Transactions of the ASME

EDITORIAL STAFF

Director, Technical Publishing
JOSEPH SANSONE
Managing Editor,
CORNELIA MONAHAN
Production Editor, SUZANNE MAGIDA
Prod. Asst., BETH DARCHI

APPLIED MECHANICS DIVISION
Chairman, R. C. DiPRIMA
Secretary, W. G. GOTTENBERG
Technical Editor, C. S. HSU
Associate Editors, S. T. ARIARATNAM
T. BELYTSCHKO
D. B. BOGY
R. J. CLIFTON
L. B. FREUND
M. HOLT
T. R. KANE
A. S. KOBAYASHI
S. LEIBOVICH
P. A. LIBBY
U. S. LINDHOLM
L. E. MALVERN
J. J. McCOY
R. D. NORDGREN
R. T. SHIELD
C. R. STEELE
C. T. SUN
T. C. T. TING
J. S. WALKER
G. A. WEMPNER

BOARD ON COMMUNICATIONS
Chairman and Vice-President
M. J. RABINS

Members-at-Large
J. E. ORTLOFF
J. W. LOCKE
W. BEGELL
J. CALLAHAN
D. KOENIG
M. KUTZ
F. LANDIS
C. PHILLIPS
K. REID

Business Staff
345 E. 47th St.
New York, N. Y. 10017
(212)644-7789

Mng. Dir., Pub., J. J. FREY

OFFICERS OF THE ASME
President, ROBERT B. GAITHER
Executive Director and Sec'y.
BURKE E. NELSON
Treasurer, ROBERT A. BENNETT

Journal of Applied Mechanics (ISSN 0021-8936) is edited and published quarterly at the offices of The American Society of Mechanical Engineers, United Engineering Center, 345 E. 47th St., New York, N. Y. 10017. ASME-TWX No. 710-581-5267, New York. Second Class postage paid at New York, N. Y., and at additional mailing offices.

CHANGES OF ADDRESS must be received at Society headquarters seven weeks before they are to be effective. Please send old label and new address.

PRICES: To members, $30.00, annually; to nonmembers, $60.00. Single copies, $20.00 each. Add $5.00 for postage to countries outside the United States and Canada.

STATEMENT from By-Laws. The Society shall not be responsible for statements or opinions advanced in papers or . . . printed in its publications (B7.1, Par. 3).

COPYRIGHT © 1981 *by the American Society of* Mechanical Engineers. Reprints from this publication may be made on condition that full credit be given the TRANSACTIONS OF THE ASME, JOURNAL OF APPLIED MECHANICS, and the author, and date of publication be stated.

INDEXED by the Engineering Index, Inc.

Journal of Applied Mechanics

Published Quarterly by The American Society of Mechanical Engineers

VOLUME 48 • NUMBER 4 • DECEMBER 1981

TECHNICAL PAPERS

689 **On the Irrotational Flow Around a Horizontal Cylinder in Waves** (81-WA/APM-18)
J. R. Chaplin

695 **A Surface Integral Numerical Solution for Laminar Developed Duct Flow**
M. S. Khader

701 **Application of the Method of Integral Relations to the Calculation of Two-Dimensional Incompressible Turbulent Boundary Layer**
W.-S. Yeung and R.-J. Yang

707 **The Plane Parallel Flow of a Binary Mixture of Fluids**
L. M. Srivastava and V. P. Srivastava

717 **On the Mean Reynolds Equation in the Presence of Surface Roughness: Squeeze-Film Bearing**
N. Phan-Thien

721 **Direct Approach to Aerodynamic Design Problems**
W. C. Chin

727 **On the Radial Oscillations of Multiple Gas Bubbles in an Incompressible Liquid**
B. E. Foody and P. W. Huber

732 **The Exact Solutions of Some Stefan Problems With Prescribed Heat Flux**
L. N. Tao

737 **On the Propagation of Weak Discontinuities Along Bicharacteristics in a Radiating Gas**
R. S. Singh and V. D. Sharma

743 **Characteristic Forms of Differential Equations for Wave Propagation in Nonlinear Media** (81-WA/APM-23)
T. C. T. Ting

749 **Calculation of the Response of an Impulsively Excited Oscillator in an Infinite Acoustic Fluid**
A. V. Clark, Jr. and A. M. Whitman

753 **Uncoupling Approximations in Fluid-Structure Interaction Problems With Cavitation**
F. L. DiMaggio, I. S. Sandler, and D. Rubin

757 **Gas-Driven Fracture Propagation**
R. H. Nilson

763 **Elastohydrodynamic Analysis of Head to Flexible Disk Interface Phenomena**
J. P. Licari and F. K. King

769 **Pendulum Analogy for Nonlinear Fluid Oscillations in Spherical Containers**
B. A. Sayar and J. R. Baumgarten

773 **On the Formulation of Strain-Space Plasticity With Multiple Loading Surfaces** (81-WA/APM-20)
P. J. Yoder and W. D. Iwan

779 **A Self-Consistent Scheme for the Relaxation Behavior of Metals** (81-WA/APM-14)
G. J. Weng

785 **Creep and Creep Recovery of 304 Stainless Steel at Low Stresses With Effects of Aging on Creep and Plastic Strains** (81-WA/APM-17)
U. W. Cho and W. N. Findley

791 **On the Applicability of Acoustoelasticity for Residual Stress Determination** (81-WA/APM-8)
G. C. Johnson

796 **A Critical Appraisal of Static Hardness Measurements**
C. Rubenstein

803 **The Effective Elastic Moduli of Porous Granular Rocks**
P. J. Digby

809 **The Continuous Damage Theory of Brittle Materials, Part 1: General Theory**
D. Krajcinovic and G. U. Fonseka

816 **The Continuous Damage Theory of Brittle Materials, Part 2: Uniaxial and Plane Response Modes**
G. U. Fonseka and D. Krajcinovic

825 **Energy-Release Rate in Elastic-Plastic Fracture Problems** (81-WA/APM-21)
S. Aoki, K. Kishimoto, and M. Sakata

830 **The Penny-Shaped Crack and the Plane Strain Crack in an Infinite Body of Power-Law Material**
M. Y. He and J. W. Hutchinson

841 **An Educational Elasticity Problem With Friction, Part 1: Loading, and Unloading for Weak Friction** (81-WA/APM-19)
J. Dundurs and M. Comninou

846 **Fatigue Failure Criteria for Unidirectional Fiber Composites**
Z. Hashin

853 **Stress Field Due to a Cylindrical Inclusion With Constant Axial Eigenstrain in an Infinite Elastic Body**
Y. Takao, M. Taya, and T. W. Chou

(Contents continued on Page 992)

Downloaded 04 May 2010 to 171.66.16.34. Redistribution subject to ASME license or copyright; see http://www.asme.org/terms/Terms_Use.cfm

859 **Nonlinear Viscoelastic Analysis of a Unidirectional Composite Material** (81-WA/APM-15)
B. G. Schaffer and D. F. Adams

866 **Residual Stresses of Czochralski-Grown Crystal**
T. Iwaki and N. Kobayashi

871 **Heat Conduction Through a Flat Punch**
M. Comninou, J. R. Barber, and J. Dundurs

876 **A Diagonally Dominant Solution for the Cylinder End Problem** (81-WA/APM-12)
T. D. Gerhardt and S. Cheng

881 **Scattering of Rayleigh Waves by a Plate Attached to a Half Space Through a Viscous Couplant** (81-WA/APM-24)
Y. C. Angel and D. B. Bogy

889 **The Rolling Contact of Two Elastic-Layer-Covered Cylinders Driving a Loaded Sheet in the Nip**
T.-C. Soong and C. Li

895 **The Deformation of a Thin, Incomplete, Elastic Ring in a Frictional Channel** (81-WA/APM-22)
R. C. Benson

900 **Theories for Elastic Plates Via Orthogonal Polynomials**
S. Krenk

905 **Optimization in a Class of Hole Shapes in Plate Structures**
S. K. Dhir

909 **On the Nonlinear Intrinsic Dynamics of Doubly Curved Shells** (81-WA/APM-9)
A. Libai

915 **Mode Interaction of Axially Stiffened Cylindrical Shells: Effects of Stringer Axial Stiffness, Torsional Rigidity, and Eccentricity** (81-WA/APM-28)
D. Hui, R. C. Tennyson, and J. S. Hansen

923 **Transverse Vibrations of Beams, Exact Versus Approximate Solutions**
J. R. Hutchinson

929 **Resonant Whirling of Aircraft Propeller-Engine Systems**
S. H. Crandall and J. Dugundji

936 **Mechanics of Ice-Lifting From a Flat Surface Through Penetration With a Sharp Blade** (81-WA/APM-27)
N. C. Huang

943 **Dynamic Behavior of Continuous Cantilevered Pipes Conveying Fluid Near Critical Velocities** (81-WA/APM-13)
J. Rousselet and G. Hermann

948 **Parametric Instability of a Rotating Shaft Due to Pulsating Torque**
A. Unger and M. A. Brull

959 **Amplitude Incremental Variational Principle for Nonlinear Vibration of Elastic Systems** (81-WA/APM-26)
S. L. Lau and Y. K. Cheung

BRIEF NOTES

Aluminum Matrix Composite Elasticity Measured Ultrasonically — 965
G. V. Blessing and W. L. Elban

Acoustoelastic Effect of Thickness Oscillations — 966
M. Hirao, Y. Miura, and H. Fukuoka

Harmonic Waves in Fiber-Reinforced Orthotropic Elastic Composites — 967
S. Nemat-Nasser and M. Yamada

Closed-Form Approximations for Forces on Conical Penetrators Into Dry Porous Rock — 971
D. B. Longcope and M. J. Forrestal

An Improvement of the Stress Calculations in Plane Elasticity by Use of Spline Functions — 972
J. C. Boyer and P. Trompette

974 Boundary Condition Independence in Coupled Thermoelasticity
E. V. Wilms and H. Cohen

975 The Annular Membrane Under Axial Load
D. J. Allman and E. H. Mansfield

976 On Plastic Strain in Porous Materials
M. M. Carroll, J. F. Schatz, and S. E. Yamada

978 Critical Compressive Stress of a Beam-Column to a Second Order
D. Chattoraj and S. K. Bose

980 On a Bénard Convection in the Presence of Dielectrophoretic Forces
A. Georgescu and O. Polotzka

DISCUSSIONS

982–987 Discussions on previously published papers by **Y. Matsuzaki** and **T. Ueda, V. A. Lubarda** and **E. H. Lee, S. Ali** (No Closure), **B. J. Hsieh**

(Contents continued on Inside Back Cover)

Downloaded 04 May 2010 to 171.66.16.34. Redistribution subject to ASME license or copyright; see http://www.asme.org/terms/Terms_Use.cfm

CONTENTS (CONTINUED)

BOOK REVIEWS

988 ***The Symmetric Eigenvalue Problem*** by **Beresford N. Parlett** . . . Reviewed by **S. H. Crandall**

Nonlinear Oscillations by **Peter Hagedorn** . . . Reviewed by **C. S. Hsu**

Turbulence in the Free Atmosphere by **N. K. Vinnichenko, N. Z. Pinus, S. M. Shmeter,** and **G. N. Shur** . . . Reviewed by **J. L. Lumley**

Injection and Mixing in Turbulent Flow by **J. A. Schetz,** edited by **M. Summerfield** . . . Reviewed by **J. L. Lumley**

700, 726	Worldwide Mechanics Meeting List
742, 756, 790, 808, 829	Applied Mechanics Symposium Proceedings
840, 865, 870, 875, 922	Applied Mechanics Symposium Proceedings
947	Announcement—Standard International Units
958	Special Notice—Mandatory Excess Page Charge for Transactions
987	Change of Address Form

Downloaded 04 May 2010 to 171.66.16.34. Redistribution subject to ASME license or copyright; see http://www.asme.org/terms/Terms_Use.cfm

J. R. Chaplin

Lecturer,
Department of Civil Engineering,
University of Liverpool,
Brownlow Street,
P. O. Box 147,
Liverpool L69 3BX, England

On the Irrotational Flow Around a Horizontal Cylinder in Waves

Milne-Thomson's circle theorem is used to study the characteristics of the two-dimensional irrotational flow around a horizontal cylinder under long-crested waves. Even when the cylinder diameter is small compared with the wavelength, the circumferential velocity and pressure distributions are unsteady and differ markedly from those corresponding to uniform ambient flow with similar velocity and acceleration vectors.

Introduction

Horizontal cylinders in waves experience an incident flow field which is qualitatively different from that around vertical cylinders. In view of the complexity of even steady ambient flow around a circular cylinder it is not surprising that in many studies of wave-induced loads the unsteady nature of the flow has come to be represented simply by an oscillating uniform ambient flow, characterized by velocity and acceleration vectors which are always parallel. Thus experiments have been carried out at the nodes of standing waves [1] or in oscillating water tunnels (e.g., by Sarpkaya [2]). Despite the presence in waves of other factors, such as the free surface and lengthwise velocity gradients, this is a reasonable approach to adopt since it reproduces one of the essential features of separated wave-induced flow around a vertical cylinder, the periodic convection of shed vorticity back toward the separation points. Vortices generated on a previous half cycle are then in close proximity to growing vortices of opposite sense of rotation, resulting in strong interactions between them. Measurements in uniform ambient flow oscillating in one direction have provided coefficients for Morison's equation over wide ranges of Keulegan-Carpenter and Reynolds numbers, and some understanding of the fluid mechanics involved [2, 3].

However, it would not be reasonable to expect that these results should be valid also for horizontal cylinders for which the incident flow may be quite different. In the simplest case of a long horizontal cylinder submerged with its axis parallel to the crests in small amplitude deep water waves, the incident flow (that occurring at the location of the cylinder in its absence) is characterized by a steadily rotating velocity vector of constant magnitude, and circular particle orbits. As in the case of a vertical cylinder, the vorticity shed from the cylinder may return to it (neglecting any drift current and self-induced wake propagation), but this time the disposition of existing positive and negative vorticity is such as to reinforce the generation process. In addition, the wake is subject to lateral pressure gradients and lift forces associated with the changing orientation of the ambient flow. Any attempt at an understanding of this complex process, whether experimental or theoretical, must begin with an appreciation of the character of the irrotational ambient flow, which in some respects is not well represented by the combination of a uniform unsteady stream and a doublet. It is the purpose of this paper to provide some illumination on the nature of the irrotational flow around horizontal cylinders beneath waves, particularly those features of it which may have a bearing on the corresponding viscous flow. Additional interest in this problem is derived from the consideration that in some situations the cylinder is too small to diffract incident waves, and too large to produce significant wake effects, so that the loading is almost entirely inertial [4].

Very few experiments have been reported on the wave-induced flow in the drag regime around horizontal cylinders away from the influence of both the free surface and the bed. Maull and Norman [5] and Rhodes [6] presented results for a range of transitional water depths in which the particle orbits of the undisturbed flow were elliptic or almost circular. For circular orbital flow Holmes and Chaplin [7] achieved higher Reynolds numbers by moving the cylinder through otherwise still water along a circular path without rotation. The present work was stimulated by these experimental measurements, from which it is clear that in wave-induced flow regular vortex shedding is locked-on to the wave frequency with an integral frequency ratio [5, 6]. Also inertia coefficients are found to be lower than expected, frequently less than unity [7], suggesting that the vortex induced lift may have a nonzero mean associated with an angular shift in the wake from the direction of the incident flow. The method of simulation used by Holmes and Chaplin effectively replaces the nonuniform wave-induced ambient flow by an unsteady uniform

Contributed by the Applied Mechanics Division and presented at the Winter Annual Meeting, Washington, D. C., November 15–20, 1981, of THE AMERICAN SOCIETY OF MECHANICAL ENGINEERS.

Discussion on this paper should be addressed to the Editorial Department, ASME, United Engineering Center, 345 East 47th Street, New York, N. Y. 10017, and will be accepted until March 1, 1982. Manuscript received by ASME Applied Mechanics Division, September, 1980; final revision, February, 1981. Paper No. 81-WA/APM-18.

Copyright © 1981 by ASME

Downloaded 01 May 2010 to 171.66.16.249. Redistribution subject to ASME license or copyright; see http://www.asme.org/terms/Terms_Use.cfm

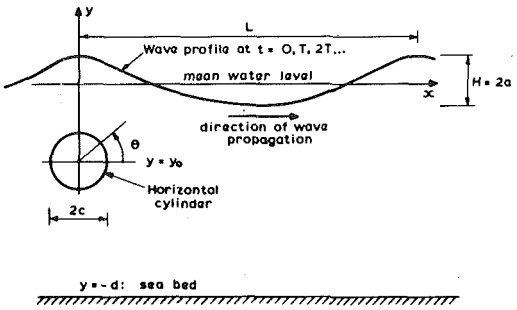


Fig. 1 Definition sketch

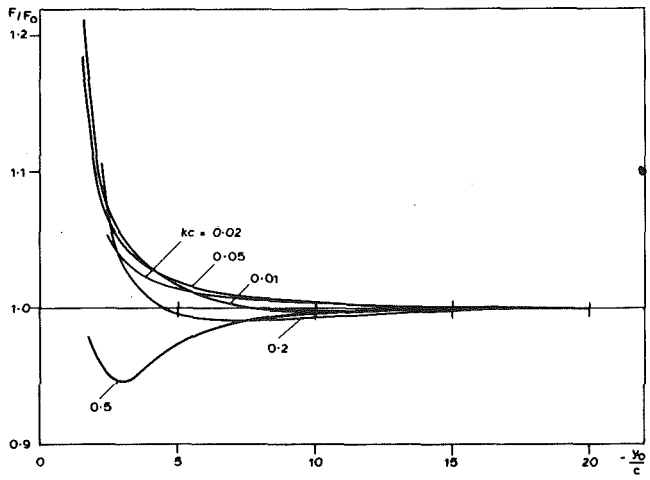


Fig. 2 The magnitude of Ogilvie's first-order force F as a function of submergence for various radii; F_0 = inertia force in uniform ambient flow

stream with velocity and acceleration vectors equal to those at the location of the cylinder in undisturbed waves. On the basis that the length scale of velocity gradients in the waves (i.e., the wavelength) was large compared to the cylinder diameter, they assumed that the nonuniformity of the flow incident on the cylinder would not be a dominant factor in determining flow-induced loading. This is an important question which may have a bearing on the interpretation of Holmes and Chaplin's results, and of results from other tests using the same convenient method of simulation. In order to study this point and as a step toward a better understanding of the flow around horizontal cylinders in waves, we proceed with an analysis of the nonuniform irrotational flow.

We show that there is a range of interest in which the irrotational flow around a horizontal cylinder, out of the influence of both the free surface and the bed, differs significantly from that in uniform ambient flow. Positions of the stagnation, maximum velocity, and maximum pressure points oscillate around the circumference of the cylinder in relation to the orientation of the incident flow. Inertia forces differ slightly from those derived [8] on the assumption that the cylinder diameter is small compared to the scale of spatial variations of fluid velocity.

Theory

We consider the irrotational flow around a long horizontal stationary circular cylinder submerged beneath long-crested waves so that its axis is perpendicular to the flow plane. Unless the cylinder is located well below the free surface, the disturbance it generates in the flow may be expected significantly to modify the characteristics of the waves. This problem was studied by Dean [9], who showed, however, that to first order there are no reflected waves. The transmitted waves undergo a phase change, which was calculated by Ogilvie [10], who also gave results for the first and second-order forces experienced by a cylinder in deep water waves. The first-order force vector rotates with constant amplitude and follows the acceleration vector of the undisturbed incident flow with a constant phase lag. The second-order force has a nonzero mean which is directed vertically upward and can be derived from the first-order velocity potential. To assess the significance of the free surface, it is of interest to compare these fluctuating forces with those derived on the assumption that the undisturbed incident flow is a uniform unbounded stream having velocity and acceleration equal to those due to the undisturbed wave at the location of the center of the cylinder.

Geometric parameters are defined in Fig. 1: in addition, $\omega = 2\pi/T$ is the wave angular frequency, $k = 2\pi/L$ its wave number, and t is time measured from the instant a crest passes the stationary line $x = 0$. For small amplitude incident waves propagating to the right in deep water the complex potential $w_0 = \phi + i\psi$ of the ambient flow is

$$w_0 = i\frac{ga}{\omega}\exp\left[-i(kz - \omega t)\right] \tag{1}$$

where $z = x + iy$ and g is gravitational acceleration, taking the positive gradient of the velocity potential as the velocity. At the location of the cylinder axis $z_0 = iy_0$, the acceleration vector has constant magnitude $gak \cdot e^{ky_0}$, and rotates steadily clockwise. Assuming that the flow around the cylinder is well represented by a doublet inserted in uniform flow, the force per unit length is then [8]

$$F_0 = 2\rho\pi c^2 gak \cdot e^{ky_0}$$

where ρ is the fluid density. The force F_0 is directed along the acceleration vector of the ambient flow.

The magnitude F of Ogilvie's oscillating first-order force is derived from his equation (27). The solutions presented later were computed from the first 20 equations of Ogilvie's infinite systems, and are indistinguishable from those obtained using only the first 10. The problem is defined in terms of the dimensionless parameters kc and ky_0, and for a range of conditions, Fig. 2 presents the ratio F/F_0. The curve for each value of kc can be taken no further to the left than $-y_0/c = 1$ since the cylinder then would not be fully submerged; for cylinder locations close to surface level the linearized expression used for the modified velocity potential must be significantly in error. However, Fig. 2 suggests that for a submergence $-y_0/c > 5$ the flow is not dominated by the presence of the free surface for the range of kc given. Bearing this restriction in mind we proceed to consider the velocity and then pressure distributions around the cylinder and find that they depart significantly from those around a cylinder in uniform flow. The velocity and pressure distributions are of concern when studying wave induced real fluid flow around horizontal cylinders because they are important factors in controlling separation and vortex shedding, on which depends much of the actual fluid loading.

Points on the surface of the cylinder are specified by the angle θ, defined in Fig. 1, measured anticlockwise from the positive x-direction. The tangential velocity on the cylinder v_θ is also measured positive anticlockwise. From Ogilvie's velocity potential, v_θ is given in terms of the undisturbed wave induced particle speed V_0 by

$$v_\theta = -\frac{2V_0\cos\psi_1}{kc}\sum_{m=1}^{\infty}\frac{m\epsilon_m}{(kc)^m}\cos\left(\omega t + \frac{m\pi}{2} - m\theta + \psi_1\right) \tag{3}$$

where ψ_1 is the phase angle between the first-order force and acceleration vectors, and ϵ_m the solutions of an infinite set of linear simultaneous equations. Equation (3) can be represented as the sum of a large number of component profiles of tangential velocity each propagating around the circumference of the cylinder with individual angular frequency ω/m. The shape of the velocity profile is thus a function of time, and its maxima and zeros oscillate in angular position with respect to the orientation of the velocity vector of the undisturbed ambient flow. For the particular case $kc = 0.2$, $ky_0 = -1.0$, Fig. 3 shows the circumferential distribution of surface velocity when $\omega t = 3\pi/2$, in other words when the incident flow is directed upward. The broken line represents the velocity profile $v_\theta = 2V_0\cos\theta$ corre-

Downloaded 01 May 2010 to 171.66.16.249. Redistribution subject to ASME license or copyright; see http://www.asme.org/terms/Terms_Use.cfm

sponding to uniform flow conditions. The distortion in the solution for nonuniform flow is evident first in the slightly increased maximum velocities, 2.097 and −2.123, and second, in their displacements through about 19° and 23°, both toward the downstream side of the cylinder. Whereas Fig. 2 suggests that for this case the effects of the distorted velocity profiles on the first-order oscillating forces are very small, in a real fluid they must affect the separation positions and thus have some bearing on the form drag and lift. Before studying further velocity and pressure distributions on a cylinder in nonuniform wave-induced flow, we introduce a simplification in neglecting the presence of the free surface to approximate the flow around the cylinder due to irregular or finite amplitude waves in finite water depth.

Approximate Theory

The irrotational flow around a cylinder at an elevation remote from both the free surface and the bed is characterized by the nonuniform nature of the ambient flow, rather than the characteristics of transmitted or reflected waves, or the kinematic boundary condition at the bed. Improved understanding of free-surface effects can come only from higher-order solutions, although the presence of the bed can be incorporated by the use of multiple images. Concluding from the previous section that there is a range of interest between conditions dominated by the surface and by the bed, we formulate below a solution neglecting both.

Milne-Thomson's circle theorem [11] states that if the cylinder $|z - z_0| = c$ is inserted into the flow whose complex potential is $w_0 = f(z)$, the resulting flow is represented by

$$w = f(z) + \bar{f}\left(\frac{c^2}{z - z_0} + \bar{z}_0\right) \tag{4}$$

where an overbar denotes the complex conjugate. The complex velocity $u - iv$ on the surface of the cylinder $z = z_0 + ce^{i\theta}$ is then

$$\frac{dw}{dz} = u - iv = f'(z) - e^{-2i\theta}\overline{f'(z)}$$
$$= 2ie^{-i\theta}(u_0 \sin\theta - v_0 \cos\theta), \tag{5}$$

where u_0 and v_0 represent the original velocity components, $u_0 - iv_0 = f'(z_0 + ce^{i\theta})$. The effect of the additional term in the complex potential (4) is thus to add at the surface of the cylinder radial and tangential velocity components whose magnitudes are equal to those of the undisturbed flow. While the radial components are in opposite directions, and so cancel, the tangential components are in the same direction. The velocity at any point on the surface of the cylinder is therefore simply two times the velocity component in the direction of the tangent to the cylinder of the undisturbed flow at the same point. Similarly, the local rate of change of the velocity potential $\partial\phi/\partial t$ on the surface of the cylinder is twice the value at the same point in the undisturbed flow. Surface velocities and pressures can in this way be computed directly from the original complex potential.

The forces acting on the cylinder can be found from Milne-Thomson's [11] extension of Blasius's theorem. Providing the cylinder is stationary, the flow-induced forces X and Y in the x and y-directions are given by

$$X - iY = \frac{1}{2}i\rho \int \left(\frac{dw}{dz}\right)^2 dz + i\rho \frac{\partial}{\partial t}\int \bar{w}d\bar{z} \tag{6}$$

where the integrations are taken around the cylinder, and w represents the complex potential given by equation (4). Milne-Thomson showed that in unbounded fluid in uniform motion at infinity the first integral vanishes and the second gives the well-known inertia forces proportional to and concurrent with the ambient flow local acceleration. When the fluid at infinity is not in uniform motion however, as in waves, the first integral does not vanish. With no circulation around the cylinder the most general form of the complex potential consistent with (4) is

$$w = \alpha_1 z' + \alpha_2 z'^2 + \alpha_3 z'^3 + \ldots \bar{\alpha}_1 \frac{c^2}{z'} + \bar{\alpha}_2 \frac{c^4}{z'^2} + \bar{\alpha}_3 \frac{c^6}{z'^3} + \ldots \tag{7}$$

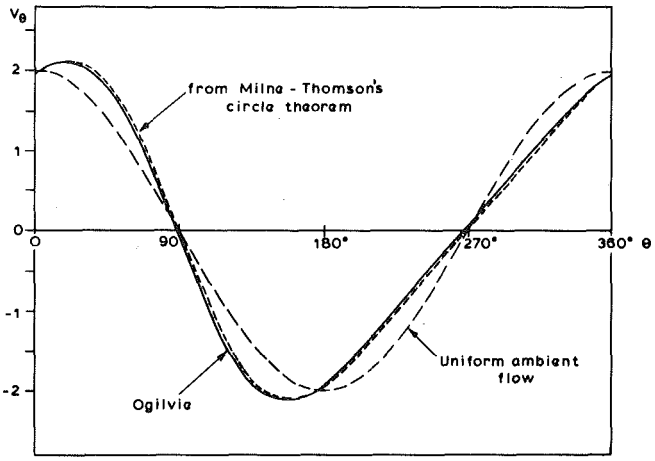


Fig. 3 Tangential velocity profiles over the circumference of the cylinder for $kc = 0.2$, $ky_0 = -1.0$ at the instant $\omega t = 3\pi/2$

where α_1, etc., are complex coefficients, and writing z' for $z - z_0$. Differentiating and squaring, the only nonzero residues come from the product of the two series, from a term in z'^{-1} whose coefficient is

$$-4a^2(\bar{\alpha}_1\alpha_2 + 3\bar{\alpha}_2\alpha_3 c^2 + 6\bar{\alpha}_3\alpha_4 c^4 + \ldots)$$

Similarly, in the second integration, only the first term in the second series has a nonzero residue. The forces are then given by

$$X - iY = 2\pi c^2\rho\left[(2\bar{\alpha}_1\alpha_2 + 6\bar{\alpha}_2\alpha_3 c^2 + 12\bar{\alpha}_3\alpha_4 c^4 + \ldots) + \frac{\partial\alpha_1}{\partial t}\right] \tag{8}$$

It is convenient to write these forces as usual in terms of the velocity and acceleration, and in this case higher spatial gradients, of the undisturbed flow at the location of the center of the cylinder. On this basis we obtain

$$X - iY = 2\pi c^2\rho\left\{\frac{\partial}{\partial t}\left(\frac{dw_0}{dz}\right) + \frac{\overline{dw_0}}{dz}\frac{d^2w_0}{dz^2} + \frac{1}{2}\frac{\overline{d^2w_0}}{dz^2}\frac{d^3w_0}{dz^3}c^2 + \frac{1}{12}\frac{\overline{d^3w_0}}{dz^3}\frac{d^4w_0}{dz^4}c^4 + \ldots\right\}_{z=z_0} \tag{9}$$

in which w_0 refers to the complex potential of the undisturbed flow. Since $dw_0/dz = u_0 - iv_0$ and $(\overline{dw_0}/dz)$. $(d^2w_0/dz^2) = (u_0(\partial u_0/\partial y) + v_0(\partial u_0/\partial y) - i(u_0(\partial v_0/\partial x) + v_0(\partial v_0/\partial y)$, equation (9) differs from the conventional formulation [8] only by the appearance of terms with $c^2, c^4, \ldots$ The significance of these terms is discussed below in the context of wave-induced flow.

A general complex potential for multicomponent waves may be written as the sum of a number of components with wave numbers k_n, frequencies ω_n, and complex phase angles β_n, as

$$w_0 = \sum_n A_n \sin(k_n z - \omega_n t - \beta_n) \tag{10}$$

We proceed in the next section to investigate the flow around a horizontal cylinder subject to this ambient flow using the results previously presented. Velocities and pressures over the surface of the cylinder are computed by the properties of the circle theorem directly from equation (10), and the total forces from equation (9).

Numerical Results

The tangential velocity profile around the circumference of the cylinder calculated by the approximate method for single component deep water waves with $kc = 0.2$, $ky_0 = -1.0$ is shown in Fig. 3. The close agreement with that previously obtained from Ogilvie's velocity potential suggests that for these conditions the flow is dominated by the nonuniformity of the ambient flow rather than by the presence of the free surface. The effects of the proximity of the free surface are, however, evident in the velocity profiles compared in Fig. 4 for $kc =$

Downloaded 01 May 2010 to 171.66.16.249. Redistribution subject to ASME license or copyright; see http://www.asme.org/terms/Terms_Use.cfm

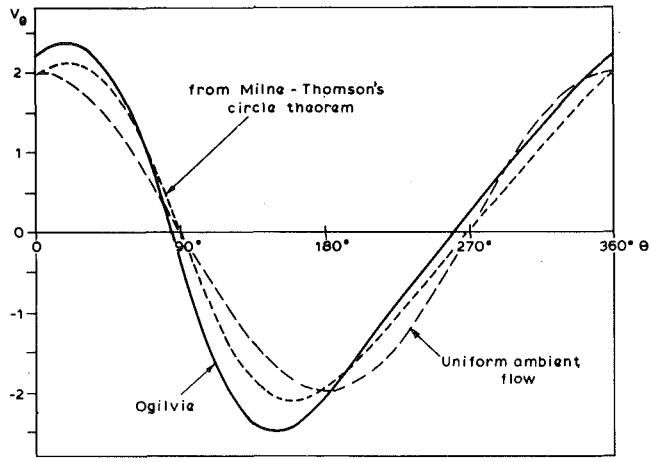


Fig. 4 As Fig. 3; $ky_0 = -0.4$

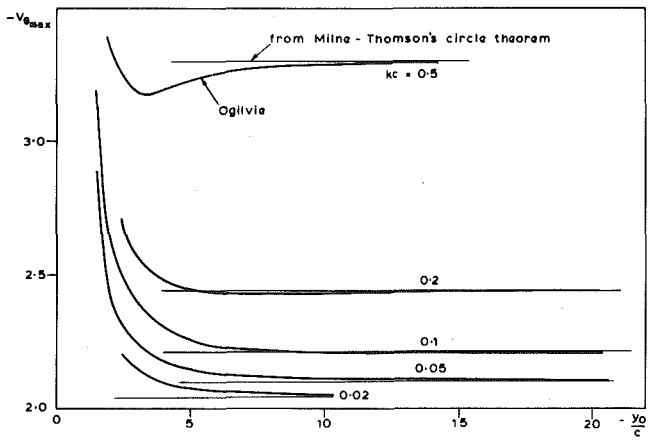


Fig. 6 Maximum tangential velocity on the upper side of the cylinder when it is beneath a crest, as a function of submergence for various radii

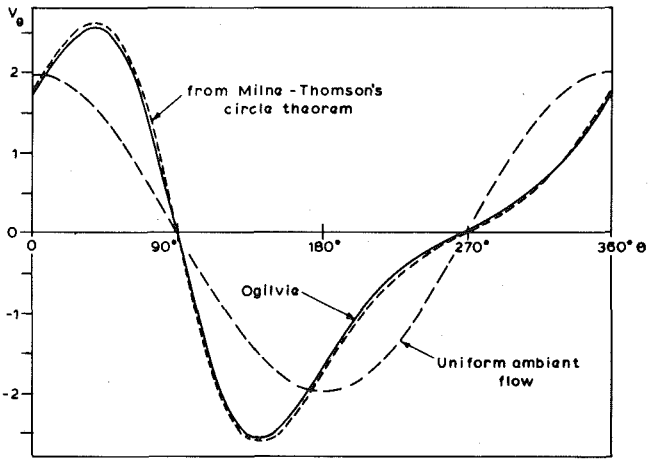


Fig. 5 As Fig. 3; $kc = 0.5$, $ky_0 = -2.5$

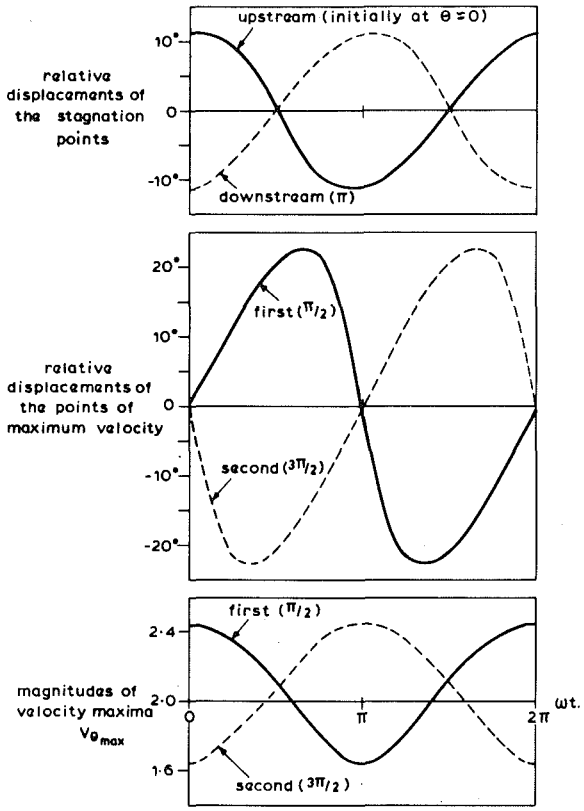


Fig. 7 Angular displacements of stagnation points and points of maximum velocity, and magnitudes of velocity maxima over the circumference of the cylinder, plotted over one wave period for linear deep water waves; $kc = 0.2$, $ky_0 = -1.0$

0.2 and $ky_0 = -0.4$. Conversely, increasing the relative radius kc at a given relative submergence $-y_0/c$ has little effect on the agreement betweeen results from Ogilvie's method and the approximate method, as shown in Fig. 5.

Another indication of the importance of free surface effects on the kinematics of flow around the cylinder is given in Fig. 6. At the instant when the cylinder is beneath a crest, the velocity on the cylinder at $\theta = \pi/2$ reaches a maximum, which is plotted in Fig. 6 as a function of relative submergence $-y_0/c$ for various values of kc. In uniform flow the relative velocity maximum $v_{\theta\,\max}/V_0$ would always be 2. Reasonable agreement between results from Ogilvie's velocity potential and the approximate method neglecting the free surface extends to $-y_0/c > 5$ for $0.02 < kc < 0.5$. It is worth noting that for greater submergences, $v_{\theta\,\max}/V_0$ quickly becomes a constant which is significantly above 2 for $kc > 0.1$.

The principle distortion evident in Figs. 3–5 from the uniform velocity profiles is the downstream movement of both points of maximum velocity. The positions of the stagnation points are almost unchanged. However, these profiles relate only to a single wave phase angle, $\omega t = 3\pi/2$, when the undisturbed flow is directed vertically upward at the position of the cylinder $x = 0$. Plotting the positions of the stagnation points and the positions and magnitudes of the velocity maxima in Fig. 7 for the conditions of Fig. 3 shows that there is a cyclic change throughout the distorted velocity profiles over the surface of the cylinder. Fig. 7 shows as functions of time over one wave period the angular departures of the two stagnation points from the positions they would occupy, 0° and 180°, from the incident velocity vector, if the ambient flow were uniform. The amplitude of their angular displacement is found to be approximately kc rad, regardless of the depth of submergence. Also shown are the angular displacements from 90° and 270° of the points at which the velocity is maximum, and its values there. The approximate amplitude of the variations in position of the velocity maximum is

$$\left(\frac{20 - 81\,k^2c^2}{10 - 4kc}\right) kc \text{ rad},$$

and the velocity maximum is in the range

$$2e^{-kc} < |v_{\theta\max}/V_0| < 2e^{kc}$$

Downloaded 01 May 2010 to 171.66.16.249. Redistribution subject to ASME license or copyright; see http://www.asme.org/terms/Terms_Use.cfm

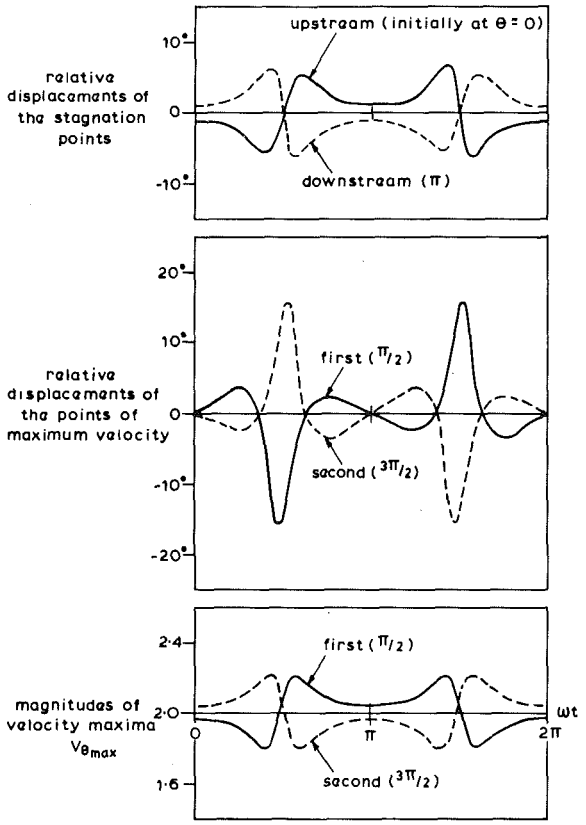


Fig. 8 As Fig. 7; $kc = 0.05$, $ky_0 = -0.25$, for linear waves with $d/L = 0.1$

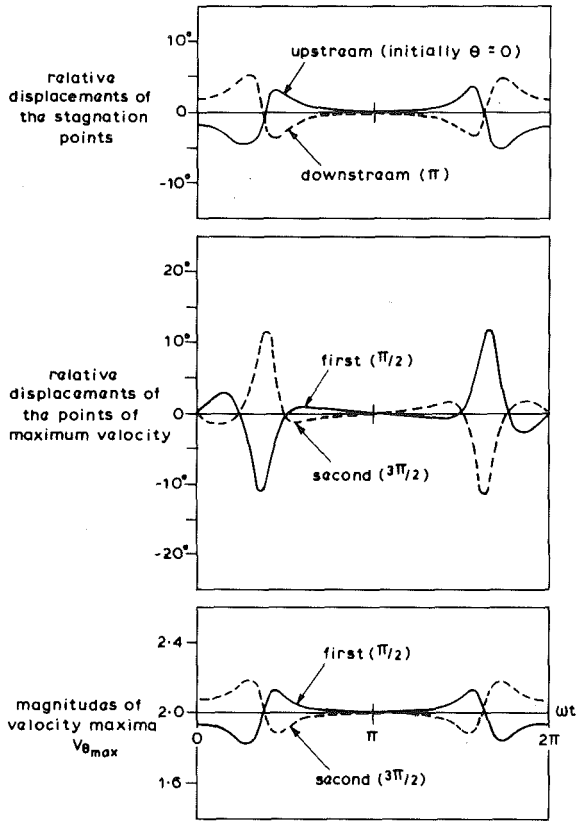


Fig. 9 As Fig. 7; $kc = 0.0337$, $ky_0 = -0.1685$ for 9th-order Dean stream function waves with $d/L_0 = 0.05$, $H/L_0 = 0.0292$ (Case 5c)

This is of course equivalent to two times the range of relative incident velocity in the undisturbed flow over the diameter of the cylinder in the vertical plane. These results are all for deep water conditions and are independent of the wave amplitude.

For waves in transitional water depths the velocity profiles undergo a more complex deformation. Fig. 8 shows results similar to those of Fig. 7 for the case $kc = 0.05$, $ky_0 = -0.25$ with $d/L = 0.1$. Surface velocities on the cylinder differ most from those in uniform ambient flow at $\omega t = \pi/2$ and $3\pi/2$, i.e., when the water surface above the cylinder crosses mean water level. However, these results are derived from the single velocity potential component of linear theory, which is realistic only for waves of very small amplitude under these conditions. To present velocities and pressures on the cylinder in finite amplitude waves we use Dean's [12] tabulated results for case 5C which represents an accurate solution of the regular wave problem for $d/L_0 = 0.05$, $H/L_0 = 0.292$, where L_0 is the small amplitude deep water wavelength, $L_0 = gT^2/2\pi$. From substituting in equation (10) the velocity potential terms derived from the 9th-order stream-function solution, surface velocity results are plotted in Fig. 9. They refer to the case of a cylinder of diameter 1m with its axis 2.5m below mean water level in waves of height 4.56m, period 10 sec in mean water depth 7.81m.

Again the strongest distortion of the velocity profile occurs when the water surface is close to mean water level, though this is now closer to the crest owing to the vertical asymmetry of the characteristic shape of the free-surface wave form. Under the long flat trough the flow is not surprisingly relatively undistorted, but close to the crest the velocity profile over the cylinder's circumference reflects the more severe velocity gradients present in the waves. The pressure distribution around the circumference of the cylinder is shown in Fig. 10 at the instant $\omega t = \pi/4$ when the orientation of the incident velocity vector is at $\theta = 309.2°$. The shape of the distribution reflects the presence of the pressure gradient superimposed on the familiar sinusoidal profile. Also shown are the pressure distributions for the uniform ambient flow case with acceleration vectors equal to the local and total accelerations, respectively, of the wave-induced flow.

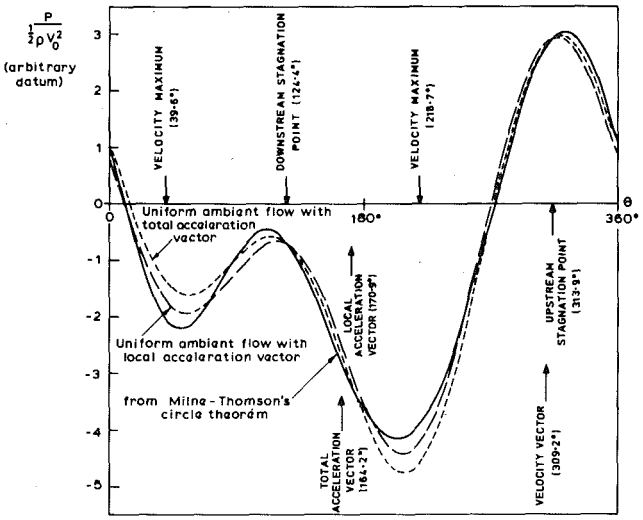


Fig. 10 Pressure distribution over the circumference of the cylinder for conditions of Fig. 9, when $\omega t = \pi/4$

Although there are some differences in the pressures the integrated forces obtained from equation (9) agree to within one percent with those obtained from uniform flow with the wave induced total acceleration vector. This is the case throughout the wave period for all the examples just presented. In other words, the irrotational flow forces are found to agree closely with the formula (force per unit length) = $-2 \times$ (cross-sectional area) $\times$ (pressure gradient), also in nonuniform wave flow.

Discussion and Conclusions

We have shown that the irrotational flow around a submerged

Downloaded 01 May 2010 to 171.66.16.249. Redistribution subject to ASME license or copyright; see http://www.asme.org/terms/Terms_Use.cfm

horizontal cylinder may be calculated using Milne-Thomson's circle theorem [11] when the cylinder is out of the influence of both the free surface and the bed. Some features of the flow differ significantly from those found from uniform ambient flow with appropriate velocity and acceleration vectors. A general form for irrotational flow forces however provides results only marginally different from those obtained with conventional inertia coefficient of 2 [8].

The oscillatory movements of the stagnation points and points of maximum velocity shown in Fig. 7 represent a significant departure from uniform flow conditions. They are independent of wave amplitude and the location of the cylinder, providing it is outside the region of influence of the bed and the free surface. Although velocity and pressure distributions over the circumference of the cylinder will be profoundly altered by separation, the nature of the external irrotational flow is of interest because it dominates the development of the attached boundary layers up to the separation points. The problem of solving boundary-layer characteristics under these complex and essentially unsteady conditions is worthy of further detailed investigation, perhaps following Telionis, et al. [13].

The nonuniform features of the external flow are absent in the simulation used by Holmes and Chaplin [7]. Further experiments in waves are required before the effects of this deficiency can be identified fully. However, one notable qualitative difference between their results and those of Maull and Norman [5] and Rhodes [6] from experiments in waves is that in the latter, vortex shedding is locked-on to the wave frequency with an integral frequency ratio. The absence of locking-on in Holmes and Chaplin's results suggests that the triggering mechanism may be the oscillating nonuniformity in the ambient flow just discussed.

Acknowledgment

This work forms part of the project "Wave Loading and Response of Small Diameter Cylinders" funded by the Science Research Council through the North Western Universities Consortium for Marine Technology.

References

1 Keulegan, G. H., and Patterson, L. H., "Forces on Cylinders and Plates in an Oscillating Fluid," *Journal of Research of the National Bureau of Standards*, Vol. 60, No. 5, 1958, pp. 423–440.

2 Sarpkaya, T., "Vortex Shedding and Resistance in Harmonic Flow About Smooth and Rough Circular Cylinders," *Proceedings of the First Conference on the Behaviour of Offshore Structures*, Trondheim, Norway, 1976, pp. 220–235.

3 Graham, J. M. R., "The Forces on Sharp-Edged Cylinders in Oscillatory Flow at Low Keulegan-Carpenter Numbers," *Journal of Fluid Mechanics*, Vol. 97, Part 1, 1980, pp. 331–346.

4 Stansby, P. K., "Inertia of a General Cylinder in an Arbitrary Flow Configuration," *Proceedings of the Institution of Civil Engineers*, Vol. 69, Part 2, 1980, pp. 63–71.

5 Maull, D. J., and Norman, S. G., "A Horizontal Circular Cylinder Under Waves," *Mechanics of Wave-Induced Forces on Cylinders*, ed., Shaw, T. L., Pitman, 1979, pp. 359–378.

6 Rhodes, T. C., "Wave-Induced Loads on a Horizontal Circular Cylinder," MSc Thesis, University of Liverpool, U.K., 1980.

7 Holmes, P., and Chaplin, J. R., "Wave Loads on Horizontal Cylinders," *Proceedings of the 16th International Conference on Coastal Engineering*, Hamburg, Germany, Chapter 149, 1978, pp. 2449–2460.

8 Isaacson, M. de St.Q., "Nonlinear Inertia Forces on Bodies," *Proceedings of the American Society of Civil Engineers*, Vol. 105, No. WW3, 1978, pp. 213–227.

9 Dean, W. R., "On the Reflexion of Surface Waves by a Submerged Circular Cylinder," *Proceedings of the Cambridge Philosophical Society*, Vol. 44, 1948, pp. 483–491.

10 Ogilvie, T. F., "First and Second-Order Forces on a Cylinder Submerged Under a Free Surface," *Journal of Fluid Mechanics*, Vol. 16, 1963, pp. 451–472.

11 Milne-Thomson, L. M., *Theoretical Hydrodynamics*, 4th ed., Macmillan, New York, 1968.

12 Dean, R. G., "Evaluation and Development of Water Wave Theories for Engineering Application," U.S. Army, Corps of Engineers, Coastal Engineering Research Center, Special Report No. 1, Vols. 1 and 2, 1974.

13 Telionis, D. P., Tsahalis, D. T., and Werle, M. J., "Numerical Investigation of Unsteady Boundary-Layer Separation," *Physics of Fluids*, Vol. 16, 1973, pp. 968–973.

Downloaded 01 May 2010 to 171.66.16.249. Redistribution subject to ASME license or copyright; see http://www.asme.org/terms/Terms_Use.cfm

M. S. Khader
Associate Professor,
Mechanical Engineering Department,
Cairo University,
Giza, Egypt
Mem. ASME

A Surface Integral Numerical Solution for Laminar Developed Duct Flow

A surface integral numerical solution for laminar developed flow in ducts of arbitrary shape cross sections is presented. The method is general for any two-dimensional duct with simple or multiple connected regions cross section. The solutions provide information for velocity distribution, friction factor, and wall shear stress. As an application of the present method, solutions for flow in circular and rectangular ducts are obtained. These solutions are used to compare the obtained results and the corresponding exact analytical solutions. Moreover, in order to illustrate the general use of the present scheme, a solution for the case of circular duct containing rod clusters is obtained. The method proved to have several interesting features and advantages over other conventional numerical and analytical techniques.

Introduction

The problem of predicting flow and heat transfer in ducts has received the attention of numerous investigators for many years [1]. The problem presents itself in many diverse areas with applications in a variety of engineering fields.

This paper is concerned with the analysis of developed laminar flow in ducts of arbitrary cross section. Consideration is given to both sections of single and multiply connected regions. The only restriction imposed on the present method is that the duct cross-section geometry does not change in the direction of the flow.

This type of duct flow is governed by a simple form of the Navier-Stokes equation, since the developed condition renders the equation linear with one velocity describing the flow field. Solution of such an equation is analytically possible if the duct boundary coincides with one of the common coordinate systems. Circular, rectangular, and special curved contours are typical examples of such cases. For those cases of "exotic" boundary shape, finding the natural system of coordinate is troublesome, and solving the governing equation in such a coordinate system is untractable analytically. However, under special conditions, the complication caused by the boundary shape can be removed by conformal transformation [2–4]. In addition, many analytical methods are devised for solving this type of flow such as orthonormal functions [5], Galerkin's method [6], and collocation technique [7]. Furthermore, methods such as finite difference and finite elements have been used extensively for numerical solutions [8–10] for ducts with geometrically complicated cross sections.

The present method provides an alternative way for solving the developed laminar duct flow with less mathematical sophistication and effort. The method, although it seems to be numerically oriented, uses an exact formulation. The surface integral method is based on casting the flow governing equation into an integral equation using the adjoint operator definition and Green's free-space function. The resulting integral equation is then, particularized to the duct boundary, as a limiting process, to become an auxiliary relation between the velocity gradients at the surface and the duct contour. This equation, which is regarded as a constraint relation, is then numerically integrated. The numerical integration is accomplished by dividing the duct contour into a finite number of flat elements and the use of a simple quadrature. This procedure, in turn, gives the values of the velocity gradient at those finite numbers of elements and accordingly the duct wall shear stress is obtained. Velocities at any interior point within the duct are calculated by direct substitution of the velocity gradients determined previously into the original integral equation.

These features result in a uniformly applicable numerical technique for solving developed duct flows with high accuracy, considerable economy, and flexibility.

Formulation of Approach

Consider a fully developed, steady, laminar incompressible fluid flow in a duct of a cross section A, and a boundary Γ, as shown in Fig. 1. The conservation of momentum equation under these conditions is given in the following compact form:

Contributed by the Applied Mechanics Division for publication in the JOURNAL OF APPLIED MECHANICS.
Discussion on this paper should be addressed to the Editorial Department, ASME, United Engineering Center, 345 East 47th Street, New York, N. Y. 10017, and will be accepted until two months after final publication of the paper itself in the JOURNAL OF APPLIED MECHANICS. Manuscript received by ASME Applied Mechanics Division, February, 1981; final revision, April, 1981.

Copyright © 1981 by ASME
Downloaded 01 May 2010 to 171.66.16.249. Redistribution subject to ASME license or copyright; see http://www.asme.org/terms/Terms_Use.cfm

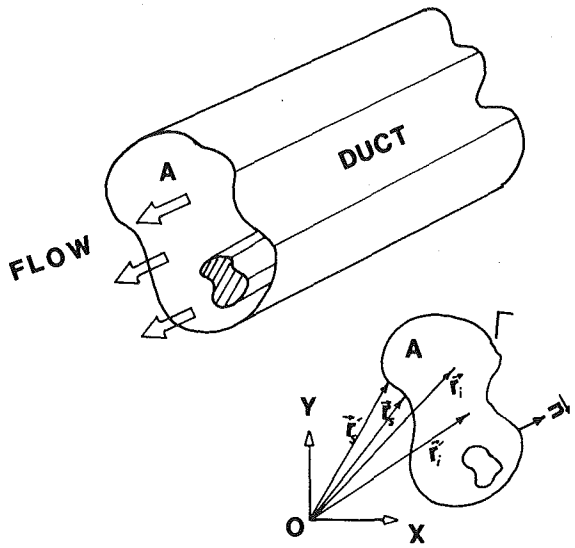


Fig. 1 Duct geometry and coordinates system

$$\nabla^2[V^*(\mathbf{r}_i)/C] = 1 \qquad \text{in} \quad A \tag{1}$$

with

$$C = -\frac{1}{\mu}\left[\frac{dP}{dZ} + \rho g\right]$$

Meanwhile, the conservation of mass, together with the condition of developed flow, restrict the velocity to be of a two-dimensional form with no variation in the flow direction z. The nonslip of the velocity at the duct boundary gives

$$V^*(\mathbf{r}_s) = 0 \qquad \text{on} \quad \Gamma \tag{2}$$

Equations (1) and (2) represent the basic formulation of the present problem. In order to facilitate the development of the basic idea of the present solution approach, equation (1) is put into operator form, i.e.,

$$L(V) = 1; \quad L(\ \ ) = \nabla^2(\ \ ) \tag{3}$$

The starting point for formulating the theory for the surface integral method is the introduction of the adjoint operator $L^*(\ \ )$. This adjoint operator is defined such that the following expression is satisfied:

$$\iint_A \phi L(V)dA = \oint_\Gamma \left(\phi \frac{\partial}{\partial n} V - V \frac{\partial \phi}{\partial n}\right) d\Gamma + \iint_A VL^*(\phi)dA \tag{4}$$

with $L^*(\phi) = \nabla^2\phi$.

This relation between the two operators L and L^* is achieved, simply, by carrying out the integration-by-parts of the left-hand side of equation (4). In expression (4), if one equates $L^*(\phi)$ to the Dirac delta function δ, the second term of the right-hand side becomes directly,

$$\iint_A V\delta(\mathbf{r}_i - \mathbf{r}_i')dA = V(\mathbf{r}_i) \tag{5}$$

This is accomplished by the use of the basic definition of the δ function [11]. The $\mathbf{r}_i$ represents any point within the duct while $\mathbf{r}_i'$ is the position vector of a pole. In addition, $(\mathbf{r}_i - \mathbf{r}_i')$ may be considered as geodesic vector (distance). The function ϕ, consequently satisfies the equation

$$L^*(\phi) = \nabla^2(\phi) = \delta(\mathbf{r}_i - \mathbf{r}_i')$$

Inserting expression (5) into equation (4) and rearranging the different terms, the velocity $V(\mathbf{r}_i)$ at any point within the duct is expressed as

$$V(\mathbf{r}_i) = \iint_A \phi(\mathbf{r}_i, \mathbf{r}_i')L(V)dA + \oint_\Gamma \phi(\mathbf{r}_i, \mathbf{r}_s') \frac{\partial}{\partial n} V(\mathbf{r}_s')d\Gamma \tag{6}$$

In the foregoing equation, the boundary condition (2) on Γ has been used to eliminate the term $V\partial/\partial n\ \phi$ on the boundary appearing in equation (4). The $\mathbf{r}_s'$ in the boundary integral represent the position vector of a pole located on the duct surface or contour. Since the operator $L(V)$ is equal to a constant value, equation (1), the integral over the duct cross section of equation (6) is reduced to contour integral. This reduction is made possible by the use of Green's identity with a simple manipulation. The expression for the velocity (6) in turn becomes

$$V(\mathbf{r}_i) = \oint_\Gamma \left[\frac{\partial}{\partial n}\psi(\mathbf{r}_i, \mathbf{r}_s') + \phi(\mathbf{r}_i, \mathbf{r}_s') \frac{\partial}{\partial n} V(\mathbf{r}_s')\right] d\Gamma \tag{7}$$

with

$$\psi = \frac{1}{4}|\mathbf{r}_i - \mathbf{r}_s'|^2 [\phi(\mathbf{r}_i, \mathbf{r}_s') - 1]$$

One notices that all the integrals appearing now in equation (7) are contour integrals. The function ϕ is readily obtained from solving $\nabla^2\phi = \delta$ and is called the free-space Green's function. The ϕ is given for the present two-dimensional case as, [11]

$$\phi(\mathbf{r}_i, \mathbf{r}_i') = \frac{-1}{2\pi} LN(|\mathbf{r}_i - \mathbf{r}_i'|) \tag{8}$$

Hence, the velocity at any interior point within the duct can be determined from equation (7) provided the value of $\partial/\partial n V(\mathbf{r}_s)$ is specified along the duct contour. Physically, if one knows the shear stress along the duct contour, the velocity field is directly obtainable by using equation (7). This proves to be impossible prior to the solution of the velocity field, in any theoretical analysis. However, if the value of the shear stress is determined experimentally, the solution for $V(r_i)$ is then feasible to be obtained.

It is then the essence of the present surface integral approach to yield the value of the unknown velocity gradient (shear stress) along the duct contour and subsequently the velocity field. This is accomplished by taking the limit of equation (7) as an interior point $\mathbf{r}_i$ approaches an arbitrary point on the duct surface $\mathbf{r}_s$. This procedure in turn yields an integral equation containing the known velocity gradient along the duct contour, which is independent of equation (7). Upon solving the resulting equation, the velocity gradient is determined. Since the velocity along the duct contour is zero by the boundary condition, the limiting form of equation (7) is

Nomenclature

A = duct cross-section area
D = hydraulic diameter
f = friction factor
g = gravitation acceleration
j = index
$L(\ \ ), L^*(\ \ )$ = differential operator
$LN[\ \ ]$ = logarithm of
M = the number of surface elements
$\mathbf{n}$ = outer normal unit vector
P = pressure
$\mathbf{r}_i, \mathbf{r}_i'$ = position vector, interior points
$\mathbf{r}_s, \mathbf{r}_s'$ = position vector, surface points
Re = Reynolds number, $\rho V_{av}D/\mu$
V^* = velocity
V = nondimensional velocity, V^*/C
V_{av} = average velocity
x, y, z = Cartesian coordinates system
Γ = duct surface
δ = Dirac delta function
μ = fluid viscosity
ρ = fluid density
τ_ω = wall shear stress
ϕ = function defined by equation (8)
∇^2 = Laplacian operator

Downloaded 01 May 2010 to 171.66.16.249. Redistribution subject to ASME license or copyright; see http://www.asme.org/terms/Terms_Use.cfm

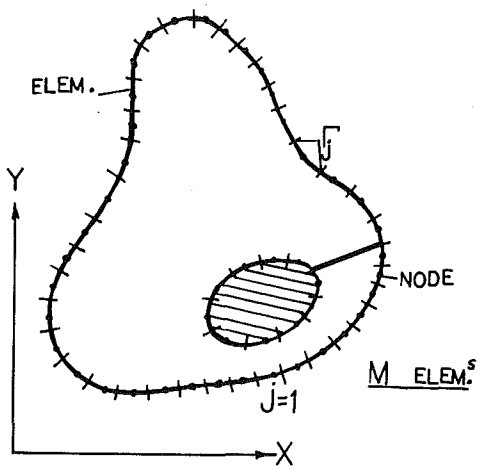


Fig. 2 Surface discretization into segments

$$0 = \oint_\Gamma \left[\frac{\partial}{\partial n}\psi(\mathbf{r}_s, \mathbf{r}'_s) + \phi(\mathbf{r}_s, \mathbf{r}'_s)\frac{\partial}{\partial n}V(\mathbf{r}_s)\right]d\Gamma \tag{9}$$

Equation (9), as one notices, is a relation between the velocity gradient and the geometry of the duct cross section for a given pressure gradient. The functions ψ and ϕ remain the same as previously defined but with $\mathbf{r}_s$ and $\mathbf{r}'_s$ replacing $\mathbf{r}_i$ and $\mathbf{r}'_i$, respectively. Equation (9) after substituting ψ takes the form

$$\oint_\Gamma \frac{1}{4}\frac{\partial}{\partial n}|\mathbf{r}_s - \mathbf{r}'_s|^2 d\Gamma = \oint_\Gamma \frac{1}{4}\frac{\partial}{\partial n}[|\mathbf{r}_s - \mathbf{r}'_s|^2 \phi(\mathbf{r}_s, \mathbf{r}'_s)]d\Gamma + \int_\Gamma \phi(\mathbf{r}_s, \mathbf{r}'_s)\frac{\partial}{\partial n}V(\mathbf{r}_s)d\Gamma \tag{10}$$

In general, no analytical methods are available for the solution of either equation (7) or equation (10). Hence, numerical schemes must be used.

In a certain application, a channel may possess a symmetrical plane and then a solution for the flow is sought for only part of the cross section. In such a case, the velocity gradient at the symmetry plane is zero with a velocity value of nonzero. Accordingly, one has to use a modified form of equation (10). You recall that $V(\partial\phi/\partial n)$ of equation (4) was equated to zero by virtue of the boundary condition (2) in development of equation (10). For the special case of nonvanishing velocity at a symmetrical plane, equation (10) takes the form

$$\oint_\Gamma \frac{1}{4}\frac{\partial}{\partial n}|\mathbf{r}_s - \mathbf{r}'_s|^2 d\Gamma = \oint_\Gamma \frac{1}{4}\frac{\partial}{\partial n}[|\mathbf{r}_s - \mathbf{r}'_s|^2 \phi(\mathbf{r}_s, \mathbf{r}'_s)]d\Gamma + \oint_\Gamma \left[\phi(\mathbf{r}_s, \mathbf{r}'_s)\frac{\partial}{\partial n}V(\mathbf{r}_s) - V(\mathbf{r}_s)\frac{\partial}{\partial n}\phi(\mathbf{r}_s, \mathbf{r}'_s)\right]d\Gamma \tag{10a}$$

Numerical Scheme

The starting point in the present numerical procedure is to divide the duct contour, under consideration, into a number M, of piecewise straight segments. Each of these segments is defined by two nodal points, see Fig. 2. Equation (10) or equation (7) is then discretized for each of these segments in the form

$$\sum_{j=1}^{M}\left[\int_{\Gamma_j}\frac{1}{4}|\mathbf{r}_s - \mathbf{r}'_s|^2_j d\Gamma\right] = \sum_{j=1}^{M}\left[\int\frac{1}{4}\frac{\partial}{\partial n}[|\mathbf{r}_s - \mathbf{r}'_s|^2_j \phi_j(\mathbf{r}_s, \mathbf{r}'_s)]d\Gamma + \sum_{j=1}^{M}\left[\int_{\Gamma_j}\phi_j(\mathbf{r}_s, \mathbf{r}'_s)\frac{\partial}{\partial n}V_j(\mathbf{r}_s)d\Gamma\right]\right. \tag{11}$$

Collocating equation (11) at each segment midpoint, a system of linear algebraic equations in the unknown velocity gradients is given. Numerical valuation of the integrals appearing in equation (11) is based on one of the following approaches, The first, is accomplished by assuming that along each segment the integrand is of a constant value while the second is based on linear variations of $\partial V/\partial n$ along the segment. In both approaches the final numerical integration is obtained using simple quadrature. For more detail concerning the linear variation approach, see reference [13].

The set of the linear algebraic equations formed in the previous step is then rearranged into a matrix form. By using a standard scheme for solving the formed matrix, all the unknown velocity gradients are obtained on the duct contour. At this point of the present scheme, most of the important hydrodynamical quantities can be calculated. The average velocity for the given duct in terms of the pressure gradient is obtained without actual evaluation of the velocity distribution. This is accomplished as follows. Green's identity [12] for the two functions V and u is

$$\iint_A [V\nabla^2 u - u\nabla^2 V]dA = \oint_\Gamma \left[V\frac{\partial u}{\partial n} - u\frac{\partial V}{\partial n}\right]d\Gamma \tag{12}$$

With the choice of $u = r^2/4$ and using the boundary condition $V = 0$ on the duct contour, equation (12) reduces to

$$V_{av} = \frac{1}{A}\iint_A V dA = \frac{1}{A}\iint_A \frac{1}{4}r^2 dA - \oint_\Gamma \frac{r^2}{4A}\frac{\partial V}{\partial n}d\Gamma \tag{13}$$

In equation (13), one recognizes the first term on the right-hand side as the polar moment of inertia for the duct area. The second term represents the polar moment of the shear force per unit axial length of the duct. Since all the values of $\partial V/\partial n$ are known, at this stage, equation (13) is discretized to become

$$V_{av} = \frac{1}{4A}I_0 - \frac{1}{A}\sum_{j=1}^{M}\left(\frac{1}{4}\int_{\Gamma_j} r^2\frac{\partial V}{\partial n}\right)_j d\Gamma \tag{14}$$

which is simply executed numerically.

The wall shear stress τ_ω is obtained using the determined, $\partial V/\partial n$, values as

$$\tau_\omega = \frac{1}{\Gamma}\int_\Gamma \frac{\partial V}{\partial n}d\Gamma \tag{15}$$

It should be mentioned here that both V_{av} and τ_ω are functions of $(1dP/\mu dz)$ as shown from equation (1). Combining equations (14) and (15) with the hydraulic diameter of the duct D gives

$$f\,\mathrm{Re} = 2\frac{\tau_\omega D}{V_{av}} = 2\frac{\partial V^*}{\partial n}\frac{D}{V^*_{av}} \tag{16}$$

where f is friction coefficient.

The information given by equation (16) completes the important hydrodynamic analysis of the flow from the practical point of view. If detailed velocity distributions or contours of isovels are needed, equation (7) is directly utilized. This is simply done by direct substitution of the values of the velocity gradient obtained before into a discretized form of equation (7) enables the numerical calculation of the velocity at any point within the duct.

Applications

The foregoing numerical surface integral method is now applied to example problems. As a rigorous test for the method predicted values, two examples of duct flow of known exact solutions are used. The first is the flow in a rectangular duct of aspect ratio 0.5 as shown in Fig. 3, where the duct contour is divided into 24 segments. The numerical results are compared with the exact solution obtained from the similar problem in elastic stress. The exact solution is calculated from a 30 term series solution given in [12]. Results of both numerical and exact solutions are shown in Fig. 3. The value of f Re predicted by the present method is within two significant digits accuracy of the theoretical one. The numerical calculations using the Standard Fortran language took about 2 sec on an AMDAHL 470 computer. The second example of a known exact solution chosen is the classical pipe flow. A pipe of diameter 4 units with 48 segments is used for the present case. The number of segments used is larger than the previous example due to the severe curvature of the boundary. Saving in the number of segments may be accomplished in this specific example

Downloaded 01 May 2010 to 171.66.16.249. Redistribution subject to ASME license or copyright; see http://www.asme.org/terms/Terms_Use.cfm

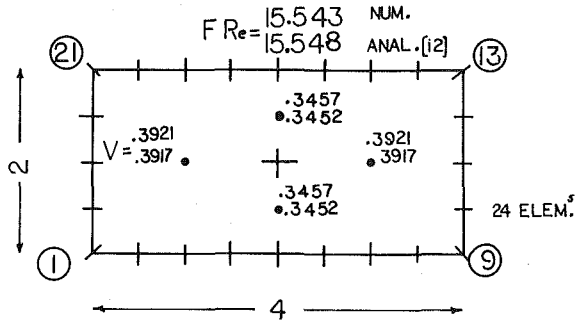


Fig. 3 A rectangular channel with aspect ratio 0.5

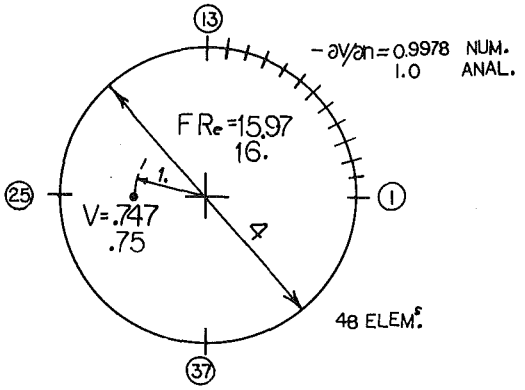


Fig. 4 A circular channel with a diameter of 4 units

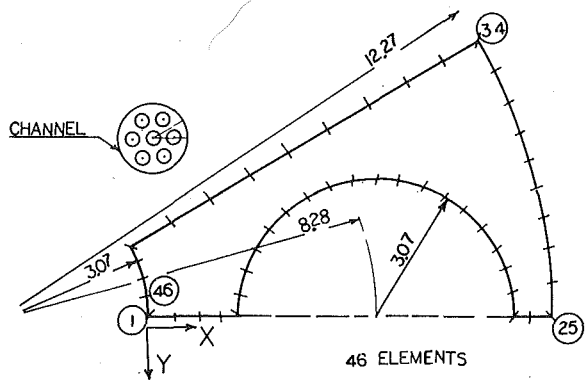


Fig. 5 A circular channel with rod clusters of reference [14]

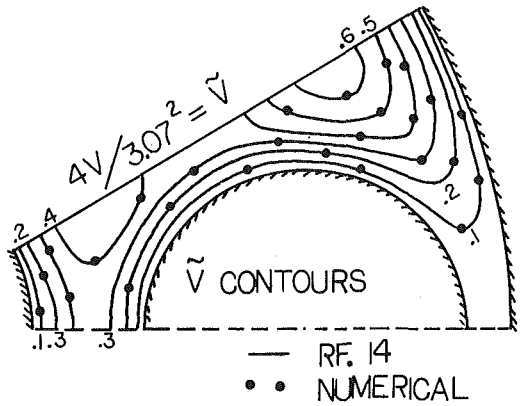


Fig. 6 Velocity contours "isovels" compared with the analytical prediction of reference [14]

if half of a duct cross section is used. However, it was decided to use the full cross section in order that solution symmetry could be checked. Results are shown in Fig. 4 and are compared with the exact values. The value f Re predicted numerically is 15.97 as compared to the exact value of 16.

Finally, a very general case of duct of multiply connected region is investigated. A circular duct containing rod clusters which represent typical cooled fuel elements of a nuclear reactor is considered Min, et al. [14], and later, Mottaghian and Wolf [15] using elegant mathematical procedures which involved transformation and series expansions obtained approximate analytical solutions for the flow field in such a duct. A typical element of such a duct is shown in Fig. 5, where the coordinate and dimensionless length parameters are used as of reference [14]. The contour of the duct element is divided into 46 segments for the present numerical solution. Fig. 6 shows the velocity contour compared to those reported in [14] for the present case. The comparison indicates that the present numerical prediction for the velocity contour "isovels" is in a good agreement with those predicted in [14]. One has to keep in mind that the results reported in [14] are approximate and not exact. For the value of friction coefficient of the present channel, the present scheme predicts a value of f Re = 18.876 as compared with a value of $\simeq$19 of [14]. The numerical calculation for the foregoing case consumed about 6 sec of the computer time. Table 1 shows the numerical results at the duct surface as obtained by the present method for this example.

These solutions for the previous flow problems, indicate that the present surface integral scheme is accurate and general for solving developed flow in ducts of arbitrary cross-section shapes. The solution predicted by equations (7) and (9) is exact in nature since no approximation is involved in its basic formulation. However, the numerical values of the solution are approximated for the purpose of its numerical evaluation. This fact is one of the unique features of the present method in contrast to the other numerical methods of finite difference and finite element.

Conclusions

The surface integral numerical method presented has no inherent limitations to geometric complexity of the duct cross section. The method is general and economical in its use. The method is most suitable for calculating the hydrodynamic parameters for fully developed duct flow without the need for calculating the velocity at every interior point within the duct. However, complete velocity distributions are directly obtainable with minimum effort. This advantage has been shown to provide a savings in computer storage time. This feature makes the method superior to available numerical methods, where the solution involves all interior points.

Another primary advantage of using the surface integral scheme rather than the original differential equation is the space reduction of the problem from two dimensions to one dimension. This, in turn, reduces the amount of effort and time involved in the solution procedure.

Moreover, the present technique has been proven to produce accurate predictions compared to other solution methods. As a matter of fact, the present scheme yields increasingly accurate numerical predictions as the number of surface elements used increases. This increase in accuracy of solution does not require any modifications in the numerical procedure or causes any numerical instabilities.

Finally, the present numerical scheme could be extended to many other problems which are governed by similar equations to equation (1). As a matter of fact, the basic features of the present method still hold true even for cases similar to the variable right-hand side of equation (1). The only restriction imposed for such cases is that the right-hand side of equation (1) should be a function of the position over the domain of interest. A brief description of this extension of the method to such cases is given in the Appendix, for completeness.

Downloaded 01 May 2010 to 171.66.16.249. Redistribution subject to ASME license or copyright; see http://www.asme.org/terms/Terms_Use.cfm

Table 1 Numerical results for rod cluster channel

Element #	$-\partial V/\partial n$	V	Element #	$-\partial V/\partial n$	V
1	0	0.138	24	0	0.3353
2	0	0.3016	25	0.1514	0
3	0	0.305	26	0.2373	0
4	0	0.1479	27	0.2944	0
5	0.6187	0	28	0.3838	0
6	0.6510	0	29	0.4826	0
7	0.6845	0	30	0.5774	0
8	0.6855	0	31	0.6642	0
9	0.6621	0	32	0.5663	0
10	0.6348	0	33	0	0.2964
11	0.6492	0	34	0	0.604
12	0.7021	0	35	0	0.6625
13	0.7703	0	36	0	0.555
14	0.8018	0	37	0	0.407
15	0.7737	0	38	0	0.335
16	0.6893	0	39	0	0.3727
17	0.5862	0	40	0	0.4646
18	0.4589	0	41	0	0.4729
19	0.3610	0	42	0	0.2324
20	0.2868	0	43	0.8351	
21	0.2286	0	44	0.6373	
			45	0.6122	
22	0.3154	0	46	0.65766	
23	0	0.18996			

Acknowledgment

The author gratefully acknowledges Mr. M. Hanna of the Electrical and Computer Engineering Department, University of South Carolina, for his help with the computer programming during this investigation.

References

1 Shah, R. K., and London, A. L., "Laminar Flow Forced Convection in Ducts," *Advances in Heat Transfer*, Supplement 1, Academic Press, 1978.

2 Tao, L. N., "Method of Conformal Mapping in Forced Convection Problems," International Division of Heat Transfer, *Proceedings of the Heat Transfer Conference*, Boulder, Colo., Part 3, 1961, pp. 598–606.

3 Sastry, U. A., "Viscous Flow Through Tubes of Doubly Connected Regions," *Indian Journal of Pure Applied Physics*, Vol. 3, 1965, pp. 230–232.

4 Sastry, U. A., "Heat Transfer by Laminar Forced Convection in a Pipe of Curvilinear Polygonal Section," *J. Sci. Engr. Res.*, Vol. 7, Part 2, 1963, pp. 281–292.

5 Sparrow, E. M., and Haji-Sheikh, A., "Flow and Heat Transfer in Ducts of Arbitrary Shape With Arbitrary Thermal Boundary Conditions," ASME Paper No. 65-WA/HT-13.

6 Hu, M. H., "Flow and Thermal for Mechanically Enhanced Heat Transfer Tubes," PhD Thesis, State University of New York at Buffalo, 1973.

7 Cheng, K. C., "Analog Solution of Laminar Heat Transfer in Noncircular Ducts by Moire' Method and Point-Matching," ASME *Journal of Heat Transfer*, Vol. 88, 1966, pp. 175–182.

8 Nakamura, S. H., and Yamada, I., "Laminar Forced Convection Flow and Heat Transfer in Arbitrary Triangular Ducts," *Heat Transfer—Japan Res.*, Vol. 1, 1972, pp. 120–122.

9 Date, A. W., and Singham, J. R., "Numerical Prediction of Friction and Heat Transfer Characteristics of Fully Developed Laminar Flow in Tubes Containing Twisted Tapes," ASME Paper No. 72-HT-17.

10 Masliyah, J. H., and Nandakumar, K., "Heat Transfer in Internally Finned Tubes," ASME *Journal of Heat Transfer*, Vol. 98, 1976, pp. 257–261.

11 Stakgold, I., *Boundary Value Problems of Mathematical Physics*, The Macmillan Co., Vols. I and II, 1967.

12 Marco, S. M., and Han, L. S., "A Note on Limiting Laminar Nusselt Number in Ducts With Constant Temperature Gradient by Analogy to Thin Plate Theory," TRANS. ASME, Vol. 77, 1955, pp. 625–630.

13 Khader, M. S., "Heat Conduction With Temperature-Dependent Thermal Conductivity," ASME Paper 80-HT-4.

14 Min, T. C., et al., "An Analysis of Axial Flow Through a Circular Channel Containing Rod Clusters," 3rd Southeastern Conference on Theoretical and Applied Mechanics, Vol. 3, 1966, pp. 667–689.

15 Mottaghian, R., and Wolf, L., "A Two-Dimensional Analysis of Laminar Fluid Flow in Rod Bundles on Arbitrary Arrangement," *International Journal of Heat and Mass Transfer*, Vol. 17, 1974, pp. 1121–1127.

APPENDIX

General Form of Equation (1)

This Appendix discusses the application of the present form to a more general class of equation (1), where the right-hand side is a function of position, i.e.,

$$\nabla^2 V = f(\mathbf{r}_i) \tag{17}$$

Following the same methodology used before in connection with equation (1) one arrives at

$$V(r_i) = \oint_\Gamma \left[\frac{\partial}{\partial n}\phi(\mathbf{r}_i, \mathbf{r}_s')V(\mathbf{r}_s) - \phi(\mathbf{r}_i, \mathbf{r}_s')\frac{\partial V}{\partial n}(\mathbf{r}_s')\right] d\Gamma + \iint_A \phi(\mathbf{r}_i, \mathbf{r}_i')f(r_i)dA \tag{18}$$

Downloaded 01 May 2010 to 171.66.16.249. Redistribution subject to ASME license or copyright; see http://www.asme.org/terms/Terms_Use.cfm

for interior points. For points located on the boundary of the region, the equivalent statement is

$$V(r_s) = \oint_\Gamma \left[\frac{\partial}{\partial n}\phi(\mathbf{r}_s, \mathbf{r}_s')V(\mathbf{r}_s) - \phi(\mathbf{r}_s, \mathbf{r}_s')\frac{\partial}{\partial n}V(\mathbf{r}_s)\right] d\Gamma + \iint_A \phi(\mathbf{r}_s, \mathbf{r}_s')f(\mathbf{r}_i)dA \quad (19)$$

If the boundary condition is of the type of vanishing values of V, then the left-hand side and the first term in the line integral of equation (19) also vanish.

The numerical statement for equation (19) will take the form

$$V_i(\mathbf{r}_s) + \sum_{j=1}^{M}\left[\int_{\Gamma_j}\left(V_j\frac{\partial}{\partial n}\phi_j - \phi_j\frac{\partial}{\partial n}V_j\right)d\Gamma_j\right] - \sum_{j=1}^{MM}\int_{A_j} f_j\phi_j dA_j = 0 \quad (20)$$

where again M represents the number of segments on the boundary. The surface integral of equation (19) is evaluated numerically using MM internal area cells. The rest of the analysis to follow is exactly the same as before.

Downloaded 01 May 2010 to 171.66.16.249. Redistribution subject to ASME license or copyright; see http://www.asme.org/terms/Terms_Use.cfm

W.-S. Yeung[1]
Assoc. Mem. ASME

R.-J. Yang
Student Mem. ASME

Materials and Molecular Research Division,
Lawrence Berkeley Laboratory,
University of California,
Berkeley, Calif. 94720

Application of the Method of Integral Relations to the Calculation of Two-Dimensional Incompressible Turbulent Boundary Layer

The orthonormal version of the Method of Integral Relations (MIR) was applied to solve for a two-dimensional incompressible turbulent boundary layer. The flow was assumed to be nonseparating. Flows with favorable, unfavorable, and zero pressure gradient were considered, and comparisons made with available experimental data. In general, the method predicted very well the experimental results for flows with favorable or zero pressure gradient; for flows with unfavorable pressure gradient, it predicted the experimental data well only up to a certain distance from the initial station. This result is due to the flow not being in equilibrium beyond that distance. Finally, the scheme was shown to be efficient in obtaining numerical solutions.

Introduction

In the vast body of literature dealing with turbulent boundary-layer calculations, two major methods have been employed: the so-called integral method and the differential method. In this report, we investigate a particular solution procedure for the two-dimensional incompressible turbulent boundary layer via the Method of Integral Relations (MIR). In particular, the efficiency and versatility of this method, as applied to turbulent boundary-layer calculations, is studied.

Formulation

The method of integral relations has previously been applied to two-dimensional turbulent boundary-layer calculations by Abbott and Deiwert [1] and by Murphy and Rose [2] at the 1968 Stanford Conference on turbulent boundary-layer calculations. Unfortunately, it was found inferior to other prediction methods presented at the same conference. Here, we shall reformulate the problem by using the modified version of MIR developed by Fletcher and Holt [3]. As a result, most of the shortcomings indicated by Murphy and Rose are overcome.

We start with the two-dimensional incompressible boundary-layer equations in the usual notations

$$u\frac{\partial u}{\partial x}+v\frac{\partial u}{\partial y}=-\frac{1}{\rho}\frac{\partial p}{\partial x}+\frac{\partial}{\partial y}\left[\left(\nu+\frac{\epsilon}{\rho}\right)\frac{\partial u}{\partial y}\right], \tag{1}$$

$$\frac{\partial u}{\partial x}+\frac{\partial v}{\partial y}=0, \tag{2}$$

where u and v are the mean velocity components in the x and y-directions, respectively, and p is the mean pressure; ρ is the density of the fluid, and ν its kinematic viscosity. The eddy viscosity, ϵ, is defined as

$$-\rho\,\overline{u'v'}=\epsilon\frac{\partial u}{\partial y} \tag{3}$$

where $-\rho\,\overline{u'v'}$ is the so-called Reynolds stress. The following nondimensional variables are chosen:

$$U=\frac{u}{u_e},\quad V=\frac{v\,\mathrm{Re}^{1/2}}{u_e},\quad \bar{x}=\frac{x}{L},\quad \bar{y}=\frac{y\,\mathrm{Re}^{1/2}}{L},\quad U_e=\frac{u_e}{u_\infty}, \tag{4}$$

where L and u_∞ are the characteristic length and velocity scales, respectively, u_e is the velocity at the outer boundary-layer edge, and the Reynolds number Re is defined as

$$\mathrm{Re}=u_\infty L/\nu \tag{5}$$

The pressure gradient is related to the outer edge velocity by Bernoulli's equation

$$-\frac{1}{\rho}\frac{\partial p}{\partial x}=u_e\frac{du_e}{dx} \tag{6}$$

[1] Present address: Department of Mechanical Engineering, University of Lowell, Lowell, Mass. 01854.

Contributed by the Applied Mechanics Division for publication in the JOURNAL OF APPLIED MECHANICS.

Discussion on this paper should be addressed to the Editorial Department, ASME, United Engineering Center, 345 East 47th Street, New York, N.Y. 10017, and will be accepted until two months after final publication of the paper itself in the JOURNAL OF APPLIED MECHANICS. Manuscript received by ASME Applied Mechanics Division, April, 1981.

Copyright © 1981 by ASME

Downloaded 01 May 2010 to 171.66.16.249. Redistribution subject to ASME license or copyright; see http://www.asme.org/terms/Terms_Use.cfm

Using (4) and (6), the original governing equations (1) and (2) become

$$U\frac{\partial U}{\partial \bar{x}} + V\frac{\partial U}{\partial \bar{y}} = \frac{1}{U_e}\frac{dU_e}{d\bar{x}}(1-U^2) + \frac{1}{U_e}\frac{\partial}{\partial \bar{y}}\left[\left(1+\frac{\epsilon}{\mu}\right)\frac{\partial U}{\partial \bar{y}}\right], \quad (7)$$

$$\frac{\partial U}{\partial \bar{x}} + \frac{\partial V}{\partial \bar{y}} = -\frac{U}{U_e}\frac{dU_e}{d\bar{x}}. \quad (8)$$

To apply the Method of Integral Relations, we define a set of linearly independent functions $\{f_i(U)\}$ such that

$$f_i(1) = 0, \quad i = 1, 2, \ldots N, \quad (9)$$

where N is the order of approximation.

Multiply equation (8) by f_i and equation (7) by f_i', defined as the first derivative of f_i with respect to U, add and integrate from $\bar{y} = 0$ to $\bar{y} \to \infty$:

$$\frac{\partial}{\partial \bar{x}}\int_0^\infty f_i U d\bar{y} = \frac{1}{U_e}\frac{dU_e}{d\bar{x}}\int_0^\infty f_i'(1-U^2)\,d\bar{y} - \frac{1}{U_e}f_i'(0)\left(\frac{\partial U}{\partial \bar{y}}\right)_0 - \frac{1}{U_e}\int_0^\infty\left(1+\frac{\epsilon}{\mu}\right)\left(\frac{\partial U}{\partial \bar{y}}\right)^2 f_i''\,d\bar{y} - \frac{1}{U_e}\frac{dU_e}{d\bar{x}}\int_0^\infty U f_i d\bar{y} \quad (10)$$

Change the variable of integration from $\bar{y}$ to U and define Z as

$$Z = \left(\frac{\partial U}{\partial \bar{y}}\right)^{-1}, \quad (11)$$

and equation (10) can be written as

$$\frac{\partial}{\partial \bar{x}}\int_0^1 f_i U Z dU = \frac{1}{U_e}\frac{dU_e}{d\bar{x}}\int_0^1 [(1-U^2)f_i' - U f_i]Z dU - \frac{1}{U_e}f_i'(0)\frac{1}{Z_0} - \frac{1}{U_e}\int_0^1\left(1+\frac{\epsilon}{\mu}\right)\frac{f_i''}{Z}dU. \quad (12)$$

Equation (12) is the basic integral relation in the present analysis.

We now further define $\{f_i\}$ as a set of orthonormal functions constructed from the Dorodnitsyn functions $(1-U)^k$, $k = 1, 2, 3 \ldots$ by the Gram-Schmidt procedure [4]. Hence

$$f_i(U) = \sum_{k=1}^{i} c_{ik}(1-U)^k, \quad (13)$$

and

$$\int_0^1 f_k f_j \frac{U}{1-U}dU = \delta_{kj}, \quad (14)$$

with δ_{kj} being the Kronecker delta. Z is then represented by

$$Z = \frac{b_0 + \sum_{i=1}^{N-1} b_j f_j(U)}{1-U} \quad (15)$$

where $b_0, b_1, b_2, \ldots$, are unknown coefficients to be found. Substitute (15) into (12) and invoking (14), we obtain an explicit set of ordinary differential equations in the coefficients $b_0, b_1, \ldots, b_{N-1}$:

$$\frac{db_0}{d\bar{x}}\int_0^1\frac{f_i U}{1-U}dU + \frac{db_i}{d\bar{x}} = \frac{1}{U_e}\frac{dU_e}{d\bar{x}}\int_0^1[(1-U^2)f_i' - U f_i]Z dU - \frac{1}{U_e}\frac{f_i'(0)}{Z_0} - \frac{1}{U_e}\int_0^1\left(1+\frac{\epsilon}{\mu}\right)\frac{f_i''}{Z}dU, \quad i = 1, 2, \ldots N-1 \quad (16a)$$

and

$$\frac{db_0}{d\bar{x}}\int_0^1\frac{f_N U}{1-U}dU = \frac{1}{U_e}\frac{dU_e}{d\bar{x}}\int_0^1[(1-U^2)f_N' - U f_N]Z dU - \frac{1}{U_e}f_N'(0)\frac{1}{Z_0} - \frac{1}{U_e}\int_0^1\left(1+\frac{\epsilon}{\mu}\right)\frac{1}{Z}f_N''\,dU \quad (16b)$$

which can be integrated subject to appropriate initial conditions at some station $\bar{x} = \bar{x}_i$. We shall discuss the initial conditions later.

The foregoing formulation is similar to that in a laminar boundary layer (Dorodnitsyn, [5]). Apart from the difficulty of evaluating the integral

$$\int_0^1\left(1+\frac{\epsilon}{\mu}\right)\frac{1}{Z}f_i''(U)dU,$$

in which some kind of eddy viscosity model for ϵ has to be used, one problem is that the approximation of Z given by (15) is not accurate unless N is rather large. This is mainly due to the highly inflected velocity profile in a turbulent boundary layer as opposed to the smooth profile in the laminar case. Thus Murphy and Rose [2] pointed out that the usual sequence $(1-U)^j$, $j = 1, 2, \ldots$ is not quite satisfactory, even when a four-parameter profile is used (i.e., $N = 4$). Instead, they judiciously assigned much larger exponents to the factor $(1-U)$ and determined in the course of their numerical solution the optimum values of those exponents. This of course destroys the completeness requirement of the original method of integral relations, and it does not guarantee in principle that the approximation will converge to the exact solution if the order of approximation tends to infinity. The sole purpose of their scheme is, to our knowledge, to better represent the Z profile in a turbulent boundary layer while using as few parameters as possible, since the traditional method of integral relations is quite impractical when too many parameters are used. However, the present orthonormal version circumvents this "high order" difficulty and enables one to preserve the completeness requirement while still using as many parameters as possible to represent faithfully the Z profile. Indeed, it has been applied to the two-dimensional laminar boundary layer to as high as $N = 15$ with little computer expense [3]. It is therefore believed that the present formulation would be efficient even for large values of N.

Turbulence Modeling

In order to calculate the last integrals in equations (16a) and (16b), a model for the eddy viscosity ϵ/μ is needed. We use the following expression for the wall region:

$$\frac{\epsilon}{\mu} = 0.04432\,[e^{0.4u^+} - 1 - 0.4u^+ - 0.08\,u^{+2}], \quad (17)$$

which was first deduced by Spalding [6] and later found independently by Kleinstein [7]. For the wake region, the Clauser model [8] is used.

$$\frac{\epsilon}{\mu} = 0.0168\,\mathrm{Re}_{\delta^*} \quad (18)$$

where $u^+ = u/u_\tau$ and $u_\tau = \sqrt{\tau_w/\rho}$, the wall frictional velocity. Re_{δ^*} is defined as

$$\mathrm{Re}_{\delta^*} = \frac{u_e\delta^*}{\nu} \quad (19)$$

with δ^* being the usual displacement thickness.

The wall shear stress, τ_w, is given by

$$\tau_w = (\mu+\epsilon)_0\left(\frac{\partial u}{\partial y}\right)_0 \quad (20)$$

where the subscript 0 denotes the wall.

Experimental data shows that the wall region extends to where the nondimensional velocity U assumes a value of roughly 0.7 (Bradshaw, [9]). In general, we denote this value by U_m. The determination of U_m will be discussed later. Hence the last integral in equation (16a) and (16b) can be evaluated as

$$\int_0^1(\ldots)dU = \int_0^{U_m}(\ldots)dU + \int_{Um}^1(\ldots)dU, \quad (21)$$

where $(\ldots)$ represents symbolically the integrand.

Before discussing the method used to calculate (21), we first derive expressions of u^+ and y^+ in terms of the present variables Z and U. We begin from equation (20)

$$\tau_w = (\mu+\epsilon)_0\left(\frac{\partial u}{\partial y}\right)_0.$$

Since $\epsilon = 0$ at $\bar{y} = 0$, we have

Downloaded 01 May 2010 to 171.66.16.249. Redistribution subject to ASME license or copyright; see http://www.asme.org/terms/Terms_Use.cfm

$$\tau_w = \mu \left(\frac{\partial u}{\partial y}\right)_0.$$

Using the definition of Z and the nondimensional variables defined in (4), it can be shown that

$$\frac{\tau_w \sqrt{\mathrm{Re}}}{\rho u_\infty{}^2} = \frac{U_e}{Z_0}$$

or

$$\left(\frac{u_\tau}{u_\infty}\right)^2 = \frac{U_e}{Z_0 \,\mathrm{Re}^{1/2}} \tag{22}$$

Hence,

$$u^+ = U\sqrt{U_e Z_0 \,\mathrm{Re}^{1/2}} \tag{23}$$

and

$$y^+ = \sqrt{\frac{U_e \mathrm{Re}^{1/2}}{Z_0}}\,\bar{y} \tag{24}$$

Thus the eddy viscosity can be written in terms of Z and U as follows:

For $0 \le U < U_m$

$$\frac{\epsilon}{\mu} = 0.04432\,[e^{0.4U\sqrt{U_e Z_0 \mathrm{Re}^{1/2}}} - 1 - 0.4U\sqrt{U_e Z_0 \mathrm{Re}^{1/2}} - 0.08U^2 U_e \mathrm{Re}^{1/2} Z_0], \tag{25}$$

and for $U_m \le U \le 1$,

$$\frac{\epsilon}{\mu} = 0.0168\, U_e\, \mathrm{Re}^{1/2} \int_0^1 (1-U)Z\,dU \tag{26}$$

and the displacement thickness δ^* has been written as

$$\delta^* = \int_0^\delta \left(1 - \frac{u}{u_e}\right) dy = \frac{L}{\mathrm{Re}^{1/2}} \int_0^1 (1-U)Z\,dU \tag{27}$$

Evaluation of Integrals

The integrals in equations (16a) and (16b) can be computed exactly except for the shear integrals, which appear as the last term in the equations. At present, these shear integrals are evaluated by using a method based on the Gaussian-Legendre rule whose algorithm is available in the Sandia Mathematical Library.

Determination of U_m

Up to now, we have only denoted the outer bondary of the wall region by U_m. As mentioned before, experimental results indicate that U_m is roughly 0.7. However, this value of U_m may not produce a continuous curve for ϵ/μ across the whole boundary layer. To be consistent with the present formulation, then, U_m must be found by determining the intersection of the ϵ/μ in the inner region with that in the outer region. Hence, equating the two expressions (25) and (26), we have

$$0.04432\,[e^{0.4U\sqrt{U_e Z_0 Re^{1/2}}} - 1 - 0.4U\sqrt{U_e Z_0\,\mathrm{Re}^{1/2}} = 0.08U^2 U_e Z_0\,\mathrm{Re}^{1/2}] = 0.0168\, U_e\, \mathrm{Re}^{1/2} \int_0^1 (1-U)Z\,dU \tag{28}$$

The aforementioned equation can be solved iteratively to yield U_m. The advantage of using Spalding's model becomes clear: this model is explicit in U and hence makes it easier to determine U_m. The solution is sought in the neighborhood of 0.7. In the case of flow with adverse pressure gradient, the wake region becomes substantial and U_m is found to be smaller than that of the flow with favorable pressure gradient or without pressure gradient. Once U_m is determined, the shear integrals can be evaluated as mentioned earlier.

Initial Conditions

The system or ordinary differential equations (ODE) resulting from our formulation of the MIR must be provided with initial conditions on the parameters b_0 and b_j at some initial station, which can be taken as zero by suitable translation of the origin. Unlike laminar boundary-layer flows, where the initial conditions are usually given by exact solutions (similarity solution), we have to rely on experimental data to determine the appropriate initial conditions. The easiest way in the present formulation is to calculate these initial values from experimental data. In general, among the experimental data, velocity profile U, boundary-layer thickness δ, displacement thickness δ^*, momentum thickness θ, and skin-friction coefficient C_f are available. One then faces the problem of choosing the most "effective" data. Our suggestion on these choices is as follows:

1 The skin-friction coefficient, C_f, is the most effective for insuring the correct behavior of the velocity profile at the wall.

2 Second in effectiveness is δ, the boundary-layer thickness. Although equation (15) satisfies the boundary conditions $\partial U/\partial \bar{y} \to 0$ automatically as $\bar{y} \to \infty$, the value of the boundary- layer thickness would not generally match the experimental data. Hence, to match the boundary-layer thickness is to secure a more correct boundary condition at the outer edge of the layer.

3 Displacement thickness, δ^*, is our third choice of data. In 1 and 2, we specify the boundary conditions at the wall and at the outer edge of the layer. By matching the displacement thickness, we expect to get a correct global behavior of the velocity profile in the boundary layer.

It was found that using the previous three conditions (i.e., C_f, δ, δ^*, for $N = 3$) to compute the flow over a flat plate, a very satisfactory result was obtained. In the case of higher approximations, more data are needed. Generally, a trial-and-error procedure is needed to choose other "effective" data. However, one can pinpoint these data after several attempts by noting that good initial conditions should behave as $|b_0| > |b_1| > |b_2| \ldots$ in equation (15). Since $U = 0$ at the wall, equation (15) becomes

$$Z_0 = b_0 + \sum_{j=1}^{N-1} b_i f_j(0) = b_0 + \sum_{j=1}^{N-1} b_j \left(\sum_{k=1}^{j} c_{jk}\right) \tag{29}$$

In the course of constructing orthonormal functions from $(1-U)^k$ by the Gram-Schmidt procedure, we found that

$$\left|\sum_{k=1}^{j-1} c_{jk}\right| < \left|\sum_{k=1}^{j} c_{jk}\right|$$

Intuitively, the contribution to Z from the subsequent term in equation (29) should become smaller as the order of approximation gets higher. Therefore, as noted, we expect that good initial conditions should yield $|b_0| > |b_1| > |b_2| > \ldots$[2]

Results and Discussion

Three kinds of flow are tested by the present formulation: (1) flow with zero pressure gradient, (2) flow with adverse pressure gradient, and (3) flow with favorable pressure gradient. Results for each case are plotted and compared with the experimental data that can be found in Cole and Hirst [10].

Flow With Zero Pressure Gradient (ID 1400).[3] Figs. 1–5 show comparisons between the predicted and measured values of the various flow quantities. Surprisingly good results were obtained with the approximation $N = 3$ just by using the initial conditions that matched C_f, δ, and δ^*. This supports the "effectiveness" of the data C_f, δ, and δ^* in the determination of initial conditions. The computer time of this approximation is about 5 sec in a CDC-7600 machine. Results of the approximations for $N = 4$ and $N = 5$ also show excellent agreement with measured values.

It should be pointed out that the CPU time for $N = 5$ (45 sec) is much greater than that for $N = 4$ (8 sec). This is due to the stiffness of the system of ODE's in equations (16a) and (16b), in which the coefficients of c_{ik} in equation (13) gets larger as N gets higher. Nev-

[2] In our calculations, however, this condition was not always met.

[3] The identity number refers to that used in reference [10].

Downloaded 01 May 2010 to 171.66.16.249. Redistribution subject to ASME license or copyright; see http://www.asme.org/terms/Terms_Use.cfm

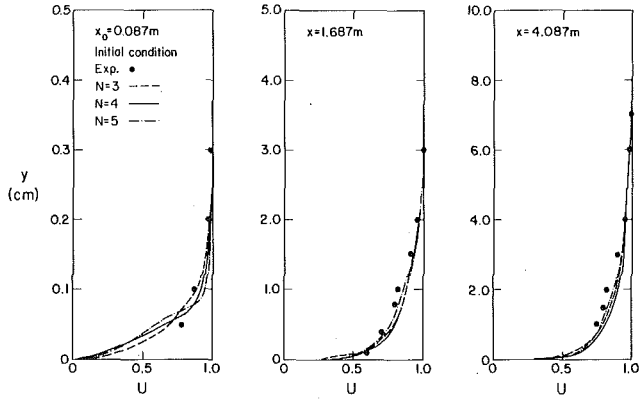


Fig. 1 Initial velocity profile and its development (ID 1400). (This and subsequent ID numbers are from reference [10].)

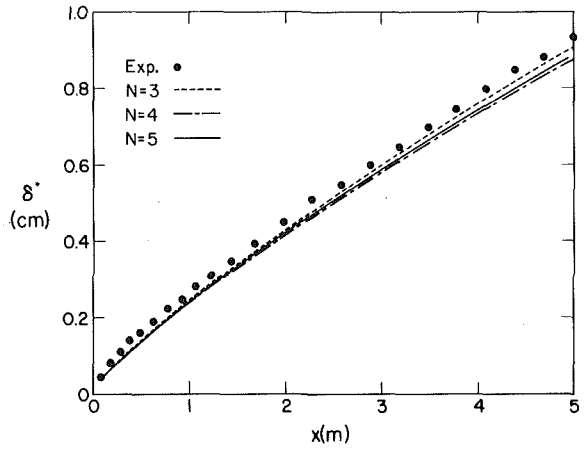


Fig. 4 Displacement thickness (ID 1400)

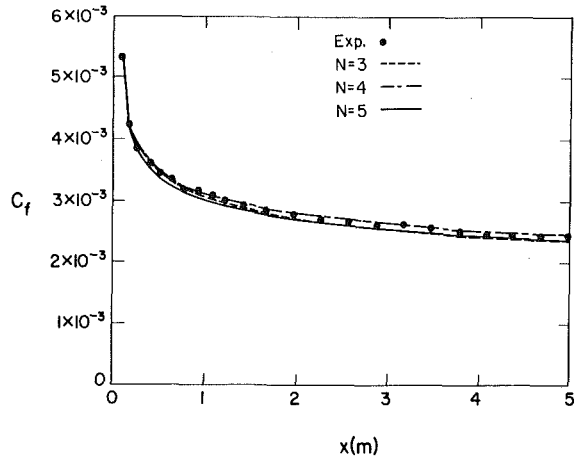


Fig. 2 Skin-friction coefficient (ID 1400)

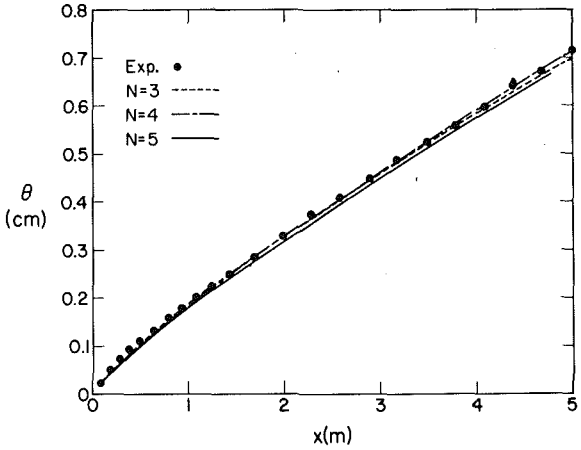


Fig. 5 Momentum thickness (ID 1400)

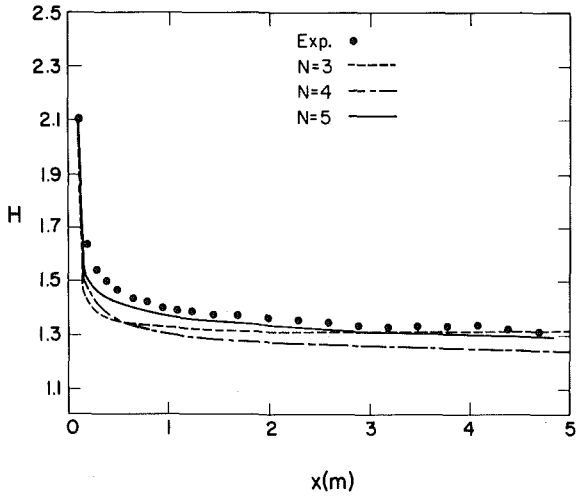


Fig. 3 Shape factor (ID 1400)

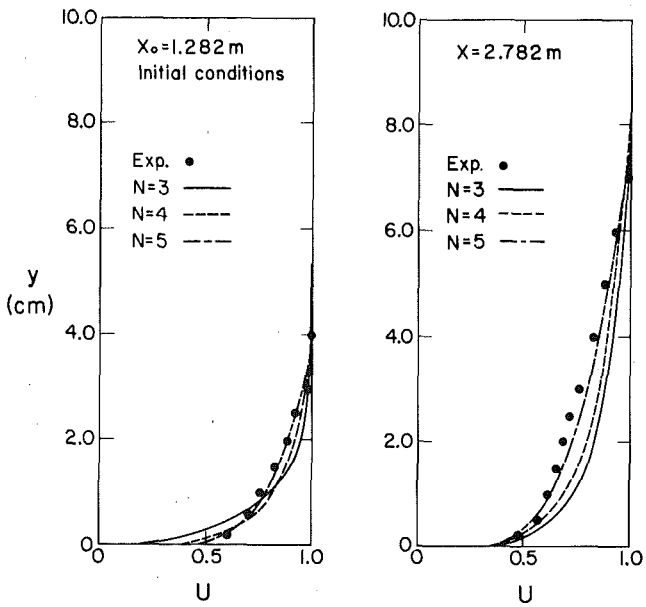


Fig. 6 Initial velocity profile and its development (ID 1100)

ertheless, the CPU times for the present formulation are smaller than those quoted in Murphy and Rose [2], taking into consideration of the different computers used.

Flow With Adverse Pressure Gradient (ID 1100). The flow, ID 1100, is not an equilibrium turbulent boundary layer beyond $x = 3m$, which was indicated by Murphy and Rose [2]. This is because the experimental data for θ, H, C_f show that they cannot satisfy the momentum integral equation.

Downloaded 01 May 2010 to 171.66.16.249. Redistribution subject to ASME license or copyright; see http://www.asme.org/terms/Terms_Use.cfm

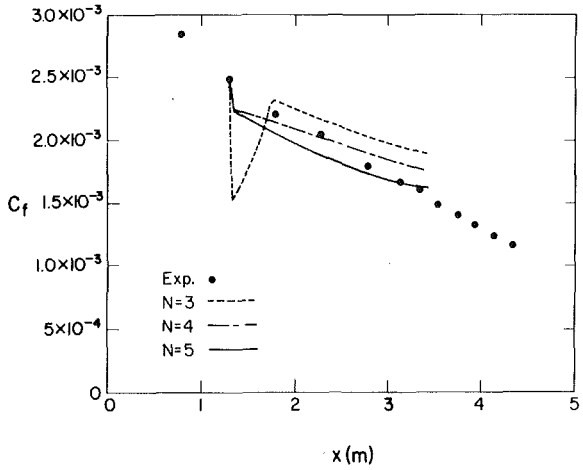


Fig. 7 Skin-friction coefficient (ID 1100)

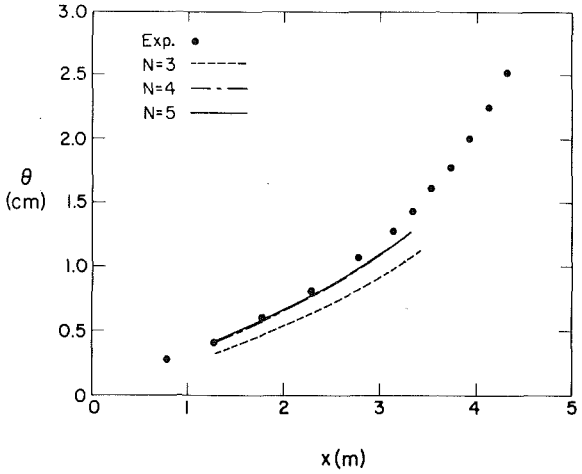


Fig. 10 Momentum thickness (ID 1100)

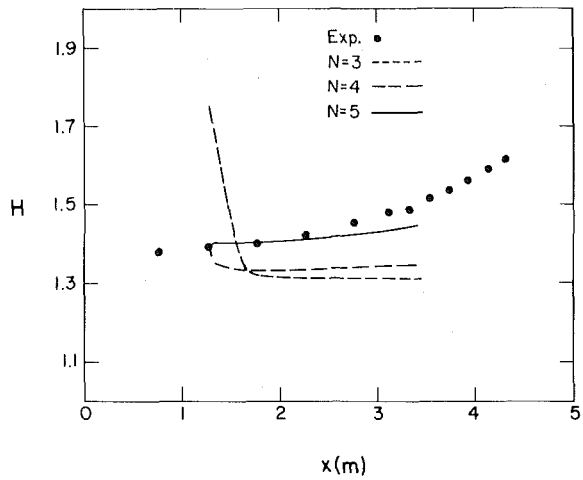


Fig. 8 Shape factor (ID 1100)

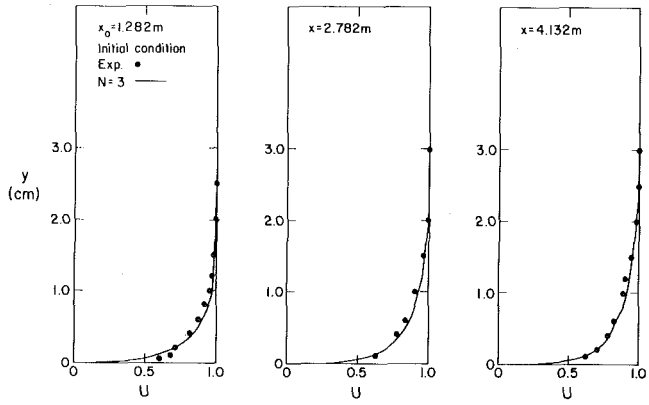


Fig. 11 Initial velocity profile and its development (ID 1300)

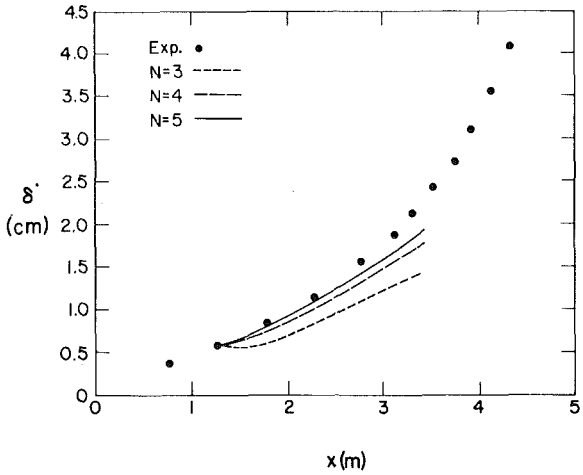


Fig. 9 Displacement thickness (ID 1100)

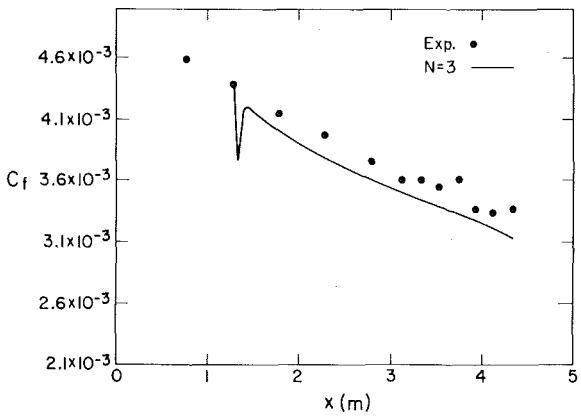


Fig. 12 Skin-friction coefficient (ID 1300)

$$\int_{x_0}^{x} \frac{d\theta}{dx}\,dx + \int_{x_0}^{x} (2+H)\,\frac{\theta}{U_\infty}\,\frac{dU_\infty}{dx}\,dx = \int_{x_0}^{x} \frac{C_f}{2}\,dx. \qquad (30)$$

Hence, we shall not discuss the predicted results beyond $x = 3m$ since the flow-satisfying equations (1) and (2) must satisfy equation (30).

Figs. 6–10 show comparisons between the predicted and measured values. The case $N = 3$ could not predict this flow accurately, unlike the first case. It was found that the wake region was substantial in the streamwise direction. In order to represent the velocity profile more accurately, one should use high-order approximations. Results of $N = 5$ show good agreement with the measured values.

Flow With Favorable Pressure Gradient (ID 1300). This is a simple flow that can be accurately predicted even in the case $N = 3$ with the initial conditions matching C_f, δ, and δ^*. Results are shown in Figs. 11–15. No attempt was made to use high-order approximation in this case.

Downloaded 01 May 2010 to 171.66.16.249. Redistribution subject to ASME license or copyright; see http://www.asme.org/terms/Terms_Use.cfm

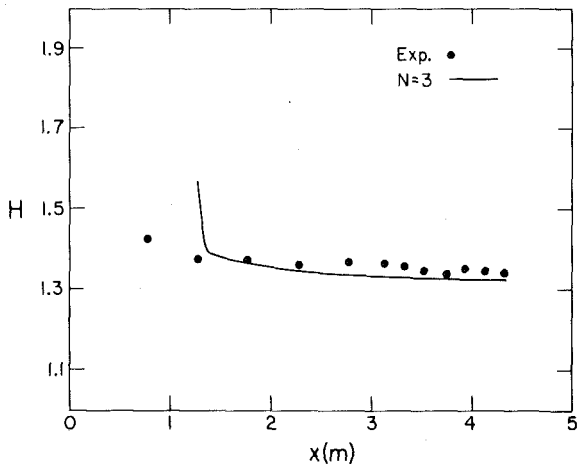


Fig. 13 Shape factor (ID 1300)

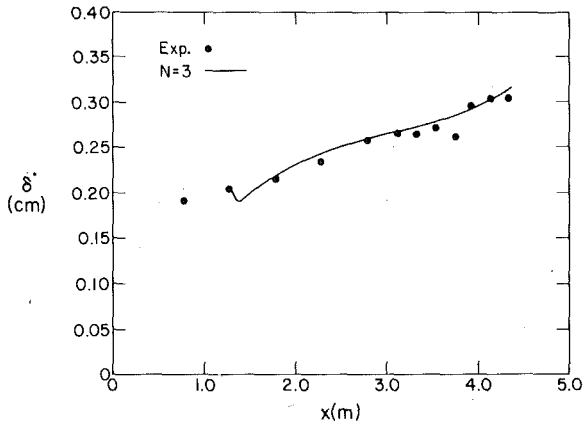


Fig. 14 Displacement thickness (ID 1300)

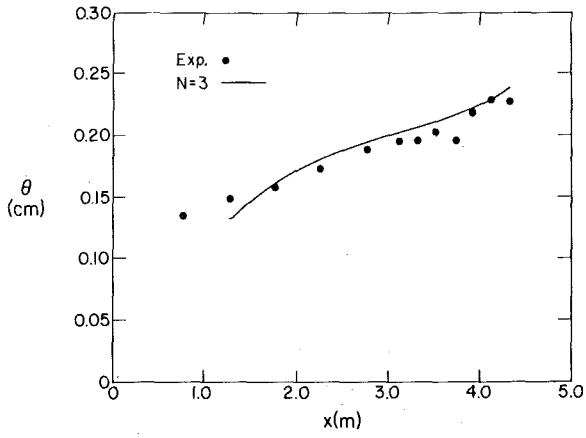


Fig. 15 Momentum thickness (ID 1300)

Conclusion

The application of the orthonormal version of the Method of Integral Relations to turbulent boundary layers has been examined. The present method circumvents the "high-order" difficulty and preserves the completeness requirement.

Three sample runs have been given. Results are shown to be in good agreement with experimental data. In addition, solutions for these flows require only 8 sec on a CDC-7600 computer when $N = 3$ or 4. This is very rapid.

A manner of determining the initial conditions from the experimental data at the initial station has been suggested and has proven to be effective. A shortcoming of this method, however, must be mentioned. It appears difficult to find initial conditions when we use high-order approximations, say $N = 6$, since the velocity profile is quite flat in turbulent boundary layers near the wall region. This high-order interpolating polynomial may be oscillatory. Furthermore, the corresponding system of ODE's becomes quite stiff and difficult to integrate. This shortcoming remains to be overcome in future research.

Acknowledgments

The authors wish to express their gratitude for the encouragement given them by A. V. Levy, program advisor and M. Holt, faculty advisor. This work was supported by the Division of Materials Sciences, Office of Basic Energy Sciences, U. S. Department of Energy, through Contract 7405-ENG-48.

References

1 Abbott, D. E., and Deiwert, G. S., "Application of the Method of Weighted Residuals to the Turbulent Boundary-Layer Equations," *Proceedings, Computation of Turbulent Boundary-Layers-1968 AFOSR-IFP-Stanford Conference*, Vol. 1, 1968, pp. 46–53.

2 Murphy, J. D., and Rose, W. C., "Application of the Method of Integral Relations to the Calculation of Incompressible Turbulent Boundary-Layers," *Proceedings, Computation of Turbulent Boundary Layers-1968 AFOSR-IFP-Stanford Conference*, Vol. 1, 1968, pp. 54–75.

3 Fletcher, C. A. J., and Holt, M., "An Improvement of the Method of Integral Relations," *Journal of Computational Physics*, Vol. 18, No. 2, 1975, pp. 154–164.

4 Isaacson, E., and Keller, H. B., *Analysis of Numerical Methods*, 1st ed., Wiley, New York, 1966, p. 199.

5 Dorodnitsyn, A. A., "General Method of Integral Relations and Its Application to Boundary Layer Theory," *Advances in Aeronautical Science*, Vol. 3, Pergamon Press, New York, 1960.

6 Spalding, D. B., "A Single Formula for the Law of the Wall," ASME JOURNAL OF APPLIED MECHANICS, Vol. 28, 1961, pp. 455–457.

7 Kleinstein, G., "Generalized Law of the Wall and Eddy-Viscosity Model for Wall Boundary Layers," *AIAA Journal*, Vol. 5, No. 8, 1967, pp. 1402–1407.

8 Clauser, F. H., "The Turbulent Boundary Layer," *Advances in Applied Mechanics*, Vol. 4, 1956, pp. 1–51.

9 Bradshaw, P., ed. *Topics in Applied Physics-Turbulence*, Vol. 12, Springer-Verlag, 1976, p. 53.

10 Coles, P., and Hirst, E., eds. *Proceedings, Computation of Turbulent Boundary Layers-1968 AFOSR-IFP Stanford Conference*, Vol. 2, Compiled Data, 1968.

Downloaded 01 May 2010 to 171.66.16.249. Redistribution subject to ASME license or copyright; see http://www.asme.org/terms/Terms_Use.cfm

L. M. Srivastava
Department of Mathematics,
University of Liberia,
Monrovia, Liberia,
West Africa.

V. P. Srivastava[1]
Department of Applied Mathematics,
Motilal Nehru Regional Engineering College,
Allahabad, India

The Plane Parallel Flow of a Binary Mixture of Fluids

The flow of a binary mixture of chemically inert incompressible, Newtonian fluids over an infinite plate, set into motion in its plane by impulse and by oscillation, is studied. The binary mixture consists of (i) two different viscous density nonstratified fluids, and (ii) two different viscous density stratified fluids. The exact solutions are obtained using two methods, (i) Laplace transform and (ii) Hankel transform. To further study the velocities and the wall shear stress, asymptotic expansion are found for small and large times. Some other results of physical importance such as results for noninteracting fluids, strongly interacting fluids, and extremely different fluids are also derived and compared analytically with other results. Finally, to gain an insight into the patterns of the flow, numerical study of the results has been made in detail using digital computer. A strong motivation of the present analysis has been the hope that such a theory of fluids is useful in providing some insight in rheological properties of complex fluids as polymers, liquid crystals and, in particular, blood in the vessels of small diameter. Also the theory of fluids might provide an improved understanding of such diverse subjects as diffusion of proteins, swimming of micro-organism and particle deposition in respiratory tract.

Introduction

The flow behavior of many substances such as suspensions, polymers, polycrystalline aggregates, granular media, bubbly liquids, liquid crystals, fluid-filled porous elastic solids, composite elastic solids, alloys, and etc., cannot be explained fully if one regards them as a single continua. In order to describe adequately the nature of such substances, it seems to be important and necessary to assume that the material consists of more than one constituent. Fluid dynamics of a continuum theory of mixture has, from historic times, been the object of scientific and engineering research. Historical discussion on the development of the subject is sufficiently available in the literature. A more fundamental and rigorous theoretical approach of the modern phase of the continuum theory of mixture can be found in the treatises of Truesdell [1], Truesdell and Toupin [2], and in papers by Eringen and Ingram [3], Green and Naghdi [4], and Mills [5, 6]. Atkin and Craine [7] have recently derived the fundamental equations of a continuum theory of mixture and given the historical development of the subject. In a subsequent paper [8], they have applied the basic theory for different types of binary chemically reacting and nonreacting mixture of fluids. Wilhelm and Vander Werff [9] studied binary mixture of Newtonian fluids in a pipe. In addition, a number of authors have worked on multiphase or two-phase flows from a different view point, much of the work being concerned with the suspension of solid particles in fluids. An extensive review of the theory of solid-fluid mixture has been given by Marble [10, 11] and Soo [12]. These studies include the work of Davidson and Harrison [13], Murray [14], Brenner [15], Digiovanni and Lee [16], Drew [17, 18], and Peddieson [19].

The theoretical study of the theory of mixture is very useful in understanding a number of diverse physical problems concerned with powder technology, fluidization, aerosol filtration, sedimentation, atmospheric fallout, combustion, Lunar ash flows, environmental pollution, etc. Lately, interest is developing in applying this theory to hydrodynamics of biological systems because it provides an improved understanding of such diverse subjects, as the diffusion of proteins, the rheology of blood, the swimming of micro-organism, and the particle deposition in respiratory tract, etc. [20–23].

Whereas all the studies just mentioned are concerned with a mixture of homogeneous materials, only little work, at least to the authors' knowledge, has been done to understand the behavior of a mixture of nonhomogeneous fluids. For the first time, Healy [24] attempted the problems of two-phase plane parallel flow of density stratified fluids. Recently, the analysis of boundary layer in the flow of such fluids is reported by Srivastava, et al. [25]. However, by considering the fluid as a single continua, literature on stratified fluids seem available. An elementary account of the basic development in this area is contained in a well-known book by Yih [26]. These studies also include the work of Kelly and Redekopp [27] and Standing [28].

The research reported here is devoted to the study of flow of a mixture of two different incompressible Newtonian viscous fluids.

[1] Present address: L.B.S. Degree College, Gonda (U.P.) India.

Contributed by the Applied Mechanics Division for publication in the JOURNAL OF APPLIED MECHANICS.

Discussion on this paper should be addressed to the Editorial Department, ASME, United Engineering Center, 345 East 47th Street, New York, N. Y. 10017, and will be accepted until two months after final publication of the paper itself in the JOURNAL OF APPLIED MECHANICS. Manuscript received by ASME Applied Mechanics Division, May, 1980; final revision, December, 1980.

Copyright © 1981 by ASME

Downloaded 01 May 2010 to 171.66.16.249. Redistribution subject to ASME license or copyright; see http://www.asme.org/terms/Terms_Use.cfm

The flow induced in such a mixture is considered in the two cases when an infinite plate moves parallel to itself (*i*) in simple harmonic motion, and (*ii*) impulsively from rest with uniform velocity. In particular, first we consider a binary mixture of chemically inert viscous density nonstratified fluids and then a mixture of two density stratified fluids (for the theory of mixture of chemically reacting fluids, readers are referred to Eringen and Ingram [3, 29] and Atkin and Craine [7]). Both exact and approximate results for small and large time are obtained. Some other results of physical importance such as results for noninteracting fluids, strongly interacting fluids, and extremely different fluids are also derived. Each of the constituents of the mixture is described by a modified Navier-Stokes equation, in which dynamic coupling of the different fluids is due to the intercomponent friction forces which satisfy the action-reaction principle [9]. It is hoped that the theory presented here is useful in providing some insight in rheological properties of blood and its possible utility in understanding adequately blood flow in blood vessels of small diameter (e.g., main veins, small veins, main arterial branches, arterioles, etc.) where spatial distribution of red blood cells is nonuniform (lower number density of red blood cells close to the wall than in the center [30, 31]). In addition the results appear to be applicable to several mixtures of fluids of the Navier-Stokes type, e.g., C_2H_5OH and H_2O, Na, and K; and A and Ne.

Formulation

Consider a mixture of two chemically inert, viscous incompressible fluids occupying a semi-infinite region $y > 0$, bounded by an infinite plate oscillating parallel to its own plane with frequency ω and amplitude U. Induced motion of the mixture is a result of the transmission of momentum produced at the plate into the interior of the mixture through the diffusion action of viscosity of fluids and the interaction between two phases. The appropriate equations describing the flow are

$$\rho_1(y)\frac{\partial u_1}{\partial t} = \mu_1\frac{\partial^2 u_1}{\partial y^2} - \frac{\rho_1(y)}{\tau_1}(u_1 - u_2) \tag{1}$$

$$\rho_2(y)\frac{\partial u_2}{\partial t} = \mu_2\frac{\partial^2 u_2}{\partial y^2} - \frac{\rho_2(y)}{\tau_2}(u_2 - u_1) \tag{2}$$

where $u_s(y, t)$ and $\rho_s(y)$, $s = 1, 2$ are the velocity and mass of the phase s per unit volume of the mixture, μ_s (constant) and τ_s (constant) are the viscosity and momentum relaxation time of the fluids in the mixture. In general τ_1 and τ_2 will be functions of the relative velocity, but for dilute particle suspension, a constant value of τ_s is justified. It should be noted that μ_s and τ_s are the properties of the mixture and not those of the individual fluid. Each constituent in the mixture will exchange momentum through the intercomponent friction forces. The intercomponent forces, satisfying the action-reaction principle, will produce no momentum change of the fluid mixture, i.e.,

$$\rho_1\tau_1^{-1}(u_1 - u_2) + \rho_2\tau_2^{-1}(u_2 - u_1) = 0 \tag{3}$$

or

$$\rho_1/\tau_1 = \rho_2/\tau_2 \quad \text{and} \quad \tau_1 \neq \tau_2 \quad \text{for} \quad \rho_1 \neq \rho_2 \tag{4}$$

for a binary mixture. The initial and boundary conditions are

$$u_s(y, 0) = 0; \quad u_s(0, t) = U\,\mathrm{Re}\,e^{i\omega t}; \quad \lim_{y\to\infty} u_s(y, t) = \text{finite} \tag{5}$$

Analysis

Exact and various approximate solutions for density stratified and nonstratified fluids are obtained using the Laplace and the finite Hankel transformations.

Density Nonstratified Fluids

In this case, we assume $\rho_s(y) = \rho_{s,0}$ (constant), where $\rho_{s,0}$ is the density of fluids at the plate ($y = 0$). An application of the Laplace transform along with the foregoing initial and boundary conditions in equations (1) and (2), gives the expression for the velocity of fluids $s = 1, 2$ as

$$u_s(y, t) = \frac{U}{2\pi i}\int_{\alpha-i\infty}^{\alpha+i\infty}\frac{p(k_1^2 - k_2^2)^{-1}}{p^2 + \omega^2}\left[[k_1^2 e^{-k_2 y} - k_2^2 e^{-k_1 y}] + \frac{p}{\nu_s}[e^{-k_1 y} - e^{-k_2 y}]\right]e^{pt}\,dp \tag{6}$$

where

$$k_{1,2} = \frac{1}{\sqrt{2}}\left[\frac{1 + p\tau_1}{\nu_1\tau_1} + \frac{1 + p\tau_2}{\nu_2\tau_2} \pm \left\{\left(\frac{1 + p\tau_1}{\nu_1\tau_1} - \frac{1 + p\tau_2}{\nu_2\tau_2}\right)^2 + \frac{4}{\nu_1\nu_2\tau_1\tau_2}\right\}^{1/2}\right]^{1/2} \tag{7}$$

and ν_s is the kinematic viscosity of the two fluids.

The steady-oscillatory solution, which is obtained by calculating residues of the integrand of equation (6) at $p = \pm i\omega$, may therefore be written as

$$u_s(y, t) = (0.5)(k_1^{+2} - k_2^{+2})^{-1}\left\{[k_1^{+2} e^{-k_2^+ y} - k_2^{+2} e^{-k_1^+ y}] \times U + \frac{i\omega U}{\nu_s}[e^{-k_1^+ y} - e^{-k_2^+ y}]\right\}e^{i\omega t} + (0.5)(k_1^{-2} - k_2^{-2})^{-1}\left\{[k_1^{-2} e^{-k_2^- y} - k_2^{-2} e^{-k_1^- y}] \times U - \frac{i\omega U}{\nu_s}[e^{-k_1^- y} - e^{-k_2^- y}]\right\}e^{-i\omega t} \tag{8}$$

where

$$k_{1,2}^{\pm} = (k_{1,2})_{p=\pm i\omega} \tag{9}$$

In view of the complicated form of $k_{1,2}$ (equation (7)) to complete the Laplace inversion of equation (6), and hence obtain the transient solution, is almost a formidable task. Instead, it is of interest for physiologists and engineers to have asymptotic solutions for small and large time. We focus our attention on the transient due to the impulsively moved plate, that is, for $\omega = 0$ in cases of small and large-time solutions.

Small-Time Solution

A solution for small time is obtained by taking $|p|$ large and in this limit equation (7) reduces to

$$k_{1,2} \sim \left(\frac{p}{\nu_{1,2}}\right)^{1/2}\left\{1 + \frac{1}{2\tau_{1,2}}\frac{1}{p} + 0\left(\frac{1}{p^2}\right)\right\} \tag{10}$$

and accordingly the expression for velocity of fluids $s = 1, 2$ are given from equation (6) as

$$\frac{u_s}{U} \sim \mathrm{erfc}\,\eta_s\left[1 + 2\eta_s^2\left(\frac{t}{\tau_s}\right)\right] - \frac{2}{\sqrt{\pi}}\eta_s e^{-\eta_s^2}\left(\frac{t}{\tau_s}\right) + O\left(\frac{t}{\tau_s}\right)^2 \tag{11}$$

where

$$\eta_s = y/2\sqrt{\nu_s t} \tag{12}$$

Equation (11) is the same as obtained by Healy [32] (up to first approximation). Thus, for small time and up to first approximation, one fluid experiences the effect of the other fluid as if the other fluid were inviscid. Again, if we take $\tau_s \to \infty$ (noninteracting fluids), the famous Stokes first problem: $u_s = U\,\mathrm{erfc}\,y/2\sqrt{\nu_s t}$ (Schlichting [33]) is recovered.

Finally, the dimensionless wall shear stress ratio becomes

$$\frac{P_{(1,2),k}}{P_{1,0}} \sim \frac{\mu_{1,2}}{\mu_1}\left(\frac{\nu_1}{\nu_{1,2}}\right)^{1/2}\left[1 + \sqrt{\nu_{1,2}}\frac{[\tau_2/\tau_1\sqrt{\nu_1} + \sqrt{\nu_2}]}{(\sqrt{\nu_1} + \sqrt{\nu_2})^2} \times (1 - \sqrt{\nu_{2,1}/\nu_{1,2}})\left(\frac{t}{\tau_2}\right)\right] + O\left(\frac{t}{\tau_2}\right)^2 \tag{13}$$

Subscript k ($= \rho_2/\rho_1 = \tau_2/\tau_1$) stands for the interacting fluids in the mixture. When the second fluid is inviscid ($\nu_2 = 0$), the shear stress ratio from equation (13) becomes

Downloaded 01 May 2010 to 171.66.16.249. Redistribution subject to ASME license or copyright; see http://www.asme.org/terms/Terms_Use.cfm

$$\frac{P_{1,k}}{P_{1,0}} \sim 1 + \left(\frac{t}{\tau_1}\right) \tag{14}$$

which is the same as obtained by Healy [32].

Large-Time Solution

A solution for large time is obtained by taking $|p|$ small and in this limit equation (7) reduces to

$$k_1 \sim \left(\frac{\nu_1\tau_1 + \nu_2\tau_2}{\nu_1\nu_2\tau_1\tau_2}\right)^{1/2}\left[1 + \frac{1}{2}\frac{\tau_1\tau_2(\nu_1{}^2\tau_1 + \nu_2{}^2\tau_2)}{(\nu_1\tau_1 + \nu_2\tau_2)^2}p + \frac{1}{8}\frac{\tau_1{}^2\tau_2{}^2[4\nu_1\nu_2\tau_1\tau_2(\nu_1 - \nu_2)^2 - (\nu_1{}^2\tau_1 + \nu_2{}^2\tau_2)^2]}{(\nu_1\tau_1 + \nu_2\tau_2)^4}p^2 + O(p^3)\right] \tag{15}$$

$$k_2 \sim \left(\frac{\tau_1 + \tau_2}{\nu_1\tau_1 + \nu_2\tau_2}P\right)^{1/2}\left[1 - \frac{\tau_1{}^2\tau_2{}^2(\nu_1 - \nu_2)^2}{2(\tau_1 + \tau_2)(\nu_1\tau_1 + \nu_2\tau_2)^2}p + \frac{1}{8}\frac{\tau_1{}^3\tau_2{}^3(\nu_1 - \nu_2)^3[\nu_1\tau_1(3\tau_2 + 4\tau_1) - \nu_2\tau_2(3\tau_1 + 4\tau_2)]}{(\tau_1 + \tau_2)^2(\nu_1\tau_1 + \nu_2\tau_2)^4}p^2 + O(p^3)\right] \tag{16}$$

and accordingly the expression for the velocity of fluids $s = 1, 2$ are given as

$$\frac{u_1}{U} \sim \operatorname{erfc}\bar{\eta}_1 + \frac{\bar{\eta}_1}{\sqrt{\pi}}\frac{\tau_1\tau_2(\nu_1 - \nu_2)}{(\nu_1\tau_1 + \nu_2\tau_2)^2} \times \left[\frac{\tau_1(\nu_1 - \nu_2)}{\tau_1 + \tau_2}\left(\bar{\eta}_1{}^2 - \frac{1}{2}\right) + \nu_2\right]e^{-\bar{\eta}_1{}^2}\left(\frac{\tau_2}{t}\right) + O\left(\frac{\tau_2}{t}\right)^2 \tag{17}$$

$$\frac{u_2}{U} \sim \operatorname{erfc}\bar{\eta}_1 + \frac{\bar{\eta}_1}{\sqrt{\pi}}\frac{\tau_1{}^2(\nu_1 - \nu_2)}{(\nu_1\tau_1 + \nu_2\tau_2)^2} \times \left[\frac{\tau_2(\nu_1 - \nu_2)}{\tau_1 + \tau_2}\left(\bar{\eta}_1{}^2 - \frac{1}{2}\right) - \nu_1\right]e^{-\bar{\eta}_1{}^2}\left(\frac{\tau_2}{t}\right) + O\left(\frac{\tau_2}{t}\right)^2 \tag{18}$$

where

$$\bar{\eta}_1 = y/2\sqrt{\nu_m t}, \quad \nu_m = \frac{(\nu_1\tau_1 + \nu_2\tau_2)}{(\tau_1 + \tau_2)} \tag{19}$$

When the second fluid is inviscid, the corresponding velocity of the fluids can be obtained from equations (17) and (18) by taking $\nu_2 = 0$, as

$$\frac{u_1}{U} \sim \operatorname{erfc}\bar{\eta} + \frac{\bar{\eta}}{\sqrt{\pi}}\frac{\tau_2}{\tau_1 + \tau_2}\left(\bar{\eta}^2 - \frac{1}{2}\right)e^{-\bar{\eta}^2}\left(\frac{\tau_2}{t}\right) + O\left(\frac{\tau_2}{t}\right)^2 \tag{20}$$

$$\frac{u_2}{U} \sim \frac{u_1}{U} - \frac{\bar{\eta}}{\sqrt{\pi}}e^{-\bar{\eta}^2}\left(\frac{\tau_2}{t}\right) + O\left(\frac{\tau_2}{t}\right)^2 \tag{21}$$

where

$$\bar{\eta} = y/2\sqrt{\bar{\nu}_1 t}, \quad \bar{\nu}_1 = \nu_1\tau_1/(\tau_1 + \tau_2) \tag{22}$$

Equations (20) and (21) are the same as obtained by Michael, et al. [34], and Healy [32]. When the time is infinitely large, i.e., $t/\tau_2 \to \infty$, the velocity of fluids from equation (17) and (18), becomes $\tilde{u} = u_1 = u_2 = \operatorname{erfc} y/2\sqrt{\nu_m t}$. Thus, from a measurement of the mean velocity $\tilde{u}$, the kinematic viscosity ν_m of the mixture can be determined. In this case, the two-phase system behaves as a single fluid of viscosity $(\mu_1 + \mu_2)$ and density $(\rho_{1,0} + \rho_{2,0})$, that is an equilibrium state has been reached. Further if one fluid is nonviscous ($\mu_2 = 0$), $u_1 = u_2 = \operatorname{erfc} y/2\sqrt{\bar{\nu}_1 t} = \operatorname{erfc} y/2\sqrt{\mu_1/(\rho_{1,0} + \rho_{2,0})}$, the system behaves as a single fluid of density $(\rho_{1,0} + \rho_{2,0})$ and hence the effect of one fluid on the other is to reduce the effective kinematic viscosity to $\nu_1/(1 + \rho_{2,0}/\rho_{1,0})$, as was noticed by Saffman [35] and Healy [32]. Again by taking $\tau_1 \to \infty$, the famous result $u_s = \operatorname{erfc} y/2\sqrt{\nu_1 t}$ [33] for noninteracting fluids is obtained.

Finally, the wall shear stress ratio becomes

$$\frac{P_{(1,2),k}}{P_{1,0}} \sim \frac{\mu_{1,2}}{\mu_1}\left(\frac{\nu_1}{\nu_m}\right)^{1/2} \times \left[1 + \frac{\tau_1}{4(\nu_1\tau_1 + \nu_2\tau_2)}\left\{2\nu_{2,1} + \frac{(\tau_1 + \tau_2)^{-1}}{(\nu_1\tau_1 + \nu_2\tau_2)}[\tau_1\tau_2(\nu_1 - \nu_2)^2 - 2\nu_1\nu_2(\tau_1 + \tau_2)^2]\right\}\left(\frac{\tau_2}{t}\right) + \frac{3}{32}\frac{\tau_1{}^3(\nu_1 - \nu_2)}{(\nu_1\tau_1 + \nu_2\tau_2)^3} \times \left\{4\nu_{2,1}[2(\nu_1\tau_1 - \nu_2\tau_2)/\tau_1 + \tau_2(\nu_1 - \nu_2)/(\tau_1 + \tau_2)] + \tau_1/(\nu_1\tau_1 + \nu_2\tau_2)\left\{\frac{\tau_2(\nu_1 - \nu_2)^2[\nu_1\tau_1(3\tau_2 + 4\tau_1) - \nu_2\tau_2(3\tau_1 + 4\tau_2)]}{\tau_1(\tau_1 + \tau_2)^2} - \frac{8\nu_1\nu_2}{\tau_1{}^2}[\nu_2\tau_2(\tau_2 + 2\tau_1) - \nu_1\tau_1(2\tau_2 + \tau_1)] - \frac{4\nu_1\nu_2\tau_2(\nu_1 - \nu_2)}{\tau_1}\right\}\left(\frac{\tau_2}{t}\right)^2\right] + O\left(\frac{\tau_2}{t}\right)^3 \tag{23}$$

When $\nu_2 = 0$, equation (23) reduces to

$$\frac{P_{1,k}}{P_{1,0}} \sim \left(1 + \frac{\tau_2}{\tau_1}\right)^{1/2}\left[1 + \frac{\tau_2}{4(\tau_1 + \tau_2)}\left(\frac{\tau_2}{t}\right) + \frac{3}{32}\frac{\tau_2(3\tau_2 + 4\tau_1)}{(\tau_1 + \tau_2)^2}\left(\frac{\tau_2}{t}\right)^2\right] + O\left(\frac{\tau_2}{t}\right)^3 \tag{24}$$

as found in [32].

Noninteracting Fluids ($\tau_s \to \infty$)

The interaction force between two interacting fluids will be eliminated by assuming the interaction time go to infinity, i.e., $\tau_s \to \infty$. In this limit

$$k_{1,2} \sim \left(\frac{p}{\nu_{1,2}}\right)^{1/2} \tag{25}$$

Use of (25) in equation (6) yields the solution

$$\frac{u_s}{U} = e^{-y\sqrt{\omega/2\nu_s}}\cos\left[\omega t - y\sqrt{\frac{\omega}{2\nu_s}}\right] - \frac{1}{\pi}\int_0^\infty \frac{r}{r^2 + \omega^2}e^{-rt}\sin\left(y\sqrt{r/\nu_s}\right)dr \tag{26}$$

which is in good agreement with Healy [32]. The first part of equation (26) is the Stokes second problem [33] with boundary-layer thickness $\delta \sim (2\nu_s/\omega)^{1/2}$.

Density Stratified Fluids

In the case of the mixture of two density stratified fluids, we assume the variation of densities of two fluids as $\rho_s = \rho_{s,0}\exp(-cy)$ where c is a constant, used to denote stratification and $\rho_{s,0}$, the density at the plate ($y = 0$). To handle equations (1) and (2) subject to present variation of density, we introduce the relation, $r^2 = \exp(-cy)$, which transforms the geometry of the problem from the plate, $0 \leqslant y < \infty$, to the cylinder, $0 \leqslant r < 1$, and the original problem into the axial flow of the mixture in an infinitely long cylinder. Equations (1) and (2) now become

$$\frac{\partial u_{1,c}}{\partial t} = \nu_{1,c}\left[\frac{\partial^2 u_{1,c}}{\partial r^2} + \frac{1}{r}\frac{\partial u_{1,c}}{\partial r}\right] - \frac{1}{\tau_1}(u_{1,c} - u_{2,c}) \tag{27}$$

$$\frac{\partial u_{2,c}}{\partial t} = \nu_{2,c}\left[\frac{\partial^2 u_{2,c}}{\partial r^2} + \frac{1}{r}\frac{\partial u_{2,c}}{\partial r}\right] - \frac{1}{\tau_2}(u_{2,c} - u_{1,c}) \tag{28}$$

where

$$\nu_{s,c} = \frac{\mu_s c^2}{4\rho_{s,0}} \tag{29}$$

The solution of equations (27) and (28), subject to the foregoing initial and boundary conditions, is carried out using a standard technique (Laplace transform) and yields the following expression for the velocity of fluids $s = 1, 2$:

Downloaded 01 May 2010 to 171.66.16.249. Redistribution subject to ASME license or copyright; see http://www.asme.org/terms/Terms_Use.cfm

$$u_{s,c}(y,t) = \frac{1}{2\pi i}\int_{\alpha-i\infty}^{\alpha+i\infty} \frac{p(\alpha_1{}^2-\alpha_2{}^2)^{-1}}{p^2+\omega^2} \times\left[\left(\alpha_1{}^2\frac{I_0(\alpha_2 e^{-cy/2})}{I_0(\alpha_2)}-\alpha_2{}^2\frac{I_0(\alpha_1 e^{-cy/2})}{I_0(\alpha_1)}\right)U + \frac{pU}{\nu_{s,c}}\left(\frac{I_0(\alpha_1 e^{-cy/2})}{I_0(\alpha_1)}-\frac{I_0(\alpha_2 e^{-cy/2})}{I_0(\alpha_2)}\right)\right] e^{pt}dp \quad (30)$$

where

$$\alpha_{1,2} = \frac{1}{\sqrt{2}}\left[\frac{1+p\tau_1}{\nu_{1,c}\tau_1}+\frac{1+p\tau_2}{\nu_{2,c}\tau_2} \pm\left\{\left(\frac{1+p\tau_1}{\nu_{1,c}\tau_1}-\frac{1+p\tau_2}{\nu_{2,c}\tau_2}\right)^2+\frac{4}{\nu_{1,c}\nu_{2,c}\tau_1\tau_2}\right\}^{1/2}\right]^{1/2} \quad (31)$$

The steady oscillatory solution is therefore written as

$$u_{s,c}(y,t) = (0.5)(\alpha_1{}^{+2}-\alpha_2{}^{+2})^{-1} \times\left[\left(\alpha_1{}^{+2}\frac{I_0(\alpha_2{}^+ e^{-cy/2})}{I_0(\alpha_2{}^+)}-\alpha_2{}^{+2}\frac{I_0(\alpha_1{}^+ e^{-cy/2})}{I_0(\alpha_1{}^+)}\right)U+\frac{i\omega U}{\nu_{s,c}} \times\left(\frac{I_0(\alpha_1{}^+ e^{-cy/2})}{I_0(\alpha_1{}^+)}-\frac{I_0(\alpha_2{}^+ e^{-cy/2})}{I_0(\alpha_2{}^+)}\right)\right] e^{i\omega t} + (0.5)(\alpha_1{}^{-2}-\alpha_2{}^{-2})^{-1} \times\left[\left(\alpha_1{}^{-2}\frac{I_0(\alpha_2{}^- e^{-cy/2})}{I_0(\alpha_2{}^-)}-\alpha_2{}^{-2}\frac{I_0(\alpha_1{}^- e^{-cy/2})}{I_0(\alpha_1{}^-)}\right)U - \frac{i\omega U}{\nu_{s,c}}\left(\frac{I_0(\alpha_1{}^- e^{-cy/2})}{I_0(\alpha_1{}^-)}-\frac{I_0(\alpha_2{}^- e^{-cy/2})}{I_0(\alpha_2{}^-)}\right)\right] e^{-i\omega t} \quad (32)$$

where

$$\alpha_{1,2}{}^{\pm} = (\alpha_{1,2})_{p=\pm i\omega} \quad (33)$$

The representation of the transient solution (equation (30)), which is associated with the residues at the zeros of $\alpha_{1,2}$ and $I_0(\alpha_{1,2})$, as real definite integrals, may be made through the application of the usual method of contour integration. But the method and expressions are so lengthy that the enormous amount of work involved would not be justified. Therefore, the problem is reattempted using a finite Hankel transform. However, some useful approximate transient results from equation (30) will be obtained in the latter part of the paper.

The use of a finite Hankel transform along with $u_s(0,t) = U$, in equations (27) and (28) yields the following expression for the velocity of fluids $s = 1, 2$:

$$\frac{u_{s,c}}{U} = 2\sum_{i=1}^{\infty}\frac{(\nu'_{1,c}+k\nu'_{2,c}+\nu'_{1,c}\,\nu'_{2,c}\,\xi_i{}^2)\,\xi_i\,J_0(\xi_i\,e^{-cy/2})}{J_1(\xi_i)} \times\left[\frac{1}{r_1 r_2}-\frac{1}{r_1-r_2}\left\{\left(\frac{\nu'_{s,c}}{\nu'_{1,c}+k\nu'_{2,c}+\nu'_{1,c}\,\nu'_{2,c}\,\xi_i{}^2}-\frac{1}{r_1}\right)e^{-r_1 t} - \left(\frac{\nu'_{s,c}}{\nu'_{1,c}+k\nu'_{2,c}+\nu'_{1,c}\nu'_{2,c}\xi_i{}^2}-\frac{1}{r_2}\right)e^{-r_2 t}\right\}\right] \quad (34)$$

Here t is the time divided by τ_2 and $\nu'_{s,c} = \mu_s\tau_2 c^2/4\rho_{s,0}$; ξ_i are the roots of $J_0(\xi) = 0$, and

$$-\begin{pmatrix} r_1 \\ r_2 \end{pmatrix} = 0.5\,[\{(\nu'_{1,c}+\nu'_{2,c})\,\xi_i{}^2+k+1\} \pm\{[(\nu'_{1,c}+\nu'_{2,c})\,\xi_i{}^2+k+1]^2 - 4[\nu'_{1,c}\nu_{2,c}{}'\xi_i{}^4+(\nu'_{1,c}+k\nu'_{2,c})\,\xi_i{}^2]\}^{1/2}] \quad (35)$$

When second fluid is inviscid ($\mu_2 = 0$), equations (34) and (35) give

$$\frac{u_{1,c}}{U} = 1-2\nu'_{1,c}\sum_{i=1}^{\infty}\frac{\xi_i J_0(\xi_i e^{-cy/2})}{(r'_1-r'_2)\,J_1(\xi_i)} \times\left[\left(1-\frac{1}{r'_1}\right)e^{-r'_1 t}-\left(1-\frac{1}{r'_2}\right)e^{-r'_2 t}\right] \quad (36)$$

$$-\begin{pmatrix} r'_1 \\ r'_2 \end{pmatrix} = 0.5\,[(k+1+\nu'_{1,c}\xi_i{}^2) \pm[(k+1+\nu'_{1,c}\xi_i{}^2)^2-4\nu'_{1,c}\xi_i{}^2]^{1/2}] \quad (37)$$

which is in complete agreement with relation obtained by Healy [24]. If the plate oscillates with velocity $U\cos\omega t$, an application of Duhamel's theorem gives the expression of the velocity of the fluids as

$$\frac{u_{s,c}}{U} = 2\sum_{i=1}^{\infty}\xi_i\frac{[\nu'_{1,c}+k\nu'_{2,c}+\nu'_{1,c}\nu'_{2,c}\,\xi_i{}^2]}{r_1-r_2}\frac{J_0(\xi_i e^{-cy/2})}{J_1(\xi_i)} \times\left[\frac{1}{\lambda^2+\omega^2}\left(\frac{\lambda\nu'_{s,c}}{\nu'_{1,c}+k\nu'_{2,c}+\nu'_{1,c}\nu'_{2,c}\xi_i{}^2}-1\right) \times(\lambda\cos\omega t+\omega\sin\omega t-\lambda e^{-\lambda t})\right]\Bigg|_{\lambda=r_2}^{\lambda=r_1} \quad (38)$$

Equation (34) is recovered by setting $\omega = 0$ in equation (38). In addition, with $k = 0$, equation (38) reduces to the same form as equation (10), page 124 of Carslaw and Jaeger [36], which corresponds to velocity profile for noninteracting fluids. The wall shear stress ratio is obtained from equation (34) as

$$\frac{P_{(s,c),k}}{P_{(1,c),0}} = \frac{\mu_s}{\mu_1}\sum_{i=1}^{\infty}\frac{\xi_i{}^2[\nu'_{1,c}+k\nu'_{2,c}+\nu'_{1,c}\nu'_{2,c}\xi_i{}^2]}{r_1-r_2} \times\left[\left(\frac{\nu'_{s,c}}{\nu'_{1,c}+k\nu'_{2,c}+\nu'_{1,c}\nu'_{2,c}\xi_i{}^2}-\frac{1}{r_1}\right)e^{-r_1 t} - \left(\frac{\nu'_{s,c}}{\nu'_{1,c}+k\nu'_{2,c}+\nu'_{1,c}\nu'_{2,c}\xi_i{}^2}-\frac{1}{r_2}\right)e^{-r_2 t}\right]\Big/\sum_{i=1}^{\infty}e^{-\xi_i{}^2\nu'_{i,c}t} \quad (39)$$

When $\mu_2 = 0$, one finds

$$\frac{P_{(1,c),k}}{P_{(1,c),0}} = \nu'_{1,c}\sum_{i=1}^{\infty}\frac{\xi_i{}^2}{r'_1-r'_2}\left[\left(1-\frac{1}{r'_1}\right)e^{-r'_1 t} - \left(1-\frac{1}{r'_2}\right)e^{-r'_2 t}\right]\Big/\sum_{i=1}^{\infty}e^{-\xi_i{}^2\nu'_{1,c}t} \quad (40)$$

as found in [24]. Again for noninteracting fluids stress ratio becomes

$$\frac{P_{(1,c),0}}{P_{(1,0),0}} = 2(\pi\nu'_{1,c}t)^{1/2}\sum_{i=1}^{\infty}e^{-\xi_i{}^2\nu'_{1,c}t} \quad (41)$$

Some Approximate Results and Discussions

There are many interesting situations of physical importance which necessitate the determination of approximate results. Thus, in order to reveal the physical implications of the general solutions obtained for interacting phases, some approximate results for small and large time, noninteracting fluids, strongly interacting and extremely different fluids, etc., are obtained. If the time is not too large, the ratio of the Bessel functions $I_0(\theta r)/I_0(\theta)$ for small $\nu'_{s,c}$ may be written as

$$\frac{I_0(\theta r)}{I_0(\theta)} \sim \frac{1}{\sqrt{r}}e^{-\theta(1-r)}\left[1-\frac{1-r}{8\theta r}\cdots\right] \quad (42)$$

where $\theta = \alpha_{1,2}$ and are large. Use of $r \sim 1 - cy/2$, etc., in (42) yields

$$\frac{I_0(\theta e^{-cy/2})}{I_0(\theta)} \sim e^{-\theta cy/2}\left[1-\frac{cy}{16\theta}+O\left(\frac{1}{\theta^2}\right)\right] \quad (43)$$

Due to degeneracy, $\lim c \to 0$ ($\nu_{s,c} \to 0$) does not give results for nonstratified fluid ($\rho = \rho_0 = $ constant). Results for nonstratified fluid can now be deduced from the results of stratified fluid (equation (30)), using the foregoing asymptotic expansion for the Bessel functions, as

$$u_{s,c} \sim \frac{U}{2\pi i}\int_{\alpha-i\infty}^{\alpha+i\infty}\frac{p(\alpha_1{}^2-\alpha_2{}^2)^{-1}}{p^2+\omega^2}\left[(\alpha_1{}^2 e^{-(cy/2)\alpha_2}-\alpha_2{}^2 e^{-(cy/2)\alpha_1}) + \frac{p}{\nu_{s,c}}(e^{-(cy/2)\alpha_1}-e^{-(cy/2)\alpha_2})\right]e^{pt}\,dp - \frac{U}{2\pi i}\frac{cy}{16}\int_{\alpha-i\infty}^{\alpha+i\infty}\frac{p(\alpha_1{}^2-\alpha_2{}^2)^{-1}}{p^2+\omega^2}\left[\frac{1}{\alpha_2}\left(\alpha_1{}^2-\frac{p}{\nu_{s,c}}\right)e^{-(cy/2)\alpha_2} - \frac{1}{\alpha_1}\left(\alpha_2{}^2-\frac{p}{\nu_{s,c}}\right)e^{-(cy/2)\alpha_1}\right]e^{pt}\,dp + O(\nu_{s,c}) \quad (44)$$

The first term in equation (44) is the velocity for nonstratified fluid

Downloaded 01 May 2010 to 171.66.16.249. Redistribution subject to ASME license or copyright; see http://www.asme.org/terms/Terms_Use.cfm

whereas the second term is the first-order contribution from the stratification. Thus, in the limit, $c \to 0$, equation (6), the velocity for nonstratified fluid, is again recovered.

Small-Time Solution

Solution for small time is obtained by taking $|p|$ large and in this limit equation (31) reduces to

$$\alpha_s \sim \left(\frac{p}{\nu_{s,c}}\right)^{1/2}\left\{1 + \frac{1}{2\tau_s}\cdot\frac{1}{p} + O\left(\frac{1}{p^2}\right)\right\} \tag{45}$$

and accordingly the expression for velocity of fluids $s = 1, 2$, using the foregoing asymptotic expansion for the Bessel functions, are given from equation (30) as

$$\frac{u_{s,c}}{U} \sim e^{cy/4}\left[\operatorname{erfc}\eta_s\left[1 + 2{\eta_s}^2\left(\frac{t}{\tau_s}\right)\right] - \frac{2}{\sqrt{\pi}}\eta_s\, e^{-{\eta_s}^2}\left(\frac{t}{\tau_s}\right)\right] - \frac{cy}{8}e^{cy/2}\sqrt{\nu_{s,c}t}\left[\frac{1}{\sqrt{\pi}}e^{-{\eta_s}^2} - \eta_s \operatorname{erfc}\eta_s\right] + O\left(\frac{t}{\tau_s}\right)^2 \tag{46}$$

Thus, for small time and up to the first approximation, one fluid in the mixture experiences the effect of other fluid as if the other fluid were inviscid. Again by taking $\tau_s \to \infty$ (noninteracting fluids) in equation (46), one can see the reflection of stratification in the Stokes first problem: $u_s = U \operatorname{erfc} y/2\sqrt{\nu_s t}$ through the second term of equation (46). Also in the limit $c \to 0$, equation (11), the velocity for nonstratified fluid, is recovered.

Finally, the dimensionless wall shear stress ratio becomes

$$\frac{P_{(1,2)c,k}}{P_{1c,0}} \sim \left[\frac{\mu_{1,2}}{\mu_2}\left(\frac{\nu_{1,c}}{\nu_{(1,2),c}}\right)^{1/2}\left\{1 + \sqrt{\nu_{(1,2),c}}\,\frac{[\tau_2/\tau_1\sqrt{\nu_{1,c}} + \sqrt{\nu_{2,c}}]}{(\sqrt{\nu_{1,c}} + \sqrt{\nu_{2,c}})^2} \times \left(1 - \sqrt{\nu_{(2,1),c}/\nu_{(1,2),c}}\left(\frac{t}{\tau_2}\right)\right\} - \frac{1}{2}\sqrt{\pi\nu_{(1,2),c}t}\right] \Big/ \left(1 - \frac{1}{2}\sqrt{\pi\nu_{1,c}t}\right) \tag{47}$$

If the second fluid is inviscid ($\nu_{2,c} = 0$), the shear stress ratio from equation (47) becomes

$$\frac{P_{1c,k}}{P_{1c,0}} \sim \frac{1 + t/\tau_1 - \frac{1}{2}\sqrt{\pi\nu_{1,c}t}}{1 - \frac{1}{2}\sqrt{\pi\nu_{1,c}t}} \tag{48}$$

which is the same as obtained by Healy [24]. Again in the limit $c \to 0$, equation (47) gives shear stress ratio for nonstratified fluid as obtained in equation (13). Further in this limit equation (48) reduces to equation (14).

Large-Time Solution

Using the approximate values of $\alpha_{1,2}$ (following equations (15) and (16)) and the foregoing asymptotic expansion for the Bessel functions, one obtains the velocity for large time as

$$\frac{u_{1,c}}{U} \sim e^{cy/4}\left[\operatorname{erfc}\bar{\eta}_{1,c} + \frac{\bar{\eta}_{1,c}\tau_1\tau_2(\nu_{1,c} - \nu_{2,c})}{\sqrt{\pi}(\nu_{1,c}\tau_1 + \nu_{2,c}\tau_2)^2}\left\{\frac{\tau_1(\nu_{1,c} - \nu_{2,c})}{\tau_1 + \tau_2} \times \left(\bar{\eta}_{1,c}{}^2 - \frac{1}{2}\right) + \nu_{2,c}\right\} e^{-\bar{\eta}_{1,c}{}^2}\left(\frac{\tau_2}{t}\right)\right] - \frac{cy}{16}e^{cy/2} \times \left[\left(-\frac{cy}{2}\right)\operatorname{erfc}\bar{\eta}_{1,c} + \frac{1}{\sqrt{\pi}}\sqrt{\nu_{m,c}t}\, e^{-\bar{\eta}_{1,c}{}^2}\right] + \frac{\tau_1{}^2\tau_2(\nu_{1,c} - \nu_{2,c})}{8\sqrt{\pi t}(\nu_{1,c}\tau_1 + \nu_{2,c}\tau_2)^4}\left(\bar{\eta}_{1,c}^2 - \frac{1}{2}\right)\left\{\frac{\tau_1\tau_2(\nu_{1,c} - \nu_{2,c})^2}{(\tau_1 + \tau_2)^2} \times [\nu_{1,c}\tau_1(3\tau_2 + 4\tau_1) - \nu_{2,c}\tau_2(3\tau_1 + 4\tau_2)] + 8\nu_{1,c}\nu_{2,c} \times [\nu_{2,c}\tau_2(\tau_2 + 2\tau_1) - \nu_{1,c}\tau_1(2\tau_2 + \tau_1)] + 4\nu_{1,c}\nu_{2,c}\tau_1\tau_2 \times (\nu_{1,c} - \nu_{2,c}) + \frac{2\tau_1{}^2\tau_2{}^2(\nu_{1,c} - \nu_{2,c})^3}{(\tau_1 + \tau_2)^2} + 2cy(\nu_{1,c} - \nu_{2,c}) \times \sqrt{\nu_{1,c}\nu_{2,c}\tau_1\tau_2(\tau_1 + \tau_2)}\,\nu_{m,c}{}^{3/2} + 4\nu_{2,c}(\tau_1 + \tau_2)(\nu_{2,c}\tau_2 - \nu_{1,c}\tau_1)\,\nu_{m,c}{}^{3/2}\right\}\left(\frac{\tau_2}{t}\right) + O\left(\frac{\tau_2}{t}\right)^2 \tag{49}$$

with

$$\bar{\eta}_{1,c} = \frac{1}{2}cy/2\sqrt{\nu_{m,c}t}, \quad \nu_{m,c} = \frac{\nu_{1,c}\tau_1 + \nu_{2,c}\tau_2}{\tau_1 + \tau_2} \tag{50}$$

Following a similar approach one can obtain the results for the second-phase velocity and the wall shear stress. When time is sufficiently large i.e., $t/\tau_2 \to \infty$, the velocity of fluids from equation (49) become

$$\tilde{u}_c = u_{1,c} = u_{2,c} = e^{cy/4}\operatorname{erfc}\bar{\eta}_{1,c} - \frac{cy}{8}e^{cy/2}\sqrt{\nu_{m,c}t} \times \left[\frac{1}{\sqrt{\pi}}e^{-\bar{\eta}_{1,c}{}^2} - \bar{\eta}_{1,c}\operatorname{erfc}\bar{\eta}_{1,c}\right] \tag{51}$$

Thus, in this case, the two-phase system behaves as a single fluid of kinematic viscosity $\nu_{m,c}$, i.e., an equilibrium state has been reached. Further, in the limit $c \to 0$, equation (18), velocity for nonstratified fluid, is recovered.

The large-time results for the velocity and the wall shear stress just obtained are so lengthy that the enormous amount of work involved in the numerical study of the expressions would not be justified. Therefore, results for sufficiently large time is again obtained from equation (34) taking $\xi_i = \xi_1$ (for large time the contribution of ξ_1 only will be significant), as

$$\frac{u_{s,c}}{U} \sim 1 - \frac{2}{\xi}\frac{J_0(\xi_1 e^{-cy/2})}{J_1(\xi_1)}e^{-{\xi_1}^2\nu'_{m,c}t}, \ (\nu'_{s,c} \text{ is not too large}) \tag{52}$$

with $\nu'_{m,c} = \nu'_{1,c}\tau_1 + \nu'_{2,c}\tau_2/(\tau_1 + \tau_2)$, is the kinematic viscosity of the mixture. Comparison of equation (52) and equation (10) of reference [38, p. 124] shows that the two-phase system behaves as a single fluid of viscosity $(\mu_1 + \mu_2)$ and density $(\rho_1 + \rho_2)$; i.e., an equilibrium state has been established.

Consequently, the wall shear stress ratio from equation (52) is given as

$$\frac{P_{(s,c,),k}}{P_{(1,c),0}} \sim \frac{\mu_s}{\mu_1}e^{-{\xi_1}^2(\nu'_{m,c} - \nu'_{1,c})t} \tag{53}$$

Noninteracting Fluids ($\tau_s \to \infty$)

The interaction force between the two interacting fluids will be eliminated by assuming the interaction time go to infinity; i.e., $\tau_s \to \infty$. In this limit, equation (31) reduces to

$$\alpha_{1,2}{}^+ \sim (1 + i)\,(\omega/2\nu_{(1,2),c})^{1/2}, \quad \alpha_{1,2}{}^- \sim i(1 + i)\,(\omega/2\nu_{(1,2),c})^{1/2} \tag{54}$$

In view of equation (54), equation (32) assumes the form

$$u_{s,c} \sim \frac{U}{2}\left[\frac{I_0(q_s e^{-cy/2})}{I_0(q_s)}e^{i\omega t} + \frac{J_0(q_s e^{-cy/2})}{J_0(q_s)}e^{-i\omega t}\right] \tag{55}$$

where

$$q_s = (1 + i)\sqrt{\frac{\omega}{2\nu_{s,c}}} \tag{56}$$

Further, use of the Bessel function $I_0(zr)$ expansions (for small and large complex arguments)

$$I_0(zr) \sim \sum_{n=0}^{\infty}(n!)^{-2}\left(\frac{zr}{2}\right)^{2n}, \quad |z|r < 1 \tag{57}$$

$$I_0(zr) \sim (2\pi\, zr)^{-1/2}\, e^{zr}\sum_{n=0}^{\infty}\frac{[(2n-1)!]^2}{n!}(8zr)^{-n}, \quad |z|r > 1 \tag{58}$$

in equation (55), yields

$$u_{s,c} \sim \frac{U}{8}[{p_s}^+ e^{i\omega t} + {p_s}^- e^{-i\omega t}], \quad \omega/\nu_{s,c} \ll 1 \tag{59}$$

$$u_{s,c} \sim \frac{U}{2}[e^{\beta_s + i\omega t + cy/4} + e^{i\beta_s - i\omega t + cy/4}], \quad e^{-cy/2}\frac{\omega}{\nu_{s,c}} \gg 1 \tag{60}$$

where

Downloaded 01 May 2010 to 171.66.16.249. Redistribution subject to ASME license or copyright; see http://www.asme.org/terms/Terms_Use.cfm

$$p_s^{\pm} = \frac{4 \pm i\omega/\nu_{s,c} e^{-cy}}{1 \pm i\omega/\nu_{s,c}} \tag{61}$$

$$\beta_s = (1+i)(e^{-cy/2} - 1)\sqrt{\omega/2\nu_{s,c}} \tag{62}$$

Using the asymptotic expansion of the Bessel function (equation (43)) in equation (55), one finds

$$u_{s,c} \sim Ue^{-(cy/2)\sqrt{\omega/2\nu_{s,c}}} \cos\left[\omega t - \frac{cy}{2}\sqrt{\frac{\omega}{2\nu_{2,c}}}\right] + \frac{cy}{16(1+i)}\sqrt{\frac{2\nu_{s,c}}{\omega}}(e^{i\omega t} - ie^{-i\omega t}) \tag{63}$$

In the limit $c \to 0$, equation (63) becomes

$$u_s \sim Ue^{-y\sqrt{\omega/2\nu_s}} \cos\left[\omega t - y\sqrt{\frac{\omega}{2\nu_s}}\right] \tag{64}$$

which is the Stokes second problem [33]. Thus the velocity for nonstratified fluid (equation (26) in absence of transient part) is recovered. It may be noted here that fluids in mixture behave as noninteracting components for oscillation periods $\omega^{-1} \ll \tau_s$.

Strongly Interacting Fluids ($\tau_s \ll \omega^{-1}$)

When oscillation frequency ω is small, the implication is that the relaxation time τ_s is small in comparison with the period of oscillation, i.e., $\tau_s \ll \omega^{-1}$, and then one-phase velocity will follow the velocity of other phase very closely and thus the fluids start interacting strongly by intercomponent friction force. In the limit $\tau_s \ll \omega^{-1}$, equation (31) reduces to

$$\alpha_1^{\pm} \sim \left(\frac{1}{\nu_{1,c}\tau_1} + \frac{1}{\nu_{2,c}\tau_2}\right)^{1/2}, \quad \alpha_2^{+} \sim (1+i)\left(\frac{\omega}{2\nu_{m,c}}\right)^{1/2}, \quad \alpha_2^{-} = i\alpha_2^{+} \tag{65}$$

also

$$O\left[\alpha_2^{+2}/\alpha_1^{+2}\right] = 0\left[\alpha_2^{-2}/\alpha_1^{-2}\right] = O\left[\omega\tau_s\right] \ll 1 \tag{66}$$

In view of equations (65) and (66), equation (32) assumes the form

$$u_{s,c} \sim \frac{U}{2}\left[\frac{I_0(\psi e^{-cy/2})}{I_0(\psi)} e^{i\omega t} + \frac{J_0(\psi e^{-cy/2})}{J_0(\psi)} \bar{e}^{i\omega t}\right] \tag{67}$$

where

$$\psi = (1+i)\sqrt{\frac{\omega}{2\nu_{m,c}}} \tag{68}$$

Use of the Bessel function expansions, equations (57) and (58) in equation (67), yields

$$u_{s,c} \sim \frac{U}{8}\left[\nu_1^{+} e^{i\omega t} + \nu_1^{-} e^{-i\omega t}\right], \quad \frac{\omega}{\nu_{m,c}} \ll 1 \tag{69}$$

$$u_{s,c} \sim \frac{U}{2}\left[e^{(\nu_2 + i\omega t + cy/4)} + e^{(i\nu_2 - i\omega t + cy/4)}\right], \quad e^{-cy/2}\frac{\omega}{\nu_{m,c}} \gg 1 \tag{70}$$

where

$$\nu_1^{\pm} = \frac{4 \pm i\omega/\nu_{m,c} e^{-cy}}{1 \pm i\omega/\nu_{m,c}} \tag{71}$$

$$\nu_2 = (1+i)(e^{-cy/2} - 1)\sqrt{\omega/2\nu_{m,c}} \tag{72}$$

Further, using the asymptotic expansion of the Bessel function (equation (44)) in equation (67), one finds

$$u_{s,c} \sim Ue^{-(cy/2)\sqrt{\omega/2\nu_{m,c}}} \cos\left[\omega t - \frac{cy}{2}\sqrt{\frac{\omega}{2\nu_{m,c}}}\right] + \frac{cy}{16(1+i)}\sqrt{\frac{2\nu_{m,c}}{\omega}}(e^{i\omega t} - i\bar{e}^{i\omega t}) \tag{73}$$

In the limit $c \to 0$, equation (73), becomes

$$u_s \sim Ue^{-y\sqrt{\omega/2\nu_m}} \cos\left[\omega t - y\sqrt{\frac{\omega}{2\nu_m}}\right] \tag{74}$$

Comparison of equations (55)–(64) and (67)–(74) shows that the two-phase system behaves as a single fluid of kinematic viscosity $\nu_{m,c}$ and hence an equilibrium state is established.

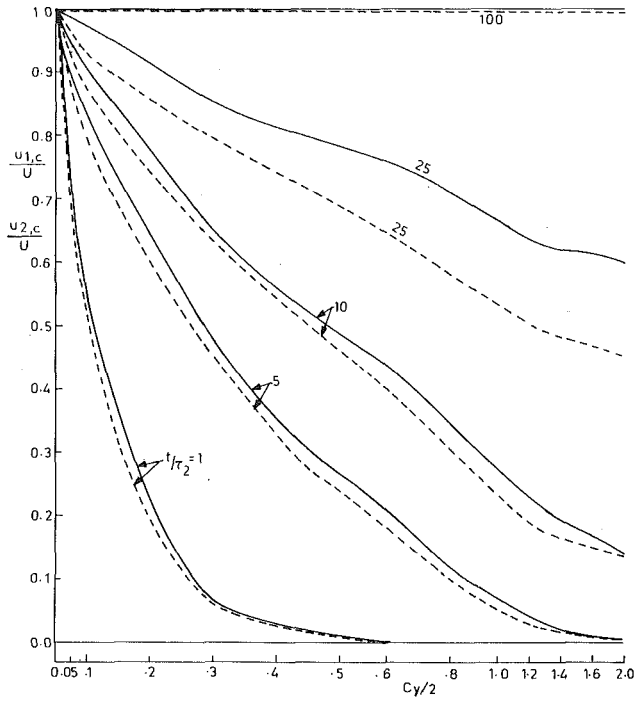


Fig. 1 Exact stratified velocity profiles for noninteracting fluids mixture for $\nu'_{1,c} = 0.01$, $\nu'_{2,c} = 0.009$; —— u_1, - - - u_2

Extremely Different Fluids ($\mu_2 \gg \mu_1$)

When the two fluids are extremely different, i.e., $\mu_2 \gg \mu_1$ (say), we can use the relation $\nu_{2,c}\tau_2 \gg \nu_{1,c}\tau_1$ as $\tau_2/\rho_2 = \tau_1/\rho_1$. If, in addition, the fluids are considered strongly interacting, i.e., $\tau_s \ll \omega^{-1}$, equation (31) reduces to

$$\alpha_1^{\pm} \sim \sqrt{1/\nu_{1,c}\tau_1}, \; \alpha_2^{+} \sim (1+i)\left(\frac{\omega}{2\bar{\nu}_{2,c}}\right)^{1/2}, \; \alpha_2^{-} = i(1+i)\left(\frac{\omega}{2\bar{\nu}_{2,c}}\right)^{1/2} \tag{75}$$

with

$$\bar{\nu}_{2,c} = \frac{\nu_{2,c}\tau_2}{\tau_1 + \tau_2} \tag{76}$$

In view of equation (75), equation (32) assumes the form

$$u_{s,c} \sim \frac{U}{2}\left[\frac{I_0(\phi e^{-cy/2})}{I_0(\phi)} e^{i\omega t} + \frac{J_0(\phi e^{-cy/2})}{J_0(\phi)} \bar{e}^{i\omega t}\right] \tag{77}$$

where

$$\phi = (1+i)\sqrt{\frac{\omega}{2\bar{\nu}_{2,c}}} \tag{78}$$

Use of the Bessel function expansions, equations (57) and (58) in equation (74), yields

$$u_{s,c} \sim \frac{U}{8}\left[\delta_1^{+} e^{i\omega t} + \delta_1^{-} e^{-i\omega t}\right], \quad \frac{\omega}{\bar{\nu}_{2,c}} \ll 1 \tag{79}$$

$$u_{s,c} \sim \frac{U}{2}\left[e^{(\delta_2 + i\omega t + cy/4)} + e^{(i\delta_2 - i\omega t + cy/4)}\right], \quad e^{-cy/2}\frac{\omega}{\bar{\nu}_{2,c}} \gg 1 \tag{80}$$

where

$$\delta_1^{\pm} = \frac{4 \pm i\omega/\bar{\nu}_{2,c} e^{-cy}}{1 \pm i\omega/\bar{\nu}_{2,c}} \tag{81}$$

$$\delta_2 = (1+i)(e^{-cy/2} - 1)\sqrt{\omega/2\bar{\nu}_{2,c}} \tag{82}$$

Downloaded 01 May 2010 to 171.66.16.249. Redistribution subject to ASME license or copyright; see http://www.asme.org/terms/Terms_Use.cfm

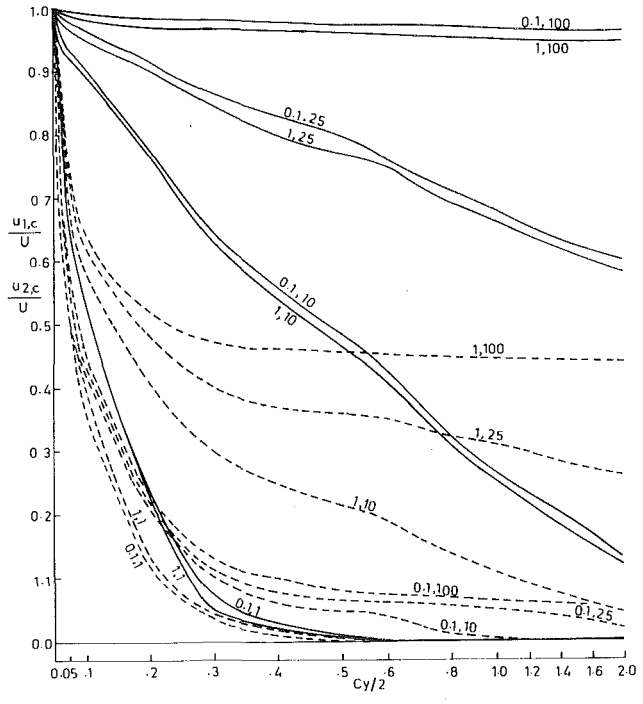


Fig. 2 Exact stratified velocity profiles for $\nu'_{1,c} = 0.01$, $\nu'_{2,c} = 0.009$; numbers k, t/τ_2; —— U_1, - - - U_2

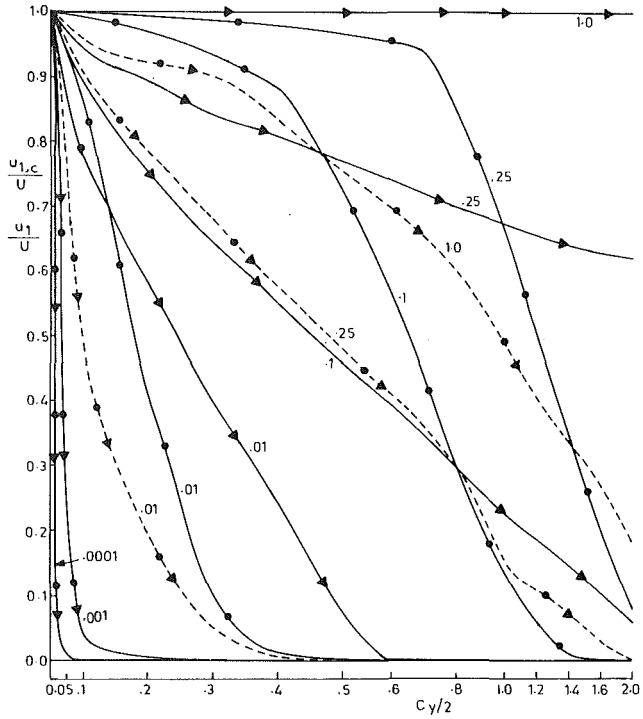


Fig. 4 Approximate velocity profiles for large and small time for noninteracting fluids mixture $\nu'_{1,c} = 0.01$, numbers $\nu'_{1,c}t$; —— stratified, - - - - nonstratified, ▶▶▶ large time, ●●● small time

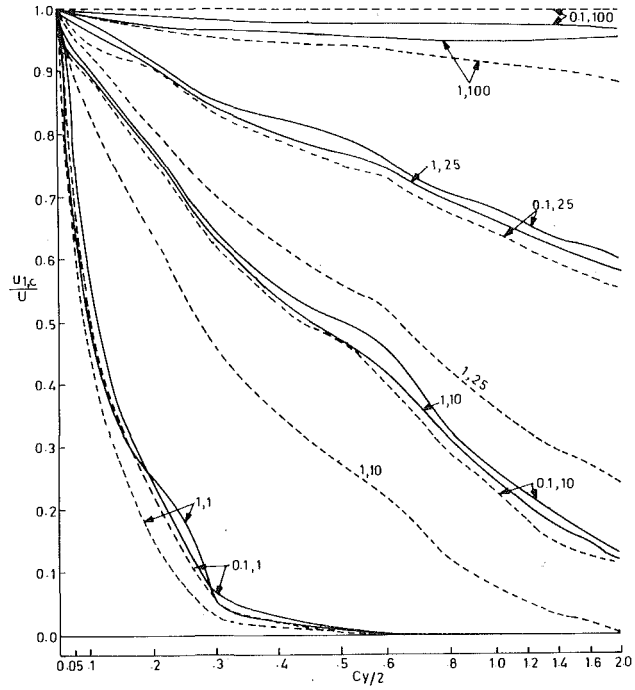


Fig. 3 Exact stratified velocity profiles for $\nu'_{1,c} = 0.01$, $\nu'_{2,c} = 0.009$; numbers k, t/τ_2; —— $\nu'_{2,c} = 0.009$, - - - $\nu'_{2,c} = 0.0$

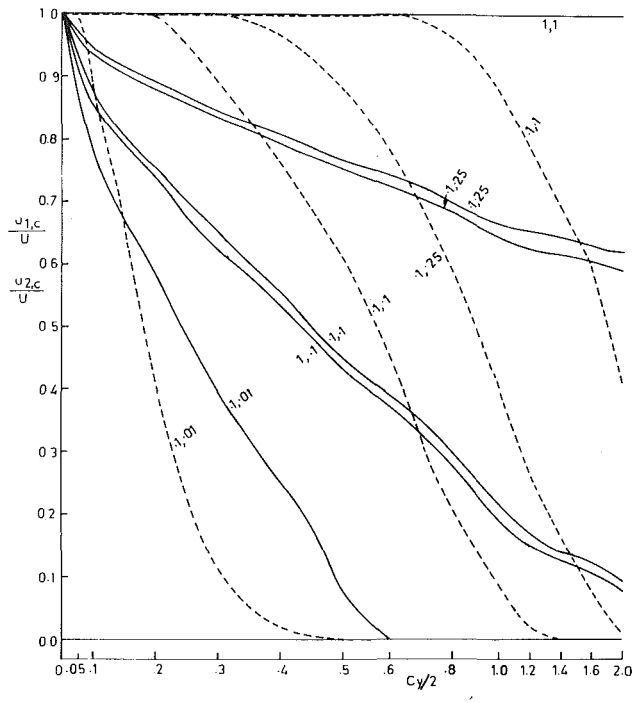


Fig. 5 Approximate velocity profiles for large time for $\nu'_{1,c} = 0.01$, $\nu'_{2,c} = 0.009$; numbers k, $\nu'_{1,c}t$, —— stratified, - - - nonstratified

Further, using the asymptotic expansion of the Bessel function (equation (43)) in equation (77), one finds

$$u_{s,c} \sim Ue^{-(cy/2)\sqrt{\omega/2\bar{\nu}_{2,c}}} \cos\left[\omega t - \frac{cy}{2}\sqrt{\frac{\omega}{2\bar{\nu}_{2,c}}}\right] + \frac{cy}{16(1+i)}\sqrt{\frac{2\bar{\nu}_{2,c}}{\omega}}(e^{i\omega t} - ie^{-i\omega t}) \quad (83)$$

In the limit $c \to 0$, equation (83) becomes

$$u_s \sim Ue^{-y\sqrt{\omega/2\bar{\nu}_2}} \cos\left[\omega t - y\sqrt{\frac{\omega}{2\bar{\nu}_2}}\right] \quad (84)$$

Comparison of equations (67)–(74) and equations (77)–(84) shows that

Downloaded 01 May 2010 to 171.66.16.249. Redistribution subject to ASME license or copyright; see http://www.asme.org/terms/Terms_Use.cfm

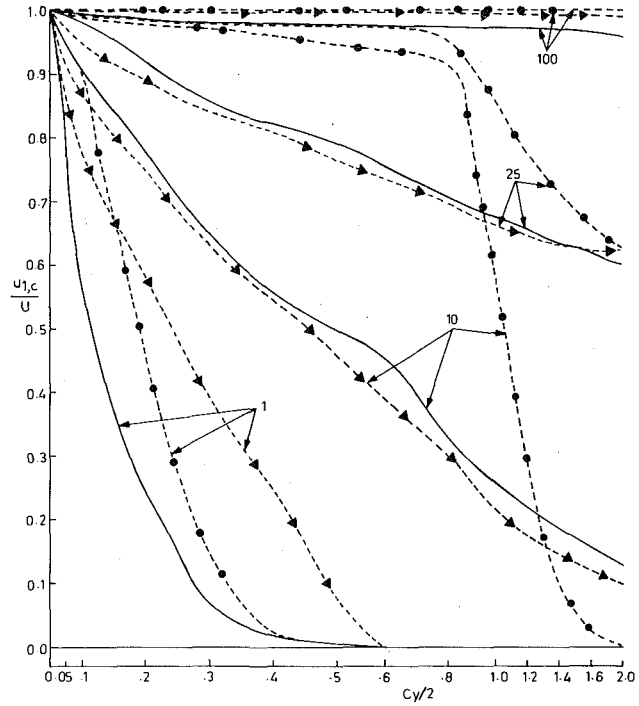


Fig. 6 Exact and asymptotic stratified velocity profiles for $k = 0.1$; $\nu'_{1,c} = 0.01$, $\nu'_{2,c} = 0.009$; numbers t/τ_2, —— exact, - - - asymptotic, ▶▶▶ large time, ●●● small time

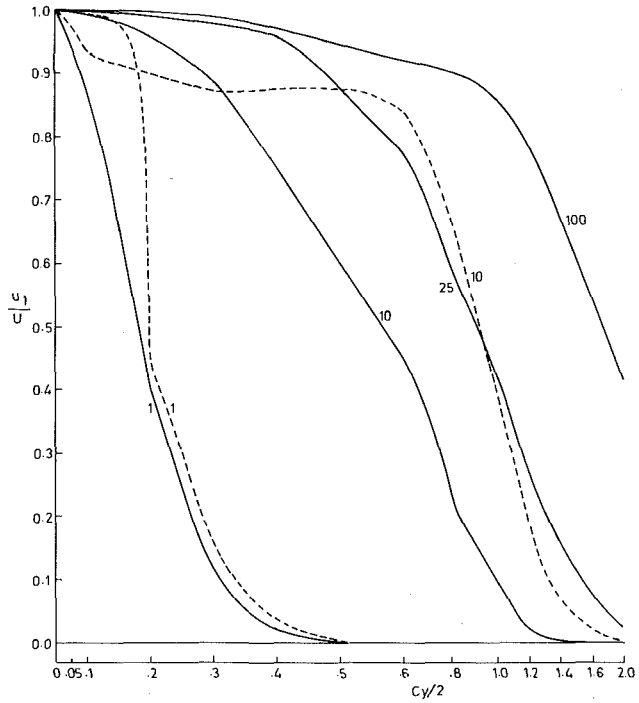


Fig. 7 Approximate nonstratified velocity profiles for large and small time for $k = 1$, $\nu'_{1,c} = 0.01$, $\nu'_{2,c} = 0.009$, numbers t/τ_2, —— large time, - - - small time

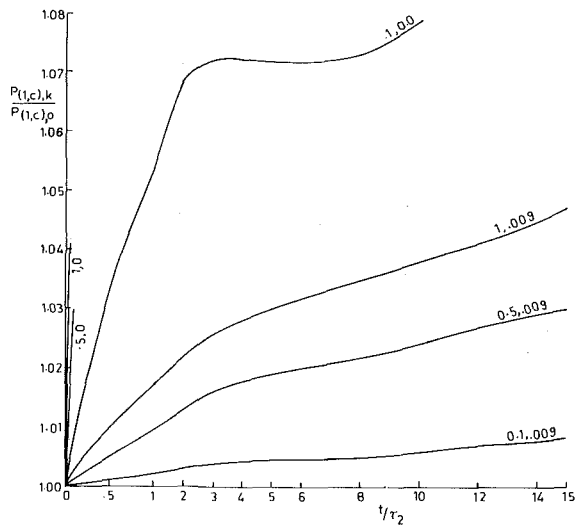


Fig. 8 Exact stratified wall shear stress for $\nu'_{1,c} = 0.01$; number k, $\nu'_{2,c}$;

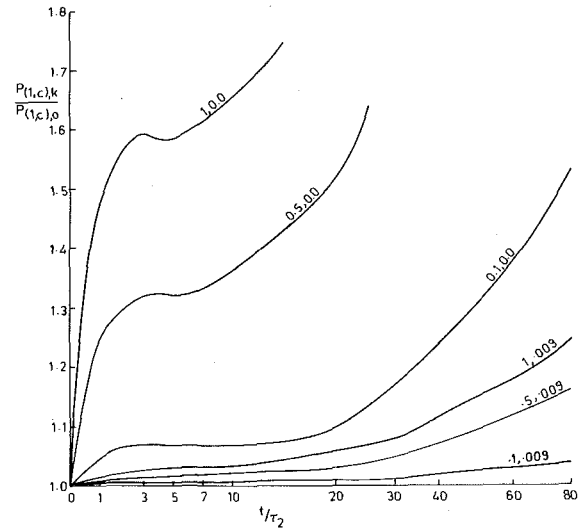


Fig. 9 Exact stratified wall shear stress for $\nu'_{1,c} = 0.01$; numbers k, $\nu'_{2,c}$

now the two-phase system behaves as a single fluid of kinematic viscosity $\mu_2/(\rho_1 + \rho_2)$ and hence the effect of one fluid on the other is to reduce the effective kinematic viscosity to $\nu_{2,c}/(1 + \rho_1/\rho_2)$. It may also be noted that in this case the system behaves as a mixture of viscous and nonviscous fluids. Further, when $\mu_1 = 0$, the results of strongly interacting fluids (equations (67)–(74)) reduce to the corresponding results of extremely different fluids (equations (77)–(84)).

Numerical Results and Discussions

To gain an insight into the patterns of flow, the exact and approximate velocity profiles for both density stratified and nonstratified fluids flow have been plotted (Figs. 1–7). Comparison between (*i*) stratified and nonstratified flows; (*ii*) exact and approximate results; (*iii*) velocity profiles of both the constituents; (*iv*) mixture of two different interacting viscous fluids and mixture of one viscous and other nonviscous interacting fluid flows; (*v*) mixture of two noninteracting fluid flows, have been shown in the graphs. The series in equations (34) and (39) have been summed using a digital computer for the first forty zeros of the Bessel function $J_0(\xi)$. The values of $\nu'_{1,c}$ and $\nu'_{2,c}$ are taken as 0.01, and 0.009, respectively. Since

$$\operatorname{erfc}\left(\frac{y}{2\sqrt{\mu_s/\rho_{s,0}\,t}}\right) = \operatorname{erfc}\left(\frac{cy/2}{2\sqrt{\nu'_{s,c}t}}\right),$$

the velocity profiles for the density nonstratified fluid flow may also be shown in the graphs of the stratified fluid flow (Figs. 4 and 5). Fig. 4 reveals that when time is small, say, $\nu'_{1,c}\,t < 0.001$, the stratification has a very small effect on the flow. But, when $\nu'_{1,c}t > 0.001$, the difference between the stratified and nonstratified profiles increases rapidly with the increase in time, in particular at a large distance from

Downloaded 01 May 2010 to 171.66.16.249. Redistribution subject to ASME license or copyright; see http://www.asme.org/terms/Terms_Use.cfm

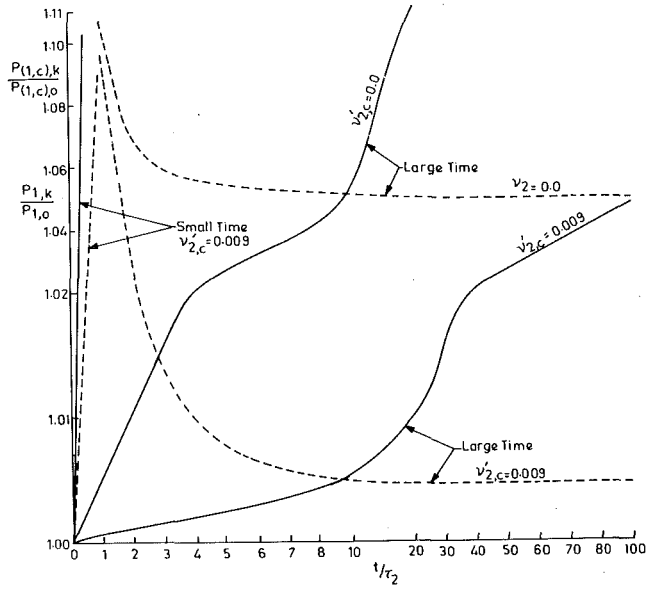


Fig. 10 Approximate stratified and nonstratified wall shear stress for large and small time, $\nu'_{1,c} = 0.01$, $k = 0.1$; —— stratified, - - - nonstratified

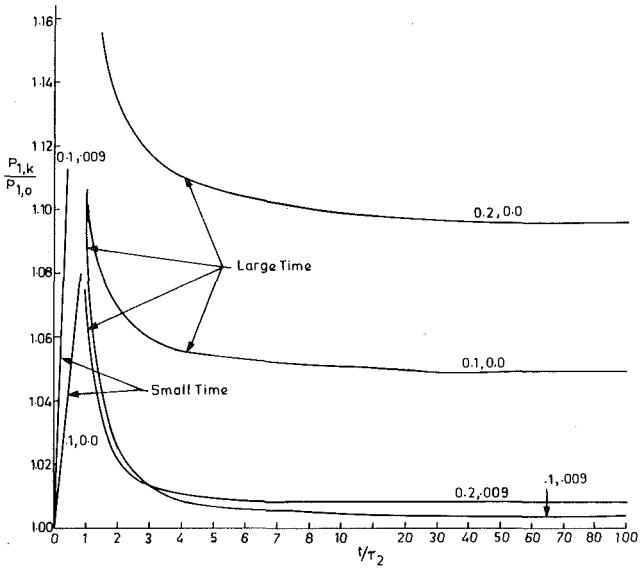


Fig. 12 Approximate nonstratified wall shear stress for large and small time; $\nu'_{1,c} = 0.01$; $k = 0.1, 0.2$; numbers k, $\nu'_{2,c}$

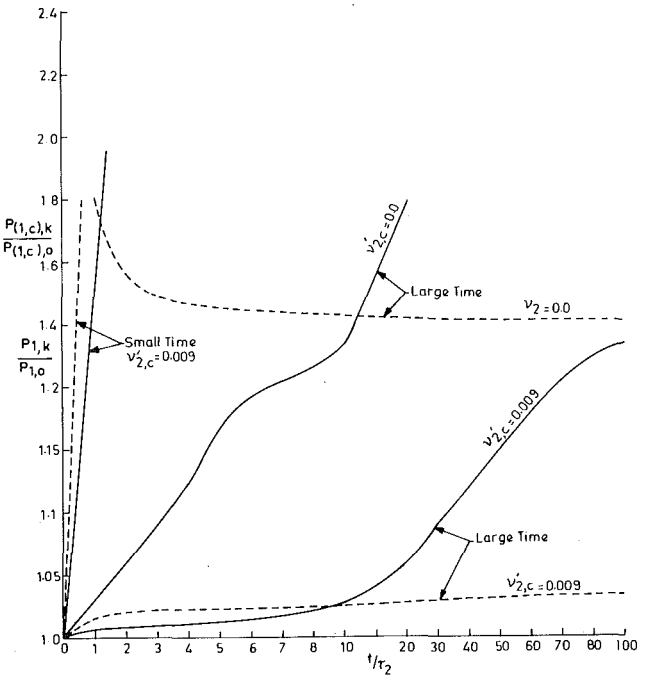


Fig. 11 Approximate stratified and nonstratified wall shear stress for large and small time, $\nu'_{1,c} = 0.01$; $k = 1$; —— stratified, - - - nonstratified

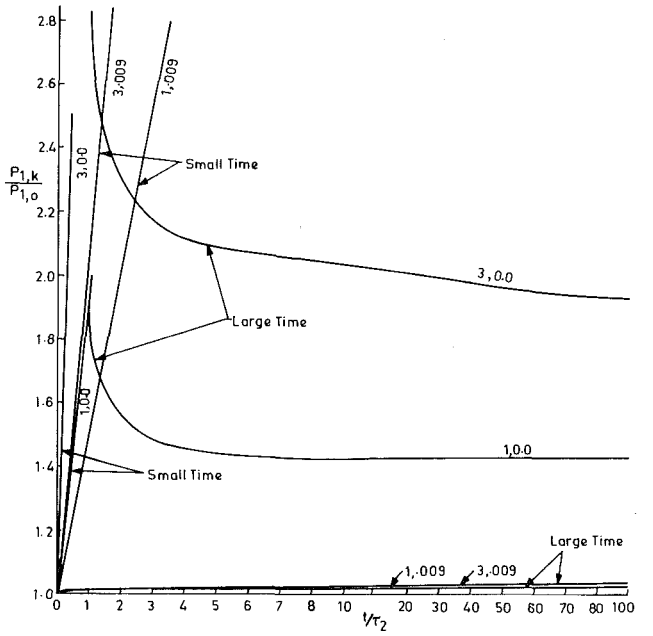


Fig. 13 Approximate nonstratified wall shear stress for large and small time; $\nu'_{1,c} = 0.01$; $k = 1, 3$; numbers k, $\nu'_{2,c}$

the plate. Fig. 6 shows that, apart from the value $t/\tau_2 \leqslant 1$, large-time asymptotic expansion gives a fairly accurate representation of velocity profiles for the stratified fluid.

Exact and asymptotic (large and small time) wall shear stress ratio for both the stratified and the nonstratified flows have been plotted in Figs. 8–13. Fig. 11 shows that for $k = 1$, the stratification has a very small effect on the shear stress ratio when $t/\tau_2 \leqslant 10$, but the difference between the stratified and the nonstratified shear stress increases rapidly with time when $t/\tau_2 > 10$. For $k = 0.1$ (Fig. 10), the difference between the stratified and the nonstratified shear stress decreases in the range $0 < t/\tau_2 < 10$, almost zero at $t/\tau_2 = 0$ and increases rapidly with time when $t/\tau_2 > 10$.

Acknowledgment

The authors gratefully acknowledge support of this work by a Project-Grant from the Ministry of Education and Social Welfare, Government of India.

References

1 Truesdell, C., *Atti Accad. Naz. Lincei Rc.*, Series 8, Vol. 22, 1957, pp. 33, 158; also translation by the author in *Continuum Mechanics II. The Rational Mechanics of Materials*, 1965, pp. 295, ed., Truesdell, C., Gordon and Breach, New York

2 Truesdell, C., and Toupin, R., "The Classical Field Theories," *Handbuch der Physik*, ed., Flügge, S., Vol. III/I, Springer-Verlag, Berlin, 1960, pp. 226.

Downloaded 01 May 2010 to 171.66.16.249. Redistribution subject to ASME license or copyright; see http://www.asme.org/terms/Terms_Use.cfm

3 Eringen, A. C., and Ingram, J. D. "A Continuum Theory of Chemically Reacting Media—I," *International Journal of Engineering Science*, Vol. 3, 1965, pp. 197–212.

4 Green, A. E., and Naghdi, P. M., "A Dynamical Theory of Interacting Continua," *International Journal of Engineering Science*, Vol. 3, 1965, pp. 231–241.

5 Mills, N., "Incompressible Mixture of Newtonian Fluids," *International Journal of Engineering Science*, Vol. 4, 1966, pp. 97–112.

6 Mills, N., "On a Theory of Multi-Component Mixture," *Quarterly Journal of Mechanics and Applied Mathematics*, Vol. 20, 1967, pp. 499–508.

7 Atkin, R. J., and Craine, R. E., "Continuum Theories of Mixtures: Basic Theory and Historical Development," *Quarterly Journal of Mechanics and Applied Mathematics*, Vol. 29, 1976, pp. 209–244.

8 Atkin, R. J., and Craine, R. E., "Continuum Theories of Mixtures: Application," *Journal of the Institute of Mathematics and Application*, Vol. 17, 1976, pp. 153–207.

9 Wilhelm, H. E., and Vander Werff, T. J., "Oscillating Flows of Miscible Fluids," *Applied Scientific Research*, Vol. 33, 1977, pp. 339–352.

10 Marble, F. E., "Dynamics of a Gas Containing Small Solid Particles," presented at the Fifth AGARD Combustion and Propulsion Colloquium, Braunschweig, 1962.

11 Marble, F. E., "Dynamics of Dusty Gas," *Annual Review of Fluid Mechanics*, Vol. 2, 1971, pp. 397–446.

12 Soo, S. L., *Fluid Dynamics of Multiphase Systems*, Blaisdell Publishing Company, Waltham, Mass., 1967.

13 Davidson, J. F., and Harrison, D., *Fluidized Particles*, Cambridge Press, London, 1963.

14 Murray, J. D., "Some Basic Aspects of One-Dimensional Incompressible Particle-Fluid Two-Phase Flows," *Astronautica Acta*, Vol. 13, 1967, pp. 417–430.

15 Brenner, H., "Rheology of Two-Phase Systems," *Annual Review of Fluid Mechanics*, Vol. 2, 1970, pp. 131–176.

16 Digiovanni, P. R., and Lee, S. L., "Impulsive Motion in a Particle-Fluid Suspension Including Particulate Volume, Density, and Migration Effects," ASME JOURNAL OF APPLIED MECHANICS, Vol. 41, 1974, pp. 35–41.

17 Drew, D. A., "Two-Phase Flows: Consitutive Equations for Lift and Brownian Motion and Some Basic Flows," *Arch Rational Mechanics and Analysis*, Vol. 62, 1976, pp. 149–163.

18 Drew, D. A., "Lubrication Flow of a Particle Fluid Mixture," ASME JOURNAL OF APPLIED MECHANICS, Vol. 6, 1979, pp. 211–213.

19 Peddison, J., "Some Unsteady Parallel Flows of Particulate Suspensions," *Applied Scientific Research*, Vol. 32, 1976, pp. 239–268.

20 Lightfoot, E. N., *Transport Phenomena and Living Systems*, Wiley, New York, 1974.

21 Hung, T. K., and Brown, T. D., "Solid-Particles Motion in Two-Dimensional Peristaltic Transport," *Journal of Fluid Mechanics*, Vol. 73, 1976, pp. 77–96.

22 Karino, T., Kwong, H. H. M., and Goldsmith, H. L., "Particle Flow Behavior in Models of Branching Vessels: 1 Vortices in 90°T-Junction," *Biorheology*, Vol. 16, 1979, pp. 231–248.

23 Srivastava, L. M., and Agarwal, R. P., "Oscillating Flow of a Conducting Fluid with a Suspension of Spherical Particles," ASME JOURNAL OF APPLIED MECHANICS, Vol. 47, 1980, pp. 196–200.

24 Healy, J. V., "The Plane Parallel Flow of a Density Stratified Fluid with and Without a Suspension of Particles," ASME JOURNAL OF APPLIED MECHANICS, Paper No. 72-APM-JJJ.

25 Srivastava, L. M., Srivastava, V. P., and Agarwal, R. P., "Boundary Layer of Density Stratified Fluid With a Suspension of Particles," *AIAA Journal*, Vol. 18, 1980, pp. 846–849.

26 Yih, C. S., *Dynamics of Nonhomogeneous Fluids*, The Macmillan Company, New York, 1965.

27 Kelly, R. E., and Redekopp, L. G., "The Development of Horizontal Boundary Layer in Stratified Flow—Part 1: Nondiffusive Flow," *Journal of Fluid Mechanics*, Vol. 42, 1970, pp. 497–511.

28 Standing, R. G., "The Rayleigh Problem for a Slightly Diffusive Density-Stratified Fluid," *Journal of Fluid Mechanics*, Vol. 48, 1971, pp. 673–688.

29 Eringen, A. C., and Ingram, J. D., "A Continuum Theory of Chemically Reacting Media—II," *International Journal of Engineering Science*, Vol. 5, 1967, pp. 289–322.

30 Bugliarello, G., and Sevilla, J., "Velocity Distribution and Other Characteristics of Steady and Pulsatile Blood Flow in Fine Glass Tubes," *Biorheology*, Vol. 7, 1970, pp. 85–107.

31 McDonald, D. A., *Blood Flow in Arteries*, 2nd ed., Edward Arnold, London, 1974.

32 Healy, J. V., and Yang, H. T., "The Stokes Problems for a Suspension of a Particle," *Astronautica Acta*, Vol. 17, 1972, pp. 851–856.

33 Schlichting, H., *Boundary-Layer Theory*, McGraw-Hill, New York, 1968.

34 Michael, D. H., and Miller, D. A., "Plane Parallel Flow of a Dusty Gas," *Mathematika*, Vol. 13, 1966, pp. 97–109.

35 Saffman, P. G., "On The Stability of Laminar Flow of a Dusty Gas," *Journal of Fluid Mechanics*, Vol. 13, 1962, pp. 120–128.

36 Carslaw, H. S., and Jaeger, J. C., *Operational Methods in Applied Mathematics*, Dover Publication Inc., New York, 1963.

Downloaded 01 May 2010 to 171.66.16.249. Redistribution subject to ASME license or copyright; see http://www.asme.org/terms/Terms_Use.cfm

N. Phan-Thien

Department of Mechanical Engineering,
University of Sydney,
New South Wales, 2006, Australia

On the Mean Reynolds Equation in the Presence of Surface Roughness: Squeeze-Film Bearing

The mean Reynolds equation in the presence of surface roughness is derived using the techniques developed by Keller. This mean equation is nonlocal in the sense that the mean pressure at all points in the flow field has some effect on the mean pressure at any particular point. The performance of a two-dimensional squeeze film bearing with homogeneous surface roughness is considered next showing that the load is enhanced by a factor of $1 + \epsilon^2 a^2 S/h^2$, *where* ϵa *is the amplitude of the roughness,* h *is the film thickness, and* S *varies between* $-3\langle m^2\rangle$, *for parallel surface roughness, to* $6\langle m^2\rangle$ *for transverse surface roughness. Here, the bearing surfaces are described by* $\epsilon a m_1$ *and* $h + \epsilon a m_2$ *and* $m = m_2 - m_1$.

Introduction

In a recent international symposium devoted to the understanding of the effects of surface roughness in lubrication [1], two types of surface roughness were distinguished: the Reynolds and the Strokes roughness [2], where the Reynolds and the Stokes equations, respectively, apply. Sun and Chen [3] demonstrated that the roughness is of the Reynolds type when its amplitude is considerably less than, and its characteristic wavelength is considerably greater than, the mean film thickness. In this case, the surfaces can be regarded as being smooth and the classical Reynolds equation [4] applies. Most of the work done in the literature has been concerned with the Reynolds roughness and involved some heuristic, or "dishonest," in the terminology of Keller [5], attempts to average the Reynolds equation [6–10]. These dishonest attempts have been shown [9] to be theoretically inadequate and the full, unmodified Reynolds equation should be used when correcting for the Reynolds roughness.

Needless to say, the description of any rough surface requires a statistical description [11]. As a result, the Reynolds equation becomes a stochastic partial differential equation with random coefficients. In reviewing the existing statistical methods for treating rough surface hydrodynamic lubrication problems of the Reynolds type, Chen and Sun [12] concluded that a general method is still not available; the method of averaging the Reynolds equation before solving it has not been handled in a satisfactory manner (the "honest" method, using Keller's [5] terminoloy). This view is not wholly agreed on here. In fact, using the techniques deveoped by Keller [5, 13] to treat wave propagation problems in random media, it is shown that the average Reynolds equation, omitting terms of $O(\epsilon^3)$, where ϵ is the dimensionless amplitude of the surface corrugations, exhibits a nonlocal character in the sense that the mean pressure gradient at all points in the flow field has some effect on the mean pressure at any particular point. This nonlocal character has been observed to be a common feature of the mean responses of random media (for a review of this subject, see Beran [14]).

The two-dimensional squeeze film bearing with homogeneous surface roughness is taken up next. Without knowing the detailed solution and if the correlation length of the surface roughness is extremely long, then it can be shown that the load enhancement is positive and depends on the statistics of the surface roughness through its mean square. Furthermore, the load enhancement is minimum and negative when the corrugations are parallel to the flow direction; and it is maximum and positive when the corrugations are transverse to the flow direction. Before proceeding with the analysis, it is worthwhile mentioning here that not much progress has been achieved with the Stokes roughness, although some tentative discussions were put forward by the present author [15, 16]. There, it was shown, with the aid of two Stokes solutions to the slider and squeeze film bearings with parallel surface roughness, that an error of about 10 percent is made when using the Reynolds equation to correct for surface roughness if $\omega h \leqslant 0.5$, where ω is a representative frequency of the corrugations and h is the mean film thickness; furthermore, if $\omega h > 1.9$, the Reynolds equation gives a wrong correction to the load-carrying capacity of the bearings, even qualitatively. Thus, in the present paper, we are only concerned with a Reynolds surface roughness where ωh is less than 0.5.

Formulation

We consider the quasi-steady flow of an incompressible viscous fluid in a quite general bearing geometry whose surfaces are described by

$$z_1 = \epsilon a m_1(x, y); \quad z_2 = h(x, t) + \epsilon a m_2(x, y) \tag{1}$$

Contributed by the Applied Mechanics Division for publication in the JOURNAL OF APPLIED MECHANICS.

Disucussion on this paper should be addressed to the Editorial Department, ASME, United Engineering Center, 345 East 47th Street, New York, N. Y. 10017, and will be accepted until two months after final publication of the paper itself in the JOURNAL OF APPLIED MECHANICS. Manuscript received by ASME Applied Mechanics Division, November, 1980; final revision, March, 1981.

Copyright © 1981 by ASME

Downloaded 01 May 2010 to 171.66.16.249. Redistribution subject to ASME license or copyright; see http://www.asme.org/terms/Terms_Use.cfm

Here $\epsilon \ll 1$ is a perturbation parameter (dimensionless amplitude of the surface roughness, $h(x, t)$, some given function of x and time, $m_k(x, y)$, $k = 1, 2$ are stochastic processes representing the surface profiles. Cartesian coordinates (x, y, z) are used throughout, with x being the primary direction of flow. Without loss of generality we assume that $m_k(x, y)$ are meaningless. Thus the bottom plate is flat, on the average, and the mean film thickness is

$$\langle H \rangle = \langle z_2 - z_1 \rangle = \langle h + \epsilon a(m_2 - m_1) \rangle = \langle h + \epsilon a m \rangle = h \quad (2)$$

To obtain analytical solution to the squeeze film bearing, the surface roughness, m, is assumed to be statistically homogeneous [17]:

$$m(\mathbf{r}) = \int e^{i\boldsymbol{\lambda}\cdot\mathbf{r}} Z(d\boldsymbol{\lambda}). \quad (3)$$

In (3) $\mathbf{r}$ and $\boldsymbol{\lambda}$ are two-dimensional vectors (x, y), (λ, μ), respectively, and the Fourier-Stieltjes double integral (the spectral representation of m [17]) is taken over the wave number space $\boldsymbol{\lambda} \epsilon (-\infty, \infty) \times (-\infty, \infty)$. Furthermore $Z(d\boldsymbol{\lambda})$ is an interval random function [17] that satisfies

$$\langle Z(d\boldsymbol{\lambda}) \rangle = 0 \quad (4)$$

$$\langle Z(d_i\boldsymbol{\lambda}) Z^*(d_j\boldsymbol{\lambda}) = \delta_{ij}\Omega(\boldsymbol{\lambda}_i) d_i\boldsymbol{\lambda} \qquad \text{(no sum)}, \quad (5)$$

where $\langle \cdot \rangle$ denotes an ensemble average, x^*, the complex conjugate of x, $d_i\boldsymbol{\lambda}$ is an (two-dimensional) interval centered at $\boldsymbol{\lambda}_i$, δ_{ij}, the Kronecker delta, and $\Omega(\boldsymbol{\lambda})$ is the spectral density of $m(\mathbf{r})$:

$$R(\mathbf{r}) = \langle m(\mathbf{r} + \mathbf{s}) m(\mathbf{s}) \rangle = \int e^{i\boldsymbol{\lambda}\cdot\mathbf{r}} \Omega(\boldsymbol{\lambda}) d\boldsymbol{\lambda} \quad (6)$$

or equivalently,

$$\Omega(\boldsymbol{\lambda}) = \frac{1}{(2\pi)^2} \int e^{-i\boldsymbol{\lambda}\cdot\mathbf{r}} R(\mathbf{r}) d\mathbf{r} \quad (7)$$

(6) and (7) are the classical Wiener-Khinchin relationship [17].

If the upper bearing plate is moving with velocity $(U, 0, V)$ and the lower plate stationary, then the Reynolds equation for an incompressible lubricant can be written as (note $V = \partial h/\partial t$)

$$\nabla \cdot (H^3 \nabla P) = 6\eta \frac{\partial}{\partial x}(HU) + 12\eta V, \quad (8)$$

subjected to the boundary conditions

$$P(0, y) = P(L, y) = 0, \quad (9)$$

where L is the bearing length.

This equation was derived by Reynolds [4] based on the assumption of smooth, slowly varying surface. In (8) P is the pressure, η, the fluid viscosity (constant), and ∇ is the two-dimensional gradient operator $(\partial/\partial x, \partial/\partial y)$. When the pressure field is obtained, the bearing performance can be evaluated by its load-carrying capacity

$$N = \int_0^L P dx = -\int_0^L \frac{\partial P}{\partial x} x dx. \quad (10)$$

Since H is a stochastic process (8)–(9) become a stochastic differential equation with random coefficients. Published methods of treating this stochastic differential equation in the lubrication literature mostly involved some dishonest arguments to evaluate cross correlation terms.

Average Reynolds Equation

To average the Reynolds equation we follow closely the procedure outlined by Keller [5, 13]. This technique (or some variation of it) has been used successfully by many workers in solving transport problems in random media (see Beran [14]).

Denoting by L, L_1, L_2 the differential operators

$$L = \nabla \cdot h^3 \nabla, \quad L_1 = 3a\nabla \cdot h^2 m \nabla, \quad L_2 = 3a^2 \nabla \cdot h m^2 \nabla, \quad (11)$$

we have,

$$(L + \epsilon L_1 + \epsilon^2 L_2 + O(\epsilon^3))\, P = 6\eta \frac{\partial}{\partial x}(hU) + 12\eta V + 6\eta\epsilon a \frac{\partial}{\partial x}(mU) \quad (12)$$

If P_0 is the solution to the corresponding smooth-bearing problem then a solution to (12) is, in symbolic notation,

$$P = P_0 + 6\epsilon\eta a L^{-1} \frac{\partial}{\partial x}(mU) - L^{-1}(\epsilon L_1 + \epsilon^2 L_2) P + O(\epsilon^3), \quad (13)$$

where, by L^{-1}, we mean the integral operator ($\mathbf{r} \equiv (x, y)$)

$$L^{-1} f(\mathbf{r}) = \int G(\mathbf{r}, \mathbf{r}') f(\mathbf{r}') d\mathbf{r}', \quad (14)$$

where $G(\mathbf{r},\mathbf{r}')$ is the Green function of the smooth-bearing, self-adjoint operator L which has the boundary conditions (9) embedded in it.

A successive iteration on (13) gives

$$P = P_0 + 6\epsilon\eta a L^{-1} \frac{\partial}{\partial x}(mU) - \epsilon L^{-1} L_1 P_0 + \epsilon^2 L^{-1} \left(L_1 L^{-1} L_1 P_0 - L_2 P_0 - 6\eta a L_1 L^{-1} \frac{\partial}{\partial x}(mU) \right) + O(\epsilon^3).$$

Hence

$$\langle P \rangle = P_0 + \epsilon^2 L^{-1} \left(\langle L_1 L^{-1} L_1 \rangle P_0 - \langle L_2 \rangle P_0 - 6\eta a \left\langle L_1 L^{-1} \frac{\partial}{\partial x}(mU) \right\rangle \right) + O(\epsilon^3) \quad (15)$$

To eliminate P_0 from (15) we keep in mind that

$$P_0 = \langle P \rangle + O(\epsilon^2)$$

whence (note that the foregoing substitute is only made in the terms of $O(\epsilon^2)$)

$$\langle P \rangle = P_0 + \epsilon^2 L^{-1} \left(\langle L_1 L^{-1} L_1 \rangle \langle P \rangle - \langle L_2 \rangle \langle P \rangle - 6\eta a \left\langle L_1 L^{-1} \frac{\partial}{\partial x}(mU) \right\rangle \right) + O(\epsilon^3). \quad (16)$$

Applying the operator L on both sides of (16) and noting that

$$L P_0 = 6\eta \frac{\partial}{\partial x}(hU) + 12\eta V,$$

we obtain

$$\frac{\partial}{\partial x_\alpha} \left[(h^3 + 3a^2 h \epsilon^2 \langle m^2 \rangle) \frac{\partial \langle P \rangle}{\partial x_\alpha} \right] - 9\epsilon^2 a^2 \left\langle \frac{\partial}{\partial x_\alpha} \left[h^2 m \frac{\partial}{\partial x_\alpha} \int G(\mathbf{x},\mathbf{x}') \cdot \frac{\partial}{\partial x_{\beta'}} \left(h^2(\mathbf{x}') m(\mathbf{x}') \frac{\partial}{\partial x_{\beta'}} \langle P(\mathbf{x}') \rangle \right) d\mathbf{x}' \right] \right\rangle = 6\eta \frac{\partial}{\partial x}(hU) + 12\eta V - 18\epsilon^2 \eta a^2 \left\langle \frac{\partial}{\partial x_\alpha} \left[h^2 m \frac{\partial}{\partial x_\alpha} \int G(\mathbf{x},\mathbf{x}') \frac{\partial}{\partial x'} (m(\mathbf{x}') U(\mathbf{x}')) d\mathbf{x}' \right] \right\rangle, \quad (17)$$

where the boundary conditions for $\langle P \rangle$ are, from (9),

$$\langle P \rangle (0, y) = \langle P \rangle (L, y) = 0.$$

Note that (17) is correct up to $O(\epsilon^2)$ and we have used the results $\langle m \rangle = 0 = \langle L_1 \rangle$ and the usual summation convention with $\alpha, \beta = 1, 2$. A more compact version of (17) can be derived with the aid of Green's theorem. However, we defer this until next section. It is observed that the mean Reynolds equation is nonlocal in the sense that the mean pressure at all points in the flow field appears in (17). The effect of the far-field mean pressure, however, is weighted by the Green function $G(\mathbf{x},\mathbf{x}')$; this two-dimensional Green function normally has a singularity at $\mathbf{x}' = \mathbf{x}$ and thus the far-field effects are confined to a finite neighborhood of $\mathbf{x}$.

Downloaded 01 May 2010 to 171.66.16.249. Redistribution subject to ASME license or copyright; see http://www.asme.org/terms/Terms_Use.cfm

Squeeze-Film Bearing

To illustrate the application of (17), we consider a two-dimensional squeeze-film bearing of length $2L$. In this flow geometry, the fluid is squeezed between two parallel (on the average) plates at a rate $V = dh/dt$. Note that V is a function of time only. If the surface roughness $m(x, y)$ is assumed to be spatially homogeneous, then $\langle m^2 \rangle$ is independent of x and y and (17) becomes

$$\left(1 + 3\epsilon^2 \frac{a^2}{h^2}\langle m^2\rangle\right)\nabla^2\langle P\rangle - 9\epsilon^2 a^2 h\left\langle \frac{\partial}{\partial x_\alpha}\left[m\frac{\partial}{\partial x_\alpha}\int G(\mathbf{x},\mathbf{x}') \cdot \frac{\partial}{\partial x_{\beta'}}\left(m(\mathbf{x}')\frac{\partial}{\partial x_{\beta'}}\langle P(\mathbf{x}')\rangle\right)d\mathbf{x}'\right]\right\rangle = 12\eta\frac{V}{h^3}. \quad (18)$$

Using the commutivity of ensemble average and linear operators and noting the homogeneous boundary conditions on $G(\mathbf{x}, \mathbf{x}')$ and $\langle P(\mathbf{x}')\rangle$, we have, on applying Green's theorem.

$$\left(1 + 3\epsilon^2 \frac{a^2}{h^2}\langle m^2\rangle\right)\nabla^2\langle P\rangle + 9\epsilon^2 a^2 h\frac{\partial}{\partial x_\alpha}\int \frac{\partial^2 G(\mathbf{x},\mathbf{x}')}{\partial x_\alpha \partial x_{\beta'}} \cdot R(\mathbf{x}-\mathbf{x}')\frac{\partial\langle P(\mathbf{x}')\rangle}{\partial x_{\beta'}}d\mathbf{x}' = 12\eta\frac{V}{h^3} \quad (19)$$

In (19) we have used $R(\mathbf{x} - \mathbf{x}') = \langle m(\mathbf{x})m(\mathbf{x}')\rangle$ and that $G(\mathbf{x},\mathbf{x}')$ is determined by

$$\nabla^2 G(\mathbf{x}, \mathbf{x}') = h^{-3}\delta(\mathbf{x} - \mathbf{x}')$$
$$G(x = \pm L) = 0 \quad (20)$$

Long Correlation Length. If the correlation length (the distance beyond which the correlation is practically zero) is long and that $\partial^2 G(\mathbf{x},\mathbf{x}')/\partial x_\alpha \partial x_{\beta'}$ do not have any long tail, then the main contribution to the integral on the left-hand side of (19) comes from $\mathbf{x}' \sim \mathbf{x}$, hence

$$\left(1 + 3\epsilon^2 \frac{a^2}{h^2}\langle m^2\rangle\right)\nabla^2\langle P\rangle + 9\epsilon^2 a^2 h R(0)\frac{\partial}{\partial x_\alpha}\int \frac{\partial^2 G(\mathbf{x},\mathbf{x}')}{\partial x_\alpha \partial x_{\beta'}} \cdot \frac{\partial\langle P(\mathbf{x}')\rangle}{\partial x_{\beta'}}d\mathbf{x}' = 12\eta\frac{V}{h^3}.$$

But $R(0) = \langle m^2\rangle$ and $\partial^2 G/\partial x_\alpha \partial x_\alpha = h^{-3}\delta(\mathbf{x} - \mathbf{x}')$ and we finally obtain

$$\left(1 - 6\epsilon^2 \frac{a^2}{h^2}\langle m^2\rangle\right)\nabla^2\langle P\rangle = 12\frac{\eta V}{h^3} \quad (21)$$

The assumption leading to (21) is analogous to the white-noise assumption, only here $R(\mathbf{r})$ is taken to be constant. From (21) the effective gap thickness is

$$H_{\text{eff}} = h\left(1 - 6\epsilon^2 \frac{a^2}{h^2}\langle m^2\rangle\right)^{1/3}. \quad (22)$$

Since the normal load is proportional to H_{eff}^{-3}, there is a load enhancement factor of

$$1 + 6\epsilon^2 \frac{a^2}{h^2}\langle m^2\rangle$$

which depends on the statistics of the surface roughness through its mean square. This turns out to be the maximum load enhancement, as will be seen later in the next section.

Homogeneous Surface Roughness. To avoid solving the integro-differential equation (18) or (19) we note that $\langle P(\mathbf{x}')\rangle$ can be replaced by $P_0(\mathbf{x}') + O(\epsilon^2)$. Thus, up to an error term of $O(\epsilon^4)$, the second term on the left-hand side of (18) becomes

$$-9\epsilon^2 a^2 h\left\langle \frac{\partial}{\partial x_\alpha}\left(m\frac{\partial}{\partial x_\alpha}I\right)\right\rangle,$$

where

$$I = \int G(\mathbf{x},\mathbf{x}')\frac{\partial}{\partial x'}\left(m(x')\frac{\partial}{\partial x'}P_0(x')\right)dx'.$$

The solution to the smooth-squeeze-film bearing is well known,

$$P_0 = -6\eta V h^{-3}(h^2 - x^2), \quad \frac{\partial P_0}{\partial x} = 12\eta V x h^{-3},$$

and if $m(\mathbf{x})$ is represented by (3), it can be shown that

$$I = \frac{12\eta V}{h^6}\int \phi(x)e^{i\mu y}Z(d\boldsymbol{\lambda}), \quad (23)$$

where (note $\boldsymbol{\lambda} = (\lambda, \mu)$)

$$\phi(x) = \left(\frac{\lambda^2 - \mu^2}{|\lambda|^4} - \frac{i\lambda}{|\lambda|^2}x\right)e^{i\lambda} - \left(\frac{\lambda^2 - \mu^2}{|\lambda|^4} - \frac{i\lambda L}{|\lambda|^2}\right)\frac{e^{i\lambda L}}{\sinh 2\mu L}\sinh\mu(L + x) - \left(\frac{\lambda^2 - \mu^2}{|\lambda|^4} + \frac{i\lambda L}{|\lambda|^2}\right)\frac{e^{-i\lambda L}}{\sinh 2\mu L}\sinh\mu(L - x). \quad (24)$$

Thus we have

$$\left\langle \frac{\partial}{\partial x_\alpha}\left(m\frac{\partial}{\partial x_\alpha}I\right)\right\rangle = 12\eta\frac{V}{h^6}\frac{d}{dx}\int\frac{d\phi}{dx}e^{-i\lambda x}\Omega(\boldsymbol{\lambda})d\boldsymbol{\lambda} = 12\eta\frac{V}{h^6}\frac{d}{dx}\int\left\{i\lambda\frac{\lambda^2 - \mu^2}{|\lambda|^4} - \frac{i\lambda}{|\lambda|^2} + \frac{\lambda^2}{|\lambda|^2}x + O\left(\frac{h}{L}\right)\right\}\Omega(\boldsymbol{\lambda})d\boldsymbol{\lambda}$$

where we have used the statistical orthogonality of $Z(d\boldsymbol{\lambda})$, $Z^*(d\boldsymbol{\lambda}')$, equation (5), and $\lambda h \sim 0.5$ which implies $\lambda L \sim O(L/h)$. The latter assumption means that the representative wavelength of the corrugations (λ^{-1}) is larger than the mean film thickness.

Neglecting terms of $O(h/L)$, and noting that

$$\nabla^2\langle P\rangle \simeq \nabla^2 P_0(1 + O(\epsilon^2)) = 12\eta V h^{-3}(1 + O(\epsilon^2)),$$

we have

$$\left(1 + 3\epsilon^2\frac{a^2}{h^2}\langle m^2\rangle - 9\epsilon^2\frac{a^2}{h^2}\int\frac{\lambda^2}{|\lambda|^2}\Omega(\boldsymbol{\lambda})d\boldsymbol{\lambda}\right)\nabla^2\langle P\rangle = 12\eta\frac{V}{h^3}. \quad (25)$$

It is important to note that (25), as well as (17) or (18) or (19) are accurate up to $O(\epsilon^2)$, since the substitution $\langle P\rangle = P_0 + O(\epsilon^2)$ is made only in the term of $O(\epsilon^2)$.

From (25) the effective film thickness is given by

$$H_{\text{eff}} = h\left(1 + 3\epsilon^2\frac{a^2}{h^2}\int_{-\infty}^{\infty}\int_{-\infty}^{\infty}\frac{2\lambda^2 - \mu^2}{\lambda^2 + \mu^2}\Omega(\lambda, \mu)\,d\lambda d\mu\right)^{1/3} \quad (26)$$

and the load-carrying capacity increases by a factor of $(1 + \epsilon^2 a^2 S/h^2)$, where

$$S = 3\int_{-\infty}^{\infty}\int_{-\infty}^{\infty}\frac{2\lambda^2 - \mu^2}{\lambda^2 + \mu^2}\Omega(\boldsymbol{\lambda})d\lambda d\mu. \quad (27)$$

We can rewrite (27) as

$$S = 6\int_{-\infty}^{\infty}\int_{-\infty}^{\infty}\Omega(\lambda, \mu)d\lambda d\mu - 9\int_{-\infty}^{\infty}\int_{-\infty}^{\infty}\frac{\mu^2}{\lambda^2 + \mu^2}\Omega(\lambda, \mu)d\lambda d\mu.$$

For a given $\langle m^2\rangle = \int_{-\infty}^{\infty}\int_{-\infty}^{\infty}\Omega(\lambda, \mu)d\lambda d\mu$, S is maximized if $\Omega(\lambda, \mu)$ takes the form $\delta(\mu)K(\lambda)$, that is, if the corrugations are transverse to the flow direction, viz., $m_k = m_k(x)$. (It should be noted that $\Omega(\boldsymbol{\lambda})$ is always positive [17].) In this case the load enhancement is

$$S = 6\langle m^2\rangle. \quad (28)$$

Similarly, by expressing

$$S = -3\int_{-\infty}^{\infty}\int_{-\infty}^{\infty}\Omega(\lambda, \mu)d\lambda d\mu + 9\int_{-\infty}^{\infty}\int_{-\infty}^{\infty}\frac{\lambda^2}{\lambda^2 + \mu^2}\Omega(\lambda, \mu)d\lambda d\mu$$

it is immediately seen that S is minimized if $\Omega = \delta(\lambda)K(\mu)$, or that the surface roughness is parallel to the flow direction, viz., $m_k = m_k(y)$. In this case, we have[1]

$$S = -3\langle m^2\rangle. \quad (29)$$

[1] In these two extreme cases, this theory is identical to that of Elrod [6] when terms of 0 (ϵ^4) are neglected in the latter.

Downloaded 01 May 2010 to 171.66.16.249. Redistribution subject to ASME license or copyright; see http://www.asme.org/terms/Terms_Use.cfm

Regular Perturbation Method. As an alternative to solving (18) or (19), a regular perturbation scheme of the type considered by Sun [9] and Phan-Thien [15, 16] can be set up. In this scheme, the pressure is expanded in a series

$$P = P_0 + \epsilon P_1 + \epsilon^2 P_2 + O(\epsilon^3), \tag{30}$$

where

$$P_0 = 12\eta \frac{V}{h^3}(x^2 - L^2)$$

is the well-known smooth-bearing squeeze-film solution. The ϵ^1-solution is governed by

$$\nabla^2 P_1 = -36\eta \frac{aV}{h^4} \frac{\partial}{\partial x}(mx)$$

$$P_1(-L) = 0 = P_1(L) \tag{31}$$

Keeping in mind the representation (3) of $m(x, y)$, it is easily shown that the representation of P_1 is

$$P_1 = -36\eta \frac{aV}{h^4} \int \phi(x) e^{i\lambda y} Z(d\boldsymbol{\lambda}), \tag{32}$$

where $\phi(x)$ is given by (24).

Next, the ϵ^2-solution is governed by

$$\nabla^2 P_2 = -3\frac{a}{h} \nabla \cdot (m \nabla P_1) - 3\frac{a^2}{h^2} \nabla \cdot (m^2 \nabla P_0)$$

$$P_2(-L) = 0 = P_2(L) \tag{33}$$

Although the spectral representation for P_2 can be found (a quadruple Fourier-Stieltjes integral) as in the ϵ^1-case, it is not necessary if only mean values of P_2 are after

$$\frac{d^2}{dx^2}\langle P_2 \rangle = -3\frac{a^2}{h^2}\langle m^2 \rangle \frac{d^2 P_0}{dx^2} - 3\frac{a}{h}\left\langle m \frac{\partial P_1}{\partial x} \right\rangle$$

$$= 12\frac{\eta V}{h^3}\left\{-3\frac{a^2}{h^2}\langle m^2 \rangle + 9\frac{a^2}{h^2}\frac{d}{dx}\int \frac{d\phi}{dx} e^{-i\lambda x} \Omega(\boldsymbol{\lambda}) d\boldsymbol{\lambda}\right\}.$$

Proceeding as before, the increase in the load-carrying capacity is given by equation (27), if terms of $O(h/L)$ are neglected.

Finally, it is worthwhile mentioning here that, for a parallel surface roughness where $m = m(y)$, the Stokes equations predict a load increase of (Phan-Thien [15])

$$S = 3\int_{-\infty}^{\infty} \left\{(\lambda h \coth \lambda h - 2)(\Omega_{22} + \Omega_{11}) + \frac{2\lambda h}{\sinh \lambda h}\Omega_{12}\right\} d\lambda, \tag{34}$$

where Ω_{ij} is the special density of m_i and m_j; $i, j = 1,2$.

Only when the characteristic dimensionless frequency of the corrugation is less than 0.5, that the prediction of the load enhancement given by the Reynolds equation is accurate to about 10 percent. Furthermore, if this characteristic frequency is greater than about 2, then the prediction of the Reynolds equation cannot be trusted, even qualitatively [15, 16]. In this sense, most rough surfaces met in practice seem to belong to the Stokes type, and further research into Stokes roughness corrections should be a welcome contribution.

Acknowledgment

I have benefited from several discussions with Dr. John D. Atkinson. This work is a byproduct of a project supported by the Australian Research Grants Committee (ARGC Grant F7915597R). This support is gratefully acknowledged.

References

1 Wilcock, D. F., "Effects of Surface Roughness in Lubrication," ASME *Journal of Lubrication Technology*, Vol. 100, 1978, pp. 6–11.

2 Elrod, H. G., "Thin-Film Lubrication Theory for Newtonian Fluids With Surfaces Possessing Striated Roughness or Grooving," ASME *Journal of Lubrication Technology*, Vol. 95, 1973, pp. 484–489.

3 Sun, D.-C., and Chen, K.-K., "First Effects of Stokes Roughness on Hydrodynamic Lubrication," ASME *Journal of Lubrication Technology*, Vol. 99, 1977, pp. 2–9.

4 Reynolds, O., "On the Theory of Lubrication and Its Application to Mr. Beauchamp Tower's Experiments," *Philosophical Transactions of the Royal Society*, Series A, Vol. 177, 1886, pp. 157–234.

5 Keller, J. B., "Wave Propagation in Random Media," *Proceedings, Symposium on Applied Mathematics*, Vol. 13, American Mathematical Society, Providence, R.I., 1962.

6 Christensen, H., "Stochastic Models forHydrodynamic Lubrication of Rough Surfaces," *Proceedings, Institution of Mechanical Engineers*, Vol. 184, 1969–1970, pp. 1013–1026.

7 Tonder, K., "Lubrication of Surfaces Having Area-Distributed Isotropic Roughness," ASME *Journal of Lubrication Technology*, Vol. 99, 1977, pp. 323–330.

8 Chow, P. L., and Saibel, E. A., "On the Roughness Effect in Hydrodynamic Lubrication," ASME *Journal of Lubrication Technology*, Vol. 100, 1978, pp. 176–180.

9 Sun, D.-C., "On the Effects of Two-Dimensional Reynolds Roughness in Hydrodynamic Lubrication," *Proceedings, Royal Society*, London, Series A, Vol. 364, 1978, pp. 89–106.

10 Tonder, K., "Simulation of the Lubrication of Isotropically Rough Surface," *ASLE Transactions*, Vol. 23, 1980, pp. 326–333.

11 Longuet-Higgins, M.S., "The Statistical Geometry of Random Surfaces," *Proceedings, Symposium on Applied Mathematics*, Vol. 13, American Mathematical Society, Providence, R.I., 1962.

12 Chen, K.-K., and Sun, D.-C., Fourth Leeds-Lyon Symposium on the Effects of Surface Roughness in Lubrication, 1977.

13 Keller, J. B., "Stochastic Equations and Wave Propagation in Random Media," *Proceedings, Sympsoium on Applied Mathematics*, Vol. 16, American Mathematical Society, Providence, R.I., 1964.

14 Beran, M. J., *Statistical Continuum Theories*, New York, Interscience, 1968.

15 Phan-Thien, N., "On the Effects of Parallel and Transverse Stationary Random Surface Roughness in Hydrodynamic Lubrication," *Proceedings of the Royal Society*, London, Series A, 1980, Vol. 374, 1981, pp. 569–591.

16 Phan-Thien, N., "On the Effects of Reynolds and Stokes Surface Roughness in a Two-Dimensional Slider Bearing," *Proceedings of the Royal Society*, London, Series A, 1981, in press.

17 Yaglom, A. M., *An Introduction to the Theory of Stationary Random Functions*, translated and edited by R. A. Silverman, Prentice-Hall, Englewood Cliffs, N.J., 1965.

Downloaded 01 May 2010 to 171.66.16.249. Redistribution subject to ASME license or copyright; see http://www.asme.org/terms/Terms_Use.cfm

W. C. Chin

Aerodynamics Consultant,
134 Needletree Lane,
Glastonbury, Conn. 06033

Direct Approach to Aerodynamic Design Problems

"Direct" small disturbance approaches to inviscid aerodynamic "inverse" or "design" problems in two and three-dimensional, subsonic, supersonic, and transonic flow, are given which extend the stream function method of Chin and Rizzetta. Our shape solutions generally involve nonlinear differential equations of mixed type for scalar "streamlike" functions Ψ which are solved with Neumann conditions related to prescribed surface pressure and "Kutta-type" constraints on edge closure or included angle specified using jumps in Ψ or its streamwise derivative. Because edge constraints are enforced automatically the methods are direct. They resemble "analysis" potential function (ϕ) methods for flows past fixed shapes where the jumps $[\phi]$ are chosen "directly" to insure smooth trailing edge flow; thus computational methods for analysis apply with minor change to design. Dualities relating the analysis problem for camber to the design problem for thickness, and the design problem for camber to the analysis problem for thickness, are given for planar flow; both closed trailing edges, and cusped ones, generally opened, which model the displacement effects of viscous wakes, are considered. These are extended to three dimensions and consequences of an inverse analogy to Prandtl's lifting line for analysis problems are explored. Transonic inverse formulations for airfoils, wings, fans, cascades, inlets, and nacelles are discussed and preliminary numerical results are presented.

Introduction

Aerodynamic inverse methods are important because they allow designers to specify pressures with desirable loadings, moments, boundary layer, and structural properties and to obtain with ease the required shapes subject to auxiliary physical conditions. Here we will develop stream-function methods in two and three-dimensional compressible flow and cite advantages both analytical and numerical: the potential function, ideally suited to analysis problems, does not adequately handle the trailing edge shape constraints usually imposed in inverse problems, because potential jumps model only changes in lift (hence, "man-in-loop" numerical decisions). Such constraints are naturally handled by prescribing jumps in the disturbance stream function Ψ or its streamwise derivative to control closure or included angle. This choice of dependent variable leads, interestingly, to Neumann surface pressure conditions, rendering the inverse formulation "analysis-like" and amenable to existing direct computational methods! A classic sign ambiguity yielding two velocities for a given mass flux, one subsonic and the other supersonic, unfortunately, renders the transonic stream-function equation indeterminate; but recently, Chin and Rizzetta [1] circumvented this difficulty for unbounded planar flows by solving an unambiguously defined integro-differential equation of mixed type. Their boundary-value problem, $(1 - M^2 + M^2(\Lambda + 1) \int_{\pm\infty}^{z} \Psi_{xx}(x, s)ds)\, \Psi_{xx} + \Psi_{zz} = 0$ with $\pm\infty$ for $z \gtrless 0$, $\Psi_z(x, 0^{\pm}) = -\frac{1}{2}(1 - M^2)C_p - M^2(\Lambda + 1)C_p{}^2/8$ specified on the chord, a vanishing jump $[\Psi]$ through the downstream "wake" for trailing edge closure and $\Psi \sim 0$ at infinity (note $z^{\pm}(x) = -\Psi(x, 0^{\pm})$ represent upper and lower surfaces), where C_p is the prescribed pressure coefficient, x and z are streamwise and transverse coordinates, M is a subsonic free-stream Mach number, and Λ is the ratio of specific heats, actually follows without approximation from the complementary analysis problem solving $(1 - M^2 - M^2(\Lambda + 1)\phi_x)\phi_{xx} + \phi_{zz} = 0$, subject to $\phi_z(x, 0^{\pm})$ specified on the chord, $[\phi]$ chosen to satisfy Kutta's condition and vanishing $\nabla\phi$ at infinity (note $C_p = -2\phi_x$). Shock conditions for mass and vorticity apply in both cases. In [1] classic solutions for ellipses and flat plates at angle of attack were obtained from known subsonic pressures; also, known supercritical airfoils, using type-dependent numerical methods, were reproduced in one case using a shock-free Korn C_p and in a second using a Jameson C_p with a strong shock. The method was also used in [2] to design families of shock-free airfoils and to examine the existence of realistic airfoils given smooth surface pressures fixed throughout a range in M. These calculations appear to have established the computational expediency of the new formulation.

Contributed by the Applied Mechanics Division for publication in the JOURNAL OF APPLIED MECHANICS.

Discussion on this paper should be addressed to the Editorial Department, ASME, United Engineering Center, 345 East 47th Street, New York, N. Y. 10017, and will be accepted until two months after final publication of the paper itself in the JOURNAL OF APPLIED MECHANICS. Manuscript received by ASME Applied Mechanics Division, December, 1980; final revision, May, 1981.

Copyright © 1981 by ASME

Downloaded 01 May 2010 to 171.66.16.249. Redistribution subject to ASME license or copyright; see http://www.asme.org/terms/Terms_Use.cfm

We stress that our approach for a given free stream *always* produces a closed airfoil for any prescribed pressure (unphysical surface "crossovers" are possible, however) and apparently contradicts the well-known work of Lighthill [3]. In brief, [3] solves Laplace's equation for the total potential Φ with the exact pressure $\Phi_x{}^2 + \Phi_z{}^2$ prescribed on the circle to which the unknown airfoil maps. This formulation, neither Neumann nor Dirichlet, insists on three existence requirements: a consistency condition on permissible surface pressures, a condition on "x closure" and one on "z closure." But, in their small disturbance model, Chin and Rizzetta enforce z closure only; their formulation, it turns out, is correct for thin airfoils nearly aligned with the free stream. This is true because, in this limit, the exact expression for C_p linearizes to the usual $-2\phi_x$ identical, of course, with $-2\Psi_z$; since Ψ_z is prescribed on the slit $z = 0$, one has an analysis-like Neumann problem for $\Psi_{xx} + \Psi_{zz} = 0$ whose uniqueness is insured by setting $\Psi = 0$ at infinity and choosing a "circulation" $[\Psi]$ consistently with edge requirements. Lighthill's inverse formulation is Neumann-like for thin airfoil flows: his first pressure constraint is satisfied automatically, x closure does not apply, leaving only a requirement on z closure correctly handled by prescribing $[\Psi]$. The difficulties discussed in [3] apply only to the inner nose problem, not addressed here, where linearization is impossible (see Thwaites [4] for a review of early inverse methods). Alternatively, we could have considered the small disturbance formulation for $\phi_{xx} + \phi_{zz} = 0$; for any chordwise $\phi_z(x, 0^\pm)$ a unique analysis solution always exists given Kutta's condition plus some statement on the leading edge singularity (constraints on ϕ_z are unnecessary even for nonzero $\int \phi_z(x, 0^\pm)dx$ if a source-like asymptote is assumed at infinity). Because our inverse formulation using Ψ is identical, the same conclusions apply without change: $\Psi_z(x, 0^\pm)$ can be prescribed arbitrarily provided vortex and source-like farfields are assumed for flows with nonzero $\int \Psi_z(x, 0^\pm)dx$ or $[\Psi]$. Prescribed trailing edge C_p's should obey Kutta's condition, but this is not required mathematically.

This paper expands on [1] by considering broader classes of aerodynamic shapes, e.g., finite wings, cascades, fans, inlets, and nacelles. While the earlier study dealt only with closed edges, the present also discusses constraints on $[\Psi_x]$ which affect included angle (in particular, a vanishing jump assures a cusped but generally opened trailing edge, modeling the inviscid displacement thickness streamline leaving the trailing edge tangent to the high Reynolds number flow far upstream). For general subsonic linear flows, analytical results derived provide a number of dualities relating analysis and design formulations, as discussed in the Abstract, which may shed insight on the more difficult but numerically tractable transonic problem. That shapes with edges both cusped and closed are possible by introducing dynamically insignificant changes to prescribed C_p's is demonstrated for linear flows, suggesting, perhaps, new variations on transonic inverse formulations. In what follows the basic ideas are developed from simple examples and extended to flows of increasing geometric and aerodynamic complexity. The role of constraints is also examined in detail.

Theory and Examples

Constant Density Planar Flows. Thin airfoil theory solves $\phi_{xx} + \phi_{zz} = 0$, with $\phi_z(x, 0^\pm)$ specified along $-1 \leq x \leq 1$, $[\phi]$ chosen for smooth trailing edge flow and $\nabla\phi \sim 0$ at infinity. The direct problem superposes solutions symmetric and antisymmetric with respect to chord: a "thickness" $\phi^{(t)}$ satisfying an equation that implies a source strength proportional to local surface slope and a "camber" $\phi^{(c)}$ (modeled by lineal vortices and) governed by an integral equation whose solution is rendered unique only by invoking Kutta's condition plus some statement on the leading edge singularity. Design problems also require auxiliary constraints. Now, any prescribed C_p can be decomposed into symmetric and antisymmetric parts. For thickness problems, we assume sources of strength f using the integral $\phi^{(t)} = \frac{1}{2\pi}\int_{-1}^{1} f(s) \log((x-s)^2 + z^2)ds$ and the boundary condition $\phi_x{}^{(t)}(x, 0^\pm) = u^{(t)}(x)$. But the resulting singular integral equation $\int_{-1}^{1} f(s)/(x - s)ds = \pi u^{(t)}(x)$ is the analysis equation for the lifting flow past a camber line if $u^{(t)}(x)$ is the surface slope and f is the sought vorticity! Thus various solutions are possible. For example, the choice

$$f(x) = \frac{1}{\pi}\left(\frac{1-x}{1+x}\right)^{1/2}\int_{-1}^{1}\left(\frac{1+s}{1-s}\right)^{1/2}\frac{u^{(t)}(s)ds}{s-x} - \frac{(1-x^2)^{-1/2}}{\pi}\int_{-1}^{1}\left(\frac{1+s}{1-s}\right)^{1/2}u^{(t)}(s)ds$$

leads to closed airfoils satisfying $\int_{-1}^{1} f(s)ds = 0$ but both edges are blunted unless the second integral vanishes (thus leaving a sharp trailing edge of zero radius); in contrast,

$$f(x) = \frac{1}{\pi}\left(\frac{1-x}{1+x}\right)^{1/2}\int_{-1}^{1}\left(\frac{1+s}{1-s}\right)^{1/2}\frac{u^{(t)}(s)ds}{s-x}$$

leads to blunted leading and cusped trailing edges generally opened. This duality between the analysis problem for lift and the design problem for thickness is complemented by one for the analysis problem for thickness and the design problem for lift. The boundary condition $\phi_x{}^{(c)}(x, 0^\pm) = \pm u^{(c)}(x)$ together with

$$\phi^{(c)} = -\frac{1}{2\pi}\int_{-1}^{1} h(s)\arctan z/(x-s)ds$$

(h is the vortex strength) now leads to an equation with the obvious solution $h(x) = 2u^{(c)}(x)$, analogous to the analysis result relating source strength to local surface slope. Now let us reconsider the foregoing using Ψ as opposed to ϕ. We solve an analysis-like problem for $\Psi_{xx} + \Psi_{zz} = 0$ with

$$\Psi = \frac{1}{\pi}\int_{-1}^{1} f(s)\arctan z/(x-s)ds$$

where f is determined from the Neumann condition $\Psi_z(x, 0^\pm) = \phi_x(x, 0^\pm) = u^{(t)}(x)$. But interestingly, we have superposed "arctangents" just like the vortex solutions used in analysis potential formulations for camber (i.e., $\phi \sim \tan^{-1}$, here, of course, "arctangent" means sources): in this sense one has "pseudovortices." Similarly, the design formulation for camber using Ψ superposes vortex singularities which analytically appear as logarithms; the analogy with potential formulations for thickness (solved taking $\phi \sim \log$) suggests the use of "pseudosources." As in "analysis potential theory," solutions to the integral equation for "pseudovortex strength," not unique, are fixed by Kutta-type conditions. A specified jump in Ψ, for example, physically measures the mass flow issuing from the trailing edge, since the stream function is constant along a streamline ($[\Psi] = 0$, equivalently $\int_{-1}^{1} f(s)ds = 0$, enforces closure); on the other hand, $[\Psi_x] = [-\phi_z] = -[dz/dx]$ fixes the included angle. The design problem for camber, again, superposes pseudosources, leading to the well-known "source equation" with unique solutions. These terms appear somewhat superficial at first, but their use in three dimensions, as will be seen, broadens the duality connecting analysis and design problems. In closing this paragraph, we stress emphatically that stream-function formulations for design, as proposed, are mathematically identical to potential ones for analysis; thus computational methods, panel, vortex-lattice, finite difference, and finite element, devised for analysis apply with minor change to design problems provided only we reinterpret inputs and outputs (again, $z^\pm(x) = -\Psi(x, 0^\pm)$). Chin and Rizzetta [1] worked this idea for planar transonic flows; this paper, again, extends [1] to problems of increased geometric and aerodynamic complexity.

A particularly important shape is the one that induces the uniform loading $u^{(t)}(x) = \beta > 0$ and possessing blunted leading and cusped trailing edges; hence, the source strength $f(x) = \beta(1-x)^{1/2}/(1+x)^{1/2}$ is singular at $x = -1$ and zero at $x = +1$ (f, as defined, equals the surface slope). Now, the upper surface satisfying $z^+(-1) = 0$ is $z^+(x) = \beta((1-x^2)^{1/2} + \frac{1}{2}\pi + \sin^{-1}x)$; thus the thickness grows monotonically with x, producing a trailing edge gap equal to $2\pi\beta$ (contrasting with the well-known thin ellipse). In the design problem, airfoils with blunted leading and cusped trailing edges *entirely closed* are therefore possible, by appending to an "original" $u^{(t)}(x)$ a constant β loading everywhere, with just enough "$2\pi\beta$" to close the final shape ("starting" and appended shapes are linearly superposed)! This constant addition has no aerodynamic significance since it modifies neither the specified pressure gradient nor the lift. The cusped edge model also provides

Downloaded 01 May 2010 to 171.66.16.249. Redistribution subject to ASME license or copyright; see http://www.asme.org/terms/Terms_Use.cfm

the inviscid displacement thickness streamline leaving the trailing edge tangent to the free stream; to obtain the "actual" airfoil, one subtracts a displacement thickness determined from simple boundary layer estimates, with closure ensured by modifying $u^{(t)}$ as discussed. Note also that the amount of closure $[\Psi]$ changes monotonically with β, just as the lift $[\phi]$ in analysis problems changes monotonically with angle of attack. This *may* also be true of weakly supercritical transonic flows (in analysis problems, high angles of attack produce strong shocks and possible losses in lift). The method of Chin and Rizzetta [1] can be reformulated to produce trailing edges both cusped and closed: drop their $[\Psi] = 0$ in favor of fixing $[\Psi_x]$ and program changes to β "intelligently" to provide the desired closure (the analysis analogy would vary angle of attack to produce a prescribed lift).

Constant Density Flows Past Finite Wings. Analysis problems solve $\phi_{xx} + \phi_{zz} + \phi_{yy} = 0$ (y is the spanwise variable) with $\phi_z(x, 0^{\pm}, y)$ specified on a flat "lifting surface," $[\phi(y)]$ chosen to satisfy Kutta's condition and regularity conditions at infinity. To demonstrate similar analysis and design analogies three-dimensionally, we must show that a "$\Psi(x, z, y)$" exists which satisfies the same boundary-value problem. The more general stream function, however, is a vector potential governed by three coupled boundary-value problems, thus diminishing somewhat our hopes. But any scalar streamlike function satisfying our demand and which also reduces to our planar formulation suffices: simply write

$$\left(\phi_x + \int_{-\infty}^{x} \phi_{yy} dx\right)_x + (\phi_z)_z = 0$$

and define

$$\Psi_z = \phi_x + \int_{-\infty}^{x} \phi_{yy} dx \text{ and } \Psi_x = -\phi_z.$$

This leads to $\Psi_{xx} + \Psi_{zz} + \Psi_{yy} = \Psi_{yy}(-\infty, z, y) = 0$, *the required equation!* For mildly swept high aspect ratio wings, since spanwise variations are small, the approximation

$$\Psi_z = \phi_x + \int_{-\infty}^{x} \phi_{yy} dx \cong \phi_x = -\tfrac{1}{2} C_p$$

provides a Neumann condition unchanged from planar theory, and the same "Kutta-type" trailing edge constraints and regularity conditions can be used. This three-dimensional formulation for $\Psi(x, z, y)$ is *identical* to the analysis formulation for $\phi(x, z, y)$ and provides the required inverse dual to lifting surface theory: numerical methods devised for analysis problems, as in planar flows, again therefore apply to design problems. Surface streamlines are computed from $dz^{\pm}(x, y)/dx = \phi_z(x, 0^{\pm}, y) = -\Psi_x(x, 0^{\pm}, y)$, that is, $z^{\pm}(x, y) = -\Psi(x, 0^{\pm}, y) + g(y)$, where the dihedral $g(y)$ vanishes in small disturbance theory (potential function design methods, assuming closure is properly handled, differentiate to obtain ϕ_z and integrate to obtain $z^{\pm}$, a procedure that may be inaccurate numerically).

In planar flows, infinite line vortices with axes perpendicular to the page create lift; for finite wings, this vortex bends into the downstream flow, but because the bound circulation $[\phi(y)]$ now varies with span, a wake forms that induces a local downwash which reduces the geometric angle of attack. Planar inverse formulations for thickness superpose pseudovortices as discussed. For finite wings, because $\Psi(x, z, y)$ satisfies Laplace's equation, our infinite line pseudovortices must likewise bend in the downstream direction. Whenever spanwise variations in $[\Psi]$ exist, Stokes' theorem requires a shed pseudovortex wake that arises from mass conservation as opposed to rotation: a wake of "source lines" carries "shed mass" that arises from spanwise differences in trailing edge ejected flow (these are generally nonzero for Kutta-type conditions in $[\Psi_x]$). Pseudovortex wakes induce changes in wing loading the way real wakes induce downwash; the "wake" vanishes for a trailing edge everywhere closed (or equally opened), for example, as a real wake would if all section loadings vanish.

Our cusped edge model is particularly relevant to high Reynolds number flows where, in fact, one has a semi-infinite chord bounded by an inviscid displacement thickness stream surface that leaves the trailing edge tangent to the uniform flow (since $[\Psi_x] = 0$, the gap will vary with span). In the direct problem, C_p is obtained, and boundary-layer wing and wake flows are solved. The inverse problem is also important: the displacement stream surface (as described) is sought that induces the prescribed C_p over a given planform (the actual wing can be obtained by subtracting a boundary-layer thickness as in the planar case). The resulting edge thickness $[\Psi(y)]$ then provides some estimate of surface viscous effects; for example, if it is large relative to the maximum thickness, the pressure is probably undesirable. This problem, easily solved numerically, also lends itself to simple analysis in the "lifting line" sense. Prandtl's solution for flat plate wings uses planar results locally based on $[\phi_x] = 0$ at the trailing edge and assumes zero tip loadings $[\phi] = 0$; here, enforce our viscous condition at each section and assume wing tip closure through $[\Psi] = 0$. Because both formulations are identical, lifting line formulas based on Glauert's classic expansion (not duplicated here) apply without change to design; for example, the total ejected mass flow depends only on the first harmonic much like the well-known result for total lift, and the edge gap can be everywhere found (unfortunately, analogies to known results for minimum induced drag do not exist because the Trefftz plane kinetic energy $\Psi_y{}^2 + \Psi_z{}^2$ is unphysical). Of course, aerodynamic twist would correspond to a variable loading $\beta(y)$; while it can be used to produce edges both cusped and closed, as discussed, in the present context it provides a means to analyze prescribed spanwise pressure gradients to prevent unwanted boundary-layer separation. Bound pseudovortices are responsible for closure while free pseudovortices induce changes in pressure.

Compressible Flows Past Finite Wings. In compressible flow we write

$$\left((1 - M^2)\phi_x - \tfrac{1}{2}M^2(\Lambda + 1)\phi_x{}^2 + \int_{-\infty}^{x} \phi_{yy} dx\right)_x + (\phi_z)_z = 0$$

and define $\Psi(x, z, y)$ through

$$\Psi_z = (1 - M^2)\phi_x - \tfrac{1}{2}M^2(\Lambda + 1)\phi_x{}^2 + \int_{-\infty}^{x} \phi_{yy} dx$$

and $\Psi_x = -\phi_z$ so that $(1 - M^2 - M^2(\Lambda + 1)\phi_x)\Psi_{xx} + \Psi_{zz} + \Psi_{yy} = 0$ assuming $\Psi_{yy}(-\infty, z, y)$ vanishes. For mildly swept high aspect ratio wings, as before, the spanwise term in Ψ_z can be neglected, so that $\pm|(1 - M^2)^2 - 2M^2(\Lambda + 1)\Psi_z|^{1/2}\Psi_{xx} + \Psi_{zz} + \Psi_{yy} = 0$ holds (the $\pm$ refers to pure subsonic and supersonic flows). For transonic flows with $M < 1$, ϕ_x decays at infinity, so that

$$\phi_x = -\int_{\pm\infty}^{z} \Psi_{xx}(x, s, y) ds$$

(if $M > 1$, surface C_p's provide the required reference): substitution produces the integrodifferential equation of [1] with an added Ψ_{yy} term. Assuming weak spanwise effects, the definition for Ψ_z and the expression $C_p = -2\phi_x$ lead to the Neumann condition $\Psi_z = -\tfrac{1}{2}(1 - M^2)C_p - M^2(\Lambda + 1)C_p{}^2/8$. Kutta-type trailing edge conditions again apply, along with the usual regularity condition at infinity for $M < 1$ or radiation conditions for $M > 1$. This analysis-like problem is amenable to existing transonic analysis methods; again, only simple code changes are required, and wherever the local type is known beforehand, the simpler "$\pm$" equation can be used (e.g., see [1] for details). For linear compressible flows, $(1 - M^2)\Psi_{xx} + \Psi_{zz} + \Psi_{yy} = 0$ holds: the dual analogy to analysis results satisfying the Prandtl-Glauert equation $(1 - M^2)\phi_{xx} + \phi_{zz} + \phi_{yy} = 0$ is exact! Thus the vast literature on subsonic and supersonic analysis methods provides an important new source of aerodynamic design information.

Flows in Fans and Cascades. An inverse approach to rectilinear cascades is easily formulated. For transonic flow, we use $(1 - M^2 - M^2(\Lambda + 1)\phi_x)\Psi_{xx} + \Psi_{zz} = 0$ with

$$\phi_x(x, z) = -\tfrac{1}{2}C_p(x, 0^{\pm}) - \int_{0\pm}^{z} \Psi_{xx}(x, s) ds,$$

taking references along the chord; if $M < 1$, for example, $+|(1 - M^2)^2 - 2M^2(\Lambda + 1)\Psi_z|^{1/2}\Psi_{xx} + \Psi_{zz} = 0$ applies upstream of the leading edge and downstream of the trailing edge. This is solved with periodicity conditions, trailing edge shape constraints, and nonzero Ψ's

Downloaded 01 May 2010 to 171.66.16.249. Redistribution subject to ASME license or copyright; see http://www.asme.org/terms/Terms_Use.cfm

specified upstream and downstream of the airfoil to enforce prescribed levels of streamline deflection. The effects of finite span and aerodynamic twist are modeled by a Ψ_{yy} term and taking $\Psi_y = 0$ along symmetry planes. For linear subsonic or supersonic flow, code development is trivial. Simply apply existing panel methods (which satisfy regularity and not periodicity conditions) to a stacked array of flat planforms with the required aspect and gap to chord ratios; the "middle flow" satisfies the periodicity requirement.

Axisymmetric Compressible Flows. Flows past axisymmetric nacelles satisfy $(1 - M^2 - M^2(\Lambda + 1)\phi_x)\phi_{xx} + \phi_{rr} + \phi_r/r = 0$ (r is the radial coordinate), with $\phi_r(x, R^{\pm}) = F_{\pm}'(x)$, where $r = R + F_{\pm}(x)$ are outer and inner surfaces and R is a mean radius, $\phi_r(x, 0) = 0$, $\nabla\phi \cong 0$ at infinity (for $M < 1$), the usual shock relations and Kutta's condition through the wake $r = R$. "Isolated inlets" are semi-infinite and tend to $r = R$ far downstream; here, the level of circulation is determined by the amount of mass flow (note $C_p = -2\phi_x$). These simple formulations extend planar theory; however, for axisymmetric nacelles, the effects of source and vortex rings are strongly coupled. For inverse problems, auxiliary conditions again appear: finite length nacelles require trailing edge constraints, as expected, but isolated inlets will enforce requirements on compressor face flow distortion. Let us write $(r(A\phi_x - \frac{1}{2}B{\phi_x}^2))_x + (r\phi_r)_r = 0$ and define $\Psi_r = r(A\phi_x - \frac{1}{2}B{\phi_x}^2)$ and $\Psi_x = -r\phi_r$ ($A = 1 - M^2$ and $B = M^2(\Lambda + 1)$ for convenience). Thus $(A - B\phi_x)\Psi_{xx} + \Psi_{rr} - \Psi_r/r = 0$ or $\pm\,|A^2 - 2B\Psi_r/r|^{1/2}\Psi_{xx} + \Psi_{rr} - \Psi_r/r = 0$ for pure subsonic or supersonic flow. For transonic flow, $\phi_r = -\Psi_x/r$ is integrated with respect to r from "r" to "R" and differentiated with respect to x. Thus

$$\phi_x(x, r) = -\tfrac{1}{2}C_p^{\pm}(x, R) + \int_r^R \frac{1}{s}\Psi_{xx}(x, s)ds,$$

where $C_p^{\pm}(x, R)$ refers to $r \gtrless R$, uniquely defining the $A - B\phi_x$ coefficient (the simpler subsonic form applies off the edges, of course, if $M < 1$). This is solved with the Neumann condition $\Psi_r(x, R^{\pm}) = -R(\frac{1}{2}AC_p + BC_p{}^2/8)$ with C_p satisfying Kutta's condition for physical consistency; also, $\Psi = 0$ at infinity and along $r = 0$, and the usual jump conditions hold. Surface coordinates are obtained from $dr^{\pm}(x)/dx = \phi_r(x, R^{\pm}) = -\Psi_x(x, R^{\pm})/R$ or $r^{\pm}(x) = -\Psi(x, R^{\pm})/R$; for closed edges, differences between trailing edge and center line Ψ's provide the disturbance mass flow. This formulation allows inlet and afterbody interaction. In some problems afterbody effects on inlet flow may be less important than a desire for distortion-free flow vital to engine flow stability and surge suppression. Such isolated inlet problems require semi-infinite nacelles with specified lip C_p's or $\Psi_r(x, R^{\pm})$. Edge closure no longer applies; instead, compressor face constraints are imposed (e.g., $\Psi_x = -r\phi_r = 0$ assures a flow without radial velocity, while $\Psi_{xx} = -r(\phi_x)_r = 0$ guarantees a uniform streamwise flow). Improved boundary conditions are computationally possible: substitute $\phi_x = -\frac{1}{2}(C_p + {\phi_r}^2) \cong -\frac{1}{2}(C_p + {\Psi_x}^2/R^2)$ in the definition for Ψ_r and evaluate Ψ_x using latest values (this formulation may be ill-posed, since $\Psi_{xx} + \Psi_{rr} - \Psi_r/r = 0$ is not Laplace's equation; however, numerical results have appeared to be stable). These methods apply to diffusers, nozzles, and wind tunnel test sections with slowly varying contours; the boundary conditions are $\Psi_r(x, R) = -R(\frac{1}{2}AC_p + BC_p{}^2/8)$, vanishing $\Psi_r(x, 0)$ or $\Psi(x, 0)$, and prescribed exit and entry plane streamline deflections specifying nonzero Ψ (again, $r(x) = -\Psi(x, R)/R$). Slender bodies of revolution are more difficult; the formula $C_p = -2\phi_x - {\phi_r}^2$ and the definitions for Ψ imply the "Neumann" condition $\Psi_r = -\frac{1}{2}Ar(C_p + {\Psi_x}^2/r^2) - Br(C_p + {\Psi_x}^2/r^2)^2/8$ where Ψ_x is evaluated using latest values. The weak dependence of Ψ_r/r on x may be useful numerically; streamlines would be obtained from $dr(x)/dx = \phi_r(x, r) = -\Psi_x(x, r)/r$. Similar ideas apply to planar flows.

Sample Calculations

The ideas outlined provide a rational basis for design codes that produce shapes satisfying pressure and auxiliary constraints automatically. Of course, the choice of C_p that yields sections free of unwanted wiggles and surface crossover remains a perennial problem. Because the success of any inverse method ultimately depends on "good" input pressure, this, in practice, would come from analysis results for shapes undergoing minor redesign. Reference [1] addressed transonic design for C_p's with and without shocks and [2] shock-free airfoil design; here, we emphasize instead alternative geometric constraints for both planar and three-dimensional flows. To highlight the basic effects we keep the pressures simple, preferring, for the present, to survey quickly various results implied within the broad scope of stream-function formulations.

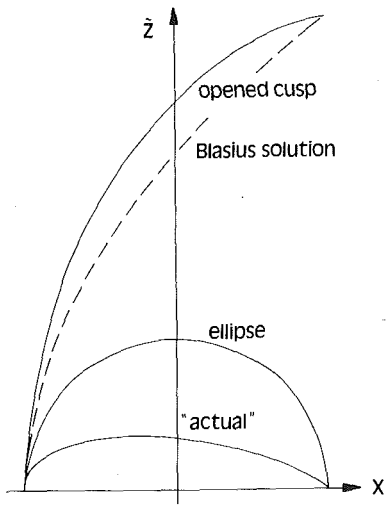


Fig. 1 Thin airfoil results

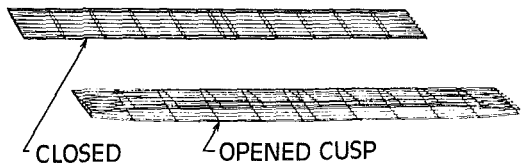


Fig. 2 High aspect ratio thin wing results

The airfoil thickness corresponding to a constant negative $C_p^{\pm} = -2\beta$ prescribed chordwise at Mach zero, assuming leading and trailing edge closure, is a thin ellipse of thickness ratio β, correctly calculated by the difference method of [1]; added "analysis wake logic" easily produced a monotonically growing shape of thickness ratio $\pi\beta$ with an opened cusp. These calculations agreed well with the analytic solutions $\tilde{z} = z^+/\beta\ (1 - x^2)^{1/2}$ and $\tilde{z} = z^+/\beta = \frac{1}{2}\pi + (1 - x^2)^{1/2} + \sin^{-1}x$ (multiples of the latter are appended to shapes whose C_p's are modified by constant β's to provide sharp cusped edges, as discussed). We also indicated how approximate displacement thicknesses could be subtracted from "opened cusp" solutions (based on "β modified" C_p's) to provide "actual" shapes. Such a shape, for example, is shown in Fig. 1, along with the opened cusp, the Blasius boundary layer having the same trailing edge gap and the classic ellipse. Finite span effects were considered taking $C_p(x, 0^{\pm}, y) = -0.2$ on a rectangular unswept planform of aspect ratio 8 at Mach zero; as before, cusped edges were obtained using wake logic, while closed edges assume single-valued Ψ's without "wakes" (for pure subsonic or supersonic flow, panel methods are very efficient, but type-dependent relaxation methods must be used transonically). Calculated midspan sections agreed with the planar shape just given, with three-dimensional effects confined to the wing tips, as shown in Fig. 2; both panel and finite-difference methods gave nearly identical results. Fully three-dimensional transonic design calculations were also pursued using nearly converged analysis pressures; however, shape recovery was hampered by the effects of blunt leading edges, wing sweep and, especially, truncation errors through shocks, present in both analysis and design modes. Unfortunately, high computational costs precluded extensive experiment.

Downloaded 01 May 2010 to 171.66.16.249. Redistribution subject to ASME license or copyright; see http://www.asme.org/terms/Terms_Use.cfm

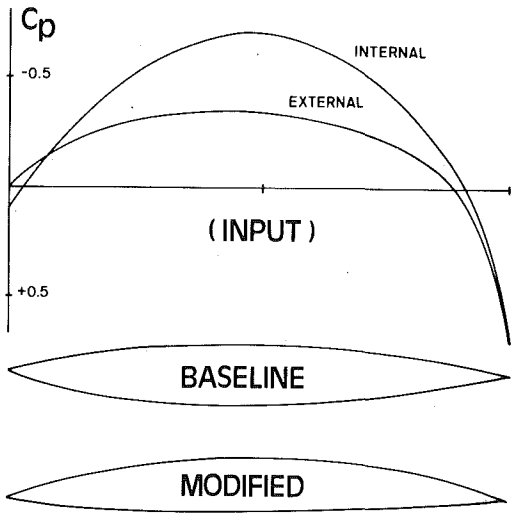


Fig. 3 Inlet/afterbody design calculation

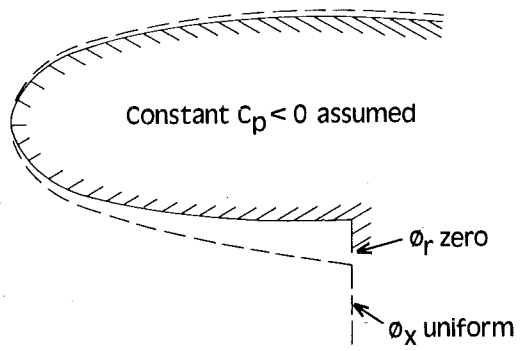


Fig. 4 Isolated inlet design results

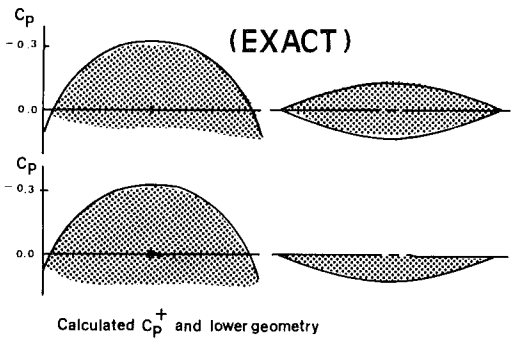


Fig. 5 Mixed analysis and design problems

For airfoils and finite wings in unbounded flow, thickness and lift decouple in small disturbance theory, and analytical and numerical simplifications are possible; in contrast, flows induced by ring sources and vortices in axisymmetric problems are highly coupled, due to center-line effects. Thus inlet, nacelle, and ringwing flow fields, which have not yet yielded to closed-form solution, must be solved numerically. But this is trivial since the difference methods just described require only ϕ_r/r or Ψ_r/r changes. Fig. 3 shows a baseline ringwing section used to generate the C_p shown; it, in turn, reproduced the baseline shape. This same C_p was next used, assuming a smaller mean radius, to produce the modified shape, which correctly shows a flatter internal (lower) surface. These constant density runs were repeated at Mach 0.8; computed shapes, not shown here, however, showed weak surface oscillations near the shock foot and slight crossover at the trailing edge. For isolated inlets, $C_p = -0.6$ at Mach zero was assumed on both internal and external lips (for the latter, this slowly vanished far downstream) with an inlet diameter to lip length ratio of 6. Results for two flow constraints, zero ϕ_r and uniform ϕ_x, as discussed, are shown in Fig. 4; the former, as expected, produces a flatter internal surface more aligned with the free stream.

Finally, consider mixed analysis and design problems (e.g., a wing is redesigned for improved tip flow, specifying stable pressures, but also inboard geometric shape to minimize root bending moment); in general, both closure and Kutta conditions apply, but existence also depends on compatible boundary conditions. No complete theory exists, in particular for small-disturbance flows, but special classic solutions are available in isolated exact examples (see [4]). We sketch an *ad hoc* approach valid three-dimensionally and transonically, but, for simplicity, consider constant density airfoil flows. At the outset, ϕ_z (geometry) and Ψ_z (pressure) are specified arbitrarily on a slit. The first iteration solves an analysis problem satisfying Kutta's condition, using ϕ_z where it is prescribed and zero elsewhere; in the second, solve a design problem satisfying closure, using Ψ_z where it is prescribed, but $\Psi_z = \phi_x$ from latest estimates otherwise. Analysis calculations then follow using $\phi_z = -\Psi_x$ as needed, followed by a design iteration, and so on. Here, pressures for a 10 percent thick unpitched biconvex section were obtained by analysis; mixed calculations specifying geometry on the upper chord and pressure on the lower, were initiated, noting that each iteration in the difference solution need not individually converge. This symmetric example is nontrivial because the circulation initially present, due to numerical asymmetry, must disappear in the converged solution; Fig. 5 shows encouraging results typical of others not reported here. The method probably applies to minor redesigns about known flows provided any slight incompatibility in boundary data is no worse than the discretization error.

Closing Remarks

Inverse problems, analysis-like under stream-function transformations, are easily solved by existing potential flow codes with minor change. References [1 and 2] pursued this idea for transonic planar flows with closed edges; this paper explores the role of constraints in flows of increased geometric and aerodynamic complexity, develops the basic ideas through simple examples, and illustrates their application using subcritical pressures. Essentially, prescribing pressure fixes the lift or vorticity strength $[\phi]$, so that the nonuniqueness, which must be related to source strength, is "directly" and naturally handled using $[\Psi]$. If nonzero, the thickness farfield is source-like, but doublet-like for completely closed trailing edges. Of special interest is the "streamlike" function $\Psi(x, z, y)$: like the more conventional vector potential, it also arises from mass conservation, but it is scalar and tractable mathematically (it is, in a sense, "harmonically conjugate" to $\phi(x, z, y)$ in three dimensions). Unfortunately, it is not possible to furnish additional calculated examples covering the broad scope of stream-function formulations, out of time, funding and length constraints; the author, through the work presented here and in [1, 2] at least, hopes to stimulate further research in this promising area.

Of course, excepting the simplest cases, we have not established existence requirements, but the formulations suggested are physically plausible; other applications, e.g., wings in ground effect, separation modeling for displacement streamlines with $[\Psi_x]$ zero or nonzero, and so on, easily lend themselves to our methodology. Finally, several research areas remain, among them, (1) the need for special "inner" design solutions near noses and wing tips (there, "Lighthill's constraints" apply, but they are known only for constant density planar flows); (2) methods to adjust C_p, to obtain "satisfactory" shapes, if *both* $[\Psi]$ and $[\Psi_x]$ are imposed; (3) heat transfer analogies for design, namely, $T_{xx} + T_{zz} + T_{yy} = 0$, specifying $T_z(x, 0^{\pm}, y)$ on the planform and $\nabla T = 0$ at infinity (closure is automatic since the temperature T is single-valued); (4) studies of any three-dimensional results inferred from the duality between $(1 - M^2)\Psi_{xx} + \Psi_{zz} + \Psi_{yy} = 0$ and $(1 -$

Downloaded 01 May 2010 to 171.66.16.249. Redistribution subject to ASME license or copyright; see http://www.asme.org/terms/Terms_Use.cfm

$M^2)\phi_{xx} + \phi_{zz} + \phi_{yy} = 0$ using classical analysis literature; and possibly, (5) the evaluation of possible exact methods, which may be implicit in $\phi_{ss} + \phi_{nn} = 0$ and $\Psi_{ss} + \Psi_{nn} = 0$, where s and n are streamline coordinates. For alternative "potential function" perspectives on inverse methods for planar and wing-like transonic flows, References [5–11] provide a representative survey.

References

1 Chin, W. C., and Rizzetta, D. P., "Airfoil Design in Subcritical and Supercritical Flows," ASME JOURNAL OF APPLIED MECHANICS, Vol. 46, Dec. 1979, pp. 761–766.

2 Chin, W. C., "Class of Shock-Free Airfoils Producing the Same Surface Pressure," *Journal of Aircraft*, Apr. 1980, pp. 286–288.

3 Lighthill, M. J., "A New Method of Two-Dimensional Aerodynamic Design," *Rep. Memor. Aero. Res. Coun.*, London, No. 2112, 1945.

4 Thwaites, B., *Incompressible Aerodynamics*, Oxford University Press, Oxford, 1960.

5 Sobieczky, H., et al., "New Method for Designing Shock-Free Transonic Configurations," *AIAA Journal*, Vol. 17, July 1979, pp. 722–729.

6 Yu, N. J., "Efficient Transonic Shock-Free Wing Redesign Procedure Using a Fictitious Gas Method," *AIAA Journal*, Vol. 18, Feb. 1980, pp. 143–148.

7 Henne, P. A., "Inverse Transonic Wing Design Method," *Journal of Aircraft*, Vol. 18, Feb. 1981, pp. 121–127.

8 Carlson, L. A., "Transonic Airfoil Design Using Cartesian Coordinates," NASA CR-2578, 1976.

9 Hicks, R. M., and Henne, P. A., "Wing Design by Numerical Optimization," AIAA Paper 77-1247, 1977.

10 Shankar, V., and Malmuth, N. D., "Computational Transonic Inverse Procedure for Wing Design With Automatic Trailing Edge Closure," AIAA Paper 80-1390, 1980.

11 Shankar, V., Malmuth, N. D., and Cole, J. D., "Computational Transonic Airfoil Design in Free Air and a Wind Tunnel," AIAA Paper 78-103, 1978.

Downloaded 01 May 2010 to 171.66.16.249. Redistribution subject to ASME license or copyright; see http://www.asme.org/terms/Terms_Use.cfm

B. E. Foody
P. W. Huber
Associate Professor.
Assoc. Mem. ASME

Department of Mechanical Engineering,
Room 3-258,
Massachusetts Institute of Technology,
Cambridge, Mass. 02139

On the Radial Oscillations of Multiple Gas Bubbles in an Incompressible Liquid

The radial oscillations of multiple gas bubbles in an incompressible liquid bounded by plane solid or free surfaces are analyzed. Derivation of the normal mode frequencies and mode shapes of two, three, and four bubble configurations in an unbounded liquid illustrate the method of analysis. Expressions for the oscillation frequencies of bubbles near free and solid surfaces are derived.

Introduction

The dynamics of a single spherical bubble oscillating radially in a liquid have been extensively investigated. Rayleigh [1] derived the basic equation governing the motion of a gas cavity in an unbounded fluid. Minnaert [2], using a simple energy method, determined the natural frequency of an oscillating gas bubble. Since that time, research on vapor bubbles and cavitation has motivated studies of vapor bubble collapse, heat transfer effects, and a wide range of other topics. Hsieh [3, 4] reviews some of this work.

No previous analysis, however, has dealt generally with the hydrodynamic relations governing interactions among multiple oscillating bubbles and their surroundings. It is well known that a solid surface attracts an oscillating bubble while a free surface repels it [5]. Cole [6] and Friedman [7] have derived expressions for the oscillation period of a single, explosively formed bubble situated between a free and solid surface. Since surfaces can be interpreted as the planes of symmetry in a multiple bubble system, these expressions also determine oscillation periods for a restricted set of multiple bubble configurations.

This paper presents a method for estimating the radial oscillation natural frequencies of any number and configuration of gas bubbles in an unbounded liquid or in a liquid bounded by plane solid or free surfaces. The analysis is limited to linear, small amplitude oscillations.

Model Assumptions

We consider the radial oscillations of N gas bubbles in an unbounded liquid. The liquid flow is assumed to be incompressible and irrotational. Gravitational and surface tension effects are ignored. Far from the bubbles, the pressure P_∞ is uniform.

Radial displacements of the bubble surfaces are taken to be small compared to bubble radii r

$$\delta r/r \ll 1. \tag{1}$$

If the velocity in the fluid varies with a period τ and is characterized by an amplitude U_0 on the bubble surface, then δr is of order $U_0\tau$. The Strouhal number, $r/U_0\tau$ is then much greater than 1 and convective accelerations in the liquid can be ignored. Equation (1) also implies that the time scale for oscillation is much smaller than that for convective distortions of the bubble geometry. We shall assume that the bubble geometry is invariant (spherical or ellipsoidal) during the oscillations analyzed. The gas is treated as ideal and adiabatic with a ratio of specific heats γ. Equation (1) can then be written

$$\delta P/3\gamma P_\infty \ll 1 \tag{2}$$

where δP is the maximum change in bubble pressure from the equilibrium.

Analysis

The kinetic energy T of a liquid bounded internally by surfaces A can be expressed as

$$T = -\tfrac{1}{2}\rho \int_A \phi \frac{\partial \phi}{\partial n} dA \tag{3}$$

where ϕ is the velocity potential and ρ is the liquid density. The normal vector n is defined as pointing *into* the liquid (i.e., outward from the gas bubbles). In our analysis, the integral is taken over the bubble surfaces.

The rate of change of the ith bubble's volume is given by

$$q_i = \int_{A_i} \frac{\partial \phi}{\partial n} dA_i \tag{4}$$

Contributed by the Applied Mechanics Division for publication in the JOURNAL OF APPLIED MECHANICS.
Discussion on this paper should be addressed to the Editorial Department, ASME, United Engineering Center, 345 East 47th Street, New York, N.Y. 10017, and will be accepted until two months after final publication of the paper itself in the JOURNAL OF APPLIED MECHANICS. Manuscript received by ASME Applied Mechanics Division, December, 1980; final revision, March, 1981.

Copyright © 1981 by ASME
Downloaded 01 May 2010 to 171.66.16.249. Redistribution subject to ASME license or copyright; see http://www.asme.org/terms/Terms_Use.cfm

where the integral is taken over the surface of the ith bubble. We define two potentials ϕ_1 and ϕ_2, whose sum is ϕ, such that ϕ_1 is uniform over each bubble surface,

$$\int_{A_i} \frac{\partial \phi_1}{\partial n} dA_i = q_i \quad \text{for} \quad i = 1, 2, \ldots N \tag{5a}$$

and

$$\int_{A_i} \frac{\partial \phi_2}{\partial n} dA_i = 0 \quad \text{for} \quad i = 1, 2, \ldots N. \tag{5b}$$

Physically, ϕ_2 is the amount by which the actual potential ϕ departs from the average potential ϕ, at any point on a bubble's surface. Except in the case of a single bubble in an unconfined liquid, $\partial\phi/\partial n$ will not be uniform over each bubble and thus $\partial\phi_2/\partial n$ may vary over each bubble.

Using the relation

$$\int_A \phi_1 \frac{\partial \phi_2}{\partial n} dA = \int_A \phi_2 \frac{\partial \phi_1}{\partial n} dA \tag{6}$$

we obtain

$$T = \tfrac{1}{2}\rho \left[\int_A \phi_1 \frac{\partial \phi_1}{\partial n} dA + \int_A \phi_2 \frac{\partial \phi_2}{\partial n} dA \right]. \tag{7}$$

The kinetic energy can therefore be defined as the sum of two terms: T_1 which depends on ϕ_1 only, and T_2 which depends on ϕ_2.

Euler's equation for highly unsteady motion,

$$-\nabla P = \rho \nabla(\partial\phi/\partial t), \tag{8}$$

requires that $\partial\phi/\partial t$ be uniform on the bubble surface since the pressure P in the liquid is uniform on that surface. Any initial nonuniformity in ϕ will thus persist through a number of oscillations. As a result, ϕ_2 and therefore T_2 will remain roughly constant over the time scales (several bubble oscillation periods) of interest in this analysis.

We note here that, as a consequence of equation (7), the kinetic energy of any bubble system with given volume rates of expansion is a minimum when ϕ is uniform over each bubble surface.

Since ϕ_1 is uniform on each bubble

$$T = -\tfrac{1}{2}\rho \mathbf{q}^T \boldsymbol{\phi}_1 + T_2 \tag{9}$$

where $\mathbf{q}$ is a column vector of the q_i and $\boldsymbol{\phi}_1$ is a column vector specifying the uniform potential ϕ_1 on each surface. Each q_i is related to $\boldsymbol{\phi}_1$ by Laplace's equation and hence varies linearly with each term of $\boldsymbol{\phi}_1$. The relation can therefore be expressed as

$$\mathbf{q} = \mathbf{C}\boldsymbol{\phi}_1 \tag{10}$$

where $\mathbf{C}$ is a square matrix depending only on geometry. $\mathbf{C}$ is analogous to the capacitance matrix in an electrostatic problem with charged conductors.

The kinetic energy may now be written

$$T = \tfrac{1}{2}\mathbf{q}^T \mathbf{M} \mathbf{q} + T_2 \tag{11}$$

where

$$\mathbf{M} \equiv -\rho \mathbf{C}^{-1}. \tag{12}$$

The potential energy of the ith bubble V_i^* is

$$V_i^* = -\int_{V_{0i}}^{V_{0i}+\delta V_i} (P_i - P_\infty) dV \tag{13}$$

where P_i is the pressure in the ith bubble, V_{0i} is its equilibrium volume and δV_i is the change in volume from V_{0i}. Assuming reversible adiabatic expansion of each gas bubble the total potential energy V^* of the multiple bubble system can be found from equation (13) and expressed as

$$V^* = \tfrac{1}{2}\boldsymbol{\delta V}^T \mathbf{K} \boldsymbol{\delta V} \tag{14}$$

where $\boldsymbol{\delta V}$ is a vector of δV_i and is a diagonal matrix whose elements are

$$K_{ii} = \frac{P_\infty \gamma}{V_{0i}}. \tag{15}$$

Lagrange's equations, with $\delta \dot{V}_i$ substituted for q_i require:

$$\frac{d}{dt}\left(\frac{\partial T}{\partial(\delta \dot{V}_i)}\right) - \frac{\partial T}{\partial(\delta V_i)} = -\frac{\partial V^*}{\partial(\delta V_i)} \quad \text{for} \quad i = 1, 2, \ldots N. \tag{16}$$

If $\mathbf{M}$ does not vary with time, we obtain

$$\mathbf{M}\boldsymbol{\delta \ddot{V}} + \mathbf{K}\boldsymbol{\delta V} = 0. \tag{17}$$

The constant term T_2 in the kinetic energy disappears in the differentiation. The eigenvalues of equation (17),

$$|-\omega^2 \mathbf{M} + \mathbf{K}| = 0, \tag{18}$$

are the natural frequencies ω of the N bubble system and the eigenvectors define the mode shapes. If the eigenvectors are known *a priori*, ω can be deduced from the Rayleigh-Ritz equation (8)

$$\omega = \sqrt{\frac{\tfrac{1}{2}\boldsymbol{\delta V}^T \mathbf{K} \boldsymbol{\delta V}}{\tfrac{1}{2}\boldsymbol{\delta V}^T \mathbf{M} \boldsymbol{\delta V}}} \tag{19}$$

where $\boldsymbol{\delta V}$ is an eigenvector. This formulation is particularly useful when the mode shapes can be deduced directly from considerations of symmetry.

The Mass Matrix. The mass matrix, equation (12), relates $\boldsymbol{\phi}$ and $\mathbf{q}$. For a single spherical bubble of radius r_0

$$\phi = -\frac{q}{4\pi r_0} \tag{20}$$

and equations (10) and (12) yield

$$M = \frac{\rho}{4\pi r_0}. \tag{21}$$

Substituting equations (21) and (15) into equation (19) yields the well-known Rayleigh bubble natural frequency (2)

$$\omega = \frac{1}{r_0}\sqrt{\frac{3P_\infty \gamma}{\rho}}. \tag{22}$$

For a single ellipsoidal bubble with semiaxes a, b, c, Smythe [9] gives

$$\phi = -\frac{q}{8\pi} \int_0^\infty [(a^2+\theta)(b^2+\theta)(c^2+\theta)]^{-1/2} d\theta. \tag{23}$$

Therefore

$$M = \frac{\rho}{8\pi} \int_0^\infty [(a^2+\theta)(b^2+\theta)(c^2+\theta)]^{-1/2} d\theta. \tag{24}$$

If the ellipsoid is prolate, equation (24) with $a = b$ can be integrated to give

$$M = \frac{\rho}{4\pi a}\left[\frac{-1}{\sqrt{(c/a)^2-1}} \log\left[(c/a) - \left[\left(\frac{c}{a}\right)^2 - 1\right]^{1/2}\right]\right] \quad c > a \tag{25a}$$

$$M = \frac{\rho}{4\pi a}\left[\frac{1}{\sqrt{1-\left(\frac{c}{a}\right)^2}}\left[\frac{\pi}{2} - \tan^{-1}\frac{1}{\sqrt{\left(\frac{a}{c}\right)^2 - 1}}\right]\right] \quad c < a, \tag{25b}$$

Fig. 1 compares bubble frequencies of single spherical and ellipsoidal bubbles of equal volume calculated using equation (19) with equation (21) or (25), respectively. The dependence of bubble frequency on bubble geometry is found to be very weak.

It is more difficult to determine the elements of $\mathbf{M}$ analytically for configurations involving two or more bubbles. Smythe [9] uses a method of images approach [10] to solve the analogous electrostatic problem: the potential energy of two charged conducting spheres of radius r_0 separated center to center by r_{12}. The solution can be expressed in terms of $\mathbf{M}$ as

$$M_{11} = M_{22} = \frac{\rho}{4\pi r_0}\left(\frac{A}{A^2 - B^2}\right) \tag{26a}$$

Downloaded 01 May 2010 to 171.66.16.249. Redistribution subject to ASME license or copyright; see http://www.asme.org/terms/Terms_Use.cfm

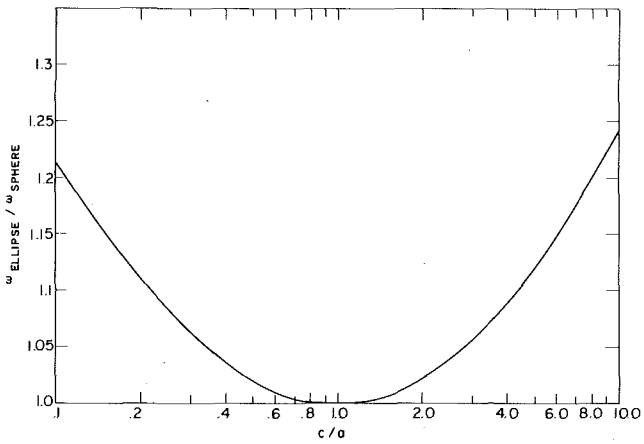


Fig. 1 Ellipsoidal bubble frequency ($\omega_{ellipse}$) compared to the frequency of a spherical bubble of the same volume; ellipsoid semiaxes are *c*, *a*, *a*

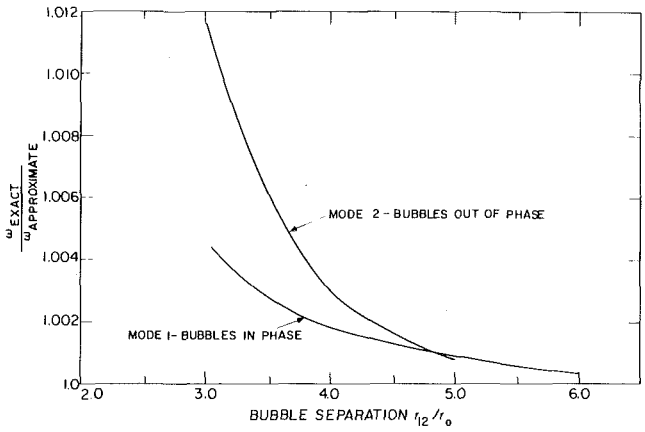


Fig. 2 Exact and approximate frequencies for two bubbles

$$M_{12} = M_{21} = \frac{\rho}{4\pi r_{12}}\left(\frac{r_{12}}{r_0}\right)\left(\frac{B}{A^2 - B^2}\right) \tag{26b}$$

where

$$A = \sinh\beta \sum_{n=1}^{\infty} \operatorname{csch}\left[(2n-1)\beta\right]$$

$$B = \sinh\beta \sum_{n=1}^{\infty} \operatorname{csch}\left[(2n)\beta\right]$$

$$\cosh\beta = \frac{r_{12}}{2r_0}.$$

Solving the eigenvalue problem of equation (18) we find that the natural frequencies are

$$\omega_1 = \sqrt{\frac{3P_\infty\gamma}{\rho}(A - B)} \tag{26c}$$

$$\omega_2 = \sqrt{\frac{3P_\infty\gamma}{\rho}(A + B)} \tag{26d}$$

The two eigenvectors can be given as the columns of a square matrix $\mathbf{A}_2$:

$$\mathbf{A}_2 = \begin{pmatrix} 1 & 1 \\ 1 & -1 \end{pmatrix} \tag{26e}$$

The first mode describes two bubbles oscillating in phase; in the second mode the bubbles are 180° out of phase. Both the phasing and the relative amplitudes of the bubble oscillation in these two normal modes could, of course, have been anticipated from the problem's symmetry.

Exact analytic solutions of **M** for more complex configurations are not available. However, a very accurate approximate expression for **M** may be derived for spherical bubbles by assuming a uniform source distribution dq' on each bubble's surface. In any multiple bubble configuration this assumption implies a nonuniform potential field ϕ' on each bubble. It follows from equation (7) that

$$T_1 < -\frac{1}{2}\rho\int_A \phi'\frac{\partial\phi'}{\partial n}dA. \tag{27}$$

The definition of the divergence, implies

$$dq' = \nabla^2\phi' dV. \tag{28}$$

Equations (27) and (28) and Green's theorem then yield

$$T_1 < -\tfrac{1}{2}\rho\int\phi' dq'. \tag{29}$$

Integrating

$$T_1 < \tfrac{1}{2}\dot{\delta\mathbf{V}}^T\mathbf{M}\dot{\delta\mathbf{V}} \tag{30}$$

where the approximate mass matrix is

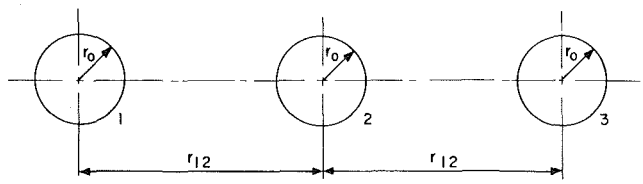


Fig. 3 Three-bubble configuration

$$M_{ij} = \frac{\rho}{4\pi r_{ij}}. \tag{31}$$

Here r_{ij} is the center-to-center separation between the ith and jth bubble if $i \neq j$, and the equilibrium bubble radius if $i = j$.

Use of the approximate mass matrix leads to an overestimate of T_1, and thus underestimates ω (equation (19)). The accuracy of the approximation is expected to increase with increasing bubble separation. The examples in the following section demonstrate that equation (31) provides a remarkably accurate estimate of ω even for bubbles in close proximity.

Multiple Bubble Configurations

Consider again two spherical bubbles of equal radii. Using equation (31) for **M** and taking $\lambda = 1/\omega^2$, equation (18) reduces to the eigenproblem

$$\begin{vmatrix} \frac{\lambda P_\infty\gamma}{V_0} - \frac{\rho}{4\pi r_0} & \frac{-\rho}{4\pi r_{12}} \\ \frac{-\rho}{4\pi r_{12}} & \frac{\lambda P_\infty\gamma}{V_0} - \frac{\rho}{4\pi r_0} \end{vmatrix} = 0. \tag{32}$$

This yields natural frequencies

$$\omega_1 = \frac{1}{r_0}\sqrt{\frac{3p_\infty\gamma}{\rho\left(1 + \frac{r_0}{r_{12}}\right)}} \tag{33a}$$

and

$$\omega_2 = \frac{1}{r_0}\sqrt{\frac{3P_\infty\gamma}{\rho\left(1 - \frac{r_0}{r_{12}}\right)}} \tag{33b}$$

with the mode shapes defined by the columns of $\mathbf{A}_2$

$$\mathbf{A}_2 = \begin{pmatrix} 1 & 1 \\ 1 & -1 \end{pmatrix}. \tag{33c}$$

Fig. 2 compares these approximate solutions (equations (33*a*) and (33*b*)) with the exact solutions (equation (26)). The approximate solutions underestimate ω for both mode shapes, as expected. How-

Downloaded 01 May 2010 to 171.66.16.249. Redistribution subject to ASME license or copyright; see http://www.asme.org/terms/Terms_Use.cfm

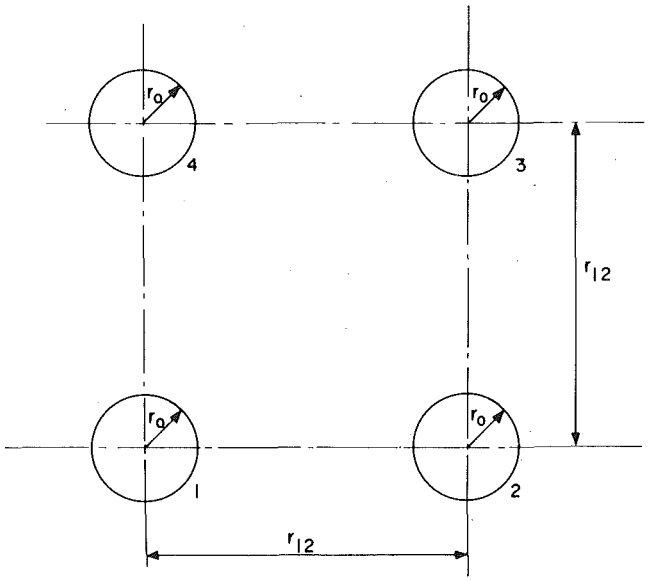


Fig. 4 Four-bubble configuration

ever, for bubble center-to-center separations as low as three bubble radii, the error is less than 1.2 percent.

Consider three aligned bubbles with center-to-center separations r_{12} (Fig. 3). The approximate **M** matrix is

$$\mathbf{M} = \frac{\rho}{4\pi}\begin{pmatrix} \frac{1}{r_0} & \frac{1}{r_{12}} & \frac{1}{2r_{12}} \\ \frac{1}{r_{12}} & \frac{1}{r_0} & \frac{1}{r_{12}} \\ \frac{1}{2r_{12}} & \frac{1}{r_{12}} & \frac{1}{r_0} \end{pmatrix} \tag{34}$$

The eigenvalues are found to be

$$\omega_1 = \frac{1}{r_0}\sqrt{\frac{3P_\infty\gamma}{\rho\left(1 + 1.6861\frac{r_0}{r_{12}}\right)}} \tag{35a}$$

$$\omega_2 = \frac{1}{r_0}\sqrt{\frac{3P_\infty\gamma}{\left(1 - 0.5\frac{r_0}{r_{12}}\right)}} \tag{35b}$$

$$\omega_3 = \frac{1}{r_0}\sqrt{\frac{3P_\infty\gamma}{\left(1 - 1.1861\frac{r_0}{r_{12}}\right)}} \tag{35c}$$

and the mode shapes are given by the columns of $\mathbf{A}_3$

$$\mathbf{A}_3 = \begin{pmatrix} 1 & 1 & 1 \\ 1.1861 & 0 & -1.6861 \\ 1 & -1 & 1 \end{pmatrix}. \tag{35d}$$

In the first mode, all the bubbles oscillate in phase. In the second, only the two outside bubbles have finite amplitudes of oscillation. The third mode has the center bubble 180° out of phase with the other two. As expected from the symmetry of the configuration, the end bubbles have the same amplitude in each mode. Comparison with the results of a numerical calculation (in which the mass matrix was accurately computed by a method of images analysis) shows that the estimated natural frequencies are in error by less than 1.7 percent for $r_{12}/r_0 \geq 3$ (11).

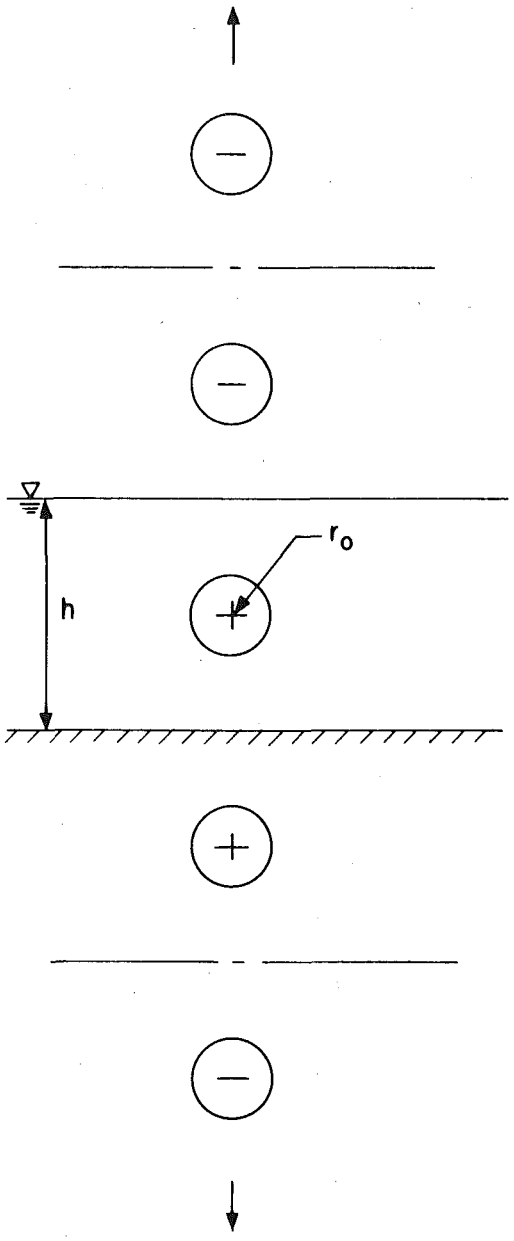


Fig. 5 Bubble between free and solid surfaces

The four bubble case shown in Fig. 4. provides a final test of the approximations inherent in equation (31). The same procedure as in the previous examples yields a matrix of eigenvectors

$$\mathbf{A}_4 = \begin{pmatrix} 1 & 1 & 1 & 1 \\ 1 & 1 & -1 & -1 \\ 1 & -1 & 1 & -1 \\ 1 & -1 & -1 & 1 \end{pmatrix} \tag{36a}$$

Again, the symmetry of the problem requires that each bubble have the same amplitude and that the normal modes involve phase differences of 0° or 180°. The eigenvectors actually found are consistent with both of these requirements.

The eigenvalues are found to be

$$\omega_1 = \frac{1}{r_0}\sqrt{\frac{3P_\infty\gamma}{\rho\left(1 + 2.707\frac{r_0}{r_{12}}\right)}} \tag{36b}$$

Downloaded 01 May 2010 to 171.66.16.249. Redistribution subject to ASME license or copyright; see http://www.asme.org/terms/Terms_Use.cfm

$$\omega_2 = \omega_4 = \frac{1}{r_0}\sqrt{\frac{3P_\infty\gamma}{\rho\left(1 - 0.707\frac{r_0}{r_{12}}\right)}} \tag{36c}$$

$$\omega_3 = \frac{1}{r_0}\sqrt{\frac{3P_\infty\gamma}{\rho\left(1 - 1.293\frac{r_0}{r_{12}}\right)}}. \tag{36d}$$

The identity of ω_2 and ω_4 results from the geometric identity of mode shapes 2 and 4 (the second and fourth columns of $\mathbf{A}_4$). These results are within 2.7 percent of an accurate numerical calculation for $r_{12}/r_0 = 3$ (11).

Free and Solid Surfaces

The normal modes for $2N$ bubbles in an infinite pool will implicitly determine the normal modes for N bubbles adjacent to a plane solid or free surface that replaces any plane of symmetry in the $2N$ bubble configuration. A first example is presented in equations (33*a*) and (33*b*) which can be interpreted as the frequencies of oscillation of a single bubble adjacent to a solid or free surface, respectively. Two bubbles aligned parallel to a free surface, twice as far apart as their distance from the surface, will have two normal modes corresponding to Modes 2 and 3 of the four bubble configuration, equations (36*c*) and (36*d*). If the surface is replaced by a solid surface, the two normal modes are given by Modes 1 and 4. These results demonstrate expected trends: proximity to a free surface raises normal mode frequencies and brings them closer together; a solid surface lowers frequencies and spreads them apart.

The analysis of bubbles oscillating near free and solid surfaces is greatly simplified by a method of images approach. When more than one free or solid surface is present, the number of image bubbles required is usually infinite, but the amplitudes and phasing of the image bubbles can be deduced in advance by inspection. Images are always of the same amplitude as the "object" bubble, in phase for a solid surface image and 180° out of phase for a free surface. When the mode shape can be determined directly, an analysis of the natural frequencies based on equation (19) is considerably simpler than an attempt to identify the appropriate eigenvalues in equation (18) when the dimensions of $\mathbf{M}$ and $\mathbf{K}$ are infinite.

For a system with N independent bubbles and an arbitrary boundary of free and solid plane surfaces there are N normal modes of oscillation. The problem can always be reduced to analyzing an $N \times N$ mass matrix whose M_{ij} element relates the potential on the ith bubble to the volume flux from the jth bubble *and* all its images. If the $j + kN$th bubble is a reflection of the jth,

$$M_{ij} = \sum_{k=0}^{\infty}\left[\frac{\rho}{4\pi r_{i\,j+kN}}\left(\frac{q_{j+kN}}{q_j}\right)\right]. \tag{37}$$

The ratio q_{j+kN}/q_j will equal ± 1 depending on the types of "reflecting" surfaces involved. The elements of the stiffness matrix $\mathbf{K}$ will be given by equation (15) as before.

Fig. 5 shows an example of a single bubble situated midway between a free and solid surface separated by a distance h. For this case,

$$M = \frac{\rho}{4\pi r_0}\left[1 + \sum_{k=1}^{\infty}(-1)^k\frac{r_0}{kh}\right] \tag{38}$$

and equation (19) then yields

$$\omega = \frac{1}{r_0}\sqrt{\frac{3P_\infty\gamma}{\rho\left(1 + \sum_{k=1}^{\infty}(-1)^k\left(\frac{r_0}{kh}\right)\right)}} \approx \frac{1}{r_0}\sqrt{\frac{3P_\infty\gamma}{\rho\left(1 - 0.693\frac{r_0}{h}\right)}}. \tag{39}$$

Cole [6] and Friedman [7] use a similar technique to describe the motion of an explosively formed bubble in a pool of finite depth.

Concluding Remarks

The small amplitude oscillations of a single spherical bubble in an unbounded liquid are analogous to those of a one-spring, one-mass system with $K = P_\infty\gamma/V_0$ and $M = \rho/4\pi r_0$. Nonspherical bubble shape has only a weak effect on predicted frequency. Multiple spherical bubbles in an unbounded liquid have normal mode frequencies and mode shapes that can be found by formulating K and M matrices as outlined in this paper and analyzing the matrix $M^{-1}K$. Use of approximate mass matrix elements greatly simplifies the construction of M with little loss of accuracy in the frequency predictions. The effects of plane pool boundaries on the elements of M can be determined by a method of images.

References

1 Rayleigh, O. M., *Philosophical Magazine*, Vol. 34, 1917, p. 94.

2 Minnaert, M., *Philosophical Magazine* Vol. 16, 1933, p. 235.

3 Hsieh, D. Y., ASME *Journal of Basic Engineering*, Vol. 87, No. 4, Dec. 1965, pp. 991–1005.

4 Hsieh, D. Y., ASME *Journal of Basic Engineering*, Vol. 94, No. 3, Sept. 1972, pp. 655–665.

5 Birkhoff and Zarentello, *Jets, Wakes, and Cavities*, Academic Press, N.Y., 1957.

6 Cole, R. H., *Underwater Explosions*, Princeton University Press, 1950.

7 Friedman, B., *Comm. on Pure and Applied Maths*, Vol. 3, No. 2, June 1950.

8 Lamb, H., *Hydrodynamics*, 6th ed., Cambridge University Press, London, 1932.

9 Smythe, W. R., *Static and Dynamic Electricity*, McGraw-Hill, New York, 1960; Shima, A., ASME *Journal of Basic Engineering*, Vol. 93, 1971, pp. 426–432 also addresses this problem.

10 Milne-Thompson, L. M., *Theoretical Hydrodynamics*, Macmillan, New York, 1968.

11 Foody, B. E., "On the Dynamics of Bubbles in Close Proximity," SM Thesis, Department of Mechanical Engineering, Massachusetts Institute of Technology, Cambridge, Mass., May 1980.

Downloaded 01 May 2010 to 171.66.16.249. Redistribution subject to ASME license or copyright; see http://www.asme.org/terms/Terms_Use.cfm

L. N. Tao

Professor of Mechanics,
Department of Mechanics and
Mech. & Aero. Engineering,
Illinois Institute of Technology,
Chicago, Ill. 60616
Mem. ASME

The Exact Solutions of Some Stefan Problems With Prescribed Heat Flux

The Stefan problem of a semi-infinite material with arbitrarily prescribed initial and flux conditions is studied. When the surface temperature is initially different from the freezing temperature, there exists a presolidification or a premelting period prior to the occurrence of a phase change. The exact solutions for both periods, before and after the appearance of a phase change, are established. This indicates that the initial condition of the Stefan problem with a prescribed heat flux at the surface cannot be assumed to be constant. Possibilities of similarity solutions of the problem are also examined. A similarity solution exists only when the heat flux is proportional to $t^{-1/2}$ and the initial and boundary conditions satisfy an inequality. The solidification of a supercooled liquid is also investigated. The exact solution is obtained.

Introduction

In a recent paper [1], the exact solution of the moving boundary problem of a semi-infinite material with arbitrarily prescribed initial and flux conditions has been found. There remain some questions unanswered. The purpose of this investigation is to gain a better and deeper understanding of the problem and to establish some new results.

There are many physical problems concerned with freezing or melting. A difficulty of these problems is the presence of a moving surface of separation between two phases of the material. The position of this surface of separation is not given *a priori* and is one of the unknowns to be solved. These problems are commonly known as the Stefan problems or moving boundary problems.

Moving boundary problems have been studied for more than a hundred years. The first known exact solution was established by Neumann in the 1860's (see [2]) and by Stefan in 1889 [3]. They considered a semi-infinite material initially at a constant temperature, which is then in contact with a different constant temperature at its surface. The temperature distributions are established in terms of the similarity variable $x/t^{1/2}$ and the position of the interfacial boundary is found to be proportional to $t^{1/2}$. This means that the partial differential equations are reducible by a similarity transformation to ordinary differential equations. A similarity transformation is possible only when the domain is semi-infinite and the initial and boundary conditions are of some special forms. Since similarity solutions to problems with other boundary and initial conditions are not generally possible, many different mathematical techniques and approximate methods have been devised to find solutions of these moving boundary problems. They have been discussed and summarized in several books [4–7], survey articles [8–11], and some recent conference proceedings [12, 13].

To seek exact solutions of moving boundary problems not by similarity transformation has been the objective of many researches. Only very recently, an analytically exact solution of the classical Stefan problem of a semi-infinite material with arbitrarily prescribed initial and boundary conditions has been found [14]. The exact solutions of the problem with arbitrarily prescribed heat flux or radiation boundary condition at its surface have also been derived [1, 15].

There are some differences between the solutions of moving boundary problems of a semi-infinite material with prescribed temperature and prescribed heat flux. One of these differences is that the position of the interfacial boundary in the former problem is of the order of $t^{1/2}$ as $t \to 0$, while in the latter it is of the order of t. One of the purposes of the present paper is to investigate this difference of the order. In the flux problem discussed in [1], the initial temperature at the surface is taken to be the freezing temperature of the material. When this condition is altered, we find that no physically admissible solution of the problem with an immediate moving boundary is possible. This does not mean that there is no solution to the problem. It is found that the solution has two parts. There is no change of phase in the early stage and a change of phase will occur only after the surface temperature has reached the freezing point. In other words, there exists a presolidification or a premelting period until the surface temperature has reached the freezing point. This might have been

Contributed by the Applied Mechanics Division for publication in the JOURNAL OF APPLIED MECHANICS.

Discussion on this paper should be addressed to the Editorial Department, ASME, United Engineering Center, 345 East 47th Street, New York, N. Y. 10017, and will be accepted until two months after final publication of the paper itself in the JOURNAL OF APPLIED MECHANICS. Manuscript received by ASME Applied Mechanics Division, July, 1980; final revision, April, 1981.

Copyright © 1981 by ASME

Downloaded 01 May 2010 to 171.66.16.249. Redistribution subject to ASME license or copyright; see http://www.asme.org/terms/Terms_Use.cfm

expected intuitively. However, this is not the case with arbitrarily prescribed temperature at its surface where a change of phase and consequently a moving boundary, will occur immediately after the contact. This leads to a conclusion that no immediate solidification is possible in a flux problem when the surface temperature is above the freezing point initially. A consequence of this result is that in a flux problem the temperature distribution immediately preceding the occurrence of a phase change cannot be arbitrarily assigned. This excludes the possibility of a constant initial state for the Stefan problem with prescribed heat flux. Any study of this problem must attend to this fact.

To further pursue the point of immediate occurrence of a phase change, we next investigate possibilities of similarity solutions. A similarity solution for the problem with a constant temperature initially and a different constant temperature at its surface (Neumann's solution) is well known. A replacement of a constant heat flux, instead of a constant temperature, at its surface does not permit a similarity solution. It is found, however, that a similarity solution does exist. It exists only when the heat flux is proportional to $t^{-1/2}$ and when the initial temperature at the surface is not far different from the freezing temperature. The latter condition is established in the form of an inequality. When this inequality is not satisfied, no solution is possible.

Finally, we intend to study a problem of a different nature, solidification of a supercooled liquid. A similarity solution for the problem with freezing temperature at its surface is known [5]. It is valid when the degree of supercooling is small. It is found that this same condition also prevails in the present problem with arbitrary heat supply. When this condition is satisfied, the exact solution is established.

Mathematical Solutions

To describe the physical problem, let us be specific and consider the solidification problem. The material is originally in a liquid state, occupying a half space $x > 0$, with an initial temperature $V(x)$ above the freezing temperature T_f. At its surface $x = 0$, there is a heat flux $-Q(t)$. Denote the solid and liquid phases of the material by subscripts I and II, respectively; then the temperature distributions satisfy

(*i*) Differential Equations:

$$\begin{aligned} \alpha_I(\partial^2 T_I/\partial x^2) &= \partial T_I/\partial t \quad 0 < x < s(t) \\ \alpha_{II}(\partial^2 T_{II}/\partial x^2) &= \partial T_{II}/\partial t \quad s(t) < x < \infty \end{aligned} \tag{1}$$

where $s(t)$ is the position of the interfacial boundary.

(*ii*) Boundary and Initial Conditions:

$$k_I(\partial T_I/\partial x)_{x=0} = Q(t), \quad T_{II}(x, 0) = V(x) \tag{2}$$

(*iii*) Interface Conditions:

$$\begin{aligned} T_I(s, t) &= T_{II}(s, t) = T_f \\ k_I(\partial T_I/\partial x)_s - k_{II}(\partial T_{II}/\partial x)_s &= \rho L(ds/dt) \\ s(0) &= 0 \end{aligned} \tag{3}$$

where ρ is the density and L is the latent heat.

To complete the description, we assume that both the boundary and initial conditions $Q(t)$ and $V(x)$ are analytic functions and expressible by power series,

$$\begin{aligned} Q(t) &= (k_I/\alpha_I^{1/2}) \sum_0 q_n t^n/n!, & q_n &= (\alpha_I^{1/2}/k_I)(d^n Q/dt^n)_0 \\ V(x) &= \sum_0 v_n (x/\alpha_{II}^{1/2})^n/n!, & v_n &= \alpha_{II}^{n/2}(d^n V/dx^n)_0 \end{aligned} \tag{4}$$

The problem now is to find the solutions of temperatures T_I and T_{II} and the interfacial boundary $s(t)$. Before we discuss these solutions, we recall that solutions of the heat equation can be expressed in products of the repeated error integral and time t. Following [14], we introduce

$$E_n(\xi) = \tfrac{1}{2}[i^n \operatorname{erfc}(-\xi) + i^n \operatorname{erfc} \xi] \tag{5}$$

$$\begin{aligned} F_n(\xi) &= \tfrac{1}{2}[i^n \operatorname{erfc}(-\xi) - i^n \operatorname{erfc} \xi] \\ G_n(\xi) &= \tfrac{1}{2}[i^n \operatorname{erfc}(-\xi) + (-1)^n i^n \operatorname{erfc} \xi] \\ &= \sum_0^{[n/2]} \xi^{n-2m}/2^{2m} m!\,(n-m)! \end{aligned} \tag{5}$$

(*Cont.*)

where $\xi = x/(4\alpha t)^{1/2}$. We note that $G_n(\xi)$ is a polynomial of order n. Properties of these functions follow directly from those of the repeated error integrals. We mention only that all three functions are unbounded at $t = 0$, but their products with $t^{n/2}$ have a definite limit,

$$\begin{aligned} (4\alpha t)^{n/2} E_n(\xi)|_{t=0} &= (4\alpha t)^{n/2} F_n(\xi)|_{t=0} = (4\alpha t)^{n/2} G_n(\xi)|_{t=0} \\ &= x^n/n! \end{aligned} \tag{6}$$

Using these functions, we introduce the temperature solutions:

$$\begin{aligned} T_I(x, t) &= \sum_0 q_n (4t)^{n+1/2} G_{2n+1}(\xi_I) + \sum_0 a_n (4t)^{n/2} E_n(\xi_I) \\ T_{II}(x, t) &= \sum_0 v_n (4t)^{n/2} G_n(\xi_{II}) + \sum_0 b_n (4t)^{n/2} i^n \operatorname{erfc} \xi_{II} \end{aligned} \tag{7}$$

These two temperature solutions satisfy the prescribed initial and boundary conditions. At $x = 0$

$$\begin{aligned} k_I(\partial T_I/\partial x)_0 &= (k_I/\alpha_I^{1/2}) \left[\sum_0 q_n (4t)^n G_{2n}(0) + \sum_0 a_{n+1} (4t)^{n/2} F_n(0)\right] \\ &= Q(t) \end{aligned}$$

As $t \to 0$,

$$T_{II}(x, 0) = \sum_0 v_n (4t)^{n/2} G_n(\xi_{II})|_{t=0} = V(x)$$

To complete the solutions, we need to find the coefficients a_n and b_n and the interfacial boundary $s(t)$ to satisfy the interface conditions. To this end, let us construct the solution of the interfacial boundary in the form

$$s(t) = t^\delta \chi(t)$$

where $\chi(0) \neq 0$. Substitutions of the equation and the temperature solutions in (3) and evaluation at $t = 0$ reveal that $\delta = \frac{1}{2}$. To determine the function $\chi(t)$, we find that it, as in many other moving boundary problems, must be expressed as a power series of $t^{1/2}$, not t, in order to satisfy the interfacial conditions. Accordingly, we introduce

$$\begin{aligned} \tau &= t^{1/2}, \quad \omega = (\alpha_I/\alpha_{II})^{1/2} \\ s(t) &= 2\alpha_I^{1/2} \sum_0 \lambda_n \tau^{n+1} \\ \eta_I(t) &= s/(4\alpha_I t)^{1/2} = \sum_0 \lambda_n \tau^n \\ \eta_{II}(t) &= s/(4\alpha_{II} t)^{1/2} = \omega \sum_0 \lambda_n \tau^n \end{aligned} \tag{8}$$

Substitution of these equations in the interface conditions and evaluation at $t = 0$ yield

$$a_0 = T_f, \quad b_0 = -(v_0 - T_f)/\operatorname{erfc}(\omega\lambda_0) \tag{9}$$

and that λ_0 satisfies

$$-\omega k_{II}(v_0 - T_f) \exp(-\omega^2\lambda_0^2) = \pi^{1/2} \rho L \alpha_I \lambda_0 \operatorname{erfc}(\omega\lambda_0) \tag{10}$$

Since $v_0 > T_f$, no positive solution of λ_0 exists [16]. Though a negative solution does exist, it is physically inadmissible. A negative λ_0 corresponds to a motion of the interfacial boundary traveling initially outside the material region. This then leads to a question: Is there a solution to the problem? It suffices to say that a solution exists. In the foregoing derivation, we have taken that $s(t)$ is an analytic function of τ and is nonzero when $t > 0$. This condition must be disregarded. Instead, it is necessary, when $v_0 > T_f$, to use a piecewise continuous function for $s(t)$. In other words, there are two parts to the solution. From (9) and (10) we readily observe that when $v_0 = T_f$ a trivial

Downloaded 01 May 2010 to 171.66.16.249. Redistribution subject to ASME license or copyright; see http://www.asme.org/terms/Terms_Use.cfm

non-negative solution of λ_0 exists, i.e., $\lambda_0 = 0$. Physically, this corresponds to the situation that there is no solidification in the early stage. Solidification will occur only after the surface temperature has lowered to the freezing point and continues to fall subsequently. It means that there is a *presolidification period*, during which the temperature of the liquid will be lowered without solidification.

The temperature distribution of the liquid $T^p_{II}(x, t)$ in this presolidification period can be easily found. Expressing the boundary and initial conditions by

$$k_{II}[\partial T^p_{II}(0, t)/\partial x] = Q(t) = (k_{II}/\alpha_{II}^{1/2}) \sum_0 \bar{q}_n t^n/n!$$

$$T^p_{II}(x, 0) = \sum_0 v_n (x/\alpha_{II}^{1/2})^n/n!$$

$$\bar{q}_n = q_n (k_I/k_{II})(\alpha_{II}/\alpha_I)^{1/2} \tag{11}$$

we have

$$T^p_{II}(x, t) = \sum_0 v_n (4t)^{n/2} E_n(\xi_{II}) - \sum_0 \bar{q}_n (4t)^{n+1/2} i^{2n+1} \operatorname{erfc} \xi_{II} \tag{12}$$

Its surface temperature is

$$T^p_{II}(0, t) = \sum_0 v_n \tau^n/\Gamma(\tfrac{1}{2}n + 1) - \sum_0 \bar{q}_n \tau^{2n+1}/\Gamma(n + \tfrac{3}{2}) \tag{13}$$

This presolidification period ends when the surface temperature reaches T_f. Let t_f ($= \tau_f^2$) be the time required for the surface temperature to reach T_f; then

$$T_f = v_0 - \tau_f \sum_0 p_n \tau_f^n \tag{14}$$

where

$$p_{2n-1} = -v_{2n}/n!, \quad p_{2n} = (\bar{q}_n - v_{2n+1})/\Gamma(n + \tfrac{3}{2})$$

The value of t_f may be found from the inverse function of this equation. To facilitate the evaluation, Faa de Bruno's formula for derivatives of a function of a function [17] will be used. Let $f = f(x)$ and $x = x(t)$. Then

$$D_t^N f = \sum_{m=0}^{N} N!\, Z_m^N(x)\, d^m f/dx^m \tag{15}$$

and

$$Z_m^N(x) = \sum_{\alpha_k} \prod_1^N [(D_t^k x/k!)^{\alpha_k}/\alpha_k!]$$

where the sum $\Sigma\alpha_k$ is extended to all non-negative integers such that

$$\sum_1^N \alpha_k = m, \quad \sum_1^N k\alpha_k = N$$

These multinomial coefficients may be found in [18].[1]

Using Lagrange's inversion formula, we find

$$t_f^{1/2} = \tau_f = \sum_0 h_n (v_0 - T_f)^{n+1}/(n + 1)! \tag{16}$$

where

$$h_n = D_\tau^n \{[T_f/(v_0 - T_f)]^{n+1}\} = \sum_{m=0}^{n} (-1)^m (n + m)!\, Z_m^n(p)/p_0^{n+m+1}$$

and

$$Z_m^n(p) = \sum_{\alpha_k} \prod_1^n [(p_k)^{\alpha_k}/\alpha_k!]$$

With known t_f, we may then proceed to solve the solidification problem. The exact solution of this solidification problem has been established recently [1]. We will only give a summary of the result without detailed derivations. Let

$$t^* = t - t_f, \quad \zeta_i = x/(4\alpha_i t^*)^{1/2}$$

$$Q(t) = (k_I/\alpha_I^{1/2}) \sum_0 q_n^* (t^*)^n/n!, \quad q_n^* = (\alpha_I^{1/2}/k_I)(d^n Q/dt^n)_{t=t_f}$$

$$V^*(x) = T^p_{II}(x, t_f) = \sum_0 v_n^* (x/\alpha_{II}^{1/2})^n/n!$$

$$v_n^* = \alpha_{II}^{n/2} \partial^n T^p_{II}(x, t_f)/\partial x^n|_0 \tag{17}$$

The complete solutions of this problem are

$$T_I(x, t^*) = \sum_0 q_n^* (4t^*)^{n+1/2} G_{2n+1}(\zeta_I) + \sum_0 a_n^* (4t^*)^{n/2} E_n(\zeta_I)$$

$$T_{II}(x, t^*) = T_f + \sum_1 v_n^* (4t^*)^{n/2} G_n(\zeta_{II}) + \sum_0 b_n^* (4t^*)^{n/2} i^n \operatorname{erfc} \zeta_{II}$$

$$s(t^*) = 2\alpha_I^{1/2} \sum_1 \lambda_n^* (\tau^*)^{n+1} \tag{18}$$

Evaluation of the interface equations at $t = 0$ yields

$$a_0^* = T_f, \quad b_0^* = 0, \quad \lambda_1^* = (k_I/2\rho L\alpha_I)\,[q_0^* - \omega(k_{II}/k_I)v_1^*] \tag{19}$$

It is seen that a positive λ_1^* exists if and only if

$$q_0^* - \omega(k_{II}/k_I)v_1^* > 0$$

This condition is satisfied if the τ derivative of the surface temperature at $\tau = 0$ is negative, i.e., the surface temperature is decreasing at $\tau = 0$. This assertion follows from (13),

$$D_\tau T^p_{II}(0, t)|_0 = (v_1 - \bar{q}_0)/\Gamma(3/2) < 0$$

or

$$q_0^* - \omega(k_{II}/k_I)v_1^* > 0 \tag{20}$$

The other coefficients a_n^*, b_n^*, and λ_n^* can be determined by a recent formula for the material time derivative of arbitrary order [19]. In the one-dimensional case where $f = f(x, t)$ and $x = x(t)$, we have

$$D_t^N f(x, t) = \sum_{n=0}^{N} \sum_{m=0}^{N-n} (N!/n!) Z_m^{N-n}(x)\, \partial_t^n \partial_x^m f$$

where $Z_m^n(x)$ is given by (15).

Successive differentiations of the interface equations (3) and evaluations at $t = 0$ yield the recurrence formulas,

$$a_1^* = b_1^* = 0$$

$$\sum_0^{[(N-1)/2]} q_n^* A_{2n+1}^N(1) + \sum_2^N a_n^* A_n^N(1) + \sum_1^{[(N-1)/2]} a_{2n+1}^* B_{2n+1}^N(1) = 0$$

$$\sum_1^N v_n^* A_n^N(\omega) + \sum_2^N b_n^* B_n^N(\omega) = 0$$

$$\sum_0^{[N/2]} q_n^* A_{2n}^N(1) + \sum_2^N a_n^* A_{n-1}^N(1) - \sum_1^{[N/2]} a_{2n+1}^* B_{2n}^N(1) - \omega(k_{II}/k_I) \sum_1^N v_n^* A_{n-1}^N(\omega) - \sum_2^N b_n^* B_{n-1}^N(\omega) = (\rho L\alpha_I/k_I)(N + 2)\lambda_{N+1}^* \tag{21}$$

where

$$A_{2n}^N(\omega) = \sum_{r=0}^{[(N/2)-1]} (2\omega)^{2r} Z_{2r}^{N-2n}(\lambda^*)/(n - r)!$$

$$A_{2n+1}^N(\omega) = \sum_{r=0}^{[(N/2)-n-1]} (2\omega)^{2r+1} Z_{2r+1}^{N-2n-1}(\lambda^*)/(n - r)!$$

[1] Reference [18] contains all multinomial coefficients for $N \le 10$. For direct computation of larger N, a calculator program has been prepared by the author and has been deposited in the Texas Instruments' Professional Program Exchange.

Downloaded 01 May 2010 to 171.66.16.249. Redistribution subject to ASME license or copyright; see http://www.asme.org/terms/Terms_Use.cfm

$$B_n^N(\omega) = \sum_{r=0}^{N-n} (-2\omega)^r Z_r^{N-n}(\lambda^*)/\Gamma\left(\frac{n-r}{2}+1\right) \quad \text{when } N \le 2n$$

$$= \sum_{r=0}^{n} (-2\omega)^r Z_r^n(\lambda^*)/\Gamma\left(\frac{n-r}{2}+1\right)$$

$$+ \pi^{-1/2} \sum_{r=0}^{[(N-1)/2-n]} (-1)^r (-2\omega)^{2r+n+1} Z_{2r+n+1}^{N-n}(\lambda^*)[(2r)!/2^{2r}r!]$$

when $N > 2n$ and $Z_m^n(\lambda^*)$ is given by (16).

From this set of algebraic equations, we may determine, starting from $N = 1$ sequentially, the coefficients a_n^*, b_n^*, and λ_n^*. The proofs of existence and uniqueness of these coefficients are given in [1]. Also, it is shown there that the resulting series solutions of the problem are absolutely and uniformly convergent. We refer to [1] for details.

It is readily seen from the present solution that as $t^* \to 0$ the interfacial boundary in a flux problem, with or without a presolidification period, can never be of the order of $t^{*1/2}$ as in the problem with a prescribed temperature at its surface. To be specific, it is of the order of t^* (or t) when (20) is satisfied. If the inequality (20) is not satisfied and is replaced by an equal sign, then the interfacial boundary would be of the order of $(t^*)^{n/2}$ $(n > 2)$. The value of n depends on the prescribed boundary and initial data. A discussion of this point has already been given in [1].

From the derived solution it is clearly seen that an immediate solidification occurs only when the initial temperature at the surface is at the freezing point. Otherwise, a presolidification period exists. This readily excludes the possibility of a constant initial state in a moving boundary problem when heat flux is prescribed at the surface. It is different from the problem with prescribed temperature at the surface where any constant temperature above the freezing temperature can be assigned as the initial condition of the liquid.

In the foregoing discussion, we have followed the usual assumption that the liquid and solid phases of the material have the same density. If the assumption is removed, then there is a convective term in the heat equation for the liquid phase. In another paper [20], it is shown that a moving boundary problem including the density jump at the interface can be transformed by some appropriate changes of the independent variables and the material constants to an associated problem in which both liquid and solid phases behave as if they had the same density. Hence, solutions of the problems without a density discontinuity can be utilized for those with a density jump at the interface. This transformation is also valid for the present problem with prescribed heat flux. This point will not be pursued further, we refer to the original paper for details.

Similarity Solution

In this section we intend to investigate possible similarity solutions of the problem. First, let us introduce a similarity variable x/t^ν. It is found that the only value of ν which will reduce the heat equation to an ordinary differential equation is $\nu = 1/2$. Hence, we introduce

$$\xi_i = x/(4\alpha_i t)^{1/2}, \quad \theta_i(\xi_i) = T_i(x, t) \tag{22}$$

The boundary and initial conditions (2) are transformed to

$$\theta_{II}(\infty) = V(x), \quad d\theta_{II}/d\xi_{II}|_\infty = 0$$

and

$$k_I(d\theta_I/d\xi_I)_0 = (4\alpha_I t)^{1/2} Q(t) \tag{23}$$

A similarity solution exists only when the boundary and initial conditions are at most functions of ξ_i. This indicates that $V(x)$ must be limited to a constant and $Q(t)$ to a function proportional to $t^{-1/2}$. Writing

$$V(x) = V_0, \quad Q(t) = Q_0/t^{1/2}, \quad \omega = (\alpha_I/\alpha_{II})^{1/2} \tag{24}$$

we find

$$T_I(x, t) = T_f + [(\pi\alpha_I)^{1/2} Q_0/k_I] (\text{erf } \xi_I - \text{erf } \lambda)$$

$$T_{II}(x, t) = V_0 - (V_0 - T_f) \text{ erfc } \xi_{II}/\text{erfc } \omega\lambda$$

$$s(t) = 2\lambda(\alpha_I t)^{1/2} \tag{25}$$

and λ satisfies

$$1 - Ke^{\lambda^2}/e^{\omega^2\lambda^2} \text{ erfc } \omega\lambda = (\rho L\alpha_I^{1/2}/Q_0)\lambda e^{\lambda^2}$$

where

$$K = (k_{II}/\sqrt{\pi\alpha_{II}}) (V_0 - T_f)/Q_0 \tag{26}$$

The aforementioned transcendental equation for λ has a positive root only when $K < 1$ [16]. This assertion follows from the fact that the RHS is monotonically increasing from 0 to ∞ and LHS is monotonically decreasing from $1 - K$ to $-\infty$, since $\exp \lambda^2 \text{ erfc } \lambda$ is monotonically decreasing from 1 to 0 [21].

Physically, this similarity solution may not be easily realized, since it requires initially an infinite heat flux. However, this infinite heat flux seems to be necessary. The initial temperature of the liquid V_0 is higher than the freezing temperature. A solidification is assumed to occur immediately after the heat flux has been applied; an infinite amount of heat extraction at $t = 0$ is needed in order to lower the surface temperature from V_0 to T_f. In addition, even when this heat flux could be achieved, a similarity solution exists only when $K < 1$. It then leads to a question: Is it possible when $K \ge 1$ to have a presolidification period so that the surface temperature of the liquid could drop to the freezing temperature by heat extraction? In contrast to the general problem discussed in the previous section, it is impossible. The temperature of the liquid without a change of phase is

$$T_{II}(x, t) = V_0 - (\sqrt{\pi\alpha_{II}}\, Q_0/k_{II}) \text{ erfc } \xi_{II}$$

The surface temperature is

$$T_{II}(0, t) = V_0 - (\pi\alpha_{II})^{1/2} Q_0/k_{II}$$

It remains unchanged for $t > 0$ and is always larger than T_f when $K > 1$. Also, when $K = 1$, the surface temperature is T_f, but the temperature distribution in the liquid at $x > 0$ is

$$T_{II}(x, t) = V_0 - (V_0 - T_f) \text{ erfc } \xi_{II} > T_f$$

Hence we conclude that no similarity solution of solidification problem could exist when

$$Q_0 \le (k_{II}/\sqrt{\pi\alpha_{II}}) (V_0 - T_f)$$

Supercooled Liquid

Another interesting problem is solidification of a supercooled liquid, which has been suggested as a possible state of solidification of a binary alloy [22–24]. A similarity solution of the problem is known [5]. It deals with a supercooled liquid of constant initial temperature $V_0 < T_f$ in a semi-infinite region of which the surface temperature at $x = 0$ is held at the freezing temperature T_f. The solution is given by

$$T_I = T_f$$

$$T_{II} = V_0 + (T_f - V_0) \text{ erfc } (\xi_{II})/\text{ erfc } \lambda$$

$$s = 2\lambda(\alpha_{II} t)^{1/2} \tag{27}$$

where λ satisfies

$$(T_f - V_0)e^{-\lambda^2}/\text{erfc } \lambda = \lambda\rho L\pi^{1/2}\alpha_{II}/k_{II}$$

This solution is physically admissible only when

$$T_f - V_0 < \rho L\alpha_{II}/k_{II} \tag{28}$$

When a supercooled liquid of initial temperature $V(x) < T_f$ is subject to a heat supply $Q(t)$ at its surface $x = 0$, the solution can also be established. We again write

Downloaded 01 May 2010 to 171.66.16.249. Redistribution subject to ASME license or copyright; see http://www.asme.org/terms/Terms_Use.cfm

$$T_{\mathrm{I}}(x,t) = -\sum_0 q_n (2\tau)^{2n+1} G_{2n+1}(\xi_{\mathrm{I}}) + \sum_0 c_n (2\tau)^n E_n(\xi_{\mathrm{I}})$$

$$T_{\mathrm{II}}(x,t) = \sum_0 v_n (2\tau)^n G_n(\xi_{\mathrm{II}}) + \sum_0 d_n (2\tau)^n i^n \operatorname{erfc} \xi_{\mathrm{II}}$$

$$s(t) = 2\alpha_{\mathrm{II}}^{1/2} \sum_0 \mu_n \tau^{n+1} \tag{29}$$

where q_n and v_n are given by (4). The interface equations yield

$$c_0 = T_f, \quad d_0 = (T_f - v_0)/\operatorname{erfc}(\omega\mu_0)$$

$$\pi^{1/2}\omega\mu_0 \exp(\omega^2\mu_0^2) \operatorname{erfc}(\omega\mu_0) = (k_{\mathrm{II}}/\rho L\alpha_{\mathrm{II}})(T_f - v_0) \tag{30}$$

We observe that this transcendental equation for determination of μ_0 is independent of q_n. In other words, the initial motion of the interfacial boundary is independent of the flux condition at its surface. Furthermore, this transcendental equation is identical to the one just given for the problem with constant T_f at its surface. This is not surprising, because the surface temperature in the present problem with prescribed heat flux is also T_f as $t \to 0$.

Since

$$\sqrt{\pi}\,\mu \exp(\mu^2) \operatorname{erfc} \mu$$

is bounded between 0 and 1 [21], a solution of μ_0 exists only when

$$T_f - v_0 < \rho L \alpha_{\mathrm{II}}/k_{\mathrm{II}} \tag{31}$$

If this condition is satisfied, the complete solution can be derived. Similar to the derivation given in the preceding sections, the coefficients c_n, d_n, and μ_n satisfy the recurrence formulas

$$\sum_1^N c_n P_n^N(1) + \sum_0^{N^*} c_{2n+1} Q_{2n+1}^N(1) - \sum_0^{N^*} q_n P_{2n+1}^N(1) = 0$$

$$\sum_1^N v_n P_n^N(\omega) + \sum_0^N d_n Q_n^N(\omega) = 0$$

$$\sum_1^N c_n P_{n-1}^{N-1}(1) - \sum_0^{N^*} c_{2n+1} Q_{2n}^{N-1}(1) - \sum_0^{N^*} q_n P_{2n}^{N-1}(1)$$

$$-\omega(k_{\mathrm{II}}/k_{\mathrm{I}}) \left[\sum_1^N v_n P_{n-1}^{N-1}(\omega) - \sum_0^N d_n Q_{n-1}^{N-1}(\omega)\right]$$

$$= (\rho L \alpha_{\mathrm{I}}/k_{\mathrm{I}})(N+1)\mu_N \tag{32}$$

where

$$P_n^N(\omega) = 2^n \sum_{m=0}^r \omega^m Z_m^{N-n}(\mu)\, G_{n-m}(\omega\mu_0)$$

$$Q_n^N(\omega) = 2^n \sum_{m=0}^r (-\omega)^m Z_m^{N-n}(\mu)\, i^{n-m} \operatorname{erfc}(\omega\mu_0)$$

$N^* = [\frac{1}{2}(N-1)]$ stands for the integer part of $\frac{1}{2}(N-1)$ and $r = \min(N-n, n)$. The existence and uniqueness of these coefficients and the convergence of the resulting series solutions for both temperature distributions and interfacial boundary can be proved analogously as in the studies of the classical Stefan problem [1, 14, 15].

As previously given, the solution of a supercooled liquid exists only when (31) is satisfied. What happens when (31) is not satisfied? Will there be a presolidification period as in a normal problem? The answer seems to be unclear. Heat supplies could raise the surface temperature of a supercooled liquid to freezing temperature T_f or any other temperature which satisfies the inequality (31), and solidification could then occur. This readily indicates that initiation of solidification might not be unique. It is believed that when (31) is not satisfied, local solidification could occur when liquid is disturbed, since supercooled liquid is not a stable state. Hence, it is conjectured that when (31) is not satisfied, the problem must be solved by a two or three-dimensional model, together with a special consideration of its stability. In view of this discussion, the inequality (31) may be considered as a necessary condition for solidification of a one-dimensional supercooled liquid.

Acknowledgment

This research is based upon work supported by the National Science Foundation under Grant CME-7921350.

References

1 Tao, L. N., "On Free Boundary Problems With Arbitrary Initial and Flux Conditions," *ZAMP*, Vol. 30, 1979, pp. 416–426.

2 Riemann, G. F. B., and Weber, H., *Die partiellen Differentialgleichungen der mathematischen Physik*, Bd. 2, 5-fl. Aufl., Braunschweig, 1912.

3 Stefan, J., "Über eininge Probleme der Theorie der Wärmeleitung," *S.-B. Wien. Akad. Mat. Natur.*, Vol. 98, 1889, pp. 473–484.

4 Rubinstein, L. I., *The Stefan Problem (English translation)*, Transl. Math. Monog. #27, American Mathematical Society, 1971.

5 Carslaw, H. S., and Jaeger, J. C., *Conduction of Heat in Solids*, 2nd ed., Clarendon Press, Oxford, 1959.

6 Crank, J., *The Mathematics of Diffusion*, 2nd ed., Clarendon Press, Oxford, 1975.

7 Ruddle, R. W., *The Solidification of Castings*, Institution of Metals, London, 1957.

8 Bankoff, S. G., "Heat Conduction or Diffusion With Change of Phase," *Adv. Chem. Eng.*, Vol. 5, 1964, pp. 75–150.

9 Muehlbauer, J. C., and Sunderland, J. E., "Heat Conduction With Freezing or Melting," *Appl. Mech. Rev.*, Vol. 18, 1965, pp. 951–959.

10 Tiller, W. A., *Principles of Solidification, in Arts and Sciences of Growing Crystals*, ed., Gilman, J. J., Wiley. New York, 1963.

11 Boley, B. A., "Survey of Recent Developments in the Fields of Heat Conduction in Solids and Thermoelasticity," *Nuclear Eng. Des.*, Vol. 18, 1972, pp. 377–399.

12 Ockendon, J. R., and Hodgkins, W. R., eds., *Moving Boundary Problems in Heat Flow and Diffusion*, Clarendon Press, Oxford, 1975.

13 Wilson, D. G., Solomon, A. D., and Boggs, P. T., eds., *Moving Boundary Problems*, Academic Press, New York, 1978.

14 Tao, L. N., "The Stefan Problem With Arbitrary Initial and Boundary Conditions," *Quarterly of Applied Mathematics*, Vol. 36, 1978, pp. 223–233.

15 Tao, L. N., "Free Boundary Problems With Radiation Boundary Conditions," *Quarterly of Applied Mathematics*, Vol. 37, 1979, pp. 1–10.

16 Tao, L. N., "The Analyticity of Solutions of the Stefan Problem," *Arch. Rational Mech. Analy.*, Vol. 72, 1980, pp. 285–301.

17 Jordan, C., *Calculus of Finite Differences*, Chelsea, New York, 1965.

18 Abramowitz, M., and Stegun, I. A., eds., *Handbook of Mathematical Functions*, Dover, New York, 1964.

19 Tao, L. N., "On the Material Time Derivative of Arbitrary Order," *Quarterly of Applied Mathematics*, Vol. 36, 1978, pp. 323–324.

20 Tao, L. N., "On Solidification Problems Including the Density Jump at the Moving Boundary," *Quarterly Journal of Mechanics and Applied Mathematics*, Vol. 32, 1979, pp. 175–185.

21. Tao, L. N., "Dynamics of Growth or Dissolution of a Gas Bubble," *J. Chem. Phys.*, Vol. 69, 1978, pp. 4189–4194.

22 Chalmers, B., *Principles of Solidification*, Wiley, New York, 1964.

23 Tao, L. N., "On Solidification of a Binary Alloy," *Quarterly Journal of Mechanics and Applied Mathematics*, Vol. 33, 1980, pp. 211–225.

24 Tao, L. N., "Solidification of a Binary Mixture With Arbitrary Heat Flux and Initial Conditions," *Arch. Rational Mech. Analy.*, in press.

Downloaded 01 May 2010 to 171.66.16.249. Redistribution subject to ASME license or copyright; see http://www.asme.org/terms/Terms_Use.cfm

R. S. Singh
Lecturer,
Department of Mechanical Engineering,
Institute of Technology,
Banaras Hindu University,
Varanasi 221005, India

V. D Sharma[1]
Visiting Associate Professor,
Department of Aerospace Engineering,
University of Maryland,
College Park, Md. 20742

On the Propagation of Weak Discontinuities Along Bicharacteristics in a Radiating Gas

The propagation of weak discontinuities along bicharacteristic curves in the characteristic manifold of the differential equations governing the flow of a radiating gas near the optically thin limit has been discussed. Some explicit criteria for the growth and decay of weak discontinuities along bicharacteristics are given. As a special case, when the discontinuity surface is adjacent to a region of uniform flow, the solution for the velocity gradient at the wave head is specialized to the plane, cylindrical, and spherical waves. For expandng waves, the attenuation induced by geometric factors and the radiative flux, and the growth induced by the upstream flow Mach number are discussed. It is shown that a compressive disturbance steepens into a shock only if the initial disturbance is sufficiently strong.

Introduction

In the theory of hyperbolic systems of partial differential equations the characteristic surfaces play an important role. One of the important properties of a characteristic surface is that the discontinuities in the derivatives of dependent variables can exist only along the characteristic surface. At any point of a characteristic surface there is a privileged direction given by the tangent of the characteristic curve passing through that point. Coburn [1], from the system of equations representing steady supersonic flow of an inviscid and nonconducting gas, derived an equation containing the derivatives only along the bicharacteristic curve. Witham [2], while studying the propagation of weak waves, derived an equation giving the rate of change of the wave amplitude along the rays (bicharacteristics). His theory has been used very successfully in computing the intensity of sonic boom produced by a supersonic plane. Gupkin [3], making assumption of short wave, derived an approximate quasi-linear equation giving the rate of change of amplitude of a weak disturbance in the bicharacteristic direction. This work was further generalized by Prasad [4] for a general system of partial differential equations. Thomas [5], using the singular surface theory, derived the transport equations for the discontinuities in the normal derivatives of the dependent variables along orthogonal trajectories for an isentropic flow with a state of rest on the rear side of singularity surface. When the singularity surface is adjacent to region of rest, it is natural to consider the transport of discontinuities along orthogonal trajectories, as has been done by Thomas [6]. But, if the discontinuity surface is adjacent to a region of uniform flow in that case, it has been shown by Elcrat [7] that it is natural to consider the transport of discontinuity along bicharacteristic curves in the characteristic manifold of the governing differential equations. In this paper, we have derived transport equations for the discontinuities in the normal derivatives of the flow parameters along the bicharacteristic curves in the characteristic manifold of the differential equations governing the flow of a radiating gas near the optically thin limit. Under this condition, the emission process dominates over the absorption one, i.e., the photon mean free path is large compared to the characteristic length of the medium. The gas is assumed to be perfect, optically grey and in thermodynamic equilibrium. It is observed that the transport equations along bicharacteristics reduce to the corresponding equations along orthogonal trajectories when the singularity surface is adjacent to a region of rest. Some explicit criteria for the growth and decay of weak discontinuities along bicharacteristics are given. The situation, in which the medium ahead of the wave is uniform, has been envisaged and the special

[1] Presently on leave from the Applied Mathematics Section, Institute of Technology, B.H.U., India.

Contributed by the Applied Mechanics Division for publication in the JOURNAL OF APPLIED MECHANICS.

Discussion on this paper should be addressed to the Editorial Department, ASME, United Engineering Center, 345 East 47th Street, New York, N. Y. 10017, and will be accepted until two months after final publication of the paper itself in the JOURNAL OF APPLIED MECHANICS. Manuscript received by ASME Applied Mechanics Division, May, 1980; final revision, May, 1981.

Copyright © 1981 by ASME

Downloaded 01 May 2010 to 171.66.16.249. Redistribution subject to ASME license or copyright; see http://www.asme.org/terms/Terms_Use.cfm

reference is made of plane, cylindrical, and spherical wave motions. The bicharacteristic curves in these cases are, of course, straight lines emanating from the center of wave propagation. The effects of radiative flux, the upstream flow Mach number, and that of wave front geometry on the growth and decay properties of weak discontinuities are discussed.

It is found that a compressive wave steepens up into a shock after a finite time only if the magnitude of initial discontinuity exceeds a critical value. Compressive waves with initial discontinuity below the critical value damp out while initial discontinuities equal to the critical value decay, but not completely. It is shown that the stabilizing influence of curvature is not strong enough to arrest the nonlinear steepening tendency of the wave surface. The decaying rate of an expansive wave is enhanced by the presence of radiative flux and the wave front curvature, whereas it is diminished by the presence of upstream flow Mach number

Speed of Propagation

The basic equations, appropriate to the case, are

$$\frac{\partial \rho}{\partial t} + u_i \rho_{,i} + \rho u_{i,i} = 0 \tag{1}$$

$$\rho \frac{\partial u_i}{\partial t} + \rho u_j u_{i,j} + p_{,i} = 0 \tag{2}$$

$$\frac{\partial p}{\partial t} + u_i p_{,i} + \gamma p u_{i,i} + Q(\gamma - 1) = 0 \tag{3}$$

where p is the gas pressure, ρ the density, u_i the gas velocity components, and γ the ratio of specific heats. The quantity $Q = 4k_p \sigma T^4$ is the rate of energy loss by the gas per unit volume through radiation, where k_p, σ, and T are the Planck mean absorption coefficient, Stefan-Boltzmann constant, and the gas temperature, respectively. Here the summation convention on repeated indices is employed and a comma followed by an index (i) denotes a partial derivative with respect to space variable x_i. Throughout this paper we shall take the spectrum of the suffixes, i, j, k to be 1, 2, 3.

Furthermore the equation of state of the gas is taken to be of the form

$$p = \rho R T \tag{4}$$

where R is the gas constant.

Equations (1)–(3), using matrix notation, can be written

$$\frac{\partial U}{\partial t} + A^i U_{,i} + B = 0 \tag{5}$$

where U is a column vector with five components (ρ, u_i, p), B is a column vector with five components, and A^i are square matrices of order five which can be read off by inspection of (1)–(3).

Let us now introduce a characteristic wave surface $\Sigma, \phi(x_1, x_2, x_3, t) = 0$, across which the set of dependent variables U and the interior derivatives of U along Σ are continuous but the exterior derivatives of U may have a jump across it. The jump, across Σ, in a quantity f is denoted by $[f]$. The square bracket stands for the value of the quantity enclosed immediately behind the wave surface Σ minus its value just ahead of the wave surface. We now introduce new coordinates $\xi^0, \xi^1, \xi^2, \xi^3$ to be chosen such that ξ^1, ξ^2, ξ^3 determine a point on Σ which is itself defined by $\phi = 0$, and set $\xi^0 = \phi$. In terms of these new coordinates, the system (5) can be written as

$$(I\phi_{,t} + A^i \phi_{,i}) U_{,\phi} + A^i \xi^j{}_{,i} U_{,\xi^j} + B = 0 \tag{6}$$

where I is the unit matrix of order five. Forming the jumps in the usual way, we obtain from (6)

$$(I\phi_{,t} + A^i \phi_{,i}) [U, \phi] = 0. \tag{7}$$

This follows because the interior derivatives $U_{,\xi^j}$ are continuous across Σ; the discontinuities existing only in the exterior derivative $U_{,\phi}$. Normalizing equation (7) by dividing by $(\phi_{,i}\phi_{,i})^{1/2}$ and setting $\phi_{,i}/(\phi_{,j}\phi_{,j})^{1/2} = n_i$ (the unit normal to the wave surface Σ) and $\phi_{,t}/(\phi_{,j}\phi_{,j})^{1/2} = -G$ (the speed of propagation of Σ along n_i), the system (7) will have a nontrivial solution if $\det(A^i n_i - GI) = 0$, which yields

$$V^3(V^2 - C_0^2) = 0 \tag{8}$$

where $V = G - u_{n0}$ is the relative speed of advance of Σ in the fluid, $C_0 = \sqrt{\gamma p_0/\rho_0}$ is the speed of sound and $U_{n0} = U_{i0} n_i$. The suffix, 0, indicates a value in the region ahead of the wave Σ.

Let us now consider the case when the wave front is propagating into a region of uniform flow. Equation (8) yields $V = \pm C_0$ and $V = 0$. The case $V = 0$, in which the surface moves with the fluid is discarded as uninteresting. Thus we consider only the advancing disturbance for which $V = C_0$, or

$$G = U_{n0} + C_0. \tag{9}$$

The order of the characteristic matrix of the system (7) is equal to five, its rank is equal to four when (9) holds. Thus, for $V = C_0$, the characteristic matrix has an eigenvector, the components of which are $(1, C_0 n_i/\rho_0, C_0^2)$. This means that the jumps in the derivatives of ρ, u_i, and p normal to the surface Σ, which we denote by ζ, λ^i, and ξ, respectively, satisfy the following relations:

$$\lambda = \rho_0^{-1} C_0 \zeta = (\rho_0 C_0)^{-1} \xi, \tag{10}$$

where $\lambda = \lambda^i n_i$.

Behavior of the Discontinuity at the Wave-Head

The transport equation for the quantity λ, which predicts the growth and decay of the discontinuity in the normal component of the fluid velocity along the bicharacteristic curves of (5) is derived in the next section in the following form:

$$\frac{d\lambda}{dt} - (C_0\Omega - \Lambda_0)\lambda + \frac{(\gamma + 1)}{2}\lambda^2 = 0, \tag{11}$$

where d/dt is the time derivative along the bicharacteristic direction, Ω is the mean curvature of the wave surface Σ, and $\Lambda_0 = 2(\gamma - 1)^2 Q/\rho_0 C_0^2$.

In the present section, we shall discuss the behavior of the solution of (11); special attention will be paid to the planar, cylindrical, and spherical wave fronts.

Equation (11) can be integrated to yield

$$\lambda = \frac{\lambda_0 \exp\left(-\Lambda_0 t + C_0 \int_0^t \Omega(t)dt\right)}{1 + \frac{\gamma + 1}{2}\lambda_0 \int_0^t \exp\left(-\Lambda_0 \hat{t} + C_0 \int_0^{\hat{t}} \Omega(\tilde{t})d\tilde{t}\right)d\hat{t}} \tag{12}$$

where λ_0 is the value of λ at $t = 0$. It follows from (12) that if $\lambda_0 > 0$ (i.e., an expansive wave front) then the discontinuity λ is finite at finite time. But, if $\lambda_0 < 0$ (i.e., a compressive wave front) then we have the criterion

$$\int_0^{t_c} \exp\left(-\Lambda_0 t + C_0 \int_0^t \Omega(\tilde{t})d\tilde{t}\right)dt = -\frac{2}{(\gamma + 1)\lambda_0}$$

for the shock formation at a finite time $t = t_c$, provided the magnitude of the initial value of the discontinuity, λ_0, exceeds a critical value λ_c given by

$$\lambda_c = \left\{\frac{(\gamma + 1)}{2}\int_0^{\infty} \exp\left(-\Lambda_0 t + C_0 \int_0^t \Omega(\tilde{t})d\tilde{t}\right)dt\right\}^{-1}.$$

1 Plane Waves. For a plane wave front $\Omega = 0$ and equation (12) reduces to

$$\frac{\lambda}{\lambda_0} = \frac{\exp(-\Lambda_0 t)}{1 + \frac{\lambda_0}{\lambda_c}(1 - \exp(-\Lambda_0 t))} \tag{13}$$

where $\lambda_c = 2\Lambda_0/(\gamma + 1)$. Equation (13) shows that if $\lambda_0 > 0$ (i.e., an expansive wave front) then $\lambda \to 0$ as $t \to \infty$, i.e., the wave decays. Also, if $\lambda_0 < 0$ (i.e., a compressive wave front) and $|\lambda_0| < \lambda_c$, then $\lambda \to 0$ as

Downloaded 01 May 2010 to 171.66.16.249. Redistribution subject to ASME license or copyright; see http://www.asme.org/terms/Terms_Use.cfm

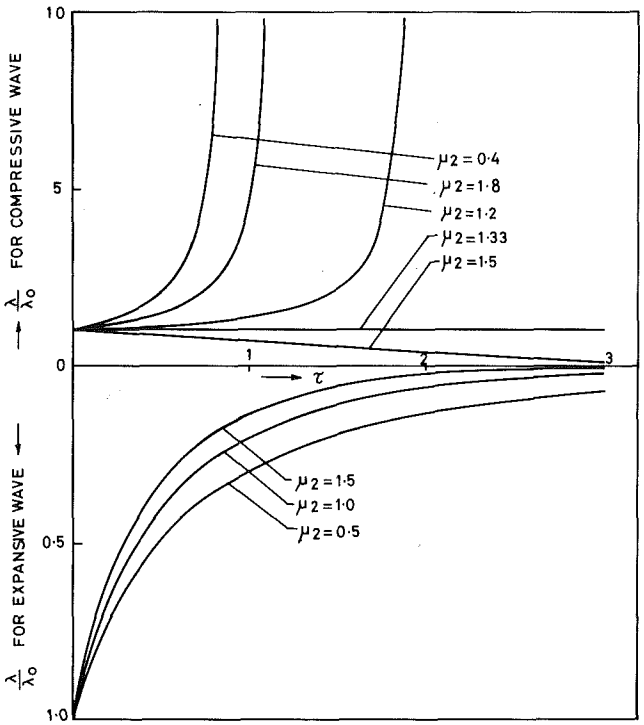


Fig. 1 Effect of radiative flux (μ_2) on the growth and decay of plane waves for $\gamma = 5/3$

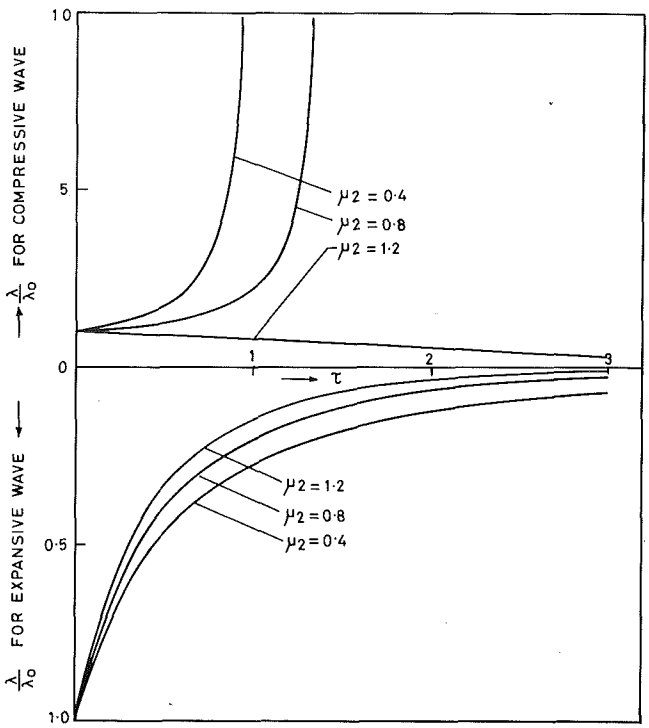


Fig. 2 Effect of radiative flux (μ_2) on the growth and decay of cylindrical waves for $\mu_3 = 0.5$, $M_0 = 0$, and $\gamma = 5/3$

$t \to \infty$. But, if $\lambda_0 < 0$ and $|\lambda_0| > \lambda_c$, then (13) shows that $|\lambda| \to \infty$ as $t \to t_c$, where t_c is given by

$$t_c = \Lambda_0^{-1} \ln \left(1 - \frac{\lambda_c}{|\lambda_0|}\right)^{-1}. \tag{14}$$

Thus, at a finite time t_c, a compressive wave steepens up into a shock if the value of the initial discontinuity $|\lambda_0|$ exceeds the critical value λ_c. Further, if $\lambda_0 < 0$ and $|\lambda_0| = \lambda_c$, then it is clear from (13) that $\lambda = \lambda_0$, i.e., the wave propagates with a constant wave form.

From (14) it follows that $(\partial t_0/\partial \Lambda_0) > 0$, i.e., an increase in Λ_0 causes an increase in t_c. Thus the radiative flux has a stabilizing effect on the shock formation in the sense that an increase in Λ_0 causes a decrease in the shock formation time. The behavior of λ/λ_0 versus $\tau(= |\lambda_0|t)$ for different values of $\mu_2 (= \Lambda_0/|\lambda_0|)$ is exhibited in Fig. 1 for the adiabatic index $\gamma = 5/3$. It is found that the effect of radiative flux causes an expansion wave of given initial discontinuity to decay at a faster rate relative to what it would be in the absence of radiative flux.

2 Cylindrical Waves. For a diverging cylindrical wave $\Omega = -1/2R$ where $R = R_0 + Gt$; R_0 being the radius of the cylindrical wave front at a time $t = 0$. In this case $G = C_0(1 + M_0)$ where $M_0 = u_0/C_0$ is the upstream flow Mach number. Then (12) becomes

$$\lambda = \frac{\lambda_0 (R/R_0)^{-\nu} \exp(\beta_0 - \beta)}{1 + \dfrac{\lambda_0}{\lambda_c}\left(1 - \dfrac{I(\nu, \beta)}{I(\nu, \beta_0)}\right)} \tag{15}$$

where $\beta = 2\nu\Lambda_0 R/C_0$, $\beta_0 = 2\nu\Lambda_0 R_0/C_0$, $\nu = 1/2(1 + M_0)$,

$$I(\nu, x) = \int_x^\infty t^{-\nu} \exp(-t) dt, \tag{16}$$

and

$$\bar{\lambda}_c = \left\{\frac{\gamma + 1}{2\Lambda_0} \beta_0^{\nu} \exp(\beta_0) I(\nu, \beta_0)\right\}^{-1}. \tag{17}$$

Since ν, β, and β_0 are all positive, it is evident from (16) that the integral I is convergent. The quantity $\bar{\lambda}_c$ just defined is a positive critical value of the initial discontinuity in the sense discussed later.

The term inside the bracket in denominator of (15) increases monotonically from 0 to 1 as R increases from R_0 to ∞. Hence if $\lambda_0 > 0$ or $\lambda_0 < 0$ and $|\lambda_0| < \lambda_c$, then it follows from (15) that $\lambda \to 0$ as $R \to \infty$, the wave decays. However, if $\lambda_0 < 0$ and $|\lambda_0| = \bar{\lambda}_c$, then at any time t the discontinuity $|\lambda|$ is given by

$$|\lambda| = \frac{2\Lambda_0 \exp(-\beta)(R/R_0)^{-\nu}}{(\gamma + 1)\beta^{\nu} I(\nu, \beta)}$$

which approaches the value $2\Lambda_0(\gamma + 1)^{-1}$, critical λ_0 for a plane wave, as $R \to \infty$. But if $\lambda_0 < 0$ and $|\gamma_0| > \bar{\lambda}_c$, then there exists a finite time $\bar{t}_c$ given by

$$I(\nu, \Lambda_0 \bar{t}_c + \beta_0) = \left(1 - \frac{\bar{\lambda}_c}{|\lambda_0|}\right) I(\nu, \beta) \tag{18}$$

such that $|\lambda| \to \infty$ as $t \to \bar{t}_c$. This signifies the appearance of a shock wave at a finite time $\bar{t}_c$. Equation (18) shows that the shock formation time $\bar{t}_c$ depends on λ_0, Λ_0, M_0, and R_0. The dependence on λ_0 is such that $(\partial \bar{t}_c/\partial |\lambda_0|) < 0$ which means that an increase in the initial value of the discontinuity leads to a rapid shock formation. Also, it follows from (18) that $\partial \bar{t}_c/\partial R_0 < 0$ which means that an increase in the initial curvature will cause the shock formation time $\bar{t}_c$ to increase. The differential equation (11) can be written in the following nondimensional form:

$$\frac{d\delta}{d\tau} - (\mu_1 - \mu_2)\delta + \frac{\gamma + 1}{2} \frac{\lambda_0}{|\lambda_0|} \delta^2 = 0 \tag{19}$$

where $\delta = \lambda/\lambda_0$, $\tau = |\lambda_0|t$, $\mu_1 = -(\nu/2)\{\mu_3^{-1} + (1 + M_0)\tau\}^{-1}$, and $\mu_3 = C_0/|\lambda_0|R_0$.

In writing (19) we have used the relation $2\Omega = -n/R$, where $n = 0$, 1, 2 for plane, cylindrical, and spherical waves, respectively. Some of the solution curves of (19) for $n = 1$ and $\gamma = 5/3$ are obtained by using Runge-Kutta method of fourth order, and these are exhibited in Figs. 2–4.

Figs. 2 and 3 indicate that the effects of radiative flux and that of the wave front curvature are to reduce the steepening rate of a compressive wave but to increase the flattening rate of an expansive wave. Fig. 4 shows that the upstream flow Mach number has exactly a reverse effect on the growth and decay properties.

Downloaded 01 May 2010 to 171.66.16.249. Redistribution subject to ASME license or copyright; see http://www.asme.org/terms/Terms_Use.cfm

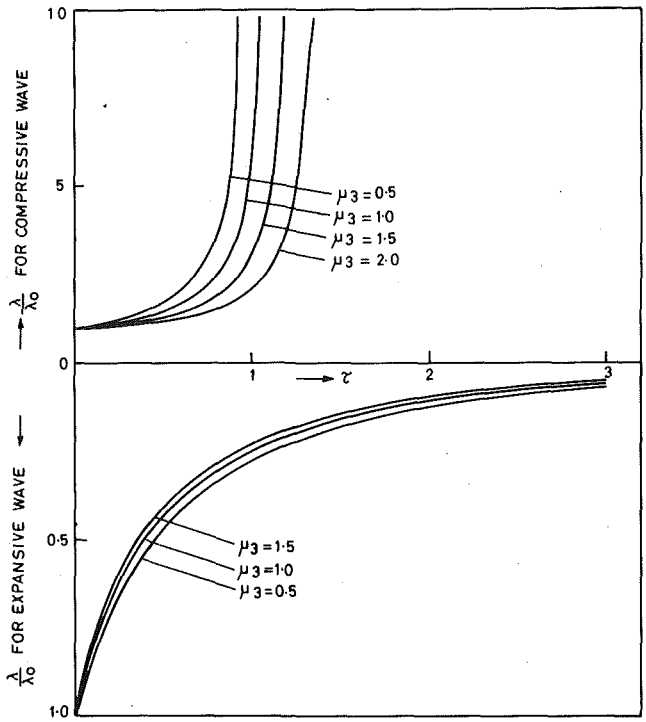


Fig. 3 Effect of the wave front curvature (μ_3) on the growth and decay of cylindrical waves for $\mu_2 = 0.4$, $M_0 = 0$, and $\gamma = 5/3$

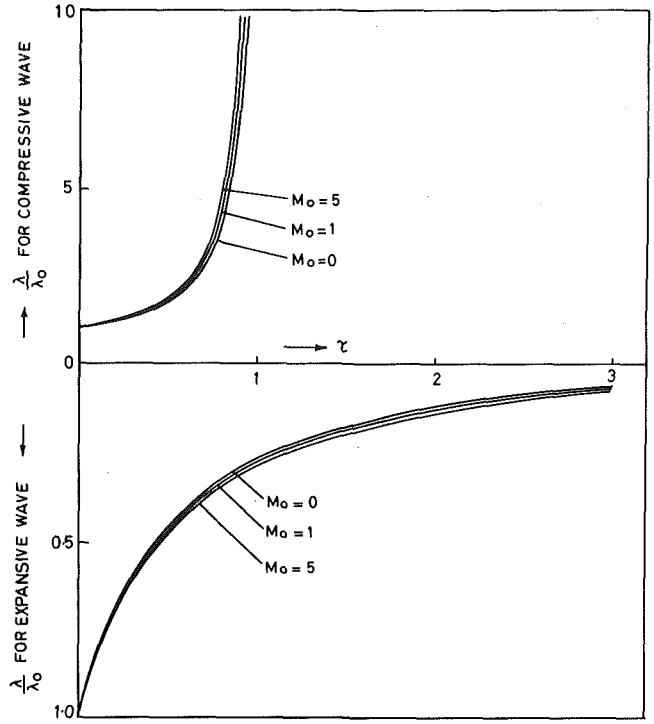


Fig. 4 Effect of the upstream flow Mach number (M_0) on the growth and decay of cylindrical waves for $\mu_2 = 0.4$, $\mu_3 = 0.5$, and $\gamma = 5/3$

3 Spherical Waves. In this case also the growth and decay phenomena are very much similar to those of plane and cylindrical waves. Now, consider an expanding wave front which at $t = 0$ is a sphere of radius R_0. Then at any time $t > 0$, the wave front is a sphere of radius $R = R_0 + Gt$. For such a wave $\Omega = -1/R$ and (12) reduces to

$$\lambda = \frac{\lambda_0 (R/R_0)^{-2\nu} \exp(\beta_0 - \beta)}{1 + \frac{\lambda_0}{\hat{\lambda}_c}\left(1 - \frac{I(2\nu, \beta)}{I(2\nu, \beta_0)}\right)}, \tag{20}$$

where

$$\hat{\lambda}_c = \left\{\left(\frac{\gamma+1}{2\Lambda_0}\right)\beta_0^2 \exp(\beta_0) I(2\nu, \beta_0)\right\}^{-1}. \tag{21}$$

It follows from (20) that for $\lambda_0 < 0$, there exists a positive critical value $\hat{\lambda}_c$ given by (21) such that waves whose initial discontinuity is less than $\hat{\lambda}_c$ damp to zero and waves whose initial discontinuity is greater than $\hat{\lambda}_c$ grow without bound in a finite time $\hat{t}_c$ given by

$$I(2\nu, \Lambda_0 \hat{t}_c + \beta_0) = \left(1 - \frac{\hat{\lambda}_c}{|\lambda_0|}\right) I(2\nu, \beta_0). \tag{22}$$

For $\lambda_0 < 0$ and $|\lambda| = \hat{\lambda}_c$, using L'Hospital's and Leibnitz rules, it turns out that $|\lambda| \to 2\Lambda_0(\nu+1)^{-1}$ (critical λ_0 for a plane wave) as $R \to \infty$. Thus a compressive wave with $|\lambda_0| = \hat{\lambda}_c$ takes ultimately a stable wave form.

A few solution curves of (20) for $n = 2$ and $\gamma = 5/3$ are exhibited in Figs. 5–7. It is evident from Figs. 5–7 that the nature of the solution curves of (20) for spherical and cylindrical waves are very much similar. However, it is interesting to note that the time taken for the shock formation in case of a spherical wave is greater than that for a cylindrical wave of the same initial strength (Figs. 2, 3, 5, 6).

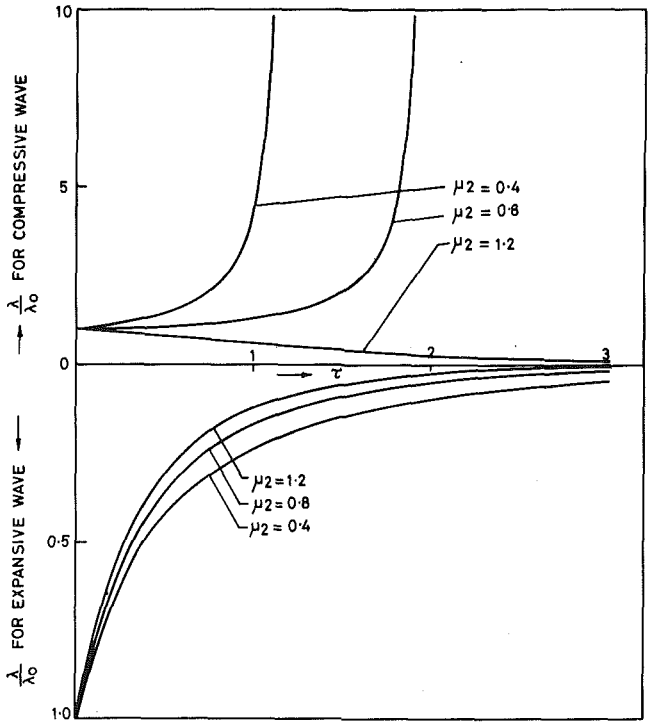


Fig. 5 Effect of radiative flux (μ_2) on the growth and decay of spherical waves for $\mu_3 = 0.5$, $M_0 = 0$, and $\gamma = 5/3$

Derivation of the Growth Equation

In this section we shall derive transport equations for the quantities λ, ξ, and ζ along orthogonal trajectories of Σ first, and then we shall pass on to the bicharacteristics. The compatibility conditions for the singularity surface Σ, which shall be needed in the derivation are the following [8].

$$[f,_{ij}] = \overline{B} n_i n_j + g^{\alpha\beta} B_{,\alpha}(n_i x_{j,\beta} + n_j x_{i,\beta}) - B g^{\alpha\beta} g^{\sigma\tau} b_{\alpha\sigma} x_{i,\beta} x_{j,\tau} \tag{23}$$

$$\left[\frac{\partial^2 f}{\partial x_i \partial_t}\right] = \left(-G\overline{B} + \frac{\delta B}{\delta t}\right) n_i - g^{\alpha\beta}(BG),_\alpha x_{i,\beta} \tag{24}$$

where $B = [f,_i] n_i$, $\overline{B} = [f,_{ij}] n_i n_j$, and $\delta f/\delta t = \partial f/\partial t + G n_i f,_i$ is the time

Downloaded 01 May 2010 to 171.66.16.249. Redistribution subject to ASME license or copyright; see http://www.asme.org/terms/Terms_Use.cfm

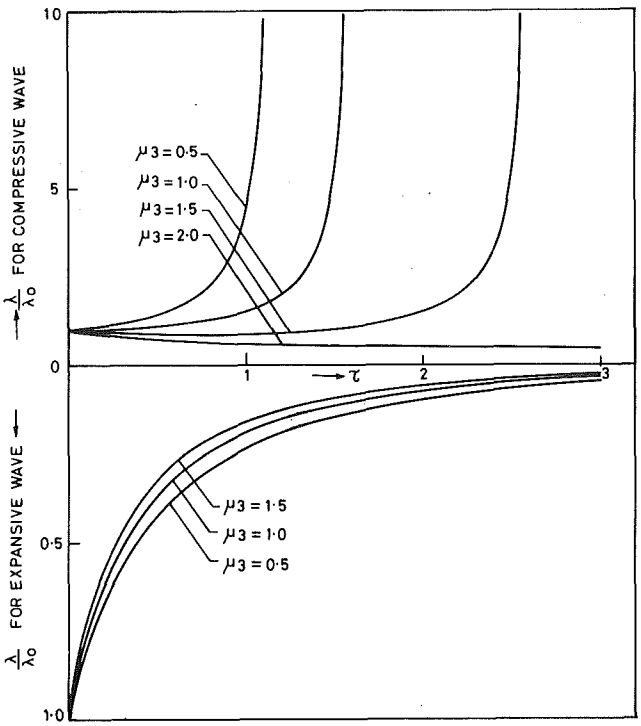


Fig. 6 Effect of the wave front curvature (μ_3) on the growth and decay of spherical waves for $\mu_2 = 0.4$, $M_0 = 0$, and $\gamma = 5/3$

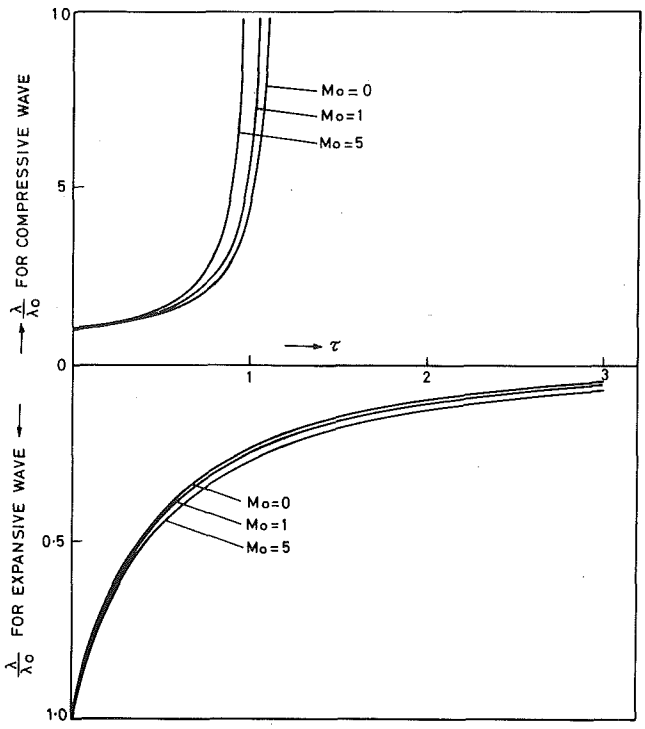


Fig. 7 Effect of the upstream-flow Mach number (M_0) on the growth and decay of spherical waves for $\mu_2 = 0.4$, $\mu_3 = 0.5$, $\gamma = 5/3$

rate of change of f along the normal n_i. Here the range of Greek indices $\alpha, \beta, \sigma, \tau$ is 1, 2. The first and second fundamental forms of Σ are denoted by $g^{\alpha\beta}$ and $b_{\alpha\beta}$, respectively. We also recall the following relations which we shall need in this program:

$$n_{i,\alpha} = -g^{\beta\sigma} b_{\beta\alpha} x_{i,\sigma}; \quad 2\Omega = g^{\alpha\beta} b_{\alpha\beta}, \tag{25}$$

where Ω is the mean curvature of Σ.

If we differentiate equations (2) and (3) with respect to x_j and evaluate on each side of Σ, and then subtract and make use of the relations (4), (9), (10), and (23)–(25), we get

$$\rho \frac{\delta\lambda}{\delta t} + \rho u^{\alpha}{}_{\lambda,\alpha} + \bar{\xi} - \rho_0 c_0 \bar{\lambda} = 0 \tag{26}$$

$$\frac{\delta\xi}{\delta t} + u_{\alpha}\xi_{,\alpha} - C_0(\bar{\xi} - \rho_0 c_0 \bar{\lambda}) - \left(2C_0\Omega - \frac{4(\gamma-1)^2 Q}{\rho_0 C_0{}^2}\right)\xi + \frac{(\gamma+1)\xi^2}{\rho_0 C_0} = 0 \tag{27}$$

where $\bar{\lambda} = \bar{\lambda}_i n_i$, $\bar{\lambda}_i = [u_{i,}{}_j k] n_j n_k$ and $\bar{\xi} = [p_{,ij}] n_i n_j$ are the quantities defined on Σ.

Eliminating $(\bar{\xi} - \rho_0 C_0 \bar{\lambda})$ from (26) with the help of (27) we get

$$\rho_0 C_0 \left(\frac{\delta\lambda}{\delta t} + u^{\alpha}\lambda_{,\alpha}\right) + \left(\frac{\delta\xi}{\delta t} + u^{\alpha}\xi_{,\alpha}\right) + \frac{(\gamma+1)\xi^2}{\rho_0 C_0} - \left(2C_0\Omega - \frac{4(\gamma-1)^2 Q}{\rho_0 C_0{}^2}\right)\xi = 0. \tag{28}$$

In view of relations (10), equation (28) yields a differential equation for λ, and therefore one for ζ and one for ξ along orthogonal trajectories of Σ. In equation (28), the terms involving surface derivatives cause some difficulty in its interpretation, but if we transform (28) to a differential equation along bicharacteristics, this difficulty disappears. Thus, to achieve this, we proceed as follows:

We first recall that a bicharacteristic curve $x_i = x_i(t)$ of the system (5) satisfies the equation [9]

$$\frac{dx_i}{dt} = \frac{\partial F}{\partial \varphi_{,i}} \Big/ \frac{\partial F}{\partial \varphi_{,t}}, \tag{29}$$

where d/dt is the time derivative moving along the wave front along the bicharacteristic curve defined as $df/dt = \partial f/\partial t + v_i \partial f/\partial x_i$, where v_i are the bicharacteristic velocity components, and $F \equiv |I\varphi_{,t} + A^i \varphi_{,i}| = 0$ is the characteristic equation for the system (5), which for the present case (i.e., $V = C_0$) takes the form

$$F \equiv \varphi_{,t} + u_i \varphi_{,i} + C_0(\varphi_{,i}\varphi_{,i})^{1/2}. \tag{30}$$

In view of (30), equation (29) yields

$$v_i = \frac{dx_i}{dt} = u_i + C_0 n_i. \tag{31}$$

Keeping in view the definition of δ-time derivative, and the relation (31), it follows immediately that

$$\frac{d}{dt} = \frac{\delta}{\delta t} + u^{\alpha} x_{i,\alpha} \frac{\partial}{\partial x_i} \tag{32}$$

where $x_{i,\alpha} = \partial x_i / \partial y^{\alpha}$; y^{α} ($\alpha = 1, 2$) being the Gaussian coordinates on the surface Σ, and $u^{\alpha} = u_i x_{i,\alpha}$ being the velocity components along the discontinuity surface Σ.

Thus, for any flow variable $f(x_i, t)$, defined on Σ, we have the relation

$$\frac{df}{dt} = \frac{\delta f}{\delta t} + u^{\alpha} f_{,\alpha}. \tag{33}$$

It can easily be seen that equation (28), on using (10) and (33), reduces to (11).

Acknowledgment

The authors are thankful to Professor Maurice Holt and the referee for making certain points more explicit. Dr. V. D. Sharma is thankful to the Ministry of Education, Government of India for the research support.

References

1 Coburn, N., "Intrinsic Form of the Characteristic Relations in Steady Supersonic Flow of a Compressible Fluid," *Quarterly of Applied Mathematics*, Vol. 15, 1957, pp. 237–248.

Downloaded 01 May 2010 to 171.66.16.249. Redistribution subject to ASME license or copyright; see http://www.asme.org/terms/Terms_Use.cfm

2 Whitham, G. B., "On the Propagation of Weak Shock Wave," *Journal of Fluid Mechanics*, Vol. 1, 1956, pp. 290–318.
3 Gubkin, K. E., "Propagation of Discontinuities in Sound Waves," *Journal of Applied Mathematics and Mechanics*, Vol. 22, 1958, pp. 787–793.
4 Prasad, P., "Approximation of the Perturbation Equations of a Quasi-Linear Hyperbolic System in the Neighborhood of a Bicharacteristic," *Journal of Mathematical Analysis and Applications*, Vol. 50, No. 3, June 1975, pp. 470–482.
5 Thomas, T. Y., "The Growth and Decay of Sonic Discontinuities in Ideal Gases," *Journal of Mathematics and Mechanics*, Vol. 6, 1957, pp. 455–469.
6 Thomas, T. Y., *Plastic Flow and Fracture in Solids*, Academic Press, New York, 1961.
7 Elcrat, A. R., "On the Propagation of Sonic Discontinuities in the Unsteady Flow of a Perfect Gas," *International Journal of Engineering Science*, Vol. 15, 1977, pp. 29–34.
8 Thomas, T. Y., "Extended Compatibility Conditions for the Study of Surfaces of Discontinuity in Continuum Mechanics," *Journal of Mathematics and Mechanics*, Vol. 6, 1957, pp. 311–322.
9 Courant, R., and Hilbert, D., *Method of Mathematical Physics*, Vol. II, Wiley, Interscience, 1962.

Downloaded 01 May 2010 to 171.66.16.249. Redistribution subject to ASME license or copyright; see http://www.asme.org/terms/Terms_Use.cfm

T. C. T. Ting

Professor of Applied Mechanics,
Department of Materials Engineering,
University of Illinois at Chicago Circle,
Chicago, Ill. 60680
Mem. ASME

Characteristic Forms of Differential Equations for Wave Propagation in Nonlinear Media

Characteristic forms of differential equations for wave propagation in nonlinear media are derived directly from equations of motion and equations which combine the constitutive equations and the equations of continuity. Both Lagrangian coordinates and Eulerian coordinates are considered. The constitutive equations considered here apply to a large class of nonlinear materials. The characteristic forms derived here clearly show which components of the stress and velocity are involved in the differentiation along the bicharacteristics. Moreover, the reduction to one-dimensional cases from three-dimensional problems is obvious for the characteristic forms obtained here. Examples are given and compared with the known solution in the literature for wave propagation in linear isotropic elastic solids and isentropic compressible fluids.

1 Introduction

For wave propagation in a medium, the equations of motion and the constitutive relation together with the continuity condition in a fixed rectangular coordinate system x_i may be written as

$$\sigma_{ij,j} = \rho_0 v_{i,t} \tag{1a}$$

$$\sigma_{ij,t} = M_{ijkp} v_{k,p} \tag{1b}$$

where σ_{ij} is the Piola-Kirchhoff stress, ρ_0 the mass density in the undeformed state, v_i the particle velocity, and M_{ijkp} are material functions which may depend on σ_{ij} and x_i. Repeated indices imply summation and a comma stands for partial derivative with respect to the space variable x_i except when a t follows a comma it implies partial derivative with respect to the time t. For many materials, M_{ijkp} have the property

$$M_{ijkp} = M_{jikp} = M_{ijpk} = M_{kpij} \tag{2}$$

This property, however, is *not* assumed in the following analyses.

Equations (1) use the Lagrangian coordinate system and apply to wave propagation in a wide class of materials. Wave propagation in hypoelastic materials [1], in hyperelastic materials [2], and in general nonlinear simple elastic materials [3] can be written in the form of equations (1). So can wave propagation in elastic-plastic materials [4–6] be written in the form of equations (1). As to wave propagation in elastic-viscoplastic materials [7, 8], equations (1) apply if we add a term which is a function of σ_{ij} to the right of equation (1b). Since addition of such a term in equation (1b) presents no difficulty in the following analysis, we omit this term for simplicity. For the same reason, we omit in equation (1a) the term which represents the body force.

It is well known that a system of partial differential equations of hyperbolic type can be transformed into a system of "interior differential equations" on the characteristic surface [9]. For one-dimensional waves, equations (1) reduce to

$$\sigma_{,x} = \rho_0 v_{,t} \tag{3a}$$

$$\sigma_{,t} = M v_{,x} \tag{3b}$$

and the characteristic form of equations (3) is the familiar relation [10],

$$\frac{d\sigma}{dt} \mp \rho_0 c \frac{dv}{dt} = 0 \quad \text{along} \quad \frac{dx}{dt} = \pm c \tag{4}$$

in which $c = \sqrt{M/\rho_0}$ is the wave speed and d/dt is the total differentiation along the characteristics. For two or three-dimensional waves, equations (1) can be rewritten in the form

$$\mathbf{A}_0 \mathbf{w}_{,t} + \mathbf{A}_i \mathbf{w}_{,i} = \mathbf{0} \tag{5}$$

in which $\mathbf{w}$ is a column matrix whose elements are σ_{ij} and v_i while $\mathbf{A}_0$, $\mathbf{A}_i$, $(i = 1, 2, 3)$ are square matrices. The characteristic form of differential equations derived from equation (5) has been obtained in [11, 12] for linear isotropic elastic solids and in [7] for elastic-viscoplastic materials.

Although equation (5) appears to be in a more compact form than equations (1), use of equation (5) in deriving the characteristic form

Contributed by the Applied Mechanics Division and presented at the Winter Annual Meeting, Washington, D.C., November 15–20, 1981, of THE AMERICAN SOCIETY OF MECHANICAL ENGINEERS.

Discussion on this paper should be addressed to the Editorial Department, ASME, United Engineering Center, 345 East 47th Street, New York, N.Y. 10017, and will be accepted until March 1, 1982. Manuscript received by ASME Applied Mechanics Division, April, 1981. Paper No. 81-WA/APM-23.

Copyright © 1981 by ASME

Downloaded 01 May 2010 to 171.66.16.249. Redistribution subject to ASME license or copyright; see http://www.asme.org/terms/Terms_Use.cfm

of wave equations has several drawbacks in practical applications. First, the matrices $\mathbf{A}_0$ and $\mathbf{A}_i$ *have to be found for a given material.* $\mathbf{A}_0$ and $\mathbf{A}_i$ are 5×5 matrices for two-dimensional waves [11] and 9×9 matrices for three-dimensional waves [12]. Therefore, the wave speeds and the eigenvectors of equation (5) are not easily obtained, specially for nonlinear materials. Second, unless the material is specified (i.e., M_{ijkp} are given explicitly), it is difficult to see how the stress and velocity components enter in the characteristic form derived from equation (5).

In Section 2, we use equations (1) instead of equation (5) to derive the characteristic form of wave equations. Each term in the characteristic form has a geometrical meaning. This is presented in Section 3. For the special case of linear and isotropic elastic materials, the characteristic form for two and three-dimensional waves are, interestingly enough, similar to the one-dimensional case, equation (4). This is shown in Section 4. Of course, the characteristic form should be the same regardless of whether it is derived from equations (1) or equation (5). It is shown that the characteristic form for elastic waves obtained from equation (5) in the literature is equivalent to the shorter form obtained here.

The use of Lagrangian coordinate system as in equations (1) is not always the most convenient in applications, especially for motions of fluids. We present in Section 5 the characteristic form of wave equations in Eulerian coordinates. For the special case of wave motion in compressible fluids, the characteristic form for three-dimensional problems is again very similar to the one for one-dimensional problems.

Finally, in Section 6, we compare the characteristic equation obtained here with the characteristic equation derived from equation (5).

2 Characteristic Form in Lagrangian Coordinates

Let the characteristic surface in the $(\mathbf{x},t)$ space be given by

$$\phi = t - \tau(\mathbf{x}) = 0, \tag{6}$$

where τ is a function of $\mathbf{x}$ only. Also, let f^* be the value of the function $f(\mathbf{x},t)$ evaluated on the characteristic surface $t = \tau(\mathbf{x})$, i.e.,

$$f^*(\mathbf{x}) = f(\mathbf{x},\tau(\mathbf{x})). \tag{7}$$

We then have

$$f^*_{,i} = f_{,i} + f_{,t}\tau_{,i} \tag{8}$$

where it is understood that $f_{,i}$ and $f_{,t}$ on the right-hand side of equation (8) are evaluated on the characteristic surface after taking the partial differentiations. By applying equation (8) to σ_{ij} and v_i in equations (1), we obtain

$$\sigma^*_{ij,j} - \sigma_{ij,t}\tau_{,j} = \rho_0 v_{i,t} \tag{9a}$$

$$\sigma_{ij,t} = M_{ijkp}(v^*_{k,p} - v_{k,t}\tau_{,p}) \tag{9b}$$

or, after eliminating $\sigma_{ij,t}$,

$$D_{ik}v_{k,t} + \sigma^*_{ij,j} - M_{ijkp}\tau_{,j}v^*_{k,p} = 0 \tag{10}$$

where

$$D_{ik} = M_{ijkp}\tau_{,j}\tau_{,p} - \rho_0\delta_{ik} \tag{11}$$

The characteristic surface $\tau(\mathbf{x})$ is a solution of the differential equation which is obtained by setting the determinant of D_{ik} to zero

$$Q(\tau_{,p}) = \|D_{ik}\| = 0 \tag{12}$$

At a fixed time t, let $\mathbf{n}$ be the unit normal vector to the characteristic surface in the $\mathbf{x}$-space pointing toward the direction of propagation of the characteristic surface and c be the normal wave speed. Then

$$\tau_{,i} = n_i/c. \tag{13}$$

Substitution of equation (13) into equation (11) and then into equation (12) yields the wave speeds c for a given $\mathbf{n}$.

Since the characteristic curves of equation (12) are the bicharacteristics of equations (1), we obtain [9]

$$b_p = \frac{dx_p}{dt} = \frac{(\partial Q/\partial\tau_{,p})}{\tau_{,k}(\partial Q/\partial\tau_{,k})} \tag{14}$$

where b_p is the wave velocity measured along the bicharacteristic direction. It follows from equations (14) and (13) that

$$b_p n_p = c \tag{15}$$

Equation (14) requires a differentiation of Q with respect to $\tau_{,p}$, an operation which is not easy to do when Q has a complicated expression. An alternate expression to equation (14) is [6],

$$b_p = l_i(M_{ijkp} + M_{ipkj})\tau_{,j}r_k/(2\rho_0 l_m r_m) \tag{16}$$

where l_i and r_i are the left and right eigenvectors of D_{ik}:

$$l_i D_{ik} = l_i(M_{ijkp}\tau_{,j}\tau_{,p} - \rho_0\delta_{ik}) = 0 \tag{17a}$$

$$D_{ik}r_k = (M_{ijkp}\tau_{,j}\tau_{,p} - \rho_0\delta_{ik})r_k = 0 \tag{17b}$$

When equation (10) is multiplied by l_i, it follows from equation (17a) that

$$l_i\sigma^*_{ij,j} - l_i M_{ijkp}\tau_{,j}v^*_{k,p} = 0 \tag{18}$$

Equation (18) is the "interior differential equation" on the characteristic surface because σ^*_{ij} and v^*_k are the values of σ_{ij} and v_k evaluated on the characteristic surface.

We define the total differentiation of a function $f(\mathbf{x},t)$ along the bicharacteristics by

$$\frac{df}{dt} = f_{,j}\frac{dx_j}{dt} + f_{,t} = f_{,j}b_j + f_{,t} \tag{19}$$

Elimination of $f_{,t}$ between equations (19) and (8) yields

$$f^*_{,i} = \frac{df}{dt}\tau_{,i} + (\delta_{ij} - \tau_{,i}b_j)f_{,j} \tag{20}$$

Therefore, equation (18) can be written as, using equations (20), (13), and (17a),

$$l_i\left(\frac{d\sigma_{ij}}{dt}n_j - \rho_0 c\frac{dv_i}{dt}\right) = -S \quad \text{along} \quad \frac{dx_i}{dt} = b_i, \tag{21a}$$

where

$$S = l_i(c\delta_{jp} - n_j b_p)\sigma_{ij,p} - l_i(M_{ijkp}n_j - \rho_0 c\delta_{ik}b_p)v_{k,p} \tag{21b}$$

The interior differentiation on the characteristic surface in the $(\mathbf{x},t)$ space is now divided into two parts. The left-hand side of equation (21a) contains differentiations along the bicharacteristics while the right-hand side contains differentiations on the part of characteristic surface which intersects the plane t = constant. Equations (21) are useful for a finite-difference approximation.

3 Geometrical Interpretation of Equations (21)

Consider the characteristic surface in the $\mathbf{x}$ space at a fixed time t = constant. On this surface, we introduce the surface coordinates (ξ_1,ξ_2) so that any point on the surface is given by

$$\mathbf{x} = \mathbf{x}(\xi_1,\xi_2) \tag{22}$$

The base vectors of the curvilinear surface coordinates are

$$\mathbf{e}_\Gamma = \partial\mathbf{x}/\partial\xi_\Gamma, \quad (\Gamma = 1, 2) \tag{23}$$

and the reciprocal base vectors $\mathbf{e}^\Delta$ $(\Delta = 1, 2)$ on the surface are defined by

$$\mathbf{e}^\Delta \cdot \mathbf{e}_\Gamma = \delta^\Delta_\Gamma \quad \text{or} \quad e^\Delta_k e^k_\Gamma = \delta^\Delta_\Gamma \tag{24}$$

where δ^Δ_Γ is the Kronecker delta.

Using equation (15), it is seen that

$$(c\delta_{jp} - n_j b_p)n_p = 0 \tag{25}$$

Downloaded 01 May 2010 to 171.66.16.249. Redistribution subject to ASME license or copyright; see http://www.asme.org/terms/Terms_Use.cfm

Hence $(c\delta_{jp} - n_j b_p)$ is, for a fixed j, perpendicular to n_p and can be written as

$$c\delta_{jp} - n_j b_p = \alpha_j^\Gamma e_\Gamma^p \tag{26}$$

To determine α_j^Γ, all we have to do is multiply both sides of equation (26) by e_p^Δ and use equation (24). The result is

$$\alpha_j^\Gamma = (c\delta_{jp} - n_j b_p) e_p^\Gamma \tag{27}$$

Similarly, using equations (17a), (13), and (15) it can be shown that

$$l_i(M_{ijkp} n_j - \rho_0 c\delta_{ik} b_p) n_p = 0 \tag{28}$$

Hence

$$l_i(M_{ijkp} n_j - \rho_0 c\delta_{ik} b_p) = \beta_k^\Gamma e_\Gamma^p \tag{29}$$

where

$$\beta_k^\Gamma = l_i(M_{ijkp} n_j - \rho_0 c\delta_{ik} b_p) e_p^\Gamma \tag{30}$$

It follows from equations (26) and (29) that equation (21b) can be written as

$$S = l_i \alpha_j^\Gamma \sigma_{ij,\Gamma} - \beta_i^\Gamma v_{i,\Gamma} \tag{31}$$

where

$$f_{,\Gamma} = e_\Gamma^p f_{,p} = \partial f / \partial \xi_\Gamma, \quad (\Gamma = 1, 2) \tag{32}$$

is the differentiation along the ξ_Γ-direction on the characteristic surface. Equation (31) shows that S indeed consists of differentiations of σ_{ij} and v_i along two curvilinear surface coordinates on the portion of characteristic surface which intersects the plane t = constant.

We now rewrite the left-hand side of equation (21a) as

$$\frac{d}{dt}(l_i \sigma_{ij} n_j) - \rho_0 c \frac{d}{dt}(l_i v_i) - \sigma_{ij} \frac{d}{dt}(l_i n_j) + \rho_0 c v_i \frac{d}{dt}(l_i) = -S \tag{33}$$

The last two terms on the left-hand side of equation (33) vanish if l_i and n_i are constants along the bicharacteristics. This happens when the material is linear and homogeneous or when the material is nonlinear but the problem is mathematically one-dimensional, such as spherically symmetric waves in which only one space variable is involved. The first two terms of equation (33) represent the differentiation along the bicharacteristics of the quantities $l_i \sigma_{ij} n_j$ and $l_i v_i$. Without loss of generality, we normalize l_i so that it is a unit vector. Since $\sigma_{ij} n_j$ is the surface traction vector on the characteristic surface, $l_i \sigma_{ij} n_j$ is the projection of the surface traction vector in the direction of l_i, Fig. 1. Similarly, $l_i v_i$ is the projection of the velocity vector in the direction l_i. Notice that if $M_{ijkp} = M_{kpij}$, l_i is identical to r_i, the polarization vector. It is the vector which a discontinuity in $v_{i,t}$ across the characteristic surface is proportional to.

In the next section, we apply the results obtained to homogeneous linear isotropic elastic materials.

4 Homogeneous Linear Isotropic Elastic Materials

For linear isotropic elastic materials,

$$M_{ijkp} = \lambda\delta_{ij}\delta_{kp} + \mu(\delta_{ik}\delta_{jp} + \delta_{ip}\delta_{jk}) \tag{34}$$

where λ and μ are the Lamé constants. Equations (11)–(13) provide two distinct wave speeds c which will be denoted by c_1 and c_2, respectively:

$$c_1 = \sqrt{(\lambda + 2\mu)/\rho}, \quad c_2 = \sqrt{\mu/\rho} \tag{35}$$

The subscript 0 of ρ is omitted for simplicity in this section. Equations (17), (16), (27), and (30) furnish the eigenvectors l_i and r_i, the bicharacteristic wave speed b_i and $\alpha_i^\Gamma, \beta_i^\Gamma$. We will now consider $c = c_1$ and c_2 separately.

(I) Characteristic Form for $c = c_1$. When $c = c_1$, we have

$$\left.\begin{aligned} l_i = r_i = n_i,\ b_i = c_1 n_i \\ \alpha_i^\Gamma = c_1 e_i^\Gamma,\ \beta_i^\Gamma = \lambda e_i^\Gamma \end{aligned}\right\} \tag{36}$$

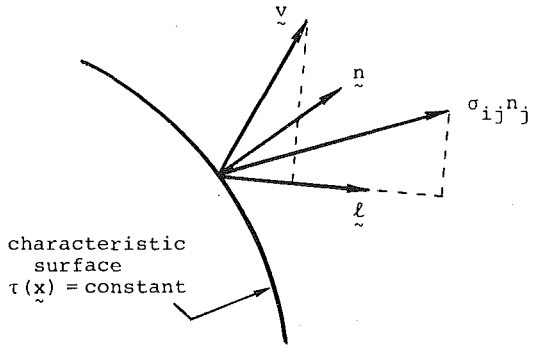


Fig. 1 Interpretation of equation (21)

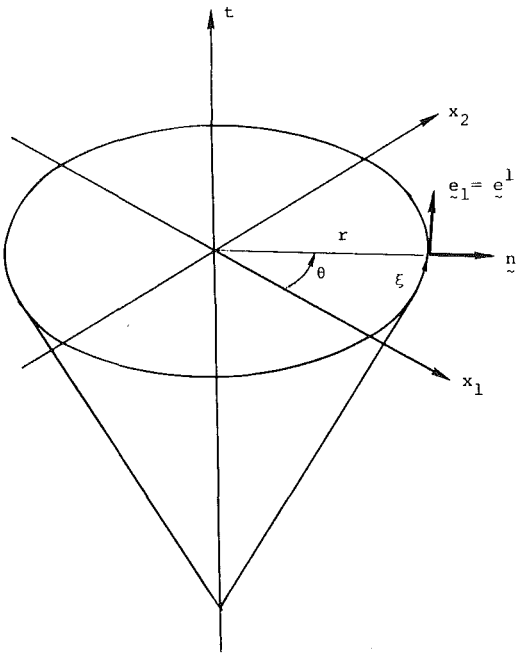


Fig. 2 Characteristic surface in Lagrangian coordinates for two-dimensional waves in linear isotropic elastic solids

Hence equations (21a) and (31) become

$$\frac{d\sigma_n}{dt} - \rho c_1 \frac{dv_n}{dt} = -S \quad \text{along} \quad \frac{dx_i}{dt} = c_1 n_i, \tag{37}$$

where

$$\left.\begin{aligned} S = c_1 n_i e_j^\Gamma \sigma_{ij,\Gamma} - \lambda e_i^\Gamma v_{i,\Gamma} \\ \sigma_n = \sigma_{ij} n_i n_j, \quad v_n = v_i n_i \end{aligned}\right\} \tag{38}$$

Notice that only the stress and velocity components normal to the characteristic surface appear in the left-hand side of equation (37). As to the right-hand side of equation (37), S vanishes for one-dimensional waves because the intersection of the characteristic surface (in this case, a line) with the plane t = constant is a point and hence there is no differentiation with respect to ξ_Γ required. Hence for one-dimensional waves equation (37) reduces to equation (4). The $\mp$ sign in front of dv/dt in equation (4) can be recovered from equation (37) if one observes that v_n for waves propagating in the negative x-direction has an opposite sign to v_n for waves propagating in the positive x-direction.

It is illuminating to see the form of S for two-dimensional waves because the characteristic surface on the t = constant plane is a plane curve. Hence only one $\mathbf{e}_\Gamma$ is needed, say $\mathbf{e}_1$. Similarly, only one $\mathbf{e}^\Gamma$ is needed, say $\mathbf{e}^1$, and $\mathbf{e}_1 \cdot \mathbf{e}^1 = 1$. As an illustration, we consider a circular cone for the characteristic surface so that its intersection on the t =

Downloaded 01 May 2010 to 171.66.16.249. Redistribution subject to ASME license or copyright; see http://www.asme.org/terms/Terms_Use.cfm

constant plane is a circle with a radius r, Fig. 2. We also choose $\xi_1 = r\theta = \xi$, say. Then,

$$\left.\begin{aligned} \mathbf{n} &= (\cos\theta, \sin\theta) \\ \mathbf{e}_1 = \mathbf{e}^1 &= (-\sin\theta, \cos\theta) \end{aligned}\right\} \tag{39}$$

and

$$S = c_1\left\{-\frac{1}{2}(\sigma_{11} - \sigma_{22})_{,\xi}\sin 2\theta + (\sigma_{12})_{,\xi}\cos 2\theta\right\} - \lambda\{-v_{1,\xi}\sin\theta + v_{2,\xi}\cos\theta\} \tag{40}$$

where

$$f_{,\xi} = (-f_{,1}\sin\theta + f_{,2}\cos\theta) \tag{41}$$

It is not difficult to show that S obtained in equation (40) is equivalent to the right-hand side of equation (14a) in [11] if α in [11] is equated to $\theta + \pi$. Similarly, it can be shown that the left-hand side of equation (37) is equivalent to the left-hand side of equation (14a) in [11]. However, the expression obtained here is in a more compact form than that of equation (14a) in [11].

For the polar coordinates shown in Fig. 2, σ_n and v_n of equation (37) are σ_{rr} and v_r, respectively. Moreover,

$$f_{,\xi} = f_{,\theta}/r \tag{42}$$

and hence equations (37) and (40) can be written as

$$\frac{d\sigma_{rr}}{dt} - \rho c_1\frac{dv_r}{dt} = -c_1\left\{\frac{1}{r}\sigma_{r\theta,\theta} + \frac{1}{r}(\sigma_{rr} - \sigma_{\theta\theta})\right\} + \lambda\left(\frac{1}{r}v_{\theta,\theta} + v_r\right) \tag{43}$$

where

$$\left.\begin{aligned} \sigma_{rr} &= \frac{1}{2}(\sigma_{11} + \sigma_{22}) + \frac{1}{2}(\sigma_{11} - \sigma_{22})\cos 2\theta + \sigma_{12}\sin 2\theta \\ \sigma_{\theta\theta} &= \frac{1}{2}(\sigma_{11} + \sigma_{22}) - \frac{1}{2}(\sigma_{11} - \sigma_{22})\cos 2\theta - \sigma_{12}\sin 2\theta \\ \sigma_{r\theta} &= -\frac{1}{2}(\sigma_{11} - \sigma_{22})\sin 2\theta + \sigma_{12}\cos 2\theta \\ v_r &= v_1\cos\theta + v_2\sin\theta \\ v_\theta &= -v_1\sin\theta + v_2\cos\theta \end{aligned}\right\} \tag{44}$$

Noticing that

$$\frac{df}{dt} = f_{,t} + f_{,r}c_1 \tag{45}$$

Equation (43) has the form

$$\sigma_{rr,t} - \left[2\mu v_{r,r} + \lambda\left(v_{r,r} + \frac{1}{r}v_{\theta,\theta} + \frac{1}{r}v_r\right)\right] = -c_1\left\{\sigma_{rr,r} + \frac{1}{r}\sigma_{r\theta,\theta} + \frac{1}{r}(\sigma_{rr} - \sigma_{\theta\theta}) - \rho v_{r,t}\right\} \tag{46}$$

Each side of equation (46), when set to zero, can be identified as one of the stress-strain laws and one of equations of motion, respectively, in the polar coordinates. This is not surprising; since the characteristic form of differential equations is derivable from a linear superposition of the original differential equations.

(II) Characteristic Form for $c = c_2$. Since c_2 is a double root, the characteristic surface is actually two surfaces merged into one. Nevertheless, we will regard the surface as two surfaces and identify them by $\Delta = 1,2$. We then have, for $c = c_2$ ($\Delta = 1,2$)

$$\left.\begin{aligned} l_i &= e^i_\Delta, \quad r_i = e^\Delta_i, \quad b_i = c_2 n_i \\ \alpha^\Gamma_i &= c_2 e^\Gamma_i, \quad \beta^\Gamma_i = \mu n_i \delta^\Gamma_\Delta \end{aligned}\right\} \tag{47}$$

Equations (21a) and (31) reduce to

$$\frac{d\sigma_{\Delta n}}{dt} - \rho c_2\frac{dv_\Delta}{dt} = -S \quad \text{along} \quad \frac{dx_i}{dt} = c_2 n_i \tag{48a}$$

where

$$S = c_2 e^i_\Delta e^\Gamma_j \sigma_{ij,\Gamma} - \mu n_i v_{i,\Delta} \tag{48b}$$

$$\sigma_{\Delta n} = \sigma_{ij} n_j e^i_\Delta, \quad v_\Delta = v_i e^i_\Delta \tag{48c}$$

The left-hand side of equation (48a) shows that only the shear stress and the velocity component which are tangential to the characteristic surface are involved in the total differentiation along the bicharacteristics.

Again, we will consider the two-dimensional case with the characteristic surface being a circular cone. Equation (39) is still applicable and equations (48a) and (48b) become

$$\frac{d\sigma_{r\theta}}{dt} - \rho c_2\frac{dv_\theta}{dt} = -c_2\{\sigma_{11,\xi}\sin^2\theta + \sigma_{22,\xi}\cos^2\theta - \sigma_{12,\xi}\sin 2\theta\} + \mu\{v_{1,\xi}\cos\theta + v_{2,\xi}\sin\theta\} \tag{49}$$

where the differentiation with respect to ξ is defined in equation (41) and $\sigma_{r\theta}$, v_θ are defined in equation (44). It can be shown that equation (49), though in a more compact form, is identical to equation (14b) of [11]. As before, one can show that equation (49) is obtainable from a superposition of one of the stress-strain relations and one of the equations of motion in the polar coordinates.

In the next section we consider the characteristic form of wave equations in an Eulerian coordinate system.

5 Characteristic Form in Eulerian Coordinates

In Eulerian coordinates, equations (1) are replaced by

$$T_{ij,j} = \rho\dot{v}_i \tag{50a}$$

$$\dot{T}_{ij} = L_{ijkp}v_{k,p} \tag{50b}$$

where T_{ij} is the Cauchy stress, ρ the mass density at time t, L_{ijkm} are the material functions, and a dot stands for material differentiation:

$$\dot{f} = f_{,t} + f_{,k}v_k. \tag{51}$$

Equations (50) therefore have the form

$$T_{ij,j} = \rho(v_{i,t} + v_{i,k}v_k) \tag{52a}$$

$$T_{ij,t} + T_{ij,k}v_k = L_{ijkp}v_{k,p} \tag{52b}$$

or, using equation (8),

$$T^*_{ij,j} - T_{ij,t}\tau_{,j} = \rho(\gamma v_{i,t} + v^*_{i,k}v_k) \tag{53a}$$

$$T^*_{ij,k}v_k + \gamma T_{ij,t} = L_{ijkp}(v^*_{k,p} - v_{k,t}\tau_{,p}) \tag{53b}$$

where

$$\gamma = 1 - v_k\tau_{,k} = 1 - v_k n_k/c = (c - v_n)/c \tag{54}$$

The second and third equality of equation (54) come from equations (13) and (38).

It should be mentioned that, for simplicity, some of the notations we use in this section are the same as the ones in the previous sections although they may not represent the same physical quantity. For instance, x_i in the previous sections are the Lagrangian coordinates while in this section they are the Eulerian coordinates. Likewise, n_i is the unit vector normal to the characteristic surface in the Lagrangian coordinates in the previous section but is the unit vector in the Eulerian coordinates in this section. We could have used different notations, but then we would have to rewrite equations such as equations (6)–(8), and (13) and many equations in Section 3.

Elimination of $T_{ij,t}$ between equations (53a) and (53b) results in the following equation:

$$B_{ik}v_{k,t} + (\gamma\delta_{jk} + \tau_{,j}v_k)T^*_{ij,k} - (L_{ijkp}\tau_{,j} + \rho\gamma v_p\delta_{ik})v^*_{k,p} = 0 \tag{55}$$

where

$$B_{ik} = L_{ijkp}\tau_{,j}\tau_{,p} - \rho\gamma^2\delta_{ik} \tag{56}$$

The vanishing of the determinant B_{ik} is, using equation (54),

Downloaded 01 May 2010 to 171.66.16.249. Redistribution subject to ASME license or copyright; see http://www.asme.org/terms/Terms_Use.cfm

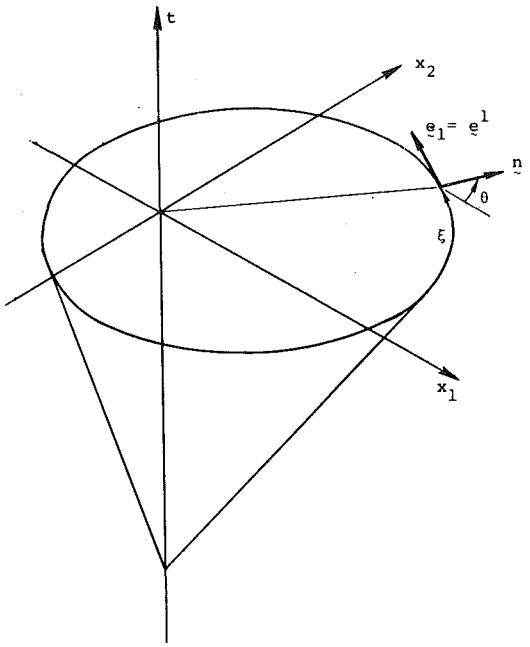


Fig. 3 Characteristic surface in Eulerian coordinates for two-dimensional isentropic flows

$$Q(\tau_{,p}) = \|L_{ijkm}\tau_{,j}\tau_{,m} - \rho(1 - v_m\tau_{,m})^2\delta_{ik}\| = 0 \tag{57}$$

The bicharacteristic wave speed b_p can be obtained by using (14). As before, an alternate expression for b_p without using equation (14) is desirable. Following the same approach in deriving equation (16) (see [6]), one obtains

$$b_p = l_i\{(L_{ijkp} + L_{ipkj})\tau_{,j} + 2\rho\gamma v_p\delta_{ik}\}r_k/(2\rho\gamma l_m r_m) \tag{58}$$

where l_i and r_i are the left and right eigenvectors of B_{ik}:

$$l_iB_{ik} = 0, \quad B_{ik}r_k = 0. \tag{59}$$

Let

$$a = c - v_kn_k = c - v_n, \tag{60}$$

be the characteristic wave speed relative to the normal particle velocity. Equations (54) and (57) become

$$\gamma = a/c, \tag{61}$$

$$\|L_{ijkp}n_jn_p - \rho a^2\delta_{ik}\| = 0 \tag{62}$$

Equation (62) provides a for a given normal n_i. The characteristic wave speed c is then obtained from equation (60). Thus, while a depends only on L_{ijkp} and n_i, c depends also on the normal particle velocity. The characteristic cone through a fixed point in the $(\mathbf{x},t)$ space is no longer symmetric with respect to the t-axis of the cone as shown in Fig. 3 for the case of a two-dimensional flow.

It follows from equations (55) and (59) that

$$l_i(\gamma\delta_{jk} + \tau_{,j}v_k)T^*_{ij,k} - l_i(L_{ijkp}\tau_{,j} + \rho\gamma v_p\delta_{ik})v^*_{k,p} = 0 \tag{63}$$

This is obviously a characteristic form of the original differential equation because T^*_{ij} and v^*_k are values of T_{ij} and v_k on the characteristic surface. The interior differentiation $T^*_{ij,k}$ and $v^*_{k,p}$ can be written in terms of differentiation along the bicharacteristics and differentiation on the plane t = constant by using equation (20). The result is, using equations (13), (54), (59), and (61),

$$l_i\left(\frac{dT_{ij}}{dt}n_j - \rho a\frac{dv_i}{dt}\right) = -S \quad \text{along} \quad \frac{dx_i}{dt} = b_i, \tag{64a}$$

where

$$S = l_i[a\delta_{jp} - n_j(b_p - v_p)]T_{ij,p} - l_i[L_{ijkp}n_j - \rho a\delta_{ik}(b_p - v_p)]v_{k,p} \tag{64b}$$

As in equation (25), one can show that the coefficient of $T_{ij,p}$ in equation (64b) vanishes when multiplied by n_p. The same statement applies to the coefficient of $v_{k,p}$. Following a similar procedure in deriving equations (25)–(31), we rewrite equation (64b) as

$$S = l_i\alpha^\Gamma_jT_{ij,\Gamma} - \beta^\Gamma_kv_{k,\Gamma} \tag{65}$$

where

$$\left.\begin{aligned}\alpha^\Gamma_j &= [a\delta_{jp} - n_j(b_p - v_p)]e^\Gamma_p\\ \beta^\Gamma_k &= l_i[L_{ijkp}n_j - \rho a\delta_{ik}(b_p - v_p)]e^\Gamma_p\end{aligned}\right\} \tag{66}$$

and e^Γ_p and $f_{,\Gamma}$ are defined in equations (24) and (32).

Equations (64a), (64b), and (65) are similar to equations (21a), (21b), and (31), respectively. Therefore, the geometrical interpretation of the terms in the characteristic form given in Section 3 can be applied here also.

As an application of the characteristic form in Eulerian coordinates, we consider the isentropic flow of compressible fluids. To this end, let

$$\left.\begin{aligned}T_{ij} &= -p\delta_{ij},\\ L_{ijkm} &= \lambda\delta_{ij}\delta_{km}\end{aligned}\right\} \tag{67}$$

where p is the pressure and $\lambda = \rho dp/d\rho$. We then have

$$\left.\begin{aligned}a &= \sqrt{\lambda/\rho} = \sqrt{dp/d\rho}\\ l_i &= r_i = n_i\\ b_i &= an_i + v_i\\ \alpha^\Gamma_i &= ae^\Gamma_i\\ \beta^\Gamma_i &= e^\Gamma_i\end{aligned}\right\} \tag{68}$$

and equations (64a) and (65) reduce to

$$\frac{dp}{dt} + \rho an_i\frac{dv_i}{dt} = -\lambda e^\Gamma_kv_{k,\Gamma} \quad \text{along} \quad \frac{dx_i}{dt} = an_i + v_i \tag{69}$$

For two-dimensional problems, let the angle between the normal vector $\mathbf{n}$ and the x_1-axis be θ, Fig. 3. Then equations (39) and (41) still apply and we have

$$\frac{dp}{dt} + \rho a\left(\cos\theta\frac{dv_1}{dt} + \sin\theta\frac{dv_2}{dt}\right) = -\lambda(-v_{1,\xi}\sin\theta + v_{2,\xi}\cos\theta) \quad \text{along} \quad \frac{dx_i}{dt} = an_i + v_i \tag{70}$$

This is, in a slightly shorter form, identical to equation (4.12) in [13]. For one-dimensional isentropic flow in the x_1-direction, equation (70) becomes the familiar relation (see [14], for example)

$$\frac{dp}{dt} \pm \rho a\frac{dv_1}{dt} = 0 \quad \text{along} \quad \frac{dx_1}{dt} = v_1 \pm a \tag{71}$$

6 Comparison With the Characteristic Equation Derived From Equation (5)

The main results of this paper are given in equations (21) and (31) for the Lagrangian coordinates and in equations (64) and (65) for the Eulerian coordinates. Once a constitutive equation is given, the matrix D_{ij} of equation (11) or B_{ij} of equation (56) is known. Since D_{ij} or B_{ij} is a 3×3 matrix, the left eigenvector l_i defined in equations (17a) and (59) is a three-dimensional vector. Equations (21) or (64) then provides the characteristic equation.

If equation (5) is used in deriving the characteristic equation, it can be shown that the characteristic equation based on equation (5) is

$$n_i\mathbf{g}^T\mathbf{A}_i\frac{d\mathbf{W}}{dt} = -S, \tag{72a}$$

$$S = (c\delta_{ij} - n_ib_j)\mathbf{g}^T\mathbf{A}_i\mathbf{W}_{,j}, \tag{72b}$$

Downloaded 01 May 2010 to 171.66.16.249. Redistribution subject to ASME license or copyright; see http://www.asme.org/terms/Terms_Use.cfm

where

$$\left.\begin{aligned} \mathbf{g}^T\mathbf{A} &= \mathbf{0} \\ \mathbf{A} &= \mathbf{A}_0 - \tau_{,i}\mathbf{A}_i \end{aligned}\right\} \tag{73}$$

b_i in equation (72b) is still given by equation (14). However, Q in equation (14) is now the determinant of $\mathbf{A}$:

$$Q = \|\mathbf{A}\| \tag{74}$$

In deriving the characteristic equation, equation (72), one has to find the matrices $\mathbf{A}_0$ and $\mathbf{A}_i$, (i = 1, 2, 3). These matrices are 5 × 5 matrices for two-dimensional problems and 9 × 9 matrices for three-dimensional problems. Accordingly, the left eigenvector $\mathbf{g}$ is a five-dimensional (or nine-dimensional) vector for two-dimensional (or three-dimensional) problems. Therefore, $\mathbf{g}$ is not easily found, especially for nonlinear problems. The same difficulty prevails in finding the wave speed c and the ray velocity b_i.

There are other drawbacks in using equations (72). Unlike equations (21) or (64), it is not clear from equations (72) which stress and velocity components are involved in the characteristic equation. Moreover, reduction from the three-dimensional characteristic equation to the two-dimensional one is not obvious from equation (72). In fact, one cannot obtain the two-dimensional characteristic equation by specializing the three-dimensional one because $\mathbf{A}_0$ and $\mathbf{A}_i$ are matrices of different dimensions in two and three-dimensional problems.

Finally, as shown in the examples, the characteristic equations obtained from equations (72) have lengthier expressions than the characteristic equations obtained from equations (21) or (64).

7 Concluding Remarks

Characteristic forms of differential equations for wave propagation in nonlinear media are derived for Lagrangian and Eulerian coordinates. Although in both cases the rectangular coordinate system is used, one could modify the analysis for general curvilinear coordinate systems. The left sides of equations (21a) and (64a) will remain essentially the same while the right-hand sides of these equations would involve covariant differentiations.

As we mentioned in the Introduction, the constitutive equations given by equations (1b)and (50b) cover a wide class of materials. For elastic-viscoplastic materials, we add a term which is a function of the stress to the right-hand side of equations (1b) and (50b). The modifications required in the analysis due to the addition of this term is straightforward. As to viscoelastic materials, if the stress σ_{ij} is a nonlinear functional of the strain ϵ_{ij}, one can write [15, 16]

$$\begin{aligned} \sigma_{ij,t} &= G_{ijkp}\epsilon_{kp,t} + H_{ij} \\ &= G_{ijkp}v_{k,p} + H_{ij} \end{aligned} \tag{75}$$

in which G_{ijkp} and H_{ij} are nonlinear functionals of ϵ_{ij}. Again, the modification required in the analysis due to equation (75) is straightforward. A characteristic form for wave propagation in one-dimensional linear viscoelastic materials whose stress-strain law is given by the Boltzman convolution integral can be found in equations (43) of [17].

Acknowledgments

The work presented here is supported by the U. S. Army Research Office—Durham, under Grant DAAG 29-80-C-0093 to the University of Illinois at Chicago Circle.

References

1 Nariboli, G. A., and Juneja, B. L., "Growth of Acceleration Waves in an Initially Stressed Hypoelastic Media," *Journal of Nonlinear Mechanics*, Vol. 6, 1971, pp. 13–25.

2 Suhubi, E. S., "The Growth of Acceleration Waves of Arbitrary Form in Deformed Hyperelastic Materials," *International Journal for Engineering Sciences*, Vol. 8, 1970, pp. 699–710.

3 Wright, T. W., "Acceleration Waves in Simple Elastic Materials," *Arch. Rat. Mech. Anal.*, Vol. 50, 1973, pp. 237–277.

4 Sauerwein, H., "Anisotropic Waves in Elastoplastic Solids," *International Journal for Engineering Sciences*, Vol. 5, 1967, pp. 455–475.

5 Lee, E. H., "Plastic-Wave Propagation Analysis and Elastic-Plastic Theory at Finite Strain," in *Shock Waves and the Mech. Properties of Solids*, eds., Burke, J. J., and Weiss, V., Syracuse University Press, 1971, pp. 3–19.

6 Ting, T. C. T., "Shock Waves and Weak Discontinuities in Anisotropic Elastic-Plastic Media," in *Propagation of Shock Waves in Solids*, ed., Varley, E., ASME, AMD-Vol. 17, 1976, pp. 41–64.

7 Bejda, J., "Propagation of Two-Dimensional Strong Discontinuity Waves in an Elastic-Viscoplastic Medium," *Arch. Mechanics*, Vol. 24, 1972, pp. 337–349.

8 Ziv, M., "Integrable Generalized Wave Equations Exhibiting a Hypoelastic Compressible Rate-Sensitive Material Flow," ASME JOURNAL OF APPLIED MECHANICS, Vol. 44, 1977, pp. 419–423.

9 Courant, R., and Hilbert, D., *Methods of Mathematical Physics, II*, Wiley-Interscience, 1962.

10 Lee, E. H., "A Boundary-Value Problem in the Theory of Plastic Wave Propagation," *Quarterly of Applied Mathematics*, Vol. 10, 1953, pp. 335–346.

11 Clifton, R. J., "A Difference Method for Plane Problems in Dynamic Elasticity," *Quarterly of Applied Mathematics*, Vol. 24, No. 1, Apr. 1967, pp. 98–116.

12 Recker, W. W., "A Numerical Solution of Three-Dimensional Problems in Dynamic Elasticity," ASME JOURNAL OF APPLIED MECHANICS, Vol. 37, 1970, pp. 116–122.

13 Butler, D. S., "The Numerical Solution of Hyperbolic Systems of Partial Differential Equations in Three Independent Variables," *Proceedings of the Royal Society*, London, Series A, Vol. 255, 1960, pp. 232–252.

14 Whitham, G. B., *Linear and Nonlinear Waves*, Wiley-Interscience, 1974, p. 122.

15 Coleman, B. D., and Gurtin, M. E., "Waves in Materials With Memory. IV. Thermodynamics and the Velocity of General Acceleration Waves," *Arch. Rat. Mech. Anal.*, Vol. 19, 1965, pp. 317–338.

16 Ting, T. C. T., "Nonlinear Effects on the Propagation of Discontinuities of All Orders in Viscoelastic Media," *Proceedings of IUTAM Symposium on Mechanics of Viscoelastic Media and Bodies*, ed., Hult, Jan. 1975, pp. 84–95.

17 Mukunoki, I. and Ting, T. C. T., "Transient Wave Propagation Normal to the Layering of a Finite Layered Medium," *International Journal of Solids and Structures*, Vol. 16, 1980, pp. 239–251.

Downloaded 01 May 2010 to 171.66.16.249. Redistribution subject to ASME license or copyright; see http://www.asme.org/terms/Terms_Use.cfm

A. V. Clark, Jr.[1]
A. M. Whitman[2]

Department of Mechanical Engineering and Applied Mechanics, University of Pennsylvania, Philadelphia, Pa. 19104

Calculation of the Response of an Impulsively Excited Oscillator in an Infinite Acoustic Fluid

The response of an impulsively excited single-degree-of-freedom oscillator submerged in an infinite acoustic fluid is considered. The character of the response is determined by the quantity ka; k is the wave number associated with the in-vacuo natural frequency of the oscillator, and a is a characteristic structural dimension. For low-frequency oscillators ($ka \ll 1$), the response consists of two parts. The first is the usual hydrodynamic solution in which the effect of the fluid on the structure is that of an added mass. The second is much smaller (of order ka) and is significant only in a "boundary layer" in time of order a/c, with c the fluid sonic velocity. For high-frequency oscillators ($ka \gg 1$), the principal effect of the fluid is a decay of oscillator vibration due to sound radiation.

Introduction

The equations which describe the interaction between a submerged elastic structure and the surrounding fluid can be cast into the form of a set of coupled integrodifferential equations for some selected set of mode amplitudes. To be specific, we write here the equation which obtains for the case of a single-degree-of-freedom impulsively excited system

$$m\frac{d^2x}{dt^2} + \int_0^t L(t-t')\frac{d^2x}{dt'^2}dt' + Kx = I\delta(t)$$

$$x = 0, \quad \frac{dx}{dt} = 0 \quad \text{at} \quad t = 0. \tag{1}$$

The fluid-solid interaction is contained in the second term which is a convolution of the acceleration and the impulse response function, L. This function can be calculated in principle, for a specific geometry and mode, from the wave equation for the fluid. However as a practical matter, analytic results have been obtained only for simple geometries (sphere, cylinder) [1].

Although equation (1) can be formally solved by Laplace transform, this is not usually done because of difficulties in evaluating the inverse transform [2]. Instead, various assumptions have been made about L in order to simplify the interaction term in equation (1) [3–6].

Now there are a few general (independent of geometry and mode) results known about L [7] which we write here for later use.

$$(a) \qquad L \sim m_p\left(\frac{c}{a}\right); \quad T = \frac{ct}{a} \to 0 \tag{2}$$

Here c is the speed of sound in the fluid, a is a characteristic dimension,

$$m_p = \rho a\, A_p$$

is the effective piston mass, ρ the fluid density, and A_p the effective piston area. If one uses equation (2) in the convolution in equation (1), that term is

$$m_p\frac{c}{a}\frac{dx}{dt}. \tag{3}$$

This was one of the first approximations of fluid-structure interaction that was tried [3] and not surprisingly it was found in general to give good results only for early times.

$$(b) \qquad L(T) = O(T^{-1}); \quad \lim T \to \infty$$

If the acceleration does not vary appreciably on the time scale T, it can be removed from the convolution in equation (1) (i.e., treated as a constant); then for $T \to \infty$ the convolution is approximately

$$m_0\frac{d^2x}{dt^2} \tag{4}$$

where m_0 is the "added mass,"

$$m_0 = \frac{a}{c}\int_0^\infty L(T)\,dT. \tag{5}$$

This approximation to the interaction was found to be valid at late

---

[1] Present address: Naval Research Laboratory, Washington, D.C. 20375.
[2] Present address: Tel-Aviv University, Tel-Aviv, Israel.

Contributed by the Applied Mechanics Division for publication in the JOURNAL OF APPLIED MECHANICS.
Discussion on this paper should be addressed to the Editorial Department, ASME, United Engineering Center, 345 East 47th Street, New York, N.Y. 10017, and will be accepted until two months after final publication of the paper itself in the JOURNAL OF APPLIED MECHANICS. Manuscript received by ASME Applied Mechanics Division, June, 1980; final revision, March, 1981.

Copyright © 1981 by ASME
Downloaded 01 May 2010 to 171.66.16.249. Redistribution subject to ASME license or copyright; see http://www.asme.org/terms/Terms_Use.cfm

times [2].

More recent types of approximation assume a form for L such that L satisfies a differential equation of finite order (note that equation (1) may be regarded as an infinite order differential equation) and which reduces the interaction term to equation (3) for early times and equation (4) for late times [6]. Thus they have the advantage of being computationally simple while retaining the correct asymptotic behavior in time.

(*c*) Here we restrict the subsequent analysis to bodies for which

$$L(T) = 0(T^{-n}); \quad \lim T \to \infty \quad n = 1, 2, \ldots$$

so that all the moments of L are finite

$$m_j = \frac{a}{c} \int_0^\infty T^j L(T) dT < \infty \tag{5'}$$

There is no general proof that $L(T)$ must have this behavior; however, the existence of the m_j makes good physical sense and those impulse response functions of finite bodies which are known analytically have this property. For example, although the added mass of an infinite circular cylinder in the breathing mode is infinite, for any finite length cylinder it is finite [8].

In the present work, we note that there are two characteristic time scales in the problem, a/c and $(m/k)^{1/2} = 1/\omega_0$, and we seek solutions of equation (1) which are valid for the asymptotic limits of their ratio. Thus we are interested in the two cases

$$\omega_0 a/c = ka \gg 1$$

and

$$\omega_0 a/c = ka \ll 1.$$

The former, we call a high frequency oscillator and the latter a low frequency oscillator. The calculation is accomplished without assuming a form for L and hence illustrates those properties of L which are most important in determining the oscillator response. The results are compared with the known exact solution for a breathing sphere and agreement between the two (to the order in ka of the calculation) is demonstrated.

High Frequency Oscillator

We render equation (1) dimensionless according to the following scheme:

$$\bar{t} = \omega_0 t \quad \bar{x} = x/a \quad \bar{I} = I/m\omega_0 a \quad \bar{\delta} = \delta/\omega_0$$

$$\kappa = m_p/m \quad \bar{L} = L/m\omega_0 = \kappa\chi/ka$$

where $\chi(T)$ is a dimensionless impulse response function such that from equation (2), $\chi(0) = 1$. Equation (1) is thus, dropping the overbars for convenience

$$\frac{d^2x}{dt^2} + \frac{\kappa}{ka} \int_0^t \chi\left(\frac{t-t'}{ka}\right) \frac{d^2x}{dt'^2} dt' + x = I\delta(t). \tag{6}$$

The forcing term in equation (6) is 0 for $t > 0$ so we can alternatively solve the homogeneous form of equation (6) subject to the initial conditions

$$x = 0, \quad dx/dt = I \quad \text{for} \quad t = 0^+. \tag{7}$$

For future reference, we note here that since d^2x/dt^2 is singular at $t = 0$, its value at $t = 0^+$ is different from zero and is, from equations (2) and (6),

$$d^2x/dt^2 = -\kappa I/ka \quad \text{for} \quad t = 0^+. \tag{8}$$

Writing a Taylor expansion for χ and evaluating the convolution in equation (6) gives

$$\frac{d^2x}{dt^2} + \frac{\kappa}{(ka)} \frac{dx}{dt} + \frac{\kappa}{(ka)^2} \chi'(0)x + O[(ka)^{-3}] + x = I\delta(t),$$

where we have used the early time property, equation (2), to evaluate the dominant term. In the limit $ka \to \infty$ the succeeding terms from the convolution are of higher order. We will take $\kappa = O(1)$ in what we do so that the ordering in ka is explicit.

Assuming a formal expansion of the type

$$x(t, ka) = \sum_{j=0}^{m} (ka)^{-j} x_j(t),$$

substituting into the homogeneous form of the equation, and equating powers of ka gives for the first three problems

$$\begin{aligned} &\frac{d^2x_0}{dt^2} + x_0 = 0 \\ &\frac{d^2x_1}{dt^2} + x_1 = -\kappa \frac{dx_0}{dt} \\ &\frac{d^2x_2}{dt^2} + x_2 = -\kappa\chi'(0)x_0 - \kappa \frac{dx_1}{dt}. \end{aligned} \tag{9}$$

The solution of these equations yields a nonuniformly valid (in t) expansion for x due to the resonant forcing terms (e.g., dx_0/dt). This type of singular perturbation problem is common and it can be treated satisfactorily by the method of multiple scales [9]. Accordingly, we take

$$x(t, ka) \equiv x(\eta, \xi, ka)$$

where $\eta = t\,[1 + \omega_2/(ka)^2]$, $\xi = t/ka$. This gives enough freedom to annihilate the resonant forcing terms (through order $(ka)^{-2}$). The result of this calculation is, in original terms,

$$x \sim e^{-\kappa t/2ka}\,(A \sin \omega t + B \cos \omega t) \tag{10}$$

with

$$\omega = 1 + \kappa[4\chi'(0) - \kappa]/8(ka)^2(10)$$

or after satisfying equation (7)

$$x = Ie^{-\kappa t/2ka} \sin \omega t + O[(ka)^{-2}]. \tag{11}$$

Thus we see that for a high frequency oscillator ($ka \gg 1$) the plane wave approximation [3] is correct up to extremely long times ($t = O[(ka)^2]$). As a practical matter, we would say that it is valid for all time since when $t \sim (ka)^2$ the response is exponentially small. Numerical work agreeing with this result have been previously reported in the literature [2].

Low Frequency Oscillator

In this limit $ka \to 0$. We write the convolution as

$$\int_0^t \chi\left(\frac{t'}{ka}\right) \frac{d^2x}{d(t-t')^2} dt'$$

and Taylor expand the acceleration term in it as

$$\frac{d^2x}{d(t-t')^2} = \frac{d^2x}{dt^2} - \frac{d^3x}{dt^3} t' + \frac{d^4x}{dt^4} \frac{t'^2}{2} + O(t'^3).$$

In terms of $T = t/ka$ the integral is

$$\int_0^{t/ka} \chi(T) \left\{\frac{d^2x}{dt^2} - (ka) \frac{d^3x}{dt^3} T + O[(ka)^2]\right\} dt.$$

Evaluating this using the moments of χ (equation (5')) and substituting into equation (6) gives

$$\frac{d^2x}{dt^2} + M_0 \frac{d^2x}{dt^2} - (ka)M_1 \frac{d^3x}{dt^3} + O[(ka)^2] + x = I\delta(t)$$

where $M_0 = m_0/m$ and $M_1 = m_1/m$. This equation is explicitly ordered in the small parameter ka provided that $M_j = O(1)$ and that all x derivatives are also order one. Assuming this is so, making the expansion

$$x(t, ka) = \sum_{i=0}^{\infty} (ka)^i x_i(t),$$

substituting into the homogeneous equation, and ordering powers of ka gives for the first two orders,

Downloaded 01 May 2010 to 171.66.16.249. Redistribution subject to ASME license or copyright; see http://www.asme.org/terms/Terms_Use.cfm

$$\left.\begin{aligned}(1+M_0)\frac{d^2x_0}{dt^2}+x_0&=0\\(1+M_0)\frac{d^2x_1}{dt^2}+x_1&=M_1\frac{d^3x_0}{dt^3}\end{aligned}\right\} \tag{12}$$

In the system of equations, equation (12) is formally equivalent to equation (9); that is, a weakly damped oscillator. Applying the method of multiple scales as before yields

$$x \sim e^{-M_1\omega_r{}^4kat/2}\,(A\sin\Omega t + B\cos\Omega t) \tag{13}$$

where

$$\Omega = \omega_r\left\{1-\frac{(\omega_r{}^2ka)^2}{8}[2M_2-5M_1{}^2\omega_r{}^2]\right\}$$

and

$$\omega_r = 1/(1+M_0)^{1/2}$$

is the reduced frequency which accounts for the inertia of the fluid. This has the same form as equation (10); only the decay constant and frequency are different. Evaluating the constants using equation (7) then gives

$$x = \frac{Ie^{-M_1\omega_r{}^4kat/2}}{\omega_r}\sin\Omega t + O[(ka)^2]$$

Differentiating this twice however gives

$$\frac{d^2x}{dt^2}\sim -M_1\,\omega_r{}^3\,ka\,I \qquad t=0^+,$$

which is contradicted by equation (8). The meaning of this contradiction is that the assumption that x derivatives are all order one is invalid near $t=0$. We can interpret equation (13) as an outer solution invalid when $t \ll 1$ and hence we cannot evaluate A and B using equation (7) [10]. Instead, we must deduce the form of the solution valid in the boundary layer and match the two solutions in their common regions of validity [11]. For this purpose we need to write equation (13) in the form it takes in this region. Now the boundary-layer scale is

$$T = t/ka \tag{14}$$

since derivatives with respect to T will remain finite in ka. Using equation (14) in equation (13), taking the limit as $ka \to 0$, and retaining the leading two terms gives on rewriting the result in terms of t

$$x = A\,\omega_r t + B + O[(ka)^2]. \tag{15}$$

We obtain an equation valid in the boundary layer by applying the transformation, equation (14), to equation (6). The appropriate dependent variable scaling is

$$q = x/ka \tag{16}$$

because that leaves the forcing term finite. Thus equation (6) becomes, in the new variables

$$\frac{d^2q}{dt^2}+\kappa\int_0^T\chi(T')\frac{d^2q}{d(T-T'^2)}\,dT' + (ka)^2\,q = I\delta(T). \tag{17}$$

Equations (7) are also transformed to

$$q=0, \quad dq/dT = I \quad \text{for} \quad t=0^+ \tag{18}$$

while equation (8) becomes

$$d^2q/dT^2 = -\kappa I \quad \text{for} \quad t=0^+. \tag{19}$$

Assuming an asymptotic expansion of the form

$$q(T,ka) = \sum_{i=0}^{\infty}(ka)^i q_i(T),$$

the dominant order equation is

$$\frac{d^2q_0}{dT^2}+\kappa\int_0^T\chi(T')\frac{d^2q_0}{d(T-T'^2)}\,dT' = I\delta(T).$$

Taking the Laplace transform of this gives

$$Q_0(s) = \frac{I}{s^2[1+\kappa\equiv(s)]}$$

where $Q_0(s)$ is the transform of $q_0(t)$ and $\equiv(s)$ is the transform of $\chi(t)$.

From a Tauberian theorem [12]

$$\lim_{T\to 0}\chi(T) = \lim_{s\to\infty} s\equiv(s)$$

and the early time property, equation (2), requires

$$\equiv(s)\to 1/s \quad \text{for} \quad s\to\infty.$$

Then

$$Q_0(s)\to 1/s^2 \quad \text{for} \quad s\to\infty$$

and the inversion integral can be evaluated by means of the residue calculus. Now the residue at the double pole at $s=0$ gives

$$\frac{I\left\{T-\kappa\left.\frac{d\equiv(s)}{ds}\right|_{s=0}\Big/[1+\kappa\equiv(0)]\right\}}{1+\kappa\equiv(0)}$$

Since $\equiv(0) = M_0/\kappa$ and $\left.\frac{d\equiv(s)}{ds}\right|_{s=0} = M_1/\kappa$ we find that

$$q(t)\sim I\,\omega_r{}^2\,(\omega_r{}^2\,M_1+T)+f(T) \tag{20}$$

where

$$f(T) = \sum_j[\text{Res}\,\{e^{s_jT}Q_0(s_j);s_j\}] + \sum_i\int_{c_i}e^{sT}\,Q_0(s)\,ds$$

is the contribution to $q(T)$ from the zeros of

$$1+\kappa\equiv(s)=0$$

at $s=s_j$ as well as any branch points of $\equiv(s)$ at $s=s_i$.

Substituting equation (14) into equation (20) and using equation (16), we obtain the two term outer representation of the one term inner expansion

$$X\sim I\omega_r{}^2t + (ka)\,IM_1\,\omega_r{}^4 \tag{21}$$

Matching this with equation (15) gives

$$A = I\omega_r \quad B = (ka)\,IM_1\omega_r{}^4.$$

Forming a uniformly valid composite expansion as a sum of the inner and outer expansions less the common part [11], equation (21), then yields

$$x = e^{-M_1\omega_r{}^4kat/2}\,I\omega_r\sin\Omega t + (ka)\left\{f\left(\frac{t}{ka}\right)+e^{-M_1\omega_r{}^4kat/2}\,IM_1\,\omega_r{}^4\cos\Omega t\right\}+O[(ka)^2]. \tag{22}$$

Equation (22) satisfies the acceleration jump condition (8) as well as the initial conditions, equation (7). To dominant the order the displacement is given by the first term in equation (22). In particular the maximum displacement is approximately

$$x_{\max}\sim I\omega_r.$$

The velocity and acceleration histories, however, depend to dominant order on the function $f(t/ka)$ or equivalently, on the impulse response function.

Comparison With an Exact Result—Breathing Sphere

It is instructive to compare the high and low frequency approximate solutions for arbitrarily shaped bodies with the corresponding exact results for a simple shape; that is, one for which the impulse response function can be computed in a closed form. A typical example of a

Downloaded 01 May 2010 to 171.66.16.249. Redistribution subject to ASME license or copyright; see http://www.asme.org/terms/Terms_Use.cfm

simple shape is a sphere. There are many possible modes of motion of a sphere; however since only single-degrees-of-freedom oscillators are considered here, it is necessary to select a particular mode.

The simplest mode for a sphere is the "breathing" mode of pure radial oscillation for which [1]

$$L(t) = 4\rho\pi ca^2 e^{-ct/a}. \tag{23}$$

From equation (23) and equation (2)

$$m_p = 4\pi\rho a^3$$

where ρ is the fluid density. We also note that

$$\chi(T) = e^{-T} \tag{24}$$

and

$$M_j = m_j/m = j!\kappa.$$

In particular, the added mass, m_0, is equal to the piston mass, m_p.

Transforming equation (24)

$$\equiv(s) = 1/(1+s) \tag{25}$$

so that $1 + \kappa \equiv (s) = 0$ has one root for which

$$s = -(1+\kappa) = -1/\omega_r{}^2;$$

consequently

$$f(T) = -I\kappa\omega_r{}^4 e^{-T/\omega_r{}^2}.$$

Collecting results we have, from equation (11),

$$x = Ie^{-\kappa t/2ka}\sin\omega t + O[(ka)^{-2}] \tag{26}$$

$$\omega = 1 - [\kappa(4+\kappa)]/8(ka)^2$$

for the high frequency oscillator and, from equation (22),

$$x = e^{-\kappa\omega_r 4kat/2} I\omega_r \sin\Omega t + (ka)\, I\kappa\omega_r{}^4\{e^{-\kappa\omega_r 4kat/2}\cos\Omega t - e^{-t/ka\omega_r{}^2}\} + O[(ka)^2] \tag{27}$$

with

$$\Omega = \omega_r\left\{1 - (ka)^2\frac{\kappa\omega_r{}^6}{8}(\kappa - 4)\right\}$$

for the low frequency oscillator.

The exact solution can be obtained by Laplace transforming equation (17). Doing this, using equation (25), and rearranging gives

$$Q(s) = \frac{I(1+s)}{s^3 + s^2/\omega_r{}^2 + (ka)^2 s + (ka)^2}. \tag{28}$$

The solution for $x(t)$ is easily found in terms of the roots of the cubic polynomial in the denominator of equation (28). In the cases that we are interested in, these can be found asymptotically using Newton diagrams [13]. The results are, first for the high frequency oscillator, lim $ka \to \infty$,

$$s_1 \sim -1 - \frac{\kappa}{(ka)^2}$$

$$s_2 \sim -i(ka) - \frac{\kappa}{2} + \frac{i}{(ka)}\frac{\kappa}{8}(4+\kappa)$$

$$s_3 = s_2{}^*.$$

On evaluating the residues at these singularities we obtain

$$x(t) = Ie^{-\kappa t/2ka}\sin\omega t + O[(ka)^{-2}]$$

$$\omega = 1 - [\kappa(4+\kappa)]/8(ka)^2$$

in agreement with equation (26) to this order. In the antithetical limit $ka \to 0$, the roots are

$$s_1 \sim -\frac{1}{\omega_r{}^2}$$

$$s_2 \sim i(ka)\omega_r - \frac{\kappa\omega_r{}^4}{2}(ka)^2 - \frac{i}{8}\kappa\omega_r{}^7(\kappa - 4)(ka)^3$$

$$s_3 = s_2{}^*$$

and evaluating residues again gives complete agreement, this time with equation (27).

Summary

In this paper we have calculated the response of a single-degree-of-freedom oscillator of arbitrary shape submerged in an infinite acoustic fluid and impulsively exicted from rest. By nondimensionalizing the oscillator equations of motion, we found that the parameter ka determines the character of the oscillator response.

For high frequency oscillators, $ka \gg 1$, the solution decays weakly on the oscillator frequency scale. The decay constant can be calculated using the plane wave approximation for the interaction.

For low frequency oscillators, $ka \ll 1$, there is an acceleration boundary layer in time whose duration is of order a/c. In this boundary layer, the details of the fluid-structure interaction must be known in order to calculate the oscillator response. The boundary-layer solution evolves into an outer solution which characterizes the oscillator period. Because the boundary-layer displacement is small, of the order of ka, the important displacement history is given by the solution in this region, which is also a weakly decaying oscillation. The oscillation frequency can be calculated to dominant order using the added mass approximation for the interaction; however in order to obtain the correct displacement one must properly account for the boundary-layer behavior. The decay constant depends dominantly on the first moment of the impulse response function. This quantity can be calculated from the Helmholtz equation as a perturbation of the incompressible flow field which gives rise to the added mass.

When mode coupling is taken into account, it may still be possible to consider groups of modes which can all be regarded as either high or low frequency. In this event, given that the mode coupling is weak in these cases [6], it would appear that the present analysis could be extended. We are presently working toward this goal.

References

1 Mnev, Y. N., and Pertsev, A. K., *Hydroelasticity of Shells*, Leningrad, USSR, trans. Foreigh Tech. Div., Wright-Patterson AFB, AD 731646, 1970.

2 Geers, T. L., ASME JOURNAL OF APPLIED MECHANICS, Vol. 36, 1969, pp. 459–469.

3 Mindlin, R. D., and Bleich, H. H., ASME JOURNAL OF APPLIED MECHANICS, Vol. 20, 1953, pp. 189–195.

4 Haywood, J. H., *Quarterly Journal of Mechanics and Applied Mathematics*, Vol. 11, 1958, pp. 129–141.

5 Geers, T. L., *JASA*, Vol. 49, 1971, pp. 1505–1510.

6 Geers, T. L., *JASA*, Vol. 64, 1978, pp. 1500–1508.

7 Clark, A. V., *Approximate Methods in Fluid-Structure Interaction Problems*, PhD Thesis, University of Pennsylvania, 1977.

8 Whitman, A. M., ASME JOURNAL OF APPLIED MECHANICS, Vol. 39, 1972, pp. 1047–1049.

9 Cole, J. D., *Perturbation Methods in Applied Mathematics*, Blaisdell, 1968.

10 Burke, W. L., *Physical Review*, Series A, Vol. 2, 1970, pp. 1501–1505.

11 VanDyke, M., *Perturbation Methods in Fluid Mechanics*, Academic, 1964.

12 VanderPol, B., and Bremmer, H., *Operational Calculus*, Cambridge University, 1950.

13 Kruskal, M. D., "Asymptotology," in *Mathematical Models in Physical Sciences*, ed., Drobot, S., Prentice-Hall, Englewood Cliffs, N.J., 1963.

Downloaded 01 May 2010 to 171.66.16.249. Redistribution subject to ASME license or copyright; see http://www.asme.org/terms/Terms_Use.cfm

F. L. DiMaggio
Professor,
Department of Civil Engineering
and Engineering Mechanics,
Columbia University,
New York, N. Y. 10027

I. S. Sandler
Partner.
Mem. ASME

D. Rubin
Senior Research Engineer.
Mem. ASME

Weidlinger Associates,
110 E. 59th Street,
New York, N. Y. 10022

Uncoupling Approximations in Fluid-Structure Interaction Problems With Cavitation

1 Introduction

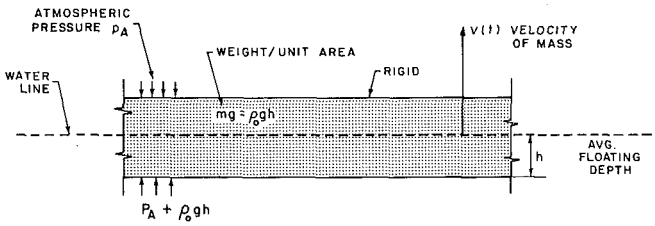
If a structure has complex internal components, the capacity of presently available computers rarely allows the use of the complete fluid equations when dynamic interaction of the structure with fluid is investigated. In most cases, it is necessary to uncouple the equations of motion of the fluid from those of the structure by assuming approximate differential (or integro-differential) relations between fluid pressure and velocity on the wet surface of the structure.

For submerged structures, cavitation often does not occur or is negligible. Many uncoupling schemes have been developed and applied for such cases [1]. When, however, a surface ship is exposed to typical underwater shock loadings, it may no longer be possible to neglect cavitation.

In this report, procedures are developed for modifying presently used uncoupling schemes to include cavitation. These permit structural response to be calculated if the free-field velocities and pressures are known. A one-dimensional problem is considered in detail and linear and nonlinear interaction approximations are developed. The results are compared with exact solutions. An extension of the methods to two-dimensional problems is currently being used for the practical numerical solution of large scale fluid-structure problems. This work will be the subject of a forthcoming paper.

2 Formulation of the One-Dimensional Problem

To study the proposed methods, consider the one-dimensional problem illustrated in Fig. 1. A model of a surface ship, consisting of a rigid mass m per unit area with an average floating depth h is subjected to an exponential pressure wave with incident gauge pressure p_0, decay time τ and cutoff time T.[1] It is desired to obtain the velocity response of the mass, $v(t)$, as a function of time t.



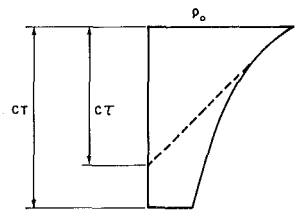


Fig. 1 1-D model

3 Free-Field Pressures and Velocities

The constitutive relation for the fluid is assumed to be the bilinear one illustrated in Fig. 2, which does not permit tension in the fluid.

Contributed by the Applied Mechanics Division for publication in the JOURNAL OF APPLIED MECHANICS.
Discussion on this paper should be addressed to the Editorial Department, ASME, United Engineering Center, 345 East 47th Street, New York, N. Y. 10017, and will be accepted until two months after final publication of the paper itself in the JOURNAL OF APPLIED MECHANICS. Manuscript received by ASME Applied Mechanics Division, November, 1980; final revision, April, 1981.

[1] The cutoff time T is intended to exercise the interactive model under the sudden reduction in pressure associated with surface reflection of the incident wave. Of course, in a 1-D problem, the surface reflection cannot be represented as such; it is included in the incident wave.

Copyright © 1981 by ASME
Downloaded 01 May 2010 to 171.66.16.249. Redistribution subject to ASME license or copyright; see http://www.asme.org/terms/Terms_Use.cfm

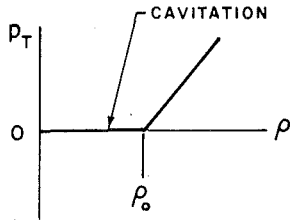
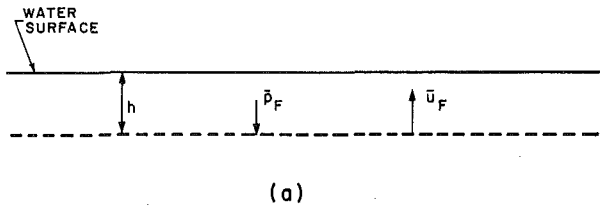
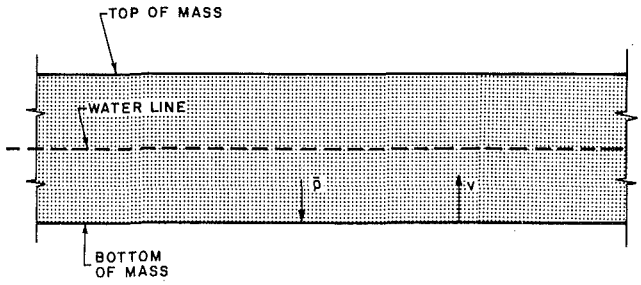


Fig. 2 Bilinear pressure-density relation





$$\bar{p} - \bar{p}_F = F\{\bar{u}_F - v\}$$

Fig. 3 Interactive approximation

Cavitation occurs when the total pressure p_T first reaches zero at a density $\rho = \rho_0$. Small deformations are assumed so that

$$|\rho - \rho_0| \ll \rho_0 \tag{1}$$

In the absence of the mass in Fig. 1, free-field pressure p_F[2] and particle velocities u_F would result in the half space. Using the cavitation model of Fig. 2 these free-field values may readily be obtained using the interactive solution of Bleich and Sandler [2]. It is only necessary to set $m = 0$ in the programs they developed.

4 Exact Response of Mass

The exact velocity of the mass, and total pressure exerted on its bottom surface, may be obtained by slight modifications of the program of Bleich and Sandler [2], to permit nonzero depth h and finite cutoff time T. These exact solutions will be used to evaluate the validity of the approximations described in the sequel.

5 Interactive Approximations

Consider the free-field pressures and particle velocities of Section 3. Let $\bar{p}_F$ and $\bar{u}_F$ denote values[3] at a depth h. If the rigid mass is replaced by a body of water of depth h, as shown in Fig. 3(a), these values may be taken as a first approximation to the pressure acting on the mass and its velocity response to that pressure. The actual values, denoted by $\bar{p}$ and v, occur when the mass is actually present as shown in Fig. 3(b). The quantities $\bar{p}_F$, $\bar{p}$, $\bar{u}_F$, and v are related by

$$\bar{p} - \bar{p}_F = F\{\bar{u}_F - v\} \tag{2}$$

in which F is an appropriately chosen functional. Equation (2) is a special case of a general interactive approach currently being developed [3], to uncouple the motion of a structure from that of the nonlinear medium with which it is in contact. In this paper, the approximation of F is studied.

(A) Linear Interactive Approximation. The simplest functional F is that corresponding to the linear (acoustic) approximation

$$\bar{p} - \bar{p}_F = \rho_0 c(\bar{u}_F - v) \tag{3}$$

In the absence of cavitation, equation (3) would be exact, with the increments on the left and right-hand side of (3) referred to as radiated pressure and velocity, respectively. From (3), the resultant pressure acting on the mass is

$$\bar{p} = \bar{p}_F + \rho_0 c\bar{u}_F - \rho_0 cv \tag{4}$$

so that the equation of motion of the mass

$$m\dot{v} = \bar{p} \tag{5}$$

becomes

$$m\dot{v} + \rho_0 cv = \bar{p}_F + \rho_0 c\bar{u}_F \tag{6}$$

It is readily seen that the fluid reaction to the motion of the mass in the linear approximation (3) is equivalent to that of a linear viscous dashpot with damping coefficient $\rho_0 c$ attached to the mass, and having base velocity $\bar{u}_F$.

After free-field values on the right-hand side of (6) are obtained as described in Section 3, equation (6) may be integrated to give $v(t)$, which can then be compared to the exact response described in Section 4.

(B) Nonlinear Interactive Approximation. The linear approximation of equation (3) will be in error when cavitation occurs. It will be most seriously in error when cavitation is present at or near the depth h because then separation takes place and the dashpot in the model of equation (6) should not be acting. In this stage the mass should be almost freely decelerating under the action of only gravity and atmospheric pressure. Equation (6) should be replaced, while cavitation occurs at the bottom of the mass, by

$$\dot{v} = -\frac{p_A + mg}{m} \tag{7}$$

When the mass again makes contact with the water, equation (6) may again be used.

The considerations just outlined suggest that a better choice for the functional F to be used in equation (2) would be defined by the following approach:

Initial Shock. Use equation (6) until such time t_1 as the condition

$$\bar{p}_T(t_1) \equiv \bar{p}(t_1) + p_A + mg = 0 \tag{8}$$

is satisfied, i.e., when the total pressure first drops to zero.

Separation and Fall. Use equation (7) until such time t_2 as the separation distance returns to zero, i.e., until the condition

$$\int_{t_1}^{t_2} (v - \bar{u}_F)dt = 0 \tag{9}$$

is satisfied

Closure. Return to equation (6) for as long as $\bar{p}_T(t) > 0$. If equation (8) is again satisfied, a new separation and fall phase begins.

Again the response $v(t)$ will be compared with the exact results described in Section 4.

[2] Unless otherwise noted, live pressure will be used in this paper, i.e., total pressure less the atmospheric and hydrostatic pressure, $p_A + \rho_0 gh$.

[3] Note that $\bar{p}_F$ and $\bar{u}_F$ include cavitation effects in the free field.

Downloaded 01 May 2010 to 171.66.16.249. Redistribution subject to ASME license or copyright; see http://www.asme.org/terms/Terms_Use.cfm

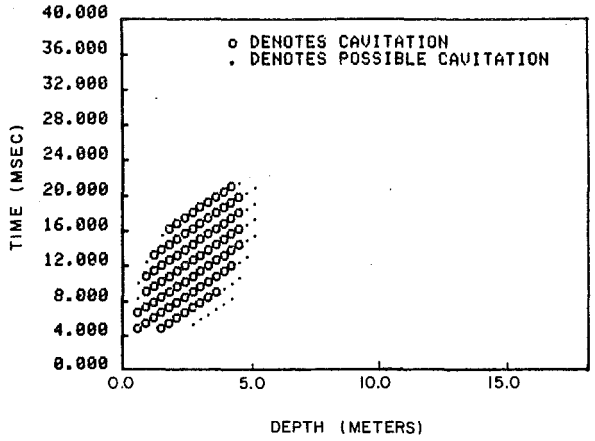


Fig. 4 Extent of cavitation region-free field, Example 1

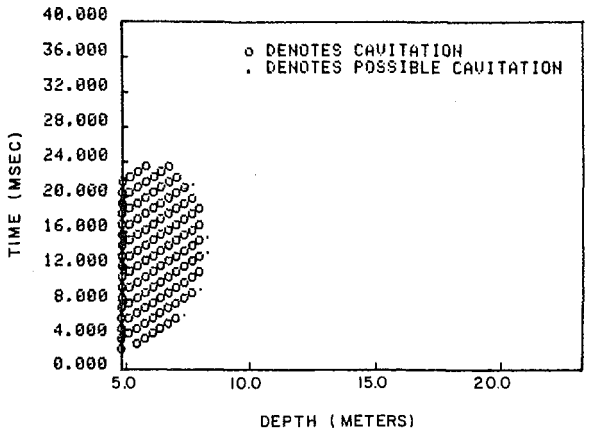


Fig. 5 Extent of cavitation region-mass present, Example 1

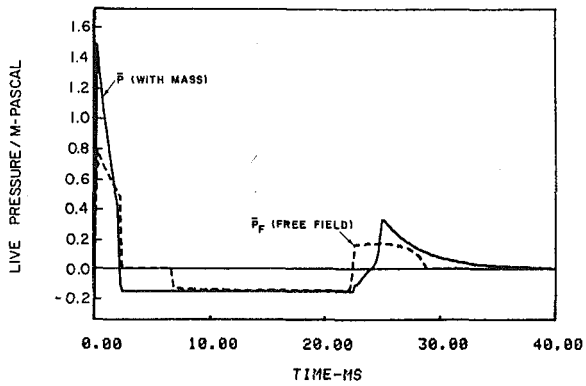


Fig. 6 Pressure at mass bottom, Example 1

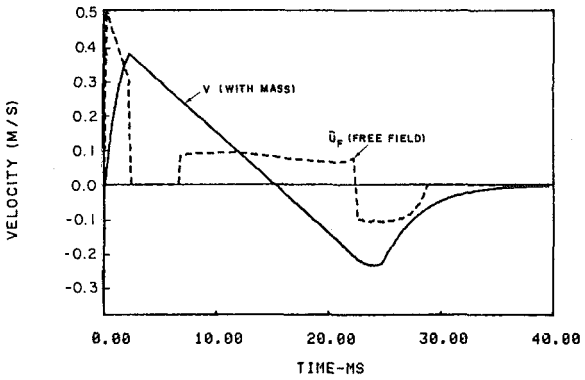


Fig. 7 Fluid velocity at mass bottom, Example 1

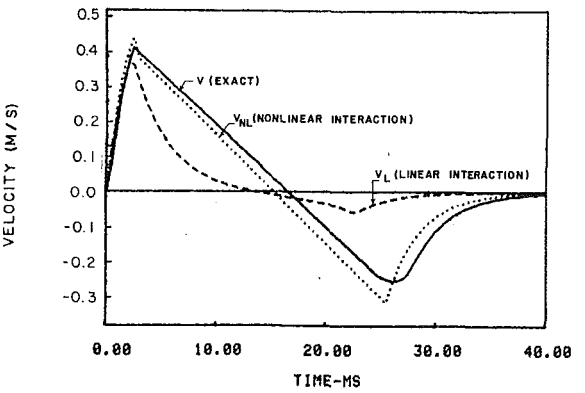


Fig. 8 Velocity of mass, Example 1

6 Numerical Examples

1 A comparison between the two approximate interactive approximations and the exact solution was first made for the following material and geometric parameters:

mg = 0.048 MPa (7 psi)
g = 9.81 m/s^2 (32.2 ft/sec^2)
c = 1524 m/s (5000 ft/sec)
p_0 = 0.786 MPa (114 psi)
τ = 4 ms
T = 2.2 ms
ρ_0 = 1000 kg/m^3 (1.94 slugs/ft^3)
p_A = 0.101 MPa (14.7 psi)

The solutions for the response in all cases were obtained by a numerical forward integration scheme.

As discussed in Sections 3 and 4, the exact free-field pressures and particle velocities, and the exact velocity response of the mass were obtained using the foregoing parameters. In Figs. 4 and 5, the cavitation fields with and without the mass present, respectively, are shown. It is seen that both the extent and duration of the cavitation are affected significantly by the presence of the mass.

In Fig. 6, the histories of live pressure at the depth h with and without the mass, denoted by $\overline{p}$ and $\overline{p}_F$, respectively, are exhibited. Note that the three phases discussed in Section 5(B) are clearly delineated for the solid curve $\overline{p}$. The initial shock, with pressure doubling, is followed by a long cavitation period in which the total pressure $\overline{p}_T = 0$, and then by the closure shock.

Fig. 7 shows the free-field particle velocity at depth h, $\overline{u}_F$, and the velocity of the mass, v, as functions of time. Again the three stages are clearly evident when the mass is present. The constant slope of the plot of v during the cavitation phase is essentially that of free deceleration given by equation (7).

Using the free-field histories at depth h, $\overline{p}_F$, and $\overline{u}_F$, the velocity of the mass was obtained with (a) the linear interaction approximation of equation (6) (and denoted by v_L) and (b) the nonlinear interaction described in Section 5(B) (and denoted by v_{NL}). These were then compared with the exact response v, previously plotted in Fig. 7. This comparison is illustrated in Fig. 8. It is seen that the linear approximation is excellent initially but becomes increasingly poorer as the long cavitation phase continues. During this phase, c should be set equal to zero in equation (6), i.e., equation (7) of the nonlinear approximation should be used. It is seen that the nonlinear interaction

Downloaded 01 May 2010 to 171.66.16.249. Redistribution subject to ASME license or copyright; see http://www.asme.org/terms/Terms_Use.cfm

approximation predicts response which is in excellent agreement with exact results through all three phases of loading

It should be pointed out that the error in the nonlinear approximation has two sources. The numerical error in the integration process due to finite time steps is primarily responsible for a parallel offset. The error in slope, however, is due to the fact that during the fall phase, the approximation does not allow for the addition to the falling mass of fluid particles from the cavitated region. The slope in the approximate solution is therefore too steep.

2 Example 1 put the proposed uncoupling schemes to a severe test. Because the mass of the ship model was so large, the cavitation phase on the wet surface was very long. For lighter masses, both approximations give better results. In the example used in [2], e.g., the mass used corresponded to

$$mg = 0.0013 \text{ MPa } (0.2 \text{ psi})$$

Using this mass (which is $\frac{1}{35}$ that of Example 1) but leaving unchanged all the other parameters of Example 1, no significant cavitation occurs on the surface of the mass and the free-field velocities, those obtained using either approximation, and the exact solution are virtually indistinguishable from one another.

8 Conclusions

A linear and a nonlinear interactive scheme have been developed to uncouple the equations of motion of a structure from those of a cavitating fluid in which it is immersed, and through which a shock wave propagates and impinges on the structure. The method has been tested numerically on one-dimensional problems for which the exact solution is obtainable. In these cases, the nonlinear interactive approximation gives especially good results, even when the cavitation phase on the wet surface of the structure is of a long duration. This method is currently being used for multidimensional applications which will be the subject of a forthcoming paper.

References

1 Ranlet, D., et al., "Elastic Response of Submerged Shells With Internally Attached Structures to Shock Loading," *Computers and Structures*, Vol. 7, 1977, pp. 355–364.

2 Bleich, H. H , and Sandler, I. S., "Interaction Between Structures and Bilinear Fluids," *International Journal of Solids and Structures*, Vol. 6, 1970, pp. 617–638.

3 Defense Nuclear Agency Contract No. DNA001-79-C-0256, "Dynamic Structure-Medium Interaction (SMI) Calculations," Weidlinger Associates, 1979–1980.

Downloaded 01 May 2010 to 171.66.16.249. Redistribution subject to ASME license or copyright; see http://www.asme.org/terms/Terms_Use.cfm

R. H. Nilson

Department of Fluid and Thermal Sciences,
Sandia National Laboratories
Division 5512,
Albuquerque, New Mex. 87185
Assoc. Mem. ASME

Gas-Driven Fracture Propagation[1]

A one-dimensional gas-flow drives a wedge-shaped fracture into a linearly elastic, impermeable half space which is in uniform compression, σ_∞, at infinity. Under a constant driving pressure, p_0, the fracture/flow system accelerates through a sequence of three self-similar asymptotic regimes (laminar, turbulent, inviscid) in which the fracture grows like an elementary function of time (exponential, near-unity power, and linear, respectively). In each regime, the transport equations are reducible under a separation-of-variables transformation. The integro-differential equations which describe the viscous flows are solved by iterative shooting methods, using expansion techniques to accomodate a zero-pressure singularity at the leading edge of the flow. These numerical results are complemented by an asymptotic analysis for large pressure ratio ($N = p_0/\sigma_\infty \to \infty$) which exploits the disparity between the fracture length and penetration length of the flow. Since the seepage losses to a surrounding porous medium are shown to be negligable in the late-time long-fracture limit, the results have application to geologic problems such as: containment evaluation of underground nuclear tests, stimulation of oil and gas wells, and permeability enhancement prior to in situ combustion processes.

1 Introduction

In a fluid-driven fracture process, it is the internal fluid pressure which wedges open the fracture and, hence, controls the rate of propagation. The fluid velocity and the induced fracture-tip velocity are generally small compared to the velocity of stress waves; so, the displacement field adjusts almost instantaneously to the changing fluid-pressure distribution. This quasi-steady strain field is representative of both the classical pump-driven hydrofracture and of the late time response of explosion-driven systems. Despite this similarity in the solid mechanics of these two cases, there is very little similarity in the fluid mechanics:

1 Liquid-driven hydrofracture of petroleum reservoirs is a well-developed practice [1]. Here the fracture-velocity is controlled by a predetermined pumping schedule, and the injected fluid is incompressible. The flow field and the elastic field are both quasi-steady. The driving pressure is only slightly greater than the confining tectonic stress, and the fluid pressure is nearly uniform along the fracture.

2 Gas-driven fracture propagation arises in a number of current or proposed applications: containment of underground nuclear tests; explosive stimulation of oil, gas, and geothermal wells; permeability enhancement of oil shale or coal prior to *in situ* combustion. Here the fracture velocity is controlled by the dynamic interaction of a compressible fluid with the elastic solid. Only the elastic field is quasi-steady. The driving pressure, p_0, may greatly exceed the resisting compressive stress, σ_∞, and the fluid pressure varies considerably along the fracture.

The latter problem is addressed in the present paper and in two previous studies [2,3].

In those previous analyses of gas-driven fracture, the conservation equations are integrated in space and time using general numerical methods which are applicable to complex geometries, to porous media, and even to multiphase flows. Although very general and informative in this regard, the previous studies suppress the fluid/solid coupling by neglecting temporal wall divergence in the flow analysis and also by imposing an arbitrary pressure at [3] or near [2] the tip, rather than enforcing continuity and a local specification of the stress state. These coupling considerations may be of little consequence when the pressure ratio $N = p_0/\sigma_\infty$ is near unity, but with increasing N, they become very important.

The present study addresses the elementary problem of a wedge-shaped, gas-driven fracture in a linearly elastic, impermeable medium. Under constant driving pressure, the flow accelerates through a sequence of self-similar, asymptotic regimes (laminar, turbulent, and inviscid) in which the conservative equations are separable, time from position. The resulting ordinary differential equations are solved, for the laminar and turbulent regimes, using standard shooting methods. The analysis reveals a number of interesting mathematical and physical features which are summarized at the end of the paper. The results are useful in estimating fracture growth rates under subsonic gas-drive. A more detailed description of the analysis and the results is available in [4] where it is also shown that the seepage interaction which occurs in a permeable medium is an early-time perturbation on the impermeable solutions which are given here.

This work was supported by the U.S. Department of Energy under Contract DE-AC04-76DP00789.

Contributed by the Applied Mechanics Division for publication in the JOURNAL OF APPLIED MECHANICS.

Discussion on this paper should be addressed to the Editorial Department, ASME, United Engineering Center, 345 East 47th Street, New York, N.Y. 10017, and will be accepted until two months after final publication of the paper itself in the JOURNAL OF APPLIED MECHANICS. Manuscript received by ASME Applied Mechanics Division, March, 1980; final revision, October, 1980.

Copyright © 1981 by ASME

Downloaded 01 May 2010 to 171.66.16.249. Redistribution subject to ASME license or copyright; see http://www.asme.org/terms/Terms_Use.cfm

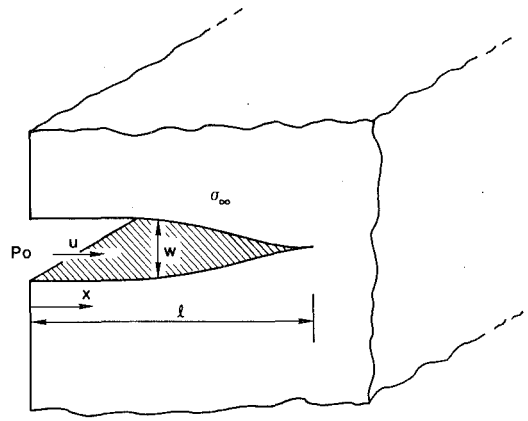


Fig. 1 Schematic of wedge-shaped fracture driven by internal gas pressure

2 Formulation

In the planar geometry of Fig. 1, a constant pressure p_0 drives a wedge-shaped fracture to a penetration depth $l(t)$. The internal gas pressure $p(x,t)$ spreads the walls of the fracture, producing a flow channel with aperture width $w(x,t)$. The considered geometry describes the vertical-plane fractures which occur in the geologic applications where the least principal stress is horizontal, and it places an upper bound on fracture growth because it neglects the fracture-closing effect of a finite fracture height and it eliminates the flow divergence which occurs in axisymmetric penny-shaped configurations.

Since the velocity of stress waves greatly exceeds the fracture velocity in a subsonic gas-drive, the displacement field adjusts almost instantaneously to the changing pressure loading. A quasi-steady stress analysis is therefore appropriate. Suppose that the tectonic stress σ_∞ (normal to the fracture plane) is uniform in the far field, that $x = 0$ is a line of symmetry, and that viscous traction is negligible. Then the aperture distribution is functionally related to the pressure distribution by the theory of linear elasticity [5–7].

$$w(\theta,t) = \frac{4(1-\nu)l}{\pi G}\int_\theta^1 \int_0^\sigma \frac{[p(\zeta)-\sigma_\infty]d\zeta}{\sqrt{\sigma^2-\zeta^2}}\frac{\sigma d\sigma}{\sqrt{\sigma^2-\theta^2}} \tag{1}$$

G and ν are the shear modulus and Poisson's ratio, respectively, and $\theta = x/l(t)$ is the normalized position variable. Note that $w(\theta,t)$ depends on t directly through $l(t)$, but that the fracture shape $w(\theta,t)/l(t)$ is preserved during fracture growth whenever $p(\theta)$ remains stationary.

The mechanics of the tip region are addressed by Barenblatt's theory of equilibrium fracture [8] which has been broadly applied [5,7,8] to geologic hydrofracture. The theory postulates that the stress must be finite at the tip of a fracture which is in mobile equilibrium. Accordingly, the pressure must satisfy an integral constraint [7,8]

$$\int_0^1 \frac{[p(\theta)-\sigma_\infty]}{\sqrt{1-\theta^2}}\,d\theta = \frac{K}{\sqrt{2l}} \simeq 0 \tag{2}$$

in which the fracture toughness or stress intensity is usually neglected (i.e., $K/\sqrt{2l} \to 0$), because the fracture-closing effect of the *in situ* compressive stress is generally much greater than the local action of molecular cohesion.

Transient compressible flow in the fracture is governed by conservation of mass and momentum, here written in the one-dimensional form [9]

$$\frac{\partial}{\partial t}(\rho w) + \frac{\partial}{\partial x}(\rho w u) = 0$$

$$\frac{\partial}{\partial t}(\rho w u) + \frac{\partial}{\partial x}(\rho w u^2) = -\rho w\left(\frac{1}{\rho}\frac{\partial P}{\partial x} + \lambda\right) \tag{3}$$

in which ρ and u are density and velocity, each averaged across the channel. The viscous shear stress λ is approximated as follows for the limiting cases of low and high Reynolds number ($\mathrm{Re}_0 = u_0 w_0 \rho_0/\mu_0$), respectively

$$\lambda \equiv \frac{2\tau_w}{w} = \frac{1}{\rho}\frac{12\mu u}{w^2} \quad \text{(laminar)}$$

$$= a\left(\frac{\epsilon}{w}\right)^b \frac{u^2}{w} \quad \text{(turbulent)}. \tag{4}$$

The former is the standard Poiseuille expression for a laminar channel flow; the latter is based on an experimental study ($a \simeq 0.1$, $b \simeq 0.5$) [10] of turbulent flow in simulated geologic fractures having roughness heights ϵ. Regarding thermodynamics, it is here assumed that the gas is both ideal and isothermal

$$\rho = \frac{p}{RT_0}, \quad \frac{dp}{d\rho} = RT_0 = \frac{c_0^2}{\gamma}, \tag{5}$$

which depicts a convenient and representative limiting case, and often places an upper bound [2] on fracture growth.

3 Analysis

The transformation to ordinary differential equations is accomplished by a separation-of-variables approach which distinguishes between global dependence on the growth rate $l(t)$ and local dependence upon the normalized position variable θ. Denoting the fracture-growth function as

$$l(t) = l_0 g(\tau), \tag{6}$$

the appropriate independent variables are

$$\theta = \frac{x}{l_0 g(\tau)}, \quad \tau = \frac{t}{t_0}. \tag{7}$$

The dependent variables w, u, p, and ρ are now presumed separable in a manner which is compatible with the constant boundary conditions on P and ρ, and is compatible with the observation that $w(\theta,t)$ increases linearly with $l(t)$, and is minimally restrictive on $u(x,t)$.

$$\begin{aligned} w(x,t) &= w_0 g(\tau) W(\theta) \quad & p(x,t) &= p_0 P(\theta) \\ u(x,t) &= u_0 f(\tau) U(\theta) \quad & \rho(x,t) &= \rho_0 \mathrm{P}(\theta) \end{aligned} \tag{8}$$

in which l_0, u_0, t_0, p_0, and ρ_0 are characteristic constants; f and g are functions of τ alone; P, P, W, and U depend upon both x and τ, but only through $\theta(x,\tau)$. Letting

$$t_0 = \frac{l_0}{u_0}, \quad w_0 = l_0\left[\frac{4(1-\nu)}{\pi}\frac{p_0}{G}\right]\frac{\pi}{2N} \ln\left(\frac{2\sqrt{e}N}{\pi}\right), \tag{9}$$

and noting that $\mathrm{P}(\theta) = P(\theta)$ in isothermal flow, and that

Nomenclature

$N = p_0/\sigma_\infty$ = pressure ratio
$\mathrm{Re} = uw\rho/\mu$ = Reynolds number
G, ν = shear modulus, Poisson's ratio
σ_∞ = tectonic stress
a, b, ϵ = constants in turbulence model as defined below equation (4)
c_0, γ, μ = sound speed, specific heat ratio, viscosity
t = time; $t_0 = l_0/u_0$; $\tau = t/t_0$
x = position along fracture
$\theta = x/l(t)$ = normalized position
$\eta = \theta\sqrt{\alpha}$; $\hat{\eta} = \theta\alpha^{2/3}$
$l = l_0 g(\tau)$ = fracture length
l_0 = reference length (usually initial l)
p_0 = driving pressure
u_0 = reference velocity in equation (15)
w_0 = reference aperture in equation (9)
p, P = pressure, p/p_0
u, U = velocity, $u/u_0 f(\tau)$
w, W = aperture, $w/w_0 g(\tau)$
ρ, P = density, ρ/ρ_0
f, g = functions of τ given in (16) and (17)

Downloaded 01 May 2010 to 171.66.16.249. Redistribution subject to ASME license or copyright; see http://www.asme.org/terms/Terms_Use.cfm

$$\frac{\partial}{\partial x} = \frac{1}{l_0 g(\tau)} \frac{\partial}{\partial \theta}, \quad \frac{\partial}{\partial t} = \frac{1}{t_0}\left(\frac{\partial}{\partial \tau} - \theta \frac{1}{g}\frac{\partial g}{\partial \tau}\frac{\partial}{\partial \theta}\right) \tag{10}$$

the problem statement (3),(4),(1) becomes as follows:

$$\theta W P' - \frac{f}{g'}(WPU)' = P(W - \theta W') \tag{11}$$

$$\gamma\left(\frac{u_0}{c_0}\right)^2 \left\{f'gU - \theta f g' U' + f^2 UU'\right\} + \frac{1}{P}P'$$

$$= -\frac{u_0}{u_l}\frac{f}{g}\frac{U}{PW^2} \quad \text{(laminar)}$$

$$= -\frac{u_0}{u_t}\frac{f^2}{g^b}\frac{U^2}{W^{(1+b)}} \quad \text{(turbulent)} \tag{12}$$

$$W = \frac{2N}{\pi \ln(2\sqrt{e}\, N/\pi)} \int_\theta^1 \int_0^\sigma \frac{[P(\zeta) - N^{-1}]d\zeta}{\sqrt{\sigma^2 - \zeta^2}} \frac{\sigma d\sigma}{\sqrt{\sigma^2 - \theta^2}}. \tag{13}$$

subject to the boundary and integral conditions (the latter from (2))

$$P(0) = 1, \quad \int_0^1 \frac{P(\theta)d\theta}{\sqrt{1-\theta^2}} = \frac{\pi}{2N}. \tag{14}$$

The primes on W, U, and P indicate derivatives with respect to θ, whereas primes on f or g represent derivatives with respect to τ. In these equations there are three different velocity scales: the sound speed c_0, the laminar velocity u_l, and the turbulent velocity u_t, with the latter two defined in the following way:

$$u_l = \left(\frac{w_0}{l_0}\right)^2 \frac{c_0^2 \rho_0 l_0}{12\mu_0 \gamma}, \quad u_t = \left[\left(\frac{w_0}{l_0}\right)\frac{c_0^2}{a\gamma}\left(\frac{w_0}{\epsilon}\right)^b\right]^{1/2} \tag{15}$$

It is hereafter assumed that the characteristic Mach number, $M_0 = u_0/c_0$, is sufficiently small that the inertial terms (in script brackets) remain negligible during the time of interest. Then, the reference velocity u_0 is taken as either u_l or u_t, in the laminar and turbulent cases, respectively, in order that there remains only one parameter, N.

The usual separation argument requires that the time functions satisfy (for small M_0) either

$$g' = \alpha_l f \quad \text{and} \quad g = f \quad \text{(laminar)}$$

or $\tag{16}$

$$g' = \alpha_t f \quad \text{and} \quad g^b = f^2 \quad \text{(turbulent)}.$$

In each, only the one separation constant, α, need be left arbitrary to maintain full generality. So, by integration of (16)

$$g = \exp(\alpha_l \tau_l) \quad \text{(laminar)}$$

or $\tag{17}$

$$g = \left(C + \frac{2-b}{2}\alpha_t \tau_t\right)^{2/(2-b)} \quad \text{(turbulent)}$$

The time variable τ is subscripted here as a reminder that the time scale ($t_0 = l_0/u_0$) is different for the laminar and turbulent periods. Since f and g are increasing with τ, the flow is accelerating from laminar dominance at early times to turbulent dominance at intermediate times, followed by inviscid inertial dominance even later. Thus the constant of integration in g is taken as unity in the laminar case to have $l = l_0$ when $t = 0$, and in the turbulent case the constant C, which drops out at late times, is determined by matching considerations at laminar/turbulent transition.

Temporal wall divergence (i.e., $\partial w/\partial t$) has a first-order influence on the flow field, as illustrated by the following rearrangement of the continuity equation (equation (11) with $f/g' = 1/\alpha$ from (16a) or (16b))

$$PU' + (U - \alpha\theta)P' = -P\left[(U - \alpha\theta)\frac{W'}{W} + \alpha\right], \tag{18}$$

in which $U - \alpha\theta$ is the local velocity of the fluid relative to the moving coordinate system (since $(dx/dt)_\theta/u_0 f = \alpha\theta$). Whenever $U - \alpha\theta > 0$, the flow experiences the axial convergence ($W_\theta < 0$) of the wedge-shaped channel, particularly near the tip where $W'/W \to \infty$. But, there is an offsetting effect ($P\alpha$ term) due to the temporal divergence ($w_\tau > 0$) of the walls at any fixed θ and this is dominant near $\theta = 0$, where $W' \to 0$. The flow, therefore, sees a diverging-converging channel.

Evacuation of the tip region due to wall divergence is favored by the smooth closure, and hence small aperture, within the leading zone. The resulting viscous stresses ($\sim 1/W^n$, $n = 2$, or $1 + b$) prevent the flow from overtaking the tip. An analogous situation occurs in liquid-driven fractures where the fracture-fluid is unable to wet the tip [7,8]. In spite of these expectations of an evacuated tip, the only justifiable *a priori* assertion is that no mass crosses the impermeable walls and hence $\rho(U_{\text{fluid}} - U_{\text{tip}}) \to 0$, or equivalently

$$P(U - \alpha\theta) \to 0 \quad \text{as} \quad \theta \to 1, \tag{19}$$

which implies either a finite fluid velocity $U \to \alpha$ or a full vacuum $P \to 0$ at the leading edge. An important aspect of the present analysis is the identification and resolution of the singularity which must be present if this condition is to be satisfied. To this end, use will be made of the jump-balance conditions [9], derived by integrating (11) and (12) across the jump or from first principles,

$$[P] = 0, \quad [P(U - \alpha\theta)] = 0 \tag{20}$$

which, respectively, insure conservation of momentum (in the degenerate, low M_0 sense) and of mass at a singular surface.

4 Early-Time Laminar Flow Structure

In laminar flow the integro-differential system (11)–(15) can be written as follows by substituting the equality $U = -P'W^2$ from (12a) into (18) and (19).

$$P(P'W^2)' + (P'W^2 + \alpha\theta)P' = -P\left[(P'W^2 + \alpha\theta)\frac{W'}{W} - \alpha\right], \tag{21}$$

$$P(0) = 1, \quad \lim_{\theta \to 1} P(P'W^2 + \alpha\theta) = 0 \tag{22}$$

$$W(\theta;N) = W(P(\theta);N), \quad \int_0^1 \frac{Pd\theta}{\sqrt{1-\theta^2}} = \frac{\pi}{2N}. \tag{23}$$

The ordinary differential equation (ODE) is second order with a like number of boundary conditions. The separation constant α affords the auxilliary degree of freedom necessary to satisfy the integral constraint.

A singularity is present at an interior point θ^* where, in keeping with (20),

$$P(\theta^*) = 0, \quad P'(\theta_-{}^*) = -\alpha\theta^*/W^2(\theta^*)$$
$$P'(\theta_+{}^*) = 0. \tag{24}$$

The last insures that $P(\theta) = 0$ for $\theta_-{}^* \leqslant \theta \leqslant 1$, so that the leading-edge boundary condition (19) is automatically satisfied. The supporting argument given in [4] rules out any other possibility on the basis of the ODE and the condition that $W'(1) = 0$, and hence $W \sim C\xi^\beta$ (C = constant > 0, $\xi = 1 - \theta$, $\beta > 1$) near $\theta = 1$. The discontinuity in P' has the character of a degenerate shock. Pressure jump is precluded by the absence of inertial terms at low Mach number, and the trailing fluid velocity is the same as the velocity of the discontinuity. The same conditions are found to occur at a contact interface in gas dynamics and at the leading edge of a porous-media flow which expands into a vacuum.

The numerical solution procedure consists of successive iterations of the sequence listed as follows, starting from the initial guess that $P(\theta)$ is linear and that $\theta^* \simeq \pi/N$ (which is based on the asymptotic large-N solution to be given shortly)

1 Calculate $W(\theta) = W[P(\theta), N]$ from the elastic representation (13) using most-recent $P(\theta)$ in the integrand. Averaging this result with previous $W(\theta)$ affords advantageous damping.

2 By application of a two-parameter shooting method, solve the problem (21), (22a), (23b), and (24) for $P(\theta)$ using most-recent $W(\theta)$ in the ODE. It is elected to regard θ^* and α as shooting parameters (rather than $P'(0)$ and α). Starting with a leftward expansion from

Downloaded 01 May 2010 to 171.66.16.249. Redistribution subject to ASME license or copyright; see http://www.asme.org/terms/Terms_Use.cfm

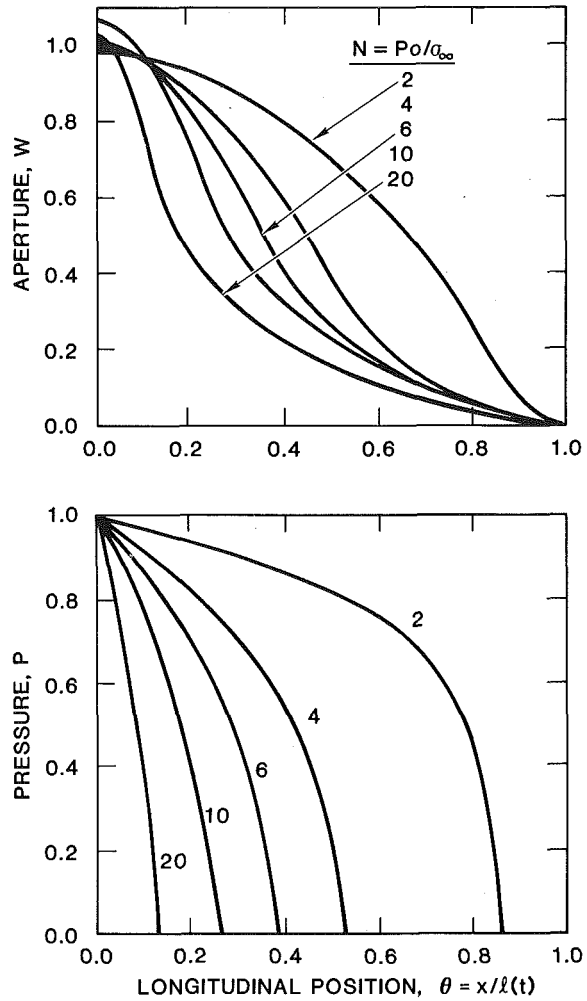


Fig. 2 Aperture and pressure distributions in laminar flow for various values of the pressure ratio, $N = p_0/\sigma_\infty$

guessed θ^*, integration proceeds backward to $\theta = 0$; thereafter checking to see whether $P(0) = 1$ and whether the integral constraint (23*b*) is met.

3 Test convergence by checking the agreement between successive iterations.

Standard library routines perform the major operations: simplex minimization iterates the shooting parameters, and a fifth-order Runge-Kutta procedure integrates the ODE such that a specified error tolerance (here 10^{-6}) is maintained by adaptive control of the forward step size.

Profiles of pressure and aperture are displayed in Fig. 2 for selected values of N. The corresponding data in Table 1 can be used to estimate the location and velocity of the tip as well as aperture, gas velocity, and mass flow at the entrance.

An asymptotic analysis for large N is based on the recognition of growing disparity between the fracture-length and the penetration depth of the fluid, θ^*. Under the coordinate transformation, $\eta = \theta\sqrt{\alpha}$, the ODE no longer depends explicitly on α. For large enough N (and hence, large α), it can then be argued that $W = 1$ and $W' \ll 1$ within the pressurized entry region, in which case $P(\eta)$ satisfies the following problem in which $()' = d()/d\eta$ (derived from (21), (22*a*), and (24)).

$$PP'' + P'(P' + \eta) = P \tag{25}$$

$$P(0) = 1$$

$$P(\eta^*) = 0, \quad P'(\eta_-{}^*) = -\eta^*, \quad P'(\eta_+{}^*) = 0. \tag{26}$$

The piecewise linear solution, which is singular at $\eta^* = 1$,

Table 1 Laminar flow results

$N = p_0/\sigma_\infty$	α	θ^*	$W(0)$	$U(0)$
2	0.29	0.86	0.98	0.29
4	1.4	0.54	0.99	0.84
6	3.2	0.40	1.0	1.4
10	9.2	0.27	1.1	2.7
20	38.0	0.13	1.0	5.4
∞	$(N/\pi)^2$	π/N	1.0	N/π

Table 2 Turbulent flow results

$N = p_0/\sigma_\infty$	α	$W(0)$	$U(0)$
2	0.73	0.82	0.68
4	2.0	0.95	1.1
6	3.4	1.0	1.5
10	7.3	0.98	1.9
20	21.0	0.98	2.8
∞	$\sim(N/\pi)^{3/2}$	~ 1.0	$(N/\pi)^{1/2}$

$$\begin{aligned} P &= 1 - \eta, \quad 0 \leqslant \eta \leqslant \eta_-{}^* \\ P &= 0 \qquad\quad \eta_+{}^* \leqslant \eta \leqslant \sqrt{\alpha} \end{aligned} \tag{27}$$

is exact in the limit ($N \to \infty$). Substitution of this profile into the integral constraint (23*b*) shows that $\alpha \to (N/\pi)^2$ as $N \to \infty$, as noted in Table 1. Convergence to this asymptotic result is apparent in Fig. 2 and is demonstrated more clearly in [4] where $P(\theta)$ from the finite-N numerical calculations is replotted versus η.

5 Intermediate-Time Turbulent Flow Structure

The integro-differential system for a turbulent flow is the same as the laminar case (21)–(23) except that the previous ODE for P is now replaced by the pair of equations (take $P'/P = -U^2/W^{1+b}$ from (12*b*) and substitute into (18))

$$U' - (U - \alpha\theta)\frac{U^2}{W^{1+b}} = -\left[(U - \alpha\theta)\frac{W'}{W} + \alpha\right] \tag{28}$$

$$P = \exp\left[-\int_0^\theta \frac{U^2}{W^{1+b}}\,d\theta\right]. \tag{29}$$

This form is chosen (over the second-order equation for P) because the ODE for U is only first order and it happens to be independent of P.

The singularity must now lie at the leading edge where

$$P \to 0 \quad \text{and} \quad U \to \alpha\theta \quad \text{as} \quad \theta \to 1. \tag{30}$$

There is no other way to satisfy the requirement that $P(U - \alpha\theta) \to 0$, as $\theta \to 1$. The supportive argument given in [4] is based on the ODE and on the behavior of W near the tip. The requirement that $U(1) = \alpha$ is the only boundary condition to be satisfied by U.

The numerical calculations are easier than in laminar flow, because α is now the only shooting parameter. Expansion from the singularity is followed by a leftward march to the origin, thereafter checking to see if the integral constraint is satisfied. The pressure, P, and the integral constraint, I, are evaluated by carrying along supplementary ODE's for $(\ln P)'$ and I'. Cyclical alternation between the ODE's and the integral equation is the same as in laminar flow. Results are presented in Fig. 3 and Table 2.

The asymptotic ($N \to \infty$) entrance-layer argument is carried over from laminar to turbulent flow. Upon transformation to the appropriate boundary-layer scaling $\hat{\eta} = \theta\alpha^{2/3}$ and $\hat{U} = U/\alpha^{1/3}$, the inner problem statement ($W = 1$, $W' \ll 1$) is again independent of α (here $()' = d()/d\hat{\eta}$)

$$\hat{U}' - (\hat{U} - \hat{\eta})\hat{U}^2 = -1 \tag{31}$$

$$P = \exp\left[-\int_0^{\hat{\eta}} \hat{U}^2 d\hat{\eta}\right] \tag{32}$$

$$\hat{U} \to \hat{\eta} \quad \text{as} \quad \hat{\eta} \to \infty. \tag{33}$$

Downloaded 01 May 2010 to 171.66.16.249. Redistribution subject to ASME license or copyright; see http://www.asme.org/terms/Terms_Use.cfm

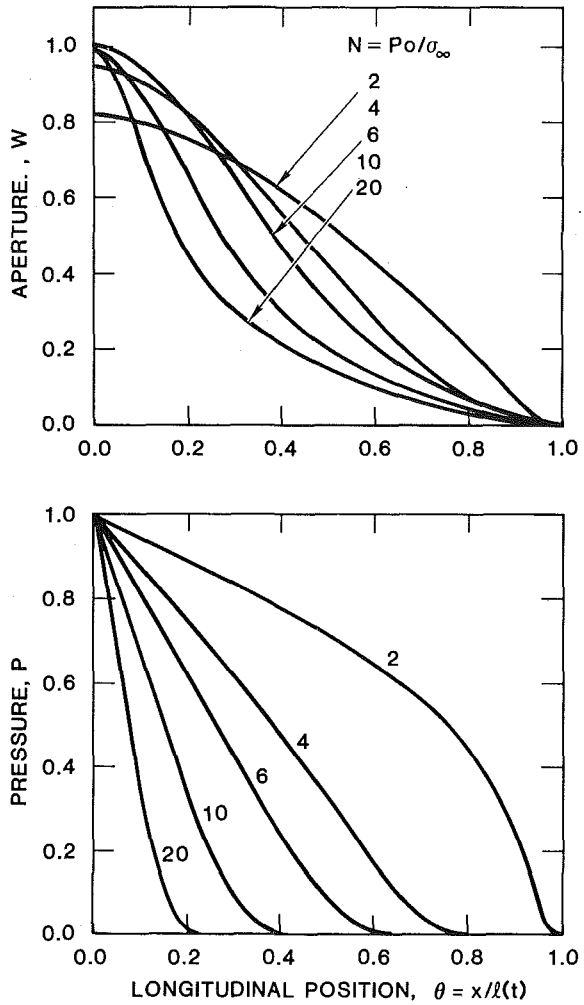


Fig. 3 Aperture and pressure distributions in turbulent flow for various values of the pressure ratio, $N = p_0/\sigma_\infty$

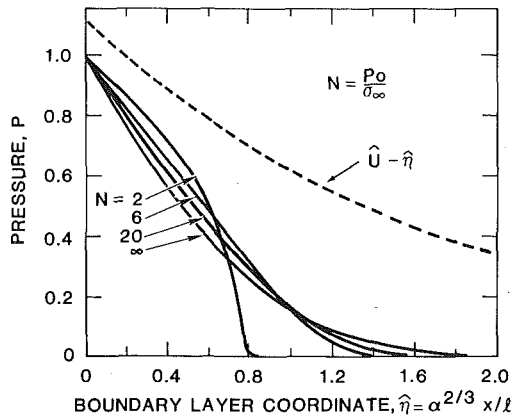


Fig. 4 Convergence of turbulent pressure distribution to the large-N, boundary-layer solution (also shown is velocity $\hat{U}$ for $N \to \infty$)

The requirement that $\hat{U} \to \hat{\eta}(U \to \alpha\theta)$ enforces agreement between the outer behavior of the inner (boundary-layer) solution and the inner behavior (leading terms) of the outer solution (tip expansion) as anticipated from the theory of matched asymptotic expansions. The numerical solution, which goes like $\hat{U} = \hat{\eta} + 2/\hat{\eta}^2$ as $\hat{\eta} \to \infty$, is plotted in Fig. 4 where the large-N convergence of $P(\hat{\eta})$ is also presented. The corresponding asymptotic entries in Table 2 are based on the following observations (from (14b) and from examination of Fig. 4):

$$\frac{\pi}{2N} = \int_0^1 \frac{P(\theta)d\theta}{\sqrt{1-\theta^2}} \to \alpha^{-2/3} \int_0^\infty P d\hat{\eta} \simeq \frac{1}{2}\alpha^{-2/3} \quad \text{as} \quad N \to \infty. \tag{34}$$

6 Transitions

The fracture-growth function $g(\tau)$ satisfies a first-order ODE, so it is possible to satisfy only one initial condition at the onset and only one matching condition at each transition. This single constant-of-integration can be interpreted as any extensive measure of the fracture/flow system such as length, volume, or elastic strain energy. The early laminar solution depends linearly upon the nonzero integration constant l_0 which characterizes the extent of the fracture at the onset of gas-drive, which might be deduced from: a preexisting fracture length, energy considerations at breakdown, or an analysis of the early-time stress-controlled elongation. At the transition from laminar to turbulent flow, roughly $\mathrm{Re} = \mathrm{Re}_0 f(\tau)g(\tau) \simeq 2{\cdot}10^3$, the integration constant of the turbulent flow, C in (17b), should be chosen so that one of the extensive measures is continuous. The matching is not, however, a critical issue since the turbulent solution eventually becomes independent of the initial data.

The dependence upon initial data is qualitatively different in the laminar and turbulent flow regimes. In the laminar solution (from (17a), (6), (7), and (15a))

$$l = l_0 \exp\left(\alpha t \left(\frac{w_0}{l_0}\right)^2 \frac{c_0^2 \rho_0}{12\mu_0\gamma}\right) \tag{35}$$

there is a lasting dependence on the initial data, l_0. But in the late-time limit of the turbulent solution, which is when it becomes asymptotically valid, (from (17b), (6), (7), and (15b) as $\tau \to \infty$)

$$l = \left(\frac{2-b}{2}\alpha t \left[\left(\frac{w_0}{l_0}\right)^{1+b} \frac{c_0^2}{a\gamma}\left(\frac{1}{\epsilon}\right)^b\right]^{1/2}\right)^{2/(2-b)} \tag{36}$$

there is no longer any dependence on the initial length scale l_0, since the ratio w_0/l_0 is given by (9) in terms of p_0,N, and the elastic constants.

The laminar-dominated and turbulent-dominated flows belong to the class called self-similar asymptotics, each being strictly valid only when the Reynolds number is either very low or very high everywhere within the channel. The transition from laminar to turbulent flow will therefore be a gradual one with turbulence taking over a longer and longer section of the fracture, and there will always be a laminar zone near the tip. The character of such a transition and the validity of the asymptotic solutions have been investigated for the closely related problem of the high-Re to low-Re transitional flow which occurs during transient fluid flow in porous media, or equivalently in narrow capillary tubes or in constant-aperture fractures [11].

Seepage interactions between a hydrofracture and a surrounding permeable medium (e.g., geologic media) may also be viewed within the context of asymptotic analysis, as described in [4] and as briefly outlined as follows. The continuity equation for the fracture (3a) is modified to include a lateral seepage velocity, v, which depends on the lateral pressure gradient; $v = -(\kappa/\mu)\partial p/\partial y$ in which κ is permeability and y is measured away from the fracture. An expression for $v(\theta,\tau)$ can then be deduced from the transport equations which describe the seepage flow (2D continuity and Darcy's law) which are written in terms of the longitudinal variable θ and the lateral variable $y^* = (\phi\mu/\kappa p_0)^{1/2} y/\sqrt{t}$. It is found that the seepage interaction becomes negligible when τ has become sufficiently large that the following parameter becomes small (here ϕ is porosity).

$$\Gamma = \left[\left(\frac{l_0}{w_0}\right)\frac{1}{u_0}\frac{p_0\phi\kappa}{\mu_0 w_0}\right]\left(\frac{\partial g}{\partial \tau}\sqrt{\tau}\right)^{-1} \ll 1 \tag{37}$$

Physically, the seepage interaction diminishes at late times because an increase in aperture, w, enhances the through-flow much more than a corresponding increase in length, l, enhances the seepage losses (i.e., enhances the surface area for seepage loss). Thus, with respect to this consideration, the present results must be viewed as late-time as-

Downloaded 01 May 2010 to 171.66.16.249. Redistribution subject to ASME license or copyright; see http://www.asme.org/terms/Terms_Use.cfm

ymptotics in permeable media. Although the seepage interaction will always result in a finite tip pressure, the zero-pressure analysis should give a good approximation so long as the pressure ratio, $p_{\text{driving}}/p_{\text{tip}}$, is large (roughly 5 or greater) as observed in the closely related problem of transient flow-through porous media or slender channels [11].

7 Summary

A problem of gas-driven fracture propagation has been solved by separation of the time and position variables, followed by numerical integration of the resulting ordinary differential equations. The considered case is a prototypic one, which reveals a number of interesting qualitative features.

1 The flow accelerates through a sequence a self-similar asymptotic regimes: laminar, turbulent, and inviscid; only the first two are reported here.

2 A strong vacuum exists at the tip of the fracture, either in an impermeable medium or in a permeable medium at late times.

3 The flow effectively experiences a diverging/converging channel, because of the competing effects of timewise wall divergence, $\partial w/\partial t$, and spacewise wall convergence, $\partial w/\partial x$.

4 If the pressure ratio ($N = p_0/\sigma_\infty$) is large, the flow is confined to a narrow entry-layer region at the entrance to the channel.

5 In laminar-dominated flow at early times: the fracture grows exponentially, the pressure goes to zero at midspan, and the pressure distribution is linear for large values of N.

6 In turbulent-dominated flow at late times: the fracture grows like a near-unity power of time, the pressure goes to zero at the tip, and the pressure distribution is exponential for large values of time.

7 The initial data (i.e., length l_0 at the onset of gas-drive) has a lasting influence in the early laminar period but not in the late-time limit of the turbulent period.

Assumptions and approximations in the analysis are self-consistent with respect to two different criteria: late-time, long-fracture limit (quasi-steady stress field, impermeable media, no tensile strength); and upper-bound on fracture extension (all above, isothermal, wedge-shaped configuration).

Quantitative results provide convenient estimates of fracture propagation rates and other engineering data.

1 Temporal variation of length, aperture and velocity is described by the analytic expressions

$$l = l_0 g(\tau), \quad w(0,t) = w_0 W(0) g(\tau), \quad u(0,t) = u_0 U(0) f(\tau)$$

in which $g(\tau)$ and $f(\tau)$ are given by (16) and (17); $\tau = t/t_0$ and $t_0 = l_0/u_0$; l_0 is the initial fracture length; w_0 and u_0 are defined in (9) and (15); and Tables 1 and 2 provide α, $W(0)$, and $U(0)$ as functions of N; see in particular equations (35) and (36) for $l(t)$.

2 Spatial variations in pressure, aperture, and velocity are presented graphically.

3 Asymptotic results for large N are particularly simple and, by demonstrating convergence, they lend verification to the numerics.

References

1 Howard, G. C., and Fast, C. R., *Hydraulic Fracturing*, Society of Petroleum Engineers of AIME, Dallas, 1970.

2 Pitts, J. H., and Brandt, H., "Gas Flow in a Permeable Earth Formation Containing a Crack," ASME JOURNAL OF APPLIED MECHANICS, Vol. 44, 1977, pp. 553–558.

3 Keller, C. E., Davis, A. H., and Stewart, J. N., "The Calculation of Steam Flow and Hydraulic Fracturing in a Porous Medium With the KRAK Code," Los Alamos Scientific Laboratory Report LA-5602-MS, 1974.

4 Nilson, R. H., "Gas-Driven Fracture Propagation," SAND79-2379, Sandia National Laboratories, Albuquerque, New Mex., 1981.

5 Daneshy, A. A., "On the Design of Vertical Hydraulic Fractures," *Journal of Petroleum Technology*, Vol. 25, Jan. 1973, pp. 83–97.

6 England, A. H., and Green, A. E., "Some Two-Dimensional Punch and Crack Problems in Classical Elasticity," *Proceedings, Cambridge Philosophical Society*, Vol. 59, 1963, pp. 489–500.

7 Geertsma, J., and De Klerk, F., "A Rapid Method of Predicting Width and Extent of Hydraulically Induced Fractures," *Journal of Petroleum Technology*, Vol. 21, Dec. 1969, pp. 1571–1581.

8 Barenblatt, G. I., "The Mathematical Theory of Equilibrium Cracks in Brittle Fracture," *Advances in Applied Mechanics*, Vol. 7, 1962, pp. 55–129.

9 Shapiro, A. H., "*The Dynamics and Thermodynamics of Compressible Fluid Flow*," II, Ronald Press, New York, 1954.

10 Huitt, J. L., "Fluid Flow in Simulated Fractures," *AIChE Journal*, Vol. 2, (2), 1956, pp. 259–264.

11 Nilson, R. H., "Transient Fluid Flow in Porous Media: Inertia-Dominated to Viscous-Dominated Transition," *Journal of Fluids Engineering*, in press, 1981.

Downloaded 01 May 2010 to 171.66.16.249. Redistribution subject to ASME license or copyright; see http://www.asme.org/terms/Terms_Use.cfm

J. P. Licari

IBM Corporation,
Information Systems Division,
Highway 52 & Northwest 37th Street,
Rochester, Minn. 55901

F. K. King[1]

Datapoint Corporation,
Peripheral Operation Division,
686 West Maud Avenue,
Sunnyvale, Calif. 94086
Mem. ASME

Elastohydrodynamic Analysis of Head to Flexible Disk Interface Phenomena

The finite-element and finite-difference techniques are used to develop an analytical model which describes the interaction between a magnetic recording head and a flexible disk. The finite-element approach is used to describe disk deformation. Both disk bending stiffness and stiffness effects due to disk rotation are included. The finite-difference scheme is used to solve the Reynold's or lubrication equation which describes the flow interaction between head and disk. The procedure used to couple the two numerical models into a complete head-to-disk interface simulator is outlined. Accuracy of the simulator is verified experimentally, and results of studies showing the sensitivities of various parameters are given.

Introduction

Development of magnetic recording input/output (I/O) devices requires a complete understanding of the head-to-tape or head-to-disk interface. In order to achieve high performance in tape or disk drives, a hydrodynamic air bearing is created between the head and recording medium which move at high relative velocities. The air bearing is usually kept within the range of 250 and 1000 nanometers to yield the desired magnetic performance. It also provides a means of controlling head/media separation as well as extending product life by minimizing effects of wear.

With the evolution of higher performance I/O devices, greater emphasis has been placed on modeling or simulating foil bearing (tape/air bearing) and hard file head-disk spacing configurations. Recently, Stahl, et al. [1], have studied the dynamic response of a foil bearing using the equation of motion for a finite length of tape coupled to the transient lubrication equation. Others such as Barmen and Elrod [2] have investigated foil bearing behavior. In a hard file I/O device, the interaction between the head and disk is described by Reynold's or lubrication equation alone [3]. Adams [4] and Greenberg [5] have addressed the two-dimensional flexible disk/head interface elasticity—lubrication problem. The purpose of this paper is to solve a similar problem. However, we use the finite-element technique to solve the disk elasticity problem, and we use a modification of the coupling algorithm to solve the combined elasticity—lubrication equations. In addition, this work developed an easy-to-use design simulation program. Some design information on the effect of head radius and disk thickness is given.

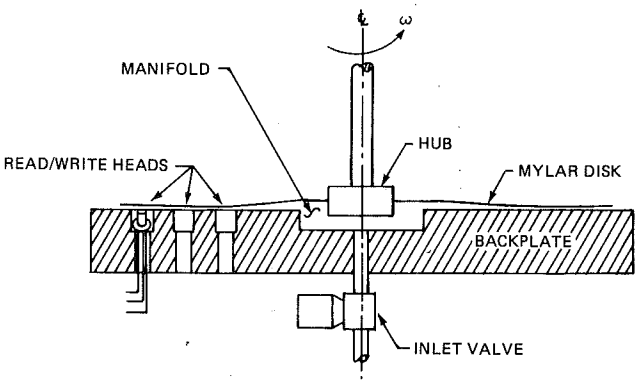


Fig. 1 Flexible disk—base plate configuration

Flexible disk files are attractive as future storage products due to their high area bit density capabilities (lower flying heights), potentially lower cost, and faster access than tape drives. In a typical configuration for this type of file, a single flexible sheet is spun near a base plate. The plate, from which the head protrudes, serves as a stabilizing plateform for the disk (Fig. 1) [6].

With the disk made of thin mylar, it is no longer possible to ignore its elasticity. We consider here the problem of a spinning elastic disk, the stiffness of which is due to the membrane stresses from its rotation and the inherent disk bending strength. The recording head pene-

[1] Formerly employed by IBM Corporation, Information Systems Division, Rochester, Minn. 55901.

Contributed by the Applied Mechanics Division for publication in the JOURNAL OF APPLIED MECHANICS.

Discussion on this paper should be addressed to the Editorial Department, ASME, United Engineering Center, 345 East 47th Street, New York, N. Y. 10017, and will be accepted until two months after final publication of the paper itself in the JOURNAL OF APPLIED MECHANICS. Manuscript received by ASME Applied Mechanics Division, December, 1980; final revision, April, 1981.

Copyright © 1981 by ASME

Downloaded 01 May 2010 to 171.66.16.249. Redistribution subject to ASME license or copyright; see http://www.asme.org/terms/Terms_Use.cfm

trates into the disk causing the disk to deform locally. An air gap or separation between the head and disk several microinches thick is developed. A coupled two-dimensional nonlinear elastic-fluid problem results. Effects of the stabilizing platform are incorporated into the simulation by applying experimentally determined external forces to the disk model.

The disk elasticity problem is solved using the finite-element method. This approach replaces the governing partial differential equation by a series of coupled algebraic equations which can be solved by standard matrix techniques. Only inertia effects associated with the disk rotation are included in this study.

The nonlinear Reynold's equation which characterizes the head/disk air lubrication is solved using an arbitrary grid finite-difference scheme. This grid, defined in Cartesian coordinates, allows direct coupling with the sector finite-element model described in cylindrical coordinates. A match of finite-element and finite-difference points is assured due to the arbitrary nature of the latter.

The development of the disk and flow models, along with a description of the procedure which couples the models to form the head-disk interface simulator, are given. Experimental results are presented which verify the models. Finally, results of a parameter study using the simulator are presented to show the sensitivity of key variables such as head radius, head penetration, and disk thickness.

Theory

Disk Model. For ease in development of this initial head/disk interface simulator, the disk was assumed to behave linearly and be homogeneous and isotropic in nature. Effects of transverse disk vibration are neglected. However, the effect of rotation on the disk stiffness is included. It is assumed that any transverse disk deflection does not appreciably alter the in-plane stress field set up by the disk rotation. Even under these simplifications, a complex nonlinear problem must be solved when coupled with the flow or lubrication equation.

The disk spinning at some angular velocity ω is assumed to be rigidly constrained at the hub against both transverse and planar displacement. The partial differential equation governing the disk deflection has the form

$$D\nabla^4 W - \frac{1}{r}\frac{\partial}{\partial r}\left[r\sigma_{rr}\frac{\partial W}{\partial r}\right] - \frac{1}{r^2}\frac{\partial}{\partial \theta}\left[\sigma_{\theta\theta}\frac{\partial W}{\partial \theta}\right] = q(r,\theta) \tag{1}$$

subject to the appropriate boundary conditions. D is the plate flexural rigidity, $W(r,\theta)$ the transverse plate deflection, and $q(r,\theta)$ the applied load. As was noted previously, both the membrane stresses σ_{rr} and $\sigma_{\theta\theta}$, due to the disk rotation, and bending effects are included in the formulation.

The finite-element technique is utilized to obtain an approximate numerical solution to (1). This approach is desirable due to geometric complexities such as holes in the disk, and the desire to determine the disk deformation for cases where all disk constraints are not known *a priori*.

The standard displacement technique is used to develop two sector shaped elements. They have the same geometry which is shown in Fig. 2. One describes the sector stiffness due to the inherent bending strength of the disk, while the other relates the disk resistance to deflect transversely due to the centrifugal stresses generated by the disk rotation.

The strain energy of deformation representing the work done by the forces acting in the middle plane of the plate during a transverse deflection is given by

$$U_1 = \frac{t}{2}\iint_A \left[\sigma_{rr}\left(\frac{\partial W}{\partial r}\right)^2 + \sigma_{\theta\theta}\frac{1}{r^2}\left(\frac{\partial W}{\partial \theta}\right)^2 + \frac{2}{r}\sigma_{r\theta}\frac{\partial W}{\partial \theta}\frac{\partial W}{\partial r}\right] r dr d\theta \tag{2}$$

where t is the disk thickness.

The in-plane stress field is assumed to be unchanged due to any transverse deflection W. The rotating disk problem [5] solved to obtain the in-plane stress field is defined in the usual way by

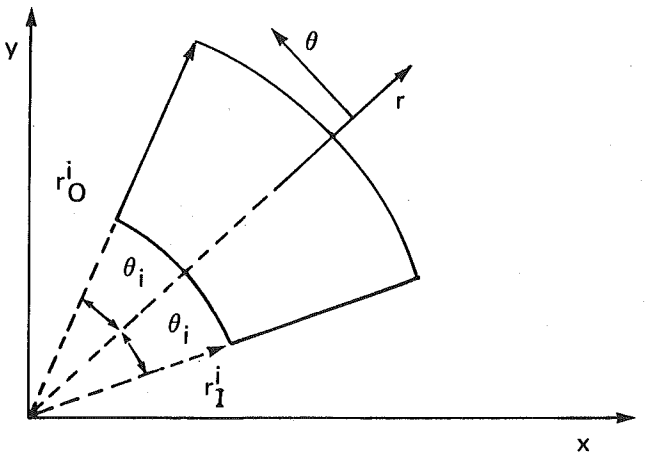


Fig. 2 Element coordinate system

$$\frac{d}{dr}(r\sigma_{rr}) - \sigma_{\theta\theta} + \rho\omega r^2 = 0 \tag{3}$$

In addition to (3) boundary conditions of zero radial displacement at the hub or inner boundary and zero radial stress at the outer boundary are needed.

The development of the finite-element stiffness model through the use of (2) requires that an approximate form for the deflection pattern $W(r,\theta)$ be assumed across the element. The local coordinate system for a typical element is shown in Fig. 2. The choice of the cylindrical coordinate system is such that for a given radial location, the elements are independent of their angular position. The local coordinate system, therefore, coincides with the global coordinate system. With four nodes or four degrees of freedom for the membrane problem, we choose for each element the expansion

$$W(r,\theta) = a_1 + a_2 r + a_3\theta + a_4 r\theta. \tag{4}$$

Substituting (4) and the solution from (3) into (2) and integrating one defines the element membrane stiffness matrix in the usual manner.

The description of the plate bending sector shaped finite element is derived similarly. The potential energy of bending in polar coordinates is

$$U_2 = \frac{D}{2}\iint_A \left\{\left(\frac{\partial^2 W}{\partial r^2} + \frac{1}{r}\frac{\partial W}{\partial r} + \frac{1}{r^2}\frac{\partial^2 W}{\partial \theta^2}\right)^2 + 2(1-\nu)\left[\left(\frac{1}{r}\frac{\partial^2 W}{\partial r\partial\theta} - \frac{1}{r^2}\frac{\partial W}{\partial\theta}\right)^2 - \frac{\partial^2 W}{\partial r^2}\left(\frac{1}{r^2}\frac{\partial^2 W}{\partial\theta^2} + \frac{1}{r}\frac{\partial W}{\partial r}\right)\right]\right\} r dr d\theta. \tag{5}$$

In this case, however, each of the sector node points has three degrees of freedom; one deflection and two rotation. Thus, for the assumed deflection pattern within the element, we chose the 12-term polynominal given by

$$W(r,\theta) = b_1 + b_2 r + b_3\theta + b_4 r\theta + b_5 r^2 + b_6\theta^2 + b_7 r^3 + b_8 r^2\theta + b_9\theta^2 r + b_{10}\theta^3 + b_{11} r\theta^3 + b_{12}\theta r^3. \tag{6}$$

Development of the sector bending finite element proceeds in the same manner as that for the sector membrane element. In this case, however, the resulting element matrix will be a 12 by 12 square matrix.

The final system of disk equations is obtained by combining the sector membrane and bending elements. This yields the following equation which relates forces and deflections for a spinning flexible disk

$$\mathbf{K}\,\overline{X} = \overline{F} \tag{7}$$

$\mathbf{K}$ is the system stiffness matrix.

Downloaded 01 May 2010 to 171.66.16.249. Redistribution subject to ASME license or copyright; see http://www.asme.org/terms/Terms_Use.cfm

Lubrication Model. The separation between the head and disk is described by the lubrication (Reynold's) equation [5]. A steady-state compressible flow is assumed. Effects of slip flow are included. In vector form the governing equation becomes

$$\nabla \cdot [H^3 P \nabla P] + 6m \nabla \cdot [H^2 P \nabla P] = \bar{\Lambda} \cdot \nabla [PH] \tag{8}$$

where

$$H = \frac{h(x,y)}{h_{\min}}; \quad P = \frac{p(x,y)}{p_{\text{ambient}}}; \quad m = \frac{(2 - S_r)}{S_r} \frac{\lambda}{h_{\min}}$$

$h(x,y) \equiv$ spacing; $p(x,y) \equiv$ pressure

$$\bar{\Lambda} = \Lambda_x \bar{i} + \lambda_y \bar{j} = \frac{6\mu \bar{V} L}{P_{\text{ambient}} h_{\min}^2} \equiv \text{gas bearing number} \tag{9}$$

$\lambda_{\text{ambient}} \equiv$ mean free path length
$S_r \equiv$ surface reflective factor
$\mu \equiv$ viscosity; $L \equiv$ bearing reference length
$\bar{V} \equiv u\bar{i} + v\bar{j} \equiv$ disk velocity

The boundary condition associated with (8) is

$$p(x,y) = P_{\text{ambient}} \tag{10}$$

along the boundary of the head and along the slots or pressure relief grooves, if any are present in the head.

Slip flow effects given by the second term on the left in (8) are included to improve results for small head/disk spacings. Given the head/disk separation $h(x,y)$, the Reynold's equation is used to solve for the resulting pressure $p(x,y)$.

An implicit pointwise over-relaxation finite-difference numerical solution technique is chosen to solve the Reynold's equation [8, 9]. The usual approach is to use a uniformly spaced finite-difference grid. However, since compatibility is required between the sector finite-element disk model and the finite-difference fluid flow model, an arbitrary grid is used. This allows a point-to-point grid match between the two different numerical models and eliminates possible additional numerical error.

The film thickness or head-to-disk spacing h is defined pointwise by the relationship

$$h = W(r,\theta) - \delta(r,\theta) \tag{11}$$

where

$W(r,\theta) \equiv$ disk deflection pattern
$\delta(r,\theta) \equiv$ geometric description of the head surface or profile

A 12-point grid arrangement is used for the finite-difference analysis. The necessary partial derivatives are calculated for each grid point using its adjacent 11 grid points with a weighting factor. One of the significant effects of the 12-point arbitrary grid algorithm developed here is to increase the rate at which convergence is achieved during the iteration process used to obtain a solution to the Reynold's equation.

The relatively fast convergence using this approach is largely due to the inclusion of more neighboring points in calculating the partial derivatives. Two rows of points upstream are used to calculate the partial derivatives at the point of interest.

Discretization of the Reynold's equation results in a set of nonlinear quadratic algebraic equations of the form

$$A_{ij}\, \theta^2_{ij} + B_{ij}\, \theta_{ij} + C_{ij} = 0 \tag{12}$$

where

$$\theta_{ij} = P_{ij}\, H_{ij}.$$

A_{ij}, B_{ij}, and C_{ij} are functions of properties described in the Reynold's equation, P_{ij} is the normalized pressure, H_{ij} the normalized spacing. An iterative scheme is used to determine the θ_{ij}. For every calculation of θ_{ij}, the current up-to-date values of the adjacent 11 grid points and the old θ_{ij} are used.

Coupling Algorithm. In addition to the necessary grid point matching between the finite-element and finite-difference models, a coupling algorithm is needed to combine the effects of the disk elasticity and the air film between the head and disk. Key to obtaining a solution, which simultaneously satisfies both models, is choosing a good starting point to begin the iteration.

In this simulator, the starting point is not guessed arbitrarily. The disk deformation due to the penetrating head is determined by the disk model alone as the initial solution to the disk-flow problem.

This initial solution is a good approximation to that region or area of the head to which the disk conforms, and it also gives the reaction forces between the head and disk.

Although uniqueness and existence are not rigorously proven from a mathematical point of view, the coupling procedure outlined in the following has been found to be very effective and efficient in obtaining a converged solution. The approach is heuristic. The ultimate proof that the solution converges to the correct result is the experimental-simulator comparison. The procedure is as follows:

1 Using the disk model alone determines the region on the head that the disk conforms to or contacts. Also determine the reaction forces between the head and disk. Do this for the desired head contour and penetration.

2 The initial disk shape and forces previously calculated are passed to the Reynold's equation solver. To calculate a first Reynold's pressure, the initial disk shape is raised to a reasonable spacing above the head. A predetermined algorithm is used to modify this spacing and hence, the initial pressure to insure a proper solution to the Reynold's equation.

3 For the iterative process, the basic equation used to relate the new disk pressure to the old disk pressure, the Reynold's pressure, and the relaxation factor has the form

$$P_{i+1} = P_i + (P_R - P_i)\, K_{i+1} \tag{13}$$

where P_R is the Reynold's pressure or the pressure resulting from the lubrication equation, K_{i+1} the relaxation factor, and P_{i+1} the new disk pressure.

For the first iteration, the relaxation factor is determined by an algorithm which considers the total or resultant Reynold's pressure and the total or resultant initial disk pressure as variables.

4(*a*) From iteration to iteration, the following is done for the $i+1$ iteration. Define the starting value for K_{i+1} as

$$K_{i+1} = \alpha K_i \tag{14}$$

where $\alpha > 1$.

This assures that the disk pressure can oscillate freely; i.e., a solution is not forced.

Equation (13) is now used to define all the new pointwise disk pressures using K_{i+1}.

Next, check to see if the following relationship holds for the total disk pressure

$$\left| \sum P_{i+1} - \sum P_i \right| < \left| \sum P_i - \sum P_{i-1} \right| \tag{15}$$

If (15) is violated, define a new K_{i+1} from

$$K_{i+1} \equiv \beta\, K_{i+1}, \qquad 0 < \beta < 1 \tag{16}$$

Apply the foregoing until a new value of K_{i+1} is found such that (15) holds. Once this value is established, do a binary search between it and the previous K_{i+1} for which (15) was violated. This homes in on the value of K_{i+1} such that (15) becomes satisfied.

4(*b*) If a head crash or physically invalid solution from the Reynold's equation solver occurs, change K_{i+1} to

$$K_{i+1} \equiv \beta\, K_{i+1} \tag{17}$$

Apply (17) until a new value of K_{i+1} does not yield a crash or invalid solution; do a binary search between this value and the previous one which gave a crash until a value of K_{i+1} is defined such that a crash or invalid solution does not occur and (15) is satisfied. The β correction

Downloaded 01 May 2010 to 171.66.16.249. Redistribution subject to ASME license or copyright; see http://www.asme.org/terms/Terms_Use.cfm

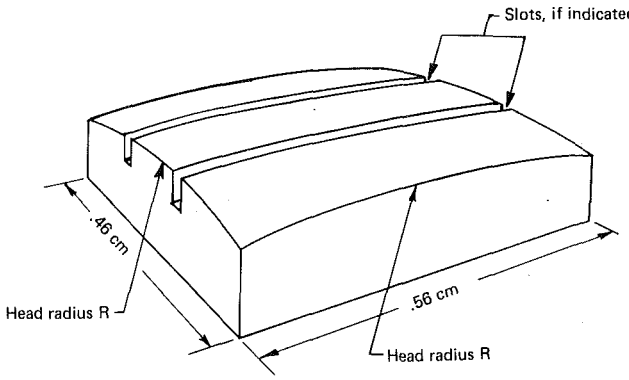


Fig. 3 Head geometry

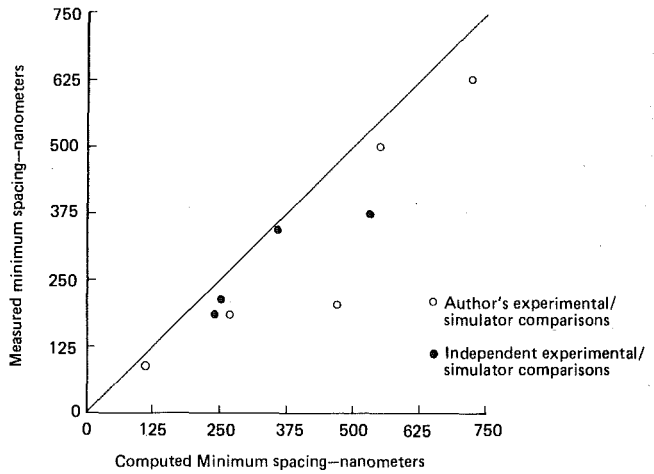


Fig. 4 Correlation between measured and computed minimum spacing for various head sizes, penetration, and disk geometries

Table 1 Comparison of calculated-to-measured flying height

Head radius	Disk thickness	Minimum measured spacing	Minimum calculated spacing
0.94 cm	0.004 cm	200 nanom	275 nanom
1.78 cm	0.004 cm	625 nanom	725 nanom
1.78 cm	0.0076 cm	0 nanom	110 nanom
1.78 cm (slotted)	0.004 cm	200 nanom	450 nanom

factor in equation (17) must be altered for cases when slots or areas of pressure relief exist in the head.

5 The pointwise convergence criteria used to define the final solution has the form

$$\Delta P_{i+1} = \frac{\sum_{j=1}^{m} (P_{i+1}^j - P_i^j)^2}{\sum_{j=1}^{m} (P_i^j)^2} \leq P_c \qquad (18)$$

where P_c is the desired convergence value and m the total number of node points used to describe the system geometry. Thus the criteria is based upon how the disk pressure changes from one iteration to the next.

The key in allowing (18) to be the convergence criteria is that the relaxation factor is not arbitrary during the iteration process. It is dynamically controlled during execution such that head crashes do not occur and (15) is satisfied.

6 Finally, form ΔP_{i+1} and use (18) to determine if a solution has been achieved. Otherwise continue iterating.

It is important to note that during the finite-difference iteration process, the Reynold's pressures are calculated for each simulator iteration by starting with all the initial pressure values at atmospheric pressure. However, the disk or elastic pressure is modified from its previous value. It is well known that a small spacing change between the head and disk can cause a large change in the calculated Reynold's pressure. Thus, to use the Reynold's pressure values from the previous simulator, iteration may cause undesirable numerical instabilities due to the spacing change from iteration to iteration. On the other hand, the magnitude of changes in the disk deformation are of less sensitive to changes in the disk or elastic pressure. Therefore, the value of the disk or elastic pressure from the previous simulator iteration can be used as a base to build the new solution.

Verification

Several tests were run to check the accuracy and sensitivity of the simulator by comparing results to white light interferometric photos of the spacing between the head and disk. Transparent heads were used in these tests. The radii of the heads were determined by an optical procedure with a 5 percent measurement error.

The effect of the stabilizing platform on the disk is incorporated into the simulator. This is done by applying a load to the disk such that the disk profile and the total head load are close to that observed experimentally. The profile of the disk was determined by radially transversing a photonic sensor over the spinning disk.

It is known that the pressure between the base plate and disk varies nonlinearly as the head penetrates the disk. As a result, the load on the head varies in a nonlinear fashion with penetration, especially for penetrations above 0.04 cm. Experimental data have indicated that the nonlinearity is due to changing pressure between the head and disk as the head protrudes and not disk nonlinearity. Thus, in the verification tests given here, comparisons were made between simulator results and experimental data for cases in which the magnitude of the head loads were within 10 percent of one another. Also, effects of disk surface roughness are not included in these tests.

Three design parameters were evaluated in these verification tests; the radius of the spherical head, the disk thickness, and the effect of slots or pressure relief grooves in the head. The geometry of a typical head is shown in Fig. 3. Table 1 shows experimental results along with the calculated minimum spacing for a head with a 0.94 cm radius with a 0.004 cm thick disk, for a 1.78 cm radius head with a 0.0076 cm disk and also a 1.78 cm radius head with two 0.0076 cm wide parallel slots 0.046 cm apart with a 0.004 cm disk. The disk is rotating at 1800 rpm.

Data from the simulator and experiment compare favorably considering the possible sources of error mentioned earlier. Even in those cases using coarse grids, not only is the minimum spacing close but the general shape of the disk region closest to the head is of the correct shape. The comparisons show that as the head radius is increased from 0.94 cm to 1.78 cm, the minimum flying height increases from 200 to 625 nanometers experimentally, and the simulator results increase from 275 to 725 nanometers. For the same 1.78 cm radius head white light data shows the minimum fly height drops to near contact when the disk thickness is nearly doubled. Corresponding simulator results show a flying height drop down to 110 nanometers.

The greatest deviation between experiment and simulator is the case of the slotted head. However, the trend to a lower fly height is correct as shown in Table 1. It is believed that the media flies higher in the simulator results since the pressure relief grooves are modeled as single lines and, hence, do not have finite width as is physically the case.

It is interesting to note from these results how sensitive the head/disk interface is to the disk bending and membrane stiffness. Not only does the fly height decrease dramatically as the disk thickness in-

Downloaded 01 May 2010 to 171.66.16.249. Redistribution subject to ASME license or copyright; see http://www.asme.org/terms/Terms_Use.cfm

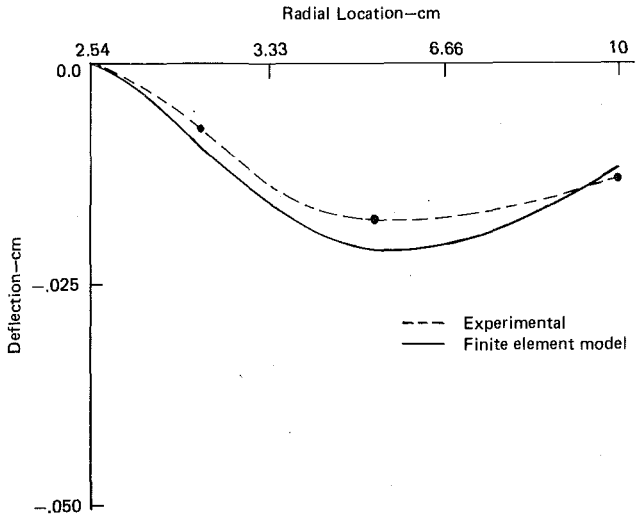


Fig. 5 Disk deflection due to pressure between rotating disk and base plate—including effect of gravity

creases, but the manner in which the disk conforms to the head also is affected.

Additional confidence in the simulator results can be obtained by plotting a correlation curve of minimum spacing only. Results from the authors and independent users experimental/simulator comparisons are shown in Fig. 4. Generally results compare favorably. The greatest deviations are in cases where slots or pressure relief grooves are added to the head. As was indicated, this effect is not adequately taken into account by the model.

Table 2 Point loaded circular plate

	Exact plate theory	Large element aspect ratio	Medium element aspect ratio	Element aspect ratios near 1
Plate deflection under point load	0.24290 cm	0.25164 cm	0.24907 cm	0.24262 cm

More insight into the model can be gained by independently considering the finite-element disk model and the Reynold's equation solver. In particular consider the disk model since comparison of the Reynold's equation solver used here to other available solutions gave results with little if any difference. The disk model involves the solution of an elastic, rotating plate with a central hole acted upon by an asymmetric load applied over a small region. Two comparisons of the disk model are made. One to exact theory and the other to experimental data.

Exact plate theory solutions are used for the first comparison. A solid 10 cm radius circular plate was clamped on its outer periphery. A point load was applied at a 6.25 cm radial location. For this comparison the size of the finite elements were varied to more closely approximate the plate domain division for a complete head to disk interface simulation. There is a good agreement as shown in Table 2 between the finite-element model and exact plate theory. Even for a finite-element breakup with large aspect ratios there is less than 4 percent error.

To incorporate disk rotation effects a comparison is made of the predicted disk deflection to the measured deflection of a flexible disk

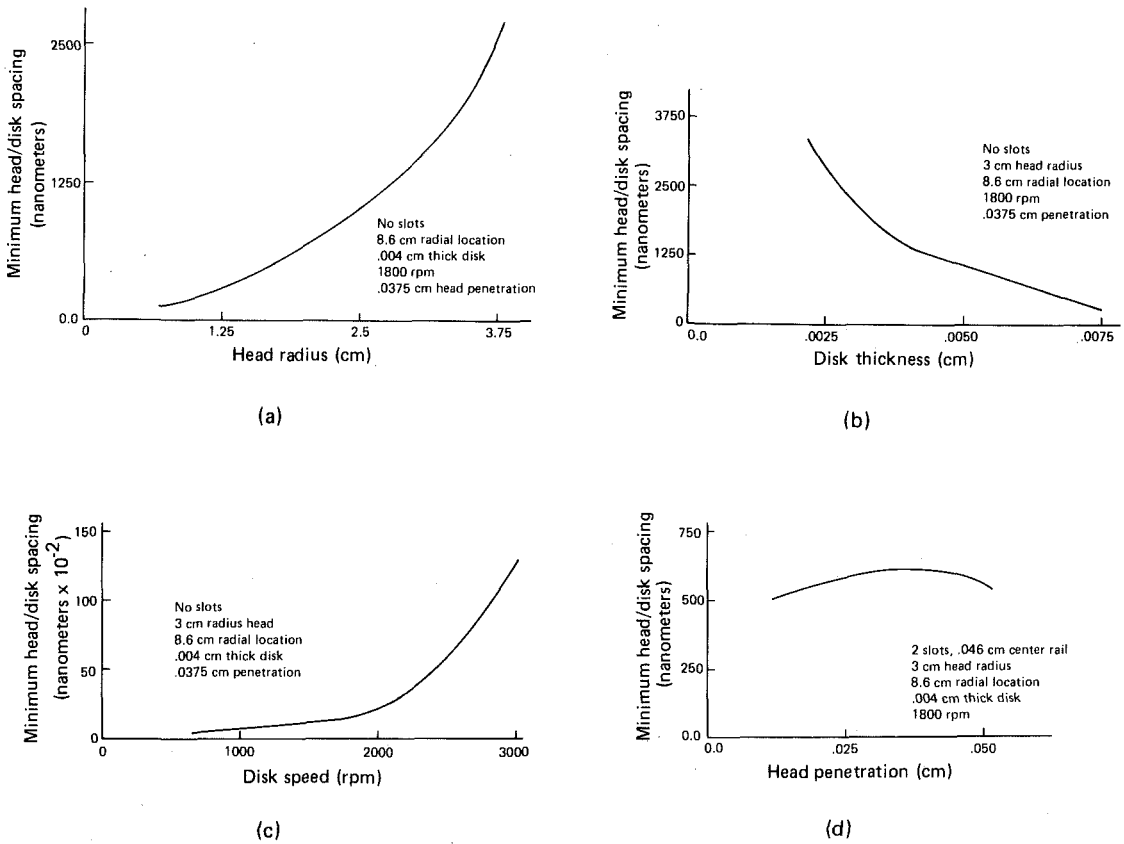


Fig. 6 Parameter study results

Downloaded 01 May 2010 to 171.66.16.249. Redistribution subject to ASME license or copyright; see http://www.asme.org/terms/Terms_Use.cfm

rotating near a base plate. The load applied to the disk includes the experimentally measured pressure between the flexible disk and base plate and the effects of gravity. Results are shown in Fig. 5. Considering the possible error in measuring the pressure loads there is good correlation.

Although the data presented is limited, it does show that the simulator not only gives qualitative trends, but reasonable quantitative results. Finally, if one does not include the effect of the pressure between the base plate and disk, test results indicate that the simulator will still yield the proper qualitative trends and sensitivities.

Parameter Study Results

Results of a parameter study utilizing the simulator are presented as follows. They illustrate the sensitivity of several of the key variables one would evaluate to obtain acceptable compliance or interaction between the head and disk.

Effects of head radius, disk thickness, and disk speed for solid spherical heads are given in Fig. 6(a–c), respectively. All results are for the head at a 8.6 cm radial location on a disk with a diameter greater than 28 cm. In addition, Fig. 6(d) shows the variation in flying height of a slotted head with head penetration. The slots are 0.046 cm apart and are modeled as lines of constant (atmospheric) pressure. For the cases presented here, all data are qualitative since the affect of the pressure generated between the disk and base plate is not included.

Conclusions

Development of an elastohydrodynamic simulator characterizing the head-to-disk interface for flexible disk devices has been presented. The coupled finite element-finite difference technique utilized here offers an efficient and accurate means to study the interaction between head and disk. The procedure used to couple the disk model to the lubrication model appears to be efficient and is a modification of other approaches used to solve coupled elastohydrodynamic problems. The steady-state solutions are well behaved, stable, and converge rapidly. Generally, solutions are obtained after 50 to 100 simulator iterations and execution times on an IBM System 370/168 are 15 to 20 min. For simulations using the pressure and deformation results of previous simulations as starting data, the run time can be cut to 5 to 10 min.

Generally, good agreement has been shown between simulator results and corresponding experimental data. However, additional simulator enhancements are needed to improve the quantitative analysis; especially the representation of pressure relief grooves in the head.

References

1 Stahl, K. J., White, J. W., and Deckert, K. L., "Dynamic Response of Self-Acting Foil Bearings," *IBM Journal of Research and Development*, Vol. 18, 1974, p. 513.

2 Barnum, T. B., and Elrod, H. G., "A Theoretical Study of the Dynamic Behavior of Foil Bearings," ASME *Journal of Lubrication Technology*, Vol. 93, 1971, p. 133.

3 Constantinescu, V. N., *Gas Lubrication*, New York, ASME, 1969.

4 Adams, G. G., "Analysis of the Flexible Disk/Head Interface," ASME *Journal of Lubrication Technology*, Vol. 102, 1980, pp. 86–90.

5 Greenberg, H. J., "Flexible Disk—Read/Write Head Interface," *IEEE Transactions, Magnetics*, MAG-14, 1978, pp. 336–338.

6 Pelech, I., and Shapiro, A. H., "Flexible Disk Rotating on a Gas Film Next to a Wall," ASME JOURNAL OF APPLIED MECHANICS, Vol. 31, 1964, pp. 577–584.

7 Wang, C.-T., *Applied Elasticity*, McGraw-Hill, New York, 1953, pp. 63–67.

8 Forsythe, G., and Wasow, W., *Finite-Difference Methods for Partial Differential Equations*, Wiley, 1967.

9 Scarborogh, J., *Numerical Mathematical Analysis*, The John Hopkins Press, Baltimore, Md., 1966.

Downloaded 01 May 2010 to 171.66.16.249. Redistribution subject to ASME license or copyright; see http://www.asme.org/terms/Terms_Use.cfm

B. A. Sayar
Assistant Professor,
Mechanical Engineering Department,
Stevens Institute of Technology,
Castle Point Station,
Hoboken, N. J. 07030
Mem. ASME

J. R. Baumgarten
Professor,
Department of Mechanical Engineering,
Iowa State University,
Ames, Iowa 50011
Mem. ASME

Pendulum Analogy for Nonlinear Fluid Oscillations in Spherical Containers

The nonlinear response of a pendulum model is compared to that of fluid motion in a spherical container undergoing lateral oscillations. It is observed that the pendulum does not duplicate the nonlinear response of the fluid except at a particular fluid height. The strong boundary curvature of the spherical container is blamed for this disagreement. Therefore, a cubic spring is included to provide sufficient elasticity to compensate for the boundary effects. The proper values for the coefficient of the cubic spring are found from an experimental observation of planar fluid motion in a spherical tank. It is also noted that, if the pendulum and the fluid are not constrained to a planar motion, at a certain excitation amplitude and frequency, both depart from the plane of excitation and rotate about a vertical axis. The upper and lower boundaries of this rotational motion of the fluid are obtained by a mathematical analysis of its analog pendulum model and compared to those measured experimentally. Mathematical predictions agreed more favorably with the experimental results after the inclusion of the cubic spring in the pendulum model.

Introduction

Mathematical analysis of fluid oscillations becomes extremely complicated if the generalized Navier-Stokes equations are employed, viscous fluid is used, and complex boundary conditions are applied. For engineering applications however, mechanical models serve the purpose and have been employed for a variety of container geometries [1]. Most of these models are designed to duplicate fluid motion in a linear range, and some in the nonlinear range; however, nonlinear modeling for spherical containers has not been attempted.

Sumner [2] has experimentally determined the parameters of a pendulum model for linear fluid oscillations in spherical containers. Sumner [3] has also measured damping of fluids oscillating in spherical containers, but has not incorporated his findings in his mechanical model. Abramson [4] has studied fluid sloshing in spherical tanks and has produced an experimental force-frequency response which has a softening character in the nonlinear range. On the other hand, Miles [5] has studied independently the response of a spherical pendulum under harmonic excitation at the support and has determined the frequency-amplitude limits beyond which the pendulum rotates about a vertical axis.

Contributed by the Applied Mechanics Division for publication in the JOURNAL OF APPLIED MECHANICS.
Discussion on this paper should be addressed to the Editorial Department, ASME, United Engineering Center, 345 East 47th Street, New York, N. Y. 10017, and will be accepted until two months after final publication of the paper itself in the JOURNAL OF APPLIED MECHANICS. Manuscript received by ASME Applied Mechanics Division, August, 1980; final revision, March, 1981.

The fluid oscillations in spherical containers exhibit similarity to the motion of a spherical pendulum in that both have softening response in the nonlinear range, and both depart from their planar oscillations at a particular excitation frequency-amplitude combination. In order to determine the adequacy of the same linear pendulum model [2] to duplicate the nonlinear response of fluid motion, the present study is conducted. First, to prevent the rotational motion of the fluid (swirl), a splitter plate was used parallel to the direction of excitation in the middle of the spherical tank and the horizontal slosh forces were measured by a load cell circuit. Second, the splitter plate was removed and the excitation amplitudes and frequencies were recorded at the instants when nonplanar motion just started. Mathematical force values and boundary limits were obtained from the analysis of the unconstrained pendulum model. Detailed analysis and further applications of the nonlinear pendulum model for fluid oscillations in spherical tanks are presented in reference [6].

Pendulum Model and Slosh Force

The pendulum model proposed by Sumner [2] duplicates the fluid oscillation in a spherical container in the linear range. However, in the nonlinear range the degree of softening of a pendulum may be different from that of the fluid motion, a fact to be determined in this research. A strong reason for a possible disagreement is the effect of curvature of the spherical container which tends to influence the restoring force of the fluid. For this reason an additional cubic spring is assumed attached to the pendulum to provide sufficient elasticity to compensate for the curvature effects of the container. To account

Copyright © 1981 by ASME
Downloaded 01 May 2010 to 171.66.16.249. Redistribution subject to ASME license or copyright; see http://www.asme.org/terms/Terms_Use.cfm

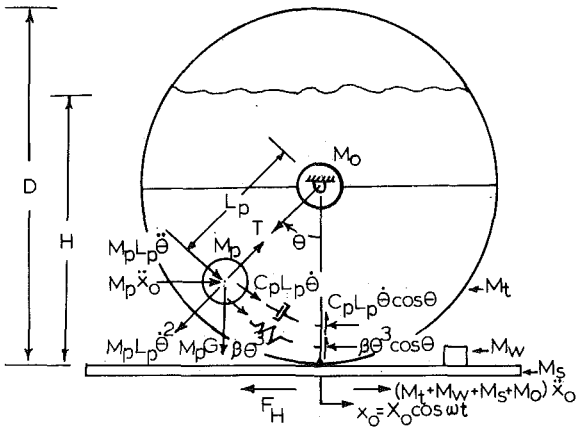


Fig. 1 Pendulum model for the spherical container partially filled with fluid

for damping, in case more viscous fluids are used, a dashpot is also attached to the same model designed in accordance with Sumner's proposed parameters. The schematic diagram of a spherical container partially filled with fluid and its analogous pendulum is shown in Fig. 1.

Referring to Fig. 1 which includes the inverse effective forces, and using D'Alembert's principle, the following equations can be written:

On the Tank and Its Attachments

$$\Sigma \text{ horizontal (external forces-effective forces)} = 0$$

$$-\beta\theta^3\cos\theta - F_H - T\sin\theta - C_pL_p\dot{\theta}\cos\theta + (M_t + M_w + M_s + M_0)\ddot{x}_0 = 0 \quad (1)$$

On the Pendulum

$$\Sigma \text{ radial (external forces-effective forces)} = 0$$

$$T - M_pG\cos\theta - M_pL_p\dot{\theta}^2 + M_p\ddot{x}_0\sin\theta = 0 \quad (2)$$

$$\Sigma \text{ tangential (external forces-effective forces)} = 0$$

$$C_pL_p\dot{\theta} + \beta\theta^3 + M_pG\sin\theta + M_p\ddot{x}_0\cos\theta + M_pL_p\ddot{\theta} = 0 \quad (3)$$

where G is the acceleration of gravity, F_H is the horizontal force, and M_p is the mass of the pendulum.

From 1, 2, and 3, the following equations for the slosh force and the pendulum motion can be written:

$$F_H = M\ddot{x}_0 - M_pL_p\dot{\theta}^2\sin\theta + M_pL_p\ddot{\theta}\cos\theta \quad (4)$$

$$\ddot{\theta} + 2\zeta_p\omega_p\dot{\theta} + \omega_p{}^2(\theta - \eta\theta^3) = \epsilon\cos\omega t \quad (5)$$

where

$$\eta = \tfrac{1}{6} - \beta/W_p \quad (6)$$

β is the coefficient of the cubic spring
$M = (M_s + M_t + M_w + M_0 + M_p)$
ζ_p is the viscous damping factor
ω_p is the natural frequency of the pendulum
$\epsilon = X_0/L_p$
ω is the excitation frequency
t is time
H is the fluid height

It should be noted that in the derivation of equation (5) $\sin\theta \simeq \theta - \theta^3/6$ and $\cos\theta \simeq 1 - \theta^2/2$ are substituted and terms of θ^4 and higher orders are discarded.

Equation (5) is Duffing's equation with damping term included and can be solved by assuming solutions of the form [5]:

$$\theta = \epsilon^{1/3}|a|\cos|\omega t - \phi| + \epsilon|a_3|\cos|3\omega t - \phi_3| + O(\epsilon)^{5/3} \quad (7)$$

where $|a|$ is a dimensionless amplitude factor and ϕ is the pendulum phase angle. Using the first term of the assumed solution and substituting in equation (5) one obtains

$$\frac{3}{4}\eta|a|^3 + V|a|^2 + \Omega_f{}^2\cos\phi = 0 \quad (8)$$

$$k|a| = \Omega_f\sin\phi \quad (9)$$

by eliminating ϕ from equations (8) and (9), one gets

$$\{|a|^2\}^3 + \frac{8V}{2}\{|a|^2\}^2 + \frac{16}{9\eta^2}(V^2 + k\Omega_f{}^2)\{|a|^2\} - \frac{16\Omega_f{}^4}{9\eta^2} = 0 \quad (10)$$

where $V = (\Omega_f{}^2 - 1)\epsilon^{-2/3}$ and $k = 2\zeta_p\epsilon^{-2/3}$ in the absence of damping.

On the other hand, the expression for the sloshing force, F_H (equation (4)), can be simplified as

$$F_H = W_p\Omega_f{}^2[(\epsilon/\mu)\cos\omega t + \theta\cos\theta + (A^2 - \theta^2)\sin\theta] \quad (11)$$

To obtain the maximum sloshing force, $|F_H|_{\max.}$, the following condition must hold:

$$dF_H/dt = 0$$

From this condition equation (11) yields

$$[\sin^2\Phi]^3 + \frac{2B}{C}[\sin^2\Phi]^2 + \frac{B^2 + E^2}{C^2}[\sin^2\Phi] - \frac{E^2}{C^2} = 0 \quad (12)$$

where

$$A = \epsilon^{1/3}|a|,$$

$$B = \left[(\epsilon/\mu A)\cos\phi - \frac{A^2}{2}(A^2 + 7) + 1\right],$$

$$C = \frac{A^2}{2}(9 + A^2)$$

$$E = (\epsilon/\mu A)\sin\phi$$

$$\Phi = \omega t - \phi$$

$$W_p = M_pG$$

$\mu = M_p/M$, mass ratio

Swirl or Rotation Boundaries

When the splitter plate is removed from the spherical tank, the fluid rotates about a vertical axis at a particular frequency and lateral excitation amplitude. The spherical pendulum, if not constrained, also exhibits similar behavior. This phenomena has been discovered earlier and has been studied both mathematically and experimentally by Hutton [7] and Berlot [8] for small amplitudes of fluid oscillations in cylindrical tanks. Bauer [9] has developed later, a mechanical model to duplicate the nonlinear fluid oscillation and to predict the swirl boundaries more accurately and has used a cylindrical container geometry for his analysis. However to include the expanding and contracting curvature effects of a spherical geometry below and above $H/D = 0.5$, in oppose to the constant circular cross section of a cylinder, further investigation seems appropriate.

Considering the pendulum model capable of leaving the plane of excitation and eliminating the damper (water viscosity is assumed negligible), one can use Miles approach [5] and for the class of differential equations

$$\left[\frac{d^2}{dt^2} + \frac{G}{L_p}\right]\theta - \frac{G}{\eta L_p}\theta^3 + \frac{1}{2}\theta\left[\frac{d^2}{dt^2} + \frac{G}{L_p}\right]\alpha^2 = \epsilon\omega^2\cos\omega t \quad (13)$$

$$\left[\frac{d^2}{dt^2} + \frac{G}{L_p}\right]\alpha - \frac{G}{\eta L_p}\alpha^3 + \frac{1}{2}\alpha\left[\frac{d^2}{dt^2} + \frac{G}{L_p}\right]\theta^2 = 0 \quad (14)$$

governing the motion of a spherical pendulum with a cubic spring, the stability boundaries can be investigated.

Using a perturbation method, and assuming the solutions

$$\theta = \epsilon^{1/3}[f_1(\Lambda)\cos\omega t + f_2(\Lambda)\sin\omega t] \quad (15)$$

and

$$\alpha = \epsilon^{1/3}[f_3(\Lambda)\cos\omega t + f_4(\Lambda)\sin\omega t] \quad (16)$$

Downloaded 01 May 2010 to 171.66.16.249. Redistribution subject to ASME license or copyright; see http://www.asme.org/terms/Terms_Use.cfm

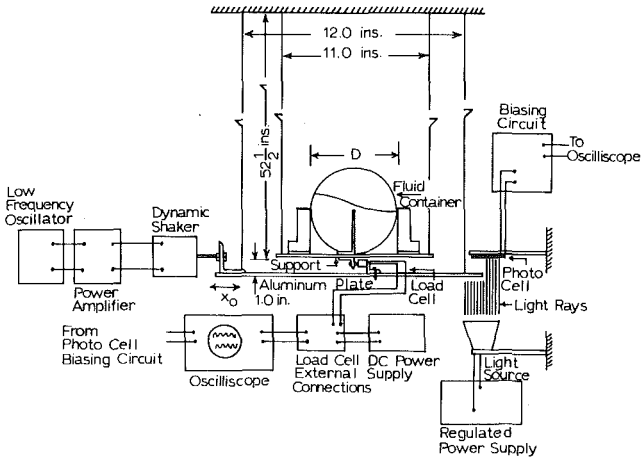


Fig. 2 Experimental setup for forced vibrations

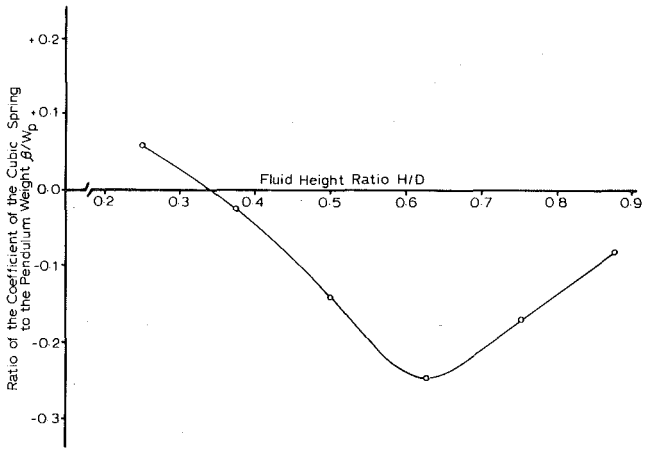


Fig. 4 Coefficients of the cubic spring

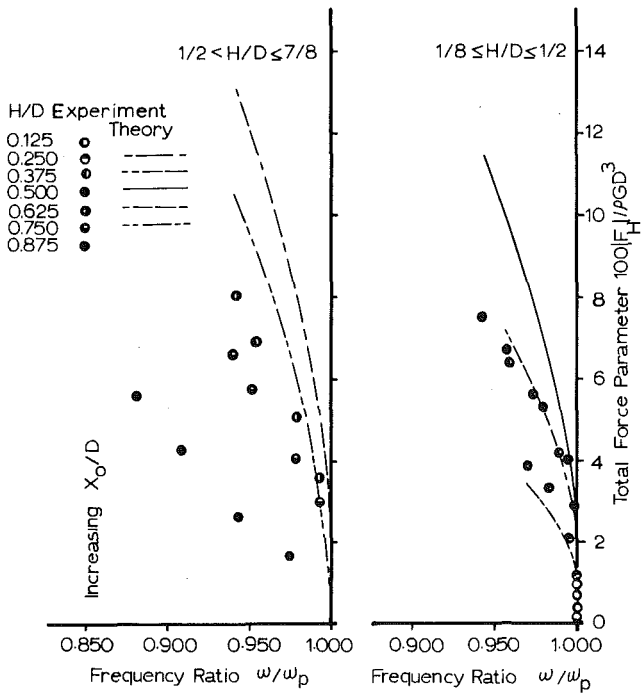


Fig. 3 Comparison of pendulum and fluid force response without the cubic spring ($\beta = 0$)

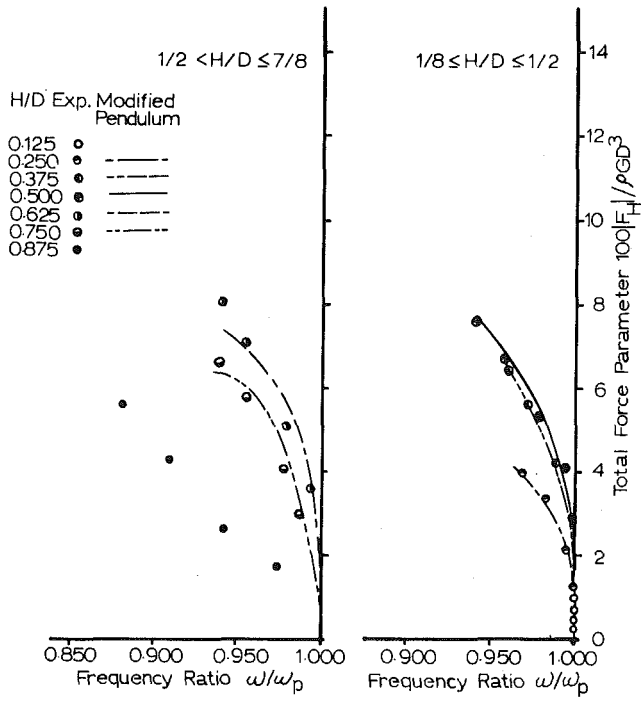


Fig. 5 Force response of modified pendulum as compared to the experiments ($\beta \neq 0$)

where $\Lambda = \frac{1}{2}\epsilon^{2/3}\omega t$, and α is the second coordinate of the spherical pendulum, the stability boundaries corresponding to the singularities are obtained as follows:

If $f_i(0)$ is a singular point, a perturbation solution of the form

$$f_i(\Lambda) = f_i(0) + C_i \exp[(\lambda - k)\Lambda] \tag{17}$$

can be assumed for $|C_i| \ll 1$. Here λ is a measure of stability of the pendulum. Such a solution approaches the singular point if $\lambda < k$, remains in the neighborhood of the singular point if $\lambda = k$, or departs from this neighborhood if $\lambda > k$. Therefore, the singular point is stable if $\lambda \leq k$ and unstable if $\lambda > k$. After manipulating similar to Miles [5] the following boundaries can be obtained:

1 Lower Boundaries

$$a = \left(\frac{2\Omega_f{}^2}{3\eta}\right)^{1/3} \tag{18}$$

2 Upper Boundaries

$$a = -\left(\frac{2\Omega_f{}^2}{9\eta}\right)^{1/3} \tag{19}$$

After substitution of equations (18) and (19) into equation (8), setting $\phi = 0$, and simplifying, the lower boundaries will be

$$X_0/D = \frac{0.4444(L_p/D)}{\sqrt{\eta}} \frac{(1 - \Omega_f{}^2)^{3/2}}{\Omega_f{}^2} \tag{20}$$

and the upper boundaries will be

$$X_0/D = \frac{0.61972(L_p/D)}{\sqrt{\eta}} \frac{(\Omega_f{}^2 - 1)^{3/2}}{\Omega_f{}^2} \tag{21}$$

where X_0 is the excitation amplitude; D is the tank diameter; and Ω_f is the frequency ratio ω/ω_p.

Comparison to Experimental Results

An experimental setup as shown in Fig. 2 was constructed and sloshing forces of the moving fluid were measured by the load cell.

Downloaded 01 May 2010 to 171.66.16.249. Redistribution subject to ASME license or copyright; see http://www.asme.org/terms/Terms_Use.cfm

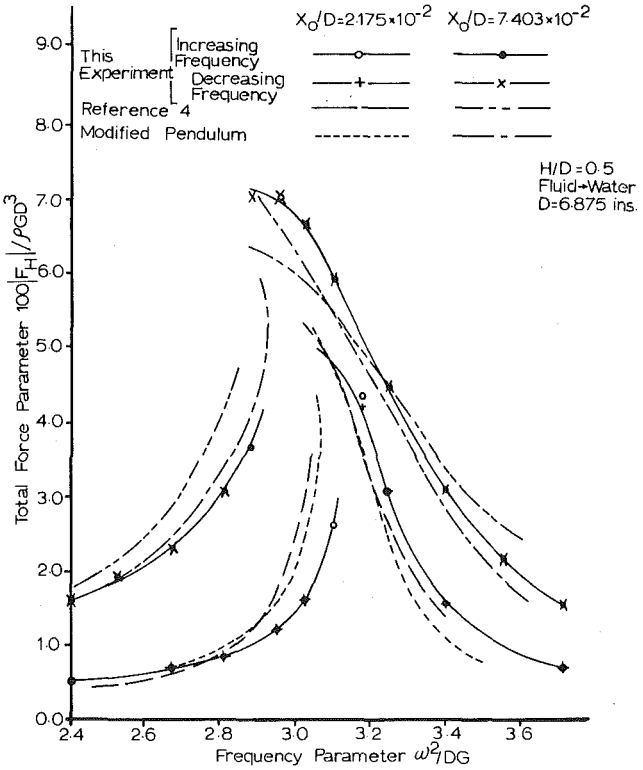


Fig. 6 Force response of the modified pendulum, present experiment, and Abramson's [4] experiments

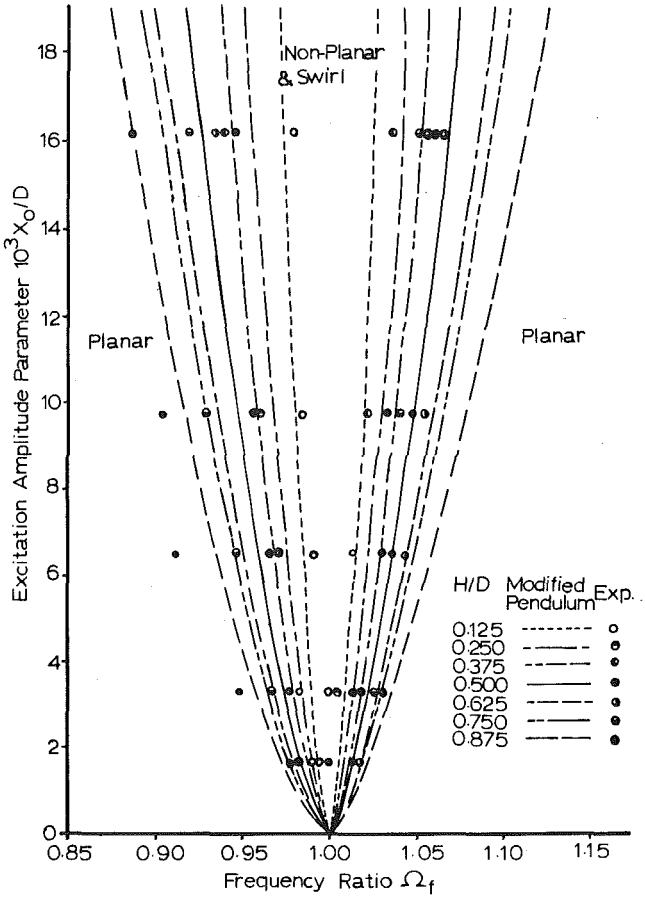


Fig. 7 Stability boundaries of the modified pendulum

Excitations were provided by the input circuit shown and output amplitudes (for other purposes) were measured by the photo-cell circuit.

Water was used as the fluid medium in a transparent plastic spherical container 6.875 in. in diameter.

Maximum pendulum forces without the cubic spring ($\beta = 0$) were calculated from equation (11) and were compared to those measured by the load cell. The comparison was not favorable except for a fluid height ratio of $H/D = 0.375$. This comparison is shown in Fig. 3.

To compensate for the curvature effect, the cubic spring with experimentally determined coefficients was employed. The β/W_p values plotted in Fig. 4 are selected for the proper fit of force response curves as shown in Fig. 5.

To insure the adequacy of the modified pendulum to duplicate the nonlinear fluid motion in spherical tanks, the pendulum response, the results of this experimentation, and that of Abramson's [4] were compared as shown in Fig. 6. The comparison proved satisfactory.

When the splitter plate was removed, the frequencies and excitation amplitudes corresponding to swirl were measured and compared to the mathematical boundaries obtained from equations (20) and (21). This comparison is shown in Fig. 7. The agreement is acceptable except at $H/D = 0.875$ at which the modified pendulum failed to duplicate fluid motion. Such disagreements are equally noticeable in Figs. 3 and 5. At this fluid height the fluid breaks into droplets and streamers which climb the dome of the container and pour over to the other side of the tank. Obviously the pendulum analogy fails at such fluid heights and this type of modeling becomes meaningless.

Conclusions

A pendulum model designed in accordance with Sumner's [2] criteria duplicates linear fluid oscillations in a spherical container very well. However this model fails to predict the fluid response in the nonlinear range except at the neighborhood of $H/D = 0.375$.

The pendulum model so designed will duplicate, with acceptable accuracy, the nonlinear fluid motion if a cubic spring is added to compensate for the curvature effects arising from the spherical geometry. Furthermore, if the modified pendulum is not restricted to planar motion, the stability boundaries of the model correspond to the swirl boundaries of the fluid motion in spherical containers.

Acknowledgments

The authors extend their sincere thanks to Professors Sisto, Tricamo, and Speziale for reading the manuscript of this paper and their valuable suggestions.

References

1 Abramson, H. N., "The Dynamic Behavior of Liquids in Moving Containers," NASA, SP-106.

2 Sumner, I. E., "Experimentally Determined Pendulum Analogy of the Liquid Sloshing in Spherical and Oblate-Spheroidal Tanks," NASA, TN-2737, Lewis Research Center, Cleveland, Ohio, Apr. 1965.

3 Sumner, I. E., and Stofan, A. J., "An Experimental Investigation of the Viscous Damping of Liquid Sloshing in Spherical Tanks," NASA, TN D-1991, Lewis Research Center, Cleveland, Ohio, Dec. 1963.

4 Abramson, H. N., Chu, W. H., and Kana, D. D., "Some Studies of Nonlinear Lateral Sloshing in Rigid Containers," ASME JOURNAL OF APPLIED MECHANICS, Vol. 33, Dec. 1966, pp. 777–784.

5 Miles J. W., "Stability of Forced Oscillation of a Spherical Pendulum," *Quarterly of Applied Mathematics*, Vol. 20, No. 1, Apr. 1962, pp. 21–32.

6 Sayar, B. A., "Fluid Slosh Dampers," PhD thesis presented to the Graduate Division of Georgia Institute of Technology, 1971, pp. 1–36.

7 Hutton, R. E., "An Investigation of Resonant, Nonlinear, Nonplanar Free Surface Oscillations of a Fluid," NASA TN D-1870, 1963.

8 Berlot, R. R., "Production of Rotation in a Confined Liquid Through Translation Motion of the Boundaries," ASME JOURNAL OF APPLIED MECHANICS, Vol. 26, Dec. 1959, pp. 513–516.

9 Bauer, H. F., "Nonlinear Mechanical Model for Description of Propellant Sloshing," *AIAA Journal*, Vol. 4, No. 9, Sept. 1966, pp. 1662–1668.

Downloaded 01 May 2010 to 171.66.16.249. Redistribution subject to ASME license or copyright; see http://www.asme.org/terms/Terms_Use.cfm

P. J. Yoder
Assistant Professor,
Department of Mechanical Engineering,
Georgia Institute of Technology,
Atlanta, Ga. 30332

W. D. Iwan
Professor of Applied Mechanics,
Division of Engineering and
Applied Science,
104-44,
California Institute of Technology,
Pasadena, Calif. 91125
Mem. ASME

On the Formulation of Strain-Space Plasticity With Multiple Loading Surfaces

An alternative formulation of plasticity is discussed in which strain rather than stress serves as the independent variable. The relationship of the formulation to traditional plasticity is examined for cases of both single and multiple loading surfaces. Conditions are given under which the stress and strain-space formulations are equivalent.

Introduction

The usual approach to solving dynamics problems in continuum mechanics is to let the displacements be the independent variables of the problem. Toward this end, one eliminates stress from the equation of motion in favor of strain and then expresses strain in terms of displacement. However, a displacement formulation will be possible only if stress is expressible as a functional of strain. A solution may then be sought by any of a number of standard methods, including separation of variables, integral transforms, and numerical techniques. The use of numerical techniques is particularly attractive when the problem is nonlinear, as is the case for plastic material behavior.

In typical *explicit* numerical algorithms, the displacement increments are found directly, or explicitly, from Newton's second law. For each time step the strain increment is obtained first, and then the stress is updated accordingly. It is obviously helpful in this case if stress may be expressed in terms of strain and strain history. A similar observation is true for *implicit* numerical algorithms, which construct a global stiffness based upon the current strain and then solve a matrix equation involving this stiffness to obtain the displacement increments. The process of forming the stiffness begins on the local level, and it is at this stage that the constitutive law enters in. So long as the law gives stress as a functional of strain, the required local stiffness can readily be extracted.

Plasticity, however, has traditionally been formulated in just the opposite manner. The classical theory treats the current stress and stress increment as independent variables and based on these, computes the corresponding strain increment. From the standpoint of numerical implementation, this poses two difficulties. First, the material response at any given instant depends upon the very quantities for which a solution is sought. This difficulty has been handled in different ways by various investigators [1–3]. However, the result is that the estimated response may be considerably in error for those parts of the domain which have just turned plastic or just reverted to elastic behavior. Moreover, additional computer storage is required and it is necessary to compute all the stresses whether or not they are of practical significance.

A second difficulty arises from the fact that conventional plasticity gives the response in terms of a compliance instead of a stiffness. Thus, after deciding whether the behavior is to be elastic or plastic, one still has to invert a matrix [1, 4].

The difficulties associated with stress-space plasticity become even more vexing when multiple yield surfaces are employed. Suppose, for example, that the last available stress state happens to lie at the intersection of m yield surfaces. Then, without knowing the stress increment, it is impossible to say which of these surfaces are active and which are inactive. There are 2^m cases in all, and each gives a different candidate for the elastoplastic stiffness. The only way to proceed is by trial and error, and there may conceivably be several "correct" answers, or perhaps none at all. It is little wonder therefore that most investigators [4, 5] sidestep this issue by forcing the surfaces to obey some arbitrary nesting rule. This must, however, be done at the expense of abandoning such features as Prager's kinematic hardening law, which specifies that a yield surface translate in the direction of its normal at the point of loading.

An alternative which avoids the inversion problem altogether, is to use a strain-space plasticity formulation. Drucker remarked about this possibility as early as 1950 [6] but he stopped short of working out the details of a strain-space formulation. Other investigators have approached plasticity from a strain-space perspective. Lenskii [7], for example, developed a model for permanently deforming media, which has since been applied to soils [8]. The model avoids the use of yield surfaces, though, and bears little resemble to traditional plasticity. In work much more akin to that reported herein, Naghdi [9, 10] showed that many of the familiar features of stress-space plasticity

Contributed by the Applied Mechanics Division and presented at the Winter Annual Meeting, Washington, D. C., November 15–20, 1981, of THE AMERICAN SOCIETY OF MECHANICAL ENGINEERS.

Discussion on this paper should be addressed to the Editorial Department, ASME, United Engineering Center, 345 East 47th Street, New York, N. Y. 10017, and will be accepted until March 1, 1982. Manuscript received by ASME Applied Mechanics Division, October, 1980; final revision, March, 1981. Paper No. 81-WA/APM-20.

Copyright © 1981 by ASME

Downloaded 01 May 2010 to 171.66.16.249. Redistribution subject to ASME license or copyright; see http://www.asme.org/terms/Terms_Use.cfm

can be carried over to strain space. He did not, however, establish equivalence between stress and strain-space loading criteria for either single or multiple loading surfaces. Nor did he pursue the possibility of expressing stress as a functional of strain for either of these cases. These topics are dealt with in this paper.

Background

To appreciate the underlying difference between a strain-space and stress-space plasticity formulation, consider a simple, one-dimensional example. Let the mechanical response of the system considered be bilinear, as suggested by the stress-strain diagrams of Figs. 1(a) and 1(b). In the traditional formulation of plasticity, the stress plays the role of the independent variable. The total strain is found by computing the strain which would arise elastically from the given stress and adding a plastic strain ϵ^P, as indicated in Fig. 1(a). Thus

$$\epsilon = \kappa\sigma + \epsilon^P \tag{1}$$

Clearly, an alternative approach would be to define an elastic interval along the strain axis such that yielding will occur only if the strain lies on the boundary of this interval and if the strain increment is directed outward from it. Then, the strain is taken as an independent variable in describing the material state. To find the stress, one could first compute that stress which would result elastically from the current strain ϵ and then subtract the amount by which the stress has been *relaxed* on account of plastic effects. Hence,

$$\sigma = c\epsilon - \sigma^R \tag{2}$$

This is shown in Fig. 1(b). Equations (1) and (2) are identical in form except for a minus sign. In a similar way, the whole framework of stress-space plasticity may be made to carry over to a strain-space formulation.

The Relaxation Surface in Strain-Space

Turning to the case of three-dimensional loading, let the elastic behavior be characterized by a Young's modulus E and a Poisson's ratio ν. Then, for elastic deformation increments,

$$d\sigma_{ij} = c_{ijkl}d\epsilon_{kl}, \quad d\epsilon_{ij} = \kappa_{ijkl}d\sigma_{kl} \tag{3}$$

where

$$c_{ijkl} = \frac{E}{1+\nu}\left(\delta_{ik}\delta_{jl} + \frac{\nu}{1-2\nu}\delta_{ij}\delta_{kl}\right),$$
$$\kappa_{ijkl} = \frac{1}{E}\left[(1+\nu)\delta_{ik}\delta_{jl} - \nu\delta_{ij}\delta_{kl}\right] \tag{4}$$

and where δ denotes the Kronecker delta.

Once the loading becomes plastic, the strain $\boldsymbol{\epsilon}$ will be taken as the independent variable for strain-space plasticity. By analogy to the scalar case, the stress will then be found by subtracting a stress relaxation $\boldsymbol{\sigma}^R$ from the stress which would arise elastically from the current strain. That is,

$$\boldsymbol{\sigma} = \mathbf{c}\boldsymbol{\epsilon} - \boldsymbol{\sigma}^R \tag{5}$$

In some contexts it will be useful to keep track not only of the cumulative stress relaxation but also of some measure of how much relaxation (of whatever sign) has occurred throughout the history of the material sample. Accordingly, let

$$L = \int\left(\frac{2}{3}d\sigma_{ij}^R d\sigma_{ij}^R\right)^{1/2} \tag{6}$$

where the integration is to be carried out over the entire stress history.

By analogy to the one-dimensional case, one expects the incremental elastic equation (3) to prevail in some simply connected region of strain space which, in the course of time, may undergo translation and/or distortion. The instantaneous strain state always lies either within the region or on its boundary. This region may be defined by a function $\hat{F}$ such that at all times $\hat{F}(\boldsymbol{\epsilon}, \boldsymbol{\sigma}^R, L) \leq 0$. Stress relaxation will be possible only if

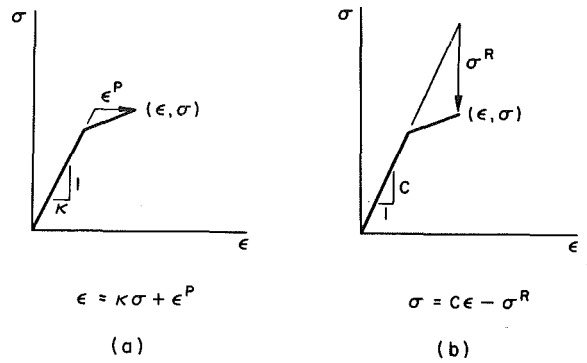


Fig. 1

$$\hat{F}(\boldsymbol{\epsilon}, \boldsymbol{\sigma}^R, L) = 0 \tag{7}$$

The boundary given by (7) will be called the *relaxation surface*. Since $\boldsymbol{\epsilon}$ and $\boldsymbol{\sigma}^R$ are symmetric, $\hat{F}$ will be symmetric with respect to both $\boldsymbol{\epsilon}$ and $\boldsymbol{\sigma}^R$. In what follows, it will be assumed that the partial derivatives of $\hat{F}$ with respect to ϵ_{ij}, σ_{ij}^R, and L exist and are continuous and that the gradient of $\hat{F}$ never vanishes.

In the case of three-dimensional loading, it is necessary to somehow assign a *direction* to the stress relaxation increment. Toward this end, one might consider an idealized experiment in which the strain throughout a material specimen moves out to the relaxation surface, advances incrementally into it, and then returns to the original state. This is the approach used by Drucker [11], as a springboard for his familiar stability hypothesis. However, rather than pursuing Drucker's analysis further, it suffices here to assume (i) that the incremental step into the plastic region of strain space produces a stress relaxation increment of the same order of magnitude; (ii) that the stress relaxation increment is independent of the recent elastic history; and (iii) that the work done on the specimen during the excursion is nonnegative. It follows readily from these assumptions that

$$d\sigma_{ij}^R = dl\frac{\partial\hat{F}}{\partial\epsilon_{ij}}, \quad dl > 0, \tag{8}$$

and that the relaxation surface is convex [12].

A similar normality rule has traditionally been used in stress-space plasticity, although its inclusion in the theory restricts somewhat the range of materials that can be modeled. In particular, experiments show that normality in stress space is violated for soils [13] and other materials that undergo permanent volume changes. One way to accommodate such behavior is to discard Assumption (iii) and allow for the possibility that plastic loading may at times feed mechanical energy into the system. The prospect of negative hysteretic damping, though, seems questionable. Another approach is to abandon Assumption (ii) and let the plastic increment depend upon the recent elastic history. This option becomes workable only if one can devise an expedient alternative to the traditional loading surface. Lacking that, the present exposition will retain traditional loading surfaces and embrace a normality rule as well.

Consistent with the foregoing, it will be assumed that the first invariants of stress and strain are linearly related to one another. Ruling out inelastic changes in volume implies that the relaxation surface is parallel to the dilatational axis $\epsilon_1 = \epsilon_2 = \epsilon_3$. The surface must therefore be a cylinder cutting at right angles through the plane of zero dilatation, $\epsilon_1 + \epsilon_2 + \epsilon_3 = 0$. The locus of intersection will hereafter be referred to as the *relaxation curve*. Once the shape of this curve is specified, the geometry of the entire relaxation surface will be determined.

Further restrictions on the relaxation curve result if it is required that the criterion for plastic response be isotropic for the virgin material and that the compressive and extensional elastic limits be equal. These requirements, along with convexity, lead to hexagonal inner and outer bounds on the relaxation curve which are identical to their stress-space counterparts [12].

Downloaded 01 May 2010 to 171.66.16.249. Redistribution subject to ASME license or copyright; see http://www.asme.org/terms/Terms_Use.cfm

Elastoplastic Constitutive Laws

Since the foregoing results follow from assumed properties of the virgin material, they really apply only to the *initial* configuration of the relaxation surface. The next question which must be addressed is how the relaxation surface evolves as the material undergoes plastic deformation. A number of answers to this question have found their way into the stress-space literature, but two stand out on account of their widespread acceptance. For isotropic hardening it is assumed that the yield surface expands (or shrinks) uniformly like a balloon. For kinematic hardening, the surface is assumed to translate parallel to the instantaneous normal at the point of loading.

Strain-Space Formulation. In the absence of any compelling rationale on how to handle the strain-space problem, it seems reasonable to incorporate analogs of isotropic and kinematic hardening. Accordingly, assume that with each increment $d\boldsymbol{\sigma}^R$, the relaxation surface translates a distance $cd\boldsymbol{\sigma}^R$ in strain space and simultaneously grows larger or smaller through the influence of the parameter L, defined by equation (6). Let c also depend upon L, in the interest of further generality, and thus set

$$\hat{F}(\boldsymbol{\epsilon}, \boldsymbol{\sigma}^R, L) = F([\boldsymbol{\epsilon} - c(L)\boldsymbol{\sigma}^R]') - k^2(L), \tag{9}$$

The prime will be used throughout to signify a deviatoric component.

The full elastoplastic constitutive law follows directly upon application of the so-called consistency condition, which says that during stress relaxation each strain increment leads from one plastic state to another, equation (7) holding both before and after. In view of (6), (8), and (9), this yields

$$d\sigma_{ij}^R = \frac{1}{D}\frac{\partial \hat{F}}{\partial \epsilon_{ij}}\frac{\partial \hat{F}}{\partial \epsilon_{mn}} d\epsilon_{mn} \tag{10}$$

where

$$D = c\frac{\partial \hat{F}}{\partial \epsilon_{ij}}\frac{\partial \hat{F}}{\partial \epsilon_{ij}} + \left(\frac{\partial \hat{F}}{\partial \epsilon_{ij}}\sigma_{ij}^R\frac{dc}{dL} + 2k\frac{dk}{dL}\right)\cdot\left(\frac{2}{3}\frac{\partial \hat{F}}{\partial \epsilon_{kl}}\frac{\partial \hat{F}}{\partial \epsilon_{kl}}\right)^{1/2} \tag{11}$$

It is assumed that $D \in (O, \infty)$. Ruling out negative values for D assures that during stress relaxation each strain increment takes a step into the current relaxation surface. The size of D governs the extent to which plastic effects dominate. For D positive but tending toward zero, a small increment of strain beyond the relaxation surface leads to a large increase in stress relaxation. Thus the relaxation surface corresponds to a nearly immovable barrier in strain space. On the other hand, as $D \to \infty$, a great deal of strain can be accommodated with minimal stress relaxation. In this limit, therefore, the material reverts to Hookean linearity.

Since $\hat{F}$ depends only upon the deviatoric part of $\boldsymbol{\epsilon}$, it may be shown that $\partial \hat{F}/\partial \epsilon_{mn}$ is purely deviatoric. Hence, if $\boldsymbol{\sigma}^R = \mathbf{0}$ initially, it will, from (10), remain purely deviatoric and (9) simplifies to

$$\hat{F}(\boldsymbol{\epsilon}, \boldsymbol{\sigma}^R, L) = F[\boldsymbol{\epsilon}' - c(L)\boldsymbol{\sigma}^R] - k^2(L) \tag{12}$$

Collecting together the pertinent statements just mentioned, one arrives at the constitutive law $[C]$ for strain-space plasticity:

$$\hat{F}(\boldsymbol{\epsilon}, \boldsymbol{\sigma}^R, L) \le 0 \text{ always.} \tag{a}$$

If

$$\hat{F}(\boldsymbol{\epsilon}, \boldsymbol{\sigma}^R, L) = 0 \tag{b}$$

and

$$\frac{\partial \hat{F}}{\partial \epsilon_{ij}} d\epsilon_{ij} > 0, \tag{c}$$

then

$$d\sigma_{ij} = c_{ijkl}d\epsilon_{kl} - \frac{1}{D}\frac{\partial \hat{F}}{\partial \epsilon_{ij}}\frac{\partial \hat{F}}{\partial \epsilon_{mn}} d\epsilon_{mn} \tag{d}$$

If (b) or (c) is violated, then

$$d\sigma_{ij} = c_{ijkl}d\epsilon_{kl}. \tag{e}$$

Throughout the foregoing, D and all derivatives of $\hat{F}$ are to be evaluated at the current values of $\boldsymbol{\epsilon}$, $\boldsymbol{\sigma}^R$, and L.

Stress-Space Formulation. The analysis just delineated parallels step by step the conventional, stress-space presentation of plasticity. This being true, there is little point in deriving here the constitutive relations for the stress-space theory. Suffice it to note that the criteria for plastic flow are expressible in terms of a yield function

$$\hat{\Phi}(\boldsymbol{\sigma}, \boldsymbol{\epsilon}^P, \Lambda) = \Phi(\boldsymbol{\sigma}' - \gamma(\Lambda)\boldsymbol{\epsilon}^P) - \kappa^2(\Lambda). \tag{13}$$

The roles played by $\hat{\Phi}$, Φ, $\boldsymbol{\sigma}$, $\boldsymbol{\epsilon}^P$, Λ, γ, and κ correspond, respectively, to those of $\hat{F}$, F, $\boldsymbol{\epsilon}$, $\boldsymbol{\sigma}^R$, L, c, and k.

For stress-space plasticity, the analytical form of the constitutive law turns out to depend strongly on the sign of the scalar quantity

$$\Delta = \gamma\frac{\partial \hat{\Phi}}{\partial \sigma_{ij}}\frac{\partial \hat{\Phi}}{\partial \sigma_{ij}} + \left(\frac{\partial \hat{\Phi}}{\partial \sigma_{ij}}\epsilon_{ij}^P\frac{d\gamma}{d\Lambda} + 2\kappa\frac{d\kappa}{d\Lambda}\right)\cdot\left(\frac{2}{3}\frac{\partial \hat{\Phi}}{\partial \sigma_{kl}}\frac{\partial \hat{\Phi}}{\partial \sigma_{kl}}\right)^{1/2} \tag{14}$$

All three cases are of physical interest; they correspond respectively to strain hardening ($\Delta > 0$), "ideal" (or "perfect") plasticity ($\Delta = 0$), and strain softening ($\Delta < 0$) behavior. No such distinction is necessary for the strain-space formulation.

For strain hardening, $\Delta > 0$, the constitutive law $[\Gamma]$ for stress-space plasticity may be summarized as follows:

$$\hat{\Phi}(\boldsymbol{\sigma}, \boldsymbol{\epsilon}^P, \lambda) \le 0 \quad \text{always.} \tag{α}$$

If

$$\hat{\Phi}(\boldsymbol{\sigma}, \boldsymbol{\epsilon}^P, \Lambda) = 0 \tag{β}$$

and

$$\frac{\partial \hat{\Phi}}{\partial \sigma_{ij}} d\sigma_{ij} > 0, \tag{γ}$$

then

$$d\epsilon_{ij} = \kappa_{ijkl}d\sigma_{kl} + \frac{1}{\Delta}\frac{\partial \hat{\Phi}}{\partial \sigma_{ij}}\frac{\partial \hat{\Phi}}{\partial \sigma_{mn}} d\sigma_{mn} \tag{δ}$$

If (β) or (γ) is violated, then

$$d\epsilon_{ij} = \kappa_{ijkl}d\sigma_{kl}. \tag{ϵ}$$

Somewhat similar relationships are obtained for the cases of ideal plasticity and strain softening.

Equivalence of the Elastoplastic Formulations

A cursory glance at constitutive laws $[C]$ and $[\Gamma]$ will reveal that they are virtually identical in form. It is therefore not surprising that they can be made equivalent. Under Hooke's law, deviatoric stress and strain increments are simply proportional to one another. This readily allows the sets of state variables $(\boldsymbol{\sigma}, \boldsymbol{\epsilon}^P, \Lambda)$ and $(\boldsymbol{\epsilon}, \boldsymbol{\sigma}^R, L)$ to be related as follows.

Let $\boldsymbol{\sigma}$ and $\boldsymbol{\epsilon}$ denote the current values of stress and strain, and assume that the elastic response and compliance tensors take the form indicated in (4). By analogy to (5) and (6), define $\boldsymbol{\epsilon}^P$ and Λ such that

$$\boldsymbol{\epsilon} = \boldsymbol{\kappa}\boldsymbol{\sigma} + \boldsymbol{\epsilon}^P \tag{15}$$

$$\Lambda = \int\left(\frac{2}{3}d\epsilon_{ij}^P d\epsilon_{ij}^P\right)^{1/2}. \tag{16}$$

Assume that $\boldsymbol{\sigma}^R = \boldsymbol{\epsilon}^P = \mathbf{0}$ for the virgin material and let $F(\boldsymbol{\epsilon}, \boldsymbol{\sigma}^R, L)$ and $\Phi(\boldsymbol{\sigma}, \boldsymbol{\epsilon}^P, \Lambda)$ be defined by (12) and (13). Suppose that either constitutive law $[C]$ or constitutive law $[\Gamma]$ holds; then the state of the material may equivalently be described by the state variables $(\boldsymbol{\epsilon}, \boldsymbol{\sigma}^R, L)$ or $(\boldsymbol{\sigma}, \boldsymbol{\epsilon}^P, \Lambda)$, and either set may be obtained from the other through the transformations

$$\begin{aligned}\boldsymbol{\sigma}^R &= \frac{E}{1+\nu}\boldsymbol{\epsilon}^P \\ L &= \frac{E}{1+\nu}\Lambda\end{aligned} \tag{17}$$

The constitutive models associated with $[C]$ and $[\Gamma]$ will be

Downloaded 01 May 2010 to 171.66.16.249. Redistribution subject to ASME license or copyright; see http://www.asme.org/terms/Terms_Use.cfm

equivalent only if the stress- and strain-space plastic parameters are properly related to one another. If, in addition to the aforementioned hypotheses it is assumed that

$$F(\mathbf{x}') = \Phi\left(\frac{E}{1+\nu}\mathbf{x}'\right) \quad \text{on} \quad \text{sym}\,(\mathbb{R}^3); \tag{18}$$

$$c(x) = \frac{1+\nu}{E}\left[\frac{1+\nu}{E}\gamma\left(\frac{1+\nu}{E}x\right)+1\right] \quad \text{on} \quad \mathbb{R}; \tag{19}$$

$$k(x) = \kappa\left(\frac{1+\nu}{E}x\right) \quad \text{on} \quad \mathbb{R}. \tag{20}$$

then,

$$k(L) = \kappa(\Lambda) \tag{21}$$

$$c(L) = \frac{1+\nu}{E}\left[\frac{1+\nu}{E}\gamma(\Lambda)+1\right], \tag{22}$$

$$F([\boldsymbol{\epsilon} - c(L)\boldsymbol{\sigma}^R]') = \Phi([\boldsymbol{\sigma} - \gamma(\Lambda)\boldsymbol{\epsilon}^P]') \tag{23}$$

$$\hat{F}(\boldsymbol{\epsilon}, \boldsymbol{\sigma}^R, L) = \hat{\Phi}(\boldsymbol{\sigma}, \boldsymbol{\epsilon}^P, \Lambda) \tag{24}$$

$$\frac{\partial \hat{F}}{\partial \epsilon_{ij}}(\boldsymbol{\epsilon}, \boldsymbol{\sigma}^R, L) = \frac{E}{1+\nu}\frac{\partial \hat{\Phi}}{\partial \sigma_{ij}}(\boldsymbol{\sigma}, \boldsymbol{\epsilon}^P, \Lambda) \tag{25}$$

$$\frac{dk(L)}{dL} = \frac{1+\nu}{E}\frac{d\kappa(\Lambda)}{d\Lambda} \tag{26}$$

$$\frac{dc(L)}{dL} = \left(\frac{1+\nu}{E}\right)^3\frac{d\gamma(\Lambda)}{d\Lambda}, \tag{27}$$

where it is understood that in each of the foregoing, $(\boldsymbol{\epsilon}, \boldsymbol{\sigma}^R, L)$ is related to $(\boldsymbol{\sigma}, \boldsymbol{\epsilon}^P, \Lambda)$ through (5), (15), and (17) [12]. Equations (21)–(27) link a number of the quantities arising in the strain-space theory with their more familiar counterparts from stress space.

The question of the equivalence of the stress and strain-space loading criterion has not been dealt with explicitly in the past [10, 11] and accordingly deserves some attention here. From the foregoing, it follows that

$$D = \Delta + \frac{E}{1+\nu}\frac{\partial \hat{\Phi}}{\partial \sigma_{mn}}\frac{\partial \hat{\Phi}}{\partial \sigma_{mn}} = \Delta + \frac{1+\nu}{E}\frac{\partial \hat{F}}{\partial \epsilon_{mn}}\frac{\partial \hat{F}}{\partial \epsilon_{mn}}. \tag{28}$$

$$(e) \text{ or } (\epsilon) \Rightarrow \frac{\partial \hat{F}}{\partial \epsilon_{kl}}d\epsilon_{kl} = \frac{\partial \hat{\Phi}}{\partial \sigma_{kl}}d\sigma_{kl}, \tag{29}$$

and *if* Δ is nonzero,

$$(d) \text{ or } (\delta) \Rightarrow \frac{1}{D}\frac{\partial \hat{F}}{\partial \epsilon_{kl}}d\epsilon_{kl} = \frac{1}{\Delta}\frac{\partial \hat{\Phi}}{\partial \sigma_{kl}}d\sigma_{kl} \tag{30}$$

This result follows directly from the properties of the inner products of deviatoric tensors and algebraic manipulation of the hypotheses [12].

It will be seen that for the case of strain hardening, for which Δ is positive as well as D, statements (29) and (30) assure that $(\partial \hat{F}/\partial \epsilon_{ij})d\epsilon_{ij}$ and $(\partial \hat{\Phi}/\partial \sigma_{ij})d\sigma_{ij}$ will always take on the same sign. It makes no difference, therefore, which of these inner products is used as a loading criterion.

That constitutive laws $[C]$ and $[\Gamma]$ are equivalent follows from statements (29) and (30), the fact that D and Δ are both positive, the definitions of the response and compliance tensors, and the observation that, under Hooke's law, deviatoric stress and strain increments are proportional to one another.

From (18), it will be seen that for a given constitutive behavior, the stress-space and strain-space models will possess loading surfaces that differ only in scale. Thus the strain-space counterpart of the Tresca yield surface is a regular hexagonal cylinder centered along the line $\epsilon_1 = \epsilon_2 = \epsilon_3$; and similarly for the von Mises surface.

One attractive feature of the strain-space formulation is its versatility. The conventional theory requires one set of constitutive relations for strain hardening, another for ideal plasticity, and yet another for strain softening. In strain space, on the other hand, just one set can accommodate all three cases. This simplification can be very significant in computer applications.

Equations (19) and (20) lead to one further observation. For isotropic hardening/softening (in stress space), $\gamma = 0$ and κ grows or shrinks as the plastic deformations proceed. Corresponding to this, $c = (1+\nu)/E$ and k varies like κ, so the loading surface in strain space translates as well as changing size. In a similar way, the strain-space models equivalent to kinematic hardening/softening and to perfect plasticity feature translating relaxation surfaces. This may seem odd in the case of perfect plasticity, but it is in fact fortunate. In stress-space computer codes for ideal plasticity, the stress point tends under loading to follow the local tangent and inevitably winds up outside the surface on account of convexity. Accordingly, investigators have had to devise schemes for returning the stress point to the yield surface [14]. The best way to handle the problem, however, may well be to circumvent it by working in strain space.

Generalization to Multiple Loading Surfaces

The constitutive models thus far considered allow for only a bilinear approximation to the observed relationship between stress and strain. Accordingly, a number of authors [5, 6, 15] have suggested extending plasticity theory to incorporate several loading surfaces. If the surfaces behave like those just described and their respective plastic contributions are summed, the resulting stress-strain law will be multilinear. This is true whether stress or strain-space surfaces are used. In light of the foregoing results, one might expect the two alternatives to yield equivalent formulations, but such is not the case. It will be shown that for equivalence to hold, there must be coupling between the surfaces. This gives rise to some analytical complications.

Incrementally Elastic Behavior. Suppose that incrementally elastic deformations are governed by response and compliance tensors of the form (4). Let it further be assumed that deviations from Hookean linearity are accounted for *either* by subtracting stress relaxations *or* by adding plastic strains, leading to the relationships

$$[C]: \quad \boldsymbol{\sigma} = \mathbf{c}\boldsymbol{\epsilon} - \sum_{\phi \in \mathcal{N}} \boldsymbol{\sigma}_\phi^R$$

or

$$[\Gamma]: \quad \boldsymbol{\epsilon} = \boldsymbol{\kappa}\boldsymbol{\sigma} + \sum_{\phi \in \mathcal{N}} \boldsymbol{\epsilon}_\phi^P \tag{31}[1]$$

where

$$\mathcal{N} = \{1, 2, 3, \ldots, N\}$$

and N is the total number of loading surfaces.

Assume that the material behaves elastically at the outset of loading so that initially $\boldsymbol{\sigma}_\phi^R = \boldsymbol{\epsilon}_\phi^P = \mathbf{0}$ for all ϕ. After loading, some plastic effects will have set in. As a measure of the influence of these effects, define L_ϕ and Λ_ϕ for each surface through relations analogous to (6) and (16). Further, let the loading surfaces depend upon parameters $\boldsymbol{\mathcal{S}}_\phi$ and $\boldsymbol{\mathcal{E}}_\phi$ defined by

$$\boldsymbol{\mathcal{S}}_\phi = \sum_{\substack{\psi \in \mathcal{N} \\ \psi \neq \phi}} \boldsymbol{\sigma}_\psi^R, \quad \boldsymbol{\mathcal{E}}_\phi = \sum_{\substack{\psi \in \mathcal{N} \\ \psi \neq \phi}} \boldsymbol{\epsilon}_\psi^P \quad \forall\, \phi \in \mathcal{N}. \tag{32}$$

This represents a specific form of coupling between surfaces. Other forms of coupling could be assumed but will in general not lead to an equivalence between the stress- and strain-space formulations.

For each constitutive model, there are N loading surfaces, and the current value of strain (or stress, for the stress-space theory) can never lie outside any of these surfaces. Thus

$$\begin{aligned} \hat{F}_\phi(\boldsymbol{\epsilon}, \boldsymbol{\mathcal{S}}_\phi, \boldsymbol{\sigma}_\phi^R, L_\phi) \leq 0 \\ \hat{\Phi}_\phi(\boldsymbol{\sigma}, \boldsymbol{\mathcal{E}}_\phi, \boldsymbol{\epsilon}_\phi^P, \Lambda_\phi) \leq 0 \end{aligned} \quad \forall\, \phi \in \mathcal{N} \tag{33}$$

At any given instant the ϕth surface can contribute to the mechanical response only if $\phi \in \mathcal{W}$ (or Ω), where

[1] The summation convention will apply only to Latin indices. Whenever there is summation over a Greek index, this will be indicated explicitly.

Downloaded 01 May 2010 to 171.66.16.249. Redistribution subject to ASME license or copyright; see http://www.asme.org/terms/Terms_Use.cfm

$$\mathcal{W} = \{\phi | \phi \in \mathcal{N} \quad \text{and} \quad \hat{F}_\phi(\boldsymbol{\epsilon}, \boldsymbol{\mathcal{E}}_\phi, \boldsymbol{\sigma}^R_\phi, L_\phi) = 0\}$$
$$\Omega = \{\phi | \phi \in \mathcal{N} \quad \text{and} \quad \hat{\Phi}_\phi(\boldsymbol{\sigma}, \boldsymbol{\mathcal{E}}_\phi, \boldsymbol{\epsilon}^P_\phi, \Lambda_\phi) = 0\} \tag{34}$$

If the instantaneous strain (or stress) happens to lie inside all N surfaces, Hooke's law will prevail incrementally.

The Hardening Law. In order to satisfy (33), the loading surfaces must in general move during plastic deformations. To prescribe these motions it suffices to assume an analytical form for the functions $\hat{F}_\phi$ (or $\hat{\Phi}_\phi$). Accordingly, set

$$\begin{aligned} \hat{F}_\phi(\boldsymbol{\epsilon}, \boldsymbol{\mathcal{E}}_\phi, \boldsymbol{\sigma}^R_\phi, L_\phi) &\equiv F(\boldsymbol{\epsilon} - b\boldsymbol{\mathcal{E}}_\phi - c\boldsymbol{\sigma}^R_\phi) - [k_\phi(L_\phi)]^2 \\ \hat{\Phi}_\phi(\boldsymbol{\sigma}, \boldsymbol{\mathcal{E}}_\phi, \boldsymbol{\epsilon}^P_\phi, \Lambda_\phi) &\equiv \Phi(\boldsymbol{\sigma} - \beta\boldsymbol{\mathcal{E}}_\phi - \gamma\boldsymbol{\epsilon}^P_\phi) - [\kappa_\phi(\Lambda_\phi)]^2 \end{aligned} \quad \forall\, \phi \in \mathcal{N} \tag{35}$$

Letting $\hat{F}_\phi$ and $\hat{\Phi}_\phi$ satisfy symmetry, continuity and differentiability conditions similar to those for the single surface case. Hypothesis (35) can accommodate either isotropic or kinematic plasticity, or, for that matter, any linear combination of the two. What is more, through parameters b and β, it allows for coupling amongst the surfaces. The strain-space models obtained by setting b to zero lend themselves readily to the calculation of elastoplastic *stiffness*.

Normality and Volumetric Strains. It was argued in the case of single-surface models that unless the stress relaxation increment points in the outward normal direction, plastic deformations may at times feed mechanical energy into the system. In view of the discussion associated with statement (34), this same reasoning applies to one of the surfaces making up a multiple-surface model, provided it is possible for the strain to lie on that surface while remaining inside of all of the others. This in fact will be true for each of the surfaces so long as the hardening law permits them to overlap. Accordingly, let

$$d\sigma^R_{ij\phi} = \begin{cases} \dfrac{1}{\sqrt{D_\phi}} x_\phi \mathrm{H}(x_\phi) \dfrac{\partial \hat{F}_\phi}{\partial \epsilon_{ij}} & \forall\, \phi \in \mathcal{W} \\ 0 & \forall\, \phi \in \mathcal{N} - \mathcal{W} \end{cases} \tag{36}$$

$$d\epsilon^P_{ij\phi} = \begin{cases} \dfrac{1}{\sqrt{\Delta_\phi}} \xi_\phi \mathrm{H}(\xi_\phi) \dfrac{\partial \hat{\Phi}_\phi}{\partial \sigma_{ij}} & \forall\, \phi \in \Omega \\ 0 & \forall\, \phi \in \mathcal{N} - \Omega \end{cases} \tag{37}$$

where H is the Heaviside step function, and

$$\begin{aligned} D_\phi &= c \frac{\partial \hat{F}_\phi}{\partial \epsilon_{ij}} \frac{\partial \hat{F}_\phi}{\partial \epsilon_{ij}} + 2k_\phi(L_\phi) \frac{dk_\phi}{dL_\phi} \left(\frac{2}{3} \frac{\partial \hat{F}_\phi}{\partial \epsilon_{ij}} \frac{\partial \hat{F}_\phi}{\partial \epsilon_{ij}} \right)^{1/2} \\ &\geq C \frac{\partial \hat{F}_\phi}{\partial \epsilon_{ij}} \frac{\partial \hat{F}_\phi}{\partial \epsilon_{ij}}, \quad C > 0 \end{aligned} \tag{38}$$

$$\begin{aligned} \Delta_\phi &= \gamma \frac{\partial \hat{\Phi}_\phi}{\partial \sigma_{ij}} \frac{\partial \hat{\Phi}_\phi}{\partial \sigma_{ij}} + 2\kappa_\phi(\Lambda_\phi) \frac{d\kappa_\phi}{d\Lambda_\phi} \left(\frac{2}{3} \frac{\partial \hat{\Phi}_\phi}{\partial \epsilon_{ij}} \frac{\partial \hat{\Phi}_\phi}{\partial \sigma_{ij}} \right)^{1/2} \\ &\geq \Gamma \frac{\partial \hat{\Phi}_\phi}{\partial \sigma_{ij}} \frac{\partial \hat{\Phi}_\phi}{\partial \sigma_{ij}}, \quad \Gamma > 0 \\ &\forall\, \phi \in \mathcal{N} \end{aligned} \tag{39}$$

The terms x_ϕ and ξ_ϕ will be determined from the principle of consistency. Throughout it is understood that all partial derivatives are evaluated holding $\boldsymbol{\mathcal{E}}_\phi$, $\boldsymbol{\sigma}^R_\phi$, L_ϕ, $\boldsymbol{\mathcal{E}}_\phi$, $\boldsymbol{\epsilon}^P_\phi$, and Λ_ϕ constant.

As in the bilinear case, the loading functions have been here assigned a mathematical form which rules out any plastic influence upon the volumetric component of strain [12].

Consistency and Loading Criteria. The quantities D_ϕ and Δ_ϕ, introduced somewhat arbitrarily in the foregoing, arise as in the one-surface models upon invoking the principle of consistency. For brevity's sake the discussion will focus upon the strain-space theory. The analysis in stress-space proceeds similarly.

Suppose the strain point lies at some instant on the ϕth relaxation surface. In view of (36) and the principle of consistency, this surface will undergo loading if and only if

$$x_\phi = \frac{1}{\sqrt{D_\phi}} \frac{\partial \hat{F}_\phi}{\partial \epsilon_{ij}} d\epsilon_{ij} - b \sum_{\substack{\psi \in \mathcal{W} \\ \psi \neq \phi}} \frac{1}{\sqrt{D_\phi D_\psi}} \frac{\partial \hat{F}_\phi}{\partial \epsilon_{ij}} \frac{\partial \hat{F}_\psi}{\partial \epsilon_{ij}} x_\psi \mathrm{H}(x_\psi) > 0 \tag{40}$$

In the case of unloading, the inequality is violated, and all that is known about x_ϕ is that it is nonpositive.

If there is just one relaxation surface, or if b equals zero, the above gives an explicit criterion for loading. The more general case is less tractable. To apply the loading test to any one surface, one needs to know in advance how much stress relaxation the other surfaces are generating. This coupling significantly complicates the situation and raises the question of just how many different sets of relaxation increments might satisfy the loading conditions at any given instant. For the constitutive model to be useful, there must clearly be one and only one.

To establish the existence of at least one set of relaxation increments, it suffices to find a set of x_ϕ (or ξ_ϕ, for the stress-space theory) satisfying

$$x_\phi = \frac{1}{\sqrt{D_\phi}} \frac{\partial \hat{F}_\phi}{\partial \epsilon_{ij}} d\epsilon_{ij} - b \sum_{\substack{\psi \in \mathcal{W} \\ \psi \neq \phi}} \frac{1}{\sqrt{D_\phi D_\psi}} \frac{\partial F_\phi}{\partial \epsilon_{ij}} \frac{\partial \hat{F}_\psi}{\partial \epsilon_{ij}} x_\psi \mathrm{H}(x_\psi) \quad \forall\, \phi \in \mathcal{W} \tag{41}$$

$$\xi_\phi = \frac{1}{\sqrt{\Delta_\phi}} \frac{\partial \hat{\Phi}_\phi}{\partial \epsilon_{ij}} d\sigma_{ij} - \beta \sum_{\substack{\psi \in \Omega \\ \psi \neq \phi}} \frac{1}{\sqrt{\Delta_\phi \Delta_\psi}} \frac{\partial \hat{\Phi}_\phi}{\partial \sigma_{ij}} \frac{\partial \hat{\Phi}_\phi}{\partial \sigma_{ij}} \xi_\psi \mathrm{H}(\xi_\psi) \quad \forall\, \phi \in \omega \tag{42}$$

This can be accomplished through a modified Picard iteration scheme, so long as

$$\begin{aligned} (N-1)|b/C| &< 1 \\ (N-1)|\beta/\Gamma| &< 1 \end{aligned} \tag{43}$$

This approach, incidently, provides a means of generating solutions to the problem. In a similar way, it can be shown using (43) that any two sets of x_ϕ satisfying (41) lead to the same set of stress relaxation increments when substituted back into (36).

Equivalence of the Strain and Stress-Space Models. As in the foregoing, constitutive relations $[C]$ and $[\Gamma]$ will be equivalent to one another if the corresponding model parameters are appropriately interrelated. Accordingly, let each individual loading surface satisfy the hypotheses set out previously for the single loading surface model. Furthermore, let

$$b = \frac{1+\nu}{E} \left(\frac{1+\nu}{E} \beta + 1 \right) \tag{44}$$

Then, if

$$\left.\begin{aligned} \boldsymbol{\sigma}^R_\phi &= \frac{E}{1+\nu} \boldsymbol{\epsilon}^P_\phi \\ L_\phi &= \frac{E}{1+\nu} \Lambda_\phi \end{aligned}\right\} \quad \forall\, \phi \in \mathcal{N} \tag{45}$$

at some moment, *at that same instant*,

$$\left.\begin{aligned} d\boldsymbol{\sigma}^R_\phi &= \frac{E}{1+\nu} d\boldsymbol{\epsilon}^P_\phi \\ dL_\phi &= \frac{E}{1+\nu} d\Lambda_\phi \end{aligned}\right\} \quad \forall\, \phi \in \mathcal{N} \tag{46}$$

To establish this result, one shows first that relations analogous to (24), (25), and (28) hold at the instant when (45) is valid. Suppose $[C]$ holds and that $\{x_\phi\}$ satisfies (41). Then, manipulating the foregoing results one finds that the positive elements of $\{\sqrt{\Delta_\phi/D_\phi} x_\phi\}$ satisfy (42). The negative elements would also satisfy (42) if they were merely rescaled by a factor D_ϕ/Δ_ϕ. Thus, for each ϕ, the quantity $\sqrt{\Delta_\phi/D_\phi} x_\phi$ satisfies either the loading or the unloading criteria in *stress* space. Equations (46) follow, then, from the uniqueness principle and (37). A similar argument applies when $[\Gamma]$ holds.

It now follows readily that the stress-space and strain-space models are equivalent.

Downloaded 01 May 2010 to 171.66.16.249. Redistribution subject to ASME license or copyright; see http://www.asme.org/terms/Terms_Use.cfm

Assertion. Under the hypotheses represented by equations (4), (6), (16), (31)–(39) and (41)–(44), equations (45) hold throughout the history of the motion. Moreover, constitutive relations $[C]$ and $[\Gamma]$ are equivalent.

Proof: Re (45). The fact that $\dot{\epsilon}_\phi^P = \sigma_\phi^R = 0$ initially implies that (45) also holds initially, in (6) and (16). But then so does (46). Thus (45) holds at the next instant, and, continuing the argument, at all subsequent times.

$Re[C] \Rightarrow [\Gamma]$. Multiply through $[C]$ by κ, and note, in view of (4), that since σ_ϕ^R is purely deviatoric, $\kappa\sigma_\phi^R = (1 + \nu)/\mathrm{E}\ \sigma_\phi^R$. The result follows, then, upon invoking (45).

$Re[\Gamma] \Rightarrow [C]$. Similar to the aforementioned.

Concluding Remarks

Once an equivalence has been established for multiple-surface models, it is only reasonable to inquire into the range of stress-strain behavior that can be accommodated by this equivalence. Statements (38) and (39) require not only that the D_ϕ but also the Δ_ϕ take on positive values. Thus, upon setting $N = 1$, one recovers only the strain-hardening case of the single loading-surface analysis. When there are several surfaces, statements (43) also come into play. This leads to a number of interesting consequences.

Consider a stress-space model with N uncoupled surfaces ($\beta = 0$). In conformity with the Assertion, the strain-space equivalent will feature coupling, with $b = (1 + \nu)/E$, as dictated by (44). To make this strain-space model well behaved, one must also impose (43), so $C > (N - 1)(1 + \nu)/E$. For purely kinematic hardening, it may be shown that this requires that the ultimate deviatroic, elastoplastic stiffness for the original stress-space model be zero when $N = 2$ and tend toward one-half the elastic value as $N \to \infty$. The Assertion guarantees the existence of an equivalent strain-space model only if the original stress-space model conforms to these specifications.

The analysis proceeds similarly for models with uncoupled strain-space surfaces. Oddly enough, though, the results are different. So long as the constitutive law falls within the strain-hardening regime, the Assertion guarantees the existence of an equivalent model in stress space, no matter how many surfaces are involved. In light of this paradoxical asymmetry, it should be emphasized that the Assertion gives only sufficient conditions for equivalence. No attempt has been made to delineate a set of necessary conditions.

From the standpoint of practical applications, the Assertion is useful but somewhat disappointing. The prospect of shifting from strain space to stress space or vice versa is considerably less appealing in the case of multiple-surface models than for the single-surface models. This is because the models featuring uncoupled surfaces are by far the easiest to use, and by virtue of (44) these cannot be made equivalent to one another. To achieve, in stress space, constitutive behavior the same as that given by an uncoupled strain-space model, one must resort to coupling, and vice versa.

From a practical viewpoint, the main conclusion to be drawn from the Assertion is that, for multiple-surface models, it is no easy matter to invert elastoplastic stiffnesses and compliances. Since the uncoupled strain-space models give stiffnesses quite readily, they appear to show great promise for applications involving extensive use of numerical techniques. Accordingly, a computer algorithm for a model of this type has been developed and used in the investigation of a variety of example problems [12].

In summary, the basis for a strain-space plasticity theory has been discussed herein. Starting with linear isotropic elasticity, most of the familiar features of traditional yield surfaces are carried over to strain-space. A normality rule is adopted, and inelastic volume changes are ruled out. In the multiple-surface case, a specific form of coupling is allowed between the surfaces, although more general forms could certainly be envisioned. Within the realm of problems characterized by these limitations, the strain-space formulation is believed to possess significant advantages over its stress-space analog. This is particularly true in applications which involve multiple yield surfaces or extensive numerical computation. With a somewhat more firm foundation thus laid, it is hoped that investigators will be encouraged to further explore the application of the strain-space formulation.

References

1 Joyner, W. B., "A Method for Calculating Nonlinear Seismic Response in Two Dimensions," *Bulletin of the Seismological Society of America*, Vol. 65, No. 5, Oct. 1975, pp. 1337–1357.

2 Hughes, T. J. R., and Prévost, J. H., "DIRT: A Finite-Element Program for the Static Analysis of Nonlinear Anisotropic Elastoplastic Hysteretic Continua Subjected to Complicated Loading Paths," California Institute of Technology, May 1977.

3 Kalev, I., and Gluck, J., "Finite-Element Analysis for Cyclic Plasticity," *Journal of the Engineering Mechanics Division*, ASCE, Vol. 103, No. EM1, Feb. 1977, pp. 189–201.

4 Prévost, J. H., "Mathematical Modelling of Monotonic and Cyclic Undrained Clay Behavior," *International Journal for Numerical and Analytical Methods in Geomechanics*, Vol. 1, No. 2, Apr.–Jun. 1977, pp. 195–216.

5 Mróz, Z., "On the Description of Anisotropic Workhardening," *Journal of the Mechanics and Physics of Solids*, Vol. 15, May 1967, pp. 163–175.

6 Drucker, D. C., "Stress-Strain Relations in the Plastic Range: A Survey of Theory and Experiment," Office of Naval Research Contract N7 onr-358, Brown University, Dec. 1950.

7 Lenskii, V. S., "Analysis of Plastic Behaviour of Metals Under Complex Loading," *Plasticity: Proceedings of the Second Symposium on Naval Structural Mechanics*, eds., Lee, E. H., and Symonds, P. S., Pergamon Press, New York, 1960, pp. 259–278.

8 Palmer, A. C., and Pearce, J. A., "Plasticity Theory Without Yield Surfaces," *Proceedings of the Symposium on the Role of Plasticity in Soil Mechanics*, Cambridge, 1973, pp. 188–200.

9 Naghdi, P. M., and Trapp, J. A., "The Significance of Formulating Plasticity Theory With Reference to Loading Surfaces in Strain Space," *International Journal of Engineering Science*, Vol. 13, No. 9/10, Sept./Oct. 1975, pp. 785–797.

10 Naghdi, P. M., "Some Constitutive Restrictions in Plasticity," *Constitutive Equations in Viscoplasticity: Computational and Engineering Aspects*, AMD, ASME, Vol. 20, 1976, pp. 79–93.

11 Drucker, D. C., "Some Implications of Work Hardening and Ideal Plasticity," *Quarterly of Applied Mathematics*, Vol. 7, No. 4, Jan. 1950, pp. 411–418.

12 Yoder, P. J., "A Strain-Space Plasticity Theory and Numerical Implementation," PhD Thesis, California Institute of Technology, 1981.

13 Prévost, J. H., "Plasticity Theory for Soil Stress-Strain Behavior," *Journal of the Engineering Mechanics Division*, ASCE, Vol. 104, No. EM5, Oct. 1978, pp. 1177–1194.

14 Krieg, R. D., and Krieg, D. B., "Accuracies of Numerical Solution Methods for the Elastic-Perfectly Plastic Model," ASME *Journal of Pressure Vessel Technology*, Vol. 99, No. 4, Nov. 1977, pp. 510–515.

15 Iwan, W. D., "On a Class of Models for the Yielding Behavior of Continuous and Composite Systems," ASME JOURNAL OF APPLIED MECHANICS, Vol. 34, Sept. 1967, pp. 612–617.

Downloaded 01 May 2010 to 171.66.16.249. Redistribution subject to ASME license or copyright; see http://www.asme.org/terms/Terms_Use.cfm

G. J. Weng

Associate Professor
Department of Mechanics
and Materials Science,
Rutgers University,
New Brunswick, N.J. 08903
Mem. ASME

A Self-Consistent Scheme for the Relaxation Behavior of Metals

We identify in this paper that stress relaxation in metals is a "strain-free" process. The corresponding self-consistent relations between the strain, and stress variations of a grain and of its aggregate are derived from Eshelby's solution of an ellipsoidal inclusion. It is shown that, under such a process, the strain in a more favorably oriented grain continues to rise and that its stress decreases more drastically than that of the aggregate; conversely, for a less favorably oriented grain, its strain decreases and its stress relaxes less. The self-consistent relations are supplemented with a temperature-dependent, physically consistent constitutive equation for the slip system. Such an equation enables us to determine the single crystal constants at one temperature from the polycrystal data at another temperature; it also makes the self-consistent scheme applicable to the varying-temperature environment. The established theory was finally applied to predict the relaxation behavior of an RR-59 aluminum alloy under combined stress; the results showed reasonably good agreement with the experimental data.

Introduction

It was recently pointed out [1] that creep in metals, unlike plastic deformation, is a truly "stress-free" process in the sense of Eshelby [2], and that Kröner's self-consistent relation [3] could be used to derive the polycrystal creep properties from those of its constituent grains. Hill's model [4], on the other hand, should be used with a modified constraint tensor involving the elastic moduli, instead of the tangent moduli, of the matrix. This is a welcome consequence because, though Hill's model is more rigorous in plasticity, it is "implicit" in nature and requires an iterative process in computations. Kröner's model, on the other hand, is characterized by a given constraint tensor, and for the calculation of creep strains of metals his model is now simple, yet rigorous.

When a metal or polycrystalline aggregate is subjected to a constant strain at elevated temperature, stress relaxation takes place. Several theories (for instance, see [5, 6]) have been proposed to calculate the relaxation behavior of metals under combined stress. Most of these theories, however, are purely phenomenological and, because they neglect the physical basis of relaxation process in each grain, and grain interactions, the estimates sometimes could be inaccurate. It appears that very few investigations have been directed toward this micromechanical process, and to the author's knowledge the only one published is that of Lin, et al. [7], who employed Lin's "equivalent body force" [8], originally proposed for time-independent plasticity. In their generally successful effort, however, no quantitative comparison with experimental data was provided.

In this paper we follow the spirit of [1] and identify that relaxation in metals, contrary to creep, is a strain-free process. This property allows us to use Eshelby's solution again to derive a self-consistent relation for the relaxation behavior of a polycrystalline material. The constitutive equations proposed in [1] will be extended to include the effect of temperature on creep rate, so that the self-consistent relations can be used to determine the creep or relaxation behavior of metals even at a different, or under changing temperature. By means of an inverse method [9] the additional single crystal constants which appear in the new constitutive equations will be determined from the creep data of its polycrystal. The self-consistent scheme finally will be applied to calculate the relaxation behavior of an aluminum alloy, and the results compared with von Mises' theory, and experiments. We again restrict our consideration to the temperature range below half the melting point (T_m), so that crystallographic slip is the main cause of creep deformation in metals. The elastic anisotropy of the grain, and grain rotation, will be neglected for simplicity under small deformation.

Self-Consistent Determination of Relaxation: A Strain-Free Stress Problem

The self-consistent relation for a relaxation process of course can be derived from the self-consistent relation for creep, and then superimposed by an incremental stress to offset the produced incremental creep strain. But it is far more elegant and revealing to consider stress relaxation directly from a strain-free process, so that the intricacies of the micromechanics between an inclusion and the matrix can be fully realized at each stage.

We consider an ellipsoidal inclusion (grain) embedded in an infi-

Contributed by the Applied Mechanics Division and presented at the Winter Annual Meeting, Washington, D.C., November 15–20, 1981, of THE AMERICAN SOCIETY OF MECHANICAL ENGINEERS.

Discussion on this paper should be addressed to the Editoral Department, ASME, United Engineering Center, 345 East 47th Street, New York, N.Y. 10017, and will be accepted until March 1, 1982. Manuscript received by ASME Applied Mechanics Division. November, 1980; final revision, March, 1981. Paper No. 81-WA/APM-14.

Copyright © 1981 by ASME

Downloaded 01 May 2010 to 171.66.16.249. Redistribution subject to ASME license or copyright; see http://www.asme.org/terms/Terms_Use.cfm

nitely extended matrix (aggregate). At any generic state the stress and total strain of the inclusion are denoted by σ and ϵ, and those of the matrix specified by the barred (averaging) quantities $\bar{\sigma}$ and $\bar{\epsilon}$, respectively. The total strain is the sum of elastic and creep strains. In a relaxation test $\bar{\epsilon}$ is held constant, and to maintain such a state, creep strain increment continuously exchanges for elastic strain increment with a consequent reduction of stress. The total strain of grain ϵ in general still varies with time, because creep deformation in the aggregate is heterogeneous. Now suppose that during a relaxation process the incremental creep strains of the inclusion and matrix are, respectively, given as $d\epsilon^c$ and $d\bar{\epsilon}^c$. The self-consistent relation can be derived from the following two steps:

1 Let the matrix and inclusion relax freely according to their respective incremental creep strains. The corresponding stress relaxations are given by

$$d\bar{\sigma} = -\mathcal{L}d\bar{\epsilon}^c, \tag{1}$$

$$d\sigma_1 = -\mathcal{L}d\epsilon^c, \tag{2}$$

where $\mathcal{L}$ is their isotropic, elastic moduli tensor, and the subscript refers to the said step. At this stage these two materials remain compatible to each other. The equilibrium condition over the grain boundary, however, is violated; this is characterized by an excessive layer of surface traction $d\mathbf{T}^*$, given by $d\mathbf{T}^* = (d\sigma_1 - d\bar{\sigma})\,\mathbf{m}$, where $\mathbf{m}$ is the unit normal to the surface of inclusion.

2 To bring these two materials to an equilibrium state, we apply an opposite surface traction $-d\mathbf{T}^*$ on the bonded interface. Then, according to Eshelby's solution [2] the generated strain and stress in the inclusion due to this traction are given by

$$d\epsilon = \mathbf{S}(d\epsilon^c - d\bar{\epsilon}^c), \tag{3}$$

$$d\sigma_2 = \mathcal{L}\mathbf{S}(d\epsilon^c - d\bar{\epsilon}^c), \tag{4}$$

where $\mathbf{S}$ is Eshelby's transformation matrix. Though $-d\mathbf{T}^*$ also disturbs the stress field of the matrix, its disturbance is confined to the neighborhood of grain boundary and therefore gives only insignificant contribution to the overall stress of the infinitely extended matrix.

Thus, at the end of a relaxation process, the matrix stress is reduced by equation (1), and the inclusion stress changed by $d\sigma = d\sigma_1 + d\sigma_2$, or

$$d\sigma = -\mathcal{L}(\mathbf{I} - \mathbf{S})d\epsilon^c - \mathcal{L}\mathbf{S}d\bar{\epsilon}^c, \tag{5}$$

where $\mathbf{I}$ is the fourth rank identity tensor. Note that the average of equation (3) over all grain orientations vanishes and the average of equation (5) leads to equation (1) of the aggregate. These relations thus satisfy the condition of "self-consistency."

If the shape of inclusion is spherical, equations (3) and (5) can be simplified to

$$d\epsilon = \beta(d\epsilon^c - d\bar{\epsilon}^c), \tag{6}$$

$$d\sigma = -2\mu(1-\beta)d\epsilon^c - 2\mu\beta d\bar{\epsilon}^c, \tag{7}$$

where μ is the shear modulus, and β, in terms of Poisson's ratio ν, is given by $\beta = 2(4-5\nu)/15(1-\nu)$. For most metals, $0 < \beta < 1$. It is thus evident from (6) and (7) that in a relaxation test, the total strain of a more favorably oriented grain, characterized by $d\epsilon^c > d\bar{\epsilon}^c$, increases and its stress relaxes more than that of the aggregate. Conversely, for a less favorably oriented grain, its total strain decreases and its stress relaxes less.

In general, when the matrix is under an arbitrary strain-controlled process, an additional strain $d\bar{\epsilon}$ and stress $\mathcal{L}d\bar{\epsilon}$ should be added to (3) and (5), respectively, to account for the strain and stress changes of the grain. This additional contribution is purely elastic, since the creep rate is independent of stress increment. Such a self-consistent relation then can be used to calculate the relaxation behavior of a polycrystalline aggregate under a constant strain (static relaxation) or changing strain (step or dynamic relaxation) condition.

Constitutive Equations

The relaxation behavior of metals is basically caused by creep deformation. Creep in metals, depending on the lattice structure, stress and temperature levels, could be caused by dislocation glide, climb, lattice twinning, diffusion in the grain and along the grain boundary. Lattice twinning usually occurs in crystals with low symmetry (e.g., hexagonal close-packed crystals). Since most structural metals have a cubic lattice their creep deformation is not likely to be caused by such a process. Also, at high stress (say, $10^{-3} \sim 10^{-1}$ of the theoretical strength) and below $T_m/2$, as illustrated in Ashby's normalized stress-homologous temperature deformation maps (see [10] for example), creep in metals is primarily caused by dislocation glide, or crystallographic slip. During the glide motion dislocation interactions, intersections and structural changes lead to active and latent hardening in slip systems. The hardening behavior hinders the flow process and causes the creep rate to decrease even at a constant stress, until a steady state is reached. The transient creep therefore needs to be described in accordance with the theory of work hardening. Recently the nature of major hardening mechanisms in metal crystals was analyzed, and classified into two categories: isotropic and kinematic hardening [11]. This analysis leads to a mixed hardening law for the slip system. Based on such a theory one set of constitutive equations for the steady and transient creep rates of the ith slip system, respectively denoted by $\overset{(i)}{\dot{\gamma}}{}^c_s$ and $\overset{(i)}{\dot{\gamma}}{}^c_t$, was proposed in [1]:

$$\overset{(i)}{\dot{\gamma}}{}^c_s = \kappa \overset{(i)}{\tau}{}^{\lambda}, \tag{8}$$

$$\overset{(i)}{\dot{\gamma}}{}^c_t = \eta\left\{\zeta \overset{(i)}{\tau}{}^{\lambda} - \left[\alpha \sum_j |\overset{(j)}{\gamma}{}^c_t| + (1-\alpha)\sum_j \cos \overset{(i,j)}{\theta} \cos \overset{(i,j)}{\phi}\, \overset{(j)}{\gamma}{}^c_t\right]\right\}, \tag{9}$$

where $\overset{(i)}{\tau}$ is its resolved shear stress, and κ, λ, η, ζ and α are single crystal constants. The parameter α is called "the degree of isotropy in work hardening," with $\alpha = 1$ and 0 corresponding to Taylor's isotropic hardening [12] and kinematic hardening [13], respectively. Further, $\overset{(i,j)}{\theta}$ denotes the angle between the slip directions of the ith and jth systems, and $\overset{(i,j)}{\phi}$ between their slip-plane normals. Equations (8) and (9) have been successfully employed in [1] to calculate the creep, recovery, and the Bauschinger effect of a 2618-T61 aluminum alloy.

Equations (8) and (9), however, are restricted to a constant temperature, and therefore they can be applied to predict the creep behavior of its polycrystal only at that specific temperature. Frequently one wishes to predict the creep or relaxation behavior of a metal at one temperature, but the single crystal constants are known at another temperature. Or more generally, a structural component may be subjected to a varying-temperature environment. Then, the constitutive equations which can properly reflect the influence of temperature on creep rates become essential. Such a study was undertaken by Mott [14], among others, who employed the Arrhenius function to describe the temperature effect on the steady creep rate of metals. This function has been shown to be adequate, and has also been used by Dorn [15] to establish the concept of "temperature-compensated time" for high temperature creep. In equations (8) and (9) the effect of temperature is embedded in the constants κ and ζ. When such an exponential function is adopted, these equations can be modified to include the (absolute) temperature T:

$$\overset{(i)}{\dot{\gamma}}{}^c_s = \kappa_0\, e^{-(\Gamma/T)} \overset{(i)}{\tau}{}^{\lambda}, \tag{10}$$

$$\overset{(i)}{\dot{\gamma}}{}^c_t = \eta\left\{\zeta_0\, e^{-(\Gamma/T)} \overset{(i)}{\tau}{}^{\lambda} - \left[\alpha \sum_j |\overset{(j)}{\gamma}{}^c_t| + (1-\alpha)\sum_j \cos \overset{(i,j)}{\theta} \cos \overset{(i,j)}{\phi}\, \overset{(j)}{\gamma}{}^c_t\right]\right\}, \tag{11}$$

where the additional material constant Γ is related to the activation energy of a slip process (indeed it is the activation energy divided by the Boltzmann constant), and κ_0 and ζ_0 are temperature-independent, connected to κ and ζ through the exponential function. Equations (10) and (11) will serve as the new basis for the self-consistent determination of creep and relaxation behavior of metals.

To assist the determination of these six single crystal constants, it is useful to introduce similar constitutive equations for the con-

Downloaded 01 May 2010 to 171.66.16.249. Redistribution subject to ASME license or copyright; see http://www.asme.org/terms/Terms_Use.cfm

stant-stress tensile creep behavior of polycrystals. At a constant temperature we write

$$\dot{\bar{\epsilon}}_s^c = a\bar{\sigma}^b, \tag{12}$$

$$\dot{\bar{\epsilon}}_t^c = c(d\bar{\sigma}^b - \bar{\epsilon}_t^c), \tag{13}$$

where a, b, c, and d are four polycrystal constants, which can be easily determined from two tensile creep curves. When the effect of temperature is explicitly included, we have

$$\dot{\bar{\epsilon}}_s^c = a_0 e^{-Q/T}\bar{\sigma}^b, \tag{14}$$

$$\dot{\bar{\epsilon}}_t^c = c(d_0 e^{-Q/T}\bar{\sigma}^b - \bar{\epsilon}_t^c), \tag{15}$$

where the additional parameter Q is again related to the activation energy of creep deformation of metals. This parameter can be determined from an additional creep curve of the metal tested at a different temperature. The constants a_0 and d_0 are related to a and d in an obvious manner.

In passing we note that the elastic moduli of metals are also temperature-dependent; the change, however, is generally small. After examining the variation of 57 elastic constants for 22 substances, Varshni [16] concluded that, though the temperature-dependence of elastic moduli can vary as T^4 or T^2 at low temperature (near $0°K$), the variation for most metals is almost linear at higher temperature.[1] Thus, within the range of room temperature to $T_m/2$, we may assume the linear function for both Young's and shear moduli

$$E = E_0 - pT, \tag{16}$$

$$G = G_0 - qT, \tag{17}$$

where E_0, G_0, p, and q are material constants. Poisson's ratio, which is needed in the self-consistent calculation, is of course given by $\nu\,(T) = E/2G - 1$.

Derivation of the Relaxation Behavior of Polycrystals

In a constant strain relaxation test when the total strain $\bar{\epsilon}$ is suddenly applied, the instantaneous reaction is elastic; the initial stress is given by $\mathcal{L}\bar{\epsilon}$. To determine how $\bar{\sigma}$ decreases from equation (1) at any generic state, the value of $d\bar{\epsilon}^c$ has to be evaluated. We take the aggregate to be composed of randomly oriented, equally sized grains. When the elastic anisotropy of the grain is neglected, $d\bar{\epsilon}^c$ is given by the average of $d\epsilon^c$ over all grain orientations. Symbolically we write

$$d\bar{\epsilon}_{ij}^c = \{d\epsilon_{ij}^c\}, \tag{18}$$

where, and hereafter, the bracket $\{\,\}$ represents the said average.

The creep strain of each grain is contributed simultaneously by the slip strain of its slip systems. We denote the slip direction of a slip system by b_i, its slip-plane normal by n_i, and define ν_{ij} as the symmetric part of the dyad $b_i n_j$

$$\nu_{ij} = \tfrac{1}{2}(b_i n_j + b_j n_i). \tag{19}$$

Then, the creep strain increment of a grain is given by

$$d\epsilon_{ij}^c = \sum_k^{(k)} \nu_{ij}^{(k)} d\gamma^c, \tag{20}$$

where the superscript k is to be summed over all slip systems, and $d\gamma^c = (\dot{\gamma}_s^c + \dot{\gamma}_t^c)\,dt$, dt being the time increment.

The steady and transient creep rates of a slip system, in view of equations (10)and (11), depend on its resolved shear stress, given by

$$\tau = \nu_{ij}\sigma_{ij}, \tag{21}$$

in terms of the current stress in the considered grain.

Stress relaxation of the aggregate now can be calculated by the self-consistent scheme. We assume, for simplicity, that temperature distribution in the aggregate is homogeneous at any instant, and that the coefficient of thermal expansion in the grain is also isotropic. If this coefficient is highly anisotropic, an additional thermal stress is introduced, which can be evaluated by means of Eshelby's solution [2]. At $t = 0$, $\sigma_{ij} = \bar{\sigma}_{ij}$ for each grain, and the initial creep rate of a slip system can be calculated from (10) and (11), in conjunction with equation (21). Then the incremental creep strain of each grain $d\epsilon_{ij}^c$, and $d\bar{\epsilon}_{ij}^c$ of the aggregate are given by (20) and (18), respectively. The stress relaxation of the aggregate now can be readily obtained from equation (1). During this process the stress in each grain decreases according to the self-consistent relation (5) or (7) when the grain is spherical. This relation provides a new stress state in each grain for the next time increment. If the applied strain is varying, an additional $\mathcal{L}d\bar{\epsilon}$ needs to be added to the internal stress of each grain. If temperature also changes in the step, current temperature and Poisson's ratio should be used. Now, with the new state of stress and slip strains in each grain, we return to equations (10) and (11) to calculate the new creep rates. This process is repeated, until the desired relaxation history of the aggregate is completely determined.

In engineering practice, von Mises' theory has been widely applied to predict the inelastic behavior of metals under combined stress. It is of obvious importance to know where this theory stands in comparison with a relaxation experiment, and perhaps also of interest to compare it to the self-consistent scheme. In terms of von Mises' generalized stress $\bar{\sigma}^*$ and strain $\bar{\epsilon}^{*c}$, the constitutive equations, following (14) and (15), may be written as

$$\dot{\bar{\epsilon}}_s^{*c} = a_0 e^{-Q/T}\bar{\sigma}^{*b}, \tag{22}$$

$$\dot{\bar{\epsilon}}_t^{*c} = c(d_0 e^{-Q/T}\bar{\sigma}^{*b} - \bar{\epsilon}_t^{*c}). \tag{23}$$

Under combined tension and shear, which will be specifically considered later,

$$\bar{\sigma}^* = (\bar{\sigma}_{11}^2 + 3\bar{\sigma}_{12}^2)^{1/2}. \tag{24}$$

The tensile and shear creep rates are related to the generalized creep rate through the Prandtl-Ruess relation

$$\dot{\bar{\epsilon}}_{11}^c = \frac{\bar{\sigma}_{11}}{\bar{\sigma}^*}\dot{\bar{\epsilon}}^{*c}, \tag{25}$$

$$\dot{\bar{\epsilon}}_{12}^c = \frac{3\bar{\sigma}_{12}}{2\bar{\sigma}^*}\dot{\bar{\epsilon}}^{*c}, \tag{26}$$

where $\dot{\bar{\epsilon}}^{*c} = \dot{\bar{\epsilon}}_s^{*c} + \dot{\bar{\epsilon}}_t^{*c}$. Then, the stress relaxations are given by

$$d\bar{\sigma}_{11} = -Ed\bar{\epsilon}_{11}^c, \tag{27}$$

$$d\bar{\sigma}_{12} = -2Gd\bar{\epsilon}_{12}^c, \tag{28}$$

where, as usually done in experiments, no lateral stresses $\bar{\sigma}_{22}$ and $\bar{\sigma}_{33}$ are applied to offset $d\bar{\epsilon}_{22}^c$ and $d\bar{\epsilon}_{33}^c$.

Determination of Single Crystal Constants From Polycrystal Data

To determine the relaxation behavior of polycrystals by the self-consistent scheme, the material constants of the constituent single crystals must be evaluated first. This could be done from the creep data of single crystals. However, a specimen-sized crystal is difficult to prepare, and expensive to grow. Particularly in view of the fact that most structural metals are alloys with specific chemical compositions, mechanical processing and heat treatment, it is even more formidable to grow such a crystal. Yet, even so prepared, the effect of grain boundary on the mechanical behavior of a crystallite still cannot be accounted. To circumvent all these difficulties an inverse method [9] was proposed to derive the grain behavior directly from the test data of its polycrystal. The derived properties of the grain are therefore *in situ*.

By applying this inverse method, and considering the initial creep rate, steady creep rate, and the initial decreasing rate of creep rate versus creep strain of the polycrystal, it was shown in [1] that

[1] To simulate the transition from the nonlinear behavior at low T to a linear relation at high T, two nonlinear functions were proposed in [16] for the entire temperature range.

Downloaded 01 May 2010 to 171.66.16.249. Redistribution subject to ASME license or copyright; see http://www.asme.org/terms/Terms_Use.cfm

$$\lambda = b, \tag{29}$$

$$\kappa = a\left\{\frac{1}{(\Sigma\nu_{11}{}^{b+1})^{1/b}}\right\}^b, \tag{30}$$

$$\kappa + \eta\zeta = \frac{a + cd}{\{\Sigma\nu_{11}{}^{b+1}\}}, \tag{31}$$

$$\eta\left\{\sum_i^{(i)}\nu_{11}\sum_j[\alpha + (1-\alpha)\cos\overset{(i,j)}{\theta}\cos\overset{(i,j)}{\phi}\overset{(j)}{]}\nu_{11}{}^b\right\} = \frac{c^2d}{\dfrac{a+cd}{\{\Sigma\nu_{11}{}^{b+1}\}} - a\left\{\dfrac{1}{(\Sigma\nu_{11}{}^{b+1})^{1/b}}\right\}^b}, \tag{32}$$

at a given temperature. Equations (29)–(32) provide four equations for the five constants. The additional relation may be obtained from a recovery curve.

When the temperature-dependent constitutive equations (10), (11), (14), and (15) are used, the new parameters κ_0, ζ_0, and Γ can be obtained from their counterparts a_0, d_0, and Q. Substituting

$$\kappa = \kappa_0 e^{-\Gamma/T},\ \zeta = \zeta_0 e^{-\Gamma/T}, \tag{33}$$

$$a = a_0 e^{-Q/T},\ d = d_0 e^{-Q/T}, \tag{34}$$

into equations (30)–(32), and noting that these relations hold at arbitrary temperature within the considered range, we arrive at

$$\Gamma = Q, \tag{35}$$

$$\kappa_0 = a_0\left\{\frac{1}{(\Sigma\nu_{11}{}^{b+1})^{1/b}}\right\}^b, \tag{36}$$

$$\kappa_0 + \eta\,\zeta_0 = \frac{a_0 + cd_0}{\{\Sigma\nu_{11}{}^{b+1}\}}, \tag{37}$$

$$\eta\left\{\sum_i^{(i)}\nu_{11}\sum_j[\alpha + (1-\alpha)\cos\overset{(i,j)}{\theta}\cos\overset{(i,j)}{\phi}\overset{(j)}{]}\nu_{11}{}^b\right\} = \frac{c^2d_0}{\dfrac{a_0+cd_0}{\{\Sigma\nu_{11}{}^{b+1}\}} - a_0\left\{\dfrac{1}{(\Sigma\nu_{11}{}^{b+1})^{1/b}}\right\}^b}. \tag{38}$$

Equations (29), (35)–(38) provide the new connections between the properties of a polycrystal and its constituent grains. It should be pointed out, however, that because of the nonlinear, heterogeneous, time-dependent behavior of creep deformation in metals, these relations can only provide the starting values for the single crystal constants in an iterative process to simulate the tensile creep and recovery data of the polycrystal. In fact, for the best fit of the entire curve, the value of λ is always slightly greater than b, and consequently Γ also differs from the exact value of Q.

In practical numerical derivation of these single crystal constants, it usually proves more convenient to use the constant-temperature constitutive equations (8), (9), (12), and (13) to derive the five single crystal constants at one temperature (say T_1) first. Then the single crystal constants at another temperature (say T_2) can be expressed as

$$\kappa_2 = \kappa_1 e^{-\Gamma(1/T_2 - 1/T_1)}, \tag{39}$$

$$\zeta_2 = \zeta_1 e^{-\Gamma(1/T_2 - 1/T_1)}, \tag{40}$$

where the subscript refers to the said temperature. The value of Γ then can be determined from the simulation of creep curve at T_2. Once Γ is known, κ_0 and ζ_0 can be found directly from equation (33).

Prediction of the Relaxation Behavior of an Aluminum Alloy

Very few creep tests were conducted under combined stress, and even less for the relaxation behavior of metals. The test of Johnson, et al. [17], on an RR-59 aluminum alloy under combined tension and shear was the only one that the author could find in open literature. Fortunately, in addition to the relaxation test they had also conducted some creep experiments for the same material [18], and thus enabled us to derive the single crystal constants. In this section we apply the self-consistent scheme to derive the relaxation behavior of this alloy. The predicted results will be compared directly with their data, and von Mises' theory.

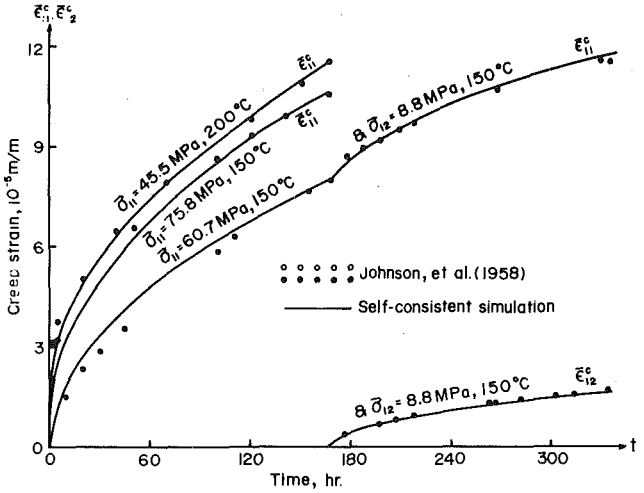


Fig. 1. Derivation of single crystal constants from creep data of an RR-59 aluminum alloy

The reported relaxation experiments were conducted at 200°C. At this temperature their tensile creep data were published only at one stress level. But at 150°C, tensile creep tests were conducted at two stress levels, followed by a superimposed shear. Though the second state was not a recovery test, we could still use the nonradial creep data to determine the degree of isotropy in work hardening α, and the other four constants at 150°C. From the two tensile creep tests the polycrystal constants a, b, c, and d can be found for this temperature. To determine the five single crystal constants we first assume $\alpha = 1$ (isotropic hardening). Then with the help of equations (29)–(32), the remaining four constants can be found so that the two tensile creep data are well simulated. These values are then used to predict the creep strains under the superimposed shear stress. Because of the assumption of isotropic hardening the predicted shear strain is usually lower than the experimental value. The value of α is then reduced to increase the kinematic component of work hardening (which tends to enhance the shear strain under a tension-shear nonradial loading). The simulation process is again repeated. With a continuous decrease of α, the two tensile and nonradial creep curves all eventually could be well simulated. The corresponding values of these constants represent the creep behavior of the grain at 150°C. Then, from the tensile creep data at 200°C, the value of Γ and subsequently of κ_0 and ζ_0 can be determined.

The experimental data of the two tensile creep tests, at $\bar{\sigma}_{11}$ = 75.8 MPa (5 tsi) and 60.7 MPa (4 tsi), and of the superimposed shear at $\bar{\sigma}_{12}$ = 8.8 MPa (7/12 tsi), each lasting for 167 hr at 150°C, are shown as filled circles in Fig. 1. By direct integration of (12) and (13), explicit relation between creep strain and time was obtained. From this relation and the two tensile creep data the polycrystal constants were found to be: $a = 1.44 \times 10^{-4}$, $b = 1.24$, $c = 3.60 \times 10^{-2}$, and $d = 2.50 \times 10^{-2}$, where stress, creep strain, and time were in the units of MPa, 10^{-5} m/m and hr, respectively. At 200°C the tensile creep data tested at $\bar{\sigma}_{11}$ = 45.5 MPa (3 tsi), are also shown in Fig. 1 as open circles. With these additional data, we found $Q = 2.89 \times 10^3$ °K, $a_0 = 0.134$, and $d_0 = 23.2$, in the same units.

The elastic constants of RR-59 aluminum alloy at 150°C or 200°C were not given by Johnson, et al. However, as pointed out by Blass and Findley [19], the property of this alloy is very similar to that of a 2618-T61 aluminum alloy. Such an alloy has the elastic moduli: E = 74.4 GPa (10.8×10^6 psi) and G = 27.6 GPa (4.0×10^6 psi) at room temperature, and E = 65.0 GPa (9.43×10^6 psi) and G = 24.6 GPa

Downloaded 01 May 2010 to 171.66.16.249. Redistribution subject to ASME license or copyright; see http://www.asme.org/terms/Terms_Use.cfm

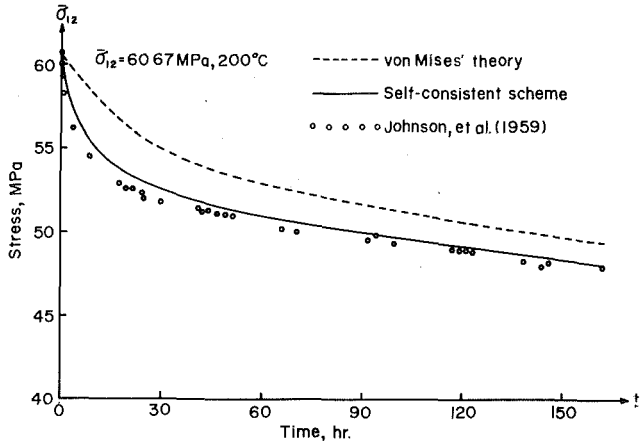


Fig. 2. Stress relaxation of an RR-59 aluminum alloy under pure shear

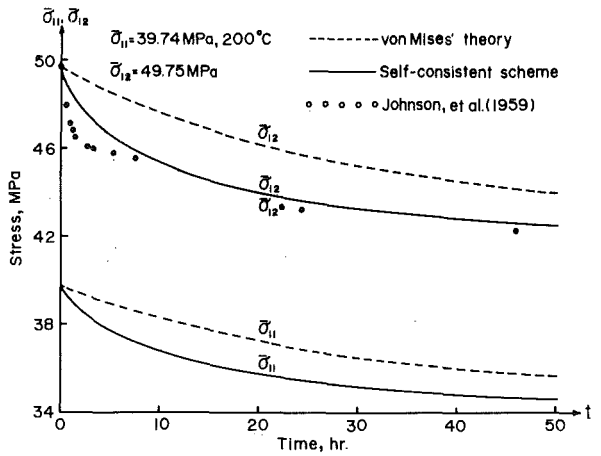


Fig. 3. Stress relaxation of an RR-59 aluminum alloy under combined tension and shear

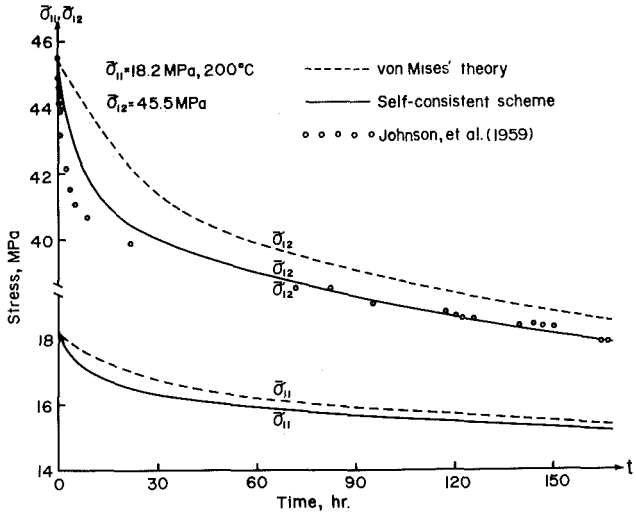


Fig. 4. Stress relaxation of an RR-59 aluminum alloy under combined tension and shear

(3.57 × 10^6 psi) at 200°C [20]. We substituted these values into equations (16) and (17), and found that E_0 = 75.75 GPa, G_0 = 28.03 GPa, p = 0.054 GPa/°C, and q = 0.017 GPa/°C. These values lead to E = 67.65 GPa and G = 25.47 GPa for the alloy at 150°C.

In the numerical calculations we adopted the same face-centered-cubic polycrystal model employed in [1]. This model consists of 75 different crystal orientations, constructed with the aid of stereographic projections in the standard triangle to simulate the three-dimensional isotropy. An f.c.c. crystal has four {111} slip planes and three ⟨110⟩ slip directions on each plane; it has 12 slip systems. The grain was assumed to be spherical. First, we apply the self-consistent scheme for creep to determine the single crystal constants; their values were so determined to provide a "best fit," by visual inspection, to the overall creep data. From the data at 150°C, we found that $\lambda = 1.40$, $\kappa = 1.38 \times 10^{-4}$, $\eta = 0.10$, $\zeta = 3.02 \times 10^{-2}$, and $\alpha = 0$, where stress, creep strain, and time are in the units of MPa, 10^{-5} m/m and hr, respectively. Together with the additional data at 200°C, we further found that $\Gamma = 3.07 \times 10^3$ °K, $\kappa_0 = 0.196$, and $\zeta_0 = 42.9$, again in the same units. With these parameters, the corresponding creep curves by the self-consistent scheme of [1] for these tested cases are also shown in Fig. 1; the experimental data are seen to be reasonably well simulated. The time increments in these creep and the following relaxation calculations, for both the self-consistent scheme and von Mises' theory, were taken as: $\Delta t = 1$ for $0 \le t < 4$; $\Delta t = 2$ for $4 \le t < 10$; $\Delta t = 5$ for $10 \le t < 30$, and $\Delta t = 10$ for $t \ge 30$, in the unit of hr.

Seven relaxation tests were reported in [17]: two by simple shear for 150 hr, two by combined tension-shear for 50 hr, and another three by combined tension-shear for 150 hr. In these experiments, though the lateral creep strains $\bar{\epsilon}^c_{22}$ and $\bar{\epsilon}^c_{33}$ were generated they were not removed by imposing $\bar{\sigma}_{22}$ and $\bar{\sigma}_{33}$. For the sake of comparison we also adopted this boundary condition in our numerical calculations. We used the foregoing six single crystal constants and the derived self-consistent scheme for relaxation to calculate the stress relaxation for all these tests. The agreement between the theory and experiments was found to be generally good. The results of three selected cases, one from each group, are shown in Figs. 2–4. The initial conditions and test periods for these three cases are: pure shear at $\bar{\sigma}_{12}$ = 60.67 MPa (4 tsi) for 150 hr, combined tension and shear at $\bar{\sigma}_{11}$ = 39.74 MPa (2.62 tsi), and $\bar{\sigma}_{12}$ = 49.75 MPa (3.28 tsi) for 50 hr, and another combined stress at $\bar{\sigma}_{11}$ = 18.2 MPa (1.2 tsi) and $\bar{\sigma}_{12}$ = 45.5 MPa (3 tsi) for 150 hr. In these figures the experimental data, the self-consistent predictions and von Mises' estimates are shown as open circles, solid and dashed lines, in turn. The self-consistent scheme is seen to give fairly accurate predictions, and because of the dominant contributions by more favorably oriented grains it can also account better the drastic decrease of stress in the early stage of the relaxation process. von Mises' theory, on the other hand, underestimates the shear stress relaxation by 12, 26, and 8 percent, respectively, at the end of these three tests.

The corresponding data for the tensile stress component was not explicitly given by Johnson, et al.; they suggested, however, that the ratio of tensile to shear stress remained constant in these relaxation processes. In Figs. 3 and 4 these ratios are 0.8 and 0.4, respectively. Starting with these values, von Mises' theory and the self-consistent scheme, respectively, gave the ratios of 0.811 and 0.815 in Fig. 3, and 0.409 and 0.414 in Fig. 4, at the end of the tests.

Conclusions

Following the spirit of [1], we identified in this paper that stress relaxation in metals is a strain-free process. The self-consistent relations between the strain, and stress of a grain and of its aggregate were established. These relations show that, even though the total strain of the aggregate is kept constant in a relaxation test, the strain of a more favorably oriented grain actually increases whereas that of a less favorably oriented grain decreases. Stress relaxation in a more favorably oriented grain also exceeds that of the aggregate, while for a less favorably oriented grain its stress relaxes less.

To improve the range of applicability of the self-consistent scheme, a new set of constitutive equations was introduced to account for the effect of temperature on creep rate, besides being consistent with a theory of active and latent hardening for slip systems. The inclusion of temperature allows us to derive the single crystal constants at one temperature from the creep data of polycrystals at another temper-

Downloaded 01 May 2010 to 171.66.16.249. Redistribution subject to ASME license or copyright; see http://www.asme.org/terms/Terms_Use.cfm

ature. With these constitutive equations, the self-consistent scheme may also be applied to predict the creep or relaxation behavior of metals under a varying-temperature environment. These equations are characterized by six single crystal constants, whose connections with the polycrystal constants have also been established.

The self-consistent scheme was applied to predict the relaxation behavior of an RR-59 aluminum alloy. We first derived the single crystal constants from the data of two tensile creep and one nonradial loading tests at 150°C and of another tensile creep at 200°C. These constants were then used in the self-consistent scheme to predict the relaxation behavior of the alloy under pure shear and under combined tension and shear at 200°C. The results of this method and of von Mises' theory were compared directly with experimental data. It was shown that the self-consistent scheme gave fairly good predictions and that von Mises' theory tended to underestimate the shear stress relaxation.

Acknowledgment

This work was supported by the National Science Foundation, Solid Mechanics Program, through Grant CME-8019546.

References

1 Weng, G. J., "Self-Consistent Determination of Time-Dependent Behavior of Metals," ASME JOURNAL OF APPLIED MECHANICS, Vol. 48, 1981, pp. 41-46.

2 Eshelby, J. D., "The Determination of the Elastic Field of an Ellipsoidal Inclusion, and Related Problems" *Proceedings of the Royal Society*, London, Series A, Vol. 241, 1957, pp. 376–396.

3 Kröner, E., "Zur Plastischen Verformung des Vielkristalls," *Acta Metallurgica*, Vol. 9, 1961, pp. 155–161.

4 Hill, R., "Continuum Micro-Mechanics of Elastoplastic Polycrystals," *Journal of the Mechanics and Physics of Solids*, Vol. 13, 1965, pp. 89–101.

5 Rabotnov, Y. N., *Creep Problems in Structural Members*, North-Holland, Amsterdam, 1969.

6 Hult, J. A., *Creep in Engineering Structures*, Blaisdell, Waltham, 1966.

7 Lin, T. H., Yu, C. L., and Weng, G. J., "Derivation of Polycrystal Creep Properties From the Creep Data of Single Crystals," ASME JOURNAL OF APPLIED MECHANICS, Vol. 44, 1977, pp. 73–78.

8 Lin, T. H., "Physical Theory of Plasticity," *Advances in Applied Mechanics*, Vol. 11, ed., Yih, C. S., Academic Press, New York, 1971.

9 Weng, G. J., "A Physically Consistent Method for the Prediction of Creep Behavior of Metals," ASME JOURNAL OF APPLIED MECHANICS, Vol. 46, 1979, pp. 800–804.

10 Ashby, M. F., "A First Report on Deformation-Mechanism Maps," *Acta Metallurgica*, Vol. 20, 1972, pp. 887–897.

11 Weng, G. J., "Dislocation Theories of Work Hardening and Yield Surfaces of Single Crystals," *Acta Mechanica*, Vol. 37, 1980, pp. 217–230.

12 Taylor, G. I., "Plastic Strain in Metals," *Journal of the Institute of Metals*, Vol. 62-1, 1938, pp. 307–324.

13 Weng, G. J., "Kinematic Hardening Rule in Single Crystals," *International Journal of Solids and Structures*, Vol. 15, 1979, pp. 861–870.

14 Mott, N. F., "A Theory of Work-Hardening of Metals II: Flow Without Slip Lines, Recovery and Creep," *Philosophical Magazine*, Vol. 44, 1953, pp. 742–765.

15 Dorn, J. E., "Some Fundamental Experiments on High Temperature Creep," *Journal of the Mechanics and Physics of Solids*, Vol. 3, 1954, pp. 85–116.

16 Varshni, Y. P., "Temperature Dependence of the Elastic Constants," *Physical Review*, Vol. B2, 1970, pp. 3952–3958.

17 Johnson, A. E., Henderson, J., and Mathur, V. D., "Complex Stress Creep Relaxation of Metallic Alloys at Elevated Temperatures," *Aircraft Engineering*, Vol. 31, 1959, pp. 75–79.

18 Johnson, A. E., Henderson, J., and Mathur, V. D., "Creep Under Changing Complex Stress Systems," *The Engineer*, Vol. 206, 1958, pp. 209–216.

19 Blass, J. J., and Findley, W. N., "Short-Time, Biaxial Creep of an Aluminum Alloy With Abrupt Changes of Temperature and State of Stress," ASME JOURNAL OF APPLIED MECHANICS, Vol. 38, 1971, pp. 489–501.

20 Findley, W. N., and Lai, J. S., "Creep and Recovery of 2618 Aluminum Alloy Under Combined Stress With a Representation by a Viscous-Viscoelastic Model," ASME JOURNAL OF APPLIED MECHANICS, Vol. 45, 1978, pp. 507–514.

Downloaded 01 May 2010 to 171.66.16.249. Redistribution subject to ASME license or copyright; see http://www.asme.org/terms/Terms_Use.cfm

U. W. Cho
Postdoctoral Fellow.
Assoc. Mem. ASME

W. N. Findley
Professor of Engineering.
Fellow ASME

Division of Engineering,
Brown University,
Providence, R.I. 02912

Creep and Creep Recovery of 304 Stainless Steel at Low Stresses With Effects of Aging on Creep and Plastic Strains

Creep and creep recovery data of 304 stainless steel are reported for experiments at low stress levels under combined tension and torsion at 593°C (1100°F). The data were represented by a viscous-viscoelastic model in which the strain was resolved into five components—elastic, plastic (time-independent), viscoelastic (time-dependent recoverable), and viscous (time-dependent nonrecoverable) which has separate positive and negative components. Only part of the creep strain at low stresses was recovered upon complete unloading following creep (as also found at high stresses), and each time-dependent strain data was well represented by a power function of time. But the stress dependence below a transition stress was approximately a linear relation with no creep limits and no cross effects such as were found in a previous analysis for higher stress levels above a transition stress. The transition stress for nonrecoverable strains agrees with the Frost-Ashby boundary between diffusional flow and dislocation creep. Aging decreased the creep rate and plastic strain. Results for different times of aging at 593°C (1100°F) under pure tension stresses were well represented by power functions of aging time up to 1000 h for each creep component and plastic strain.

Introduction

In a recent paper [1] on the present program, creep and creep recovery data of type 304 stainless steel at 593°C (1100°F) were analyzed by using a viscous-viscoelastic model [2] in which the strain was resolved into five components; elastic ϵ^E, time-independent plastic ϵ^P, time-dependent-recoverable viscoelastic ϵ^{VE}, time-dependent-nonrecoverable viscous positive ϵ^V(pos), and time-dependent-nonrecoverable viscous negative ϵ^V(neg) components. In [1] creep limits were defined below which creep strains might be negligible; and the stress dependence of the time-dependent strains at the stress levels tested were found to be nonlinear and synergistic.

In order to check the foregoing facts at low stress levels several tests at stresses below the apparent creep limits were performed. It was found that creep occurred below the apparent "creep limits" found in [1]. The amount of such creep may not be negligible compared to creep above the creep limit, particularly at stress levels just above the creep limits. The data were found to be well represented by a linear stress-strain relation below the apparent creep limit with nonlinear relations above the creep limits as defined in [1].

Also a considerable aging effect was found from tests for four different aging times from 2 up to 1000 h at the same pure tension stress. The strain components of the viscous-viscoelastic model were fitted to an exponential function of aging time. The results were satisfactorily employed in the analysis of long time creep under variable stresses, to be reported later.

Material and Specimen

Type 304 stainless steel, reference heat No. 9T2796, supplied by Oak Ridge National Laboratory, had a chemical composition in percent of 0.059 C, 1.26 Mn, 0.44 Si, 18.6 Cr, 9.5 Ni, 0.033 P, 0.015 S, 0.35 Mo, and 0.25 Cu. 12-ft bars, 4.88 cm (1.92 in.) in diameter, were machined into test specimens of thin-walled tubes of which the nominal outside diameter, wall thickness, and gage length were 2.540, 0.1524, and 10.16 cm (1.000, 0.060, and 4.00 in.), respectively. The rough machined specimens were reannealed in an argon-filled vertical tube at 1107°C (2025°F). They were at temperature for 30 min and then cooled exponentially at a minimum cooling rate of 4°C per sec at 538°C (1000°F). The ASTM grain size was 3 and the number of grain

Contributed by the Applied Mechanics Division and presented at the Winter Annual Meeting, Washington, D.C., November 15–20, 1981, of THE AMERICAN SOCIETY OF MECHANICAL ENGINEERS.

Discussion on this paper should be addressed to the Editorial Department, ASME, United Engineering Center, 345 East 47th Street, New York, N.Y. 10017, and will be accepted until March 1, 1982. Manuscript received by ASME Applied Mechanics Division, August, 1980; final revision, March, 1981. Paper No. 81-WA/APM-17.

Copyright © 1981 by ASME

Downloaded 01 May 2010 to 171.66.16.249. Redistribution subject to ASME license or copyright; see http://www.asme.org/terms/Terms_Use.cfm

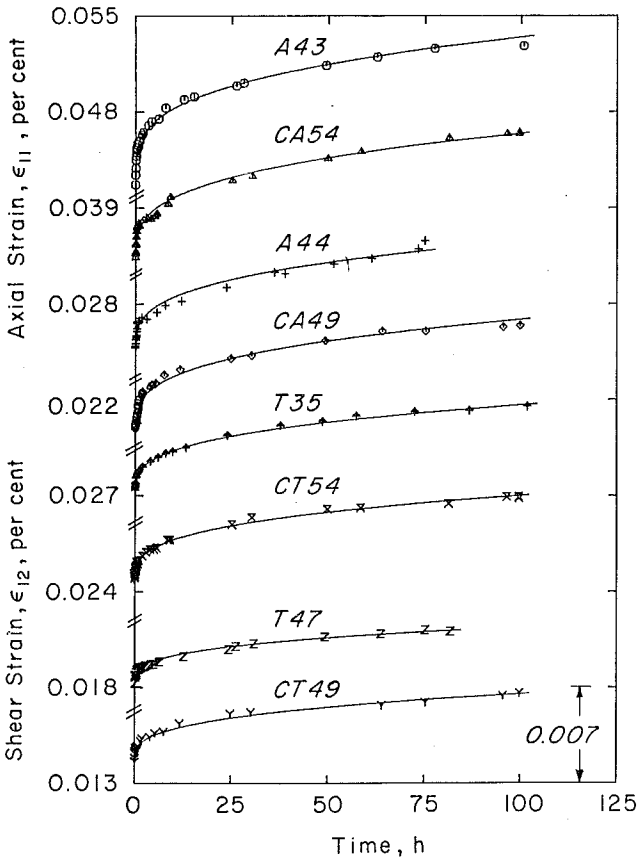


Fig. 1 Creep curves for axial or shear strains at low stresses under pure tension (A), pure torsion (T), and combined tension and torsion (C); numbers on curves indicate test numbers; see Table 1 for stresses; solid lines are equation (2)

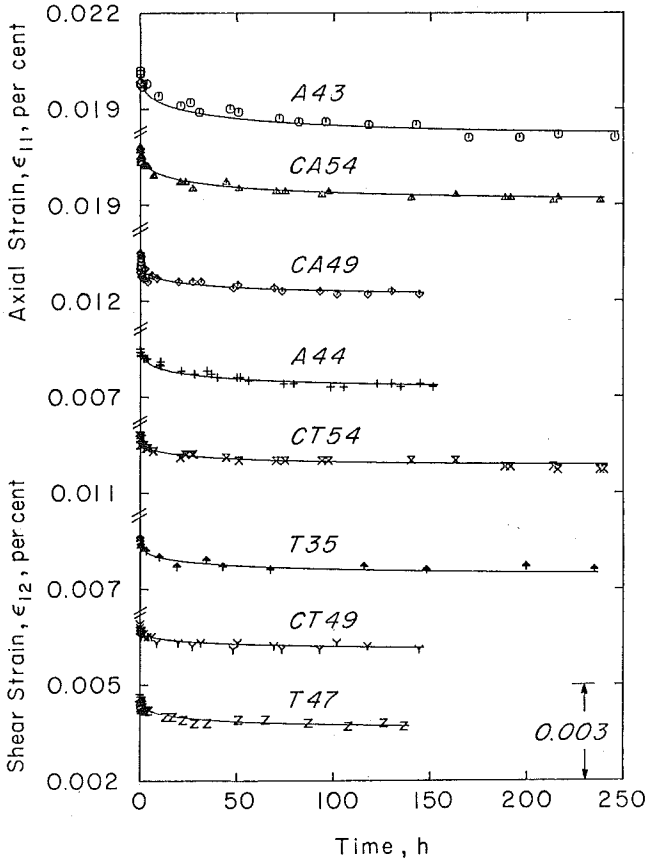


Fig. 2 Recovery curves for axial or shear strains following pure tension (A), pure torsion (T), and combined tension and torsion (C), creep in Fig. 1; numbers on curves indicate test numbers; see Table 1 for stresses; solid lines are equation (4)

boundaries across the wall thickness was 20 including twins. The hardness was as received C35 after heat-treatment A37, after 1 percent creep A45. A more complete description of material and specimens is given in [1, 3]. Heat No. 9T2796 has been investigated extensively in several laboratories [4–8]. The microstructure was described in [4–6] and the effect of aging was described in [8].

Experimental Apparatus and Procedure

The combined tension and torsion machine used for these experiments was described in [9]. Some modifications for high temperature use were described in [1]. The temperature control and measurement employed resulted in an apparent temperature drift of less than ±0.6°C (±1°F) through the whole test (see [1] for details).

Except as noted the specimen was allowed to soak at the test temperature of 593°C (1100°F) for about 20 h prior to loading. A final strain reading just before loading was taken as the zero point. The gage length was measured before heating and no correction was made for thermal expansion.

The required load was applied by means of dead weights. One-step loading and unloading was performed by manual control of a jack in less than 10 sec without shock. The time at which the weight was fully applied or released was taken as zero time for the time-dependent creep strains.

Experimental Results

In the present paper six creep and creep-recovery tests, performed at a temperature of 593°C (1100°F), were included in the analysis of the data at low stress levels. The tests included two pure tension, two pure torsion, and two combined tension and torsion. Both the combined tests had the same ratio of axial and shear stress and one of them, C54 had the same axial stress as the pure tension test, A44, and had almost the same shear stress as the pure torsion test, T47. The creep and creep recovery data are shown in Figs. 1 and 2, respectively. The results of analysis are also shown in Figs. 1–5 by solid lines.

Four creep experiments were performed with different aging times of 2, 20, 120, 1000 h under a pure tension stress $\sigma = 86.2$ MPa (12.5 ksi). The results for creep and creep recovery data are shown in Fig. 5. Also the results of analysis are shown in Fig. 6.

For all the aforementioned tests, the creep period was about 100 h and the creep recovery period was about 250 h. All tests are listed in Table 1.

Analysis of Data

Creep Below Creep Limits. By a viscous-viscoelastic model [2] the total creep strain was separated into the five components [1]

$$\epsilon = \epsilon^E + \epsilon^P + \epsilon^{VE} + \epsilon^V(\text{pos}) + \epsilon^V(\text{neg}), \tag{1}$$

where ϵ^E is an elastic strain, ϵ^P is a plastic strain (time-depepdent), ϵ^{VE} is a viscoelastic strain (time-dependent recoverable), and ϵ^V is a viscous strain (time-dependent nonrecoverable). Separate positive and negative parts of ϵ^V allow for creep in either sense and reversal of stress. Assuming a power function of time for the viscoelastic and viscous strains, equation (1) was rewritten as

$$\epsilon_{ij} = \epsilon_{ij}^E + \epsilon_{ij}^P + \epsilon_{ij}^{\pm VE} t^{n_1} + \epsilon_{ij}^{\pm V} t^{n_2}. \tag{2}$$

"Creep limits" were defined in [1] as limiting stresses below which the creep strain was zero or negligibly small. New test results below the creep limits showed that some creep occurred and the amount could not be neglected, compared to creep at stresses just above the creep limits. It was also interesting to find that only part of the creep

Downloaded 01 May 2010 to 171.66.16.249. Redistribution subject to ASME license or copyright; see http://www.asme.org/terms/Terms_Use.cfm

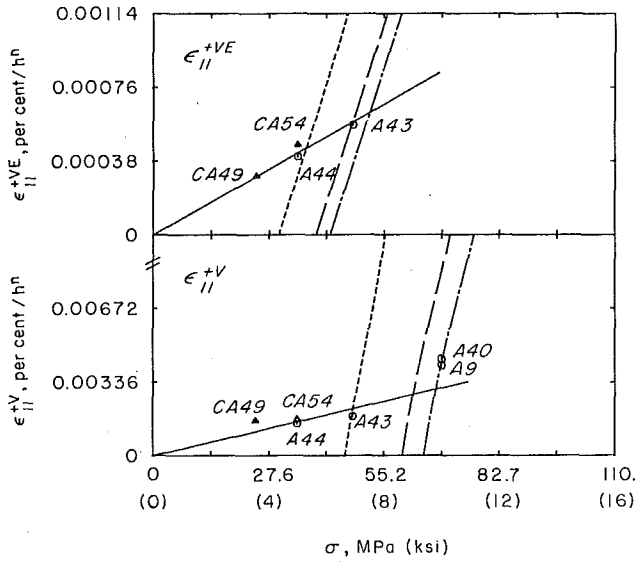


Fig. 3 Recoverable ϵ_{11}^{+VE} and nonrecoverable ϵ_{11}^{+V} strain coefficients versus tensile stress σ for low stresses; numbers indicate test numbers in Table 1. Tests 9 and 40 were taken from reference [1]. The solid lines indicate equations (7) and (9) and the dot-dash lines are for pure tension at high stresses; the dash lines and dotted lines are for combined tension and torsion with ratios of 4.102 and 1.739, respectively.

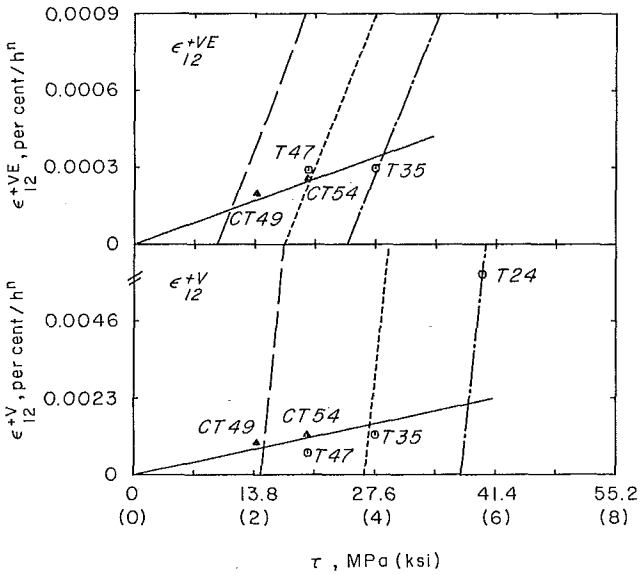


Fig. 4 Recoverable ϵ_{12}^{+VE} and nonrecoverable ϵ_{12}^{+V} strain coefficients versus shearing stress τ for low stresses; numbers indicate test numbers in Table 1. Test 24 was taken from reference [1]. The solid lines indicate equations (8) and (10) and the dot-dash lines are for pure torsion at high stresses; the dash lines and dotted lines are for combined tension and torsion with ratios of 4.102 and 1.739, respectively.

Table 1 The values of N, n_1 in equations (3) and (4) and the strain components for equation (2) with $n_1 = n_2 = 0.315$

Test	Tension, σ		Torsion, τ		Aging time, t_s, h	Duration of creep t_1, h	Exponents		Strain Components With $N = n_1 = n_2 = 0.315$			
	MPa	(ksi)	MPa	(ksi)			N	n_1	ϵ^E, %	ϵ^{+VE} 10^{-2}%/h^n	ϵ^{+V} 10^{-2}%/h^n	ϵ^P, %
A43	47.8	(6.928)	0	(0)	20	101	0.215	0.596	0.0325	0.0559	0.1795	0.0109
A44	34.5	(5.000)	0	(0)	20	75	0.333	0.563	0.0240	0.0396	0.1445	0.0007
CA49	24.4	(3.543)	14.0	(2.037)	20	100	0.213	0.353	0.0166	0.0296	0.1590	0.0032
CA54	34.5	(5.000)	19.8	(2.875)	20	100	0.323	0.304	0.0236	0.0457	0.1659	0.0118
T35	0	(0)	27.6	(4.000)	20	102	0.301	0.165	0.0249	0.0296	0.1204	0.0023
T47	0	(0)	19.9	(2.887)	20	82	0.349	0.254	0.0174	0.0289	0.0651	0.0010
CT49	24.4	(3.543)	14.0	(2.037)	20	100	0.261	0.258	0.0127	0.0197	0.0957	0.0019
CT54	34.5	(5.000)	19.8	(2.875)	20	100	0.277	0.490	0.0180	0.0255	0.1198	0.0068
A55	86.2	(12.5)	0	(0)	2	100	0.372	0.528	0.0604	0.3019	3.4743	0.2001
A38	86.2	(12.5)	0	(0)	20	100	0.384	0.545	0.0596	0.2867	2.1026	0.1489
A42	86.2	(12.5)	0	(0)	120	101	0.393	0.510	0.0578	0.1830	1.2525	0.1168
A46	86.2	(12.5)	0	(0)	1000	99	0.430	0.335	0.0557	0.1336	1.0429	0.0986

strain below the creep limits was recoverable even at a very small stress level.

The creep and creep recovery data were well represented by the following equations:

For Creep;

$$\epsilon_{ij} = \epsilon_{ij}^0 + \epsilon_{ij}^{+} t^N. \tag{3}$$

For creep recovery after unloading at time t_1:

$$\epsilon_{ij} = A_{ij} + \epsilon_{ij}^{+VE} \{t^{n_1} - (t - t_1)^{n_1}\}, \tag{4}$$

where

$$A_{ij} = \epsilon_{ij}^P + \epsilon_{ij}^{+V} t_1^{n_2}.$$

Then, from equations (2) and (4)

$$\epsilon_{ij}^E = \epsilon_{ij}|_{t=t_1} - A_{ij} - \epsilon_{ij}^{+VE} t_1^{n_1}. \tag{5}$$

And from creep data, rewriting equation (2)

$$\epsilon_{ij} - (\epsilon_{ij}^E + \epsilon_{ij}^{+VE} t^{n_1}) = \epsilon_{ij}^P + \epsilon_{ij}^{+V} t^{n_2}. \tag{6}$$

The values of N and n_1 (see Table 1), computed from equations (3) and (4) for the tests below the creep limits showed no definite trend with stress and yielded an average $N = n_1 = 0.328$. Since this was close to the value ($n = 0.315$) used in the previous analysis [1] of creep and creep recovery data above the creep limit, the value of $N = n_1 = n_2 = 0.315$ was used again in the analysis of the creep results below the creep limits. The value of n_2 in equation (6) was not obtained separately, because $N = n_1$ implies $N = n_2$ from equations (2) and (3). Using $n = 0.315$, the strain components were recomputed by equations (2)–(6) and the results are shown in Table 1. The creep and creep re-

Downloaded 01 May 2010 to 171.66.16.249. Redistribution subject to ASME license or copyright; see http://www.asme.org/terms/Terms_Use.cfm

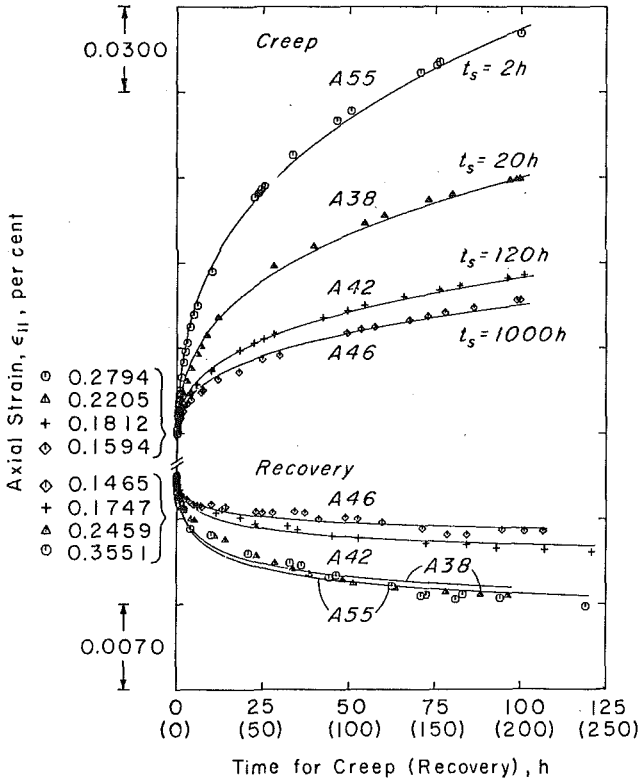


Fig. 5 Creep and recovery curves for axial strains under pure tension of 86.2 MPa (12.5 ksi) after different aging times t_s; numbers indicate test numbers in Table 1; solid lines equation (2) for creep; equation (4) for recovery

covery curves using these components are shown as solid lines together with test data in Figs. 1 and 2, respectively.

As shown in Table 1 and Figs. 3 and 4, the data of ϵ_{ij}^{+VE}, ϵ_{ij}^{+V} versus σ or τ suggested a linear relation between creep strain and stress at low stress levels including stresses below the apparent creep limits. The results of the combined tension and torsion tests C49 and C54 also suggested that there was no cross effect under combined stress at low stress levels. If a cross effect exists it appears to be within the possible scatter of data due to material variability and unknown factors.

The relation between creep strain and stress may be continuous for all stress levels, but in this analysis the data at low stresses were fitted to linear equations with transition points to the nonlinear relations (with creep limits) at higher stresses determined in the previous analysis [1], as shown in Figs. 3 and 4.

The linear equations up to the transition points, shown as solid straight lines in Figs. 3 and 4, were as follows:

$$\epsilon_{11}^{+VE} = 0.8311^* \times 10^{-4}\,\sigma, \quad \sigma \leqslant 51.7 \text{ MPa (7.492 ksi)}, \tag{7}$$

$$\epsilon_{12}^{+VE} = 0.8488^* \times 10^{-4}\,\tau, \quad \tau \leqslant 28.4 \text{ MPa (4.126 ksi)}, \tag{8}$$

$$\epsilon_{11}^{+V} = 3.089^* \times 10^{-4}\,\sigma, \quad \sigma \leqslant 67.6 \text{ MPa (9.801 ksi)}, \tag{9}$$

$$\epsilon_{12}^{+V} = 3.840^* \times 10^{-4}\,\tau, \quad \tau \leqslant 38.2 \text{ MPa (5.545 ksi)}. \tag{10}$$

In Figs. 3 and 4, are also shown the nonlinear curves with creep limits as dot-dash lines for pure tension or pure torsion, and as dotted and dashed lines for combined tension and torsion of two particular ratios of σ/τ, taken from [1]. The transition points were determined as the intersections of the nonlinear curves above the creep limits with the linear straight lines of equations (7)–(10) as shown in Figs. 3 and 4.

Employing the linear relation below the transition points and the nonlinear relations with creep limits above the transition points, predictions were made for creep under varying loading histories, to be reported later.

* These coefficients are for ksi input. For MPa input, they are 12.05, 12.31, 44.80, and 55.69, respectively.

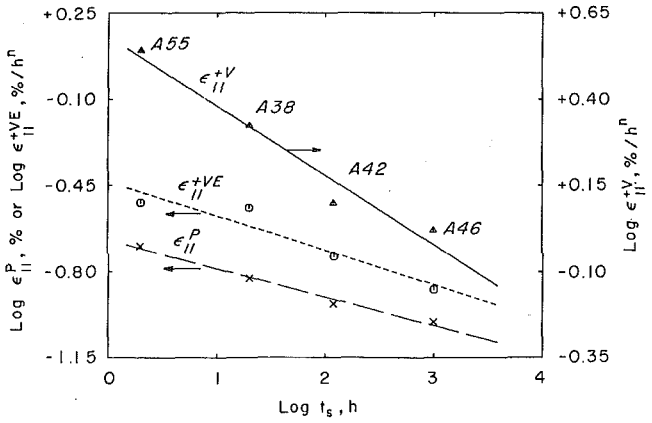


Fig. 6 Effect of aging time t_s on nonrecoverable ϵ_{11}^{+V}, recoverable ϵ_{11}^{+VE}, strain coefficients and plastic strain ϵ_{11}^{P}; numbers indicate test numbers in Table 1; lines indicate equations (11), (12), or (13)

Effects of Aging. Four aging tests were performed under a pure tension of $\sigma = 86.2$ MPa (12.5 ksi) at 593°C (1100°F) for 100 h creep and 250 h creep recovery. These tests were performed after aging times of 2, 20, 120, and 1000 h, respectively, at 593°C (1100°F).

Creep and creep recovery data of the aging tests were analyzed in the same manner as in the previous section for creep data at low stresses. Using equations (3) and (4), the values of N and n_1 were found as shown in Table 1. The results suggested that the exponent N for 100 h creep was not so different for the four different aging tests but that it might be taken as a constant for all aging times. Since the values of N were close to the average $n = 0.315$, which was used for all other data, $N = n_1 = n_2 = 0.315$ was also used for analysis of the aging tests. Using $n = 0.315$, strain components were recomputed by equations (4)–(6) and the results are shown in Table 1. Using these components, creep and creep recovery curves for the four aging tests are shown as solid lines together with the data in Fig. 5. As these results indicated, increasing aging caused all components to decrease. The effect on the time-dependent strain components were larger than the time-independent plastic strain and the effect on the elastic strain, though a regular decrease, was small enough to neglect for this analysis.

The data of ϵ_{11}^{+VE}, ϵ_{11}^{+V}, and ϵ_{11}^{P} versus the aging time prior to the first loading are shown in Fig. 6. These data could be described by power functions of aging time, t_s, shown as straight lines in the log-log plot of ϵ_{11}^{+V}, ϵ_{11}^{+VE}, ϵ_{11}^{P} versus t_s in Fig. 6. The constants of the power functions for each component were obtained by least squares separately as follows:

$$\epsilon_{11}^{+V} = 3.8165\, t_s^{-0.2016}, \tag{11}$$

$$\epsilon_{11}^{+VE} = 0.3671\, t_s^{-0.1397}, \tag{12}$$

$$\epsilon_{11}^{P} = 0.2124\, t_s^{-0.1158}, \tag{13}$$

where t_s is the aging time at 593°C (1100°F) from the start of heating of the specimen up to the time of the first load application. In Fig. 6 ϵ_{11}^{+V}, ϵ_{11}^{+VE}, and ϵ_{11}^{P} are shown by a solid line, a dotted line, and a dashed line, respectively.

As shown in the results, more aging time made the material more creep resistant. The relations between the strain components and aging time obtained from aging tests under pure tension as in the foregoing, were very successful in predicting the long time creep under variable stresses under combined tension and torsion, to be reported later.

Discussions on the Results of Analysis

The Transition Points. In the present analysis of creep data at low stress levels, some transition points were introduced to divide two different regions of stress dependence, where creep above the transition points was described by a nonlinear relation with apparent creep

Downloaded 01 May 2010 to 171.66.16.249. Redistribution subject to ASME license or copyright; see http://www.asme.org/terms/Terms_Use.cfm

limits using the multiple integral representation [10] and creep below the transition points was approximated by linear relations with no creep limits. Johnson's [11] creep experiments on several materials over a fairly wide stress range also showed a transition of stress dependence between high and low stress levels for primary creep strain. Also it has been reported [12] that the stress dependence of the steady-state creep rate could be divided into three stress ranges: low, intermediate, and high. These results suggest that the nonlinear stress-strain relation of creep behavior cannot be represented by a single analytical equation.

In reference [5] a Deformation Mechanism Map for AISI 304 stainless steel developed by J. H. Frost and M. F. Ashby was reported and compared with tensile creep and tensile test data for the same heat of steel as in the present investigation. When the transition point for ϵ_{12}^{+V}, from equation (10), $\tau/G = 38.2\ \text{MPa}/5.56 \times 10^4\text{MPa} = 6.87 \times 10^{-4}$, was plotted together with the test temperature, 593°C, on the Frost-Ashby deformation-mechanism map in [5] it fell slightly above the line marking the transition between diffusional flow and dislocation creep. Similarly when the transition point for ϵ_{11}^{+V} from equation (9), $\sigma/2G = 67.6\text{MPa}/2 \times 5.56 \times 10^4\text{MPa} = 6.08 \times 10^{-4}$, was plotted it fell slightly below the same transition line.

The corresponding transition points τ/G for ϵ_{12}^{+VE} and $\sigma/2G$ for ϵ_{11}^{+VE} were 5.11×10^{-4} and 4.65×10^{-4}, respectively. These both fell below the line marking the transition between diffusional flow and dislocation creep. Thus it appears possible that creep at low stresses having a linear behavior was diffusional flow, whereas, creep at stresses above a transition having a nonlinear synergistic behavior was dislocation creep.

A study of substructures developed during creep of the same heat of steel was reported in [6]. For the small strains and stresses involved in the present work the study reported in [6] indicated that the change in dislocation density was too small to measure, no cells formed and the major alteration of the substructure was the precipitation of $M_{23}C_6$ carbides on grain and twin boundaries and some dislocations.

The Effect of Aging. The effect of aging on material properties including creep is well known. Since the aging effect is usually quite different for different materials, temperature and aging time, little attention has been given to aging in the formulation of creep theories. Aging effects were reported in [8] for 304 stainless steel of the same heat as the present tests, reannealed for 30 min at 1093°C (2000°F) and air-cooled. Table 7 of [8] shows that the minimum creep rate at a stress of 207MPa (30ksi) and temperature of 593°C (1100°F) decreased from 8.38×10^{-2} to 7.86×10^{-2} percent per h following aging at the test temperature for 4000 and 10,000 h, respectively. Also the loading strain in the same tests decreased from 8.63 to 6.35 percent. This decrease represents a decrease in plastic strain on loading. These results agree with the trends for creep and plastic strains found in the present investigation. However, results for other heats given in [8] caused the authors of [8] to conclude that aging of 304 stainless steel increased the minimum creep rate.

As generally known, the features of aging effects may be quite different according to the range of aging time as well as different heats of the same material.

For creep of the 304 stainless steel in the present tests at 593°C (1100°F), the aging effect was found to be considerable for creep tests of 100–1000 h duration. The aging time-creep strain relation could be described as a power function of aging time. This function indicated about a 30 percent decrease in creep rate from a 20 h to a 120 h aging time. The aging effect was not considered during the 100 h of creep after either aging period, yet the values of N, n_1 were about the same. In studying this question the creep data after 2, 20, 120, 1000 h of aging were fitted by a power function of time, as in equation (3), considering data only from $t = 0$ to t', where $t' = 2, 10, 20, 50, 100$ h, respectively. The resulting values of the exponent N for the best fit to the data for the different values of t' are shown in Table 2.

Other data at different stress levels after 20 h aging showed similar values of N to those of A38 in Table 2. The foregoing results suggested that the aging effect during creep might be included in the exponent N. Since N was considered only for the first 100 h creep data, such as

Table 2 Effect of duration of creep t' on exponent N

Test	Aging	t'=2	10	20	50	100 h
A55	2 h	0.794	0.528	0.470	0.420	0.372
A38	20 h	0.776	0.637	0.506	0.439	0.384
A42	120 h	0.479	0.538	0.508	0.436	0.393
A46	1000 h	0.355	0.462	0.437	0.442	0.430

0.384 for A38 and 0.393 for A42, no significant difference in N between 20 h and 120 h aging times was observed. Thus the average N was used for the analysis. As indicated in the above results of N, the average N could not be used for representation of the first 2 h of creep after 2 or 20 h of aging. But all the creep periods used for the present test program were more than 50 h and the analysis of the data using the average N presented no problem.

The coefficients, ϵ_{ij}^{+V} or ϵ_{ij}^{+VE} determined by using the average N for 100 h creep after 20 h aging included the aging effect by neglecting the difference in N between 2 h and 100 h. Since aging between 120 h and 220 h made less than a 9 percent difference in coefficients according to equations (11) and (12) and the exponent N between the first 2 h and 100 h data after 120 h aging (A42) showed no significant difference, the coefficients determined by using the average N for 100 h creep after 120 h aging were a good approximation. This fact also suggests no difficulty in using the average N for all the other test programs involving more than 120 h. As the 100 h creep data were used for determination of all constants, the present analysis presented no explicit problem in spite of the disagreement for 2 h creep data after 2 or 20 h of aging. Short time creep tests after short aging times perhaps should consider N as a function of aging time.

Conclusions

The stress-strain relation for creep of 304 stainless steel at low stresses and 593°C (1100°F) was approximately linear with no synergistic effect under combined stress and no creep limit. Above a transition stress the behavior was nonlinear, synergistic, and had an apparent creep limit. The transition stress for the recoverable strain component was less than that for the nonrecoverable strain component. The transition for nonrecoverable creep agrees with the Frost-Ashby boundary between diffusion flow for low stresses and dislocation creep for higher stresses.

Aging was found to decrease the creep rate and plastic strain. The aging time versus creep strain and aging time versus plastic strain for 304 stainless steel aged and tested at 593°C (1100°F) were well described by power functions of aging time over the range of aging times investigated, 2 to 1000 h.

Acknowledgments

This work was supported by the National Science Foundation under Grant No. ENG76-02519. The material tested was supplied by the Oak Ridge National Laboratory. The authors are grateful to R. M. Reed for assistance in experiments and Ms. P. C. Orzechowski for typing the manuscript.

References

1 Cho, U. W., and Findley, W. N., "Creep and Creep Recovery of 304 Stainless Steel Under Combined Stress With a Representation of a Viscous-Viscoelastic Model," ASME JOURNAL OF APPLIED MECHANICS, Vol. 47, 1980, pp. 755–761.

2 Findley, W. N., and Lai, J. S., "Creep and Recovery of 2618 Aluminum Under Combined Stress With a Representation by a Viscous-Viscoelastic Model," ASME JOURNAL OF APPLIED MECHANICS, Vol. 45, 1978, pp. 504–514.

3 Findley, W. N., and Mark, R., "Multiaxial Creep Behavior of 304 Stainless Steel," Annual Report No. 1 (Brown University Report EMRL-55, Oct. 1972), No. 2 (EMRL-58, Nov. 1973), No. 3 (EMRL-62, Nov. 1974), No. 4 (EMRL-63, July 1975) to Oak Ridge National Laboratory.

4 Bhargava, R., Moteff, J., and Swindeman, R. W., "Correlation of the Microstructure With the Creep and Tensile Properties of AISI 304 Stainless

Downloaded 01 May 2010 to 171.66.16.249. Redistribution subject to ASME license or copyright; see http://www.asme.org/terms/Terms_Use.cfm

Steel," ASME Symposium on Structural Materials for Service at Elevated Temperatures in Nuclear Power Generation, Doc. MPC-1, 1975, pp. 31–54.

5 Bhargava, R. K., Moteff, J., and Swindeman, R. W., "The Dislocation Substructure, Carbides, and the Deformation Mechanism Map for AISI 304 Stainless Steel," *Met. Trans.*, Vol. 7A, 1976, pp. 879–884.

6 Swindeman, R. W., et al., "Substructures Developed During Creep and Cyclic Tests of Type 304 Stainless Steel (Heat 9T2796)," Oak Ridge National Laboratory, ORNL-5293, Sept. 1977.

7 Swindeman, R. W., "Correlation of Rupture Life, Creep Rate, and Microstructure for Type 304 Stainless Steel," Oak Ridge National Laboratory, ORNL-5523, June 1979.

8 Sikka, V. K., Brinkman, C. R., and McCoy, H. E., "Effect of Thermal Aging on Tensile and Creep Properties of Types 304 and 316 Stainless Steel," ASME Symposium on Structural Materials for Service at Elevated Temperatures in Nuclear Power Generation, Doc. MPC-1, 1975, pp. 316–350.

9 Findley, W. N., and Gjelsvik, A., "A Biaxial Testing Machine for Plasticity, Creep, or Relaxation Under Variable Principal-Stress Ratios," *Proceedings, ASTM*, Vol. 62, 1962, pp. 1103–1118.

10 Findley, W. N., Lai, J. S., and Onaran, K., *Nonlinear Creep and Relaxation of Viscoelastic Materials, With an Introduction to Linear Viscoelasticity*, North-Holland, Amsterdam, 1976.

11 Johnson, A. E., "Creep Under Complex Stress Systems at Elevated Temperature," *Proceedings, Institution of Mechanical Engineers*, Vol. 164, 1951, pp. 432–446.

12 Lagneborg, R., "Dislocation Mechanisms in Creep," *International Metallurgical Reviews*, Vol. 17, 1972, pp. 130–146.

Downloaded 01 May 2010 to 171.66.16.249. Redistribution subject to ASME license or copyright; see http://www.asme.org/terms/Terms_Use.cfm

G. C. Johnson

Assistant Professor,
Department of Mechanical Engineering,
University of California,
Berkeley, Calif. 94720
Assoc. Mem. ASME

On the Applicability of Acoustoelasticity for Residual Stress Determination

Acoustoelasticity has recently been used for the nondestructive evaluation of residual stresses. In making such measurements the assumption has been made that the plastic flow leading to the residual stress state did not change the acoustic response of the material. This paper examines the extent to which that assumption holds for three aluminum alloys. The acoustoelastic theory is summarized and results are presented for tests of specimens under uniaxial tension which are subjected to plastic deformation followed by complete unloading. It is shown that the assumption made does not hold for all materials and that further theoretical development is required for general quantitative residual stress determination.

Introduction

Determination of the state of stress within a structure has been the focus of considerable research in experimental mechanics. Along with a variety of other methods, several acoustic techniques have been developed for the nondestructive evaluation of the stress within a body [1–3].

Acoustoelasticity [1] (see also [4]), the most widely explored ultrasonic method, makes measurement of the changes in the propagation speeds of various waves due to changes in stress. The majority of the work has been devoted to the study of simple, controlled states of stress which are within the elastic region, although acoustoelasticity has also been used to determine residual stresses in specimens with more complicated geometries [5–7].

In studies which use acoustoelasticity as a residual stress measurement technique the assumption is made that the plastic deformation which led to the residual stress has not changed the acoustic response of the material. This assumption actually includes two points: first that the acoustoelastic constants for elastic loading are the same as for unloading from a plastic state, and second that the velocity at a given stress level is independent of the loading path. This paper examines the validity of the two facets of this assumption for three aluminum alloys. Velocity changes are measured throughout the loading cycle of uniaxial tension test specimens which are subjected to plastic deformation. It is shown that the standard residual stress assumptions do not hold for all materials and that careful acoustic characterization of material is necessary for accurate stress determination.

Theory and Experimental Method

Previous work [1] has indicated that the velocity change for waves propagating through an elastically deformed medium is proportional to the applied stress. In this study only longitudinal waves propagating normal to the plane of a specimen which is in a state of plane stress were examined. Acoustoelastic theory states that the velocity of such a wave should change with stress as

$$\frac{\Delta V}{V_0} = p(\sigma_1 + \sigma_2) \tag{1}$$

where ΔV is the difference between the current longitudinal wave speed and the initial (unstressed) wave speed, V_0, σ_1, and σ_2 are the principal inplane stresses, and p is the material's acoustoelastic constant for velocity. The value of p can be obtained experimentally and is expressible in terms of the Lamé constants λ and μ, and Murnaghan's (third-order) constants l, m, and n as

$$p = \frac{\mu l - \lambda(m + \lambda + 2\mu)}{\mu(3\lambda + 2\mu)(\lambda + 2\mu)} \tag{2}$$

Experimental results were obtained using the double-pulse-echo technique, the details of which may be found in reference [1]. This method does not measure the velocity directly, but determines the transit time of a wave propagating through the specimen by setting up a special phase condition, called a null. The frequency of the wave which establishes this phase relation is called the null frequency and is the variable actually measured. Its change is related to the change in velocity and the change in specimen thickness as

$$\frac{\Delta f}{f_0} = \frac{\Delta V}{V_0} - \epsilon_t \tag{3}$$

Contributed by the Applied Mechanics Division and presented at the Winter Annual Meeting, Washington, D. C., November 15–20, 1981, of THE AMERICAN SOCIETY OF MECHANICAL ENGINEERS.

Discussion on this paper should be addressed to the Editorial Department, ASME, United Engineering Center, 345 East 47th Street, New York, N. Y. 10017, and will be accepted until March 1, 1982. Manuscript received by ASME Applied Mechanics Division, February, 1980; final revision, December, 1980. Paper No. 81-WA/APM-8.

Copyright © 1981 by ASME

Downloaded 01 May 2010 to 171.66.16.249. Redistribution subject to ASME license or copyright; see http://www.asme.org/terms/Terms_Use.cfm

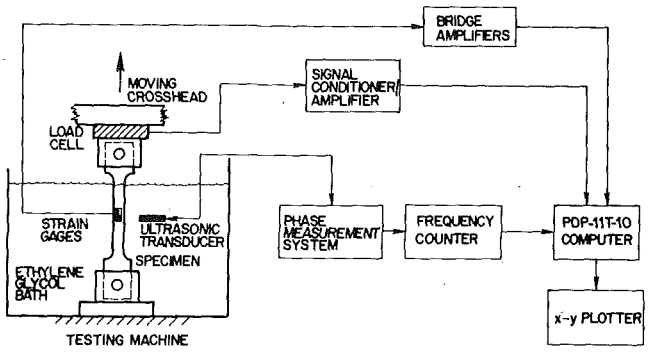


Fig. 1 Schematic of experimental arrangement; details of phase measurement system may be found in [1]

where Δf is the difference between the current null frequency and the initial null frequency, f_0, and ϵ_t is the transverse strain of the plane-stress specimen.

When the deformation is elastic the transverse strain is proportional to the sum of the principal in-plane stresses and the frequency relation becomes

$$\frac{\Delta f}{f_0} = P(\sigma_1 + \sigma_2) \tag{4}$$

where the acoustoelastic constant for frequency, P, is directly measurable using the double-pulse-echo technique and is expressed as

$$P = \frac{2\mu l - \lambda(2m + \lambda + 2\mu)}{2\mu(3\lambda + 2\mu)(\lambda + 2\mu)} \tag{5}$$

It should be emphasized that equation (4) holds only for elastic states when the transverse strain is proportional to the sum of the stresses, but is valid for either loading or unloading provided the proper reference frequency, f_0, is used.

In making the measurements a transducer with 12.5 MHz center frequency and 3 mm dia active area was coupled to the metal specimens by an ethylene glycol bath. Two sets of strain gages were mounted on the specimens to monitor longitudinal and transverse strain. Measurements of null frequency, applied load, and strain were taken as the loading progressed. All readings were made directly by a mini-computer (PDP—11T-10) with the load cell and strain gage outputs entered through analog to digital converters and frequency entered as binary coded decimal. A schematic of the experimental setup is shown in Fig. 1.

Experimental Results

Uniaxial tension test specimens with nominal cross sections of 10 mm by 15 mm over a length of 60 mm were machined from plates of 2024-T351, 6061-T651, and 7075-T651 aluminum with the specimen axis parallel to the plate rolling direction. These specimens were mounted in the pinned grips of a hydraulic testing machine which allowed displacement control. They were subjected to a loading cycle which caused significant plastic deformation followed by complete unloading.

Several investigators have previously examined the effects of plastic deformation on the acoustic response of a material. Rollins showed that plastic flow did not affect the acoustic birefringence of shear waves in C1018 steel [8] and 1100-F aluminum [9]. Bergman and Shahbender [10] made measurements on loading only, thus their results cannot be used in evaluating the assumption in question. Each of these tests produced about 10 data points. Using the data acquisition system described in the previous section, around 1000 data points were taken in each test presented here.

Fig. 2 shows the stress-strain curve for the 2024-T351 specimen. It indicates a sharp yield point and slight strain hardening. Plots of relative frequency change versus stress and strain are presented in Fig. 3. The null frequency increased along a nearly linear path in the

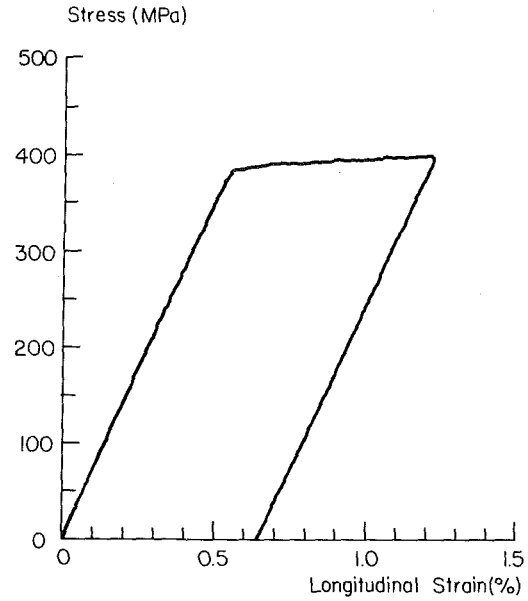


Fig. 2 Uniaxial stress-strain curve for 2024-T351 aluminum

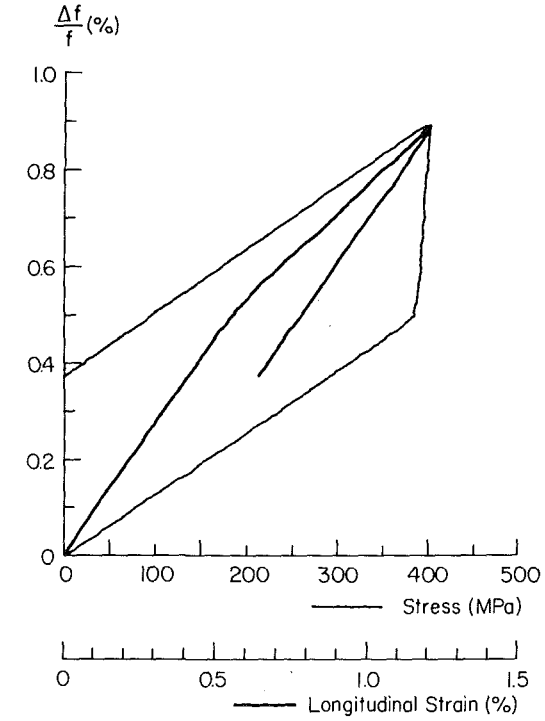


Fig. 3 Relative frequency change for longitudinal waves versus uniaxial stress and strain in 2024-T351 aluminum

elastic zone as predicted by equation (4). After yielding, the frequency continued to increase as the strain increased. On complete unloading, it was found that the null frequency was 0.38 percent higher than it had been at the start of the test. The slope of the plot of frequency versus stress gives the value for the acoustoelastic constant P. On loading P was 13.2×10^{-6} MPa^{-1} while on unloading it was 13.3×10^{-6} MPa^{-1}, a difference of 0.8 percent. Through use of equation (3) and the measured transverse strain the relative velocity change was calculated. Fig. 4 shows the plots of relative velocity change versus stress and strain. The velocity of propagation increased linearly up to yield, held virtually constant during plastic flow, then returned to within 0.01 percent of its original value after complete unloading. The

Downloaded 01 May 2010 to 171.66.16.249. Redistribution subject to ASME license or copyright; see http://www.asme.org/terms/Terms_Use.cfm

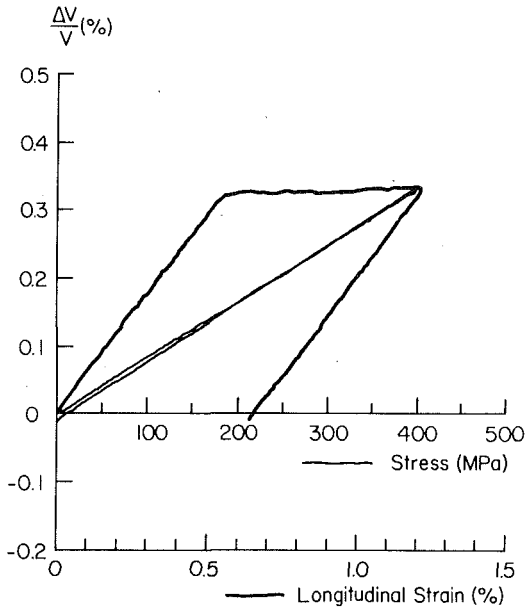


Fig. 4 Relative velocity change for longitudinal waves versus uniaxial stress and strain in 2024-T351 aluminum

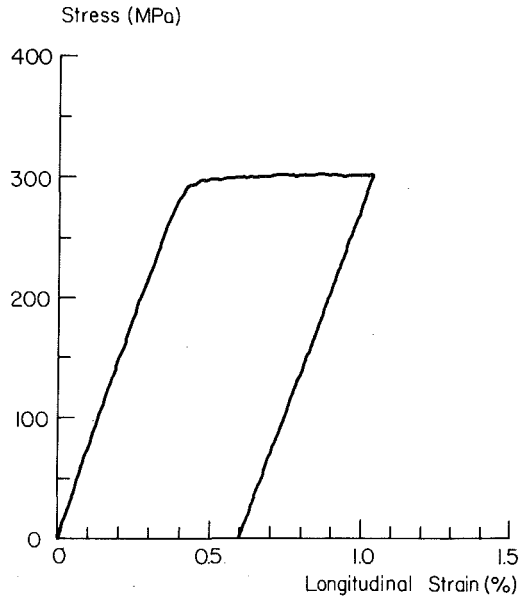


Fig. 5 Uniaxial stress-strain curve for 6061-T651 aluminum

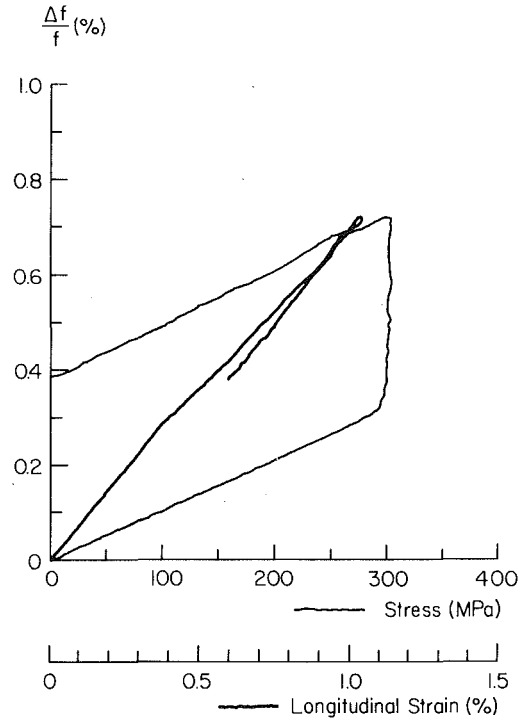


Fig. 6 Relative frequency change for longitudinal waves versus uniaxial stress and strain in 6061-T651 aluminum

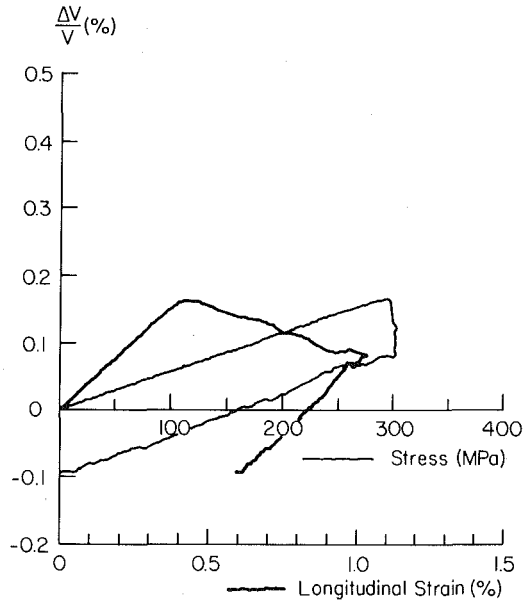


Fig. 7 Relative velocity change for longitudinal waves versus uniaxial stress and strain in 6061-T651 aluminum

change in the acoustoelastic constant for velocity, p, between loading and unloading was 1.2 percent, increasing from 8.6×10^{-6} MPa^{-1} to 8.7×10^{-6} MPa^{-1}.

The small differences between the acoustoelastic constants of loading and unloading and the slight decrease in velocity caused by yield lead to the conclusion that this material would be suitable for residual stress measurements without modification of the standard assumptions outlined in the Introduction. Yielding did not significantly change the acoustoelastic character of this material.

Figs. 5–7 are plots of the stress-strain curve, relative frequency change curves, and relative velocity change curves, respectively, for the specimen of 6061-T651 aluminum. This material has a well-defined yield point and experiences moderate strain hardening (Fig. 5). The relative frequency change curves (Fig. 6) have the same general characteristics as the corresponding curves for 2024-T351, with the final change in null frequency (after complete unloading) being 0.38 percent. The acoustoelastic constant for frequency, P, increased by 2.8 percent during yield, going from 10.6×10^{-6} MPa^{-1} to 10.9×10^{-6} MPa^{-1}. When velocity change is plotted (Fig. 7) a marked difference between 6061-T651 and 2024-T351 is seen. As loading progressed beyond the yield point the propagation velocity decreased by 0.08 percent. After complete unloading the velocity was 0.09 percent lower than at the start of the test. This decrease is of significant magnitude considering that the maximum increase in velocity during elastic deformation amounted to only 0.17 percent. The constant p increased from 5.7×10^{-6} MPa^{-1} to 6.1×10^{-6} MPa^{-1} for a 7.0 percent change.

Downloaded 01 May 2010 to 171.66.16.249. Redistribution subject to ASME license or copyright; see http://www.asme.org/terms/Terms_Use.cfm

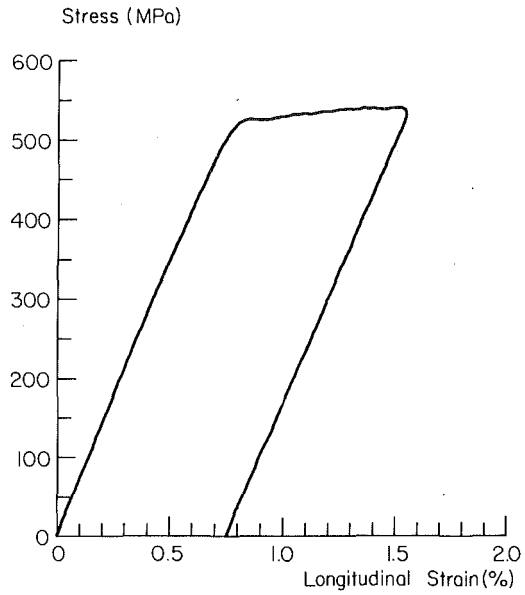
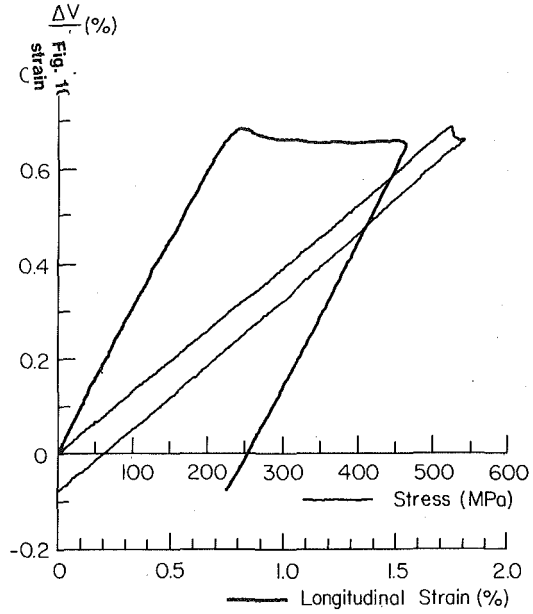


Fig. 8 Uniaxial stress-strain curve for 7075-T651 aluminum



) Relative velocity change for longitudinal waves versus stress and in 7075-T651 aluminum

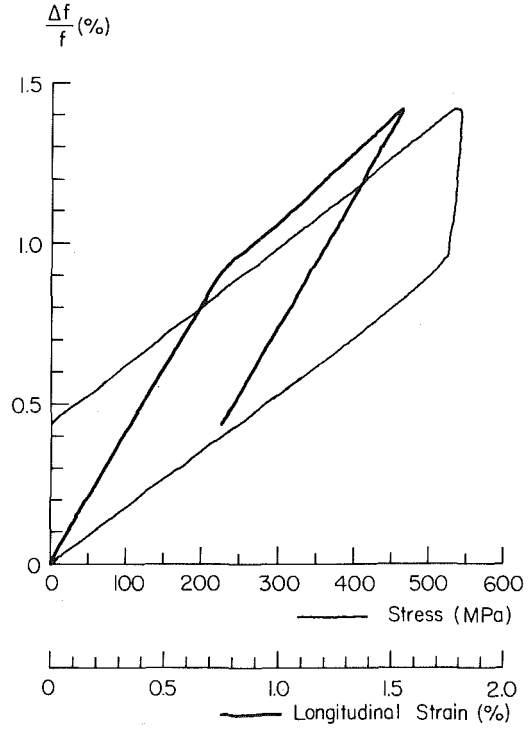


Fig. 9 Relative frequency change for longitudinal waves versus stress and strain in 7075-T651 aluminum

Table 1 Summary of test results

ALLOY	YIELD STRENGTH, MPa	VELOCITY CHANGE AT YIELD, %	FINAL PLASTIC STRAIN, %	CHANGE IN ACOUSTOELASTIC CONSTANT, %		FINAL VELOCITY CHANGE, %
				p	P	
2024-T351	385	0.33	0.64	0.8	1.2	-0.01
6061-T651	295	0.17	0.59	2.8	7.0	-0.09
7075-T651	525	0.69	0.76	3.4	3.8	-0.07

For 6061-T651 the assumption that yielding does not appreciably change the acoustoelastic response is not valid. The acoustoelastic constants did not change drastically, but the large drop in velocity during plastic flow would distort any quantitative residual stress measurements made under the standard assumptions.

The plots of stress-strain, frequency change, and velocity change curves for the specimen of 7075-T651 aluminum are shown in Figs. 8–10. Again a well-defined yield point and moderate hardening were observed (Fig. 8), and again the general shape of the relative frequency change curves (Fig. 9) is the same as for the other materials. The final null frequency was 0.45 percent higher than its initial value, while P changed by 3.4 percent from 17.6×10^{-6} MPa^{-1} to 18.2×10^{-6} MPa^{-1}. Fig. 10 shows that the velocity decreased immediately after the onset of plastic flow, followed by a region of nearly constant velocity. This velocity drop led to a final decrease of 0.07 percent, while p changed from 13.2×10^{-6} MPa^{-1} to 13.7×10^{-6} MPa^{-1}, a 3.8 percent change.

This material, then, falls between the previous two terms of its usability in ultrasonic residual stress measurements. The acoustoelastic constants p and P did not change significantly, but the velocity changed during yield by 0.07 percent. Although this is the same order of magnitude as the change for 6061-T651, it represents only 10 percent of the value of the maximum velocity increase which occurred during elastic loading.

A summary of the results for the three alloys is given in Table 1.

Conclusion

Considerable material characterization is required for accurate residual stress determination using acoustoelasticity. It has been demonstrated that plastic deformation caused changes in the acoustic response to various degrees depending upon the material. The alloy 6061-T651 would require that considerably more analysis be performed in order to use it in residual stress evaluation. On the other hand, 2024-T351 would be suitable for such tests under the simplifying assumption that plastic flow does not change the acoustic response. In general, each material considered for testing must be examined to determine its suitability, given the current state of acoustoelastic theory.

In every case the acoustoelastic constant p changed less than 7 percent during the test, indicating that the velocity versus stress curves were nearly parallel on loading and unloading. This leads to the conclusion that had the unloading occurred at a smaller value of

Downloaded 01 May 2010 to 171.66.16.249. Redistribution subject to ASME license or copyright; see http://www.asme.org/terms/Terms_Use.cfm

plastic strain, the final velocity change that would have resulted can be approximated by the change in velocity from the yield point to the point of unloading. The error involved in this approximation is given by the change in p between loading and unloading. For larger plastic strains it is more difficult to anticipate the results as the velocity change versus strain curve might undergo further changes at large strains. (The leveling off of Fig. 10 after yield is an example of such a change.) It is reasonable to expect, though, that the final velocity changes of such tests would still be dominated by the change in velocity which occurs during plastic flow.

Two main areas of further research are apparent. First, a unifying theory including elastic-plastic deformations should be developed. Such a theory would aid in identifying parameters which are important in the yielding process as well as add predictive capabilities to residual stress testing. The second area of research is in shear wave response. A set of experiments similar to those presented here would show how acoustic birefringence changes with plastic flow, and thus how shear waves can be used in quantitative residual stress analysis.

The question of whether the acoustoelastic technique can be expected to be of use in determining an arbitrary residual stress state has not been answered. It seems, though, that for plane stress states in a well-characterized material one should be able to make reasonable estimates of the residual stress using acoustoelasticity. Further work on the acoustoelastic response in three-dimensional stress states must be undertaken for the method to be extended to more general states of residual stress.

Acknowledgments

The author would like to thank J. B. Hunter and A. R. Selfridge and Professors G. S. Kino, C. R. Steele, D. M. Barnett, and G. Herrmann of Stanford University for their help and advice throughout the course of this work. Support for this research was provided by NSF Contract No. DMK-76-00726 through the Center for Materials Research at Stanford University and by EPRI Contract No. RP-609-1.

References

1 Kino, G. S., et al., "Acoustoelastic Imaging of Stress Fields," *Journal of Applied Physics*, Vol. 50, 1979, pp. 2607–2613.

2 Blinka, J., and Sachse, W., "Application of Ultrasonic-Pulse-Spectroscopy Measurements to Experimental Stress Analysis," *Experimental Mechanics*, Vol. 16, 1976, pp. 448–453.

3 Gerhart, G. R., "Rayleigh Wave Velocity for a Stress-Induced Slightly Anisotropic Solid," *Journal of the Acoustical Society of America*, Vol. 60, 1976, pp. 1085–1088.

4 Johnson, G. C., "Acoustoelasticity: Stress Measurements Using Ultrasonics," PhD Dissertation, Stanford University, 1979.

5 Crecraft, D. I., "The Measurement of Applied and Residual Stresses in Metals Using Ultrasonic Waves," *Journal of Sound and Vibration*, Vol. 5, 1967, pp. 173–192.

6 Fukuoka, H., Toda, H., and Yamane, T., "Acoustoelastic Stress Analysis of Residual Stress in a Patch-welded Disk," *Experimental Mechanics*, Vol. 18, 1978, pp. 277–280.

7 Scott, M. P., Barnett, D. M., and Ilić, D. B., "The Nondestructive Determination of Residual Stress in Extruded Billets From Acoustoelastic Measurements," *1979 IEEE Ultrasonics Symposium Proceedings*, New Orleans, La.

8 Rollins, F. R., "Ultrasonic Methods for Nondestructive Measurement of Residual Stress," WADD Technical Report 61-42, Part I, 1961.

9 Rollins, F. R., Korbett, D. R., and Jones, J. L., "Ultrasonic Methods for Nondestructive Measurement of Residual Stress," WADD Technical Report 61-42, Part II, 1962.

10 Bergman, R. H., and Shahbender, R. A., "Effect of Statically Applied Stresses on the Velocity of Propagation of Ultrasonic Waves," *Journal of Applied Physics*, Vol. 29, 1958, pp. 1736–1739.

Downloaded 01 May 2010 to 171.66.16.249. Redistribution subject to ASME license or copyright; see http://www.asme.org/terms/Terms_Use.cfm

C. Rubenstein[1]

Visiting Fellow,
Department of Production and
Industrial Engineering,
Hong Kong Polytechnic,
Hung Hom, Kowloon, Hong Kong

A Critical Appraisal of Static Hardness Measurements

A semiempirical analysis of the indentation process is made as a result of which the hardness indentation data obtained with ball, cone and square-based pyramid indenters are related to the uniaxial stress-strain curve of the indented material. It is shown that deductions from the analysis are valid only for annealed materials. The factors liable to result in erroneous hardness readings are considered and the influence of residual stresses in the surface and the subsurface layers of the material under examination are shown to explain (i) the dependence of cone and pyramid hardness on the applied load and (ii) the anomalous influence of cone angle on the measured hardness when large angle indenters are pressed into materials which have been strain-hardened prior to the hardness measurement.

Introduction

Empirically, Meyer [1] found that when ball-ended indenters are pressed into ductile materials under a load sufficient to cause plastic deformation, the indenter sinks into the specimen to a depth such that the diameter, d, of the circular projected area of contact is related to the applied load, L, by a relation

$$L = \mathbf{a}d^n,$$

and, further, that the constant **a** is related to the diameter of the indenter, D, by a relation of the form $\mathbf{a}D^{n-2}$ = a constant.

Böklen [2] combined and rearranged these equations in the form

$$(p_m)_b = HMU\,(d/D)^m \tag{1}$$

where $(p_m)_b$ is the Meyer hardness; i.e., $L/(\pi/4)d^2$; $HMU = (4\mathbf{a}/\pi)D^m$ is the ultimate Meyer hardness; i.e., the Meyer hardness obtained when the ball is indented up to its diametral plane ($d = D$) and $m = n - 2$.

Böklen presented numerous sets of indentation data as $(p_m)_b$ versus d/D on logarithmic scales and showed that the data were well represented by equation (1).

Tabor [3] assumed that $(p_m)_b$ was proportional to the initial yield stress of the specimen material when subjected to uniaxial tension or frictionless compression, that d/D was proportional to the representative strain produced by the indentation process and that the indented material deformed plastically in tension according to the equation [4]

$$\sigma = b\epsilon^x \tag{2}$$

and he obtained the equation

$$(p_m)_b = K\,(d/D)^x \tag{3}$$

where $K \equiv bc_bq^x$.

c_b is given by $(p_m)_b = c_bY$, Y is the initial yield stress of the specimen material and q is given by $\epsilon = qd/D$.

Empirically, Tabor found that with $c_b = 3$ and $q = 0.2$ for all values of the d/D ratio, ball indentation data obtained on ductile metals fell close to the true stress-natural strain curve of the specimen material provided the applied loads were sufficiently great to cause the material below the ball to become *fully* plastic. Noting the identity between equations (1) and (3) we see that the simple analysis offered by Tabor leads to the empirical observations made by Meyer [1] and, as such, lend support to the suggestion that indentation data may be expressed in terms of equivalent tensile stresses and strains.

Atkins and Tabor [5] fitted cone indentation data to the stress-strain curves of copper and steel by allowing the parameter c_c (given by $c_c = (p_m)_c/Y$) to vary with cone angle in an unexpected manner, viz., first decreasing, then increasing and finally decreasing as cone angle increased. Subsequently, Beeuwkes, Chait, and Lin [6] repeated and extended the work of Atkins and Tabor and found, essentially, the same results. This raises the question as to why c_c should be found to vary so oddly with cone angle when it has been observed that an essentially similar parameter, c_b, is independent of the d/D ratio. In

[1] Permanent Address after September 30, 1981: Department of Mechanical Engineering, Ben Gurion University of the Negev, P. O. Box 653, Beer Sheva, Israel.

Contributed by the Applied Mechanics Division for publication in the JOURNAL OF APPLIED MECHANICS.

Discussion on this paper should be addressed to the Editorial Department, ASME, United Engineering Center, 345 East 47th Street, New York, N. Y. 10017, and will be accepted until two months after final publication of the paper itself in the JOURNAL OF APPLIED MECHANICS. Manuscript received by ASME Applied Mechanics Division, June, 1980; final revision, May, 1981.

Copyright © 1981 by ASME

Downloaded 01 May 2010 to 171.66.16.249. Redistribution subject to ASME license or copyright; see http://www.asme.org/terms/Terms_Use.cfm

addition we seek expressions for the representative strain produced by a cone or by a square-based pyramid indenting a ductile material.

Analysis

In the absence of a rigorous solution to the elastoplastic problem of indentation by a rigid indenter, we will adopt a semiempirical approach and begin by proposing the hypothesis that the functions relating the representative strain in the material below a rigid indenter to the indenter geometry are similar when the indented material is either elastically or plastically deformed. Thus, if, for a particular indenter, the equivalent uniaxial strain in the elastic region, ϵ_e, is given by $\epsilon_e = q_e f(\phi)$, where $f(\phi)$ is the relevant function of the indenter geometry, then the hypothesis states that when the material below the indenter is fully plastic, the equivalent uniaxial strain will be $\epsilon_p = q_p f(\phi)$ where $q_p \neq q_e$.

Ball Indentation. Consider, now, indentation by a ball indenter of diameter D which has been pressed into a semi-infinite elastic medium of Young's modulus, E, and Poisson's ratio, ν, under a load L such that the projected area of contact is a circle of radius r and all the material below the ball is elastically strained.

Then r is given by [7]

$$r^3 = \frac{3LD}{8E}(1-\nu^2)$$

hence the mean stress

$$(p_m)_b = \frac{L}{\pi r^2} = \frac{8}{3\pi}\cdot\frac{E}{1-\nu^2}\cdot\frac{r}{D}$$
$$= \frac{4}{3\pi}\cdot\frac{E}{1-\nu^2}\cdot\frac{d}{D} \tag{4}$$

where $d = 2r$ is the diameter of the projected area of contact. Here a second hypothesis will be proposed, viz., that the mean indentation stress p_m is related to the equivalent uniaxial stress, σ, by the relation $p_m = C\sigma$.

Hence for ball indentation

$$(p_m)_b = C_b\sigma$$

Substituting this in equation (4) we obtain

$$\sigma = E\frac{4}{3\pi C_b}\cdot\frac{1}{1-\nu^2}\cdot\frac{d}{D}$$

But since the material is elastically deformed

$$\sigma = E\,(\epsilon_b)_e$$

that is,

$$(\epsilon_b)_e = \frac{4}{3\pi C_b}\cdot\frac{1}{1-\nu^2}\cdot\frac{d}{D}$$
$$= (q_b)_e \cdot d/D$$

where

$$(q_b)_e = \frac{4}{3\pi C_b}\cdot\frac{1}{1-\nu^2}$$

It follows from the first hypothesis that when the material below the ball is plastically deformed, the equivalent uniaxial tensile strain is

$$(\epsilon_b)_p = (q_b)_p \cdot d/D$$

From the second hypothesis, the equivalent uniaxial stress is given by

$$\sigma_p = p_m/(C_b)_p$$

Assuming that the uniaxial stress-strain curve of the indented material in the plastic region can be represented by equation (2), then

$$\sigma_p = b\epsilon_p^x$$

and hence, for a ball indentation

$$(p_m)_b = b\cdot(C_b)_p\,(q_b)_p^x\,(d/D)^x$$

which can be written as

$$(p_m)_b = HMU\,(d/D)^x \tag{5}$$

Thus this analysis has led to Böklen's expression (equation (1) relating the mean stress acting over the projected area of contact to the d/D ratio. Empirically Böklen found that for a given specimen material (i.e., b, x fixed), HMU is constant, independent of the value of d/D hence we may infer that $(C_b)_p$ and $(q_b)_p$ are independent of the strain produced by the indentation.

Cone Indentation. Repeating this procedure consider indentation into a semi-infinite elastic medium of Young's modulus E and Poisson's ratio ν by a rigid conical indenter of apex angle 2ϕ under an applied load L. Then, $L = E\pi r^2\cot\phi/2(1-\nu^2)$ where r is the radius of the circle of contact [8]. The mean stress, $p_m = L/\pi r^2 = [E/2(1-\nu^2)]\cot\phi$. Again, utilizing the second hypothesis $p_m = C_c\sigma$. Hence $\sigma = (E/2C_c\,(1-\nu^2))\cot\phi$. However $\sigma = E(\epsilon_c)_e$ since, in this instance, the deformation is completely elastic; hence

$$(\epsilon_c)_e = \cot\phi/2C_c\,(1-\nu^2)$$
$$= (q_c)_e\cot\phi$$

where

$$(q_c)_e \equiv [2C_c(1-\nu^2)]^{-1}$$

It follows from the first hypothesis that when the material below the conical indenter is plastically deformed, the equivalent uniaxial strain $(\epsilon_c)_p$ is given by $(\epsilon_c)_p = (q_c)_p\cdot\cot\phi$.

Assuming, as before, that the equivalent uniaxial stress is given by $\sigma_p = (p_m)_c/(C_c)_p$ and that the uniaxial stress-strain curve of the material in the plastic region is represented by $\sigma_p = b\epsilon_p^x$, we have

$$(p_m)_c = b(C_c)_p(q_c)_p^x\cdot(\cot\phi)^x$$
$$= [(p_m)_c]_{90}\cdot(\cot\phi)^x \tag{6}$$

where $[(p_m)_c]_{90}$ is the cone hardness determined with a cone having an apex angle of 90°.

Thus the analysis suggests that cone hardness data presented as the mean hardness pressure versus the cotangent of the semiapex angle on logarithmic scales should be linearly related, the slope of the line being the work-hardening index of the indented material.

Square-Based Pyramid Indentation. Here, unfortunately, we cannot follow similar procedures in order to obtain an expression for the equivalent uniaxial strain since we lack an expression relating the load to the depth of penetration of a pyramid into an elastic medium. However, as an approximation, we will assume that the strain produced by a square-based pyramid, the sides of which are inclined to each other at an angle of 2ϕ is equal to the strain produced by a cone of the same angle, i.e., $(\epsilon_p)_p = (\epsilon_c)_p = (q_c)_p\cdot\cot\phi$. Assuming, as before, that $\sigma_p = (p_m)_p/(C_p)_p$ and that the stress-strain curve in the plastic region can be represented as $\sigma_p = b\epsilon_p^x$ we obtain

$$(p_m)_p = b(C_p)(q_c)_p^x\,(\cot\phi)^x$$
$$= [(p_m)_p]_{90}\,(\cot\phi)^x \tag{7}$$

The Parameters C and q. Consider now the situation when a flat punch is pressed into a rigid-perfectly plastic material, the yield stress of which is Y. Then a permanent indentation will be formed when the mean pressure over the contact area is of the order of $3Y$. Now for small d and large D a ball indentation approaches an indentation by a flat punch so that for an indentation into a rigid-perfectly plastic solid by a ball at small d/D, the mean hardness pressure $(p_m)_b \sim 3Y$. But for a rigid-perfectly plastic solid, $\sigma = Y$ and hence, $(p_m)_b \sim 3\sigma$, i.e., $(C_b)_p \sim 3$ for values of d/D approaching zero. If now, we introduce the third hypothesis, viz., that the parameters $(C_b)_p$, $(C_c)_p$, and $(C_p)_p$ are constant, independent of the strain produced by the indentation process it follows that $(C_b)_p \sim 3$ for all values of d/D—a conclusion consistent with Tabor's empirical findings [3]. Similarly, as $\phi \to 90°$, cone and square-based pyramid indenters approach flat punches

Downloaded 01 May 2010 to 171.66.16.249. Redistribution subject to ASME license or copyright; see http://www.asme.org/terms/Terms_Use.cfm

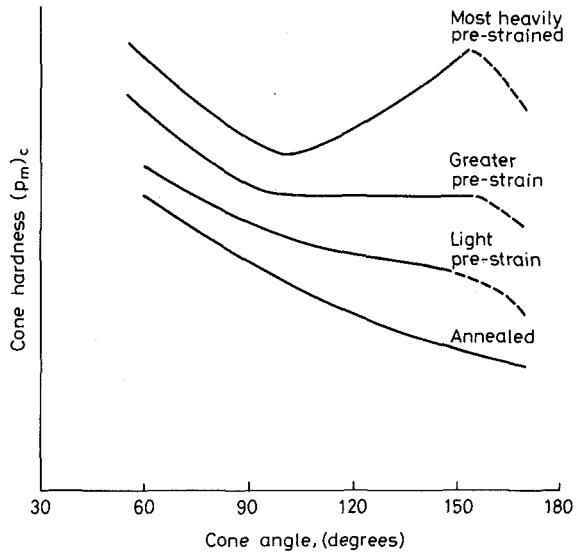


Fig. 1 Schematic representation of the variation of the measured value of the cone hardness with cone angle observed with a metal subjected to different amounts of prestrain

hence it follows from the hypothesis that $(C_c)_p = (C_p)_p \doteq 3$ independent of cone or pyramid apex angle.

Taking $(C_b)_p = (C_c)_p = (C_p)_p = 3$, it follows from equation (5) that $HMU = 3\,b(q_b)_p{}^x$ and, from equations (6) and (7), that $[(p_m)_c]_{90} = [(p_m)_p]_{90} = 3b(q_c)_p^x$.

Böklen [2] showed empirically that if the Meyer hardness $(p_m)_b$ is plotted against d/D on logarithmic scales, the data are linearly related (in accordance with equation (1)) and, further, that if the hardness obtained with a 90° cone, i.e., $[(p_m)_c]_{90}$ is plotted on the same diagram at the abscissa $d/D = 1$, the point so obtained lies on or close to the line through the ball data, i.e., $[(p_m)_c] = HMU$; hence $3b(q_c)_p^x = 3b(q_b)_p^x$. That is, $(q_c)_p = (q_b)_p$. Empirically, Tabor (3) found $(q_b)_p = 0.2$; hence $(q_c)_p = (q_p)_p = (q_b)_p = 0.2$.

Accordingly, we are led to conclude that the equivalent stress is represented by $\frac{1}{3}(p_m)$ and the equivalent strain is represented by 0.2 d/D for ball indentations and by 0.2 cot ϕ for cone and square-based pyramid indentations and that presented in this way, indentation data should lie close to the uniaxial stress-strain curve of the indented material.

Discussion

Comparison With Experimental Data. *The Strain Induced by a Vickers Pyramid.* If we accept that the strain produced by a square-based pyramid is equal to that produced by a cone of the same apex angle, then the strain produced by a Vickers pyramid indenter is given by $\epsilon_p = 0.2 \cot \frac{1}{2}(136°) = 0.08$. This agrees very well with the empirical finding by Tabor [3] that a Vickers pyramid induces a strain of between 8 and 10 percent.

Cone Hardness. Published data on the influence of indenter angle on the measured hardness are not consistent [5] in that evidence exists showing that the measured hardness (*a*) increases as the indenter angle increases [9–11]; (*b*) is almost independent of indenter angle [12]; (*c*) decreases as the indenter angle increases [13, 14].

Atkins and Tabor [5] showed that all three relationships between measured hardness and indenter angle could be observed with a given material which had been prestrained by different amounts. If the material is in the annealed state or is only lightly prestrained then the measured hardness decreases as the indenter angle increases but with increasing amounts of prestrain (and, particularly with indenters having apex angles greater than 90°), the tendency is for the measured hardness to increase as the indenter angle increases—their results are shown schematically in Fig. 1. In the light of these results it is clear

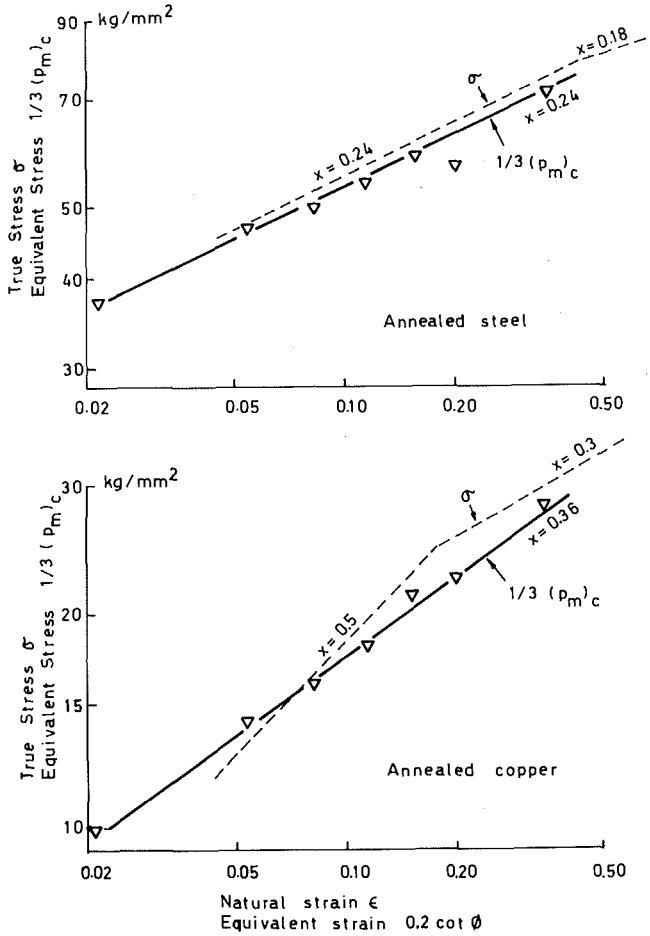


Fig. 2 Cone indentation data obtained by Atkins and Tabor [5] presented as $(p_m)_c/3$ versus 0.2 cot ϕ along with the stress-strain curve obtained in compression; 1 kg/mm² = 9.8 MPa

that while the analysis just given might be capable of explaining the dependence of the measured hardness on indenter angle for annealed or lightly worked materials, it cannot explain observations made when heavily worked materials are indented.

To explain their observations, Atkins and Tabor made the tacit assumption that the *only* effect introduced by prestraining the specimen is that the uniaxial tensile stress corresponding to the hardness pressure measured with a given cone indenting a metal prestrained by X percent and that corresponding to the hardness pressure measured by indenting the metal in its annealed state are displaced (on the stress-strain curve) one from the other by a strain of X percent. They then argued that since for the most heavily worked materials the yield stress is constant and that $(p_m)_c = c_c Y$, then the values of c_c for each cone can be obtained by computing the values of $(p_m)_c/Y$ using the cone hardness measurements obtained for the most heavily worked specimens. From Fig. 1 it is clear that this procedure results in c_c first decreasing, then increasing and finally decreasing as the cone angle increases. It is extremely difficult to see why c_c should behave so oddly with cone angle—all the more so when it is recalled that an essentially similar parameter, c_b, has been shown to be constant, independent of d/D [3]. The only basis for presuming that c_c should vary with cone angle is the theoretically derived variation in the ratio p/Y obtained for the indentation of a rigid-perfectly plastic solid by wedges [15] when it was deduced that p/Y increases *monotonically* as the wedge angle increases.

An alternative approach (and this has been adopted in the present work) is to assume that $(C_c)_p$ is a constant, independent of cone angle, that prestraining the material under examination introduces more than one effect and that at least one of these effects results in the

Downloaded 01 May 2010 to 171.66.16.249. Redistribution subject to ASME license or copyright; see http://www.asme.org/terms/Terms_Use.cfm

measured hardness being an overestimate of the true hardness, the degree of overestimation being most pronounced when the prestrain is greatest and the cone angle is greatest. Then (*i*) only with annealed metals and alloys can we expect agreement between experiment and theoretical prediction, but (*ii*) with materials in the annealed state, agreement should be obtained with a single, constant value of C_c.

In Fig. 2, data obtained by Atkins and Tabor with annealed specimens of steel and copper are presented on logarithmic scales as $\frac{1}{3}(p_m)_c$ versus the equivalent tensile strain, viz., 0.2 cot ϕ and it can be seen that the data are in reasonable accord with the deduced relation $(p_m)_c \propto (\cot \phi)^x$. The fact that the indentation data lie close to straight lines is consistent with the assumption that $(C_c)_p$ is a constant over the whole range of cone angles examined (60°–170°). Also shown in Fig. 2 are the stress-strain data of the materials obtained from compression tests and it can be seen that over the range of strain induced by the conical indenters the same strain-hardening index is obtained for annealed steel from the compression tests and from the indentation tests, viz., $x = 0.24$. For annealed copper, the indentation data can be seen to conform well with the deduced relation and a strain-hardening index of $x = 0.36$ is obtained from the slope of the line through the data. However, it can be seen that in this case the compression data do not conform to equation (2) with a single value of the strain-hardening index over the whole range of strain induced by the indenters but, instead, the compression data are better represented by $x = 0.5$ up to a strain of 0.18 and, thereafter with $x = 0.3$. Despite this, as can be seen, the indentation data would suggest that a single value of the strain-hardening index would suffice in order to express the relation between the stress and the strain in compression. While no explanation for this discrepancy can be offered, we will see, subsequently, that indentation data obtained by Hankins [13] conforms very well with the stress-strain curve obtained by Atkins and Tabor with annealed copper. Thus, to the extent that cone indentation data obtained with annealed metals conform with prediction and, at least in the case of annealed steel, the same strain-hardening index is obtained from compression and from indentation data we may conclude that the analysis can explain the results obtained when annealed metals are indented by cones and the data are consistent with the hypothesis that $(C_c)_p$ is constant, independent of cone angle. The fact that indentation data presented as $\frac{1}{3}(p_m)_c$ versus 0.2 cot ϕ lie close to true stress-natural strain data obtained from compression tests suggests that the values $(C_c)_p = 3$ and $(q_c)_p = 0.2$ are reasonable.

It has been postulated in the foregoing that prestraining the specimen material by compression introduces factors which influence the measured value of the hardness in addition to the obvious strain-hardening influence and these additional factors will now be considered. Beeuwkes, et al. [6], have suggested that friction between the indenter surface and the specimen material and the release of elastic stresses on unloading will cause false hardness readings. Interfacial friction will influence hardness measurements made both on annealed and on prestrained materials so that the anomalous behavior observed with heavily compressed specimens cannot be attributed to this factor.

Regarding elastic recovery, Beeuwkes, et al., proposed an equation to compensate for this effect on the measured hardness. This equation suggests that the overestimation of the true hardness is a constant proportion of the measured hardness. We will now consider the implications of this suggestion. Suppose that the true hardness is p_m, the measured hardness is p_a, that $p_m = K (\cot \phi)^x$ and that the equation proposed by Beeuwkes, et al., is a valid representation of the effect of elastic recovery, viz., that $p = p_m - p_a = -kp_a$. Then $p_m = p_a (1 - k) = K (\cot \phi)^x$, i.e., $p_a = K' (\cot \phi)^x$ where $K' = K/(1 - k)$ is a constant. Thus presenting the measured hardness against cot ϕ on logarithmic scales will still result in a linear relation of the correct (strain hardening) slope although the values of the hardness are overestimates. However, we see that the Beeuwkes, et al., equation *cannot* be invoked to explain the variation of hardness with indenter angle observed when indentations are made in a heavily prestrained specimen.

One possible mechanism by which the observed influence of indenter angle on measured hardness could be explained is via the influence of residual stresses in the surface layers of the specimen under examination. Now even though the specimens used by Atkins and Tabor were compressed between lubricated plattens, it is not unreasonable to expect that compressive residual stresses would be induced in the surface layers and that these would reduce as we progress in depth below the surface until, eventually, the residual stresses become tensile. If we compare the depths reached with a 60° and a 170° cone under a given load we find that if we are indenting a material for which the strain-hardening index is 0.4, the 60° cone penetrates 11 times deeper than does the 170° cone while, for a fully work-hardened material ($x = 0$), the penetration ratio increases to 20. Thus the larger the included angle of the cone the higher are the compressive stresses in the material which is in contact with the indenter faces and hence, the more will the measured hardness be an overestimate of the true hardness. Plausible as this suggestion is, it must be viewed with some degree of caution, at least as far as an attempt to use it to explain the observations of Atkins and Tabor goes for they make the point that their measured hardness values were *not* a function of load. In fact, they used 5 kg and 20 kg loads when determining the hardness of copper and 20 kg and 50 kg loads to measure the hardness of steel so that for any indenter the penetration into the heavily prestrained copper was something like twice as deep at the higher load than it was at the lower load while for the heavily prestrained steel the depth ratio would be of the order of 1.6:1. Clearly, the penetration ratio obtained by varying the load is an order of magnitude less than that achieved by changing the indenter angle from 60° to 170° when indenting a fully work-hardened material but, for all that, some influence of load should have been evident, particularly with the large angled cones since the stress gradients would be steepest in the layers immediately below the surface.

In contrast to the observations by Atkins and Tabor, there is evidence that cone and Vickers hardness values may depend on load; sometimes the hardness is found to increase as the load increases, sometimes it is found that the hardness is independent of the load and yet other investigations reveal that the measured hardness decreases as the load increases. In fact, this is consistent with the suggestion that residual stresses influence the measured value of the hardness, for if the pretreatment of the material under examination is such as to generate compressive residual stresses in the surface layers (e.g., cold rolling) then the measured hardness will *decrease* as the load (and hence the penetration) increases but if the pretreatment generates residual tensile stresses in the surface layers (e.g., a thermal quench) then the measured hardness will *increase* as the load increases. Results presented by Fisher [16] are given in Table 1 and show that with a high nickel-chrome alloy (the pretreatment of which was not mentioned and hence we may infer that it was not subjected to a thermal treatment) the hardness decreases as the load increases while for a 0.37 percent carbon steel which had been subjected to an oil quench, the hardness increases as the load increases. When this same steel was normalized the measured hardness still increased as the load was increased but the increase is much more modest and this, again, is consistent with the suggestion that residual stresses affect the measured hardness since the normalization process would be expected to reduce the residual tensile stresses (induced by the previous oil quench) considerably. Further evidence is furnished by O'Neill [17] who quotes the variation of $(p_m)_p$ obtained with a Vickers pyramid as the load is increased for soft and for cold-rolled copper and for four steels. In all cases but one, the measured hardness decreases as the load increases—oddly enough, the one case in which the hardness was found to increase as the load increased was when the cold-rolled copper was indented but we will see subsequently that this behavior is explicable.

In Figs. 3(*a*) and 3(*b*), the ball and cone indentation data obtained by Hankins [13] are presented on logarithmic scales and from these data we can compare the influence of cold working and normalizing (graphs 3 and 4). Here we see that for the cold-worked steel the cone data lie above the line through the ball data, consistent with the suggestion that compressive residual surface stresses cause the

Downloaded 01 May 2010 to 171.66.16.249. Redistribution subject to ASME license or copyright; see http://www.asme.org/terms/Terms_Use.cfm

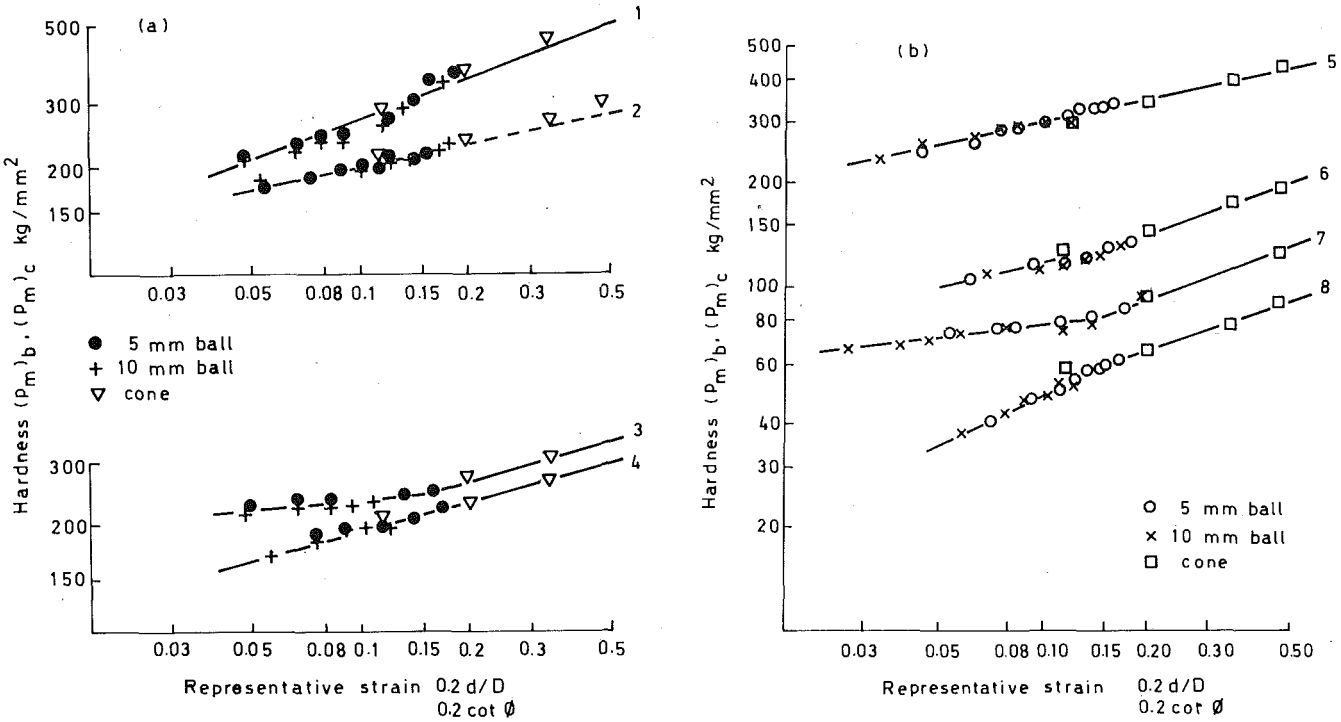


Fig. 3 Ball and cone indentation hardness presented against the representative strain—data obtained by Hankins [13]; (*a*) graph 1: Manganese steel; graph 2: 0.48 percent carbon steel; graph 3: B.E.P. steel, cold-worked; graph 4: B.E.P. steel, normalized and (*b*) graph 5: Tool steel, annealed; graph 6: Mild steel; graph 7: Copper, cold-rolled; graph 8: Copper, annealed; 1 kg/mm^2 = 9.8 MPa

Table 1 Data obtained by Fisher [16] showing that the Vickers hardness may increase or decrease as the applied load increases according to the pretreatment to which the material under examination has been subjected; note loads quoted in kg: 1 kg = 9.8 N

High Nickel-chrome alloy		0.37% Carbon steel			
		Oil quenched		normalised	
Load kg	HV	Load kg	HV	Load kg	HV
1	234	1	532	1	150
5	188	5	570	5	150
10	176	10	585	10	153
20	166	20	588	20	153
40	158	40	592	40	153
60	154	60	590	60	154
80	151	80	590	80	154
100	150	100	590	100	156
				120	155

Downloaded 01 May 2010 to 171.66.16.249. Redistribution subject to ASME license or copyright; see http://www.asme.org/terms/Terms_Use.cfm

measured hardness to be an overestimate of the true hardness while the normalized steel produces cone hardness values which lie on the line through the ball data. Similarly the cone data are close to the line through the ball data when indentations are made in annealed tool steel (graph 5). In contrast, data obtained with annealed copper (graph 8) seem to be grouped about two different lines according to whether we are dealing with ball data or cone data. It appears that as with the stress-strain curve for annealed copper obtained by Atkins and Tabor (Fig. 1) so also here, there is evidence that the data cannot be represented by equation (2) with a single value of the strain-hardening index but that, by chance, the ball data produce strains in the range where one value of the strain-hardening index is appropriate while the cone data fall in the range of strain where another (smaller) value is applicable. What is astonishing is the agreement between the slopes of the two lines drawn in graph 8 and the slopes of the two lines drawn through the stress-strain data shown in Fig. 2. From Fig. 2 the stress-strain curve for annealed copper can be represented with a value of $x = 0.5$ up to a strain of 0.18 and by a value of $x = 0.3$ at higher strains while from graph 8, Fig. 3(b) the line through the ball data has a slope of 0.5 and the line through the cone data has a slope of 0.32, the two lines intersecting at a strain of 0.17.

Any attempt to explain the data obtained with rolled copper (graph 7) in terms of the stress-strain curve being represented by equation (2) with different values of the strain-hardening index in different ranges of strain would require the strain-hardening index above a strain of 0.15 being *higher* than the strain-hardening index below this strain—an unlikely eventuality. More likely is the suggestion that here (and also in graphs 3, 6, and 7) we are seeing the influence of residual compressive stresses causing the measured hardness values to be overestimates, the degree of overestimation increasing as the strain decreases. (No comment is offered concerning the data shown in graph 1 since the data there are subject to too much scatter to warrant any deduction being made.)

It would appear then that available experimental data are quite consistent with the suggestion that residual surface stresses influence the value of the measured hardness, and further, that notwithstanding the fact that Atkins and Tabor could not detect any dependence of the cone hardness on load, the behavior they observed when heavily prestrained specimens were indented is consistent with the suggestion that the surface layers of the specimens were subject to compressive residual stresses.

It is unfortunate that the generation of compressive residual stresses is not the only complication which is introduced when specimens are heavily prestrained. Siebe [18] has shown that the hardness of compressed specimens increases as we progress from the surface to the center and this would tend to cause the measured hardness to increase either as the load increases or as the indenter angle decreases. This, perhaps, offers an explanation of the observation just quoted that with cold-rolled copper, the hardness was found to increase as the load was increased despite the fact that we would anticipate exactly the opposite effect if residual compressive stresses alone were influencing the measured value of the hardness. From all this we might conclude that indentations into materials other than in the annealed or a normalized condition are liable to produce data which are extremely difficult to interpret with confidence.

Square-Based Pyramid Hardness. Little by way of data obtained during a systematic investigation of the influence of pyramid indenter angle on the measured hardness exists. Haddow and Johnson [14] have indented tellurium-lead and aluminum, both annealed and in the work-hardened condition with both rough and smooth triangular-based and square-based pyramids. They measured the depth of unloaded indentations and, as Atkins and Tabor [19] have indicated, the hardness values computed from their measurements of applied load/(depth of recovered indentation)^2 are likely to be in error because of elastic recovery, piling-up and sinking-in effects. We have seen above, however, that although the actual value of the hardness may be erroneous as a result of elastic recovery, the form of the dependence of the measured value of $(p_m)_p$ on pyramid angle should be unaffected. In Fig. 4 the computed values of the pyramid hardness, $(p_m)_p$,

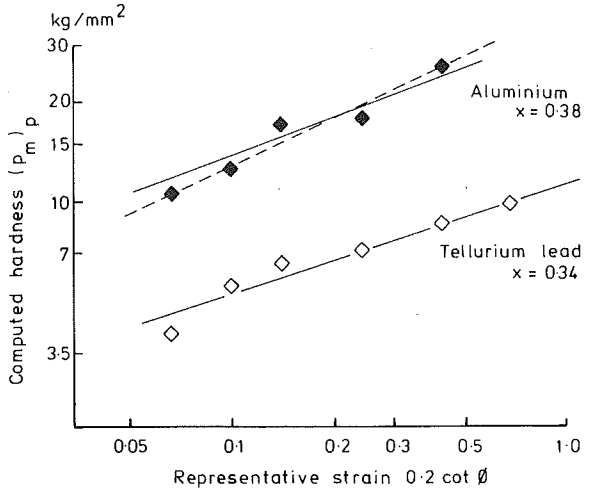


Fig. 4 The pyramid hardness, calculated from the data obtained by Haddow and Johnson [14] presented against the representative strain 0.2 cot ϕ; 1 kg/mm^2 = 9.8 MPa

for annealed aluminum and tellurium-lead are presented against values of the representative strain on logarithmic scales and the data are seen to be distributed about straight lines. The slope of the line through the data obtained with tellurium-lead is 0.34 which agrees quite well with the strain-hardening index obtainable from the stress-strain curve given by Haddow and Johnson, viz., $x = 0.32$. Rather less satisfactory is the agreement between the strain-hardening index obtained from the stress-strain curve for aluminum ($x = 0.35$) and the slope of the line through the indentation data obtained with aluminum for although the solid line drawn through the data has a slope of 0.38, the dashed line could equally well be drawn through the data and this has a slope of 0.49.

Relation Between Cone and Vickers Hardness. Böklen [20] quotes hardness values obtained by Koschella [21] who measured $(p_m)_c$ using 92° and 142° diamond cones and, also, the Vickers hardness of 20 materials. If we accept the approximation proposed in the foregoing that a square-based pyramid generates the same mean stress and the same representative strain as a cone of the same apex angle, then from a knowledge of the cone hardness values we should be able to estimate the Vickers hardness and these estimates can be compared with the measured values of the Vickers hardness.

Assuming that the true stress-natural strain curve of the material can be expressed as $\sigma = b\epsilon^x$ then we may write $\frac{1}{3}(p_m)_c' = b(0.2 \cot 46°)^x$ and $\frac{1}{3}(p_m)_c'' = b(0.2 \cot 71°)^x$ where $(p_m)_c'$ and $(p_m)_c''$ are the cone hardness values determined with a 92° and a 142° cone, respectively. Hence, $(p_m)_c''/(p_m)_c' = z = (\cot 71/\cot 46)^x$; that is,

$$x = \log z/(\log \cot 71 - \log \cot 46)$$

$$= \log z/\log 0.3566$$

so that from a knowledge of $(p_m)_c''$ and $(p_m)_c'$ we can calculate a value for x. Now $\frac{1}{3}(p_m)_p = b(0.2 \cot 68)^x$; that is, $(p_m)_p = (p_m)_c' (\cot 68/\cot 46)^x = (p_m)_c' (0.4148)^x$.

Tabor [3] has shown that the Vickers hardness, HV, is related to $(p_m)_p$ by the equation $HV = 0.93\ (p_m)_p$; hence, $HV = 0.93\ (p_m)_c' (0.4148)^x$.

In Table 2, the calculated values of x and of HV are given and the latter may be compared with the measured values of HV; hence it can be seen that generally the agreement between the measured and the calculated values is surprisingly good. These results taken in conjunction with the prediction that a Vickers pyramid induces a strain of about 8 percent lend support to the suggestion, proposed above, that the mean stress and the representative strain produced by a cone and by a square-based pyramid of the same apex angle are approximately the same.

Downloaded 01 May 2010 to 171.66.16.249. Redistribution subject to ASME license or copyright; see http://www.asme.org/terms/Terms_Use.cfm

Conclusions

1 The semi-empirical analysis just given has shown that

(*a*) For ball indentation an equation of the same form as Böklen's empirical equation (which embodies Meyer's laws) can be derived.

(*b*) Cone hardeness, $(p_m)_c$, can be related to the cotangent of the semiapex angle of the cone in terms of the cone hardness obtained with a 90° cone and the work-hardening index of the indented material.

(*c*) The hardness obtained with a square-based pyramid can be related to the cotangent of the semiapex angle of the pyramid in terms of the hardness obtained with a 90° square-based pyramid and the work-hardening index of the indented material.

(*d*) A Vickers pyramid induces a strain of about 8 percent—a result in agreement with empirical observation.

(*e*) Indentation data obtained with annealed or with lightly prestrained materials can be related to the uniaxial stress-strain curve of the material by taking $\frac{1}{3}$ of the mean hardness pressure as the representative stress. For ball indenters the equivalent strain is $0.2\ (d/D)$ where D is the indenter diameter and d is the diameter of the projected, circular area of the permanent indentation while, for cones and square-based pyramids of semiapex angle ϕ, the equivalent strain is $0.2 \cot \phi$.

(*f*) The Vickers hardness predicted from a knowledge of the cone hardness values measured with a 92° and a 142° cone agrees very well with measured values of the Vickers hardness.

2 If the effect of elastic recovery on unloading is as expressed by the equation proposed by Beeuwkes, et al. [6], then the value of the strain-hardening index obtained by plotting the measured cone hardness against cot ϕ on logarithmic scales will be unaffected by elastic recovery although the value of the hardness measured after unloading will be an overestimate of the true hardness.

3 Pretreatments resulting in the surface layers of the material under examination being subjected to compressive residual stresses will cause the measured hardness obtained with a given cone or pyramid to decrease as the load is increased and will cause the measured hardness obtained at a given load to be an overestimate of the true hardness, the extent of the overestimation increasing as the indenter angle increases and as the magnitude of the residual compressive stress increases.

4 Pretreatments resulting in the surface layers of the specimen material being subject to compressive residual stresses will tend to cause the measured hardness obtained at a given load to increase as the indenter angle increases. This explains the observations made when cold-worked materials were indented by wedges [9], cones [5, 10], and by pyramids [11].

5 Pretreatments resulting in the surface layers of the specimen material being subject to tensile residual stresses will produce results exactly opposite to those quoted in 5 and 6.

Table 2 Showing the values of the Vickers hardness calculated from cone data and, for comparison, the measured values of the Vickers hardness; data quoted by Böklen [20]

	MATERIAL	x	HV measured	HV calculated
1.	ST 37 k	- 0.01	202	186
		- 0.04	206	191
2.	ST 37 k normalised	0.15	124	115
3.	C 45	0.05	222	224
		0.07	205	212
4	C 45 normalised	0.11	181	185
		0.08	207	206
5	C 60	0.08	226	212
6	C 60 normalised	0.09	212	215
		0.11	196	201
7	37 Mn. Si 5	0.04	267	258
8	37 Mn. Si 5 normalised	0.08	224	224
9.	12 Cr. Ni 18	0.11	247	243
10	12 Cr. Ni 18 quenched	0.31	161	163
11	VC Mo 135	0.03	320	296
12	Al_{99} F8	0.11	28	25
13	Al_{99} F12	- 0.05	42	36
14	AlBz5 F30	0.16	108	105
		- 0.02	171	165
15	AlBz5 F45	- 0.03	175	172
16	Al Zn Mg Cu	- 0.05	190	181
17	Ms 58 F 37	0.15	108	112
18	Ms 58 F 44	0.15	119	122
19	Al Cu Mg 2 F 38	0.03	128	127
20	Al Cu Mg 2 F 44	0.04	142	143

References

1 Meyer, E., "Untersuchungen über Härteprüfung und Härte," *Zeitschrift V.D.I.*, Vol. 52, 1908, pp. 645–654.

2 Böklen, R., "Die bezogene Härtekurve und die Ludwik'sche Kegeldruckhärte," *Zeitschrift für Metallkunde*, Vol. 35, 1943, pp. 14–18.

3 Tabor, D., "A Simple Theory of Static and Dynamic Hardness," *Proceedings of the Royal Society*, Series A, Vol. 192, 1948, pp. 247–274.

4 Nadai, A., *Plasticity*, McGraw-Hill, New York, 1931, p. 83.

5 Atkins, A. G., and Tabor, D., "Plastic Indentation in Metals With Cones," *Journal of the Mechanics and Physics of Solids*, Vol. 13, 1965, pp. 149–164.

6 Beeuwkes, R., Chait, R., and Lin, H. H., "The Science of Hardness Testing and Its Research Applications," American Society for Metals, Metals Park, Ohio, 1971, p. 75.

7 Timoshenko, S. P., and Goodier, J. N., *Theory of Elasticity*, 3rd ed., McGraw-Hill, New York, 1970, p. 412.

8 Sneddon, I. N., *Fourier Transforms*, McGraw-Hill, New York, 1951, p. 466.

9 Dugdale, D. S., "Wedge Indentation Experiments With Cold-Worked Metals," *Journal of the Mechanics and Physics of Solids*, Vol. 2, 1953, pp. 14–26.

10 Dugdale, D. S., "Cone Indentation Experiments," *Journal of the Mechanics and Physics of Solids*, Vol. 2, 1954, pp. 265–277.

11 Dugdale, D. S., "Experiments With Pyramidal Indenters—Part I," *Journal of the Mechanics and Physics of Solids*, Vol. 3, 1955, pp. 197–205.

12 Bishop, R. F., Hill, R., and Mott, N. F., "The Theory of Indentation and Hardness Tests," *Proceedings of the Physical Society*, Vol. 57, 1945, pp. 147–159.

13 Hankins, G. A., "Report on the Effects of Adhesion Between the Indenting Tool and the Material in Ball and Cone Indentation Hardness Tests," *Proceedings of the Institution of Mechanical Engineers*, Vol. 1, 1925, pp. 611–645.

14 Haddow, J. B., and Johnson, W., "Indenting With Pyramids—II Experimental," *International Journal of Mechanical Science*, Vol. 4, 1962, pp. 1–13.

15 Hill, R., Lee, E. H., and Tupper, S. J., "The Theory of Wedge Indentation of Ductile Materials," *Proceedings of the Royal Society*, Series A, Vol. 188, 1947, pp. 273–290.

16 Fisher, A., "A Neglected Factor in Diamond Pyramid Hardness Testing," *Machinery*, London, Vol. 53, 1939, pp. 654–655.

17 O'Neill, H., *Hardness Measurement of Metals and Alloys*, Chapman and Hall, London, 1967, p. 44.

18 von Siebe, P., "Härteverlauf in gestauchten Kupferzylindern," *Zeitschrift für Metallkunde*, Vol. 19, 1927, pp. 366–373.

19 Atkins, A. G., and Tabor, D., "On 'Indenting With Pyramids'," *International Journal of Mechanical Science*, Vol. 7, 1965, pp. 647–650.

20 Böklen, R., "Neues Verfahren zur Ermittlung der Streckgrenze aus Eindrücken mit einem spitzen Diamantkegel," *Zeitschrift für Metallkunde*, Vol. 55, 1964, pp. 371–373.

21 Koschella, J., "Diplomarbeit," Technische Hochschule Stuttgart, 1962.

Downloaded 01 May 2010 to 171.66.16.249. Redistribution subject to ASME license or copyright; see http://www.asme.org/terms/Terms_Use.cfm

P. J. Digby[1]

Department of Mathematics
and General Research,
Koninklijke Shell Exploration
and Production Laboratory,
Volmerlaan 6,
Rijswijk (ZH),
The Netherlands

The Effective Elastic Moduli of Porous Granular Rocks

A porous granular rock is modeled by an aggregate of identical, randomly stacked, spherical particles. Contacting particles are initially bonded together across small areas. A theory is developed for the deformation of two such spherical particles under equal and opposite forces acting through the line joining their centers. The theory is used to calculate the effective elastic moduli of the medium. The dependence of the derived elastic wave speeds on the confining pressure and adhesion radius of the contacting particles is then predicted.

1 Introduction

In the present paper, we consider the calculation of the effective elastic moduli of porous, granular rocks. The rock will always be elastically isotropic and homogeneous over lengths large compared with the radii of the individual particles of which the rock is composed. Many earlier papers treating this problem (for example, Deresiewicz [2] and Duffy and Mindlin [3]) concentrate on regular packings of identical solid spherical particles. The results obtained in such special cases are very useful. All predict effective elastic moduli whose values are directly proportional to the cube root of the confining pressure, no matter what kind of regular packing model is selected. One limitation of this model is, of course, that the material will not be elastically isotropic. Another is that values of the effective elastic moduli have so far only been predicted for a few descrete values of the porosity.

Brandt [1], in his elegant treatment of the porous, granular rock proposed an alternative model. A random packing of spherical particles of different radii was used. He was able to calculate explicitly the effective bulk modulus of an elastically isotropic, homogeneous porous rock as a function of the confining pressure, porosity, and liquid saturation. Values of the effective shear modulus, and the pressure and shear wave speeds were then derived, assuming that the effective Poisson's ratio for the rock was known.

In the present paper, we shall calculate explicitly *both* the effective bulk and the effective shear modulus of a porous granular rock modeled by a random packing of identical solid spherical particles. We shall also consider the effect of the initial bonding of the particles on the calculated values of the effective bulk and effective shear moduli. In all of the earlier papers just described, the particles (grains) composing the rock were not actually bonded together initially. Rather, the particles were forced to come into contact over small areas by subjecting a specimen of the modeled rock to large confining pressures.

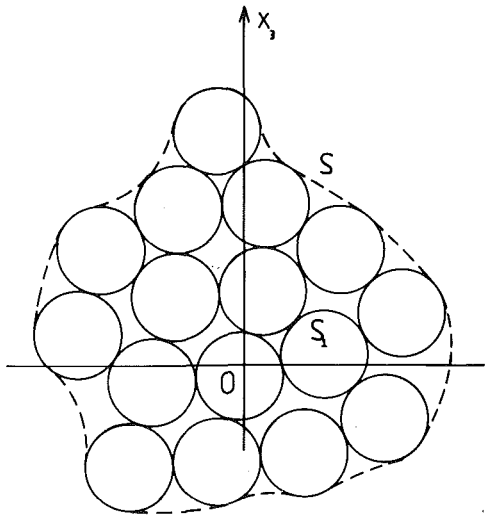


Fig. 1 Set of spheres in the medium intersected by an arbitrary plane S_1 normal to the Ox_3-axis; externally applied stress is transmitted to the particles across a surface S enclosing a large number of particles in the medium

We shall deal with the more general case in which the granular rock is modeled by a random packing of bonded spheres of different radii in a later paper. This exercise will enable the effects of porosity and liquid saturation to be included in the calculations.

2 Model of the Rock

We consider a random packing of identical solid spherical particles of radius R. Each particle (grain) is elastically isotropic and homogeneous with shear modulus, Poisson's ratio, and density, μ, ν, and ρ, respectively. A bar over any of these quantities denotes the corre-

[1] From *present to September, 1981:* Lobelialaan 48, 2555 PJ, The Hague, The Netherlands: *After October, 1981:* Department of Rock Mechanics, University of Lulea, S-951 87 Lulea, Sweden.

Contributed by the Applied Mechanics Division for publication in the JOURNAL OF APPLIED MECHANICS.

Discussion on this paper should be addressed to the Editorial Department, ASME, United Engineering Center, 345 East 47th Street, New York, N. Y. 10017, and will be accepted until two months after final publication of the paper itself in the JOURNAL OF APPLIED MECHANICS. Manuscript received by ASME Applied Mechanics Division, September, 1980; final revision, March, 1981.

Copyright © 1981 by ASME

Downloaded 01 May 2010 to 171.66.16.249. Redistribution subject to ASME license or copyright; see http://www.asme.org/terms/Terms_Use.cfm

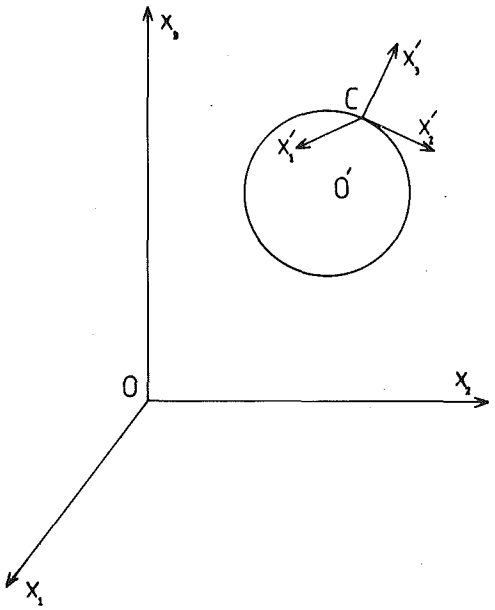


Fig. 2 $Ox_1x_2x_3$ is a right-handed set of axes embedded in the rock; C is a contact point on the surface with center $0'$; $Cx'_1x'_2x'_3$ is a right-handed set of axes on the surface of the sphere with Cx'_3 normal to the surface

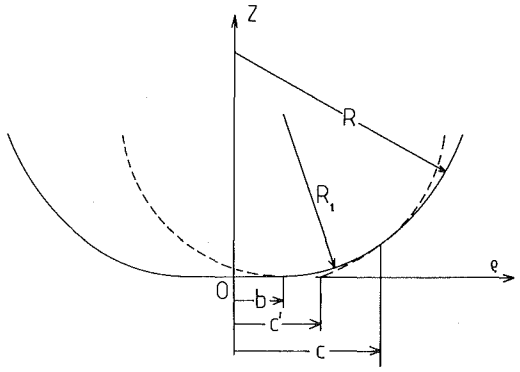


Fig. 3 Cross section of the surface profile of a spherical particle near an adhesion region before deformation

sponding effective elastic modulus or density of the medium we are considering. Neighboring particles are initially firmly bonded across small, flat, circular regions of the same average radius b. Outside the adhesion surfaces, the particles are assumed to be smooth. Consider an aggregate of these particles enclosed by the surface S shown in Fig. 1. The dimensions of S are large compared with the radius of any particle. The surface S transmits an external pressure P to the particles. Under such a purely hydrostatic stress condition, we suppose that the particles deform in such a way that the contact regions of all neighboring particles remain flat, circular, and have the same average radius $a(>b)$ small compared with R. Under purely hydrostatic externally applied stresses we assume that the contact forces are normal to the contact surfaces and have the same average value. Each sphere has the same average number of contacts K.

3 Some Preliminary Definitions

We define a right-handed set of orthogonal unit vectors $\mathbf{i}_1, \mathbf{i}_2, \mathbf{i}_3$ along axes Ox_1, Ox_2, Ox_3, respectively, embedded in the rock we are considering, as shown in Fig. 2. At a given contact point C on the sphere with center O' we define an analogous set of unit vectors $\mathbf{i}'_1, \mathbf{i}'_2, \mathbf{i}'_3$ along the axes Cx'_1, Cx'_2, Cx'_3 with $\mathbf{i}'_3$ normal to the surface of the sphere. Referred to axes Ox_1, Ox_2, Ox_3, the unit vectors $\mathbf{i}'_r$ $(r = 1, 2, 3)$ have the components

$$\mathbf{i}'_r = (\alpha_{r1}, \alpha_{r2}, \alpha_{r3}) \tag{1}$$

The position and displacement vectors have components x_i and u_i, respectively, and the components of the applied stress and strain tensors are written p_{ij}, e_{ij} $(i, j = 1, 2, 3)$ referred to the same axes. Corresponding primed quantities denote components referred to the axes $Cx'_1x'_2x'_3$. $u_i{}^c$ and $u_i{}^0$ $(i = 1, 2, 3)$ denote the displacement components of the points C and O', respectively, for the sphere center O'. Contact forces at C have the components N'_{31}, N'_{32}, and N'_{33} along axes $\mathbf{i}'_1, \mathbf{i}'_2, \mathbf{i}'_3$, respectively.

4 Calculation Procedure

We suppose the medium is initially subjected to a uniform hydrostatic pressure $P = -p_{kk}/3$. e_{kk} is the corresponding uniform strain field. We now superimpose on this uniform field, small, arbitrary applied stresses δp_{ij} $(i, j = 1, 2, 3)$. Let δe_{ij} be the corresponding strain field. δp_{ij} and δe_{ij} are supposed uniform over lengths large compared with R. We suppose that under the given applied stresses, each grain undergoes zero rotation, that is, no couple stresses act in the medium. We then have

$$\delta p_{ij} = \bar{\kappa}\delta_{ij}\delta e_{kk} + 2\bar{\mu}(\delta e_{ij} - \tfrac{1}{3}\delta_{ij}\delta e_{kk}) \tag{2}$$

As usual, δ_{ij} is the Kronecker delta symbol and, unless stated otherwise, summation is performed over repeated subscripts.

Our problem is to calculate explicitly the effective bulk and the effective shear moduli $\bar{\kappa}$ and $\bar{\mu}$ in equation (2). A similar problem has been solved by Duffy and Mindlin [3] for a special type of regular packing. However, rigorous application of their methods, for rocks modeled by random packings of spheres, would be a hopelessly complex task. We must therefore construct an approximate method.

We suppose first that the increment of displacement of a contact point on the surface of any sphere in the medium, relative to its center, $\delta(u_j{}^c - u_j{}^o)$, $(j = 1, 2, 3)$ can be uniquely determined from the uniform applied strain field δe_{ij}, that is,

$$\delta(u_j{}^c - u_j{}^o) = R\alpha_{3k}\delta e_{jk} \tag{3}$$

In Section 6, we consider the number of spheres in the medium intersected by an arbitrary plane. Variations in contact forces, $\delta N'_{3i}$ $(i = 1, 2, 3)$ are related to the arbitrary variations in the applied stresses δp_{ij} by deriving a force equilibrium equation for all spheres cut by the plane. This problem is considered in Section 7. It will be seen that the values of the effective elastic moduli (given in equations (33) and (34) later) can be explicitly calculated, if the relative displacements of the centers of neighboring, bonded spheres can be related to the contact forces. This problem is considered in the following section.

5 Contact Problem With Adhesion

(a) Boundary Conditions. Fig. 3 shows a plane section normal to the contact surface and through the center of a typical spherical particle (grain) in the medium before deformation has occurred. The surface profile in the adhesion region consists of two circular arcs of radii R and $R_1(R_1 < R)$ joining smoothly at a point distant c from the axis of symmetry. The circular arc of radius R intersects the adhesion region (of radius b) produced at a point distant c' from the axis of symmetry. If c is sufficiently small, the equation of the surface profile in Fig. 3 can be written locally as

$$\begin{aligned} z &= 0 && \text{for} \quad \rho \leqslant b \\ &= (\rho - b)^2/2R_1 && \text{for} \quad c \geqslant \rho \geqslant b \\ &= (\rho^2 - c'^2)/2R && \text{for} \quad \rho \geqslant c \end{aligned} \tag{4}$$

Each surface profile is smooth in the neighborhood of the bonding surface. We therefore have the condition

$$R_1 = R(c - b)/c \tag{5}$$

It can then be assumed that when purely normal forces acting through the centers of the spheres are applied, there are no singularities in the

Downloaded 01 May 2010 to 171.66.16.249. Redistribution subject to ASME license or copyright; see http://www.asme.org/terms/Terms_Use.cfm

normal stress $p_{zz}(\rho)$ at the boundaries of the adhesion and contact regions. Furthermore, the normal stress vanishes at the boundary of the contact region. We must calculate the distance 2δ by which the centers of two adhering spheres approach one another when a purely normal force Y acting through the center of each sphere is applied. We approximate this by a "half plane" problem, as in the classical Hertz theory. The normal displacements in the contact region are prescribed. From equations (4) one obtains the following

$$\begin{aligned} u &= \delta - \frac{(\rho^2 - c'^2)}{2R} \quad \text{for } a \geq \rho \geq c \geq b \\ &= \delta - \frac{(\rho - b)^2}{2R_1} \quad \text{for } a \geq c \geq \rho \geq b \\ &= \delta \qquad\qquad\quad \text{for } a \geq c \geq b \geq \rho \end{aligned} \tag{6}$$

Outside the contact region ($\rho \geq a$) all stresses $p_{zz}(\rho)$, $p_{\rho z}(\rho)$ vanish. Inside the contact region ($\rho \leq a$) the shear stress $p_{\rho z}(\rho)$ again vanishes since we have two identical spheres pushed together by purely normal forces acting along the line joining their centers. The normal stress $p_{zz}(\rho)$ has a resultant equal to Y.

(b) Solution of the Boundary-Value Problem. The adhesion and contact surfaces of the adhering spheres in Fig. 3 join smoothly for all $Y \geq 0$. We can therefore assume that the normal stress $p_{zz}(\rho)$ is continuous for all values of ρ, $0 \leq \rho < \infty$. We can therefore follow the procedure given in Sneddon's book [5]. One obtains the following expression for the normal displacement of the contact surface $u_z(\rho, 0)$, $(0 \leq \rho \leq a)$

$$\pi\mu u_z(\rho, 0) = 2(1-\nu) \int_0^\rho \frac{dt}{(\rho^2 - t^2)^{1/2}} \int_t^a \frac{\rho' p_{zz}(\rho') d\rho'}{(\rho'^2 - t^2)^{1/2}} \tag{7}$$

From equations (6) and (7) we then have

$$\begin{aligned} 2(1-\nu) &\int_0^\rho \frac{dt}{(\rho^2 - t^2)^{1/2}} \int_t^a \frac{\rho' p_{zz}(\rho') d\rho'}{(\rho'^2 - t^2)^{1/2}} \\ &= \pi\mu \left\{ \delta - \frac{(\rho^2 - c'^2)}{2R} \right\} \quad \text{if} \quad c \leq \rho \leq a \\ &= \pi\mu \left\{ \delta - \frac{(\rho - b)^2}{2R_1} \right\} \quad \text{if} \quad b \leq \rho \leq c \leq a \\ &= \pi\mu\delta \qquad\qquad\qquad\quad \text{if} \quad 0 \leq \rho \leq b \end{aligned} \tag{8}$$

We then find, for $0 \leq \rho \leq a$,

$$p_{zz}(\rho) = -\frac{2a^2}{\pi\rho} \frac{d}{d\rho} \int_{\rho/a}^1 \frac{tF(t)dt}{\left[t^2 - \frac{\rho^2}{a^2}\right]^{1/2}} \tag{9}$$

where

$$\begin{aligned} F(t) &= \frac{\mu\delta}{a(1-\nu)} + \frac{\mu bt}{R_1(1-\nu)} \left\{ \sin^{-1}\left(\frac{c}{at}\right) - \sin^{-1}\left(\frac{b}{at}\right) \right\} \\ &\quad - \frac{\mu at}{R_1(1-\nu)} \left(t^2 - \frac{b^2}{a^2}\right)^{1/2} - \frac{\mu at}{(1-\nu)} \left(\frac{1}{R} - \frac{1}{R_1}\right) \left(t^2 - \frac{c^2}{a^2}\right)^{1/2} \\ &\quad \text{if} \quad 1 \geq t \geq c/a > b/a > 0 \\ &= \frac{\mu\delta}{a(1-\nu)} + \frac{\mu bt}{R_1(1-\nu)} \left\{ \frac{\pi}{2} - \sin^{-1}\left(\frac{b}{at}\right) \right\} \\ &\quad - \frac{\mu at}{R_1(1-\nu)} \left(t^2 - \frac{b^2}{a^2}\right)^{1/2} \quad \text{if} \quad c/a \geq t \geq b/a > 0 \\ &= \frac{\mu\delta}{a(1-\nu)} \quad \text{if} \quad b/a \geq t > 0 \end{aligned} \tag{10}$$

We can show from equations (5)and (9) that the condition that the normal stress $p_{zz}(\rho)$ has no singularity as $\rho \to a - 0$ (and in fact vanishes at $\rho = a$) is that $F(1)$ vanishes. We then obtain,

$$\frac{\delta}{a} + \frac{b}{R_1} \left\{ \sin^{-1}\left(\frac{c}{a}\right) - \sin^{-1}\left(\frac{b}{a}\right) \right\} + \frac{a}{cR_1} \left\{ b\left(1 - \frac{c^2}{a^2}\right)^{1/2} - c\left(1 - \frac{b^2}{a^2}\right)^{1/2} \right\} = 0 \quad \text{if} \quad a \geq c > b > 0 \tag{11}$$

(*Cont.*)

An explicit expression for the resultant normal force, Y, can also be derived. We find

$$\begin{aligned} Y &= \frac{4\mu a\delta}{(1-\nu)} + \frac{2\mu ba^3}{3R_1 c(1-\nu)} \left(2 + \frac{c^2}{a^2}\right) \left(1 - \frac{c^2}{a^2}\right)^{1/2} \\ &\quad - \frac{2\mu a^3}{3R_1(1-\nu)} \left(2 + \frac{b^2}{a^2}\right) \left(1 - \frac{b^2}{a^2}\right)^{1/2} \\ &\quad + \frac{2\mu a^2 b}{R_1(1-\nu)} \left\{ \sin^{-1}\left(\frac{c}{a}\right) - \sin^{-1}\left(\frac{b}{a}\right) \right\} \quad \text{if} \quad a \geq c > b > 0 \end{aligned} \tag{12}$$

For the case $c \geq a > b > 0$ one obtains the following corresponding results:

$$\frac{\delta}{a} + \frac{b}{R_1} \left\{ \frac{\pi}{2} - \sin^{-1}\left(\frac{b}{a}\right) \right\} - \frac{a}{R_1} \left(1 - \frac{b^2}{a^2}\right)^{1/2} = 0 \tag{13}$$

and

$$\begin{aligned} Y &= \frac{4\mu a\delta}{(1-\nu)} - \frac{2\mu a^3}{3R_1(1-\nu)} \left(2 + \frac{b^2}{a^2}\right) \left(1 - \frac{b^2}{a^2}\right)^{1/2} \\ &\quad + \frac{2\mu a^2 b}{R_1(1-\nu)} \left\{ \frac{\pi}{2} - \sin^{-1}\left(\frac{b}{a}\right) \right\} \end{aligned} \tag{14}$$

From equations (11) and (12) (or (13) and (14)) together, we find by differentiation that

$$\frac{dY}{d\delta} = \frac{4\mu a}{(1-\nu)} \tag{15}$$

for either $a \geq c > b > 0$ or $c \geq a > b > 0$.

Suppose that a small tangential force dT is now superimposed on the normal force Y. Suppose the centers of the spheres undergo a relative tangential displacement $2\,ds$. Mindlin's results [4], show that

$$\frac{dT}{ds} = \frac{8\mu b}{(2-\nu)} \tag{16}$$

We now present the limiting forms of the results given in equations (11) and (12) (valid for $a \geq c > b > 0$). We let $c \to b + 0$. We find that

$$\delta = a(a^2 - b^2)^{1/2}/R \tag{17}$$

and

$$Y = \frac{4\mu}{(1-\nu)} \left\{ a\delta - \frac{(a^2 - b^2)^{3/2}}{3R} \right\} \tag{18}$$

The use of the limiting forms for Y and δ (equations (17) and (18)) in the following sections of this paper will simplify the subsequent analysis considerably. Equations (17) and (18) reduce to those of the classical Hertz theory when we put b equal to zero. Equations (15)–(18) derived in the foregoing now enable us to relate relative displacements of the centers of neighboring bonded spheres, to small, arbitrary variations in the contact forces.

6 Some Statistical Modeling

We now consider in Fig. 1, the set of spheres in the medium intersected by an arbitrary plane S_1 normal to the Ox_3-axis. We consider the portions of these intersected spheres lying on the side of S_1 whose unit normal points along the positive Ox_3-axis, as shown in Fig. 4. We suppose that the surface area of S_1, denoted by A is large compared with the surface area of any particle. Suppose that the circle of intersection of S_1 with a given sphere subtends an angle 2θ at the center of this sphere (Fig. 4). Suppose there are $n(\theta)$ such spheres. $A(1-\alpha)$ is the total area bounded by all the circles of intersection of S_1 with the spheres, where α is the porosity of the aggregate. The number of spheres per unit bulk volume of the medium is $3(1-\alpha)/4\pi R^3$. The number of spheres cut by S_1 at an angle greater than or equal to θ is therefore $3A(1-\alpha)(1+\cos\theta)/4\pi R^2$. The total number of spheres $n(\theta)$

Downloaded 01 May 2010 to 171.66.16.249. Redistribution subject to ASME license or copyright; see http://www.asme.org/terms/Terms_Use.cfm

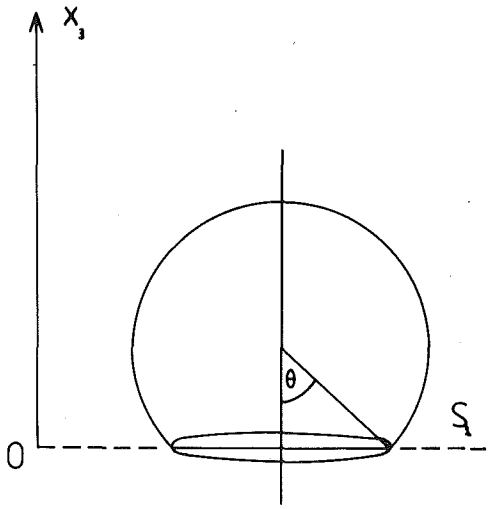


Fig. 4 Portion of intersected spherical particle lying on side of S_1 whose unit normal points along the positive Ox_3-axis; circle of intersection of S_1 with the sphere subtends an angle 2θ at the center of the sphere

cut at between θ and $\theta + \delta\theta$ is therefore equal to $3A(1 - \alpha) \sin \theta\delta\theta/4\pi R^2$. We then have

$$\sum_{\theta} n(\theta) \sin^4 \theta = \sum_{\theta} 3A(1-\alpha) \sin^5 \theta\delta\theta/4\pi R^2 = \frac{3A(1-\alpha)}{4\pi R^2} \int_0^{\pi} \sin^5 \theta d\theta = \frac{4A(1-\alpha)}{5\pi R^2} \tag{19}$$

Similarly, we have

$$\sum_{\theta} n(\theta) \sin^2 \theta = A(1-\alpha)/\pi R^2 \tag{20}$$

Equation (20) can in any case be derived independently of the arguments just given. In later calculations we shall suppose that the K contact points on the surface of a given sphere are distributed over the surface with uniform probability, or at any rate approximately. There are then $K/4\pi$ contacts per unit solid angle distributed over the surface of the sphere. Considering now the portion of the given sphere cut by S_1 (as previously defined) we then easily derive the following results (for $r = 1, 2, 3$) which are also needed in later sections of this paper,

$$\sum_{\text{contacts}} \alpha_{3r} = \tfrac{1}{4} \delta_{3r} K \sin^2 \theta \tag{21}$$

$$\sum_{\text{contacts}} \alpha_{33}{}^2 \alpha_{3r} = \frac{\delta_{3r} K \sin^2 \theta}{8} (2 - \sin^2 \theta) \tag{22}$$

$$\sum_{\text{contacts}} \alpha_{3p}{}^2 \alpha_{3r} = \frac{\delta_{3r} K \sin^4 \theta}{16} \quad \text{for} \quad p = 1, 2 \tag{23}$$

$$\sum_{\text{contacts}} \alpha_{31}\alpha_{32}\alpha_{33} = 0 \tag{24}$$

7 Force Equilibrium Equations

We now derive force equilibrium equations for the set of spheres intersected by the plane S_1. The force increments acting on the portions of the spheres (defined in Section 6) are first due to the force increments acting on the plane S_1 of area A. We suppose that the force increments are the resultant of the uniform applied stress increments δp_{ij} distributed over the plane S_1. Thus the resultant force acting on S_1 has the components $A\delta p_{3r}$, $(r = 1, 2, 3)$. Equilibrium of this set of spheres will be maintained if each of these components is equal to the corresponding component of resultant contact forces acting on the same set of spheres, that is,

$$A\delta p_{3r} = \sum_{\substack{\text{all} \\ \text{spheres}}} \sum_{\text{contacts}} \alpha_{1r}\delta N'_{31} + \alpha_{2r}\delta N'_{32} - \alpha_{3r}\delta N'_{33} \tag{25}$$

for $r = 1, 2, 3$. We can also write (from equations (1) and (3)), for $r = 1, 2, 3$:

$$\delta(u_r{}^{c\prime} - u_r{}^{0\prime}) = R\alpha_{rp}\alpha_{3k}\delta e_{pk} \tag{26}$$

After some algebra, it can then be shown, from the results of Section 5 (equations (15) and (16)) and equations (25) and (26), that, for $r = 1, 2, 3$,

$$A\delta p_{3r} = \sum_{\theta} \sum_{\text{contacts}} \frac{8\mu b n(\theta)}{(2-\nu)} \alpha_{3p}\delta e_{rp} - \alpha_{3r}(\alpha_{3p}\alpha_{3q})\delta e_{pq} + \sum_{\theta} \sum_{\text{contacts}} \frac{4\mu a n(\theta)}{(1-\nu)} \alpha_{3r}(\alpha_{3p}\alpha_{3q})\delta e_{pq} \tag{27}$$

where θ and $n(\theta)$ have been defined in Section 6. We note that only the components of the unit normals to the surfaces of the spheres intersected by the plane S_1 arise in the equilibrium equation (27). It should also be noted that the coefficients of the terms α_{3p} and $\alpha_{3r}(\alpha_{3p}\alpha_{3q})$ for $p, q, r = 1, 2, 3$ are constant over the surface of any sphere. Using equations (21)–(24) derived in Section 5, one obtains from equation (27)

$$A\delta p_{3r} = \sum_{\theta} \frac{K\mu bRn(\theta) \sin^2 \theta}{(2-\nu)} \delta e_{3r}(2 - \sin^2 \theta) + \sum_{\theta} \frac{K\mu aRn(\theta) \sin^4 \theta}{2(1-\nu)} \delta e_{3r} \quad \text{for} \quad r = 1, 2 \tag{28}$$

and

$$A\delta p_{33} = \sum_{\theta} \frac{K\mu bRn(\theta) \sin^4 \theta}{2(2-\nu)} (3\delta e_{33} - \delta e_{kk}) + \sum_{\theta} \frac{K\mu aRn(\theta) \sin^2 \theta}{4(1-\nu)} \{\delta e_{33}(4 - 3\sin^2 \theta) + \delta e_{kk} \sin^2 \theta\} \tag{29}$$

From equation (29) we then derive the following results:

$$\bar{\lambda} = \sum_{\theta} \frac{K\mu Rn(\theta) \sin^4 \theta}{2A} \left\{\frac{a}{2(1-\nu)} - \frac{b}{(2-\nu)}\right\} \tag{30}$$

and

$$2\bar{\mu} = \sum_{\theta} \frac{K\mu Rn(\theta) \sin^2 \theta}{2A} \left\{\frac{a(4 - 3\sin^2 \theta)}{2(1-\nu)} + \frac{3b \sin^2 \theta}{(2-\nu)}\right\} \tag{31}$$

From equation (28) one also obtains

$$2\bar{\mu} = \sum_{\theta} \frac{K\mu Rn(\theta) \sin^2\theta}{A} \left\{\frac{a \sin^2 \theta}{2(1-\nu)} + \frac{b(2 - \sin^2 \theta)}{(2-\nu)}\right\} \tag{32}$$

Equations (31) and (32) appear to be inconsistent. However, we assume that the material we are considering is isotropic. The coefficients of the terms $n(\theta) \sin^2 \theta$ and $n(\theta) \sin^4 \theta$ in equations (30)–(32) are then independent of θ. We can then show, with the help of equations (19) and (20), that equations (31) and (32) are identical. In fact, one finally obtains

$$\bar{\lambda} = \frac{\mu K(1-\alpha)}{5\pi R} \left\{\frac{a}{(1-\nu)} - \frac{2b}{(2-\nu)}\right\} \tag{33}$$

and

$$2\bar{\mu} = \frac{\mu K(1-\alpha)}{5\pi R} \left\{\frac{2a}{(1-\nu)} + \frac{6b}{(2-\nu)}\right\} \tag{34}$$

We can derive a further result from equation (25) with the help of our results given in Section 5. Under a purely hydrostatic increment of stress, δP, we have,

$$A\delta P = \sum_{\substack{\text{all} \\ \text{spheres}}} \sum_{\text{contacts}} \alpha_{33}\delta N'_{33} \tag{35}$$

Under the assumptions outlined in Section 2, and using equations (20)–(24) one obtains

Downloaded 01 May 2010 to 171.66.16.249. Redistribution subject to ASME license or copyright; see http://www.asme.org/terms/Terms_Use.cfm

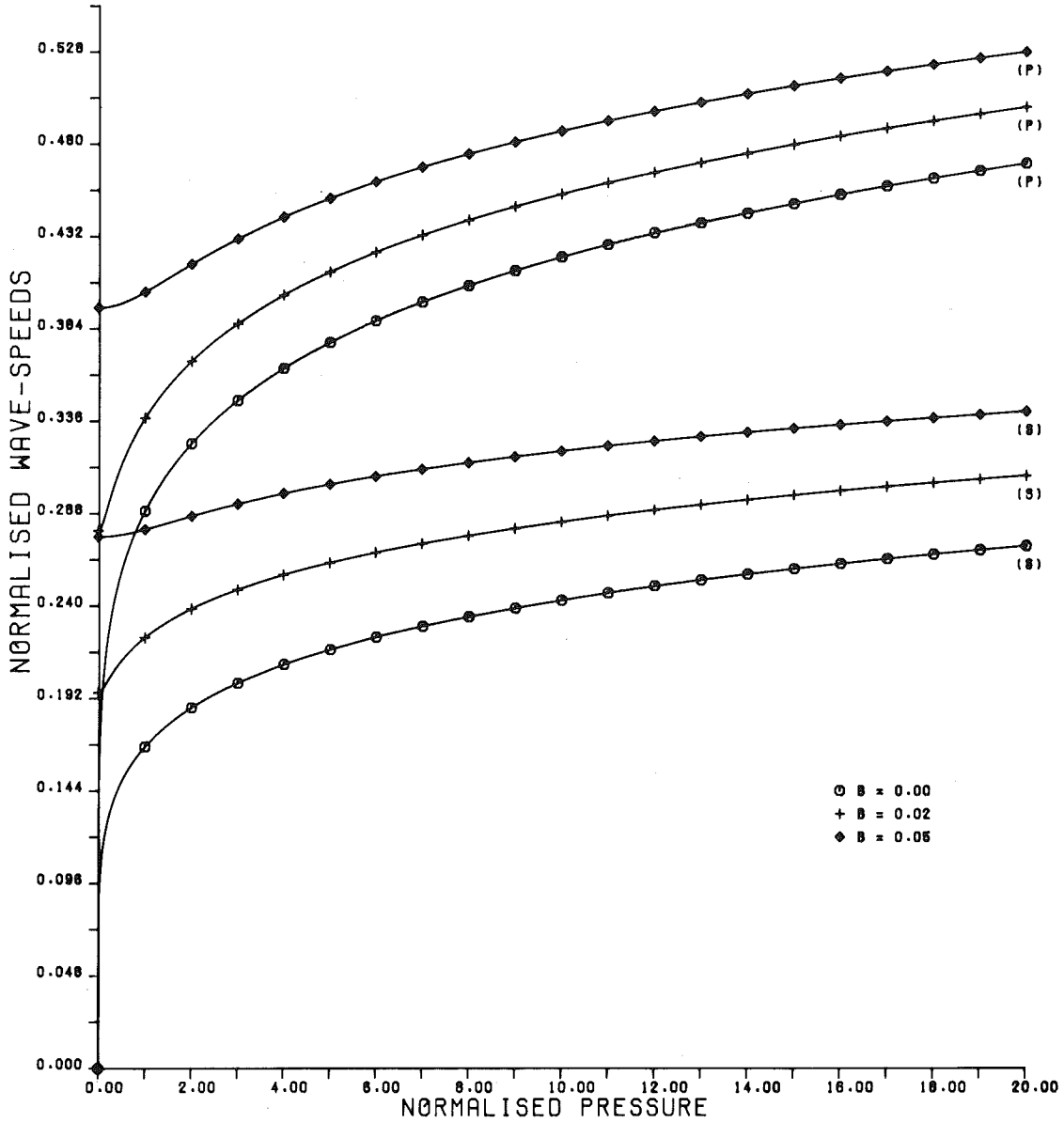


Fig. 5 Normalized wave speeds plotted as functions of the normalized pressure for some fixed values of the normalized adhesion radius $B = b/R$

$$\frac{4\pi R^2 \delta P}{(1-\alpha)} = K\delta N'_{33} = K\delta Y \tag{36}$$

where Y is defined in Section 4. We therefore have, if up to the pressure P, the loading was purely hydrostatic,

$$\frac{4\pi R^2 P}{(1-\alpha)} = KY \tag{37}$$

This result agrees exactly with equation (16) in Brandt's paper [1], for the special case of a "dry" packing of spheres, when, in Brandt's paper we put $C_{\phi\epsilon} = 1$ and $K = 8.84$. It can also be shown, in this case, that the effective density of the medium is given by

$$\bar{\rho} \simeq \rho(1-\alpha)\left(1 + 3\left(\frac{\delta}{R}\right)\right) \tag{38}$$

to order δ/R, where δ has been defined in Section 4 and ρ is the grain density.

From equations (17), (18), and (37) one obtains the following equation for the normalized contact radius, a/R,

$$a/R = \{(x/R)^2 + (b/R)^2\}^{1/2} \tag{39}$$

where x/R satisfies the cubic equation

$$\left(\frac{x}{R}\right)^3 + \frac{3}{2}\left(\frac{b}{R}\right)^2\left(\frac{x}{R}\right) - \frac{3\pi}{2K}\left(\frac{1-\nu}{1-\alpha}\right)\left(\frac{P}{\mu}\right) = 0 \tag{40}$$

Equations (39) and (40), together with equations (33) and (34), enable us to determine explicitly the effective bulk and effective shear modulus of the granular rock we are considering as a function of the confining pressure P and the adhesion radius b of the adhering particles. One can also derive the corresponding numerical values of the elastic wave speeds (using also equation (38))—as is done in the next section. Walton [6], however, has shown that this procedure is only strictly valid for seismic waves of sufficiently low frequency ω, namely, those for which $\rho\omega^2R^2/(\lambda + 2\mu) < \rho\omega^2R^2/\mu \ll 1$.

8 Results

Fig. 5 shows values of the normalized wave speeds $((\bar{\lambda} + 2\bar{\mu})\rho/\mu\bar{\rho})^{1/2}$ and $(\bar{\mu}\rho/\mu\bar{\rho})^{1/2}$ plotted as functions of the normalized confining

Downloaded 01 May 2010 to 171.66.16.249. Redistribution subject to ASME license or copyright; see http://www.asme.org/terms/Terms_Use.cfm

pressure P/μ, for some fixed values of the normalized adhesion radius $B = b/R$. The values selected for the grain Poisson's ratio ν, and the grain shear modulus μ were 0.2 and 38 GPa, respectively. Values of P/μ range from 0 to 18.10×10^{-4}. The values of α and K are the same as those used in Brandt's paper [1]; namely, 0.392 and 8.84, respectively.

References

1 Brandt, H., "A Study of the Speed of Sound in Porous Granular Media," ASME JOURNAL OF APPLIED MECHANICS, Vol 22, 1955, pp. 479–486.

2 Deresiewicz, H., "Stress-Strain Relations for a Simple Model of a Granular Medium," ASME JOURNAL OF APPLIED MECHANICS, Vol 25, 1958, pp. 402–406.

3 Duffy, J., and Mindlin, R. D., "Stress-Strain Relations and Vibrations of a Granular Medium," ASME JOURNAL OF APPLIED MECHANICS, Vol. 24, 1957, pp. 585–593.

4 Mindlin, R. D., "Compliance of Elastic Bodies in Contact," ASME JOURNAL OF APPLIED MECHANICS, Vol. 16, 1949, pp. 259–268.

5 Sneddon, I. N., *Mixed Boundary-Value Problems in Potential Theory*, North Holland Publishing Company, Amsterdam, 1966.

6 Walton, W., "Elastic Wave Propagation in Model Sediments—I," *Geophysical Journal of the Royal Astronomical Society*, Vol. 48, pp. 461–478.

Downloaded 01 May 2010 to 171.66.16.249. Redistribution subject to ASME license or copyright; see http://www.asme.org/terms/Terms_Use.cfm

D. Krajcinovic
Professor,
Department of Materials Engineering,
University of Illinois at Chicago Circle,
Chicago, Ill. 60680
Mem. ASME

G. U. Fonseka[2]
Mechanical Engineer,
NUTECH,
6835 Via de Oro,
San Jose, Calif. 95119

The Continuous Damage Theory of Brittle Materials[1]

Part 1: General Theory

The paper focuses on the establishment of the damage law consistent with the adopted physical interpretation of the damage. The model is developed within the framework of the general thermodynamics theory. In addition, the model incorporates a rigorous mathematical description of the damage growth kinematics including both cleavage and slip modes.

I Introduction

The crystalline structure of a typical structural material is at each stage of the loading characterized by a certain arrangement of dislocations, microcracks, voids and other flaws and defects. The energy associated with a subsequent load increment is accommodated, in case of a purely mechanical system, by changes in:

- the elastic strain energy,
- the plastic flow (redistribution of dislocations)
- the damage pattern (reflecting the growth of the existing defects and nucleation of new microcracks).

The two latter, dissipative processes are distinctly different not only in their nature but even more significantly in the manner in which they affect the compliance of the material. For example, the carefully conducted axial compression tests on unconfined rock or concrete specimens exhibit in general:

1 The "softening" of the specimen (i.e., negative slope of the stress-strain curve) in the "postfailure" domain.

2 Positive dilatancy (volumetric strain) in the later stages of the test.

3 The gradual change of elastic properties (mainly elastic modulus) in subsequent cycles of a repetitive loading program.

None of these phenomena can be satisfactorily interpreted within the framework of the plasticity theory. In addition, except in case of very ductile materials at high temperatures the relation between the plastic strains and the ultimate failure is somewhat tenuous. Hence, there is need for a theory which will recognize the difference between the plastic flow and microcracking.

The exact description of the actual evolution of the microcrack pattern would not only defy our computational capability but would also represent a meaningless task in view of the fact that the details of the crack pattern will to a significant degree differ from one experiment to the other. Hence, instead of trying to reproduce the fine details of the microdefect pattern it appears reasonable to introduce a set of kinematic variables reflecting the damage in an appropriately chosen smoothed sense. A phenomenological theory established along these lines ignores the fine details of the stress distribution around the crack tip, branching, and forking of cracks, etc. Quite naturally, a theory of this kind is also unsuitable in cases when the response is governed by a single well-developed crack.

The description of the state of damage by means of internal variables is reminiscent of the manner in which the plasticity theory describes the rearrangement of the dislocations. A very detailed description of the cracking pattern around a generic point would require a large number of the variables, or as suggested by Kröner [1] a large number of the statistical momenta of a single variable. As in plasticity, it can further be assumed that the higher momenta of the microcrack pattern unnecessarily encumber the analysis for no apparent gain in insight or accuracy.

Such a conclusion is supported by the successful application of the Kachanov's model [2] in a variety of one-dimensional problems, although his measure of the damage (void density in a given cross section) is in Kröner's sense only the zeroth approximation. The description of the increase in damage by the gradual decrease in the effective, load-carrying, area (i.e., increase in the relative void area) is much too attractive to be abandoned for a more esoteric model solely on the basis of the mathematical expedience. The clear physical insight into the problem is, in addition, paramount for the proper identification of the material parameters.

[1] This work was supported by the U.S. National Science Foundation Grant to the University of Illinois at Chicago Circle.

[2] Formerly, graduate student at the University of Illinois at Chicago Circle.

Contributed by the Applied Mechanics Division for publication in the JOURNAL OF APPLIED MECHANICS.

Discussion on this paper should be addressed to the Editorial Department, ASME, United Engineering Center, 345 East 47th Street, New York, N. Y. 10017, and will be accepted until two months after final publication of the paper itself in the JOURNAL OF APPLIED MECHANICS. Manuscript received by ASME Applied Mechanics Division, February, 1981; final revision, May, 1981.

Copyright © 1981 by ASME

Downloaded 01 May 2010 to 171.66.16.249. Redistribution subject to ASME license or copyright; see http://www.asme.org/terms/Terms_Use.cfm

The objective of this paper is to generalize the original Kachanov's model preserving its physical meaning. It is, nevertheless, too optimistic to expect that a single model will suffice for the description of both brittle and ductile, trans- and intergranular, flat, or spherical microcracks. Therefore, for present purposes, it appears reasonable to focus exclusively on the progressive deterioration of brittle materials emphasizing a multitude of flat, penny-shaped planar microdefects.

2 Damage Variable

Even a superficial perusal of the literature reveals the profound disagreement regarding the choice and the mathematical nature of the damage variable. Thus a concise critical appraisal of some of the published literature appears to be appropriate.

The original Kachanov's model [2] considers the damage to be a scalar. Further modifications of the scalar model were suggested by Hayhurst and Leckie [3, 4], Hayhurst, et al. [5], Leckie [6], Lémaitre and Chaboche [7], and many others including Rabotnov, Odquist, Broberg, Leland and others. The scalar representation could obviously be useful in case of the very ductile materials characterized by damage in form of a sufficiently dilute concentration of spheroidal voids. However, the micrographs published by Hayhurst and Leckie [3–5] strongly emphasize thin, planar microcracks perpendicular to the direction of the principal tensile strain. Concious of the directional nature of this type of damage both the originator [8] and one of the main protagonists [6] openly admit the limited appeal of the scalar model when "the stress field has large rotations."

A comprehensive thermomechanical model based on the vectorial representation of the damage was formulated by Davison and Stevens [9]. The planar void was correctly defined by "a vector normal to the plane of the crack and of magnitude equal to the area of the crack."

The first characterization of the damage in form of a second-order tensor is due to Vakulenko and Kachanov [10] who correctly pointed out that a void can grow in either cleavage (Mode I) or the slip (Modes II, III) mode. They defined the damage tensor as a dyadic product of the normal n_i to the void and the relative displacement b_j of two points separated by the void surface, i.e., $\omega_{ij} = n_i b_j$. The lack of the distinction between the damage growth and the damage itself is the inherent shortcoming of this model. Consider an experiment in which the damage ω_{11} was created applying tension in the direction 1. Upon unloading the specimen is subjected to pure shear for which only $d\omega_{12} \neq 0$. Since the already accumulated damage due to the tension is stored in ω_{11} the model ignores it and starts accumulating new damage ω_{12} in the same cross section on the top of the already existing voids. This is a logical consequence of the fact that the definition of damage in [10] involves change (b_j) rather than state.

The second-order tensor model was further developed by Dragon and Mroz [11], Dougill [12–14], Bazant and Kim [15] (who do not consider tension cracking), Srinivasan, et al. [16], Kratochvil and Dillon [17, 18] and again Kachanov [19].

A formal mathematical generalization of the Kachanov's model was suggested by Chaboche [20, 21] who proposed an eight-order tensor damage characterization (in order to preserve the objectivity). The formidable problems in dealing with an eight-order tensor inspired a somewhat flawed second-order tensor characterization by Murakami and Ohno [22], a fairly complex second-order tensor characterization by Sidoroff and Cordebois [23] and a fourth-order tensor model by Chaboche [24].

Of all other models based on the statistical strength theories, the divagation theory or variations of the endochronic theory of special interest is the model suggested by Seaman, Curran, and Shockey [25] who developed a computer model which attempts to bridge the gap between the material sciences and the continuum mechanics. A very interesting model based on the statistical approach and a fourth-order tensor representation of damage was proposed by Chudnovski [26]. His definition of damage, though, contains again the jump in the displacement across the crack which is characteristic of the change of the state and not the state itself.

The present considerations are restricted to damage defined as a multitude of flat, plane penny-shaped microdefects. The shape of the voids is considered to be of little significance. Thus the geometry of such a void is fully defined locally by a vector $\mathbf{D}(X_I,t)$. Consistent with the nature of the theory the components of the damage vector are related to the void densities in the projection planes. The proposed representation is supported by the experimental evidence for rock, concrete, ceramics, and most metals subjected to typical loading conditions and ambient temperatures.

3 Theoretical Preliminaries

The thermodynamics with internal variables developed originally by Coleman and Noll [27] provides a very suitable framework for the establishment of a general form of the continuous damage theory. The comprehensive recapitulation of the theory is hardly necessary in view of many excellent papers such as those already mentioned [9, 17, 18] as well as those by Rice [28, 29] and a host of others. Nevertheless, for the complete understanding of the model it is necessary to highlight several basic ideas.

Disregarding the electrical and chemical processes the basic state functions of a thermodynamic system (perceived as a collection of continuous matter) are as follows:

Helmholtz free energy Ψ
Stress $\boldsymbol{\sigma}$
Heat flux $\mathbf{Q}$
Entropy S

The state variables defining the reversible processes are as follows:

Elastic strain $\boldsymbol{\epsilon}$
Temperature τ
Thermal gradient grad τ

In view of the two diverse processes, the internal (hidden) variables defining irreversible or dissipative processes are classified into two distinctly different groups:

Kinematic variables reflecting the rearrangement of dislocations (plastic flow and hardening), and damage parameters $\mathbf{D}^{(\alpha)}$ ($\alpha = 1, 2, \ldots n$) defining the microdefect pattern locally (truly permanent memory).

In order to focus the attention on the microcracking the internal variables of the first group will not be considered. Furthermore, the consideration will be restricted to materials for which the basic functions depend only on the instantaneous values of the state and internal variables, i.e., "on the current pattern of structural arrangement, on the microscale, of material parameters" (Rice [29]). Finally, the deformations are considered to be small and the process isothermal. Despite of these simplifying assumptions the general framework within which the theory will be developed is sufficiently general for further extensions.

The state functions and variables previously listed are related through the balance laws which can in case of sufficient smoothness be written in form of differential equations. The recital of these equations is in view of [9, 17, 18, 28, 29] superfluous.

4 Analytical Model

4.1 Response Functions. The Helmholtz free energy for a small deformation of a perfectly brittle body subjected to statically applied loading and isothermal conditions is a scalar-valued function of the elastic strain tensor $\boldsymbol{\epsilon}$ and the damage vector $\mathbf{D}$, invariant with respect to the choice of the coordinate system. Making use of the irreducible integrity basis for the representation of a polynomial scalar invariant of the second order tensor $\boldsymbol{\epsilon}$ and vector $\mathbf{D}$ (see, for example, Davison and Stevens [9], or Pipkin and Rivlin [30]) the Helmholtz free-energy density $\Psi(\boldsymbol{\epsilon},\mathbf{D},\tau)$ can be written in form quadratic in strain (for small deformations)

Downloaded 01 May 2010 to 171.66.16.249. Redistribution subject to ASME license or copyright; see http://www.asme.org/terms/Terms_Use.cfm

$$\rho\Psi = \tfrac{1}{2}(\lambda + 2\mu)\epsilon_{KK}\epsilon_{LL} - \mu(\epsilon_{KK}\epsilon_{LL} - \epsilon_{KL}\epsilon_{LK}) + \overline{C}_1 D_K{}^{(\alpha)}\epsilon_{KL}D_L{}^{(\beta)}\epsilon_{MM} + \overline{C}_2 D_K{}^{(\alpha)}\epsilon_{KL}\epsilon_{LM}D_M{}^{(\beta)} \quad (\alpha,\beta = 1, 2, \ldots) \tag{1}$$

where ρ is the mass density (to be taken constant in view of the flatness of the considered defects), while $\overline{C}_i = \hat{C}_i(X_I, D_K D_K, \tau)$ are the scalar-valued material parameters. The Helmholtz free energy must be invariant in case $D^{(\alpha)} \to -D^{(\alpha)}$, where α and β denote damage fields which cannot be added as vectors (see [9]). the Lamé parameters λ and μ can, in general, also depend on τ and D_K. The latter assumption leads, however, to the isotropic damage model [31] insensitive to the orientation change. The superscripts α and β allow consideration of several independent damage fields.

For an isothermal process (see Rice [29]) the stress is

$$\sigma_{IJ} = \rho \frac{\partial \Psi}{\partial \epsilon_{IJ}} \quad (\mathbf{D} \text{ fixed}) \tag{2}$$

From (1) and (2)

$$\sigma_{IJ} = K_{IJKL}\epsilon_{KL} \tag{3}$$

where for a single damage field $\alpha = \beta = 1$ (as in [9])

$$K_{IJKL} = \lambda\delta_{IJ}\delta_{KL} + 2\mu\delta_{IK}\delta_{JL} + \overline{C}_1(\delta_{IJ}D_K D_L + \delta_{KL}D_I D_J) + \overline{C}_2(\delta_{JK}D_I D_L + \delta_{IL}D_J D_K) \tag{4}$$

The incremental form of the stress-strain relationship can be derived from (2) in form

$$d\sigma_{IJ} = \rho \frac{\partial^2 \Psi}{\partial \epsilon_{IJ}\partial \epsilon_{KL}} d\epsilon_{KL} + \rho \frac{\partial^2 \Psi}{\partial \epsilon_{IJ}\partial D_M} dD_M \tag{5}$$

or

$$d\sigma_{IJ} = K_{IJKL}d\epsilon_{KL} + \overline{K}_{IJM}dD_M \tag{6}$$

where from (4) for constant $\overline{C}_i$

$$\overline{K}_{IJM} = \overline{C}_1\epsilon_{KL}[\delta_{IJ}(\delta_{KM}D_L + \delta_{LM}D_K) + \delta_{KL}(\delta_{IM}D_J + \delta_{JM}D_I)] + \overline{C}_2\epsilon_{KL}[\delta_{JK}(\delta_{IM}D_L + \delta_{LM}D_I) + \delta_{IL}(\delta_{JM}D_K + \delta_{KM}D_J)] \tag{7}$$

According to (3) the stress is a quadratic function of $\mathbf{D}$, while Kachanov's model suggests a linear relationship between the stress and the damage $\boldsymbol{\omega}$ (void density). The two models are readily reconciled if

$$\mathbf{D} = D_N\mathbf{N} = \omega_N{}^{1/2}\mathbf{N} \tag{8}$$

where

$$\boldsymbol{\omega} = \omega_N\mathbf{N} \tag{9}$$

with ω_N being the void density in the cross section with normal $\mathbf{N}$. This contrasts the Davison, Stevens [9] model according to which $\mathbf{D} = \omega_N\mathbf{N}$ in present notation. With (8) and (9) the tensors (4) and (7) can be rewritten in form

$$K_{IJKL} = \lambda\delta_{IJ}\delta_{KL} + 2\mu\delta_{IK}\delta_{JL} + C_1(\delta_{IJ}\omega_K\omega_L + \delta_{KL}\omega_I\omega_J) + C_2(\delta_{JK}\omega_I\omega_L + \delta_{IL}\omega_J\omega_K) \tag{10}$$

and since $\overline{C}_i$ are not constant as for (7)

$$\overline{K}_{IJM} = C_1\epsilon_{KL}[\delta_{IJ}(\delta_{KM}\omega_L + \delta_{LM}\omega_K) + \delta_{KL}(\delta_{IM}\omega_J + \delta_{JM}\omega_I)] + C_2\epsilon_{KL}[\delta_{JK}(\delta_{IM}\omega_L + \delta_{LM}\omega_I) + \delta_{IL}(\delta_{JM}\omega_K + \delta_{KM}\omega_J)] + 2[C_1(\delta_{IJ}\omega_K\omega_L + \delta_{KL}\omega_I\omega_J) + C_2(\delta_{JK}\omega_I\omega_L + \delta_{IL}\omega_J\omega_K)]\frac{\omega_M}{\omega_P\omega_P}\epsilon_{KL} \tag{11}$$

where

$$C_i(\omega_N,\tau) = \frac{\overline{C}_i(\tau)}{\sqrt{\omega_p\omega_p}} \tag{12}$$

The incremental stress-strain law (6) is, therefore, finally

$$d\sigma_{IJ} = K_{IJKL}d\epsilon_{KL} + \overline{K}_{IJM}d\omega_M \tag{13}$$

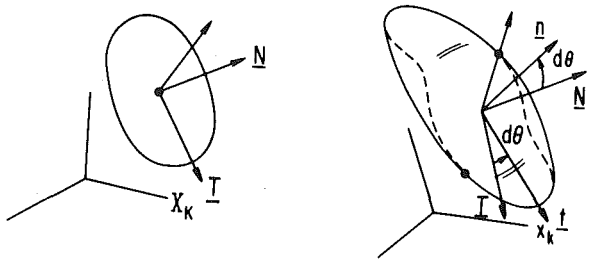


Fig. 1 The original void geometry and the geometry of the incremented void (actual void sketched using the dashed line)

The generalized thermodynamic force conjugate to the kinematic damage variable is

$$R_I{}^{(\alpha)} = -\rho \frac{\partial \Psi}{\partial D_I{}^{(\alpha)}} \quad (\boldsymbol{\epsilon},\tau \text{ fixed}) \tag{14}$$

From (1) for a single damage field ($\alpha = \beta = 1$) and constant $\overline{C}_i$

$$R_I = -2\overline{C}_1\epsilon_{MM}\epsilon_{IL}D_L - 2\overline{C}_2\epsilon_{IL}\epsilon_{LK}D_K = a_{IJ}D_J \tag{15}$$

The strong form of the Clausius-Duhem inequality (proposed by Truesdell and Noll, see Malvern [32]) requires that the local entropy production and the entropy production by heat conduction are separately non-negative. Thus

$$R_I dD_I \geq 0 \tag{16}$$

for all generalized forces and fluxes. Inequality (16) provides the range of admissible values for the material parameters C_i.

As a result of the symmetry of the matrix, a_{IJ} the relation (15) satisfies the Onsager's reciprocity theorem [32]. The relation existing between the generalized thermodynamic force R_I and the "crack resistance force" (i.e., energy-release rate) will be discussed in Appendix A of this paper.

4.2 Kinematics of the Void Growth. The kinematics of the void growth is perhaps the most arbitrary and certainly the most debatable part of the existing damage models. The void growth is in most cases formally legislated on the basis of general considerations and/or simple one-dimensional material science models. Most of these models are insufficiently general and of dubious mathematical heritage. The purpose of this paper is to suggest a rigorous continuum mechanics kinematic model compatible with the adopted physical interpretation of damage (consisting of a multitude of flat, penny-shaped voids).

Generally, the change in the void geometry will involve a combination of two basic modes: dilation and change of orientation (slip). Indeed, from (8) $\dot{\mathbf{D}} = \dot{D}_N\mathbf{N} + D_N\dot{\mathbf{N}}$ where the dot signifies the rate of change. Inherent to this representation is the assumption that a flat void on a curved surface (Fig. 1) is mechanically equivalent to its largest projection. Since the proposed model actually deals with the projections of the damage vector (10) and (11) this assumption does not appear overly restrictive.

A rational description of the void growth kinematics, reminiscent of the procedure leading to the concept of the strain, involves a transformation mapping a void dA_K at a state $(\Psi,\boldsymbol{\sigma},\mathbf{Q}^f,S)$ into a void da_k at a state $(\Psi + d\Psi,\boldsymbol{\sigma} + d\boldsymbol{\sigma},\mathbf{Q}^f + d\mathbf{Q}^f,S + dS)$. Denoting by X^K the material and by x^k the spatial coordinates (Fig. 1) the mapping relation can be written (see Eringen [33]) in form

$$da_k = JX^K{}_{,k}dA_K \tag{17}$$

where J is the Jacobian of the coordinate transformation. The square of the incremented void area is (see again [33])

$$(da)^2 = J^2\overset{-1}{C}{}^{KL}dA_K dA_L \tag{18}$$

where $\overset{-1}{C}{}^{KL}$ is the inverse of the contravariant Green's deformation tensor. The measure of the change in the void area is then

$$(da)^2 - (dA)^2 = (J^2\overset{-1}{C}{}^{KL} - G^{KL})dA_K dA_L = 2d\Omega^{KL}dA_K dA_L \tag{19}$$

Downloaded 01 May 2010 to 171.66.16.249. Redistribution subject to ASME license or copyright; see http://www.asme.org/terms/Terms_Use.cfm

where

$$2\,d\Omega^{KL} = J^{2}\overset{-1}{C}{}^{KL} - G^{KL} \tag{20}$$

with G^{KL} being the contravariant metric tensor of the void geometry.

The second-order tensor $d\Omega^{KL}$ provides the measure of the change in the void geometry.[3] Borrowing from the nonlinear elasticity theory [32, 33] the void dilation or "stretch" is

$$\frac{da}{dA} = \left(J^{2}\overset{-1}{C}{}^{KL}\frac{dA_K}{dA}\frac{dA_L}{dA}\right)^{1/2} = [(2\,d\Omega^{KL} + G^{KL})N_K N_L]^{1/2} \tag{21}$$

where

$$N^K = dA^K/dA$$

is the cosine director of the normal N to the "initial" void surface dA. In the principal void coordinates NT (where T is the direction of slip) the dilation of the void area is

$$\frac{da}{dA_N} = \left(1 + 2\frac{d\Omega^{(NN)}}{G^{(NN)}}\right)^{1/2} \tag{22}$$

where the parentheses around indices suppress the summation. Accordingly, for a small increment in the void area and the orthogonal system of coordinates

$$d\Omega_{NN} = \left(\frac{da - dA}{dA}\right)_N \tag{23}$$

Thus the first diagonal term of the tensor $d\Omega_{NT}$ represents the relative increase in the area of a void in the plane perpendicular to its normal.

In a manner quite similar to one leading to the definition of the shear it can be deduced that the off-diagonal component $d\Omega_{NT}$ represents the angle between the normal **N** and **n** generated by the rotation about the axis perpendicular to **N** and **T** (see Fig. 1 and Appendix B), i.e.,

$$2\,d\Omega_{NT} = \sin(\mathbf{N}, \mathbf{n}) \simeq d\theta \tag{24}$$

At this point it is convenient to establish the relationship between the components of the tensor $d\Omega_{NT}$ and the Kachanov's [2] measure of the damage ω_N which can be written as

$$\omega_N = \frac{dA_N}{A_N} \quad \text{i.e.,} \quad d\omega_N = \left(\frac{da - dA}{A}\right)_N \tag{25}$$

where A_N is the area of the cross section with normal N. Hence, from (22) and (25) follows the scalar equation (no summation)

$$d\omega_N = \omega_N d\Omega_{NN} \tag{26}[4]$$

Since the damage parameter is a vector $\omega_i = \omega_N n_i$ where ω_N is a scalar, the kinematics of the damage growth is defined by

$$d\omega_i = d\omega_N n_i + \omega_N dn_i \tag{27}$$

The relation (24) can be rewritten using the skew-symmetric tensor e_{ijk} in indicial form as

$$dn_i = \frac{1}{2}e_{ijk}d\Omega_{kj} \tag{28}$$

Consequently, substituting (26) and (28) into (27) leads to the vector equation

$$d\omega_i = \omega_N\left(d\Omega_{NN}n_i + \frac{1}{2}e_{ijk}d\Omega_{kj}\right) \tag{29}$$

[3] It should be noted that in general the Helmholtz free energy could depend on $d\Omega^{KL}$ as well. Nevertheless, the assumption that $\Psi = \Psi(\boldsymbol{\epsilon}, \mathbf{D}, \tau)$ is consistent with the premise that the basic function depends only on the current pattern of the microcracking.

[4] In its present form the proposed model is restricted to the growth of already existing microdefects. In view that the original defects can be arbitrarily small, this does not appear to be a serious limitation.

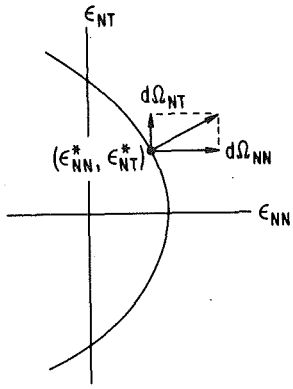


Fig. 2 A damage surface in the strain space

4.3 Damage Law. The concluding step in establishment of the analytical model consists of the determination of the constitutive relationship relating the increments in strain $d\epsilon_{ij}$ and damage growth $d\Omega_{NM}$ ($M = N, T$). This task can be accomplished either by prescribing a damage evolution law (as in [9, 10, 20], etc.) or by using the concept of the damage surface (as in [11–14] or in Paul [34]).

In view of the existence of the load paths along which the damage remains constant the latter approach is definitively preferable. The damage surface is simply an experimentally defined function of state and internal variables $f = \hat{f}(\boldsymbol{\epsilon}, \boldsymbol{\omega}, \tau)$ enveloping all states of stress which can be reached without further increase in damage (change in the recorded history).

In absence of specific experimental data it is possible only to hypothesize on the general shape of the damage surface. If ϵ_{NN} and ϵ_{NT} are the strains normal and tangential to the void surface, it is possible to speculate that

$$d\Omega_{NN} = d\Omega_{NT} = 0 \text{ if } \epsilon_{NN} \leq 0,\ \epsilon_{NT} = 0 \tag{30a}$$

$$d\Omega_{NN} > 0,\ d\Omega_{NT} = 0 \text{ if } \epsilon_{NN} = \epsilon^*_{NN},\ \epsilon_{NT} = 0 \tag{30b}$$

$$d\Omega_{NN} > 0,\ |d\Omega_{NT}| > 0 \text{ if } \epsilon_{NN} = 0,\ \epsilon_{NT} = \epsilon^*_{NT} \tag{30c}$$

$$f(\epsilon^*_{NN}, \epsilon^*_{NT}, \boldsymbol{\omega}, \tau) = f(\epsilon^*_{NN}, -\epsilon^*_{NT}, \boldsymbol{\omega}, \tau) \tag{30d}$$

where the asterisk denotes a point on the damage surface (Fig. 2).

In addition it will be assumed (as in [11–14]) that the damage rate is normal to the damage surface. Thus

$$\begin{aligned} d\Omega_{NN} &= \kappa\, G(\boldsymbol{\epsilon}, \boldsymbol{\omega}, \tau)\left(\frac{\partial f}{\partial \epsilon_{NN}}d\epsilon_{NN} + \frac{\partial f}{\partial \epsilon_{NT}}d\epsilon_{NT}\right)\frac{\partial f}{\partial \epsilon_{NN}} \\ d\Omega_{NT} &= \kappa\, G(\boldsymbol{\epsilon}, \boldsymbol{\omega}, \tau)\left(\frac{\partial f}{\partial \epsilon_{NN}}d\epsilon_{NN} + \frac{\partial f}{\partial \epsilon_{NT}}d\epsilon_{NT}\right)\frac{\partial f}{\partial \epsilon_{NT}} \end{aligned} \tag{31}$$

where $G(\boldsymbol{\epsilon}, \boldsymbol{\omega}, \tau)$ is a non-negative scalar-valued function of the invariants of the state and internal variables, while

$$\kappa = 1 \quad \text{if} \quad f = 0 \quad \text{and} \quad \frac{\partial f}{\partial \epsilon_{IJ}}d\epsilon_{IJ} > 0; \quad \kappa k = 0 \quad \text{otherwise} \tag{32}$$

A possible form of a fracture surface consistent with stipulations (30) is shown in Fig. 2. The extent to which the fracture surface penetrates the domain of negative normal studies ϵ_{NN} and the validity of the normalcy rule depends on the friction between two faces of the void (see Drucker [35] or Mandel [36]). The presence of plastic strains (prior to the onset of damage propagation) will also complicate the issue for $\epsilon_{NN} < 0$.

Downloaded 01 May 2010 to 171.66.16.249. Redistribution subject to ASME license or copyright; see http://www.asme.org/terms/Terms_Use.cfm

The scalar-valued G in (31) cannot be selected arbitrarily. From the consistency equation

$$d\omega_N = -\kappa \left(\frac{\partial f}{\partial \omega_N}\right)^{-1} \left(\frac{\partial f}{\partial \epsilon_{NN}} d\epsilon_{NN} + \frac{\partial f}{\partial \epsilon_{NT}} d\epsilon_{NT}\right) \tag{33}$$

Thus, in conjunction with (26) and (31), the equation (33) provides the expression for the "softening" parameter G

$$G(\epsilon,\omega,\tau) = -\left[\omega_N \frac{\partial f}{\partial \omega_N}\left(\frac{\partial f}{\partial \epsilon_{NN}}\right)\right]^{-1} \tag{34}$$

Finally, it is necessary to relate the strains in the (N, T) system with strains in an arbitrary global coordinate system. Considering, for convenience, the principal axes 1, 2, 3 and the plane strain case it follows that

$$\begin{aligned} \epsilon_{NN} &= \cos^2\theta\epsilon_{11} + \sin^2\theta\epsilon_{22} \\ \epsilon_{NT} &= -\sin\theta\cos\theta\,(\epsilon_{11} - \epsilon_{22}) \end{aligned} \tag{35}$$

where θ is the angle subtended by N and axis 1. Differentiating (35) and using (24) it is readily derived that

$$\begin{aligned} d\epsilon_{NN} &= \cos^2\theta d\epsilon_{11} + \sin^2\theta d\epsilon_{22} - 2(\epsilon_{11} - \epsilon_{22})\,(\sin 2\theta) d\Omega_{NT} \\ d\epsilon_{NT} &= \sin\theta\cos\theta\,(d\epsilon_{11} - d\epsilon_{22}) - 2(\epsilon_{11} - \epsilon_{22})\,(\cos 2\theta) d\Omega_{NT} \end{aligned} \tag{36}$$

4.4 Summary of the Derived Equations. Arranging the components of the stress and strain tensors into vectors all of the derived equations can be conveniently written in matrix notation. Thus

$$\{d\sigma\} = [K]\{d\epsilon\} + [\overline{K}]\{d\omega\} \tag{13'}$$

$$\{d\omega\} = [A]\{d\Omega\} \tag{29'}$$

$$\{d\Omega\} = \kappa[B]\{d\epsilon\} \tag{31'}$$

and

$$\{d\bar{\epsilon}\} = [C]\{d\epsilon\} + [H]\{d\Omega\} \tag{36'}$$

where $\{\bar{\epsilon}\}$ is the vector with components $(\epsilon_{NN}, \epsilon_{NT})$. After some simple manipulations

$$\{d\omega\} = \kappa[A][B][R]\{d\epsilon\} \tag{37}$$

where

$$[R] = ([I] - \kappa[H][B])^{-1}[C] \tag{38}$$

Finally, the incremental stress-strain law can be written in a customary way as

$$\{d\sigma\} = [K_\omega]\{d\epsilon\} \tag{39}$$

where the material property matrix consists of two parts:

$$[K_\omega] = [K] + \kappa[\overline{K}][A][B][R] \tag{40}$$

The second term exists only during loading (32). The first term in view of (10) contains already accumulated damage. In other words, the elastic parameters of the material are gradually changed as a result of the existing cracking (see, for example, Budiansky, O'Connell [37] or Walsh [38]). This is, of course, in sharp contrast to the corresponding matrices governing the plastic deformation of solids.

5 Summary and Conclusions

The proposed analytical model, governing the mechanical response of a perfectly brittle solid under isothermal conditions, which consists of the derived constitutive equation (39), balance laws and the associated initial and boundary conditions:

1 Constitutes a well-posed boundary-value problem the solution of which should provide reasonably reliable estimates of the stress, strain, and damage fields associated with an arbitrarily general loading history (loading path).

2 Is based on an acceptable and clearly defined physical interpretation of the damage and the mathematically rigorous description of the damage growth (incorporating both cleavage and slip modes).

3 Has a sound thermomechanical constitution satisfying all thermomechanical requirements (objectivity, entropy production inequality, etc.).

4 Provides a suitable framework for future extensions to more general materials and processes.

5 Can be readily incorporated into the existing computer codes for nonlinear analyses of structures.

In other words, in contrast to some other existing models, the present model is not a purely mathematical artifice. The physical nature of the model enables unambiguous identification of material parameters and establishment of connections to the Fracture Mechanics and Statistical Strength Theories. This is, naturally, of utmost importance in the experimental determination of the material parameters and use of results obtained elsewhere.

It should be noted again that the suggested model, established as a phenomenological continuum theory, is inherently incapable to predict the fine details of the propagation of a particular crack and the stress field around its tip. In this respect the proposed theory is rather similar to the plasticity theory (and its relation to a particular dislocation).

References

1 Kröner, E., "Dislocation: A New Concept in the Continuum Theory of Plasticity," *Journal of Mathematics and Physics*, Vol. 42, 1962, pp. 27–37.

2 Kachanov, L. M., "On the Creep Fracture Time," *Izv. AN SSR, Otd. Tekhn. Nauk*, No. 8, 1958, pp. 26–31 (in Russian).

3 Hayhurst, D. R., and Leckie, F. A., "The Effect of Creep Constitutive and Damage Relationships Upon the Rupture Time of a Solid Circular Torsion Bar," *Journal of Mechanics and Physics of Solids*, Vol. 21, 1973, pp. 431–446.

4 Leckie, F. A., and Hayhurst, D. R., "Creep Rupture of Structures," *Proceedings of the Royal Society*, London, Series A, Vol. 340, 1974, pp. 323–347.

5 Hayhurst, D. R., Dimmer, P. R., and Chernuka, M. W., "Estimates of the Creep Rupture Lifetime of Structures Using the Finite-Element Method," *Journal of Mechanics and Physics of Solids*, Vol. 23, 1975, pp. 335–355.

6 Leckie, F. A., "The Constitutive Equations of Continuum Creep Damage Mechanics," *Philosophical Transactions of the Royal Society*, London, Series A, Vol. 288, 1978, pp. 27–47.

7 Lemaitre, J., and Chaboche, J. L., "Aspect Phenomenologique de la Rupture par Endommagement," *Journal de Mecanique Appliquee*, Vol. 2, 1978, pp. 317–365.

8 Kachanov, L. M., "Creep and Fracture at Complex Loading," *Problemi Prochnosti*, 1977, No. 6, pp. 3–5 (in Russian).

9 Davison, L., and Stevens, A. L., "Thermomechanical Constitution of Spalling Elastic Bodies," *Journal of Applied Physics;* Vol. 44, 1973, pp. 667–674.

10 Vakulenko, A. A., and Kachanov, M. L., "Continuum Theory of Cracked Media," *Mekh. Tverdogo Tela*, Vol. 6, 1971, pp. 159–166 (in Russian).

11 Dragon, A., and Mroz, A., "A Continuum Model for Plastic-Brittle Behavior of Rock and Concrete," *International Journal of Engineering Science*, Vol. 17, 1979, pp. 121–137.

12 Dougill, J. W., "Some Remarks on Path Independence in the Small in Plasticity," *Quarterly of Applied Mathematics*, Vol. 33, 1975, pp. 233–243.

13 Dougill, J. W., "On Stable Progressively Fracturing Solids," *ZAMP*, Vol. 27, 1976, pp. 423–437.

14 Dougill, J. W., Lau, J. C., and Burt, N. J., "Toward a Theoretical Model for Progressive Failure and Softening in Rock, Concrete and Similar Materials" in *Mechanics in Engineering*, ASCE-EMD 1976, University of Waterloo Press, 1977, pp. 335–355.

15 Bazant, Z. P., and Kim, S. S., "Plastic-Fracturing Theory for Concrete," *Journal of Engineering Mechanics Division Proceedings, ASCE*, Vol. 105, 1979, pp. 429–446.

16 Srinivasan, M. G., et al., "The Distributed Damage Theory and Its Application in Dynamically Loaded Structures," 16th Annual Meeting SES, Northwestern University, 1979, pp. 24–25.

17 Kratochvil, J., and Dillon, O. W., Jr., "Thermodynamics of Elastic-Plastic Materials as a Theory With Internal State Variables," *Journal of Applied Physics*, Vol. 40, 1969, pp. 3207–3218.

18 Kratochvil, J., and Dillon, O. W., Jr., "Thermodynamics of Crystalline Elastic-Visco-Plastic Materials," *Journal of Applied Physics*, Vol. 44, 1970, pp. 1470–1478.

19 Kachanov, M., "Continuum Model of Medium With Cracks," *Journal of Engineering Mechanics Division, Proceedings, ASCE*, Vol. 106, 1980, pp. 1039–1051.

20 Chaboche, J. L., "Description Thermodynamique et Phenomenologique de la Viscoplasticite Cyclique avec Endommagement," ONERA, Publ. No. 1978-3, 1978.

Downloaded 01 May 2010 to 171.66.16.249. Redistribution subject to ASME license or copyright; see http://www.asme.org/terms/Terms_Use.cfm

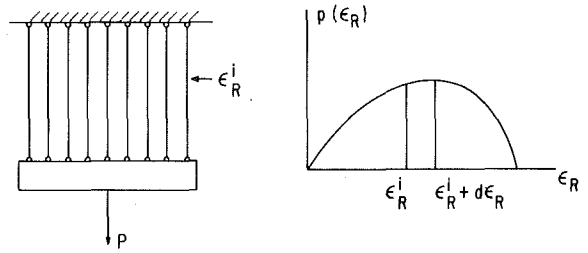


Fig. 3 The parallel bar model, and the probability density function of rupture strains

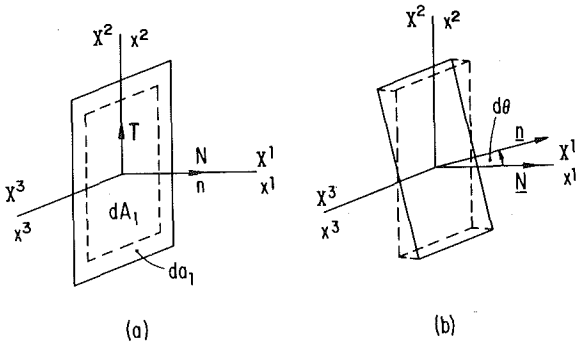


Fig. 4 Dilation (*a*) and slip (*b*) modes of the void growth

21 Chaboche, J. L., "The Continuous Damage Mechanics: A Tool to Describe Phenomena Before Crack Initiation," 2nd Int. Seminar on Incl. Analysis and Life Prediction in High Temp. Env., 1979, pp. C9–C14.

22 Murakami, S., and Ohno, N., "A Constitutive Equation of Creep Damage in Polycrystalline Metals," IUTAM Colloquium Euromech 111, Marienbad, 1978.

23 Cordebois, J. P., and Sidoroff, F., "Anisotropic elastique induite per endommagement," Colloquium Euromech 115, grenoblr, 1979.

24 Chaboche, J. L., "Le Concept de Contrainte Effective Appliquee a l'elasticite et a Viscoplasticite en Presence d'un Endommagement Anisotrope," Colloquium Euromech 115, grenoble 1979.

25 Seaman, L., Curran, D. R., and Shockey, D. A., "Computational Models for Ductile and Brittle Fracture," *Journal of Applied Physics*, Vol. 47, 1976, pp. 4814–4826.

26 Chudnovsky, A. I., "A Theory of Long-Time Strength in Fatigue and Creep," Workshop on a Continuum Mechanics Approach to Damage and Life Prediction, May 1980, pp. 79–87.

27 Coleman, B. D., and Noll, W., "The Thermodynamics of Elastic Materials With Heat Conduction and Viscosity," *Arch. Rat. Mech. Anal.*, Vol. 13, 1963, pp. 167–178.

28 Rice, J. R., "Inelastic Constitutive Relations for Solids: An Internal Variable Theory and Its Application to Plasticity," *Journal of the Mechanics and Physics of Solids*, Vol. 19, 1971, pp. 433–455.

29 Rice, J. R., "Continuum Mechanics and Thermodynamics of Plasticity in Relation to Microscale Deformation Mechanisms," in *Constitutive Equations in Plasticity*, ed., Argon, A. S., The MIT Press, 1975.

30 Pipkin, A. C., and Rivlin, R. S., "The Formulation of Constitutive Equations in Continuum Physics I," *Arch. Rat. Mech. Anal.*, Vol. 4, 1959, pp. 129–144.

31 Boade, R. R., Grady, D. E., and Kipp, M. E., "Dynamic Rock Fragmentation Oil Shale Application," SAND 80-0857, Sandia Nat. Cal., 1980,

32 Malvern, L. E., *Introduction to the Mechanics of a Continuous Medium*, Prentice-Hall, Englewood Cliffs, N.J., 1969.

33 Eringen, A. C., *Nonlinear Theory of Continuous Media*, McGraw-Hill, New York, 1962.

34 Paul, B., "A Modification of the Coulomb-Mohr Theory of Fracture," ASME JOURNAL OF APPLIED MECHANICS, Vol. 28, 1961, pp. 259–268.

35 Drucker, D. C., "A Definition of Stable Inelastic Material," ASME JOURNAL OF APPLIED MECHANICS, Vol. 26, 1959, pp. 101–106.

36 Mandel, J., "Conditions de Stabilite et Postulat de Drucker," in *Rheology and Soil Mechanics*, eds., Kravtchenko and Sirieys, Springer-Verlay 1966, pp. 58–68.

37 Budiansky, B., and O'Connell R. J., "Elastic Moduli of a Cracked Solid," *International Journal of Solids and Structures*, Vol. 12, 1976, pp. 81–97.

38 Walsh, J. B., "The Effects of Cracks in Rocks on Poisson's Ratio," *Journal of Geophysics Research*, Vol. 70, No. 20, 1965, pp. 5249–5257.

APPENDIX *A*

Parallel Bar Model

The original Kachanov's model can be readily recovered from the presented theory approximating the axially stretched solid specimen by a parallel bar model (Fig. 3) for which $\nu = 0$ such that only $\epsilon_{11} \neq 0$. In this case from (3) and (4) follows the familiar relationship

$$\sigma_{11} = E(1 - D\omega)\epsilon_{11} \tag{41}$$

where $D = -2(C_1 + C_2)/(\lambda + 2\mu) = -1$ and $\omega_N = \omega$.

Since in this case $\epsilon_{11} = \epsilon_{NN} = \epsilon$ from (33) it follows

$$d\omega = \kappa\lambda(\epsilon,\omega,\tau)d\epsilon \tag{42}$$

where

$$\lambda = \frac{\partial f/\partial\epsilon}{\partial f/\partial\omega} \tag{43}$$

In certain special cases equation (42) can be integrated and the damage law recovered in a closed form. In case of the parallel bar system the proposed model can be related to the statistical strength theories by prescribing a specific probability density function $p(\epsilon_R)$ (Fig. 3) for the rupture strain ϵ_R of individual bars. Since $p(\epsilon_R)d\epsilon_R$ represents the number of bars which will be ruptured when the strain is increased from $\epsilon_R{}^i$ to $\epsilon_R{}^i + d\epsilon_R$ it can be readily seen that the damage ω (ratio of the number of ruptured bars and the total number of bars) is in the fact the cumulative distribution function of a continuous random variable ϵ_R, i.e.,

$$\omega = P(\bar{\epsilon}_R) = \int_0^{\bar{\epsilon}_R} p(\epsilon_R)d\epsilon_R \tag{44}$$

where $\bar{\epsilon}_R = \epsilon_{\max}$.

Comparing (43) and (44) it follows that $\lambda = \lambda(\epsilon,\tau)$ which presents a valuable clue in establishing a suitable expression for the damage surface $f(\epsilon,\omega,\tau)$.

The Helmholtz free-energy density for the parallel bar model is from (1)

$$\rho\Psi = \tfrac{1}{2}E\epsilon^2 + (C_1 + C_2)\epsilon^2\omega \tag{45}$$

Consequently, the thermodynamic force R (14) associated with the damage parameter is

$$R = -\rho\frac{\partial\Psi}{\partial\omega} = -(C_1 + C_2)\epsilon^2 \tag{46}$$

The Griffith's criterion used extensively in the Fracture Mechanics reads

$$\sigma_c = \sqrt{\frac{E\gamma}{b}} \tag{47}$$

where $b \sim 3.10^{-8}$ cm is the atomic distance while $\gamma = 10^3$ ergs/cm^2 is the true surface energy. Comparing (46) and (47) in conjunction with $\epsilon = \sigma/E$ it further follows that

$$-\frac{R}{C_1 + C_2} = \frac{\gamma}{Eb} = \frac{K_I{}^2}{b} \tag{48}$$

where K_I is the stress-intensity factor (in cleavage mode). Thus the thermodynamic force R is actually the crack resistance force or the energy release rate (as noted previously by Chaboche [20]).

APPENDIX *B*

Kinematics of the Void Growth

The kinematics of the void growth is defined by a coordinate transformation mapping the "original" void area dA_K into the "incremented" void area da_k. Neglecting the influence of the change of the void shape (a higher moment of the void distribution in sense of Kröner [1]) it is sufficient to consider only three modes:

1 Dilation or cleavage for which the direction of the normal remains unchanged.

Downloaded 01 May 2010 to 171.66.16.249. Redistribution subject to ASME license or copyright; see http://www.asme.org/terms/Terms_Use.cfm

2 Two slips or rotations about the axes perpendicular to the normal **N**.

Consider first, the dilation mode of a void perpendicular to the coordinate axis χ^1 (Fig. 4(a). The governing coordinate transformation can be written as

$$x^1 = b_1 X^1 \quad x^2 = b_2 X^2 \quad x^3 = b_2 X^3 \quad \text{for all} \quad X^I \in dA^1 \tag{49}$$

The Green deformation tensors computed from the well-known relations (see, for example, references [32, 33]) are

$$C_{KL} = x^i{}_{,K} x^i{}_{,L} \qquad \overset{-1}{C}{}^{KL} = X^K{}_{,i} X^L{}_{,i} \tag{50}$$

such that

$$2d\Omega^{KL} = J^2 \overset{-1}{C}{}^{KL} - G^{KL} = \begin{Vmatrix} b_2{}^4 - 1 & 0 & 0 \\ 0 & 0 & 0 \\ 0 & 0 & 0 \end{Vmatrix} \tag{51}$$

where $b_1 = (b_2)^{-1}$. If the change in the void area is small, i.e., if $b_2 = 1 + \epsilon$ where $\epsilon \ll 1$ then

$$d\Omega^{11} = (1 + 4\epsilon - 1)^{\frac{1}{2}} = 2\epsilon \tag{52}$$

while directly from the Fig. 4(a) with $A = 1$

$$\frac{da - dA}{dA} = \frac{(1 + \epsilon)^2 - 1}{1} \approx 2\epsilon \tag{53}$$

Thus the component $d\Omega^{11}$ indeed presents the void dilation or stretch.

The coordinate transformation governing the slip mode shown in Fig. 4(b) can be written in form of

$$x^1 = X^1 - \beta X^2 \quad x^2 = X^2 \quad x^3 = X^3 \tag{54}$$

Hence, using relations (42) it follows that for the slip

$$2d\Omega^{KL} = J^2 C^{-1}{}_{KL} - G^{KL} = \begin{Vmatrix} \beta^2 & \beta & 0 \\ \beta & 0 & 0 \\ 0 & 0 & 0 \end{Vmatrix} \sim \begin{Vmatrix} 0 & \beta & 0 \\ \beta & 0 & 0 \\ 0 & 0 & 0 \end{Vmatrix} \tag{55}$$

for $\beta^2 \ll \beta \ll 1$. The angle subtended by two normals **N** and **n** is by inspection of the Fig. 4(b) equal to

$$\tan d\theta \approx d\theta = \beta \tag{56}$$

i.e., as stated in the text (24)

$$2d\Omega^{12} = d\theta \tag{57}$$

where the first index denotes the direction of the original normal and the second superscript the tangent to the void which changes its direction. The missing index defines the tangent which does not change its orientation during the slip.

Downloaded 01 May 2010 to 171.66.16.249. Redistribution subject to ASME license or copyright; see http://www.asme.org/terms/Terms_Use.cfm

G. U.Fonseka[2]
Mechanical Engineer,
NUTECH,
6835 Via de Oro,
San Jose, Calif. 95119

D. Krajcinovic
Professor,
Department of Materials Engineering,
University of Illinois at Chicago Circle,
Chicago, Ill. 60680
Mem. ASME

The Continuous Damage Theory of Brittle Materials[1]

Part 2: Uniaxial and Plane Response Modes

This part of the paper focuses on the application of the analytical model developed in Part 1 on the uniaxial tension, uniaxial compression, and plane problems (including rotating strain fields and unproportional loading). Identification of the material parameters is discussed in view of the derived results.

1 Introduction

The acid test of every new theory is in its ability to duplicate the experimental measurements over a wide range of diverse response modes. This is especially true when a theory operates with an admittedly modest number of material parameters. Moreover, the sometimes helpful ambiguity can be further reduced if the newly introduced material parameters have clearly identifiable physical nature which in effect pinpoints the specific test from which a particular parameter can and should be determined.

In the present case, the actual process of correlating the analytical results and the published experimental data is somewhat inhibited by

1 The relative dearth of the test data for the materials which can be considered purely brittle.

2 The disappointing paucity of the test results reflecting the influence of the loading path on the microcracking.

It was, therefore, necessary to select a material of some practical importance, which is reasonably brittle and for which a sufficiently well developed test data base exists. While certain rocks and ceramic materials would probably be more suitable materials it was decided to compare the analytical results with the test data for the high strength concrete. In other words, the availability of experimental results and the practical importance of the concrete outweighs the fact that even the high strength concrete inevitably demonstrates a certain degree of ductility especially in confined conditions.

2 Damage Surface

In order to arrive at some numerical results it is first necessary to select a specific damage function based on the general considerations outlined in Part 1 of this paper. In selecting the damage function it would be unwise to ignore the so-called Mohr-Coulomb relations (see Zienkiewicz and Pande [39] or Jaeger and Cook [40]). It should be noted, though, that Zienkiewicz and Pande use the Mohr-Coulomb criterion as a yield condition and Jaeger and Cook as the ultimate fracture criterion. In the context of this theory the damage function $f(\epsilon,\omega)$ is merely a locus of all points in the strain space separating the accessible from inaccessible states. The curve $f(\epsilon_{NN},\epsilon_{NT},\omega_N,\tau) = 0$ defining the damage surface in the $\epsilon_{NN},\epsilon_{NT}$ plane envelopes all accessible states. Thus the Jaeger and Cook [40] fracture surface can be conceived as the ultimate position of the damage surface characterizing the onset of the gross failure (as noted by Paul [34]). Nevertheless, it is probably not entirely wrong to hypothesize that the shape of the damage surface does not radically change during the process leading to the ultimate loss of the integrity.

Similarly as in the theory of plasticity (see, for example, Martin [41]) the unloading can be defined as a strain path along which the recorded history remains unchanged. In other words, if ϵ is on the damage surface $f(\epsilon,\omega,\tau) = 0$ then the new point lies within the damage surface $f(\epsilon + d\epsilon,\omega,\tau) < 0$. Hence, the unloading is defined as

$$df|_{\omega=\text{const}} < 0 \quad \text{when} \quad f = 0$$

or for a continuously differentiable damage surface (see also Dougill [12])

$$f(\epsilon,\omega,\tau) = 0 \quad \text{and} \quad \frac{\partial f}{\partial \epsilon_{IJ}} d\epsilon_{IJ} < 0 \quad (I,J, = N,T) \tag{1}$$

On the other side, a strain increment $d\epsilon_{IJ}$ imposed on the damage surface for which $d\phi(\epsilon + d\epsilon,\omega,\tau) > 0$ must be associated with a change in damage (so that the point $\epsilon + d\epsilon,\omega + d\omega$ represents an admissible state $f \leq 0$). Hence, the loading path is defined as a path along which the recorded history changes

$$f(\epsilon,\omega,\tau) = 0 \quad \text{and} \quad \frac{\partial f}{\partial \epsilon_{IJ}} d\epsilon_{IJ} > 0 \quad (I,J = N,T) \tag{2}$$

Finally, for the neutral loading,

---

[1] This work was sponsored by the U.S. National Science Foundation Grant to the University of Illinois at Chicago Circle.

[2] Formerly, graduate student at the University of Illinois at Chicago Circle.

Contributed by the Applied Mechanics Division for publication in the JOURNAL OF APPLIED MECHANICS.

Discussion on this paper should be addressed to the Editorial Department, ASME, United Engineering Center, 345 East 47th Street, New York, N. Y. 10017, and will be accepted until two months after final publication of the paper itself in the JOURNAL OF APPLIED MECHANICS. Manuscript received by ASME Applied Mechanics Division, February, 1981; final revision, May, 1981.

Copyright © 1981 by ASME

Downloaded 01 May 2010 to 171.66.16.249. Redistribution subject to ASME license or copyright; see http://www.asme.org/terms/Terms_Use.cfm

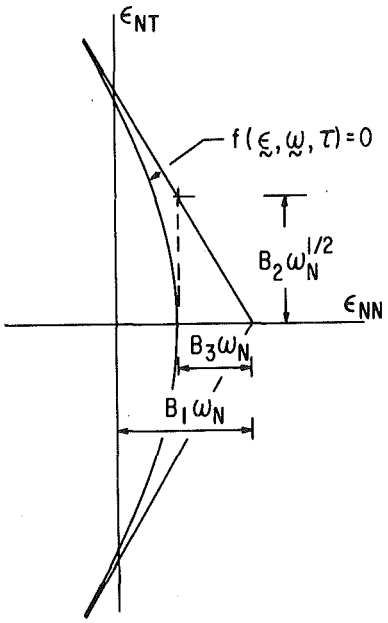


Fig. 1 The damage surface in the ϵ_{NN},ϵ_{NT} plane

$$f(\epsilon,\omega,\tau) = 0 \quad \text{and} \quad \frac{\partial f}{\partial \epsilon_{IJ}} d\epsilon_{IJ} = 0 \quad (I,J = N,T) \tag{3}$$

Naturally, since the damage is a physically irreversible process (except in case of polymers, see Wool [42]) the damage surface should be selected such that $d\omega \geq 0$.

While the orientation of the initial defect (damage) field in concrete may depend on the direction of casting it will be assumed that in case of small initial void ratio $\omega_N \ll 1$ the orientation of initial defects is for all practical purposes random. The experimental evidence indicates that the very small microdefects nucleate primarily in the cleavage mode. Hence for $\omega_N \ll 1, d\Omega_{NN} \gg d\Omega_{NT}$, i.e., for small ω_N the damage surface should approach a straight line perpendicular to the ϵ_{NN}-axis. In other words, if the damage surface is selected in form of a hyperbola (reminiscent of the Mohr-Coulomb type of curves), the angle subtended by its asymptotes must depend on the incured damage ω_N. The preceeding considerations lead to a hyperbola shown in Fig. 1 and given by the equation

$$f = \epsilon_{NN} + B_3\bar{\omega}_N^{1/2}\sqrt{B_2^{-2}\epsilon_{NT}^2 + \bar{\omega}_N} - B_1\bar{\omega}_N = 0 \tag{4}$$

where B_1,B_2, and B_3 are material parameters (dependent in general on the temperature τ) while $\bar{\omega}_N$ is the largest recorded damage. The consistency equation which must be satisfied during the loading (2) can be written in form

$$(B_1\bar{\omega}_N - \epsilon_{NN})d\epsilon_{NN} + \left(\frac{B_3}{B_2}\right)^2 \bar{\omega}_N\epsilon_{NT}d\epsilon_{NT} + \left[B_1\epsilon_{NN} + \frac{1}{2}\left(\frac{B_3}{B_2}\epsilon_{NT}\right)^2 - (B_1^2 - B_3^2)\bar{\omega}_N\right] d\omega_N = 0 \tag{5}$$

for ϵ_{NN},ϵ_{NT}, and $\bar{\omega}_N$ satisfying the conditions (2).

It can be readily seen that the selected damage surface (4) conforms to the requirements listed in Part 1 of this paper. For example, it is obviously symmetric with respect to the axis ϵ_{NN}. Moreover in case of pure cleavage (i.e., uniaxial tensile test $\epsilon_{NT} = d\epsilon_{NT} = 0$) from (4) and (5) it follows that

$$\epsilon_{NN} - (B_1 - B_3)\bar{\omega}_N = 0 \tag{6}$$

and

$$d\epsilon_{NN} - (B_1 - B_3)d\omega_N = 0 \tag{7}$$

If an existing damage field is subjected to a pure slip for which $\epsilon_{NN} = 0$ then from (4)

$$\left(\frac{B_3}{B_2}\right)^2 \epsilon_{NT}^2 - (B_1^2 - B_3^2)\bar{\omega}_N = 0 \tag{8}$$

while from the consistency equation (5)

$$B_1 d\epsilon_{NN} + \left(\frac{B_3}{B_2}\right)^2 \epsilon_{NT}d\epsilon_{NT} - \frac{1}{2}(B_1^2 - B_3^2)d\omega_N = 0 \tag{9}$$

Notice that in a specimen subjected to pure slip the damage field "rotates" such that $d\epsilon_{NN} \neq 0$. In other words, pure slip is but an instant in the general loading process. This is, of course, entirely in agreement with the well-known Fracture Mechanics result (see, for example, Broek [43]) according to which the pure shear of a crack results in the extension of the crack and the change of the orientation (i.e., the crack propagates at an angle of $\sim 70°$ with respect to the original plane of the crack).

It is interesting to note that the "damage evolution laws" (6) and (7) are the same ones used by Janson and Hult [44], Krajcinovic [45], and Krajcinovic, et al. [46, 47]. This, naturally, by no means implies that the selected form of the damage surface (4) is the only correct one or even the most suitable one. It merely means that the absence of carefully recorded experimental results necessitated selection of an appropriate function $f(\epsilon_{NN},\epsilon_{NT},\omega_N)$ satisfying some very general considerations imposed by the physical nature of the phenomenon. The correlation between the analytical and experimental results will provide the ultimate criterion of the suitability and applicability of every specific damage function $f(\epsilon,\omega,\tau)$.

3 Simple Response Modes-Proportional Loading

As an illustration of the proposed theory it is convenient to start with simple uniaxial problems. In order to test the accuracy of the derived equations the following procedure was devised. A cylindrical specimen manufactured from the high strength concrete is subjected to the uniaxial tension in direction 1. The material parameters are determined fitting the published experimental data (i.e., from the "tensile strength"). Subsequently, an "identical" specimen is subjected to the unconfined uniaxial compression. The analytical results are computed using the material parameters obtained previously on the basis of the tensile test. The closeness of the fit existing between the experimental data and the analytical results is the first indication of the validity of the developed theory.

In order to examine the "postfailure" (softening) response both tests are strain-controlled (i.e., conducted using the stiff testing device).

3.1 Uniaxial Tension Test. Even though the orientation of the initial microdefects is in all probability a random variable only those defects which are perpendicular to the maximum tensile strain will show substantial growth. Thus the damage field will be dominated by the defects perpendicular to the direction of the loading. This conclusion is supported by all of the published experimental data. The governing equations, deduced from (Part 1–(3), (4)) can be written in the matrix form

$$\begin{bmatrix}\sigma_1\\0\\0\end{bmatrix} = Ek\begin{bmatrix}1+(C_1+C_2)\omega & \bar{\nu}+\frac{1}{2}C_1\omega & \bar{\nu}+\frac{1}{2}C_1\omega\\ \bar{\nu}+\frac{1}{2}C_1\omega & 1 & \bar{\nu}\\ \bar{\nu}+\frac{1}{2}C_1\omega & \bar{\nu} & 1\end{bmatrix}\begin{bmatrix}\epsilon_{11}\\\epsilon_{22}\\\epsilon_{33}\end{bmatrix} \tag{10}$$

where

$$\bar{\nu} = \frac{\nu}{1-\nu} \qquad k = \frac{1-\nu}{(1+.\nu)(1-2\nu)}$$

while $\omega \equiv \omega_1$ is the damage perpendicular to the direction of the principal strain ϵ_{11}. The constants C_i are divided for convenience by Ek. The incremental form of the stress-strain relations is obtained from (Part 1—(6)) in form

Downloaded 01 May 2010 to 171.66.16.249. Redistribution subject to ASME license or copyright; see http://www.asme.org/terms/Terms_Use.cfm

$$\begin{Bmatrix} d\sigma_{11} \\ 0 \\ 0 \end{Bmatrix} = Ek \begin{bmatrix} 1+(C_1+C_2)\omega & \bar{\nu}+\frac{1}{2}C_1\omega & \bar{\nu}+\frac{1}{2}C_1\omega \\ \bar{\nu}+\frac{1}{2}C_1\omega & 1 & \bar{\nu} \\ \bar{\nu}+\frac{1}{2}C_1\omega & \bar{\nu} & 1 \end{bmatrix} \begin{Bmatrix} d\epsilon_{11} \\ d\epsilon_{22} \\ d\epsilon_{33} \end{Bmatrix}$$

$$+ \mathrm{Ek} \begin{Bmatrix} (C_1+C_2)\epsilon_{11}+\frac{1}{2}C_1(\epsilon_{22}+\epsilon_{33}) \\ \frac{1}{2}C_1\epsilon_{11} \\ \frac{1}{2}C_1\epsilon_{11} \end{Bmatrix} d\omega \quad (11)$$

The associated "damage rule" is deduced from the damage surface (4)

$$f = \epsilon_{11} + (B_3 - B_1)\omega = 0 \quad \text{for} \quad \epsilon_{11} d\epsilon_{11} > 0 \quad (12)$$

and the associated consistency equation (5)

$$d\epsilon_{11} = (B_1 - B_3)d\omega \quad \text{for} \quad f = 0, \quad \epsilon_{11} d\epsilon_{11} > 0 \quad (13)$$

while

$$d\omega = 0 \quad \text{if} \quad f < 0$$
$$\text{or} \quad f = 0 \quad \text{and} \quad \epsilon_{11} d\epsilon_{11} < 0 \quad (14)$$

Consider first, the process of loading defined by conditions (2). According to the selected expression for the damage surface (4) the damage will start propagating when

$$\epsilon_{11} \geq \epsilon_{11}^{\circ} = (B_1 - B_3)\omega^{\circ} \quad (15)$$

where ω° is some initial damage (void density) reflecting the nature of the manufacturing process (casting in case of the concrete) or the previous loading history. The strain ϵ°_{11} at the onset of the void nucleation can be experimentally identified as the strain at the proportionality limit. From the equation (11)

$$d\epsilon_{22} = d\epsilon_{33} = -(1-\nu)\left(\frac{\nu}{1-\nu} + \frac{C_1}{B_1 - B_3}\epsilon_{11}\right) d\epsilon_{11} \quad \text{for} \quad \epsilon_{11} \geq \epsilon^{\circ}_{11}$$

and

$$d\epsilon_{22} = d\epsilon_{33} = -(1-\nu)\left(\frac{\nu}{1-\nu} + \frac{1}{2}C_1\omega_0\right) d\epsilon_{11} \quad \text{for} \quad \epsilon_{11} < \epsilon^{\circ}_{11} \quad (16)$$

Equations (16) can be integrated leading to a simple expression

$$\epsilon_{22} = \epsilon_{33} = -(1-\nu)\left(\frac{\nu}{1-\nu} + \frac{1}{2}\frac{C_1}{B_1 - B_3}\epsilon_{11}\right)\epsilon_{11} \quad \text{for} \quad \epsilon_{11} > \epsilon^{\circ}_{11}$$

$$\epsilon_{22} = \epsilon_{33} = -(1-\nu)\left(\frac{\nu}{1-\nu} + \frac{1}{2}C_1\omega^{\circ}\right)\epsilon_{11} \quad \text{for} \quad \epsilon_{11} < \epsilon^{\circ}_{11} \quad (17)$$

Substituting (16) and (17) into (11) and integrating the obtained equation, with the initial condition $\sigma_{11} = \sigma^{\circ}_{11}$ when $\epsilon_{11} = \epsilon^{\circ}_{11}$, leads to the closed-form solution for the uniaxial tensile problem of the brittle material with gradually increasing microdefect population,

$$\frac{1}{Ek}\sigma_{11} = \left(1 - \frac{2\nu^2}{1-\nu}\right)\epsilon_{11} + \frac{1}{B_1 - B_3}[C_2 + (1-2\nu)C_1]\epsilon_{11}^2$$
$$- \frac{1-\nu}{2}\frac{C_1^2}{(B_1 - B_3)^2}\epsilon_{11}^3 \quad \text{for} \quad \epsilon_{11} > \epsilon^{\circ}_{11} \quad (18)$$

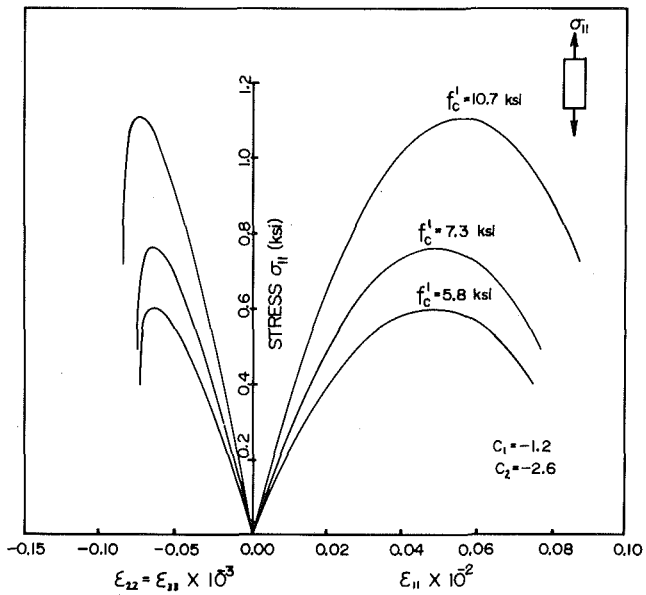


Fig. 2 Stress-strain curves—uniaxial tension of three concrete specimens

In unloading, defined by the conditions (1) the damage remains constant $d\omega = 0$. Thus

$$\epsilon_{22} = \epsilon_{33} = -\left(\nu + \frac{1-\nu}{2}C_1\bar{\omega}\right)\epsilon_{11} \quad (19)$$

while

$$\sigma_{11} = Ek\left[1 - \frac{2\nu^2}{1-\nu} + C_1(1-2\nu)\bar{\omega} + C_2\bar{\omega} - \frac{1-\nu}{2}C_1\bar{\omega}^2\right]\epsilon_{11} \quad (20)$$

where $\bar{\omega}$ is the maximum value of the previously accumulated damage, i.e., recorded history. Note that there is no residual strain, i.e., for $\sigma_{11} = 0$, $\epsilon_{11} = 0$. The slope of the unloading straight line is a constant dependent on $\bar{\omega}$ (reduced elastic modulus).

The thermodynamic force conjugate to the damage variable is from (Part 1—(14)) and (Part 1—(15)) given by

$$R_1 = -\rho\frac{\partial\psi}{\partial\omega_1} = -Ek(C_1\epsilon_v\epsilon_{11} + C_2\epsilon_{11}^2) \quad (21)$$

Since the volumetric strain ϵ_v is during the loading positive the Clausius-Duhem inequality $R_I d\omega_I \geq 0$ (Part 1—(16)) is unconditionally satisfied if both C_1 and C_2 are nonpositive functions of the temperature τ. The local entropy production vanishes in unloading since by definition $d\omega = 0$.

The stress-strain curves for uniaxial tension of three specimens manufactured of three different grades of concrete ($f_c' = 10.7$ ksi (73.8 MPa), 7.3 ksi (50.3 MPa) and 5.8 ksi (40.0 MPa)) are computed from the equation (18) and plotted in Fig. 2. The existence of the postfailure domain, characterized by the negative $d\sigma_{11}/d\epsilon_{11}$ ratio, is assured since the strain is controlled. In absence of the precise data the material parameters are determined assuming that the peak stress in tension $\sigma_{11}{}^{M}$ is 10 percent of the peak stress in compression $\sigma_{11}{}^{M}$. Leaving the discussion of the exact procedure for the numerical identification of material parameters for a more appropriate place it is sufficient to list the numerical values used in computation

For $f_c' = 10.7$ ksi (73.8 MPa) $E = 4.0.10^6$ psi $(27.6 \cdot 10^3$ MPa) $B_1 - B_3 = 4.149.10^{-3}$
For $f_c' = 7.3$ ksi (50.3 MPa) $E = 3.1.10^6$ psi $(21.4 \cdot 10^3$ MPA) $B_1 - B_3 = 3.676.10^{-3}$
For $f_c' = 5.8$ ksi (40.0 MPa) $E = 2.5.10^6$ psi $(17.2 \cdot 10^3$ MPa) $B_1 - B_3 = 3.597.10^{-3}$

While $\nu = 0.2$, $\epsilon^{\circ}_{11} = 0.4 \times 10^{-4}$ and $C_1 = -1.2$, $C_2 = -2.6$ for all three grades of concrete.

The stress-strain curves, obtained on the basis of equations (17) and (18) and the listed parameters are plotted in Fig. 2. The postfailure region is well developed and the strain at failure is almost twice as large as the strain ϵ^{M} at the peak stress.

Downloaded 01 May 2010 to 171.66.16.249. Redistribution subject to ASME license or copyright; see http://www.asme.org/terms/Terms_Use.cfm

The apparent Poisson's ratio ($-\epsilon_{22}/\epsilon_{11}$) versus ϵ_{11} is computed from (17) and plotted in Fig. 3. The relative softening in the direction of the maximum tensile strain is quite obvious. The Poisson's ratio at fracture is roughly 50 percent of the initial value.

The plots of the volumetric strain ($\epsilon_{11}+\epsilon_{22}+\epsilon_{33}$) versus ϵ_{11} is shown in Fig. 4(a). As expected the volumetric strain is always positive. Finally, as a result of the selected damage law the damage variable ω is a linear function of the axial strain ϵ_{11}. The damage at $\sigma_{11}{}^{\max}$ is $\omega \simeq 0.13$ while at rupture $\omega \simeq 0.21$ (Fig. 4(b)).

3.2 Uniaxial Compressive Test. In case of the uniaxial compression of an unconfined concrete specimen it is pretty well understood that the "failure occurs . . . by splitting at right angles to the direction of the load" (see, Neville [48, p. 229]). Moreover, to quote from the same source and same page "there are strong indications that it is not a limiting stress but a limiting tensile strain that determines the strength of the concrete." The same conclusion is valid in rock mechanics (see, for example, the book by Jaeger and Cook [40]). Hence, it was appropriate to select the elastic strain as a state variable and not the stress as in Dragon and Mroz [11] (which results in an unnecessary complication necessitating the use of the deviatoric stresses when $\sigma_{ii} < 0$, while the total stresses have to be used when $\sigma_{ii} > 0$).

The dominant microcracks will nucleate in the directions perpendicular to the two tensile strains $d\epsilon_{11}, d\epsilon_{22}$ (the compressive load acts along the axis 3, i.e., $d\epsilon_{33} < 0$). Thus, from (Part 1—(3), (4)) the governing equations are

$$\begin{Bmatrix} 0 \\ 0 \\ \sigma_{33} \end{Bmatrix} = Ek \begin{bmatrix} 1+(C_1+C_2)\omega^\alpha & \bar{\nu}+\tfrac{1}{2}C_1(\omega^\alpha+\omega^\beta) & \bar{\nu}+\tfrac{1}{2}C_1\omega^\alpha \\ \bar{\nu}+\tfrac{1}{2}C_1(\omega^\alpha+\omega^\beta) & 1+(C_1+C_2)\omega^\beta & \bar{\nu}+\tfrac{1}{2}C_1\omega^\beta \\ \bar{\nu}+\tfrac{1}{2}C_1\omega^\alpha & \bar{\nu}+\tfrac{1}{2}C_1\omega^\beta & 1 \end{bmatrix} \times \begin{Bmatrix} \epsilon_{11} \\ \epsilon_{22} \\ \epsilon_{33} \end{Bmatrix} \quad (22)$$

where ω^α and, ω^β are two independent mutually perpendicular microcrack fields which cannot be added vectorially. For simplicity, assume that no bias was created during the casting of concrete, i.e., assume that the two initial damage fields are equal in magnitude. Since their increments have no reason to be different in view of $d\epsilon_{11} = d\epsilon_{22}$ it follows that $\omega^\alpha = \omega^\beta = \omega$ in terms of the magnitude (they remain mutually perpendicular). Thus the incremental stress-strain law can for this case be inferred from (Part 1—(13))

$$\begin{Bmatrix} 0 \\ 0 \\ d\sigma_{33} \end{Bmatrix} = Ek \begin{bmatrix} 1+(C_1+C_2)\omega & \bar{\nu}+C_1\omega & \bar{\nu}+\tfrac{1}{2}C_1\omega \\ \bar{\nu}+C_1\omega & 1+(C_1+C_2)\omega & \bar{\nu}+\tfrac{1}{2}C_1\omega \\ \bar{\nu}+\tfrac{1}{2}C_1\omega & \bar{\nu}+\tfrac{1}{2}C_1\omega & 1 \end{bmatrix} \times \begin{Bmatrix} d\epsilon_{11} \\ d\epsilon_{22} \\ d\epsilon_{33} \end{Bmatrix} + Ek \begin{bmatrix} \tfrac{1}{2}C_1(\epsilon_{33}+4\epsilon_{11})+C_2\epsilon_{11} \\ \tfrac{1}{2}C_1(\epsilon_{33}+4\epsilon_{22})+C_2\epsilon_{22} \\ C_1\epsilon_{11} \end{bmatrix} d\omega \quad (23)$$

In view of the existence of two mutually independent damage fields it is necessary to introduce two independent damage surfaces. In both cases, for loading, from equation (7)

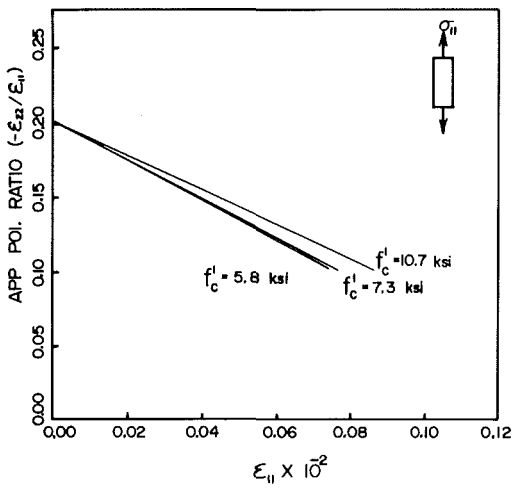


Fig. 3 The apparent Poisson's ratio—uniaxial tension test

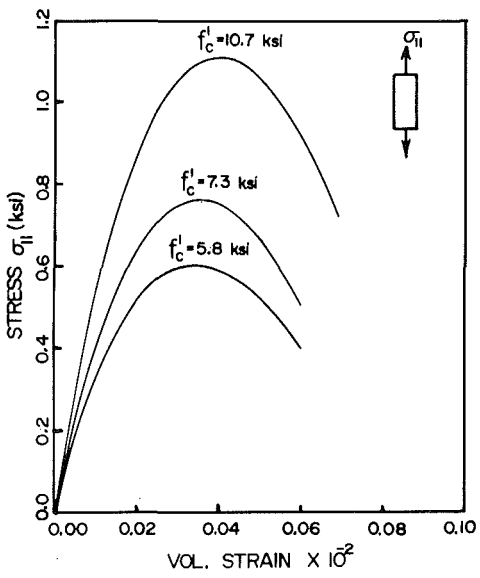


Fig. 4(a)

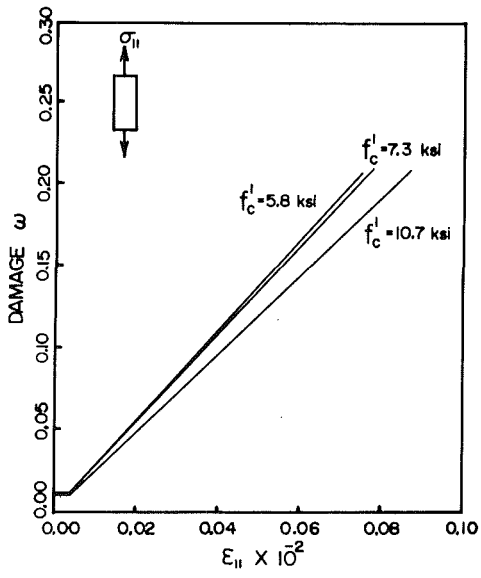


Fig. 4(b)

Fig. 4 (a) The volumetric strain; (b) Accumulated damage—uniaxial tension test

Downloaded 01 May 2010 to 171.66.16.249. Redistribution subject to ASME license or copyright; see http://www.asme.org/terms/Terms_Use.cfm

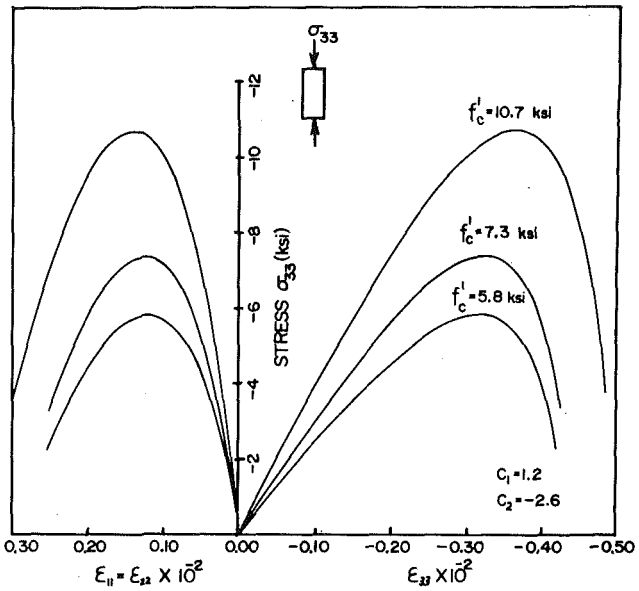


Fig. 5 Stress-strain curves—uniaxial compression test of three concrete specimens

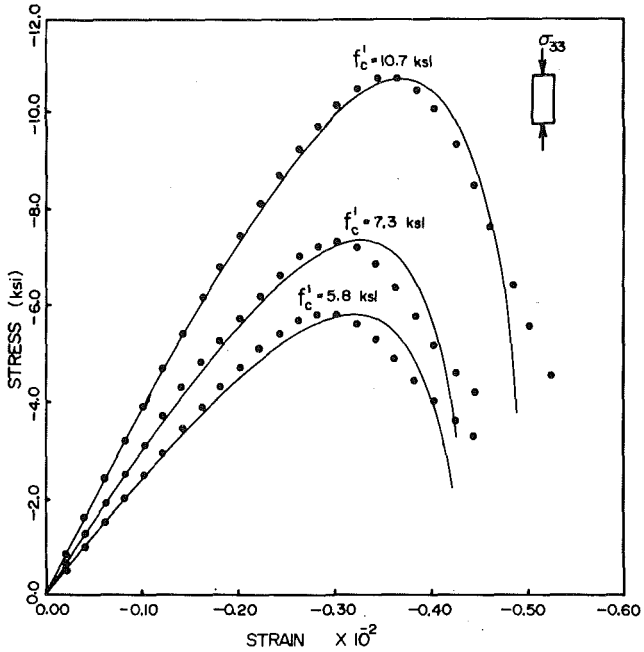


Fig. 6 Correlation of the computed data and the experimental results [53] for the three concrete specimens subjected to uniaxial compression

$$d\epsilon_{11} = (B_1 - B_3)d\omega^\alpha \quad \text{for} \quad \epsilon_{11} > \epsilon_0$$

$$d\epsilon_{22} = (B_1 - B_3)d\omega^\beta \quad \text{for} \quad \epsilon_{22} > \epsilon_0 \tag{24}$$

A simple closed-form solution relating σ_{33} with ϵ_{33} as in case of the tension cannot be derived in this case. Instead, the system of equations (23) can be reduced to three simultaneous differential equations

$$d\epsilon_{11} = d\epsilon_{22} = -(\bar{\nu} + \tfrac{1}{2}C_1\omega)\left[\frac{1}{1-\nu} + (2C_1 + C_2)\omega + \frac{C_1}{B_1 - B_3}(\tfrac{1}{2}\epsilon_{33} + 2\epsilon_{11}) + \frac{C_2\epsilon_{11}}{B_1 - B_3}\right]^{-1} d\epsilon_{33}$$

$$d\sigma_{33} = Ek\left[d\epsilon_{33} + (2\bar{\nu} + C_1\omega + \frac{C_1}{B_1 - B_3}\epsilon_{11})d\epsilon_{11}\right] \quad \text{for} \quad \epsilon_{11} > \epsilon_0$$

and

$$d\omega = (B_1 - B_3)^{-1}d\epsilon_{11} \quad \text{for} \quad f = 0; \frac{\partial f}{\partial \epsilon_{11}}d\epsilon_{11} > 0 \tag{25}$$

For a given point in the strain space ($\epsilon_{11} = \epsilon_{22}, \epsilon_{33}$) and a given strain decrement $d\epsilon_{33}$ it is, therefore, possible to compute $d\epsilon_{11}, d\omega$, and ultimately $d\sigma_{33}$ from the differential equations (25).

The thermodynamic forces conjugate to the two damage variables are

$$R^\alpha = -\rho\frac{\partial \psi}{\partial \omega^\alpha} = -EkC_1\epsilon_v\epsilon_{11} - EkC_2{\epsilon_{11}}^2$$

$$R^\beta = -\rho\frac{\partial \psi}{\partial \omega^\beta} = -EkC_1\epsilon_v\epsilon_{22} - EkC_2{\epsilon_{22}}^2 \tag{26}$$

The second law of thermodynamics requires that $R^\alpha d\omega^\alpha \geq 0$ and $R^\beta d\omega^\beta \geq 0$. Experimental data for the axial compression of the unconfined concrete (see Neville [48], Kupter and Gerstle [49], Wang, Shah, and Naaman [50] and others) and brittle rock specimens (see Jaeger, Cook [40], Brace, Paulding, and Scholz [51], Crouch [52] and others) indicate that the dilatancy (volumetric strain) is initially negative but may become positive at the advanced stage of damage. Thus, since $d\omega \geq 0$, the entropy production inequalities $R^i d\omega^i \geq 0$ are unconditionally satisfied if $C_1 > 0$ and $C_2 < 0$. In view of the previous considerations for the tensile test $C_1 = -\bar{C}_1$ sign (ϵ_v), $C_2 < 0$ in order to satisfy the Clausius-Duhem inequality for both tension and compression.

The stress-strain curves for the uniaxial compression test of three unconfined concrete specimens computed from (25), using the values for the material parameters as determined from the tensile test, are plotted in Fig. 5. The postfailure domain is again quite prominent. The computed results are compared with the experimental data published by Wang [53] in Fig. 6. The correlation is very good especially for the high strength concrete which is less ductile than the lower grades of concrete.

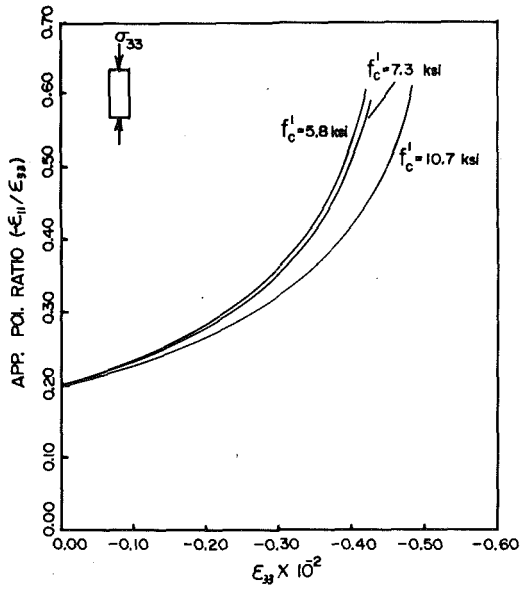


Fig. 7 Apparent Poisson's ratio—uniaxial compression

The apparent Poisson's ratio $(-\epsilon_{11}/\epsilon_{33})$ versus ϵ_{11}, plotted in Fig. 7, shows rather dramatic decrease in lateral "stiffness." The ultimate apparent Poisson's ratio is three times larger than the initial one. The increasing curvature of the plotted curves indicate that the apparent Poisson's ratio may easily exceed unity. The computed values correlate rather well with the data obtained by Walsh [38] according to which the ultimate Poisson's ratio for the rocks is more than two times larger than the initial.

The dramatic increase of the apparent Poisson's ratio results in the

Downloaded 01 May 2010 to 171.66.16.249. Redistribution subject to ASME license or copyright; see http://www.asme.org/terms/Terms_Use.cfm

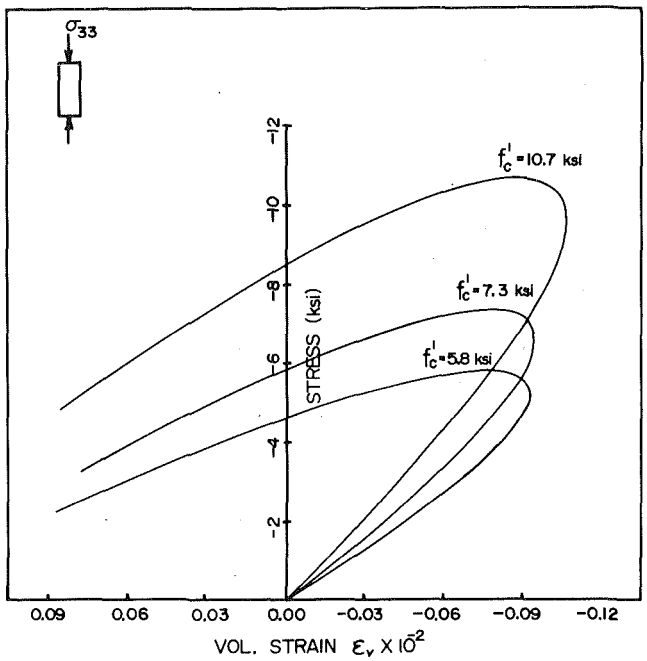


Fig. 8 Volumetric strain (dilatancy)—uniaxial compression test

change in sign of the dilatancy (volumetric strain) Fig. 8 which correlates well with experimental results for concrete (Kupfer, Hilsdorf, Rüsch [54]) and rocks (Brace, Paulding, and Scholz [51], Crouch [52], etc.).

It should finally be noted that this rather remarkable correlation with experimental data was obtained using only three constants (C_1, C_2 and $B_3 - B_1$) on the basis of incomplete test results on a material which is not perfectly brittle. In addition, the Helmholtz free energy parameters C_i are taken to be constants rather than functions of the recorded history ω_N. Finally, it is quite likely that a more accurate damage surface will be eventually determined on the basis of a more complete experimental data bank. Since the basic trends and features of the investigated phenomenal can be readily duplicated with this rather simple scheme there is little doubt that a finer fit may be achieved later if desired.

4 Plane Problem

Consider a general two-dimensional problem for which $\sigma_{13} = \sigma_{23} = 0$, $\epsilon_{13} = \epsilon_{23} = 0$ and $\omega_3 = d\omega_3 = 0$. The governing equations of the problem in Cartesian coordinates can be deduced from (Part 1—(3)) and written in matrix form

$$\begin{Bmatrix} \sigma_{11} \\ \sigma_{22} \\ \sigma_{33} \\ \sigma_{12} \end{Bmatrix} = [K] \begin{Bmatrix} \epsilon_{11} \\ \epsilon_{22} \\ \epsilon_{33} \\ \epsilon_{12} \end{Bmatrix} \tag{27}$$

where $[K]$ is a fourth-order square material property matrix which in view of (Part 1—(10)) reads

$$K = Ek\frac{1}{\omega}\begin{bmatrix} \omega + (C_1 + C_2)\omega_1^2 & \bar{\nu}\omega + \frac{1}{2}C_1\omega^2 & \bar{\nu}\omega + \frac{1}{2}C_1\omega_1^2 & \frac{1}{2}(C_1 + C_2)\omega_1\omega_2 \\ \bar{\nu}\omega + \frac{1}{2}C_1\omega^2 & \omega + (C_1 + C_2)\omega_2^2 & \bar{\nu}\omega + \frac{1}{2}C_1\omega_2^2 & \frac{1}{2}(C_1 + C_2)\omega_1\omega_2 \\ \bar{\nu}\omega + \frac{1}{2}C_1\omega_1^2 & \bar{\nu}\omega + \frac{1}{2}C_1\omega_2^2 & \omega & \frac{1}{2}C_1\omega_1\omega_2 \\ \frac{1}{2}(C_1 + C_2)\omega_1\omega_2 & \frac{1}{2}(C_1 + C_2)\omega_1\omega_2 & \frac{1}{2}C_1\omega_1\omega_2 & \frac{1-2\nu}{2(1-\nu)}\omega + \frac{1}{4}C_2\omega^2 \end{bmatrix} \tag{28}$$

where $\omega = \sqrt{\omega_1^2 + \omega_2^2}$.

The incremental stress strain relationship can be written from (Part 1—(6)) in the matrix form (Part 1—(13)) where $\{d\omega\} = \{d\omega_1\ d\omega_2\}^T$. The (4×2) rectangular matrix $\overline{K}$ is best written element by element from (Part 1—(11))

$$\overline{K}_{11} = \frac{Ek}{\omega}[(C_1 + C_2)(2\omega_1\epsilon_{11} + \omega_2\epsilon_{12}) + C_1\omega_1(\epsilon_{22} + \epsilon_{33}) + L_1\omega_1]$$

$$\overline{K}_{21} = \frac{Ek}{\omega}[C_1\omega_1\epsilon_{11} + (C_1 + C_2)\omega_2\epsilon_{12} + L_2\omega_1]$$

$$\overline{K}_{31} = \frac{Ek}{\omega}[C_1\omega_1\epsilon_{11} + C_1\omega_2\epsilon_{12} + L_3\omega_1]$$

$$\overline{K}_{41} = \frac{Ek}{\omega}[\tfrac{1}{2}(C_1 + C_2)\omega_2(\epsilon_{11} + \epsilon_{22}) + \tfrac{1}{2}C_1\omega_2\epsilon_{33} + C_2\omega_1\epsilon_{12} + L_4\omega_1]$$

$$\overline{K}_{12} = \frac{Ek}{\omega}[C_1\omega_2\epsilon_{22} + (C_1 + C_2)\omega_1\epsilon_{12} + L_1\omega_2]$$

$$\overline{K}_{22} = \frac{Ek}{\omega}[C_1\omega_2(\epsilon_{11} + \epsilon_{33}) + (C_1 + C_2)(2\omega_2\epsilon_{22} + \omega_1\epsilon_{12}) + L_2\omega_2]$$

$$\overline{K}_{32} = \frac{Ek}{\omega}[C_1\omega_2\epsilon_{22} + C_1\omega_1\epsilon_{12} + L_3\omega_2]$$

$$\overline{K}_{42} = \frac{Ek}{\omega}[\tfrac{1}{2}(C_1 + C_2)\omega_1(\epsilon_{11} + \epsilon_{22}) + \tfrac{1}{2}C_1\omega_1\epsilon_{33} + C_2\omega_2\epsilon_{12} + L_4\omega_2] \tag{29}$$

where

$$L_1 = -\frac{1}{\omega^2}[(C_1 + C_2)\omega_1(\omega_1\epsilon_{11} + \omega_2\epsilon_{12}) + \tfrac{1}{2}C_1(\omega^2\epsilon_{22} + \omega_1^2\epsilon_{33})]$$

$$L_2 = -\frac{1}{\omega^2}[(C_1 + C_2)\omega_2(\omega_2\epsilon_{22} + \omega_1\epsilon_{12}) + \tfrac{1}{2}C_1(\omega^2\epsilon_{11} + \omega_2^2\epsilon_{33})]$$

$$L_3 = -\frac{C_1}{2\omega^2}(\omega_1^2\epsilon_{11} + \omega_2^2\epsilon_{22} + 2\omega_1\omega_2\epsilon_{12})$$

$$L_4 = -\frac{1}{2\omega^2}[(C_1 + C_2)\omega_1\omega_2(\epsilon_{11} + \epsilon_{22}) + C_1\omega_1\omega_2\epsilon_{33} + C_2\omega^2\epsilon_{12}] \tag{30}$$

The kinematics of the void growth is defined by (Part 1—(29), (29′)). For the selected form of the damage surface (1) the relation between the increments of the strain in the (N,T) coordinate system and the increments in damage (Part 1—(31), (31′)), i.e., the damage evolution law, reads

$$\{d\Omega\} = \kappa[B]\{d\bar{\epsilon}\} \tag{31}$$

where in view of (Part 1—(31))

$$[B] = G\begin{bmatrix} 1 & g \\ g & g^2 \end{bmatrix} \tag{32}$$

with

$$g = \frac{\partial f}{\partial \epsilon_{NT}} = -\omega\left(\frac{B_3}{B_2}\right)^2 \epsilon_{NT}(\epsilon_{NN} - B_1\omega)^{-1} \tag{33}$$

From (Part 1—(34))

$$G = \frac{1}{\omega_N}(\epsilon_{NN} - B_1\omega)\left[B_1\epsilon_{NN} + \frac{1}{2}\left(\frac{B_3}{B_2}\epsilon_{NT}\right)^2 - (B_1^2 - B_3^2)\omega\right]^{-1} \tag{34}$$

The strains in the (1)–(3) coordinate system (which is not necessary principal) and the strains in the void coordinate system (N,T) are related through the rotational matrix

Downloaded 01 May 2010 to 171.66.16.249. Redistribution subject to ASME license or copyright; see http://www.asme.org/terms/Terms_Use.cfm

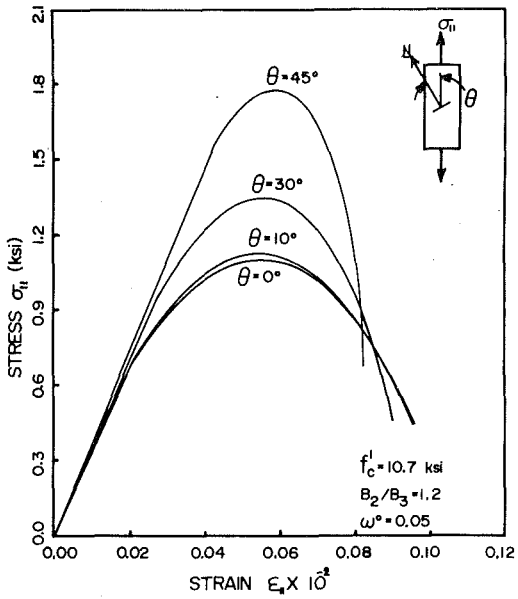


Fig. 9 Uniaxial tension test of a damaged concrete specimen; the normal to the previously inflicted damage subtends an angle θ with the direction of the applied tension

$$\begin{Bmatrix} \epsilon_{NN} \\ \epsilon_{NT} \end{Bmatrix} = \begin{bmatrix} \cos^2\theta & \sin^2\theta & 0 & \frac{1}{2}\sin 2\theta \\ -\frac{1}{2}\sin 2\theta & \frac{1}{2}\sin 2\theta & 0 & \frac{1}{2}\cos 2\theta \end{bmatrix} \begin{Bmatrix} \epsilon_{11} \\ \epsilon_{22} \\ \epsilon_{33} \\ 2\epsilon_{12} \end{Bmatrix} \tag{35}$$

or

$$\{\bar{\epsilon}\} = [C]\{\epsilon\} \tag{35'}$$

From (31) and (Part 1—(36′)) after some elementary matrix algebra

$$\{d\bar{\epsilon}\} = [R]\{d\epsilon\} \tag{36}$$

with

$$[R] = ([I] - \kappa[H][B])^{-1}[C] \tag{37}$$

where $[I]$ is the identity matrix, $\kappa = 1$ for loading and $\kappa = 0$ for unloading. The matrix $[H]$ is from (Part 1—(26)) a (2×2) square matrix

$$[H] = 2\begin{bmatrix} 0 & (\epsilon_{22} - \epsilon_{11})\sin 2\theta + 2\epsilon_{12}\cos 2\theta \\ 0 & (\epsilon_{22} - \epsilon_{11})\cos 2\theta - 2\epsilon_{12}\sin 2\theta \end{bmatrix} \tag{38}$$

Hence, the (2×4) rectangular matrix $[R]$ can finally be written in form

$$[R] = \frac{1}{P_1P_4 - P_2P_3}\begin{bmatrix} \left(P_4\cos^2\theta + \frac{P_2}{2}\sin^2\theta\right) & \left(P_4\sin^2\theta - \frac{P_2}{2}\sin 2\theta\right) & 0 & \frac{1}{2}(P_4\sin 2\theta - P_2\cos 2\theta) \\ -\left(P_3\cos^2\theta + \frac{P_1}{2}\sin 2\theta\right) & -\left(P_3\sin^2\theta - \frac{P_1}{2}\sin 2\theta\right) & 0 & \frac{1}{2}(P_3\sin 2\theta - P_1\cos 2\theta) \end{bmatrix} \tag{39}$$

in which

$$\begin{aligned} P_1 &= (1 - 4\kappa g G\epsilon_{NT}) \\ P_2 &= g(P_1 - 1) \\ P_3 &= 2\kappa g G[(\epsilon_{11} - \epsilon_{22})\cos 2\theta + 2\epsilon_{12}\sin 2\theta] \\ P_4 &= gP_3 + 1 \end{aligned} \tag{40}$$

where g and G are defined by (33) and (34).

The incremental stress-strain relationship can subsequently be written in form of (Part 1—(39)) with the material property matrix depending on the mode (loading or unloading) and the already accumulated damage,

$$\{d\sigma\} = [K_\omega]\{d\epsilon\} \tag{41}$$

where the material property matrix of the degraded material is given by

$$[K_\omega] = [K] + \kappa[\overline{K}][A][B][R] \tag{42}$$

The matrices on the right-hand side of (42) are defined by relations (28), (29), (Part 1—(33)), (32), and (39), respectively. The second term on the right-hand side of (42) exists only in loading. However, even the matrix $[K]$, being the function of the already accumulated damage, reflects the level to which the material properties have deteriorated during the loading history.

4.1 Rotational Nature of Damage. During a general loading program a structural component is subjected to a sequence of diverse loadings which differ not only in magnitude but often in the direction of application as well. Thus it is often necessary to consider a case when the direction of the principal strain is not perpendicular to the plane of microdefects generated by a previous system of external loads and/or temperature fields.

In order to examine this problem it is sufficient to consider a case of the uniaxial tension of a specimen for which the normal to the previously incured damage subtends an angle θ with the direction of the applied tension. In view of (35) both ϵ_{NN} and ϵ_{NT} will exist on the face of the crack. This will lead to a simultaneous increase in void density $d\Omega_{NN} > 0$ and change in void orientation $d\Omega_{NT} \neq 0$. This is, of course, in agreement with the well-known Fracture Mechanics result for a crack subjected to tensile and shear stress (Erdogan, Sih [55]).

It is somewhat surprising that this important problem did not attract more attention in the literature. Except for an effort by Kachanov [8] and a series of the reverse torsion creep experiments carried out by Hayhurst, Trampczynski, and Leckie [56] this problem was virtually ignored. Even the models designed to deal with multiaxial states of stress (such as [9, 11], etc.) were not tested on a problem of this kind. The inherent inability of the tensor models to cope with this type of a problem was discussed in Part 1 of this paper.

The present theory based on the physical notion of damage and a rigorous mathematical description of the kinematics of the damage growth (incorporating both the cleavage and the slip) is ideally suited for the analysis of this class of problems. The governing equations are readily deduced from the equations for the plane case writing $\omega_1 = \omega\cos\theta$, $\omega_2 = \omega\sin\theta$. The angle θ(e,ω) is the angle subtended by the axis of principal strain ("1" in this case) and the normal **N** to the damage field.

To determine the cleavage to slip ratio it is necessary to know the slope (B_2/B_3) of the asymptote to the damage surface. In a virtual absence of the pertinent experimental data assume that $(B_2/B_3) = 1.0$ and 1.2 while $(B_1/B_3) = 3$. With the assumed value for B_2/B_3 the analysis was carried out for the four high strength concrete specimens with the initial damage characterized by the void density of $\omega_N = 0.05$ (roughly 35 percent of the damage at the peak stress in tensile test) and normals subtending angles of $\theta = 0°$, 10°, 30°, and 45° with the principal tensile strain axis. The other material parameters are those determined on the basis of the uniaxial tensile test. The computed σ_{11} versus ϵ_{11} curves for the two (B_2/B_3) ratios and four different orientations of the previously incured damage are plotted in Figs. 9 and 10. The difference in the maximum stress achieved for torsion-tension

Downloaded 01 May 2010 to 171.66.16.249. Redistribution subject to ASME license or copyright; see http://www.asme.org/terms/Terms_Use.cfm

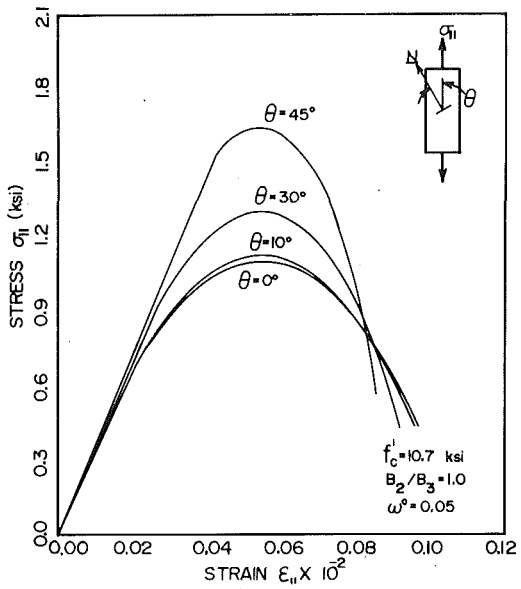


Fig. 10 Uniaxial tension test of a damaged concrete specimen (material parameters changed)

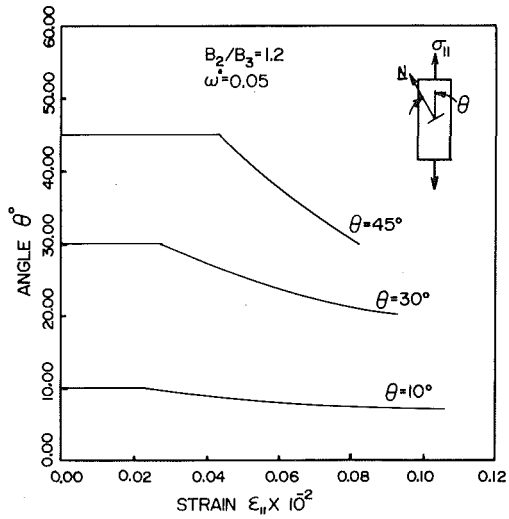


Fig. 11 Change of the damage orientation

test ($\theta = 45°$) versus tension-tension test ($\theta = 0°$) is so large (~50 percent) that a rather insensitive experiment should suffice for the determination of the material parameter B_2 (or a different and hopefully improved damage surface). These results indicate a strongly directional nature of the damage (alluded to by Leckie [6] and suspected by many others) consistent with the void geometry.

The curves showing the change in the damage orientation (i.e., rotation of the normal to the void, in sense of the Fig. 1, Part 1) are plotted in Fig. 11 for $B_2 = 1.2B_3$. In each case the damage is initially constant until the loading path in the strain space reaches the current damage surface. Subsequently, (since $d\Omega_{NN} > 0$) the angle θ decreases as the damage grows predominantly in the plane perpendicular to the principal tensile strain.

4.2 Path Dependence. In the final example two identical specimens manufactured of the high strength concrete with cylinder strength of $f_c' = 10.7$ ksi are subjected to two different loading programs. In the first specimen the stress σ_{11} is gradually increased from 0 to 1.10 ksi keeping $\sigma_{22} = 0$. Next, keeping σ_{11} at 1.1 ksi, σ_{22} is slowly increased from 0 to $\sigma_{22} = \sigma_{11}$. The second specimen is subjected to the proportional loading with stresses $\sigma_{11} = \sigma_{22}$ increased gradually from

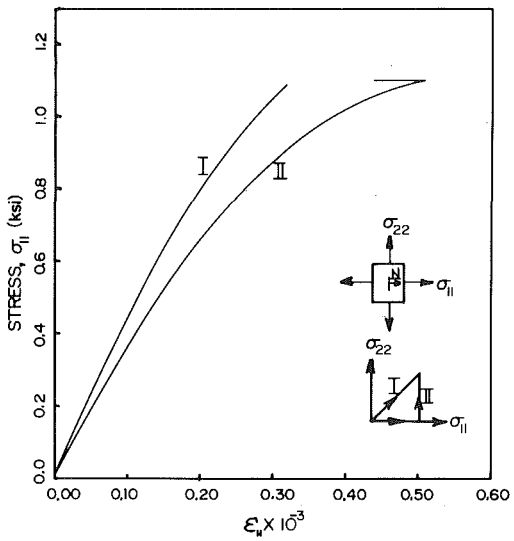


Fig. 12 Stress-strain curve—path-dependent test

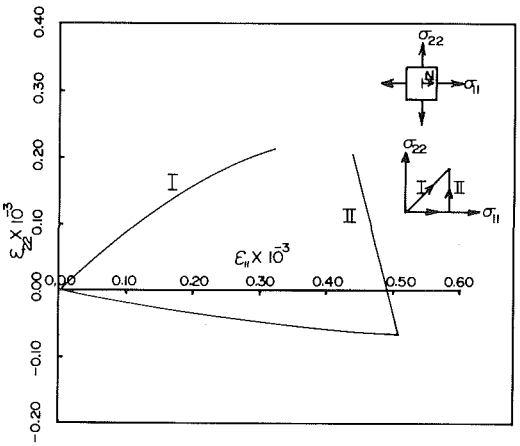


Fig. 13 Strain curves—path-dependent test

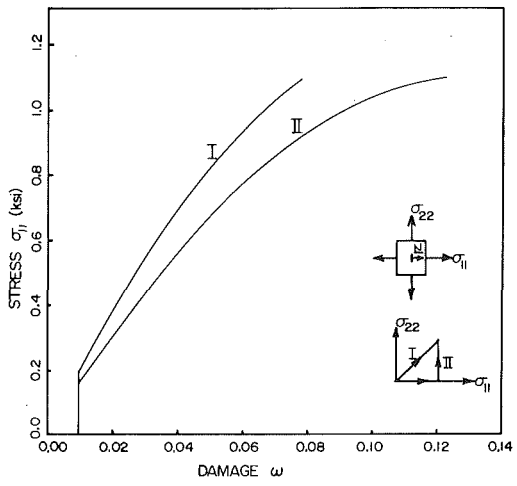


Fig. 14 Gradual damage accumulation—path-dependent test

zero to 1.1 ksi. The initial damage was in both cases $\omega_N = 0.01$, while all other material parameters are those determined from the tensile test in addition to $B_2 = 1.2B_3$ and $B_1 = 3B_3$.

The computed results are plotted in Figs. 12–14. The accumulated

Downloaded 01 May 2010 to 171.66.16.249. Redistribution subject to ASME license or copyright; see http://www.asme.org/terms/Terms_Use.cfm

damage and the axial strain are substantially larger (~33 percent) for the nonproportional loading (specimen 2). The same is true for the lateral strain ϵ_{22} (Fig. 14). These results appear again to be quite reasonable. A fairly simple experiment would suffice for the confirmation of these results and could serve for a more accurate determination of the damage surface.

Note that it was assumed that no initial damage in any other direction exists. The analysis would change somewhat if the original damage exists in all directions.

Identification of Material Parameters

One of the major problems with some of the recent, more sophisticated theories is a rather alarming degree of ambiguity in determination of the material parameters. And yet, quite obviously, the output of a computation can never be more accurate than the input.

In the case of the proposed theory the analysis of the uniaxial tension and compression requires the knowledge of three parameters C_1, C_2 and $(B_1 - B_3)$. Two of the parameters can be determined from the peak stress $\sigma_{11}{}^M$ and the corresponding strain $\epsilon_{11}{}^M$ in tension, i.e., from the equation (18) and

$$\left.\frac{\partial \sigma_{11}}{\partial \epsilon_{11}}\right|_{(\sigma^M, \epsilon^M)} = \left(1 - \frac{2\nu^2}{1-\nu}\right) + \frac{2C_2}{B_1 - B_3}\epsilon_{11}{}^M + \frac{C_1}{B_1 - B_3}\left[2(1-2\nu) - \frac{3}{2}\frac{C_1}{B_1 - B_3}(1-\nu)\epsilon_{11}{}^M\right]\epsilon_{11}{}^M = 0 \quad (43)$$

In order to determine the third parameter it is necessary, for example, to determine the void ratio ω^M at the peak stress (i.e., for $\epsilon_{11}{}^M$). This will provide the third equation since according to (12)

$$B_1 - B_3 = \epsilon_{11}{}^M/\omega^M \quad (44)$$

Naturally, ω^M is not equal to unity as per the original Kachanov's model [2]. In case of the simple model used by Janson and Hult [44] and Krajcinovic [45–47] (in the case when the Poisson's ratio is equal to zero) the maximum value of damage is $\omega_{max} = 0.5$. The number and size distribution of cracks was measured by Curran, et al. [57], for a polycarbonate plate, Shockey, et al. [58], for the α-titanium (the reduction of area at fracture was found to be about 50 percent), McHugh, et al. [59], for the oil shale rocks, etc. Hence, the void ratio can indeed be measured at the peak stress. The measured value is probably a material parameter for a fixed temperature and strain rate.

Once the three material parameters are determined from the tensile test on the basis of equations (18), (43), (44) it is possible to determine the response during the compressive test without further fitting. In the present case in absence of the experimental results for concrete ω^M was taken to be 0.15.

It is, of course, possible to determine the third constant from either the apparent Poisson's ratio or the peak strain in compressive test and predict the void ratio at failure.

In case of the plane problems it is necessary to have the constant B_2 and B_3 as well. These constants can be determined, for example, on the basis of the two loading cases examined in the text.

Finally, the initial void ratio ω_0 can be determined as the proportionality limit on the basis of equation (15). However, the analysis is fairly insensitive with respect to the exact value of the initial void ratio (if $\omega \ll 1$).

Summary and Conclusions

The results presented in this part of the paper clearly demonstrate that the proposed theory enables the stress analysis of a brittle, progressively damaging, solid subjected to a general (at this time, time-independent) loading regime. The four material parameters introduced by the theory can be determined in a straightforward manner from the simple uniaxial tests. It is very encouraging that the established analytical model (based on a simple damage surface) predicts all response trends and correlates surprisingly well with the experimental data.

Nevertheless, it is quite obvious that a host of especially designed experiments are needed to test this theory in the future. This is especially true for the case of nonproportional and sequential loading programs.

It should be finally emphasized that the proposed model should be in principle related to one developed in a series of excellent papers by Rice and Tracey [60], Needleman [61], Gurson [62], etc., in order to consider the growth of voids in a plastic continuum. Despite some superficial similarities, the actual relation between the two models is far from being apparent.

It should also be emphasized that the present model is focused on plane, penny-shaped, microdefects (of infinitely small thickness) consistent with the assumption of constant density. A more general model incorporating the spheroidal and cylindrical cavities will be one of the topics of future studies.

References

39 Zienkiewicz, O. C., and Pande, G. N., "Some Useful Forms of Isotropic Yield Surfaces for Soil and Rock Mechanics," in *Finite Elements in Geomechanics*, ed., Gudehus, G., Wiley, 1977, pp. 179–190.

40 Jaeger, J. C., and Cook, N. G. W., *Fundamentals of Rock Mechanics*, third ed., Chapman and Hall, London, 1979.

41 Martin, J. B., *Plasticity: Fundamentals and General Results*, The MIT Press, Cambridge, Mass., 1975.

42 Wool, R. P., "Material Damage in Polymers," in *Workshop on a Continuum Mechanics Approach to Damage and Life Prediction*, May 1980, pp. 28–35.

43 Broek, D., *Elementary Engineering Fracture Mechanics*, Sijthoff and Noordhoff, The Netherlands, 1978.

44 Janson, J., and Hult, J., "Fracture Mechanics and Damage Mechanics, a Combined Approach," *Journal de Mecanique Applique*, Vol. 1, 1977, pp. 69–84.

45 Krajcinovic, D., "Distributed Damage Theory of Beams in Pure Bending, ASME JOURNAL OF APPLIED MECHANICS, Vol. 46, 1979, pp. 592–596.

46 Krajcinovic, D., et al., "Progressive Damage of Dynamically Loaded Brittle Rod," ASCE Preprint 80-522, 1980.

47 Fonseka, G. U., Krajcinovic, D., and Srinivasan, M. G., "Dynamic Response of Progressively Damaging Structures," presented at 51st Shock and Vibration Symp., San Diego, Calif., 1980.

48 Neville, A. M., *Properties of Concrete*, Wiley, New York, 1963.

49 Kupfer, H. B., and Gerstle, K. H., "Behavior of Concrete Under Biaxial Stress," *Proceedings, ASCE*, Vol. 99, *Journal of Engineering Mechanics Division* EM4, 1973, pp. 852–866.

50 Wang, P. T., Shah, S. P., and Naaman, A. E., "Stress-Strain Curves of Normal and Lightweight Concrete in Compression," *Journal of the American Concrete Institute*, Vol. 75, 1978, pp. 603–611.

51 Brace, W. F., Paulding, B. W. Jr., and Scholz, C., "Dilatancy in the Fracture of Crystalline Rocks," *Journal of Geophysical Research*, Vol. 71, 1966, pp. 3939–3953.

52 Crouch, S. L., "Experimental Determination of Volumetric Strains in Failed Rock," *International Journal of Rock Mech. Min. Sci.*, Vol. 7, 1970, pp. 589–603.

53 Wang, P. T., "Complete Stress-Strain Curve of Concrete and Its Effect on Ductility of Reinforced Concrete Members," PhD Thesis, University of Illinois at Chicago Circle, Oct. 1977.

54 Kupfer, H. B., Hilsdorf, H. K., and Rüsch, H., "Behavior of Concrete Under Biaxial Stress," *Journal of the American Concrete Institute*, Vol. 66, 1969, pp. 656–666.

55 Erdogan, F., and Sih, G. C., "On the Crack Extension in Plates Under Plane Loading and Transverse Shear," ASME *Journal of Basic Engineering*, Vol. 88, 1963, pp. 519–527.

56 Hayhurst, D. R., Trampczynski, W. A., and Leckie, F. A., "Creep Rupture Under Nonproportional Loading," *Acta Metallurgica*, Vol. 28, 1980, pp. 1171–1183.

57 Curran, D. R., Shockey, D. A., and Seaman, L., Dynamic Fracture Criteria for a Polycarbonate," *Journal of Applied Physics*, Vol. 44, 1973, pp. 4025–4038.

58 Shockey, D. A., Dao, K. C., and Jones, R. L., "Effect of Grain Size on the Static and Dynamic Fracture Behavior of α-Titanium," SRI International Report (undated).

59 McHugh, Curran, D. R., and Seaman, L., "The Nag-Frag Computational Fracture Model and Its Use for Simulating Fragmentation and Fracture," presented at the 1980 SESA meeting, Ft. Lauderdale, Oct. 1980.

60 Rice, J. R., and Tracey, D. M., "On the Ductile Enlargement of Voids in Triaxial Stress Fields," *Journal of the Mechanics and Physics of Solids*, Vol. 17, 1969, pp. 201–217.

61 Needleman, A., "Void Growth in an Elastic-Plastic Medium," ASME JOURNAL OF APPLIED MECHANICS, Vol. 39, 1972, pp. 964–970.

62 Gurson, A. L., "Continuum Theory of Ductile Rupture by Void Nucleation and Growth: Part I—Yield Criteria and Flow Rules for Porous Ductile Media," ASME *Journal of Engineering Materials and Technology*, Vol. 99, 1977, pp. 2–15.

Downloaded 01 May 2010 to 171.66.16.249. Redistribution subject to ASME license or copyright; see http://www.asme.org/terms/Terms_Use.cfm

S. Aoki
Associate Professor.

K. Kishimoto
Research Associate.

M. Sakata
Professor.

Department of Physical Engineering,
Tokyo Institute of Technology,
Ookayama, Meguroku,
Tokyo 152, Japan

Energy-Release Rate in Elastic-Plastic Fracture Problems

It is shown that the energy-release rates associated with the translation, rotation, self-similar expansion and distortion of the fracture process region are expressed by the newly introduced integrals, $\hat{J}$, $\hat{L}$, $\hat{M}$, and $\hat{I}$. These integrals can be defined even if there exist plastic deformation, thermal strains, body forces, and inertia forces. They include as special cases the J, L, and M integrals which have been defined by Knowles and Sternberg and discussed by Budiansky and Rice.

1 Introduction

As shown by Broberg [1], there exists a fracture process region near a crack tip where fracture process such as nucleation of voids or microcracks and their coalescence take place and usual continuum mechanics does not work. In general the shape of the process region varies during crack extension. The size of the process region for quasi-brittle fracture is so small as to be usually neglected. However, in order to quantify ductile fracture, it will be necessary to take the finiteness of the process region into consideration. Although usual continuum mechanics does not work for the microstructural processes going on in the process region, the system energy balance has to be satisfied and energy-release rate may play an important role.

In this paper, new integrals $\hat{J}$, $\hat{L}$, $\hat{M}$, and $\hat{I}$ are introduced and are related to the energy-release rate associated with the deformation of the process region near a crack tip in an elastic-plastic material. These integrals involve line integrals and an area integral over the area inside the path of the line integrals, and can be defined even if there exist plastic deformations, thermal strains, body forces, and inertia forces. These integrals are extensions of the J, L, and M integrals which were defined by Knowles and Sternberg [2] and were related by Budiansky and Rice [3] to energy-release rate due to the cavitation or cracking of elastostatic materials.

Energy-Release Rate Due to Deformation of Process Region

We consider the two-dimensional problem of a crack in an elastic-plastic material, as shown in Fig. 1, where Γ_{end} represents the boundary of the process region A_{end}, Γ is an arbitrary curve which surrounds the curve Γ_{end}, Γ_s are curves along the crack surfaces, and A is the region surrounded by the curves Γ, Γ_s, and Γ_{end}. $O - X_1, X_2$ is the fixed frame with the origin O being at the crack tip.

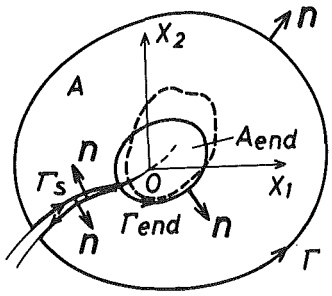


Fig. 1 Fracture process region, A_{end}

We assume that an infinitesimal crack extension virtually takes place with the contour of the process region Γ_{end} varing as shown in Fig. 1. The system energy balance equation of the material in $A + A_{end}$ is written as

$$P + Q = (d/dt)K + (d/dt)U + \Phi \tag{1}$$

where P is the power of the external forces, and Q the heat energy per unit time. $(d/dt)K$ and $(d/dt)U$ are, respectively, the time rates of changes of total kinetic and internal energies of the material instantaneously in A. Φ represents the energy-release rate, i.e., the time rate of the energy change referred to the process region, A_{end}. Although we cannot represent Φ directly in terms of usual continuum mechanics, we can relate Φ to the quantities (such as stress σ_{ij} and displacement u_i) of the regular region A through the system energy balance equation (1). Freund [4] has used a similar system energy balance equation and derived the expression of the energy-release rate

Contributed by the Applied Mechanics Division and presented at the Winter Annual Meeting, Washington, D. C., November 15–20, 1981, of THE AMERICAN SOCIETY OF MECHANICAL ENGINEERS.

Discussion on this paper should be addressed to the Editorial Department, ASME, United Engineering Center, 345 East 47th Street, New York, N. Y. 10017, and will be accepted until March 1, 1982. Manuscript received by ASME Applied Mechanics Division, October, 1980; final revision, February, 1981. Paper No. 81-WA/APM-21.

Copyright © 1981 by ASME

Downloaded 01 May 2010 to 171.66.16.249. Redistribution subject to ASME license or copyright; see http://www.asme.org/terms/Terms_Use.cfm

due to the linear dynamic extension of a crack in a linearly elastic solid.

The left-hand side of equation (1) is represented as

$$P+Q=\left\{\int_{\Gamma+\Gamma_s} T_i\dot{u}_i d\Gamma+\iint_A F_i\dot{u}_i dA\right\}+\left\{\int_{\Gamma+\Gamma_s}(-q_i n_i)d\Gamma+\iint_A \rho\gamma dA\right\}=\int_{\Gamma+\Gamma_s}(T_i\dot{u}_i-q_i n_i)d\Gamma+\iint_A(F_i\dot{u}_i+\rho\gamma)dA \quad (2)$$

where T_i is the surface traction, F_i the body force, q_i the heat flux, γ the heat produced by internal heat sources, ρ the density, and n_i the unit normal to the curve Γ or Γ_s, which points to the right of the curve when looking along it in the positive direction (see Fig. 1). A dot $(\cdot)$ designates the material-time derivative. It is noted that the line integral is carried out over the curves $\Gamma+\Gamma_s$ with Γ_{end} excluded, since the material in $A+A_{\text{end}}$ is surrounded by $\Gamma+\Gamma_s$. The area integral is carried out over A with A_{end} excluded because the energy change referred to A_{end} is included in Φ.

Since the shape of the process region A_{end} changes during the crack extension and therefore the deformation of the curve Γ_{end} takes place, the region A is time-dependent. The time rate of change of the total kinetic energy in A equals the total time rate of change of kinetic energy density in A plus the flux of kinetic energy density out of the bounding surface of A, i.e.,

$$\frac{d}{dt}K=\iint_A \rho\dot{k}dA+\int_{\Gamma_{\text{end}}}\rho k V_i(-n_i)d\Gamma \quad (3)$$

where k is the kinetic energy per unit mass, n_i the unit normal to Γ_{end}, which points out of the process region (see Fig. 1), and V_i the velocity of the curve Γ_{end}. More precise description of V_i will be given later. There is a sign difference between Freund's expression [4] and equation (3), which is due to the difference of the positive direction of n_i. Similarly, $(d/dt)U$ is written as

$$\frac{d}{dt}U=\iint_A \rho\dot{e}dA+\int_{\Gamma_{\text{end}}}\rho e V_i(-n_i)d\Gamma \quad (4)$$

where e is the internal energy per unit mass.

Substituting equations (2)–(4) into equation (1) and making use of the Gauss theorem, we obtain

$$\Phi=\int_{\Gamma_{\text{end}}}\{\rho(k+e)V_i n_i+T_i\dot{u}_i-q_i n_i\}d\Gamma \quad (5)^1$$

where we have assumed the strain is infinitesimal and used the equation of motion, the relation between strain ϵ_{ij} and displacement u_i, the first law of continuum thermodynamics (in local form), the definition of k, and stress-traction relation, i.e.,

$$\begin{aligned}
&\sigma_{ij,j}+F_i=\rho\ddot{u}_i && \text{in } A\\
&\epsilon_{ij}=(u_{i,j}+u_{j,i})/2 && \text{in } A\\
&\rho\dot{e}=\sigma_{ij}\dot{\epsilon}_{ij}-q_{i,i}+\rho\gamma && \text{in } A\\
&\rho\dot{k}=\rho\ddot{u}_i\dot{u}_i && \text{in } A\\
&T_i=\sigma_{ij}n_j && \text{on } \Gamma,\ \Gamma_s, \text{ and } \Gamma_{\text{end}}
\end{aligned} \quad (6)$$

3 Decomposition of Energy-Release Rate

In order to obtain a detailed expression of the velocity of Γ_{end}, i.e., V_i, we introduce a moving rectangular frame $0-x_1, x_2$ and also a moving polar frame $0-r, \theta$, which are attached to the crack tip as shown in Fig. 2. We assume that the moving frames $0-x_1, x_2$ and $0-r, \theta$ have the same velocity v_i and the same angular velocity ω_3 as the moving crack tip. The line $\theta=0$ coincides with the x_1-axis and the moving frame $0-x_1, x_2$ is in coincidence with the fixed frame $O-X_1, X_2$ at the time origin, $t=t_0$. The position of a point, say C, on the curve Γ_{end} at the time $t=t_0$ is denoted by a vector $\mathbf{r}(\theta, t_0)$ $(0\leqq\theta\leqq 2\pi)$ that extends from the current crack tip O to the point C.

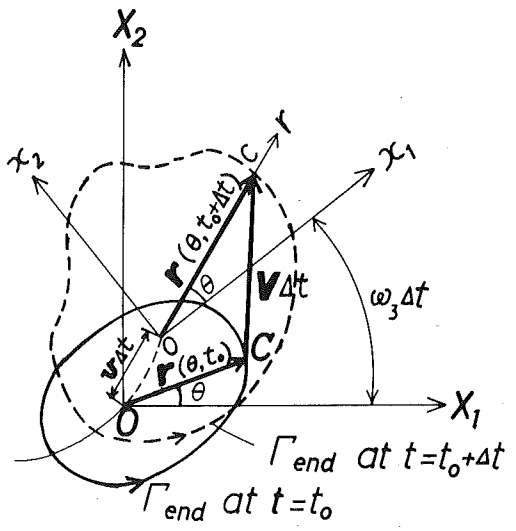


Fig. 2 Definition of the velocity of Γ_{end}, V

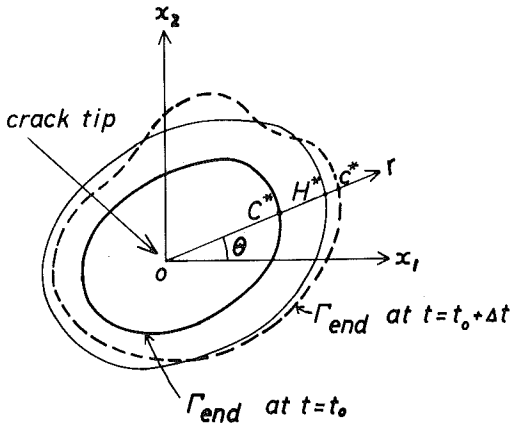


Fig. 3 Configuration of fracture process region viewed from the moving frames

After the time increases by Δt, the crack propagates by $\mathbf{v}\Delta t$ and the deformations of Γ_{end} take place as in Fig. 2, where the crack is assumed to propagate along a rather arbitrary but smooth trajectory. We select a point, say c, on the deformed spatial curve Γ_{end} in such a way that the numerical value of the moving angular coordinate θ of the point is the same as that of the point C. The point c is represented by a vector $\mathbf{r}(\theta, t_0+\Delta t)$ as shown in Fig. 2. We define the velocity of Γ_{end}, $\mathbf{V}(\theta, t_0)$ as

$$\mathbf{V}(\theta, t_0)\Delta t=\mathbf{v}\Delta t+\mathbf{r}(\theta, t_0+\Delta t)-\mathbf{r}(\theta, t_0) \quad (7)$$

As shown in Fig. 2, $\mathbf{V}\Delta t$ is the vector connecting the points C and c. Letting $\Delta t\to 0$, we obtain

$$\mathbf{V}=\mathbf{v}+\frac{\partial\mathbf{r}}{\partial t}=\mathbf{v}+\frac{\partial(r\mathbf{e}_r)}{\partial t}=\mathbf{v}+r\frac{\partial\mathbf{e}_r}{\partial t}+\frac{\partial r}{\partial t}\mathbf{e}_r \quad (8)$$

where r is the length of $\mathbf{r}$ and $\mathbf{e}_r$ is a unit vector having the same direction as $\mathbf{r}$.

[1] In reference [5], the system energy balance equation has been written as

$$P=\iint_A(\rho\dot{k}+\sigma_{ij}\dot{\epsilon}_{ij})dA+\Psi$$

and the energy-release rate has been defined by Ψ. The relation between Ψ and Φ is given as

$$\Psi=\Phi-\int_{\Gamma_{\text{end}}}\{\rho(k+e)V_i n_i-q_i n_i\}d\Gamma$$

Downloaded 01 May 2010 to 171.66.16.249. Redistribution subject to ASME license or copyright; see http://www.asme.org/terms/Terms_Use.cfm

Fig. 3 shows schematically the shapes of Γ_{end} at $t = t_0$ and $t = t_0 + \Delta t$, which are viewed from the moving frame $0 - x_1, x_2$. Since the values of the moving angular coordinate θ of the point c is the same as that of C, the points 0, C, and c are observed as if they were on a straight line. The points C^* and c^* in Fig. 3 correspond, respectively, to the points C and c in Fig. 2. The shape of the thin curve in Fig. 3 is proportional to that of the solid curve, i.e., Γ_{end} at $t = t_0$, and the area within the thin curve is the same as that of the dashed curve, i.e., Γ_{end} at $t = t_0 + \Delta t$. The point H^* is the intersection of the thin curve and the line $\overline{0c}^*$. From Fig. 3, we obtain

$$\overline{0c}^* - \overline{0C}^* = \overline{C^*H^*} + \overline{H^*c^*} \tag{9}$$

Noting that the lengths of $\overline{0c}^*$ and $\overline{0C}^*$ are, respectively, identical to $r(\theta, t_0 + \Delta t)$ and $r(\theta, t_0)$, we rewrite equation (9) as

$$r(\theta, t_0 + \Delta t) - r(\theta, t_0) = ar(\theta, t_0)\Delta t + h(\theta, t_0)\Delta t \tag{10}$$

where $ar(\theta, t_0)\Delta t$ is the length of $\overline{C^*H^*}$ and the constant a is determined by equating the area within the thin curve to that within the dashed curve, i.e.,

$$\int_0^{2\pi} r^2(\theta, t_0 + \Delta t)d\theta = (1 + a\Delta t)^2 \int_0^{2\pi} r^2(\theta, t_0)d\theta \tag{11}$$

The length of $\overline{H^*c^*}$ is denoted by $h(\theta, t_0)\Delta t$. As $\Delta t \to 0$, we obtain from equations (10) and (11)

$$\partial r/\partial t = ar + h \tag{12}$$

where

$$a = \frac{\int_0^{2\pi} \frac{\partial r^2}{\partial t} d\theta}{2\int_0^{2\pi} r^2 d\theta} \tag{13}$$

Noting that the moving frames rotate with the angular velocity $\boldsymbol{\omega} = (0, 0, \omega_3)$, we obtain

$$\frac{\partial \mathbf{e}_r}{\partial t} = \boldsymbol{\omega} \times \mathbf{e}_r \tag{14}$$

Substitution of equations (12) and (14) into equation (8) leads to

$$\mathbf{V} = \mathbf{v} + \boldsymbol{\omega} \times \mathbf{r} + a\mathbf{r} + \mathbf{h} \tag{15}$$

i.e.,

$$V_i = v_i + e_{i3l}\omega_3 x_l + ax_i + h_i \tag{16}$$

where $\mathbf{h} = h\mathbf{e}_r = (h_1, h_2, 0)$ and e_{i3l} denotes the alternating tensor. It is seen from equation (16) that V_i is decomposed into the components of translation with velocity v_i, the rotation with angular velocity $\boldsymbol{\omega}_3$, the self-similar expansion a, and the distortion (nonself-similar deformation) of the process region h_i.

Let $\partial u_i/\partial t|_{\Gamma_{end}}$ denote the time rate of u_i on the spatial line Γ_{end}:

$$\left.\frac{\partial u_i}{\partial t}\right|_{\Gamma_{end}} = \lim_{\Delta t \to 0} \times \frac{u_i(X_1 + V_1\Delta t, X_2 + V_2\Delta t, t + \Delta t) - u_i(X_1, X_2, t)}{\Delta t} \tag{17}$$

Expanding equation (17) into a Taylor's series, we obtain

$$\left.\frac{\partial u_i}{\partial t}\right|_{\Gamma_{end}} = \frac{\partial u_i(X_1, X_2, t)}{\partial t} + \frac{\partial u_i}{\partial X_j} V_j \tag{18}$$

Since $\dot{u}_i$, the velocity of a particle on Γ_{end} is identical to $\partial u_i(X_1, X_2, t)/\partial t$, equation (18) becomes

$$\dot{u}_i = \left.\frac{\partial u_i}{\partial t}\right|_{\Gamma_{end}} - \frac{\partial u_i}{\partial X_j} V_j \tag{19}$$

Combining equations (16), (19), and (5), and considering $x_i = X_i$ at the time $t = t_0$, we obtain

$$\Phi = v_\alpha \hat{J}_\alpha + \omega_3 \hat{L}_3 + a\hat{M} + \hat{I} \quad (\alpha = 1, 2) \tag{20}$$

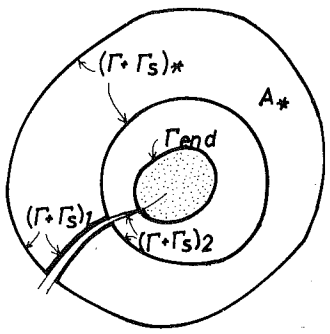


Fig. 4 Path used to show path-independence of $\hat{J}$, $\hat{L}$, and $\hat{M}$ with respect to the contour $\Gamma + \Gamma_s$

where

$$\hat{J}_\alpha = \int_{\Gamma_{end}} \left\{\rho(k + e)n_\alpha - T_i \frac{\partial u_i}{\partial X_\alpha}\right\} d\Gamma \tag{21}$$

$$\hat{L}_3 = \int_{\Gamma_{end}} e_{i3l}X_l \left\{\rho(k + e)n_i - T_j \frac{\partial u_j}{\partial X_i}\right\} d\Gamma \tag{22}$$

$$\hat{M} = \int_{\Gamma_{end}} X_i \left\{\rho(k + e)n_i - T_j \frac{\partial u_j}{\partial X_i}\right\} d\Gamma \tag{23}$$

$$\hat{I} = \int_{\Gamma_{end}} \left\{\rho(k + e)h_i n_i + T_i \left(\left.\frac{\partial u_i}{\partial t}\right|_{\Gamma_{end}} - \frac{\partial u_i}{\partial X_j} h_j\right) - q_i n_i\right\} d\Gamma \tag{24}$$

It is noted that $\hat{J}_\alpha$, L_3, $\hat{M}$, and $\hat{I}$ are the components of the energy-release rate associated, respectively, with the translation, rotation, self-similar expansion, and distortion of the process region.

4 Formulas for $\hat{J}$, $\hat{L}$, and $\hat{M}$

$\hat{J}_\alpha$, $\hat{L}_3$, and $\hat{M}$ are given in the form of line integrals on Γ_{end} in equations (21)–(23). In order to calculate these values for cracked structures, it may be convenient [6] to obtain formulas in the form of integrals over the regular region outside the process region. The use of the Gauss theorem leads to

$$\int_{\Gamma+\Gamma_s-\Gamma_{end}} T_i \frac{\partial u_i}{\partial X_\alpha} d\Gamma = \iint_A \left\{(\rho\ddot{u}_i - F_i)\frac{\partial u_i}{\partial X_\alpha} + \sigma_{ij}\frac{\partial \epsilon_{ij}}{\partial X_\alpha}\right\} dA \tag{25}$$

$$\int_{\Gamma+\Gamma_s-\Gamma_{end}} e_{i3l}X_l T_j \frac{\partial u_j}{\partial X_i} d\Gamma = \iint_A e_{i3l}\left\{\sigma_{jl}\frac{\partial u_j}{\partial X_i} + X_l(\rho\ddot{u}_j - F_j)\frac{\partial u_j}{\partial X_i} + X_l\sigma_{jk}\frac{\partial \epsilon_{jk}}{\partial X_i}\right\} dA \tag{26}$$

and

$$\int_{\Gamma+\Gamma_s-\Gamma_{end}} X_i T_j \frac{\partial u_j}{\partial X_i} d\Gamma = \iint_A \left\{X_j(\rho\ddot{u}_i - F_i)\frac{\partial u_i}{\partial X_j} + X_l\sigma_{ij}\frac{\partial \epsilon_{ij}}{\partial X_l} + \sigma_{ij}\epsilon_{ij}\right\} dA \tag{27}$$

where the negative sign of Γ_{end} means to integrate along Γ_{end} in the clockwise sense. Substituting equations (25)–(27) into equations (21)–(23), we obtain

$$\hat{J}_\alpha = -\int_{\Gamma+\Gamma_s} T_i \frac{\partial u_i}{\partial X_\alpha} d\Gamma + \int_{\Gamma_{end}} \rho(k + e)n_\alpha d\Gamma + \iint_A \left\{(\rho\ddot{u}_i - F_i)\frac{\partial u_i}{\partial X_\alpha} + \sigma_{ij}\frac{\partial \epsilon_{ij}}{\partial X_\alpha}\right\} dA \tag{28}$$

$$\hat{L}_3 = -\int_{\Gamma+\Gamma_s} e_{i3l}X_l T_j \frac{\partial u_j}{\partial X_i} d\Gamma + \int_{\Gamma_{end}} e_{i3l}X_l\rho(k + e)n_i d\Gamma + \iint_A e_{i3l}\left\{\sigma_{jl}\frac{\partial u_j}{\partial X_i} + X_l(\rho\ddot{u}_j - F_j)\frac{\partial u_j}{\partial X_i} + X_l\sigma_{jk}\frac{\partial \epsilon_{jk}}{\partial X_i}\right\} dA \tag{29}$$

Downloaded 01 May 2010 to 171.66.16.249. Redistribution subject to ASME license or copyright; see http://www.asme.org/terms/Terms_Use.cfm

and

$$\hat{M} = -\int_{\Gamma+\Gamma_s} X_i T_j \frac{\partial u_j}{\partial X_i} d\Gamma + \int_{\Gamma_{end}} X_i \rho(k+e) n_i d\Gamma + \iint_A \left\{ X_j(\rho\ddot{u}_i - F_i)\frac{\partial u_i}{\partial X_j} + X_l \sigma_{ij}\frac{\partial \epsilon_{ij}}{\partial X_l} + \sigma_{ij}\epsilon_{ij} \right\} dA \quad (30)$$

We note that these integrals, equations (28)–(30), are dependent on Γ_{end}, but for a prescribed Γ_{end} they are independent of the path $\Gamma + \Gamma_s$ irrespective of the constitutive equation (elastic, inelastic, homogeneous, nonhomogeneous, isotropic, or anisotropic); see the Appendix.

For homogeneous materials, more detailed expressions are possible. In order to find such expressions, we decompose the strain into the components of elastic strain $\epsilon_{ij}{}^e$ and the eigenstrain $\epsilon_{ij}{}^*$: i.e.,

$$\epsilon_{ij} = \epsilon_{ij}{}^e + \epsilon_{ij}{}^* \quad (31)$$

where the eigenstrains are inelastic, stress-free strains[2] [7] which are typically exemplified by thermal strains or plastic strains. The elastic strain is related to the stress and the elastic strain-energy density $W^e(\epsilon_{ij}{}^e)$ as

$$\partial W^e(\epsilon_{ij}{}^e)/\partial \epsilon_{ij}{}^e = \sigma_{ij} \quad (32)$$

Substitution of equations (31) and (32) into equation (25) gives, for a homogeneous material:

$$\int_{\Gamma+\Gamma_s-\Gamma_{end}} T_i \frac{\partial u_i}{\partial X_\alpha} d\Gamma = \int_{\Gamma+\Gamma_s-\Gamma_{end}} W^e n_\alpha d\Gamma + \iint_A \left\{ (\rho\ddot{u}_i - F_i)\frac{\partial u_i}{\partial X_\alpha} + \sigma_{ij}\frac{\partial \epsilon_{ij}{}^*}{\partial X_\alpha} \right\} dA \quad (33)$$

Here, the word "homogeneous" implies that the elastic strain-energy density W^e has the same functional form at every point in the region A; hence it does not depend explicitly on the coordinates X_1, X_2, and X_3, although there is certainly an implicit dependence [8].

From equations (33) and (21) we obtain a formula of $\hat{J}$:

$$\hat{J}_\alpha = \int_{\Gamma+\Gamma_s} \left(W^e n_\alpha - T_i \frac{\partial u_i}{\partial X_\alpha} \right) d\Gamma + \int_{\Gamma_{end}} \{\rho(k+e) - W^e\} n_\alpha d\Gamma + \iint_A \left\{ (\rho\ddot{u}_i - F_i)\frac{\partial u_i}{\partial X_\alpha} + \sigma_{ij}\frac{\partial \epsilon_{ij}{}^*}{\partial X_\alpha} \right\} dA \quad (34)$$

Similarly, employing the elastic strain energy density W^e, we obtain

$$\int_{\Gamma+\Gamma_s-\Gamma_{end}} e_{i3l} X_l T_j \frac{\partial u_j}{\partial X_i} d\Gamma = \int_{\Gamma+\Gamma_s-\Gamma_{end}} e_{i3l}\{X_l W^e n_i + T_i u_l\} d\Gamma + \iint_A e_{i3l}\left\{ (\rho\ddot{u}_i - F_i)u_l + 2\sigma_{lj}\epsilon_{ij}{}^* + X_l \sigma_{mn}\frac{\partial \epsilon_{mn}{}^*}{\partial X_i} \right\} dA \quad (35)$$

for isotropic material where $e_{i3l}\sigma_{lj}\epsilon_{ij}{}^e = 0$. Combining equations (35) and (22) gives a formula of $\hat{L}_3$:

$$\hat{L}_3 = \int_{\Gamma+\Gamma_s} e_{i3l}\left\{ X_l\left(W^e n_i - T_j \frac{\partial u_j}{\partial X_i} \right) + T_i u_l \right\} d\Gamma + \int_{\Gamma_{end}} e_{i3l}\left[\{\rho(k+e) - W^e\} X_l n_i - T_i u_l \right] d\Gamma + \iint_A e_{i3l}\left\{ 2\sigma_{lj}\epsilon_{ij}{}^* + u_l(\rho\ddot{u}_i - F_i) + X_l(\rho\ddot{u}_j - F_j)u_{j,i} + X_l \sigma_{mn}\frac{\partial \epsilon_{mn}{}^*}{\partial X_i} \right\} dA \quad (36)$$

[2] For example, consider an elastic-plastic material. The Prandtl-Reuss constitutive relation has a form as

$$d\sigma_{ij} = \lambda(d\epsilon_{kk} - d\epsilon_{kk}{}^p)\delta_{ij} + 2\mu(d\epsilon_{ij} - d\epsilon_{ij}{}^p) = \lambda(d\epsilon_{kk}{}^e)\delta_{ij} + 2\mu d\epsilon_{ij}{}^e$$

where λ and μ are the Lamé constants. It is seen from this equation that the increments of plastic strain $d\epsilon_{ij}{}^p$ are not explicitly associated with any stress.

In case that the stress is linear in the elastic components of strain ($W^e = \sigma_{ij}\epsilon_{ij}{}^e/2$), we have

$$\int_{\Gamma+\Gamma_s-\Gamma_{end}} X_i T_j \frac{\partial u_j}{\partial X_i} d\Gamma = \int_{\Gamma+\Gamma_s-\Gamma_{end}} W^e X_i n_i d\Gamma + \iint_A \{(\rho\ddot{u}_i - F_i)u_{i,j}X_j + \sigma_{ij}\epsilon_{ij,l}{}^* X_l + \sigma_{ij}\epsilon_{ij}{}^*\} dA \quad (37)$$

From equations (37) and (23), we obtain a formula of $\hat{M}$:

$$\hat{M} = \int_{\Gamma+\Gamma_s}\left(W^e n_i - T_j \frac{\partial u_j}{\partial X_i} \right) X_i d\Gamma + \int_{\Gamma_{end}} \{\rho(k+e) - W^e\} X_i n_i d\Gamma + \iint_A \{(\rho\ddot{u}_i - F_i)u_{i,j}X_j + \sigma_{ij}\epsilon_{ij,l}{}^* X_l + \sigma_{ij}\epsilon_{ij}{}^*\} dA \quad (38)$$

It is noted that the $\hat{J}_\alpha$, $\hat{L}_3$, and $\hat{M}$ given in equations (34), (36), and (38) coincide with the J_α, L_3, and M integrals [3, 8] for voids or cracks without a fracture process region in elastic materials, where F_i, $\rho\ddot{u}_i$, $\epsilon_{ij}{}^*$, and the quantities q_i, γ, and $e_{i3l}\,T_i u_l$ on Γ_{end} are neglected.

References

1 Broberg, K. B., "Crack-Growth Criteria and Nonlinear Fracture Mechanics," *Journal of the Mechanics and Physics of Solids*, Vol. 19, 1971, pp. 407–418.

2 Knowles, J. K., and Sternberg, E., "On a Class of Conservation Laws in Linearized and Finite Elastostatics," *Archive for Rational Mechanics and Analysis*, Vol. 44, No. 3, 1972, pp. 187–211.

3 Budiansky, B., and Rice, J. R., "Conservation Laws and Energy-Release Rates," ASME JOURNAL OF APPLIED MECHANICS, Vol. 40, Mar. 1973, pp. 201–203.

4 Freund, L. B., "Energy Flux Into the Tip of an Extending Crack in an Elastic Solid," *Journal of Elasticity*, Vol. 2, No. 4, Dec. 1972, pp. 341–349.

5 Kishimoto, K., Aoki, S., and Sakata, M., "On the Path-Independent Integral-$\hat{J}$," *Engineering Fracture Mechanics*, Vol. 13, No. 4, 1980, pp. 841–850.

6 Kishimoto, K., Aoki, S., and Sakata, M., "Dynamic Stress-Intensity Factors Using $\hat{J}$-Integral and Finite Element Method," *Engineering Fracture Mechanics*, Vol. 13, No. 2, pp. 387–394.

7 Eshelby, J. D., "The Determination of the Elastic Field of an Ellipsoidal Inclusion, and Related Problems," *Proceedings of the Royal Society*, London, Series A, Vol. 241, 1957, pp. 376–396.

8 Eshelby, J. D., "The Calculation of Energy Release Rate," *Prospects of Fracture Mechanics*, eds., Sih, G. C., Van Elst, H. C., and Broek, D., Noordhoff, 1974, pp. 69–84.

APPENDIX

Path-Independence of $\hat{J}_\alpha$, $\hat{L}_3$, and $\hat{M}$ With Respect to $\Gamma + \Gamma_s$.

Consider two possible choices of $\Gamma + \Gamma_s$, say $(\Gamma + \Gamma_s)_1$, and $(\Gamma + \Gamma_s)_2$, as shown in Fig. 4 and let $\hat{J}_{\alpha(1)}$ and $\hat{J}_{\alpha(2)}$ denote the associated values of $\hat{J}_\alpha$-integral. The curve $(\Gamma + \Gamma_s)_1 - (\Gamma + \Gamma_s)_2$ forms a complete closed curve, say $(\Gamma + \Gamma_s)_*$. The region A_* is enclosed by $(\Gamma + \Gamma_s)_*$. It can be shown by the use of the Gauss theorem for material having any constitutive relation that

$$\begin{aligned}
\hat{J}_{\alpha(1)} - \hat{J}_{\alpha(2)} &= -\int_{(\Gamma+\Gamma_s)_1} T_i \frac{\partial u_i}{\partial X_\alpha} d\Gamma + \int_{\Gamma_{end}} \rho(k+e) n_\alpha d\Gamma + \iint_{A_1}\left\{ (\rho\ddot{u}_i - F_i)\frac{\partial u_i}{\partial X_\alpha} + \sigma_{ij}\frac{\partial \epsilon_{ij}}{\partial X_\alpha} \right\} dA \\
&\quad - \left[-\int_{(\Gamma+\Gamma_s)_2} T_i \frac{\partial u_i}{\partial X_\alpha} d\Gamma + \int_{\Gamma_{end}} \rho(k+e) n_\alpha d\Gamma + \iint_{A_2}\left\{ (\rho\ddot{u}_i - F_i)\frac{\partial u_i}{\partial X_\alpha} + \sigma_{ij}\frac{\partial \epsilon_{ij}}{\partial X_\alpha} \right\} dA \right] \\
&= -\int_{(\Gamma+\Gamma_s)_*} T_i \frac{\partial u_i}{\partial X_\alpha} d\Gamma + \iint_{A_*}\left\{ (\rho\ddot{u}_i - F_i)\frac{\partial u_i}{\partial X_\alpha} + \sigma_{ij}\frac{\partial \epsilon_{ij}}{\partial X_\alpha} \right\} dA \\
&= 0
\end{aligned}$$

Downloaded 01 May 2010 to 171.66.16.249. Redistribution subject to ASME license or copyright; see http://www.asme.org/terms/Terms_Use.cfm

where A_1 and A_2 denote the regions enclosed by $(\Gamma + \Gamma_s)_1$ and Γ_{end}, and by $(\Gamma + \Gamma_s)_2$ and Γ_{end}, respectively.

Similarly,

$$\hat{L}_{3(1)} - \hat{L}_{3(2)} = -\int_{(\Gamma+\Gamma_s)_\bullet} e_{i3l} X_l T_j \frac{\partial u_j}{\partial X_i} d\Gamma + \iint_{A_\bullet} e_{i3l} \left\{ \sigma_{jl} \frac{\partial u_j}{\partial X_i} + X_l(\rho \ddot{u}_j - F_j) \frac{\partial u_j}{\partial X_i} + X_l \sigma_{jk} \frac{\partial \epsilon_{jk}}{\partial X_i} \right\} dA = 0$$

and

$$\hat{M}_{(1)} - \hat{M}_{(2)} = -\int_{(\Gamma+\Gamma_s)_\bullet} X_i T_j \frac{\partial u_j}{\partial X_i} d\Gamma + \iint_{A_\bullet} \left\{ X_j(\rho \ddot{u}_i - F_i) \frac{\partial u_i}{\partial X_j} + X_l \sigma_{ij} \frac{\partial \epsilon_{ij}}{\partial X_l} + \sigma_{ij} \epsilon_{ij} \right\} dA = 0$$

Thus $\hat{J}_\alpha$, $\hat{L}_3$, and $\hat{M}$ are proved to be independent of the path $\Gamma + \Gamma_s$.

Downloaded 01 May 2010 to 171.66.16.249. Redistribution subject to ASME license or copyright; see http://www.asme.org/terms/Terms_Use.cfm

M. Y. He
Institute of Mechanics,
Chinese Academy of Sciences,
Beijing, China

J. W. Hutchinson
Division of Applied Sciences,
Harvard University,
Cambridge, Mass. 02138
Mem. ASME

The Penny-Shaped Crack and the Plane Strain Crack in an Infinite Body of Power-Law Material

A study is carried out of the problem of a penny-shaped crack in an infinite body of power-law material subject to general remote axisymmetric stressing conditions. The plane strain version of the problem is also examined. The material is incompressible and is characterized by small strain deformation theory with a pure power relation between stress and strain. The solutions presented also apply to power-law creeping materials and to a class of strain-rate sensitive hardening materials. Both numerical and analytical procedures are employed to obtain the main results. A perturbation solution obtained by expanding about the trivial state in which the stress is everywhere parallel to the crack leads to simple formulas which are highly accurate even when the remote stress is perpendicular to the crack.

1 Statement of Problems

Within the context of small strain theory we consider an incompressible, power-law solid characterized in simple tension by

$$\epsilon/\epsilon_0 = \alpha(\sigma/\sigma_0)^n \tag{1}$$

where ϵ_0 and σ_0 are a reference strain and stress and α is an extra constant introduced for convenience of application. For J_2 deformation theory, (1) generalizes to

$$\frac{\epsilon_{ij}}{\epsilon_0} = \frac{3}{2}\alpha\left(\frac{\sigma_e}{\sigma_0}\right)^{n-1}\frac{s_{ij}}{\sigma_0} \tag{2}$$

where s_{ij} is the stress deviator and σ_e is the effective stress defined by

$$\sigma_e = \left(\frac{3}{2}s_{ij}s_{ij}\right)^{1/2} \tag{3}$$

It is also convenient to define an effective strain

$$\epsilon_e = \left(\frac{2}{3}\epsilon_{ij}\epsilon_{ij}\right)^{1/2} \tag{4}$$

which coincides with the tensile strain in uniaxial tension so that σ_e and ϵ_e satisfy (1).

Two crack problems are analyzed below. The first is a penny-shaped crack of radius a subject to general remote axisymmetric stress conditions (see Fig. 1(a))

$$\sigma_{11}^{\infty} = \sigma_{33}^{\infty} = T, \quad \sigma_{22}^{\infty} = S \tag{5}$$

The second is the plane strain problem ($\epsilon_{33} = 0$) with a crack of half length a subject to inplane remote stresses (see Fig. 1(b))

$$\sigma_{11}^{\infty} = T, \quad \sigma_{22}^{\infty} = S \quad \left(\text{with } \sigma_{33}^{\infty} = \frac{1}{2}(S+T)\right) \tag{6}$$

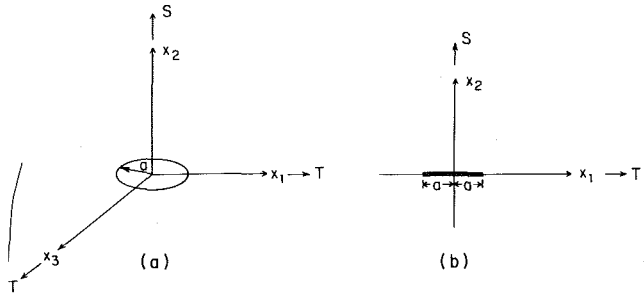


Fig. 1 Conventions: (*a*) penny-shaped crack, (*b*) plane strain crack

In both problems the crack is traction-free. A number of fully plastic crack problems of this type have been analyzed [1–4], and an estimation scheme has been proposed for using these solutions together with linear elastic solutions to interpolate from small to large-scale yielding behavior [4–6].

The solutions presented as follows also apply to power-law creeping materials under steady-state creep conditions. The following pre-

Contributed by the Applied Mechanics Division for publication in the JOURNAL OF APPLIED MECHANICS.

Discussion on this paper should be addressed to the Editorial Department, ASME, United Engineering Center, 345 East 47th Street, New York, N. Y. 10017, and will be accepted until two months after final publication of the paper itself in the JOURNAL OF APPLIED MECHANICS. Manuscript received by ASME Applied Mechanics Division, March, 1981.

Copyright © 1981 by ASME

Downloaded 01 May 2010 to 171.66.16.249. Redistribution subject to ASME license or copyright; see http://www.asme.org/terms/Terms_Use.cfm

sentation will use the time-independent formulation but conversion of the results to the steady creep interpretation is immediate. If S and T are increased (or decreased) monotonically in fixed proportion, the solution to the fully plastic crack problem has the property that the stress components also increase in fixed proportion at each point in the body. Consequently, the solutions are also exact solutions based on the J_2 flow (incremental) theory of plasticity fit to the same uniaxial relation (1), as discussed more fully in [1].

The fully plastic solutions can be used in addition to generate solutions to a class of strain-rate-dependent hardening solids [7, 8] which in simple tension satisfy

$$\sigma/\sigma_0 = \beta(\epsilon/\epsilon_0)^k(\dot{\epsilon}/\epsilon_0)^m \tag{7}$$

and for multiaxial states satisfy

$$\frac{s_{ij}}{\sigma_0} = \frac{2}{3}\beta\left(\frac{\epsilon_e}{\epsilon_0}\right)^{k-1}\left(\frac{\dot{\epsilon}_e}{\epsilon_0}\right)^m \frac{\epsilon_{ij}}{\epsilon_0} \tag{8}$$

where $(\dot{\ })$ here denotes the time rate of change. The solution to the fully plastic problem governed by (2) is of the form

$$u_i = \lambda\bar{u}_i, \quad \epsilon_{ij} = \lambda\bar{\epsilon}_{ij}, \quad \sigma_{ij} = \lambda^{1/n}\bar{\sigma}_{ij} \tag{9}$$

where λ is taken as a strain-based load parameter which is directly related to S and T. Spatial dependence is contained in the barred quantities. The corresponding solution to the strain-rate-dependent hardening problem governed by (8) in which the same load parameter varies with time according to $\lambda(t)$ is

$$u_i = \lambda\bar{u}_i, \quad \epsilon_{ij} = \lambda\bar{\epsilon}_{ij}, \quad \dot{\epsilon}_{ij} = \dot{\lambda}\bar{\epsilon}_{ij}, \quad \sigma_{ij} = \lambda^k\dot{\lambda}^m\bar{\sigma}_{ij} \tag{10}$$

where $k + m = 1/n$ and $\beta = (1/\alpha)^{1/n}$. The stressing is again proportional at each point in the body and, as long as λ varies such that σ_e does not decrease, the solution from (8) is as well a solution to the J_2 flow theory version of the constitutive law.

The family of power-law materials (2) includes an isotropic, incompressible linear elastic solid at one end of the range we will consider ($n = 1$) and a rigid-perfectly plastic solid with the yield condition $\sigma_e = \sigma_0$ at the other ($n = \infty$). The plane strain problem becomes hyperbolic with the possibility of discontinuous displacements across certain slip lines in the rigid-perfectly plastic limit. On the other hand, the axisymmetric problem for the penny-shaped crack is elliptic for all n including the limit $n = \infty$ so that discontinuities in strains and displacements are not possible. The differences in the characters of the two solutions for large n will be brought out in the following.

The outline of the paper is as follows. The theoretical background to the numerical solution is given in Section 2. The numerical method is described in Section 3 and results for the penny-shaped crack are then presented. A perturbation method is employed in Section 4 to generate solutions for remote stressing conditions departing only slightly from the trivial state in which $S = 0$ and $T \neq 0$. These relatively simple results are found to give highly accurate predictions even under remote tension conditions ($S > 0$, $T = 0$). The paper concludes with Section 5 in which numerical results for the plane strain problem are given.

2 Theoretical Background

Minimum Principle for Infinite Body. The displacement-based minimum principle for the infinite body given in [9] will be used. The principle is the standard minimum potential energy principle modified such that volume or area integrals remain bounded when applied to an infinite region. Let $\boldsymbol{\sigma}^\infty$, $\boldsymbol{\epsilon}^\infty$, and $\mathbf{u}^\infty$ denote the uniform fields associated with the uncracked body subject to prescribed S and T. Let an additional displacement field $\tilde{\mathbf{u}}$ be introduced such that the total displacement is

$$\mathbf{u} = \mathbf{u}^\infty + \tilde{\mathbf{u}} \tag{11}$$

where $u_{i,i} = u^\infty_{i,i} = \tilde{u}_{i,i} = 0$. With

$$\epsilon_{ij} = \frac{1}{2}(u_{i,j} + u_{j,i}) \quad \text{and} \quad \tilde{\epsilon}_{ij} = \frac{1}{2}(\tilde{u}_{i,j} + \tilde{u}_{j,i}) \tag{12}$$

the total strain is given by $\boldsymbol{\epsilon} = \boldsymbol{\epsilon}^\infty + \tilde{\boldsymbol{\epsilon}}$. It will be assumed that the additional displacement field decays faster than $r^{-1/2}$ as $r = (x_i x_i)^{1/2}$ becomes large. Then, among all admissible additional displacement fields satisfying this condition, the solution minimizes

$$\Phi(\tilde{\mathbf{u}}) = \int_V [W(\boldsymbol{\epsilon}) - W(\boldsymbol{\epsilon}^\infty) - \sigma^\infty_{ij}\tilde{\epsilon}_{ij}]dV - \int_S \sigma^\infty_{ij} n_j \tilde{u}_i dS \tag{13}$$

where V is the infinite region surrounding the crack, S is the crack surface, $\mathbf{n}$ is the unit normal to S pointing into V, and

$$W(\boldsymbol{\epsilon}) = \int_0^{\boldsymbol{\epsilon}} \sigma_{ij} d\epsilon_{ij} = \frac{n}{n+1}\alpha\sigma_0\epsilon_0\left(\frac{\epsilon_e}{\alpha\epsilon_0}\right)^{n+1/n} \tag{14}$$

Subject to the admissibility conditions on the decay of $\tilde{\mathbf{u}}$, the minimum principle holds in the limit $n = \infty$ with $\boldsymbol{\epsilon}^\infty \propto \mathbf{s}^\infty$ imposed and $\sigma^\infty_e = \sigma_0$. As will be discussed further, the condition on the decay of $\tilde{\mathbf{u}}$ is satisfied for the axisymmetric problem but not for the plane strain problem when $n = \infty$.

Relation Between Energy-Release Rate and $\Phi_{\min}$. Consider the penny-shaped crack centered in a solid sphere of material of radius R (which will subsequently be permitted to become unbounded) and let tractions $T^\infty_i \equiv \sigma^\infty_{ij} n_j$ be imposed on the outer surface S_R of the sphere. (For the plane strain problem the crack is taken to be centered in a cylinder of radius R, but otherwise the argument which follows applies to plane strain as well.) The potential energy of the cracked body V_R subject to $\mathbf{T}^\infty$ on S_R is

$$PE(a) = \int_{V_R} W(\boldsymbol{\epsilon})dV - \int_{S_R} T^\infty_i u_i \, dS \tag{15}$$

For an increase of radius of the crack from a to $a + da$ with $\mathbf{T}^\infty$ held fixed, the energy-release rate per unit length of crack edge is

$$J = -\frac{1}{2\pi a}\frac{dPE}{da} \tag{16}$$

Next, we show that $dPE/da = d\Phi_{\min}/da$ when $R \to \infty$. By the principle of virtual work

$$\int_{S_R} T^\infty_i \tilde{u}_i dS = \int_{V_R} \sigma^\infty_{ij}\tilde{\epsilon}_{ij}\, dV + \int_S \sigma^\infty_{ij} n_j \tilde{u}_i dS \tag{17}$$

where $\tilde{\mathbf{u}}$ is the additional displacement defined in (11) and on the surface of the crack, S, the unit normal $\mathbf{n}$ points into V_R. Use (17) to rewrite (15) as

$$PE(a) = \int_{V_R} [W(\boldsymbol{\epsilon}) - W(\boldsymbol{\epsilon}^\infty) - \sigma^\infty_{ij}\tilde{\epsilon}_{ij}]dV - \int_S \sigma^\infty_{ij} n_j \tilde{u}_i dS + C \tag{18}$$

where the terms comprising C depend only on the uniform state $\boldsymbol{\sigma}^\infty$ and are independent of a. Subject to the same decay conditions on $\tilde{\mathbf{u}}$ required for the minimum principle, $PE - C$ becomes $\Phi_{\min}$ as R becomes unbounded and therefore

$$dPE/da = d\Phi_{\min}/da \tag{19}$$

By dimensional considerations $\Phi_{\min}$ must have the functional form

$$\Phi_{\min} = \sigma_0\epsilon_0 a^3 f(n, S/T, S/\sigma_0) \tag{20}$$

and thus

$$d\Phi_{\min}/da = 3\sigma_0\epsilon_0 a^2 f = 3\Phi_{\min}/a \tag{21}$$

It follows then from (16), (19), and (21) that

$$J = -\frac{3}{2\pi a^2}\Phi_{\min} \tag{22}$$

For any admissible additional displacement field $\tilde{\mathbf{u}}$, $\Phi(\tilde{\mathbf{u}}) \geq \Phi_{\min}$ and thus an estimate of J using

$$J = -\frac{3}{2\pi a^2}\Phi(\tilde{\mathbf{u}}) \tag{23}$$

is necessarily a *lower bound.* Equation (23) will be used to obtain our numerical estimates of J.

Downloaded 01 May 2010 to 171.66.16.249. Redistribution subject to ASME license or copyright; see http://www.asme.org/terms/Terms_Use.cfm

For the plane strain crack (16), (20), and (22) are replaced by, respectively,

$$J = -\frac{1}{2}\frac{dPE}{da} \tag{24}$$

$$\Phi_{\min} = \sigma_0 \epsilon_0 a^2 f(n, S/T, S/\sigma_0) \tag{25}$$

$$J = -\Phi_{\min}/a \tag{26}$$

Analogous relations based on a modified complementary potential energy functional can also be formulated. For statically admissible stress fields, the complementary formulation generates upper bound estimates of J. This alternative approach has not been used here. In [3], both of the unmodified minimum principles have been used to produce numerical estimates of J for problems involving cracks in finite geometries. The numerical results in [3] do appear to provide the corresponding lower and upper bounds, even though it is unlikely that the strict bounding properties, which hold for the infinite body, apply to finite geometries.

Crack-Tip Fields and the Relation Between J and the M-Integral for the Penny-Shaped Crack. For the plane strain problem J as defined here is equal to the line integral definition of J [10]. The singular crack-tip fields are of the form

$$\sigma_{ij} = \sigma_0 \left(\frac{J}{\alpha \sigma_0 \epsilon_0 I_n r}\right)^{1/n+1} \tilde{\sigma}_{ij}(\theta, n), \quad \epsilon_{ij} = \alpha \epsilon_0 \left(\frac{J}{\alpha \sigma_0 \epsilon_0 I_n r}\right)^{n/n+1} \tilde{\epsilon}_{ij}(\theta, n) \tag{27}$$

where (r, θ) are planar polar coordinates centered at the crack tip and where details of the θ-variations and the normalizing constant I_n are given in [11, 12].

The plane strain singular fields (27) also hold at the edge of a penny-shaped crack, where r and θ are then local coordinates in a plane perpendicular to the edge of the crack. Because the circumferential strain is bounded at the crack edge, the singular field is necessarily a plane strain field with the same functional dependence on r and θ as in (27). The easiest way to see that J, which has been defined here as the energy-release rate in (16), is the amplitude of the singular fields in (27) is to invoke a surface-independent integral [13] called the M-integral in [14]. For the power-law material (2),

$$M = \int_S \left[W x_i n_i - \sigma_{ij} n_j u_{i,k} x_k - \left(\frac{2n-1}{n+1}\right) \sigma_{ij} n_j u_i \right] dS \tag{28}$$

where S is any closed surface which encloses the crack and $\mathbf{n}$ is the unit outward normal to S at each point. In [14] it is shown that M/a is the total energy-release rate with respect to a. Thus, for our definition of J in (16), it follows that

$$J = M/(2\pi a^2) \tag{29}$$

Now deform the surface S in (28) to a torus-like surface ringing the edge of the penny-shaped crack. (The integrand vanishes on the faces of the crack.) As the torus is shrunk down to the edge of the crack, only the singular terms in the integrand of (28) contribute to M, and it is readily seen that $M/(2\pi a^2)$ is just the line-integral definition of J for plane strain. This establishes that J as defined in (16) for the penny-shaped crack is indeed the amplitude of the singular crack-tip fields as it appears in (27).

3 Numerical Solution for Penny-Shaped Crack

A numerical procedure based on the approximate minimization of Φ in (13) as developed in [9, 15] will be employed. A stream function $\psi(x, y)$ is used to generate the additional axisymmetric displacements according to

$$\tilde{u}_x = x^{-1}\psi_{,y} \quad \text{and} \quad \tilde{u}_y = -x^{-1}\psi_{,x} \tag{30}$$

where x and y are radial and axial cylindrical coordinates (which coincide with x_1 and x_2, respectively, in the trace plane $x_3 = 0$) and $\tilde{u}_x$ and $\tilde{u}_y$ are the associated additional displacements.

To expedite numerical integration the region outside the crack in the trace plane $x_3 = 0$ is mapped onto the interior of the unit circle in the ζ-plane (see Fig. 2) using

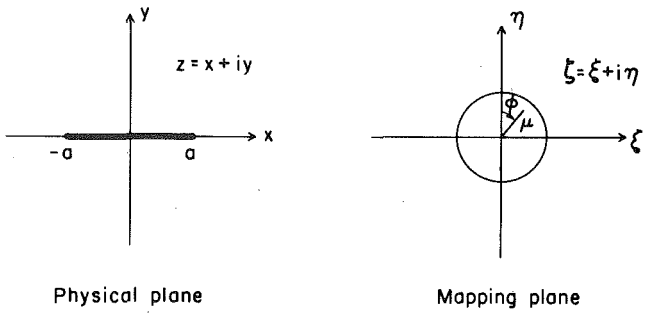


Fig. 2 Mapping of physical trace plane onto interior of the unit circle in the ζ-plane

$$z \equiv x + iy = \omega(\zeta) = \frac{a}{2}(\zeta + \zeta^{-1}) \quad (i = \sqrt{-1}) \tag{31}$$

With μ and ϕ as planar-polar coordinates in the mapping plane as shown in Fig. 2 and with ψ regarded as a function of these coordinates,

$$\tilde{u}_x = \frac{1}{x}\left(\psi_{,\mu}\frac{\partial \mu}{\partial y} + \psi_{,\phi}\frac{\partial \phi}{\partial y}\right), \quad \tilde{u}_y = -\frac{1}{x}\left(\psi_{,\mu}\frac{\partial \mu}{\partial x} + \psi_{,\phi}\frac{\partial \phi}{\partial x}\right) \tag{32}$$

where, with $\Omega = \zeta(d\omega/d\zeta)$,

$$\frac{\partial \mu}{\partial x} + i\frac{\partial \mu}{\partial y} = \mu\frac{\Omega}{|\Omega|^2}, \quad \frac{\partial \phi}{\partial y} - i\frac{\partial \phi}{\partial x} = -\frac{\Omega}{|\Omega|^2} \tag{33}$$

Expressions for the additional strain components from $\psi(\mu, \phi)$ are given in the Appendix.

An approximate representation of the stream function is taken as

$$\psi(\mu, \phi) = F(\mu, \phi)\left[A_0 + \sum_{k=1}^{N}\sum_{j=0}^{M} A_{kj}\mu^j \mu_k(\phi)\right] \tag{34}$$

where

$$F(\mu, \phi) = (1 - \mu^\beta \sin^2\phi)\cos\phi \tag{35}$$

The A's and β are treated as variables in the minimization of Φ. In terms of the polar mapping coordinates, $\mu = 1$ corresponds to the crack surface while $\mu \to 0$ corresponds to $x^2 + y^2 \to \infty$. The range of ϕ is from 0 to π with ψ being symmetric in ϕ about $\phi = \pi/2$. The choice of F in (34) and (35) insures a uniform representation leading to admissible behavior at the poles and a smooth opening of the crack, as will be discussed later. The terms in the square brackets in (34) are derived from a complete double series which has been truncated consistent with admissibility conditions. These require that u_k is symmetric about $\phi = \pi/2$ and that $u_k(0) = u_k'(0) = 0$. The set of orthogonal eigenfunctions used for the ϕ-variation in (34) is

$$u_k(\phi) = \cos\lambda_k\left(\phi - \frac{\pi}{2}\right) + b_k \cosh\lambda_k\left(\phi - \frac{\pi}{2}\right) \tag{36}$$

where the λ_k satisfy

$$\cos\left(\frac{\lambda_k\pi}{2}\right)\sinh\left(\frac{\lambda_k\pi}{2}\right) + \sin\left(\frac{\lambda_k\pi}{2}\right)\cosh\left(\frac{\lambda_k\pi}{2}\right) = 0 \tag{37}$$

and

$$b_k = \sin\left(\frac{\lambda_k\pi}{2}\right)/\sinh\left(\frac{\lambda_k\pi}{2}\right) \tag{38}$$

The first four λ_k and b_k are

$$\begin{aligned} \lambda_1 &= 1.5056187 & b_1 &= 0.1328565 \\ \lambda_2 &= 3.5000107 & b_2 &= -5.792274 \times 10^{-3} \\ \lambda_3 &= 5.5000000 & b_3 &= 2.503110 \times 10^{-4} \\ \lambda_4 &= 7.5000000 & b_4 &= -1.08169 \times 10^{-5} \end{aligned} \tag{39}$$

With $\psi = A_0 F(\mu, \phi)$, the crack opening displacement $\delta(x) = u_y(x, 0^+) - u_y(x, 0^-)$ is

Downloaded 01 May 2010 to 171.66.16.249. Redistribution subject to ASME license or copyright; see http://www.asme.org/terms/Terms_Use.cfm

Table 1 h_1, h_2, and h_3 for penny-shaped crack

$h_1(n, S/T)$

S/σ_e^∞	S/T	n = 1	n = 1.5	n = 2	n = 3	n = 5	n = 10	n = ∞
1	∞	0.9549	1.094	1.194	1.331	1.484	1.639	1.841
2	2.0	3.819	4.372	4.758	5.248	5.734	6.141	6.669
3	1.50	8.594	10.05	11.12	12.55	14.12	15.75	18.24
4	1.33	15.28	18.59	21.23	25.30	31.03	39.13	55.65
5	1.25	23.87	30.45	36.35	47.09	65.42		
0.5	-1.0	0.2387	0.2736	0.2978	0.3297	0.3641	0.3983	0.4448
0.2	-0.25	0.03819	0.04386	0.04774	0.05279	0.05815	0.06338	0.07030
0.1	-0.111	0.009549	0.01097	0.01195	0.01320	0.01453	0.01581	0.01748

$h_2(n, S/T)$

S/σ_e^∞	S/T	n = 1	n = 1.5	n = 2	n = 3	n = 5	n = 10	n = ∞
1	∞	4.000	4.575	4.992	5.554	6.159	6.709	7.270
2	2.0	8.000	9.232	10.08	11.17	12.41	12.83	14.90
3	1.5	12.00	14.74	16.92	19.99	23.78	28.83	38.96
4	1.33	16.00	21.19	25.94	34.83	50.29	75.96	130.6
5	1.25	20.00	28.64	37.87	57.77	97.52		
0.5	-1.0	2.000	2.289	2.492	2.761	3.053	3.347	3.749
0.2	-0.25	0.8000	0.9179	0.9992	1.105	1.219	1.330	1.480
0.1	-0.111	0.4000	0.4594	0.5002	0.5529	0.6087	0.6631	0.7342

$$\delta(x) = \frac{6}{a^3} A_0 \sqrt{a^2 - x^2} \tag{40}$$

Contributions from the other terms in (34) result in an opening displacement of the form $f(x)\sqrt{a^2 - x^2}$ where f is bounded at $x = a$. Thus (34) only contains the correct behavior for δ as $x \to a$ for the case $n = 1$. For $n > 1$, (34) can only approximate the correct behavior (i.e., $\delta \propto (a - x)^{1/n+1}$). In the neighborhood of the crack edge ($\mu = 1, \phi \approx \pi/2$)

$$\tilde{u}_x \cong -\frac{\beta}{3\left(\frac{\pi}{2} - \phi\right)} u_y \cong -\frac{\beta}{4}\left[A_0 + \sum_{k=1}^{N}\sum_{j=0}^{M} A_{kj}(1 + b_k)\right] \tag{41}$$

By allowing β to be a free variable in the minimization process, we remove the constraint between $\tilde{u}_x$ and u_y implied by (41) when β is fixed. (For $n = 1$, β turns out to be essentially zero and is always less in magnitude than 0.3.)

The surface integral contribution to Φ in (13) when evaluated using the representation (34) is just

$$-\int_S \sigma_{ij}^\infty n_j \tilde{u}_i \, dS = 4\pi \, \sigma_{22}^\infty A_0 \tag{42}$$

In terms of the coordinate variables μ and ϕ, the volume integral in (13) becomes an iterated double integral with the ranges $0 \le \mu \le 1$ and $0 \le \phi \le \pi/2$. For given numerical values of β and the A's, this integral is evaluated using an iterated application of a 10-point Gaussian integration formula. Minimization of Φ with respect to a given set of the free variables, β and the A's, is achieved using a numerically implemented Newton-Raphson method, which is described in more detail in [9]. For given numerical values of the free variables the volume integral in (13) is accurate to at least four significant figures. Thus the lower bound character of our estimates of J is preserved to this level of accuracy.

The functional form of the solution is

$$\begin{aligned} \frac{J}{\sigma_e^\infty \epsilon_e^\infty a} &= h_1\left(n, \frac{S}{T}\right) \\ \frac{\Delta V}{\epsilon_e^\infty a^3} &= h_2\left(n, \frac{S}{T}\right) \\ \frac{\delta}{\epsilon_e^\infty a} &= h_3\left(n, \frac{S}{T}\right) \end{aligned} \tag{43}$$

where ΔV is the volume of the opened crack and $\delta = u_y(0,0^+) - u_y(0,0^-)$ is opening of the crack at its center. For the axisymmetric problem

$$\sigma_e^\infty = |S - T| \tag{44}$$

and ϵ_e^∞ is related to σ_e^∞ by (1). Numerical results for h_1, h_2, and h_3 for various S/T and n are given in Table 1.

An indication of the convergence of the lower bound estimates of h_1 as dependent on the number of free parameters in (34) can be seen in Table 2 for the case of remote uniaxial tension ($S > 0$, $T = 0$). For the linear problem ($n = 1$) only 5 free parameters are required to give h_1 exactly to four significant figures. For the rigid-perfectly plastic problem ($n = \infty$) the convergence is slower with a 5 percent difference between the calculation with ($N = 2, M = 3$) and that with ($N = 3, M = 3$). The results in Table 1 for the case of remote uniaxial tension were determined with ($N = 3, M = 3$) for a total of 11 free parameters. The other results were obtained with ($N = 2, M = 3$) for a total of 8 free parameters.

Plots of the normalized J and ΔV as functions of the ratio S/σ_e^∞ are given in Figs. 3 and 4. With $\sigma_m^\infty = (S + 2T)/3$ as the remote mean stress, remote triaxiality is measured by

$$\frac{\sigma_m^\infty}{\sigma_e^\infty} = \frac{S}{\sigma_e^\infty} - \frac{2}{3}$$

for $S - T > 0$. The very strong dependence of ΔV on triaxiality for

Downloaded 01 May 2010 to 171.66.16.249. Redistribution subject to ASME license or copyright; see http://www.asme.org/terms/Terms_Use.cfm

Table 1 (Continued)

$h_3(n, S/T)$

S/σ_e^∞	S/T	n = 1.0	n = 1.5	n = 2.0	n = 3.0	n = 5.0	n = 10	n = ∞
1	∞	1.909	2.093	2.218	2.375	2.525	2.637	2.690
2	2.0	3.818	4.069	4.226	4.415	4.671	4.753	5.358
3	1.5	5.727	6.496	7.059	7.760	8.595	9.812	12.30
4	1.333	7.637	9.395	10.92	13.85	19.16	28.27	47.75
5	1.250	9.546	12.79	16.23	23.92	40.07		
0.5	-1.0	0.9546	1.091	1.183	1.320	1.426	1.545	1.698
0.2	-0.25	0.3824	0.4428	0.4852	0.5405	0.5996	0.6570	0.7329
0.1	-0.111	1.910	0.2224	0.2445	0.2734	0.3045	0.3348	0.3746

Table 2 h_1 for different numbers of free parameters ($S > 0$, $T = 0$)

	N = 1, M = 3	N = 2, M = 2	N = 2, M = 3	N = 3, M = 3
n = 1.0	0.9549	0.9549	0.9549	0.9549
n = 1.5	1.089	1.090	1.092	1.094
n = 5	1.423	1.432	1.453	1.484
n = ∞	1.680	1.716	1.756	1.841

$\sigma_m^\infty/\sigma_e^\infty$ above unity when n is 3 or greater is similar to the dependence of the dilatation of a spherical void on triaxiality [9, 16].

The profile of the opened crack is shown in Fig. 5 for several n-values for the case of remote uniaxial tension ($S > 0$, $T = 0$; or $S/\sigma_e^\infty = 1$). Contours on which the effective strain is a constant are shown in Fig. 6 for $n = 5$ and in Fig. 7 for $n = \infty$, both for the case of remote uniaxial tension and both with $\epsilon_e^\infty = 1$.

4 Perturbation Solution

Penny-Shaped Crack. The uniform state $\sigma_{22} = 0$, $\sigma_{11} = \sigma_{33} = T$ is a trivial solution to the penny-shaped crack problem. In this section we develop an exact perturbation solution about this state. For the linear problem ($n = 1$) nothing new will be learned from this solution. However, for the nonlinear problems ($n \neq 1$) we will obtain relatively simple results which not only hold for remote stressing conditions slightly perturbed from the trivial state but also for remote uniaxial tension with a fairly high degree of accuracy.

In the uniform trivial state ($S = 0$, $T < 0$) the crack remains closed, J is zero and the nonzero strain components from (2) are

$$\epsilon_{22} = -2\epsilon_{11} = -2\epsilon_{33} = \epsilon_e = \alpha\epsilon_0(|T|/\sigma_0)^n \tag{45}$$

Onto this trivial state we superimpose an increment of remote tensile stress $\dot{\sigma}^\infty$ parallel to the x_2-axis and perpendicular to the traction-free crack so that

$$\sigma_{22}^\infty \equiv S = \dot{\sigma}^\infty \quad \text{and} \quad \sigma_{11}^\infty = \sigma_{33}^\infty \equiv T \tag{46}$$

From (2), the increments in deviatoric stress and strain throughout the body satisfy

$$\dot{s}_{ij} = L_{ijkl}\dot{\epsilon}_{kl} \quad (\dot{\epsilon}_{kk} = 0) \tag{47}$$

where the incremental moduli are

$$L_{ijkl} = 2\mu\left\{\frac{1}{2}(\delta_{ik}\delta_{jl} + \delta_{il}\delta_{jk}) - \frac{1}{3}\delta_{ij}\delta_{kl} + \frac{2}{3}\frac{(1-n)}{n}\epsilon_{ij}\epsilon_{kl}\epsilon_e^{-2}\right\} \tag{48}$$

with

$$\mu = \frac{1}{3}\frac{\sigma_e}{\epsilon_e} \tag{49}$$

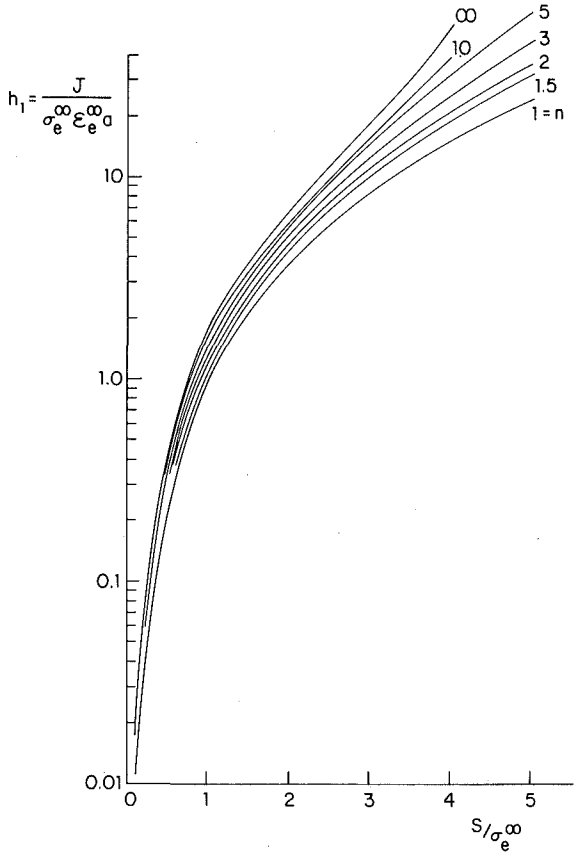


Fig. 3 Normalized J for penny-shaped crack

The incremental problem is a standard linear elastic crack problem for an incompressible material with uniform moduli (48) which are transversely isotropic with respect to the x_2-axis. The solution to this problem has been given in the literature but we have had some difficulty in gleaning the information desired here from published studies. In what follows, we sketch out the details for obtaining J, ΔV, and δ for the present incremental problem following for the most part a solution procedure used in [17] for the more general problem of an elliptical crack in a linear anisotropic solid. In this section it is important not to lose sight of the fact that it is the *linear incremental problem* which is being analyzed. When $S \neq 0$ it is always possible to find a zone sufficiently near the tip where the perturbation breaks down regardless of how small S is. Nevertheless, the perturbation solution does provide a rigorous expansion of J and ΔV for small S.

Downloaded 01 May 2010 to 171.66.16.249. Redistribution subject to ASME license or copyright; see http://www.asme.org/terms/Terms_Use.cfm

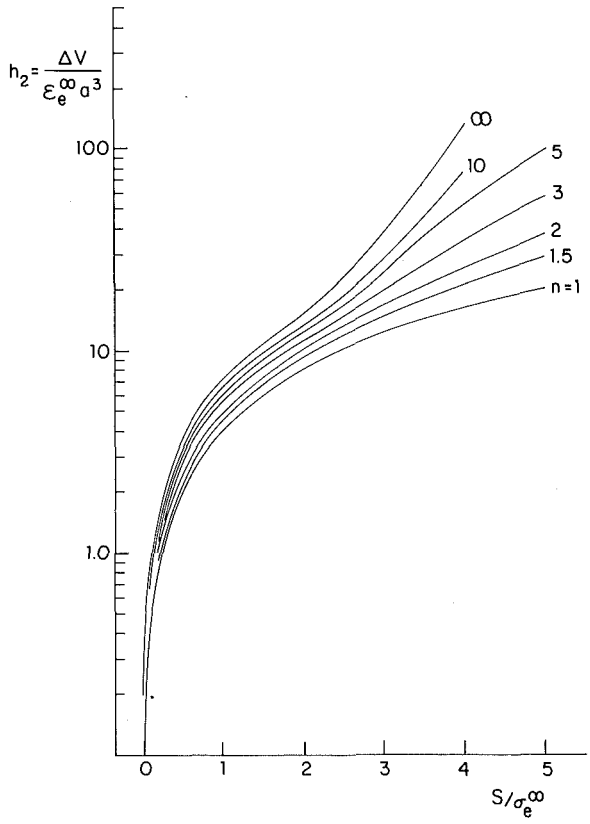


Fig. 4 Normalized volume of opened penny-shaped crack

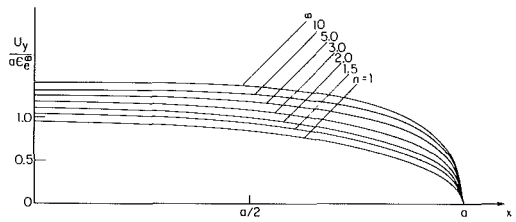


Fig. 5 Crack opening displacements for penny-shaped crack subject to remote uniaxial tension

In addition, the expansion of the crack opening displacement at any fixed point away from the tip is asymptotically correct as S approaches zero.

From the fundamental work on the general ellipsoidal inclusion problems [18] it is known that an elliptical crack in a homogeneous linear elastic solid opens into an ellipsoid. In the present incremental problem for the penny-shaped crack, both the moduli and the loading preserve axial symmetry about the x_2-axis and thus the opening of the crack is necessarily given by

$$\delta(R) = c(\dot{\sigma}^\infty/\mu)\,(a^2 - R^2)^{1/2} \tag{50}$$

where R is the distance from the center of the crack in its plane and c is an unknown dimensionless factor which, by dimensional analysis, depends only on n. The volume of the opened crack is

$$\Delta V = 2\pi \int_0^a \delta(R) R dR = \frac{2\pi}{3} c(\dot{\sigma}^\infty/\mu) a^3 \tag{51}$$

Next, consider the total energy released by creating a crack of radius a in a linear solid subject to a remote stress $\dot{\sigma}^\infty$ for which the opening displacement is (50); it is

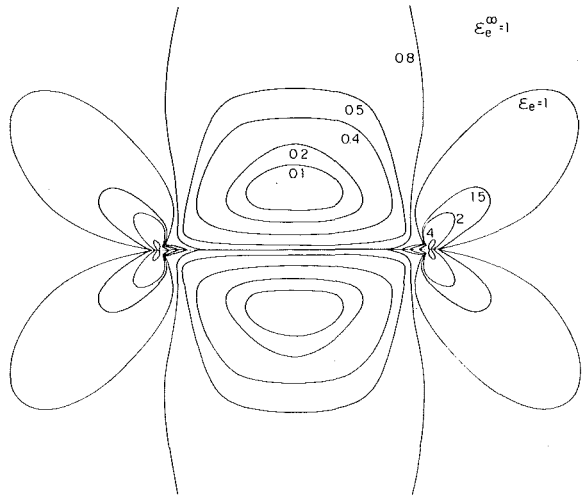


Fig. 6 Contours of constant effective strain ϵ_e for penny-shaped crack subject to remote uniaxial tension with $\epsilon_e^\infty = 1$ for $n = 5$

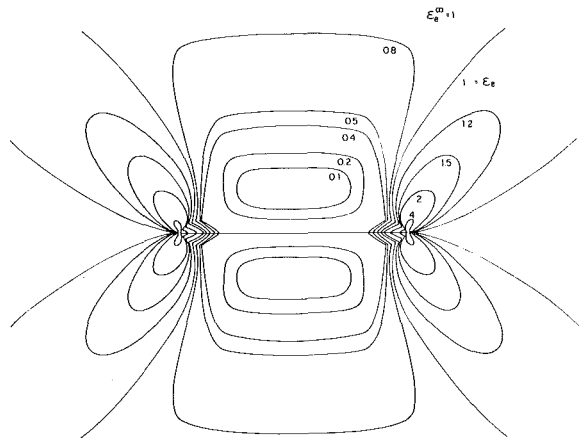


Fig. 7 Contours of constant effective strain ϵ_e for penny-shaped crack subject to remote uniaxial tension with $\epsilon_e^\infty = 1$ for $n = \infty$

$$E = \frac{1}{2} 2\pi \int_0^a \delta(R)\dot{\sigma}^\infty R dR = \frac{1}{2}\dot{\sigma}^\infty \Delta V \tag{52}$$

With J as the energy-release rate per unit length of crack edge, as defined earlier, it follows from (51) and (52) that

$$J = \frac{1}{2\pi a}\frac{dE}{da} = \frac{c}{2\mu}(\dot{\sigma}^\infty)^2 a \tag{53}$$

Another independent expression for J can be obtained by calculating the work done by the singular stresses at the crack edge through the crack opening for an incremental advance of the crack with $\dot{\sigma}^\infty$ held constant, i.e.,

$$J = \lim_{\Delta a \to 0} \frac{1}{2\Delta a} \int_0^{\Delta a} \dot{\sigma}_{22}(\xi, a)\delta(\xi, a + \Delta a) d\xi \tag{54}$$

where $\xi = R - a$. Here $\dot{\sigma}_{22}(\xi,a)$ denotes the stress acting at $R = a + \xi$ on the plane of the crack $x_2 = 0$ when the crack has radius a, and $\delta(\xi, a + \Delta a)$ is the crack opening at the same point associated with a crack of radius $a + \Delta a$. The singularity of $\dot{\sigma}_{22}$ at the crack edge necessarily has the form

$$\dot{\sigma}_{22} = \frac{k\dot{\sigma}^\infty \sqrt{a}}{\sqrt{2\pi\xi}} \tag{55}$$

for the incremental problem where k can only depend on n. Performing the calculation in (54) using (50) and (55), we find

Downloaded 01 May 2010 to 171.66.16.249. Redistribution subject to ASME license or copyright; see http://www.asme.org/terms/Terms_Use.cfm

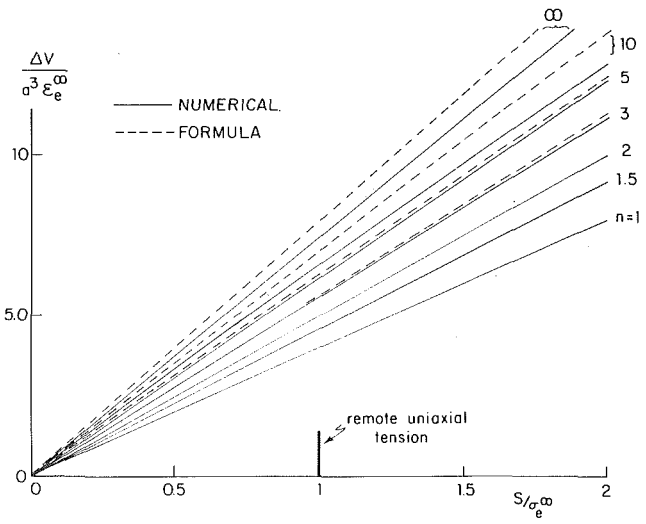


Fig. 8 Comparison between analytical results (64) and numerical results for penny-shaped crack

$$J = \frac{\sqrt{\pi}}{4}\frac{ck}{\mu}(\dot{\sigma}^{\infty})^2 a \tag{56}$$

By comparing (56) with (53) we see immediately that $k = 2/\sqrt{\pi}$, giving the classical result for a penny-shaped crack in an isotropic material. Thus the stress singularity on the plane of the crack is independent of n, i.e., independent of the degree of transverse anisotropy for this class of incremental, incompressible problems.

It remains to determine c. This is achieved by carrying out a local singularity analysis at the edge of the crack and then reconciling the result with (50) and (55). The singularity field at the edge of the penny-shaped crack is a plane strain field. Let ξ and η be local Cartesian coordinates in the plane $x_3 = 0$ with origin at the crack edge and parallel to the x_1 and x_2 axes, respectively. For the singularity field in the local coordinates, $\dot{\epsilon}_{33} = 0$ and $\dot{\epsilon}_{11} + \dot{\epsilon}_{22} = 0$. The latter constraint implies the existence of a stream function $\psi(\xi,\eta)$ such that $\dot{u}_1 = \psi_{,\eta}$ and $\dot{u}_2 = -\psi_{,\xi}$. Incremental equilibrium requires

$$\psi_{,\xi\xi\xi\xi} + \left(\frac{3}{n} - 1\right)\psi_{,\xi\xi\eta\eta} + \psi_{,\eta\eta\eta\eta} = 0 \tag{57}$$

where (48) has been used to express the stresses in terms of ψ in the equilibrium equations. Traction-free conditions on the crack flanks require

$$\left.\begin{aligned}\psi_{,\xi\xi} - \psi_{,\eta\eta} &= 0\\ 3\psi_{,\xi\xi\eta} + n\psi_{,\eta\eta\eta} &= 0\end{aligned}\right\}\ (\xi < 0, \eta = \pm 0) \tag{58}$$

Only the pertinent details of the singularity field solution of (57) and (58) will be given here. These are

$$\dot{\sigma}_{22} = A\xi^{-1/2} \quad (\xi > 0, \eta = 0) \tag{59}$$

and

$$\delta = \dot{u}_2(\xi, 0^+) - \dot{u}_2(\xi, 0^-) = \frac{4}{\mu}\left(1 + \frac{3}{n}\right)^{-1/2} A(-\xi)^{1/2} \quad (\xi < 0) \tag{60}$$

where A is an amplitude factor which is undetermined by the singularity analysis. Equations (59) and (55) (with $k = 2/\sqrt{\pi}$) imply

$$A = \dot{\sigma}^{\infty}(2a)^{1/2}/\pi \tag{61}$$

Near the edge of the crack (50) becomes $\delta = c(\dot{\sigma}^{\infty}/\mu)(-2a\xi)^{1/2}$; thus from (60) and (61) we find

$$c = \frac{4}{\pi}\left(1 + \frac{3}{n}\right)^{-1/2} \tag{62}$$

To further reduce the expressions for ΔV in (51) and J in (53) note that by (46) and (49)

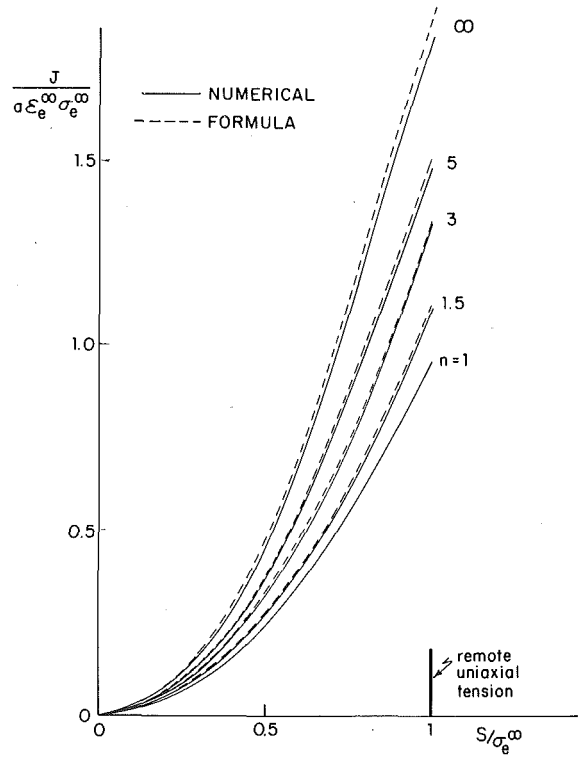


Fig. 9 Comparison between analytical results (65) and numerical results for penny-shaped crack

$$\frac{\dot{\sigma}^{\infty}}{\mu} = 3\epsilon_e^{\infty}\frac{\dot{\sigma}^{\infty}}{\sigma_e^{\infty}} = 3\epsilon_e^{\infty}\frac{S}{\sigma_e^{\infty}} \tag{63}$$

Equations (51) and (53) can therefore be written as

$$\frac{\Delta V}{\epsilon_e^{\infty} a^3} = 8\left(1 + \frac{3}{n}\right)^{-1/2}\frac{S}{\sigma_e^{\infty}} \tag{64}$$

and

$$\frac{J}{\sigma_e^{\infty}\epsilon_e^{\infty} a} = \frac{6}{\pi}\left(1 + \frac{3}{n}\right)^{-1/2}\left(\frac{S}{\sigma_e^{\infty}}\right)^2 \tag{65}$$

In applying these formulas we will take σ_e^{∞} as $|S - T|$ rather than $|T|$ since the difference in doing so involves terms of order $(\dot{\sigma}^{\infty})^3$ which have already been neglected. With $\sigma_e^{\infty} = |S - T|$ and ϵ_e^{∞} obtained from σ_e^{∞} by (1), (64) and (65) are exact for all S and T when $n = 1$. For $n \neq 1$, the error in (64) is of order $(S/\sigma_e^{\infty})^3$ since $\Delta V/\epsilon_e^{\infty}$ is odd in S/σ_e^{∞}; and, similarly, the error in J given by (65) is of order $(S/\sigma_e^{\infty})^4$.

The prediction of (64) is compared with the numerical results for h_2 from Table 1 in Fig. 8 for S/σ_e^{∞} ranging from 0 to 2. A comparison of (65) with the numerical results for h_1 is shown in Fig. 9. For remote uniaxial tension (64) and (65) become

$$\frac{\Delta V}{\epsilon_e^{\infty} a^3} = 8\left(1 + \frac{3}{n}\right)^{-1/2} \tag{66}$$

and

$$\frac{J}{\sigma_e^{\infty}\epsilon_e^{\infty} a} = \frac{6}{\pi}\left(1 + \frac{3}{n}\right)^{-1/2} \tag{67}$$

and these are compared with the most accurate set of numerical results (with $N = 3$ and $M = 3$) in Fig. 10. Equation (67) exceeds the numerical results by less than 5 percent, with the greatest difference occurring for the rigid-perfectly plastic limit. Furthermore, it is conceivable that (67) is even more accurate than Fig. 10 suggests since the numerical results give a lower bound curve.

Plane Strain Crack. The perturbation solution of the plane strain problem proceeds along similar lines so only the main results will be given. There is, however, an important mathematical difference

Downloaded 01 May 2010 to 171.66.16.249. Redistribution subject to ASME license or copyright; see http://www.asme.org/terms/Terms_Use.cfm

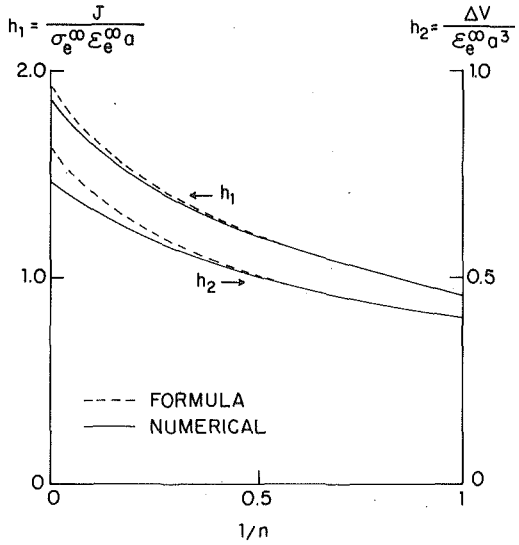


Fig. 10 Comparison of analytical results (66) and (67) with numerical results for penny-shaped crack under remote uniaxial tension ($S > 0$, $T = 0$)

between the two problems which is brought out very nicely by the perturbation solutions and this will be discussed.

The trivial state is now $\sigma_{11} = T < 0$, $\sigma_{22} = 0$, and $\sigma_{33} = T/2$ with $\sigma_e = \sqrt{3}|T|/2$ and

$$\epsilon_{22} = -\epsilon_{11} = \sqrt{3}\epsilon_e/2, \quad \epsilon_{33} = 0 \tag{68}$$

where ϵ_e is given in terms of σ_e by (1). An increment of remote plane strain tension $\sigma_{22} \equiv S = \dot{\sigma}^\infty$ is superimposed onto the trivial state. The results for this incremental problem are listed in the order developed for the penny-shaped crack in the following.

Equations (50), (51), and (53) are replaced by

$$\delta(x_1) = c(\dot{\sigma}^\infty/\mu)(a^2 - x_1^2)^{1/2} \tag{69}$$

$$\Delta A = \frac{\pi}{2} c(\dot{\sigma}^\infty/\mu)a^2 \tag{70}$$

$$J = \frac{\pi c}{4\mu}(\dot{\sigma}^\infty)^2 a \tag{71}$$

where ΔA is the area of the opened crack and μ is again given by (49). Equations (55) and (56) still hold in plane strain; and, by comparing (71) and (56), we see that $k = \sqrt{\pi}$ for all n.

In terms of the stream function $\psi(x_1, x_2)$ with $\dot{u}_1 = \psi_{,2}$ and $\dot{u}_2 = -\psi_{,1}$, equation (57) is replaced by

$$\psi_{,1111} + \left(\frac{4}{n} - 2\right)\psi_{,1122} + \psi_{,2222} = 0 \tag{72}$$

with boundary conditions

$$\left.\begin{aligned} \psi_{,11} - \psi_{,22} &= 0 \\ (4-n)\psi_{,112} + n\psi_{,222} &= 0 \end{aligned}\right\} (|x_1| < a, x_2 = \pm 0) \tag{73}$$

With $\xi = x_1 - a$, the singularity analysis gives

$$\dot{\sigma}_{22} = A\xi^{-1/2} \quad (\xi > 0, x_2 = 0) \tag{74}$$

and

$$\delta = \frac{2}{\mu}\sqrt{n}\, A(-\xi)^{1/2} \quad (\xi < 0) \tag{75}$$

Comparing (74) and (75) with (38) and (69), we find

$$c = \sqrt{n} \tag{76}$$

By (63), (70), and (71) become

$$\frac{\Delta A}{\epsilon_e^\infty a^2} = \frac{3\pi\sqrt{n}}{2}\frac{S}{\sigma_e^\infty} \tag{77}$$

and

$$\frac{J}{\sigma_e^\infty \epsilon_e^\infty a} = \frac{3\pi\sqrt{n}}{4}\left(\frac{S}{\sigma_e^\infty}\right)^2 \tag{78}$$

These formulas are again exact for all S and T when $n = 1$ if σ_e^∞ is taken as $\sqrt{3}|S - T|/2$ and ϵ_e^∞ is obtained from (1).

The solutions to the axisymmetric incremental problem are well behaved as $n \to \infty$. The governing equations (e.g., (57)) remain elliptic in this limit. In contrast, the normalized results for ΔA and J in plane strain, (77) and (78), are unbounded as $n \to \infty$ and this is associated with the loss of ellipticity of (72) in this limit. These behaviors mirror the corresponding behaviors in the rigid-perfectly plastic limit of the fully nonlinear problems. That is, the axisymmetric problem for $n \to \infty$ remains elliptic and well behaved, while the plane strain problem becomes hyperbolic admitting the possibility of discontinuous displacements and/or displacement gradients.

5 Numerical Solution for Plane Strain Crack

The numerical solution for the plane strain problem parallels that given in Section 3 for the penny-shaped crack. In fact, it is simpler to choose a representation for the stream function in the plane problem. On the other hand, the plane strain problem is ill-behaved as $n \to \infty$, as already discussed, and this makes it more difficult to generate accurate results for large n. In the axisymmetric problem it was possible to carry out calculations using the minimum principle with $n = \infty$. The plane strain solution does not obey the admissibility conditions associated with the minimum principle when $n = \infty$.

The geometry of the problem is shown in Fig. 1(*b*) and the mapping function (31) is again employed to map the slit plane onto the interior of the unit circle in the ζ-plane as in Fig. 2. Incompressibility implies the existence of a stream function ψ such that the additional displacements are given by

$$\tilde{u}_1 = \psi_{,2} \quad \text{and} \quad \tilde{u}_2 = -\psi_{,1} \tag{79}$$

In terms of the coordinates μ and ϕ in the mapping plane (see Fig. 2), ψ is taken as

$$\psi(\mu, \phi) = \sum_{k=1}^{N}\sum_{j=1}^{M} A_{kj}[\mu^{j-1}\sin 2k\phi - (-1)^k 2k(\phi - \pi/2)] \tag{80}$$

where the A's are free parameters chosen to minimize Φ. This choice meets the required symmetry of the solution with respect to the two Cartesian coordinate axes. The crack opening from (80) is of the form $f(x)\sqrt{a^2 - x_1^2}$ where $f(a)$ is bounded, and therefore (80) can only approximate the solution when $n \neq 1$.

The second term in (13) is

$$-\int_S \sigma_{ij}^\infty n_j \tilde{u}_i dS = 4\pi S \sum_{k=1}^{N}\sum_{j=1}^{M} k(-1)^k A_{kj} \tag{81}$$

The effective strain is computed using

$$\epsilon_e^2 = \frac{2}{3}\epsilon_{ij}\epsilon_{ij} = \frac{4}{3}[(\psi_{,12} - \epsilon_{11}^\infty)^2 + \frac{1}{4}(\psi_{,11} - \psi_{,22})^2] \tag{82}$$

and otherwise the numerical procedure is similar to that described

Table 3 h_1, h_2, and h_3 for plane strain crack

	S/σ_e^∞	S/T	n = 1	n = 1.5	n = 2.0	n = 3.0	n = 5.0
$h_1 = \frac{J}{a\sigma_e^\infty \epsilon_e^\infty}$	$2/\sqrt{3}$	∞	3.142	3.851	4.448	5.422	6.754
	$1/\sqrt{3}$	-1.0	0.7853	0.9591	1.100	1.333	1.639
	$4/\sqrt{3}$	2.0	12.57	15.44	17.73	22.12	27.16
$h_2 = \frac{\Delta A}{a\epsilon_e^\infty}$	$2/\sqrt{3}$	∞	5.441	6.686	7.757	9.523	11.86
	$1/\sqrt{3}$	-1.0	2.721	3.325	3.819	4.657	5.521
	$4/\sqrt{3}$	2.0	10.88	13.62	15.81	19.68	24.56
$h_3 = \frac{\delta}{a\epsilon_e^\infty}$	$2/\sqrt{3}$	∞	3.463	4.116	4.650	5.491	6.610
	$1/\sqrt{3}$	-1.0	1.732	2.095	2.391	2.854	3.340
	$4/\sqrt{3}$	2.0	6.926	8.124	9.002	10.63	12.87

Downloaded 01 May 2010 to 171.66.16.249. Redistribution subject to ASME license or copyright; see http://www.asme.org/terms/Terms_Use.cfm

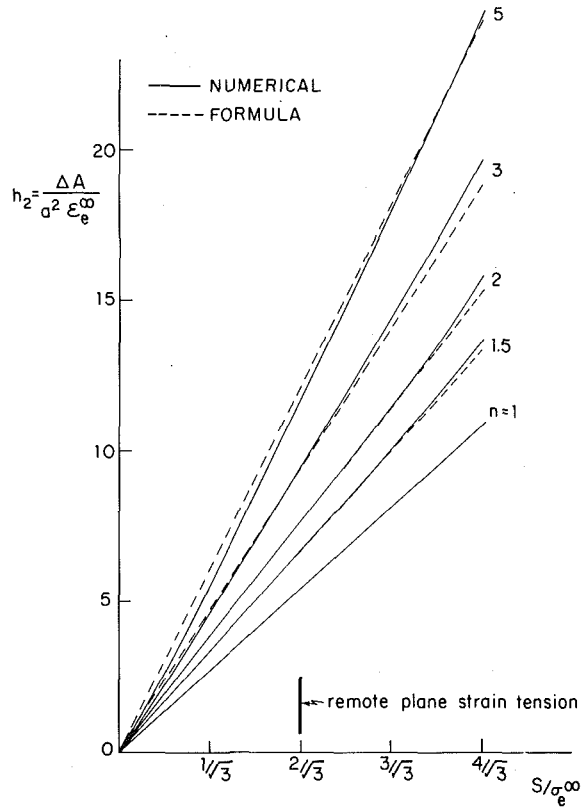


Fig. 11 Normalized crack opening area for plane strain crack; dashed line curves from (77)

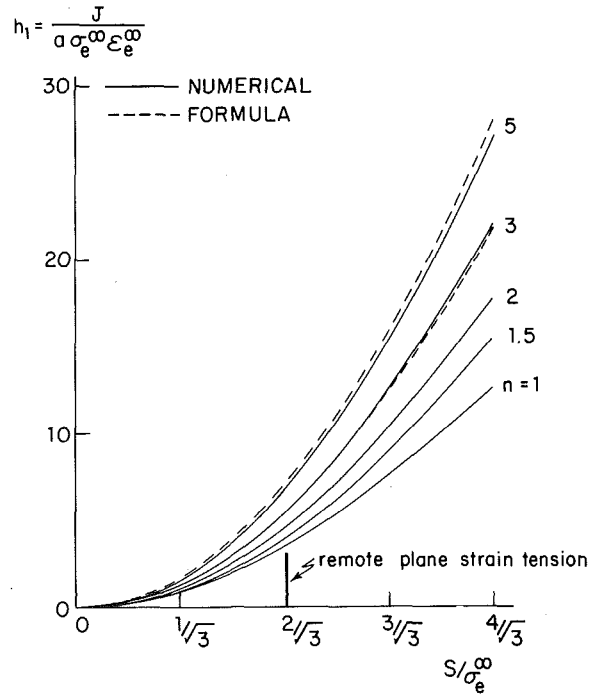


Fig. 12 Normalized J for plane strain crack; dashed line curve from (78)

for the axisymmetric problem. It can be shown that the decay of the additional displacements for large r satisfies the conditions required for application of the minimum principle as long as n is finite.

On the basis of numerical experimentation with different N and M, it is felt that the calculations with $N = 3$ and $M = 3$ give results

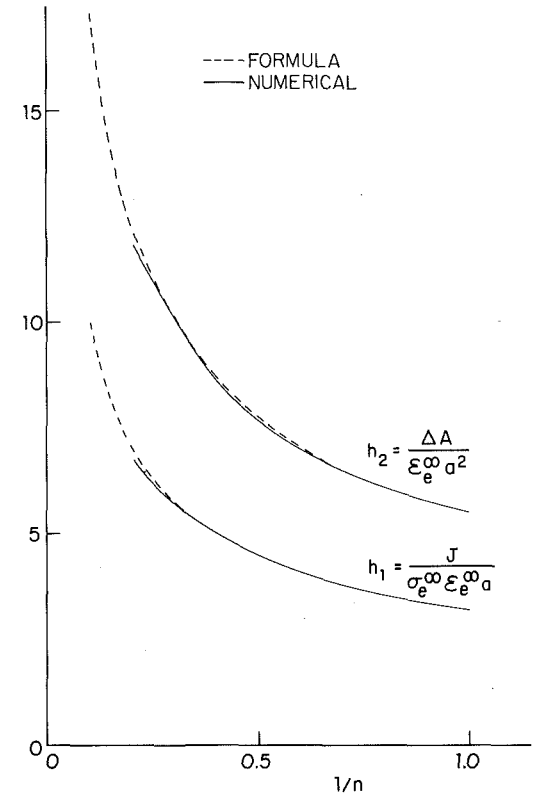


Fig. 13 Comparison between numerical results and analytical results (85) for plane strain crack in plane strain tension

for J in Table 3 which are low by not more than about 5 percent for $n < 3$. With $N = 3$ and $M = 4$, the same level of accuracy appears to be achieved for $n = 3$ and 5. For n larger than 5 the strain concentrates in rather narrow bands emanating from the tips, and it is not expected that our numerical method can accurately represent the solution unless many more terms are included in (82). The numerical results in Table 3 are for h_1, h_2, and h_3 which are defined by

$$\frac{J}{\sigma_e^\infty \epsilon_e^\infty a} = h_1\left(n, \frac{S}{T}\right)$$
$$\frac{\Delta A}{\epsilon_e^\infty a^2} = h_2\left(n, \frac{S}{T}\right) \tag{83}$$
$$\frac{\delta}{\epsilon_e^\infty a} = h_3\left(n, \frac{S}{T}\right)$$

where $\delta = u_2(0, 0^+), -u_2(0, 0^-)$, $\sigma_e^\infty = \sqrt{3}|S - T|/2$, and ϵ_e^∞ is related to σ_e^∞ by (1). In plane strain $\sigma_{33}^\infty = (\sigma_{11}^\infty + \sigma_{22}^\infty)/2$, $\sigma_m^\infty \equiv \sigma_{kk}^\infty/3 = (S + T)/2$ and, for $S - T > 0$,

$$\frac{S}{\sigma_e^\infty} = \frac{2}{\sqrt{3}}\left(\frac{\sigma_m^\infty}{\sigma_e^\infty} + \frac{1}{2}\right) \tag{84}$$

Curves of h_1 and h_2 as functions of S/σ_e^∞ are shown in Figs. 11 and 12 where the dashed curves are obtained from formulas (77) and (78) and the solid curves are from Table 3. For $n \leq 5$ at least, it appears that the formulas will be sufficiently accurate for many purposes for $\sigma_m^\infty/\sigma_e^\infty$ as large as $\frac{3}{2}$. Fig. 13 displays the results as plots against $1/n$ for plane strain tension ($S > 0$, $T = 0$) for which (77) and (78) become simply

$$\frac{\Delta A}{\epsilon_e^\infty a^2} = \pi\sqrt{3n} \quad \text{and} \quad \frac{J}{\sigma_e^\infty \epsilon_e^\infty a} = \pi\sqrt{n} \tag{85}$$

The relationship between (85) and those of [4] for a crack of length $2a$ in an infinite strip of width $2b$ subject to remote plane strain tension ($S > 0$, $T = 0$) is displayed in Fig. 14. In the present notation, the function h_1 of [4] is defined as

Downloaded 01 May 2010 to 171.66.16.249. Redistribution subject to ASME license or copyright; see http://www.asme.org/terms/Terms_Use.cfm

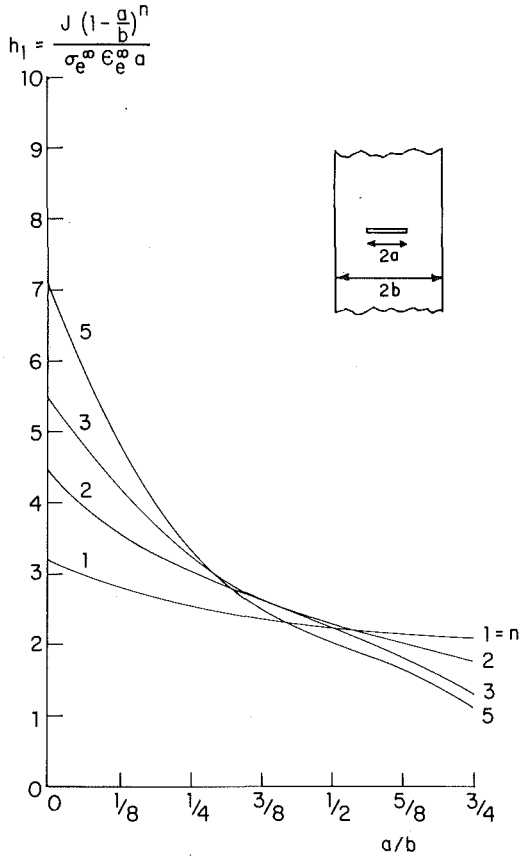


Fig. 14 Normalized J for plane strain center-cracked strip subject to plane strain tension; values for $a/b = 0$ from (85) and for $a/b > 0$ from [4]

$$h_1\left(\frac{a}{b}, n\right) = \frac{J}{\sigma_e^\infty \epsilon_e^\infty a}\left(1 - \frac{a}{b}\right)^n \tag{86}$$

which coincides with the present definition of h_1 in plane strain tension when $a/b = 0$. It is seen that $h_1(a/b, n)$ is a strong function of a/b when a/b is small and $n \neq 1$. Some care should be exercised in using the results for the infinite geometry to model the finite geometry and vice versa.

Finally, contours of constant effective strain are shown in Fig. 15 for plane strain tension with $\epsilon_e^\infty = 1$ for $n = 5$. A comparison of this figure with the corresponding plot for the penny-shaped crack in Fig. 6 reveals the substantially larger strain concentration in the plane strain problem at a given distance from the crack tip. In addition, it is noted that there is a large dead zone directly above and below the center of the plane strain crack in which the effective strain is almost zero.

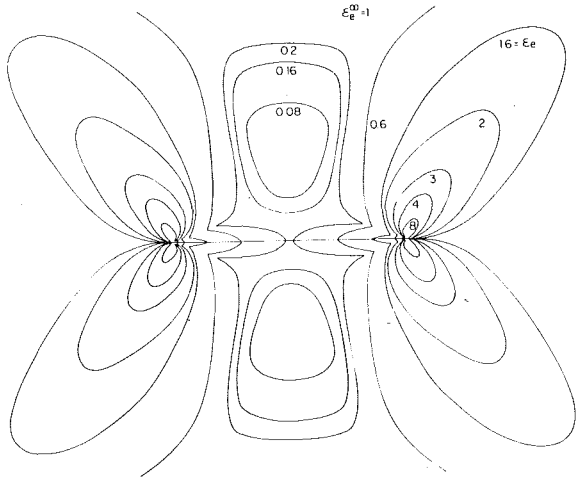


Fig. 15 Contours of constant effective strain ϵ_e for the plane strain crack subject to remote plane strain tension with $\epsilon_e^\infty = 1$ and $n = 5$

Acknowledgment

The work of M.Y.H. was supported in part by the Chinese Academy of Sciences and by the National Science Foundation under Grant ENG-78-10756. The work of J.W.H. was supported in part by the National Science Foundation under Grants DMR-79-23597 and ENG-78-10756, and by the Division of Applied Sciences, Harvard University.

References

1 Goldman, N. L., and Hutchinson, J. W., "Fully Plastic Crack Problems: The Center-Cracked Strip Under Plane Strain," *International Journal of Solids and Structures*, Vol. 11, 1975, pp. 575–591.

2 Amazigo, J. C., "Fully Plastic Center-Cracked Strip Under Antiplane Shear," *International Journal of Solids and Structures*, Vol. 11, 1975, pp. 1291–1299.

3 Ranaweera, M. P., and Leckie, F. A., "The Use of Optimization Techniques in the Analysis of Cracked Members by the Finite-Element Displacement and Stress Methods," *Computer Methods in Applied Mechanics and Engineering*, Vol. 19, 1979, pp. 367–389.

4 Kumar, V., Shih, C. F., and German, M. D., *The Handbook for Elastic-Plastic Fracture Analysis*, in preparation by the General Electric Company.

5 Shih, C. F., "J-Integral Estimates for Strain-Hardening Materials in Antiplane Shear Using Fully Plastic Solutions," in *Mechanics of Crack Growth*, ASTM STP 590, 1976, pp. 3–22.

6 Shih, C. F., and Hutchinson, J. W., "Fully Plastic Solutions and Large-Scale Yielding Estimates for Plane Stress Crack Problems," ASME *Journal of Engineering Materials and Technology*, Vol. 98, 1976, pp. 289–295.

7 Hill, R. and Storåkers, B., "Plasticity and Creep of Pressurized Membranes: A New Look at the Small-Deflection Theory," *Journal of Mechanics and Physics of Solids*, Vol. 28, 1980, pp. 27–48.

8 Hult, J., "On the Stationarity of Stress and Strain Distributions in Creep," in *Proceedings of the International Symposium on Second-Order Effects in Elasticity, Plasticity and Fluid Dynamics*, Haifa, Pergamon Press, 1962, pp. 352–361.

9 Budiansky, B., Hutchinson, J. W., and Slutsky, S., "Void Growth and Collapse in Viscous Solids," Harvard University Report, Division of Applied Sciences, MECH-15, Feb. 1980, to be published in *Mechanics of Solids*, The Rodney Hill 60th Anniversary Volume, eds., Hopkins, H. G., and Sewell, M. J., Pergamon Press, 1981.

10 Rice, J. R., "A Path-Independent Integral and the Approximate Analysis of Strain Concentration by Notches and Cracks," ASME JOURNAL OF APPLIED MECHANICS, Vol. 35, 1968, pp. 379–386.

11 Hutchinson, J. W., "Singular Behavior at the End of a Tensile Crack in a Hardening Material," *Journal of Mechanics and Physics of Solids*, Vol. 16, 1968, p p. 13–31.

12 Rice, J. R., and Rosengren, G. F., "Plane-Strain Deformation Near a Crack Tip in a Power-Law Hardening Material," *Journal of Mechanics and Physics of Solids*, Vol. 16, 1968, pp. 1–12.

13 Knowles, J. K., and Sternberg, E., "On a Class of Conservation Laws in Linearized and Finite Elastostatics," *Archive for Rational Mechanics and Analysis*, Vol. 44, 1972, pp. 187–211.

14 Budiansky, B., and Rice, J. R., "Conservation Laws and Energy-Release Rates," ASME JOURNAL OF APPLIED MECHANICS, Vol. 40, 1973, pp. 201–203.

15 Budiansky, B., and Hutchinson, J. W., "Self-Similar Shapes and Asymptotic Dilatation-Rates for Voids in Viscous Solids," in *Proceedings of the XVth International Congress of Theoretical and Applied Mechanics* (Postprints), eds., Rimrott, F. P. J., and Tabarrok, B., North-Holland Publishing Company, Amsterdam, 1980, pp. 243–249.

16 Rice, J. R., and Tracey, D. M., "On the Ductile Enlargement of Voids in Triaxial Stress Fields," *Journal of Mechanics and Physics of Solids*, Vol. 17, 1969, pp. 201–217.

17 Hoenig, A., "The Behavior of a Flat Elliptical Crack in an Anisotropic Elastic Body," *International Journal of Solids and Structures*, Vol. 14, 1978, pp. 925–934.

18 Eshelby, J. D., "The Determination of the Elastic Field of an Ellipsoidal Inclusion, and Related Problems," *Proceedings of the Royal Society*, London, Series A, Vol. 241, 1957, pp. 376–396.

Downloaded 01 May 2010 to 171.66.16.249. Redistribution subject to ASME license or copyright; see http://www.asme.org/terms/Terms_Use.cfm

APPENDIX

Additional Strains for Axisymmetric Problem

With (x, θ, y) as radial, circumferential, and axial coordinates, the additional strains are related to ψ by

$$\epsilon_x = x^{-1}\psi_{,xy} - x^{-2}\psi_{,y}, \quad \epsilon_\theta = x^{-2}\psi_{,y}, \quad \epsilon_y = -\epsilon_x - \epsilon_\theta,$$
$$2\epsilon_{xy} = x^{-2}[x(\psi_{,yy} - \psi_{,xx}) + \psi_{,x}]$$

By change of variables to μ and ϕ

$$\psi_{,x} = \psi_{,\mu}\frac{\partial\mu}{\partial x} + \psi_{,\phi}\frac{\partial\phi}{\partial x}$$

$$\psi_{,xx} = \left[\psi_{,\mu\mu}\frac{\partial\mu}{\partial x} + \psi_{,\mu\phi}\frac{\partial\phi}{\partial x}\right]\frac{\partial\mu}{\partial x} + \psi_{,\mu}\frac{\partial^2\mu}{\partial x^2} + \left[\psi_{,\phi\mu}\frac{\partial\mu}{\partial x} + \psi_{,\phi\phi}\frac{\partial\phi}{\partial x}\right]\frac{\partial\phi}{\partial x} + \psi_{,\phi}\frac{\partial^2\phi}{\partial x^2}$$

with similar expressions for the other partial derivatives of ψ. The derivatives $\partial\mu/\partial x$ and $\partial\phi/\partial x$ are given in (33), while

$$\frac{\partial^2\mu}{\partial x^2} + i\frac{\partial^2\mu}{\partial x\partial y} = \frac{\partial\mu}{\partial x}\frac{\Omega}{|\Omega|^2} + \mu\frac{\Omega'}{|\Omega|^2\omega'} - \frac{2\mu\Omega}{|\Omega|^4}\mathrm{Re}\left[\frac{\bar{\Omega}\Omega'}{\omega'}\right]$$

$$\frac{\partial^2\mu}{\partial x\partial y} + i\frac{\partial^2\mu}{\partial y^2} = \frac{\partial\mu}{\partial y}\frac{\Omega}{|\Omega|^2} + i\frac{\mu\Omega'}{|\Omega|^2\omega'} - \frac{2\mu\Omega}{|\Omega|^4}\mathrm{Re}\left[\frac{i\bar{\Omega}\Omega'}{\omega'}\right]$$

$$\frac{\partial^2\phi}{\partial x\partial y} - i\frac{\partial^2\phi}{\partial x^2} = -\frac{\Omega'}{|\Omega|^2\omega'} + \frac{2\Omega}{|\Omega|^4}\mathrm{Re}\left[\frac{\bar{\Omega}\Omega'}{\omega'}\right]$$

$$\frac{\partial^2\phi}{\partial y^2} - i\frac{\partial^2\phi}{\partial x\partial y} = -\frac{i\Omega'}{|\Omega|^2\omega'} + \frac{2\Omega}{|\Omega|^4}\mathrm{Re}\left[\frac{i\bar{\Omega}\Omega'}{\omega'}\right]$$

Downloaded 01 May 2010 to 171.66.16.249. Redistribution subject to ASME license or copyright; see http://www.asme.org/terms/Terms_Use.cfm

John Dundurs
Professor,
Department of Civil Engineering,
Northwestern University,
Evanston, Ill. 60201
Fellow ASME

Maria Comninou
Associate Professor,
Department of Civil Engineering,
University of Michigan,
Ann Arbor, Mich. 48109
Mem. ASME

An Educational Elasticity Problem With Friction

Part 1: Loading, and Unloading for Weak Friction

The paper treats an elasticity problem with friction that can be solved in closed form. It involves an unbounded solid with a semi-infinite cut. The solid is compressed in a direction perpendicular to the cut, but the cut is induced to separate and slip locally by applying a concentrated force at the tip of the cut. The first part deals with the initial loading phase and includes unloading for weak friction.

Introduction

Although contact problems with friction have received considerable attention in recent years (see Gladwell [1] and Goodman [2] for references), analytical as well as computational difficulties have tended to obscure some of their essential features. Indeed, there are very few available solutions that further the understanding of friction in elasticity either from the viewpoint of insight gained, or by exposing instructively the difficulties encountered in such problems.

The present article gives the solution of an elasticity problem which in itself is not of much practical significance. However, its simplicity allows one to follow potentially complicated issues such as the history of loading, residual stresses left upon unloading, and the distinction between weak and strong friction. The problem can thus serve as a basis for modeling other more realistic situations, and its purpose is mainly educational.

The article is divided into two parts. The first part treats loading and the simpler case of unloading for weak friction. Unloading for strong friction, reloading and periodically fluctuating loads will be discussed in the second part.

Problem and Mathematical Preliminaries

Consider an unbounded elastic solid with a straight semi-infinite cut, as indicated in Fig. 1. The solid is first compressed in a direction normal to the cut by the uniform applied pressure p^∞ and subsequently subjected to a concentrated force at the tip of the cut. The angle α between the cut and the force can be restricted to the range $0 \leq \alpha \leq \pi$ without loss of generality. It is anticipated that, for angles $0 < \alpha < \pi/2$, the concentrated force makes the faces of the cut separate near the tip and slip on an adjacent part, while the faces stick on the rest of the cut because of friction (see Fig. 1). Slip without separation is expected for $\pi/2 \leq \alpha < \pi$. However, emphasis is put on the first case, or $0 < \alpha < \pi/2$.

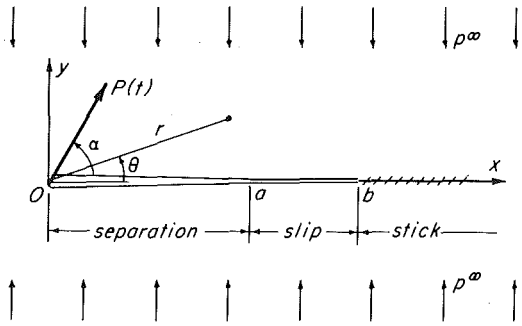


Fig. 1 Geometry of the problem

The boundary conditions on the cut involve the normal tractions

$$N(x) = \sigma_{yy}(x, 0) \tag{1}$$

the shearing tractions

$$S(x) = \sigma_{xy}(x, 0) \tag{2}$$

the gap

$$g(x) = u_y(x, 0+) - u_y(x, 0-) \tag{3}$$

the tangential shift between the faces of the cut

$$h(x) = u_x(x, 0+) - u_x(x, 0-) \tag{4}$$

and the slip velocity

$$V(x) = dh(x)/dt \tag{5}$$

It is important to note that elasticity problems with friction require

Contributed by the Applied Mechanics Division and presented at the Winter Annual Meeting, Washington, D. C., November 15–20, 1981, of THE AMERICAN SOCIETY OF MECHANICAL ENGINEERS.

Discussion on this paper should be addressed to the Editorial Department, ASME, United Engineering Center, 345 East 47th Street, New York, N. Y. 10017, and will be accepted until March 1, 1982. Manuscript received by ASME Applied Mechanics Division, January, 1981. Paper No. 81-WA/APM-19.

 Copyright © 1981 by ASME

Downloaded 01 May 2010 to 171.66.16.249. Redistribution subject to ASME license or copyright; see http://www.asme.org/terms/Terms_Use.cfm

that the deformation process be followed in time, because the elastic fields depend on the history of loading. As the concentrated force changes, so do the displacements and stresses, but it is asumed that the rates are sufficiently low and that the effect of inertia can be neglected. The time-dependence of the field quantities will not be indicated explicitly unless there is a need to do so.

The boundary conditions are

$$N(x) = 0, \quad S(x) = 0 \tag{6a, b}$$

$$g(x) > 0 \tag{7}$$

in the separation zone $0 < x < a$,

$$g(x) = 0, \quad |S(x)| = f_k|N(x)| \tag{8a, b}$$

$$N(x) < 0, \quad \text{sgn } S(x) = \text{sgn } V(x) \tag{9a, b}$$

in the slip zone $a < x < b$, and

$$g(x) = 0, \quad V(x) = 0 \tag{10a, b}$$

$$N(x) < 0, \quad |S(x)| < f_s|N(x)| \tag{11a, b}$$

in the stick zone $b < x < \infty$, where f_k and f_s denote, respectively, the coefficients of kinetic and static friction ($f_k \leq f_s$).

The applied pressure and the concentrated force for $0 < \alpha < \pi/2$ are incorporated in the solution through the Airy stress function [3]

$$U = -\frac{1}{2}p^\infty x^2 + \frac{1}{2\pi}(Ar\theta \sin\theta + Br\theta\cos\theta) \tag{12}$$

in which the coefficients A and B are determined by the requirement that all closed contours surrounding the origin transmit the net force ($P\cos\alpha$, $P\sin\alpha$), with P denoting the instantaneous magnitude of the concentrated force. The Airy stress function (12) gives the following quantities on the cut $0 < x < \infty$:

$$N(x) = -p^\infty, \quad S(x) = 0, \qquad -\infty < x < \infty \tag{13a, b}$$

$$g(x) = -A\frac{\kappa - 1}{4\mu}, \qquad 0 < x < \infty \tag{14}$$

$$h(x) = -B\frac{\kappa - 1}{4\mu}, \quad V(x) = -\dot{B}\frac{\kappa - 1}{4\mu}, \qquad 0 < x < \infty \tag{15a, b}$$

where μ denotes the shear modulus, $\kappa = 3 - 4\nu$ for plane strain, and ν is Poisson's ratio. It is clear from these expressions that the Airy stress function (12) by itself satisfies none of the set of conditions for separation, slip, or stick.

The boundary conditions on the cut are enforced by distributing edge dislocations over the separation and slip zones. The separation zone $0 < x < a$ is covered by a distribution of climb dislocations (Burgers vectors in the y-direction) with the density $B_y(x)$. Glide dislocations (Burgers vectors in the x-direction) with the density $B_x(x)$ are distributed over both the separation and slip zones, or on $0 < x < b$. The dislocation distributions give [4]

$$N(x) = -\frac{2\mu}{\pi(\kappa+1)}\int_0^a \frac{B_y(\xi)d\xi}{\xi - x}, \qquad -\infty < x < \infty \tag{16}$$

$$S(x) = -\frac{2\mu}{\pi(\kappa+1)}\int_0^b \frac{B_x(\xi)d\xi}{\xi - x}, \qquad -\infty < x < \infty \tag{17}$$

$$g(x) = -\int_0^x B_y(\xi)d\xi, \qquad 0 < x < \infty \tag{18}$$

$$h(x) = -\int_0^x B_x(\xi)d\xi, \qquad 0 < x < \infty \tag{19}$$

Initial Loading Phase for Case of Separation

We consider first the loading phase when the concentrated force starts from zero and increases steadily in magnitude, or $P(0) = 0$ and $\dot{P}(t) > 0$. Then

$$A = -P\cos\alpha, \quad B = P\sin\alpha \tag{20a, b}$$

For $0 \leq \alpha < \pi/2$, separation starts immediately as the concentrated force is applied. This is seen from the solution for a concentrated force in the unbounded solid without a cut [3] which involves infinite tension on $y = 0$ at $x = 0+$. Combining (13a) and (16), the boundary condition (6a) yields the integral equation

$$\int_0^a \frac{B_y(\xi)d\xi}{\xi - x} = -\frac{\pi(\kappa+1)}{2\mu}p^\infty, \quad 0 < x < a \tag{21}$$

The solution of (21) must be bounded at the transition from separation to contact, or at $x = a$ [5]. A solution which is bounded at both ends of the separation zone is not possible because the right side of (21) does not satisfy the consistency condition [6] of the singular Cauchy integral equation. Consequently, the solution of (21) must be singular at $x = 0$. Recalling that the solution of

$$\int_{-1}^1 \frac{\phi(u)du}{u - s} = f(s), \quad -1 < s < 1 \tag{22}$$

which contains a singularity at $s = -1$ is [9]

$$\phi(s) = -\frac{1}{\pi^2}w(s)\int_{-1}^1 \frac{f(u)du}{w(u)(u - s)}, \quad -1 < s < 1 \tag{23}$$

with

$$w(s) = \left(\frac{1-s}{1+s}\right)^{1/2} \tag{24}$$

we have

$$B_y(x) = \frac{\kappa+1}{2\mu}p^\infty\left(\frac{a}{x} - 1\right)^{1/2}, \quad 0 < x < a \tag{25}$$

Substituting (25) into (16) and taking into account (13a), the total normal tractions of $y = 0$ become

$$N(x) = -p^\infty\left(1 - \frac{a}{x}\right)^{1/2}, \quad -\infty < x < 0, \quad a < x < \infty \tag{26}$$

The extent of the separation zone is determined by the condition

$$g(a) = \frac{\kappa - 1}{4\mu}P\cos\alpha - \int_0^a B_y(\xi)d\xi = 0 \tag{27}$$

and

$$a = \frac{\kappa - 1}{\pi(\kappa+1)}\frac{P\cos\alpha}{p^\infty} \tag{28}$$

The gap follows from (14) and (18) as

$$g(x) = \frac{\kappa+1}{4\mu}p^\infty a\left\{\frac{\pi}{2} + \sin^{-1}\left(1 - \frac{2x}{a}\right) - 2\left[\frac{x}{a}\left(1 - \frac{x}{a}\right)\right]^{1/2}\right\}, \quad 0 < x < a \tag{29}$$

Since $g(0) > 0$, $g(a) = 0$ and $dg(x)/dx \neq 0$ on $0 < x < a$, the inequality (7) is satisfied.

It is also clear that there is some slip to the right of the separation zone for any level of friction. This follows from the fact that the governing integral equation in the absence of a slip zone would be

$$\int_0^a \frac{B_x(\xi)d\xi}{\xi - x} = 0, \quad 0 < x < a \tag{30}$$

which can only have solutions that are singular at both ends of the interval, and that it becomes impossible to satisfy (11b) for any value of f_s. Taking into account (13b) and (17), boundary condition (6b) requires that

$$\int_0^b \frac{B_x(\xi)d\xi}{\xi - x} = 0, \quad 0 < x < a \tag{31}$$

The tangential shift given by (15a) suggests that $V(x) < 0$ and consequently $S(x) < 0$ in the slip zone. Then (8b) can be replaced with

Downloaded 01 May 2010 to 171.66.16.249. Redistribution subject to ASME license or copyright; see http://www.asme.org/terms/Terms_Use.cfm

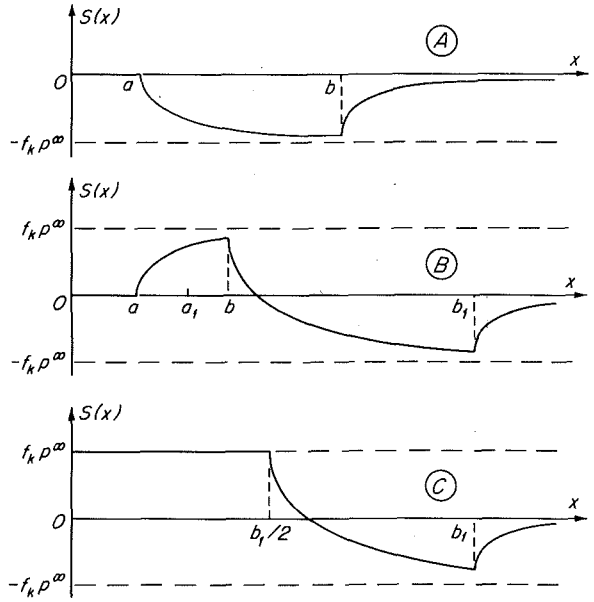


Fig. 2 Schematic distribution of the shearing tractions on the cut. (*A*) initial phase of loading; (*B*) unloading with weak friction; (*C*) residual tractions left upon complete unloading with weak friction

$$S(x) = f_k N(x) \tag{32}$$

Substituting from (13*b*), (17), and (26) into (32),

$$\int_0^b \frac{B_x(\xi)d\xi}{\xi - x} = \frac{\pi(\kappa+1)}{2\mu} f_k p^\infty \left(1 - \frac{a}{x}\right)^{1/2}, \quad a < x < b \tag{33}$$

The two conditions (31) and (33) can be combined into the single integral equation

$$\int_0^b \frac{B_x(\xi)d\xi}{\xi - x} = \frac{\pi(\kappa+1)}{2\mu} f_k p^\infty \times \left(1 - \frac{a}{x}\right)^{1/2} H(x-a), \quad 0 < x < b \tag{34}$$

Similarly to the distribution of the climb dislocations, $B_x(x)$ must be bounded at $x = b$ [5], but a solution that is also bounded at $x = 0$ is not possible because the right side of (34) does not satisfy the consistency condition. Consequently $B_x(x)$ must be singular at $x = 0$, and we get solving (34)

$$B_x(x) = -\frac{\kappa+1}{2\mu} f_k p^\infty \begin{cases} \left(\frac{b}{x} - 1\right)^{1/2} - \left(\frac{a}{x} - 1\right)^{1/2}, & 0 < x < a \\ \left(\frac{b}{x} - 1\right)^{1/2}, & a < x < b \end{cases} \tag{35}$$

The shearing tractions from (13*b*) and (17) are then

$$S(x) = -f_k p^\infty \begin{cases} \left(1 - \frac{a}{x}\right)^{1/2}, & a < x < b \\ \left(1 - \frac{a}{x}\right)^{1/2} - \left(1 - \frac{b}{x}\right)^{1/2}, & -\infty < x < 0, \quad b < x < \infty \end{cases} \tag{36}$$

The extent of the slip zone is determined by the condition

$$h(b) = -\frac{\kappa-1}{4\mu} P \sin\alpha - \int_0^b B_x(\xi)d\xi = 0 \tag{37}$$

and

$$b = a + \frac{\kappa-1}{\pi(\kappa+1)} \frac{P\sin\alpha}{f_k p^\infty} = a\left(1 + \frac{\tan\alpha}{f_k}\right) \tag{38}$$

The tangential shift follows from (15*a*) and (19) as

$$h(x) = -\frac{\kappa+1}{4\mu} f_k p^\infty b \left\{\frac{\pi}{2}\left(1 - \frac{a}{b}\right) + \sin^{-1}\left(1 - \frac{2x}{b}\right) - 2\left[\frac{x}{b}\left(1 - \frac{x}{b}\right)\right]^{1/2}\right\} + \frac{\kappa+1}{4\mu} \times f_k p^\infty a \begin{cases} \sin^{-1}\left(1 - \frac{2x}{a}\right) - 2\left[\frac{x}{a}\left(1 - \frac{x}{a}\right)\right]^{1/2}, & 0 < x < a \\ -\frac{\pi}{2}, & a < x < b \end{cases} \tag{39}$$

and the slip velocity is

$$V(x) = -\frac{\kappa+1}{4\mu} f_k p^\infty b \left\{\frac{\pi}{2} + \sin^{-1}\left(1 - \frac{2x}{b}\right)\right\}, \quad a < x < b \tag{40}$$

Equations (36) and (40) show that (9*b*) is satisfied.

Moreover, it is clear from (26), (27), (36), and (37) that the conditions (10*a*, *b*) and (11*a*, *b*) in the stick zone are satisfied. A notable feature of the results is that the coefficient of static friction does not enter the calculations and, thus, none of the field quantities are affected by it. The distribution of $S(x)$ is shown schematically in Fig. 2. The shearing tractions in the stick zone have an infinite slope at the transition to slip. This is in agreement with the asymptotic analysis of such a transition [5].

It is interesting to note from (28) and (38) that the extents of the separation and slip zones are proportional to the magnitude P of the concentrated force and inversely proportional to the applied pressure p^∞.

Loading Phase for Case Without Separation

No separation develops between the faces of the cut when the angle α falls in the range $\pi/2 \le \alpha \le \pi$. To treat this case, the Airy stress function (12) is replaced with

$$U = -\frac{1}{2} p^\infty x^2 + \frac{1}{2\pi}\left\{Ar\theta\sin\theta + Br\theta\cos\theta + \frac{\kappa-1}{\kappa+1}(Cr\log r\cos\theta + Dr\log r\sin\theta)\right\} \tag{41}$$

where again

$$A = -P\cos\alpha, \quad B = P\sin\alpha \tag{42a, b}$$

The constant C is determined by the condition that there be no interpenetration of material, and

$$C = P\cos\alpha \tag{43}$$

The faces of the cut stick if $\sin\alpha + f_s\cos\alpha < 0$ or $f_s > |\tan\alpha|$, and (41) is the complete solution with

$$D = P\sin\alpha \tag{44}$$

If $\sin\alpha + f_s\cos\alpha > 0$ or $f_s < |\tan\alpha|$, there is slip on $0 < x < b$ and, considering the friction law (8*b*) very near to the origin, it is seen that

$$D = -f_k P\cos\alpha \tag{45}$$

The derivations for this case will be omitted, as it is not difficult to show that the following results satisfy the conditions of the problem for $\dot{P}(t) > 0$:

$$B_x(x) = -\frac{\kappa+1}{2\mu} f_k p^\infty \left(\frac{b}{x} - 1\right)^{1/2}, \quad 0 < x < b \tag{46}$$

$$b = \frac{\kappa-1}{\pi(\kappa+1)} \frac{P\cos\alpha}{f_k p^\infty}(f_k + \tan\alpha) \tag{47}$$

Downloaded 01 May 2010 to 171.66.16.249. Redistribution subject to ASME license or copyright; see http://www.asme.org/terms/Terms_Use.cfm

$$N(x) = -p^\infty \left\{1 - \frac{f_k}{f_k + \tan\alpha}\frac{b}{2|x|}\right\}, \quad -\infty < x < \infty \tag{48}$$

$$S(x) = f_k p^\infty \frac{f_k}{f_k + \tan\alpha}\frac{b}{2|x|} - f_k p^\infty \begin{cases} 1, & 0 < x < b \\ 1 - \left(1 - \dfrac{b}{x}\right)^{1/2}, & -\infty < x < 0, b < x < \infty \end{cases} \tag{49}$$

$$h(x) = -\frac{\kappa+1}{4\mu} f_k p^\infty b \left\{\frac{\pi}{2} + \sin^{-1}\left(1 - \frac{2x}{b}\right) - 2\left[\frac{x}{b}\left(1 - \frac{x}{b}\right)\right]^{1/2}\right\}, \quad 0 < x < b \tag{50}$$

The slip velocity is given by (40).

Unloading

Suppose that the magnitude of the concentrated force reaches a maximum value P_1 and then starts to decrease. The solution for the unloading phase with $P(t) < P_1$ and $\dot{P}(t) < 0$ can be constructed by adding a correction (denoted by subscripts or superscripts c) to the elastic fields corresponding to the load P_1 which are viewed as locked in residual fields (denoted by subscripts 1). Considering the case $0 \le \alpha < \pi/2$, the coefficients in the Airy stress function (12) for the corrective part of the solution are

$$A_c = (P_1 - P)\cos\alpha, \quad B_c = -(P_1 - P)\sin\alpha \tag{51a, b}$$

The tractions, gap and tangential shift for the Airy stress function are given by (12a)–(15b). Taking the separation zone for P_1 as $0 < x < a_1$, and that caused by the instantaneous force with the smaller magnitude P as $0 < x < a$, we distribute on $0 < x < a_1$ climb dislocations with the density $B_y^c(x)$ such that, first, the gap is closed on $a < x < a_1$ and, second, zero normal tractions are maintained on $0 < x < a$. The normal tractions induced by $B_y^c(x)$ are

$$N_c(x) = -\frac{2\mu}{\pi(\kappa+1)}\int_0^{a_1} \frac{B_y^c(\xi)d\xi}{\xi - x}, \quad -\infty < x < \infty \tag{52}$$

and the new gap is

$$g(x) = g_1(x) - \frac{\kappa-1}{4\mu}(P_1 - P)\cos\alpha - \int_0^x B_y^c(\xi)d\xi, \quad 0 < x < a_1 \tag{53}$$

where $g_1(x)$ is the gap on $0 < x < a_1$ caused by P_1. It can be obtained from (29) by replacing P with P_1 and a with a_1. The requirement that $N_c(x) = 0$ on $0 < x < a$ gives

$$\int_0^a \frac{B_y^c(\xi)d\xi}{\xi - x} = -\int_a^{a_1} \frac{B_y^c(\xi)d\xi}{\xi - x}, \quad 0 < x < a \tag{54}$$

Since $g(x) = 0$ on $a < x < a_1$,

$$g_1(x) - \frac{\kappa-1}{4\mu}(P_1 - P)\cos\alpha - \int_0^x B_y^c(\xi)d\xi = 0, \quad a < x < a_1 \tag{55}$$

and

$$B_y^c(x) = \frac{dg_1(x)}{dx} = -\frac{\kappa+1}{2\mu}p^\infty\left(\frac{a_1}{x} - 1\right)^{1/2}, \quad a < x < a_1 \tag{56}$$

Substituting from (56) into the right side of (54), we get the integral equation

$$\int_0^a \frac{B_y^c(\xi)d\xi}{\xi - x} = \frac{p^\infty(\kappa+1)}{2\mu}\int_a^{a_1}\left(\frac{a_1}{\xi} - 1\right)^{1/2}\frac{d\xi}{\xi - x}, \quad 0 < x < a \tag{57}$$

The solution of (57) that is bounded at $x = a$ but unbounded at $x = 0$ is

$$B_y^c(x) = -\frac{\kappa+1}{2\mu}p^\infty\left\{\left(\frac{a_1}{x} - 1\right)^{1/2} - \left(\frac{a}{x} - 1\right)^{1/2}\right\}, \quad 0 < x < a \tag{58}$$

Using (56) and (58) in (52), the corrective normal tractions are

$$N_c(x) = -p^\infty\left\{\left(1 - \frac{a}{x}\right)^{1/2} - \left(1 - \frac{a_1}{x}\right)^{1/2}H(x - a_1)\right\}, \quad a < x < \infty \tag{59}$$

The total normal tractions are obtained by adding $N_c(x)$ to $N_1(x)$, for which the latter follows from (26) with a replaced by a_1. Thus

$$N(x) = -p^\infty\left(1 - \frac{a}{x}\right)^{1/2}, \quad a < x < \infty \tag{60}$$

The extent of the separation zone is determined by the condition that $g(a) = 0$, and using (58) in (53),

$$a = \frac{\kappa-1}{\pi(\kappa+1)}\frac{P\cos\alpha}{p^\infty} \tag{61}$$

The last two results could be anticipated, because the distribution of the climb dislocations in the present problem does not depend on the slip process.

The residual shearing tractions that are locked in when the concentrated force, having reached the magnitude P_1, starts to decrease are from (36)

$$S_1(x) = f_k p^\infty\left\{-\left(1 - \frac{a_1}{x}\right)^{1/2}H(x - a_1) + \left(1 - \frac{b_1}{x}\right)^{1/2}H(x - b_1)\right\}, \quad 0 < x < \infty \tag{62}$$

If at any time during the unloading process the existing distribution of glide dislocations is $B_x^c(x)$ on the interval $0 < x < c$, the corrective shearing tractions are

$$S_c(x) = -\frac{2\mu}{\pi(\kappa+1)}\int_0^c \frac{B_x^c(\xi)d\xi}{\xi - x}, \quad 0 < x < \infty \tag{63}$$

The total shearing tractions on the cut are

$$S(x) = S_1(x) + S_c(x) \tag{64}$$

One may expect at first that there is a zone of backslip on the interval $a < x < b$. It is not known, however, whether $a_1 < b$ or $b < a_1$, and two cases must be explored. The mathematical formulation of the two cases is quite different because, in the first case ($a_1 < b$), the slip zone spreads into a previous stick zone, whereas in the second case ($b < a_1$), the slip zone, if there is one, contracts on one side and previously slipping parts of the cut start to stick. We restrict the present article to the first case which, as will be seen, corresponds to weak friction.

Weak Friction. The active slip zone $a < x < b$ with $a_1 < b$ for the unloading phase is modeled by distributing on $0 < x < b$ glide dislocations with the density $B_x^c(x)$ which serves to correct the shearing tractions on the cut. It will be assumed in the analysis that $b < b_1$ which can be confirmed later. The total shearing tractions on the cut are from (62)–(64)

$$S(x) = -f_k p^\infty\left(1 - \frac{a_1}{x}\right)^{1/2}H(x - a_1) - \frac{2\mu}{\pi(\kappa+1)}\int_0^b \frac{B_x^c(\xi)d\xi}{\xi - x}, \quad 0 < x < b \tag{65}$$

It is expected that $V(x) > 0$ and $S(x) > 0$ during the unloading phase with backslip, so that (6b) and (8b) can be replaced with

$$S(x) = -f_k N(x), \quad 0 < x < b \tag{66}$$

The condition (66), which incorporates the requirement that the shearing tractions vanish in the separation zone and obey the friction law in the slip zone, gives upon substitution of (60) and (65) the integral equation

$$\int_0^b \frac{B_x^c(\xi)d\xi}{\xi - x} = -\frac{\pi(\kappa+1)}{2\mu}f_k p^\infty\left\{\left(1 - \frac{a}{x}\right)^{1/2}H(x - a) + \left(1 - \frac{a_1}{x}\right)^{1/2}H(x - a_1)\right\}, \quad 0 < x < b \tag{67}$$

Downloaded 01 May 2010 to 171.66.16.249. Redistribution subject to ASME license or copyright; see http://www.asme.org/terms/Terms_Use.cfm

The physically suitable solution of (67) is

$$B_x^c(x) = \frac{\kappa+1}{2\mu} f_k p^\infty \left\{ -\left(\frac{a}{x}-1\right)^{1/2} H(a-x) - \left(\frac{a_1}{x}-1\right)^{1/2} H(a_1-x) + 2\left(\frac{b}{x}-1\right)^{1/2} \right\}, \quad 0 < x < b \tag{68}$$

The extent of the slip zone is determined by the condition that $h_c(b) = 0$, or

$$\frac{\kappa-1}{4\mu}(P_1 - P)\sin\alpha - \int_0^b B_x^c(\xi)d\xi = 0 \tag{69}$$

where the first term comes from the corrective part of the Airy stress function. Using (61) and (68) in (69), the result is

$$b = \frac{1}{2}(a_1 + a) + \frac{1}{2}(a_1 - a)\frac{\tan\alpha}{f_k} \tag{70}$$

from which we can deduce that the assumption of $a_1 < b$ requires that

$$f_k < \tan\alpha \tag{71}$$

and that indeed $b < b_1$. It is important to note that

$$\dot{b} = \frac{1}{2}\dot{a}\left(1 - \frac{\tan\alpha}{f_k}\right) \tag{72}$$

and, since $\dot{a} < 0, \dot{b} > 0$ meaning that the slip zone expands to the right as the load is being reduced. For $f_k = \tan\alpha, b = a_1 =$ constant. The total shearing tractions computed from (65) are

$$S(x) = f_k p^\infty \left\{ \left(1-\frac{a}{x}\right)^{1/2} H(x-a) - 2\left(1-\frac{b}{x}\right)^{1/2} H(x-b) + \left(1-\frac{b_1}{x}\right)^{1/2} H(x-b_1) \right\}, \quad 0 < x < \infty \tag{73}$$

and it is seen that $S(x) > 0$ on $a < x < b$. The distribution of the shearing tractions is shown schematically in Fig. 2.

In order to check the assumption made about the direction of slip we also compute the tangential shift

$$h_c(x) = \frac{\kappa-1}{4\mu}(P_1 - P)\sin\alpha - \int_0^x B_x^c(\xi)d\xi, \quad 0 < x < \infty \tag{74}$$

Using (68)

$$h_c(x) = \frac{\kappa+1}{4\mu} f_k p^\infty \left\{ \pi\left(b - \frac{1}{2}a_1\right) - a_1\left\{\sin^{-1}\left(1-\frac{2x}{a_1}\right) - 2\left[\frac{x}{a_1}\left(1-\frac{x}{a_1}\right)\right]^{1/2}\right\} + 2b\left\{\sin^{-1}\left(1-\frac{2x}{b}\right) - 2\left[\frac{x}{b}\left(1-\frac{x}{b}\right)\right]^{1/2}\right\}\right\}, \quad a < x < a_1 \tag{75}$$

$$h_c(x) = \frac{\kappa+1}{4\mu} f_k p^\infty \left\{ \pi b + 2b\left\{\sin^{-1}\left(1-\frac{2x}{b}\right) - 2\left[\frac{x}{b}\left(1-\frac{x}{b}\right)\right]^{1/2}\right\}\right\}, \quad a_1 < x < b \tag{76}$$

The slip velocity from (75) and (76) is

$$V(x) = \frac{\kappa+1}{4\mu} f_k p^\infty \dot{b}\left\{\pi + 2\sin^{-1}\left(1-\frac{2x}{b}\right)\right\}, \quad a < x < b \tag{77}$$

and it is seen that $V(x) > 0$ as was assumed in writing the friction law.

It is important to note that, if the concentrated force is removed altogether, residual shearing tractions remain locked in on the cut. The size of the slip zone at the instant just before the concentrated force reaches zero magnitude is obtained from (70) by setting $a = 0$, and

$$b = \frac{1}{2}a_1\left(1 + \frac{\tan\alpha}{f_k}\right) = \frac{1}{2}b_1 \tag{78}$$

The residual shearing tractions from (73) then are

$$S(x) = f_k p^\infty \left\{ 1 - 2\left(1-\frac{b}{x}\right)^{1/2} H(x-b) + \left(1-\frac{b_1}{x}\right)^{1/2} H(x-b_1)\right\}, \quad 0 < x < \infty \tag{79}$$

and their distribution is shown schematically in Fig. 2.

One could also follow the unloading process as the concentrated force is reduced to zero and then allowed to reverse direction. However, this case will not be pursued here.

Acknowledgment

The support by the office of Naval Research through the Contract No. DRDA-81-1903-P1 is greatly acknowledged.

References

1 Gladwell, G. M. L., *Contact Problems in the Classical Theory of Elasticity*, Sijthoff and Noordhoff, Alphen an den Rijn, The Netherlands, 1980.

2 Goodman, L. E., "Contributions of Continuum Mechanics to the Analysis of the Sliding of Unlubricated Solids," *Solid Contact and Lubrication*, eds., Cheng, H. S., and Keer, L. M., AMD—Vol. 39, ASME, New York, 1980.

3 Timoshenko, S. P., and Goodier, J. N., *Theory of Elasticity*, 3rd ed., McGraw-Hill, New York, 1970.

4 Bilby, B. A., and Eshelby, J. D., "Dislocations and the Theory of Fracture," *Fracture*, ed., Liebowitz, H., Vol. I, Academic Press, New York, 1968.

5 Comninou, M., and Dundurs, J., "Some Consequences of the Inequality Conditions in Contact and Crack Problems," *Journal of Elasticity*, Vol. 9, 1979, pp. 71–82.

6 Muskhelishvili, N. I., *Singular Integral Equations*, P. Noordhoff, Groningen, 1953.

Downloaded 01 May 2010 to 171.66.16.249. Redistribution subject to ASME license or copyright; see http://www.asme.org/terms/Terms_Use.cfm

Z. Hashin[2]

Professor and Chairman,
Department of Solid Mechanics,
Materials and Structures,
Tel Aviv University,
Ramat-Aviv,
Tel Aviv 69978, Israel.
Fellow ASME

Fatigue Failure Criteria for Unidirectional Fiber Composites[1]

Three-dimensional fatigue failure criteria for unidirectional fiber composites under states of cyclic stress are established in terms of quadratic stress polynomials which are expressed in terms of the transversely isotropic invariants of the cyclic stress. Two distinct fatigue failure modes, fiber mode, and matrix mode, are modeled separately. Material information needed for the failure criteria are the S-N curves for single stress components. A preliminary approach to incorporate scatter into the failure criteria is presented.

1 Introduction

A fundamental problem concerning the engineering uses of fiber composites is the determination of their resistance to combined states of cyclic stress. This problem is of much greater importance for fiber composites than for metals. For the latter there are many applications where the predominant state of stress is one-dimensional. Then the fatigue resistance for constant amplitude cycling is defined by the S-N curve for this stress component. By contrast, even in the simplest fiber composite laminate the unidirectionally reinforced laminae are in states of combined stress. In many applications it is sufficient to deal with plane stress while in others, however, a full three-dimensional state of stress must be considered. The latter case arises predominantly near holes in laminates and at laminate edges. These are complicated cases which require stress analysis by finite-element methods. Analysis of fatigue failure based on the stresses obtained is not possible without failure criteria for three-dimensional cyclic stress.

In view of the complexity of microstructural damage accumulation during fatigue cycling there is little hope for resolving such problems by micromechanics methods, even for the simpler case of cycling by one stress component only. It therefore appears that at the present time the only realistic approach to such problems is to construct fatigue failure criteria for combined cyclic stress in terms of fatigue failure criteria for simple states of stress, e.g., the S-N curves for single cyclic stress components.

In this sense the problem has first been considered in [1] but only for the case of cyclic plane stress with tensile normal stresses.

Fatigue failure under combined stress has been extensively investigated in the context of metal fatigue. Early work was mostly based on such simple assumptions that principal normal stress, principal shear stress, strain-energy density or distortional strain-energy density associated with the cyclic stresses determine the fatigue failure. A more rational approach to the problem, of curve fitting nature, was introduced in [2]. For review of these and other approaches; see, e.g., [3, 4]. A systematic approach to the problem has recently been given in [5]. This was based on isotropy of the material which is a reasonable assumption for metals. Consequently, the failure criteria were developed in terms of isotropic invariants of the stress tensor. The present case is much more complicated because of the pronounced anisotropy of fiber composites. However, a related approach is still feasible based on the transverse isotropy of the unidirectional material and recognition of its different failure modes. This approach is closely related to a recent method of establishment of static failure criteria, [6].

2 General Considerations

The present discussion is concerned with some general characteristics of phenomenological failure criteria for combined cyclic stress. It is assumed that cyclic stress with average σ_{ij} is statistically homogeneous. Averages are defined over representative volume elements (RVE) and the statistical homogeneity implies that averages are independent of RVE location. It is further assumed that all stresses cycle at same frequency and that the maximum and minimum amplitudes, denoted σ_{ij}^2 and σ_{ij}^1, respectively, of each stress component remain constant during the cycling, Fig. 1. The mean stresses σ_{ij}^m and alternating stresses σ_{ij}^a are defined by

$$\sigma_{ij}^m = \tfrac{1}{2}(\sigma_{ij}^2 + \sigma_{ij}^1)$$
$$\sigma_{ij}^a = \tfrac{1}{2}(\sigma_{ij}^2 - \sigma_{ij}^1) \tag{1}$$

If the stress cycles are sinusoidal then the cyclic state of stress is uniquely defined by the magnitudes of (1) and the phase lags δ_{ij} of

[1] Supported by Naval Air Systems Command and Office of Naval Research under Contract N 00014-78-C-0544 with the University of Pennsylvania.

[2] Also, Adjunct Professor, College of Engineering and Applied Sciences, University of Pennsylvania, Philadelphia, Pa. 19104.

Contributed by the Applied Mechanics Division for publication in the JOURNAL OF APPLIED MECHANICS.

Discussion on this paper should be addressed to the Editorial Department, ASME, United Engineering Center, 345 East 47th Street, New York, N.Y. 10017, and will be accepted until two months after final publication of the paper itself in the JOURNAL OF APPLIED MECHANICS. Manuscript received by ASME Applied Mechanics Division, September, 1980; final revision, January, 1981.

Copyright © 1981 by ASME

Downloaded 01 May 2010 to 171.66.16.249. Redistribution subject to ASME license or copyright; see http://www.asme.org/terms/Terms_Use.cfm

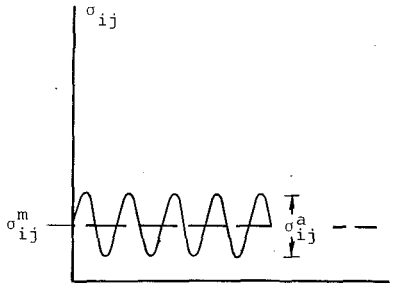


Fig. 1 Cyclic stress

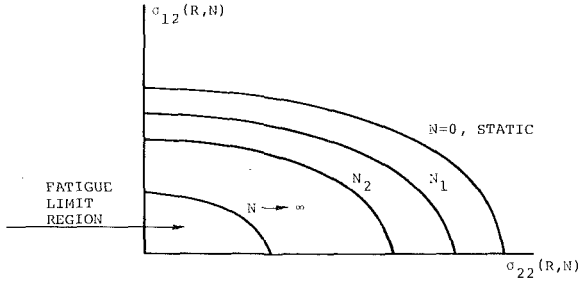


Fig. 2 Fatigue failure surface family

the individual stress components. It is thus assumed that for any given specimen the number of cycles to failure N is determined by the stress amplitudes and the phase lags. In general, therefore, the failure condition is

$$F(\sigma_{ij}^m, \sigma_{ij}^a, \delta_{ij}, N) = 1 \tag{2}$$

It may be noted in passing that the problem may be further complicated by allowing stress cycle amplitudes to change during cycling. An important special case is application of one stress cycle component first and then another. This situation would require cumulative damage theory under combined stress and will not be considered here.

Phase lags are encountered when the stresses are due to a number of cyclic forces which are not in phase. The writer is not aware of consideration in the literature of their influence on failure under combined stress. It will be henceforth assumed that all stresses cycle in phase and thus the δ_{ij} vanish. Then (2) becomes

$$F(\sigma_{ij}^m, \sigma_{ij}^a, N) = 1 \tag{3}$$

It should be noted that sign reversal of any σ_{ij}^a produces a cycling which is half a cycle out of phase with respect to other cycling. Thus this specific out of phase cycling is included in the formulation.

Two important special cases are vanishing alternating stress and vanishing mean stress. In the first case

$$F(\sigma_{ij}^m, 0, N) = F(\sigma_{ij}^m) = 1 \tag{4}$$

which is the static failure criterion, while in the second

$$F(0, \sigma_{ij}^a, N) = 1 \tag{5}$$

which is a failure criterion for reversed cycling.

The situation is now further simplified by assuming that the ratio

$$R_{ij} = \sigma_{ij}^1/\sigma_{ij}^2 \tag{6}$$

has the same value R for all stress component cycles. This is the case when the body remains elastic under cycling since then all stresses vary linearly with the instantaneous values of the applied cyclic forces. In view of (1) and (6), (3) can be written as

$$F[\tfrac{1}{2}\sigma_{ij}^2(1+R), \tfrac{1}{2}\sigma_{ij}^2(1-R), N] = 1 \tag{7}$$

which will from now on be written

$$F(\sigma_{ij}, R, N) = 1 \tag{8}$$

where it is understood that σ_{ij} represent the maximum amplitudes of stress cycles. Since (8) is dependent on the value of R, any single component S-N curve to be used in obtaining information about the failure criterion must have this same R.

It is useful to note that by the definition (6) different cases of cyclic stress are defined by numerical ranges of R as follows:

$R < 0$	tension-compression
$0 \le R < 1$	tension-tension
$1 < R$	compression-compression
$R = -1$	reversed cycling
$R = 1$	static stress

It appears that all previous work on the subject is based on the form (8) thus tacitly incorporating the assumptions which have been previously pointed out. Consideration of failure criteria of type (3) would introduce tremendous additional complexity.

It is conceptually helpful to adopt the usual stress space representation of failure criteria. In such a description (8) for a fixed N is a surface in six-dimensional stress space (or in three-dimensional principal stress space). The surface is the locus of all cyclic stress states (with same frequency and same R ratio) which produce failure after N cycles. When N varies (8) becomes a parametric family of surfaces with parameter N, Fig. 2. The static failure criterion is defined by the surface $N = 0$. At the other extremity are states of cyclic stress which will not produce failure for any practically attainable, theoretically infinite, number of cycles. These define a region in stress space which contains no failure points and may be called the fatigue limit region, Fig. 2.

A state of stress σ_{ij} which produces failure after N cycles may be regarded as a vector in stress space connecting the origin to the appropriate point on the N failure surface. It is to be expected on physical grounds that if all σ_{ij} are increased in fixed mutual ratios the number of cycles to failure will decrease. It follows that the failure surface for N_2 is contained within the failure surface for $N_1 < N_2$. Consequently (8) is a nonintersecting family of surfaces which are all contained within the static failure surface, Fig. 2. (It should be noted that the foregoing reasoning disregards scatter.)

Since infinite failure stresses do not occur in nature the failure surfaces should be closed. However, an infinite failure stress may at times be a convenient mathematical idealization to express the fact that a failure stress for one situation is larger by an order of magnitude than for another. For example: failure under hydrostatic compression as compared to failure under uniaxial stress. A well-known case is the Mises representation of a plasticity yield surface as a cylinder which extends to infinity in octahedral direction.

3 Failure Criteria

For the purpose of establishment of failure criteria under combined cyclic stress it is essential to recognize the different fatigue failure modes of unidirectional fiber composites.

The most common fiber composite consists of polymeric matrix reinforced by glass, graphite, carbon, or boron fibers. When a specimen of such a composite is subjected to tension-tension cycling in fiber direction it is mostly observed that damage accumulates randomly in the form of many small cracks in fiber direction (axial) and normal to the fibers (transverse). The axial cracks are in the matrix while the transverse cracks rupture fibers and matrix. It is the accumulation of the latter which reduces the carrying capacity of the specimen resulting finally in specimen failure with a jagged irregular failure surface, Fig. 3. This kind of failure mode is very different from a metal fatigue failure mode which consists of the initiation and propagation of a single crack.

Downloaded 01 May 2010 to 171.66.16.249. Redistribution subject to ASME license or copyright; see http://www.asme.org/terms/Terms_Use.cfm

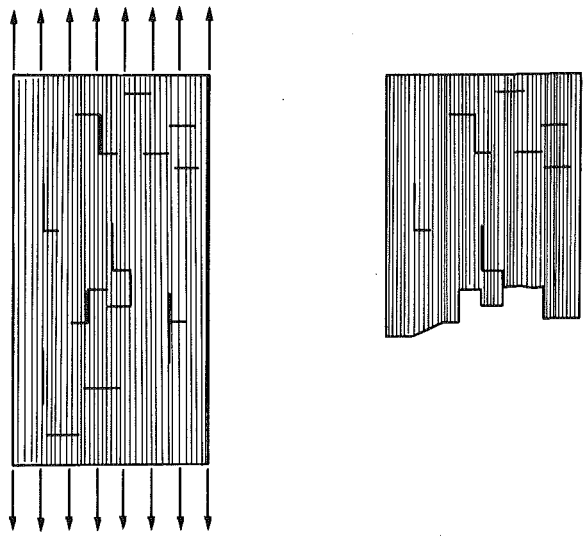


Fig. 3 Fiber failure mode; (*a*) damage accumulation and (*b*) failure

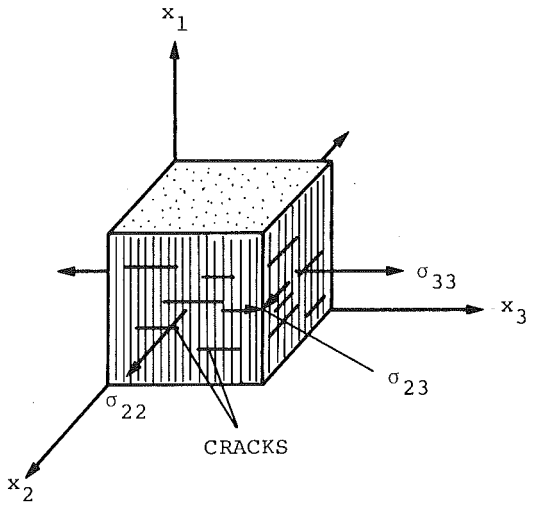


Fig. 4 Transverse plane cracks have no effect on transverse stress

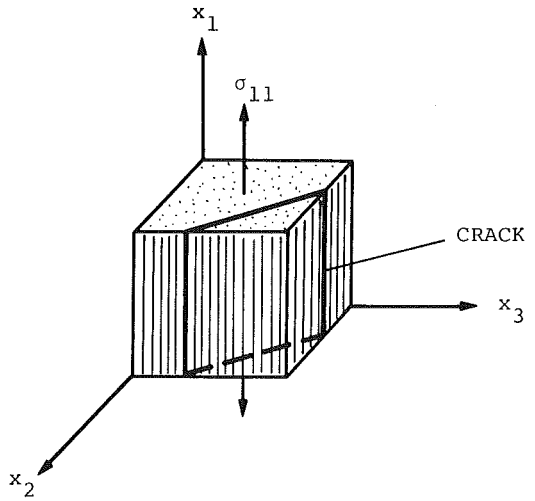


Fig. 5 Axial crack has no effect on axial stress

No doubt transverse crack propagation in a fiber composite is inhibited by the fibers since they are much stiffer and stronger than the matrix. But it must be borne in mind that the transverse properties of the fibers are the ones which are important here. Glass and boron fibers are reasonably isotropic, thus have high transverse stiffness. By contrast carbon and graphite are very anisotropic and have low transverse stiffness—at times as low as twice the polymeric matrix stiffness. Indeed, the damage accumulation mode is mostly observed in the case of glass and boron fibers while for carbon and graphite a sudden transverse crack propagation mode also occurs. The common feature of the two modes is that failure takes place by fiber rupture through transverse cracks. Thus this type of failure will be called *fiber mode.*

Consider a homogeneous anisotropic elastic brittle element which has the elastic symmetry of a unidirectional fiber composite, thus is transversely isotropic, Fig. 4, and contains transverse cracks. Let the element be subjected to a homogeneous stress state σ_{ij}. Evidently, the cracks have no effect on the stress components σ_{22}, σ_{33}, and σ_{23}. Therefore crack criticality depends only on the stress components σ_{11}, σ_{12}, and σ_{13}. It is an open question whether cracks in a fiber composite obey the laws of anisotropic fracture mechanics, but it may be expected that the situation with respect to the effect of the average components σ_{22}, σ_{33}, and σ_{23} will be similar. It will consequently be assumed that the fiber failure mode depends only on the average stress components σ_{11}, σ_{12}, and σ_{13}.

When the cycling is other than tension-tension the situation is less clear. It may be reasoned that for tension-compression cycling the preceding arguments are still acceptable because of the presence of the tension component and thus the assumption of independence of failure of σ_{22}, σ_{33}, and σ_{23} can be retained.

The failure mechanisms in compression-compression cycling are much less understood than for tension-tension. There is sufficient evidence that in static compression in fiber direction the composite fails because of fiber buckling. Approximate stability analyses [7, 8] have indicated that the compressive strength is proportional to the matrix shear modulus. The matter of the failure mechanism in compression-compression cycling is an open question. It is possible that the fibers will buckle at cyclic load much lower than static buckling load because of deterioration of matrix shear modulus due to cycling and/or due to opening of longitudinal cracks at fiber/matrix interfaces. In view of all of these uncertainties it is difficult to form an opinion whether or not transverse cyclic normal and shear stress will affect the longitudinal compressive cyclic failure stress.

The second primary failure mode of a unidirectional composite consists of a planar crack in fiber direction, in between the fibers, and is called the *matrix mode.* This occurs in static and cyclic loading and is best demonstrated with off-axis specimens (see, e.g., [1]). Such cracks occur suddenly without warning and propagate at once through the specimen. This is in contrast to fatigue cracks in metals which grow slowly with the cycling.

In a thin flat specimen in plane stress the fracture surface of the matrix mode is plane perpendicular to the specimen plane. It is to be expected, that for a three-dimensional state of stress the fracture surface will be a plane in fiber direction oriented at some angle in the transverse plane, Fig. 5. The stress σ_{11} has no effect on the propagation of such a crack and it is therefore assumed that it does not enter into the matrix failure criterion.

There arises again the question whether the failure mode described also occurs for tension-compression and compression-compression fatigue. Pending thorough experimental investigation of this question it seems reasonable to expect that the directionality of fibers will lead also in these cases to the same kind of plane matrix failure mode.

Assuming that all stress components cycle in phase with same R ratios the failure criteria are of the form (8). In view of the foregoing discussion of failure modes the fiber and matrix failure criteria have the forms

$$F_f(\sigma_{11}, \sigma_{12}, \sigma_{13}, R, N) = 1 \tag{9a}$$

Downloaded 01 May 2010 to 171.66.16.249. Redistribution subject to ASME license or copyright; see http://www.asme.org/terms/Terms_Use.cfm

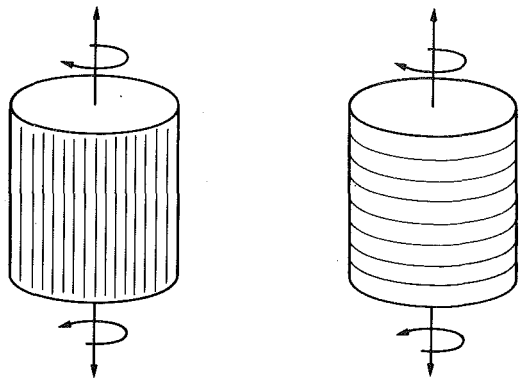


Fig. 6 Thin-walled torsion specimens

$$F_m(\sigma_{22}, \sigma_{33}, \sigma_{12}, \sigma_{23}, \sigma_{13}, R, N) = 1 \tag{9b}$$

where subscripts f and m indicate fiber and matrix modes, respectively, and all stresses are maximum amplitudes. It should be recalled that the reasoning leading to (9a) does not necessarily apply to compression-compression fatigue.

A unidirectional fiber composite is initially transversely isotropic in the macrosense with respect to the x_1-axis in fiber direction. It is not unreasonable to assume that the material will retain this macrosymmetry during the cycling until failure occurs. It follows that the failure criteria must be functions of the transversely isotropic invariants of the cyclic stress tensor and thus can be developed by a method similar to one employed in [6]. The invariants are

$$I_1 = \sigma_{11} \tag{10a}$$

$$I_2 = \sigma_{22} + \sigma_{33} \tag{10b}$$

$$I_3 = \sigma_{23}^2 - \sigma_{22}\sigma_{33} \quad \text{or} \quad \tfrac{1}{4}(\sigma_{22} - \sigma_{33})^2 + \sigma_{23}^2 \tag{10c}$$

$$I_4 = \sigma_{12}^2 + \sigma_{13}^2 \tag{10d}$$

$$I_5 = 2\sigma_{12}\sigma_{23}\sigma_{13} - \sigma_{22}\sigma_{13}^2 - \sigma_{33}\sigma_{12}^2 \tag{10e}$$

The second of (10c) and (10d) are squares of principal shear stresses in transverse and axial planes, respectively. It follows that (9) assume the forms

$$F_f(I_1, I_4, R, N) = 1; \quad F_m(I_2, I_3, I_4, I_5, R, N) = 1 \tag{11}$$

Assuming failure criteria which are quadratic in the stresses (see [6] for discussion of this common approximation) (11) reduce to

$$A_f I_1 + B_f I_1^2 + D_f I_4 = 1$$

$$A_m I_2 + B_m I_2^2 + C_m I_3 + D_m I_4 = 1 \tag{12}$$

where the coefficients are functions of R and N.

Specializing (12) to the cases of pure transverse and axial cyclic shears, σ_{23} and σ_{12} (or σ_{13}), respectively, it follows at once that

$$C_m = 1/\tau_T^2$$

$$D_m = D_f = 1/\tau_A^2 \tag{13}$$

where

$$\tau_T = \tau_T(R, N)$$

$$\tau_A = \tau_A(R, N) \tag{14}$$

are the fatigue shear failure stresses as represented by the S-N curves for these stresses. Similarly, let the S-N curves for cyclic stress σ_{11} in fiber direction and σ_{22} or σ_{33} transverse to fibers be given by

$$\sigma_A = \sigma_A(R, N)$$

$$\sigma_T = \sigma_T(R, N) \tag{15}$$

It follows from (12) and (10) that

$$A_f\sigma_A + B_f\sigma_A^2 = 1$$

$$A_m\sigma_T + B_m\sigma_T^2 = 1 \tag{16}$$

Since this is insufficient information to determine the coefficients it is in general necessary to perform combined cyclic stress failure tests, e.g., cyclic σ_{11}, σ_{12} or cyclic σ_{22}, σ_{12} to obtain necessary additional equations from (12). Such tests can be carried out by combined torsion-axial force cycling of thin-walled cylinders in which the fibers are either in axial or in circumferential direction, Fig. 6. Such tests are, however, quite expensive because of the high cost of the specimens.

It will now be shown that in the case of fully reversed cycling, i.e., mean stresses vanish, thus $R = -1$ for all stress cycles, all of the coefficients in (16) are easily determined. The reason is that a change of sign of reversed cyclic stress cannot affect the lifetime (number of cycles to failure) for it merely displaces all cycles by half a period. Consequently (16) must be valid with same coefficients for $\sigma_A, -\sigma_A$ and $\sigma_T, -\sigma_T$. It follows that

$$A_f = A_m = 0$$

$$B_f = 1/\sigma_A^2$$

$$B_m = 1/\sigma_T^2 \tag{17}$$

Consequently, the failure criteria for reversed cycling are as follows:

Fiber Mode

$$\left(\frac{\sigma_{11}}{\sigma_A}\right)^2 + \frac{\sigma_{12}^2 + \sigma_{13}^2}{\tau_A^2} = 1 \tag{18a}$$

Matrix Mode

$$\left(\frac{\sigma_{22} + \sigma_{33}}{\sigma_T}\right)^2 + \frac{\sigma_{23}^2 - \sigma_{22}\sigma_{33}}{\tau_T^2} + \frac{\sigma_{12}^2 + \sigma_{13}^2}{\tau_A^2} = 1 \tag{18b}$$

where

$$\sigma_A = \sigma_A(-1, N) \quad \sigma_T = \sigma_T(-1, N)$$

$$\tau_A = \tau_A(-1, N) \quad \tau_T = \tau_T(-1, N) \tag{19}$$

are the failure stresses for reversed cycling as given by their S-N curves. For any given state of cyclic stress (18) and (19) should be regarded as equations with unknown N, the number of cycles to failure, also called—the fatigue life. Each of (18) and (19) is solved separately and failure is determined by the criterion which leads to the smaller N. This procedure determines fatigue life and failure mode.

In view of the simplicity of (18) and (19), it is tempting to use them also for the more general case when the mean cyclic stresses do not vanish, in which case the cyclic failure stresses are (14) and (15). It is possible to advance some fracture mechanics arguments that such a presentation would be appropriate for tension-tension cycling, but only testing data under combined stress can form a basis for examination of such an assumption. Given all the uncertainties and the significant scatter of fatigue data the writer believes that the failure criteria (18) and (19) can probably be used on an ad hoc basis for nonreversed cycling. Some evidence for this is known for plane stress and will be shown further in the following.

An essential problem in the definition of the failure criteria is the experimental determination of the failure stresses (14) and (15) or (19). The simplest is σ_A which is obtained from the S-N curve for stress in fiber direction, using flat unidirectional specimens. The σ_T S-N curve can in principle be obtained with similar specimens in which the fibers are in transverse (90°) direction but experience shows that such specimens are not suitable because of the very large scatter of the test data. To obtain the τ_A S-N curve directly it is necessary to employ thin-walled tubes in torsion. Since fatigue testing requires many specimens this is a very expensive procedure. A better alternative is to obtain the σ_T and τ_A S-N curves by use of off-axis specimens. This will be discussed later.

Experimental determination of τ_T is a notoriously difficult problem

Downloaded 01 May 2010 to 171.66.16.249. Redistribution subject to ASME license or copyright; see http://www.asme.org/terms/Terms_Use.cfm

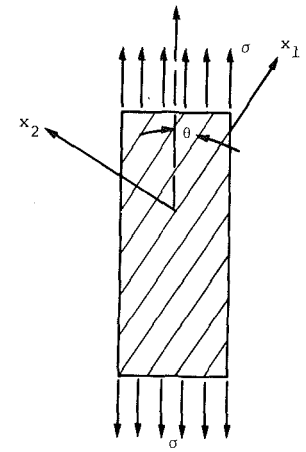
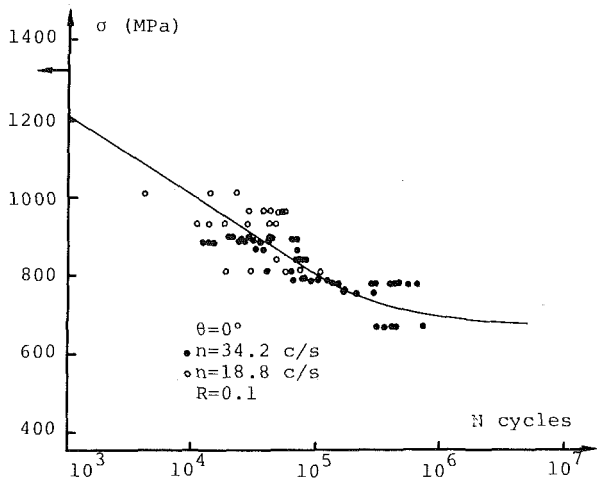


Fig. 7 Off-axis specimen



S-N curve for stress in fiber direction

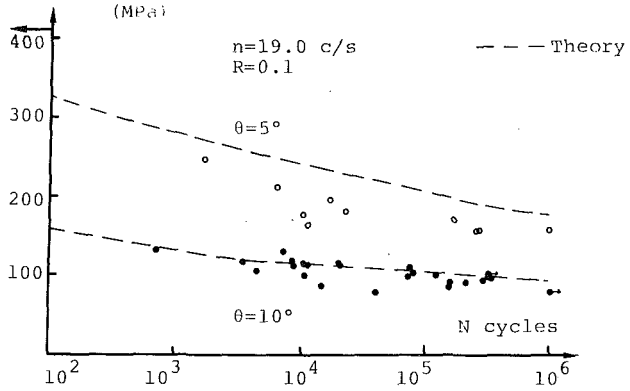


Fig. 8 Test data for off-axis specimens and theory

even for static loading. The primary difficulties are that torsion cannot be used and that flat specimens must be made with fibers normal to their planes. Such specimens can only be produced by transverse cuts through unidirectional specimens and therefore their sizes must be small. One possibility is to employ a new device for producing pure shear, [9], which can be used with very small specimens. In the absence of other information it is reasonable to assume that τ_T is the matrix shear failure stress.

The basic state of stress of a unidirectional lamina within a laminate is uniform plane stress. If x_1 is in fiber direction, x_2 transverse to it in the plane of the lamina and x_3 normal to the lamina then the plane components of stress are σ_{11}, σ_{22}, σ_{12} all others vanish. The failure criteria (18) and (19) reduce to

Fiber Mode

$$\left(\frac{\sigma_{11}}{\sigma_A}\right)^2 + \left(\frac{\sigma_{12}}{\tau_A}\right)^2 + 1 \tag{20a}$$

Matrix Mode

$$\left(\frac{\sigma_{22}}{\sigma_T}\right)^2 + \left(\frac{\sigma_{12}}{\tau_A}\right)^2 = 1 \tag{20b}$$

Failure will occur in the mode which corresponds to lower fatigue lifetime.

Next, there is considered the case of a rectangular flat specimen subjected to cyclic uniform uniaxial stress unidirectionally reinforced at direction θ with respect to specimen axis, Fig. 7. The stresses with respect to the material system of axes x_1, x_2 are

$$\begin{aligned} \sigma_{11} &= \sigma \cos^2\theta \\ \sigma_{22} &= \sigma \sin^2\theta \\ \sigma_{12} &= \sigma \cos\theta \sin\theta \end{aligned} \tag{21}$$

Insertion of (21) into (20) leads to

$$\left(\frac{\sigma}{\sigma_A}\right)^2 \cos^4\theta + \left(\frac{\sigma}{\tau_A}\right)^2 \cos^2\theta \sin^2\theta = 1 \tag{22a}$$

$$\left(\frac{\sigma}{\sigma_T}\right)^2 \sin^4\theta + \left(\frac{\sigma}{\tau_A}\right)^2 \cos^2\theta \sin^2\theta = 1 \tag{22b}$$

When an off-axis specimen is cycled to failure for different stress levels the test data can be summarized by the S-N curve $\sigma(R, N)$. Equations (22) may be regarded as relations among $\sigma(R, N)$, $\sigma_A(R, N)$, $\sigma_T(R, N)$, and $\tau_T(R, N)$. It is easily realized that the fiber failure mode (22a) will apply for angles $0 \le \theta \le \theta_0$ while the matrix mode (22b) will apply for angles $\theta_0 \le \theta \le 90°$. The transition angle θ_0 is defined by simultaneous satisfaction of the failure criteria (22). This defines θ_0 as

$$\tan\theta_0 = \sqrt{\sigma_T/\sigma_A} \tag{23}$$

This angle is generally small for polymer matrix composites since $\sigma_T \ll \sigma_A$.

In order to find the S-N curves $\tau_T(R, N)$ and $\tau_A(R, N)$ it is best to fail the specimen in matrix modes using specimens with several different θ. Using two convenient values θ_1, θ_2, equation (22b) becomes

$$\begin{aligned} \frac{\sin^4\theta_1}{\sigma_T^2(R,N)} + \frac{\cos^2\theta_1 \sin^2\theta_1}{\tau_A^2(R,N)} &= \frac{1}{\sigma^2(R,N)} \\ \frac{\sin^4\theta_2}{\sigma_T^2(R,N)} + \frac{\cos^2\theta_2 \sin^2\theta_2}{\tau_A^2(R,N)} &= \frac{1}{\sigma^2(R,N)} \end{aligned} \tag{24}$$

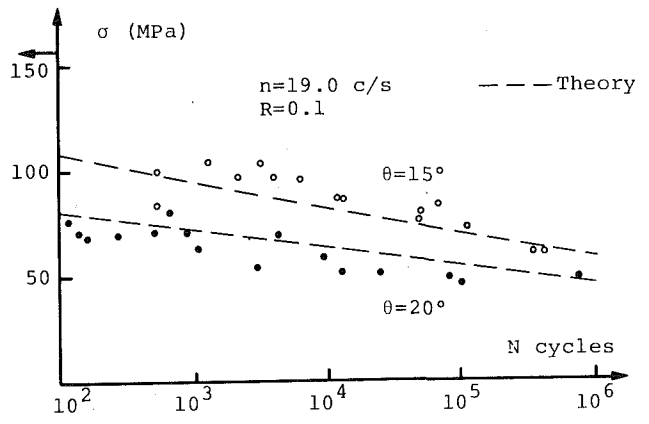
which can be solved for σ_T and τ_A.

Such a procedure has been successfully used, [1], to represent unidirectional glass/epoxy test data. In this work the simple failure criterion $\sigma_{11} = \sigma_A$ was used instead of (20a). Figs. 8–9, taken from [1], show the fit of the failure criteria to the experimental data for fatigue failure tests of glass/epoxy off axis specimens with various angles of reinforcement. It is seen that there is reasonably good agreement with the data although (20) are applicable to reversed cycling and not necessarily for the present case which includes mean stress; R = 0.1.

4 The Problem of Scatter

An intrinsic characteristic of fatigue test data is large scatter. It is not unusual to observe a decade of scatter for fatigue lives associated with same cyclic stress. The role of a deterministic failure criterion

Downloaded 01 May 2010 to 171.66.16.249. Redistribution subject to ASME license or copyright; see http://www.asme.org/terms/Terms_Use.cfm



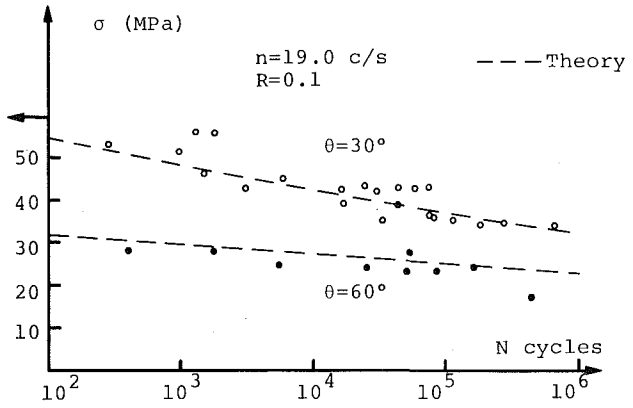


Fig. 9 Test data for off-axis specimens and theory

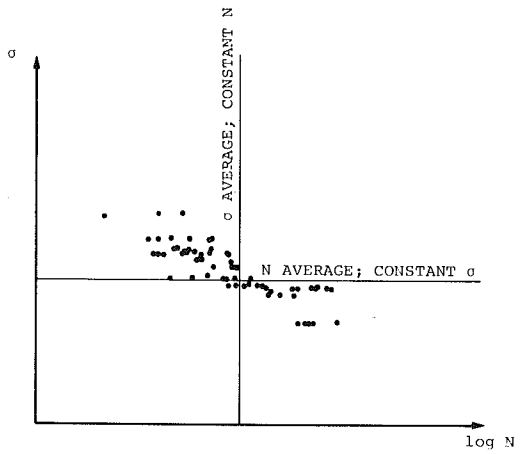


Fig. 10 Test data averaging

vis-a-vis such scattered data is not clear and does not appear to have been explored. It is customary to draw the failure locus on a plot of the test data and to be satisfied when the locus passes "through" the data. A more rational-point of view may be proposed: given the scattered data for simple tests such as expressed by the S-N curves (14) and (15). To predict statistical aspects such as means and variances for failure under combined states of cyclic stress. A possible approach to this problem is given in the following.

It is reasonable to assume that the scatter in lifetimes of specimens which are subjected to identical cyclic stress states is due to the differences in microstructures and consequent different evolution of microfailures in test specimens. Conversely, it is reasonable to assume that if a specimen could be reproduced exactly, in all microdetails, in any number of replicas, the resulting specimens would exhibit no lifetime scatter whatsoever. In what follows such hypothetical specimens will be called *clones* and clones of a certain kind will be called a *clone species.*

Evidently a clone species obeys some deterministic failure criterion which is unknown and can unfortunately not be experimentally investigated since clone specimens are not available. It is however possible to relate any proposed deterministic failure criterion to scattered experimental data in indirect fashion. Suppose that a group of specimens has been tested to failure under identical cyclic stress states. Each specimen is regarded as a member of a hypothetical clone species. It therefore obeys a deterministic failure criterion which results in an expression for failure prediction, involving certain parameters (e.g., one-dimensional cyclic failure stresses (14) and (15)). Since however, such parameters are different for different species, the failure criterion predicts a different lifetime and different states of failure stress for each specimen; i.e., for it's clone species. Therefore the predicted failure stress statistics is determined by the specimen parameter statistics in terms of the analytical expressions or procedures resulting from the failure criterion proposed. Consequently, experimental tests of a failure criterion should consist of comparisons of such quantities as probabilities, means and variances of failure stress components and lifetimes as predicted by the theory and as determined by experiment.

This approach will be illustrated by a simple example. Suppose that the state of stress is plane and the specimens all fail in the matrix mode obeying the failure criterion (20b). Consider stress states for which the ratio σ_{12}/σ_{22} is constant. Thus

$$\sigma_{22} = \sigma s_{22}$$
$$\sigma_{12} = \sigma s_{12} \tag{25}$$

where s_{22} and s_{12} are given nondimensional numbers and σ has dimensions of stress. Let the mth specimen have cyclic failure stresses $\sigma_{Tm}(R, N)$ and $\tau_{Am}(R, N)$. Then from (25) the failure stress $\sigma_m(R, N)$ for this specimen is given by

$$\sigma_m(R, N) = \sigma \left[\left(\frac{s_{22}}{\sigma_{Tm}}\right)^2 + \left(\frac{s_{12}}{\tau_{Am}}\right)^2\right]^{-1/2} \tag{26}$$

which defines the failure stresses (25) for this specimen and for its clone species.

If failure tests with cyclic stress (25) are conducted with M specimens then the mean of σ is given by

$$\langle\sigma\rangle(R, N) = \frac{1}{M}\sum_{m=1}^{M} \sigma_m[\sigma_{Tm}(R, N), \tau_{Am}(R, N)] \tag{27}$$

and the variance v is

$$v(R, N) = \frac{1}{M}\sum_{m=1}^{M} [\sigma_m - \langle\sigma\rangle]^2 \tag{28}$$

The mean (27) defines through (25) the mean failure stresses

$$\langle\sigma_{22}\rangle = \langle\sigma\rangle s_{22}$$
$$\langle\sigma_{12}\rangle = \langle\sigma\rangle s_{12} \tag{29}$$

If this procedure is carried out for different values of s_{22} and s_{12} there is obtained a *mean failure locus* defined by the stresses (29) and the associated variances are given by (28).

Often static failure criteria such as (22) are used with scattered data by substituting for σ_A, σ_T, and τ_A their means obtained by one-dimensional failure experiments. It should be emphasized that the procedure previously outlined is entirely different from such an arbitrary approach. Only when there is little scatter, thus small variance, can these two different approaches be expected to give similar results.

Downloaded 01 May 2010 to 171.66.16.249. Redistribution subject to ASME license or copyright; see http://www.asme.org/terms/Terms_Use.cfm

It must now be pointed out that the present procedure for obtaining mean failure stresses and variances for combined cyclic stress involves a serious *practical* difficulty. It is seen that the averaging in (27) is carried out for constant N. However, fatigue tests are carried out for constant stress with the scatter in associated N since stress can be controlled by a testing machine but N cannot. To carry out the required "vertical" stress average, Fig. 10, it is necessary either to have a very large number of test data or to devise the joint probability function for σ and N. It should, however, be emphasized that the present method is equally valid for static failure criteria where that difficulty does not arise.

The problem of obtaining statistical information for the scattered N associated with given state of cyclic stress also involves serious difficulties. In order to average N (26) must first be solved for N but this is not possible since the functional dependence of σ_m, σ_{Tm}, and τ_{Am} on N is not known for a clone species.

5 Conclusions

The problem of establishment of fatigue failure criteria for unidirectional fiber composite subjected to three-dimensional cyclic stress has been considered in terms of quadratic approximations and on the basis of the transverse isotropy of the material. A fundamental ingredient of the approach is the identification of different fatigue failure modes—fiber and matrix modes, and their individual modeling. It should of course be admitted that mode separation is an idealization. It is entirely possible that mode intersection points on the failure surface represent in actuality small domains in which both modes are operative simultaneously. This situation is reminiscent of corners in plasticity yield surfaces.

A special interesting situation is reversed cycling for in this case the one-dimensional cyclic failure stresses σ_A, σ_T, τ_A, and τ_T as defined by their S-N curves are sufficient information to determine the failure criteria within the frame of the quadratic approximation. For cyclic stresses with any R ratio some testing information for combined stress cycling is needed. It may be that the simple failure criteria for reversed cycling are suitable approximations for this more general case. Some experimental evidence to this effect, for plane-stress cycling, has been presented.

Fatigue failure criteria for three-dimensional cyclic stress are of particular importance for fatigue failure analysis of notched laminates, an important aeronautical engineering problem. The states of stress in the laminae near the notch are three-dimensional and can only be obtained by numerical methods such as finite-element methods. The failure criteria can be used to predict after how many cycles and at which location first failure occurs and in which mode. Location means a specific finite element. If the element fails in the fiber mode then it may be assumed that its axial (in fiber direction) Young's modulus is zero. If it fails in the matrix mode, the transverse Young's modulus and the shear stiffness may be assumed negligible. The numerical analysis can now be continued with the new properties until more elements fail, etc. Such an approach is illustrated by a notched laminate analysis given in [10].

An important additional failure mode which is specific to laminates is delamination, that is separation of the bond between two laminae due to shear and normal stresses. This failure mode has not been considered here since the work is concerned with unidirectional materials.

Finally, the incorporation of the statistics of the failure test data is a most important aspect of fatigue failure criteria. A preliminary approach to this problem has been given here but further treatment to overcome the difficulties mentioned is needed.

References

1 Hashin, Z., and Rotem, A., "A Fatigue Failure Criterion for Fiber-Reinforced Materials," *Journal of Composite Materials*, Vol. 7, 1973, pp. 448–464.

2 Gough, H. J., and Pollard, H. V., "The Strength of Metals Under Combined Alternating Stresses," *Proceedings of the Institute of Mechanical Engineers*, London, Vol. 131, 1935, p. 3.

3 Rotvel, F., "Biaxial Fatigue Tests With Zero Mean Stresses," *International Journal of the Mechanical Sciences*, Vol. 12, 1970, pp. 597–612.

4 McDiarmid, D. L., "A General Criterion for Fatigue Failure Under Multiaxial Stress," *Proceedings of the 2nd International Conference on Pressure Vessel Technology*, Part II, ASME, 1973, pp. 851–862.

5 Hashin, Z., "Fatigue Failure Criteria for Combined Cyclic Stress," *International Journal of Fracture*, Vol. 17, 1981, pp. 101–109.

6 Hashin, Z., "Failure Criteria for Unidirectional Fiber Composites," ASME JOURNAL OF APPLIED MECHANICS, Vol. 47, 1980, pp. 329–334.

7 Rosen, B. W., "Strength of Uniaxial Fibrous Composites," *Mechanics of Composite Materials*, Wendt, F. W., Liebowitz, H., and Perrone, N., eds., Pergamon Press, 1970, pp. 621–651.

8 Schuerch, H., "Prediction of Compressive Strength in Uniaxial Fiber-Metal Matrix Composite Materials," *AIAA Journal*. Vol. 4, 1966, pp. 102–106.

9 Voloshin, A., and Arcan, L., "Failure of Glass-Epoxy Lamina—Fractographic Study," *Journal of Composite Materials*, Vol. 13, 1979, pp. 240–246.

10 Humphreys, E. A., and Rosen, B. W., "Development of a Realistic Stress Analysis of Notched Composite Laminates," NASA CR-159119, May 1979.

Downloaded 01 May 2010 to 171.66.16.249. Redistribution subject to ASME license or copyright; see http://www.asme.org/terms/Terms_Use.cfm

Y. Takao[2]
Research Associate.

M. Taya
Assistant Professor.
Assoc. Mem. ASME

T. W. Chou
Professor.

Department of Mechanical and Aerospace Engineering,
University of Delaware,
Newark, Del. 19711

Stress Field Due to a Cylindrical Inclusion With Constant Axial Eigenstrain in an Infinite Elastic Body[1]

This paper examines an important aspect of the hygrothermal effect in fiber composite materials, the deformation induced by matrix shrinkage. The physical problem is simulated by prescribing a constant axial eigenstrain to the fiber material and the boundary-value problem is then solved in the context of an "inclusion" problem. The complete stress field due to a cylindrical inclusion with constant axial eigenstrain in an infinite elastic body are obtained by representing the eignestrain and displacements in Fourier integral forms. The solutions for stresses are expressed in terms of gamma and hypergeometric functions. The results are also compared with the existing solution of a special case.

1 Introduction

Consider an elastic infinite body containing a subdomain in which the eigenstrains (transformation strains) are given. The elastic moduli of the infinite body and the subdomain are assumed to be the same. The subdomain is called "inclusion." A number of inclusion problems have been solved since the pioneering work of Eshelby [1]. Most of them are for ellipsoidal inclusions (see, for example, [2–5]). The problem of nonellipsoidal inclusions has recently been solved for the cases of cuboidal [6–11] and rectangular [12–13] shapes.

In this paper a cylindrical inclusion problem is examined for the case where a uniform axial eigenstrain is prescribed. General expressions of the stress field inside and out of the cylindrical inclusion are formulated by use of Fourier integrals (see, for example, [14]).

The study of this problem was motivated by the experimental observations of the deformation of fiber composite materials under adverse environmental conditions [15]. Ashbee and coworkers [16, 17], for instance, examined the failure of glass fiber-reinforced plastics due to water damage. They observed dimensional changes of the resin matrix due to water immersion at temperatures of 20, 60, and 100° C. At each temperature, the first response of the composite to diffused water was resin swelling. In hot water, the swelling was then followed by shrinkage. The magnitude of the shrinkage increased as the duration of immersion was prolonged. It is believed that the shrinkage is due to the leaching of low molecular weight materials from the resin. The glass fiber embedded in a shrinking matrix then acted as a rigid indenter. Consequently, conical-shaped cracks were observed at fiber ends and interfacial debonding also occurred. The deformation field induced by a shrinking matrix can be partially simulated by prescribing a constant eigenstrain to the fiber material, which is modeled as a cylindrical inclusion in the present investigation. It is understood that the nonhomogeneity aspect of the inclusion problem is not considered here. The solution of the problem should shed some light on the interfacial failure and crack initiation of fiber composites in hygrothermal environment.

In the following, we first show that the strains induced by the eigenstrain in the cylindrical inclusion can be expressed in terms of triple integrals, which can be reduced to one-dimensional integrals. Then a special numerical integration technique is applied to obtain the stress fields. Finally, numerical results are presented and compared with the analytical ones by Eshelby for a special case.

2 Formulation

In the theoretical model we consider an infinite elastic body containing a cylindrical inclusion as shown in Fig. 1. Let the domain of the infinite body and the cylindrical inclusion be denoted by D and Ω, respectively. Hence the domain of the matrix is $D - \Omega$. The cylinder

[1] This research was supported by the National Science Foundation under Grant No. CME-7918249.

[2] On leave from Kyushu University, Research Institute for Applied Mechanics, Higashi-ku, Fukuoka, Japan.

Contributed by the Applied Mechanics Division for publication in the JOURNAL OF APPLIED MECHANICS.

Discussion on this paper should be addressed to the Editorial Department, ASME, United Engineering Center, 345 East 47th Street, New York, N. Y. 10017, and will be accepted until two months after final publication of the paper itself in the JOURNAL OF APPLIED MECHANICS. Manuscript received by ASME Applied Mechanics Division, March, 1981; final revision, May, 1981.

 Copyright © 1981 by ASME

Downloaded 01 May 2010 to 171.66.16.249. Redistribution subject to ASME license or copyright; see http://www.asme.org/terms/Terms_Use.cfm

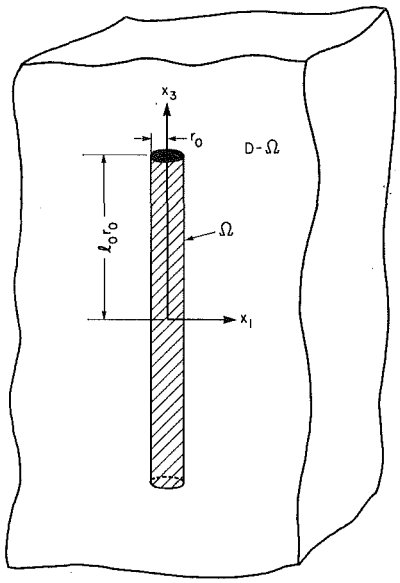


Fig. 1 A calculation model; l_0 is one half of the cylinder length normalized by the radius of the cylinder r_0

direction is taken along the x_3-axis. The eigenstrain ϵ^*_{ij} is so defined that it assumes some value in Ω but vanishes in $D - \Omega$. For the present problem, we prescribe ϵ^*_{ij}in such a way that ϵ^*_{33} is constant and the other components vanish in Ω.

For a prescribed eigenstrain ϵ^*_{ij} in Ω, the resulting stress σ_{ij} is given by [1]

$$\sigma_{ij} = C_{ijkl}\,(\epsilon_{kl} - \epsilon^*_{kl}) \qquad \text{in } D \tag{1}$$

where C_{ijkl} is the elastic stiffness tensor of the matrix and ϵ_{kl} denotes the strain induced by ϵ^*_{kl}. The eigenstrains ϵ^*_{ij} can be expressed in Fourier integral form

$$\epsilon^*_{ij}(\mathbf{x}) = \int\int\int \bar{\epsilon}^*_{ij}\,(\boldsymbol{\xi})\, e^{i\boldsymbol{\xi}\cdot\mathbf{x}} d\boldsymbol{\xi} \tag{2}$$

with

$$\bar{\epsilon}^*_{ij}\,(\boldsymbol{\xi}) = (2\pi)^{-3} \int_{-\infty}^{\infty}\int\int \epsilon^*_{ij}\,(\mathbf{x})\, \bar{e}^{i\boldsymbol{\xi}\cdot\mathbf{x}} d\mathbf{x} \tag{3}$$

where $d\boldsymbol{\xi}$ and $d\mathbf{x}$ designate $d\xi_1\, d\xi_2\, d\xi_3$ and $dx_1\, dx_2\, dx_3$, respectively. Likewise the displacement field u_k is expressed in Fourier integral as

$$u_k(\mathbf{x}) = \int_{-\infty}^{\infty}\int\int \bar{u}_k(\boldsymbol{\xi}) e^{i\boldsymbol{\xi}\cdot\mathbf{x}} d\boldsymbol{\xi} \tag{4}$$

Hence, the displacement gradient is given by

$$u_{k,l}(\mathbf{x}) = \int_{-\infty}^{\infty}\int\int i\xi_l \bar{u}_k(\boldsymbol{\xi}) e^{i\boldsymbol{\xi}\cdot\mathbf{x}} d\boldsymbol{\xi} \tag{5}$$

A substitution of equaions (2) and (5) into equation (1) yields

$$\sigma_{ij}(\mathbf{x}) = C_{ijkl} \int_{-\infty}^{\infty}\int\int \{i\xi_l\, \bar{u}_k(\boldsymbol{\xi}) - \bar{\epsilon}^*_{kl}(\boldsymbol{\xi})\} e^{i\boldsymbol{\xi}\cdot\mathbf{x}} d\boldsymbol{\xi} \tag{6}$$

It should be noted in equation (6) that the symbol i in front of ξ_l and $\boldsymbol{\xi}$ is defined as $\sqrt{-1}$ and is distinguished from the subscript i. $\bar{u}_k$ can be solved by applying stress equilibrium $\sigma_{ij,j} = 0$ and can be expressed in terms of $\bar{\epsilon}^*_{ij}$ (see Chapter 1 of [14] for details). By using the relation between strain ϵ_{ij} and displacement u_i: $\epsilon_{ij}(\mathbf{x}) = (u_{i,j}(\mathbf{x}) + u_{j,i}(\mathbf{x}))/2$ we arrive at

$$\epsilon_{mn}(\mathbf{x}) = (2\pi)^{-3} \int\int\int_{\Omega} \times \int_{-\infty}^{\infty}\int\int \frac{1}{2} C_{ijkl}\, \epsilon^*_{ij}(\mathbf{x}') T_{mnkl}\,(\boldsymbol{\xi}) e^{-i\boldsymbol{\xi}\cdot(\mathbf{x}'-\mathbf{x})} d\boldsymbol{\xi} d\mathbf{x}' \tag{7}$$

where

$$T_{mnkl}(\boldsymbol{\xi}) = \xi_l\, \{\xi_n M_{km}(\boldsymbol{\xi}) + \xi_m M_{kn}(\boldsymbol{\xi})\} \tag{8}$$

with

$$M_{ij}(\boldsymbol{\xi}) = \frac{\delta_{ij}}{\mu\xi^2} - \left(\frac{\lambda+\mu}{\lambda+2\mu}\right)\frac{\xi_i\xi_j}{\mu\xi^4} \tag{9}$$

In the foregoing equation λ and μ are the Lamé constants and $\xi^2 = \xi_k\xi_k$. Let us consider the following integral which is the portion of equation (7) related to $\mathbf{x}'$

$$A_{33}(\boldsymbol{\xi}) = \int_{\Omega}\int\int \epsilon^*_{33}(\mathbf{x}') e^{-i\boldsymbol{\xi}\cdot\mathbf{x}'} d\mathbf{x}' \tag{10}$$

Without losing generality we take $\epsilon^*_{33}(\mathbf{x}') = 1$ in Ω and obtain

$$A_{33}(\boldsymbol{\xi}) = -\frac{2\pi}{i\xi_3}\{e^{-i\xi_3 l_0} - e^{i\xi_3 l_0}\}\frac{J_1(\sqrt{\xi_1^2+\xi_2^2})}{\sqrt{\xi_1^2+\xi_2^2}} \tag{11}$$

where l_0 is the ratio of one half of the cylinder length to the cylinder radius. In the aforementioned derivation, the following relations [18] have been used:

$$J_0(r) = \frac{1}{2\pi}\int_{\alpha}^{2\pi+\alpha} e^{-ir\sin\theta} d\theta \tag{12}$$

$$\frac{r}{\beta} J_1(\beta r) = \int r\, J_0(\beta r)\, dr \tag{13}$$

The variables with dimension of length are all normalized by the radius of the cylinder. Hence the actual length of the cylinder becomes $2l_0r_0$ where r_0 is the radius of the cylinder (see Fig. 1). In the foregoing equations J_i is the first kind of Bessel function of the ith order.

We substitute equations (8), (9), and (11) into (7) to obtain

$$\epsilon_{mn}(\mathbf{x}) = (2\pi)^{-2} \int_{-\infty}^{\infty}\int\int \frac{1}{2} C_{kl33} \frac{1}{(-i\xi_3)} \times \{e^{-i\xi_3 l_0} - e^{i\xi_3 l_0}\}\frac{J_1(\sqrt{\xi_1^2+\xi_2^2})}{\sqrt{\xi_1^2+\xi_2^2}} \cdot \left[\xi_l\xi_n\left\{\frac{\delta_{km}}{\mu\xi^2} - \left(\frac{\lambda+\mu}{\lambda+2\mu}\right)\frac{\xi_k\xi_m}{\mu\xi^4}\right\} + \xi_l\xi_m\left\{\frac{\delta_{kn}}{\mu\xi^2} - \left(\frac{\lambda+\mu}{\lambda+2\mu}\right)\frac{\xi_k\xi_n}{\mu\xi^4}\right\}\right] \cdot e^{i\boldsymbol{\xi}\cdot\mathbf{x}} d\boldsymbol{\xi} \tag{14}$$

In order to express the strains in cylindrical coordinates, we take x_1, x_2, and x_3-axes along the r, θ, and z-directions, respectively, and set $x_2 = 0$, $\xi_1 = R\cos\theta$ and $\xi_2 = R\sin\theta$ in equation (14) to obtain

$$\epsilon_{rr}(\mathbf{x}) = (2\pi)^{-2} \int_0^{\infty}\int_{-\infty}^{\infty}\int_0^{2\pi} B(\xi_3,R)\left\{\frac{\lambda}{(\lambda+2\mu)}\frac{1}{(R^2+\xi_3^2)} - 2\left(\frac{\lambda+\mu}{\lambda+2\mu}\right)\frac{\xi_2^2}{(R^2+\xi_3^2)^2}\right\} \cdot R^2\cos^2\theta\, e^{i(x_1 R\cos\theta + x_3\xi_3)} d\theta\, d\xi_3 dR \tag{15}$$

$$\epsilon_{\theta\theta}(\mathbf{x}) = (2\pi)^{-2} \int_0^{\infty}\int_{-\infty}^{\infty}\int_0^{2\pi} B(\xi_3,R)\left\{\frac{\lambda}{(\lambda+2\mu)}\frac{1}{(R^2+\xi_3^2)} - 2\left(\frac{\lambda+\mu}{\lambda+2\mu}\right)\frac{\xi_3^2}{(R^2+\xi_3^2)^2}\right\} \cdot R^2\sin^2\theta\, e^{i(x_1 R\cos\theta + x_3\xi_3)} d\theta\, d\xi_3\, dR \tag{16}$$

$$\epsilon_{zz}(\mathbf{x}) = (2\pi)^{-2} \int_0^{\infty}\int_{-\infty}^{\infty}\int_0^{2\pi} B(\xi_3,R)\left\{\left(\frac{3\lambda+4\mu}{\lambda+2\mu}\right)\frac{1}{(R^2+\xi_3^2)} - 2\left(\frac{\lambda+\mu}{\lambda+2\mu}\right)\frac{\xi_3^2}{(R^2+\xi_3^2)^2}\right\} \times \xi_3^2\, e^{i(x_1 R\cos\theta + x_3\xi_3)} d\theta\, d\xi_3\, dR \tag{17}$$

$$\epsilon_{rz}(\mathbf{x}) = (2\pi)^{-2} \int_0^{\infty}\int_{-\infty}^{\infty}\int_0^{2\pi} B(\xi_3,R)\, 2\left(\frac{\lambda+\mu}{\lambda+2\mu}\right)\left\{\frac{1}{(R^2+\xi_3^2)} - \frac{\xi_3^2}{(R^2+\xi_3^2)^2}\right\} \cdot R\xi_3\cos\theta\, e^{i(x_1 R\cos\theta + x_3\xi_3)} d\theta\, d\xi_3\, dR \tag{18}$$

where

Downloaded 01 May 2010 to 171.66.16.249. Redistribution subject to ASME license or copyright; see http://www.asme.org/terms/Terms_Use.cfm

$$B(\xi_3,R) = \frac{1}{-i\xi_3}\{e^{-i\xi_3 l_0} - e^{i\xi_3 l_0}\} J_1(R) \tag{19}$$

$\epsilon_{r\theta}$ and $\epsilon_{\theta z}$ vanish due to axial-symmetry.

Next, we reduce the triple integrals in equations (15)–(18) to single integrals with respect to R. To this end the following relations are used:

$$\begin{aligned}
&\int_0^{2\pi} \cos^2\theta\, e^{ix_1R\cos\theta} d\theta = \pi\{J_0(x_1R) - J_2(x_1R)\}\\
&\int_0^{2\pi} \sin^2\theta\, e^{ix_1R\cos\theta} d\theta = \pi\{J_0(x_1R) + J_2(x_1R)\}\\
&\int_0^{2\pi} e^{ix_1R\cos\theta} d\theta = 2\pi J_0(x_1R)\\
&\int_0^{2\pi} \cos\theta\, e^{i(x_1R\cos\theta)} d\theta = 2\pi i J_1(x_1R)
\end{aligned} \tag{20}$$

and

$$\begin{aligned}
&\int_{-\infty}^{\infty} \frac{e^{ia\xi}}{\xi} d\xi = i\pi\,\mathrm{sgn}\,(a)\\
&\int_{-\infty}^{\infty} \frac{\xi e^{ia\xi}}{(\xi^2+R^2)} d\xi = i\pi\, e^{-|a|R}\,\mathrm{sgn}\,(a)\\
&\int_{-\infty}^{\infty} \frac{e^{ia\xi}}{(\xi^2+R^2)^2} d\xi = \frac{\pi}{2R^3}(1+|a|R\, e^{-|a|R})\\
&\int_{-\infty}^{\infty} \frac{\xi e^{ia\xi}}{(\xi^2+R^2)^2} d\xi = i\frac{\pi|a|}{2R} e^{-|a|R}\,\mathrm{sgn}\,(a)
\end{aligned} \tag{21}$$

where

$$\mathrm{sgn}\,(a) = \begin{cases} 1 & \text{for } a>0\\ 0 & \text{for } a=0\\ -1 & \text{for } a<0 \end{cases} \tag{22}$$

Equations (20) can be derived from the definition of Bessel function [18]

$$J_n(z) = \frac{1}{\pi i^n}\int_0^{\pi} e^{iz\cos\theta}\cos n\theta\, d\theta \tag{23}$$

and equations (21) are recapitulated from [18].

Substituting equations (20) and (21) into equations (15)–(18), the strain components are obtained in terms of single integrals

$$\begin{aligned}
\epsilon_{rr} = \int_0^{\infty} \Bigg[&\Bigg\{\frac{\lambda}{4(\lambda+2\mu)}(e^{-|x_3-l_0|R}-1)\\
&+\frac{1}{4}\left(\frac{\lambda+\mu}{\lambda+2\mu}\right)|x_3-l_0|\, e^{-|x_3-l_0|R}R\Bigg\} J_1(R)\{J_0(x_1R)\\
&- J_2(x_1R)\}\,\mathrm{sgn}\,(x_3-l_0) - \Bigg\{\frac{\lambda}{4(\lambda+2\mu)}(e^{-|x_3+l_0|R}-1)\\
&+\frac{1}{4}\left(\frac{\lambda+\mu}{\lambda+2\mu}\right)|x_3+l_0|\, e^{-|x_3+l_0|R}R\Bigg\}\\
&\times J_1(R)\{J_0(x_1R) - J_2(x_1R)\}\,\mathrm{sgn}\,(x_3+l_0)\Bigg] dR
\end{aligned} \tag{24}$$

$$\begin{aligned}
\epsilon_{zz} = \int_0^{\infty} \Bigg[&-\frac{1}{2}\Bigg\{e^{-|x_3-l_0|R}\\
&+\left(\frac{\lambda+\mu}{\lambda+2\mu}\right)|x_3-l_0|\, e^{-|x_3-l_0|R}R\Bigg\} J_1(R)J_0(x_1R)\,\mathrm{sgn}\,(x_3-l_0)\\
&+\frac{1}{2}\Bigg\{e^{-|x_3+l_0|R}+\left(\frac{\lambda+\mu}{\lambda+2\mu}\right)|x_3+l_0|\, e^{-|x_3+l_0|R}R\Bigg\}\\
&\times J_1(R)J_0(x_1R)\,\mathrm{sgn}\,(x_3+l_0)\Bigg] dR
\end{aligned} \tag{25}$$

$$\begin{aligned}
\epsilon_{rz} = \int_0^{\infty} \Bigg[&-\frac{1}{2}\left(\frac{\lambda+\mu}{\lambda+2\mu}\right)\{e^{-|x_3-l_0R|} + |x_3-l_0|\\
&\times e^{-|x_3-l_0|R}R\} J_1(R)J_1(x_1R) + \frac{1}{2}\left(\frac{\lambda+\mu}{\lambda+2\mu}\right)\{e^{-|x_3+l_0|R}\\
&+ |x_3+l_0|\, e^{-|x_3+l_0|R}R\} J_1(R)J_1(x_1R)\Bigg] dR
\end{aligned} \tag{26}$$

The expression of $\epsilon_{\theta\theta}$ is the same as that of ϵ_{rr} except that the negative sign in front of $J_2(x_1R)$ should be replaced by the positive sign.

For the case of $|x_3 \pm l_0| \neq 0$, the equations (24)–(26) can be simplified by the use of the following relation [18]:

$$\begin{aligned}
&\int_0^{\infty} R^{\rho-1} e^{-\alpha R} J_n(\beta R)\, J_\nu(\gamma R)\, dR\\
&= \frac{\beta^n\gamma^\nu}{\Gamma(\nu+1)}\cdot 2^{-\nu-n}\alpha^{-\rho-n-\nu}\sum_{m=0}^{\infty}\frac{\Gamma(\rho+n+\nu+2m)}{m!\,\Gamma(n+m+1)}\\
&\quad\times F\left(-m,-n-m;\nu+1;\frac{\gamma^2}{\beta^2}\right)\left(-\frac{\beta^2}{4\alpha^2}\right)^m
\end{aligned} \tag{27}$$

where the previous equation is valid for $R_e(\rho+n+\nu)>0$ and $R_e(\alpha \pm i\beta \pm i\gamma)>0$. Γ and F in equation (27) denote gamma and hypergeometric function, respectively.

For the case of $|x_3 \pm l_0| = 0$, equation (27) cannot be used for the evaluation of the terms containing $e^{-|x_3 \pm l_0|R}$. However, those terms become zero in equations (24) and (25) since sgn $|x_3 \pm l_0| = 0$. For equation (26), the following relation [18] is useful, for the case of $|x_3 \pm l_0| = 0$,

$$\begin{aligned}
&\int_0^{\infty} J_1(R)J_1(x_1R)dR = \frac{\sqrt{\pi}\,x_1}{2(1+x_1^2)^{3/2}}\\
&\times\left[1+\frac{\frac{3}{4}\cdot\frac{5}{4}}{2\cdot 1!}\frac{4x_1^2}{(1+x_1^2)^2}+\frac{\frac{3}{4}\left(\frac{3}{4}+1\right)\frac{5}{4}\left(\frac{5}{4}+1\right)}{2\cdot 3\cdot 2!}\left\{\frac{4x_1^2}{(1+x_1^2)^2}\right\}^2+\cdots\right]\\
&= \frac{\sqrt{\pi}\,x_1}{2(1+x_1^2)^{3/2}} F\,(3/4, 5/4; 2; 4x_1^2(1+x_1^2)^{-2})
\end{aligned} \tag{28}$$

Furthermore, the following relations also have been used for the evaluation of equations (24) and (25)

$$\int_0^{\infty} J_1(R)J_0(x_1R) = \begin{cases} 1 & 0\le x_1<1\\ 0.5 & \text{for } x_1=0\\ 0 & x_1>1 \end{cases}$$

$$\int_0^{\infty} J_1(R)J_2(x_1R) = \begin{cases} 0 & 0\le x_1<1\\ 0.5 & \text{for } x_1=0\\ x_1^{-2} & x_1>1 \end{cases} \tag{29}$$

Finally, by the use of equations (27)–(29), the strain (equations (24)–(25)) and stress (equation (1)) components can be computed.

It should be noted that when the value of x_1 is large or that of $|x_3 \pm l_0|$ is small, the convergence of the series on the right-hand side of equation (27) becomes very slow. A special numerical integration technique has been adopted to evaluate the left-hand side of equation (27) directly. The detail of this technique is given in the Appendix. The stress and strain field along the cylindrical axis ($x_1 = 0$) can be obtained in closed form as

$$\begin{aligned}
\epsilon_{\theta\theta} = \epsilon_{rr} = &\left[\frac{-\lambda}{4(\lambda+2\mu)}\frac{(x_3-l_0)}{((x_3-l_0)^2+1)^{1/2}}\right.\\
&\left.+\frac{(\lambda+\mu)}{4(\lambda+2\mu)}\frac{(x_3-l_0)}{((x_3-l_0)^2+1)^{3/2}}\right]\\
&-\left[\frac{-\lambda}{4(\lambda+2\mu)}\frac{(x_3+l_0)}{((x_3+l_0)^2+1)^{1/2}}+\frac{(\lambda+\mu)}{4(\lambda+2\mu)}\frac{(x_3+l_0)}{((x_3+l_0)^2+1)^{3/2}}\right]
\end{aligned} \tag{30}$$

Downloaded 01 May 2010 to 171.66.16.249. Redistribution subject to ASME license or copyright; see http://www.asme.org/terms/Terms_Use.cfm

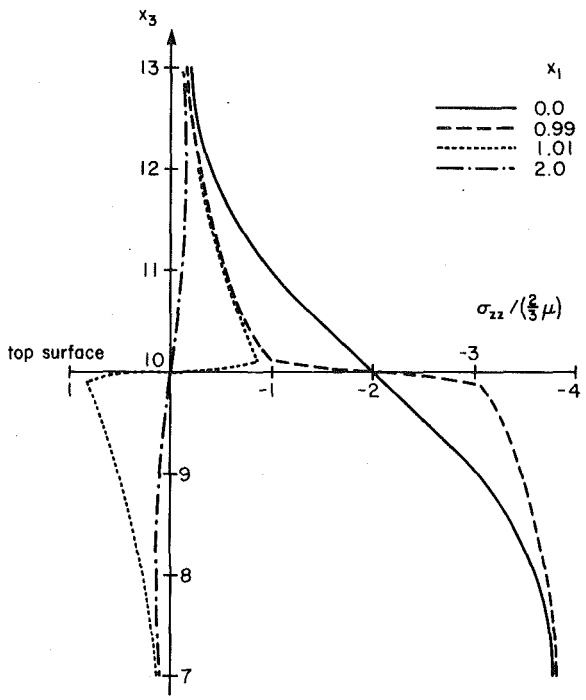


Fig. 2 The distributions of σ_{zz} normalized by $2\mu/3$ along the longitudinal direction

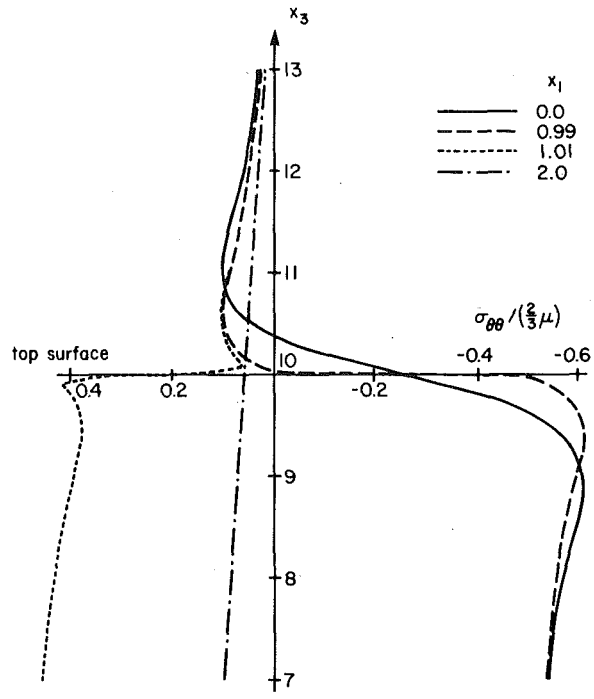


Fig. 4 The distributions of $\sigma_{\theta\theta}$ normalized by $2\mu/3$ along the longitudinal direction

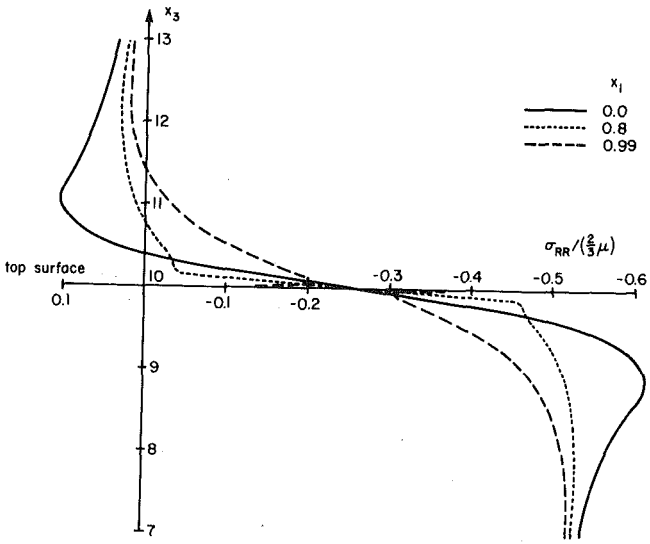


Fig. 3 The distributions of σ_{rr} normalized by $2\mu/3$ along the longitudinal direction

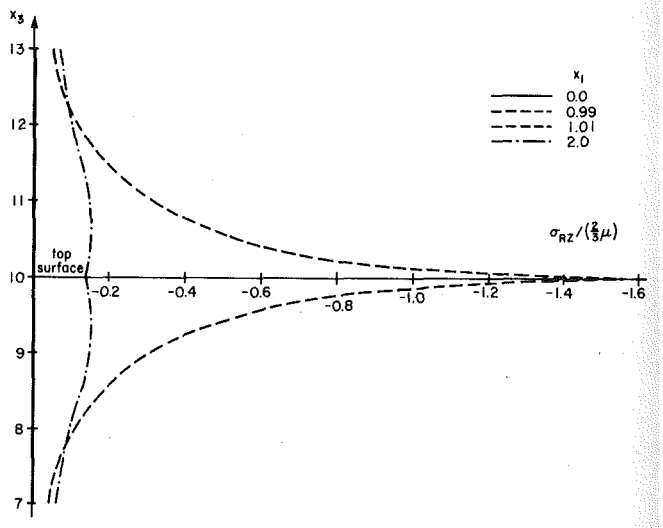


Fig 5 The distributions of σ_{rz} normalized by $2\mu/3$ along the longitudinal direction

$$\epsilon_{zz} = \left[\frac{1}{2}\frac{(x_3 - l_0)}{((x_3 - l_0)^2 + 1)^{1/2}} - \frac{(\lambda + \mu)}{2(\lambda + 2\mu)}\frac{(x_3 - l_0)}{((x_3 - l_0)^2 + 1)^{3/2}}\right] - \left[\frac{1}{2}\frac{(x_3 + l_0)}{((x_3 + l_0)^2 + 1)^{1/2}} - \frac{(\lambda + \mu)}{2(\lambda + 2\mu)}\frac{(x_3 + l_0)}{((x_3 + l_0)^2 + 1)^{3/2}}\right] - \frac{1}{2}[\text{sgn}\,(x_3 - l_0) - \text{sgn}\,(x_3 + l_0)] \quad (31)$$

$$\epsilon_{rz} = 0 \quad (32)$$

3 Numerical Results

The Poisson's ratio of the matrix (ν) and the aspect ratio of the cylinder ($l_0 r_0/r_0$) are assumed to be 0.25 and 10.0, respectively, throughout the computation. Note that $\lambda = \mu$ for $\nu = 0.25$. Due to the axial-symmetry, the domain of numerical computation is taken as $0 \le x_1 \le 2.0$ and $7 \le x_3 \le 13$. In the domain outside $x_1 = 2.0$ and $x_3 = 13.0$, the numerical values of stresses become almost constant. (It should be noted that $x_1 = 1.0$ corresponds to the side surface and $x_3 = 10.0$ to the top surface of the cylinder.)

The distributions of σ_{zz}, σ_{rr}, $\sigma_{\theta\theta}$, and σ_{rz} along the direction parallel to the x_3-axis are plotted in Figs. 2–5, respectively. These stresses are normalized by $2\mu/3$. It should be noted in Fig. 5 that the distributions of shear stress at $x_1 = 0.99$ and $x_1 = 1.01$ almost coincide, hence they are represented by one broken curve. The numerical results show that σ_{rz} (Fig.5) is unbounded as x_1 approaches 1, i.e., at the corner of the cylinder ($x_1 = 1$ and $x_3 = 10$). Figs. 6(a–c) show the radial distributions of σ_{zz}, σ_{rr}, and $\sigma_{\theta\theta}$, respectively. Three radial sections, i.e., $x_3 = 0$, 9.5, and 10.5 have been used. It follows from Fig. 6 that σ_{rr} is continuous across the side surface, while σ_{zz} and $\sigma_{\theta\theta}$ are discontinuous

Downloaded 01 May 2010 to 171.66.16.249. Redistribution subject to ASME license or copyright; see http://www.asme.org/terms/Terms_Use.cfm

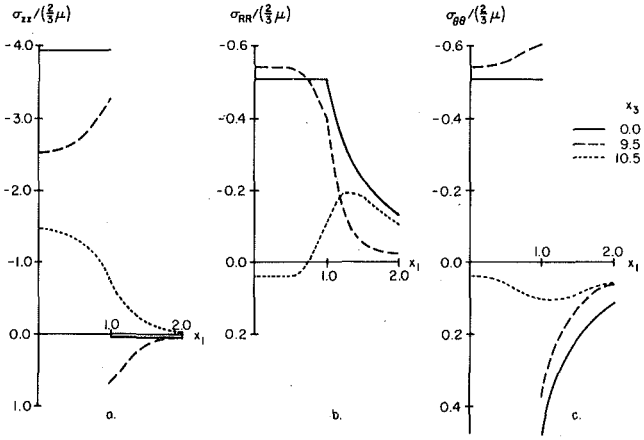


Fig. 6 The distributions of stresses σ_{zz} (a), σ_{rr} (b), and $\sigma_{\theta\theta}$ (c) along the radial direction; the stresses are normalized by $2\mu/3$

across the side surface. By defining $[\sigma] = \sigma_{\text{out}} - \sigma_{\text{in}}$ with subscripts "out" and "in" indicating $r = 1.0^+$ and 1.0^-, respectively, the numerical results show $[\sigma_{zz}] \cong 4.0$ and $[\sigma_{\theta\theta}] \cong 1.0$.

4 Discussions

Five major points are discussed as follows:

4.1 Comparison With Eshelby's Solution. It is expected that the values of strains on the plane of $x_3 = 0$ in a long cylinder should approach those obtained by Eshelby's inclusion method for the ellipsoid elongated along the x_3-axis. For the choice of $\nu = 0.25$ and $\epsilon^*_{33} = 1.0$, the analytical results by Eshelby's inclusion method for an infinitely long ellipsoid give $\epsilon_{zz} = 0.0$ and $\epsilon_{rr} = 0.16$. The present numerical results when l_0 is set as ∞ in equations (30) and (31) coincide exactly with the Eshelby's results.

4.2 Stress Jumps Across the Matrix-Inclusion Interface. The stress jumps across the matrix-inclusion interface is given by [2, 19]

$$[\sigma_{pq}] = C_{pqmn}\{-C_{klij}\epsilon^*_{ij}n_l n_n M_{km}(\mathbf{n}) + \epsilon^*_{mn}\} \tag{33}$$

Here, $[\sigma_{pq}]$ is defined in the previous section, and $M_{km}(\mathbf{n})$ is given by equation (8) with $\boldsymbol{\xi}$ replaced by $\mathbf{n}$ and $\mathbf{n}$ is the unit vector normal to the interface with the positive direction being toward the outside of the inclusion. Let the side and top surfaces be denoted by surfaces A and B, respectively. Then

$$\begin{aligned} \mathbf{n}_A &= (0, 0, 1) \\ \mathbf{n}_B &= (1, 0, 0) \end{aligned} \tag{34}$$

For a given ϵ^*_{ij}, i.e., $\epsilon^*_{33} = 1.0$ and other components being zero, the jumps in stresses across the interface are obtained as

$$\begin{aligned} [\sigma_{pq}]_A &= 0 \\ [\sigma_{rr}]_B &= 0 \\ [\sigma_{\theta\theta}]_B &= 2\lambda\mu/(\lambda + 2\mu) \\ [\sigma_{zz}]_B &= 4\mu(\lambda + \mu)/(\lambda + 2\mu) \\ [\sigma_{rz}]_B &= 0 \end{aligned} \tag{35}$$

For $\nu = 0.25$ and by normalizing the stresses by $2\mu/3$, equations (35) yield

$$\begin{aligned} [\sigma_{\theta\theta}]_B &= 1.0 \\ [\sigma_{zz}]_B &= 4.0 \end{aligned} \tag{36}$$

Equation (36) agrees well with our numerical results given in Figs. 6.

4.3 Normal Stresses at $x_3 = l_0$. The normal stresses at $x_3 = l_0$ and $x_1 > 1$ can be obtained from equations (1), (24), and (25) in closed forms:

$$\begin{aligned} \sigma_{zz} &= 0 \\ \sigma_{rr} &= -\frac{2\mu}{3}\cdot\frac{1}{4x_1{}^2} \\ \sigma_{\theta\theta} &= \frac{2\mu}{3}\cdot\frac{1}{4x_1{}^2} \end{aligned} \tag{37}$$

The analytical results of equation (37) for σ_{rr} $(= -\sigma_{\theta\theta})$ at $x_3 = l_0$ and $x_1 > 1$ as well as the corresponding numerical values are given in Table 1 where all the stresses are normalized by $2\mu/3$. It follows from Table 1 that a good agreement between the analytical and numerical results has been obtained.

The analytical results for σ_{zz}, σ_{rr} $(= \sigma_{\theta\theta})$ for the domain of $x_3 = l_0$ and $0 \le x_1 < 1$ can be obtained as follows:

$$\begin{aligned} \sigma_{zz} &= -\frac{2\mu}{3}\cdot 2 \\ \sigma_{rr} = \sigma_{\theta\theta} &= -\frac{2\mu}{3}\cdot\frac{1}{4} \end{aligned} \tag{38}$$

In the foregoing derivation, the condition of stress continuity across the top surface was used (see equation (35)). The numerical results corresponding to equation (38) are depicted in Figs. 2–4 and they also agree well with the analytical ones.

4.4 Singularity of Shear Strain ϵ_{rz} at the Corner of the Cylinder. In order to study the behavior of ϵ_{rz} at the corner of the cylinder, we first substitute $x_3 = l_0$ into equation (26). Then the dominant term in ϵ_{rz} is the first term

$$\epsilon_{rz} \cong -\frac{(\lambda + \mu)}{2(\lambda + 2\mu)}\int_0^\infty J_1(R)J_1(x_1R)\,dR \tag{39}$$

The integral in equation (39) has been expressed in the hypergeometric function $F(\alpha, \beta; \gamma; z)$ (see equation (28)), which diverges when $|z| = 1$ [18], i.e., $x_1 = 1$ since $\text{Re}(\alpha + \beta - \gamma) = 0$. Thus the shear strain ϵ_{rz} and hence, stress σ_{rz} diverges at $x_3 = l_0$ and $x_1 = 1$. Next, we examine the nature of the singularity of ϵ_{rz}. To this end, the integral domain, $0 \sim \infty$ in equation (39) is divided into two domains, $0 \sim R^*$ and $R^* \sim \infty$ where the value of R^* is large but remains finite. For $R > R^*$ the Bessel function $J_\nu(R)$ is approximately equal to $\sqrt{2/(\pi R)} \times \cos(R - (2\pi + 1)\pi/4)$. Consequently ϵ_{rz} can be approximated as:

$$\epsilon_{rz} \cong \frac{(\lambda + \mu)}{2\pi(\lambda + 2\mu)}\{-\text{si}((x_1 + 1)R^*) + \text{ci}((x_1 - 1)R^*)\} \tag{40}$$

where si and ci are sine and cosine integral functions, respectively. As $x \to 0$, $\text{si}(x)$ remains finite, but $\text{ci}(x)$ approaches $\ln|x|$. Thus ϵ_{rz}, as $x_1 \to 0$, is further approximated by

Table 1

x_1	1.01	1.05	1.1	1.2	1.3	1.5	2.0
Numerical results $\sigma_{rr}/(2\mu/3)$	−0.246	−0.228	−0.208	−0.175	−0.149	−0.112	−0.063
Numerical results $\sigma_{\theta\theta}/(2\mu/3)$	0.244	0.226	0.206	0.173	0.147	0.110	0.062
Analytical results $\sigma_{\theta\theta}/(2\mu/3) = -\sigma_{rr}/(2\mu/3)$	0.225	0.227	0.207	0.174	0.148	0.111	0.063

Downloaded 01 May 2010 to 171.66.16.249. Redistribution subject to ASME license or copyright; see http://www.asme.org/terms/Terms_Use.cfm

$$\epsilon_{rz} \cong \frac{(\lambda + \mu)}{2\pi(\lambda + 2\mu)} \ln |x_1 - 1| \tag{41}$$

Therefore, both the shear strain ϵ_{rz} and stress σ_{rz} have the logarithmic singularity at $x_3 = l_0$ and $x_1 = 1$.

4.5 The Possible Direction of Crack Initiation at the Corner of the Cylinder. Due to the singularity of σ_{rz} at the corner, it is possible that a crack may initiate at the corner. Then the question arises as to along which direction this corner crack will propagate. There are two possible directions: (*i*) along the matrix-inclusion interface and (*ii*) along some plane extending into the matrix. It is clear from Fig. 6(*b*) that σ_{rr} is in compression along the interface near the corner. Hence the corner crack is less likely to propagate along the interface. On the other hand, the normal stresses near the corner are finite and the direction of the maximum principal stress direction is at an angle of 135° with respect to the positive x_1-axis. Moreover, the magnitude of the maximum principal stress approaches to infinity as x_3 and x_1 approach to l_0 and 1, respectively. It follows from the foregoing reasoning that the corner crack is more likely to propagate along the 45° line to the positive x_1-axis. Hence the shape of a crack so initiated resembles an inverted cone emanated from the circular edge of the cylindrical inclusion. If the difference in the stiffness of the matrix and inclusion is neglected, the previously mentioned results can be used to simulate the experimental observations of Ashbee, et al. [17]. Their work showed that for glass/resin composites immersed in hot water, resin swelling first occurred due to the presence of diffused water. This is then followed by matrix shrinkage as a result of the leaching of low molecular weight materials from the resin. The glass fibers embedded in a shrinking matrix acted like indenters and conical-shaped cracks were observed at fiber ends. The observed cone angle and location is in close agreement with the predictions of the present theory. Furthermore, the observed debonding near fiber ends can be understood from the presence of high interfacial shear stress as discussed in Section 4.4.

Finally, we note that the present approach can be extended to the case of constant radial eigenstrain which still remains to be solved.

References

1 Eshelby, J. D., "The Determination of the Elastic Field of an Ellipsoidal Inclusion, and Related Problems," *Proceedings, Royal Society*, London, Series A, Vol. 241, 1957, pp. 376–396.

2 Walpole, L. J., "The Elastic Field of an Inclusion in an Anisotropic Medium," *Proceedings, Royal Society*, London, Series A, Vol. 300, 1967, pp. 270–289.

3 Willis, J. R., "Anisotropic Elastic Inclusion Problem," *Quarterly Journal of Mechanics and Applied Mathematics*, Vol. 17, 1964, pp. 157–174.

4 Kinoshita, N., and Mura, T., "Elastic Fields of Inclusions in Anisotropic Media," *Physica Status Solidi*, Vol. (a) 5, 1971, pp. 759–768.

5 Asaro, R. J., and Barnett, D. M., "The Non-Uniform Transformation Strain Problem for an Anisotropic Ellipsoidal Inclusion," *Journal of the Mechanics and Physics of Solids*, Vol. 23, 1975, pp. 77–83.

6 Faivre, G., "Déformations de cohérence d'un précipité quadratique," *Physica Status Solidi*, Vol. 35, 1964, pp. 249–259.

7 Sankaran, R., and Laird, C., "Deformation Field of a Misfitting Inclusion," *Journal of the Mechanics and Physics of Solids*, Vol. 24, 1976, pp. 251–262.

8 Lee, J. K., and Johnson, W. C., "Elastic Strain Energy and Interactions of Thin Square Plates Which Have Undergone a Simple Shear," *Scripta Metallurgica*, Vol. 11, 1977, pp. 477–484.

9 Chiu, Y. P., "On The Stress Field Due to Initial Strains in a Cuboid Surrounded by an Infinite Elastic Space," ASME JOURNAL OF APPLIED MECHANICS, Vol. 44, 1977, pp. 587–590.

10 Lee, J. K., and Johnson, W. C., "Calculation of the Elastic Strain Field of a Cuboidal Precipitate in an Anisotropic Matrix," *Physica Status Solidi*, Vol. 46, 1978, pp. 267–272.

11 Chiu, Y. P., "On the Stress Field and Surface Deformation in a Half Space With Cuboidal Zone in Which Initial Strains Are Uniform," ASME JOURNAL OF APPLIED MECHANICS, Vol. 45, 1978, pp. 302–306.

12 Owen, D. R. J., "Analysis of Fibre-Reinforced Materials by an Initial Strain Method," *Fibre Science and Technology*, Vol. 5, 1972, pp. 37–59.

13 Chiu, Y. P., "On the Internal Stresses in a Half Plane and a Layer Containing Localized Inelastic Strains or Inclusions," ASME JOURNAL OF APPLIED MECHANICS, Vol. 47, 1980, pp. 313–318.

14 Mura, T., *Micromechanics of Defects in Solids*, to be published, Noordoff International Publishing, 1981.

15 Vinson, J. K., and Chou, T. W., *Composite Materials and Their Use in Structures*, Elsevier-Applied Science, London, 1975.

16 Ashbee, K. H. G., Frank, F. C., and Wyatl, R. C., "Water Damage in Polyester Resins," *Proceedings, Royal Society*, London, Series A, Vol. 300, 1967, pp. 415–419.

17 Ashbee, K. H. G., and Wyatl, R. C., "Water Damage in Glass Fibre/Resin Composites," *Proceedings, Royal Society*, London, Series A, Vol. 312, 1969, pp. 553–564.

18 Gradshteyn, I. S., and Ryzhik, I. M., *Table of Integrals, Series, and Products*, Academic Press, 1965.

19 Mura, T., and Cheng, P. C., "The Elastic Field Outside an Ellipsoidal Inclusion," ASME JOURNAL OF APPLIED MECHANICS, Vol. 44, 1977, pp. 591–594.

APPENDIX

In order to discuss the special numerical integration technique more clearly, the left-hand side of equation (27) is rewritten as

$$I = \int_0^\infty R^{\rho-1} e^{-|x_3 \pm l_0|R} J_1(R) J_\nu(x_1 R)\, dR \tag{42}$$

where $\rho = 1$ or 2 and $\nu = 0$, 1, or 2. Consider the following integral:

$$I_i = \int_0^{R_i} R^{\rho-1} e^{-|x_3 \pm l_0|R} J_1(R) J_\nu(x_1 R)\, dR \tag{43}$$

As R_i increases, the value of I_i oscillates with narrower amplitude. We start counting M peaks and valleys of I_i just after the perturbation of I_i becomes within some limit. The values of the peaks and valley are denoted by $I_{\max(1)}, I_{\max(2)}, \ldots, I_{\max(M)}$ and $I_{\min(1)}, I_{\min(2)}, \ldots, I_{\min(M)}$, respectively. The value of the integral I can be approximated by the average of $I_{\max(i)}$ and $I_{\min(i)}$ for $i = 1, M$.

In order to check the validity of this method, we apply it for the computation of $\int_0^\infty J_0(x)\, dx$. The analytical result of this integral is 1.0, whereas the value obtained by the aforementioned numerical integration is 1.00001. The interval of the integral, $R_{i+1} - R_i$ is chosen so as not to exceed the interval between two neighboring zero points of the Bessel functions which is nearly equal to π. The region $R_{i+1} - R_i$ is divided into four equal intervals for which the numerical integration technique of Newton-Cote [18] has been applied.

Downloaded 01 May 2010 to 171.66.16.249. Redistribution subject to ASME license or copyright; see http://www.asme.org/terms/Terms_Use.cfm

B. G. Schaffer[1]
Graduate Student.
Student Mem. ASME

D. F. Adams
Professor.
Mem. ASME

Department of Mechanical Engineering,
University of Wyoming,
Laramie, Wyo. 82071

Nonlinear Viscoelastic Analysis of a Unidirectional Composite Material

The single-integral nonlinear viscoelastic constitutive equations developed by Schapery from thermodynamic theory have been adapted to analyze the time-dependent response of a unidirectional composite material. This viscoelastic analysis has been combined with an existing time-independent elastoplastic micromechanics analysis, to permit the study of nonlinear time-dependent response of materials loaded beyond their elastic limit. Literature values as well as a brief series of creep-recovery tests on a typical epoxy resin were used to characterize the nonlinear viscoelastic response of the matrix constituent of a composite material. Composite response under transverse loading at various stress levels was then predicted, and the results compared with actual composite creep data.

Introduction

The viscoelastic behavior of a composite material can be of paramount importance when it is subjected to repeated loading cycles or substantial loads at moderately high temperatures for long periods of time. Environmental cycling or fluctuations of the ambient temperature and/or relative humidity can also have considerable influence on the performance of the composite. Under such conditions, the internal stress distributions and overall strain of the composite could ultimately change enough with time to cause failure of the component. Alternatively, the stress state could also change so as to relieve high stress states in certain areas of the composite, preventing failure of the component.

In order to experimentally characterize the time-dependent behavior of a composite material, a number of tests must be conducted. There are many factors (e.g., temperature, moisture, loading rate, and stress level) that affect the viscoelastic properties of a composite. Thus an extensive amount of testing must be undertaken to determine how and to what extent each of these factors will affect the composite. While a particular composite material system might be adequately characterized by such a testing program, if a designer wishes to use a different fiber-matrix combination, he must re-evaluate all the properties determined in the previous testing program. This can be a problem since there are numerous fiber-matrix combinations available to a designer.

To overcome this difficulty, a micromechanics analysis has been developed by the authors [1] which includes time-dependent effects. Since only the individual constituent properties need to be determined experimentally, this analysis becomes extremely cost-effective considering the amount of time and experimental testing saved by not having to evaluate all fiber-matrix combinations. Also, most fibers do not exhibit time-dependence. Therefore, only the candidate matrix materials need be tested. By inputting the appropriate constituent viscoelastic properties, the designer can try any combination of fiber and matrix material, to determine if that composite will satisfy his needs.

To model the various fiber-matrix combinations, the analysis uses a finite-element model capable of simulating a unidirectional composite subjected to any combination of longitudinal and transverse normal loadings, as well as hygrothermal loading. Time-independent nonlinear (elastoplastic) material behavior is included, as is a creep formulation which uses stresses as the independent state variable. The analysis also contains two failure criteria, viz., an octahedral shear stress criterion and a hydrostatic criterion.

Background

Whether considering creep or relaxation there are numerous theories available, each having its strong and weak points. A review of these various theories is presented in reference [1], the relative advantages and disadvantages of each being discussed. Most of these formulations are primarily phenomenological, models being constructed and equations written to describe specific experimental data. In creep, actual values of strain (response) depend upon the entire stress (input) history and not just the current value of stress. In order to account for this, a more mathematical representation is needed. One of these mathematical forms is the differential operator method. A generalization to multiaxial stress states can easily be written, and is given by Findley and Lai [2]. A common solution technique utilizes the Correspondence Principle [2]. Of course, it is possible to find a solution without using the Correspondence Principle, but the differential equations can become cumbersome and extremely difficult to solve.

Another and more widely used mathematical model is the integral

[1] Currently with Hughes Aircraft, Culver City, Calif.

Contributed by the Applied Mechanics Division and presented at the Winter Annual Meeting, Washington, D. C., November 15–20, 1981, of THE AMERICAN SOCIETY OF MECHANICAL ENGINEERS.

Discussion on this paper should be addressed to the Editorial Department, ASME, United Engineering Center, 345 East 47th Street, New York, N. Y. 10017, and will be accepted until March 1, 1982. Manuscript received by ASME Applied Mechanics Division, August, 1980; final revision, January, 1981. Paper No. 81-WA/APM-15.

Copyright © 1981 by ASME

Downloaded 01 May 2010 to 171.66.16.249. Redistribution subject to ASME license or copyright; see http://www.asme.org/terms/Terms_Use.cfm

representation [2–8]. The advantages of this method over the differential operator form are the relative ease of incorporating measured experimental data and the inclusion of temperature and moisture effects. Probably the simplest of the integral representations is the Boltzmann superposition principle [2]. A slightly more general integral form was proposed by Leaderman [9]. Multiple integral representations [5, 6] are very attractive in that they are completely general in nature and can account for any degree of nonlinearity. Difficulty arises when the material exhibits a high degree of nonlinearity, making simplification of many terms impossible. Without such simplification the kernels, i.e., the stress, temperature, and moisture-dependent parameters in the equations, are extremely difficult to evaluate experimentally.

Schapery has developed much simpler, single-integral nonlinear constitutive equations, derived from thermodynamic theory in terms of strains [7] or stresses [8]. These equations contain kernels which are written in terms of linear viscoelastic properties, and are much easier to evaluate than those in the multiple integral forms. The theory developed by Schapery [8] was chosen for use in the present analysis.

As demonstrated in reference [1], it is quite easy to incorporate the measured material parameters into the equations derived by Schapery [8]. Also, it has been demonstrated by Schapery [10] that for a multiaxially stressed material, the properties can be expressed as a function of the local octahedral shear stress in the material. This allows one to completely characterize a material by a series of uniaxial tests. In order to include the effects of temperature and moisture, one need simply repeat the aforementioned uniaxial tests for a range of constant temperature and moisture levels, to determine the dependence of certain constants in the constitutive equations upon these parameters.

Nonlinear Viscoelastic Constitutive Equations

The single integral nonlinear viscoelastic constitutive equation derived by Schapery [8] for an isotropic material under isothermal conditions and uniaxial loading can be written as

$$\epsilon(t) = g_0 D_0 \sigma(t) + g_1 \int_{0^-}^{t} \Delta D(\Psi - \Psi') \frac{d[g_2\sigma(t)]}{d\tau'} d\tau' \qquad (1)$$

where D_0 is the initial (time-independent) value of the compliance and $\Delta D(\Psi)$ is the transient (time-dependent) value of the compliance. Note that $\Delta D(\Psi)$ is a function of reduced time Ψ. The reduced time is defined as

$$\Psi \equiv \int_0^t \frac{dt'}{a_\sigma} \quad \text{and} \quad \Psi' \equiv \int_0^{\tau'} \frac{dt'}{a_\sigma}. \qquad (2)$$

The terms g_0, g_1, g_2, and a_σ are all functions of stress and have certain thermodynamic significance [8]; for example, g_0, g_1, and g_2 reflect stress-dependence on Gibb's free energy while changes in a_σ signify effects of both entropy production and free energy. The term a_σ in equation (2) is also a function of temperature, and for certain composites, moisture content. This factor tends to accelerate or decelerate the influence of time, meaning that changes in temperature, moisture, or stress produce the same output of events (with respect to some reference value), but at a faster or slower rate.

Multiaxial viscoelastic relationships as defined by Schapery [8] are somewhat more complicated in that they allow for any degree of coupling between the applied stresses. In the present analysis [1] it is assumed that this viscoelastic coupling (other than that due to Poisson's effects) is of higher order and is neglected, except as influenced by elastoplastic (Prandtl-Reuss) material response. The constitutive equations used in the present analysis can be written in the simple form

$$\epsilon_{ij}(t) = D_{ijkl}(t, T, M, \sigma)\sigma_{kl} \qquad (3)$$

where $D_{ijkl}(t, T, M, \sigma)$ is the time-dependent nonlinear creep compliance tensor, and is a function of time, temperature, moisture, and applied stress level.

In order to use equation (3), it becomes necessary to simplify the convolution integrals (equation (1)) contained in D_{ijkl}. In the current formulation [1] an incremental analysis procedure is used, all loading, temperature, and moisture increments being applied in time-independent steps. That is, these increments are assumed to occur instantaneously, and to be held constant during succeeding time steps. Time-dependent response is determined by the application of finite increments of time; no increments of stress, temperature, or moisture are permitted during a time increment. In other words, stress is a constant during any time increment.

By substituting $\sigma(t) = \sigma_a$ (a constant value) and integrating, equation (1) yields

$$\epsilon(t) = [g_0 D_0 + g_1 g_2 \Delta D(t/a_\sigma)]\sigma_a. \qquad (4)$$

Details of this integration are presented in reference [1]. Note that ΔD is a function of the ratio of real time to the time shift factor a_σ.

From equation (4), the nonlinear creep compliance for a constant applied stress σ_a is defined as

$$\hat{D} = \frac{\epsilon(t)}{\sigma_a} = g_0 D_0 + g_1 g_2 \Delta D(t/a_\sigma) \qquad (5)$$

where the term $g_0 D_0$ is the instantaneous (time-independent) portion and the term $g_1 g_2 D(t/a_\sigma)$ is the transient (time-dependent) portion of the creep compliance.

If the material is isotropic (as is typically the case of the matrix material in a composite), the creep compliance tensor in equation (3) is simplified to three time-dependent terms, two of which are independent. The isotropic elastic constitutive equations for multiaxial loading, written in tensorial form, are [11]

$$\epsilon_{ij} = \frac{(1+\nu)}{E}\sigma_{ij} - \frac{\nu}{E}\sigma_{kk}\delta_{ij} \qquad (6)$$

where E is the elastic (Young's) modulus and ν is Poisson's ratio. By using equation (5) (for the special case of constant externally applied stresses), making Poisson's ratio time-dependent, and substituting into equation (6), the time-dependent constitutive equations (equations (3)) become

$$\epsilon_{ij}(t) = \hat{D}[1 + \nu(t)]\sigma_{ij} - \hat{D}\nu(t)\sigma_{kk}\epsilon_{ij} \qquad (7)$$

Equations (7) are valid for any isotropic, time-dependent material subject to a constant externally applied load.

Elastoplastic Constitutive Equations

Since the nonlinear viscoelastic constitutive equations are to be used in conjunction with (time-independent) elastoplastic constitutive relations to model composite response beyond the elastic limit, it is appropriate to briefly summarize these later relations also.

The present analysis incorporates an octahedral shear yield criterion, and assumes that the plastic deformation is governed by the Prandtl-Reuss flow rule. While these two criteria have been used by a number of other investigators as well, e.g., see references [12–16], they have not been fully accepted for use with polymers. However, for lack of better criteria, they are tolerated, if not fully accepted. It should be noted that the present analysis, as well as most others, could be readily converted to the use of any improved criterion, should one be found at any time.

The tangent modulus method [12, 16–19] is used to model the nonlinear material behavior in the inelastic range, requiring that the loads be applied incrementally. Thus the analysis is linearized within these small load steps. The resulting incremental constitutive equation is

$$\dot{\epsilon}_{ij} = \frac{(1+\nu)}{E}\dot{\sigma}_{ij} - \frac{\nu}{E}\dot{\sigma}_{kk}\,\delta_{ij} + \frac{s_{ij}s_{kl}\dot{\sigma}_{kl}}{6\,\tau_0^2 M_T} + \dot{\epsilon}_0\,\delta_{ij} \qquad (8)$$

where s_{ij} is the deviatoric component of the stress and δ_{ij} is the Kronecker delta. The dot over a quantity indicates an incremental value. The term τ_0 is the octahedral shear stress

$$\tau_0 = (\tfrac{1}{3} s_{ij}s_{ij})^{1/2} \qquad (9)$$

and $2M_T$ is the tangent modulus of the octahedral shear stress-oc-

Downloaded 01 May 2010 to 171.66.16.249. Redistribution subject to ASME license or copyright; see http://www.asme.org/terms/Terms_Use.cfm

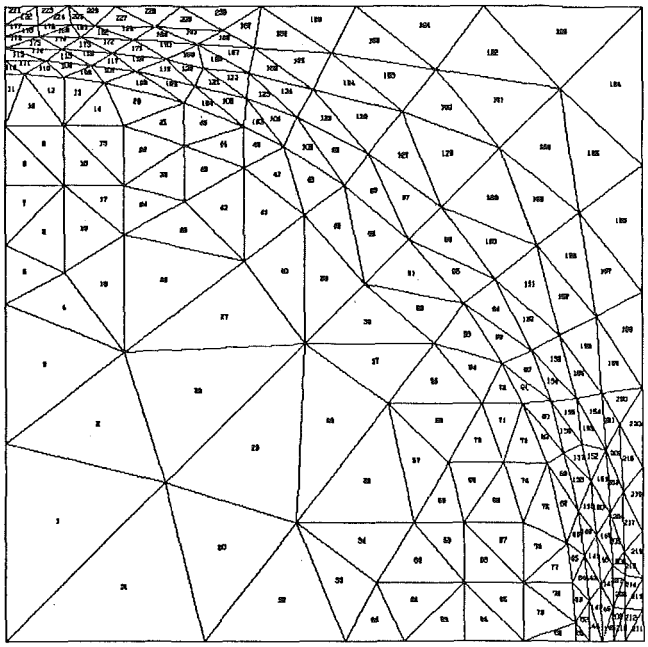


Fig. 1 The finite-element grid used in the present analysis

tahedral plastic shear strain curve. The term $\dot{\epsilon}_0\,\delta_{ij}$ accounts for dilatational strain increments induced by temperature and/or moisture changes. Equation (8) must be inverted for use in the present analysis. Complete details are given in reference [17].

Method of Solution

In the present study, it was desired to model a unidirectional composite material. This relatively complex boundary-value problem is difficult to solve, a finite-element micromechanics analysis being the generally accepted method of solution [15, 16, 18, 20]. A finite-element grid of the internal structure of the composite is constructed, allowing the examination of the internal stresses due to a variety of external conditions. The cross-sectional arrangement of fibers in most unidirectional fibrous composites typically tends to be random. However, there is usually little loss of generality in the analysis if some periodicity is assumed [21]. A detailed discussion of the various possible types of fiber packing, and the ramifications of assuming each type, is presented in references [15–20], among others. In the present analysis, the fibers have been assumed to be arranged in a square array. Symmetry arguments can be invoked which require only one quarter of a fiber to be modeled. The finite-element grid used in the present analysis is shown in Fig. 1. Also, to simulate a small continuum in a rectangular array of fibers in a composite, certain boundary conditions must be satisfied. These are discussed in detail in references [1, 15–20].

In the finite-element analysis, nodal point forces are generated due to the creep strains. The magnitudes of these induced nodal forces are a function of the geometry of an element and the time-dependent material properties of that element. These node point forces are calculated using equation (7) and the elemental stresses at the beginning of the time increment. To accomplish this, equation (7) is differentiated with respect to time and evaluated at the time corresponding to the midpoint of the time increment. By assuming the elemental stresses to remain constant throughout the time interval, and multiplying through by the time increment Δt, a linear approximation of the incremental creep strain for that time increment is obtained. For this reason it is necessary to keep the time increments, which are input into the analysis, very small when the value of the creep compliance is changing rapidly.

While the following equations are written to emphasize the time-dependent incremental formulation, the general procedure is similar for the time-independent portion of the analysis. Details of the strain-displacement relations, shape functions, and basic finite-element formulation for the time-independent formulation are given in references [16–20], but will be summarized here. The equation which relates nodal forces to displacements can be written as [16, 19].

$$\{\dot{F}\}_i = [K]_i\{\dot{\delta}\}_i + \{\dot{F}_{\epsilon_0}\}_i \tag{10}$$

where $\{\dot{F}\}_i$ is the incremental nodal force vector of the ith element due to externally applied loads, $\{\dot{F}_{\epsilon_0}\}_i$ is the incremental nodal force vector due to temperature, moisture, and time changes, $[K]_i$ is the element stiffness matrix, and $\{\dot{\delta}\}_i$ is the incremental element nodal displacement vector. During a time increment, $\{\dot{F}\}_i$ must be zero since loads can only be applied during time-independent increments. Also, no changes in temperature or moisture content can occur. Thus $\{\dot{F}_{\epsilon_0}\}_i$ is the incremental nodal force due to incremental strain changes caused by creep or the time-dependent properties only.

The element stiffness matrix is defined as [16, 19]

$$[K]_i = [B]_i^T[D]_i[B]_i t_i \Delta_i \tag{11}$$

where $[B]_i$, sometimes referred to as the shape matrix, relates the node point displacements and the element strains, t_i is the thickness of the element in the out-of-plane direction (which is assumed to be unity in the present analysis), and Δ_i is the cross-sectional area of the element. The elemental material properties matrix $[D]_i$ is found by evaluating the time-dependent parameters such as $\hat{D}$ (see equation (5)) and $\nu(t)$ at the time corresponding to the midpoint of the time increment, and then substituting into the following matrix for an isotropic material under generalized plane-strain conditions:

$$[D] = \frac{(1-\nu^*)}{D^*\,(1+\nu^*)\,(1-2\nu^*)}\begin{bmatrix} 1 & \nu^*/(1-\nu^*) & 0 & \nu^*/(1-\nu^*) \\ & 1 & 0 & \nu^*/(1-\nu^*) \\ & & [(1-2\nu^*)/2(1-\nu^*)] & 0 \\ \text{symmetric} & & & 1 \end{bmatrix} \tag{12}$$

The terms D^* and ν^* are the creep compliance and the time-dependent Poisson's ratio, respectively, evaluated at the particular time just defined.

Using equation (10) and the finite-element analysis, the incremental displacements can now be solved for if the incremental forces $\{\dot{F}_{\epsilon_0}\}_i$ due to the creep strains are known. The expression for $\{\dot{F}_{\epsilon_0}\}_i$ is [14]

$$\{\dot{F}_{\epsilon_0}\}_i = [B]_i^T\,[D]\,\{\dot{\epsilon}_0\}t_i\Delta_i \tag{13}$$

where $\{\dot{\epsilon}_0\}$ is the incremental creep strain.

Evaluation of $\{\dot{\epsilon}_0\}$ for an element is accomplished by the use of equations (7) and the element stresses at the beginning of the increment. To get $\{\dot{\epsilon}_0\}$, the derivative with respect to time is taken of equations (7) and all of the time-dependent properties evaluated at the time corresponding to the midpoint of the time interval. Using the first of equations (7) as an example, i.e.,

$$\epsilon_x = \hat{D}\sigma_x - \hat{D}\nu(t)\sigma_y - \hat{D}\nu(t)\sigma_z \tag{14}$$

its derivative with respect to time is

$$\frac{d}{dt}(\epsilon_x) = \frac{d}{dt}(\hat{D})\sigma_x - \left\{\left[\frac{d}{dt}(\hat{D})\right]\nu(t) + \left[\frac{d}{dt}\nu(t)\right]\hat{D}\right\}\sigma_y - \left\{\left[\frac{d}{dt}(\hat{D})\right]\nu(t) + \left[\frac{d}{dt}\nu(t)\right]\hat{D}\right\}\sigma_z \tag{15}$$

Downloaded 01 May 2010 to 171.66.16.249. Redistribution subject to ASME license or copyright; see http://www.asme.org/terms/Terms_Use.cfm

Table 1 Time-independent constituent material properties

Material	Longitudinal Modulus GPa (Msi) E_ℓ	Transverse Modulus GPa (Msi) E_t	Major Poisson's Ratio* $\nu_{\ell t}$	In-Plane Poisson's Ratio* ν_{tt}	Coefficient of Thermal Expansion (10^{-6}/°C) Longitudinal α_ℓ	Transverse α_t	Coefficient of Moisture Expansion (10^{-3}/%M) Longitudinal β_ℓ	Transverse β_t
S2 Glass Fiber [25]	86.9 (12.6)	86.9 (12.6)	0.22	0.22	5	5	0	0
AS Graphite Fiber [26]	221 (32.0)	13.8* (2.0)	0.20	0.25	-0.36	18	0	0
3501-6 Epoxy Resin [27]	4.1 (0.6)	4.1 (0.6)	0.34	0.34	40	40	2	2

* Estimated Values [28]

It has been determined by several investigators [22–24] that Poisson's ratio is time-independent or a very weak function of time. For this reason, it was decided that certain terms in equation (15) could be considered higher-order effects and therefore be dropped from the equations, viz., the terms involving time rates of change of Poisson's ratio. With this simplification, equation (15) becomes

$$\frac{d}{dt}(\epsilon_x) = \frac{d}{dt}(\hat{D})\sigma_x - \left[\frac{d}{dt}(\hat{D})\right]\nu(t)\sigma_y - \left[\frac{d}{dt}(\hat{D})\right]\nu(t)\sigma_z. \quad (16)$$

The terms g_0, D_0, g_1, g_2, and a_σ in the nonlinear creep compliance $\hat{D}$ (equation (5)), are functions of stress, temperature and moisture only, and are required to be constant throughout a time increment in this analysis. Thus, when equation (16) is evaluated at a time corresponding to the midpoint of the time increment and multiplied throughout by Δt, a linear approximation of the incremental creep strain ϵ_x is obtained.

A similar argument is applied to the relations for ϵ_y, ϵ_z, and γ_{xy}; the resulting equations are given as follows:

$$\frac{d}{dt}(\epsilon_y) = -\left[\frac{d}{dt}(\hat{D})\right]\nu(t)\sigma_x + \frac{d}{dt}(\hat{D})\sigma_y - \left[\frac{d}{dt}(\hat{D})\right]\nu(t)\sigma_z$$

$$\frac{d}{dt}(\epsilon_z) = -\left[\frac{d}{dt}(\hat{D})\right]\nu(t)\sigma_x - \left[\frac{d}{dt}(\hat{D})\right]\nu(t)\sigma_y + \frac{d}{dt}(\hat{D})\sigma_z$$

$$\frac{d}{dt}(\gamma_{xy}) = \left[\frac{d}{dt}(\hat{D})\right][1 + \nu(t)]\tau_{xy} \quad (17)$$

Once these incremental values of strain are known, the analysis solves for the incremental node point displacements, which are later used to find the new values for elemental stress. When this has been accomplished, the solution procedure returns for the next increment of time, temperature, moisture, or load. Since an incremental procedure is used, to permit the linearization of material response within each increment (tangent modulus method, as previously discussed), this also facilitates the combination of nonlinear viscoelastic and elastoplastic reponse. The time increments are also selected to be sufficiently small so that the stresses within a given finite element can be assumed to remain essentially constant over the time increment. Adjustments of these stress values to maintain equilibrium conditions can then be made between time increments, using the governing elastoplastic (Prandtl-Reuss) flow rule. While obviously an approximation, it is of the same order as the incremental analysis itself, and consistent with the approximate nature of the finite-element analysis. That is, the approximation can be improved as required by using smaller elements, smaller load increments, and smaller time increments.

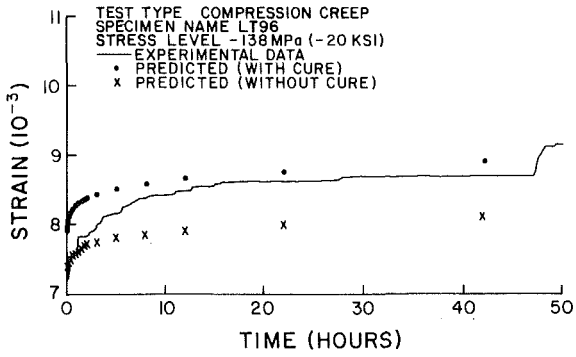


Fig. 2 Plot of strain versus time for an S2 glass/epoxy composite (Hercules 3501-6 epoxy resin) subject to a 50 hr creep test at room temperature (21°C); predicted values are shown by the symbols while the solid line represents experimental data [29]

Numerical Examples

The material properties for Hercules 3501-6 epoxy resin and S2 glass and Hercules AS graphite fibers given in Table 1 were used in generating all of the numerical results presented here. The assumed properties of the fibers were based upon available experimental data as referenced. Since the transverse properties of the fibers (i.e., E_t, ν_{lt}, ν_{tt}, α_t) are not well-characterized, their values are estimates based upon the existing literature. In all of the following examples, the fibers are assumed to behave time-independently, i.e., to show no viscoelastic behavior. Longitudinal creep data generated by Beckwith [22] and Irion [29] for unidirectional glass and graphite composites support this assumption.

A number of comparisons between the predictions of the present analysis and experimental results for various transverse compressive loadings of both glass/epoxy and graphite/epoxy [29] were made. One such comparison is shown in Fig. 2. Additional results are included in reference [1]. It should be noted that the strain scale has been expanded to show detail, thus exaggerating the deviations between theory and experiment. Two predictions were actually made, one including a cure simulation and one without a cure simulation. The predictions with a cure, represented by the solid circles in Fig. 2, involved simulating a cooldown from the 177°C cure temperature to room temperature (21°C). This was done using six time-independent temperature increments to achieve 21°C, and was followed by a 140-hr relaxation period. The relaxation time was arbitrary and was included in order to simulate what would happen to the stresses in a composite

Downloaded 01 May 2010 to 171.66.16.249. Redistribution subject to ASME license or copyright; see http://www.asme.org/terms/Terms_Use.cfm

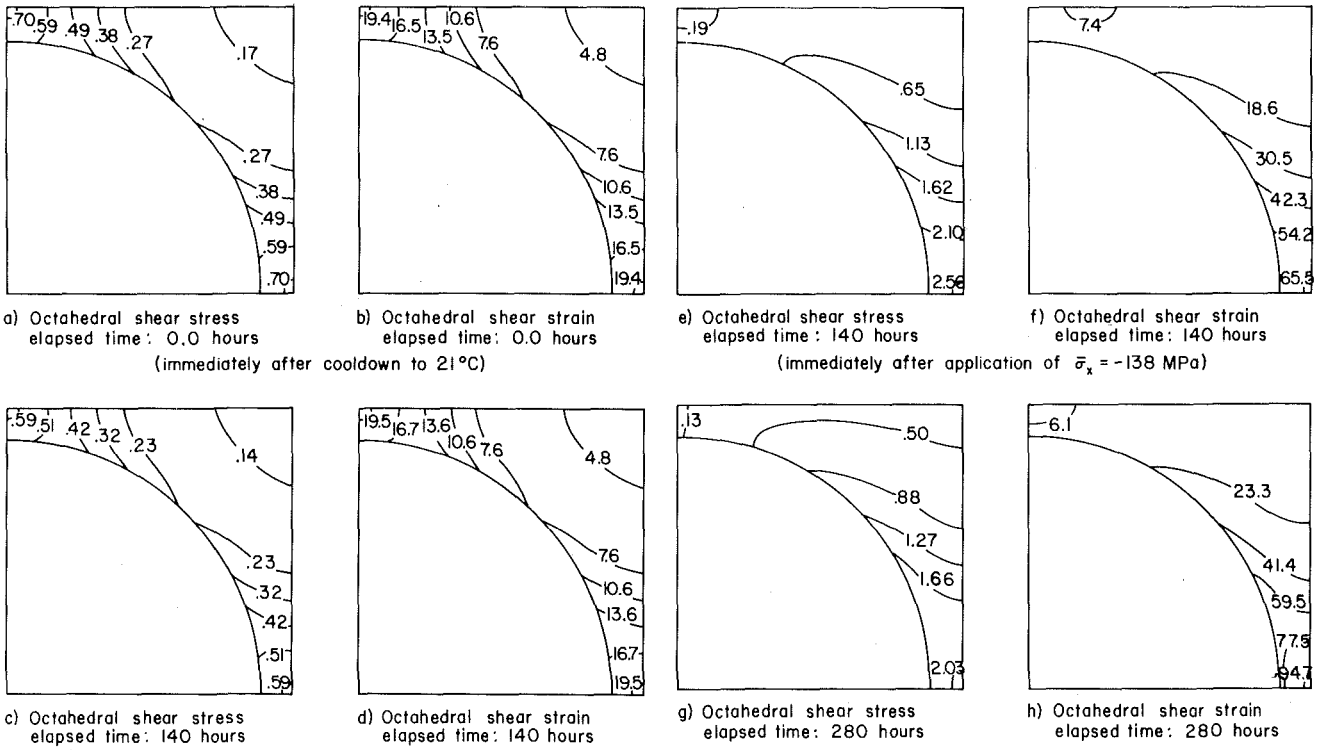


Fig. 3 Octahedral shear stress (normalized) and octahedral shear strain plots for glass/epoxy subjected to a cooldown from the 177°C cure temperature to 21°C, followed by a 140 hr relaxation period, and then a −138 MPa (−20 ksi) stress for another 140 hr

after it had been cured and allowed to "stand" for several hours. It was demonstrated that longer relaxation times tend to produce lower and more uniform stress states.

After this relaxation period, the load was applied and the composite allowed to creep. In examining Fig. 2 it will be noted that the creep strains for the simulation which involved a cure cycle are higher than those for the simulation which did not involve a cure cycle. The reason is that the initial internal stresses in an uncured composite are zero, while the internal stresses in the composite cooled from the cure temperature are very high. These initial stresses are caused primarily by the difference in the coefficients of thermal expansion between the fiber and the matrix.

Both "with" and "without cure" predictions were made in order to obtain a "range" in which the experimental data might lie. In other words, the subsequent response of a composite is a function of how long it has been since the specimen was fabricated. In theory, the internal stresses should be very small and uniform after a very long relaxation time. It is expected that the actual experimental data will lie somewhere within this range, and the predictions shown in Fig. 2 seem to confirm this. There is considerable scatter in the experimental data found in reference [29]. The errors between the predictions and these experiments, as shown here in Fig. 2, and in the additional comparisons in reference [1], are of the same magnitude as the experimental scatter. Thus the agreement between the predictions and experiment is quite reasonable considering the limited amount of data available.

Stress contour plots for the glass/epoxy composite for both the with and without cure cycles are also of interest. Figs. 3(a) and 3(b) show octahedral shear stress and strain contours immediately after cooldown of the composite, while Figs. 3(c) and 3(d) show the composite after 140 hr of relaxation. Figs. 3(e) and 3(f) show octahedral shear stress and strain contours, respectively, for the composite just after application of a compressive stress in the x-direction, and Figs. 3(g) and 3(h) show these two plots for the composite after this stress has been applied for 140 hr. It will be noted that the octahedral shear stress plots for all of the following examples have been normalized by dividing by the yield value of the octahedral stress. Thus a contour value greater than one signifies that the region has yielded.

It is clear from Figs. 3(a) and 3(c) that the internal stresses are relaxing from the cure cycle, as expected. It is also interesting to compare the contour values of the octahedral shear stresses in Figs. 3(e) and 3(g). After 140 hr of elapsed time after application of the load, the high stress state in the lower right-hand corner has been relieved somewhat.

The octahedral shear strain plots (Figs. 3(b) and 3(d) reveal only minute changes of the internal strain during relaxation, as exhibited by both the shapes and magnitudes of the contour lines. This is reasonable since a change in temperature creates a symmetric loading and the net force on the boundary due to this type of loading is zero. Figs. 3(f) and 3(h) illustrate the change in octahedral shear strain immediately after the load has been applied, and 140 hr later. During this time the strain in the lower right-hand corner is seen to substantially increase, while only moderate increases in strain are observed for the upper portions of the model. These changes in strain are responsible for the redistribution of stresses during this time period.

In Fig. 4, plots of the normal stress and tangential shear stress on the fiber-matrix interface are shown for the foregoing simulation, immediately after cure and immediately after application of the load. Plots corresponding to 140 hr after cure and 140 hr after load application indicated significant reductions in both normal and shear stresses, as expected.

Fig. 5 represents the glass/epoxy composite in which curing was not simulated. The first two plots are octahedral shear stress and octahedral shear strain contour plots for the instant immediately after application of the load, while the last two are for 140 hr after application of the load. Since the internal stresses are lower in this model than in the previous model (see Figs. 3(e) and 3(g)), there is less redistribution of the stresses, as evidenced by Figs. 5(a) and 5(c).

The octahedral shear strain (Figs. 5(b) and 5(d)) is again seen to increase significantly in the lower right-hand corner (where the stress is high), with only moderate increases in the upper portion of the

Downloaded 01 May 2010 to 171.66.16.249. Redistribution subject to ASME license or copyright; see http://www.asme.org/terms/Terms_Use.cfm

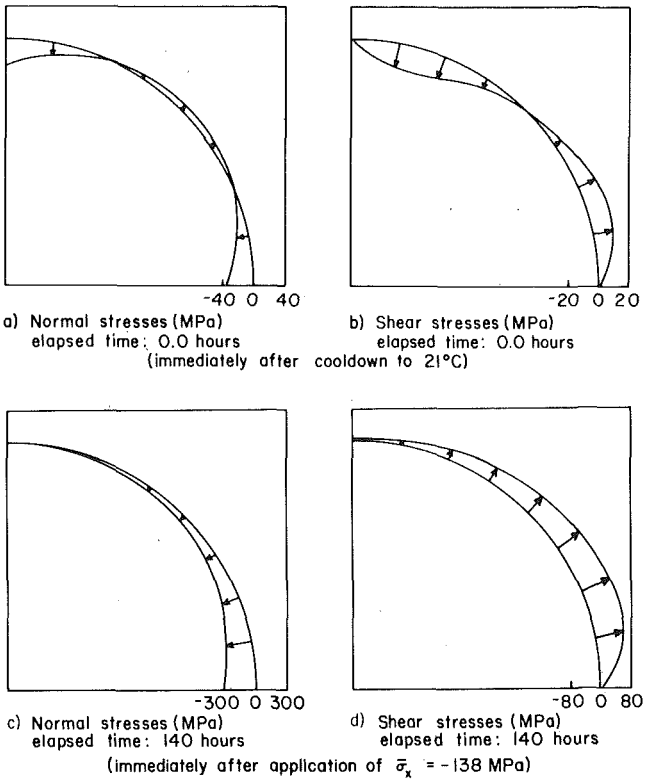


Fig. 4 Interface stresses for glass/epoxy subjected to a cooldown from the 177°C cure temperature to 21°C followed by a 140 hr relaxation period, and then a −138 MPa (−20 ksi) stress

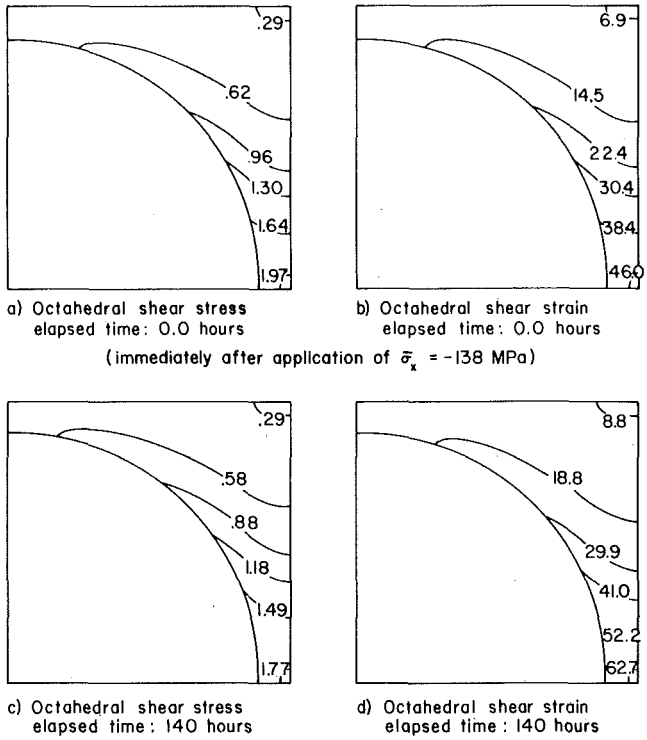


Fig. 5 Octahedral shear stress (normalized) and octahedral shear strain plots for glass/epoxy subjected to a −138 MPa (−20 ksi) stress for 140 hr (no prior temperature history)

model. This is also caused by the lower initial stress state present in this composite than in the composite with the cure. Thus a higher stress state in a composite corresponds to a greater amount of creep strain, which in turn causes a greater redistribution of the stresses.

Discussion of Results

The single example just presented demonstrates only one of the many potential applications of the analysis. It is possible to simulate complicated loading histories, such as multiaxial cycling, thermal cycling, etc., to model many different situations. A number of additional examples, and comparisons with other experimental data, are included in reference [1].

In summary, the analysis is capable of modeling any unidirectional composite subjected to longitudinal and/or transverse normal and/or hygrothermal loadings. It solves problems which involve changes of stress, temperature, and moisture content with time as a series of step loadings. That is, no increments of load, temperature, or moisture are permitted during a time increment. However, increments of load, temperature, and/or moisture may be applied simultaneously using a time-independent increment.

The nonlinear viscoelastic parameters for the matrix material which are input to the analysis can be determined by means of a series of creep-recovery tests at different stress levels, as demonstrated in reference [1]. To include the effects of temperature and moisture, a series of creep-recovery tests at various temperatures and moisture contents must be run. An important feature of the present analysis is that only constituent material properties need to be evaluated. This avoids the difficulty of having to evaluate the time-dependent parameters of all fiber-matrix combinations. Usually only matrix materials need to be tested for time-dependence since most fibers do not show (or show very little) viscoelastic behavior. Thus a designer can model the time-dependent behavior of many different types of composite systems with only a small amount of experimental data.

In general, the results obtained for uniaxial loading compare very well with the experimental data available. Comparisons with the data generated by Irion [29] proved the analysis to be within experimental error. While only a limited amount of data was available for comparison, it is felt that future comparisons will be equally accurate.

Acknowledgments

This study was performed under Grant DAAG 29-79-C-0189 for the U.S. Army Research Office, with Dr. John C. Hurt as Program Monitor. Appreciation is also due to Dr. Richard A. Schapery of Texas A & M University for his many valuable discussions and suggestions during the course of the investigation.

References

1 Schaffer, B. G., and Adams, D. F., "Nonlinear Viscoelastic Behavior of a Composite Material Using a Finite-Element Micromechanics Analysis," Department Report UWME-DR-001-101-1, Department of Mechanical Engineering, University of Wyoming, Laramie, Wyo., June 1980.

2 Findley, W. M., and Lai, J. S., *Creep and Relaxation of Nonlinear Viscoelastic Materials*, North Holland Publishing Co., New York, 1976.

3 Flügge, W., *Viscoelasticity*, Blaisdell Publishing Co., Waltham, Mass., 1967, pp. 3–31.

4 Halpin, J. C., "Introduction to Viscoelasticity," *Composite Materials Workshop*, Progress in Materials Science Series, Vol. 1, Technomic Publishing Co., Westport, Conn., 1968, pp. 87–151.

5 Green, A. E., and Rivlin, R. S., "The Mechanics of Nonlinear Materials With Memory—Part I," *Archive of Rational Mechanics Analysis*, Springer-Verlag, Berlin, Germany, 1957, pp. 1–21.

6 Green, A. E., Rivlin, R. S., and Spencer, A. J. M., "The Mechanics of Nonlinear Materials With Memory—Part II," *Archive of Rational Mechanics Analysis*, Springer-Verlag, Berlin, Germany, 1959, pp. 387–404.

7 Schapery, R. A., "Application of Thermodynamics to Thermomechanical, Fracture, and Birefringent Phenomenon in Viscoelastic Media," *Journal of Applied Physics*, Vol. 35, No. 5, May 1964, pp. 1451–1465.

8 Schapery, R. A., "Further Development of a Thermodynamic Constitutive Theory: Stress Formulation," Report No. 69-2, School of Aeronautics, Astronautics, and Engineering Sciences, Purdue University, Lafayette, Ind., Feb. 1969.

9 Leaderman, H., "Elastic and Creep Properties of Filamentous Materials and Other High Polymers," The Textile Foundation, Washington, D.C., 1943.

10 Schapery, R. A., and Lou, Y. C., "Viscoelastic Characterization of a

Downloaded 01 May 2010 to 171.66.16.249. Redistribution subject to ASME license or copyright; see http://www.asme.org/terms/Terms_Use.cfm

Nonlinear Fiber-Reinforced Plastic," *Journal of Composite Materials*, Vol. 5, Apr. 1971, pp. 208–234.

11 Fung, Y. C., *A First Course in Continuum Mechanics*, Prentice-Hall Inc., Englewood Cliffs, N.J., 1977.

12 Swedlow, J. L., and Yang, W. H., "Stiffness Analysis of Elastoplastic Plates," Report AFRPL-TR-66-5, Air Force Rocket Propulsion Laboratory, Albuquerque, New Mex., Jan. 1966.

13 Marcel, P. V., and King, I. P., "Elastic-Plastic Analysis of Two-Dimensional Stress Systems by the Finite-Element Method," *International Journal of Mechanical Sciences*, Vol. 9, 1967, pp. 143–155.

14 Yamada, Y., Yoshimura, and Sakurai, T., "Plastic Stress-Strain Matrix and Its Application for the Solution of Elastic-Plastic Problems by the Finite-Element Method," *International Journal of Mechanical Sciences*, Vol. 10, 1968, pp. 343–354.

15 Lin, T. H., Salinas, D., and Ito, Y. M., "Elastic-Plastic Analysis of Unidirectional Composites," *Journal of Composite Materials*, Vol. 6, Jan. 1972, pp. 48–60.

16 Miller, A. K., and Adams, D. F., "Inelastic Finite-Element Analysis of a Heterogeneous Medium Exhibiting Temperature and Moisture Dependent Material Properties," *Fibre Science and Technology*, Vol. 13, Mar.–Apr. 1980, pp. 135–153.

17 Adams, D. F., "An Elastoplastic Analysis of Crack Propagation in a Unidirectional Composite," Report R-1070-PR, The Rand Corporation, Santa Monica, Calif., Mar. 1973.

18 Adams, D. F., "Elastoplastic Crack Propagation in a Transversely Loaded Unidirectional Composite," *Journal of Composite Materials*, Vol. 8, Jan. 1974, pp. 38–54.

19 Miller, A. K., and Adams, D. F., "Micromechanical Aspects of the Environmental Behavior of Composite Materials," Department Report UWME-DR-7011111, Department of Mechanical Engineering, University of Wyoming, Laramie, Wyo., Jan. 1977.

20 Foye, R. L., "Inelastic Micromechanics of Curing Stresses in Composites," *Inelastic Behavior of Composite Materials*, ed. Herakovich, C. T., ASME New York, 1975, pp. 177–211.

21 Adams, D. F., and Tsai, S. W., "The Influence of Random Filament Packing on the Transverse Stiffness of Unidirectional Composites," *Journal of Composite Materials*, Vol. 3, July 1969, pp. 368–381.

22 Beckwith, S. W., "Viscoelastic Characterization of a Nonlinear, Glass/Epoxy Composite Including the Effects of Damage," PhD Dissertation, Mechanics and Materials Research Center, Texas A & M University, College Station, Texas, Oct. 1974.

23 Altoulami, S. A. A., "Theoretical and Experimental Studies on the Creep Behavior of a Graphite/Epoxy Composite Material," PhD Dissertation, Engineering Mechanics Department, Drexel University, Philadelphia, Pa., June 1975.

24 Yeow, Y. T., "The Time-Temperature Behavior of Graphite/Epoxy Laminates," PhD Dissertation, Engineering Mechanics Department, Virginia Polytechnic Institute and State University, Blacksburg, Va., May 1978.

25 "Textile Fibers for Industry," Owens-Corning Fiberglass Corporation, Toledo, Ohio, 1971.

26 Hercules Magnamite Graphite Fibers," Hercules Incorporated, Wilmington, Del., 1978.

27 Unpublished experimental data for Hercules 3501-6 epoxy resin, Mechanical Engineering Department, University of Wyoming, Laramie, Wyo., 1978.

28 Ishikawa, T., Koyama, K., and Kobayashi, S., "Elastic Moduli of Carbon/Epoxy Composites and Carbon Fibers," *Journal of Composite Materials*, Vol. 11, July 1977, pp. 332–344.

29 Irion, M. N., "Compression Creep Testing of Composite Materials," MS Thesis, Department of Mechanical Engineering, University of Wyoming, Laramie, Wyo., May 1980.

Downloaded 01 May 2010 to 171.66.16.249. Redistribution subject to ASME license or copyright; see http://www.asme.org/terms/Terms_Use.cfm

T. Iwaki
Lecturer.

N. Kobayashi
Assistant Professor.

Faculty of Engineering,
Toyama University,
Takaoka 933, Japan

Residual Stresses of Czochralski-Grown Crystal

The residual stresses in a Czochralski-grown crystal during and after pulling are obtained analytically by using a linear isotropic thermoelastic model. It is assumed that the physical properties of crystal are independent of temperature and that the crystal has a semi-infinite cylindrical shape as it is withdrawn from a melt with a constant pulling rate. Moreover the problem is considered to be a quasi-stationary one. Numerical results show that the Biot number is a prime factor affecting the residual stress and that the maximum residual stress occurs at the cylindrical surface when the Biot number is small and at the center of the crystal when it is large, respectively. An explanation for the experimental results is given.

Introduction

The residual stress is one of the most important factors determining the quality of single crystals. The stress in the crystal has been studied theoretically by Penning [1], Brice [2], and Avdonin, et al. [3]. They assumed that the shape of the crystal is an infinite circular cylinder and gave the thermal stresses induced by only radially nonuniform temperature distribution. The relation between the thermal stress and the dislocation density was discussed in [1, 3]. However, in these investigations, the axial temperature gradient was neglected and the effect of the Biot number on the stress distribution and on the magnitude of stress was not correctly described.

On the other hand, the residual stress in a Czochralski-grown crystal is not only the thermal stress induced by the nonuniform temperature distribution but also the stress stored through the solidification process of the crystal. Kishigami gave the thermal and residual stresses in full and hollow circular cylinders, and in a sphere [4, 5]. However, these models differ from the Czochralski-grown crystal.

In this paper, an analytical solution is presented for the residual stresses in the Czochralski-grown crystal during and after pulling using a more practical model which has a semi-infinite cylindrical shape and radial and axial temperature gradients. An explanation for the experimental results [3, 6] is given by the present model.

Statement of Problem

The Czochralski-grown crystal which has a semi-infinite circular cylindrical shape and a planar solid-liquid interface is withdrawn with a constant pulling rate (Fig. 1). At the cylindrical surface, heat transfers by Newton's law of cooling, and at the interface the temperature is at the melting point.

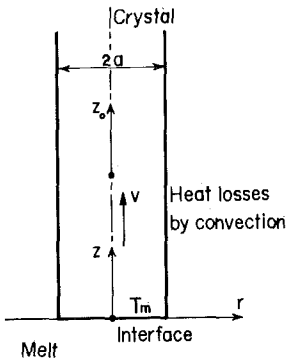


Fig. 1 Present model

The residual stresses during and after pulling are found using linear isotropic thermoelastic theory. It is further assumed that all physical properties of crystal are constant, the temperature variations in the crystal with time are slow, and a stress-free layer is formed at the interface as the crystal grows. The problem is treated as a quasi-stationary one.

Temperature Distribution

By symmetry with respect to the z_0-axis, the Fourier heat-conduction equation has the form

$$\left(\frac{\partial^2}{\partial r^2}+\frac{1}{r}\frac{\partial}{\partial r}+\frac{\partial^2}{\partial z_0^2}\right)T=\frac{1}{\kappa}\frac{\partial T}{\partial t}. \tag{1}$$

Another coordinates system (r, θ, z) is introduced to solve the problem. Then we have

$$z = z_0 + vt. \tag{2}$$

Contributed by the Applied Mechanics Division for publication in the JOURNAL OF APPLIED MECHANICS.

Discussion on this paper should be addressed to the Editorial Department, ASME, United Engineering Center, 345 East 47th Street, New York, N. Y. 10017, and will be accepted until two months after final publication of the paper itself in the JOURNAL OF APPLIED MECHANICS. Manuscript received by ASME Applied Mechanics Division, April, 1980; final revision, March, 1981.

Copyright © 1981 by ASME

Downloaded 01 May 2010 to 171.66.16.249. Redistribution subject to ASME license or copyright; see http://www.asme.org/terms/Terms_Use.cfm

Since $\partial T/\partial z_0 \simeq \partial T/\partial z$, $\partial T/\partial t = (\partial T/\partial z_0)(dz_0/dt) + \partial T/\partial t$ and for quasi-stationary state $\partial T/\partial t = 0$, equation (1), in the dimensionless form, becomes

$$\Delta^* T^* = 2c(\partial T^*/\partial \zeta). \tag{3}$$

The boundary conditions are

$$T^* = 1 \quad (\zeta = 0), \tag{4a}$$

$$(\partial T^*/\partial \rho) + BT^* = 0 \quad (\rho = 1), \tag{4b}$$

$$T^* = 0 \quad (\zeta = \infty). \tag{4c}$$

With the usual technique of separation of variables we find the solution to equation (3) subjected to the boundary conditions (4)

$$T^* = \sum_{n=1}^{\infty} A_n J_0(s_n \rho) e^{-\alpha_n \zeta}, \tag{5}$$

where s_n is the nth root of the transcendental equation

$$sJ_1(s) - BJ_0(s) = 0 \tag{6}$$

and A_n and α_n are given by

$$A_n = 2B/\{(B^2 + s_n{}^2)J_0(s_n)\}, \tag{7a}$$

$$\alpha_n = -c + \sqrt{c^2 + s_n{}^2}. \tag{7b}$$

Thermal Stresses

First, let us find the thermal stresses $(\sigma_{ij}^*)^T$ induced in a semi-infinite circular cylinder by the temperature distribution T^*. The displacement potential $\phi_0{}^*$ and the Love stress function $\phi_l{}^*$ have to, respectively, satisfy the following differential equations:

$$\Delta^* \phi_0{}^* = T^*, \tag{8}$$

and

$$\Delta^* \Delta^* \phi_l{}^* = 0. \tag{9}$$

The thermal stresses are given by

$$(\sigma_{ij}^*)^T = (\sigma_{ij}^*)_0 + (\sigma_{ij}^*)_l, \tag{10}$$

where

$$(\sigma_{\rho\rho}^*)_0 = \partial^2 \phi_0{}^*/\partial \rho^2 - \Delta^* \phi_0{}^*, \tag{11a}$$

$$(\sigma_{\theta\theta}^*)_0 = (1/\rho)(\partial \phi_0{}^*/\partial \rho) - \Delta^* \phi_0{}^*, \tag{11b}$$

$$(\sigma_{\zeta\zeta}^*)_0 = \partial^2 \phi_0{}^*/\partial \zeta^2 - \Delta^* \phi_0{}^*, \tag{11c}$$

$$(\sigma_{\rho\zeta}^*)_0 = \partial^2 \phi_0{}^*/\partial \rho \partial \zeta, \tag{11d}$$

and

$$(\sigma_{\rho\rho}^*)_l = \partial\{\nu \Delta^* \phi_l{}^* - \partial^2 \phi_l{}^*/\partial \rho^2\}/\partial \zeta, \tag{12a}$$

$$(\sigma_{\theta\theta}^*)_l = \partial\{\nu \Delta^* \phi_l{}^* - (1/\rho)(\partial \phi_l{}^*/\partial \rho)\}/\partial \zeta, \tag{12b}$$

$$(\sigma_{\zeta\zeta}^*)_l = \partial\{(2 - \nu)\Delta^* \phi_l{}^* - \partial^2 \phi_l{}^*/\partial \zeta^2\}/\partial \zeta, \tag{12c}$$

$$(\sigma_{\rho\zeta}^*)_l = \partial\{(1 - \nu)\Delta^* \phi_l{}^* - \partial^2 \phi_l{}^*/\partial \zeta^2\}/\partial \rho. \tag{12d}$$

The boundary conditions are

$$(\sigma_{\rho\rho}^*)^T = 0 \quad (\rho = 1), \tag{13a}$$

$$(\sigma_{\rho\zeta}^*)^T = 0 \quad (\rho = 1), \tag{13b}$$

$$(\sigma_{\zeta\zeta}^*)^T = 0 \quad (\zeta = 0), \tag{14a}$$

$$(\sigma_{\rho\zeta}^*)^T = 0 \quad (\zeta = 0), \tag{14b}$$

and

$$(\sigma_{ij}{}^*)^T = 0 \quad (\zeta = \infty). \tag{15}$$

Substituting equation (5) in equation (8), we have a particular solution

$$\phi_0{}^* = \sum_{n=1}^{\infty} B_n J_0(s_n \rho) e^{-\alpha_n \zeta} \tag{16}$$

where

$$B_n = -A_n/(2c\alpha_n). \tag{17}$$

The stress function $\phi_l{}^*$ is constructed in the form

$$\phi_l{}^* = \phi_1{}^* + \phi_2{}^* \tag{18}$$

and the stresses $(\sigma_{ij}^*)_1$ and $(\sigma_{\rho\rho}^*)_2$ are derived from $\phi_1{}^*$ and $\phi_2{}^*$, respectively.

A solution of $\phi_1{}^*$, suitable for our purpose, becomes

$$\phi_1{}^* = \sum_{n=1}^{\infty} \{C_n J_0(\alpha_n \rho) e^{-\alpha_n \zeta} + D_n \rho J_1(\alpha_n \rho) e^{-\alpha_n \zeta}\}. \tag{19}$$

The unknown coefficients C_n and D_n are determined so as to satisfy the boundary conditions at the cylindrical surface

$$(\sigma_{\rho\rho}^*)_1 + (\sigma_{\rho\rho}^*)_1 = 0 \quad (\rho = 1), \tag{20a}$$

$$(\sigma_{\rho\zeta}^*)_0 + (\sigma_{\rho\zeta}^*)_1 = 0 \quad (\rho = 1). \tag{20b}$$

Consequently, we have

$$C_n = B_n[s_n J_1(s_n)\{2(1 - \nu)J_1(\alpha_n) - \alpha_n{}^2 J_1(\alpha_n) + 2\alpha_n(1 - \nu)J_0(\alpha_n)\} - \alpha_n{}^2 J_0(s_n)\{2(1 - \nu)J_1(\alpha_n) + \alpha_n J_0(\alpha_n)\}]/(\alpha_n{}^2 \Delta_n), \tag{21a}$$

$$D_n = B_n\{s_n J_1(s_n)J_0(\alpha_n) - \alpha_n J_0(s_n)J_1(\alpha_n)\}/\Delta_n \tag{21b}$$

where

$$\Delta_n = \{\alpha_n{}^2 - 2(1 - \nu)\}J_1{}^2(\alpha_n) + \alpha_n{}^2 J_0{}^2(\alpha_n).$$

To satisfy the boundary conditions (14), the stress function $\phi_2{}^*$ is taken in the following form [7]:

$$\phi_2{}^* = FJ_0(\lambda\rho)e^{\lambda\zeta} + G\rho J_1(\lambda\rho)e^{\lambda\zeta}. \tag{22}$$

The stresses which are derived from $\phi_2{}^*$ must satisfy the boundary conditions at the cylindrical surface

$$(\sigma_{\rho\rho}^*)_2 = 0 \quad (\rho = 1), \tag{23a}$$

$$(\sigma_{\rho\zeta}^*)_2 = 0 \quad (\rho = 1). \tag{23b}$$

Nomenclature

a = radius of crystal
v = pulling rate
κ = thermal diffusivity
h = convective heat-transfer coefficient
k = thermal conductivity
E = modulus of elasticity
ν = Poisson's ratio
α = coefficient of thermal expansion
T_m = melting point
T_∞ = temperature of environment
T = temperature at point (r, θ, z)
t = time
(r, θ, z_0) = coordinates fixed to crystal
(r, θ, z) = coordinates fixed to solid-liquid interface
$\rho = r/a$
$\zeta = z/a$
$\Delta^* = (\partial^2/\partial \rho^2) + (1/\rho)(\partial/\partial \rho) + (\partial^2/\partial \zeta^2)$
$T^* = (T - T_\infty)/(T_m - T_\infty)$
$c = av/(2\kappa)$, Peclet number
$B = ha/k$, Biot number
$\phi_0{}^* = \phi_0(1 - \nu)/\{(1 + \nu)(T_m - T_\infty)\alpha a^2\}$
$\phi_l{}^* = \phi_l(1 - \nu)/\{(1 + \nu)(T_m - T_\infty)\alpha a^3\}$
$\sigma_{ij}^* = \sigma_{ij}(1 - \nu)/\{(T_m - T_\infty)\alpha E\}$, $(i, j = \rho, \theta, \zeta)$
$\tau^* = \tau(1 - \nu)/\{(T_m - T_\infty)\alpha E\}$, maximum principal shearing stress
$(\ )^T$ = "thermal stress"
$(\ )^D$ = "residual stress during pulling"
$(\ )^A$ = "residual stress after pulling"
$J_0(x), J_1(x)$ = Bessel function of first kind of order zero and one, respectively

Downloaded 01 May 2010 to 171.66.16.249. Redistribution subject to ASME license or copyright; see http://www.asme.org/terms/Terms_Use.cfm

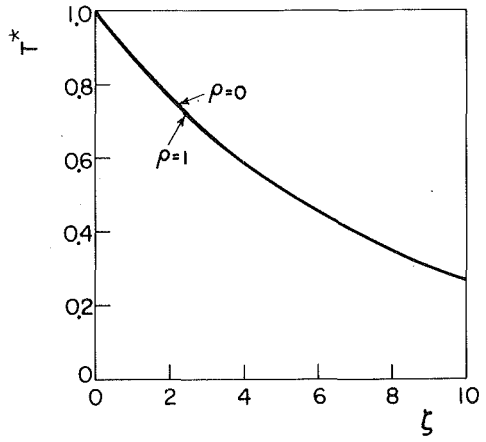


Fig. 2 Axial temperature distribution

Then we have

$$F\{\lambda J_0(\lambda) - J_1(\lambda)\} + G\{2\nu J_0(\lambda) - J_0(\lambda) + \lambda J_1(\lambda)\} = 0, \quad (24a)$$

$$F\{-\lambda J_1(\lambda)\} + G\{2(1-\nu)J_1(\lambda) + \lambda J_0(\lambda)\} = 0. \quad (24b)$$

For the solution of equations (24) to be nontrivial the determinant must be zero. Hence λ is the root of the transcendental equation

$$\{\lambda^2 - 2(1-\nu)\}J_1^2(\lambda) + \lambda^2 J_0^2(\lambda) = 0. \quad (25)$$

This equation has an infinite number of complex roots. If the nth root is defined by λ_n whose real and imaginary parts are positive, $\bar{\lambda}_n$, $-\lambda_n$, and $-\bar{\lambda}_n$ are also the roots of equation (25). We take $-\lambda_n$ as a root because of boundary condition (15) and truncate an infinite number of roots at $n = N$. Consequently, the function ϕ_2^* is written in the following form:

$$\phi_2^* = \sum_{n=1}^{N} H_n\{F(\lambda_n)J_0(\lambda_n\rho)e^{-\lambda_n\zeta} + G(\lambda_n)\rho J_1(\lambda_n\rho)e^{-\lambda_n\zeta}\} \quad (26)$$

where

$$F(\lambda_n) = 2(1-\nu)J_1(\lambda_n) + \lambda_n J_0(\lambda_n), \quad (27a)$$

$$G(\lambda_n) = \lambda_n J_1(\lambda_n) \quad (27b)$$

and H_n is an unknown complex coefficient.

The unknown complex coefficients are determined by the least-squares method so that the boundary conditions (14) may be satisfied at a number of midpoints (ρ_m, $m = 1, 2\cdots M$) across the interface, this number being larger than N. Thus we obtain the simultaneous equations

$$\begin{vmatrix} \mathrm{Re}[Q_{m,n}] & -\mathrm{Im}[Q_{m,n}] \\ \mathrm{Re}[S_{m,n}] & -\mathrm{Im}[S_{m,n}] \end{vmatrix} \begin{vmatrix} \mathrm{Re}[H_n] \\ \mathrm{Im}[H_n] \end{vmatrix} = \begin{vmatrix} U_m \\ V_m \end{vmatrix} \quad (28)$$

where

$$Q_{m,n} = \lambda_n{}^2\{F(\lambda_n)\lambda_n J_0(\lambda_n\rho_m) - G(\lambda_n)Y_q(\lambda_n\rho_m)\}, \quad (29a)$$

$$S_{m,n} = \lambda_n{}^2\{F(\lambda_n)\lambda_n J_1(\lambda_n\rho_m) - G(\lambda_n)Y_s(\lambda_n\rho_m)\}, \quad (29b)$$

$$U_m = -\sum_{n=1}^{\infty}\{B_n s_n{}^2 J_0(s_n\rho_m) + C_n\alpha_n{}^3 J_0(\alpha_n\rho_m) - D_n\alpha_n{}^2 Y_q(\alpha_n\rho_m)\}, \quad (29c)$$

$$V_m = -\sum_{n=1}^{\infty}\{B_n s_n\alpha_n J_1(s_n\rho_m) + C_n\alpha_n{}^3 J_1(\alpha_n\rho_m) - D_n\alpha_n{}^2 Y_s(\alpha_n\rho_m)\} \quad (29d)$$

and

$$Y_q(x) = 2(2-\nu)J_0(x) - xJ_1(x), \quad (30a)$$

$$Y_s(x) = 2(1-\nu)J_1(x) + xJ_0(x). \quad (30b)$$

Table 1 Accuracy of stress value

N	10	20	20
M	21 (ρ=0∿1 step 0.05)	21 (ρ=0∿1 step 0.05)	29 (ρ=0∿0.9 step 0.05; ρ=0.9∿1 step 0.01)
$\lvert\tau^*\rvert^D_{max}$	0.1106 ×10⁻²	0.1105 ×10⁻²	0.1105 ×10⁻²

Residual Stresses

When the crystal is pulled a length $\Delta\zeta$, the temperature distribution in an arbitrary layer (ζ) changes from T^*_ζ to $T^*_{\zeta+\Delta\zeta}$. The stresses $(\sigma^*_{ij})^T_{\zeta+\Delta\zeta} - (\sigma^*_{ij})^T_\zeta$ induced by the temperature difference $T^*_{\zeta+\Delta\zeta} - T^*_\zeta$ are stored in the layer. Consequently, the residual stresses $(\sigma^*_{ij})^D_\zeta$ during pulling are given by

$$(\sigma^*_{ij})^D_\zeta = \int_0^\zeta \{\partial(\sigma^*_{ij})^T_\zeta/\partial\zeta\}d\zeta = (\sigma^*_{ij})^T_\zeta - (\sigma^*_{ij})^T_\zeta = 0. \quad (31)$$

Equation (31) also shows that all stress components are zero at the interface and no tractions are at the cylindrical surface.

Moreover, when the crystal has been pulled out and attains very slowly to the uniform temperature $T^* = 0$, the residual stresses $(\sigma^*_{ij})^A_\zeta$ after pulling are given by

$$(\sigma^*_{ij})^A_\zeta = (\sigma^*_{ij})^D_\zeta - (\sigma^*_{ij})^T_\zeta. \quad (32)$$

Substitution of equation (31) into equation (32) yields

$$(\sigma^*_{ij})^A_\zeta = -(\sigma^*_{ij})^T_{\zeta=0}. \quad (33)$$

Putting $\zeta = \infty$ in equation (31) and using equation (15), we have

$$(\sigma^*_{ij})^D_{\zeta=\infty} = -(\sigma^*_{ij})^T_{\zeta=0} \quad (34)$$

and therefore

$$(\sigma^*_{ij})^A_\zeta = (\sigma^*_{ij})^D_{\zeta=\infty}. \quad (35)$$

With the usual technique of transformation of coordinates we find the three principal shearing stresses which act, respectively, on the mutually perpendicular planes.

Numerical Results

The dimensionless parameters, i.e., the Peclet number, the Biot number, and Poisson's ratio are chosen as $c = 0.01$, $B = 0.01$, and $\nu = 0.3$ (typical values for germanium). The infinite series in equation (5) is truncated at $n = N_s$ so as to obtain the results to four significant digits. Then we have $N_s = 13$. The infinite series in equation (19) is also truncated at $n = N_a$. We take $N_a = N_s$ because of equation (7b). The results for a few combinations of M and N are shown in Table 1 to compare the stress values. For the combination of $M = 21$ and $N = 10$, the stresses $(\sigma^*_{\zeta\zeta})^T$ and $(\sigma^*_{\rho\zeta})^T$ at $\zeta = 0$ which must be zero are less than 0.5 percent of $(\sigma^*_{\theta\theta})^T_{\max}$ or $(\sigma^*_{\rho\rho})^T_{\max}$ at $\zeta = 0$. Consequently, we choose $M = 21$ and $N = 10$ for all calculations.

Fig. 2 shows the axial temperature distributions. It is seen that the curves for $\rho = 0$ and $\rho = 1$ almost agree and that the axial temperature gradient is greater than the radial one.

We will discuss the stresses with the absolutely maximum principal shearing stress, defined by $|\tau^*|$, of three principal shearing stresses.

Fig. 3 shows the stress distributions in the axial direction at $\rho = 0$ and $\rho = 1$ during pulling, because the extreme values of stress occur at these positions in almost every cross section. It also shows from equation (35) that the stresses at $\zeta = \infty$ give the residual stresses after pulling. The stress at $\rho = 1$ increases rapidly to the peak value which occurs at $\zeta = 1$ and then decreases gradually. On the other hand, the stress at $\rho = 0$ increases gradually for $\zeta > 6$, and becomes greater than that at $\rho = 1$ far from the interface. It is found that the stress at $\rho = 1$ and $\zeta = 1$ during pulling is the maximum stress which the crystal undergoes.

Downloaded 01 May 2010 to 171.66.16.249. Redistribution subject to ASME license or copyright; see http://www.asme.org/terms/Terms_Use.cfm

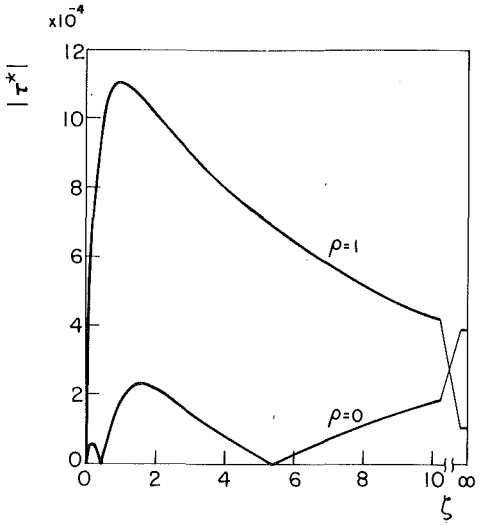


Fig. 3 Axial residual stress distribution

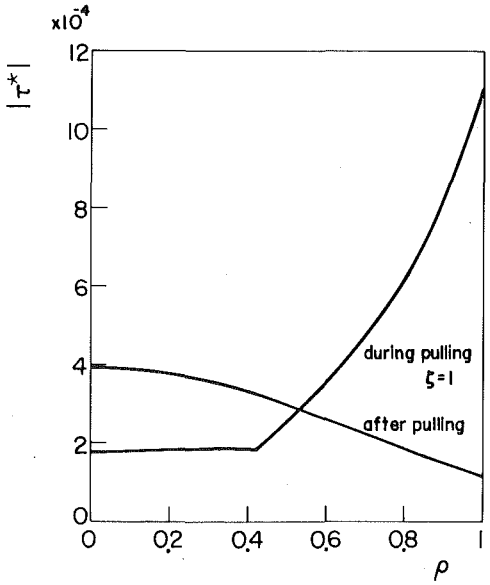


Fig. 4 Radial residual stress distribution

Fig. 4 shows the stress distributions in the radial direction at $\zeta = 1$ and $\zeta = \infty$ (after pulling). The sharp break in the curve for $\zeta = 1$ at $\rho \simeq 0.4$ is due to the change of the plane in which the maximum principal shearing stress occurs. A considerably higher stress occurs at the circumference during pulling. Conversely, after pulling, the stress near the center is greater than that at the circumference and the stress distribution is flatter than the one during pulling.

Dislocations are induced by plastic deformation so that we may expect a higher dislocation density in the deformed regions in the crystal. We can estimate qualitatively the regions deformed plastically from the elastic residual stress distributions. As shown in [1], if dislocations are caused by shearing stress, it can be expected that a region of high dislocation density is present near the circumference and that a low dislocation density is present between the center and the circumference in the crystal. This estimation agrees with the experimental results [3].

The Peclet number, c, has a small effect on the maximum stress during pulling although the stress decreases with increasing c, as shown in Fig. 5.

Fig. 6 illustrates how the Biot number, when varied over the range 0.005 to 1, affects the maximum stresses during and after pulling.

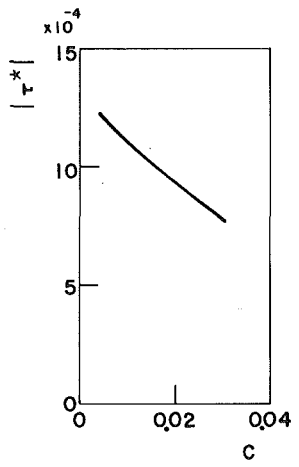


Fig. 5 Residual stress during pulling versus c

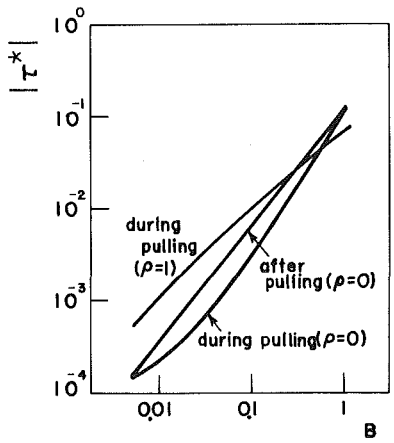


Fig. 6 Residual stress versus B

These stresses increase approximately linearly on a log-log scale as B increases. It is obvious that the residual stress is strongly affected by the Biot number. It is interesting that the stress at $\rho = 1$ during pulling is larger than that after pulling for small values of B. On the other hand, for large values of B, for example, $B = 1$, the stress at $\rho = 0$ is always larger than that at $\rho = 1$ and its maximum value which occurs at $\zeta = \infty$ (or after pulling) is about 3.6 times as large as the stress at $\rho = 1$. Thus we can explain that brittle materials such as oxide crystals (for which B is large) are easily cracked near the center without plastic deformation, as shown by experiment [4]. This fact cannot be explained by the models neglecting the axial temperature gradient [2, 3].

Conclusions

1 The Biot number is a prime factor affecting the residual stress.

2 For low values of the Biot number, the maximum residual stress occurs at the cylindrical surface during pulling, and for large values of the Biot number, it occurs at the center of the crystal.

3 Some of experimental facts are explained by this model.

Acknowledgment

The authors wish to express their hearty thanks to Prof. Kazyu Miyao of Toyama University for his valuable advices.

References

1 Penning, P., "Generation of Imperfections in Germanium Crystals by Thermal Strain," *Philips Res. Repts*, Vol. 13, 1958, pp. 79–97.

2 Brice, J. C., "The Cracking of Czochralski-Grown Crystals," *Journal of Crystal Growth*, Vol. 42, 1977, pp. 427–430.

3 Avdonin, N. A., et al., "Influence of the Temperature Field and the

Downloaded 01 May 2010 to 171.66.16.249. Redistribution subject to ASME license or copyright; see http://www.asme.org/terms/Terms_Use.cfm

Thermal Stress Field Upon the Formation of the Dislocation Structure in Gallium-Arsenide Single Crystals Grown by the Czochralski Method," *Soviet Physics-Doklady*, Vol. 16, No. 9, 1972, pp. 772–775.

4 Kishigami, H., "Thermal Stresses and Residual Stresses With Moving Solidification Front (First Report; Case of Long Circular Cylinder)," *Transactions of the Japan Society of Mechanical Engineers* (in Japanese), Vol. 38, No. 313, 1972, pp. 2179–2184.

5 Kishigami, H., "Thermal Stresses and Residual Stresses With Moving Solidification Front (Case of Hollow Cylinder and Sphere)," *Transactions of the Japan Society of Mechanical Engineers* (in Japanese), Vol. 39, No. 318, 1973, pp. 441–449.

6 Drafall, L. E., and Spear, K. E., "Czochralski Growth of $Ba_2Ge_2TiO_8$," *Journal of Crystal Growth*, Vol. 33, 1976, pp. 180–182.

7 Chu, W. H., and Dodge, F. T., "End Thermal Stresses in a Long Circular Rod," ASME JOURNAL OF APPLIED MECHANICS, Vol. 35, 1968, pp. 267–273.

Downloaded 01 May 2010 to 171.66.16.249. Redistribution subject to ASME license or copyright; see http://www.asme.org/terms/Terms_Use.cfm

Maria Comninou
Associate Professor,
Department of Civil Engineering.
Mem. ASME

J. R. Barber[1]
Associate Professor,
Department of Mechanical Engineering
and Applied Mechanics.

University of Michigan,
Ann Arbor, Mich. 48109

John Dundurs
Professor,
Department of Civil Engineering,
Northwestern University,
Evanston, Ill. 60201
Fellow ASME

Heat Conduction Through a Flat Punch

An elastic half plane is indented by a perfectly conducting rigid flat punch, which is maintained at a different temperature from the half plane. It is found that, depending on the magnitude and direction of the total heat flux, one of the following states occurs: separation at the punch corners, perfect thermal contact throughout the punch face, or an imperfect contact region at the center with adjacent perfect contact regions.

Introduction

This paper is concerned with the steady-state, two-dimensional thermoelastic problem of a frictionless elastic half plane indented by a perfectly conducting rigid flat punch. The punch is maintained at a different temperature from the half plane. In problems of this type, difficulties concerning existence can arise if the punch is cooled and the boundary conditions require continuity of temperature in regions of mechanical contact (perfect thermal contact) and complete insulation in regions of separation. These difficulties have already been exposed [1–4] and will not be elaborated here. They can be avoided by assuming a thermal contact resistance with magnitude inversely related to pressure [3]. The limit, in which the transition from perfect contact to insulation occurs over an infinitesimal range of pressure, leads to the boundary condition of "imperfect contact," introduced in [3], and subsequently used in the solution of a number of thermoelastic contact problems [5, 6].

Statement of the Problem

The geometry of the problem is illustrated in Fig. 1. The rigid punch of width $2b$ is pressed into the half plane $y < 0$ by a compressive force P as shown. The symbols μ, ν, α, k, respectively, denote the shear modulus, Poisson's ratio, coefficient of thermal expansion, and thermal conductivity for the half plane. It is also convenient to define the material constants

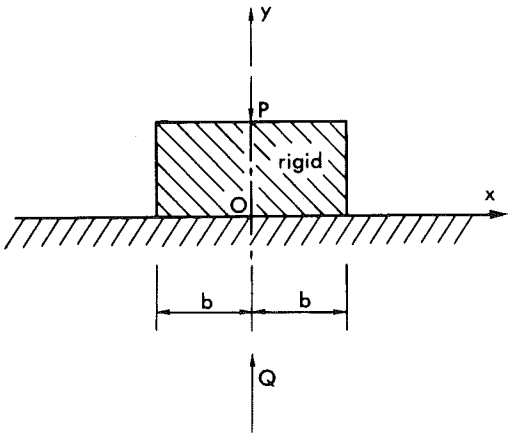


Fig. 1 Geometry of the flat punch

$$\kappa = 3 - 4\nu, \quad \delta = \alpha(1 + \nu)/k \tag{1}$$

δ being the thermal distortivity of the half plane.

The total heat flux from the half plane to the punch is Q. The case of most physical interest is $Q > 0$, since it leads to imperfect contact, but results are also given for $Q < 0$ in the interests of completeness.

The problem is analogous to the axisymmetric problem of the cylindrical flat punch treated in [6], although the mathematical formulation is very different. Pursuing this analogy, we anticipate that a central region of imperfect contact will be developed for $Q > 0$ and that separation will occur near the edges for $Q < 0$. However, if P/Q is sufficiently large, perfect contact will be maintained throughout

[1] Formerly, Department of Mechanical Engineering University of Newcastle upon Tyne, Newcastle upon Tyne, NE1 7RU, England.

Contributed by the Applied Mechanics Division for publication in the JOURNAL OF APPLIED MECHANICS.

Discussion on this paper should be addressed to the Editorial Department, ASME, United Engineering Center, 345 East 47th Street, New York, N. Y. 10017, and will be accepted until two months after final publication of the paper itself in the JOURNAL OF APPLIED MECHANICS. Manuscript received by ASME Applied Mechanics Division, January, 1981; final revision, May, 1981.

Copyright © 1981 by ASME

Downloaded 01 May 2010 to 171.66.16.249. Redistribution subject to ASME license or copyright; see http://www.asme.org/terms/Terms_Use.cfm

the punch face for either direction of heat flow. It is therefore convenient to treat this straightforward case first.

Perfect Contact Solution

If there is perfect thermal contact throughout the punch face, the temperature difference τ and the normal displacement discontinuity, or gap g must be constant in $|x| < b$, $y = 0$. Using the results and notation of [7], these conditions give

$$\frac{d\tau}{dx} = 0 \quad \text{or} \quad \int_{-b}^{b} \frac{\Lambda(\xi)d\xi}{\xi - x} = 0, \quad |x| < b \tag{2}$$

$$\frac{dg}{dx} = 0 \quad \text{or} \quad \frac{\kappa + 1}{4\pi\mu} \int_{-b}^{b} \frac{F_y(\xi)d\xi}{\xi - x} + \delta \int_{0}^{x} \Lambda(\xi)d\xi = 0, \quad |x| < b \tag{3}$$

where $\Lambda(\xi)$ is the surface heat flux density out of the half plane and $F_y(\xi)$ is the distribution of normal traction at the interface. The lower limit in the second integral term of (3) is set equal to zero in order to recover the symmetric solution ($F_y(x) = F_y(-x)$) corresponding to the force P being applied along the line of symmetry.

The total heat flux and load are regarded as prescribed quantities and hence we have

$$\int_{-b}^{b} \Lambda(\xi)d\xi = Q \tag{4}$$

$$\int_{-b}^{b} F_y(\xi)d\xi = -P \tag{5}$$

The heat-conduction problem defined by (2) and (4) is not influenced by the contact stress distribution and is of standard form with solution

$$\Lambda(x) = \frac{Q}{\pi(b^2 - x^2)^{1/2}} \tag{6}$$

Substituting this result into (3), we find

$$\int_{-b}^{b} \frac{F_y(\xi)d\xi}{\xi - x} = -\frac{4\mu\delta Q}{\kappa + 1} \sin^{-1}(x/b), \quad |x| < b \tag{7}$$

which has the solution [8]

$$F_y(x) = \frac{4\mu\delta Q}{\pi^2(\kappa + 1)(b^2 - x^2)^{1/2}} \int_{-b}^{b} \frac{(b^2 - \xi^2)^{1/2} \sin^{-1}(\xi/b)}{\xi - x} d\xi - \frac{C}{(b^2 - x^2)^{1/2}}, \quad |x| < b, \tag{8}$$

Finally, the constant C is determined from the condition (5) for the total load P. Substituting (8) into (4) and performing the integrations we find

$$C = P/\pi \tag{9}$$

and hence

$$F_y(x) = (b^2 - x^2)^{-1/2} \times \left[-\frac{P}{\pi} + \frac{4\mu\delta Q}{\pi^2(\kappa + 1)} \int_{-b}^{b} \frac{(b^2 - \xi^2)^{1/2} \sin^{-1}\frac{\xi}{b}}{\xi - x} d\xi \right], \quad |x| < b \tag{10}$$

The integral in (10) cannot be evaluated in closed form for general values of x. However, it is an even function of x which varies monotonically from $x = 0$ to $x = b$, the extreme values being

$$\int_{-b}^{b} \frac{(b^2 - \xi^2)^{1/2} \sin^{-1}(\xi/b)}{\xi} d\xi = 2b(2G - 1) \tag{11}$$

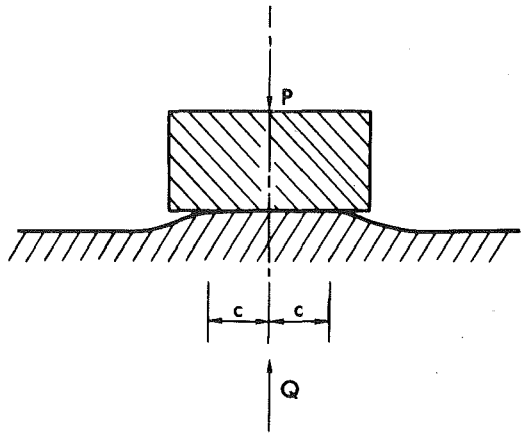


Fig. 2 Geometry for perfect contact and separation

and

$$\int_{-b}^{b} \frac{(b^2 - \xi^2)^{1/2} \sin^{-1}(\xi/b)}{\xi - b} = -2b \tag{12}$$

where $G = 0.915965\ldots$ is Catalan's constant [9].

It follows that (10) will define a negative (compressive) contact stress throughout $|x| < b$ if and only if

$$-1.57 < \lambda < 1.89 \tag{13}$$

where

$$\lambda = \frac{4\mu\delta bQ}{(\kappa + 1)P} \tag{14}$$

For $\lambda < -1.57$, corresponding to a sufficiently large heat flux into the half plane from the punch, tensile contact stresses are predicted near $|x| = b$ and we would anticipate separation to occur in this region. For $\lambda > 1.89$, $F_y(x)$ becomes tensile near $x = 0$, but it is shown in [10] that separation cannot occur in such an enclosed region. Also, an asymptotic analysis [4] shows that the smooth transition from perfect thermal contact to separation is impossible for $Q > 0$. We therefore anticipate a region of imperfect contact centered on $x = 0$. These two conditions are treated in the following two sections.

Separation Solution

If $\lambda < -1.57$, separation will occur at the edges of the punch, leaving a region of perfect contact $|x| < c < b$ as shown in Fig. 2. The contact length $2c$ is unknown and must be determined as a function of λ from the continuity condition at the transition. In all other respects the analysis is identical with that of the previous section, c replacing b throughout. In particular,

$$F_y(x) = (c^2 - x^2)^{-1/2} \left[-\frac{P}{\pi} + \frac{4\mu\delta Q}{\pi^2(\kappa + 1)} \times \int_{-c}^{c} \frac{(c^2 - \xi^2)^{1/2} \sin^{-1}(\xi/c)}{\xi - x} d\xi \right], \quad |x| < c, \tag{15}$$

(cf. equation (10)).

Using equation (12), it follows that $F_y(x)$ will be bounded at $|x| = c$ if and only if

$$\frac{P}{\pi} + \frac{8\mu\delta cQ}{\pi^2(\kappa + 1)} = 0 \tag{16}$$

or

$$\frac{c}{b} = -\frac{\pi}{2\lambda} \tag{17}$$

Substituting this result into (15) we find

Downloaded 01 May 2010 to 171.66.16.249. Redistribution subject to ASME license or copyright; see http://www.asme.org/terms/Terms_Use.cfm

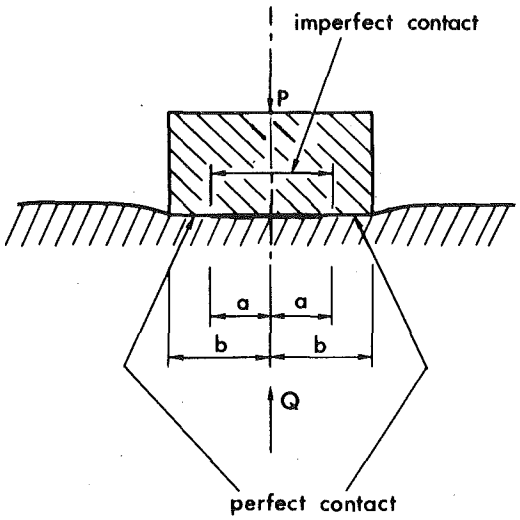


Fig. 3 Geometry for perfect and imperfect contact

$$F_y(x) = -\frac{4\mu\delta Q}{\pi^2}(c^2 - x^2)^{1/2}\int_{-c}^{c}\frac{\sin^{-1}(\xi/c)}{(c^2-\xi^2)^{1/2}(\xi - x)}\,d\xi, \quad |x| < c \tag{18}$$

which is compressive for all $|x| < c$ as required as long as $Q < 0$.

The geometry of the problem demands that $c < b$ and hence $x \leq -1.57$. The separation solution therefore continues the perfect contact solution into large negative values of λ as expected (cf. (13)).

Imperfect Contact Solution

If $\lambda > 1.89$, we anticipate a region of imperfect contact $|x| < a$ enclosed by two strips of perfect contact $a < |x| < b$ as shown in Fig. 3. The boundary condition (3) for mechanical contact applies throughout the punch face and is conveniently written

$$\Lambda(x) = -\frac{(\kappa+1)}{4\pi\mu\delta}\frac{d}{dx}\int_{-b}^{b}\frac{F_y(\xi)d\xi}{\xi - x}, \quad |x| < b \tag{19}$$

but equation (2), prescribing continuity of temperature, applies only in $a < |x| < b$. We can express this condition in the integrated form

$$\int_0^b \Lambda(\xi)\log\left|\frac{x^2-\xi^2}{b^2}\right|d\xi = -C \quad a < |x| < b \tag{20}$$

where C is an arbitrary constant, and the fact that $\Lambda(x)$ is an even function has been used to reduce the range of integration.

In the remainder of the contact area, $|x| < a$, we have imperfect contact and hence the contact stress is infinitesimal [3], i.e.,

$$F_y(x) = 0, \quad |x| < a \tag{21}$$

The contact stress distribution will have a square root singularity at $x = b^-$ and it is convenient to extract it by writing

$$F_y(x) = \frac{A}{(b^2 - x^2)^{1/2}} + G(x), \quad |x| < b \tag{22}$$

where A is a constant. It follows that

$$G(x) = -\frac{A}{(b^2-x^2)^{1/2}}, \quad |x| < a \tag{23}$$

from (21).

Substituting (22) into (19) we find

$$\Lambda(x) = -\frac{(\kappa+1)}{4\pi\mu\delta}\frac{d}{dx}\left[\int_{-b}^{b}\frac{A}{(b^2-\xi^2)^{1/2}}\frac{1}{\xi - x}\,d\xi + \int_{-b}^{b}\frac{G(\xi)}{\xi - x}\,d\xi\right], \tag{24}$$

but the first term vanishes leaving

$$\Lambda(x) = -\frac{\kappa+1}{4\pi\mu\delta}\frac{d}{dx}\int_{-b}^{b}\frac{G(\xi)}{\xi - x}\,d\xi, \quad |x| < b \tag{25}$$

Finally, we substitute this expression into (20), noting that $G(x)$ is an even function and using (23) to evaluate the integral in $|x| < a$, obtaining

$$\int_0^b \log\left|\frac{x^2-\xi^2}{b^2}\right|\frac{d}{d\xi}\left[\int_a^b G(\eta)\left(\frac{1}{\eta-\xi} - \frac{1}{\eta+\xi}\right)d\eta - A\int_0^a\left(\frac{1}{\eta-\xi} - \frac{1}{\eta+\xi}\right)\frac{d\eta}{(b^2-\eta^2)^{1/2}}\right] = -C, \quad a < x < b \tag{26}$$

Integrating by parts and using the Poincaré-Bertrand result to reverse the order of integration we have

$$\pi^2 G(x) - \int_a^b G(\eta)\left[K(\eta,x) + \frac{2b}{b^2-\eta^2}\log\left(1 - \frac{x^2}{b^2}\right)\right]d\eta + \frac{2aA}{b(b^2-a^2)^{1/2}}\log\left(1-\frac{x^2}{b^2}\right) + A\int_0^a \frac{K(\eta,x)}{(b^2-\eta^2)^{1/2}}\,d\eta = -C, \quad a < x < b, \tag{27}$$

where

$$K(\eta,x) = \frac{1}{\eta - x}\log\left|\frac{(b-x)(b+\eta)}{(b+x)(b-\eta)}\right| + \frac{1}{\eta+x}\log\left|\frac{(b+x)(b+\eta)}{(b-x)(b-\eta)}\right| \tag{28}$$

This integral equation contains two unknown constants, A, C, and the unknown extent of the contact region a. It is convenient to regard a as a prescribed quantity and to allow Q (equation (51)) to float. We then have equation (4) for P (essentially a scaling condition) and a continuity condition at $x = a^+$ to determine the remaining constants.

Asymptotic arguments [4] show that $F_y(x)$ must tend to zero at the edge of the perfect contact region and hence

$$G(a^+) = -\frac{A}{(b^2-a^2)^{1/2}} \tag{29}$$

This equation is used to substitute for A in (27), which can now be solved numerically (see next section) for the function $G(x)/C$. We then find A/C from (29) and C from (4), which can be put in the form

$$P = -2A\cos^{-1}(a/b) - 2\int_a^b G(\xi)d\xi \tag{30}$$

using (22).

The total heat flux—now a dependent variable for given a/b—can be obtained by substituting (25) into (5) and is

$$Q = \frac{\kappa+1}{2\pi\mu\delta}\int_a^b \frac{2bG(\eta)}{b^2-\eta^2}\,d\eta - \frac{2aA}{b(b^2-a^2)^{1/2}} \tag{31}$$

while the distribution of heat flux through the contact area is

$$\Lambda(x) = -\frac{\kappa+1}{4\pi\mu\delta}\frac{d}{dx}\left\{\int_a^b \frac{2\xi G(\xi)d\xi}{\xi^2 - x^2} + \frac{A}{(b^2-x^2)^{1/2}}\log\left|\frac{(a-x)\,[b^2+ax-(b^2-a^2)^{1/2}(b^2-x^2)^{1/2}]}{(a+x)\,[b^2-ax-(b^2-a^2)^{1/2}(b^2-x^2)^{1/2}]}\right|\right\} \quad a < x < b, \tag{32}$$

from (25) and (23). It may be verified that $\Lambda(x)$ exhibits correctly the singular behavior predicted by the asymptotic analysis [4].

Numerical Solution

The Cauchy integrals appearing in the expression for $F_y(x)$ (equations (10) and (18)) were evaluated using the Erdogan and Gupta quadrature [11]. For the numerical integration of the Fredholm integral equation (27) the Gauss-Jacobi quadrature [12] with weight function 1 was used. Accordingly, the integration points were chosen as the roots of Legendre polynomials. The collocation points were also chosen as the roots of the same polynomials and L'Hôpital's rule was applied when necessary.

Downloaded 01 May 2010 to 171.66.16.249. Redistribution subject to ASME license or copyright; see http://www.asme.org/terms/Terms_Use.cfm

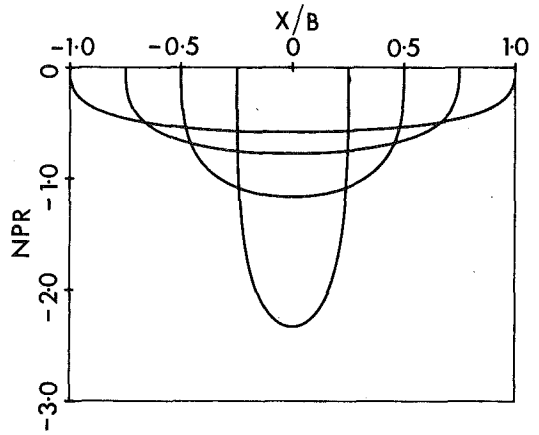


Fig. 4(*a*) Contact pressure distribution for perfect contact and separation ($NPR = F_y(x)b/P$, $X/B = x/b$)

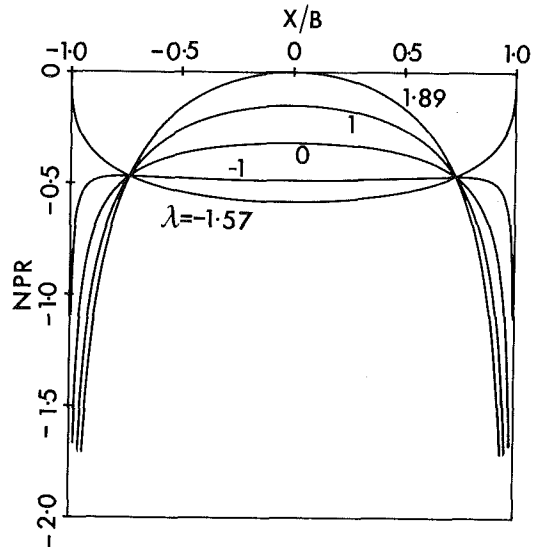


Fig. 4(*b*) Contact pressure distribution for perfect contact ($NPR = F_y(x)b/P$, $X/B = x/b$)

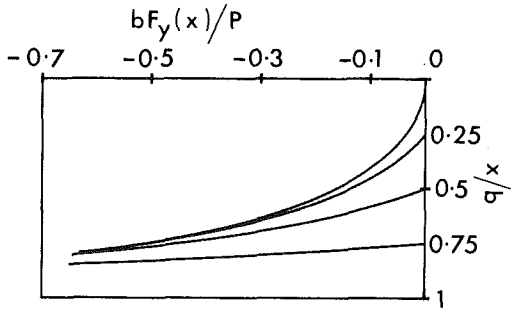


Fig. 4(*c*) Contact pressure distribution for perfect and imperfect contact

Results and Discussion

The state of the system is best described in terms of the nondimensional parameter λ defined by equation (14).

For $\lambda < -1.57$, separation occurs at the punch corners, leaving a contact width $2c$ which varies inversely with λ as defined by equation (17). Typical contact pressure distributions for this region are shown nondimensionally in Fig. 4(*a*) for $c/b = 0.25, 0.5, 0.75, 1$. Note that the contact pressure tends to zero at the edge of the contact region as in the isothermal Hertzian problem.

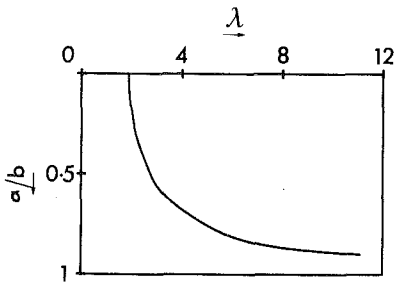


Fig. 5 Ratio a/b versus λ

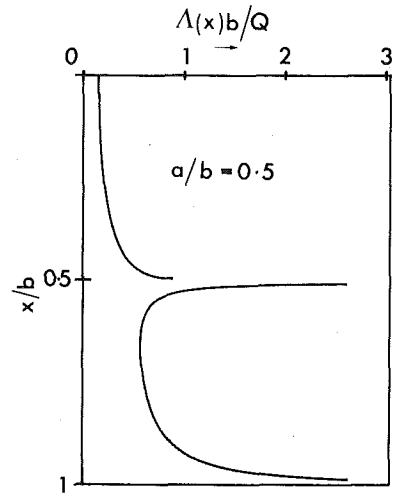


Fig. 6 Typical heat flux distribution

For $-1.57 < \lambda < 1.89$, perfect contact is maintained throughout the punch face and there is a square root singularity in pressure at the sharp edge of the punch except for the transitional case $\lambda = -\pi/2$. Typical pressure profiles are shown in Fig. 4(*b*). Notice that as λ is increased the pressure becomes more concentrated at the edges of the punch at the expense of the center until, at $\lambda = 1.89$, the central pressure is zero.

For $\lambda > 1.89$, a central region of imperfect contact of width $2a$ is developed. The ratio a/b increases monotonically with λ in this range as shown in Fig. 5. Corresponding pressure distributions are given in Fig. 4(*c*) and exhibit a square root singularity near $x = b$ and a linear behavior near $x = a$ as required by the asymptotic analysis.

A typical heat flux distribution (for the case $a/b = 0.5$) is shown in Fig. 6. There is always a square root singularity in flux at the outer edge of the contact region, but a weaker (logarithmic) singularity is developed on both sides of the perfect-imperfect contact transition.

References

1 Barber, J. R., "The Effect of Thermal Distortion on Constriction Resistance," *International Journal of Heat and Mass Transfer*, Vol. 14, 1971, pp. 751–766.

2 Barber, J. R., "Indentation of the Semi-Infinite Elastic Solid by a Hot Sphere," *International Journal of Mechanical Sciences*, Vol. 15, 1973, pp. 813–819.

3 Barber, J. R., "Contact Problems Involving a Cooled Punch," *Journal of Elasticity*, Vol. 8, 1978, pp. 404–423.

4 Comninou, M., and Dundurs, J., "On the Barber Boundary Conditions for Thermoelastic Contact," ASME JOURNAL OF APPLIED MECHANICS, Vol. 46, 1979, pp. 849–853.

5 Comninou, M., Dundurs, J., and Barber, J. R., "Planar Hertz Contact With Heat Conduction," *Solid Contact and Lubrication*, eds., Cheng, H. S., and Keer, L. M., ASME, NewYork, 1980.

6 Barber, J. R., "Indentation of an Elastic Half-Space by a Cooled Flat Punch," *Quarterly Journal of Mechanics and Applied Mathematics*, in press.

Downloaded 01 May 2010 to 171.66.16.249. Redistribution subject to ASME license or copyright; see http://www.asme.org/terms/Terms_Use.cfm

7 Dundurs, J., and Comninou, M., "Green's Function for Planar Thermoelastic Contact Problems-Interior Contact," *Mechanics Research Communications*, Vol. 6, 1979, pp. 317–321.

8 Muskhelishvilli, N. I., *Singular Integral Equations*, P. Noordhoff, Groningen, 1953.

9 Gradshteyn, I. S., and Ryzhik, I. W., *Tables of Integrals, Series and Products*, 4th ed., Academic Press, New York, 1965.

10 Barber, J. R., "The Effect of Heat Flow on the Contact Area Between a Continuous Rigid Punch and a Frictionless Elastic Half-Space," *Zeitschrift für angewandte Mathematik und Physik*, Vol. 27, 1976, pp. 439–445.

11 Erdogan, F., and Gupta, G., "On the Numerical Solution of Singular Integral Equations," *Quarterly of Applied Mathematics*, Vol. 29, 1979, pp. 525–529.

12 Stroud, A. H., and Secrest, D., *Gaussian Quadrature Formulas*, Prentice-Hall, Englewood Cliffs, N.J., 1966.

Downloaded 01 May 2010 to 171.66.16.249. Redistribution subject to ASME license or copyright; see http://www.asme.org/terms/Terms_Use.cfm

T. D. Gerhardt
Research Engineer,
USDA-Forest Service,
Forest Products Laboratory,
P.O. Box 5130,
Madison, Wisc. 53705
Assoc. Mem. ASME

Shun Cheng
Professor,
Department of Engineering Mechanics,
University of Wisconsin,
Madison, Wisc. 53706
Mem. ASME

A Diagonally Dominant Solution for the Cylinder End Problem

An improved elasticity solution for the cylinder problem with axisymmetric torsionless end loading is presented. Consideration is given to the specification of arbitrary stresses on the end of a semi-infinite cylinder with a stress-free lateral surface. As is known from the literature, the solution to this problem is obtained in the form of a nonorthogonal eigenfunction expansion. Previous solutions have utilized functions biorthogonal to the eigenfunctions to generate an infinite system of linear algebraic equations for determination of the unknown expansion coefficients. However, this system of linear equations has matrices which are not diagonally dominant. Consequently, numerical instability of the calculated eigenfunction coefficients is observed when the number of equations kept before truncation is varied. This instability has an adverse effect on the convergence of the calculated end stresses. In the current paper, a new Galerkin formulation is presented which makes this system of equations diagonally dominant. This results in the precise calculation of the eigenfunction coefficients, regardless of how many equations are kept before truncation. By consideration of a numerical example, the present solution is shown to yield an accurate calculation of cylinder stresses and displacements.

Introduction

The end problem in the field of elasticity has generated extensive attention in the literature during the past 20 years. Typically, end problems are solved through expansion of the prescribed end conditions in terms of nonorthogonal eigenfunctions which satisfy homogeneous lateral conditions. In a fairly recent work concerning the orthotropic strip problem [3] and in the solution of other end problems [1,2,4,5], the unknown eigenfunction coefficients are determined through implementation of certain biorthogonality relationships. This approach provides accurate solutions for problems with mixed end conditions, since each unknown coefficient is expressed in terms of known boundary data. However, for the physically more appealing stress or displacement end problems, the biorthogonality formulation generates an infinite system of linear algebraic equations for determination of the eigenfunction coefficients. Both Spence [6] and the present authors, in consideration of the strip and cylinder end problems, respectively, have found these equations to have matrices which lack diagonal dominance, leading to numerical instability in the calculated eigenfunction coefficients when the number of equations kept before truncation is varied. This instability subsequently has an adverse effect on the convergence of the calculated stresses as the number of equations kept before truncation is increased.

Contributed by the Applied Mechanics Division and presented at the Winter Annual Meeting, Washington, D.C., November 15–20, 1981, of THE AMERICAN SOCIETY OF MECHANICAL ENGINEERS.

Discussion on this paper should be addressed to the Editorial Department, ASME, United Engineering Center, 345 East 47th Street, New York, N.Y. 10017, and will be accepted until March 1, 1982. Manuscript received by ASME Applied Mechanics Division, June, 1980; final revision, January, 1981. Paper No. 81-WA/APM-12.

In this paper a new elasticity solution is presented for the problem of a solid isotropic cylinder with a stress-free curved surface and prescribed axisymmetric end stresses. This problem has been considered by Fama [1], Little and Childs [2], and many others. For a fairly complete review of previous work, one may consult references [7, 8]. The formulation presented in this work utilizes a Galerkin approach to generate a diagonally dominant system of equations for determination of the unknown eigenfunction coefficients. Families of functions which can combine linearly to construct the cylinder biorthogonal functions are used as the weighting functions.

A numerical example is presented. It illustrates that the proposed diagonally dominant solution yields a more stable and accurate calculation of the eigenfunction coefficients than the biorthogonal formulation. This results in the improved calculation of stresses and displacements by the diagonally dominant solution, for any number of equations kept before truncation.

The Biorthogonal Solution

Consider a semi-infinite, solid, isotropic, elastic cylinder of radius a occupying the region $0 \leq \rho \leq 1$ and $0 \leq \alpha < \infty$, where $\rho = r/a$ and $\alpha = z/a$ are dimensionless cylindrical coordinates. Let u and w be the displacements in the ρ and α-directions, respectively, G the shear modulus, and ν is Poisson's ratio. Assume that only axisymmetric torsionless end conditions are prescribed on $\alpha = 0$ and that the lateral surface of the cylinder is stress-free, i.e.

$$\sigma_{\rho\rho} = \sigma_{\rho\alpha} = 0 \quad \text{for} \quad \rho = 1 \text{ and } 0 \leq \alpha < \infty \tag{1}$$

Also, assume all stresses and displacements approach zero as α approaches infinity. The eigensolution to this problem is well known in the literature [1, 2, 10].

Copyright © 1981 by ASME

Downloaded 01 May 2010 to 171.66.16.249. Redistribution subject to ASME license or copyright; see http://www.asme.org/terms/Terms_Use.cfm

$$\frac{2G}{a}\{u, w\} = \sum_{k=1}^{\infty} a_k\{\phi_k^{(3)}(\rho), \phi_k^{(4)}(\rho)\}e^{-\lambda_k\alpha}$$

$$\{\sigma_{\alpha\alpha}, \sigma_{\alpha\rho}\} = \sum_{k=1}^{\infty} a_k\{\phi_k^{(1)}(\rho), \phi_k^{(2)}(\rho)\}e^{-\lambda_k\alpha}$$

$$\{\sigma_{\rho\rho}, \sigma_{\theta\theta}\} = \sum_{k=1}^{\infty} a_k\{\phi_k^{(5)}(\rho), \phi_k^{(6)}(\rho)\}\, e^{-\lambda_k\alpha} \tag{2}$$

For the sake of brevity, the elements of a one-column matrix are arranged horizontally. The use of braces indicates the transposition. The functions $\phi_k^{(i)}(\rho)$ $(i = 1, 6)$ and the characteristic equation which determines the eigenvalues, λ_k, are defined in the Appendix. The series solutions (2) are summed on all λ_k with positive real part. The unknown eigenfunction coefficients, a_k, must be determined as to satisfy the specified end conditions on $\alpha = 0$. Since the biorthogonal formulation [1, 2] adequately determines the eigenfunction coefficients for problems involving mixed end conditions, only the stress (3*a*) or displacement (3*b*) problems will be considered in this work. Thus, on $\alpha = 0$, one of the following sets of conditions may be specified.

$$\sigma_{\alpha\alpha} = \sigma_b, \quad \sigma_{\rho\alpha} = \tau_b \tag{3a}$$

$$u = \left(\frac{a}{2G}\right)u_b, \quad w = \left(\frac{a}{2G}\right)w_b \tag{3b}$$

The subscript b indicates a given function.

Both Fama [1] and Little and Childs [2] obtained, by different formulations, a family of functions, $\{W_j\}$, biorthogonal to the eigenfunctions $\phi_k^{(i)}$ $(i = 1, 2, 3, 4)$. The biorthogonal relationships developed led to an infinite system of linear algebraic equations for determination of the eigenfunction coefficients for either problem (3*a*) or (3*b*). The infinite system of equations obtained for the stress problem (3*a*) is given as follows [1, 2]:

$$a_j = G_j + \sum_{k=1}^{\infty} S_{jk}a_k \tag{4}$$

where

$$G_j = \frac{2}{N_j}\int_0^1 [W_j^{(1)}\sigma_b + W_j^{(2)}\tau_b]\rho d\rho, \quad S_{jj} = 0$$

$$S_{jk} = \frac{2}{N_j}\int_0^1 [W_j^{(3)}\phi_k^{(3)} + W_j^{(4)}\phi_k^{(4)}]\rho d\rho, \quad \text{if } j \neq k$$

$$\{W_j\} = \{W_j^{(1)}, W_j^{(2)}, W_j^{(3)}, W_j^{(4)}\} = K_j\{\phi_j^{(4)}, -\phi_j^{(3)}, -\phi_j^{(2)}, \phi_j^{(1)}\}$$

$$K_j = \frac{1}{2j_{1j}^2\lambda_j^2}, \quad N_j = A[-\lambda_j j_{1j}^2 + Aj_{0j}j_{1j} - 2\lambda_j j_{0j}^2]$$

where $A = 2(1 - \nu)$, $k = 0, 1, 2, \ldots, j_{0k} = J_0(\lambda_k), j_{1k} = J_1(\lambda_k)$ and J_0 and J_1 are Bessel functions of the first kind of order zero and one, respectively.

Neither Little and Childs [2] nor Fama [1] published the closed-form expressions for the matrix coefficients S_{jk}. However, this is necessary for the discussion that follows. By repeated integration by parts and by use of the characteristic equation (21), the following representation can be obtained for S_{jk}, valid for $\lambda_j \neq \lambda_k$.

$$S_{jk} = \frac{2}{N_j}(Aj_{1j}j_{1k} - 2\lambda_j\lambda_k c_{jk})\left[\frac{\lambda_k j_{1k}}{\lambda_j j_{1j}}\right]\left[\frac{\nu(\lambda_j + \lambda_k)^2 - 2\lambda_j\lambda_k}{(\lambda_j - \lambda_k)(\lambda_j + \lambda_k)^2}\right], \tag{5}$$

where

$$c_{jk} = \frac{1}{\lambda_j^2 - \lambda_k^2}[\lambda_j j_{0k}j_{1j} - \lambda_k j_{0j}j_{1k}]$$

Kantorovich and Krylov [9] have considered infinite systems of linear algebraic equations expressed in the form of equation (4). In that classical text, a regular system is defined as one which is diagonally dominated in the sense that

$$\sum_{k=1}^{\infty} |S_{jk}| < 1 \quad (j = 1, 2, 3 \ldots) \tag{6}$$

For infinite systems which satisfy the stringent criteria (6), the authors are able to prove that the unknown coefficients a_j can, in fact, be determined by truncation. For regular systems, the convergence of the calculated coefficients to the appropriate values is guaranteed, as the number of equations kept before truncation is increased.

It can be readily shown that the system of equations (4) is not regular. The asymptotic relation for the eigenvalues in the first quadrant, γ_n $(n = 1, 2, 3, \ldots)$, is given as follows [2]:

$$\gamma_n \to \left[n\pi - \frac{\ln(4n\pi)}{4n\pi}\right] + \frac{i}{2}\ln(4n\pi) \tag{7}$$

Thus, for large n, the real part of γ_n is substantially larger than the imaginary part. But the complex conjugate of $\gamma_n, \bar{\gamma}_n$, is also an eigenvalue. Therefore, the matrix terms S_{jk} which contain $(\gamma_n - \bar{\gamma}_n)$ in the denominator might be expected to be large. This can be illustrated by a numerical computation. The eigenvalues with positive real parts, λ_n, are labeled in the following manner:

$$\lambda_{2n-1} = \gamma_n, \quad \lambda_{2n} = \bar{\gamma}_n, \quad (n = 1, 2, 3 \ldots) \tag{8}$$

Then by direct calculation, $|S_{39,40}| = 1.18$ for $\nu = 0.30$. Clearly, this system of equations is not regular, at least for $\nu = 0.30$.

A More Diagonally Dominant Solution

In this section a new method is presented for the determination of the coefficients a_k for the stress problem (3*a*). Spence [6], in consideration of a semi-infinite strip with unmixed end conditions, obtained a regular system of equations [9] to determine the unknown eigenfunction coefficients. A Galerkin approach was used with arbitrary linear combinations of the strip eigenfunctions as weighting functions. However, this method cannot be applied to the cylinder problem due to the different natures of the solutions of the cylinder and strip end problems. For the strip problem, the biorthogonal functions are linear combinations of the eigenfunctions. In fact, the method developed in [6] is, to a large extent, based on this phenomenon. For the cylinder problem, the biorthogonal functions are not linear combinations of the eigenfunctions.

The authors developed a new approach suitable for the cylinder problem. Two families of functions able to combine linearly to construct the biorthogonal family of functions are required. Apparently, it is this property that allows terms to combine in a manner conducive to producing a diagonally dominant set of equations for determination of the eigenfunction coefficients. Using an arbitrary linear combination of these functions as weighting functions, an infinite set of equations is generated. The introduced constants are chosen in such a way as to eliminate the factors $(\lambda_j - \lambda_k)^n$ $(n = 1, 2, 3)$ in the denominators of all the terms in the matrix coefficients. Thus the resulting system of equations will be more diagonally dominated than the biorthogonal system of equations (4). This results in the calculation of more accurate eigenfunction coefficients when numerical examples are considered.

The authors believe that this new approach can be applied to other end problems. However, finding suitable weighting functions may not be a trivial task since, as is the case for the cylinder problem, the biorthogonal functions are of fairly complex form and depend on Poisson's ratio. For the cylinder problem, two suitable families of weighting functions, $\{\psi_j\}$ and $\{\phi_j'\}$, were found. The functions $\psi_j^{(i)}$ $(i = 1, 2, 3, 4)$ are obtained by differentiating products of the eigenfunctions and $\rho^n (n = 0, 1)$. While the functions $\phi_j'^{(i)}$ $(i = 1, 2, 3, 4)$ differ from the eigenfunctions only by a factor of λ_j.

$$\psi_j^{(1)} = \frac{1}{\lambda_j}\frac{1}{\rho}\frac{d}{d\rho}[\rho\phi_j^{(3)}] = (\lambda_j^2 j_{0j} - 2\nu\lambda_j j_{1j})J_0(\lambda_j\rho) + \lambda_j^2 j_{1j}\rho J_1(\lambda_j\rho)$$

$$\psi_j^{(2)} = \frac{1}{\lambda_j}\frac{d}{d\rho}[\phi_j^{(4)}] = (A\lambda_j j_{1j} - \lambda_j^2 j_{0j})J_1(\lambda_j\rho) + \lambda_j^2 j_{1j}\rho J_0(\lambda_j\rho)$$

$$\psi_j^{(3)} = \frac{1}{\lambda_j}\frac{d}{d\rho}[\phi_j^{(1)}] = (\lambda_j^3 j_{0j} - 2\lambda_j^2 j_{1j})J_1(\lambda_j\rho) - \lambda_j^3 j_{1j}\rho J_0(\lambda_j\rho)$$

$$\psi_j^{(4)} = \frac{1}{\lambda_j}\frac{1}{\rho}\frac{d}{d\rho}[\rho\phi_j^{(2)}] = (2\lambda_j^2 j_{1j} - \lambda_j^3 j_{0j})J_0(\lambda_j\rho) - \lambda_j^3 j_{1j}\rho J_1(\lambda_j\rho) \tag{9}$$

Downloaded 01 May 2010 to 171.66.16.249. Redistribution subject to ASME license or copyright; see http://www.asme.org/terms/Terms_Use.cfm

$$\phi_j^{\prime(i)} = \frac{1}{\lambda_j}\phi_j^{(i)}, \quad (i = 1, 2); \quad \phi_j^{\prime(i)} = \lambda_j \phi_j^{(i)}, \quad (i = 3, 4) \qquad (9)$$
(Cont.)

The biorthogonal family of functions $\{W_j\}$ can now be expressed as linear combinations of $\{\phi_j'\}$ and $\{\psi_j\}$.

$$W_j^{(1)} = K_j\left(\frac{1}{A}\right)[(-2 + 4\nu)\,\phi_j^{\prime(1)} + 2\nu\psi_j^{(1)}],$$

$$W_j^{(2)} = K_j[2\phi_j^{\prime(2)} - \psi_j^{(2)}]$$

$$W_j^{(3)} = K_j\left(\frac{1}{A+2}\right)[2\phi_j^{\prime(3)} + A\psi_j^{(3)}], \quad W_j^{(4)} = K_j\psi_j^{(4)} \qquad (10)$$

where $K_j = 1/(2j_{1j}^2\lambda_j^2)$.

The families of functions $\{\psi_j\}$ and $\{\phi_j'\}$ provide useful candidates for generating the weighting functions needed for the proposed solution. Consider now the stress problem (3*a*). As weighting functions in a Galerkin approach, $\{\chi_j\}$ will be assumed in the form

$$\chi_j^{(i)} = (-1)^i(M_i - F_i)\phi_j^{\prime(i)} + F_i\psi_j^{(i)}, \quad (i = 1, 2) \qquad (11)$$

The constants M_i and F_i are arbitrary and will be chosen as to make the infinite system of equations that will be generated diagonally dominant. Also define the integrals $I_{jk}^{(i)}(M_i, F_i)$

$$I_{jk}^{(i)}(M_i, F_i) = \int_0^1 \phi_k^{(i)}\chi_j^{(i)}\rho d\rho \quad (i = 1, 2; \text{ no sum on } i) \qquad (12)$$

Expanding the prescribed end stresses (3*a*) in terms of the eigenfunctions and using the weighting functions $\chi_j^{(i)}$ (11) in a Galerkin formulation and then adding the resulting equations together yields

$$\sum_k a_k[I_{jk}^{(1)} + I_{jk}^{(2)}] = \int_0^1 [\chi_j^{(1)}\sigma_b + \chi_j^{(2)}\tau_b]\,\rho d\rho \qquad (13)$$

The infinite system of equations (13) is in a quite general form, yielding a solution to the cylinder end problem for all values of M_i and $F_i (i = 1, 2)$. In fact, by picking $M_2 = M_1, F_2 = -M_1, F_1 = (2\nu/A)M_1$, and $M_1 = K_j$ (for each j), the biorthogonal solution (4) to this problem is obtained. In order to make the system (13) diagonally dominant, the integrals $I_{jk}^{(i)}(M_i, F_i)$ were evaluated. The following results were obtained, valid for $\lambda_j \neq \lambda_k$:

$$\begin{aligned} I_{jk}^{(1)}(M_1, F_1) + I_{jk}^{(2)}(M_2, F_2) &= 4\lambda_j^2\lambda_k^3 j_{1j}j_{1k}[2M_1\lambda_j\lambda_k - M_2(\lambda_j^2 + \lambda_k^2)]\left[\frac{c_{jk}}{(\lambda_j^2 - \lambda_k^2)^2}\right] \\ &+ 2A\lambda_k j_{1j}^2 j_{1k}^2[-M_1(\lambda_j^4 + \lambda_k^4) + M_2\lambda_j\lambda_k(\lambda_j^2 + \lambda_k^2)]\left[\frac{1}{(\lambda_j^2 - \lambda_k^2)^2}\right] \\ &+ 2A\lambda_j^2\lambda_k^2 j_{1j}j_{1k}[F_1\lambda_j + F_2\lambda_k]\left[\frac{c_{jk}}{(\lambda_j^2 - \lambda_k^2)}\right] \\ &+ A^2\lambda_j\lambda_k j_{1j}^2 j_{1k}^2[-F_1\lambda_j - F_2\lambda_k]\left[\frac{1}{(\lambda_j^2 - \lambda_k^2)}\right] \\ &+ 2M_1A\lambda_k j_{1j}^2 j_{1k}^2 \end{aligned} \qquad (14)$$

where

$$c_{jk} = \frac{1}{(\lambda_j^2 - \lambda_k^2)}[\lambda_j j_{0k}j_{1j} - \lambda_k j_{0j}j_{1k}]$$

The constants $M_i, F_i (i = 1, 2)$ are now chosen to eliminate the factors $(\lambda_j - \lambda_k)^n$ $(n = 1, 2, 3)$ in the denominators of various terms in equation (14). Taking $M_2 = M_1$ and $F_2 = -F_1$, equation (14) is reduced to a form which has the factor $(\lambda_j - \lambda_k)$ in the denominators. This factor can be removed from the demoninator of both terms by taking $F_1 = M_1/A$. Thus for $\lambda_j \neq \lambda_k$.

$$I_{jk}^{(1)}\left(M_1, \frac{M_1}{A}\right) + I_{jk}^{(2)}\left(M_1, -\frac{M_1}{A}\right) = 2M_1\lambda_j^2\lambda_k^2 j_{1j}j_{1k}\left[\frac{c_{jk}(\lambda_j - \lambda_k)}{(\lambda_j + \lambda_k)^2}\right] - AM_1\lambda_j\lambda_k j_{1j}^2 j_{1k}^2\left[\frac{(\lambda_j - \lambda_k)}{(\lambda_j + \lambda_k)^2}\right] \qquad (15)$$

By use of equation (15) the system of equations (13) can be written in the following form:

$$a_j = Q_j + \sum_{k=1}^{\infty} O_{jk}a_k \qquad (16)$$

where

$$O_{jk} = \frac{2}{N_j}(Aj_{1j}j_{1k} - 2\lambda_j\lambda_k c_{jk})\left[\frac{\lambda_k j_{1k}}{\lambda_j j_{1j}}\right]\left[\frac{A(\lambda_j - \lambda_k)}{2(\lambda_j + \lambda_k)^2}\right], \quad \text{if } j \neq k$$

$$O_{jj} = 0, \quad Q_j = \frac{2}{N_j}\int_0^1 [\chi_j^{(1)}\sigma_b + \chi_j^{(2)}\tau_b]\rho d\rho$$

The arbitrary constant M_1 has been taken as $M_1 = A/(2\lambda_j^2 j_{1j}^2) = AK_j$ (for each λ_j). For this choice of M_1,

$$I_{jj}^{(1)}\left(M_1, \frac{M_1}{A}\right) + I_{jj}^{(2)}\left(M_1, -\frac{M_1}{A}\right) = \frac{N_j}{2} \quad (\lambda_j = \lambda_k)$$

Finally, the weighting functions $\chi_j^{(1)}$ and $\chi_j^{(2)}$ are determined from equations (9) and (11).

$$\begin{aligned} \chi_j^{(1)} &= AK_j[(\lambda_j^2 j_{0j} - \lambda_j j_{1j})J_0(\lambda_j\rho) + \lambda_j^2 j_{1j}\rho J_1(\lambda_j\rho)] \\ \chi_j^{(2)} &= AK_j[(-\lambda_j^2 j_{0j} - \lambda_j j_{1j})J_1(\lambda_j\rho) + \lambda_j^2 j_{1j}\rho J_0(\lambda_j\rho)] \end{aligned} \qquad (17)$$

It should be noted from equations (5) and (16) that the expressions for the matrix coefficients S_{jk} and O_{jk} differ only in the final term. However, it is obvious that whenever the factor $(\lambda_j - \lambda_k)$ becomes small, the proposed solution will have significantly smaller matrix coefficients than the biorthogonal solution. For eigenvalues in the first quadrant, it can be shown [7] that

$$|O_{jk}| \sim \frac{k^2}{k^2} \quad \text{for a fixed } j \text{ and large } k.$$

Clearly, $|O_{jk}|$ does not tend to zero as k becomes large for the eigenvalues in the first quadrant. Thus the regularity condition (6) cannot be satisfied. However, this system has greater diagonal dominance than the biorthogonal system. This can be illustrated by a numerical computation. Previously it was stated that $|S_{39,40}| = 1.18$ for $\nu = 0.30$. By a similar computation, $|O_{39,40}| = 0.016$ for $\nu = 0.30$. Thus, although neither system is regular, more accurate values of the eigenfunction coefficients can be calculated by using the present solution due to its increased diagonal dominance. This will be more apparent when the numerical example is considered in the next section.

Finally, the similarities of the two solutions should be noted. The weighting functions $\chi_j^{(i)}$ and $W_j^{(i)}$ defined in equations (17) and (4), differ only by the presence of the constant A in different locations. These weighting functions are therefore identical when $\nu = 0.50$, since $A = 2(1 - \nu)$. It can also be observed from equations (5) and (16) that the matrix coefficients S_{jk} and O_{jk} are identical when $\nu = 0.50$.

Repeating the same procedure, a more diagonally dominant solution can also be obtained for the displacement problem (3*b*). These results are presented in [7].

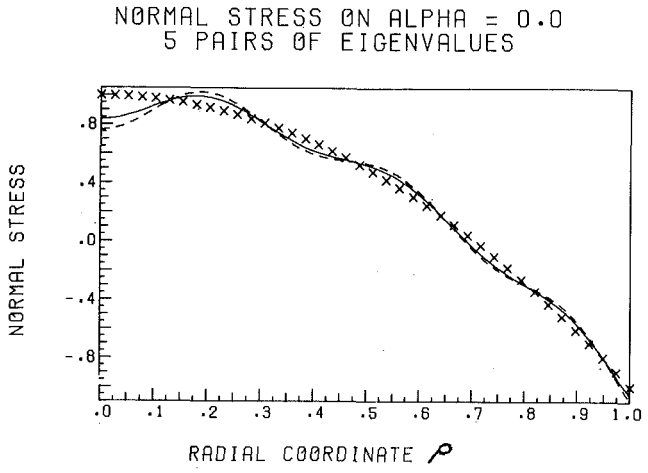
Numerical Solutions and Conclusions

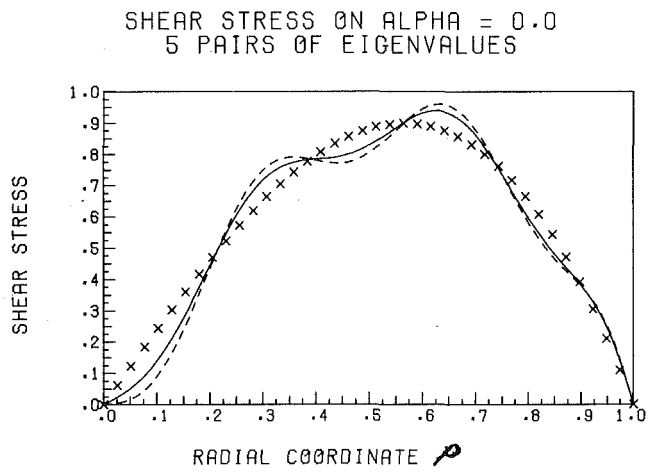
The problem of specified axisymmetric end stresses will be considered. The restriction on the specified end stresses (3*a*) necessary to ensure decaying solutions [1] is that the resultant normal force must be zero, i.e.,

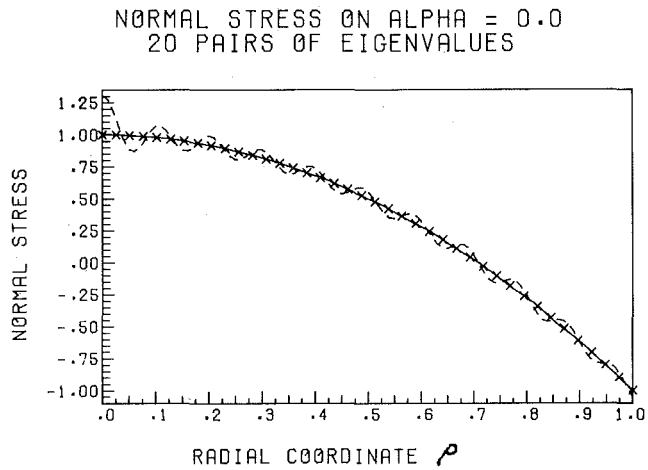
$$\int_0^1 \sigma_b\rho d\rho = 0.$$

The stresses calculated by both the biorthogonal and diagonally dominant solutions were evaluated at $\alpha = 0$ and compared with the specified end conditions by graphical means and by a goodness-of-fit parameter ER defined by

Downloaded 01 May 2010 to 171.66.16.249. Redistribution subject to ASME license or copyright; see http://www.asme.org/terms/Terms_Use.cfm







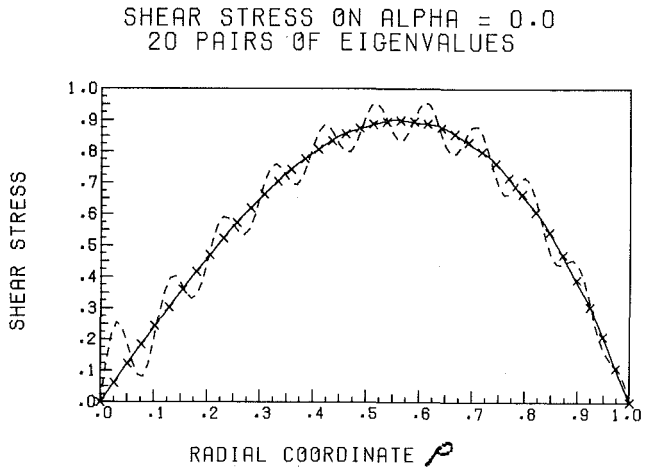


Fig. 1 Normal Stress on $\alpha = 0$; xxxxxx specified normal stress; - - - biorthogonal solution; —— diagonally dominant solution

Fig. 2 Shear stress on $\alpha = 0$; xxxxxx specified shear stress; - - - biorthogonal solution; —— diagonally dominant solution

$$ER^2 = \frac{1}{P}\sum_{i=1}^{P}\left[\{\sigma_b(\rho_i) - \sum_{k=1}^{2N} a_k \phi_k^{(1)}(\rho_i)\}^2 + \{\tau_b(\rho_i) - \sum_{k=1}^{2N} a_k \phi_k^{(2)}(\rho_i)\}^2\right] \tag{18}$$

where

$$P = 101, \rho_i = \frac{i-1}{P-1}, \quad (i = 1, 2, \ldots, P), N = 5, 10, 15, 20$$

The same specified end stresses considered in [2] were used for numerical computation:

$$\begin{aligned} \sigma_b &= 1 - 2\rho^2 \qquad 0 \le \rho \le 1 \\ \tau_b &= 2.4\rho - 2.6\rho^3 + 0.2\rho^5 \quad 0 \le \rho \le 1 \end{aligned} \tag{19}$$

Poisson's ration for the cylinder was taken to be 0.30.

The eigenvalue coefficients, a_k, were calculated for this example using both the biorthogonal (4) and diagonally dominant (16) formulations. Solutions were obtained with various numbers of equations ($2N$) kept before truncation, i.e., using N pairs of complex conjugate eigenvalues in (4) and (16). For both solutions, a_k and its congugate, $\bar{a}_k$, ($k = 1, 2, \ldots N$) are eigenfunction coefficients, resulting in real displacements and stresses after series summation (2). A complete compilation of all the calculated coefficients, as well as, results from an additional numerical example are available in [7]. The values of two coefficients, a_4 and a_9, are presented in Table 1. It should be noted that even for $N = 5$, a_4 is computed quite accurately by the diagonally dominant solution. This solution clearly shows improved stability of the calculated eigenfunction coefficients, as the number of equations kept before truncation is varied.

Table 1

N	Biorthogonal solution	Diagonally dominant solution
	Eigenfunction coefficient $a_4 \times 10^3$	
5	$0.1556 + 0.2111\,i$	$0.1232 + 0.2031\,i$
10	$0.1288 + 0.2023\,i$	$0.1276 + 0.2024\,i$
15	$0.1276 + 0.2022\,i$	$0.1276 + 0.2023\,i$
20	$0.1279 + 0.2023\,i$	$0.1275 + 0.2022\,i$
	Eigenfunction coefficient $a_9 \times 10^5$	
10	$-0.0019 + 0.3434\,i$	$-0.2707 + 0.2746\,i$
15	$-0.2643 + 0.2616\,i$	$-0.2715 + 0.2669\,i$
20	$-0.2478 + 0.2628\,i$	$-0.2739 + 0.2647\,i$

The improved eigenfunction coefficient calculation by the diagonally dominant solution is reflected in better results for the calculated stresses. This can be observed by a comparison of the end stresses calculated by each solution. In Figs. 1 and 2, normal and shear end stresses calculated by both solution techniques are compared to the prescribed values (19), for $N = 5$ and 20. Note for $N = 5$, the curve obtained by the diagonally dominant solution lies between the curve obtained by the biorthogonal solution and the specified end stresses. For $N = 20$, the biorthogonal solution no longer converges to the prescribed values. A curve which oscillates about these values is ob-

Downloaded 01 May 2010 to 171.66.16.249. Redistribution subject to ASME license or copyright; see http://www.asme.org/terms/Terms_Use.cfm

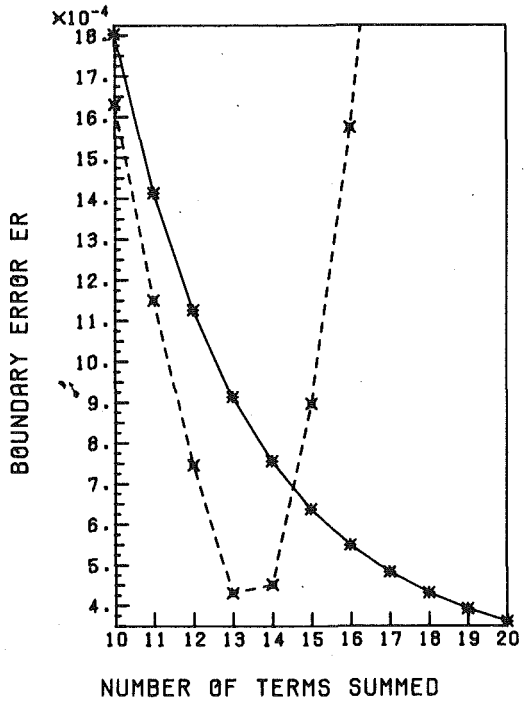


Fig. 3 Deviation from the specified end conditions, 20 pairs of eigenvalues; --- biorthogonal solution, — diagonally dominant solution

Table 2 $ER \times 10^3$

N	Biorthogonal solution	Diagonally dominant solution
5	10.879	7.569
10	3.483	1.864
15	0.807	0.639
20	8.779	0.361

tained. However, the curve obtained by the diagonally dominant solution converges closely to the specified values for $N = 20$.

This lack of convergence is illustrated in Table 2, in which the goodness-of-fit parameter (ER) was computed for various N. Note from the calculated ER-values that for any N, the diagonally dominant solution gives a more accurate representation of the prescribed boundary stresses. These results indicate that for the biorthogonal solution, the end stresses are most accurately represented when $N = 15$. By increasing the number of pairs of eigenvalues used in the biorthogonal computation to $N = 20$, the representation of the prescribed end conditions is substantially less accurate. This occurrence, although surprising, is actually caused by the inaccurate calculation of the last few eigenfunction coefficients by the biorthogonal formulation. Examination of Fig. 3 illustrates this fact. In this figure 20 pairs of eigenvalues are considered. ER is plotted against the number of conjugate pairs of terms used in the series summation (2). For the biorthogonal solution, the minimum value of ER ($ER = 0.432 \times 10^{-3}$) is obtained by discarding the last seven pairs of terms of the summation. However, a better representation of the prescribed end stresses is obtained by using all 20 pairs of terms in the diagonally dominant solution. In fact, Fig. 3 shows that all of the coefficients from the diagonally dominant solution contribute to the accuracy of the solution. It is clear that if all the calculated biorthogonal coefficients are used in the summations, accurate convergence of the solutions on $\alpha = 0$ is not guaranteed as N increases.

This example clearly demonstrates that the diagonally dominant solution is preferable over the biorthogonal solution. The diagonally dominant solution satisfies the prescribed end conditions more accurately due to a more precise caculation of the eigenfunction coefficients. Furthermore, unlike the biorthogonal solution, an accurate representation of the prescribed end conditions is obtained when all the calculated coefficients are used in the series summations. Thus the problem of deciding and justifying which coefficients to discard never arises.

References

1 Fama, M. E. D., "Radial Eigenfunctions for the Elastic Circular Cylinder," *Quarterly Journal of Mechanics and Applied Mathematics*, Vol. 25, 1972, pp. 470–495.

2 Little, R. W., and Childs, S. B., "Elastostatic Boundary Region Problem in Solid Cylinders," *Quarterly of Applied Mathematics*, Vol. 25, 1967, pp. 261–274.

3 Choi, I., and Horgan, C. O., "Saint-Venant's Principle and End Effects in Anisotropic Elasticity," ASME JOURNAL OF APPLIED MECHANICS, Vol. 44, 1977, pp. 424–430.

4 Johnson, M. W., and Little, R. W., "The Semi-Infinite Elastic Strip," *Quarterly of Applied Mathematics*, Vol. 22, 1964, pp. 335–344.

5 Klemm, J. L., and Little, R. W., "The Semi-Infinite Elastic Cylinder Under Self-Equilibrated End Loading," *Siam Journal of Applied Mathematics*, Vol. 19, 1970, pp. 712–729.

6 Spence, D. A., "Mixed Boundary-Value Problems for the Elastic Strip," Math. Research Center Report No. 1863, University of Wisconsin-Madison, 1978.

7 Gerhardt, T. D., "A Diagonally Dominant Solution for the Cylinder End Problem and a NonAxisymmetric Elasticity Solution for a Truncated Spherical Dome," Doctoral Dissertation, University of Wisconsin-Madison, 1979.

8 De la Penha, G. M., "The End Problem for a Torsionless Hollow Circular Cylinder," Doctoral Dissertation, University of Houston, 1968.

9 Kantorovich, L. V., and Krylov, V. I., *Approximate Methods of Higher Analysis*, Interscience, Inc., 1964, New York.

10 Flügge, W., and Kelkar, V. S., "The Problem of an Elastic Circular Cylinder," *International Journal of Solids and Structures*, Vol. 4, 1968, pp. 397–420.

11 Power, L. O., and Childs, S. B., "Axisymmetric Stresses and Displacements in a Finite Circular Bar," *International Journal for Engineering Science*, Vol. 9, 1971, pp. 241–255.

APPENDIX

Eigenfunctions for Equation (2)

$$\phi_k^{(1)}(\rho) = (-\lambda_k^3 j_{0k} + 2\lambda_k^2 j_{1k}) J_0(\lambda_k\rho) - \lambda_k^3 j_{1k}\rho J_1(\lambda_k\rho)$$

$$\phi_k^{(2)}(\rho) = -\lambda_k^3 j_{0k} J_1(\lambda_k\rho) + \lambda_k^3 j_{1k}\rho J_0(\lambda_k\rho)$$

$$\phi_k^{(3)}(\rho) = (\lambda_k^2 j_{0k} + A\lambda_k j_{1k}) J_1(\lambda_k\rho) - \lambda_k^2 j_{1k}\rho J_0(\lambda_k\rho)$$

$$\phi_k^{(4)}(\rho) = (\lambda_k^2 j_{0k} - A\lambda_k j_{1k}) J_0(\lambda_k\rho) + \lambda_k^2 j_{1k}\rho J_1(\lambda_k\rho)$$

$$\phi_k^{(5)}(\rho) = (\lambda_k^3 j_{0k} + \lambda_k^2 j_{1k}) J_0(\lambda_k\rho) - (\lambda_k^2 j_{0k} + A\lambda_k j_{1k}) \frac{1}{\rho} J_1(\lambda_k\rho) + \lambda_k^3 j_{1k}\rho J_1(\lambda_k\rho)$$

$$\phi_k^{(6)}(\rho) = (\lambda_k^2 j_{0k} + A\lambda_k j_{1k}) \frac{1}{\rho} J_1(\lambda_k\rho) - (1 - 2\nu)\lambda_k^2 j_{1k}\rho J_0(\lambda_k\rho) \quad (20)$$

The Characteristic Equation

$$\lambda_k[\lambda_k^2 j_{0k}^2 + (\lambda_k^2 - A) j_{1k}^2] = 0 \quad (21)$$

where $A = 2(1 - \nu)$, $k = 0, 1, 2, \ldots, j_{0k} = J_0(\lambda_k)$, $j_{1k} = J_1(\lambda_k)$ and J_0 and J_1 are Bessel functions of the first kind of order zero and one, respectively. Accurate roots of the characteristic equation (21) are presented in [2]. The eigenfunction associated with $\lambda_0 = 0$ can be shown to produce a constant axial stress ($\sigma_{\alpha\alpha}$) and no other nonzero stresses [11]. For the decaying solutions considered in this work, this eigenfunction is not needed.

Downloaded 01 May 2010 to 171.66.16.249. Redistribution subject to ASME license or copyright; see http://www.asme.org/terms/Terms_Use.cfm

Y. C. Angel[1]
D. B. Bogy
Professor.
Mem. ASME

Department of Mechanical Engineering,
University of California,
Berkeley, Calif. 94720

Scattering of Rayleigh Waves by a Plate Attached to a Half Space Through a Viscous Couplant

The steady time-harmonic problem is reduced to a system of singular integral equations for determining the tractions generated at the interface between the plate and half space where a thin viscous couplant is applied. These equations are found to have different types of singular solutions depending on the parameter values. They are solved numerically for a specific set of physical parameters that includes a wide range of values of the couplant viscosity and incident wavelength. The reflected and transmitted powers are calculated and the reflected power is plotted as a function of incident wavelength for various values of couplant viscosity. The wavelengths at which resonances occur in these functions are found to be strongly dependent on the couplant.

1 Introduction

The problem considered here is relevant to several engineering applications. One, which arises in the context of seismic studies, is the interaction of earthquake-generated ground motions with various structures, either man-made or natural. Another, which arises in the field of nondestructive evaluation, is the interaction of the detecting transducer with the ultrasonic wave motion generated in a structure by actively growing flaws or scattered from a passive flaw. These latter Nondestructive Testing (NDT) applications motivate our work.

In NDT work the object is to locate a flaw and characterize its geometry and orientation. The frequency content of the detected signals and the propagation characteristics of the test piece dictate the need to consider wavelengths that are comparable to the dimensions of the active element in the transducer. These active elements are usually piezoelectric circular disks about 1 to 2 cm dia and 1 to 5 mm thick. This plate can be housed and mounted in a variety of ways. In practice the mounting usually incorporates some type of viscous fluid couplant at the interface between the transducer and structure. The complete analysis requires taking into account all these aspects of the problem in addition to the electrical impedance of the circuit to which the transducer is connected. Most of these items pose no conceptual difficulties, and the somewhat idealized analysis of this paper will be extended in a future paper to cover those generalizations necessary for our purposes. The most serious difficulty associated with the needed generalizations of the analysis presented here is the derivation of an appropriate approximate (plate) theory for treating the strongly coupled piezoelectric transducer element (usually PZT). This has been completed and is presented in Bugdayci and Bogy [1, 2].

The present work addresses the problem of the interaction of elastic waves in a structure with an elastic plate when the two are attached together through a viscous couplant. In order to make the problem tractable without altering the important physical effects, we consider the plane-strain problem of the interaction between an elastic half space and the plate. The new elements of this work are the viscous couplant and the allowance for the bending as well as the extensional deformations in the plate. Previously published works most closely related to ours are those of Luco and Westmann [3] and Simons [4, 5]. Somewhat less related is the paper by Fruend and Achenbach [6]. The first of these considered a rigid plate perfectly bonded to an elastic half space (which they assumed to be incompressible in their numerical calculations for reasons related to the type of stress singularity that occurs at the corners of the plate). On the other hand, Simons [4] considered an elastic membrane (with no bending stiffness) perfectly bonded to an elastic half space. Both of these problems are recovered from our analysis as special cases arising in certain limits of the couplant viscosity and material parameters. We use a purely elastic plate in the context of classical plate theory that includes both bending and extension. It is recognized that classical theory does not give suitable results for the plate motion in dynamical problems where short wavelengths are of interest. The piezoelectric plate theory in [1] includes effects of transverse shear and rotatory inertia and so these effects will be included in the same generalization. Fruend and

[1] Permanent Address: 10 Allée Arcadie, Le Barriot, 69570 Dardilly, France.

Contributed by the Applied Mechanics Division and presented at the Winter Annual Meeting, Washington, D. C., November 15–20, 1981, of THE AMERICAN SOCIETY OF MECHANICAL ENGINEERS.

Discussion on this paper should be addressed to the Editorial Department, ASME, United Engineering Center, 345 East 47th Street, New York, N. Y. 10017, and will be accepted until March 1, 1982. Manuscript received by ASME Applied Mechanics Division, September, 1980; final revision, March, 1981. Paper No. 81-WA/APM-24.

Copyright © 1981 by ASME

Downloaded 01 May 2010 to 171.66.16.249. Redistribution subject to ASME license or copyright; see http://www.asme.org/terms/Terms_Use.cfm

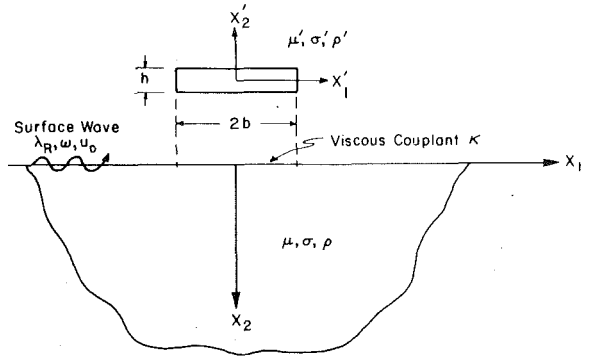


Fig. 1 Geometry, material properties and coordinates for half space, plate and couplant. Plate and half space are in contact over $|x_1| < b$, i.e., couplant thickness is neglected

Achenbach [6] consider the problem of longitudinal waves incident on the surface of a half space where a semi-infinite plate is in smooth contact.

The particular problem considered here is that of scattering of an incoming Rayleigh wave by the attached plate. Thus we look at a steady time-harmonic problem in which the incoming wave has a specified frequency and the wavelength is determined by the requirements for the Rayleigh wave. The half-space Green's functions for the scattered wave can be obtained from Lamb [7]. Many subsequent investigators have reconsidered this problem with variations. Several references to these can be found in the books by Ewing, Jardetsky, and Press [8], Fung [9], Achenbach [10], and Miklowitz [11]. Because of our need to be certain about the treatment of several issues related to singularities that arise in Lamb's problem and also in anticipation of future need for a transient analysis, the steady time-harmonic solution of Lamb's problem was rederived in [15] as a limit of the corresponding transient solution. This analysis will not be repeated here. Readers interested in these details are referred to [15], where the required results are given in Appendix A.

In Section 2, the problem to be solved is formulated considering the plate as a three-dimensional continuum. The resulting two-dimensional plate problem with arbitrary normal and shearing tractions on one face is then formulated and solved in Appendix B of [15].

In Section 3, the problem under consideration is first decomposed into physically symmetric and antisymmetric parts. Then each of these problems is reduced to a system of two integral equations that determine the interface normal and shearing stress over the contact region between the plate and half space. Various limits of the parameters are considered to illustrate how the previously solved problems in references [3, 4] emerge from the one considered here.

Section 4 is concerned with the analysis of the singular integral equations. Here the types of singular solutions for the different parameter values are revealed. In Section 5, the integral equations are replaced by their corresponding algebraic equations that result from use of the quadrature methods dictated by the type of singularities in the solution.

The numerical solutions of the systems of linear equations are presented in Section 6 for a limited range of the seven dimensionless parameters. Finally, a brief discussion is given in Section 7.

2 Formulation of the Problem

We consider the steady-state time-harmonic plane-strain problem of a plate attached through a viscous couplant to a half space (see Fig. 1). The plate has thickness h, width $2b$ and is unbounded in the direction perpendicular to the plane of motion. It is assumed to be isotropic with shear modulus μ', Poisson's ratio σ', and density ρ'. The half space is also isotropic with shear modulus μ, Poisson's ratio σ, and density ρ. The plate, considered in the context of classical plate theory, occupies the two-dimensional region $x_2 = 0$, $|x_1| < b$, $|x_3| < \infty$, which coincides with a portion of the boundary of the half space. The plate is attached to the half space over this contact region by a viscous couplant with viscous parameter κ. The inertia effects of the couplant layer are ignored and it is assumed that the vertical displacements of the plate coincide with those of the half space in the contact region while the horizontal velocity difference is proportional to the interface shear stress. The problem reduces to the determination of the normal and shearing traction distributions over this contact region.

Let $u_\alpha'(x_1', x_2', t)$ and $\sigma_{\alpha\beta}'(x_1', x_2', t)$, $\alpha, \beta = 1, 2$, represent the two-dimensional plane-strain components of the displacement and stress fields in the plate when it is considered as a three-dimensional continuum. Let $u_\alpha(x_1, x_2, t)$ and $\sigma_{\alpha\beta}(x_1, x_2, t)$ be the corresponding quantities for the half space. In this context the boundary conditions for the plate are (see Fig. 1)

$$\sigma_{22}'\left(x_1', \frac{h}{2}, t\right) = \sigma_{21}'\left(x_1', \frac{h}{2}, t\right) = 0, \quad |x_1'| < b,$$

$$\sigma_{11}'(b, x_2', t) = \sigma_{12}'(b, x_2', t) = \sigma_{11}'(-b, x_2', t) = \sigma_{12}'(-b, x_2', t) = 0, \quad |x_2'| < h/2,$$

$$-\sigma_{22}'\left(x_1', -\frac{h}{2}, t\right) = t_2'(x_1', t), \quad -\sigma_{21}'\left(x_1', -\frac{h}{2}, t\right) = t_1'(x_1', t), \quad (1)$$

in which $t_1'(x_1', t)$ and $t_2'(x_1', t)$ represent the components of the traction vector applied to the bottom surface of the plate.

The half space is assumed to be traction-free on the boundary outside the contact region. So the half-space boundary conditions are

$$\sigma_{22}(x_1, 0, t) = \begin{cases} 0, & |x_1| > b \\ -t_2(x_1, t), & |x_1| < b \end{cases}$$

$$\sigma_{21}(x_1, 0, t) = \begin{cases} 0, & |x_1| > b \\ -t_1(x_1, t), & |x_1| < b \end{cases} \quad (2)$$

The viscous contact conditions between the plate and half space are expressed as

$$u_2(x_1, 0, t) = -u_2'(x_1, t), \quad \sigma_{21}(x_1, 0, t) = \kappa[\dot{u}_1(x_1, 0, t) - \dot{u}_1'(x_1, t)],$$

$$t_1(x_1, t) = -t_1'(x_1, t), \quad t_2(x_1, t) = t_2'(x_1, t), \quad |x_1| < b. \quad (3)$$

in which $u_1'(x_1, t)$ and $u_2'(x_1, t)$ represent the extensional and bending displacement components of the two-dimensional plate considered in Appendix B of [15].

We assume an incident Rayleigh wave with $e^{-i\omega t}$ time-dependence traveling in the half space in the x_1-direction is scattered by the plate. Therefore the displacement and stress fields in the half space are decomposed into their incident and scattered parts as

$$u_\alpha = u_\alpha^{(I)} + u_\alpha^{(S)}, \quad \sigma_{\alpha\beta} = \sigma_{\alpha\beta}^{(I)} + \sigma_{\alpha\beta}^{(S)}, \quad (4)$$

in which $u_\alpha^{(I)}$ and $\sigma_{\alpha\beta}^{(I)}$ are prescribed by the incident Rayleigh wave.

3 Reduction of the Problem to Integral Equations

It will be convenient to decompose the problem into its *physically* symmetric and antisymmetric parts with respect to x_1. Superscripts "S" and "A" will be used to denote elements of this decomposition. It is easily shown that displacement and traction quantities $u_1^{(S)A}$, $u_2^{(S)S}$, $u_1'^A$, $u_2'^S$, t_1^A, and t_2^S are *mathematically* symmetric functions of x_1 while $u_1^{(S)S}$, $u_2^{(S)A}$, $u_1'^S$, $u_2'^A$, t_1^S, and t_2^A are antisymmetric functions of x_1 on $|x_1| < b$.

Since the time-dependence enters the time-harmonic problem only through the factor $e^{-i\omega t}$, we will deal with the time-reduced problem in which real time-dependent quantities $f_{\alpha\beta}(x_\gamma, t)$ are related to time-reduced $\bar{f}_{\alpha\beta}(x_\gamma)$ by

$$f_{\alpha\beta}(x_\gamma, t) = \mathrm{Re}\,\{\bar{f}_{\alpha\beta}(x_\gamma)e^{-i\omega t}\}, \quad (5)$$

where, in general, $\bar{f}_{\alpha\beta}(x_\gamma)$ represent complex-valued quantities. When unlikely to cause confusion, the bar will be deleted from $\bar{f}_{\alpha\beta}(x_\gamma)$ and it will be written simply as $f_{\alpha\beta}(x_\gamma)$.

The scattered fields in the half space can be derived from Lamb's [7] solution. A complete derivation of this steady time-harmonic solution is given in [15] as the limit of the solution of a related initial-

Downloaded 01 May 2010 to 171.66.16.249. Redistribution subject to ASME license or copyright; see http://www.asme.org/terms/Terms_Use.cfm

value problem. For our purposes we need to express the scattered interface displacements in terms of the scattered interface tractions, which are the same as the total interface tractions since the incident Rayleigh wave produces no surface tractions. When the surface tractions $t_1(x_1), t_2(x_1)$ vanish for $|x_1| > b$, equations (A.45) of [15] give the results

$$u_\alpha^{(S)S}(x_1, 0) = \int_{-b}^{b} G_{\alpha\beta}(x_1 - \xi) t_\beta^S(\xi) d\xi,$$

$$u_\alpha^{(S)A}(x_1, 0) = \int_{-b}^{b} G_{\alpha\beta}(x_1 - \xi) t_\beta^A(\xi) d\xi, \quad (6)$$

in which the displacement Green's functions $G_{\alpha\beta}$ are defined in (A.38)–(A.42) of [15] and summation is implied over repeated indices. As indicated earlier, the bar has been deleted from the time-reduced functions and $G_{\alpha\beta}(x)$ has been written in place of $G_{\alpha\beta}(x, 0)$.

The time-harmonic plate solution satisfying boundary conditions (1) is derived in Appendix B of [15], using classical plate theory. In the context of plane-strain plate theory, the displacements u_α' depend only on x_1' and t, and we decompose the plate problem into *extension* with displacement $u_1'(x_1', t)$ and *bending* with displacement $u_2'(x_1', t)$. Using the same symmetry decomposition with respect to x_1' as before, we write the time-reduced plate solution from (B.9) of [15] as

$$u_1'^S(x_1') = \int_{-b}^{b} G_1'^S(x_1', \xi) t_1'^S(\xi) d\xi,$$

$$u_1'^A(x_1') = \int_{-b}^{b} G_1'^A(x_1', \xi) t_1'^A(\xi) d\xi,$$

$$u_2'^S(x_1') = \int_{-b}^{b} G_{2\beta}'^S(x_1', \xi) t_\beta'^S(\xi) d\xi,$$

$$u_2'^A(x_1') = \int_{-b}^{b} G_{2\beta}'^A(x_1', \xi) t_\beta'^A(\xi) d\xi, \quad (7)$$

where the quantities $G_1'^S$, $G_1'^A$, $G_{2\alpha}'^S$, $G_{2\alpha}'^A$, $\alpha = 1, 2$, are defined in (B.10)–(B.11) of [15] for $0 \le x_1' \le b, 0 \le \xi \le b$ and are extended here according to the indicated symmetries to $|x_1'| \le b, |\xi| \le b$. This extension requires $G_1'^A, G_{2\beta}'^S$ be symmetric and $G_1'^S, G_{2\beta}'^A$ be antisymmetric in x_1' while it requires $G_1'^A, G_{21}'^A, G_{22}'^S$ be symmetric and $G_1'^S, G_{21}'^S, G_{22}'^A$ be antisymmetric in ξ. The symmetry extension also requires introduction of the factor 1/2.

Finally, we consider the incident Rayleigh wave. In Appendix C of [15] the time-reduced form is recorded with the desired symmetry decomposition. From (C.7) and (C.9) of [15] we have (with the bar deleted from the time-reduced expressions)

$$u_1^{(I)S}(x_1, 0) = iu_0 \sin(\omega s_R x_1), \quad u_2^{(I)S}(x_1, 0) = iu_0 P(\eta_R) \cos(\omega s_R x_1),$$

$$u_1^{(I)A}(x_1, 0) = u_0 \cos(\omega s_R x_1), \quad u_2^{(I)A}(x_1, 0) = -u_0 P(\eta_R) \sin(\omega s_R x_1),$$

$$P(\eta_R) = (2\sqrt{(1 - \epsilon^2\eta_R^2)(1 - \eta_R^2)} + \eta_R^2 - 2)/\eta_R^2\sqrt{1 - \eta_R^2},$$

$$\eta_R = s_2/s_R, \quad \epsilon = s_1/s_2. \quad (8)$$

The integral equations determining $t_\alpha(x_1)$ result from the use of (5)–(8) in (1)–(4) and they can be written formally as follows:

$$\frac{1}{i\omega\kappa} t_1^S(x_1) - \int_{-b}^{b} [t_1^S(\xi) G_{11}(x_1 - \xi) + t_2^S(\xi) G_{12}(x_1 - \xi)] d\xi$$

$$- \int_{-b}^{b} t_1^S(\xi) G_1'^S(x_1, \xi) d\xi = iu_0 \sin(\omega s_R x_1),$$

$$\frac{1}{i\omega\kappa} t_1^A(x_1) - \int_{-b}^{b} [t_1^A(\xi) G_{11}(x_1 - \xi) + t_2^A(\xi) G_{12}(x_1 - \xi)] d\xi$$

$$- \int_{-b}^{b} t_1^A(\xi) G_1'^A(x_1, \xi) d\xi = u_0 \cos(\omega s_R x_1),$$

$$\int_{-b}^{b} [t_1^S(\xi) G_{21}(x_1 - \xi) + t_2^S(\xi) G_{22}(x_1 - \xi)] d\xi$$

$$- \int_{-b}^{b} [t_1^S(\xi) G_{21}'^S(x_1, \xi) - t_2^S(\xi) G_{22}'^S(x_1, \xi)] d\xi \quad (9)$$

$$= -iu_0 P(\eta_R) \cos(\omega s_R x_1), \int_{-b}^{b} [t_1^A(\xi) G_{21}(x_1 - \xi)$$

$$+ t_2^A(\xi) G_{22}(x_1 - \xi)] d\xi - \int_{-b}^{b} [t_1^A(\xi) G_{21}'^A(x_1, \xi)$$

$$- t_2^A(\xi) G_{22}'^A(x_1, \xi)] d\xi = u_0 P(\eta_R) \sin(\omega s_R x_1). \quad (9)$$

(*Cont.*)

We note that the first and third of (9) provide a pair of two integral equations for t_1^S and t_2^S while the second and fourth provide a different pair for t_1^A and t_2^A. For $0 < \kappa < \infty$ and $u_0 \neq 0$ they are inhomogeneous equations of the second kind. The limit $\kappa \to 0$ represents perfectly lubricated contact in which case the first two of (9) imply t_1^S and t_1^A both vanish and the second two then become uncoupled equations of the first kind for t_2^S and t_2^A. The limit $\kappa \to \infty$ represents perfect bond in which case the first two of (9) become equations of the first kind, the first and third again determine t_1^S and t_2^S while the second and fourth determine t_1^A and t_2^A. In the next section, an equivalent set of singular integral equations will be derived from (9). They will then be analyzed to determine the singular nature of their solution, i.e., the interface tractions. This, in turn, will dictate the quadrature schemes for solving the equations numerically.

4 Analysis of Integral Equations

The system of integral equations obtained in the previous section has kernels with logarithmic singularities. We anticipate that the solution may be singular and we must determine the order of these singularities before the equations can be solved numerically. Before proceeding with this determination it is advantageous to introduce dimensionless variables and write the equations in a more compact form. First, the dimensionless variables are defined by

$$x = x_1/b, \quad \tilde{s} = \omega b s, \quad \tilde{u}_0 = u_0/b, \quad \alpha = \mu/\omega\kappa b, \quad k = \mu'/\mu,$$

$$\tilde{t}_\alpha^L(\xi) = \mu^{-1} t_\alpha^L(b\xi), \quad \tilde{G}_{\alpha\beta}(x) = \mu G_{\alpha\beta}(bx),$$

$$\tilde{G}_1'^L(x, \xi) = \mu' G_1'^L(bx, b\xi),$$

$$\tilde{G}_{2\beta}'^L(x, \xi) = \mu' G_{2\beta}'^L(bx, b\xi), \quad L = S, A. \quad (10)$$

Then (9) can be written as

$$-i\alpha\tilde{t}_1^L(x) - \int_{-1}^{1} [\tilde{G}_{1\beta}(x - \xi)\tilde{t}_\beta^L(\xi) + k^{-1}\tilde{G}_1'^L(x, \xi)\tilde{t}_1^L(\xi)] d\xi = f_1^L(x),$$

$$\int_{-1}^{1} [\tilde{G}_{2\beta}(x - \xi)\tilde{t}_\beta^L(\xi) + (-1)^\beta k^{-1}\tilde{G}_{2\beta}'^L(x, \xi)\tilde{t}_\beta^L(\xi)] d\xi$$

$$= f_2^L(x), \quad L = S, A \quad (11)$$

where

$$f_1^S(x) = i\tilde{u}_0 \sin(\tilde{s}_R x), \quad f_1^A(x) = \tilde{u}_0 \cos(\tilde{s}_R x),$$

$$f_2^S(x) = -i\tilde{u}_0 P(\eta_R) \cos(\tilde{s}_R x), \quad f_2^A(x) = \tilde{u}_0 P(\eta_R) \sin(\tilde{s}_R x). \quad (12)$$

In order to determine the order of singularities in $\tilde{t}_\beta(x)$ at $x = \pm 1$ we need to differentiate (11) with respect to x. Also the numerical solution will require the integral of (11) from -1 to x. Let $F(x)$ be any of the functions defined on the interval $-1 < x < 1$. Then we define $\hat{F}(x)$ and $\check{F}(x)$ by

$$\hat{F}(x) = \frac{d}{dx} F(x), \quad \check{F}(x) = \int_{-1}^{x} F(y) dy. \quad (13)$$

Upon differentiation of (11) we obtain with the use of (A.51) of [15] and [12, Section 13],

$$i\alpha\tilde{t}_{1,1}^L(x) - \frac{\epsilon^2}{2(1 - \epsilon^2)} \tilde{t}_2^L(x) + \int_{-1}^{1} \left[-\frac{1}{2\pi(1 - \epsilon^2)} \frac{\tilde{t}_1^L(\xi)}{(x - \xi)} \right.$$

$$\left. + K_{1\beta}(x - \xi)\, \tilde{t}_\beta^L(\xi) + k^{-1}\hat{G}_1'^L(x, \xi)\tilde{t}_1^L(\xi) \right] d\xi = -\hat{f}_1^L(x), \quad (14)$$

Downloaded 01 May 2010 to 171.66.16.249. Redistribution subject to ASME license or copyright; see http://www.asme.org/terms/Terms_Use.cfm

$$-\frac{\epsilon^2}{2(1-\epsilon^2)}\tilde{t}_1^L(x)+\int_{-1}^{1}\left[\frac{1}{2\pi(1-\epsilon^2)}\frac{\tilde{t}_2^L(\xi)}{(x-\xi)}-K_{2\beta}(x-\xi)\tilde{t}_\beta^L(\xi)\right.$$
$$\left.-(-1)^\beta k^{-1}\check{G}'^L_{2\beta}(x,\xi)\tilde{t}_\beta^L(\xi)\right]d\xi=-\tilde{f}_2^L(x),\quad L=S,A \quad (14)$$
(Cont.)

in which $K_{\alpha\beta}$ are defined by (A.52) of [15] while $\check{G}'^L_1$, $\check{G}'^L_{2\beta}$ are defined by (B.15) and (B.16) of [15] for $0 \leqq x \leqq 1, 0 \leqq \xi \leqq 1$. Upon integration of (11) we obtain

$$\int_{-1}^{1}[i\alpha H(x-\xi)\tilde{t}_1^L(\xi)+\check{G}_{1\beta}(x,\xi)\tilde{t}_\beta^L(\xi)$$
$$+k^{-1}\check{G}'^L_1(x,\xi)\tilde{t}_1^L(\xi)]d\xi=-\check{f}_1^L(x)$$
$$\int_{-1}^{1}[\check{G}_{2\beta}(x,\xi)\tilde{t}_\beta^L(\xi)+(-1)^\beta k^{-1}\check{G}'^L_{2\beta}(x,\xi)\tilde{t}_\beta^L(\xi)]d\xi$$
$$=\check{f}_2^L(x),\quad L=S,A \quad (15)$$

in which $\check{G}_{\alpha\beta}(x,\xi)$ are defined by (A.53) of [15] while $\check{G}'^L_1$, $\check{G}'^L_{2\beta}$ are derived from (B.14), (B.17), and (B.18) of [15] and from the symmetries discussed after (7).

Four different treatments of the integral equations are required depending on the values of the two parameters α and ϵ, which are defined in terms of μ, σ, ω, b, and the viscosity parameter κ by

$$\alpha=\mu/\omega\kappa b,\quad \epsilon=\left[\frac{1-2\sigma}{2(1-\sigma)}\right]^{1/2}.$$

Case 1: $0<\alpha<\infty, 0 \leqq \epsilon \leqq 1/\sqrt{2}$ (Viscous Coupling). In order to analyze this case we assume the functions $\tilde{t}_\alpha(\xi)$ have integrable singularities. Then using the properties of $\tilde{G}_{1\beta}$ and $\tilde{G}'^L_1$, which are defined in (A.48), (A.38)–(A.42) and (B.10)–(B.12), all of [15], we conclude from the first of (11) that $\tilde{t}_1^L(x)$ is bounded. With this result the second of (14) can be used to determine the order of singularity in $\tilde{t}_2^L(x)$, which we assume has the form

$$\tilde{t}_2^L(x)=\frac{\phi_2^L(x)}{(1-x^2)^{\gamma_2}},\quad 0<\gamma_2<1, \quad (16)$$

where $\phi_2^L(x)$ is Hölder continuous on $-1 \leqq x \leqq 1$ and does not vanish at $x=\pm 1$. Using the methods for singular integrals given in Muskhelishvili [12], we conclude that $\gamma_2=1/2$.

In order to solve the integral equations by numerical quadrature methods we need to know more about $\tilde{t}_1^L$ than merely the fact that it is bounded. Using this fact and the knowledge that $\tilde{t}_2^L$ has a square root singularity, we can show from the first of (14) that $\tilde{t}_{1,1}^L$ also has a square root singularity. To do so we assume the form

$$\tilde{t}_1^L(x)=a_1^L+b_1^L x+\phi_1^L(x)(1-x^2)^{\gamma_1},\quad 0<\gamma_1, \quad (17)$$

where a_1^L and b_1^L are constants determined by the values of $\tilde{t}_1^L$ at $x \pm 1$, and $\phi_1(x)$ is Hölder continuous and does not vanish at $x=\pm 1$. Use of this assumed form for $\tilde{t}_1^L$ in the first of (14) leads one to the conclusion that $\gamma_1=1/2$, which is the result required to determine the quadrature formulas for the numerical integration of the integral equations.

Case 2. $\alpha \to \infty, 0 \leqq \epsilon \leqq 1/\sqrt{2}$ (Inviscid Coupling). In this case the first of (11) implies that $\tilde{t}_1^L=0$, i.e., no shear stress is transmitted between the half space and plate. Then the second of (14) yields the result that $\tilde{t}_2^L$ has a square root singularity at the points $x=\pm 1$.

Case 3. $\alpha=0, \epsilon=0$ (Perfect Bond, Incompressible Half Space). In this case the equations in (14) become singular integral equations of the first kind. Both $\tilde{t}_1^L$ and $\tilde{t}_2^L$ are found to have square root singularities at $x=\pm 1$. This agrees with the result obtained by Luco and Westmann [3] under similar circumstances for the case of a rigid plate.

Case 4. $\alpha=0, 0<\epsilon \leqq 1/\sqrt{2}$ (Perfect Bond, Compressible Half Space). In this case the equations (14) become singular integral equations of the second kind. Both $\tilde{t}_1^L$ and $\tilde{t}_2^L$ are found to have oscillating square root singularities of the type that occur when a rough rigid punch indents a half space. This is also in agreement with results obtained by Luco and Westmann [3] for the case of a rigid plate.

We are interested here in the case of viscous coupling between the plate and half space and therefore confine our attention to Case 1.

Hence the solutions $\tilde{t}_\alpha^L(\xi)$ we seek have the forms given in (16) and (17), where γ_1 and γ_2 both have the value 1/2. Three different forms of the integral equations are given by (11), (14), and (15). For the purpose of numerical solution, the most suitable pair is composed of the first of (15) together with the last of (14). Therefore, the systems we wish to solve numerically can be written in the form

$$C_{\alpha\beta}\tilde{t}_\beta^L(x)+\int_{-1}^{1}\left[\frac{D_{\alpha\beta}}{x-\xi}+M_{\alpha\beta}(x,\xi)-k^{-1}M'^L_{\alpha\beta}(x,\xi)\right]\tilde{t}_\beta^L(\xi)d\xi$$
$$=\tilde{f}_\alpha^L(x),\quad L=S,A. \quad (18)$$

in which

$$C_{11}=C_{12}=C_{22}=0,\quad C_{21}=-\epsilon^2/2(1-\epsilon^2),$$
$$D_{11}=D_{12}=D_{21}=0,\quad D_{22}=1/2\pi(1-\epsilon^2),$$
$$M_{11}(x,\xi)=i\alpha H(x-\xi)+\check{G}_{11}(x,\xi),\quad M_{12}(x,\xi)=\check{G}_{12}(x,\xi),$$
$$M_{2\alpha}(x,\xi)=-K_{2\alpha}(x-\xi),\ M'^L_{11}(x,\xi)=-\check{G}'^L_1(x,\xi),$$
$$M'^L_{12}(x,\xi)=0,\quad M'^L_{2\alpha}(x,\xi)=(-1)^\alpha\check{G}'^L_{2\alpha}(x,\xi),$$
$$\tilde{f}_1^S(x)=(i\tilde{u}_0/\tilde{s}_R)[\cos(\tilde{s}_R x)-\cos(\tilde{s}_R)],$$
$$\tilde{f}_2^S(x)=-i\tilde{u}_0\tilde{s}_R P(\eta_R)\sin(\tilde{s}_R x),$$
$$\tilde{f}_1^A(x)=-(\tilde{u}_0/\tilde{s}_R)[\sin(\tilde{s}_R x)+\sin(\tilde{s}_R)],$$
$$\tilde{f}_2^A(x)=-\tilde{u}_0\tilde{s}_R P(\eta_R)\cos(\tilde{s}_R x). \quad (19)$$

Because of the differentiation involved, the second equation in the system (18) is not equivalent to the last two of (9). The constraint required to make them equivalent (i.e., to determine the integration constant) is obtained from the evaluation of the second of (15) at $x=1$. Because of the symmetry of the involved functions, no constraint is obtained from the antisymmetric equation (i.e., for $L=A$). For $L=S$ the second of (15) evaluated at $x=1$ yields

$$\int_{-1}^{1}[\check{G}_{2\beta}(1,\xi)\tilde{t}_\beta^S(\xi)+(-1)^\beta k^{-1}\check{G}'^S_{2\beta}(1,\xi)\tilde{t}_\beta^S(\xi)]d\xi=$$
$$-2i(\tilde{u}_0/\tilde{s}_R)P(\eta_R)\sin(\tilde{s}_R). \quad (20)$$

The linear algebraic system of equations resulting from the quadrature formulas appropriate to (18) subject to (20) will be derived in the next section.

5 Algebraic System Obtained From Singular Integral Equations

In this section the algebraic system of equations approximating the integral equations (18)–(20) is derived. For this purpose, it is useful to write (18)–(20) again in expanded form as

$$i\alpha\int_{-1}^{x}\tilde{t}_1^L(\xi)d\xi+\int_{-1}^{1}\check{G}_{11}(x,\xi)\tilde{t}_1^L(\xi)d\xi$$
$$+k^{-1}\int_0^1\check{G}'^L_1(x,\xi)\tilde{t}_1^L(\xi)d\xi+\int_{-1}^{1}\check{G}_{12}(x,\xi)\tilde{t}_2^L(\xi)d\xi=\tilde{f}_1^L(x),$$
$$\frac{\epsilon^2}{2(1-\epsilon^2)}\tilde{t}_1^L(x)+\int_{-1}^{1}K_{21}(x-\xi)\tilde{t}_1^L(\xi)d\xi$$
$$-k^{-1}\int_0^1\check{G}'^L_{21}(x,\xi)\tilde{t}_1^L(\xi)d\xi$$
$$+\frac{1}{2\pi(1-\epsilon^2)}\int_{-1}^{1}\frac{\tilde{t}_2^L(\xi)}{\xi-x}d\xi+\int_{-1}^{1}\operatorname{sgn}(x-\xi)\,\overline{K}_{22}(x-\xi)\tilde{t}_2^L(\xi)d\xi$$
$$+k^{-1}\int_0^1\check{G}'^L_{22}(x,\xi)\tilde{t}_2^L(\xi)d\xi=-\tilde{f}_2^L(x),$$
$$\int_{-1}^{1}\check{G}_{21}(1,\xi)\tilde{t}_1^S(\xi)d\xi+\int_{-1}^{1}\check{G}_{22}(1,\xi)\tilde{t}_2^S(\xi)d\xi$$
$$+k^{-1}\int_0^1\check{G}'^S_{22}(1,\xi)\tilde{t}_2^S(\xi)d\xi=\tilde{f}_3, \quad (21)$$

where $\overline{K}_{22}(x-\xi)$ is defined in (A.61), (A.52) of [15] and

$$\tilde{f}_3=-2i(\tilde{u}_0/\tilde{s}_R)P(\eta_R)\sin\tilde{s}_R. \quad (22)$$

Next we recall from (16), (17) and the analysis of the previous section that

Downloaded 01 May 2010 to 171.66.16.249. Redistribution subject to ASME license or copyright; see http://www.asme.org/terms/Terms_Use.cfm

$$\tilde{t}_1^L(x) = \tilde{t}_1^L(1)e^L(x) + (1 - x^2)^{1/2}\phi_1^L(x),$$

$$\tilde{t}_2^L(x) = \frac{\phi_2^L(x)}{(1 - x^2)^{1/2}}, \quad L = S, A \tag{23}$$

where

$$e^L(x) = \begin{cases} x, & \text{if } L = S \\ 1, & \text{if } L = A \end{cases} \tag{24}$$

The first term in the first of (21) and the sgn $(x - \xi)\overline{K}_{22}$ term in the second of (21) require special treatment. With use of (23) we obtain

$$\int_{-1}^{x} \tilde{t}_1^L(\xi)d\xi = E^L(x)\tilde{t}_1^L(1) + F(x)\phi_1^L(x) + \int_{-1}^{x} (1 - \xi^2)^{1/2}[\phi_1^L(\xi) - \phi_1^L(x)]d\xi \tag{25}$$

where

$$E^L(x) = \begin{cases} -(1 - x^2)/2, & \text{if } L = S \\ 1 + x, & \text{if } L = A \end{cases} \tag{26}$$

and

$$F(x) = \int_{-1}^{x} (1 - \xi^2)^{1/2}d\xi = \tfrac{1}{2}x(1 - x^2)^{1/2} + \tfrac{1}{2}\arcsin(x) + \frac{\pi}{4}. \tag{27}$$

Also, the sgn $(x - \xi)\overline{K}_{22}$ term yields

$$\int_{-1}^{1} \operatorname{sgn}(x - \xi)\overline{K}_{22}(x - \xi)\tilde{t}_2^L(\xi)d\xi = \phi_2^L(x) \int_{-1}^{1} \frac{\operatorname{sgn}(x - \xi)}{(1 - \xi^2)^{1/2}} \overline{K}_{22}(x - \xi)d\xi + \int_{-1}^{1} \frac{\operatorname{sgn}(x - \xi)}{(1 - \xi^2)^{1/2}} \overline{K}_{22}(x - \xi)[\phi_2^L(\xi) - \phi_2^L(x)]d\xi \tag{28}$$

Next, we recall from Erdogan and Gupta [14] the following approximation formulas when the functions $\tilde{t}_\alpha^L(x)$ in (21) appear in integrals with Cauchy kernels or with regular kernels. For Cauchy kernels we have

$$\frac{1}{\pi}\int_{-1}^{1} \frac{\phi_1^L(\xi)(1 - \xi^2)^{1/2}}{\xi - y_j}d\xi = \sum_{k=1}^{n} \frac{(1 - \zeta_k^2)\phi_1^L(\zeta_k)}{(n + 1)(\zeta_k - y_j)}, \quad j = 1, 2, \ldots, (n + 1),$$

$$\frac{1}{\pi}\int_{-1}^{1} \frac{\phi_2^L(\xi)}{(1 - \xi^2)^{1/2}(\xi - x_j)}d\xi = \sum_{k=1}^{n} \frac{\phi_2^L(\eta_k)}{n(\eta_k - x_j)}, \quad j = 1, 2, \ldots, (n - 1), \tag{29}$$

where the collocation points y_j, x_j and the interpolation points ζ_k, η_k are determined as roots of Chebychev polynomials and are given by

$$\zeta_k = \cos\left(\frac{\pi k}{n + 1}\right), \; y_j = \cos\left[\frac{(2j - 1)\pi}{2(n + 1)}\right], \quad k = 1, 2, \ldots, n; \quad j = 1, 2, \ldots, (n + 1) \tag{30}$$

and

$$\eta_k = \cos\left[\frac{(2k - 1)\pi}{2n}\right], \quad x_j = \cos\left(\frac{\pi j}{n}\right), \quad k = 1, 2, \ldots, n; \quad j = 1, 2, \ldots, (n - 1) \tag{31}$$

For integrals with regular kernels $M(x, \xi)$ the results are

$$\frac{1}{\pi}\int_{-1}^{1} \phi_1^L(\xi)(1 - \xi^2)^{1/2}M(x, \xi)d\xi = \sum_{k=1}^{n} \frac{1}{n + 1} \phi_1^L(\zeta_k)(1 - \zeta_k^2)M(x, \zeta_k),$$

$$\frac{1}{\pi}\int_{-1}^{1} \frac{\phi_2^L(\xi)}{(1 - \xi^2)^{1/2}} M(x, \xi)d\xi = \sum_{k=1}^{n} \frac{1}{n} \phi_2^L(\eta_k)M(x, \eta_k), \tag{32}$$

where ζ_k and η_k are again given by (30), (31).

We observe from (30), (31) that

$$\zeta_{n+1-k} = -\zeta_k, \quad y_{n+2-j} = -y_j, \quad \eta_{n+1-k} = -\eta_k, \quad x_{n-j} = -x_j. \tag{33}$$

This together with the symmetries of ϕ_α^L allows us to replace (32), for n an even integer, by

$$\int_{-1}^{1} \phi_1^L(\xi)(1 - \xi^2)^{1/2}M(x, \xi)d\xi = \frac{\pi}{n + 1} \sum_{k=1}^{n/2} \phi_1^L(\zeta_k) \times (1 - \zeta_k^2)[M(x, \zeta_k) + (-1)^L M(x, -\zeta_k)],$$

$$\int_{-1}^{1} \frac{\phi_2^L(\xi)}{(1 - \xi^2)^{1/2}} M(x, \xi)d\xi = \frac{\pi}{n} \sum_{k=1}^{n/2} \phi_2^L(\eta_k) \times [M(x, \eta_k) - (-1)^L M(x, -\eta_k)], \tag{34}$$

where

$$(-1)^L = \begin{cases} -1, & \text{if } L = S \\ 1, & \text{if } L = A \end{cases} \tag{35}$$

Similarly, the approximation formulas (29) can be written in terms of $\phi_1^L(\zeta_k)$, $\phi_2^L(\eta_k)$, $k = 1, 2 \ldots, n/2$. Also, when the limits of integration are 0 to 1 instead of -1 to 1, we have

$$\int_{0}^{1} \phi_1^L(\xi)(1 - \xi^2)^{1/2}M(x, \xi)d\xi = \frac{\pi}{n + 1} \sum_{k=1}^{n/2} \phi_1^L(\zeta_k)(1 - \zeta_k^2)M(x, \zeta_k),$$

$$\int_{0}^{1} \frac{\phi_2^L(\xi)}{(1 - \xi^2)^{1/2}} M(x, \xi)d\xi = \frac{\pi}{n} \sum_{k=1}^{n/2} \phi_2^L(\eta_k)M(x, \eta_k). \tag{36}$$

When $\phi_\alpha^L(x)$ appears in the equations outside of integrals as in (25) and (28), we use Lagrange interpolation polynomials [16] together with (33) and the symmetries of $\phi_\alpha^L(x)$ to obtain

$$\phi_1^S(x) = \sum_{k=1}^{n/2} \frac{x}{\zeta_k} \Delta_k^1(x)\phi_1^S(\zeta_k), \quad \phi_1^A(x) = \sum_{k=1}^{n/2} \Delta_k^1(x)\phi_1^A(\zeta_k),$$

$$\phi_2^S(x) = \sum_{k=1}^{n/2} \Delta_k^2(x)\phi_2^S(\eta_k), \quad \phi_2^A(x) = \sum_{k=1}^{n/2} \frac{x}{\eta_k} \Delta_k^2(x)\phi_2^A(\eta_k), \tag{37}$$

where

$$\Delta_k^1(x) = \frac{(x^2 - \zeta_1^2) \ldots (x^2 - \zeta_{k-1}^2)(x^2 - \zeta_{k+1}^2) \ldots (x^2 - \zeta_{n/2}^2)}{(\zeta_k^2 - \zeta_1^2) \ldots (\zeta_k^2 - \zeta_{k-1}^2)(\zeta_k^2 - \zeta_{k+1}^2) \ldots (\zeta_k^2 - \zeta_{n/2}^2)},$$

$$\Delta_k^2(x) = \frac{(x^2 - \eta_1^2) \ldots (x^2 - \eta_{k-1}^2)(x^2 - \eta_{k+1}^2) \ldots (x^2 - \eta_{n/2}^2)}{(\eta_k^2 - \eta_1^2) \ldots (\eta_k^2 - \eta_{k-1}^2)(\eta_k^2 - \eta_{k+1}^2) \ldots (\eta_k^2 - \eta_{n/2}^2)}. \tag{38}$$

The collocation points are not restricted in (34)–(38). These results are valid for all values of x in $-1 < x < 1$. Since a Cauchy kernel appears, with $\tilde{t}_2^L$, in the second of (21), the collocation points in that equation are given by x_j in (31). For reasons related to the number of unknowns represented by $\phi_1^L(\zeta_k)$, $\phi_2^L(\eta_k)$, $\tilde{t}_1^L(1)$ and the number of equations needed from (21), we choose for the first of (21) the collocation points y_j in (30).

Using the approximation formulas (34)–(38), we obtain from (21) the following algebraic system:

$$[i\alpha E^L(y_j) + \check{G}_{11}^L(y_j) + k^{-1}\check{G}_1'^L(y_j)]\tilde{t}_1^L(1) + \frac{\pi}{n + 1} \sum_{k=1}^{n/2} \{i\alpha A_k^L(y_j) + (1 - \zeta_k^2)[\check{G}_{11}^L(y_j, \zeta_k) + k^{-1}\check{G}_1'^L(y_j, \zeta_k)]\}\phi_1^L(\zeta_k) + \frac{\pi}{n} \sum_{k=1}^{n/2} \check{G}_{12}^L(y_j, \eta_k)\phi_2^L(\eta_k) = \tilde{f}_1^L(y_j), \quad j = 1, 2, \ldots, \frac{n}{2} + 1$$

$$\left[\frac{\epsilon^2}{2(1 - \epsilon^2)} e^L(x_j) + \check{K}_{21}^L(x_j) - k^{-1}\check{G}_{21}'^L(x_j)\right]\tilde{t}_1^L(1) + \frac{\pi}{n + 1} \sum_{k=1}^{n/2} \left\{\frac{n + 1}{\pi} \frac{\epsilon^2}{2(1 - \epsilon^2)} (1 - x_j^2)^{1/2} D_k^{1L}(x_j)\right. \tag{39}$$

Downloaded 01 May 2010 to 171.66.16.249. Redistribution subject to ASME license or copyright; see http://www.asme.org/terms/Terms_Use.cfm

$$+ (1 - \zeta_k^2)[K_{21}^L(x_j, \zeta_k) - k^{-1}\hat{G}_{21}'^L(x_j, \zeta_k)]\Big\}\phi_1^L(\zeta_k)$$

$$+ \frac{\pi}{n}\sum_{k=1}^{n/2}\left[\frac{1}{2\pi(1-\epsilon^2)}C^L(x_j, \eta_k) + B_k^L(x_j) + k^{-1}\hat{G}_{22}'^L(x_j, \eta_k)\right]\phi_2^L(\eta_k)$$

$$= -\tilde{f}_2^L(x_j), \quad j = \begin{cases} 1, 2, \ldots, n/2 - 1 & \text{if } L = S \\ 1, 2, \ldots, n/2 & \text{if } L = A \end{cases}$$

$$\hat{G}_{21}^S(1)\tilde{t}_1^S(1) + \frac{\pi}{n+1}\sum_{k=1}^{n/2}(1-\zeta_k^2)\hat{G}_{21}^S(1, \zeta_k)\phi_1^S(\zeta_k) + \frac{\pi}{n}\sum_{k=1}^{n/2}[\hat{G}_{22}^S(1, \eta_k) + k^{-1}\hat{G}'^S_{22}(1, \eta_k)]\phi_2^S(\eta_k) = \tilde{f}_3 \quad (39)$$

(*Cont.*)

where we have used the notation $\hat{G}_{\alpha\beta}^L$, $\hat{G}_{\alpha\beta}'^L$, and $\hat{G}_{\alpha}'^L$ in place of $\check{\check{G}}_{\alpha\beta}^L$, $\check{\check{G}}_{\alpha\beta}'^L$, and $\check{\check{G}}_{\alpha}'^L$ that appeared in (A.64) and (B.24) of [15], and where

$$A_k^L(x) = M(x)D_k^{1L}(x) + (1 - \zeta_k^2)[H(x - \zeta_k) + (-1)^L],$$

$$B_k^L(x) = N(x)D_k^{2L}(x) + [\operatorname{sgn}(x - \eta_k)\overline{K}_{22}(x - \eta_k) - (-1)^L\overline{K}_{22}(x + \eta_k)],$$

$$C^S(x, \eta_k) = 2x/(\eta_k^2 - x^2), \quad C^A(x, \eta_k) = 2\eta_k/(\eta_k^2 - x^2),$$

$$D_k^{1S}(x) = (x/\zeta_k)\Delta_k^1(x), \quad D_k^{1A}(x) = \Delta_k^1(x),$$

$$D_k^{2S}(x) = \Delta_k^2(x), \quad D_k^{2A}(x) = (x/\eta_k)\Delta_k^2(x),$$

$$M(x) = \frac{n+1}{2\pi}[x(1-x^2)^{1/2} + \arcsin(x)] - \sum_{j=1}^{n/2}(1-\zeta_j^2)H(x - \zeta_j)$$

$$N(x) = \frac{n}{\pi}\int_{-1}^{1}\frac{\operatorname{sgn}(x-\xi)}{(1-\xi^2)^{1/2}}\overline{K}_{22}(x-\xi)d\xi - \sum_{j=1}^{n/2}[\operatorname{sgn}(x - \eta_j)\overline{K}_{22}(x - \eta_j) + \overline{K}_{22}(x + \eta_j)]. \quad (40)$$

Equation (39) is a complex $(n + 1)$ by $(n + 1)$ linear algebraic system determining the $n + 1$ complex unknowns $\tilde{t}_1^L(1)$, $\phi_1^L(\zeta_k)$, $\phi_2^L(\eta_k)$, $k = 1, 2, \ldots, n/2$. The first of (39) yields $(n/2) + 1$ equations for $L = S$ or A. The second of (39) yields $(n/2) - 1$ equations for $L = S$ and in this case the third of (39) yields the remaining equation. On the other hand, when $L = A$ the second of (39) yields $n/2$ equations and the third of (39) does not apply.

6 Numerical Results

The linear algebraic system of equations (39) was solved numerically for several sets of the physical parameters. There are eight such primary parameters:

Poisson's ratios of half space and plate:	σ, σ'
Ratio of shear moduli, plate/half space:	$k = \mu'/\mu$
Ratio of densities, plate/half space:	$\tilde{\rho} = \rho'/\rho$
Dimensionless viscosity parameter:	$\kappa^* = \kappa/\sqrt{\mu\rho}$
Aspect ratio of plate:	$\tilde{h} = h/b$
Dimensionless amplitude of Rayleigh wave:	$\tilde{u}_0 = u_0/b$
Dimensionless wavelength of Rayleigh wave:	$\tilde{\lambda}_R = \lambda_R/b$

The choice of parameter values for the results given here was dictated more by our interest in exhibiting certain phenomena than a desire to solve a particular physical system. However, it is not difficult to find material combinations with parameters that are represented by the values we chose, which are

$$\sigma = 0.25, \quad \sigma' = 0.25, \quad k = 2, \quad \tilde{\rho} = 0.5,$$

$$\kappa^* = (0.01, 0.1, 1, 10, 100), \quad \tilde{h} = (0.2, 0.01),$$

$$\tilde{u}_0 = 1, \quad 2/\tilde{\lambda}_R = (0.1 \text{ through } 1.4), \quad (41)$$

Therefore, our numerical study focuses primarily on the dependence of the solution on the viscosity parameter κ^* and the wavelength parameter $\tilde{\lambda}_R$. The number of parameters that need to be specified can be reduced to seven if we define $\tilde{\mu}$ by

$$\tilde{\mu} = k^{-1}(1 - \sigma'). \quad (42)$$

The other parameters that appear in the solution are related to the primary parameters as follows:

$$\tilde{s}_R = 2\pi/\tilde{\lambda}_R, \quad \tilde{s}_2 = \eta_R\tilde{s}_R,$$

$$\epsilon^2 = (1 - 2\sigma)/2(1 - \sigma), \quad \alpha = (\kappa^*\tilde{s}_2)^{-1}, \quad (43)$$

where η_R^2 is the real root in $0 < \eta^2 < 1$ of the Rayleigh equation

$$\eta^6 - 8\eta^4 + (24 - 16\epsilon^2)\eta^2 - 16(1 - \epsilon^2) = 0 \quad (44)$$

and

$$\tilde{M}^2 = \tilde{s}_2^2\tilde{\rho}\tilde{\mu}/2, \quad \tilde{N}^2 = \tilde{s}_2(6\tilde{\rho}\tilde{\mu})^{1/2}/\tilde{h},$$

$$k_*^{-1}p_1 = \tilde{\mu}/2\tilde{h}\tilde{M}, \quad k^{-1}p_{21} = 3\tilde{\mu}/2(\tilde{h}\tilde{N})^2, \quad k^{-1}p_{22} = 3\tilde{\mu}/(\tilde{h}\tilde{N})^3. \quad (45)$$

It is required by the plate solution given in Appendix B of [15] that

$$\sin(2\tilde{M}) \neq 0, \quad \cos(2\tilde{N})\cosh(2\tilde{N}) \neq 1. \quad (46)$$

After all the complex functions in the problem were decomposed into their real and imaginary parts, the real linear system represented by (39) with matrix components given in Appendix D of [15] was programmed in FORTRAN and executed on the Lawrence Berkeley Laboratory CDC 7600 computer. The solution of this system gives the values

$$\{\tilde{t}_1^{LR}(1), \phi_1^{LR}(\zeta_1), \ldots, \phi_1^{LR}(\zeta_{n/2}), \phi_2^{LR}(\eta_1), \ldots, \phi_2^{LR}(\eta_{n/2})\},$$

$$\{\tilde{t}_1^{LI}(1), \phi_1^{LI}(\zeta_1), \ldots, \phi_1^{LI}(\zeta_{n/2}), \phi_2^{LI}(\eta_1), \ldots, \phi_2^{LI}(\eta_{n/2})\}$$

for $L = A$ and S. Graphical results for these quantities are given in [15] for $\kappa^* = 0.01$, 1, and 100 for the values $2/\tilde{\lambda}_R = 0.7$ and 1.4.

The numerical solution converged in a practical sense in each case, as indicated by test computations with larger order systems, but the value of n needed for convergence depends on the parameters. Larger values of n were required for larger values of the couplant viscosity κ^* and smaller values of wavelength $\tilde{\lambda}_R$. While suitable results were obtained with $n = 10$ for $\kappa^* = 0.01$ and $2/\tilde{\lambda}_R = 0.7$, the value of n had to be increased to $n = 40$ for the case $\kappa^* = 100$ and $2/\tilde{\lambda}_R = 1.4$. This latter value of κ^* approaches the case for welded contact for which the stress singularity is oscillatory. Therefore, large variations in the solution are expected near $|x| = 1$ and this was indeed seen in the results. Such variations require a relatively large number of interpolation points near $|x| = 1$, and since the distribution of these points is given by (30) and (31) we can accomplish this only by increasing n.

In order to compare the solution obtained here with experiments, we need to calculate the reflected and transmitted surface waves. For this we use asymptotic expressions for the limit $|x| \to \infty$. From (A.49) of [15] we may write

$$\lim_{|x|\to\infty}\tilde{u}_\alpha^L(x) = \overset{\infty}{u}{}_\alpha^L(x) = \int_{-1}^{1}\overset{\infty}{G}{}_{\alpha\beta}(x - \xi)\tilde{t}_\beta^L(\xi)d\xi \quad (47)$$

where

$$\overset{\infty}{G}{}_{\alpha\beta}(x) = \lim_{|x|\to\infty}\tilde{G}_{\alpha\beta}(x). \quad (48)$$

Therefore, from (A.38), (A.48) of [15] and an asymptotic analysis similar to that in Ewing, et al. [8, pp. 52, 53],

$$\overset{\infty}{G}{}_{11}(x) = iP_{11}(\eta_R)e^{i\tilde{s}_R|x|}, \quad \overset{\infty}{G}{}_{12}(x) = -\operatorname{sgn}(x)P_{12}(\eta_R)e^{i\tilde{s}_R|x|};$$
$$\overset{\infty}{G}{}_{21}(x) = -\overset{\infty}{G}{}_{12}(x), \quad \overset{\infty}{G}{}_{22}(x) = iP_{22}(\eta_R)e^{i\tilde{s}_R|x|}. \quad (49)$$

where $P_{ij}(\eta)$ are defined in (A.39) of [15] as

$$P_{11}(\eta) = \eta^2\sqrt{1 - \eta^2}/\hat{R}(\eta), \quad P_{12}(\eta) = (2 - \eta^2 - 2\sqrt{1 - \epsilon^2\eta^2}\sqrt{1 - \eta^2})/\hat{R}(\eta) \quad (50)$$

Downloaded 01 May 2010 to 171.66.16.249. Redistribution subject to ASME license or copyright; see http://www.asme.org/terms/Terms_Use.cfm

$$P_{22}(\eta) = \eta^2\sqrt{1-\epsilon^2\eta^2}/\hat{R}(\eta),$$

$$\hat{R}(\eta) = \frac{4\eta^2(1-\epsilon^2)[(3-2\eta^2)\sqrt{1-\epsilon^2\eta^2} - \sqrt{1-\eta^2}]}{\sqrt{1-\epsilon^2\eta^2}\sqrt{1-\eta^2}(\sqrt{1-\eta^2}+\sqrt{1-\epsilon^2\eta^2})} \quad (50)$$

(Cont.)

Equation (47) defines the scattered or reflected Rayleigh wave according as $x \to \infty$ or $x \to -\infty$, respectively. In view of (47)–(49) we can write (47) in the form

$$\overset{\infty}{u}{}^L_1(x) = \tilde{u}^{sL}_0 e^{i\tilde{s}_R x}, \quad \overset{\infty}{u}{}^L_2(x) = i\tilde{u}^{sL}_0 P(\eta_R) e^{i\tilde{s}_R x}, \quad x \to \infty,$$

$$\overset{\infty}{u}{}^L_1(x) = \tilde{u}^{rL}_0 e^{-i\tilde{s}_R x}, \quad \overset{\infty}{u}{}^L_2(x) = -i\tilde{u}^{rL}_0 P(\eta_R) e^{-i\tilde{s}_R x}, \quad x \to -\infty, \quad (51)$$

where $P(\eta_R)$ is defined in (8). These displacement fields have the proper functional forms for Rayleigh waves propagating in the positive and negative x-directions, respectively. Furthermore, the dimensionless complex displacement amplitudes $\tilde{u}^{sL}_0$ and $\tilde{u}^{rL}_0$ are given by

$$\tilde{u}^{sL}_0 = iP_{11}(\eta_R)\int_{-1}^{1}\tilde{t}^L_1(\xi)e^{-i\tilde{s}_R\xi}d\xi - P_{12}(\eta_R)\int_{-1}^{1}\tilde{t}^L_2(\xi)e^{-i\tilde{s}_R\xi}d\xi,$$

$$\tilde{u}^{rL}_0 = iP_{11}(\eta_R)\int_{-1}^{1}\tilde{t}^L_1(\xi)e^{i\tilde{s}_R\xi}d\xi + P_{12}(\eta_R)\int_{-1}^{1}\tilde{t}^L_2(\xi)e^{i\tilde{s}_R\xi}d\xi. \quad (52)$$

From this we observe the relationship

$$\tilde{u}^{sS}_0 = -\tilde{u}^{rS}_0, \quad \tilde{u}^{sA}_0 = \tilde{u}^{rA}_0. \quad (53)$$

Next, we define the reflection coefficient A_r and the transmission coefficient A_t by

$$A_r = \tilde{u}^r_0/\tilde{u}_0, \quad A_t = 1 + \tilde{u}^s_0/\tilde{u}_0 \quad (54)$$

in which $\tilde{u}_0$ is the dimensionless, real, incident Rayleigh wave amplitude and

$$\tilde{u}^r_0 = \tilde{u}^{rS}_0 + \tilde{u}^{rA}_0, \quad \tilde{u}^s_0 = \tilde{u}^{sS}_0 + \tilde{u}^{sA}_0 \quad (55)$$

so that, with use of (53)

$$A_r = (\tilde{u}^{sA}_0 - \tilde{u}^{sS}_0)/\tilde{u}_0, \quad A_t = 1 + (\tilde{u}^{sA}_0 + \tilde{u}^{sS}_0)/\tilde{u}_0. \quad (56)$$

The algebraic expressions for $\tilde{u}^{sS}_0$ and $\tilde{u}^{sA}_0$ are obtained from (52) using the methods of Section 5 and they appear as

$$\tilde{u}^{sS}_0 = C^S P_{11}(\eta_R)\tilde{t}^S_1(1) + 2P_{11}(\eta_R)\frac{\pi}{n+1}\sum_{k=1}^{n/2}(1-\zeta_k^2)\sin(\tilde{s}_R\zeta_k)\phi^S_1(\zeta_k) - 2P_{12}(\eta_R)\frac{\pi}{n}\sum_{k=1}^{n/2}\cos(\tilde{s}_R\eta_k)\phi^S_2(\eta_k)$$

$$\tilde{u}^{sA}_0 = iC^A P_{11}(\eta_R)\tilde{t}^A_1(1) + 2iP_{11}(\eta_R)\frac{\pi}{n+1}\sum_{k=1}^{n/2}(1-\zeta_k^2)\cos(\tilde{s}_R\zeta_k)\phi^A_1(\zeta_k) + 2iP_{12}(\eta_R)\frac{\pi}{n}\sum_{k=1}^{n/2}\sin(\tilde{s}_R\eta_k)\phi^A_2(\eta_k), \quad (57)$$

where

$$C^S = 2(\tilde{s}_R^{-1}\sin\tilde{s}_R - \cos\tilde{s}_R)/\tilde{s}_R, \quad C^A = 2\tilde{s}_R^{-1}\sin\tilde{s}_R. \quad (58)$$

Finally, we note that A_r and A_t as defined in (56) are complex numbers which can be written as

$$A_r = \text{Mod}\,(A_r)e^{i\,\text{Phase}(A_r)}, \quad A_t = \text{Mod}\,(A_t)e^{i\,\text{Phase}(A_t)}. \quad (59)$$

Fig. 2(a) shows the normalized reflected power (i.e., $[\text{Mod}\,(A_r)]^2$) as a function of $2b/\lambda_R$ in $0 < 2b/\lambda_R \leq 1.4$ for $\kappa^* = 0.01, 0.1, 1$, and 10. The two curves in Fig. 2(a) for the less viscous couplants ($\kappa^* = 0.01, 0.1$) are similar in shape and show the often observed phenomenon of quarter wavelength resonance in reflected power, namely, maximums at $2b/\lambda_R$ near 0.25, 0.75, and 1.25. This behavior is not preserved for the two curves corresponding to the more viscous couplants ($\kappa^* = 1.0$, 10) for which only two resonances appear in this wavelength range rather than three. Therefore for the highly viscous couplants quarter wavelength resonance does not occur; it appears to be closer to half wavelength resonance. The curves presented in Fig. 2(a) were found to be good indications for convergence of the numerical solutions. If the number of interpolation points is too small, the antiresonances will not be sharply defined.

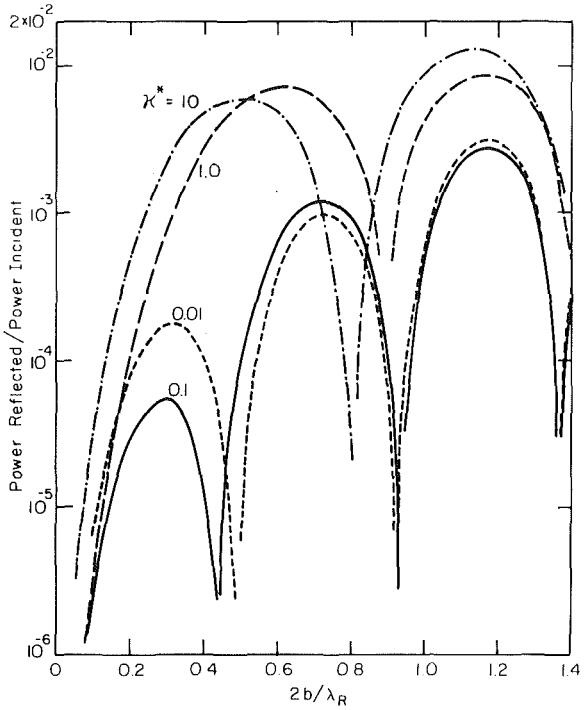


Fig. 2(a) Power of reflected surface wave versus incident wave number for parameter values $\sigma = \sigma' = 0.25$, $\mu'/\mu = 2$, $\rho'/\rho = 0.5$, $h/b = 0.2$, $u_0/b = 1$, and $\kappa^* = (0.01, 0.1, 1, 10)$

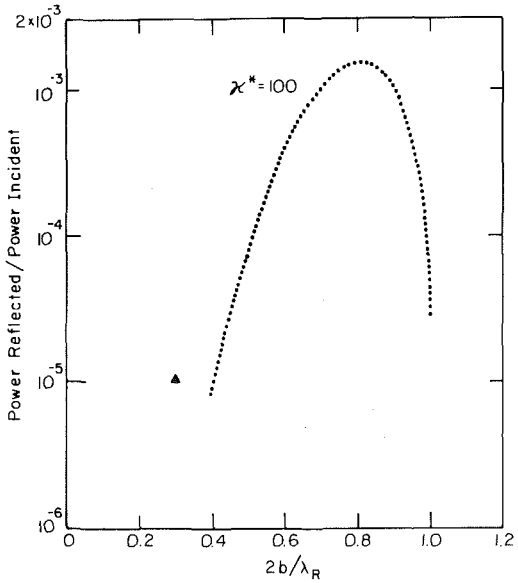


Fig. 2(b) Same as Fig. 2(a) except $h/b = 0.01$ and $\kappa^* = 100$

Fig. 2(b) gives the reflected power curve for the case $\tilde{h} = 0.01$ and $\kappa^* = 100$, i.e., a very thin plate with a highly viscous couplant. With these parameters the bending effects of the plate should be very small and the conditions of welded bond should be approximated. Therefore the model approaches that in Simons [4] where an extensible membrane was perfectly bonded to the half space. The results in Fig. 2(b)

Downloaded 01 May 2010 to 171.66.16.249. Redistribution subject to ASME license or copyright; see http://www.asme.org/terms/Terms_Use.cfm

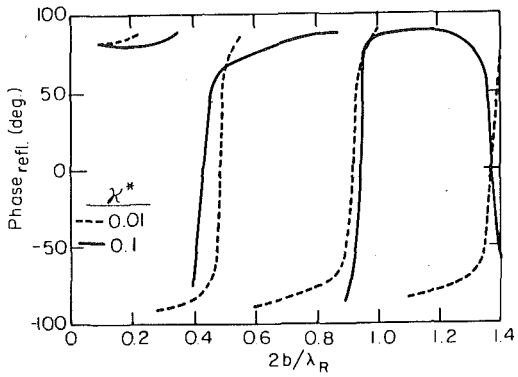


Fig. 3(*a*) Phase of reflected surface wave versus incident wave number for parameter values $\sigma = \sigma' = 0.25$, $\mu'/\mu = 2$, $\rho'/\rho = 0.5$, $h/b = 0.2$, $u_0/b = 1$ and $\kappa^* = (0.01, 0.1)$.

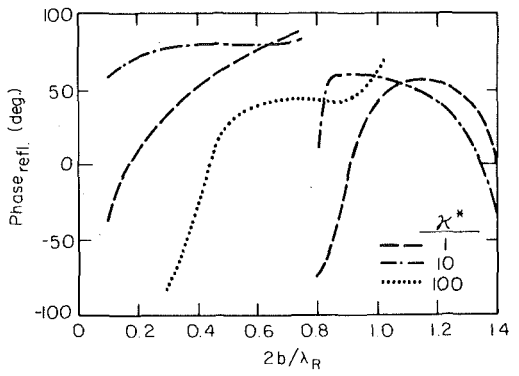


Fig. 3(*b*) Same as Fig. 3(*a*) except $\kappa^* = (1, 10)$ and for . . . $h/b = 0.01$, $\kappa^* = 100$

required $n = 40$ and were rather expensive to obtain so the range of $2b/\lambda_R$ was restricted to 0.3–1.0. Evidently antiresonances occur between the values 0.3 and 0.4 and near 1.0 while a resonance is seen near $2b/\lambda_R = 0.8$. These features of resonance and antiresonance are in agreement with Simons [4] and the numerical values are within the expected agreement given the differences in the material parameters.

Figs. 3(*a*) and 3(*b*) show the phase of the reflected surface wave [i.e., Phase (A_r), with range $(-90, 90)$ degrees as calculated from the arctangent function] as a function of $2b/\lambda_R$. In Fig. 3(*a*) results for the two less viscous cases, $\kappa^* = 0.01$ and 0.1, are given. In Fig. 3(*b*) the two more viscous cases, $\kappa^* = 1$ and 10, are shown. Also, in Fig. 3(*b*) the result is given for the $\tilde{h} = 0.01$, $\kappa^* = 100$ example considered in Fig. 2(*b*). In Fig. 3(*a*) the phase curves are discontinuous at the antiresonance values of $2b/\lambda_R$. The phase curves show a more complicated behavior for the more viscous cases in Fig. 3(*b*).

7 Discussion and Conclusions

The plane-strain elastodynamic solution is presented for the interaction of an elastic half space with a classical elastic plate attached through a viscous couplant. Incident on this system is a variable frequency Rayleigh wave. The solution can easily be changed to accommodate any other incident wave of plane strain. The viscous couplant is modeled by assuming in the contact region continuous normal stress and displacements, together with shear stress that is proportional to the tangential velocity difference. The model could be changed to also relate the contact normal stress to a normal velocity difference.

The solution revealed some essential differences for different values of the viscous couplant. Low viscosity couplants produced resonances in the reflected power beginning at the quarter wavelength and at half wavelengths thereafter, but this was not the case for the high viscosity couplants for which the first resonance occurs at the half wavelength.

From the limited results presented here it is apparent that the type of couplant used in attaching electromechanical transducers to the test piece will have a strong influence on the recorded result when the wavelengths are comparable to the dimensions of the transducer. A more complete study of the effects of the various parameters on the solution will be undertaken after the present computing scheme has been made more efficient.

Acknowledgment

This work was sponsored by the National Science Foundation, Engineering Division, Solid Mechanics Program, Grant (ENG 77-17150).

References

1 Bugdayci, N., and Bogy, D. B., "A Two-Dimensional Theory for Piezoelectric Layers Used in Electromechanical Transducers. Part I, Derivation," to appear in *International Journal of Solids and Structures*, 1981.

2 Bugdayci, N., and Bogy, D. B., "A Two-Dimensional Theory for Piezoelectric Layers Used in Electromechanical Transducers. Part II, Application," to appear in *International Journal of Solids and Structures*, 1981.

3 Luco, J. E., and Westmann, R. A., "Dynamic Response of a Rigid Footing Bonded to an Elastic Half Space," ASME JOURNAL OF APPLIED MECHANICS, Vol. 39, June 1972, pp. 527–534.

4 Simons, D. A., "Scattering of Normally Incident Rayleigh Waves by Thin Strips," *Journal of the Acoustical Society of America*, Vol. 60, 5, 1976, pp. 1100–1107.

5 Simons, D. A., "Reflection of Rayleigh Waves by Strips, Grooves, and Periodic Arrays of Strips and Grooves," *Journal of the Acoustical Society of America*, Vol. 63, 1978, pp. 1292–1301.

6 Freund, L. B., and Achenbach, J. D., "Waves in a Semi-Infinite Plate in Smooth Contact With a Harmonically Disturbed Half-Space," *International Journal of Solids and Structures*, Vol. 4, 1968, pp. 605–621.

7 Lamb, H., "On the Propagation of Tremors Over the Surface of an Elastic Solid," *Philosophical Transactions of the Royal Society*, London, Series A, Vol. 203, 1904, pp. 1–42.

8 Ewing, W. M., Jardetsky, W. S., and Press, F., *Elastic Waves in Layered Media*, McGraw-Hill, New York, 1957.

9 Fung, Y. C., *Foundations of Solid Mechanics*, Prentice-Hall, Englewood Cliffs, N.J., 1965.

10 Achenbach, J. D., *Wave Propagation in Elastic Solids*, North-Holland/American Elsevier, Amsterdam/New York, 1973.

11 Miklowitz, J., *The Theory of Elastic Waves and Waveguides*, North-Holland, 1978.

12 Muskhelishvili, N. I., *Singular Integral Equations*, Noordhoff Int. Pub., 1977.

13 Naghdi, P. M., "The Theory of Shells and Plates," *Handbuch der Physik*, VIa/2, 425–640, Springer-Verlag, 1972.

14 Erdogan, F., and Gupta, G. D., "On the Numerical Solution of Singular Integral Equations," *Quarterly of Applied Mathematics*, Vol. 30, 1972, pp. 525–534.

15 Angel, Y. C., Scattering of Rayleigh Waves by a Plate Attached to a Half-Space Through a Viscous Couplant, PhD thesis, Department of Mechanical Engineering, University of California, Berkeley, June 1980.

16 Hildebrand, F. B., *Introduction to Numerical Analysis*, McGraw-Hill, New York, 1974.

Downloaded 01 May 2010 to 171.66.16.249. Redistribution subject to ASME license or copyright; see http://www.asme.org/terms/Terms_Use.cfm

T.-C. Soong
Principal Engineer.

C. Li
Technical Specialist.

Xerox Corporation,
Xerox Square,
Rochester, N. Y. 14603

The Rolling Contact of Two Elastic-Layer-Covered Cylinders Driving a Loaded Sheet in the Nip

A circular stress function is used for the steady rolling contact of two cylinders. Each cylinder has an elastic layer bonded to a hard core, and an elastic thin sheet is compressed in the contact arc and being driven by the system. An asymmetric stress distribution is caused by a pushing or pulling force acting at the tail end of the sheet. The effect of the normal load and the tail force on the speed ratios of the two cylinders and the sheet, and also the local slippage in the contact arc are studied by enforcing the exact conditions at the contact zone. The resulting equations are solved by the collocation method and an iterative procedure which stepwisely unlocked the nonslip contacting points whenever the calculated interface shear exceeds the local Coulomb friction.

Introduction

In the recent literature of rolling contact of elastic layer-covered cylinders, Bentall and Johnson [1] studied rolling contact between an elastic strip and cylinders, Hahn and Levinson [2] investigated the gross slippage of a cylinder in contact with a hard cylinder, and Soong and Li [3] analyzed the steady rolling contact of two layered cylinders with a sheet in the nip.

The present paper extends Soong and Li's symmetric study [3] to the asymmetric case where the sheet in the nip is being pulled or pushed by a tangential force at the tail end while it is being driven in a steady state through the nip of the rollers. The geometry of the elastic layers in the cylinders, the normal force, and the tail force on the sheet, determine the relative speeds between the sheet and the two rollers and also the local slippage in the contact zone. By increasing the tail force from zero upward, the analysis shifts from the symmetric case to the extreme case of gross slippage where the drag force is equal to or greater than the Coulomb friction between the driver and the sheet.

In reference [2], Hahn and Levinson obtained their gross slippage solution by a numerically complicated series method. The present paper used a simpler collocation method, which was shown in reference [4] to be of comparable accuracy, to solve the equations obtained through the exact enforcement of the conditions prevailing in the contact zone. Numerical results showed the speed ratios for the

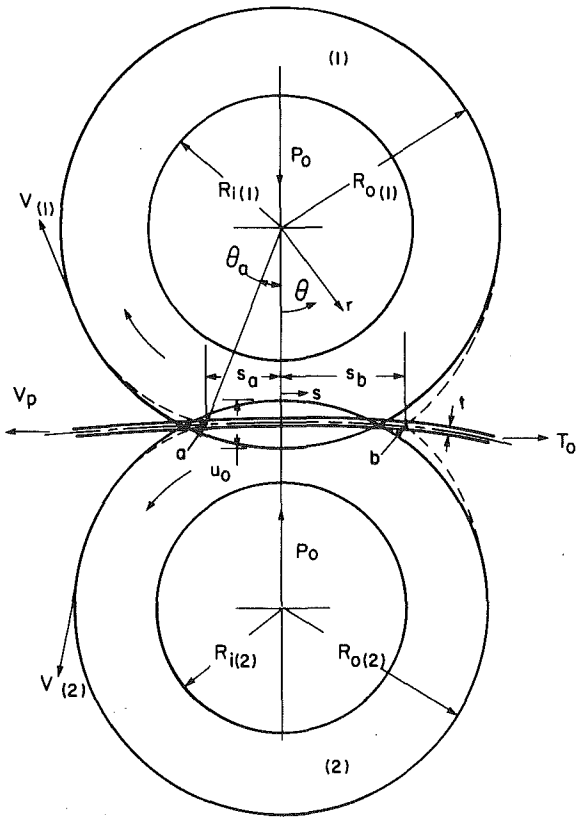


Fig. 1 Notations; subscript (1) and (2) refer to cylinder (1) and (2)

Contributed by the Applied Mechanics Division for publication in the JOURNAL OF APPLIED MECHANICS.

Discussion on this paper should be addressed to the Editorial Department, ASME, United Engineering Center, 345 East 47th Street, New York, N. Y. 10017, and will be accepted until two months after final publication of the paper itself in the JOURNAL OF APPLIED MECHANICS. Manuscript received by ASME Applied Mechanics Division, December, 1980; final revision, June, 1981.

Copyright © 1981 by ASME

Downloaded 01 May 2010 to 171.66.16.249. Redistribution subject to ASME license or copyright; see http://www.asme.org/terms/Terms_Use.cfm

steady-state rolling of the sheet in the nip with respect to the two rollers, and the distribution of slip zone in the nip as a function of the tail force. It is interesting to note that for the plain strain case as is given in the numerical example, the speed ratio of the sheet to the roller increases monotonically as the tail force changes from pulling to pushing.

Fig. 1 shows the notations.

General Equation Derivations

General Stress and Strain Expressions of a Layered Soft-Roll. A general stress function, in cylindrical coordinates, which is used for the soft layer of the circular cylinder under external loads is given by

$$U = a_0 \ln r + \frac{1}{2} b_0 r^2 + c_0 r^2 \ln r + (b_1 r^3 + c_1 r^{-1} + d_1' r \ln r) \cos\theta + \frac{1}{2} d_1 r\theta \sin\theta + \sum_{n=2}^{\infty} (a_n r^n + b_n r^{n+2} + c_n r^{-n} + d_n r^{-n+2}) \cos n\theta + e_1 \theta r^2 + e_2 \theta + (b_1^* r^3 + c_1^* r^{-1} + d_1'^* r \ln r) \sin\theta - \frac{1}{2} d_1^* r\theta \cos\theta + \sum_{n=2}^{\infty} (a_n^* r^n + b_n^* r^{n+2} + c_n^* r^{-n} + d_n^* r^{-n+2}) \sin n\theta \quad (1)$$

The radial, circumferential, and shear stresses are given by

$$\sigma_r = \frac{1}{r}\frac{\partial U}{\partial r} + \frac{1}{r^2}\frac{\partial^2 U}{\partial \theta^2},$$

$$\sigma_\theta = \frac{\partial^2 U}{\partial r^2},$$

and

$$\tau_{r\theta} = -\frac{\partial}{\partial r}\left(\frac{1}{r}\frac{\partial U}{\partial \theta}\right) \quad (2)$$

Denoting u and v as radial and circumferential displacements, respectively, the corresponding stress-strain relationships for isotropic, elastic material are,

$$E\frac{\partial u}{\partial r} = \kappa\sigma_r - \beta\sigma_\theta, \quad (3a)$$

$$E\left(\frac{u}{r} + \frac{1}{r}\frac{\partial v}{\partial \theta}\right) = \kappa\sigma_\theta - \beta\sigma_r, \quad (3b)$$

and

$$E\left(\frac{1}{r}\frac{\partial u}{\partial \theta} + \frac{\partial v}{\partial r} - \frac{v}{r}\right) = 2(1+\nu)\tau_{r\theta}, \quad (3c)$$

where E is the soft layer's Young's modulus and κ and β are related to the Poisson's ratio as follows: $\kappa = 1 - \nu^2, \beta = \nu(1+\nu)$ in the case of plane strain, and $\kappa = 1, \beta = \nu$ in the case of plane stress.

In what follows, quantities are nondimensionalized as

$$\bar{\sigma}_r = \sigma_r/E, \quad \bar{\sigma}_\theta = \sigma_\theta/E, \quad \bar{\tau}_{r\theta} = \tau_{r\theta}/E, \quad \bar{r} = r/R_0,$$

$$\bar{u} = u/R_0, \quad \bar{v} = v/R_0, \quad \bar{d}_1' = d_1'/ER_0$$

$$\bar{a}_n = R_0^{n-2} a_n/E, \quad \bar{b}_n = R_0^n b_n/E, \quad n = 0, 1, 2, \ldots,$$

$$\bar{c}_n = R_0^{-n-2} c_n/E, \quad \bar{d}_n = R_0^{-n} d_n/E, \quad n = 1, 2, \ldots \quad (4)$$

and similar definitions are given for the starred quantities, $\bar{a}_n^*, \bar{b}_n^*, \bar{c}_n^*$, and $\bar{d}_n^*$, with $n = 1, 2, \ldots$ and $\bar{d}_1'^*$. The $\bar{a}_1$ and $\bar{a}_1^*$ are constants to be given later.

The three stresses, σ_r, σ_θ, and $\tau_{r\theta}$ can be obtained from equations (1) and (2), and the displacements u and v can be obtained from integrating equations (3a) and (3b). Their expressions are omitted [5]. However, the constraining relationships among the coefficients in the stress function pertaining to the present analysis should be stated which are derived as follows.

Let $f(\theta)$ and $g(\bar{r})$ be the integration constants when $\bar{u}$ and $\bar{v}$ are derived from equations (3a) and 3b), respectively. Substitution of these equations into equation (3c) yields the compatibility condition among the coefficients:

$$\int f(\theta)d\theta + \frac{df(\theta)}{d\theta} - \bar{r}\frac{dg(\bar{r})}{d\bar{r}} - g(\bar{r}) + \sin\theta[2(\beta - \kappa - 1 - \nu)\bar{d}_1' + \bar{d}_1(\beta - \kappa)] - \cos\theta[2(\beta - \kappa - 1 - \nu)\bar{d}_1^* + (\beta - \kappa)\bar{d}_1^*] + 2(\kappa - \beta + 1 + \nu)\bar{e}_1\bar{r} - 2(1+\nu)\bar{r}^{-1}\bar{e}_2 = 0. \quad (5)$$

A solution is

$$g(\bar{r}) = -(1+\nu)\bar{e}_2\bar{r}^{-1} - 2(\beta - \kappa - 1 - \nu)\bar{e}_1\bar{r}\ln\bar{r} + q\bar{r}$$

$$f(\theta) = -\frac{1}{2}[2(\beta - \kappa - 1 - \nu)\bar{d}_1' + (\beta - \kappa)\bar{d}_1]\theta\sin\theta + \frac{1}{2}[2(\beta - \kappa - 1 - \nu)\bar{d}_1'^* + (\beta - \kappa)\bar{d}_1^*]\theta\cos\theta + \bar{a}_1\cos\theta + \bar{a}_1^*\sin\theta \quad (6)$$

where $\bar{a}_1$, $\bar{a}_1^*$, and q are integration constants.

Since θ should be single-valued and $1 + \nu \equiv \kappa + \beta$, we have, in the stress, strain, and displacement expressions, the following relationships among the coefficients:

$$\bar{c}_0 = \bar{e}_1 = 0$$

$$\bar{d}_1' = \frac{\beta - \kappa}{4\kappa}\bar{d}_1$$

$$\bar{d}_1'^* = \frac{\beta - \kappa}{4\kappa}\bar{d}_1^*$$

$$g(\bar{r}) = -(1+\nu)\bar{e}_2\bar{r}^{-1} + q\bar{r}$$

$$f(\theta) = \bar{a}_1\cos\theta + \bar{a}_1^*\sin\theta$$

$$\int f(\theta)d\theta = \bar{a}_1\sin\theta - \bar{a}_1^*\cos\theta \quad (7)$$

The undetermined value of the arbitrary constants $\bar{a}_1$, and $\bar{a}_1^*$ and q are to be used to satisfy given stresses at the boundary.

Boundary Conditions at the Contact Zone and Beyond. The boundary conditions at the inner and outer radii of the hard-cored soft-roll, with the radial and shear stress at the outer radius expressed by Fourier series, are

$$\bar{u} = \bar{v} = 0, \qquad \text{on } \bar{r} = R_i/R_0 = \bar{R}_i$$

$$\bar{\sigma}_r = \sum_{n=0}^{\infty} A_n \cos n\theta + \sum_{n=1}^{\infty} A_n^* \sin n\theta, \quad \text{on } \bar{r} = 1, \quad -\pi \le \theta \le \pi$$

$$\bar{\tau}_{r\theta} = \sum_{n=1}^{\infty} B_n \sin n\theta + \sum_{n=0}^{\infty} B_n^* \cos n\theta, \quad \text{on } \bar{r} = 1, \quad -\pi \le \theta \le \pi. \quad (8)$$

where A_n, B_n, A_n^*, and B_n^* are constants.

Assume that the two stresses at the contact nip which extends from $-\theta_a$ to θ_b are expressed by two Fourier series,

$$\bar{\sigma}_{r\langle\bar{r}=1\rangle} = \sum_{m=0}^{M} \frac{\pi}{\Omega} h_m \cos\frac{m\pi\theta}{\Omega} + \sum_{m=1}^{M} \frac{\pi}{\Omega} h_m^* \sin\frac{m\pi\theta}{\Omega} \quad (9)$$

$$\bar{\tau}_{r\theta\langle\bar{r}=1\rangle} = \sum_{m=1}^{\tilde{M}} \frac{\pi}{\Omega} q_m \sin\frac{m\pi\theta}{\Omega} + \sum_{m=0}^{\tilde{M}} \frac{\pi}{\Omega} q_m^* \cos\frac{m\pi\theta}{\Omega} \quad (10)$$

for $-\theta_a \le \theta \le \theta_b$, and vanish for θ outside the region. Here M and $\tilde{M}$ are integers and $\Omega = \frac{1}{2}(\theta_b + \theta_a)$.

Since the Fourier series of equation (8) covers the entire range of θ, coefficients A_n, B_n, A_n^*, and B_n^* can be related to h_m, h_m^*, q_m, and q_m^* by the following equations:

$$A_0 = h_0,$$

$$B_0^* = q_0^*.$$

$$\begin{Bmatrix} A_n \\ A_n^* \end{Bmatrix} = \sum_{m=0}^{M}\sum_{i=1}^{2} h_m \begin{Bmatrix} f_{sc}(i,m,n) \\ (-1)^i f_{ss}(i,m,n) \end{Bmatrix} + \sum_{m=1}^{M}\sum_{i=1}^{2} h_m^* \begin{Bmatrix} f_{ss}(i,m,n) \\ -(-1)^i f_{sc}(i,m,n) \end{Bmatrix} \quad (11)$$

Downloaded 01 May 2010 to 171.66.16.249. Redistribution subject to ASME license or copyright; see http://www.asme.org/terms/Terms_Use.cfm

$$\begin{Bmatrix} B_n \\ B_n^* \end{Bmatrix} = \sum_{m=1}^{M} \sum_{i=1}^{2} q_m \begin{Bmatrix} -(-1)^i f_{sc}(i,m,n) \\ f_{ss}(i,m,n) \end{Bmatrix} + \sum_{m=0}^{\tilde{M}} \sum_{i=1}^{2} q_m^* \begin{Bmatrix} (-1)^i f_{ss}(i,m,n) \\ f_{sc}(i,m,n) \end{Bmatrix} \quad n = 1, 2, 3 \ldots \quad (11)$$

(Cont.)

where, written in matrix form,

$$\begin{Bmatrix} f_{sc}(i,m,n) \\ f_{ss}(i,m,n) \end{Bmatrix} = \frac{\sin(m\pi + (-1)^i n\Omega)}{m\pi + (-1)^i n\Omega} \begin{Bmatrix} \cos[(m\pi + (-1)^i n\Omega)\delta/\Omega] \\ \sin[(m\pi + (-1)^i n\Omega)\delta/\Omega] \end{Bmatrix} \quad (12)$$

where $\delta = (\theta_b - \theta_a)/2$.

Substituting the stress and displacement expressions into equations (8), one gets the relationships between the coefficients of the stress function and the coefficients A_n, A_n^*, B_n, and B_n^* in equations (8), which then can be expressed in terms of h_m, h_m^*, q_m, and q_m^* through equations (11). To enforce the conditions at the contact nip, we need to have $\bar{u}(\theta)$ and ϵ_θ expressed in terms of h_m, h_m^*, q_m, and q_m^*. These are written as follows:

$$\begin{aligned} \bar{u} &= \bar{u}_{(\bar{r}=1)} \\ &= \alpha_0 h_0 \\ &+ \sum_{m=0}^{M} h_m \left\{ \sum_{n=1}^{\infty} \sum_{i=1}^{2} \alpha_n (\cos n\theta f_{sc}(i,m,n) + (-1)^i \sin n\theta f_{ss}(i,m,n)) \right\} \\ &+ \sum_{m=1}^{M} h_m^* \left\{ \sum_{n=1}^{\infty} \sum_{i=1}^{2} \alpha_n (\cos n\theta f_{ss}(i,m,n) - (-1)^i \sin n\theta f_{sc}(i,m,n)) \right\} \\ &+ \sum_{m=1}^{\tilde{M}} q_m \left\{ \sum_{n=1}^{\infty} \sum_{i=1}^{2} \tilde{\alpha}_n (-(-1)^i \cos n\theta f_{sc}(i,m,n) - \sin n\theta f_{ss}(i,m,n)) \right\} \\ &+ \sum_{m=0}^{\tilde{M}} q_m^* \left\{ \sum_{n=1}^{\infty} \sum_{i=1}^{2} \tilde{\alpha}_n ((-1)^i \cos n\theta f_{ss}(i,m,n) - \sin n\theta f_{sc}(i,m,n)) \right\} \\ &\qquad - \theta_a \le \theta \le \theta_b \end{aligned} \quad (13)$$

and

$$\begin{aligned} \epsilon_\theta &= \epsilon_\theta(\theta)_{(\bar{r}=1)} \\ &= \beta_0 h_0 \\ &+ \sum_{m=0}^{M} h_m \left\{ \sum_{n=1}^{\infty} \sum_{i=1}^{2} \beta_n (\cos n\theta f_{sc}(i,m,n) + (-1)^i \sin n\theta f_{ss}(i,m,n)) \right\} \\ &+ \sum_{m=1}^{M} h_m^* \left\{ \sum_{n=1}^{\infty} \sum_{i=1}^{2} \beta_n (\cos n\theta f_{ss}(i,m,n) - (-1)^i \sin n\theta f_{sc}(i,m,n)) \right\} \\ &+ \sum_{m=1}^{\tilde{M}} q_m \left\{ \sum_{n=1}^{\infty} \sum_{i=1}^{2} \tilde{\beta}_n (-(-1)^i \cos n\theta f_{sc}(i,m,n) - \sin n\theta f_{ss}(i,m,n)) \right\} \\ &+ \sum_{m=0}^{\tilde{M}} q_m^* \left\{ \sum_{n=1}^{\infty} \sum_{i=1}^{2} \tilde{\beta}_n ((-1)^i \cos n\theta f_{ss}(i,m,n) - \sin n\theta f_{sc}(i,m,n)) \right\} \\ &\qquad - \theta_a \le \theta \le \theta_b \end{aligned} \quad (14)$$

where the α's and β's are given in Appendix 1.

Equations (9), (10), (13), and (14) expressed as functions of the coefficients h_m, h_m^*, q_m, and q_m^* are required for a solution of the rolling contact problem.

Equations at the Contact Arc

There are four conditions to be satisfied at each contact point along the center line of the sheet which is taken as the theoretical contact line of the nip. Let s be the coordinate measured along the nip. The two ends of the contact arc are $s = -s_a$ and $s = s_b$, and define

$$s_L = (s_b + s_a)/2 \quad (15)$$

The first two conditions of contact refer to the normal pressure and the indentation of the two cylinders with respect to the undeformed geometry

$$(E\bar{\sigma}_r)_{(1)} = (E\bar{\sigma}_r)_{(2)} \quad (16)$$

$$(\bar{u}R_0)_{(1)} + (\bar{u}R_0)_{(2)} + t = u_0 + (s^2/2)[(1/R_0)_{(1)} + (1/R_0)_{(2)}] \quad (17)$$

where the subscripts (1) and (2) refer to quantities related to the two cylinders, respectively. The thickness of the sheet is t and u_0 is the total interference of the two cylinders, and $(u_0 - t)$ is a negative quantity. Equation (17), derived from small deflection geometric consideration, simply states that the combined indentation of the two cylinders, with adjustment made to allow the presence of the thickness of the sheet, should be equal to the interference at s.

In equations (13) and (14), the coordinate s is related to the coordinate θ in each cylinder through

$$s = (\theta R_0)_{(1)} = (\theta R_0)_{(2)} \quad (18)$$

The third and fourth conditions are related to the consideration of nonslip or slip between each cylinder and the sheet. If at a contact point s, the local material point of cylinder (1) moves with the same velocity as the local speed of the sheet at the point, the two speeds should satisfy the following condition:

$$V_p/V_{(1)} = (1 + \epsilon_{\theta(1)})/(1 + \epsilon_p(s)) \quad (19)$$

where $V_{(1)}$ is the nominal, unstressed, peripheral speed of cylinder (1), V_p is the speed of the unstressed sheet at the exit end of the contact nip, and ϵ_p is the longitudinal strain of the sheet at s:

$$\epsilon_p(s) = \frac{1}{(Et)_p} \left\{ \int_{-s_a}^{s} [(E\bar{\tau}_{r\theta})_{(1)} + (E\bar{\tau}_{r\theta})_{(2)}] ds \right\} \quad -s_a \le s \le s_b \quad (20)$$

where $(Et)_p$ is the extensional stiffness per unit width of the sheet. A proof of equation (19) is given in Appendix 2.

Integration of equation (20) yields

$$\epsilon_p(s) = \sum_{i=1}^{2} \frac{(ER_0)_{(i)}}{(Et)_p} \left\{ \sum_{m=1}^{\tilde{M}} \frac{1}{m} q_{m(i)} \left(\cos\frac{m\pi s_a}{s_L} - \cos\frac{m\pi s}{s_L} \right) + \sum_{m=0}^{\tilde{M}} \frac{1}{m} q_{m(i)}^* \left(\sin\frac{m\pi s_a}{s_L} + \sin\frac{m\pi s}{s_L} \right) \right\} \quad -s_a \le s \le s_b \quad (21)$$

Since ϵ_θ and ϵ_p are small compared with unity, expanding $(1 + \epsilon_p(s))^{-1}$ into power series in equation (19) and dropping high-order terms of the product of strains yield the following linearized equation:

$$\frac{V_p}{V_{(1)}} - \epsilon_{\theta(1)} + \epsilon_p(s) \cong 1 \quad (22)$$

It should be noted that equation (19) is nonlinear in terms of the unknown speed V_p and the unknown coefficients q_m and q_m^* appearing in the strains, whereas equation (22) is linear. It would be numerically easier to solve equation (22) than equation (19).

If slip occurs, then shear has to be equal to the Coulomb friction and equation (22) should be replaced by

$$\mu_{rp(1)} |(E\bar{\sigma}_r)_{(1)}| = |(E\bar{\tau}_{r\theta})_{(1)}| \quad (23)$$

where μ_{rp} is the coefficient of friction between the sheet and the roll.

Similarly, for cylinder (2), we have, either, for nonslip,

$$\frac{V_p}{V_{(2)}} - \epsilon_{\theta(2)} + \epsilon_p(s) = 1 \quad (24)$$

or, for slip, replacing equation (24) by

$$\mu_{rp(2)} |(E\bar{\sigma}_r)_{(2)}| = |(E\bar{\tau}_{r\theta})_{(2)}| \quad (25)$$

Stress Conditions at the Two Ends of the Contact Arc. For the present problem with an undermined boundary, the radial stress and the shear stress at the end of the contact arc will vanish. Or, by specifying the two end points, s_a and s_b, the correct interference u_0 and the drag force at s_b on the sheet should be of such magnitude that the two stresses at each of the two ends should vanish. Simple calculation shows that the equations for the vanishing of the stresses at the two ends are identical in terms of their coefficients. Therefore, we may enforce the stress conditions for just one end, say at $s = -s_a$.

Based on equations (9) and (10), we have

Downloaded 01 May 2010 to 171.66.16.249. Redistribution subject to ASME license or copyright; see http://www.asme.org/terms/Terms_Use.cfm

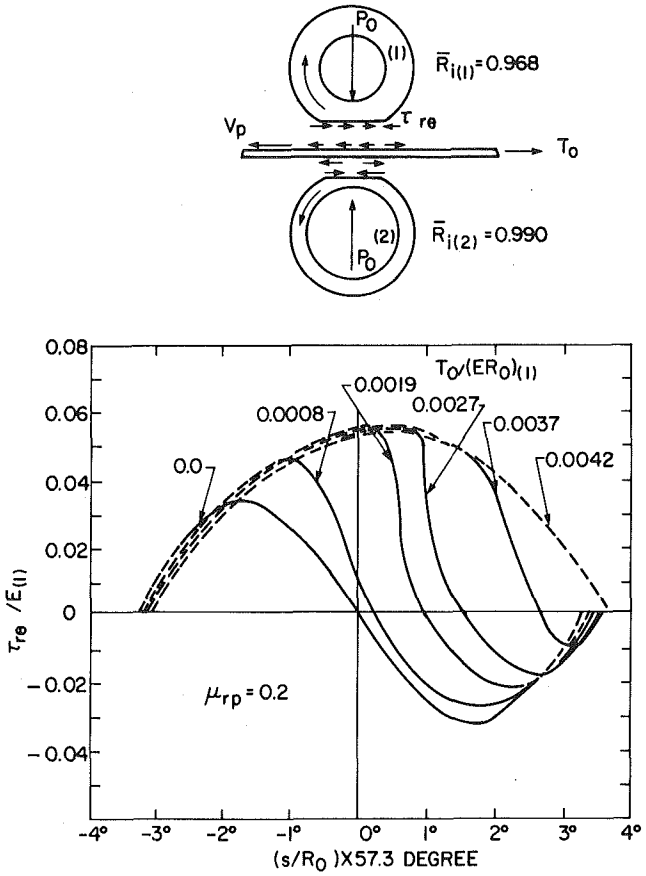


Fig. 2 Shear stress on cylinder (1) with different drag force T_0 acting at the end $s = s_b$ of the sheet; dotted line indicates the region of slipping and solid line indicates nonslip; $P_0/E_{(1)}R_0 = 0.021$; $E_p/E_{(1)} = 600$

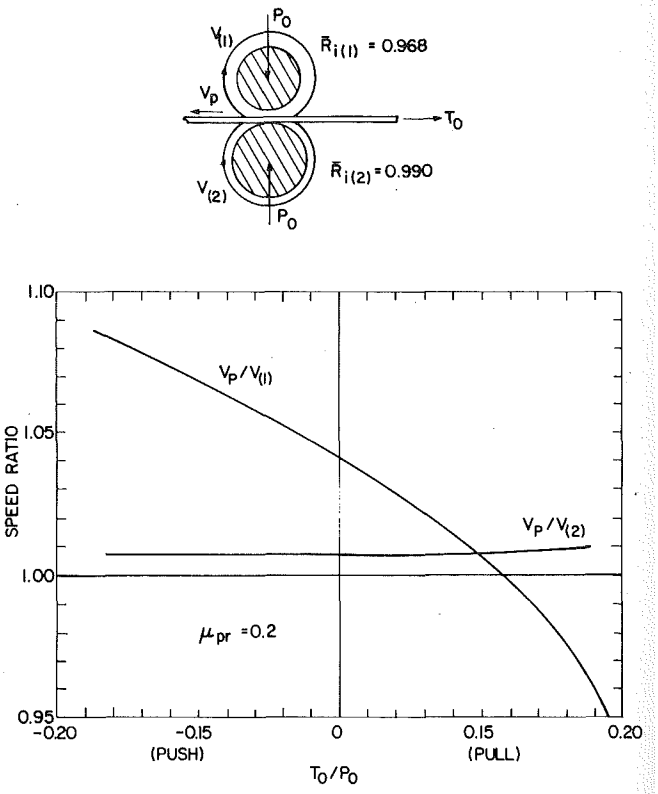


Fig. 3 Effect of T_0 change on speed ratios for constant P_0

$$\sum_{m=0}^{M} h_{m(1)} \cos\frac{m\pi s_a}{s_L} - \sum_{m=1}^{M} h^*_{m(1)} \sin\frac{m\pi s_a}{s_L} = 0 \tag{26}$$

$$-\sum_{m=1}^{\tilde{M}} q_{m(1)} \sin\frac{m\pi s_a}{s_L} + \sum_{m=0}^{\tilde{M}} q^*_{m(1)} \cos\frac{m\pi s_a}{s_L} = 0 \tag{27}$$

$$-\sum_{m=1}^{\tilde{M}} q_{m(2)} \sin\frac{m\pi s_a}{s_L} + \sum_{m=0}^{\tilde{M}} q^*_{m(2)} \cos\frac{m\pi s_a}{s_L} = 0 \tag{28}$$

The vanishing of the radial stress at cylinder (2) is automatically satisfied due to equations (16) and (26).

Equilibrium Condition of the Sheet and the Idler Cylinder. Assume cylinder (1) is the driver, cylinder (2) is an idler, and the pulling force T_0 as applied to the sheet at $s = s_b$ is providing a steady-state drag to the forward motion of the sheet. Then the equilibrium of the sheet and that of cylinder (2) require, respectively,

$$T_0 = \int_{-s_a}^{s_b} [(E\bar{\tau}_{r\theta})_{(1)} + (E\bar{\tau}_{r\theta})_{(2)}]ds \tag{29}$$

and

$$\int_{-s_a}^{s_b} (E\bar{\tau}_{r\theta})_{(2)} ds = 0. \tag{30}$$

Substitution of the shear expression into equations (29) and (30) yields

$$T_0 = (ER_0)_{(1)} \left\{ \sum_{m=1}^{\tilde{M}} \frac{1}{m} q_{m(1)} \left(\cos\frac{m\pi s_a}{s_L} - \cos\frac{m\pi s_b}{s_L} \right) + \sum_{m=0}^{\tilde{M}} \frac{1}{m} q^*_{m(1)} \left(-\sin\frac{m\pi s_a}{s_L} + \sin\frac{m\pi s_b}{s_L} \right) \right\} \tag{31}$$

and

$$\sum_{m=1}^{\tilde{M}} \frac{1}{m} q_{m(2)} \left(\cos\frac{m\pi s_a}{s_L} - \cos\frac{m\pi s_b}{s_L} \right) + \sum_{m=0}^{\tilde{M}} \frac{1}{m} q^*_{m(2)} \left(-\sin\frac{m\pi s_a}{s_L} + \sin\frac{m\pi s_b}{s_L} \right) = 0 \tag{32}$$

Solution by Collocation Method and Numerical Results

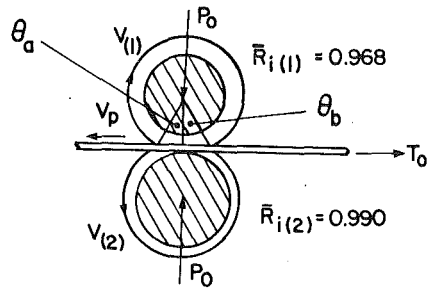
Given the coordinates of the two ends of the contact arc, namely, $-s_a$ and s_b, the coefficients h_m, h^*_m, q_m, and q^*_m, of equations (9) and (10) can be solved in terms of the geometry, the unknown u_o in equation (17), unknown $V_p/V_{(1)}$ in equation (22), and the unknown $V_p/V_{(2)}$ in equation (24). The four general equations, equations (16), (17), (22), or (23), and (24) or (25), which depends on slip or nonslip, should be satisfied at any contact from $-s_a$ to s_b, including the two end points themselves. Equations (26)–(28) and (32) supply four additional equations to solve for the three unknowns, namely, u_0 and the two speed ratios. The tail force T_0 can be calculated from equation (31), which can either be pulling (positive) or pushing (negative). It is to be noted that due to trigonometrical identities, one needs only to enforce equation (16) to one of the end points, $-s_a$ or s_b, but not both.

As in reference [4], the collocation method may be used to solve for the problem. Dividing equally the length $s_a + s_b$ into N subdivisions, we have $4N + 7$ equations. The total number of unknowns is $4M + 4\tilde{M} + 7$. Therefore, $N = M + \tilde{M}$.

In the computation, all points in the contact zone, except the two end points, are assumed to be nonslip in the beginning, then the resulting shear and normal stress at the contact points are checked. If the shear stress is greater than the product of the normal stress and the coefficient of friction at a point, the slip condition is to replace the nonslip condition at the point and calculation is resumed. Thus consecutive points are unlocked in a stepwise manner until all points satisfied the appropriate slip or nonslip criteria.

As a numerical example, we use two cylinders of equal radius but with different layer thickness:

Downloaded 01 May 2010 to 171.66.16.249. Redistribution subject to ASME license or copyright; see http://www.asme.org/terms/Terms_Use.cfm



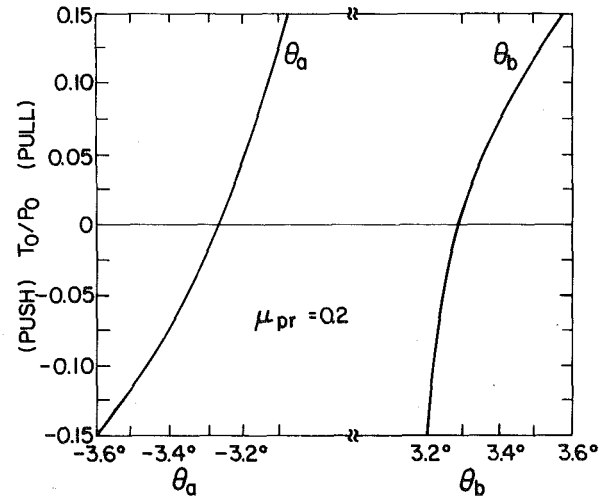


Fig. 4 Effect of T_0 change on contact angles for constant P_0

$$\bar{R}_{i(1)} = 0.968 \quad \bar{R}_{i(2)} = 0.990$$

Other geometrical and material properties are

$$t/R_0 = 0.004 \quad E_p/E_{(1)} = E_p/E_{(2)} = 600$$

$$\mu_{rp} = 0.2$$

The normal force P_0 is kept constant while the tail force T_0 is varied. In the computation, maximum n in the Fourier series is 450, and N is taken as 10 which makes $M = \bar{M} = 5$.

The numerical results are shown in Figs. 2–4, all for the plane strain case. Fig. 2 shows the changes in the distribution of the shear stress and the slip zone in the contact nip as the tail force on the sheet is increased from zero to the gross-slip value. In Fig. 2, the dotted line indicates the slip region between cylinder (1) and the sheet, and the solid line region indicates nonslip. The total normal pressure P_0 is maintained at a constant value of $P_0/E_{(1)}R_0 = 0.021$.

Fig. 3 shows the speed ratio variation versus T_0 change for the same problem. It is to be noted that there is a slight difference in having the same T_0 pulling at the exit end of the sheet instead of pushing at the inlet end and vice versa, but the difference is small.

Fig. 4 shows the shifting of the two ends of the contact arc as the tail force is changed.

Conclusion

The present analysis suggests a procedure to solve for asymmetric, steady-state rolling contact problem for two elastic layered cylinders with an elastic thin sheet in the nip, driven by the two cylinders. The asymmetric deformation is caused by a tail force, pulling or pushing, at the tail end of the sheet. The maximum drag force that can be applied is when gross slippage occurs. Boundary conditions at the contact surface are rigorously enforced.

References

1 Bentall, R. H., and Johnson, K. L., "An Elastic Strip in Plane Rolling Contact," *International Journal of Mechanical Sciences*, Vol. 10, 1968, pp. 637–663.

2 Hahn, H. T., and Levinson, M., "Indentation of an Elastic Layer Bonded to a Rigid Cylinder," *International Journal of Mechanical Sciences*, Vol. 16, 1974, pp. 489–502 and 503–514.

3 Soong, T. C., and Li, C., "The Steady Rolling Contact of Two Elastic Layer Bonded Cylinders With a Sheet in the Nip," *International Journal of Mechanical Sciences* Vol. 23, 1981, pp. 263–273.

4 Soong, T. C., and Li, C., "On the Unbonded Contact Between Plates and Layered Cylinders," ASME JOURNAL OF APPLIED MECHANICS, Vol. 47, Dec. 1980, pp. 841–846.

5 Little, R. W., *Elasticity*, Prentice-Hall, Englewood Cliffs, N. J., 1973, pp. 166–167.

APPENDIX 1

Functions given in equations (13) and (14)

$$\{\alpha_0, \beta_0\} = \frac{(\kappa^2 - \beta^2)}{(\kappa + \beta)\bar{R}_i^{-1} + (\kappa - \beta)\bar{R}_i} \{(-\bar{R}_i + \bar{R}_i^{-1}), (\bar{R}_i^{-1} - \bar{R}_i)\}$$

$$\{\alpha_1, \tilde{\alpha}_1)\} = (\kappa - 3\beta)(1 - \bar{R}_i^2)\{b_{13}, b_{12}\} + (\kappa + \beta)(1 - \bar{R}_i^2)\{b_{23}, b_{22}\} - \left(\kappa - \frac{(\kappa - \beta)^2}{4\kappa}\right) ln\, \bar{R}_i \{b_{33}, b_{32}\}$$

$$\{\alpha_n, \tilde{\alpha}_n\} = -(\kappa + \beta)n\{c_{n14}, c_{n13}\} - (\kappa(n-2) + \beta(n+2))\{c_{n24}, c_{n23}\} + (\kappa + \beta)n\{c_{n34}, c_{n33}\} + (\kappa(n+2) + \beta(n-2))\{c_{n44}, c_{n43}\} \quad n = 2, 3, \ldots, \infty$$

$$\{\beta_1, \tilde{\beta}_1\} = 2(3\kappa - \beta)\{b_{13}, b_{12}\} + 2(\kappa + \beta)\{b_{23}, b_{22}\} - \left(\frac{(\kappa - \beta)^2}{4\kappa} + \beta\right)\{b_{33}, b_{32}\}$$

$$\{\beta_n, \tilde{\beta}_n\} = n(n-1)(\kappa + \beta)\{c_{n14}, c_{n13}\} + (\kappa(n^2 + 3n + 2) - \beta(2 + n - n^2))\{c_{n24}, c_{n23}\} + (\kappa + \beta)(n + n^2)\{c_{n34}, c_{n33}\} + (\kappa(n^2 - 3n + 2) + \beta(n^2 + n - 2))\{c_{n44}, c_{n43}\} \quad n = 2, 3, \ldots, \infty \quad (33a\text{–}e)$$

where $\bar{R}_i = R_i/R_0$, b_{ij} and c_{nij} denote the (ij)th element of the inverted matrices $[B]^{-1}$ and $[C_n]^{-1}$, respectively.

Matrices $[B]$ and $[C_n]$ are given as follows:

$$[B] = \begin{bmatrix} (6\kappa - 2\beta)\bar{R}_i^2 & 2(\kappa + \beta)\bar{R}_i^{-2} & -\beta - \dfrac{(\kappa - \beta)^2}{4\kappa} \\ 2 & -2 & \dfrac{\beta - \kappa}{4\kappa} \\ 2 & -2 & 1 + \dfrac{\beta - \kappa}{4\kappa} \end{bmatrix}$$

$$[C_n] = \begin{bmatrix} -(\kappa + \beta)n\bar{R}_i^{n-1} & -[\kappa(n-2) + \beta(n+2)]\bar{R}_i^{n+1} & \dfrac{(\kappa + \beta)n}{\bar{R}_i^{n+1}} & \dfrac{\kappa(n+2) + \beta(n-2)}{\bar{R}_i^{n-1}} \\ (\kappa + \beta)nR_i^{-n-1} & [\kappa(n+4) + \beta n]\bar{R}_i^{n+1} & \dfrac{(\kappa + \beta)n}{\bar{R}_i^{n+1}} & \dfrac{\kappa(n-4) + \beta n}{\bar{R}_i^{n-1}} \\ n(n-1) & n(n+1) & -n(n+1) & -n(-1) \\ -n(n-1) & -(n-2)(n+1) & -n(n+1) & -(n+2)(n-1) \end{bmatrix}$$

$$n = 2, 3, \ldots, \infty \quad (34a, b)$$

Downloaded 01 May 2010 to 171.66.16.249. Redistribution subject to ASME license or copyright; see http://www.asme.org/terms/Terms_Use.cfm

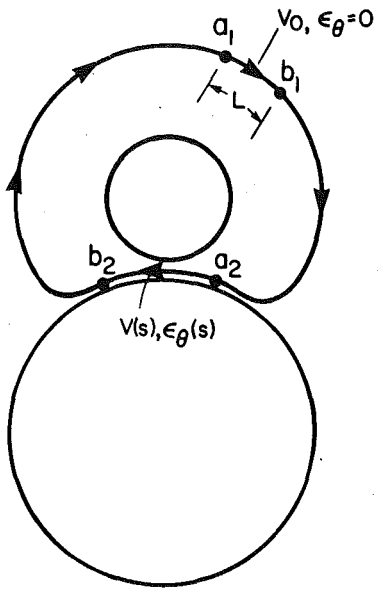


Fig. 5 A sketch for steady-state rotation

APPENDIX 2

A Proof of the Relationship Between the Local Speed and Strain

Assume an elastic material point moving along the circumferential trajectory of the boundary as shown in Fig. 5, where a_1 and b_1 are two global coordinate points with an arbitrary distance L apart. Without loss of generality, assume the region between a_1 and b_1 has zero tangential strain. Consequently, the speed of a moving point will be constant, say V_0, when crossing this region.

Assume the moving point reaches the coordinate point a_2 from a_1 after a certain time. Then, another point, starting at the same time from b_1, should reach a different point, say b_2, which is shown in the figure. Assume the a_2 and b_2 points are now located in a stressed region.

Since the motion is assumed to be of steady state, the time spent on traveling from a_1 to b_1 should be the same as the time spent on moving across a_2 to b_2, because the time required to move across b_1 to a_2 is the same for both points. The time from a_1 to b_1, or from a_2 to b_2 is evidently L/V_0.

Let us calculate what should be the length $\widehat{a_2b_2}$.

Assume $V(s)$ is the local speed of the moving point within a_2 and b_2 where s is the circumferential coordinate, then

$$\widehat{a_2b_2} = \int_0^{L/V_0} V(s)dt, \tag{35}$$

where t is the time.

Since the motion is steady-state, we may change the variable t to s,

$$s = tV_0. \tag{36}$$

Substitution of equation (36) into (35) yields

$$\widehat{a_2b_2} = \int_0^L V(s)ds/V_0. \tag{37}$$

However, the segment from a_2 to b_2 should be the stretched length of the unstressed element a_1b_1 when that element is moved to occupy the stressed region a_2 to b_2. Let $\epsilon_\theta(s)$ be the local tangential elongation of a unit length, which is known as the circumferential strain; then

$$\widehat{a_2b_2} = \int_0^L [1 + \epsilon_\theta(s)]ds. \tag{38}$$

It to be noted that in equation (38), only the engineering definition of the strain is used and there is no need to ascertain how it is related to the displacements.

Equating expressions (37) to (38) yields

$$\int_0^L \{V(s) - V_0[1 + \epsilon_\theta(s)]\}\, ds = 0. \tag{39}$$

Since L is arbitrary and equation (39) is true for every $L \geq 0$, it follows that, for all s,

$$\frac{V(s)}{V_0} = 1 + \epsilon_\theta(s). \tag{40}$$

This basic relationship leads immediately to equation (28).

Downloaded 01 May 2010 to 171.66.16.249. Redistribution subject to ASME license or copyright; see http://www.asme.org/terms/Terms_Use.cfm

R. C. Benson

Assistant Professor,
Department of Mechanical
and Aerospace Sciences,
University of Rochester,
Rochester, N. Y. 14627
Assoc. Mem. ASME

The Deformation of a Thin, Incomplete, Elastic Ring in a Frictional Channel

The deformation of a thin, incomplete, elastic ring being pushed through a frictional channel is analyzed. The problem is formulated using the nonlinear theory of the elastica and it is found that, depending on the channel geometry, either two deformed shapes for the ring are possible, or else no solution is possible. The results are applied to the design of machines such as plain-paper copiers, self-threading tapes, and sewing machines.

1 Introduction

An interesting class of modern machinery is designed for the handling of lightweight, flexible materials such as paper in a copier or film in a movie camera. When passing through the frictional channels of the machine these objects can undergo large deflections, perhaps to the point of inducing a failure. It is the purpose of this paper to treat a representative problem and to provide a mathematical description for effects such as (in colloquial terms) "jam," "stall," and "roll-over."

The object in the channel is modeled as an incomplete, elastic ring, an approximation say of a length of tape wound off a spool and still possessing a residual curvature. The equations of deformation are then derived and nondimensionalized. Using the theory of the elastica the problem is reduced to a set of elliptic integrals which are observed to possess integrable singularities. A numerical scheme for integration, including the singular point is described, and the nonlinearity of the problem is manifested by the result that either two physically meaningful solutions are possible or else none exists.

The consequence of no solution is interpreted as a jam of the ring in the channel, and a mathematical description of the threshold of jamming is given. The two modes are interpreted physically and contrasted. It is concluded that one mode is preferable to the other, as it requires less of a drive force and lies flatter in the channel. These results are used to optimize the channel geometry so the ring is passed through in the most desirable configuration.

The theory of the elastica is well understood. One of the earliest and most thorough treatments is by Love [1] who shows the possibility of multiple solutions, and determines a condition for stability. Other texts on elastic stability, such as by Timoshenko and Gere [2] have an introduction to the large deflection of beams. The most comprehensive work is by Frisch-Fay [3] who studies a variety of cantilevered beam and closed-ring problems. The book by Hancock [4] is useful for the treatment of the elliptic integrals that naturally arise in problems of the elastica.

Among recent articles Mitchell [5] gives an especially clear and compact derivation of the equations for a cantilevered bar with distributed loading and a curvilinear stress-free state. The large deformation of circular rings, the geometry of the present paper, is studied by Conway [6], Wu and Plunkett [7], and Antman [8]. Application to industrial problems is exemplified by the papers by Soong [9] on loosely fit beams, and Lloyd, et al. [10], who study the folding of heavy fabric sheets. Numerical techniques described by Carnahan [11] will be used later.

The contribution of the present paper lies in the study that is made of physical limits to a common mechanical engineering problem. It has long been known that the nonlinear theory of the elastica admits multiple solutions, but far less work has gone into the study of the effect of the boundary conditions on physical admissibility. This paper will examine such effects as frictional loading, and will balance the conflicting design requirements for driving the ring through the channel with least amount of force and the least likelihood of a jam.

2 Problem Formulation

Fig. 1 shows the geometry of the problem. A thin, incomplete elastic ring of radius r and flexural rigidity $\mathcal{D}$, is forced (left-to-right in the figure) through a channel with rigid, frictional walls of coefficient μ. The lower wall is flat and is used as a horizontal reference line, while the upper wall may be curved. Assuming plane-strain, inextensible bending the ring may be regarded as a wide, constantly curved, Euler-Bernoulli "beam."

Neglecting gravity and transient effects, the differential equation for finite deflection is

$$\mathcal{D}\frac{d^2\phi}{ds^2} = f\cos(\phi + \theta), \tag{1}$$

Contributed by the Applied Mechanics Division and presented at the Winter Annual Meeting, Washington, D. C., November 15–20, 1981, of THE AMERICAN SOCIETY OF MECHANICAL ENGINEERS.

Discussion on this paper should be addressed to the Editorial Department, ASME, United Engineering Center, 345 East 47th Street, New York, N. Y. 10017, and will be accepted until March 1, 1982. Manuscript received by ASME Applied Mechanics Division, December, 1980. Paper No. 81-WA/APM-22.

Copyright © 1981 by ASME

Downloaded 01 May 2010 to 171.66.16.249. Redistribution subject to ASME license or copyright; see http://www.asme.org/terms/Terms_Use.cfm

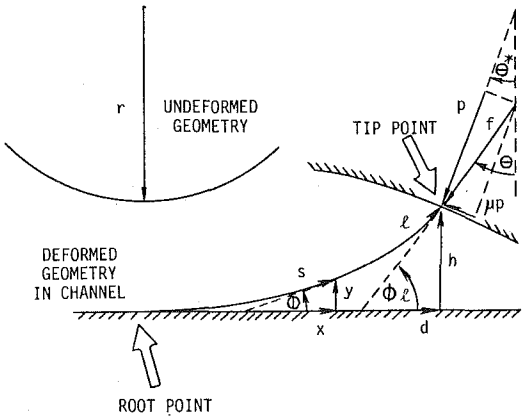


Fig. 1 Geometry

where s is a curvilinear coordinate measured along the length of the deformed beam, and $\phi(s)$ is the slope at s measured with respect to the horizontal. The reaction force exerted on the lead edge of the beam by the upper wall has magnitude f and orientation θ away from the vertical. This may alternatively be broken down into a component p, normal to the surface at angle θ^*, and a frictional drag μp. The former representation is preferred however, as the reaction angle

$$\theta = \theta^* + \tan^{-1}(\mu), \tag{2}$$

combines both the effect of upper surface pitch and friction into a *single known parameter.*

The point where the beam first lifts off the flat wall will be called the "root point" and marked as $s = 0$. Here we have the boundary conditions

$$\phi(0) = 0, \quad \frac{d\phi}{ds}(0) = 0, \tag{3}$$

and at the beam tip, an unknown length $s = l$ away, the curvature is unchanged

$$\frac{d\phi}{ds}(l) = \frac{1}{r}. \tag{4}$$

The zero curvature condition in equation (3) is due to the action of the tip force rolling the beam out along the flat wall until the resulting bending moment balances the initial curvature

$$df\cos(\theta) - hf\sin(\theta) = D/r. \tag{5}$$

The quantities d and h are the span and tip height of the deflected beam length

$$d = \int_0^l \cos\phi(s)ds, \quad h = \int_0^l \sin\phi(s)ds. \tag{6}$$

Behind the root point, $s < 0$, the beam lies flat as only the constant moment of equation (5) is present; the shear from the tip force being balanced by a reaction at the root point. The transmitted bending moment is balanced at an indeterminant distance behind the root point, but presumably close enough to prevent buckling of the flat length.

Equations (1), (3), (4), and (6) are next nondimensionalized by dividing lengths by r, and forces by $\mathcal{D}/r^2$, and using capital letters to denote nondimensional counterparts

$$H = h/r, \quad F = fr^2/\mathcal{D}, \quad \text{etc.}, \tag{7}$$

$$\frac{d^2\phi}{dS^2} = F\cos(\phi + \theta), \tag{8}$$

$$\phi(0) = 0, \quad \frac{d\phi}{dS}(0) = 0, \tag{9}$$

$$\frac{d\phi}{dS}(L) = 1, \tag{10}$$

$$D = \int_0^L \cos\phi(S)dS, \quad H = \int_0^L \sin\phi(S)dS. \tag{11}$$

This forms a well-posed system of equations where $(9)_1$, $(9)_2$, (10), and $(11)_2$ are used to solve for the unknown reaction force F, span length L, and two constants of integration produced by (8). It is also useful to treat the problem where F replaces H as a known value and constraint $(11)_2$ is dropped. This facilitates the computation of multiple solutions, a topic of Section 3. In later sections we will return to the physical problem at hand.

3 Deflected Beam Shapes—Admissible Solutions

The weakly nonlinear differential equation (8) may be integrated once, after first multiplying through by $d\phi/dS$, to produce the strongly nonlinear first-order equation

$$\frac{1}{2}\left(\frac{d\phi}{dS}\right)^2 = F\sin(\phi + \theta) + C, \tag{12}$$

where C is a constant of integration. This is eliminated by applying both of equations (9) to get

$$\frac{d\phi}{dS} = +\{2F[\sin(\phi + \theta) - \sin\theta]\}^{1/2}. \tag{13}$$

Here the positive root is chosen to reflect the fact that the beam's slope is increasing from the root point to the tip.

Applying boundary condition (10) allows for the solution of the slope at the lead edge of the beam, $\phi_L \equiv \phi(L)$, in terms of F and θ

$$\phi_L = \sin^{-1}\left(\frac{1}{2F} + \sin\theta\right) - \theta. \tag{14}$$

The potential for more than one solution presents itself here, as inverse sine has an infinite number of values. However, only two are of physical interest. They are

$$\begin{aligned} \phi_L{}^{(a)} &= \alpha - \theta, \\ \phi_L{}^{(b)} &= \pi - \alpha - \theta, \end{aligned} \tag{15}$$

where α is the principal value of the inverse sine. Since F and θ are both positive this puts α in the range

$$\theta < \alpha = \text{P.V. } \sin^{-1}\left(\frac{1}{2F} + \sin\theta\right) \le \pi/2. \tag{16}$$

Consequently $\phi_L{}^{(a)}$ and $\phi_L{}^{(b)}$ will be bounded by

$$0 < \phi_L{}^{(a)} \le (\pi/2) - \theta \le \phi_L{}^{(b)} < \pi - 2\theta. \tag{17}$$

A final inequality to note is that, in order to have real solutions to (15), F must have a lower bound

$$F \ge 0.5/(1 + \sin\theta). \tag{18}$$

When (18) becomes an equality $\phi_L{}^{(a)}$ and $\phi_L{}^{(b)}$ coincide

$$\phi_L{}^{(a)} = \phi_L{}^{(b)} = (\pi/2) - \theta; \quad F = 0.5/(1 + \sin\theta). \tag{19}$$

Other choices for ϕ_L are rejected for one of two reasons. Selecting $\phi_L > \phi_L{}^{(b)}$ leads to deflected shapes with lead edge (or "tip") angles in excess of 2π, thus requiring the beam to penetrate itself or the upper wall. A choice of $\phi_L < \phi_L{}^{(a)}$ has similar penetration problems, and leads to geometries with inflection points between the root point and tip. Love [1] shows that such solutions, with greater than the minimum number of inflections, are unstable. Only $\phi_L{}^{(a)}$ and $\phi_L{}^{(b)}$ lead to admissible shapes, with a single inflection at the root point, and no penetrations.

In Fig. 2, the lead edge angle ϕ_L is plotted against the reaction angle θ for various force levels F. The juncture of the two solutions, as given by (19), is plotted as a dashed line.

Returning to equation (13) we may solve for the differential element dS, and then integrate in ϕ to get:

$$L = \int_0^{\phi_L} \{2F[\sin(\phi + \theta) - \sin\theta]\}^{-1/2}d\phi. \tag{20}$$

This will yield two values for the deflected beam length, due to the

Downloaded 01 May 2010 to 171.66.16.249. Redistribution subject to ASME license or copyright; see http://www.asme.org/terms/Terms_Use.cfm

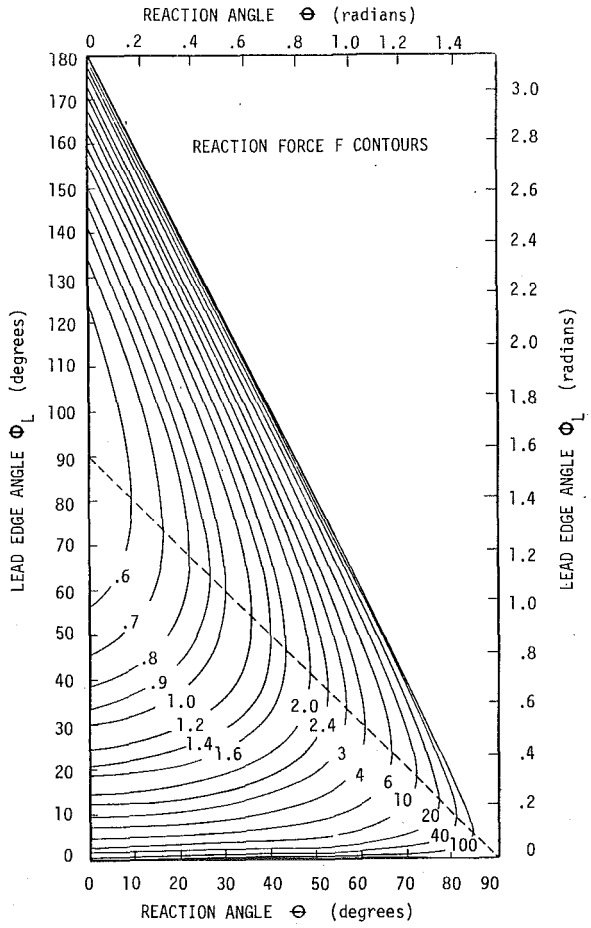


Fig. 2 Lead edge angle

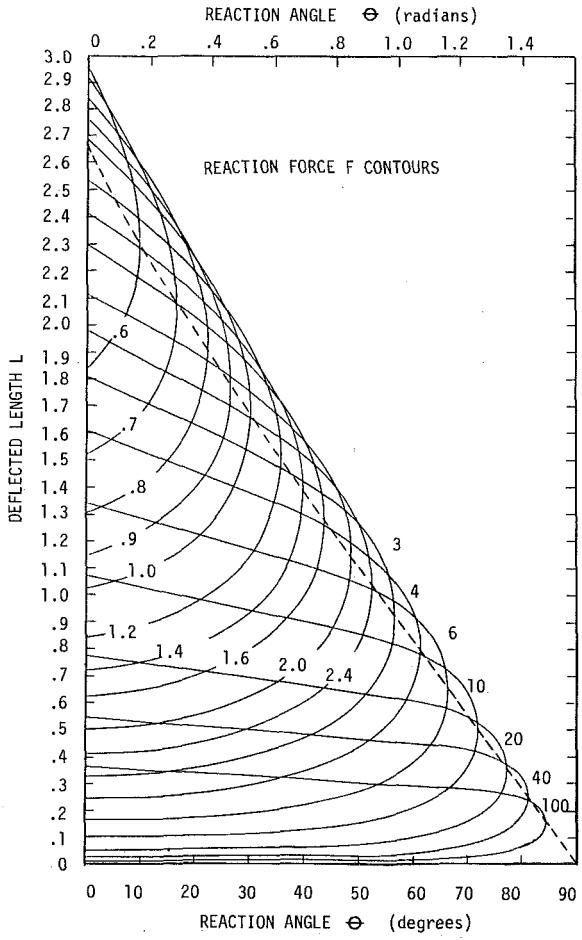


Fig. 3 Deflected length

two choices for the upper limit. Similarly equations (11) may be integrated to give

$$D = \int_0^{\phi_L} \{2F[\sin(\phi + \theta) - \sin\theta]\}^{-1/2} \cos\phi d\phi, \tag{21}$$

$$H = \int_0^{\phi_L} \{2F[\sin(\phi + \theta) - \sin\theta]\}^{-1/2} \sin\phi d\phi. \tag{22}$$

These elliptic integrals are typical elastica solutions, slightly complicated by the square root singularities which occur at the lower limits of (20) and (21); a consequence of the slope and curvature vanishing simultaneously at the root point. The singularity in equation (22) is removable. Making the variable substitution, $u = \sin(\phi + \theta)$ transforms equation (20) to

$$L = \int_{\sin\theta}^{\sin\theta + 1/(2F)} [-2F(u - \sin\theta)(u - 1)(u + 1)]^{-1/2} du, \tag{23}$$

which Hancock [4] shows is equivalent to

$$L = F^{-1/2} \tilde{F}\left\{\frac{1}{2}[1 - \sin\theta]^{1/2}, \left[\frac{2}{F(1 + \cos 2\theta) + (1 - \sin\theta)}\right]^{1/2}\right\}. \tag{24}$$

Here $\tilde{F}$ stands for the standard elliptic integral of the first kind. Equations (21) and (22) may be similarly transformed to standard, albeit complicated, forms.

For the purposes of this paper it it simpler to integrate equations (20)–(22) by the following technique. Near the singular lower limit the integrands are expressed as the product of a first-order Taylor series and $\phi^{-1/2}$, and then integrated in closed form. Away from the singular point integration is performed numerically using Simpson's rule [11]. The results are shown in Fig. 3–5, in a format similar to Fig. 2. Observe that, in each of these figures, the constant force contours overlap to form a region of dual solutions, and an envelope beyond which no solution exists. The envelope in Fig. 5 is particularly important since it sets a demarcation of solution and nonsolution in terms of known quantities; the channel height H, and reaction angle θ.

4 Nonsolution Geometries

The lack of a solution outside of the envelope in Fig. 5 corresponds to a jam of the beam in the channel. Physically, as trailing points slide in along the lower wall, the tip of the beam merely rocks about a fixed point on the upper surface. A typical consequence is to have a finite length beam run free of the drive mechanism before the tip emerges from the channel, hence a jam.

Mathematically, the curve of the jam envelope in Fig. 5 is described by

$$\left.\frac{dH}{dF}\right|_\theta = 0. \tag{25}$$

Substituting (22) into (25) gives

$$-\frac{1}{2F}\int_0^{\phi_L} \{2F[\sin(\phi + \theta) - \sin\theta]\}^{-1/2} \sin\phi d\phi + \{2F[\sin(\phi_L + \theta) - \sin\theta)]\}^{-1/2} \sin\phi_L \frac{d\phi_L}{dF} = 0. \tag{26}$$

Noting that the integral above is H, and that $\phi_L = \phi_L{}^{(b)}$ on the envelope, the second equation of (15) is substituted into (26) to give

$$FH = \sin\theta + \cos\theta \frac{\frac{1}{2F} + \sin\theta}{\left[1 - \left(\frac{1}{2F} + \sin\theta\right)^2\right]^{1/2}}. \tag{27}$$

Downloaded 01 May 2010 to 171.66.16.249. Redistribution subject to ASME license or copyright; see http://www.asme.org/terms/Terms_Use.cfm

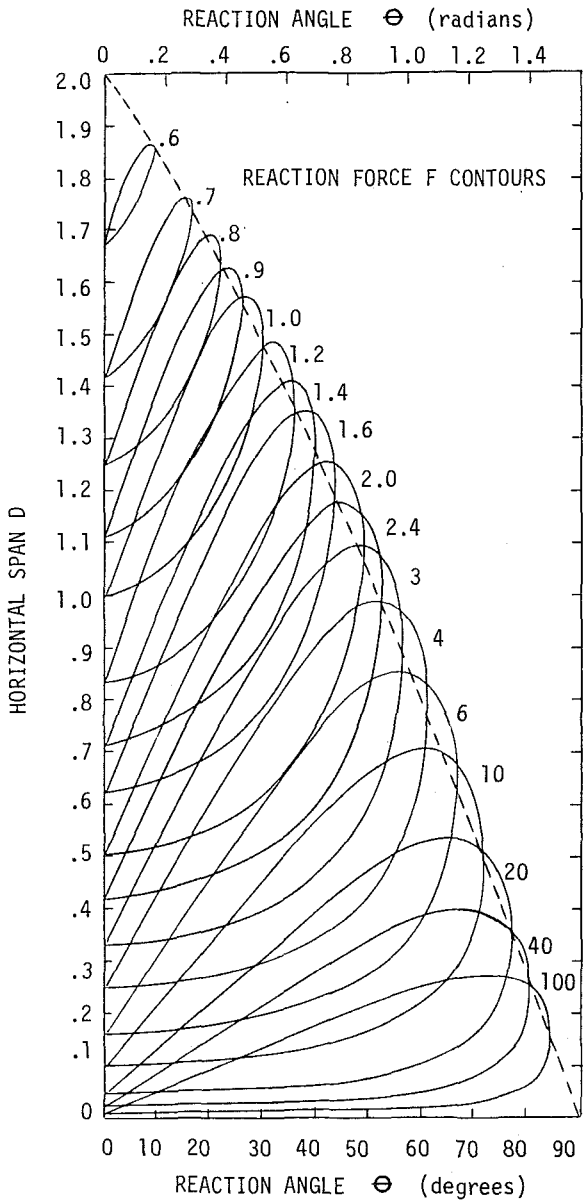


Fig. 4 Horizontal span

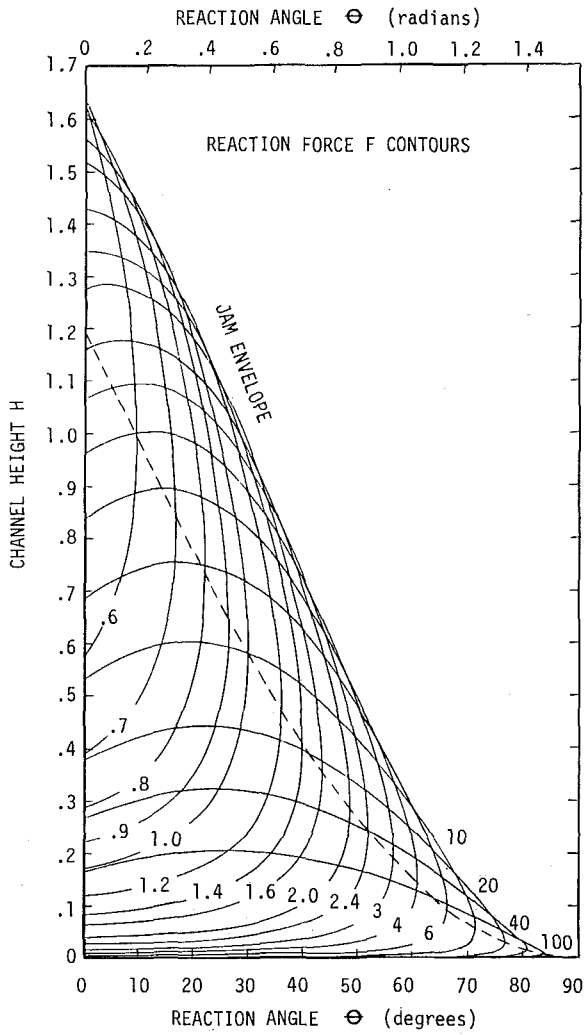


Fig. 5 Channel height

Equations (22) and (27) provide an implicit means of relating any two of the quantities F, H, and θ to the third, along the jam envelope. Subsequently, one could go back to equations (20) and (21), or Figs. 3 and 4 to find the critical values of deflected beam length L and span D. Such results have been plotted in Fig. 6 with θ as the independent variable. It should be noted that the critical curves for L and D in Fig. 6 are not the same as the envelopes in Fig. 3 and 4, respectively.

5 Dual Solution Geometries

Attention is turned next to the region inside of the jam envelope, and a comparison is made of the two modes which exist for a given H and θ. Three quantities are of interest; the magnitude of the reaction force, F, the lead edge angle, ϕ_L, and the excess beam length in a given length of the channel, L-D. "Mode 1" will be assigned to the deformation with the lesser reaction force magnitude, and "Mode 2" to the greater. Subscripts 1 and 2 will be used for distinction of the modes.

From Figs. 2–5 the following inequalities are found:

$$F_1 \leq F_2, \quad \phi_{L1} \leq \phi_{L2}, \quad L_1 - D_1 \leq L_2 - D_2. \tag{28}$$

Each of these becomes equal on the jam envelope where the two modes coincide, and becomes more accentuated at points further in from the envelope. Physically, the Mode 2 beam is more difficult to push through the channel, is bent back further, and requires a greater length to be fed into the channel before the tip traverses a given distance. These are all potential design flaws.

Fig. 7 shows results for a typical channel geometry, and will be used to illustrate the topics of this section. It is seen that the resistance to forward tip motion is over 18 times greater for the second mode, and it is possible that a mechanism designed to drive beams of the Mode 1 type might stall if a Mode 2 shape develops. Such a failure might be mistaken for a jam since in both cases the beam does not complete its travel through the channel. Unlike a jam however, a stalled beam does not continue to deform, and its progress through the channel can be resumed if a sufficient amount of drive force is applied through the root point. No amount of drive force can correct a jam which is entirely a consequence of beam and channel geometry and the friction coefficient between them.

Observe also in Fig. 7 that the point furthest progressed in the channel is the tip of the first mode, whereas for the second mode it is an intermediate point between the root and tip. A leading point, S^*, not at the tip, occurs when the slope of the beam is vertical, $\phi = \pi/2$. Substituting this for the upper limit of equation (20) gives

$$S^* = \int_0^{\pi/2} \{2F[\sin(\phi + \theta) - \sin\theta]\}^{-1/2} d\phi, \tag{29}$$

where F is determined by constraint (22). Numerically, or else through Figs. 2, 5, and 6, it is found that both modes can develop vertical

Downloaded 01 May 2010 to 171.66.16.249. Redistribution subject to ASME license or copyright; see http://www.asme.org/terms/Terms_Use.cfm

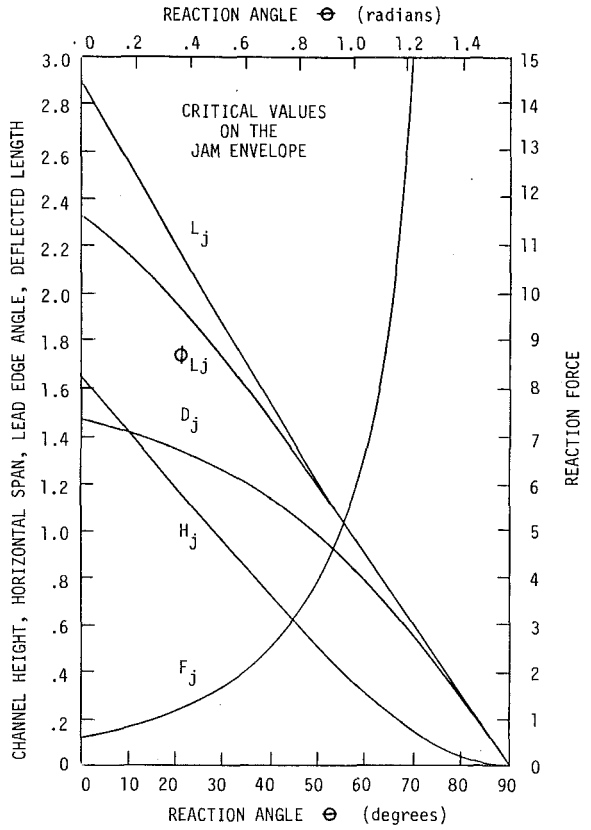


Fig. 6 Jam envelope values

slopes, depending on the channel geometry. An increase in the reaction angle θ causes the tip angles ϕ_{L1} and ϕ_{L2} to decrease, and if they drop below $\pi/2$ a vertical slope cannot be achieved. The maximum θ which still admits a vertical slope for the first mode (depending on the channel height) is about $\pi/5$ (36°). For the second mode the limit is $\pi/4$ (45°).

Decreasing the channel height, H, causes ϕ_{L1} to become smaller and ϕ_{L2} to become larger, perhaps to the point where Mode 2 has a vertical slope but Mode 1 does not. Such is the case in Fig. 7. This leads to a design flaw called rollover, when the desired configuration of Mode 1 is replaced by Mode 2. Rollover can be induced by a temporary jam of the beam. If the tip of a Mode 1 beam encounters an anamolous rough spot on the upper surface, it may jam. Subsequently the tip angle increases and a leading bulge is developed. If by chance the tip rocks free of the rough spot the beam will resume its progress through the channel, this time in the Mode 2 state. The design problems associated with rollover are usually manifested when portions of the beam exit the channel ahead of the anticipated lead edge.

Again referring to Fig. 7 it is seen that an additional 0.419 nondimensional units of length must be pushed into the channel for the tip of the Mode 2 beam to coincide with the tip of the Mode 1 beam. This could lead to timing problems.

6 Conclusions

The quasi-static motion of an incomplete, elastic ring (or curved beam) through a frictional channel has been studied. It has been found that either two physically meaningful solutions exist, or none exists. The latter possibility corresponds to a jam in the channel and is induced by increasing the height of the channel, decreasing the radius of curvature of the ring, increasing the friction coefficient of the upper surface, or increasing the pitch of the upper surface. A mathematical description of the threshold of jamming (jam envelope) has been given.

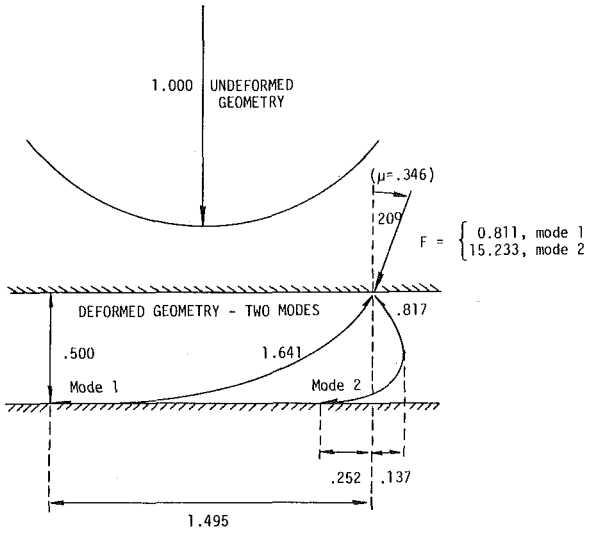


Fig. 7 Example results

When two solutions exist one is more desirable than the other. With lesser drag and a flatter configuration, the favored mode is less apt to stall or rollover in the channel. The distinction between the two modes is diminished as jamming channel geometries are approached.

The results of this paper are particularly useful when designing a channel to handle incomplete rings of statistically varying radii and flexural rigidity. For example, the increased possibility of a jam caused by widening the channel might be regarded as an acceptible tradeoff for the decreased drag that also results. Other changes, such as decreasing the friction coefficient of the upper surface, have only beneficial effects.

The general results and techniques of this paper may be applied to related problems involving the impingement of an elastic, incomplete ring (or plate) on a frictional surface, particularly with regard to regions of multiple or no solution. The geometry studied here has been chosen as being broadly representative of such problems.

Acknowledgment

This study was begun while the author was an employee of the Xerox Corporation in Rochester, N. Y. The author would like to thank his former colleagues of the Applied Mechanics Group for their excellent advice on this and other technical matters.

References

1 Love, A. E. H., *A Treatise on the Mathematical Theory of Elasticity*, Dover Publications, New York, 4th ed., Chapter 19, 1944.

2 Timoshenko, S. P., and Gere, J. M., *Theory of Elastic Stability*, McGraw-Hill, New York, Chapter 2.7, 2nd ed., 1961.

3 Frisch-Fay, R., *Flexible Bars*, Butterworth and Co. LTD., Washington, 1962.

4 Hancock, H., *Elliptic Integrals*, Dover Publications, New York, 1958.

5 Mitchell, T. P., "The Nonlinear Bending of Thin Rods," ASME JOURNAL OF APPLIED MECHANICS, Vol. 26, Mar. 1959, pp. 40–43.

6 Conway, H. D., "The Nonlinear Bending of Thin Circular Rods," ASME JOURNAL OF APPLIED MECHANICS, Vol. 23, Mar. 1956, pp. 7–10.

7 Wu, C-H., and Plunkett, R., "On the Contact Problem of Thin Circular Rings," ASME JOURNAL OF APPLIED MECHANICS, Vol. 32, Mar. 1965, pp. 11–20.

8 Antman, S., "General Solutions for Plane Extensible Elasticae Having Nonlinear Stress-Strain Laws," *Quarterly of Applied Mathematics*, Vol. 26, No. 1, 1968, pp. 35–47.

9 Soong, T. C., "Large Deflection Analysis of Loosely Fit Beams," *Recent Advances in Engineering Science, Proceedings, 15th Annual Meeting Society of Engineering Science Inc.*, Dec. 1978, pp. 267–273.

10 Lloyd, D. W., Shanahan, W. J., and Konopasek, M., "The Folding of Heavy Fabric Sheets," *International Journal of Mechanical Science*, Vol. 20, No. 8, 1978, pp. 521–527.

11 Carnahan, B., Luther, H. A., and Wilkes, J. O., *Applied Numerical Methods*, Wiley, New York, Chapter 2, 1969.

Downloaded 01 May 2010 to 171.66.16.249. Redistribution subject to ASME license or copyright; see http://www.asme.org/terms/Terms_Use.cfm

S. Krenk[1]

Department of Applied Mathematics
and Computer Science,
University of Virginia,
Charlottesville, Va. 22901

Theories for Elastic Plates Via Orthogonal Polynomials

A complementary energy functional is used to derive an infinite system of two-dimensional differential equations and appropriate boundary conditions for stresses and displacements in homogeneous anisotropic elastic plates. Stress boundary conditions are imposed on the faces a priori, and this introduces a weight function in the variations of the transverse normal and shear stresses. As a result the coupling between the two-dimensional differential equations is described in terms of a single difference operator. Special attention is given to a truncated system of equations for bending of transversely isotropic plates. This theory has three boundary conditions, like Reissner's, but includes the effect of transverse normal strain, essentially through a reinterpretation of the transverse displacement function. Full agreement with general integrals to the homogeneous three-dimensional equations is established to within polynomial approximation.

1 Introduction

Various methods can be used to develop two-dimensional plate equations from the three-dimensional equations of elasticity. Ideally an exact solution to the three-dimensional equations is desired, and such solutions can in fact be constructed systematically by algebraic manipulation of differential operators as demonstrated by Lur'e [1] and Cheng [2]. A basic problem encountered in application of this integral is the lack of explicit methods allowing for prescription of detailed boundary conditions. It is also uncertain if the truncation of this integral to a finite, and in practice small, number of terms gives an optimal solution within this number of terms. For example, it is well known that simple truncation of a Fourier expansion of a function may not yield the most desirable approximation.

This leaves ample scope for plate theories based on explicit representation of the thickness distribution of displacements and stresses. The simplest of these is the classical plate theory, where displacement derivatives and stresses can be derived directly from the transverse displacement of the midplane. This theory only allows satisfaction of two boundary conditions, but it was shown by Nordgren [3] and Simmonds [4] that the accuracy of the displacement and stress fields could be increased and explicit global error bounds obtained by a more detailed interpretation of the solution given in terms of the transverse midplane displacement. The more detailed interpretation makes use of kinematically and statically admissible fields and bounds the error by the hypersphere theorem of Prager and Synge [5, 6], but does not allow satisfaction of additional boundary conditions.

The plate theory of Reissner [7, 8] contains two important differences from classical plate theory; it makes explicit use of a three-dimensional statically admissible field and allows an extra boundary condition. Also for this theory a hypersphere error estimate can be obtained [9], but it is less useful, because the field equations in this case depend on the plate thickness.

The kinematically admissible fields used in [4, 9] include a cubic term in the representation of the displacements parallel to the midplane, and in [10] Reissner incorporated such a term explicitly in these displacements and the corresponding stresses. The resulting equations—(14) and (15) of [10]—are very close to those of the general integral of [1, 2]. In fact the only differences are terms proportional to $\nu(z/b)^2$ in the biharmonic part and the use of a parabolic distribution instead of a sinusoidal one in the rotational part. The first of these discrepancies can be traced to the effect of transverse strain and can be avoided as shown in Section 6 of the present paper. The effect of the latter is mainly a change of the thickness-shear vibration frequency to $\sqrt{10}/\pi = 1.0066$ times the correct value as discussed by Mindlin [11].

In the present paper the three-dimensional equations of elasticity are transformed into an infinite system of two-dimensional equations by polynomial representation of the thickness variation. The two-dimensional differential equations and the corresponding boundary conditions are derived from an energy functional in which both displacements and stresses appear as independent variables. The displacement field is required to satisfy the displacement boundary conditions, while the stresses are required to satisfy the equilibrium conditions as well as the stress boundary conditions. Thus truncation of the system will lead to only approximate satisfaction of Hooke's law. The strain energy associated with the discrepancy in Hooke's law is used to discuss different truncation schemes. The equations allow identification of the three types of general integrals described by Cheng [2], and surface loads and volume forces are included to allow application to plate vibration problems. Particular attention is given to the simplest theory of plate bending in terms of kinematically and

---

[1] On leave from Risø National Laboratory, 4000 Roskilde, Denmark.

Contributed by the Applied Mechanics Division for publication in the JOURNAL OF APPLIED MECHANICS.

Discussion on this paper should be addressed to the Editorial Department, ASME, United Engineering Center, 345 East 47th Street, New York, N. Y. 10017, and will be accepted until two months after final publication of the paper itself in the JOURNAL OF APPLIED MECHANICS. Manuscript received by ASME Applied Mechanics Division, April, 1981.

 Copyright © 1981 by ASME

Downloaded 01 May 2010 to 171.66.16.249. Redistribution subject to ASME license or copyright; see http://www.asme.org/terms/Terms_Use.cfm

statically admissible fields resulting in inclusion of transverse strain and general loading in Reissner's refined theory [10].

2 Problem and Notation

Let $\{x_\alpha, z\}$, $\alpha = 1, 2$ be a Cartesian coordinate system. A homogenous linear elastic body is bounded by the planes $z = \pm h$ and generators parallel to the z-axis through a curve C in the x_α-plane. The stress components are denoted $\{\sigma_{\alpha\beta}, \sigma_\alpha, \sigma\}$ corresponding to omission of the index 3. The theory is formulated for static problems, and the stresses therefore satisfy the equilibrium equations

$$\sigma_{\alpha\beta,\beta} + \sigma_{\alpha,3} + q_\alpha = 0 \tag{1}$$

$$\sigma_{\alpha,\alpha} + \sigma_{,3} + q = 0 \tag{2}$$

where a comma denotes differentiation, and the summation convention for repeated indices is adopted. $\{q_\alpha, q\}$ is the volume force.

The displacements are denoted $\{u_\alpha, w\}$, $\alpha = 1, 2$. The strains are not introduced explicitly, and Hooke's law therefore takes the form

$$\frac{1}{2}(u_{\alpha,\beta} + u_{\beta,\alpha}) = \frac{\partial B}{\partial \sigma_{\alpha\beta}} \tag{3}$$

$$u_{\alpha,3} + w_{,\alpha} = \frac{\partial B}{\partial \sigma_\alpha} \tag{4}$$

$$w_{,3} = \frac{\partial B}{\partial \sigma} \tag{5}$$

$B = B(\sigma_{\alpha\beta}, \sigma_\alpha, \sigma)$ is the complementary energy density, which in the present case of a linear elastic material is a positive-definite quadratic form in the stress components.

The independent field quantities are the stresses $\{\sigma_{\alpha\beta}, \sigma_\alpha, \sigma\}$ and the displacements $\{u_\alpha, w\}$. Stress boundary conditions will be assumed on the faces $z = \pm h$, and in static problems the volume forces $\{q_\alpha, q\}$ will be prescribed. The stress field will be required to satisfy the conditions on $z = \pm h$ *a priori*. It is noted that if the equilibrium equation (2) is satisfied at $z = \pm h$, not only $\sigma(\pm h)$ but also the derivative $\sigma_{,3}(\pm h)$ follows directly from the boundary conditions on $z = \pm h$.

When stresses and displacements are the independent field quantities, the field equations and the boundary conditions not satisfied *a priori* can be derived from the generalized complementary energy functional given by Washizu [12, p. 35]:

$$\Phi = \iint_A \int_{-h}^{h} \{B(\sigma_{\alpha\beta}, \sigma_\alpha, \sigma) + (\sigma_{\alpha\beta,\beta} + \sigma_{\alpha,3} + q_\alpha)u_\alpha + (\sigma_{\alpha,\alpha} + \sigma_{,3} + q)w\}\, dz dA + \int_{C_1} \int_{-h}^{h} \{(\sigma_{\alpha\beta}n_\beta - \bar{t}_\alpha)u_\alpha + (\sigma_\alpha n_\alpha - \bar{t})w\}\, dz ds + \int_{C_2} \int_{-h}^{h} \{\bar{u}_\alpha \sigma_{\alpha\beta} + \bar{w}\sigma_\beta\}\, n_\beta\, dz ds \tag{6}$$

A is the area within the contour C, C_1 is the part of C where the stress vector $\{\bar{t}_\alpha, \bar{t}\}$ is prescribed, while C_2 is the remaining part of C where the displacement vector $\{\bar{u}_\alpha, \bar{w}\}$ is prescribed. n_α is the outward normal. The functional (6) incoporates the *a priori* stress boundary conditions on $z = \pm h$.

3 Polynomial Representation

The z-dependence of displacements and stresses will be represented in terms of polynomials. As truncation is envisaged as the omission of terms of degree greater than a certain maximum associated with each series, the actual form of the expansion is not of fundamental importance. It will however influence the form of the resulting two-dimensional equations, and is therefore of practical importance. More important is the fact that the constraints on σ_α and σ at the faces $z = \pm h$ limit the number of independent variations and also influence the z-dependence of these variations.

No weight functions are present in the energy functional (6), and it is therefore convenient to represent the stresses and displacements in terms of Legendre polynomials $P_j(\zeta)$, [13], where the dimensionless coordinate $\zeta = z/h$ has been introduced. To suppress variations at $z = \pm h$, alternative expansions are provided for the displacements and the stress components σ_α and σ. These alternative expansions are used to define the z-dependence of the independent variations, and coefficients in these expansions will therefore not appear in the final equations.

$$\begin{Bmatrix} u_\alpha(x_\phi, z) \\ w(x_\phi, z) \end{Bmatrix} = \sum_{j=0}^{\infty} \begin{Bmatrix} u_\alpha{}^j(x_\phi) \\ w^j(x_\phi) \end{Bmatrix} P_j(\zeta)$$

$$= \begin{Bmatrix} u_\alpha{}^+(x_\phi) + u_\alpha{}^-(x_\phi)\zeta \\ w^+(x_\phi) + w^-(x_\phi)\zeta \end{Bmatrix} + (1 - \zeta^2) \sum_{j=0}^{\infty} \begin{Bmatrix} \tilde{u}_\alpha{}^j(x_\phi) \\ \tilde{w}^j(x_\phi) \end{Bmatrix} P_j{}^{(1,1)}(\zeta) \tag{7}$$

$$\begin{Bmatrix} \sigma_\alpha(x_\phi, z) \\ \sigma(x, z) \end{Bmatrix} = \sum_{j=0}^{\infty} \begin{Bmatrix} \sigma_\alpha{}^j(x_\phi) \\ \sigma^j(x_\phi) \end{Bmatrix} P_j(\zeta)$$

$$= \begin{Bmatrix} \sigma_\alpha{}^+(x_\phi) + \sigma_\alpha{}^-(x_\phi)\zeta \\ \sigma^+(x_\phi) + \sigma^-(x_\phi)\zeta \end{Bmatrix} + (1 - \zeta^2) \sum_{j=0}^{\infty} \begin{Bmatrix} \tilde{\sigma}_\alpha{}^j(x_\phi) \\ \tilde{\sigma}^j(x_\phi) \end{Bmatrix} P_j{}^{(1,1)}(\zeta) \tag{8}$$

The first term in the alternative expansion extracts the values at $z = \pm h$. Thus

$$u_\alpha{}^+(x_\phi) = \frac{1}{2}[u_\alpha(x_\phi, h) + u_\alpha(x_\phi, -h)]$$

$$u_\alpha{}^-(x_\phi) = \frac{1}{2}[u_\alpha(x_\phi, h) - u_\alpha(x_\phi, -h)] \tag{9}$$

and similarly for w, σ_α, and σ. This extraction uniquely defines the factor $(1 - \zeta^2)$ in the remaining part of the expansion, whereas the use of the Jacobi polynomials $P_j{}^{(1,1)}(\zeta)$, [13], in this expansion is merely a matter of convenience. In the present case of stress boundary conditions $\sigma_\alpha{}^\pm$ and $\sigma^\pm$ are not subject to variations. With displacement boundary conditions on $z = \pm h$ no variations would be associated with $u_\alpha{}^\pm$ and $w^\pm$ in (7). The remaining stress components are simply represented as

$$\sigma_{\alpha\beta}(x_\phi, z) = \sum_{j=0}^{\infty} \sigma_{\alpha\beta}{}^j(x_\phi) P_j(\zeta) \tag{10}$$

Similar expansions are used for the volume force $\{q_\alpha, q\}$, the boundary stress vector $\{\bar{t}_\alpha, \bar{t}\}$ on C_1 and the boundary displacement vector $\{\bar{u}_\alpha, \bar{w}\}$ on C_2.

4 Two-Dimensional Equations

The first variation of the functional (6) is

$$\delta\Phi = \iint_A \int_{-h}^{h} \left\{ -(\sigma_{\alpha\beta,\beta} + \sigma_{\alpha,3} + q_\alpha)\delta u_\alpha - (\sigma_{\alpha,\alpha} + \sigma_{,3} + q)\delta w + \left[\frac{1}{2}(u_{\alpha,\beta} + u_{\beta,\alpha}) - \frac{\partial B}{\partial \sigma_{\alpha\beta}}\right] \delta\sigma_{\alpha\beta} + \left[u_{\alpha,3} + w_{,\alpha} - \frac{\partial B}{\partial \sigma_\alpha}\right]\delta\sigma_\alpha + \left[w_{,3} - \frac{\partial B}{\partial \sigma}\right]\delta\sigma \right\} dz dA + \int_{C_1} \int_{-h}^{h} \{(\sigma_{\alpha\beta}n_\beta - \bar{t}_\alpha)\delta u_\alpha + (\sigma_\alpha n_\alpha - \bar{t})\delta w\}\, dz ds - \int_{C_2} \int_{-h}^{h} \{(u_\alpha - \bar{u}_\alpha)\delta\sigma_{\alpha\beta} + (w - \bar{w})\delta\sigma_\beta\}\, n_\beta\, dz ds \tag{11}$$

Due to the constraints on the stress components σ_α and σ the corresponding variations contain the factor $(1 - \zeta^2)$. This feature is not present in the Galerkin method recently used by Mengi [14] to obtain equations for vibrating plates. It turns out to be convenient also to use the alternative expansion to define the variations of the displacements, but in this case also the surface terms contribute.

The variations $\delta u_\alpha{}^+$, δw^+, $\delta u_\alpha{}^-$, *and* δw^- give rise to four equilibrium equations

Downloaded 01 May 2010 to 171.66.16.249. Redistribution subject to ASME license or copyright; see http://www.asme.org/terms/Terms_Use.cfm

$$h(\sigma_{\alpha\beta,\beta}{}^0 + q_\alpha{}^0) + \sigma_\alpha{}^- = 0 \tag{12}$$

$$h(\sigma_{\alpha,\alpha}{}^0 + q^0) + \sigma^- = 0 \tag{13}$$

$$\frac{h}{3}(\sigma_{\alpha\beta,\beta}{}^1 + q_\alpha{}^1) - \sigma_\alpha{}^0 + \sigma_\alpha{}^+ = 0 \tag{14}$$

$$\frac{h}{3}(\sigma_{\alpha,\alpha}{}^1 + q^1) - \sigma^0 + \sigma^+ = 0 \tag{15}$$

The equations (12)–(14) are easily recognized as the statically determinate equations of equilibrium of in-plane force, transverse force, and moment, respectively.

The equilibrium equations corresponding to $\delta\tilde{u}_\alpha{}^k$ are

$$\sum_{j=0}^{\infty}\int_{-1}^{1}\left[(\sigma_{\alpha\beta,\beta}{}^j + q_\alpha{}^j)P_j(\zeta) + \sigma_\alpha{}^j\frac{j+1}{2h}P_{j-1}{}^{(1,1)}(\zeta)\right] \times P_k{}^{(1,1)}(\zeta)(1-\zeta^2)d\zeta = 0, \quad k = 0, 1, \ldots \tag{16}$$

where the relation, [13],

$$\frac{d}{d\zeta}P_j(\zeta) = \frac{j+1}{2}P_{j-1}{}^{(1,1)}(\zeta), \quad j = 0, 1, \ldots \tag{17}$$

has been used. The last term is integrated by use of the orthogonality relation for the Jacobi polynomials $P_j{}^{(1,1)}(\zeta)$, [13], while the first is integrated by use of the formula

$$\int_{-1}^{1}P_j(\zeta)P_k{}^{(1,1)}(\zeta)(1-\zeta^2)d\zeta = \mp\frac{k+1}{k+3/2}\frac{1}{j+1/2}, \quad j = k+1\pm 1 \tag{18}$$

derived in the Appendix. The integral (18) vanishes for $j - k - 1 \neq \pm 1$. The two relations (17) and (18) are the reason behind the choice of the Jacobi polynomials $P_j{}^{(1,1)}(\zeta)$ in the alternative expansions. This choice leads to minimal coupling between the two-dimensional equations corresponding to different values of the index k. The resulting equations are conveniently written by use of a modified central difference operator $\mathcal{D}$ defined by

$$\mathcal{D}y^j = \frac{h}{2j+3}y^{j+1} - \frac{h}{2j-1}y^{j-1} \tag{19}$$

The denominator is recognized from the orthogonality relation of the Legendre polynomials $P_j(\zeta)$.

The resulting equilibrium equation corresponding to $\delta\tilde{u}_\alpha{}^k$ is

$$\sigma_\alpha{}^{k+1} = \mathcal{D}(\sigma_{\alpha\beta,\beta}{}^{k+1} + q_\alpha{}^{k+1}), \quad k = 0, 1, \ldots \tag{20}$$

and corresponding to $\delta\tilde{w}^k$

$$\sigma^{k+1} = \mathcal{D}(\sigma_{\alpha,\alpha}{}^{k+1} + q^{k+1}), \quad k = 0, 1, \ldots \tag{21}$$

In [4] Simmonds expressed σ_α and σ in terms of integrals, which in the present formulation are replaced by the difference operator $\mathcal{D}$.

The derivatives of $B(\sigma_{\alpha\beta}, \sigma_\alpha, \sigma)$ with respect to the arguments $\sigma_{\alpha\beta}$, σ_α, and σ are linear and can therefore be written as

$$\frac{\partial B}{\partial\sigma_{\alpha\beta}} = \sum_{j=0}^{\infty}\frac{\partial B^j}{\partial\sigma_{\alpha\beta}{}^j}P_j(\zeta) \tag{22}$$

where $B^j = B(\sigma_{\alpha\beta}{}^j, \sigma_\alpha{}^j, \sigma^j)$. Similar expressions apply for $\partial B/\partial\sigma_\alpha$ and $\partial B/\partial\sigma$. Orthogonality of the Legendre polynomials immediately gives the following relation corresponding to $\delta\sigma_{\alpha\beta}{}^k$.

$$\frac{1}{2}(u_{\alpha,\beta}{}^k + u_{\beta,\alpha}{}^k) = \frac{\partial B^k}{\partial\sigma_{\alpha\beta}{}^k}, \quad k = 0, 1, \ldots \tag{23}$$

The remaining equations representing Hooke's law follow by use of (17) and (18). Corresponding to $\delta\tilde{\sigma}_\alpha{}^k$

$$u_\alpha{}^{k+1} = \mathcal{D}\left(w_{,\alpha}{}^{k+1} - \frac{\partial B^{k+1}}{\partial\alpha^{k+1}}\right), \quad k = 0, 1, \ldots \tag{24}$$

and from $\delta\tilde{\sigma}^k$

$$w^{k+1} = -\mathcal{D}\frac{\partial B^{k+1}}{\partial\sigma^{k+1}}, \quad k = 0, 1, \ldots \tag{25}$$

The boundary conditions on C_1 take the simple form of coefficient matching,

$$\sigma_{\alpha\beta}{}^k n_\beta = \bar{t}_\alpha{}^k, \quad k = 0, 1, \ldots \tag{26}$$

$$\sigma_\alpha{}^k n_\alpha = \bar{t}^k, \quad k = 0, 1, \ldots \tag{27}$$

while the boundary conditions on C_2 are derived from the constrained stress variations in the form

$$u_\alpha{}^k = \bar{u}_\alpha{}^k, \quad k = 0, 1, \ldots \tag{28}$$

$$\mathcal{D}w^{k+1} = \mathcal{D}\bar{w}^{k+1}, \quad k = 0, 1, \ldots \tag{29}$$

The occurrence of the difference operator $\mathcal{D}$ in (29) turns out to be of importance for the interpretation of the transverse displacement and in identification of the effect of transverse strain.

5 Bending of Transversely Isotropic Plates

The two-dimensional equations of Section 4 cover general anisotropic materials, and approximate solutions can be obtained by suitable truncation of the expansions (7), (8), and (10). If the stress field is statically admissible, i.e., satisfies the equilibrium equations and the static boundary conditions, and the displacements satisfy the kinematic boundary conditions, an error bound in terms of strain energy can be obtained according to the hypersphere concept of Prager and Synge [5, 6]. The local contribution is simply the strain energy density associated with the terms in the brackets in the functional (11). By increasing the degree of approximation these terms are made orthogonal to an increasingly complete set of variations thus securing convergence.

In practice, however, the complications of such an approach will be severe, and the important question is more likely to be, how to obtain a good approximation within a given degree of complexity. Here this question will be limited to transversely isotropic plates, where the x_α plane is a plane of elastic symmetry. This symmetry allows separation of the bending problem from the stretching problem under the present boundary conditions. The isotropy of the x_α plane gives a central role to the Laplace operator, and enables identification of three types of solutions as discussed by Cheng [2].

The complementary energy density of a transversely isotropic material can be expressed in terms of the five elasticity parameters E, ν, G, E_3, ν_3. Hooke's law (3)–(5) then takes the form

$$\frac{1}{2}(u_{\alpha,\beta} + u_{\beta,\alpha}) = \frac{1+\nu}{E}\sigma_{\alpha\beta} - \frac{\nu}{E}\delta_{\alpha\beta}\sigma_{\gamma\gamma} - \frac{\nu_3}{E_3}\delta_{\alpha\beta}\sigma \tag{30}$$

$$u_{\alpha,3} + w_{,\alpha} = \frac{1}{G}\sigma_\alpha \tag{31}$$

$$w_{,3} = \frac{1}{G_3}\sigma - \frac{\nu_3}{E_3}\sigma_{\alpha\alpha} \tag{32}$$

E and ν identify the in-plane elastic properties, G the transverse shear stiffness, and E_3, ν_3 the effect of transverse normal stress and strain.

The corresponding two-dimensional elasticity relations follow from (23)–(25), where it is convenient to use (23) to obtain the stresses in terms of displacements.

$$\sigma_{\alpha\beta}{}^k = \frac{E}{1-\nu^2}\left[\frac{1-\nu}{2}(u_{\alpha,\beta}{}^k + u_{\beta,\alpha}{}^k) + \nu\delta_{\alpha\beta}u_{\gamma,\gamma}{}^k\right] + \frac{E}{1-\nu}\frac{\nu_3}{E_3}\delta_{\alpha\beta}\sigma^k, \quad k = 0, 1, \ldots \tag{33}$$

$$u_\alpha{}^{k+1} = \mathcal{D}\left(w_{,\alpha}{}^{k+1} - \frac{1}{G}\sigma_\alpha{}^{k+1}\right), \quad k = 0, 1, \ldots \tag{34}$$

$$w^{k+1} = -\mathcal{D}\left(\frac{1}{E_3}\sigma^{k+1} - \frac{\nu_3}{E_3}\sigma_{\gamma\gamma}{}^{k+1}\right), \quad k = 0, 1, \ldots \tag{35}$$

As a first step and in order to obtain a practically useful theory the minimal number of terms needed for a statically admissible stress field is sought. The shear stress σ_α must be quadratic in ζ in order to satisfy boundary conditions at $z = \pm h$ and still retain an independent re-

Downloaded 01 May 2010 to 171.66.16.249. Redistribution subject to ASME license or copyright; see http://www.asme.org/terms/Terms_Use.cfm

sulting transverse force. σ must satisfy boundary conditions on $z = \pm h$, but also $\sigma_{,3}$ is prescribed via the equilibrium equation (2), so σ must be cubic in ζ. The equilibrium condition (2) can be satisfied in two different ways. If σ is considered as fully prescribed *a priori*, the equation only contains one unknown, $\sigma_{\alpha,\alpha}$, and accordingly the displacement w need only one expansion coefficient, w^0. By this procedure the effect of transverse normal strain is eliminated. A superior representation of w is obtained if only the boundary values of σ are considered as constraints. It would then take three independent terms in δw to enforce pointwise satisfaction of the equilibrium equation. Thus a quadratic representation of w is adopted.

The choice of the degree of u_α is determined by the transverse shear equation (24). Because σ_α has been restricted to a quadratic representation, only the equation for ${u_\alpha}^1$ remains, and therefore the minimal representation of u_α and $\sigma_{\alpha\beta}$ is linear. The possibility of interpretation of the results in terms of a cubic representation will be discussed later.

The stress coefficients ${\sigma_{\alpha\beta}}^1$ are directly related to the moments and ${\sigma_\alpha}^0$ to the transverse shear force.

$$M_{\alpha\beta} = \int_{-h}^{h} \sigma_{\alpha\beta} z dz = \frac{2h^2}{3} {\sigma_{\alpha\beta}}^1 \tag{36}$$

$$Q_\alpha = \int_{-h}^{h} \sigma_\alpha dz = 2h {\sigma_\alpha}^0 \tag{37}$$

In this notation the equilibrium equations (13) and (14) are

$$Q_{\alpha,\alpha} + 2\sigma^- + 2hq^0 = 0 \tag{38}$$

$$M_{\alpha\beta,\beta} - Q_\alpha + 2h{\sigma_\alpha}^+ + \frac{2h^2}{3} {q_\alpha}^1 = 0 \tag{39}$$

When the discussion is restricted to bending of transversely isotropic plates, the boundary conditions on $z = \pm h$ and the remaining equilibrium (21) give

$${\sigma_\alpha}^2 = {\sigma_\alpha}^+ - \frac{1}{2h} Q_\alpha \tag{40}$$

$$\sigma^1 = \frac{6}{5}\sigma^- + \frac{h}{5}({\sigma_{\alpha,\alpha}}^+ + q^0 + q^2) \tag{41}$$

$$\sigma^3 = -\frac{1}{5}\sigma^- - \frac{h}{5}({\sigma_{\alpha,\alpha}}^+ + q^0 + q^2) \tag{42}$$

Superscripts + and − refer to the notation of (9). In the present case they refer to the value at $z = h$.

As suggested by the form of the boundary condition (29) and the elasticity relation (34) the transverse displacement will be represented in the field equations by $\mathcal{D}w^1$ and not by w^0. After having obtained a solution in terms of $\mathcal{D}w^1$ (35) is used to determine w^2 and thereby w^0. The remaining two independent functions will be chosen to be ${u_{\alpha,\alpha}}^1$ and $e_{\alpha\beta}{u_{\alpha,\beta}}^1$, where $e_{\alpha\beta}$ is the permutation symbol.

A differential equation for $e_{\alpha\beta}{u_{\alpha,\beta}}^1$ is obtained by use of (34), (20), and (14).

$$e_{\alpha\beta}{u_{\alpha,\beta}}^1 = -\frac{2}{5}\frac{h^2}{G}(e_{\alpha\beta}{\sigma_{\alpha\gamma,\gamma\beta}}^1 + e_{\alpha\beta}{q_{\alpha,\beta}}^1) + \frac{h}{G} e_{\alpha\beta}{\sigma_{\alpha,\beta}}^+ \tag{43}$$

The unknown stresses are substituted from (33).

$$\left(1 - \frac{1}{5}\frac{h^2}{G}\frac{E}{1+\nu}\partial_\gamma\partial_\gamma\right)(e_{\alpha\beta}{u_{\alpha,\beta}}^1) = \frac{2}{5}h^2 e_{\alpha\beta}{q_{\alpha,\beta}}^1 + \frac{h}{G} e_{\alpha\beta}{\sigma_{\alpha,\beta}}^+ \tag{44}$$

When the same procedure is followed using the operator ∂_α instead of $e_{\alpha\beta}\partial_\beta$ the result is

$${u_{\alpha,\alpha}}^1 - \mathcal{D}{w_{,\alpha\alpha}}^1 = -\frac{6}{5G}(\sigma^- + hq^0) - \frac{h}{5G}{\sigma_{\alpha,\alpha}}^+ \tag{45}$$

The last equation follows from elimination of ${\sigma_\alpha}^0$ between the equilibrium equations (13) and (14), followed by substitution of (33). The result,

$$\frac{h^2}{3}\left(\frac{E}{1-\nu^2}{u_{\alpha,\alpha\beta\beta}}^1 + \frac{E}{1-\nu}\frac{\nu_3}{E_3}{\sigma_{,\alpha\alpha}}^1 + {q_{\alpha,\alpha}}^1\right) = -(\sigma^- + hq^0 + h{\sigma_{\alpha,\alpha}}^+) \tag{46}$$

is expressed in terms of $\mathcal{D}w^1$ by use of (45).

$$\frac{h^2}{3}\frac{D}{1-\nu^2}(\mathcal{D}w^1)_{,\alpha\alpha\beta\beta} = -\left(1 - \frac{2h^2}{5G}\frac{E}{1-\nu^2}\partial_\beta\partial_\beta\right)(\sigma^- + hq^0) - h\left(1 - \frac{h^2}{15G}\frac{E}{1-\nu^2}\partial_\beta\partial_\beta\right){\sigma_{\alpha,\alpha}}^+ - \frac{h^2}{3}{q_{\alpha,\alpha}}^1 - \frac{h^2}{3}\frac{E}{1-\nu}\frac{\nu_3}{E_3}{\sigma_{,\alpha\alpha}}^1 \tag{47}$$

The last term σ^1 is to be substituted from (41).

In [2] Cheng identified three types of integrals to the three-dimensional equations of an isotropic elastic plate. Contributions to each of these types by the present theory can be identified from the homogeneous form of (44), (45), and (47). The so-called biharmonic solution corresponds to the following integral of the homogeneous form of (45):

$${u_\alpha}^1 = \mathcal{D}{w_\alpha}^1 + \frac{2}{5}\frac{h^2}{G}\frac{E}{1-\nu^2}\mathcal{D}{w_{,\gamma\gamma\alpha}}^1 \tag{48}$$

when $\mathcal{D}w^1$ satisfies the homogeneous biharmonic equation. If instead ${u_\alpha}^1 = \mathcal{D}{w_\alpha}^1$ is taken as the integral of (45) a solution without transverse shear resultant arises. Both of these solutions are irrotational, $e_{\alpha\beta}{u_{\alpha,\beta}}^1 = 0$. A solution to (47) of the form ${u_\alpha}^1 = e_{\alpha\beta}U_{,\beta}$ with $\mathcal{D}w^1 \equiv 0$ is of the shear type in Cheng's terminology. As also the biharmonic solution produces transverse shear resultants, it may be more appropriate to identify this type by its rotational character.

The three static boundary conditions to equations (44), (45), and (47) are specified in terms of expansion coefficients by (26) and (27) with $k = 1$ and $k = 0$, respectively. They can also be specified in terms of moments and shear forces following from (33) and (34).

$$M_{\alpha\beta} = \frac{2h^2}{3}\frac{E}{1-\nu^2}\left[\frac{1-\nu}{2}({u_{\alpha,\beta}}^1 + {u_{\beta,\alpha}}^1) + \nu\delta_{\alpha\beta}{u_{\gamma,\gamma}}^1\right] + \frac{2h^2}{3}\frac{E}{1-\nu}\frac{\nu_3}{E_3}\delta_{\alpha\beta}\left[\frac{6}{5}\sigma^- + \frac{h}{5}({\sigma_{\alpha,\alpha}}^+ + q^0 + q^2)\right] \tag{49}$$

$$Q_\alpha = \frac{5}{3}G({u_\alpha}^1 - \mathcal{D}{w_{,\alpha}}^1) + \frac{h}{3}{\sigma_\alpha}^+ \tag{50}$$

Kinematic boundary conditions are given in terms of ${u_\alpha}^1$ and $\mathcal{D}w^1$.

6 Interpretation of Stress and Displacement Fields

As indicated by the analyses of Nordgren [3, 9] and Simmonds [4] the major contribution to the hypersphere error bound arises from the discrepancy between the transverse shear predicted by displacements and stresses. The variational formulation (11) would require an additional quartic term in $\delta\sigma_\alpha$ to enforce pointwise satisfaction of the transverse shear component of Hooke's law. In general this would increase the order of the resulting differential equations and the number of boundary conditions. Alternatively, cubic terms may be included in u_α and $\sigma_{\alpha\beta}$ simply as a more detailed interpretation of the solution already provided by (44), (45), and (47). This would not allow any additional boundary conditions and would require a volume force ${q_\alpha}^3$ to satisfy the equilibrium equation (1).

The shear component of Hooke's law can be satisfied identically by introducing a term ${u_\alpha}^3$ determined by (34), $k = 2$.

$${u_\alpha}^3 = -\frac{h}{5}{w_{,\alpha}}^2 + \frac{1}{10G}Q_\alpha \tag{51}$$

For $w^2 = 0$ this corresponds to the correction introduced by Reissner in [10]. The term ${\sigma_{\alpha\beta}}^3$ follows from (33), $k = 3$.

Downloaded 01 May 2010 to 171.66.16.249. Redistribution subject to ASME license or copyright; see http://www.asme.org/terms/Terms_Use.cfm

$$\sigma_{\alpha\beta}{}^3 = \frac{1}{10}\frac{1}{G}\frac{E}{1-\nu^2}\left[\frac{1-\nu}{2}(Q_{\alpha,\beta}+Q_{\beta,\alpha})+\nu\delta_{\alpha\beta}Q_{\gamma,\gamma}\right]$$
$$-\frac{1}{5}\frac{E}{1-\nu}\frac{\nu_3}{E_3}\delta_{\alpha\beta}[\sigma^- + h(\sigma_{\gamma,\gamma}{}^+ + q^0 + q^2)]$$
$$-\frac{h}{5}\frac{E}{1-\nu^2}[(1-\nu)w_{,\alpha\beta}{}^2 + \nu\delta_{\alpha\beta}w_{,\gamma\gamma}{}^2] \quad (52)$$

Both of these relations contain w^2 determined by (35) and (33).

$$w^2 = -\frac{1}{2h}\frac{\nu_3}{E_3}M_{\gamma\gamma} + \frac{10}{105}\frac{h}{E_3}\sigma^- + \frac{4}{105}\frac{h^2}{E_3}(\sigma_{\alpha,\alpha}{}^+ + q^0 + q^2) \quad (53)$$

This formula also determines w^0 from $\mathcal{D}w^1$.

$$w^0 = -\frac{1}{h}\mathcal{D}w^1 + \frac{1}{5}w^2 \quad (54)$$

The mere length of the explicit formulas for the stress and displacement fields for general loads would defy the purpose of listing them, and the following expressions are therefore limited to the case of vanishing loads.

$$u_\alpha(x_\phi, z) = \frac{z}{h}\left[1 - \frac{h^2}{10}\frac{E}{1-\nu}\frac{\nu_3}{E_3}\left(1 - \frac{5}{3}\frac{z^2}{h^2}\right)\partial_\gamma\partial_\gamma\right]\mathcal{D}w_{,\alpha}{}^1$$
$$-\frac{3}{4G}\frac{z}{h}\left(1 - \frac{1}{3}\frac{z^2}{h^2}\right)Q_\alpha \quad (55)$$

$$w(x_\phi, z) = -\frac{1}{h}\left[1 - \frac{h^2}{10}\frac{E}{1-\nu}\frac{\nu_3}{E_3}\left(1 - 5\frac{z^2}{h^2}\right)\partial_\gamma\partial_\gamma\right]\mathcal{D}w^1 \quad (56)$$

$$\sigma_{\alpha\beta}(x_\phi, z) = \frac{E}{1-\nu^2}\frac{z}{h}[(1-\nu)\partial_\alpha\partial_\beta + \nu\delta_{\alpha\beta}\partial_\gamma\partial_\gamma]\mathcal{D}w^1$$
$$+\frac{3}{8}\frac{1}{G}\frac{E}{1+\nu}\frac{z}{h}\left(1 - \frac{1}{3}\frac{z^2}{h^2}\right)(Q_{\alpha,\beta}+Q_{\beta,\alpha})$$
$$-\frac{h^2}{10}\frac{\nu_3 E}{1-\nu^2}\frac{E}{E_3}\frac{z}{h}\left(1 - \frac{5}{3}\frac{z^2}{h^2}\right)\mathcal{D}w_{,\gamma\gamma\alpha\beta}{}^1 \quad (57)$$

$$\sigma_\alpha(x_\phi, z) = \frac{3}{4h}\left(1 - \frac{z^2}{h^2}\right)Q_\alpha \quad (58)$$

The biharmonic part of these formulas can be checked with the corresponding isotropic results of Lur'e [1] and Cheng [2], when Q_α is eliminated by use of (48). Complete correspondence is found, when $\mathcal{D}w^1$ is related to the biharmonic potential W of [1, 2] by

$$-\frac{1}{h}\mathcal{D}w^1 = W + \frac{h^2}{10}\frac{E}{1-\nu}\frac{\nu_3}{E_3}W_{,\gamma\gamma} \quad (59)$$

This does not affect the definition of the shear force of the biharmonic solution through (48).

The terms proportional to the shear force Q_α in (55)–(58) can also be compared with the first rotational solution in [2]. The length scale of the defining field equation (44) differs by the factor $\sqrt{10}/\pi = 1.0066$, and the trigonometric dependence on z/h from [2] is replaced by two term polynomial expansions. It is noted that this difference is necessary, because the terms proportional to Q_α are part of the biharmonic solution.

7 Conclusions

An infinite system of two-dimensional differential equations with appropriate boundary conditions for stresses and displacements in a homogeneous anisotropic elastic plate has been derived from a complementary energy functional. By imposing the stress boundary conditions on the faces *a priori* the variations $\delta\sigma_\alpha$ and $\delta\sigma$ are provided with the weight function $(1-\zeta^2)$. This in turn leads to a system of equations with limited coupling, expressed solely in terms of the difference operator $\mathcal{D}$, defined in (19). The derivation of this system of equations does not make use of any assumptions regarding the order of magnitude of the various terms involved.

A more detailed analysis has been carried out of a truncated system for bending of transversely isotropic plates. This system deviates from that of Reissner [10] by an alternative interpretation of the function associated with the transverse displacement and by including slightly more elaborate cubic terms in u_α and $\sigma_{\alpha\beta}$. Hereby the effect of transverse strain, which may be important in contact problems, is conserved. Furthermore full agreement with the general biharmonic solution by Lur'e [1] of the homogeneous isotropic three-dimensional equations is obtained. The present equations also incorporate the first of the rotational solutions to the three-dimensional equations found by Cheng [2]. In this case the trigonometric thickness variation is replaced by its polynomial variation. However, the bending equations allow only three boundary conditions, and therefore the good agreement with the form of general integrals only implies accuracy to the extent these boundary conditions are representative.

Acknowledgment

The author appreciates conversations with Prof. J. G. Simmonds during the course of this work.

References

1 Lur'e, A. I., *Three-Dimensional Problems of the Theory of Elasticity*, Interscience Publishers, New York, 1964.

2 Cheng, S., "Elasticity Theory of Plates and a Refined Theory," ASME JOURNAL OF APPLIED MECHANICS, Vol. 46, 1979, pp. 644–650.

3 Nordgren, R. P., "A Bound on the Error in Plate Theory," *Quarterly of Applied Mathematics*, Vol. 28, 1971, pp. 587–595.

4 Simmonds, J. G., "An Improved Estimate for the Error in the Classical Linear Theory of Plate Bending," *Quarterly of Applied Mathematics*, Vol. 29, 1971, pp. 439–447.

5 Prager, W., and Synge, J. L., "Approximations in Elasticity Based on the Concept of Function Space," *Quarterly of Applied Mathematics*, Vol. 5, 1947, pp. 241–269.

6 Synge, J. L., "The Method of the Hypercircle in Elasticity When Body Forces are Present," *Quarterly of Applied Mathematics*, Vol. 6, 1948, pp. 15–19.

7 Reissner, E., "The Effect of Transverse Shear Deformation on the Bending of Elastic Plates," ASME JOURNAL OF APPLIED MECHANICS, Vol. 12, 1945, pp. A69–A77.

8 Reissner, E., "On Bending of Elastic Plates," *Quarterly of Applied Mathematics*, Vol. 5, 1947, pp. 55–68.

9 Nordgren, R. P., "A Bound on the Error in Reissner's Theory of Plates," *Quarterly of Applied Mathematics*, Vol. 29, 1972, pp. 551–556.

10 Reissner, E., "On Transverse Bending of Plates Including the Effect of Transverse Shear Deformation," *International Journal of Solids and Structures*, Vol. 11, 1975, pp. 569–573.

11 Mindlin, R. D., "Influence of Rotatory Inertia and Shear on Flexural Motions of Isotropic, Elastic Plates," ASME JOURNAL OF APPLIED MECHANICS, Vol. 18, 1951, pp. 31–38.

12 Washizu, K., *Variational Methods in Elasticity and Plasticity*, Pergamon Press, Oxford, 1975.

13 Erdelyi, A., *Higher Transcendental Functions*, Vol. II, McGraw-Hill, New York, 1953.

14 Mengi, Y., "A New Approach for Developing Dynamic Theories for Structural Elements. Part I: Application to Thermoelastic Plates," *International Journal of Solids and Structures*, Vol. 16, 1980, pp. 1155–1168.

APPENDIX

The Jacobi polynomials can be defined by Rodrigues' formula, [13].

$$(1-\zeta^2)^n P_j{}^{(n,n)}(\zeta) = \frac{(-1)^j}{2^j j!}\left(\frac{d}{d\zeta}\right)^j(1-\zeta^2)^{j+n} \quad (60)$$

By this formula and integration by parts the following relation is obtained

$$\int_{-1}^{1} P_j(\zeta)P_k{}^{(1,1)}(\zeta)(1-\zeta^2)d\zeta$$
$$= \frac{(-1)^k}{2^{j+k}j!k!}\int_{-1}^{1}(1-\zeta^2)^j\left(\frac{d}{d\zeta}\right)^{k+j}(1-\zeta^2)^{k+1}d\zeta$$
$$= \frac{(-1)^j}{2^{j+k}j!k!}\int_{-1}^{1}(1-\zeta^2)^{k+1}\left(\frac{d}{d\zeta}\right)^{k+j}(1-\zeta^2)^j d\zeta \quad (61)$$

The boundary terms are all of the form (60) and therefore vanish due to the presence of the factor $(1-\zeta^2)$. The integrand in the second expression of (61) vanishes for $k+j > 2(k+1)$, while the integrand of the last expression vanishes for $k+j > 2j$. Due to antisymmetry the integral is zero for $j-k$ odd, leaving the only nonvanishing cases $j=k$ and $j=k+2$. The results follow simply from (61) and are given in (18).

Downloaded 01 May 2010 to 171.66.16.249. Redistribution subject to ASME license or copyright; see http://www.asme.org/terms/Terms_Use.cfm

S. K. Dhir

Numerical Structural Mech. Br. (1844), Computation, Math. & Logistics Department, David W. Taylor Naval Ship R & D Center, Bethesda, Md. 20084

Optimization in a Class of Hole Shapes in Plate Structures

An analytical/numerical procedure has been developed which yields the optimum geometry for a constrained hole shape in a large plate under prescribed boundary stresses at infinity. The optimality criterion is based on the minimization of a certain stress integral taken around the hole boundary. Muskhelishvili's method is used to first obtain the symbolic stress expressions for a given mapping function with unknown coefficients. These stress expressions are then squared and integrated around the hole boundary to obtain the stress integral. A sample problem is worked out in detail to demonstrate this procedure. The optimum shape of a square-like (double-barrel shape) hole with rounded corners was determined by restricting the mapping function to only one specific unknown coefficient. Modification of this shape by introduction of an additional term is also discussed. Numerical stress-concentration values for this case are compared with those from other sources. Most of the algebraic and numerical calculations presented in this paper were performed using MACSYMA, a symbolic manipulation package developed at M.I.T and in regular use at the David W. Taylor Naval Ship R&D Center.

Introduction

One of the most important problems in the design of plate structures is to determine and minimize the stress concentration due to the presence of holes and other discontinuities. The literature contains a great deal of information on this age-old problem; however, most of this information is concerned with direct determination of stresses for given geometry and load conditions. Some recent exceptions are the experimental results reported by Durelli and Rajaiah [1], the harmonic hole concept discussed by Bjorkman and Richards [2, 3], and the optimization approach developed by Schnack [4]. The experimental results of Durelli and Rajaiah were obtained by step-by-step machining of hole boundaries in a photoelastic model until the stress (related directly to the order of isochromatic fringe for load free boundaries) was observed to be approximately constant in both the tensile and compressive boundary regions. This technique is effective, but it does call for a series of experiments for each unique situation. The harmonic hole concept of Bjorkman and Richard conserves the first stress invariant; however, it appears to have limited application as an optimization procedure because it results in somewhat unpractical hole shapes. Schnack's procedure, an interesting finite-element approach based on the fade-away law developed by Neuber [5], is in a way the numerical equivalent of Durelli and Rajaiah's experimental method. Some other investigators [6–9] have also studied similar problems. Neuber [6] in his study has stated the requirement of a constant tangential stress along the notch boundary. This appears to be the case in the results obtained by the proposed method.

The present paper is a step toward practical design optimization, in that the technique permits the designer to have some control over the general shape of the hole. The problem can thus be formulated: Determine the geometry of a given type of hole (e.g., square-like) which, when placed in a uniformly uni- or biaxially loaded large plate, produces boundary stresses which minimize a certain stress integral. Such an optimum hole appears to lead, in most practical cases, to a more desirable overall stress field.

The approach involves first determining the symbolic boundary stress expression for a desired mapping function in a fairly general form following the well-established Muskhelishvili method. This step may require considerable algebra depending on the mapping function. In the present case most of these algebraic operations and the following steps were accomplished by MACSYMA: a symbolic manipulation package developed at M.I.T. The next step is to square this expression and integrate it around the hole so that the tensile and compressive stresses do not annihilate each other during integration. The last step is to minimize this expression with respect to the mapping function coefficients. These extreme values of coefficients contain the necessary information to define the geometry of the desired opening.

Stress Determination

Let the mapping function be represented by

Contributed by the Applied Mechanics Division for publication in the JOURNAL OF APPLIED MECHANICS.

Discussion on this paper should be addressed to the Editorial Department, ASME, United Engineering Center, 345 East 47th Street, New York, N. Y. 10017, and will be accepted until two months after final publication of the paper itself in the JOURNAL OF APPLIED MECHANICS. Manuscript received by ASME Applied Mechanics Division, July, 1980; final revision, March, 1981.

Copyright © 1981 by ASME

Downloaded 01 May 2010 to 171.66.16.249. Redistribution subject to ASME license or copyright; see http://www.asme.org/terms/Terms_Use.cfm

$$z(\zeta) = \zeta + \frac{m_1}{\zeta} + \frac{m_3}{\zeta^3} + \frac{m_5}{\zeta^5} + \frac{m_7}{\zeta^7} \tag{1}$$

a function which can map a unit circle in ζ-plane ($\zeta = e^{\alpha+i\beta}$) into a hole with at least two axes of symmetry in the z-plane ($z = x + iy$). The coefficients m_n ($n = 1, 3, 5, 7$) are assumed to be real and have the usual limitations on them which assure that $z'(\zeta) \neq 0$ for $\zeta \geq 1$ (prime indicates differentiation with respect to the argument). The stress field can be represented by

$$\sigma_\alpha + \sigma_\beta = 2\left[\frac{\phi'(\zeta)}{z'(\zeta)} + \overline{\frac{\phi'(\zeta)}{z'(\zeta)}}\right] \tag{2}$$

and

$$\sigma_\beta - \sigma_\alpha + 2\,i\,\tau_{\alpha\beta} = \frac{2\zeta^2}{\rho^2\overline{z'(\zeta)}}\left[\overline{z(\zeta)}\,\Phi'(\zeta) + \psi'(\zeta)\right] \tag{3}$$

where $\Phi(\zeta) = \phi'(\zeta)/z'(\zeta)$; σ_α, σ_β, and $\tau_{\alpha\beta}$ are the usual plane stresses; ρ is the absolute value of ζ; and bar $(-)$ over a function represents its complex conjugate. The functions $\phi(\zeta)$ and $\psi(\zeta)$ are known to have the form

$$\phi(\zeta) = S\zeta + \sum_1^\infty \frac{a_n}{\zeta^n} \tag{4}$$

$$\psi(\zeta) = D\zeta + \sum_0^\infty \frac{b_n}{\zeta^n} \tag{5}$$

where a_n and b_n are constants to be determined and

$$S = \frac{p+q}{4}$$

$$D = -\frac{p-q}{2}e^{-2i\theta} \tag{6}$$

where p and q represent the uniform stresses at infinity at an angle θ to the x and y-axes, respectively. The a_n were determined using Muskhelishvili's procedure for a load-free hole boundary and $\theta = 0$, and are given in the Appendix for completeness sake.

Optimization Procedure

Since the hole boundary ($\rho = 1$) is assumed to be load-free ($\sigma_\alpha = \tau_{\alpha\beta} = 0$), the stresses around its boundary can be described by equation (2) which requires the determination of $\phi(\zeta)$, i.e., a_n only. Now the mapping function $z(\zeta)$, given by equation (1), can be redefined in terms of Q_n, such that

$$\left.\begin{aligned} m_1 &= \sum_{i=1}^{4} Q_i \\ m_3 &= -\frac{1}{3}\sum_{i=1}^{3}\sum_{j=i+1}^{4} Q_iQ_j \\ m_5 &= \frac{1}{5}\sum_{i=1}^{2}\sum_{j=i+1}^{3}\sum_{k=j+1}^{4} Q_iQ_jQ_k \\ m_7 &= -\frac{Q_1\,Q_2\,Q_3\,Q_4}{7} \end{aligned}\right\} \tag{7}$$

These substitutions, which can be reduced to a cubic equation for determining Q_n, permit $z'(\zeta)$ to be given by

$$z'(\zeta) = \prod_{n=1}^{4}\left(1 - \frac{Q_n}{\zeta^2}\right) \tag{8}$$

Clearly, $|Q_n| < 1$, and the stresses then can be represented at the hole boundary by

$$\sigma_\beta = 4\,\mathrm{Re}\frac{S - \sum_{n=1}^{4}\frac{(2n-1)a_{2n-1}}{\sigma^{2n}}}{\prod_{n=1}^{4}\left(1 - \frac{Q_n}{\sigma^2}\right)} \tag{9}$$

which can conveniently be simplified to

$$\sigma_\beta = 4\,\mathrm{Re}\left[S + \sum_{n=1}^{4}\frac{P_n}{\sigma^2\left(1 - \frac{Q_n}{\sigma^2}\right)}\right] \tag{10}$$

where the P_n are defined as follows:

$$P_1 = -\frac{Q_1^4S - Q_1^3a_1 - 3Q_1^2a_3 - 5Q_1a_5 - 7a_7}{(Q_2 - Q_1)(Q_3 - Q_1)(Q_4 - Q_1)}$$

P_2, P_3, and P_4 can be obtained by cyclically rotating Q_n in the foregoing expression. Equation (10) reduces to

$$\sigma_\beta = 4\left[S + \sum_{n=1}^{\infty}(P_1Q_1^{n-1} + P_2Q_2^{n-1} + P_3Q_3^{n-1} + P_4Q_4^{n-1})\cos 2n\beta\right] \tag{11}$$

Although the constants P_n and Q_n can be individually complex, the expression to be summed in equation (11) will always be real for symmetrically located holes and $\theta = 0$. Parseval's theorem can now be used to show that

$$I = \frac{1}{16\pi}\int_0^{2\pi}\sigma_\beta^2 d\beta = 2S^2 + \sum_1^4\sum_1^4\frac{P_mP_n}{1 - Q_mQ_n} \tag{12}$$

where I is some form of a measure of the strain energy around the hole. It should be noted that the integration in equation (12) is performed around β and not with respect to the arc length ds which would be necessary to obtain the strain energy itself in a thin region around the hole boundary. Equation (12) can now be differentiated with respect to Q_n and equated to zero to minimize I.

This optimization procedure is thus based on minimizing the L^2-norm, a special case of the so-called L^p-norms in a continuous function space [10, 11]. The L^2-norm is also referred to as the Euclidean or the well known and most highly developed least-square norm. The other two alternatives considered were based on minimizing the L^1-norm, which is related to the absolute boundary stress values in the present problem, and the L^∞-norm (sometimes referred to as the Chebyshev norm), which is related to the minimax problem. The last two optimization approaches did not appear to be feasible for the present analytical formulation. The underlying principle, which is the same for all three approaches, depends on minimizing a general distance function involving positive quantities only. Nevertheless, it should be noted that, since the three approaches differ in the weighting of the stress distribution, they could lead to different minimum values. Whereas the L^1-norm emphasizes equally all the absolute values during the integration process, the L^2-norm emphasizes the peaks more than the other values, and the L^∞-norm very strongly emphasizes the peaks only.

The procedure followed in the present optimization approach leads within the constraints, to a relatively constant boundary stress distribution with attenuated peaks. It should be noted that this procedure simultaneously achieves a weighted minimum of the boundary strain energy which tends to approximate the harmonic field condition, a condition which guarantees absolute minimum stress concentrations around unloaded hole boundaries [2]. Thus, in the present situation, this procedure should succeed in reducing the stress concentrations around the opening. If desired, additional constraints could be introduced by using Lagrange's multipliers in order to achieve specific stress and/or displacement conditions rather than simply the overall reduction of boundary stresses. This may, however, necessitate a numerical treatment of the problem.

Whenever more than one constant, m_n or Q_n, is involved in the mapping function, the expression for I, equation (12) explicit in Q_n only, becomes so complex that its derivatives with respect to Q_n produce unwieldy expressions. For this reason, it may be desirable in such cases to simply compute the numerical values of I over a range of parameters and thus determine the minimum point.

Equations (7)–(12) have been developed for the mapping function

Downloaded 01 May 2010 to 171.66.16.249. Redistribution subject to ASME license or copyright; see http://www.asme.org/terms/Terms_Use.cfm

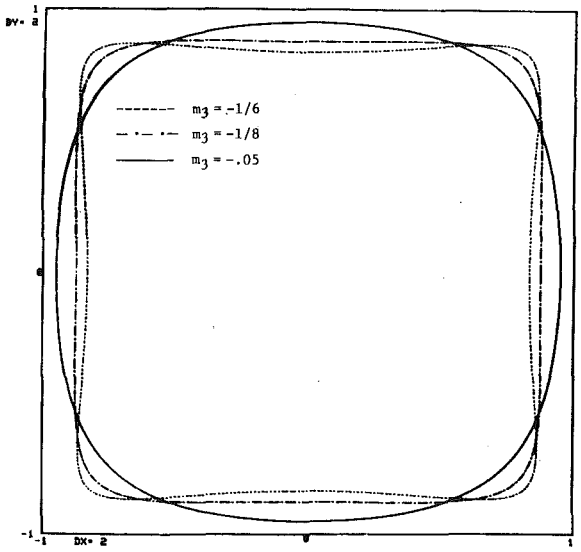


Fig. 1 Comparison of hole shapes

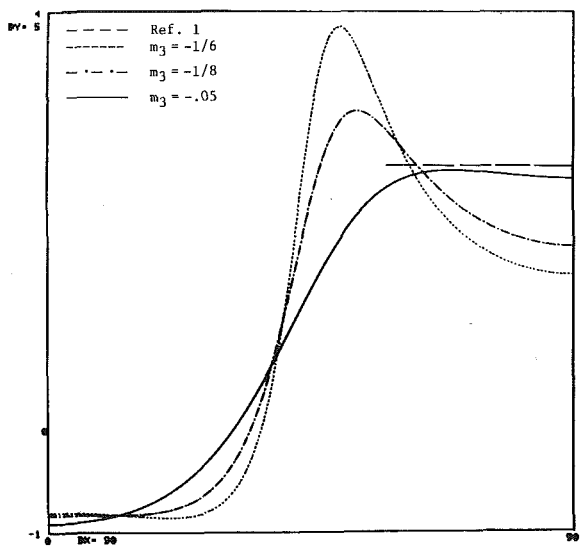


Fig. 2 Comparison of boundary stresses

given by equation (1). Therefore, these expressions should be directly reducible to accommodate other mapping functions with any of the m_n equal to zero. While this is generally true, some expressions, such as the cyclic definitions of P_n, appear to have poles in some situations. However, these are not real poles and are easily removable as the reader can verify. Special attention should be paid when programming these general expressions for a computer.

Example I

Let the mapping function be given by

$$z = \zeta + \frac{m_3}{\zeta^3}, \quad |m_3| < 1/3; \tag{13}$$

which for nonzero values of m_3 can map a unit circle into a square with rounded corners. The actual geometry of the opening (e.g., rounded corners) depends on the value of m_3. Equations (7) and (10) can be used to obtain

$$\left.\begin{aligned} Q_1 &= -Q_2 = \sqrt{3m_3} \\ Q_3 &= Q_4 = 0 \\ P_1 &= SQ_1 + \frac{3D}{2(3 - Q_1^2)} \\ P_2 &= SQ_2 + \frac{3D}{2(3 - Q_2^2)} \\ P_3 &= P_4 = 0 \end{aligned}\right\} \tag{14}$$

The expressions for Q_n and P_n given in equations (14) can be substituted in equation (11) and reduced to

$$\sigma_\beta = 4\,\frac{(1 - m_3)(1 - 9m_3^2)S + (1 - 3m_3)D\cos 2\beta}{(1 - m_3)(1 + 9m_3^2 - 6m_3\cos 4\beta)} \tag{15}$$

These values of Q_n and P_n, when substituted in equation (12), yield the integral I as

$$I = -2S^2 + \frac{4S^2}{1 - 9m_3^2} + \frac{D^2}{(1 - m_3)^2(1 - 9m_3^2)} \tag{16}$$

The first derivative of this integral with respect to m_3 yields the following condition for extremum values of I:

$$36\,S^2m_3^4 - 108\,S^2m_3^3 + 18(D^2 + 6S^2)m_3^2 - 9(D^2 + 4S^2)m_3 - D^2 = 0 \tag{17}$$

The symbolic solution of equation (17) was obtained as a function of S and D, but it is not included here because of space limitations. Four specific cases were considered:

(*i*) Isotropic loading, $p = q = 1$.
(*ii*) Uniaxial loading, $p = 1, q = 0$.
(*iii*) Biaxial loading, $p = 2, q = 1$.
(*iv*) Shear loading, $p = 1, q = -1$.

The values of m_3 which were found, using the solution of equation (17), to be within the bound of equation (13) (i.e., $|m_3| < \frac{1}{3}$ for the four cases) are, respectively:

(*i*) $m_3 = 0$.
(*ii*) $m_3 = -0.049297$ (≈ -0.05).
(*iii*) $m_3 = -0.0107713$ (≈ -0.01).
(*iv*) $m_3 = -0.0936$ (≈ -0.09).

Case (*i*). The first case is obvious, since $m_3 = 0$ represents a circular opening which is optimum in an isotropic stress field characterized by $p = q = 1$. The value of I is 0.5.

Case (*ii*). The second case ($m_3 = -0.05, p = 1, q = 0$) is worthy of comment. The value of m_3 used by Savin [12] for a square hole with rounded corners and somewhat concave sides is $-1/6$. A modified version with fairly straight sides and rounded corners can be obtained by taking $m_3 = -\frac{1}{8}$. For comparison, the values of the inegral, I, for this case were found to be 0.3627, 0.3958, and 0.4532 for $m_3 = -0.05$, $-\frac{1}{8}$, and $-\frac{1}{6}$, respectively. Fig. 1 compares the shape of this optimized hole ($m_3 = -0.05$) with the shapes of holes obtained by setting $m_3 = -\frac{1}{8}$ and $-\frac{1}{6}$. Fig. 2 compares the boundary stress distribution for these holes plotted as a function of β. The highest stress is smallest in the case of optimized shape. The boundary stresses for the optimized shape discussed by Durelli and Rajaiah [1] are also included; however, a complete distribution as a function of β could not be plotted as the relationship between β and the polar angle for this shape is not known.

Case (*iii*). The third case ($m_3 = -0.01, p = 2, q = 1$) represents only a slight perturbation on a circular hole; nevertheless, for this stress field, it is the optimum shape for a hole whose boundary is constrained by a function given by equation (13). The value of the integral for this case is 1.3723.

The calculations which have been performed for equation (13) were repeated for the elliptical shape, i.e.,

$$z = \zeta + \frac{m_1}{\zeta}; \quad |m_1| < 1 \tag{18}$$

The value of the integral in this case was found to be

Downloaded 01 May 2010 to 171.66.16.249. Redistribution subject to ASME license or copyright; see http://www.asme.org/terms/Terms_Use.cfm

$$I = 2S^2 + \frac{(2Sm_1 + D)^2}{1 - m_1^2} \tag{19}$$

which for a minimum value requires

$$m_1 = -D/2S \tag{20}$$

It is interesting to note that this value of m_1 coincides with that of Bjorkman and Richards [2] for their harmonic hole. The value of the integral in this case is simply $2S^2$, i.e., 1.125 when $p = 2$ and $q = 1$ and $m_1 = \frac{1}{3}$.

A comparison of this elliptical case with Case (*iii*) of the square-like hole (equation (13)) shows that, of all the shapes considered, the elliptical hole produces the smallest stress concentrations under a biaxial stress field. On the basis of the work of Bjorkman and Richards [2], this conclusion can be generalized to include any hole shape. However, if the hole shape is constrained to a shape given by equation (13), then Case (*iii*) represents the optimum situation. Thus, whenever m_1 is present in the mapping function, an optimization procedure (without additional constraints) as presented here leads to the trivial solution of all m_n except m_1 equal to zero, when m_1 is given by equation (20). Other nontrivial situations could be investigated by imposing additional constraints such as *a priori* assignment of numerical values to other m_n. It should be emphasized, however, that the elliptical optimum shape holds true only in the case of biaxial stress fields.

Case *iv*. The fourth case ($m_3 = -0.09$, $p = 1$, $q = -1$) represents pure shear loading, which does not permit an optimum elliptical shape. However, the present constrained optimization procedure leads m_3 to -0.09, at which point $I = 0.9077$. This optimized hole is also square-like (double barrel shape) with rounded corners. For comparison, the circular hole in this stress field will produce an $I = 1.0$. The maximum stress concentration is 3.07 at $\beta = 23.6°$ ($\beta = 0$ corresponds to one of the applied stress directions) which compares favorably with a stress concentration of 4 for a circular hole in a large plate under pure shear.

Example II

The cases discussed so far dealt with the mapping function containing only one term. Inclusion of an additional term in the mapping function leads to considerable complexity in the algebraic manipulations. The mapping function considered was

$$z = \zeta = \frac{m_3}{\zeta^3} + \frac{m_7}{\zeta^7} \tag{21}$$

In this case, the symbolic expression for I, the stress integral, and its derivatives were obtained; however, these were so unwieldy that a direct numerical approach was followed. It was found that, in the case of a uniaxial stress field ($p = 1$, $q = 0$), the minimum value of $I = 0.3623$ occurred at $m_3 = -0.05$ and $m_7 = 0.0035$. It is interesting to note that this case implies an improvement over the shape obtained by Case (*ii*) of the last example. The actual difference between the two cases is, however, very small.

Conclusions

A stress integral has been developed which can be effectively used to optimize a number of hole shapes in structures consisting of large plates. For example, it has been possible to obtain a stress-concentration factor of 2.47 for a square-like (double barrel shape) hole with rounded corners. This value is about 3 percent lower than the optimized quasi-square shape and about 5 percent lower than the double barrel shape described by Durelli and Rajaiah [1]. Both shapes occurred in uniaxially loaded plates.

In the case of pure shear loading of large plates, another square-like (double barrel shape) hole shape has been found which reduces the maximum stress concentration to 3.07 from a value of 4 for a circular hole.

References

1 Durelli, A. J., and Rajaiah, K., "Quasi-Square Hole With Optimum Shape in an Infinite Plate Subjected to In-Plane Loading," Oakland University ONR Report No. 49, Jan. 1979.

2 Bjorkman, G. S., and Richards, R., "Harmonic Holes—An Inverse Problem in Elasticity," ASME JOURNAL OF APPLIED MECHANICS, Vol. 43, 1976, pp. 414–418.

3 Bjorkman, G. S., and Richards, R., "Harmonic Holes for Nonconstant Field," ASME JOURNAL OF APPLIED MECHANICS, Vol. 46, 1979, pp. 573–576.

4 Schnack, E., "An Optimization Procedure for Stress Concentration by the Finite-Element Technique," *International Journal for Numerical Methods in Engineering*, Vol. 14, 1979, pp. 115–124.

5 Neuber, H., *Kerbspannungslehre Grundlagen für genaue Festigkeitsberechnung*, 2nd ed., Springer-Verlag, Berlin, 1958.

6 Neuber, H., "Zur Optimierung der Spannungskonzentration," *Continuum Mechanics and Related Problems of Analysis*, Moskau, Nauka, 1972, pp. 375–380.

7 Cherepanov, G. P., "Inverse Problems of the Plane Theory of Elasticity," *Journal of Applied Mathematics and Mechanics* (Translation of Soviet *J. PMM*), Vol. 38, 1974, pp. 963–979.

8 Banichuk, N. V., "On a Variational Problem With Unknown Boundaries and the Determination of Optimal Shapes of Elastic Bodies," *Journal of Applied Mathematics and Mechanics* (Translation of Soviet *J. PMM*), Vol. 39, 1975, pp. 1082–1092.

9 Wheeler, L., "On the Role of Constant-Stress Surfaces in the Problem of Minimizing Elastic Stress Concentration," *International Journal of Solids and Structures*, Vol. 12, 1976, pp. 779–789.

10 Korevaar, J., *Mathematical Methods*, Academic Press, New York, 1968.

11 Davis, P. J., *Interpolation and Approximation*, Dover Publications, New York, 1975.

12 Savin, G. N., *Concentration of Stress Around Holes*, translated by E. Gros and edited by W. Johnson, Pergamon Press, 1961.

APPENDIX

Constants for Equations (4) and (5)

$$a_7 = -m_7 S$$

$$a_5 = ((15 m_5 m_7^3 + ((-9 m_3 - 5)m_5 - 6 m_1 m_3 + 6 m_1)m_7^2 + (3 m_1 m_5^2 + (-6 m_3 + m_1^2 + 3)m_5 - 2 m_1)m_7 + 3 m_5^3 + m_1 m_5^2 + (m_3 - 1)m_5)S + 3 D m_7^2 - D m_7)/(15 m_7^3 + (9 m_3 - 5)m_7^2 + (-3 m_1 m_5 - m_1^2 - 3)m_7 - 3 m_5^2 - m_1 m_5 - m_3 + 1)$$

$$a_3 = ((15 m_3 m_7^3 + (-10 m_1 m_5 + 9 m_3^2 + 5 m_3)m_7^2 + (-10 m_5^2 - 3 m_1 m_3 m_5 + 6 m_3^2 + (m_1^2 - 3)m_3 - 2 m_1^2)m_7 - 3 m_3 m_5^2 + (m_1 m_3 - 2 m_1)m_5 + m_3^2 - m_3)S - D m_1 m_7 - D m_5)/(15 m_7^3 + (9 m_3 - 5)m_7^2 + (-3 m_1 m_5 - m_1^2 - 3)m_7 - 3 m_5^2 - m_1 m_5 - m_3 + 1)$$

$$a_1 = ((15 m_1 m_7^3 + (30 m_5 + 9 m_1 m_3 - 5 m_1)m_7^2 + ((-3 m_1^2 - 10)m_5 - 6 m_1 m_3 - m_1^3 + 3 m_1)m_7 - 3 m_1 m_5^2 + (-6 m_3 - m_1^2)m_5 - m_1 m_3 - m_1)S + 3 D m_7 - D)/(15 m_7^3 + (9 m_3 - 5)m_7^2 + (-3 m_1 m_5 - m_1^2 - 3)m_7 - 3 m_5^2 - m_1 m_5 - m_3 + 1)$$

Downloaded 01 May 2010 to 171.66.16.249. Redistribution subject to ASME license or copyright; see http://www.asme.org/terms/Terms_Use.cfm

A. Libai

Professor,
Department of Aeronautical Engineering,
Technion—Israel Institute of Technology,
Haifa 32000, Israel

On the Nonlinear Intrinsic Dynamics of Doubly Curved Shells

The field equations of motion and compatibility for the nonlinear dynamics of doubly curved shells are recast in an intrinsic form, in terms of the metric and curvature functions of their reference surfaces. For appropriate input, the motion of the shell is described without the need for an external reference coordinate system or the use of vector quantities such as position, velocity, and acceleration. The equations are shown to be readily applicable to time integration schemes. Such cases, as the (spatially) constant load problem and the inextensional dynamics problem, are also considered. The need for further work in the area is emphasized.

1 Introduction

The purpose of this study is to present an "intrinsic" formulation of the nonlinear dynamics of shells. The word intrinsic implies here, as is usual in shell theory, that the metric and curvature tensors of the shell reference surface (together with their space and time derivatives and integrals) are used directly as the field variables of the shell problem. The components of the displacement, velocity, and acceleration vectors of points on the shell reference surface are to be excluded from the field equations (although they can be calculated from the basic variables, if needed. See Appendix B.)

It should be made clear from the outset that the usefulness of the results is mainly to those shell theories which can be defined in terms of the deformation of their respective reference surfaces. Application of the results to more "refined" theories would necessitate modifications. The same is true for other intrinsic theories.

The intrinsic approaches to the statics of plates and shells has its roots in the stress-formulation of two-dimensional elasticity, where a compatibility equation can be used instead of the strain-displacement relations. Its development in shell theory has been based on the use of the Gauss and Codazzi compatibility equations instead of the strain-displacement and change of curvature-displacement relations. In common applications the number of its field equations is six: three equilibrium and three compatibility equations (see, for example, equations 3.15–3.18 of [1] or 4.14–4.17 of [2]). The use of appropriate constitutive laws can lead to equations in terms of strains and curvatures or in terms of direct forces and curvatures. The latter has been simplified by using stress and deformation functions to reduce the system in some important cases to essentially two-field equations (the $F - W$ approach to plate and shell analysis may be considered as one particularly useful example). The development of the intrinsic approach through the years since Chien's paper [3] has made it a well-established procedure for the formulation of the shell static problem, especially when nonlinear effects are to be considered. For some references, see [1–5, 15]. No attempt was made to cover the field.

The situation is less clear when nonlinear dynamic effects are to be taken into account. The vector equations of motion contain the second time derivatives of the position vector. The extrication of these terms from the equations and their replacement with appropriate time (and space) derivatives of the metric and curvature tensors of the reference surface are major tasks. In an early paper [6] (written many years ago), the author has attempted an approximate derivation which necessitated, however, the omission of some terms. The results could be used to restricted classes of problems. The introduction of a rotation vector has been helpful in the formulation of semi-intrinsic shell dynamics.

The present paper formulates the intrinsic dynamic problem for the large class of shells whose reference surfaces possess nonvanishing Gaussian curvatures. The equations are presented in several alternate forms. The preferred ones (B;C) seem to be the rate formulations which are especially useful for stepwise time integrations. An alternative formulation (A) where the compatibility equation is time-independent is also presented.

The study is divided into several parts which are presented in a logical sequence. First, a useful theorm from the geometry of surfaces and associated vector fields is presented and discussed. The kinematics of motion are then introduced in terms of the intrinsic variables. Appropriate compatibility equations as well as other interrelationships are derived. Next to follow is a short discussion of the (common) equations of motion for shells, the main purpose being to introduce the terms and transform the equations into a form which would be convenient for further use. The main section follows next with the presentation of three alternate intrinsic formulations and discussion of their equivalence to the original equations. Such topics as the response to spatially uniform loads and numerical integration procedures are also included in this section. Remarks related to pos-

Contributed by the Applied Mechanics Division and presented at the Winter Annual Meeting, Washington, D. C., November 15–20, 1981, of THE AMERICAN SOCIETY OF MECHANICAL ENGINEERS.

Discussion on this paper should be addressed to the Editorial Department, ASME, United Engineering Center, 345 East 47th Street, New York, N. Y. 10017, and will be accepted until March 1, 1982. Manuscript received by ASME Applied Mechanics Division, November, 1980. Paper No. 81-WA/APM-9.

Copyright © 1981 by ASME

Downloaded 01 May 2010 to 171.66.16.249. Redistribution subject to ASME license or copyright; see http://www.asme.org/terms/Terms_Use.cfm

sible applications are left to the conclusion section. An approach to the calculation of displacements is left to an Appendix.

All along there is no special development of constitutive laws. These are assumed to be available in a form which expresses the force and moment stress resultants in terms of the intrinsic variables and their time rates. No additional restrictions need be made.

2 Preliminary Mathematics

Let $\mathbf{R}(u^1;u^2)$ be the position vector of a surface in space, with curvi-linear coordinates $u^\alpha(\alpha = 1, 2)$. Associated with the surface are the usual geometrical quantities: Base vector-normal triad $\mathbf{R}_{,\alpha}$; $\mathbf{n}$, metric tensor $a_{\alpha\beta}$, curvature tensor $b_{\alpha\beta}$, permutation tensor $\epsilon_{\alpha\beta}$, and Gaussian curvature K. Raising and lowering of indices is performed with respect to the $a_{\alpha\beta}$, except that the "hat" notation is used to raise indices with respect to the permutation tensor, so that

$$C^{\alpha\beta} = a^{\alpha\gamma}a^{\beta\delta}C_{\lambda\delta} \quad \text{whereas} \quad \hat{C}^{\alpha\beta} = \epsilon^{\alpha\gamma}\epsilon^{\beta\delta}C_{\gamma\delta}$$

A "bar" denotes covariant differentiation with respect to surface variables and geometry, whereas a comma denotes partial differentiation with respect to the appropriate variable.

Let $\mathbf{F}(u^1;u^2)$ be a space (three-dimensional) differentiable vector field defined on $\mathbf{R}$. Then a surface tensor can be constructed from the mixed scalar products of the partial derivatives of $\mathbf{R}$ and $\mathbf{F}$ with respect to surface coordinates as follows:

$$F_{\alpha\beta} = \mathbf{R}_{,\alpha} \cdot \mathbf{F}_{,\beta}$$

This tensor will be termed the "tangential gradient tensor" of $\mathbf{F}$ on $\mathbf{R}$, since it contains the components of the $\mathbf{F}_{,\beta}$ which lie in the tangent plane only, and does not involve the normal components $\mathbf{n}\cdot\mathbf{F}_{,\beta}$. The process of obtaining the tangential gradient tensor is not reversible. In fact, whereas every (differentiable) vector field has an associated tangential gradient tensor, a given surface tensor would not have an associated vector field unless it fulfills additional requirements. The situation is covered by the retrieval theorem:

Theorem 1: A tensor $f_{\alpha\beta}$ of class C^2 defined on a surface with a nonvanishing Gaussian curvature is the tangential gradient tensor of a vector field $\mathbf{F}$ provided that it satisfies the differential equation ("integrability condition"):

$$D(f_{\alpha\beta}) = \epsilon^{\beta\gamma}\left[\left(\frac{1}{K}\hat{b}^{\alpha\delta}f_{\alpha\beta}|_\gamma\right)\Big|_\delta + b_\gamma{}^\alpha f_{\alpha\beta}\right] = 0 \tag{1}$$

Furthermore, $\mathbf{F}$ is then uniquely determined by the $f_{\alpha\beta}$ up to a constant (space) vector.

To prove the theorem, assume that $f_{\alpha\beta}$ is a tangential gradient tensor of some vector field $\mathbf{F}$. Then the partial derivatives of $\mathbf{F}$ can be expressed in the form

$$\mathbf{F}_{,\beta} = f_{\alpha\beta}\mathbf{R},^\alpha + f_\beta\mathbf{n}$$

Note that the f_β which are the components of $\mathbf{F}_{,\beta}$ in the direction normal to the surface, are as yet undetermined. The necessary and sufficient condition for the integrability of the $\mathbf{F}_{,\beta}$ is the vector equation:

$$\epsilon^{\beta\gamma}\mathbf{F}|_{\beta\gamma} = 0$$

or, in component form

$$\epsilon^{\beta\gamma}(f_{\alpha\beta}|_\gamma - b_{\alpha\gamma}f_\beta) = 0 \tag{2}$$

$$\epsilon^{\beta\gamma}(f_\beta|_\gamma + b_{\alpha\gamma}f^\alpha{}_\beta) = 0 \tag{3}$$

Equations (2) can be transformed by algebraic manipulations into

$$Kf_\beta = -b_{\alpha\beta}\hat{f}^{\alpha\gamma}|_\gamma \tag{4}$$

Provided that $K \neq 0$, f_β can now be eliminated from the equations: Substitution of (4) into (3) yields condition (1). Furthermore, substitution into the expression for $\mathbf{F}_{,\beta}$ yields

$$\mathbf{F}_{,\beta} = f_{\alpha\beta}\mathbf{R},^\alpha - \frac{1}{K}b_{\alpha\beta}\hat{f}^{\alpha\gamma}|_\gamma\mathbf{n} \tag{5}$$

The latter equations determine $\mathbf{F}$ to within a constant vector in terms of the $f_{\alpha\beta}$ (and the known surface geometry) only. This completes the proof.

For some applications it is convenient to represent $f_{\alpha\beta}$ in terms of its symmetric and antisymmetric parts. Define

$$f_{\alpha\beta} = \bar{f}_{\alpha\beta} + f\epsilon_{\alpha\beta}$$

then the integrability condition (1) reduces to

$$L(f) + D(\bar{f}_{\alpha\beta}) = 0 \tag{6}$$

where

$$L(f) = \hat{b}^{\alpha\beta}\left(\frac{1}{K}f_{,\alpha}\right)\Big|_\beta + b_\alpha{}^\alpha f \tag{7}$$

Particular cases of Theorem 1 have been implicitly used in the past for generating stress functions [7, 9] and for the study of the infinitesimal deformation of surfaces [7–9]. In the latter use, the equation $L(f) = 0$ was termed by Bianchi the "characteristic equation" of the surface [8, p. 375].

In the special case of developable surfaces ($K = 0$) the elimination process fails. Equation (4) takes the form

$$b_{\alpha\beta}\hat{f}^{\alpha\gamma}|_\gamma = 0 \tag{8}$$

Equation (8) is the integrability condition. One of equations (2) plus equation (3) may then be used in order to obtain the f_β (note that the second equation (2) cannot be used because of the vanishing of the determinant). The process involves the integration of a differential equation and the f_β are determined to within an arbitrary function only. Hence, the extension of Theorem 1 to this case would be

If $K = 0$ then an associated vector field exists, provided condition (8) is satisfied, but $\mathbf{F}$ is not uniquely determined by the $f_{\alpha\beta}$.

Developable surfaces are not considered in the rest of the paper.

3 Kinematics and Compatibility

Let $\mathbf{R}(u^1;u^2;t)$ be the time-dependent position vector of the reference surface of a shell. From here on, $\mathbf{R}$ will always be taken as a function of time, unless otherwise noted. The u^α will be taken as material coordinates on the surface. All tensorial operations refer to the current system.

Denoting by a dot partial differentiation with respect to time holding the u^α constant, then $\dot{\mathbf{R}}$ becomes the velocity vector of a material point on the surface, and $\ddot{\mathbf{R}} = \partial^2/\partial t^2\,\mathbf{R}$—is the corresponding acceleration vector. Also associated with the motion of the surface are the metric and curvature time-rates $\dot{a}_{\alpha\beta}$; $\dot{b}_{\alpha\beta}$ and higher time derivatives such as $\ddot{a}_{\alpha\beta}$, etc. The metric and curvature tensors and their various time derivatives are considered to be the intrinsic quantities, as opposed to the "extrinsic" quantities $\mathbf{R}$; $\dot{\mathbf{R}}$; $\ddot{\mathbf{R}}$.

Define the velocity tangential gradient tensor $d_{\alpha\beta}$ by

$$d_{\alpha\beta} = \mathbf{R}_{,\alpha} \cdot \dot{\mathbf{R}}_{,\beta} \tag{9}$$

The time rates of the metric and curvature tensors can be readily expressed in terms of $d_{\alpha\beta}$. In fact, results may be copied from studies on the infinitesimal deformation of surfaces. Use of (34) and (43) of [9] yields

$$\dot{a}_{\alpha\beta} = d_{\alpha\beta} + d_{\beta\alpha} \tag{10}$$

$$\dot{b}_{\alpha\beta} = -\left(\frac{1}{K}\dot{b}_{\alpha\delta}\hat{d}^{\delta\gamma}|_\gamma\right)\Big|_\beta + b_\beta{}^\gamma d_{\gamma\alpha} \tag{11}$$

The $d_{\alpha\beta}$ may be conveniently separated into its symmetric and antisymmetric parts. The symmetric part is exactly $\frac{1}{2}\dot{a}_{\alpha\beta}$. Let

$$\Omega = \tfrac{1}{2}\epsilon^{\alpha\beta}d_{\alpha\beta} \tag{12}$$

be the antisymmetric part. Then

$$d_{\alpha\beta} = \tfrac{1}{2}\dot{a}_{\alpha\beta} + \Omega\epsilon_{\alpha\beta} \tag{13}$$

so that the curvature rate tensor can be expressed in terms of $\dot{a}_{\alpha\beta}$ and Ω as follows:

Downloaded 01 May 2010 to 171.66.16.249. Redistribution subject to ASME license or copyright; see http://www.asme.org/terms/Terms_Use.cfm

$$\dot{b}_{\alpha\beta} = \epsilon_{\gamma\alpha}\left[\left(\frac{1}{K}\hat{b}^{\gamma\delta}\Omega|_{\delta}\right)\Big|_{\beta} + b_{\beta}{}^{\gamma}\Omega\right] - \frac{1}{2}\left[\left(\frac{1}{K}b_{\alpha\delta}\hat{a}^{\delta\gamma}|_{\gamma}\right)\Big|_{\beta} + b_{\beta}{}^{\gamma}\dot{a}_{\gamma\alpha}\right] \quad (14)$$

The function of Ω is seen to act as a generating function for the curvature rates (in addition to the strain rates). It is adopted as an intrinsic quantity and is termed the "curvature rate function."

The metric and curvature rates are interrelated through the requirement for the existence of a velocity vector. The relationship follows from Theorem 1 which implies that the $d_{\alpha\beta}$ determine the velocity vector up to rigid-body translation provided that the requirement

$$D(d_{\alpha\beta}) = 0 \quad (15)$$

is satisfied. Equivalently, in terms of metric and curvature rates

$$L(\Omega) + \tfrac{1}{2}D(\dot{a}_{\alpha\beta}) = 0 \quad (15a)$$

Equation (15) or (15a) is the rate-compatibility equation of the surface. Together with equations (11) or (14) for generating the curvature rates, they assure that the $\dot{a}_{\alpha\beta}$ and $\dot{b}_{\alpha\beta}$ belong to a real surface in space.

Note that it coincides with the symmetry requirement for the $\dot{b}_{\alpha\beta}$.

The acceleration tangential gradient tensor $A_{\alpha\beta}$ is defined in the same manner as the $d_{\alpha\beta}$

$$A_{\alpha\beta} = \mathbf{R}_{,\alpha}\cdot\ddot{\mathbf{R}}_{,\beta}$$

It can be tied to the time derivatives of the metric and to the curvature rate function by taking the partial derivatives of equations (9) and (10) with respect to time and combining:

$$\dot{d}_{\alpha\beta} = A_{\alpha\beta} + C_{\alpha\beta} \quad (16)$$

$$\ddot{a}_{\alpha\beta} = A_{\alpha\beta} + A_{\beta\alpha} + 2C_{\alpha\beta} \quad (17)$$

where

$$C_{\alpha\beta} = \dot{\mathbf{R}}_{,\alpha}\cdot\dot{\mathbf{R}}_{,\beta} = d^{\gamma}{}_{\alpha}d_{\gamma\beta} + \frac{1}{K^2}b_{\gamma\alpha}b_{\lambda\beta}\hat{d}^{\gamma\delta}|_{\delta}\hat{d}^{\lambda\mu}|_{\mu} \quad (18)$$

is an expression involving the $\dot{a}_{\alpha\beta}$ and Ω only, with the geometry of the surface as coefficients.

It follows from equation (17) that the terms $(\frac{1}{2}\ddot{a}_{\alpha\beta} - C_{\alpha\beta})$ represent the symmetric part of the $A_{\alpha\beta}$. The antisymmetric part is $(\psi\epsilon_{\alpha\beta})$, where ψ is given by

$$\psi = \tfrac{1}{2}\epsilon^{\alpha\beta}A_{\alpha\beta} \quad (19)$$

In order to assure the existence of an acceleration vector, Theorem 1 can be invoked, yielding a compatibility-like equation

$$L(\psi) + D(\tfrac{1}{2}\ddot{a}_{\alpha\beta} - C_{\alpha\beta}) = 0 \quad (20)$$

The compatibilities at the rate level (15a) and acceleration level (20) are not, however, independent of each other. In fact, time differentiation of equation (13) and comparison with equation (16) yields

$$(\Omega\epsilon_{\alpha\beta})^{\cdot} = \psi\epsilon_{\alpha\beta} \quad (21)$$

or

$$\psi = \frac{1}{\sqrt{a}}(\sqrt{a}\Omega)^{\cdot} \quad (21a)$$

where $a = \det(a_{\alpha\beta})$. This direct relationship between ψ and Ω connects the two compatibility equations and, in fact, makes one of them essentially superfluous if the other is used. The final expression for $A_{\alpha\beta}$ in terms of the metric and curvature function becomes

$$A_{\alpha\beta} = \tfrac{1}{2}\ddot{a}_{\alpha\beta} - C_{\alpha\beta} + (\Omega\epsilon_{\alpha\beta})^{\cdot} \quad (22)$$

4 Equations of Motion

The vector equation for the linear motion of a shell element is commonly expressed in the form

$$\mathbf{T}^{\alpha}|_{\alpha} + \mathbf{q} = \rho\ddot{\mathbf{R}} \quad (23)$$

where $\mathbf{q}$ is the load intensity vector and ρ is the mass intensity, both per unit area of $\mathbf{R}$. Here, the $\mathbf{T}^{\alpha}$ are the force resultant vectors whose components with respect to the current geometry are expressed in terms of the force ($n^{\alpha\beta}$) and moment ($m^{\alpha\beta}$) stress resultants as follows:

$$\mathbf{T}^{\alpha} = n^{\alpha\beta}\mathbf{R}_{,\beta} + m^{\beta\alpha}|_{\beta}\mathbf{n}$$

In order to make the point clearly, one of the simpler forms of the equations of motion was chosen, with the effects of rotary inertia and other fine points of integration through the thickness omitted (more elaborate theories can be incorporated, however, without special difficulties).

It follows from the definition of the acceleration tangential gradient tensor that it can be expressed in terms of the forces and loads as follows:

$$A_{\alpha\beta} = \mathbf{R}_{,\alpha}\cdot\left[\frac{1}{\rho}\left(\mathbf{T}^{\alpha}|_{\alpha} + \mathbf{q}\right)\right]_{,\beta} \quad (24)$$

Additional manipulations yield an expression for the $A_{\alpha\beta}$ in terms of the tensorial components of the forces and loads:

$$A_{\alpha\beta} = \left[\frac{1}{\rho}\left(n^{\gamma}{}_{\alpha}|_{\gamma} - b_{\alpha\lambda}m^{\gamma\lambda}|_{\gamma}\right)\right]\Big|_{\beta} - \frac{1}{\rho}b_{\alpha\beta}(n^{\gamma\lambda}b_{\gamma\lambda} + m^{\gamma\lambda}|_{\gamma\lambda}) + q_{\alpha\beta} \quad (25)$$

with the "loading tensor" $q_{\alpha\beta}$ given by

$$q_{\alpha\beta} = \mathbf{R}_{,\alpha}\cdot\left(\frac{1}{\rho}\mathbf{q}\right)_{,\beta} = \left(\frac{1}{\rho}q_{\alpha}\right)\Big|_{\beta} - \frac{1}{\rho}b_{\alpha\beta}q_{n} \quad (25a)$$

where $(q_{\alpha};q_{n})$ are the components of $\mathbf{q}$ with respect to the current geometry.

In the sequel, $A_{\alpha\beta}$ will *always* be taken as representing the right side of equations (25), that is, an explicitly given function of the moments, forces, loading tensor, mass, and current geometry.

To equation (25) is appended the equation for the behavior of ρ, which results from the requirement for the conservation of mass

$$(\rho\sqrt{a})^{\cdot} = 0 \quad \text{or} \quad \dot{\rho} = -\rho d_{\alpha}{}^{\alpha} = -\tfrac{1}{2}\rho\dot{a}_{\alpha}{}^{\alpha} = -\tfrac{1}{2}\rho a^{\alpha\beta}\dot{a}_{\alpha\beta} \quad (26)$$

To complete the listing of shell equations, constitutive laws of the form

$$n^{\alpha\beta} = n^{\alpha\beta}(a_{\gamma\delta};\, b_{\gamma\delta};\, \dot{a}\gamma\delta;\, \dot{b}_{\gamma\delta}) \quad (27)$$

$$m^{\alpha\beta} = m^{\alpha\beta}(a_{\gamma\delta};\, b_{\gamma\delta};\, \dot{a}_{\gamma\delta};\, \dot{b}_{\gamma\delta}) \quad (28)$$

are to be used. The metric and curvature enter the equations through their respective increments from a reference state $\mathbf{R}^{(0)}$ which is usually taken as a stress-free state.

The exact form of the constitutive laws is an important part of shell theory. Nevertheless, it is not a critical issue to the particular aspects of the theory which are under study in this paper. Hence, it is assumed that equations of the type (27); (28) are in existence and available. Futhermore, if the requirements of a particular integration procedure would require a different set of constitutive laws (e.g., an inverted form or a rate form), it will be assumed to be available too.

5 Formulations for Nonlinear Intrinsic Shell Dynamics

In the three formulations, equations will mainly be gathered from previous sections and then discussed. For the sake of completeness, some of the equations presented before will be repeated in this section. The equations are divided into: (a) main field equations, which are four in number and (b) auxiliary equations which are used to express some variables in terms of the others.

A listing of the auxiliary equations is as follows:

$$A_{\alpha\beta} = \left[\frac{1}{\rho}(n^{\gamma}{}_{\alpha}|_{\gamma} - b_{\alpha\delta}m^{\gamma\delta}|_{\gamma})\right]\Big|_{\beta} - \frac{1}{\rho}b_{\alpha\beta}\left(n^{\gamma\lambda}b_{\gamma\lambda} + m^{\gamma\lambda}\Big|_{\gamma\lambda}\right) + q_{\alpha\beta} \quad (25)$$

Downloaded 01 May 2010 to 171.66.16.249. Redistribution subject to ASME license or copyright; see http://www.asme.org/terms/Terms_Use.cfm

$$C_{\alpha\beta} = a_{\alpha\beta}\Omega^2 + \tfrac{1}{4}\dot{a}_\alpha{}^\gamma\dot{a}_{\gamma\beta} + \frac{1}{K^2}b_{\gamma\alpha}b_{\lambda\beta}(\epsilon^{\gamma\delta}\epsilon^{\lambda\mu}\Omega_{,\delta}\Omega_{,\mu} + \tfrac{1}{4}\hat{a}^{\gamma\delta}|_\delta\hat{a}^{\lambda\mu}|_\mu) \tag{23}$$

$$\dot{b}_{\alpha\beta} = \epsilon_{\gamma\alpha}\left[\left(\frac{1}{K}\hat{b}^{\gamma\delta}\Omega_{,\delta}\right)\Big|_\beta + b_\beta{}^\gamma\Omega\right] - \left[\left(\frac{1}{K}b_{\alpha\delta}\hat{a}^{\delta\gamma}\Big|_\gamma\right)\Big|_\beta + b_\beta{}^\gamma\dot{a}_{\gamma\alpha}\right] \tag{14}$$

$$n^{\alpha\beta} = n^{\alpha\beta}(a_{\gamma\delta};\, b_{\gamma\delta};\, \dot{a}_{\gamma\delta};\, \dot{b}_{\gamma\delta}) \tag{27}$$

$$m^{\alpha\beta} = m^{\alpha\beta}(a_{\gamma\delta};\, b_{\gamma\delta};\, \dot{a}_{\gamma\delta};\, \dot{b}_{\gamma\delta}) \tag{28}$$

$$\dot{\rho} = -\tfrac{1}{2}\rho\dot{a}_\alpha{}^\alpha \tag{26}$$

Formulation A. The field equations for this formulation are Equation of Motion:

$$\ddot{a}_{\alpha\beta} = A_{\alpha\beta} + A_{\beta\alpha} + 2C_{\alpha\beta} \tag{17}$$

Equation of Compatibility:

$$L(\Omega) + \tfrac{1}{2}D(\dot{a}_{\alpha\beta}) = 0 \tag{15a}$$

This system, together with the auxiliary system forms a complete set of shell equations.

According to Theorem 1 and the further explanation in the section on compatibility, equivalence of equation (17) to the original equations of motion is assured with the help of (15*a*), up to constant vector in space. This leaves the problem of the behavior of the shell under a constant loading vector still open.

The discussion of this point is deferred to the end of the section. The main disadvantage of "Formulation *A*" is that it is a mixed system in the sense that some of the equations are essentially rate equations, whereas the compatibility equation is not in a rate form. This makes the system more difficult to solve numerically by direct time integration methods.

Formulation B. In this formulation, the three equations of motion remain as before

$$\ddot{a}_{\alpha\beta} = A_{\alpha\beta} + A_{\beta\alpha} + 2C_{\alpha\beta} \tag{17}$$

However, the compatibility equation is replaced by the following equation: which is obtained by combining (19) and (21*a*)

$$\frac{1}{\sqrt{a}}(\sqrt{a}\Omega)^{\cdot} = \tfrac{1}{2}\epsilon^{\alpha\beta}A_{\alpha\beta} \tag{29}$$

Equations (17) and (29), together with the auxiliary system again form a complete set. However, all the equations are now either rate equations or define quantities in terms of others. This set is easier to deal with numerically, as will be seen later.

The deletion of the compatibility equation from the field equations again raises the question of the equivalence of system (17), (29) to the original equations of motion. The proof of equivalence is based on the fact that the four $A_{\alpha\beta}$ are *defined* in equation (25) in terms of the three components of the space vector $(1/\rho)(\mathbf{T}^\alpha|_\alpha + \mathbf{q})$. The elimination of the three components from the four equations (17), (29) yields precisely the compatibility condition (20). For proof, see Appendix *A*. This assures the existence of an acceleration vector and retrieves it, according to Theorem 1, up to a constant vector. The discussion on the constant (load) vector is again deferred to the end of the section.

It should be made clear at this stage that equation (29) does not introduce an additional independent time integration into the system, since the first integrals of (17), (29) are still restricted by (15*a*) for their time-independent parts. The same holds regarding the time integrals of the $\dot{a}_{\alpha\beta}$ and $\dot{b}_{\alpha\beta}$. The six integrals are still restricted by the Gauss and Codazzi equations for their time-independent parts, so that only three of the time integrations are strictly independent.

Formulation C. This formulation is theoretically similar to *B* but the separation into symmetric and antisymmetric parts is not performed. The complete set of equations is as follows:

$$\dot{d}_{\alpha\beta} = \left[\frac{1}{\rho}\left(n^\gamma{}_\alpha|_\gamma - b_{\alpha\delta}m^{\gamma\delta}|_\gamma\right)\right]\Big|_\beta - \frac{1}{\rho}b_{\alpha\beta}\left(n^{\gamma\lambda}b_{\gamma\lambda} + m^{\gamma\lambda}|_{\gamma\lambda}\right) + q_{\alpha\beta} + d^\gamma{}_\alpha d_{\gamma\beta} + \frac{1}{K^2}b_{\gamma\alpha}b_{\theta\beta}\hat{d}^{\gamma\delta}|_\delta\hat{d}^{\theta\mu}|_\mu \tag{30}$$

$$\dot{a}_{\alpha\beta} = d_{\alpha\beta} + d_{\alpha\beta} \tag{10}$$

$$\dot{b}_{\alpha\beta} = -\left(\frac{1}{K}b_{\alpha\delta}\hat{d}^{\delta\gamma}|_\gamma\right)\Big|_\beta + b_\beta{}^\gamma d_{\gamma\alpha} \tag{11}$$

$$\dot{\rho} = -\rho d_\alpha{}^\alpha \tag{26}$$

$$n^{\alpha\beta} = n^{\alpha\beta}(a_{\gamma\delta};\, b_{\alpha\delta};\, \dot{a}_{\gamma\delta};\, \dot{b}_{\gamma\delta}) \tag{27}$$

$$m^{\alpha\beta} = m^{\alpha\beta}(a_{\gamma\delta};\, b_{\gamma\delta};\, \dot{a}_{\gamma\delta};\, \dot{b}_{\gamma\delta}) \tag{28}$$

This is a more direct system of equations with a smaller number of dependent variables. Nevertheless, comparison with the previous formulation shows that the actual computational effort remains the same. Formulation *B* has the additional advantage in that the physical meaning of the variables is more clearly seen. An example at hand is the case of inextensible motion which can be easily derived from *B* (see Conclusion).

6 The Constant Load Problem

Loading vectors of the form: $(1/\rho)\mathbf{q} = \mathbf{C}(t)$ (a function of time only), drop out in the differentiations leading to the $q_{\alpha\beta}$ and therefore do not appear in the differential equations of the intrinsic system. This is coincident to the fact that the intrinsic systems are equivalent to the original equations of motion only to within a (spatially) constant acceleration vector. The question as to whether or not this constitutes a deficiency of the intrinsic systems can be clarified by a simple example:

Consider an initially stress-free shell with a free boundary (L) and uniform mass per unit area. Let the shell be subjected to a (spatially) constant loading $\mathbf{q} = \mathbf{q}(t)$. Then, from considerations of elementary mechanics, it follows that the correct solution to the shell dynamics problem is a stress-free parallel rigid body motion of the shell ($\ddot{\mathbf{R}} = (1/\rho)\mathbf{q}$; $\dot{a}_{\alpha\beta}{}^{\cdot} = \dot{b}_{\alpha\beta}{}^{\cdot} = 0$). The only obstacle to such a motion could come from the boundary (in the form of kinematical restraints or boundary forces). It is thus seen that the rigid-body response is a "natural" internal solution to the constant-load dynamic shell problem, to be corrected by boundary impositions (and/or initial stresses). It follows that a correct formulation of intrinsic shell dynamics should not include constant loads in its differential equations of motion, but rather in the boundary conditions only. This is indeed the case in the intrinsic field equations developed here. To give an example of how the loading enters the boundary conditions, consider the completely held boundary. Here, $\mathbf{R} = \mathbf{R}^{(0)}$ for all t on L, so that

$$\mathbf{T}^\alpha|_\alpha = -\mathbf{q}(t) \quad \text{on} \quad L$$

Therefore, the kinematic restraint has led to a boundary condition which involves $\mathbf{q}$ directly.

7 Numerical Integration Procedures

Formulations *B* and *C* are amenable to direct stepwise time integration procedures. The type of integration, ranging from the simplest

$$y_{i+1} = y_i + a(t_i;\, y_i)\Delta t$$

to more elaborate schemes, is immaterial here. At each step, the quantity in the equation having the highest time derivative ("left side") is stepwise integrated at all points over a mesh in the $(u^1; u^2)$-plane. The other terms ("right side") being either specified, taken from an earlier stage in the integration cycle, or taken from the previous cycle. Wherever spatial differentiation has to be performed in the right side, a central difference scheme is used. The integration cycle (using Formulation *C* as an example) is as follows:

1 Calculate $d_{\alpha\beta}$, using equation (30). Moments, forces, mass

Downloaded 01 May 2010 to 171.66.16.249. Redistribution subject to ASME license or copyright; see http://www.asme.org/terms/Terms_Use.cfm

density, loading, the $d_{\alpha\beta}$ and the geometry are taken from the results of the previous cycle. Differentiations on the right side are carried out using a central difference scheme.

2 Calculate $a_{\alpha\beta}$ using equation (10), with $d_{\alpha\beta}$ taken from the previous step.

3 Calculate $b_{\alpha\beta}$ using a symmetrized version of equation (11): $\frac{1}{2}(\dot{b}_{\alpha\beta} + \dot{b}_{\alpha\beta})$. This procedure should decrease cumulative error. The $d_{\alpha\beta}$ are from Step 1 and the other remarks of Step 1 apply too.

4 Calculate a new ρ using either (26) or, preferably, calculate it using $\rho = \rho_0\sqrt{a_0/a}$ with $(\rho_0; \sqrt{a_0})$ belonging to a known reference state and $\sqrt{a}$ calculated from Step 2.

5 Update all geometrical quantities, based on the results of Steps 2 and 3.

6 Calculate extensional and bending strain measures based on the results of this cycle and updated geometry.

7 Calculate moments and forces using constitutive laws (27), (28), and results of this cycle, including updated geometry.

8 Calculate new loading tensor $q_{\alpha\beta}$ from equation (25a), using updated geometry and known loading input at cumulative time t. Note that $q_{\alpha\beta}$ must be known at each step either as a direct input or, at most, in terms of the updated geometry. If the loads are referred to extrinsic coordinates ("dead loads" are a good example), one may still calculate the $q_{\alpha\beta}$ with the help of a continually calculated position vector (see Appendix B), but the advantages of the intrinsic approach as compared with an extrinsic formulation become questionable. Repeat.

The remarks made regarding the loading apply also to other types of input (such as boundary conditions) which have to be expressed in terms of the intrinsic variables. If the transformation to intrinsic variables is very cumbersome and involves many additional calculations, its advantages may be overwhelmed by the complications.

8 Conclusions and Further Comments

Three specific formulations have been developed for the field equations of the nonlinear intrinsic dynamics of shells, without the need to refer to an external reference frame or to vector quantities. The results are valid only to shells whose reference surfaces have nonvanishing Gaussian curvatures. The main feature of these surfaces, which makes the formulations feasible, is the capability (due to the double curvature) for an implicit definition of three-dimensional vector fields on the surfaces entirely in terms of their tangential gradients.

Although the method as such does not apply to developable surfaces, it is possible that other methods using curvature potential functions might apply there, utilizing the reversibility law for the order of covariant differentiation.

The equations are in a form which seem to be simple to time-integrate. However, at the time of writing, no solution to a specific problem has been attempted. It is important to do so since only then will it be possible to judge if the method offers practical (besides theoretical or philosophical) advantages in specific problems, over established extrinsic approaches.

The intrinsic approach offers considerable advantages in its application to inextensional shell dynamics. The differential equations for this case are arrived at by the rather simple process of the suppression of $\dot{a}_{\alpha\beta}$ and $\ddot{a}_{\alpha\beta}$ in the field equations, together with the deletion of constitutive laws (27) for the force resultants. The metric of the evolving surface (and consequently K) is that of the known reference state and the curvature tensor depends on Ω only, which becomes the sole geometrical variable of the shell problem.

Formulations A and B in their modified forms exist as before, but there is no simple stepwise time integration procedure since equation (17) is not in a rate form any more. Equation (15a) in its modified form

$$L(\Omega) = 0 \tag{15b'}$$

describes the field of possible motions of the shell in complete analogy to small displacement inextensional statics. The difference is, however, that (15b) is still nonlinear: the coefficients of the differential operator (equation 7) depend on the $b_{\alpha\beta}$ and these, in turn, depend on Ω through the modified equation (14):

$$\dot{b}_{\alpha\beta} = \epsilon_{\gamma\alpha}\left[\left(\frac{1}{K}\,\dot{b}^{\gamma\delta}\Omega_{,\delta}\right)\Big|_{\beta} + b_{\beta}{}^{\gamma}\Omega\right] \tag{14b}$$

It is apparent that the definition of a convenient integration scheme for either formulation, while taking into account appropriate contracted boundary conditions [10] and initial conditions, would be an important step in this specific theory as well as in the more general field of nonlinear inextensional analysis which does not suffer from an overabundance of solutions even in its simpler static form [13, 14].

Acknowledgment

The work was initiated while the author was a member of The Center for Advanced Studies at the University of Virginia. Its continuation and completion were supported by a grant from the Research Support Fund of the Israel Institute of Technology.

References

1 Danielson, D. A., "Simplified Intrinsic Equations for Arbitrary Elastic Shells," *International Journal of Engineering Science*, Vol. 8, 1970, pp. 251–259.

2 Koiter, W. T., and Simmonds, J. G., "Foundations of Shell Theory," Report No. 473, Laboratory of Engineering Mechanics, Delft University of Technology, 1972; also *Proceedings, 13th International Congress of Theoretical Applied Mechanics*, Moscow, 1972, Springer-Verlag, 1973, pp. 150–176.

3 Chien, W. Z., "The Intrinsic Theory of Thin Shells and Plates," *Quarterly of Applied Mathematics*, Vol. 1, No. 4; Vol. 2, Nos. 1–2, 1944.

4 Valid, P., "An Intrinsic Formulation for the Nonlinear Theory of Shells and Some Approximations," *Computers and Structures*, Vol. 10, 1979, pp. 183–194.

5 Libai, A., "The Nonlinear Membrane Shell With Application to Noncircular Cylinders," *International Journal of Solids and Structures*, Vol. 8, 1972, pp. 923–943.

6 Libai, A., "On the Nonlinear Elastokinetics of Shells ard Beams," *Journal of the Aerospace Sciences*, Vol. 29, No. 10, Oct. 1962, pp. 1190–1195, 1209.

7 Vekua, I. N., *Generalized Analytic Functions*, Pergamon Press, 1962, pp. 389–657.

8 Eisenhart, L. P., *A Treatise on the Differential Geometry of Curves and Surfaces*, Dover Publications, 1960, Chapter XI.

9 Libai, A., "Invariant Stress and Deformation Functions for Doubly Curved Shells," ASME JOURNAL OF APPLIED MECHANICS, Vol. 34, Mar. 1967, pp. 43–48.

10 Reissner, E., "Variational Methods and Boundary Conditions in Shell Theory," *Studies in Optimization*, SIAM, 1970, pp. 78–94.

11 Budiansky, B., "Notes on Nonlinear Shell Theory," ASME JOURNAL OF APPLIED MECHANICS, Vol. 35, 1968, pp. 393–401.

12 Simmonds, J. G., and Danielson, D. A., "Nonlinear Shell Theory With Finite Rotation and Stress Function Vectors," ASME JOURNAL OF APPLIED MECHANICS, Vol. 39, 1972, pp. 1085–1090.

13 Simmonds, J. G., and Libai, A., "Exact Equations for the Inextensional Deformation of Cantilevered Plates," ASME JOURNAL OF APPLIED MECHANICS, Vol. 46, 1979, pp. 631–636.

14 Hornach, R., and Rothert, H., "On the Theory of Inextensional Bending of Shell Structures," *International Journal of Solids and Structures*, Vol. 12, 1976, pp. 359–376.

15 Koiter, W. T., *The Intrinsic Equations of Shell Theory With Some Applications, Mechanics Today*, Nemat-Nasser, ed., Vol. 5, Pergamon Press, 1980, pp. 139–154.

APPENDIX *A*

Elimination and Integrability

Let the three components of a vector $\mathbf{F}$ with respect to the triad $(\mathbf{R}_{,\alpha}; \mathbf{n})$ be $(F_\alpha; F_n)$, respectively, then its tangential gradient tensor $F_{\alpha\beta}$ is related to the components by

$$F_{\alpha\beta} = F_\alpha|_\beta - b_{\alpha\beta}F_n$$

These are four equations in terms of the three components, so that an equation which interrelates the $F_{\alpha\beta}$ can be obtained by a process of elimination. Differentiate both sides and multiply by $\epsilon^{\beta\gamma}$

$$\begin{aligned}\epsilon^{\beta\gamma}F_{\alpha\beta}|_\gamma &= \epsilon^{\beta\gamma}(F_\alpha|_{\beta\gamma} - b_{\alpha\beta}|_\gamma F_n - b_{\alpha\beta}F_{n,\gamma}) \\ &= K\epsilon_{\mu\alpha}F^\mu - \epsilon^{\beta\gamma}b_{\alpha\beta}F_{n,\gamma}\end{aligned}$$

where the rule for reversing the order of covariant differentiation as

Downloaded 01 May 2010 to 171.66.16.249. Redistribution subject to ASME license or copyright; see http://www.asme.org/terms/Terms_Use.cfm

well as the Codazzi equations were used. If $K \neq 0$, the foregoing equation can be inverted to the form

$$F_{n,\mu} = b_\mu{}^\delta F_\delta - \frac{1}{K} b_{\mu\delta} \hat{F}^{\delta\gamma}|_\gamma$$

Differentiate both sides covariantly with respect to u^ν and multiply through by $\epsilon^{\mu\nu}$. Using the first equation, the result is

$$\epsilon^{\mu\nu}\left[b_\mu{}^\delta(F_{\delta\nu} + b_{\delta\nu}F_n) + \left(\frac{1}{K} b_{\mu\delta}\hat{F}^{\delta\gamma}|_\gamma\right)\right]\Bigg|_\nu$$

Noting that $\epsilon^{\mu\nu}b_\mu{}^\delta b_{\delta\nu} = 0$, this reduces to

$$\epsilon^{\mu\nu}\left[b_\mu{}^\delta F_{\delta\nu} + \left(\frac{1}{K} b_{\mu\delta}\hat{F}^{\delta\gamma}|_\gamma\right)\Bigg|_\nu\right] = 0$$

But the last equation is precisely condition (1). It follows that the elimination process is equivalent to the integrability condition (1).

APPENDIX *B*

Displacements and Displacement Gradients

Let $\mathbf{R}^{(0)}(u^1; u^2)$ be a known, time-independent reference state of the shell. This can possibly be the undeformed state, but any intermediate state in the evolution of the reference surface can be used too, as long as $K^{(0)} \neq 0$. $\mathbf{R}^{(0)}$ is used in this Appendix as the surface with respect to which all geometrical, tensorial, and differential operations are performed.

Define the displacement vector and displacement tangential gradient tensor, respectively, by

$$\mathbf{V} = \mathbf{R}(u^1; u^2; t) - \mathbf{R}^{(0)}(u^1; u^2)$$

$$V_{\alpha\beta} = \mathbf{R}_{,\alpha}{}^{(0)} \cdot \mathbf{V}_{,\beta} \tag{31}$$

It follows from Theorem 1 that $\mathbf{V}_{,\beta}$ can be represented in the form

$$\mathbf{V}_{,\beta} = V^\alpha{}_\beta \mathbf{R}_{,\alpha}{}^{(0)} - \frac{1}{K^{(0)}} b_{\alpha\beta}{}^{(0)} \hat{V}^{\alpha\gamma}\|_\gamma \mathbf{n}^{(0)} \tag{32}$$

Here, the double bar denotes covariant differentiation with respect to the reference state. Expressions for the base vectors and velocity gradients of the current state are

$$\mathbf{R}_{,\beta} = \mathbf{R}_{,\beta}{}^{(0)} + \mathbf{V}_{,\beta} = (\delta_\beta{}^\alpha + V^\alpha{}_\beta)R_{,\alpha}{}^{(0)} - \frac{1}{K^{(0)}} b_{\alpha\beta}{}^{(0)} \hat{V}^{\alpha\beta}\|_\gamma \mathbf{n}^{(0)} \tag{33}$$

$$\dot{\mathbf{R}}_{,\beta} = \dot{\mathbf{V}}_{,\beta} = \dot{V}^\alpha{}_\beta \mathbf{R}_{,\alpha}{}^{(0)} - \frac{1}{K^{(0)}} b_{\alpha\beta}{}^{(0)} \dot{\hat{V}}^{\alpha\gamma}\|_\gamma \mathbf{n}^{(0)} \tag{34}$$

The aforementioned can be used to express the $d_{\alpha\beta}$ of the main text in terms of the $V_{\alpha\beta}$ and their time derivatives:

$$d_{\alpha\beta} = \dot{V}_{\alpha\beta} + V^\lambda{}_\alpha \dot{V}_{\lambda\beta} + \frac{1}{K^{(0)_2}} b_{\lambda\alpha}{}^{(0)} b_{\epsilon\beta}{}^{(0)} \hat{V}^{\lambda\gamma}\|_\gamma \dot{\hat{V}}^{\epsilon\theta}\|_\theta \tag{35}$$

The results presented here can be used as an adjunct to the intrinsic analysis whenever the displacements are desired or the input necessitates the actual calculation of the position vector in terms of a fixed reference state. The method of calculation in a stepwise integration procedure involves repeated integration of (35) for $V_{\alpha\beta}$, with the $d_{\alpha\beta}$ taken from step (1) and the nonlinear terms taken from the previous cycle. The results are then introduced into (32) or (33), depending on the particular needs.

Another interesting use is that of formulating the shell problem entirely in terms of the $V_{\alpha\beta}$. For example, equation (33) expresses the current base vectors in terms of the $V_{\alpha\beta}$, and can serve as the basis for a formulation of nonlinear shell statics, since all the terms which enter the three equilibrium equations can be expressed in terms of $\mathbf{R}_{,\beta}$ and consequently in terms of the $V_{\alpha\beta}$. The fourth equation would be the compatibility equation

$$D^{(0)}(V_{\alpha\beta}) = 0 \tag{36}$$

The equilibrium equations are highly nonlinear, but (36) is linear, since its coefficients are those of the reference state.

The equations of nonlinear shell statics have been formulated in the past in terms of displacements [11] and rotations [12]. It is not at all clear whether the $V_{\alpha\beta}$ formulation offers any specific advantage over existing formulations. The method is introduced here in the hope that some use might be found for it in the future.

Downloaded 01 May 2010 to 171.66.16.249. Redistribution subject to ASME license or copyright; see http://www.asme.org/terms/Terms_Use.cfm

David Hui
Research Associate.
Assoc. Mem. ASME

R. C. Tennyson
Professor.

J. S Hansen
Associate Professor.

University of Toronto,
Institute for Aerospace Studies,
4925 Dufferin Street,
Downsview, Ontario, Canada M3H 5T6

Mode Interaction of Axially Stiffened Cylindrical Shells: Effects of Stringer Axial Stiffness, Torsional Rigidity, and Eccentricity

This paper deals with the effect of stringer axial stiffness, torsional rigidity, and eccentricity on the panel initial postbuckling behavior and mode interaction of axially stiffened cylindrical shells. As far as the local panel mode is concerned, the cylinder is taken to be integrally stiffened and the postbuckling redistribution of the axial load-carrying capacity between the skin and stringers is investigated. It is found that although the buckling analysis is more or less identical to previous analyses, there are significant changes in the quartic term of the potential energy of the local mode and hence, the imperfection-sensitivity of the structure is altered. These changes are due to the interaction between the stringers and the skin in the postbuckling analysis. In addition, to assess the effect of a nonlinear prebuckling state resulting from the presence of local imperfections, Koiter's theory of amplitude modulation of the local mode is applied to an example problem of interest.

Introduction

It has been theoretically observed that the interaction between simultaneous buckling modes may result in highly imperfection-sensitive structures with the conclusion that coincident buckling between competing modes may not yield an optimal design. Of particular interest here are investigations of the imperfection-sensitivity of periodically stiffened structures such as stringer or ring-reinforced cylindrical shells or stringer-reinforced flat plates. The reason for this interest is that local buckling of the panel between stringers and overall buckling of the structure may occur more or less concurrently.

Using the general theory of elastic stability first introduced by Koiter [1-3], several authors have studied a variety of mode interaction problems and imperfection-sensitivity of optimal structural designs [4–14]. Of these, one of the most commonly investigated structural optimization problems of significant practical interest is that of an integrally stringer reinforced cylindrical shell subjected to axial compression. For this problem, the imperfection-sensitivity of overall buckling has been examined [15, 16] using a smeared-out analysis which is valid when the number of circumferential half waves involves at least two or more stringers. This last assumption can be verified *a posteriori* and it is generally accepted that many practical structures satisfy this requirement. However, in the local panel analysis, the structure must be treated as integrally stiffened; thus necessitating assumptions concerning the behavior of the stringers. For example, in Koiter's study [17] of the local buckling and postbuckling behavior of stiffened panels, it was assumed that the stringers cannot bend out-of-plane and the tangential bending stiffness of the stringer was neglected. In addition, the applied load was considered to act only on the skin and not on the stringers and thus slippage between stringer and skin in the axial direction was permitted, although, as it turns out, this assumption is quite reasonable when analyzing the local sheet mode alone. Later, Stephens [18] incorporated the possibility that the stringers provide rotational constraint of the skin about the line of attachment.

In the present work, Stephens' model has been modified such that stringers and skin are now subjected to the same applied stress and postbuckling redistribution of the axial load due to the interaction between skin and stringers is taken into account in the local panel mode analysis. This modification is essential in the analysis of the interaction between overall and local buckling because the axial constraint between stiffeners and sheet has a significant stabilizing effect on the local sheet mode in the post-buckling range. The results of Koiter's analysis in [14] and the curves associated with Koiter's and Stephens boundary conditions will be shown (Fig. 3) to yield unduly conservative buckling loads.

As far as the overall mode post-buckling analysis is concerned, it is identical to that presented in [15] and requires no modification. The final portion of the analysis studies the two-mode interaction problem

Contributed by the Applied Mechanics Division for presentation at the Winter Annual Meeting, Washington, D. C., November 15–20, 1981, of THE AMERICAN SOCIETY OF MECHANICAL ENGINEERS.

Discussion on this paper should be addressed to the Editorial Department, ASME, United Engineering Center, 345 East 47th Street, New York, N. Y. 10017, and will be accepted until March 1, 1982. Manuscript received by ASME Applied Mechanics Division, June, 1980; final revision, March, 1981. Paper No. 81-WA/APM-28.

Copyright © 1981 by ASME

Downloaded 01 May 2010 to 171.66.16.249. Redistribution subject to ASME license or copyright; see http://www.asme.org/terms/Terms_Use.cfm

using the quartic terms found in the foregoing local and overall mode analyses in conjunction with Koiter's theory of amplitude modulation of the local model [14]. Unlike Koiter's general theory [1], the theory of local amplitude modulation is valid for larger values of the imperfection amplitude. It should be noted that local distortion of the stringer cross section has been ignored in the analysis.

Potential Energy of the Cylindrical Panel

Consider an axially stiffened circular cylindrical shell subjected to combined axial compressive and lateral pressure loads. The prebuckling state for the local mode is assumed to be linear so that the cylindrical panel is in a state of uniform compression prior to buckling. The potential energy of the skin based on the Donnell assumptions and the nonlinear strain-displacement relations can be written as [1]:

$$PE = (Et^3)\,(P_2{}^0[u] + P_2{}'[u] + P_3{}^0[u] + P_4{}^0[u] + \ldots) \quad (1a)$$

where

$$P_2{}^0[u] = \left(\frac{1}{2(1-\nu^2)q_0{}^2}\right) \times \int_0^{\pi\theta}\int_0^{q_0L/R} \{u_{,x}{}^2 + (v_{,y}+w)^2 + 2\nu(u_{,x})\,(v_{,y}+w) + \tfrac{1}{2}(1-\nu)\,(u_{,y}+v_{,x})^2 + (c^2/3)\,[w_{,xx}{}^2 + w_{,yy}{}^2 + 2\nu\, w_{,xx}w_{,yy} + 2(1-\nu)w_{,xy}{}^2]\}dx\,dy$$

$$P_2{}'[u] = \left(\frac{1}{2(1-\nu^2)}\right)\int_0^{\pi\theta}\int_0^{q_0L/R} \{(c_1+\nu c_2)\,(w_{,x}{}^2) + (c_2+\nu c_1)\,(w_{,y}{}^2)\}dx\,dy$$

$$P_3{}^0[u] = \frac{c}{(1-\nu^2)\,(q_0)^2}\int_0^{\pi\theta}\int_0^{q_0L/R} \{(w_{,x}{}^2)\,[u_{,x}+\nu(v_{,y}+w)] + (w_{,y}{}^2)\,[\nu u_{,x}+(v_{,y}+w)] + (1-\nu)\,(w_{,x}w_{,y})\,(u_{,y}+v_{,x})\}dx\,dy \quad (1b)$$

$$P_4{}^0[u] = \frac{3}{2(q_0)^2}\int_0^{\pi\theta}\int_0^{q_0L/R} (w_{,x}{}^2 + w_{,y}{}^2)^2\,dx\,dy \quad (1b)\ (Cont.)$$

In the foregoing, c_1 and c_2 are found to be [22],

$$c_1 = [-t/(Rc)]\,[\sigma(1+\alpha_s) + p\nu]/(1+E_n\alpha_s)$$

$$c_2 = [t/(Rc)]\,[\sigma\,\nu\,(1+\alpha_s) + (p)\,(1+E_n\alpha_s\,(1-\nu^2))]/(1+E_n\alpha_s) \quad (2a)$$

and in the important special case of zero lateral pressure and equal Young's moduli,

$$c_1 + \nu c_2 = [t/(Rc)]\,(-\sigma)\,(1-\nu^2) \quad \text{and} \quad c_2 + \nu c_1 = 0 \quad (2b)$$

Furthermore, σ is the axial load (positive for compression) and p is the lateral pressure (positive for internal pressure). Note that unlike the conventional Koiter notation, the applied load is incorporated into the $P_2{}'[u]$ expression. Moreover, integration is only carried out over half of the cylindrical panel between adjacent stringers, where $y = 0$ corresponds to the stringer edge. In addition to the aforementioned, the stringer contribution to the total potential energy must also be included. Thus the potential energy of any one stringer on passing from the prebuckling state to a neighboring state can also be arranged in the form of equation (1) where

$$P_2{}^0[u] = [1/(2q_0)]\int_0^{q_0L/R} \{(E_n\alpha_s d_s/R)\,[u_{,x} - 2c(e_s/t)w_{,xx}]^2 + \beta_s(d_s/R)\,(w_{,xx})^2 + (\gamma/q_0)\,(w_{,xy})^2\}dx$$

$$P_2{}'[u] = (1/q_0)E_n\alpha_s(d_s/R)\,(c_1R/t) \times \int_0^{q_0L/R} \{cw_{,x}{}^2 + 2c^2(e_s/t)^2\,(t/R)\,(w_{,xy})^2\}dx$$

$$P_3{}^0[u] = (1/q_0)E_n\alpha_s(d_s/R)\int_0^{q_0L/R} \{[u_{,x} - 2c(e_s/t)w_{,xx}]. [c(w_{,x})^2 + 2c^2(e_s/t)^2(t/R)\,(w_{,xy})^2]\}dx \quad (3)$$

Nomenclature

Dimensional Quantities

A_s = cross-sectional area of a stringer
e_s = stringer eccentricity
$d_s = (2\pi R)/M_s$; stringer spacing
$D = Et^3/(4c^2)$
E, E_s = Young's modulus of the skin and stringer, respectively
F = Airy stress function
G, G_s = shear modulus of the skin and stringer, respectively
I_s, I_t = out-of-plane and tangential moment of inertia of a stringer
J_s = torsional constant of a stringer
L = length of the shell
M_x, M_y, M_{xy} = bending stress resultants
N_x, N_y, N_{xy} = skin stress resultants
$\bar{p}$ = applied lateral pressure, positive for internal pressure
$Q_s = 2\,e_s - t$; height of the stringer defined only for rectangular stringer
R = radius of the shell
t = skin thickness
t_t = tangential thickness of the stringer, defined only for rectangular stringer
U, V = axial and circumferential in-plane displacements, respectively
W = out-of-plane displacement
X, Y = axial and circumferential coordinates, respectively
$\bar{\sigma}$ = applied axial stress

Nondimensional Quantities

a, b = related to the cubic and quartic terms of the potential energy of a single mode system
b_1, b_2 = quartic term of the overall mode and the local panel mode
$e = \sqrt{3(1-\nu^2)}$
$\bar{e}$ = related to the eigenvector of the overall mode
$E_n = E_s/E$
$f = 2cF/(Et^3)$
$h(x, y)$ = amplitude of the local mode which is a slowly varying function of the coordinates
m, n = number of axial half waves and number of circumferential full waves, respectively
M_s = total number of equally spaced stringers
$p = \bar{p}R^2c/(Et^2)$, applied lateral pressure (positive for internal pressure)
$q_0 = \sqrt{(2cR/t)}$
$r = \sigma_c{}^{(1)}/\sigma_c{}^{(2)}$, ratio of the overall to the local buckling load
S_x, S_y = as defined in text
$u, v = (q_0/t)(U, V)$
$w = W/t$
$x, y = (q_0/R)(X, Y)$
$z = [\lambda/(2\theta)]^2$
$Z = [L^2/(Rt)]\sqrt{(1-\nu^2)}$, Batdorf parameter
$\alpha_s = A_s/(d_st)$, area ratio
β_0 = angle in radians between adjacent stringers
$\beta_s = (E_sI_s)/(Dd_s)$, out-of-plane bending stiffness ratio
$\beta_t = E_sI_t/(Dd_s)$, tangential bending stiffness ratio
$\gamma_s = (q_0G_sJ_s)/(DR)$, torsional rigidity ratio
δ/t = amplitude of the local panel mode over the skin thickness
$\bar{\delta}$ = amplitude of local imperfection
$\theta = q_0/M_s$, flatness parameter
λ = ratio of the wavelength of the local mode in the circumferential direction to that in the axial direction
λ^* = as defined in the text
ν = Poisson's ratio
ξ_1 = amplitude of the overall mode with respect to the skin thickness
$\sigma = \bar{\sigma}(Rc/Et)$, nondimensional axial stress relative to the lighter weight unstiffened cylindrical shell
τ = torsional factor which varies from 0.14 for square-shaped stringer to 0.333 for thin-walled rectangular stringer

Note: A comma preceding subscripts indicates differentiation with respect to the variables shown.

Downloaded 01 May 2010 to 171.66.16.249. Redistribution subject to ASME license or copyright; see http://www.asme.org/terms/Terms_Use.cfm

$$P_4^0[u] = [1/(2q_0)]E_n\alpha_s(d_s/R)\int_0^{q_0L/R}\{c^2(w_{,x})^4 + [2c^2(e_s/t)^2(t/R)]^2(w_{,xy})^4 + 4c^2(e_s/t)^2(t/R)c(w_{,x})^2(w_{,xy})^2\}dx \quad (3)$$

(*Cont.*)

It should be noted that not all the aforementioned stringer energy contribution is considered by both Koiter and Stephens and it will be shown that, in general, it is highly significant in the computation of the quartic term of the potential energy of the local mode.

Consistent with Koiter's general theory of elastic stability, the total displacements can be expressed as the sum of the prebuckling deformation, the buckling mode, and the second-order field in the following form:

$$\{u_t, v_t, w_t\} = \{u_p, 0, w_p\} + (\delta/t)\{u_c, v_c, w_c\} + (\delta/t)^2\{u_2, v_2, w_2\} \quad (4)$$

where δ/t is the amplitude of the buckling mode normalized with respect to the skin thickness. In the postbuckling regime, it was shown [1, 2] that the equilibrium states are specified by

$$\left(1 - \frac{\sigma}{\sigma_c}\right)(\delta/t) + a(\delta/t)^2 + b(\delta/t)^3 = (\sigma/\sigma_c)(\bar{\delta}/t) \quad (5)$$

where the a and b coefficients are related to the cubic and quartic terms of the potential energy, respectively, $\bar{\delta}$ is the amplitude of the local imperfection which is taken to be of the same form as the buckling mode. In this expression, the cubic term a of the local mode vanishes, provided that the number of axial half waves is even, the number of stringers is even or the shell is infinitely long. Since local buckling of a stiffened shell of sufficiently high Z (>200) generally results in many local buckles, and due to symmetry considerations, the cubic term is assumed to be negligible. Thus a negative value of b indicates that the structure is imperfection-sensitive while a positive value indicates a lack of imperfection-sensitivity. In order to compute the b coefficient, it is necessary to determine the second-order field in addition to the buckling mode. Furthermore, the second-order field (u_2, v_2, and w_2) is obtained by imposing the appropriate orthogonal conditions and by minimizing the quadratic and cubic terms of the potential energy. That is, the minimization

$$\delta P_2^{\lambda}[u_2] + \delta P_3^0[u_c] = 0$$

yields the following three-differential equations [1, 19],

$$u_{2,xx} + \tfrac{1}{2}(1-\nu)u_{2,yy} + \tfrac{1}{2}(1+\nu)v_{2,xy} + \nu w_{2,x} = -c\{2w_{c,x}w_{c,xx} + (1+\nu)w_{c,xy}w_{c,y} + (1-\nu)w_{c,x}w_{c,yy}\}$$

$$\tfrac{1}{2}(1+\nu)u_{2,xy} + v_{2,yy} + \tfrac{1}{2}(1-\nu)v_{2,xx} + w_{2,y} = -c\{2w_{c,y}w_{c,yy} + (1+\nu)w_{c,x}w_{c,xy} + (1-\nu)w_{c,xx}w_{c,y}\}$$

$$(u_{2,x})\left(\frac{\nu}{1-\nu^2}\right) + (v_{2,y})\left(\frac{1}{1-\nu^2}\right) + \nabla^4 w_2 + 2S\,w_{2,xx} - 2p\,w_{2,yy} + (w_2)\left(\frac{1}{1-\nu^2}\right) = 2c\left\{f_{c,yy}w_{c,xx} + f_{c,xx}w_{c,yy} + (-2)f_{c,xy}w_{c,xy} - \left(\frac{\nu w_{c,x}^2 + w_{c,y}^2}{2(1-\nu^2)}\right)\right\} \quad (6)$$

where S is defined to be

$$S = (\sigma)\left[(1+\alpha_s)/(1+E_n\alpha_s)\right] - (p\nu)\left[(E_n\alpha_s)/(1+E_n\alpha_s)\right] \quad (7)$$

and it should be noted that $S = \sigma$ in the important special case ($p = 0, E_n = 1, \alpha_s \neq 0$) or in the case $\alpha_s = 0$. Furthermore, the Airy stress function f_c is related to u_c, v_c, and w_c by

$$(1-\nu^2)(f_{c,xx}) = \nu u_{c,x} + (v_{c,y} + w_c)$$

$$(1-\nu^2)(f_{c,yy}) = u_{c,x} + \nu(v_{c,y} + w_c)$$

$$-2(1+\nu)(f_{c,xy}) = u_{c,y} + v_{c,x} \quad (8)$$

In addition to the continuity requirements of the displacements at the stringer edge, i.e., $u^+ = u^-$, $v^+ = v^-$, $w^+ = w^-$, and $w^+_{,y} = w^-_{,y}$, the four jump conditions at the stringer edge (presented in dimensional form for clarity purposes) are given by

$$U = 0 \quad \text{or} \quad N^+_{xy} - N^-_{xy} + (E_sA_s)(\epsilon^+_x - e_s W^+_{,XX} + \tfrac{1}{2}e_s{}^2 W^+_{,XY}{}^2)_{,X} = 0$$

$$V = 0 \quad \text{or} \quad N^+_y - N^-_y - E_sI_t V^+_{,XXXX} = 0$$

$$W = 0 \quad \text{or} \quad (-D)(W^+_{,YYY} - W^-_{,YYY}) + e_sN^+_{s,XX} - E_sI_sW^+_{,XXXX} + N^+_s W^+_{,XX} = 0$$

$$W_{,Y} = 0 \quad \text{or} \quad D(W^+_{,YY} - W^-_{,YY}) + G_sJ_sW^+_{,XXY} + e_s{}^2 N^+_s W^+_{,XXY} + e_s{}^2 N^+_{s,X} W^+_{,XY} = 0 \quad (9a)$$

where subscripts "+" and "−" denote the positive and negative sides of a stringer as measured in the circumferential direction. Moreover, N_s is the axial force applied at the centroid of the stringer and it is given by

$$N_s = (E_sA_s)(\epsilon_x - e_sW_{,XX} + \tfrac{1}{2}e_s{}^2W_{,XY}{}^2) \quad (9b)$$

The desired jump conditions for the buckling state and for the second-order field computations are obtained by substituting $u_t = u_p + (\delta/t)u_c(x, y) + (\delta/t)^2 u_2(x, y)$ into the foregoing conditions and collecting terms involving (δ/t) and $(\delta/t)^2$, respectively. They will be presented subsequently.

Classical Local Buckling Load

As the applied load is increased from zero, the classical buckling load is defined to be the smallest eigenvalue which causes the quadratic terms of the potential energy to vanish. Due to symmetry considerations, the local buckling mode $u_c(x, y)$, $v_c(x, y)$, $w_c(x, y)$ must be composed of either even or odd functions with respect to the stringer edge. It is found in the example problem that the smallest eigenvalue corresponds to the condition that $u_c(x, y)$ and $w_c(x, y)$ are odd functions while $v_c(x, y)$ is an even function with respect to the stringer edge. This implies that $u_c(x, y = 0) = w_c(x, y = 0) = 0$ and thus the corresponding jump conditions can be neglected. If the shell is assured to be sufficiently long such that there are many local waves in the axial direction, then the buckling mode is expressible in the form

$$u_c(x, y) = u_c(y)\cos[\lambda x/(2\theta)]$$

$$v_c(x, y) = v_c(y)\sin[\lambda x/(2\theta)]$$

$$w_c(x, y) = w_c(y)\sin[\lambda x/(2\theta)] \quad (10)$$

The boundary conditions at the stringer edge are

$$u_c(y = 0) = 0$$

$$w_c(y = 0) = 0$$

$$v_c(y = 0)_{,y} - \pi(1-\nu^2)(\beta_t)(\theta/q_0^2)(\lambda/2\theta)^4 v_c(y = 0) = 0$$

$$[\lambda^2/(8\theta^3)](\gamma_s)w_c(y = 0)_{,y} - w_c(y = 0)_{,yy} = 0 \quad (11)$$

where β_t is the nondimensional stringer tangential bending stiffness ratio and γ_s is related to the torsional rigidity of the stringer. Since the tangential bending energy of the stringer is usually small compared with the out-of-plane bending energy and the purpose of the present paper is to study the effect of stringer eccentricity and cross-sectional area on the imperfection-sensitivity of the cylindrical panel, the quantity β_t is set to zero for comparison purposes with Stephens' paper [18]. Making such a simplification, the present eigenvalue problem is identical to that examined by Stephens. In the computation of the buckling load, the mixed formulation is used instead of the UVW formulation due to its simplicity.

The ordinary differential equations are

$$w_c(y)_{,yyyy} - 2(z+p)w_c(y)_{,yy} + (z^2 - 2zS)w_c(y) - zf_c(y) = 0$$

$$f_c(y)_{,yyyy} - 2zf_c(y)_{,yy} + z^2f_c(y) + zw_c(y) = 0 \quad (12)$$

Downloaded 01 May 2010 to 171.66.16.249. Redistribution subject to ASME license or copyright; see http://www.asme.org/terms/Terms_Use.cfm

where $z = [\lambda/(2\theta)]^2$ and S is defined in equation (7). The four boundary conditions at the stringer edge are

$$w_c(y = 0) = 0, \quad (z/2)\gamma_s w_c(y = 0)_{,y} - w_c(y = 0)_{,yy} = 0,$$

and

$$f_c(y = 0) = 0, \quad f_c(y = 0)_{,yy} = 0 \tag{13}$$

while the boundary conditions at the midpanel are

$$w_c(y = \pi\theta)_{,y} = 0, \quad w_c(y = \pi\theta)_{,yyy} = 0,$$

and

$$f_c(y = \pi\theta)_{,y} = 0, \quad f_c(y = \pi\theta)_{,yyy} = 0 \tag{14}$$

The foregoing ordinary differential equations with boundary conditions can be solved using a central finite-difference scheme in conjunction with the computation of the determinants as was done by Stephens and others using a modification of Potter's method [21]. However, since only the smallest eigenvalue is of interest, it is felt that the previous method can be replaced in the following way by a more efficient technique. First, the resulting system of linear finite-difference equations were rearranged into the standard form $Ax = \sigma Bx$ where A and B are both banded matrices and B is singular (the matrix B should not be confused with the interaction parameter B employed in [14]). The shifted inverse power method was then used to compute the eigenvector and eigenvalue, details of which can be found in [22, 23]. This obviates the need to compute determinants and drastically reduces the computation time. Second, a more efficient linear equation solver [20] was used instead of Potter's method. The classical buckling load was found by computing the smallest eigenvalue for all possible wavelengths λ (usually the optimum λ ranges between one and two). It was observed that the quartic term measured by the b coefficient, was considerably more sensitive to the wavelength parameter than was the buckling load. Consequently, 61 finite-difference grid points were employed instead of the 30 stations used by Stephens [18]. Nevertheless, the convergence is so rapid that it usually requires very few iterations.

Second-Order Fields of the Local Mode

Upon substituting $w_c(x, y), f_c(x, y)$ into equation (6), the solutions for u_2, v_2, and w_2 can be expressed in the form

$$u_2(x, y) = (x)(u_0) + u_\beta(y) \sin(\lambda x/\theta),$$
$$v_2(x, y) = v_\alpha(y) + v_\beta(y) \cos(\lambda x/\theta)$$
$$w_2(x, y) = w_0 + w_\alpha(y) + w_\beta(y) \cos(\lambda x/\theta) \tag{15}$$

Consequently, the partial differential equations can be decoupled into two sets of ordinary differential equations in terms of $v_\alpha(y)$, $w_\alpha(y)$ and $u_\beta(y)$, $v_\beta(y)$, $w_\beta(y)$, respectively. For brevity, they are called the alpha and beta problems. The differential equations for the alpha problem are then given by

$$v_\alpha(y)_{,yy} + w_\alpha(y)_{,y} = (-c)[w_c(y)_{,y} w_c(y)_{,yy} + \nu z w_c(y) w_c(y)_{,y}]$$

and

$$w_\alpha(y)_{,yyyy} - 2p\, w_\alpha(y)_{,yy} + \left(\frac{1}{1-\nu^2}\right)[w(y)] + \left(\frac{1}{1-\nu^2}\right)[v_\alpha(y)]$$
$$= c[-z w_c(y) f_c(y)_{,yy} - z w_c(y)_{,yy} f_c(y) - 2z w_c(y)_{,y} f_c(y)_{,y}]$$
$$- \left(\frac{c}{2(1-\nu^2)}\right)[\nu z w_c(y)^2 + w_c(y)_{,y}{}^2] - \left(\frac{1}{1-\nu^2}\right)(\nu u_0 + w_0) \tag{16}$$

From symmetry considerations, $v_2(x, y = 0) = 0$ and $w_2(x, y = 0)_{,y} = 0$ and hence the corresponding jump conditions can be neglected. Thus, for the alpha problem, the jump condition with respect to w_2 implies that $w_\alpha(y = 0)_{,yyy} = 0$. The boundary conditions at the midpanel due to symmetry are: $v_\alpha(y = \pi\theta) = 0$, $w_\alpha(y = \pi\theta)_{,y} = 0$, $w_\alpha(y = \pi\theta)_{,yyy} = 0$. In a similar manner, the ordinary differential equations for the beta problem are

$$[-(\lambda/\theta)^2 u_\beta(y) + \tfrac{1}{2}(1-\nu) u_\beta(y)_{,yy}] - \tfrac{1}{2}(1+\nu)(\lambda/\theta) v_\beta(y)_{,y}$$
$$- \nu(\lambda/\theta) w_\beta(y) = \left(\frac{c}{2}\right)\left(\frac{\lambda}{2\theta}\right)\{(2z)[w_c(y)]^2 - (1+\nu)[w_c(y)_{,y}]^2$$
$$- (1-\nu) w_c(y) w_c(y)_{,yy}\}$$

$$\tfrac{1}{2}(1+\nu)\left(\frac{\lambda}{\theta}\right) u_\beta(y)_{,y} + [v_\beta(y)_{,yy}$$
$$- \tfrac{1}{2}(1-\nu)(\lambda/\theta)^2 v_\beta(y)] + w_\beta(y)_{,y} = (-c)[-w_c(y)_{,y} w_c(y)_{,yy}$$
$$+ (z) w_c(y) w_c(y)_{,y}]$$

$$\left[\left(\frac{\nu}{1-\nu^2}\right)(\lambda/\theta) u_\beta(y)\right] + \left(\frac{1}{1-\nu^2}\right)[v_\beta(y)_{,y}]$$
$$+ \left\{w_\beta(y)_{,yyyy} + [-2(\lambda/\theta)^2 - 2p][w_\beta(y)_{,yy}] + \left[(\lambda/\theta)^4 - (2S)(\lambda/\theta)^2 + \left(\frac{1}{1-\nu^2}\right)\right] w_\beta(y)\right\} = (c)\,[z w_c(y) f_c(y)_{,yy} + z w_c(y)_{,yy} f_c(y)$$
$$-2 z w_c(y)_{,y} f_c(y)_{,y}] + [c/(2(1-\nu^2))]\,[-\nu z w_c(y)^2 + w_c(y)_{,y}{}^2] \tag{17}$$

Again, using symmetry at the stringer edge, $v_\beta(y = 0) = 0$ and $w_\beta(y = 0)_{,y} = 0$ and the corresponding jump conditions with respect to v_2 and $w_{2,y}$ may be neglected. The jump conditions with respect to u_2 and w_2 are

$$u_\beta(y = 0)_{,y} - \{[(E_n\alpha_s)(2\pi\theta)(1+\nu)(\lambda/\theta)^2]$$
$$\times [u_\beta(y = 0) + (2c)(e_s/t)(\lambda/\theta) w_\beta(y = 0)$$
$$+ (c^2/4)(t/R)(e_s/t)^2 (\lambda/\theta) w_c(y = 0)_{,y}{}^2]\} = 0 \tag{18}$$

$$w_\beta(y = 0)_{,yyy} + [c/(1+\nu)](e_s/t)(\lambda/\theta) u_\beta(y = 0)_{,y}$$
$$+ [\beta_s \pi\, \theta(\lambda/\theta)^4 + (E_n\alpha_s)(c)(c_1)(2\pi R/t)$$
$$\times \theta(\lambda/\theta)^2]\, w_\beta(y = 0) = 0 \tag{19}$$

Again, from symmetry conditions, the four boundary conditions at the midpanel are $u_\beta(y = 0)_{,y} = 0$, $v_\beta(y = 0) = 0$, $w_\beta(y = 0)_{,y} = 0$ and $w_\beta(y = 0)_{,yyy} = 0$. The uncoupled alpha and beta problems are then solved using a central finite-difference scheme.

Note that values for the constants u_0 and w_0 [equation (15)] cannot be obtained from the jump conditions but are obtained by minimizing

$$(P_2[u_2] + P_{21}[u_c, u_2])_{\text{skin}} + (P_2[u_2] + P_{21}[u_c, u_2])_{\text{stringer}} \tag{20}$$

with respect to u_0 and w_0. After some algebra, they are found as [22],

$$u_0 = (R_1 - R_2)/[(1-\nu^2)(1 + E_n\alpha_s)]$$
$$w_0 = \{[1 + (1-\nu^2)(E_n\alpha_s)](R_2) - \nu R_1\}/[(1-\nu^2)(1 + E_n\alpha_s)] \tag{21a}$$

where R_1 and R_2 are defined by

$$R_1 = (-c/2)\,[z H_1 + \nu H_2] - [(1-\nu^2)(E_n\alpha_s)]$$
$$\times [(c^2)(e_s/t)^2 (t/R)(z) w_c(y = 0)_{,y}{}^2]$$
$$R_2 = (-c/2)\,[z\nu H_1 + H_2]$$
$$H_1 = [1/(\pi\theta)] \int_0^{\pi\theta} \{w_c(y)^2\} dy,$$
$$H_2 = [1/(\pi\theta)] \int_0^{\pi\theta} \{w_c(y)_{,y}{}^2\} dy \tag{21b}$$

In the special case of zero torsional rigidity, one obtains,

$$H_1 = 1/2, \quad H_2 = 1/(8\theta^2), \quad w_c(y = 0)_{,y} = 1/(2\theta), z = [\lambda/(2\theta)]^2 \tag{21c}$$

so that

Downloaded 01 May 2010 to 171.66.16.249. Redistribution subject to ASME license or copyright; see http://www.asme.org/terms/Terms_Use.cfm

$$u_0 = [1/(1 + E_n\alpha_s)]\,[-c/(16\,\theta^2)][1 + (E_n\alpha_s)(e_s/t)^2(t/R)(c/\theta^2)]$$

$$w_0 = [1/(1 + E_n\alpha_s)][-c/(16\theta^2)]\{1 + (E_n\alpha_s) - (c/\theta^2)(e_s/t)^2(t/R)]\} \tag{22}$$

It can be seen that the constants u_0 and w_0 converge to Koiter's result [17] for no applied pressure, $\lambda = 1$, $e_s/t = 0$, and $\alpha_s = 0$.

Initial Postbuckling Behavior

The potential energy expression of a single mode symmetric system, evaluated at the classical buckling load is (note that the geometric initial imperfection is taken to be of the same shape as the buckling mode)

$$P.E./(Et^3) = (A_4)(\delta/t)^4 + (\sigma - \sigma_c)(d)(\delta/t)^2 + (2d\sigma)(\delta/t)(\bar{\delta}/t) \tag{23a}$$

where $(\bar{\delta}/t)$ is the amplitude of the imperfection. Moreover, in the present stringer reinforced cylindrical panel problem, A_4 and d are computed from

$$A_4 = (P_4{}^0[u_c] - (P_2{}^0[u_2] + P_2{}'[u_2]))_{\text{skin}} + (P_4{}^0[u_c] - (P_2{}^0[u_2] + P_2{}'[u_2]))_{\text{stringer}}$$

$$d = \left(\frac{\partial}{\partial\sigma} P_2{}'[u_c]\right)_{\text{skin}} + \left(\frac{\partial}{\partial\sigma} P_2{}'[u_c]\right)_{\text{stringer}} \tag{23b}$$

Thus the equilibrium equation can be written as,

$$b(\delta/t)^3 + [1 - (\sigma/\sigma_c)](\delta/t) = (\sigma/\sigma_c)(\bar{\delta}/t) \tag{24a}$$

where the b coefficient of the present local problem is

$$b = (4A_4)/[(-2d)(\sigma_c)] \tag{24b}$$

The structure is imperfection-sensitive if the b coefficient is negative. Since the buckling mode u_c and the second-order field u_2 are now known quantities, it is straightforward to compute the individual terms of the b coefficient. The quartic term of the potential energy for the skin (from stringer edge to the midpanel) is

$$\{P_4{}^0[u_c] - (P_2{}^0[u_2] + P_2{}'[u_2])\}_{\text{skin}} = Q_1 - (Q_2 + Q_3 + Q_4) \tag{25a}$$

where

$$Q_1 = P_4{}^0[u_c]_{\text{skin}} = [1/(1 - \nu^2)](c/4)(t/R)[q_0L/(8R)] \times \int_0^{\pi\theta} \{[(3\lambda^4)/(16\theta^4)]w_c(y)^4 + 3w_c(y)_{,y}{}^4 + [\lambda^2/(2\theta^2)][w_c(y)^2 w_c(y)_{,y}{}^2]\}dy$$

$$Q_2 = \left(\frac{1}{2(1-\nu^2)}\frac{L}{q_0R}\right)\int_0^{\pi\theta} \{[w_\alpha(y) + v_\alpha(y)_{,y}]^2 + [w_\alpha(y) + v_\alpha(y)_{,y}](2w_0 + 2\nu u_0) + (c^2/3)[w_\alpha(y)_{,yy}{}^2] + q_0{}^2(c_2 + \nu c_1)[w_\alpha(y)_{,y}{}^2]\}\,dy$$

$$Q_3 = \left(\frac{1}{4(1-\nu^2)q_0{}^2}\right)\left(\frac{q_0L}{R}\right)\int_0^{\pi\theta} \{(\lambda/\theta)^2[u_\beta(y)]^2 + [w_\beta(y) + v_\beta(y)_{,y}]^2 + 2\nu(\lambda/\theta)u_\beta(y)[w_\beta(y) + v_\beta(y)_{,y}] + \tfrac{1}{2}(1-\nu)[u_\beta(y)_{,y} - (\lambda/\theta)v_\beta(y)]^2 + (c^2/3)[(\lambda/\theta)^4 w_\beta(y)^2 + w_\beta(y)_{,yy}{}^2 - 2\nu(\lambda/\theta)^2 w_\beta(y)w_\beta(y)_{,yy} + 2(1-\nu)(\lambda/\theta)^2[w_\beta(y)_{,y}{}^2] + q_0{}^2[(c_1 + \nu c_2)(\lambda/\theta)^2 w_\beta(y)^2 + (c_2 + \nu c_1)[w_\beta(y)_{,y}{}^2]]\}\,dy$$

$$Q_4 = \left[\frac{1}{4(1-\nu^2)}\frac{\beta_0 L}{R}\right](u_0{}^2 + w_0{}^2 + 2\nu u_0 w_0) \tag{25b}$$

In addition, the stringer contribution to the quartic term is (upon dividing the result by two since only half a cylindrical panel between adjacent stringers has been considered)

$$\{P_4{}^0[u_0] - (P_2{}^0[u_2] + P_2{}'[u_2])\}_{\text{stringer}} = S_1 - S_2$$

where

$$S_1 = P_4{}^0[u_c]_{\text{stringer}} = \tfrac{1}{4}E_n\alpha_s(d_s/R)(L/R) \times [3/(32\theta^4)]c^4(e_s/t)^4(t/R)^2\lambda^4[w_c(y=0)_{,y}]^4$$

$$S_2 = P_2{}^0[u_2]_{\text{stringer}} = \tfrac{1}{4}E_n\alpha_s(d_s/R)(L/R) \times [u_0{}^2 + \tfrac{1}{2}(\lambda/\theta)^2 u_\beta(y=0)^2] \tag{26}$$

Also for the skin,

$$P_2{}'[u_c]_{\text{skin}} = (\sigma_c)\left[(-1/16)(q_0L/R) \times (t/Rc)(\lambda/\theta)^2 \int_0^{\pi\theta} w_c(y)^2\,dy\right] \tag{27a}$$

and for the stringer (again, upon dividing by two),

$$P_2{}'[u_c]_{\text{stringer}} = (\sigma_c)\,[(-t/Rc)E_n\alpha_s(e_s/t)^2c^2(d_s/R)z \times [w_c(y=0)_{,y}]^2 \cdot \tfrac{1}{2} \cdot (L/R)] \tag{27b}$$

Mode Interaction by Amplitude Modulation of the Local Mode

In order to investigate imperfection-sensitivity due to local and overall mode interactions, Koiter's theory of amplitude modulation of the local mode [14] was used to compute the two-mode potential energy expression. This necessitates incorporating the appropriate terms to account for axial stiffness, torsional rigidity, and eccentricity of the stringers. For brevity, only the final form of the potential energy expression is given (for details, refer to [22]),

$$\frac{P.E.}{(Et)(2\pi RL)} = [1 - (\lambda^*/r)](a_1)^2 + (1 - \lambda^*)\iint h(x,y)^2\,ds + (C_1/2)(a_1)^4 + (b_2/2)\iint h(x,y)^4\,dS + (2B)(a_1)\iint\{(\sqrt{2})\,[\sin(m\pi X/L)\sin(nY/R)]h(x,y)^2\}\,dS - (2)\,(\lambda^*/r)(\bar{a}_1a_1) - (2\lambda^*)\iint \bar{h}(x,y)\,h(x,y)\}\,dS \tag{28}$$

where $dS = (dX\,dY)/(2\pi RL)$, $h(x,y)$ is the modulated amplitude of the local mode normalized with respect to the skin thickness, barred quantities refer to imperfections, b_2 is the b coefficient of the local mode. The overall mode [15] and the modulated local mode are

$$\{W_c{}^{(1)}, F_c{}^{(1)}\} = \xi_1\{t, Et^3\bar{e}\}\sin(m\pi X/L)\sin(nY/R) \tag{29a}$$

$$W_c{}^{(2)} = (t)\,h(x,y)\,[\sin(\lambda\pi X/d_s)\,w_c(y)] \tag{29b}$$

Furthermore, $a_1, \bar{a}_1, B, C_1, \lambda^*$, and r are defined to be

$$a_1 = (\xi_1)\sqrt{(Z_1/Z_2)},\quad \bar{a}_1 = (\bar{\xi}_1)\sqrt{(Z_1/Z_2)}$$

$$B = Z_3/[(2)\,(\sqrt{Z_1Z_2})],\quad C_1 = (Z_2/Z_1)(b_1)$$

$$\lambda^* = \sigma/\sigma_c{}^{(2)},\quad r = \sigma_c{}^{(1)}/\sigma_c{}^{(2)},\quad \sigma/\sigma_c{}^{(1)} = \lambda^*/r \tag{30}$$

where $\sigma_c{}^{(1)}$ and $\sigma_c{}^{(2)}$ are the overall and local buckling loads, respectively, b_1 is the b coefficient of the overall mode. In the foregoing expressions, Z_1, Z_2, and Z_3 are defined as

$$Z_1 = [\sigma_c{}^{(1)}/(8c)][(1 + \alpha_s)(m\pi)^2(t/R)^3\,(R/L)^2]$$

$$Z_2 = \sigma_c{}^{(2)}\,[H_1/(16c)](t/R)^3(\lambda M_s)^2$$

$$Z_3 = [1/(4\sqrt{2})]\,(t/R)^2(M_s)^2[(S_x\lambda^2)(H_1/4) + S_y\theta^2H_2] \tag{31}$$

where H_1 and H_2 are defined in equations (21b) and (21c) and S_x, S_y are (using classical simple support conditions at $X = 0, L$),

$$S_x = [-A_{xx}(m\pi)^2(t/L)^2 - A_{xy}n^2(t/R)^2](\bar{e}) + [-(\bar{B}_{xx})(m\pi)^2(t/L)^2 - \bar{B}_{xy}n^2(t/R)^2]$$

$$S_y = [-A_{yy}n^2(t/R)^2 - A_{yx}(m\pi)^2(t/L)^2](\bar{e}) + [(-\bar{B}_{yy})n^2(t/R)^2 - \bar{B}_{yx}(m\pi)^2(t/L)^2] \tag{32}$$

and $A_{xx}, A_{xy}, A_{yx}, A_{yy}, \bar{B}_{xx}, \bar{B}_{xy}, \bar{B}_{yx}$, and $\bar{B}_{yy}$ can be obtained from Hutchinson and Amazigo's paper [15].

Finally, in the presence of only a local imperfection, the bifurcation load (due to the influence of the local imperfection triggering bifur-

Downloaded 01 May 2010 to 171.66.16.249. Redistribution subject to ASME license or copyright; see http://www.asme.org/terms/Terms_Use.cfm

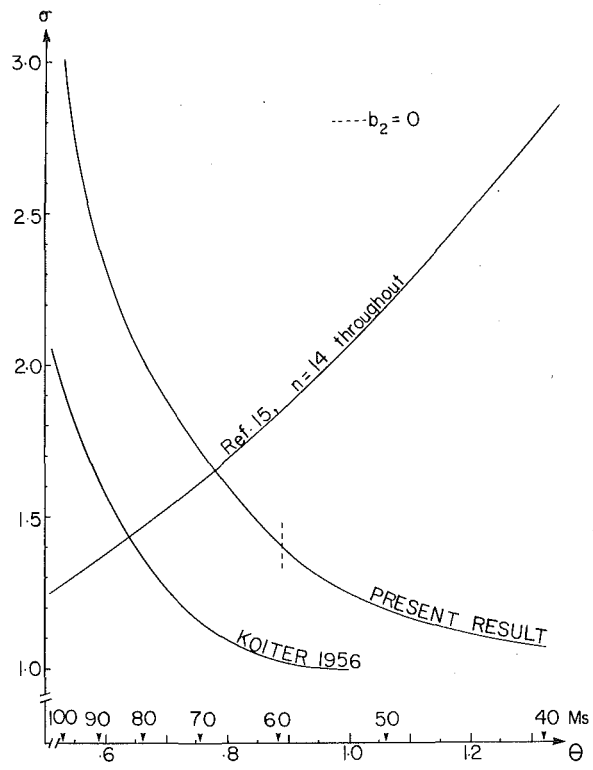


Fig. 1 Classical buckling load versus flatness parameter

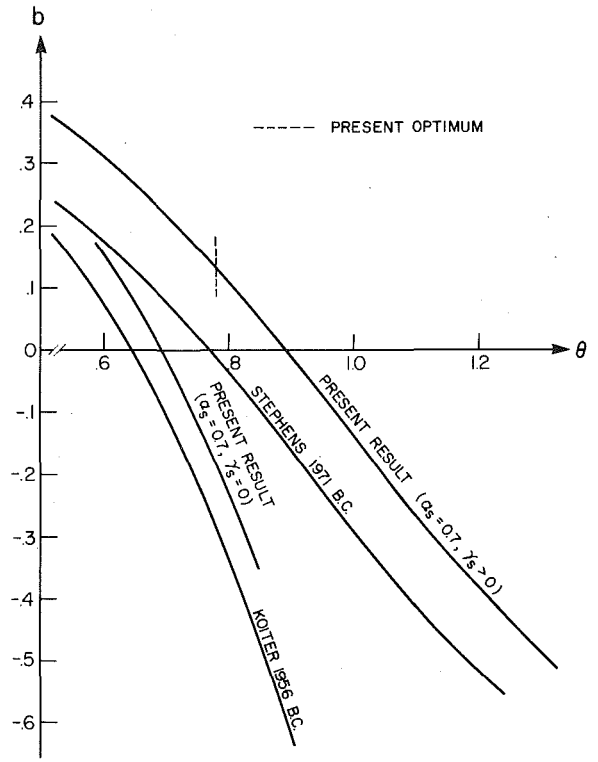


Fig. 2 *b* coefficient of the local mode versus flatness parameter

cation into the overall mode) of the imperfect system $\lambda_c{}^*$ is related to the amplitude of the local imperfection h_0 by [22]

$$(1-\lambda_c{}^*)\left(\frac{2B^2-2b_2(1-\lambda_c{}^*/r)}{2B^2-3b_2(1-\lambda_c{}^*/r)}\right)\left(\frac{(1-\lambda_c{}^*)(1-\lambda_c{}^*/r)}{2B^2-3b_2\,(1-\lambda_c{}^*/r)}\right)^{1/2} = (\lambda_c{}^*)\,(\pm h_0) \quad (33)$$

In the event that the b coefficient of the local panel mode turns out to be positive, the previous relation yields a lower bound given by [14]

$$L.B. = (r)\{1-[(2B^2)/(3b_2)]\} \quad (34)$$

Example Problem

To illustrate the effects of stringer eccentricity, axial stiffness, and torsional rigidity on buckling, imperfection-sensitivity, and mode interaction, example problems have been chosen from the relevant published literature [6, 9, 14, 24, 25] details of which can be found in [22]. However, for brevity, only one example will be presented here based on the following shell parameters taken from Byskov and Hutchinson [6]. The fixed parameters are

$$\alpha_s = 0.7, \quad Z = 810.848, \quad R/t = 850, \quad \nu = 0.3, \quad q_0 = 52.998$$
$$R/L = 1.0, \quad E_n = 1.0, \quad t_t/t = 4.09, \quad \beta_t = 10.6558. \quad (35)$$

Note that since the stringers are constrained to be of rectangular shape and α_s, t_t/t are held constant, then changing the number of stringers requires changes in the stringer height Q_s as well as

$$\theta = q_0/M_s, \quad Q_s/t = [\alpha_s/(t_t/t)]\,(2\pi/M_s)(R/t), \quad e_s/t = (1/2)\,[1+(Q_s/t)]$$
$$\beta_s = (E_n\alpha_s)\,(c^2/3)\,(Q_s/t), \quad d_s/t = (t_t/t)\,(Q_s/t)\,(1/\alpha_s) \quad (36)$$

The torsional rigidity ratio can be obtained from

$$\gamma_s = [(12\pi E_n\theta)(\tau)\ \text{minimum}\ (\beta_s, \beta_t)/(1+\nu)] - (E_n\alpha_s)(e_s/t)^2(8\pi c_1)(c^2\theta) \quad (37)$$

where τ is the torsional constant which ranges from 0.14 for square shape stringers to 0.333 for thin-walled stringers. The second term in equation (37) refers to the axial shortening of the stringer due to twisting and is usually quite small compared with the first term.

Using these values, the classical buckling load normalized with respect to the lighter weight unstiffened cylindrical shell classical buckling load is plotted against the flatness parameter θ and number of stringers M_s in Fig. 1. It should also be pointed out that this analysis differs from that of Stephens since the permissible wave number λ is treated as discrete and axial shortening of the stringers due to twisting is included. However, buckling loads close to Stephens' result were obtained, thus substantiating that significant increases in local panel buckling loads arise primarily from the inclusion of stringer torsional rigidity. Based on the smeared-out overall buckling analysis of [15] (classical simple support, $X = 0, L$), it can be seen in Fig. 1 that the simultaneous occurrence of local and overall buckling occurs at $\theta = 0.78$ ($M_s = 68$) with $\sigma = 1.66$ instead of $\theta = 0.64$ ($M_s = 83$) with $\sigma = 1.43$ found in [6, 24].

When the variation in the local b coefficient with θ (Fig. 2) is considered, the effect of stringer eccentricity and axial stiffness shows essentially a constant shift from Stephens' result [18]. This is due to the fact that the area ratio α_s is kept constant and that the percentage transfer of the axial stress from the skin to the stringer is a function of α_s. By examining the change in the axial strain via the constant u_0 in equation (15), an approximate formula for the aforementioned percentage transfer of the axial stress is [22],

$$\text{percent transfer} = [\alpha_s/(1+\alpha_s)]\ (100\ \text{percent}) \quad (38)$$

Moreover, the transition between stable and unstable postbuckling behavior is indicated by the sign change in the b coefficient which occurs at $\theta = 0.89$ (with $M_s = 60$) rather than at $\theta = 0.775$ (with $M_s = 68$) which is predicted by Stephens [18]. From Fig. 1, it may be seen that coincident buckling occurs at $\theta = 0.78$ which corresponds to $b = 0.137$. Thus the local mode alone is postbuckling stable. It is important to distinguish the b coefficients discussed in [17, 18] (which refer to the quartic term of the skin only) and the b coefficient of the present analysis (which refers to the quartic term of the entire skin and stringer combination). For example, in Fig. 2 this difference can be

Downloaded 01 May 2010 to 171.66.16.249. Redistribution subject to ASME license or copyright; see http://www.asme.org/terms/Terms_Use.cfm

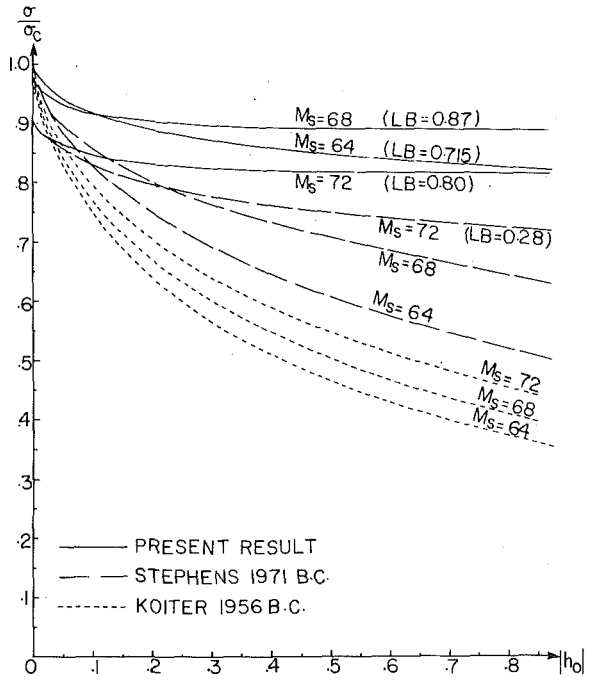


Fig. 3 Bifurcation load normalized with respect to $\sigma_c^{(2)}$ versus local imperfection amplitude normalized with respect to the skin thickness

seen by first comparing the present results for $\alpha_s = 0.7$, $\gamma_s = 0$, with those of Koiter [17]. The shift in curves is due to the inclusion of the axial stiffness parameter α_s (and stringers) in calculating the postbuckling redistribution of the compressive load. As predicted by Koiter, the difference is rather small. However, when the torsional stiffness is also considered ($\gamma_s > 0$), it is evident that very large changes in the b coefficient occur.

At this point, it is of particular interest to study the effect of a nonlinear prebuckling state (due to the presence of a local imperfection alone) on the previous local and overall mode interaction problem. The four parameters required to specify the two-mode potential energy expression are: the transformed b coefficient of the overall mode C_1, the b coefficient of the local mode b_2, the interaction cubic term B, and the ratio of the overall to the local buckling load r. Based on the computation of these parameters for the three designs being considered ($M_s = 64, 68$, and 72), the bifurcation load normalized with respect to the classical buckling load of the local mode $\sigma/\sigma_c^{(2)}$ (it should be cautioned that $\sigma_c^{(2)}$ differs between the present and Koiter's 1956 analyses) is plotted against the amplitude of the local imperfection in Fig. 3. Comparing these solutions, one can conclude that significant differences arise due to the inclusion of axial stiffness and torsional rigidity of the stringers. The present curves tend to "level off" quite rapidly for imperfection amplitudes likely to be encountered in practice. Table 1 summarizes the essential results together with the lower bound estimates (from equation (34)) when b_2 is positive. Furthermore, it should be noted that the value of the b coefficient of the overall mode has no effect whatsoever in Fig. 3 (see [14]). It was also found that each circumferential half wave of the overall mode involved about two to three stringers, thus indicating that the smeared-out overall mode analysis is a reasonable approximation for this case.

Finally, it should be emphasized that several other example problems based on different shell configurations have been examined. It was found that all these investigations yield qualitatively similar results. Experimental results confirming the present buckling and initial postbuckling behavior of the local mode can be found in [25].

Acknowledgments

The authors wish to gratefully acknowledge the contributions made at various stages in the development of this work by Prof. J. W. Hutchinson of Harvard University, who first suggested the problem to us. In addition, Prof. W T. Koiter provided valuable guidance at the outset of the program. Financial support of our research was received from the National Sciences and Engineering Research Council under Grants A-2783 and A-3663.

References

1 Koiter, W. T., "On the Stability of Elastic Equilibrium," Thesis, Delft University, Amsterdam 1945; English translations: NASA TT-F10,833, 1967 and AFFDL-TR-70-25, 1970.

2 Budiansky, B., and Hutchinson, J. W., "Dynamic Buckling of Imperfection-Sensitive Structures," *Proceedings of the 11th International Congress of Applied Mechanics*, Munich, 1964, pp. 636–651.

3 Thompson, J. M. T., and Hunt, G. W., *A General Theory of Elastic Stability*, Wiley, New York, 1973.

4 Van der Neut, A., "The Interaction of Local Buckling and Column Failure of Thin-Walled Compression Members," *Proceedings of the 12th International Congress of Applied Mechanics*, Springer-Verlag, Berlin, 1969, pp. 389–399.

5 Graves Smith, T. R., "The Ultimate Strength of Locally Buckled Columns of Arbitrary Length," *Thin-Walled Steel Structures, Their Design and Use in Building*, eds., Rockey, K. C., and Hill, H. V., Crosby Lockwood & Son Ltd., 1967, pp. 35–60.

6 Byskov, E., and Hutchinson, J. W., "Mode Interaction in Axially Stiffened Cylindrical Shells," *AIAA Journal*, Vol. 15, July 1977, pp. 941–948.

7 Gilbert, R. B , and Calladine, C. R , "Interaction Between the Effects of Local and Overall Imperfections on the Buckling of Elastic Columns," *Journal of the Mechanics and Physics of Solids*, Vol. 22, 1974, pp. 519–540.

8 Hunt, G. W., "Algorithm for the Nonlinear Analysis of Compound Bifurcation," Apr. 1980 (a copy from private communication).

9 Tvergaard, V., "Imperfection-Sensitivity of a Wide Integrally Stiffened Panel Under Compression," *International Journal of Solids and Structures*, Vol. 9, 1973, pp. 177–192.

10 Grimaldi, A., and Pignataro, M., "Postbuckling Behaviour of Thin-Walled Open Cross-Section Compression Members," *Journal of Structural Mechanics*, Vol. 7, 1979, pp. 143–159.

11 Koiter, W. T., and Kuiken, G. D. C., "The Interaction Between Local Buckling and Overall Buckling on the Behaviour of Built-Up Columns," Delft University of Technology, Report WTHD 23, May 1971.

12 Svensson, S. E., and Croll, J. G. A., "Interaction Between Local and Overall Buckling," *International Journal of Mechanical Sciences*, Vol. 17, 1975, pp. 307–321.

13 Koiter, W. T., and Pignataro, M., "A General Theory for the Interaction Between Local and Overall Buckling of Stiffened Panels," Delft University of Technology, Report WTHD 83, Apr. 1976.

14 Koiter, W. T., "General Theory of Mode Interaction in Stiffened Plate and Shell Structures," Delft University of Technology, Report WTHD 91, Sept. 1976.

15 Hutchinson, J. W., and Amazigo, J. C., "Imperfection-Sensitivity of Eccentrically Stiffened Cylindrical Shells," *AIAA Journal*, Vol. 5, Mar. 1967, pp. 392–401.

16 Hutchinson, J. W., and Frauenthal, J. C., "Elastic Postbuckling Behavior of Stiffened and Barreled Cylindrical Shells," ASME JOURNAL OF APPLIED MECHANICS, Vol. 36, Dec. 1969, pp. 784–790.

17 Koiter, W. T., "Buckling and Post-Buckling Behaviour of a Cylindrical Panel Under Axial Compression," National Aeronautical Research Institute, Amsterdam, Report S-476, May 1956.

18 Stephens, W. B., "Imperfection-Sensitivity of Axially Compressed Stringer Reinforced Cylindrical Panels Under Internal Pressure," *AIAA Journal*, Vol. 9, Sept. 1971, pp. 1713–1719.

19 Hutchinson, J. W , "Initial Post-Buckling Behaviour of Toroidal Shell Segments," *International Journal of Solids and Structures*, Vol. 3, 1967, pp. 97–115.

Table 1 Summary of mode interaction parameters

M_s	θ	r	B	b_2 (present)	b_2 (Stephens)	Lower bound (present)	Lower bound (Stephens)
64	0.828	1.144	0.158	0.044	−0.0922	0.715	No *L.B.*
68	0.779	1.0045	0.1665	0.137	−0.00457	0.8695	No *L.B.*
72	0.736	0.8842	0.1741	0.211	0.064	0.799	0.2788

Downloaded 01 May 2010 to 171.66.16.249. Redistribution subject to ASME license or copyright; see http://www.asme.org/terms/Terms_Use.cfm

20 Dongarra, J. J., et al., Linpact Working Notes #9 and #10, Applied Mathematics Division, Argonne National Laboratory, Argonne, Ill., 60439, U.S.A.; also appears as "LINPACK Users' Guide," published by Society for Industrial and Applied Mathematics, Philadelphia, 1979.

21 Blum, R. E., and Fulton, R. E., "A Modification of Potters' Method for Solving Eigenvalue-Problems Involving Tridiagonal Matrices," *AIAA Journal*, Vol. 4, Dec. 1966, pp. 2231–2232.

22 Hui, D , "Interaction Between Local and Overall Modes in Axially Stiffened Cylindrical Shells," PhD thesis, UTIAS Report Number 247, 1980.

23 Hui, D., and Hansen, J. S., "Effect of Stringer Torsional Rigidity on Buckling of Integrally Stiffened Angle Ply Plates," *Fibre Science and Technology Journal*, 1981, in press.

24 Byskov, E., and Hansen, J. C., "Postbuckling and Imperfection-Sensitivity Analysis of Axially Stiffened Cylindrical Shells With Mode Interaction," Technical University of Denmark, DCAMM Report No. 163, Aug. 1979.

25 Tennyson, R. C., Booton, M., and Hui, D., "Changes in Cylindrical Shell Buckling Behaviour Resulting From System Parameter Variations," *Proceedings of the 15th International Congress of Applied Mechanics*, Aug. 1980, pp. 417–428.

Downloaded 01 May 2010 to 171.66.16.249. Redistribution subject to ASME license or copyright; see http://www.asme.org/terms/Terms_Use.cfm

J. R. Hutchinson
Professor,
Department of Civil Engineering,
University of California,
Davis, Calif. 95616
Mem. ASME

Transverse Vibrations of Beams, Exact Versus Approximate Solutions

An exact solution for the natural frequencies of vibration of a finite length free-free beam with a circular cross section is found and compared to approximate solutions. This exact solution is a series solution of the general linear elasticity equations which converges to correct natural frequencies. Correctness of the frequencies is established by comparison to previous experiments. Comparison of the exact to approximate solutions is made with the Pochhammer-Chree approximation, the Timoshenko beam approximation and the Pickett approximation. The comparisons clearly show the range of applicability of the approximate methods as well as their accuracy. The correct shear coefficient for use in the Timoshenko beam approximation is investigated and conclusions which differ with, yet at the same time complement, those of previous researchers are reached.

Introduction

In a recent paper by this author [1] an exact solution for the vibrations of a solid isotropic linearly elastic cylinder with traction-free boundaries was developed. The transverse vibrations of beams represents an important subset of that exact solution. Many approximate solutions have been developed for beam vibrations and this exact solution provides an excellent criteria for determining the accuracy and range of applicability of the various approximate methods.

The governing equations for the transverse vibrations of slender beams is generally credited to Euler and Bernoulli. Rayleigh [2] introduced rotary inertia, and in 1921, Timoshenko [3] showed that shear deformation was as important as rotary inertia for nonslender beams.

Much research has been done on choosing a correct value for the shear coefficient, k, which appears to the Timoshenko beam equation. Timoshenko himself used several different values for k. Of particular interest is the value which is derived from Timoshenko's 1922 paper [4] in which he matched the Pochhammer-Chree solution for long wavelengths. That value is $(6 + 12\nu + 6\nu^2)/(7 + 12\nu + 4\nu^2)$ where ν is Poisson's ratio. The shear coefficient, as pointed out by Timoshenko, is also a function of the shape of the cross section. Since in this paper only beams of circular cross section are considered, all k-values discussed are for circular cross sections. In 1931, Goens [5] used a k-value of 0.9 based on static analysis. It should be pointed out that early researchers recognized that k was not only a function of cross section and Poisson's ratio, but also to some extent a function of frequency. In 1948, Davies [6] showed plots of the match between the Timoshenko beam equation and the first dispersion curve of the Pochhamer-Chree solution. In 1954, Mindlin and Deresiewicz [7] proposed a value of k of 0.847 based on matching the thickness shear vibrations in an infinitely long rod. In 1966, Cowper [8] introduced a shear coefficient of $(6 + 6\nu)/(7 + 6\nu)$ based on a static elasticity analysis. In 1970, Spence and Seldin [9] computed the shear coefficient for the first three modes for selected length to diameter ratios and values of Poisson's ratio based on matching a solution developed by Pickett [10]. In 1978, Stephan [11] showed the variation of the shear coefficient with frequency by matching the first dispersion curve of the Pochhammer-Chree solution, In a 1975 review paper, Kaneko [12] strongly supports the value found in Timoshenko's 1922 paper. Kaneko lists many of the shear coefficient values which have been used for rectangular as well as circular beams. In a 1974 paper, Aalami and Atzori [13] compared the Timoshenko beam theory with an extended Rayleigh-Ritz method for simply supported beams, and proposed the use of two shear coefficients.

The problem of the vibrating solid cylinder was first investigated in terms of the general elasticity equations by Pochhammer in 1876 and independently by Chree in 1889. An account of this treatment can be found in Love [14]. The Pochhammer-Chree solution is for an infinitely long solid circular rod which is traction free on its circumferential boundary. The solution does not, however, permit traction free ends. In 1945, Pickett [10] introduced an elasticity solution using the same basic functions as the Pochhammer-Chree solution which satisfy the boundary conditions on the circumferential boundary. Pickett combined two forms of the elasticity solution in order to make the resultant moment and resultant shear on the beam ends equal to zero. While he did not satisfy the true end boundary conditions of zero surface traction, his solution is highly accurate for a beam of any reasonable length. In 1960, Tefft [15] carried out the numerical solution of Pickett's equations and made some experimental comparisons. The computations for k by Spence and Seldin [9] were made

Contributed by the Applied Mechanics Division for publication in the JOURNAL OF APPLIED MECHANICS.
Discussion on this paper should be addressed to the Editorial Department, ASME, United Engineering Center, 345 East 47th Street, New York, N. Y. 10017, and will be accepted until two months after final publication of the paper itself in the JOURNAL OF APPLIED MECHANICS. Manuscript received by ASME Applied Mechanics Division, October, 1980; final revision, April, 1981.

Copyright © 1981 by ASME
Downloaded 01 May 2010 to 171.66.16.249. Redistribution subject to ASME license or copyright; see http://www.asme.org/terms/Terms_Use.cfm

using Tefft's numerical data. It was found necessary for comparison purposes to develop a computer program for evaluation of the Pickett solution. The results of that program differ slightly with those of Tefft and hence with those of Spence and Seldin.

The exact solution which is used as a basis for comparison in this study is the $n = 1$ case of the general solution developed in reference [1]. It must be noted that what is called an exact solution in this paper is a series solution and hence subject to truncation error. Thus it must be realized that the numerical results may be in error if enough terms are not chosen. It was found in reference [1] that for a diameter to length ratio of one, four place accuracy could be achieved with only three terms in each series; however, for other diameter-to-length ratios the convergence was not as good. The comparison with the experimental work of McMahon [16] in reference [1] showed excellent agreement.

Solutions

The solution forms for the various analytic solutions considered in this paper are presented in the following section. Derivations are omitted and only brief descriptions are given. The Euler-Bernoulli and Timoshenko beam solutions are concisely derived in reference [17]. The Pochhammer-Chree solution is derived in Love [14]. The Pickett solution is derived in reference [10], and the exact solution is derived in reference [1].

1 Euler-Bernoulli Solution. The well-known Euler-Bernoulli beam equation is

$$EI\frac{\partial^4 v}{\partial x^4} + \rho A\frac{\partial^2 v}{\partial t^2} = 0 \tag{1}$$

where E is the modulus of elasticity, I is the moment of inertia, v is the transverse displacement, ρ is the density, and A is the cross-sectional area.

Assuming sinusoidal motion and applying the boundary conditions for free ends leads to the following characteristic equation:

$$\cos\bar{\lambda}_n \cosh\bar{\lambda}_n = 1 \tag{2}$$

Equation (2) yields an infinite number of discrete values $\bar{\lambda}_n$. The relationship between the frequency parameter $\bar{\lambda}_n$ and the natural frequency p_n is

$$p_n = \frac{\bar{\lambda}_n^2}{L^2}\left[\frac{EI}{\rho A}\right]^{1/2} \tag{3}$$

where L is the length of the rod. Values for $\bar{\lambda}_n$ can be found tabulated in reference [17].

2 Timoshenko Beam Solution. The Timoshenko beam solution includes the additional effects of rotary inertia and shear deformation. The differential equation can be expressed as

$$EI\frac{\partial^4 v}{\partial x^4} + \rho A\frac{\partial^2 v}{\partial t^2} - \rho I\left(1 + \frac{E}{kG}\right)\frac{\partial^4 v}{\partial x^2\partial t^2} + \frac{\rho^2 I}{kG}\frac{\partial^4 v}{\partial t^4} = 0 \tag{4}$$

where G is the shear modulus and k is the shear coefficient.

For modes which are symmetric about the center (i.e., modes 1, 3, 5. . .) the characteristic equation is

$$\tan\frac{\bar{\beta}}{2} + \frac{\bar{\beta}}{\bar{\alpha}}\left(\frac{\bar{\alpha}^2 + \bar{p}^2}{\bar{\beta}^2 - \bar{p}^2}\right)\tanh\frac{\bar{\alpha}}{2} = 0 \tag{5}$$

For the antisymmetric modes the characteristic equation is

$$\tan\frac{\bar{\beta}}{2} - \frac{\bar{\alpha}}{\bar{\beta}}\left(\frac{\bar{\beta}^2 - \bar{p}^2}{\bar{\alpha}^2 - \bar{p}^2}\right)\tanh\frac{\bar{\alpha}}{2} = 0 \tag{6}$$

where

$$\left.\begin{matrix}\bar{\alpha}^2\\ \bar{\beta}^2\end{matrix}\right\} = \frac{\bar{p}^2}{2}\left\{\mp\left(1 + \frac{E}{kG}\right) + \left[\left(1 - \frac{E}{kG}\right)^2 + \frac{64}{\bar{p}^2}\left(\frac{L}{D}\right)^2\right]^{1/2}\right\} \tag{7}$$

and

$$\bar{p} = pL/Co \tag{8}$$

Co is the thin rod velocity, $(E/\rho)^{1/2}$, and D is the rod diameter. The term E/G can be expressed in terms of Poisson's ratio, ν, as $2(1 + \nu)$. To solve for the natural frequencies one assumes physical constants ν, L/D, and k, and solves the characteristic equation for $\bar{p}$ by iteration. A similar process can be carried out to solve for k if $\bar{p}$ is known from the exact solution.

Table 1 Solutions of elasticity equations. Columns (1), (2), and (3) represent the three solution forms. The fourth column is a common multiplier. J_n ( ) denotes the nth-order Bessel function of the first kind. Primes denote differentiation with respect to the argument. The dimensionless wave numbers, α, β, and δ and the frequency parameter ω are related by $\alpha^2 + \delta^2 = \omega^2(1 - 2\nu)/2(1 - \nu)$ and $\alpha^2 + \beta^2 = \omega^2$.

	(1)	(2)	(3)	Multiplier
u	$2\delta J_1'(\delta r)$	$-\alpha\beta J_1'(\beta r)$	$-J_1(\beta r)/r$	$\left\{\begin{matrix}\cos\alpha z\\ \sin\alpha z\end{matrix}\right\}\cos\theta$
v	$-2J_1(\delta r)/r$	$\alpha J_1(\beta r)/r$	$\beta J_1'(\beta r)$	$\left\{\begin{matrix}\cos\alpha z\\ \sin\alpha z\end{matrix}\right\}\sin\theta$
w	$2\alpha J_1(\delta r)$	$\beta^2 J_1(\beta r)$	0	$\left\{\begin{matrix}-\sin\alpha z\\ \cos\alpha z\end{matrix}\right\}\cos\theta$
σ_r	$(2\alpha^2-\omega^2)J_1(\delta r)-2\delta J_0(\delta r)/r$	$\beta^2\alpha J_1(\beta r)+\alpha\beta J_0(\beta r)/r$	$-\beta J_0(\beta r)/r$	$\left\{\begin{matrix}\cos\alpha z\\ \sin\alpha z\end{matrix}\right\}\cos\theta$
σ_z	$(2\delta^2-\omega^2)J_1(\delta r)$	$-\beta^2\alpha J_1(\beta r)$	0	$\left\{\begin{matrix}\cos\alpha z\\ \sin\alpha z\end{matrix}\right\}\cos\theta$
$\tau_{r\theta}$	$-4\delta J_0(\delta r)/r$	$2\alpha\beta J_0(\beta r)/r$	$-\beta^2 J_1(\beta r)-2\beta J_0(\beta r)/r$	$\left\{\begin{matrix}\cos\alpha z\\ \sin\alpha z\end{matrix}\right\}\sin\theta$
τ_{rz}	$4\alpha\delta J_1'(\delta r)$	$\beta(\beta^2-\alpha^2)J_1'(\beta r)$	$-\alpha J_1(\beta r)/r$	$\left\{\begin{matrix}-\sin\alpha z\\ \cos\alpha z\end{matrix}\right\}\cos\theta$
$\tau_{\theta z}$	$-4\delta J_1(\delta r)/r$	$(\alpha^2-\beta^2)J_1(\beta r)/r$	$\alpha\beta J_1'(\beta r)$	$\left\{\begin{matrix}-\sin\alpha z\\ \cos\alpha z\end{matrix}\right\}\sin\theta$

Downloaded 01 May 2010 to 171.66.16.249. Redistribution subject to ASME license or copyright; see http://www.asme.org/terms/Terms_Use.cfm

For plotting purposes a frequency parameter λ is introduced such that

$$\lambda^2 = 4\bar{p}L/D \tag{9}$$

This is introduced so that for a small D/L ratio this parameter will approach the $\bar{\lambda}$ found from equation (7).

3 Pochhammer-Chree Solution. The Pochhammer-Chree solution is formed from a linear combination of the three solutions to the general linear elasticity equations. The three solution forms are tabulated in Table 1. The fourth column of that table is a common multiplier to the three solution forms found in columns 1, 2, and 3. All symbols used in the table are dimensionless. The radial displacement u, tangential displacement v, and axial displacement w are made dimensionless by dividing by the radius. All stress quantities are made dimensionless by dividing by the shear modulus. The wave numbers α, β, and δ are made dimensionless by multiplying by the radius. The frequency is made dimensionless by multiplying by the radius and dividing by the shear wave velocity.

The frequency is often nondimensionalized by dividing by the thin rod velocity rather than the shear velocity. Such a frequency parameter will be denoted by $\bar{\omega}$. The relation between ω and $\bar{\omega}$ is

$$\omega = \bar{\omega}\sqrt{2(1+\nu)} \tag{10}$$

The relationship between $\bar{\omega}$ and the previously defined parameter λ is

$$\lambda = 2(L/D)\sqrt{2\bar{\omega}} \tag{11}$$

Using the three basic solution forms in Table 1 and satisfying the boundary conditions along the cylindrical surface leads to the following characteristic equation:

$$\begin{vmatrix} \sigma_{r1} & \sigma_{r2} & \sigma_{r3} \\ \tau_{r\theta 1} & \tau_{r\theta 2} & \tau_{r\theta 3} \\ \tau_{rz1} & \tau_{rz2} & \tau_{rz3} \end{vmatrix} = 0 \tag{12}$$

where σ_{r1} is the solution form listed in the first column (hence subscript 1) of the σ_r row of the table. The other eight terms in the determinant are similarly defined. All nine terms are evaluated at r equal to one.

Using the two relationships between α, β, δ, ω, and ν expressed in Table 1, it can be seen that the determinant in equation (12) can be solved by iteration for the relationship between α and ω. Plots can then be constructed of either α^2 versus $\bar{\omega}^2$ as done by Pickett [10] or dispersion curves of normalized phase velocity C/Co (i.e., $\bar{\omega}/\alpha$) versus α as done by Davies [6] or Abramson [18].

4 Pickett Solution. The Pickett solution also uses a linear combination of the three solution forms and identical satisfaction of the boundary conditions on the cylindrical surface. In his solution of equation (12) Pickett found two real values of α^2 for each $\bar{\omega}$. For low values of $\bar{\omega}$ one of the α^2-values was positive the other negative. For $\bar{\omega} > 1.693/(1+\nu)$ Pickett found both roots to be positive. Using the solution forms for thoese two roots it is possible to partially satisfy the end boundary conditions. Pickett approximated the free end condition by making the moment resultant and shear resultant vanish. This leads to another transcendental equation of the form

$$f(\alpha_1, \alpha_2, \bar{\omega}, D/L) = 0 \tag{13}$$

where α_1 and α_2 are the two roots found from equation (12). For details of this equation see equation (21) reference [10]. The solution process is to assume values of ν and ω, compute the two roots α from equation (12) and then solve equation (13) for D/L by iteration.

In carrying out the numerical work it was found that the modified equations presented by Tefft [15] had some computational advantages over the equations presented by Pickett. It was also found that for $\bar{\omega}$ greater than approximately 1.64 (roughly independent of Poisson's ratio) that additional roots of α appeared. Since this value of $\bar{\omega}$ is relatively high it was decided this represented a logical cutoff point for the theory. It was further noted that the root α^2 which is always positive corresponds to the first dispersion curve as defined by Abramson [18]. The root α^2 which is negative for low $\bar{\omega}$ corresponds to the second dispersion curve, and the roots that emerge for $\bar{\omega} > 1.64$ correspond to the third and higher dispersion curves.

The Pickett solution is much more accurate than the Timoshenko solution but still only represents an approximation of the end boundary conditions. Thus, for long beams, it should be very accurate, but will not represent a good solution for very short beams. Pickett "believed that these simplifications introduce very little error in the solution for the cylinder for diameter-to-length ratios up to unity for the mode of lowest frequency," and he was right.

5 Exact Solution. The exact solution also makes use of the three solution forms given in Table 1. These solution forms are grouped into three series. The expression for the radial displacement, for example, is

$$u = \sum_{i=1}^{M} A_i u_{Ai} + \sum_{j=1}^{N} B_j u_{Bj} + \sum_{k=1}^{M} C_k u_{Ck} \tag{14}$$

with similar expressions for the other displacement and stress components. In equation (14) A_i, B_j, and C_k are constants. The term u_{Ai} is a linear combination of terms from columns 1 and 2 of Table 1 (including the multiplier). The term u_{Bj} is a linear combination of terms from columns 1 and 2 with α and δ and α and β exchanged. The term u_{Ck} is a linear combination of terms from columns 1 and 3. The series expressions for the other displacement and stress components are formed in identical fashion. The A and C series can be viewed as Fourier series in the axial coordinate and the B series can be viewed as a Bessel series in the r-coordinate, therefore, M will be referred to as the number of terms in the axial direction and N as the number of terms in the radial direction. In reporting the number of terms used, the axial number will be listed first.

It is possible to select the linear combinations involved in each series together with the wave numbers α_i, α_j, α_k so that three of the required six boundary conditions satisfied identically are

$$\tau_{rz}(r, \theta, L/D) = 0 \tag{15}$$

$$\tau_{rz}(1, \theta, Z) = 0 \tag{16}$$

$$\tau_{\theta z}(r, \theta, L/D) = 0 \tag{17}$$

where L/D represents the end of the beam which has its origin at the center and the axial coordinate normalized with respect to the radius. The remaining three boundary conditions are satisfied by orthogonality as follows:

$$\int_0^{L/D} \sigma_r(1, \theta, z) \begin{Bmatrix} \cos \alpha_{Ai} Z \\ \sin \alpha_{Ai} Z \end{Bmatrix} dz = 0 \tag{18}$$

$$\int_0^1 \sigma_z(r, \theta, L/D) r J_1(\alpha_{Bj} r) dr = 0 \tag{19}$$

$$\int_0^{L/D} \tau_{r\theta}(1, \theta, z) \begin{Bmatrix} \cos \alpha_{Ck} \\ \sin \alpha_{Ck} \end{Bmatrix} dz = 0 \tag{20}$$

The upper term in the braces correspond to the symmetric modes (i.e., transverse displacement an even function of z) and the lower term is for the antisymmetric modes.

Satisfying equations (18)–(20) leads to the following characteristic equation:

$$\begin{vmatrix} \lfloor a \rfloor & [b] & \lfloor c \rfloor \\ [\bar{a}] & \lfloor \bar{b} \rfloor & [\bar{c}] \\ [\hat{a}] & [\hat{b}] & \lfloor \hat{c} \rfloor \end{vmatrix} = 0 \tag{21}$$

where the notation $\lfloor \quad \rfloor$ indicates a diagonal matrix.

The solution process involves choosing ν and D/L and a reasonable number of terms in each series. Then equation (21) is solved for ω by iteration. The number of terms in the series are increased until sufficient accuracy results.

Downloaded 01 May 2010 to 171.66.16.249. Redistribution subject to ASME license or copyright; see http://www.asme.org/terms/Terms_Use.cfm

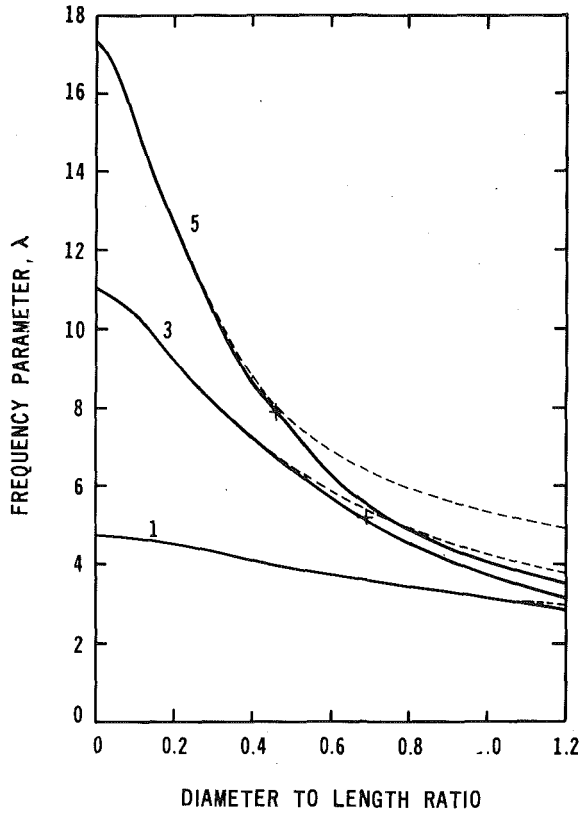


Fig. 1 Frequency parameter λ versus the diameter-to-length ratio for the three lowest symmetric modes, $\nu = 0.3$; — exact solution, - - - Timoshenko solution with $k = 0.9$, + limits of Pickett solution

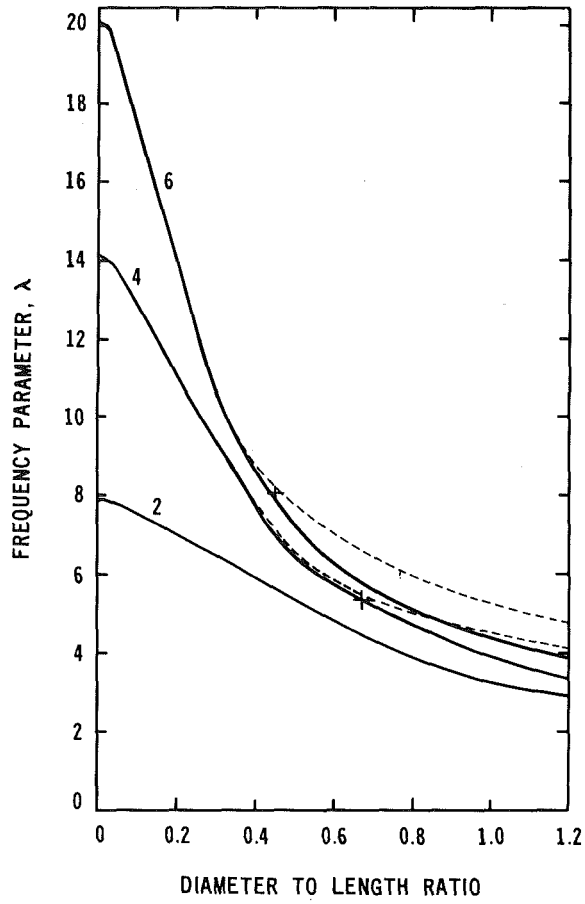


Fig. 2 Frequency parameter λ versus the diameter-to-length ratio for the three lowest antisymmetric modes, $\nu = 0.3$; — exact solution, - - - Timoshenko solution with $k = 0.9$, + limits of Pickett solution

Table 2 Comparison of the frequency parameter $\bar{\omega}$ computed by the exact method and the Pickett method. "*D/L*" refers to the diameter-to-length ratio. "Terms" refers to the number of terms in the exact solution series in the axial and radial direction, respectively. The subscript on $\bar{\omega}$ refers to the type of solution and mode, thus, $\bar{\omega}_{E3}$ refers to the third mode computed from the exact solution. All values are for a Poisson's ratio of 0.3.

D/L	0.1	0.2	0.3	0.4	0.5	0.6
TERMS	40x20	40x20	40x20	40x20	40x20	20x12
$\bar{\omega}_{E1}$	0.02762	0.10222	0.21014	0.33876	0.47980	0.62831
$\bar{\omega}_{P1}$	0.02727	0.10206	0.21005	0.33873	0.47986	0.62838
$\bar{\omega}_{E2}$	0.07238	0.24738	0.46612	0.69032	0.88760	1.03150
$\bar{\omega}_{P2}$	0.07203	0.24724	0.46609	0.69036	0.88768	1.03141
$\bar{\omega}_{E3}$	0.13402	0.42295	0.74858	1.05271	1.29688	1.47851
$\bar{\omega}_{P3}$	0.13369	0.42284	0.74860	1.05283	1.29862	1.48848

D/L	0.7	0.8	0.9	1.0	1.1	1.2
TERMS	20x14	20x16	20x18	20x20	20x20	20x20
$\bar{\omega}_{E1}$	0.78062	0.93451	1.08757	1.23662	1.37568	1.49292
$\bar{\omega}_{P1}$	0.78102	0.93543	1.08957	1.24121	1.38752	1.52490
$\bar{\omega}_{E2}$	1.12893	1.20400	1.27052	1.33403	1.39666	1.45910
$\bar{\omega}_{P2}$	1.12953	1.20585	1.27412	1.33994	1.40547	1.47150

Results

Plots of the frequency parameter λ versus the diameter-to-length ratio is shown in Figs. 1 and 2. The solid curve is for the exact solution and the dashed curve is for the Timoshenko beam equation with k equal to 0.9. The Euler-Bernoulli equation gives constant values for λ corresponding to those of zero D/L ratio. On these curves the Pickett solution corresponds so well with the exact solution that it cannot be shown as a separate curve. The cutoff values for the Pickett solution have, however, been shown. The cutoff values, corresponding to $\bar{\omega} = 1.64$, also represent points at which the Timoshenko solution begins diverging greatly from the exact solution and consequently would be useful upper bounds on the Timoshenko beam solution as well.

The close correlation between the exact solution and the Pickett solution is shown in Table 2. It can be seen that for small values of the diameter-to-length ratio the Pickett solution gives lower values for the frequency whereas for higher values of the D/L ratio the opposite is true. Although it has not been proven, it is believed that both solutions represent upper bounds on the frequency. If this is the case, then the Pickett solution is more accurate than the exact solution for smaller D/L for the limited number of terms used in the exact solution. For higher D/L, however, the exact solution converges much better and gives the more correct solutions.

Table 3 is partially taken from Tefft [15]. It shows a comparison of experimental results computed from the Pickett solution by both Tefft and this author as well as from the exact solution. Instead of the previously defined frequency parameters Tefft uses a parameter T which can be interpreted as the actual modulus of elasticity divided by the apparent modulus which would result from the Euler-Bernoulli beam theory. In terms of the previously defined parameters,

$$T_n = (\bar{\lambda}_n/\lambda_n)^4 \tag{22}$$

Table 3 serves several purposes. The slight differences between Tefft's calculations and mine, as pointed out in the Introduction, can be seen. More importantly the close correlation between experiment and theory is clearly demonstrated.

Downloaded 01 May 2010 to 171.66.16.249. Redistribution subject to ASME license or copyright; see http://www.asme.org/terms/Terms_Use.cfm

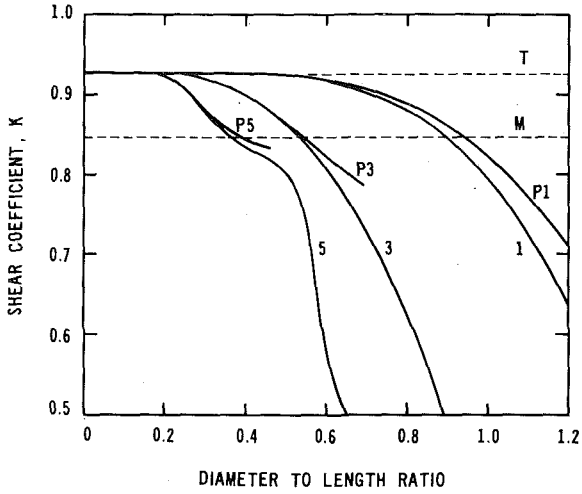


Fig. 3 Shear coefficient k versus the diameter-to-length ratio of the three lowest symmetric modes, $\nu = 0.3$; — exact solution labeled 1, 3, 5 and Pickett solution labeled P1, P3, P5; - - - Timoshenko's constant labeled *T*, and Mindlin and Deresiewicz's constant labeled *M*

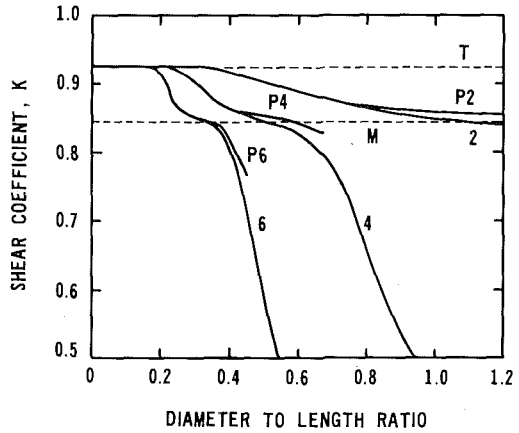


Fig. 4 Shear coefficient k versus the diameter-to-length ratio for the three lowest antisymmetric modes, $\nu = 0.3$; — exact solution labeled 2, 4, 6 and Pickett solution labeled P2, P4, P6; - - - Timoshenko's constant labeled *T*, and Mindlin and Deresiewicz's constant labeled *M*

Figs. 3 and 4 show the value the shear coefficient would have to obtain in order to produce the same answers as the exact solution or the Pickett solution. It can be seen that the best value of k for small D/L is that given by Timoshenko in 1922. As D/L is increased the k-values decrease monotonically and in some cases have a stationary value near the value predicted by Mindlin and Deresiewicz. The results from both the exact and the Pickett solution are in essential agreement but near the cutoff point do show significant differences.

The variation of the shear coefficient as a function of Poisson's ratio is shown in Fig. 5. This plot was for D/L of one half. It can be seen that for the first mode reasonable agreement is found with the Timoshenko expression, whereas for the third and fourth modes the Mindlin and Deresiewicz value would be best. The k-value found by Cowper represents a compromise between the two.

Fig. 6 shows the variation of the shear coefficient as a function of frequency. It was found that the first mode stood by itself while modes 2–6 fell in a relatively narrow band. Also shown on the plot are the shear coefficient values based on matching the first two dispersion curves of the Pochhammer-Chree solution. It should be noted that while Stephan [11] based his comparison on only the first dispersion curve these results come out between the two. In fact preliminary investigation of higher modes using the Pickett solution indicates that

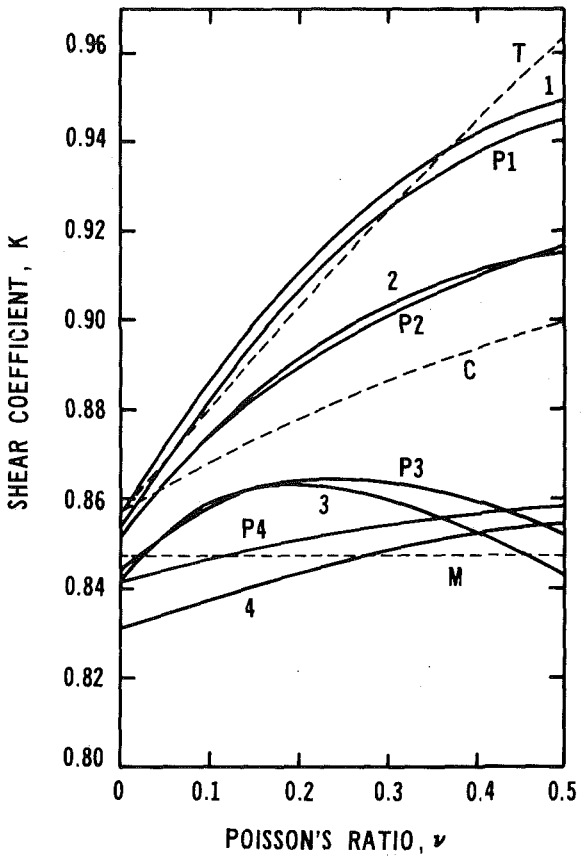


Fig. 5 Shear coefficient k versus Poisson's ratio ν for the lowest four modes; — exact solution labeled 1, 2, 3, 4, and Pickett solution labeled P1, P2, P3, P4; - - - Timoshenko's value labeled *T*, Cowper's value labeled *C*, and Mindlin and Dereciewicz's value labeled *M*

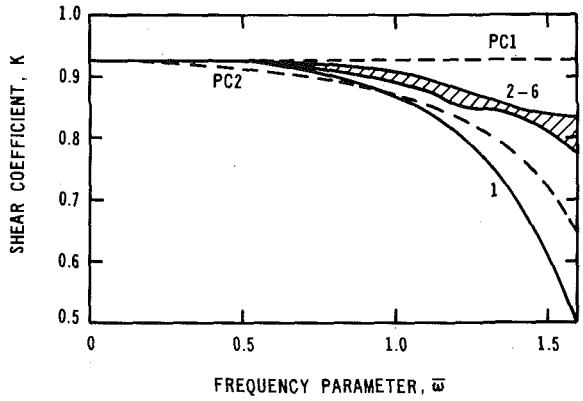


Fig. 6 Shear coefficient k versus frequency parameter $\bar{\omega}$ for the six lowest frequencies; — fundamental frequency labeled 1, frequencies 2–6 shown as band; - - - Pochhammer-Chree solution, matching of first and second dispersion curves labeled PC1 and PC2, respectively

the behavior of up to the 40th mode is similar to the behavior for modes 2–6.

Experimental verification of the exact solution was accomplished in reference [1] by comparison with the experimental work of McMahon [16]. The correlation was excellent, but the range of parameters is not totally inclusive of those considered in this paper. McMahon used solid steel and aluminum cylinders with D/L ranging from 0.6 to 10; whereas for transverse beam vibrations the range of interest is 0 to 1.2. The experiments of Spinner, et al. [19], were on steel specimens with a D/L ranging from 0.09 to 0.5. Comparison of

Downloaded 01 May 2010 to 171.66.16.249. Redistribution subject to ASME license or copyright; see http://www.asme.org/terms/Terms_Use.cfm

Table 3 A comparison of theoretical and experimental values of the correction factor T for two specimens cut from a single bar of soft steel, $\nu = 0.2879$. Specimen A has $D/L = 0.27871$ and specimen B has $D/L = 0.45039$. The subscript on T refers to the specimen and the mode. The experimental values are from Tefft [14]. The column labeled Tefft shows Teffts calculated values. The column labeled Pickett is the result of this authors calculations using Pickett's (and Tefft's) method. The column labeled Exact is the solution with 72 × 20 terms used for specimen A and 45 × 20 terms used for specimen B. The last three columns give the percent deviation from the experimental results of the Tefft, Pickett, and Exact solutions, respectively.

	Experimental	Tefft	Pickett	Exact	Tefft % Error	Pickett % Error	Exact % Error
T_{A1}	1.3790	1.3787	1.3785	1.3780	-0.02	-0.04	-0.07
T_{A2}	2.0498	2.0503	2.0490	2.0490	+0.02	-0.04	-0.04
T_{A3}	2.9770	2.9814	2.9768	2.9773	-0.15	-0.01	+0.01
T_{B1}	1.9251	1.9257	1.9248	1.9250	+0.03	-0.02	-0.005

the first mode data of Spinner, et al., with my Pickett computer solution showed errors in T between +0.4 percent and −0.3 percent which while not as close as the agreement found by Tefft (Table 3) is still within the range of experimental error. Spence and Seldin [9] give experimental results for two circular aluminum rods with L/D equal to 36.17 and 18.02; for both of these the agreement for k is to within experimental accuracy. Zemanek and Rudnick [20] determined the lowest 306 resonant frequencies of an aluminum beam whose diameter-to-length ratio was 1/240. They concluded that k decreased monotonically from 0.96 to 0.94 as the frequency increased. Their value for k is higher than the theory predicts, but the changes in k with frequency are of the order predicted.

Conclusions

The Pochhammer-Chree approximation, while not satisfying the end boundary conditions, does give some indication of the type of change one can expect in the shear coefficient with frequency. Further, matching the Pochhammer-Chree solution for long waves with the Timoshenko beam solution to derive a shear coefficient provides an excellent value of the shear coefficient for $\bar{\omega} < 0.5$.

The Pickett approximation is highly accurate particularly for low values of $\bar{\omega}$. It was found that for practical computational purposes the Pickett solution was preferable to the exact solution for $\bar{\omega} < 0.5$. In that region the Pickett solution gives answers to greater accuracy than experimentalists have been able to determine, and does so with much less computational effort than the exact solution. The cutoff frequency of $\bar{\omega} = 1.6$ appears to be a reasonable choice for an upper bound on both the Pickett solution and the Timoshenko solution.

The choice of a shear coefficient of $(6 + 12\nu + 6\nu^2)/(7 + 12\nu + 4\nu^2)$ in the Timoshenko beam theory produces excellent results for $\bar{\omega} < 0.5$, however, for $\bar{\omega} > 0.5$ k decreases monotonically with increasing $\bar{\omega}$ while showing a stationary value $k = 0.847$. Thus both Timoshenko and Mindlin and Deresiewicz predicted correct values within appropriate regions. To make a reasonable choice for k one must therefore know the region and assign a value of k accordingly.

The Pochhammer-Chree, Pickett, and exact solutions are all limited, at least in their present form, to beams of circular cross section. The Timoshenko beam approximation, however, has no such limitations. While all quantitative comparison in this paper are for beams of circular cross section, many similar conclusions on an appropriate shear coefficient for use in the Timoshenko beam equation can be drawn for beams of noncircular cross section. One can expect the shear coefficient to be a function of the cross section and Poisson's ratio for low $\bar{\omega}$, to diminish monotonically with increasing $\bar{\omega}$ and to approach the values predicted by Mindlin and Deresiewicz for higher values of $\bar{\omega}$.

References

1 Hutchinson, J. R., "Vibrations of Solid Cylinders," ASME JOURNAL OF APPLIED MECHANICS, Vol. 47, 1980, pp. 901–907.

2 Rayleigh, J. W. S., *The Theory of Sound*, Dover, New York, Vol. I, 1945, pp. 293–294.

3 Timoshenko, S. P., "On the Correction for Shear of the Differential Equation for Transverse Vibrations of Prismatic Bars," *Philosophical Magazine*, Vol. 41, 1921, pp. 744–746.

4 Timoshenko, S. P., "On the Transverse Vibrations of Bars of Uniform Cross Section," *Philosophical Magazine*, Vol. 43, 1922, pp. 125–131.

5 Goens, E., "Über die Bestimmung des Elastizitatmoduls von Staben mit Hilfe von Beigungsschwingungen," *Annelen Der Physik*, Vol. 11, 1931, pp. 649–678.

6 Davies, R. M., "A Critical Study of the Hopkinson Pressure Bar," *Philosophical Transactions of the Royal Society*, London, Series A, Vol. 24, 1948, pp. 375–457.

7 Mindlin, R. D., and Deresiewicz, H., "Timoshenko Shear Coefficient for Flexural Vibrations of Beams," *Proceedings of 2nd U.S. National Congress of Applied Mechanics*, ASME, New York, 1954, pp. 175–178.

8 Cowper, G. R., "The Shear Coefficient in Timoshenko's Beam Theory," ASME JOURNAL OF APPLIED MECHANICS, 1966, Vol. 33, pp. 335–340.

9 Spence, G. B., and Seldin, E. J., "Sonic Resonances of a Bar and Compound Torsion Oscillator," *Journal of Applied Physics*, Vol. 41, 1970, pp. 3383–3389.

10 Pickett, G., "Flexural Vibration of Unrestrained Cylinders and Disks," *Journal of Applied Physics*, Vol. 16, 1945, pp. 820–831.

11 Stephen, N. G., "On the Variation of Timoshenko's Shear Coefficient With Frequency," ASME JOURNAL OF APPLIED MECHANICS, Vol. 45, 1978, pp. 695–697.

12 Kaneko, T., "On Timoshenko's Correction for Shear in Vibrating Beams," *Journal of Applied Physics*, Vol. 8, 1975, pp. 1927–1936.

13 Aalami, B., and Atzori, B., "Flexural Vibrations and Timoshenko's Beam Theory," *AIAA Journal*, Vol. 12, No. 5, 1974, pp. 679–685.

14 Love, A. E. H., *A Treatise on the Mathematical Theory of Elasticity*, Dover, New York, 1944, pp. 287–291.

15 Tefft, W. E., "Numerical Solution of the Frequency Equations for the Flexural Vibrations of Cylindrical Rods," *Journal of Research*, NBS, Vol. 64B, 1960, pp. 237–242.

16 McMahon, G. W., "Experimental Study of the Vibrations of Solid Isotropic Elastic Cylinders," *Journal of the Acoustical Society of America*, Vol. 36, 1964, pp. 85–92.

17 Young, D., "Continuous Systems," *Handbook of Engineering Mechanics*, ed., Flügge, W., McGraw-Hill, New York, 1962, Section 61, pp. 6–18.

18 Abramson, H. N., "Flexural Waves in Elastic Beams of Circular Cross Section," *Journal of the Acoustical Society of America*, Vol. 29, 1957, pp. 42–46.

19 Spinner, S., Reichard, T. W., and Tefft, W. E., "A Comparison of Experimental and Theoretical Relations Between Young's Modulus and the Flexural and Longitudinal Resonance Frequencies of Uniform Bars," *Journal of Research*, NBS, Vol. 64A, 1960, pp. 147–155.

20 Zemanek, J., Jr., and Rudnick, I., "Attenuation and Dispersion of Elastic Waves in a Cylindrical Bar," *Journal of the Acoustical Society of America*, Vol. 33, 1961, pp. 1283–1288.

Downloaded 01 May 2010 to 171.66.16.249. Redistribution subject to ASME license or copyright; see http://www.asme.org/terms/Terms_Use.cfm

S. H. Crandall
Ford Professor of Engineering,
Department of Mechanical Engineering.
Fellow ASME

J. Dugundji
Professor,
Department of Aeronautics and Astronautics,

Massachusetts Institute of Technology,
Cambridge, Mass. 02139

Resonant Whirling of Aircraft Propeller-Engine Systems

At a critical speed, a light aircraft can experience severe vibrations in steady flight in which the propeller blades vibrate at one frequency while the engine block vibrates at a lower frequency. A model is presented which explains this phenomenon. A three-bladed propeller-engine system is considered to have six rigid-body degrees of freedom plus six blade vibration degrees of freedom. This system is analyzed and simplified by introducing a constraint based on observation of the flight phenomenon. Multiblade coordinates are introduced and a linear eigenvalue problem is derived which describes whirling motions of the engine coupled to progressive waves of blade deformation which circle the propeller disk. These whirling motions are excited by harmonics of the transverse forces on the engine due to the explosive gas pressures in the cylinders. The effects of varying the propeller blade pitch angle are studied and a high-speed instability mechanism is examined.

Introduction

We consider a three-bladed propeller driven at uniform rate of rotation Ω by a six-cylinder, four-stroke cycle, horizontally opposed internal combustion engine as shown in Fig. 1. Torsional vibrations of such systems have been thoroughly investigated and practical procedures for controlling torsional vibrations are routinely employed [1]. We consider here a less common phenomenon: the transverse whirling of the engine block coupled to a whirling pattern of vibration of the propeller blades. In such modes the frequency of the blade vibrations differs from the frequency of engine-block whirling by the frequency Ω of propeller rotation. These modes can be excited by the explosive gas forces in the cylinders when a harmonic of the cyclinder firing frequency (which is $\Omega/2$ in a four-stroke cycle engine) resonates with the natural frequency of whirling. For example, at a particular engine speed Ω_r the third harmonic of the firing frequency could excite a whirling motion of the engine block at frequency $1.5\Omega_r$ accompanied by propeller blade vibrations at frequency $2.5\Omega_r$. The resulting level of vibration can be sufficiently severe as to require restrictions against operation of the aircraft at speed Ω_r.

In order to explain this phenomenon we consider a simplified dynamic model in which the engine with its deformable case, pistons, rods, and crankshaft is represented by a rigid body with mass m_e acted on by exciting forces and torques generated by the small deformations due to the explosive gas forces. The elastic propeller is represented as consisting of three independent blades each having two degrees of freedom. The resulting model has 12 degrees of freedom in addition to the imposed rotation Ω of the propeller: the six degrees of freedom of the rigid engine-block plus the total of six degrees of freedom for the three blades. For simplicity, the center of mass of the engine-block is taken to lie on the axis of the propeller shaft and this axis is taken to be an axis of inertial symmetry of the system; i.e., it is itself a principal axis of inertia and the moments of inertia about all perpendicular axes emanating from a point on it are equal. The weight, torque, and thrust in steady flight are transmitted from the engine to the aircraft by soft rubber mounts. Since the resonant frequencies

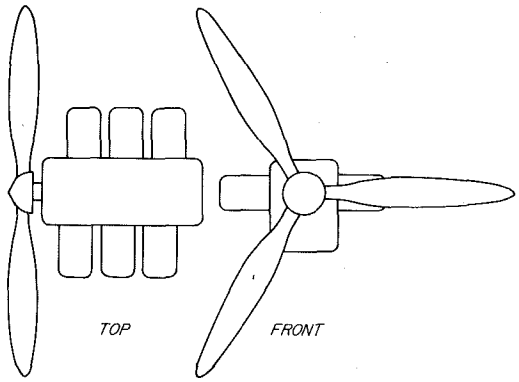


Fig. 1 Propeller-engine system

Contributed by the Applied Mechanics Division for publication in the JOURNAL OF APPLIED MECHANICS.

Discussion on this paper should be addressed to the Editorial Department, ASME, United Engineering Center, 345 East 47th Street, New York, N. Y. 10017, and will be accepted until two months after final publication of the paper itself in the JOURNAL OF APPLIED MECHANICS. Manuscript received by ASME Applied Mechanics Division, March, 1981; final revision, June, 1981.

Copyright © 1981 by ASME

Downloaded 01 May 2010 to 171.66.16.249. Redistribution subject to ASME license or copyright; see http://www.asme.org/terms/Terms_Use.cfm

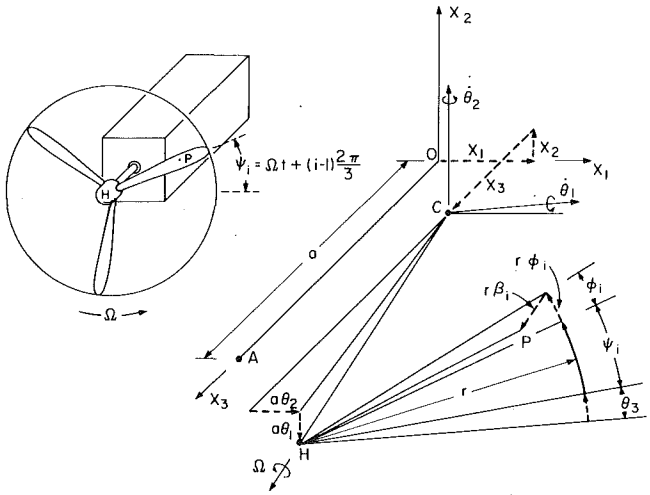


Fig. 2 Generalized coordinates for propeller-engine system are rigid-body displacements x_i and rotations θ_i, plus angular deflections ϕ_i and β_i of the elastically restrained blades

of the mounts are very low in comparison with the whirling frequencies we are interested in, we further simplify our model by removing the mounts, neglecting gravity and all aerodynamic forces, and taking the system to be floating in a gravity-free vacuum environment.

In the following we analyze this model and show that it decomposes into three subsystems: a two-degree-of-freedom longitudinal system, a two-degree-of-freedom torsional system, and an eight-degree-of-freedom transverse system. The system is then further simplified by imposing a particular mode of propeller blade vibration based on observation. This is accomplished by imposing a fixed ratio on the two coordinates of each blade thereby reducing the total number of degrees of freedom by three. The effect on the transverse system is to reduce it to a six-degree-of-freedom system which has three independent whirling modes plus three zero-frequency modes. The nature of the whirling modes is studied in some detail. In particular, the effects of propeller blade pitch angle are examined and the possibilities of resonant excitation by harmonics of the firing frequency are discussed. The results obtained for resonant whirling are qualitatively similar to those obtained previously [2] for a planar model. The addition of the yaw and pitch degrees of freedom do, however, introduce a third whirling mode and an unexpected instability mechanism at high rotational speeds Ω.

Analytical Formulation

Linear equations of motion are derived by Lagrange's method from energies which are correct to second order in the small generalized coordinates. The procedure is essentially straightforward although complicated by the presence of the finite propeller rotation rate Ω and the finite blade rotation angles

$$\psi_i = \Omega t + (i-1)2\pi/3 \tag{1}$$

of the blades $i = 1, 2, 3$. The coordinates used are displayed in Fig. 2. The center of mass of the entire system is at the origin 0 in the reference position. The propeller hub is at A, distance a from the origin, on the axis x_3. A general small rigid-body displacement of the system carries the segment OA into the position CH. The displacement of the mass center has coordinates x_1, x_2, and x_3 where x_1 is transverse horizontal, x_2 is transverse vertical, and x_3 is longitudinal. The rotation of the engine-block is described by the Euler angles θ_1, θ_2, and θ_3 where θ_2 is measured about an axis parallel to x_2, θ_1 is measured about the nodal line (nearly parallel to x_1 when θ_2 is small), and θ_3 is measured about the displaced axis of the propeller. If at $t = 0$ the ith blade makes the angle $(i-1)2\pi/3$ with the x_1-axis, then at time t the angle made by a rigid blade would be $\theta_3 + \psi_i$. We now take the blade to have independent in-plane and out-of-plane elastic deformations. For simplicity we take the deformation to be concentrated in the hub and assume that the blade acts as an elastically restrained rigid pendulum pivoted at the hub. In the plane of the propeller disk the angular displacement is ϕ_i and the elastic restoring torque at the hub is $k_{\text{in}}\,\phi_i$. Normal to this plane the angular displacement is β_i and the elastic restoring torque at the hub is $k_{\text{out}}\beta_i$. The 12 coordinates in addition to the prescribed rotation angles (1) are x_i, θ_i, ϕ_i, β_i $(i = 1, 2, 3)$. For convenience, these are all treated as first-order small quantities although we note that due to Newtonian relativity the final equations of motion should not be affected by the addition of an arbitrary *uniform* linear velocity to the entire system; i.e., the equations should be invariant under a transformation which replaces the x_i by $x_i + V_i t$ where the V_i are constant.

Kinematic analysis of Fig. 2 yields the following velocity components for the point P at radius r on blade i:

$$\begin{aligned}
V_{\text{rad}} &= [\dot{x}_1 + (a + r\beta_i)\dot{\theta}_2 - \dot{x}_3\theta_2]\cos(\theta_3 + \psi_i + \phi_i) \\
&\quad + [\dot{x}_2 - (a + r\beta_i)\dot{\theta}_1 + \dot{x}_3\theta_1]\sin(\theta_3 + \psi_i + \phi_i) \\
V_{\text{tang}} &= [\dot{x}_2 - (a + r\beta_i)\dot{\theta}_1 + \dot{x}_3\theta_1]\cos(\theta_3 + \psi_i + \phi_i) \\
&\quad + r(\dot{\theta}_3 + \Omega + \dot{\phi}_i - \theta_1\dot{\theta}_2)\cos\beta_i \\
&\quad - [\dot{x}_1 + (a + r\beta_i)\dot{\theta}_2 - \dot{x}_3\theta_2]\sin(\theta_3 + \psi_i + \phi_i) \\
V_{\text{axial}} &= \dot{x}_3 + r\dot{\beta}_i + r\dot{\theta}_1\sin(\theta_3 + \psi_i + \phi_i) \\
&\quad - r\dot{\theta}_2\cos(\theta_3 + \psi_i + \phi_i)
\end{aligned} \tag{2}$$

correct to second order in the coordinates and their derivatives. The kinetic energy of the ith blade is obtained by integrating

$$T_i = \int_0^L \tfrac{1}{2} V^2(r)\,dm \tag{3}$$

where V^2 is the sum of the squares of the components (2) and L is the length of the blade. The mass distribution of the blade enters through the parameters

$$m = \int_0^L dm \quad S = \int_m^L r\,dm \quad I = \int_0^L r^2\,dm \tag{4}$$

called the blade mass, static moment, and moment of inertia, respectively. The kinetic energy of the propeller is the sum over i of the expressions (3). In performing this sum it is convenient to note the identities

$$\begin{aligned}
\sum_{i=1}^{3}\sin\psi_i = \sum_{i=1}^{3}\cos\psi_i = \sum_{i=1}^{3}\sin\psi_1\cos\psi_i = 0 \\
\sum_{i=1}^{3}\sin^2\psi_i = \sum_{i=1}^{3}\cos^2\psi_i = \tfrac{3}{2}
\end{aligned} \tag{5}$$

The result, for the kinetic energy of the propeller correct to second order, is

$$\begin{aligned}
T_p &= \tfrac{3}{2}m[(\dot{x}_1 + a\dot{\theta}_2)^2 + (\dot{x}_2 - a\dot{\theta}_1)^2 + \dot{x}_3^2] \\
&\quad + S\sum_i [\dot{x}_3\dot{\beta}_i - (\dot{x}_1 + a\dot{\theta}_2)(\Omega\phi_i\cos\psi_i + \dot{\phi}_i\sin\psi_i) \\
&\quad - (\dot{x}_2 - a\dot{\theta}_1)(\Omega\phi_i\sin\psi_i - \dot{\phi}_i\cos\psi_i)] \\
&\quad + \tfrac{1}{2}I\left[\tfrac{3}{2}(\dot{\theta}_1^2 + \dot{\theta}_2^2) + 3(\dot{\theta}_3 + \Omega - \dot{\theta}_2\theta_1)^2 + \sum_i\{\dot{\phi}_i^2 + \dot{\beta}_i^2 - \Omega^2\beta_i^2\right. \\
&\quad \left. + 2\dot{\beta}_i(\dot{\theta}_1\sin\psi_i - \dot{\theta}_2\cos\psi_i) - 2\Omega\beta_i(\dot{\theta}_1\cos\psi_i + \dot{\theta}_2\sin\psi_i)\}\right]
\end{aligned} \tag{6}$$

Turning next to the engine-block we note that in the reference configuration in Fig. 2 the mass center of the block is located at $(0, 0, -b)$ where

$$m_e b = 3ma \tag{7}$$

Let the centroidal moments of inertia of the block be denoted by I_1, I_2, and I_3 where according to the assumption of inertial symmetry $I_1 = I_2$. The kinetic energy of the engine-block is

Downloaded 01 May 2010 to 171.66.16.249. Redistribution subject to ASME license or copyright; see http://www.asme.org/terms/Terms_Use.cfm

$$T_e = \tfrac{1}{2} m_e[(\dot{x}_1 - b\dot{\theta}_2)^2 + (\dot{x}_2 + b\dot{\theta}_1)^2 + \dot{x}_3^2] + \tfrac{1}{2} I_1(\dot{\theta}_1^2 + \dot{\theta}_2^2) + \tfrac{1}{2} I_3 \dot{\theta}_3^2 \quad (8)$$

The total kinetic energy of the system is the sum of (6) and (8). It is convenient here to introduce the system inertia parameters

$$M = 3m + m_e \quad I_d = 3(\tfrac{1}{2} I + ma^2) + I_1 + m_e b^2 \quad (9)$$

where M is the total mass of the propeller plus engine, and I_d is the diametral moment of inertia of the entire system about any transverse axis through the system center of mass. With the aid of (7) and (9) the total kinetic energy of the system reduces to

$$\begin{aligned} T = {} & \tfrac{1}{2} M(\dot{x}_1^2 + \dot{x}_2^2 + \dot{x}_3^2) + \tfrac{1}{2} I_d(\dot{\theta}_1^2 + \dot{\theta}_2^2) + \tfrac{1}{2} I_3 \dot{\theta}_3^2 \\ & + S \sum_i [\dot{x}_3 \dot{\beta}_i - (\dot{x}_1 + a\dot{\theta}_2)(\Omega\phi_i \cos\psi_i + \dot{\phi}_i \sin\psi_i) \\ & - (\dot{x}_2 - a\dot{\theta}_1)(\Omega\phi_i \sin\psi_i - \dot{\phi}_i \cos\psi_i)] \\ & + \tfrac{1}{2} I \sum_i [(\dot{\theta}_3 + \Omega + \dot{\phi}_i - \dot{\theta}_2\theta_1)^2 + \dot{\beta}_i^2 - \Omega^2\beta_i^2 \\ & - 2\dot{\theta}_i(\Omega\beta_i \cos\psi_i - \dot{\beta}_i \sin\psi_i) \\ & - 2\dot{\theta}_2(\Omega\beta_i \sin\psi_i + \dot{\beta}_i \cos\psi_i)] \quad (10) \end{aligned}$$

The potential energy associated with the elastic restoring torques in the propeller hub is

$$V = \frac{1}{2} \sum_i (k_{\text{in}} \phi_i^2 + k_{\text{out}} \beta_i^2) \quad (11)$$

The excitation resulting from the distortions in the engine-block due to the explosions in the horizontal cylinders is represented by a force $f_1(t)$ acting at the origin parallel to the x_1-axis and a torque $\tau_2(t)$ about the x_2-axis.

Lagrange's equations for the energies (10) and (11) and the generalized forces representing the excitation are 12 coupled linear differential equations. Because of the rotation angles ψ_i in (10) these equations have time-varying coefficients. It is possible to introduce a simple time-varying transformation of coordinates which removes the time-varying coefficients from the energies and leads to differential equations of motion with constant coefficients. In place of the blade deflection angles ϕ_1, ϕ_2, ϕ_3 and β_1, β_2, β_3 we introduce the multiblade coordinates [3] ξ_0, ξ_1, ξ_2 and η_0, η_1, η_2 defined by the transformations

$$\begin{aligned} \{\phi_i\} &= [A]\{\xi_j\} \quad \{\xi_j\} = [A]^{-1}\{\phi_i\} \\ \{\beta_i\} &= [A]\{\eta_j\} \quad \{\eta_j\} = [A]^{-1}\{\beta_i\} \end{aligned} \quad (12)$$

where

$$[A(t)] = \begin{bmatrix} 1 & 1 & 1 \\ -\sin\psi_1 & -\sin\psi_2 & -\sin\psi_3 \\ \cos\psi_1 & \cos\psi_2 & \cos\psi_3 \end{bmatrix}$$

$$[A(t)]^{-1} = \frac{1}{3} \begin{bmatrix} 1 & 1 & 1 \\ -2\sin\psi_1 & -2\sin\psi_2 & -2\sin\psi_3 \\ 2\cos\psi_1 & 2\cos\psi_2 & 2\cos\psi_3 \end{bmatrix} \quad (13)$$

The transformation matrix A varies periodically with time because of the time dependence of the rotation angles ψ_i; see equation (1). The nature of the in-plane multiblade coordinates ξ_j is illustrated in Fig. 3 which shows the blade deformation pattern at two instants of time for unit values of the ξ_j. The coordinate ξ_0 describes a uniform deflection of all three blades. The coordinate ξ_1 describes a time-varying pattern of deflection which always has as its resultant a horizontal (parallel to x_1) displacement of the center of mass of the propeller while the coordinate ξ_2 describes a complementary time-varying pattern of deflection which always has as its resultant a vertical (parallel to x_2) displacement of the center of mass of the propeller. The pattern of deflection due to fixed values of ξ_1 and ξ_2 can be described as a progressive displacement wave moving around the propeller disk with phase velocity Ω in the opposite sense to the rotation. This can be seen by writing the first of (12), for $\xi_0 = 0$, in the form

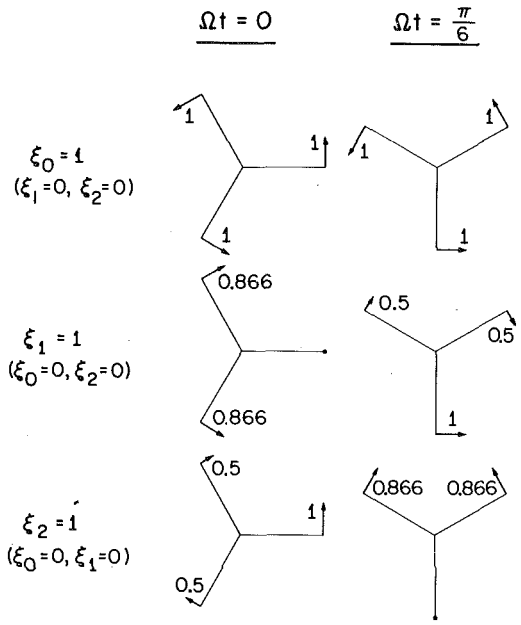


Fig. 3 Pattern of in-plane blade deflections for the multiblade coordinates ξ_0, ξ_1, and ξ_2 at $t = 0$ when $\psi_1 = 0$ and at $t = \pi/(6\Omega)$ when $\psi_1 = \pi/6$

$$\phi_i(t) = -\xi_1 \sin[\Omega t + (i-1)2\pi/3] + \xi_2 \cos[\Omega t + (i-1)2\pi/3] \quad (14)$$

which represents a wave whose phase advances incremently by angles of $2\pi/3$ in space while advancing continuously in time. The wave number is unity and the frequency is Ω. The phase velocity is Ω in the direction of decreasing index i; i.e., opposite to the direction of rotation. Each blade vibrates with amplitude $(\xi_1^2 + \xi_2^2)^{1/2}$ and frequency Ω but is 120° out-of-phase with the others.

When the blade deflection angles ϕ_i and β_i in (10) and (11) are replaced by the multiblade coordinates ξ_j and η_j defined by (12) and (13) the energies T and V are given by the following expressions:

$$\begin{aligned} 2T = {} & M(\dot{x}_1^2 + \dot{x}_2^2 + \dot{x}_3^2) + I_d(\dot{\theta}_1^2 + \dot{\theta}_2^2) + I_3\dot{\theta}_3^2 \\ & + S_p[2\dot{x}_3\dot{\eta}_0 + (\dot{x}_1 + a\dot{\theta}_2)\dot{\xi}_1 + (\dot{x}_2 - a\dot{\theta}_1)\dot{\xi}_2] \\ & + I_p[(\dot{\theta}_3 + \Omega + \dot{\xi}_0 - \dot{\theta}_2\theta_1)^2 + (\dot{\xi}_1^2 + \dot{\xi}_2^2)/2 + \Omega(\dot{\xi}_1\xi_2 - \dot{\xi}_2\xi_1) \\ & + \Omega^2(\xi_1^2 + \xi_2^2)/2 + \dot{\eta}_0^2 + (\dot{\eta}_1^2 + \dot{\eta}_2^2)/2 + \Omega(\dot{\eta}_1\eta_2 - \dot{\eta}_2\eta_1) \\ & - \dot{\theta}_1\dot{\eta}_1 - \dot{\theta}_2\dot{\eta}_2 + 2\Omega(\eta_1\dot{\theta}_2 - \eta_2\dot{\theta}_1) - \Omega^2\eta_0^2] \\ 2V = {} & 3k_{\text{in}}[\xi_0^2 + (\xi_1^2 + \xi_2^2)/2] + 3k_{\text{out}}[\eta_0^2 + (\eta_1^2 + \eta_2^2)/2] \end{aligned} \quad (15)$$

where the propeller parameters

$$S_p = 3S \quad I_p = 3I \quad (16)$$

have been introduced in place of the blade parameters of (4). The time-varying coefficients $\sin\psi_i$ and $\cos\psi_i$ are absent in (15) and the corresponding Lagrange's equations have constant coefficients. At this stage, we do not write out these equations explicitly but simply point out that the 12 equations split into three decoupled subsystems. One subsystem, in x_3 and η_0, describes longitudinal motions parallel to the x_3-axis. A second subsystem, in θ_3 and ξ_0, describes rolling motions about the x_3-axis. The third subsystem with eight degrees of freedom describes transverse motions of the system, x_1 and x_2, with pitch θ_1 and yaw θ_2, coupled to deflections of the propeller blades described by ξ_1 and ξ_2 in the plane of rotation and by η_1 and η_2 normal to that plane.

Here we make a final simplification of the system based on observation of the vibration mode encountered in practice. The propeller

Downloaded 01 May 2010 to 171.66.16.249. Redistribution subject to ASME license or copyright; see http://www.asme.org/terms/Terms_Use.cfm

blade has several natural modes of vibration involving bending and twisting. Although some of these have lower natural frequencies, the mode of vibration which occurs in the whirling resonance considered here involves rigid pendulum motion of the blade, pivoting at the hub, with the direction of motion parallel to the orientation of the blade section near the tip of the blade. As indicated in Fig. 4 the motion of a single blade can be described by a single pendulum angle q_i measured in the plane through the blade section. The angle between this plane and the plane of rotation of the propeller is the blade pitch angle α. In this mode the angles ϕ_i and β_i are locked together as components of the angle q_i

$$\begin{aligned} \phi_i &= q_i \cos \alpha \\ \beta_i &= q_i \sin \alpha \end{aligned} \tag{17}$$

Because of this the multiblade coordinates ξ_j and η_j are also locked together. As a parallel to (12) we introduce a new set of multiblade coordinates ζ_0, ζ_1, ζ_2 where

$$\{q_i\} = [A]\{\zeta_j\} \quad \{\zeta_j\} = [A]^{-1}\{q_i\} \tag{18}$$

from which follows

$$\begin{aligned} \xi_j &= \zeta_j \cos \alpha \\ \eta_j &= \zeta_j \sin \alpha \end{aligned} \tag{19}$$

When these are substituted into the energies of (15) the number of degrees of freedom in the system reduces to nine. Lagrange's equation, correct to first order, split into two decoupled subsystems. One subsystem in x_3, θ_3, ζ_0 describes coupled longitudinal and rotational motions about the x_3-axis by means of the following equations:

$$\begin{aligned} M\ddot{x}_3 + S_p\ddot{\zeta}_0 \cos \alpha &= 0 \\ (I_p + I_3)\ddot{\theta}_3 + I_p\ddot{\zeta}_0 \cos \alpha &= 0 \\ S_p\ddot{x}_3 \cos \alpha + I_p\ddot{\theta}_3 \cos \alpha + I_p[\ddot{\zeta}_0 + (\omega_0^2 + \Omega^2 \sin^2 \alpha)\zeta_0] &= 0 \end{aligned} \tag{18}$$

where ω_0^2, the square of the natural frequency of vibration of a single blade in its pendulum mode when the propeller hub is restrained against motion, is given by

$$\omega_0^2 = \frac{k_{\text{in}} \cos^2 \alpha + k_{\text{out}} \sin^2 \alpha}{I} \tag{19}$$

The other subsystem describes the transverse motion, x_1 and x_2, pitch and yaw, θ_1 and θ_2, and the progressive wave modes of the propeller defined by ζ_1 and ζ_2 by means of equations of motion which can be written in matrix form

$$[M]\{\ddot{X}\} + [G]\{\dot{X}\} + [K]\{X\} = \{F\} \tag{20}$$

with the generalized vector displacement $\{X\}$ and generalized vector excitation $\{F\}$ defined by

$$\begin{aligned} \{X\}^t &= \{x_1, x_2, \theta_1, \theta_2, \zeta_1, \zeta_2\} \\ \{F\}^t &= \{f_1, 0, 0, \tau_2, 0, 0\} \end{aligned} \tag{21}$$

and with the inertia matrix $[M]$, the gyroscopic matrix $[G[$, and the stiffness matrix $[K]$ defined as follows:

$$2[M] = \begin{bmatrix} 2M & 0 & 0 & 0 & S_p \cos \alpha & 0 \\ 0 & 2M & 0 & 0 & 0 & S_p \cos \alpha \\ 0 & 0 & 2I_d & 0 & -I_p \sin \alpha & -a\, S_p \cos \alpha \\ 0 & 0 & 0 & 2I_d & a\, S_p \cos \alpha & -I_p \sin \alpha \\ S_p \cos \alpha & 0 & -I_p \sin \alpha & a\, S_p \cos \alpha & I_p & 0 \\ 0 & S_p \cos \alpha & -a\, S_p \cos \alpha & -I_p \sin \alpha & 0 & I_p \end{bmatrix} \tag{22}$$

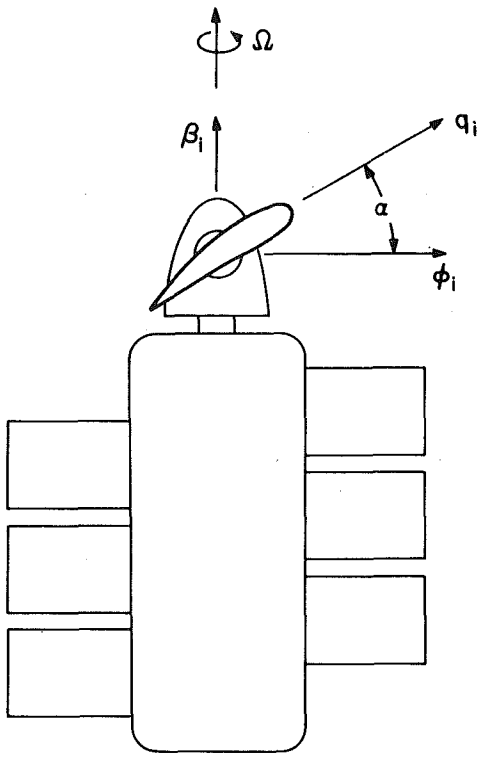


Fig. 4 Replacement of independent in-plane angular deflation ϕ_I and out-of-plane angular deflection β_I by a single angular deflection q_I in the plane making the angle α with the plane of rotation

$$[G] = I_p\Omega \begin{bmatrix} 0 & 0 & 0 & 0 & 0 & 0 \\ 0 & 0 & 0 & 0 & 0 & 0 \\ 0 & 0 & 0 & 1 & 0 & -\sin \alpha \\ 0 & 0 & -1 & 0 & \sin \alpha & 0 \\ 0 & 0 & 0 & -\sin \alpha & 0 & 1 \\ 0 & 0 & \sin \alpha & 0 & -1 & 0 \end{bmatrix} \tag{23}$$

$$2[K] = I_p \begin{bmatrix} 0 & 0 & 0 & 0 & 0 & 0 \\ 0 & 0 & 0 & 0 & 0 & 0 \\ 0 & 0 & 0 & 0 & 0 & 0 \\ 0 & 0 & 0 & 0 & 0 & 0 \\ 0 & 0 & 0 & 0 & \omega_0^2 - \Omega^2 \cos^2 \alpha & 0 \\ 0 & 0 & 0 & 0 & 0 & \omega_0^2 - \Omega^2 \cos^2 \alpha \end{bmatrix} \tag{24}$$

The whirling motions considered here are taken to be described by (20).

Whirling Modes

The natural vibratory motions of the system (20) are solutions of the homogeneous system obtained by temporarily setting $\{F\} = 0$. Because of the inertial and elastic symmetry of the model these natural motions are symmetric whirls of the form

Downloaded 01 May 2010 to 171.66.16.249. Redistribution subject to ASME license or copyright; see http://www.asme.org/terms/Terms_Use.cfm

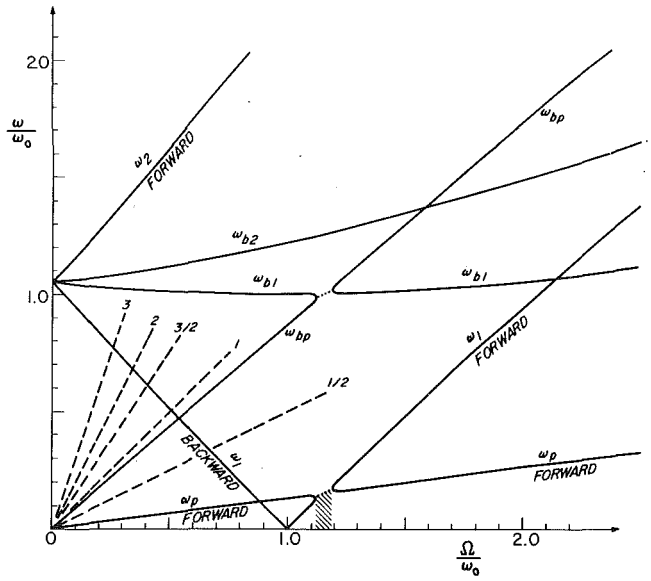


Fig. 5 Whirling frequencies ω_n, ω_2, and ω_p, and corresponding blade vibration frequencies ω_{b1} ω_{b2}, and ω_{bp} for propeller-engine system with parameters (29) and blade angle $\alpha = 0°$; dashed lines show frequencies of engine-order excitation harmonics

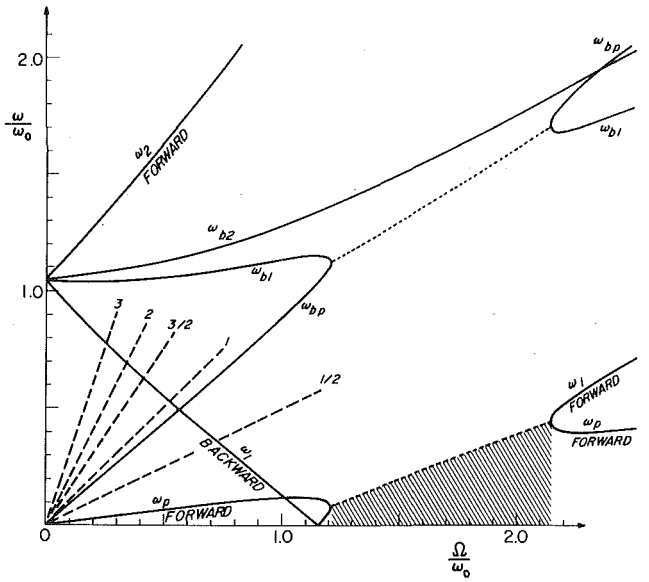


Fig. 6 Same as Fig. 5 except blade angle $\alpha = 30°$

$$\{x_1, x_2, \theta_1, \theta_2, \zeta_1, \zeta_2\}^t = \text{Re}\,[\{x, -ix, \theta, -i\theta, \zeta, -i\zeta\}^t e^{i\omega t}] \quad (25)$$

When (25) is inserted in the homogeneous system an eigenvalue problem is obtained for the whirling frequency ω and the whirling mode $\{x, \theta, \zeta\}^t$. The resulting eigenvalue problem has the Hermitian form

$$\begin{bmatrix} -2M\omega^2 & 0 & -S_p\omega^2\cos\alpha \\ 0 & 2\omega(I_p\Omega - I_d\omega) & I_p(\omega^2 - 2\Omega\omega)\sin\alpha - iaS_p\omega^2\cos\alpha \\ -S_p\omega^2\cos\alpha & I_p(\omega^2 - 2\Omega\omega)\sin\alpha + iaS_p\omega^2\cos\alpha & I_p(\omega_0^2 - \omega^2 + 2\Omega\omega - \Omega^2\cos^2\alpha) \end{bmatrix} \begin{Bmatrix} x \\ \theta \\ \zeta \end{Bmatrix} = 0 \quad (26)$$

The eigensolution depends on the blade angle α and three independent dimensionless parameters

$$R = \frac{2I_d}{I_p} \quad \gamma = \frac{a\,S_p}{I_p} \quad \epsilon = \frac{{S_p}^2}{2MI_p} \quad (27)$$

describing the inertia distribution in the system. For fixed values of α and the parameters (27) there are generally three independent solutions to (26) for each value of the rotation rate Ω. In each solution the system centroid C whirls in a circle of radius x, the propeller axis traces out a conical path with cone angle θ and the multiblade coordinates ζ_1 and ζ_2 whirl with amplitude ζ all in synchronism at the whirling frequency ω. The individual propeller blades vibrate with the angles $q_i(t)$ given by

$$q_i(t) = \zeta \sin\,[(\omega - \Omega)t - (i-1)2\pi/3] \quad (28)$$

which follow from (25), (18), and (12). The pattern of blade vibration is that of a progressive wave of angular displacement advancing around the propeller disk with amplitude ζ and phase velocity $\omega - \Omega$.

The eigensolutions of (26) have been calculated for several blade angles α for the following fixed values of the parameters (27):

$$R = 15 \quad \gamma = 1 \quad \epsilon = 9/320 \quad (29)$$

which are representative of light aircraft installations. The whirling frequencies and blade frequencies are displayed in Figs. 5–9 for blade angles of $\alpha = 0°$, $\alpha = 30°$, $\alpha = 45°$, $\alpha = 60°$, and $\alpha = 90°$. The three whirling frequencies are denoted by ω_1, ω_2, and ω_p. The corresponding blade vibration frequencies are denoted by ω_{b1}, ω_{b2}, and ω_{bp}.

For low rotation rates $\Omega \ll \omega_0$ the modes labeled 1 and 2 are characterized by considerable blade vibration at frequencies near ω_0, the natural frequency of a blade with fixed hub. The mode labeled p has very little blade deformation and resembles very closely the precession mode of a free-floating system consisting of a completely rigid propeller spinning on a rigid engine-block. The precession rate (nutation frequency) of such a system would be $\omega_p = \Omega I_p/I_d$ as can be seen from (26) by setting $\zeta = 0$ and considering the whirling problem for x and θ which remains.

The whirling modes 1 and 2, in which blade vibration is important, derive from the natural modes of the nonrotating system. When $\Omega = 0$, the system has a pair of natural modes which, because of the axial symmetry, have the same natural frequency. These modes involve blade vibration and rocking of the engine block. They may be taken so that there is independent rocking about the yaw and pitch axes or about any other pair of orthogonal diametral axes. Alternatively, they may be taken as independent forward and backward circular whirling motions. Since the inertia of the engine-block is much greater than that of the propeller blades, the repeated natural frequency for $\Omega = 0$ is only slightly greater than ω_0, which can be considered as the limiting natural frequency for the hypothetical case where the inertia of the engine-block is increased without limit. When the propeller is forced to rotate ($\Omega > 0$) the pair of modes with repeated natural frequency at $\Omega = 0$ split into forward and backward circular whirls with unequal whirling frequencies. The mode labeled 1 is a backward whirl and its whirling frequency ω_1 decreases as the rotation rate Ω increases. The mode labeled 2 is a forward whirl and its whirling frequency ω_2 increases as Ω increases. The corresponding blade vibration frequencies $\omega_{b1} = |-\omega_1 - \Omega|$ and $\omega_{b2} = \omega_2 - \Omega$ change slowly with Ω when the blade angle α is zero because there is no centrifugal stiffening for a centrifugal pendulum pivoted at the axis and oscillating in the plane of rotation. As α and the out-of-plane component of vibration increases, centrifugal stiffening causes both ω_{b1} and ω_{b2} to increase with Ω at increasingly rapid rates. This behavior is evident in the sequence of figures from Figs. 5–9.

The nature of the backward-whirl mode is sketched in Fig. 10 for the case where the parameters (27) have the values (29) and the

Downloaded 01 May 2010 to 171.66.16.249. Redistribution subject to ASME license or copyright; see http://www.asme.org/terms/Terms_Use.cfm

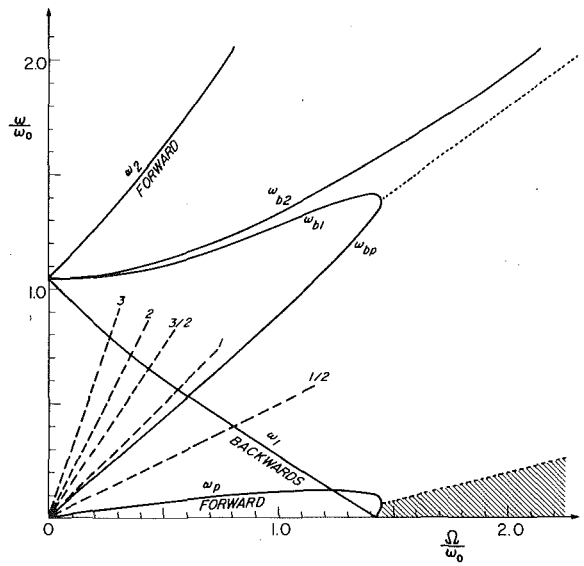


Fig. 7 Same as Fig. 5 except blade angle $\alpha = 45°$

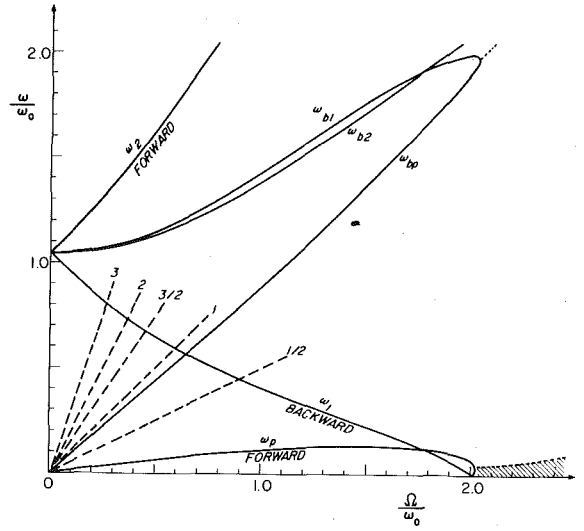


Fig. 8 Same as Fig. 5 except blade angle $\alpha = 60°$

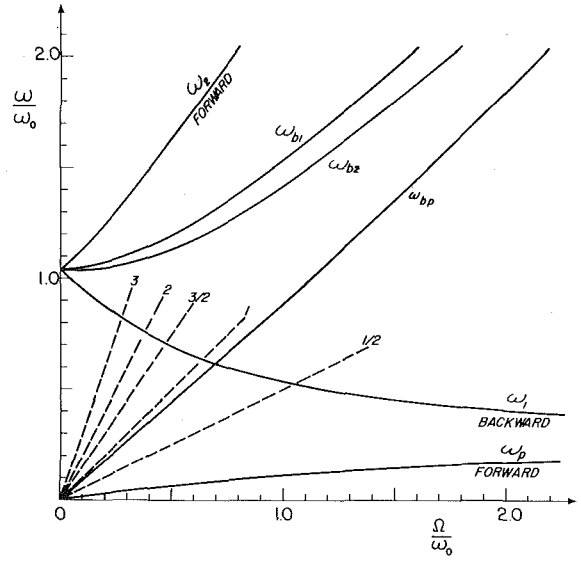


Fig. 9 Same as Fig. 5 except blade angle $\alpha = 90°$

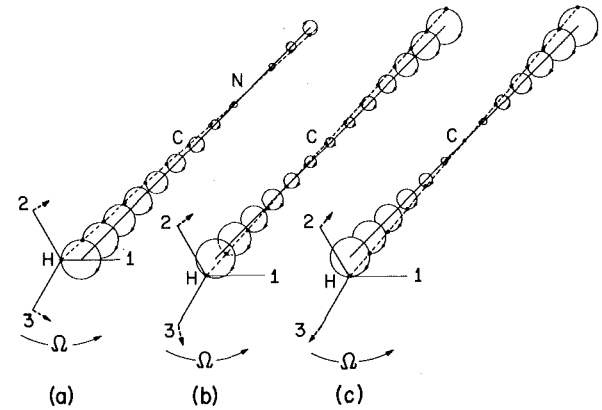


Fig. 10 Backward-whirling mode of propeller-engine system with parameters (29) when $\Omega = \omega_0/2$ and (*a*) $\alpha = 0°$; (*b*) $\alpha = 45°$; (*c*) $\alpha = 90°$

rotation rate is $\Omega = \omega_0/2$. The effects of changing the blade angle α are indicated by the three cases shown: (*a*) $\alpha = 0°$, (*b*) $\alpha = 45°$, and (*c*) $\alpha = 90°$. In (*a*) the propeller axis executes a conical whirl with a node at N. At the instant shown the deflections of blades 2 and 3 in the plane of rotation have shifted the center of mass of the propeller to the right of the hub H. As a consequence the point C, which is the center of mass of the undeformed propeller-engine system, is at the left of its reference position. In (*c*) the deflections of blades 2 and 3 are normal to the plane of rotation giving rise to an angular shift of the propeller inertia. Here the point C remains the system mass center and is the nodal point for the conical whirl of the propeller axis. In (*b*) the blade angle is $\alpha = 45°$ and there are both linear and angular shifts in the propeller inertia. The instantaneous position of the propeller axis is skew with respect to its reference position. All points along it execute circular whirls. There is no nodal point but there is a point, between N and C, which whirls in a circle of minimum radius.

Resonance and Instability

Returning to equation (20) we consider the excitation $\{F\}$ due to the cylinder detonations. With each pressure pulse in a cylinder there is a small deformation of the engine-block, piston, connecting-rod, crank shaft, bearing system. The inertia forces associated with these motions can be taken as dynamic loads on the rigid engine-block model just described. Because of the horizontal orientation of the cylinders it is expected that the important loads of this type will also be horizontal. The time histories of the resultant force $f_1(t)$ and torque $\tau_2(t)$ depend on the structural details of the engine. They will be periodic time functions with fundamental frequency $\Omega/2$ and the strength of the various harmonics will depend on the pressure histories of the individual cylinders and on their firing sequence. The nth harmonic of the horizontal force $f_1(t)$ can be decomposed into a forward-whirling excitation and a backward-whirling excitation with whirling frequencies $\pm n\Omega/2$. The nth harmonic of the torque $\tau_2(t)$ can be decomposed in a similar manner. The resulting excitation is called an excitation of engine-order $n/2$. When applied to the system of equation (20) there will be a backward-whirl resonance if $\omega_1 = n\Omega/2$ and a forward-whirl resonance if $\omega_2 = n\Omega/2$.

In Figs. 5–9, the frequencies of several engine-order excitations are indicated by dashed lines. It can be seen that backward-whirl resonance can occur for all engine-orders in the range of engine speeds from $0 < \Omega < 0.75\ \omega_0$ which corresponds to normal practice provided that the blade angle α is not too large. For blade angles much greater than 30° the resonance with the 1/2 order of fundamental firing frequency can no longer be reached in that speed range but all higher order backward-whirl resonances can be reached for any blade angle α. Forward-whirl resonance can occur in the normal speed range but

Downloaded 01 May 2010 to 171.66.16.249. Redistribution subject to ASME license or copyright; see http://www.asme.org/terms/Terms_Use.cfm

only for the higher orders; i.e., order 3 or higher for most blade angles.

Severe resonances of this type have been observed with backward whirls of engine-order 3/2. From Figs. 5–9 it can be seen that as the blade angle increases from $\alpha = 0°$ to $\alpha = 90°$ the critical engine speed increases from $\Omega = 0.41\omega_0$ to $\Omega = 0.47\omega_0$ while the propeller blade vibration frequency at resonance increases from $\omega_{b1} = 1.02\omega_0$ to $\omega_{b1} = 1.18\omega_0$. In other words, for the parameter values (29), this particular backward-whirl resonance is not very sensitive to variations in the propeller blade pitch angle.

It was previously noted that the propeller blade motion observed in these resonances was essentially that of a rigid pendulum hinged at the hub and oscillating so that the blade section moved in the direction of the blade pitch angle α. We conjecture that the reason this particular mode is involved in strong resonances rather than a blade bending or twisting mode, which involves transverse motion of the blade section, is that blade section vibration parallel to the section chord has smaller aerodynamic damping. In [4] it is shown that minimum damping occurs when the blade section oscillates along the line that bisects the angle between the chord and the average direction of the inlet air flow.

For blade angles in the range $0° \leq \alpha < 90°$ as the engine speed Ω increases the backward-whirl frequency ω_1 decreases to zero and then changes sign to represent a forward whirl. As Ω is increased further ω_1 coalesces with ω_p and an instability range appears. This is represented by the shaded regions in Figs. 5–8. In these speed ranges the linearized undamped model predicts exponential growth of a whirling mode. The nature of the instability is similar to that for helicopter ground resonance [5] where the frequency of a backward-whirl rotor mode decreases to zero, changes sign, and then coalesces with the low frequency of the helicopter vibrating on its flexible undercarriage. A similar phenomena would doubtlessy occur for the propeller-engine system if the model had included the low frequency modes of the engine on its soft rubber mounts. In the present model the low frequency mode is provided by the precession mode which behaves much like the corresponding rigid-system precession except in the range where its blade vibration frequency ω_{bp} comes close to ω_{b1}. For fixed values of the parameters (27) the location of the unstable speed range depends on the blade angle α. In Fig. 5 for $\alpha = 0°$ the unstable range extends from $\Omega_{onset} = 1.13\omega_0$ to $\Omega_{exit} = 1.18\omega_0$. In Fig. 6 for $\alpha = 30°$ the unstable range extends from $\Omega_{onset} = 1.22\omega_0$ to $\Omega_{exit} = 2.14\omega_0$. As α increases both Ω_{onset} and Ω_{exit} increase without limit. First, $\Omega_{exit} \to \infty$ when $\alpha \to 38.8°$, i.e., for blade angles greater than 38.8° stability is not regained at higher speeds. Then $\Omega_{onset} \to \infty$ when $\alpha \to 90°$ so that for large blade angles instability does not begin until the speed Ω is very great and finally, when $\alpha = 90°$, there no longer is instability for any speed.

Conclusions

The simplified propeller-engine model analyzed here provides an explanation of the backward-whirl resonance encountered in some light aircraft. The whirl is excited by a harmonic of the cylinder detonation pulses. The engine-block whirls in a conical mode which is coupled to a progressive wave of blade deformation which circles the propeller disk. The modes and frequencies involved are obtained by solving an eigenvalue problem (26) whose parameters depend on the inertia distribution in the system (27), the blade natural frequency ω_0, the blade pitch angle α, and the speed Ω. The effects on the mode shape and the whirling frequencies due to varying α are displayed in Fig. 10 and Figs. 5–9. The model predicts an unstable range of operating speeds above the speed range of normal operation. Further research is required to give quantitative estimates of the excitation and to include the effects of engine mounts and system damping.

References

1 Den Hartog, J. P., *Mechanical Vibrations*, 4th ed., McGraw-Hill, New York, 1956, pp. 210–224.

2 Crandall, S. H., and Dugundji, J., "Forced Backward Whirling of Aircraft Propeller-Engine Systems," *Proc. 2nd Intl. Conf. Vibns. Rotating Machinery*, Institution of Mechanical Engineers, 1980, pp. 265–270.

3 Hohenemser, K. K., and Yin, S. K., "Some Applications of the Method of Multiblade Coordinates," *Journal of the American Helicopter Society*, Vol. 17, July 1972, pp. 3–12.

4 Peters, D. A., "An Approximate Closed-Form Solution for Lead-Lag Damping of Rotor Blades in Hover," NASA TM X-62,425, Apr. 1975.

5 Coleman, R. P., and Feingold, A. M., "Theory of Self-Excited Mechanical Oscillations of Helicopter Rotors With Hinged Blades, NACA TR 1351, 1958.

Downloaded 01 May 2010 to 171.66.16.249. Redistribution subject to ASME license or copyright; see http://www.asme.org/terms/Terms_Use.cfm

N. C. Huang

Associate Professor,
Department of Aerospace
and Mechanical Engineering,
University of Notre Dame,
Notre Dame, Ind. 46556
Mem. ASME

Mechanics of Ice-Lifting From a Flat Surface Through Penetration With a Sharp Blade[1]

This paper is concerned with the mechanism of ice-lifting from a flat surface through penetration of the interface by means of a sharp blade. We first considered a static case in which the lifted ice was treated as an elastic Timoshenko beam of the cantilever type. The principle of the balance of energy was used in formulating the problem. Our objective was to find the relationship between the applied thrust and the length of the crack at the interface. Special attention has been focused on the instability phenomenon associated with crack propagation. An experimental program has been conducted for comparing the measured critical thrust for instability with the theoretical predictions. The static problem was then generalized to the case of dynamic loading where the sharp blade penetrated the interface through the action of an impact. In the dynamic case, the speed of the blade was found to decrease continuously when time increases. Our interest was to determine the relationship between the applied impulse and the maximum length of the crack generated at the interface.

Introduction

Among existing techniques of ice removal from the surface of a road, the most common and reliable method is the utilization of mechanical tools such as shovels, chisels, spades, or hammers. Blackburn and St. John compared different physical alternatives for highway deicing [1] and concluded that, at present, mechanical methods through the application of steady impact stresses of blade action were still the one with the most technical and operational feasibility and economical and environmental acceptability. In order to design a mechanical tool for ice removal, we need to first understand the mechanism involved in such a process. Two types of failure mode can be expected, namely, the ice-chipping behavior caused by the crack propagation in the ice and the ice-lifting phenomenon due to the crack propagation along the ice-road interface. The study of the first type of failure involves assessing the stress distribution in the ice layer caused by the penetration of the blade. The second type of failure can be investigated by means of a stability analysis. As we shall see later, when the penetration of the blade reaches a certain magnitude, the ice layer can be lifted due to the loss of stability.

Our study will first be focussed on the stability behavior of the lifted ice layer. In the analysis, the lifted ice is treated as a cantilever beam with an increasing length. The deformation of the ice layer is caused by the penetration of a sharp blade under the action of a horizontal thrust. Consequently a separation between the ice layer and the road surface is generated. Our objective is to find the relationship between the applied thrust and the distance of separation.

The Timoshenko beam theory is used in our analysis. With the penetrated distance of the blade as an independent variable, a differential equation can be formulated between the applied thrust and the distance of separation. Another relation between the thrust and the distance of separation can be derived by means of the balance of energy. In our problem, the sum of the work done by the applied force, the frictional force at the interface, and the weight of the lifted ice is equal to the sum of the elastic strain energy due to the deformation of the lifted ice and the surface energy caused by the separation between the ice layer and the road surface. An eigenvalue problem can be formulated for the study of crack propagation along the interface.

An experimental program is set up to compare the measured critical thrust with theoretical predictions. We first measure the surface energy per unit area between the ice and a smooth surface of aluminum alloy, using a procedure proposed by Williams [2] for the experiments of the propagation of a penny-shaped crack bonded to a disk under internal pressure. Once the critical pressure for crack initiation is

[1] This work has been supported by the Department of Transportation, Urban Mass Transportation Administration, under Contract IN-06-0009 titled Cold Weather Transit Technology Program.

Contributed by the Applied Mechanics Division and presented at the Winter Annual Meeting, Washington, D. C., November 15–20, 1981, of THE AMERICAN SOCIETY OF MECHANICAL ENGINEERS.

Discussion on this paper should be addressed to the Editorial Department, ASME, United Engineering Center, 345 East 47th Street, New York, N. Y. 10017, and will be accepted until March 1, 1982. Manuscript received by ASME Applied Mechanics Division, January, 1981; final revision, April, 1981. Paper No. 81-WA/APM-27.

Copyright © 1981 by ASME

Downloaded 01 May 2010 to 171.66.16.249. Redistribution subject to ASME license or copyright; see http://www.asme.org/terms/Terms_Use.cfm

measured, the product of elastic modulus and surface energy can be calculated. A separate experiment is set up for the test of the penetration of a sharp blade into the ice-aluminum alloy interface where the penetrated distance of the blade is measured under different magnitudes of thrust. The maximum thrust can be determined directly from the measured penetration curve. This experiment is then compared to the theory developed in this paper.

The static analysis of ice-lifting has been generalized to a case of dynamic loading where the blade penetrates into the interface through the action of an impact. In the dynamic case, the applied thrust is caused by the inertia force introduced through the change in the speed of the blade. In our formulation, we have neglected the effect of stress propagation in the ice. Our objective is to find the relationship between the applied impulse and the maximum length of the crack at the interface. A numerical method is established for handling this type of fracture problem.

Deflection of the Ice Layer

Let us consider a layer of ice with width b, thickness t bonded to a horizontal flat surface. The ice layer is lifted by a sharp blade with wedge angle α as shown in Fig. 1(a). In the following analysis, we shall regard the ice as a linearly elastic material. Under the action of a horizontal thrust F, the blade penetrates by a distance a into the interface and the tip of the ice is lifted by a distance h. It is evident that

$$h = a \tan \alpha. \tag{1}$$

The ice layer separates from the surface by a distance l. Our objective is to find the relation between l and F.

Note that there is friction between the blade and the surface. Let the angle of friction be ψ. In the case of friction between the ice and the metal blade, the coefficient of friction is approximately 0.1. When the ice is wet, its value is even smaller. In the following, we shall neglect the friction between the blade and the ice. The compressive force P between the blade and the ice is perpendicular to the blade surface. It is

$$P = F \frac{\cos \psi}{\sin (\alpha + \psi)}. \tag{2}$$

The vertical and horizontal components of the force acting on the ice tip are therefore

$$V = P \cos \alpha = F \frac{\cos \alpha \cos \psi}{\sin (\alpha + \psi)}, \tag{3}$$

and

$$H = P \sin \alpha = F \frac{\sin \alpha \cos \psi}{\sin (\alpha + \psi)}. \tag{4}$$

If we consider that the force from the blade is acting at a point on the center line of the ice layer as shown in Fig. 1(b), we need to apply an additional couple M_0 at the end of the ice layer. In the case of a small deformation of the ice layer, this couple is

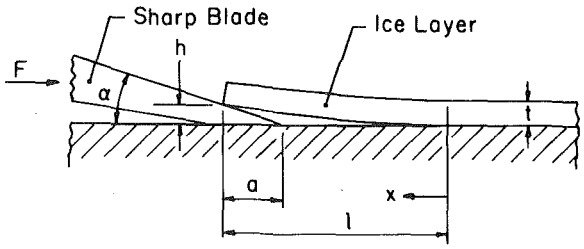
$$M_0 = Ht/2 = \frac{Ft}{2} \frac{\sin \alpha \cos \psi}{\sin (\alpha + \psi)}. \tag{5}$$

In our analysis, we shall assume the flat surface as rigid and treat the lifted ice as a slightly deformed Timoshenko beam of the cantilever type. Let ρ be the density of the ice, E the modulus of elasticity, and ν Poisson's ratio. The shear modulus of the ice is $G = \frac{1}{2}E/(1 + \nu)$ and the bending rigidity of the ice layer is $EI = Ebt^3/12$. Let us set the origin of a horizontal axis $x = 0$ at the point where separation between the ice and the surface initiates as shown in Fig. 1(a). The shear force and the bending moment at any point of the lifted ice is

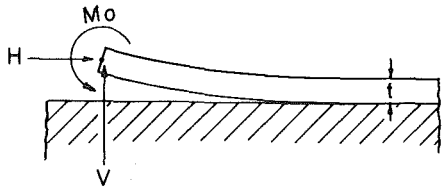
$$S(x) = V - \rho bt(l - x) \tag{6}$$

and

$$M(x) = V(l - x) - M_0 - \tfrac{1}{2} \rho bt(l - x)^2, \tag{7}$$



(a) Geometry of the problem



(b) Forces and moment acting on the ice layer

Fig. 1 Lifting of an ice layer by a sharp blade

Nomenclature

a = penetration
b = width of the ice layer
E = modulus of elasticity of the ice
F = horizontal thrust
F_f = friction
F_1 = effective applied force
f = equation (25)
G = shear modulus of the ice
g = gravitation constant
H = horizontal force acting on ice
h = lift at the end of the ice layer
I = moment of inertia about the centroidal axis of the cross section
l = distance of separation between the ice and the flat surface
l_0 = initial crack length
M = bending moment
M_0 = end moment acting on the ice layer
P = compression between the blade and the ice
S = shear force
T = surface energy per unit area
t = thickness of the ice
t_0 = time
U_1 = elastic strain energy
U_2 = surface energy
V_b = velocity of the blade
v = deflection of the ice
v_a = deflection due to bending
v_b = equation (42)
v_s = deflection due to shear
W_1 = work done by the effective applied force
W_2 = work done by the weight of the ice
W_3 = work done by the end moment
W_b = weight of the blade
x = horizontal distance
α = blade angle
β = equation (25)
β_c = critical value of β
γ = equation (25)
γ_0 = equation (25)
γ_1 = shear strain
λ = equation (25)
μ = equation (25)
ν = Poisson's ratio of the ice
ρ = density of the ice
σ_b = maximum tensile stress
σ_s = maximum shear stress
τ = equation (42)
τ_b = equation (37)
τ_s = equation (37)
ψ = angle of friction

Downloaded 01 May 2010 to 171.66.16.249. Redistribution subject to ASME license or copyright; see http://www.asme.org/terms/Terms_Use.cfm

respectively. The upward deflection at any point due to bending is

$$v_a(x) = \frac{1}{6EI} Vx^2(3l - x) - \frac{1}{2EI} M_0 x - \frac{1}{24EI} \rho btx^2(6l^2 - 4lx + x^2). \quad (8)$$

The maximum shear strain occurs at the neutral plane of the beam. It is

$$\gamma_1 = 3S/(2btG). \quad (9)$$

The deflection at any point due to shear deformation is

$$v_s(x) = \int_0^x \gamma_1 dx = \frac{3Vx}{2btG} - \frac{3\rho}{2G}\left(lx - \frac{x^2}{2}\right). \quad (10)$$

Thus the total deflection is

$$v(x) = v_a(x) + v_s(x) = \frac{1}{6EI} Vx^2(3l - x) - \frac{1}{2EI} M_0 x^2 - \frac{1}{24EI} \rho btx^2(6l^2 - 4lx + x^2) + \frac{2Vx}{3btG} - \frac{3\rho}{2G}\left(lx - \frac{x^2}{2}\right). \quad (11)$$

The horizontal displacement of the blade is found from equation (1) as

$$a = v(l)\cot\alpha = \frac{1}{3EI} Fl^3 \frac{\cos\alpha\cot\alpha\cos\psi}{\sin(\alpha+\psi)} - \frac{1}{4EI} Fl^2 t \frac{\cos\alpha\cos\psi}{\sin(\alpha+\psi)} - \frac{1}{8EI}\rho btl^4\cot\alpha + \frac{3Fl}{2btG}\frac{\cos\alpha\cot\alpha\cos\psi}{\sin(\alpha+\psi)} - \frac{3\rho l^2}{4G}\cot\alpha. \quad (12)$$

In the following, we shall regard a as a parameter and consider F and l as functions of a. The differential form of equation (12) is

$$\left[\frac{1}{3EI} l^3 \frac{\cos\alpha\cot\alpha\cos\psi}{\sin(\alpha+\psi)} - \frac{1}{4EI} l^2 t \frac{\cos\alpha\cos\psi}{\sin(\alpha+\psi)} + \frac{3l}{2btG}\frac{\cos\alpha\cot\alpha\cos\psi}{\sin(\alpha+\psi)}\right]\delta F + \left[\frac{1}{EI} Fl^2 \frac{\cos\alpha\cot\alpha\cos\psi}{\sin(\alpha+\psi)} - \frac{1}{2EI} Flt \frac{\cos\alpha\cos\psi}{\sin(\alpha+\psi)} - \frac{1}{2EI}\rho btl^3\cot\alpha + \frac{3F}{2btG}\frac{\cos\alpha\cot\alpha\cos\psi}{\sin(\alpha+\psi)} - \frac{3\rho l}{2G}\cot\alpha\right]\delta l = \delta a. \quad (13)$$

In order to obtain solutions for δF and δl, we need an additional equation which can be derived by considering the balance of energy.

Balance of Energy

The concept of the balance of energy was first employed by Griffith in the study of crack propagation in an infinite elastic plate [3]. This concept has been extended later in the investigation of the propagation of cracks of different shapes [2, 4]. The balance of energy has also been generalized to include the effects of plastic deformation in the vicinity of the crack [5, 6] and kinetic energy associated with crack propagation [7].

In order to apply the principle of the balance of energy to our problem, let us consider an effective applied force F_1 as the difference between the applied force F and the friction acting on the blade at the interface F_f, i.e.,

$$F_1 = F - F_f = F\frac{\cos\psi\sin\alpha}{\sin(\alpha+\psi)}. \quad (14)$$

The work done by the effective applied force through displacement a is

$$W_1 = \int_0^a F_1 da = \frac{\cos\psi\sin\alpha}{\sin(\alpha+\psi)}\int_0^a F da. \quad (15)$$

The work done by the weight of the ice is negative. It is

$$W_2 = -\int_0^l \rho btv(x)dx. \quad (16)$$

Substituting equation (11) with equation (16) and using equations (2), (3), and (8), we obtain

$$W_2 = -\frac{1}{8EI}\rho btl^4 F\frac{\cos\alpha\cos\psi}{\sin(\alpha+\psi)} + \frac{1}{12EI}\rho bt^2 l^3 F\frac{\sin\alpha\cos\psi}{\sin(\alpha+\psi)} + \frac{1}{20EI}\rho^2 b^2 t^2 l^5 - \frac{3\rho Fl^2}{4G}\frac{\cos\alpha\cos\psi}{\sin(\alpha+\psi)} + \frac{1}{2G}\rho^2 btl^3. \quad (17)$$

The work done by the end moment M_0 through the rotation of the cantilever introduced by the thrust is

$$W_3 = -\frac{1}{4EI} M_0 Vl^2 + \frac{1}{2EI} M_0^2 l = -\frac{1}{8EI} F^2 tl^2 \frac{\sin\alpha\cos\alpha\cos^2\psi}{\sin^2(\alpha+\psi)} + \frac{1}{8EI} F^2 t^2 l \frac{\sin^2\alpha\cos^2\psi}{\sin^2(\alpha+\psi)} \quad (18)$$

The elastic strain energy associated with the bending and shear deformation of the lifted ice is

$$U_1 = \frac{1}{2EI}\int_0^l M^2 dx + \frac{3}{4AG}\int_0^l S^2 dx, \quad (19)$$

where A is the cross-sectional area of the ice layer. Substituting equations (6) and (7) into equation (19) and using equations (2), (3), and (5), we obtain

$$U_1 = \frac{1}{EI}\left[\frac{1}{6}F^2 l^3 \frac{\cos^2\alpha\cos^2\psi}{\sin^2(\alpha+\psi)} + \frac{1}{8}F^2 t^2 l\frac{\sin^2\alpha\cos^2\psi}{\sin^2(\alpha+\psi)} + \frac{1}{40}\rho^2 b^2 t^2 l^5 - \frac{1}{4}F^2 tl^2\frac{\sin\alpha\cos\alpha\cos^2\psi}{\sin^2(\alpha+\psi)} - \frac{1}{8}F\rho btl^4\frac{\cos\alpha\cos\psi}{\sin(\alpha+\psi)} + \frac{1}{12}F\rho bt^2 l^3\frac{\sin\alpha\cos\psi}{\sin(\alpha+\psi)}\right] + \frac{3}{4btG}\left[F^2 l\frac{\cos^2\alpha\cos^2\psi}{\sin^2(\alpha+\psi)} - \rho btFl^2\frac{\cos\alpha\cos\psi}{\sin(\alpha+\psi)} + \frac{1}{3}\rho^2 b^2 t^2 l^3\right]. \quad (20)$$

The energy required for breaking the molecular bond between the ice and the surface is assumed to be proportional to the area of separation. Let the surface energy required for separating a unit area of ice from the surface be T. In the following, we shall assume that there is an initial crack of length l_0 between the ice and the surface caused by the application of pressure to the ice through the tip of the blade. The melting point of the ice can be reduced by the applied pressure resulting in an initial penetration of the tip of the blade into the melted ice. The total surface energy for separating the ice from the surface by a distance $l - l_0$ is

$$U_2 = Tb(l - l_0). \quad (21)$$

We shall first consider the ice-lifting action as quasi-static and disregard the effect of kinetic energy. We have the following equation of the balance of energy

$$W_1 + W_2 + W_3 - U_1 - U_2 = 0. \quad (22)$$

The differential form of equation (22) reads

Downloaded 01 May 2010 to 171.66.16.249. Redistribution subject to ASME license or copyright; see http://www.asme.org/terms/Terms_Use.cfm

$$\left[-\frac{1}{3EI}Fl^3\frac{\cos^2\alpha\cos^2\psi}{\sin^2(\alpha+\psi)}+\frac{1}{4EI}Ftl^2\frac{\sin\alpha\cos\alpha\cos^2\psi}{\sin^2(\alpha+\psi)}-\frac{3}{2btG}Fl\frac{\cos^2\alpha\cos^2\psi}{\sin^2(\alpha+\psi)}\right]\delta F$$
$$+\left[\frac{1}{8EI}\rho^2b^2t^2l^4-\frac{1}{2EI}F^2l^2\frac{\cos^2\alpha\cos^2\psi}{\sin^2(\alpha+\psi)}+\frac{1}{4EI}F^2tl\frac{\sin\alpha\cos\alpha\cos^2\psi}{\sin^2(\alpha+\psi)}+\frac{3}{4G}\rho^2btl^2-\frac{3}{4btG}F^2\frac{\cos^2\alpha\cos^2\psi}{\sin^2(\alpha+\psi)}-Tb\right]\delta l+F\frac{\cos\psi\sin\alpha}{\sin(\alpha+\psi)}\delta a=0. \quad (23)$$

The initial condition is that

$$l=l_0 \quad \text{when} \quad F=0. \quad (24)$$

Equations (13), (23), and (24) are the governing equations for the deformation of the ice layer caused by the penetration of the blade.

Governing Equations

Let us first introduce the following dimensionless quantities:

$$\mu=(1+\nu)\cot^2\alpha,\quad f=\frac{F\cos\alpha\cot\alpha\cos\psi}{\rho bt^2\sin(\alpha+\psi)},$$
$$\lambda=\frac{2EIT\cot^4\alpha}{\rho^2bt^6}=\frac{ET\cot^4\alpha}{6\rho^2t^3},$$
$$\gamma=\frac{l\cot\alpha}{t},\quad \gamma_0=\frac{l_0\cot\alpha}{t},\quad \beta=\frac{EIa\cot^3\alpha}{\rho bt^5}=\frac{Ea\cot^3\alpha}{12\rho t^2}. \quad (25)$$

Equations (13), (23), and (24) can be expressed in terms of the dimensionless quantities as

$$\delta\beta=\frac{1}{12}[\gamma(4\gamma^2-3\gamma+3\mu)\delta f+3(4f\gamma^2-2f\gamma-2\gamma^3+\mu f-\mu\gamma)\delta\gamma], \quad (26)$$

$$\delta\beta=\frac{1}{24f}[2f\gamma(4\gamma^2-3\gamma+3\mu)\delta f-3(\gamma^4-4f^2\gamma^2+2f^2\gamma+\mu\gamma^2-\mu f^2-4\lambda)\delta\gamma] \quad (27)$$

and

$$\gamma=\gamma_0 \quad \text{when} \quad f=0. \quad (28)$$

Equations (26) and (27) can be combined as

$$[f^2(4\gamma^2-2\gamma+\mu)-2f\gamma(\mu+2\gamma^2)+\gamma^4+\mu\gamma^2-4\lambda]\delta\gamma=0. \quad (29)$$

We have either

$$\delta\gamma=0, \quad (30)$$

or

$$f^2(4\gamma^2-2\gamma+\mu)-2f\gamma(\mu+2\gamma^2)+\gamma^4+\mu\gamma^2-4\lambda=0. \quad (31)$$

Equation (30) corresponds to the case of no crack propagation. From equation (31), we find the $f-\gamma$ relation for a propagating crack as

$$f=\frac{\gamma(\mu+2\gamma^2)+[\gamma^2(\mu+2\gamma^2)^2-(4\gamma^2-2\gamma+\mu)(\gamma^4+\mu\gamma^2-4\lambda)]^{1/2}}{4\gamma^2-2\gamma+\mu}. \quad (32)$$

Thus, for given γ_0, we can find the critical value f_c for crack propagation. When $f<f_c$, the blade simply penetrates into the initial crack without introducing any crack propagation. In general, the penetration is related to the thrust by equation (12) which can be expressed in a dimensionless form as

$$\beta=\frac{\gamma}{24}[\gamma(8f\gamma-6f-3\gamma^2)+3\mu(2f-\gamma)]. \quad (33)$$

Before crack propagation, we set $\gamma=\gamma_0$ in equation (33) and find the relation between f and γ. After crack propagation, the $f-\beta$ relation is given by equations (32) and (33) where γ is regarded as a parameter.

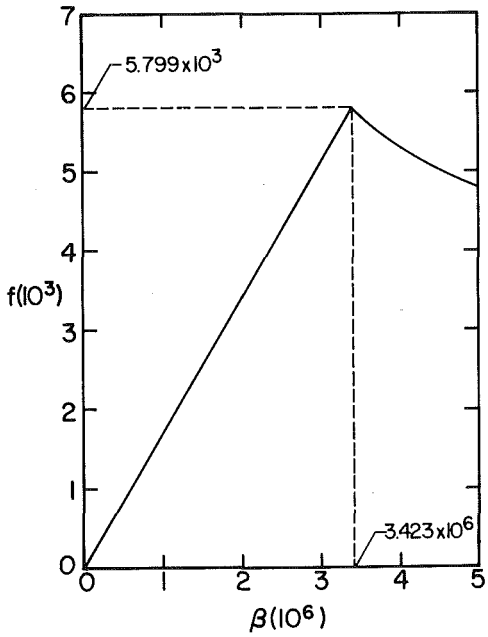


Fig. 2 f versus β curve for $\mu = 48.25$, $\gamma_0 = 11.34$, $\lambda = 4.529 \times 10^9$

Numerical Solution

In the numerical computation and experimental measurements, we are working with an ice layer of width $b = 1$ in. (25.4 mm) and thickness $t = \frac{1}{4}$ in. (6.35 mm) and length 4 in. (101.6 mm) bonded to a smooth surface of aluminum alloy. The ice layer is lifted by penetrating the interface with a sharp blade made of aluminum alloy with wedge angle of 10°. Our experiments are performed at a temperature of 20°F (−6.7°C). The angle of friction between the blade and the flat surface is measured by a sliding test at the same temperature. It is found that the angle of friction is $\psi = 14°$. The surface energy between the ice and aluminum alloy is measured by a method similar to the one used by Williams for the measurement of surface energy between polyurethane rubber and glass [2]. The apparatus for the surface energy measurement was designed by Prof. L. H. N. Lee at the University of Notre Dame. It consists of a circular disk of radius 3 in. (76.2 mm) and thickness $\frac{1}{2}$ in. (12.7 mm) with a central hole which is covered by a thin layer of wax of radius $\frac{3}{8}$ in. (9.55 mm). A layer of ice is manufactured on the surface of the disk with an initial penny-shaped crack produced by the covered wax. An internal pressure is applied gradually through the central hole under the initial crack. When the internal pressure reaches a critical value, the crack propagates in the radial direction. It is noted that fracture in the ice occurs immediately after the crack propagation. The surface energy per unit area between the ice and the disk can be determined from the critical pressure for crack propagation. Due to a lack of data, we shall assume that Poisson's ratio of the ice is $\nu = 0.5$. It is found that $ET = 453$ lb²/in.³ (547 N²/cm³) for ice bonded to the surface of the aluminum alloy. The surface energies for the ice bonded on copper and bonded on stainless steel were measured by Lee and found to be in the same range as that of ice bonded on aluminum alloy.

We shall consider the specific weight of the ice as 0.92 and the initial

Downloaded 01 May 2010 to 171.66.16.249. Redistribution subject to ASME license or copyright; see http://www.asme.org/terms/Terms_Use.cfm

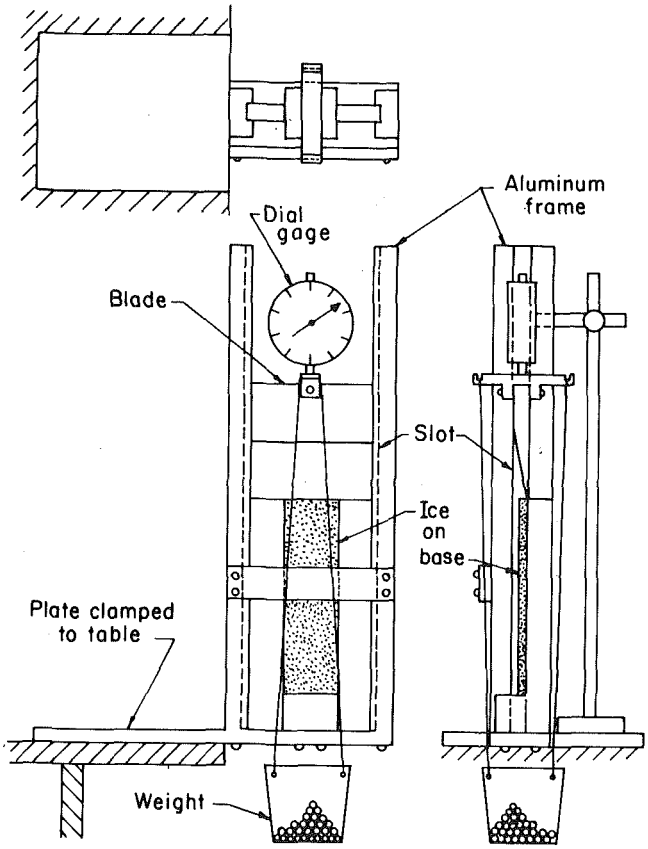


Fig. 3 Penetration test on ice-aluminum interface

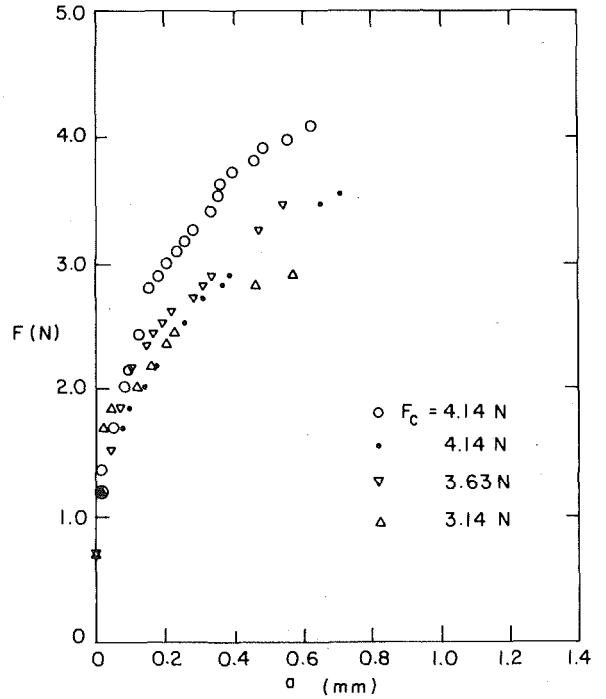


Fig. 4 Measured force versus blade penetration curve for $b = 25.4$ mm, $\tau = 6.35$ mm, $\alpha = 10°$, $\psi = 14°$, and $l_0 = 12.7$ mm

length of the crack in the penetration test as $l_0 = \frac{1}{2}$ in. (12.7 mm). We have the following geometrical and physical constants for our numerical computation: $\mu = 48.25$, $\gamma_0 = 11.34$, $\lambda = 4.529 \times 10^9$.

In Fig. 2, we plot f versus β for $\mu = 48.25$, $\gamma_0 = 11.34$, and $\lambda = 4.529 \times 10^9$. It is found that the critical thrust for bifurcation is $f_c = 5799$ which corresponds to $F_c = 0.904$ lb. (4.02 N). The critical value of β is $\beta_c = 3.423 \times 10^6$. When $\beta > \beta_c$, f decreases with increasing β. Hence the critical load for crack propagation is also the maximum load. Once the crack propagates, the lifted ice is unstable and the crack will continue to propagate indefinitely along its interface. This type of instability associated with crack propagation is similar to the behavior of propagation of a penny-shaped crack at the center of the interface of a circular thin plate bonded to a solid base caused by internal pressure [2].

Fracture of Ice

During the ice-lifting process, fracture may occur as a result of excessive stress due to bending or shear action. The maximum bending moment occurs at $x = 0$. It is

$$M_{\max} = Vl - M_0 - \tfrac{1}{2}\rho b t l^2. \tag{34}$$

The maximum tensile stress in the ice due to the combined action of bending and direct compression is

$$\sigma_b = \frac{6M_{\max}}{bt^2} - \frac{H}{bt} = \frac{2F\cos\psi}{bt^2\sin(\alpha+\psi)}(3l\cos\alpha - 2t\sin\alpha) - \frac{3\rho l^2}{t}. \tag{35}$$

The maximum shear stress occurs at the end of the ice layer. It is approximately equal to

$$\sigma_s = \frac{3V}{2bt} = \frac{3F}{2bt}\frac{\cos\alpha\cos\psi}{\sin(\alpha+\psi)}. \tag{36}$$

Let us introduce the following dimensionless quantities:

$$\tau_b = \frac{\sigma_b}{\rho t}\cot^2\alpha, \quad \tau_s = \frac{\sigma_s}{\rho t}\cot\alpha. \tag{37}$$

Equation (36) and (37) can be expressed as

$$\tau_b = 2f(3\gamma - 2) - 3\gamma^2 \tag{38}$$

and

$$\tau_s = 1.5f. \tag{39}$$

When the value of τ_b or τ_s exceeds the critical value, fracture will be introduced. It is seen that in order to enlarge the size of the ice chip, we must have smaller values of f/τ_b and f/τ_s. In either case, the value of F after instability occurs must be kept as small as possible. This condition can perhaps be obtained by the installation of an elastic spring to the blade where the thrust is applied through the spring.

Penetration Experiments

The penetration experiments were performed in a cold chamber with controlled temperature. A 10° aluminum alloy blade was penetrated vertically into the ice aluminum alloy interface by gradually increasing the weight applied to the blade as shown in Fig. 3. The motion of the blade was guided by two vertical slots. The displacement was measured by a dial gage. The dimensions of the ice layer and the physical properties of the ice are given in the foregoing section. An initial crack of length $\frac{1}{2}$ in. (12.7 mm) was generated at the interface by a thin layer of vaseline applied at the end of the surface. To minimize the diffusion of vaseline into the water before ice formation, the base upon which the ice was formed was precooled to 18°F (−7.8°C) and the water was precooled to 33°F (0.6°C). Thus the water froze immediately after it made contact with the metal surface.

It is well known that ice exhibits viscoelastic properties. Under a given thrust, the ice layer would deform gradually with time. In our test, we increased the thrust after the blade ceased to penetrate. The thrust versus penetration curve is shown in Fig. 4. As the thrust reached a maximum value, the crack propagated violently and fracture of the ice followed. The measured critical thrust was found to vary from 0.710 lb (3.14 N) to 0.935 lb (4.14 N). The theoretical value

Downloaded 01 May 2010 to 171.66.16.249. Redistribution subject to ASME license or copyright; see http://www.asme.org/terms/Terms_Use.cfm

showed $F = 0.904$ lb (4.02 N). The size of ice chip varied from $1\frac{1}{2}$ in. (38.1 mm) to 4 in. (101.6 mm).

Dynamic Theory of Ice-Lifting

In the following, we shall generalize the static theory of ice-lifting to the case of dynamic loading. The blade in this case has an initial velocity due to the application of an impulsive load. Let us denote the weight of the blade by W_b which is assumed to be small in comparison with the contact force between the ice and the blade. Again, we assume that there exists an initial crack of length l_0 at the interface. The zero time $t_0 = 0$ is set at the instant of the application of the impulsive load. The velocity of the blade is

$$V_b = da/dt_0, \tag{40}$$

and the initial velocity is $V_b(0) = V_0$. The inertia force of the blade is

$$F = -\frac{W_b}{g}\frac{d^2a}{dt_0{}^2}, \tag{41}$$

where g is the gravitation constant. Note that with F defined by equation (41), W_1 in equation (15) would be the negative of the sum of the change in kinetic energy of the blade and the work done by friction. In our analysis, we shall neglect the effect of stress wave propagation in the ice. Hence the effect of the deformation of the ice on the motion of the blade is analogous to a nonlinear spring. The deformation of the ice is generated by the inertia force F of equation (41) and is governed by equations (24) and (29).

Let us introduce the following dimensionless quantities:

$$\tau = \left[\frac{EIg\cot^2\alpha\sin(\alpha+\psi)}{W_b t^3\cos\alpha\cos\psi}\right]^{1/2}$$

$$t_0 = \left[\frac{gEb\cot^2\alpha\sin(\alpha+\psi)}{12W_b\cos\alpha\cos\psi}\right]^{1/2} t_0,$$

$$v_b = \left[\frac{EW_b\cot^4\alpha\cos\alpha\cos\psi}{12\rho^2t^4gb\sin(\alpha+\psi)}\right]^{1/2} V_b. \tag{42}$$

Equations (40) and (41) can be written as

$$v_b = d\beta/d\tau, \tag{43}$$

$$f = -d^2\beta/d\tau^2. \tag{44}$$

At $\tau = 0$, we have the following initial conditions:

$$\beta(0) = f(0) = 0, \quad \gamma(0) = \gamma_0 \quad \text{and} \quad v_b(0) = v_0, \tag{45}$$

where v_0 is related to V_0 by a relation identical to that given in equation (42). When τ is sufficiently small, there is no crack propagation. Hence $\delta\gamma = 0$ and β is related to f by equation (33). If the magnitude of the initial velocity of the blade is sufficiently large, the initial crack can propagate as f reaches a critical value. During the crack propagation f is related to γ by equation (32).

In the following, we shall establish a numerical scheme for the solution of our initial value problem. Let $\delta\tau$ be any time increment. Utilizing Taylor's expansion, we can express $\delta\beta$ approximately as

$$\delta\beta = \frac{d\beta}{d\tau}\delta\tau + \frac{1}{2}\frac{d^2\beta}{d\tau^2}(\delta\tau)^2. \tag{46}$$

With $d\beta/d\tau$ and $d^2\beta/d\tau^2$ given by equations (43) and (44), we have

$$\delta\beta = v_b\delta\tau - \tfrac{1}{2}f(\delta\tau)^2. \tag{47}$$

From equation (47), we can solve for $\delta\tau$ as

$$\delta\tau = \frac{1}{f}[v_b - (v_b{}^2 - 2f\delta\beta)^{1/2}]. \tag{48}$$

Note that equation (48) cannot be used for the computation of the first time increment because $f(0) = 0$. In this case, we can employ

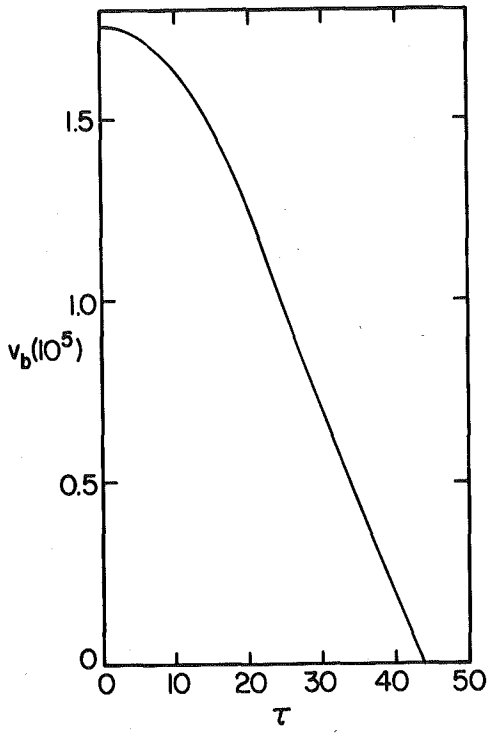


Fig. 5 v_b versus τ curve for $\mu = 48.25$, $\gamma_0 = 11.34$, $\lambda = 4.529 \times 10^9$, and $v_0 = 1.75 \times 10^5$

$$\delta\tau = \frac{1}{v_b}\delta\beta \tag{49}$$

as the approximation of the first time increment. From equations (43) and (44), we have

$$\frac{dv_b}{d\tau} = -f, \tag{50}$$

which leads to

$$\delta v_b = -f\delta\tau. \tag{51}$$

The numerical procedure can be described as follows: For given values of μ, λ, γ_0, and v_0, we first assign values for f which do not exceed the critical value of f for bifurcation as given by equation (32). We then compute β from equation (33), $\delta\tau$ from equation (48) or equation (49) and δv_b from equation (51). The new values of τ and v_b are $\tau + \delta\tau$ and $v_b + \delta v_b$, respectively. Since there is no crack propagation under these values of f, γ remains constant in each step. If v_0 is sufficiently large, there would be crack propagation as f reaches the value for bifurcation. After the point of bifurcation is reached, we assign values for γ and determine $f, \beta, \delta\tau$, and δv_b from equations (32), (33), (48) (or (49)) and (51), respectively. Again the new values of τ and v_b are $\tau + \delta\tau$ and $v_b + \delta v_b$, respectively. This incremental numerical procedure continues until v_b changes its sign. Since the increment in f is prescribed before bifurcation and the increment in γ is prescribed after bifurcation, it is impossible for us to find a real value for $\delta\tau$ in the neighborhood of $v_b = 0$. Thus, in the computation process, we decrease the increment whenever this situation occurs.

In Fig. 5, the speed of the blade versus time is plotted for $\mu = 42.85$, $\gamma_0 = 11.34$, $\lambda = 4.529 \times 10^9$, and $v_0 = 1.75 \times 10^5$. It is seen that the speed of the blade decreases continuously with increasing time. At $\tau = 19.7$, the crack begins to propagate and at $\tau = 43.9$, $v_b = 0$. The maximum length of the crack is found to be $\gamma_{max} = 13.52$. For $\tau > 43.9$, the frictional force will prevent the blade from moving backward. It is found that when the initial speed of the blade is sufficiently small, the motion of the blade can stop without introducing any crack propagation. The critical initial velocity for dynamic crack propagation is $v_c = 133{,}000$ which corresponds to $V_0 = 2.925$ in./s (7.43 cm/s)

Downloaded 01 May 2010 to 171.66.16.249. Redistribution subject to ASME license or copyright; see http://www.asme.org/terms/Terms_Use.cfm

for $W_b = 0.05$ lb (22.7 gm), and $E = 3.40 \times 10^5$ psi (2.34×10^6 kPa). In Fig. 6, the maximum growth of crack length is plotted against the initial blade velocity for $\mu = 42.85$, $\gamma_0 = 11.34$, and $\lambda = 4.529 \times 10^9$. As we may expect, the maximum crack length increases with the initial velocity of the blade.

Conclusions

The following conclusions can be drawn from our study:

1 In order to lift the ice statically or dynamically, it is necessary to have an initial crack existing in the interface. The initial crack can be generated by the repeated application of thrust through the blade. The high pressure at the tip of the blade can reduce the melting point of the ice and create an initial crack at the interface.

2 In the case of static loading, the applied thrust increases with penetration until it reaches the bifurcation load. The crack propagates indefinitely at the bifurcation load. As a result of viscoelastic properties of the ice, the maximum thrust for instability as measured by experiments checks with the theoretical value within the tolerance of experiments only when creep deformation is allowed at each increment of the thrust.

3 In the case of impulsive loading, the speed of the blade decreases continuously and the motion of the blade stops after its speed becomes zero. In order to introduce crack propagation, the initial speed of the blade must be large enough that the inertia force due to the deceleration of the blade reaches the bifurcation load of the static case. It is found that the crack length increases with the initial velocity of the blade. However, as a result of the conservation of energy, there is no dynamic instability under impulsive loading.

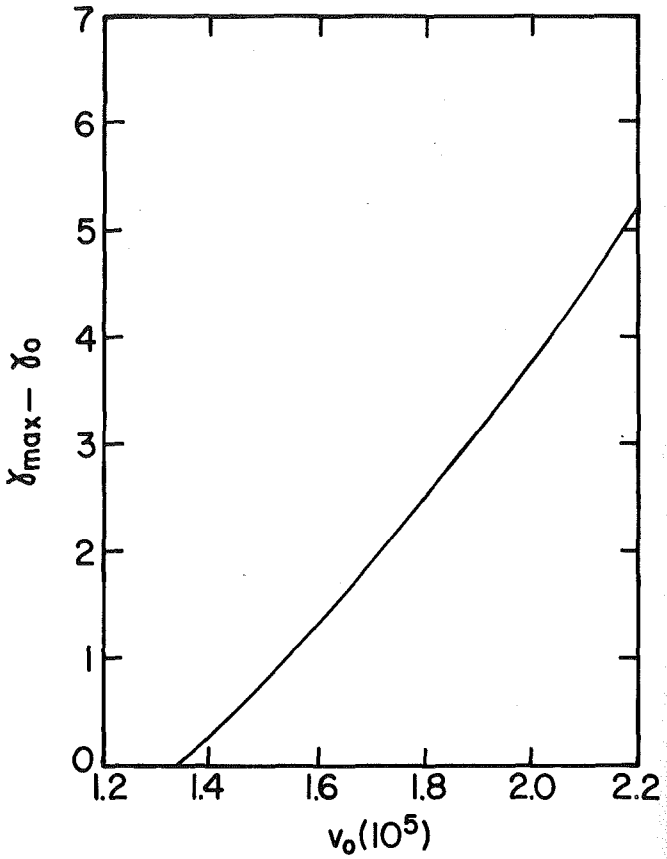


Fig. 6 $\gamma_{max} - \gamma_0$ versus v_0 curve for $\mu = 42.85$, $\gamma_0 = 11.34$, and $\lambda = 4.529 \times 10^9$

Acknowledgment

The author wishes to express his appreciation and thanks to the Department of Transportation for the support of the research grant; to Professor L. H. N. Lee for discussions and the loan of the apparatus for measurement of surface energy; to Mr. K. H. Liu for his assistance in experimental measurements and preparation of illustrations; to Mr. J. Hupp for his assistance in designing the apparatus for the penetration test.

References

1 Blackburn, R. R., and St. John, A. D., "Physical Alternatives to Chemicals for Highway Deicing," Vol. I: Phase I Results—Development of Concepts, Interim Report No. 1, Contract No. DOT-FH-11-9126, Midwest Research Institute, May 1977.

2 Williams, M. L., "The Continuum Interpretation for Fractures and Adhesion," *Journal of Applied Polymer Sciences*, Vol. 13, 1969, pp. 29–40.

3 Griffith, A. A., "The Phenomena of Rupture and Flow in Solids," *Philosophical Transactions of the Royal Society*, Series A, Vol. 221, 1921, pp. 163–198.

4 Williams, M. L., and Schapery, R. A., "Spherical Flow Instability in Hydrostatic Tension," *International Journal of Fracture Mechanics*, Vol. 1, 1965, pp. 64–72.

5 Irwin, G. R., "Fracture Mechanics," *Structural Mechanics*, eds., Goodier, J. N., and Hoff, N. J., *Proceedings of the First Symposium on Naval Mechanics*, 1960, pp. 557–594.

6 Sanders, J. L., "On the Griffith-Irwin Fracture Theory," ASME JOURNAL OF APPLIED MECHANICS, Vol. 27, 1960, pp. 352–353.

7 Rice, J. R., "An Examination of the Fracture Energy Balance," *Proceedings of International Conference on Fracture*, Sandai, Japan, 1965, pp. 309–340.

Downloaded 01 May 2010 to 171.66.16.249. Redistribution subject to ASME license or copyright; see http://www.asme.org/terms/Terms_Use.cfm

J. Rousselet[2]
Associate Professor,
Ecole Polytechnique de Montreal,
Montreal, Quebec H3C 3A7,
Canada
Assoc. Mem. ASME

G. Herrmann
Professor and Chairman,
Division of Applied Mechanics,
Department of Mechanical Engineering,
Stanford University,
Stanford, Calif. 94305
Fellow ASME

Dynamic Behavior of Continuous Cantilevered Pipes Conveying Fluid Near Critical Velocities[1]

The plane motion of a cantilevered pipe conveying fluid is examined when the flow velocity is in the neighborhood of that generating flutter. In contrast to previous studies, the flow velocity is not prescribed as a constant, but is determined from the laws of motion. We are thus led to a system of two nonlinear partial differential equations which are coupled through the nonlinear terms. The solution is found by the use of the Krylov-Bogoliubov averaging method and the results are discussed indicating the effect of nonlinearities.

Introduction

The dynamic behavior of continuous and articulated pipes, with one end restrained and one end free, has received considerable attention in the past. Bourrières [1] in 1939 investigated, analytically and experimentally, the flutter-type instability of a cantilevered pipe conveying fluid and found most of the characteristics of the phenomena. However this work remained unknown to subsequent researchers until Paidoussis [2] discovered its existence in 1974. In 1955, Long [3] studied the motion of cantilevered pipes and notices the damping effect of the fluid flow. Yet, his analysis did not reveal the existence of flutter at high flow velocity. Benjamin [4,5] in 1961 investigated thoroughly a system of articulated pipes and found that both buckling and flutter could occur. In 1966, Gregory and Paidoussis made a theoretical and experimental investigation of the behavior of a continuous cantilivered pipe conveying fluid and concluded that flutter was the only type of instability possible for such a system. All the studies just mentioned assume that the flow velocity is a known prescribed parameter and also that the amplitudes of motion are infinitesimal. Hence, the critical velocity, that is the flow velocity at which flutter appears, is determined from the solution of a single linear differential equation. In reality, for finite amplitudes of the oscillation, the flow velocity is affected by the transverse motion of the pipe. Therefore the magnitude of the initial disturbulance to which the system is subjected becomes important in determining the treshold of stability, and hence a nonlinear formulation of the problem is necessary. This formulation requires a separate equation of motion for the fluid, which will be coupled through its nonlinear terms to the transverse equation of motion of the pipe.

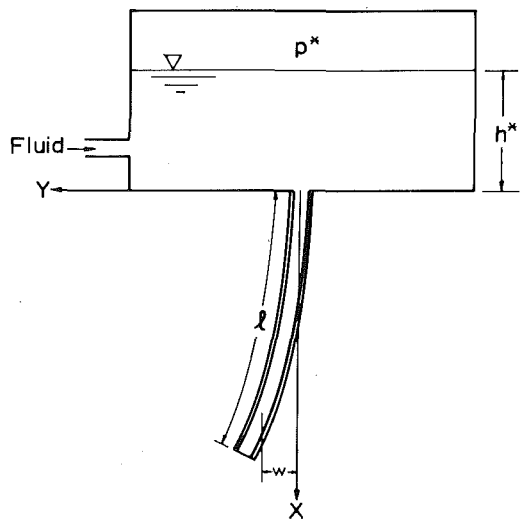


Fig. 1 Reservoir—cantilevered pipe system

The particular system considered here is a continuous cantilevered pipe hanging vertically under the influence of gravity, Fig. 1. The fluid is entering the pipe from a reservoir maintained at constant pressure. After its passage through the pipe, the fluid is discharged, tangentially to the end of the pipe, into the atmosphere.

The present work will thus present the complete nonlinear set of

[1] This work was supported in part by the Air Force Office of Scientific Research Grant AFOSR 74-2669 and National Aeronautics and Space Administration Grant NGL 05-020-397 to Stanford University.

[2] Formerly, Research Assistant, Division of Applied Mechanics, Stanford University, Assoc. Mem. ASME

Contributed by the Applied Mechanics Division and presented at the Winter Annual Meeting, Washington, D.C., November 15–20, 1981, of THE AMERICAN SOCIETY OF MECHANICAL ENGINEERS.

Discussion on this paper should be addressed to the Editorial Department, ASME, United Engineering Center, 345 East 47th Street, New York, N.Y. 10017, and will be accepted until March 1, 1982. Manuscript received by ASME Applied Mechanics Division, July, 1980; final revision, February, 1981. Paper No. 81-WA/APM-13.

Copyright © 1981 by ASME

Downloaded 01 May 2010 to 171.66.16.249. Redistribution subject to ASME license or copyright; see http://www.asme.org/terms/Terms_Use.cfm

equations of motion for the continuous cantilevered pipe. An analysis of these equations is made which shows how the critical velocity is affected by the transverse amplitudes of motion of the pipe and conclusions are drawn as to the necessity of such a nonlinear analysis.

Equations of Motion

The derivation of the equations of motion can be obtained by the use of a variational principle, as done in [7], or by direct application of Newton's law. This second method will be employed here.

Let us then consider one element of the cantilevered pipe, Fig. 2. At a given time t the position of element x is known from the components of displacement u_1 and w. The forces and moments acting on the element are N, P, M, Q which represent the tension force in the pipe, the compression force on the fluid cross section, the bending moment and the shear force, respectively. The lower part of Fig. 2 shows all the inertia terms. If we assume that the pipe is slender, the rotatory inertia can be neglected and therefore the resultant moment on the element must be zero, which leads to $Q = \partial M/\partial x$ where the moment-curvature relationship will be taken in the form $M = -EIw''/\sqrt{1-w'^2}$. The application of Newton's law in the X and Y-direction generates the following two equations:

$$[(N-P)C\theta]' - (QS\theta)' + (m_1+m_2)q = (m_1+m_2)\ddot{u}_1 + m_1\ddot{v}C\theta - m_1\dot{v}^2S\theta/R - 2m_1\dot{v}\dot{\theta}S\theta \quad (1)$$

$$[(N-P)S\theta]' + (QC\theta)' = (m_1+m_2)\ddot{w} + 2m_1\dot{v}\dot{\theta}C\theta + m_1\dot{v}^2C\theta/R + m_1\ddot{v}S\theta \quad (2)$$

where[3] m_1 and m_2 are the mass per unit length of the fluid and the pipe, respectively, g is the acceleration of gravity, $\dot{v}$ is the relative velocity of the fluid with respect to the pipe, θ or $\sin^{-1}w'$ is the angle between the element and the X-axis and R is the radius of curvature of the pipe element. The combination of the two equations obtained first by the multiplication of equation (1) by $-\tan\theta$ followed by its addition to equation (2) and second by the integration of equation (1) from x to 1, leads to

$$Q'/C\theta - (m_1+m_2)g\tan\theta - (m_1+m_2)(-\ddot{u}_1\tan\theta + \ddot{w}) - m_1\dot{v}^2/(RC\theta) - 2m_1\dot{v}\dot{\theta}/C\theta - \left\{-QS\theta - (m_1+m_2)g(1-x) + \int_x^l (m_1+m_2)\ddot{u}_1 dx + \int_x^l m_1\ddot{v}C\theta dx + \int_x^l [-m_1\dot{v}^2/(RS\theta) - 2m_1\dot{v}\dot{\theta}S\theta]\,dx\right\}(\tan\theta') = 0 \quad (3)$$

where

$$\ddot{u}_1 = \int_0^x \left[-\frac{\ddot{w}'w'}{\sqrt{1-w'^2}} - \frac{\dot{w}'^2}{(1-w'^2)^{3/2}}\right]dx$$

and where the fact that Q and $(N-P)$ are zero at $x = l$ has been used to eliminate two boundary condition terms.

The equation governing the motion of the fluid is obtained by the application of Newton's law, in the tangential direction, to an element of the fluid. The resulting equation is then integrated over the length of the pipe and leads to

$$P_0 - L\dot{v}^2 + \int_0^l m_1gC\theta dx - \int_0^l m_1\ddot{v}dx - \int_0^l m_1(\ddot{u}_1C\theta + \ddot{w}S\theta)dx = 0 \quad (4)$$

where P_0 is the compressive force acting on the fluid cross-section at $x = 0$ and $L\dot{v}^2$ is the sum of the friction forces between the fluid and the pipe. L is a constant which depends on the roughness of the pipe

[3] A prime or a dot affecting an expression indicates a differentiation of the expression with respect to x or t, respectively. Also, $C\theta$ and $S\theta$ are used in the place of $\cos\theta$ and $\sin\theta$; similarly, use is made of $S\psi$, $C\psi$, $S2\psi$, $C2\psi$, $S3\psi$, $C3\psi$, $C^2\psi$, $S^2\psi$.

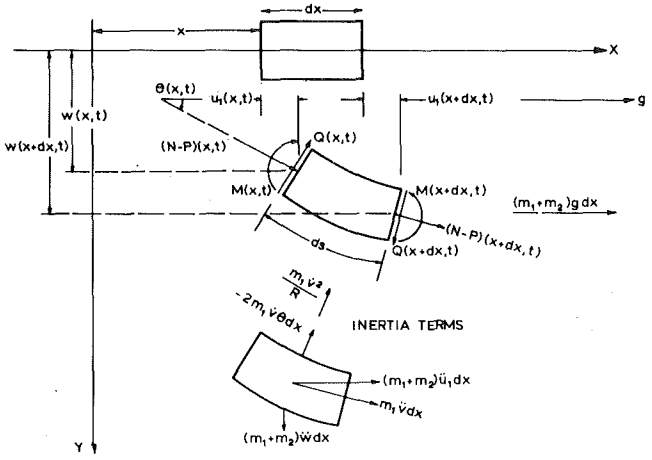


Fig. 2 Free-body diagram of an element of the pipe

and on the density of the fluid. To relate P_0 to p^*, the pressure in the reservoir, we use (neglecting small losses) Bernoulli's equation:

$$\frac{\dot{v}^2}{2} + \frac{P_0}{m} = gh^* + \frac{p^*}{\rho} \quad (5)$$

which is now combined with equation (4) to yield, after nondimensionalization and removal of nonlinear terms of order higher than three,

$$\Delta\ddot{u} + [(1+2L_0)\dot{u}_0/\gamma^{0.5}]\Delta\dot{u} = -\gamma^{0.5}\left[\frac{M}{2}\int_0^1 \eta'^2 d\xi + \int_0^1\int_0^\xi (-\ddot{\eta}'\eta' - \dot{\eta}'^2)d\xi d\xi + \int_0^1 \ddot{\eta}\eta' J\xi\right] \quad (6)$$

where

$$L_0 = L/m_1, \quad \dot{u} = (m_1/EI)^{0.5}\dot{v}l, \quad \eta = w/l$$

$$\xi = x/l, \quad \gamma = m_1/(m_1+m_2), \quad M = (m_1+m_2)gl^3/EI$$

$$\dot{u}_0 = \frac{p^* + M\gamma(1+H^*)}{(L_0+1/2)}, \quad H^* = \frac{h^*}{l}, \quad P^* = \frac{p^*Al^2}{EI}$$

The nondimensional flow velocity $\dot{u}$ has been approximated by $\dot{u}_0 + \Delta\dot{u}$ where $\Delta\dot{u} \ll \dot{u}_0$ in order to make the foregoing flow equation linear in $\Delta\dot{u}$. This approximation is justified since the variation in the flow velocity is due exclusively to nonlinear terms. The transverse equation of motion (3) after the elimination of nonlinear terms of order higher than three and the use of the nondimensional quantities defined before becomes

$$-\eta'''' - \ddot{\eta} - \dot{u}_0^2\eta'' - 2\gamma^{1/2}\dot{u}_0\dot{\eta}' = M\eta' - M(1-\xi)\eta'' + \eta''''\eta'^2 + 4\eta'''\eta''\eta' + \eta''^3 + M\eta'^3/2 + \int_0^\xi (\ddot{\eta}'\eta' + \dot{\eta}'^2)d\xi\eta' + 2\dot{u}_0\Delta\dot{u}\eta'' + 2\gamma^{1/2}\Delta\dot{u}\dot{\eta}' + \dot{u}_0^2\eta''\eta'^2 + 2\gamma^{1/2}\dot{u}_0\dot{\eta}'\eta'^2 - (3/2)M(1-\xi)\eta''\eta'^2 - \left[\int_\xi^1\int_0^\xi (\ddot{\eta}'\eta' + \dot{\eta}'^2)d\xi d\xi + \int_\xi^1 (\dot{u}_0^2\eta''\eta' + 2\gamma^{1/2}\dot{u}_0\dot{\eta}'\eta')d\xi - (1-\xi)\gamma^{1/2}\Delta\dot{u}\right]\eta''$$

$$\text{B.C.} \quad \eta = \eta' = 0 \text{ at } \xi = 0, \quad \eta'' = \eta''' = 0 \text{ at } \xi = 1 \quad (7)$$

The terms on the right-hand-side of this equation are nonlinear of order three except the first two terms which represent the linear affect of gravity. The nonlinear terms can be considered small for obvious reasons and a calculation shows that M, for γ equal to 0.5, has values of 0.01 and 0.3, respectively, for a steel and a plastic pipe 1/4 in. in di-

Downloaded 01 May 2010 to 171.66.16.249. Redistribution subject to ASME license or copyright; see http://www.asme.org/terms/Terms_Use.cfm

ameter and 2 ft in length. A less slender cantilever would lead to even smaller values of M. If we compare these values of M to the coefficients of the other linear terms in η'' and η', $\dot{u}_0^2$ and $2\gamma^{1/2}\dot{u}_0\omega$, we find that the gravity terms are very small. Indeed, a linear analysis made by Gregory and Paidoussis [6] shows that for $\gamma = 0.5$, $\dot{u}_0 = 9.5$, and $\omega = 26$ in the critical region. The gravity terms are therefore more than a hundred times smaller than the others and they are grouped with the small nonlinear terms on the right-hand side of the equation.

Solution of the Equations of Motion

Equations (6) and (7) constitute a coupled set of nonlinear equations with the coupling occurring only through the nonlinear terms. Their smallness permits us to use the following procedure to obtain the solution: (*a*) find the homogeneous solution to equation (7); (*b*) substitute this homogeneous solution into the right-hand-side of equation (6) and determine $\Delta\dot{u}$ and Δu; (*c*) substitute the homogeneous solution, $\Delta\dot{u}$ and Δu into the right-hand side of equation (7) and solve with the aid of the Krylov-Bogoliubov's method.

Following reference [6], the solution of the homogeneous part of the transverse equation of motion (7) is assumed in the form:

$$\eta(\xi,\tau) = \mathrm{Re}\left[\sum_{j=1}^{4} A_j e^{i\alpha_j \xi} e^{i(\omega\tau+\phi)}\right] \tag{8}$$

since it is linear and of fourth order in η and the satisfaction of the four boundary conditions requires the following determinant to be zero:

$$\begin{vmatrix} 1 & 1 & 1 & 1 \\ \alpha_1 & \alpha_2 & \alpha_3 & \alpha_4 \\ \alpha_1^2 e^{i\alpha_1} & \alpha_2^2 e^{i\alpha_2} & \alpha_3^2 e^{i\alpha_3} & \alpha_4^2 e^{i\alpha_4} \\ \alpha_1^3 e^{i\alpha_1} & \alpha_2^3 e^{i\alpha_2} & \alpha_3^3 e^{i\alpha_3} & \alpha_4^3 e^{i\alpha_4} \end{vmatrix} = 0 \tag{9}$$

The substitution of the trial function into equation (7) reduces to the following requirement:

$$\alpha^4 - \dot{u}_0^2\alpha^2 - 2\gamma^{1/2}\dot{u}_0\omega\alpha - \omega^2 = 0 \tag{10}$$

To attempt an analytical solution of equations (9) and (10) for the possible values of ω and α would be a desperate undertaking. We will therefore proceed in the following manner: (*a*) for a given value of $\dot{u}_0$, assume a value for ω; (*b*) numerically find the four roots of equation (10); (*c*) substitute these four values into equation (9); (*d*) if equation (9) is satisfied, the ω chosen is acceptable and represents the natural frequency of the system and using three of the four equations represented by equation (9) in conjunction with the four α's already found, we obtain the mode shape of the motion. If equation (9) is not satisfied we start again, with a different ω.

We can now consider η as a known quantity except for the fact that since equation (9) possesses only three independent equations, one of the A_j is free to take any value. This freedom permits us to assume that

$$\eta = \frac{L}{\bar{A}}\,\mathrm{Re}\left[\sum_{1}^{4} A_j e^{i\alpha_j\xi} e^{i(\omega\tau+\phi)}\right] \tag{11}$$

where

$$A_4 \equiv 1$$

$$\bar{A} = \left|\sum_{1}^{4} A_j e^{i\alpha_j}\right|$$

This normalization is such that L represents the amplitude of η at $\xi = 1$. We now solve equation (6) where the right-hand-side is treated as a forcing function. Its solution is of the form [7]

$$\Delta\dot{u} = (L/\bar{A})^2(K + U_1 S_{2\psi} + U_2 C_{2\psi}) \tag{12}$$

where K, U_1, and U_2 are constants and where ψ represents $(\omega\tau + \phi)$.

Since η and $\Delta\dot{u}$ are known values at this stage, we now solve equation (7) using the well-known Krylov-Bogoliubov method. We thus are led to

$$(\dot{L}_{av}/\bar{A})\omega \int_0^1 [I_0^2 + J_0^2 d\xi = \frac{\omega}{2\pi}\int_0^{\omega}\int_0^1 \{\mathrm{Small}\}[I_0 S_\psi + J_0 C_\psi]d\xi\, d\tau \tag{13}$$

$$(L/\bar{A})\omega\dot{\phi}_{\mathrm{av}} \int_0^1 [I_0^2 + J_0^2]d\xi = \frac{\omega}{2\pi}\int_0^{\omega}\int_0^1 \{\mathrm{Small}\}[I_0 C_\psi - J_0 S_\psi]d\xi\, d\tau \tag{14}$$

where the subscript av indicates that the quantity has been averaged over a cycle, where an integration over the length of the pipe was performed to eliminate the ξ dependence, where I_0 and J_0 are constants related to the mode shapes and where {Small} represents all the small terms on the right-hand side of equation (7). The expansion of {Small} is extremely tedious and leads to terms exhibiting a function of time of one of the following six forms: C_ψ^3, S_ψ^3, $S_\psi^2 C_4$, $S_\psi C_\psi^2$, S_ψ, C_ψ. It turns out that the integration over time in equations (13) and (14) eliminates all terms in $S_{3\psi}$, $C_{3\psi}$, and $S_\psi C_\psi$. The effective part of {Small} is therefore

$$\{\mathrm{Small}\} = \left(\frac{L}{A}\right)^3 [\Pi_1 C_\psi + \Pi_2 S_\psi] + \left(\frac{L}{A}\right) M[(I_1 - (1-\xi)I_2)C_\psi - (J_1 - (1-\xi)J_2)S_\psi] \tag{15}$$

where Π_1, Π_2, I_1, I_2, J_1, J_2 are extremely complex functions, of the mode shapes, which are not given here to save space.

Before we substitute equation (15) into equations (13) and (14), we have to consider the contribution of slight damping, positive or negative, to the system. This positive or negative damping is generated by a flow velocity which is smaller or greater than the critical flow velocity. In the foregoing derivation the frequency of motion ω was assumed to be a real number since the linear critical frequency was considered. If we are not exactly at the critical velocity, ω has an imaginary part: $\omega = (\bar{\omega} + ik)$ where $k \ll \bar{\omega}$. Thus equation (8) can be rewritten as

$$\eta = \mathrm{Re}\,[A(\xi)e^{-kt}e^{i\psi}] \tag{16}$$

This solution of the homogeneous part of the transverse equation of motion is also a solution to the slightly damped simple oscillator

$$\ddot{\eta} + 2k\dot{\eta} + \bar{\omega}^2\eta = 0$$

or

$$\ddot{\eta} + \bar{\omega}^2\eta = -2k\dot{\eta} \tag{17}$$

We thus see that the removal of the damping in the homogeneous part of equation (7) can be carried out in the following manner:

$$\ddot{\eta} + \eta'''' + \dot{u}_0^2\eta'' + 2\gamma^{1/2}\dot{u}_0\dot{\eta}^1 - 2k\dot{\eta} = -2k\dot{\eta} \tag{18}$$

Therefore, by adding $+2k\dot{\eta}$ to the right-hand side of equation (7), or in effect to {Small}, we can account for flow velocities other than critical. We therefore rewrite {Small} as

$$(L/\bar{A})^3[\Pi_1 C_\psi + \Pi_2 S_\psi] + (L/\bar{A})\{M[(I_1 - (1-\xi)I_2)C_\psi - (J_1 - (1-\xi)J_2)S_\psi] + 2k\omega[-I_0 S_\psi - J_0 C_\psi]\} \tag{19}$$

which, after substitution into equations (13) and (14) reduces to

$$(\dot{L}_{\mathrm{av}}/\bar{A})\omega\int_0^1 (I_0^2 + J_0^2)d\xi = (L/\bar{A})^3/2\int_0^1 [I_0\Pi_2 + J_0\Pi_1]d\xi + (L/\bar{A})M/2\int_0^1 [J_0(I_1 - (1-\xi)I_2) - I_o(J_1 - (1-\xi)J_2)]d\xi - (L/\bar{A})k\omega\int_0^1 (I_0^2 + J_0^2)d\xi \tag{20}$$

$$\omega\dot{\phi}_{\mathrm{av}}\int_0^1 [I_0^2 + J_0^2]d\xi = (L/\bar{A})^2/2\int_0^1 (I_0\Pi_1 - J_0\Pi_2)d\xi + M/2\int_0^1 [I_0(I_1 - (1-\xi)I_2] + J_0(J_1 - (1-\xi)J_2)]d\xi \tag{21}$$

Downloaded 01 May 2010 to 171.66.16.249. Redistribution subject to ASME license or copyright; see http://www.asme.org/terms/Terms_Use.cfm

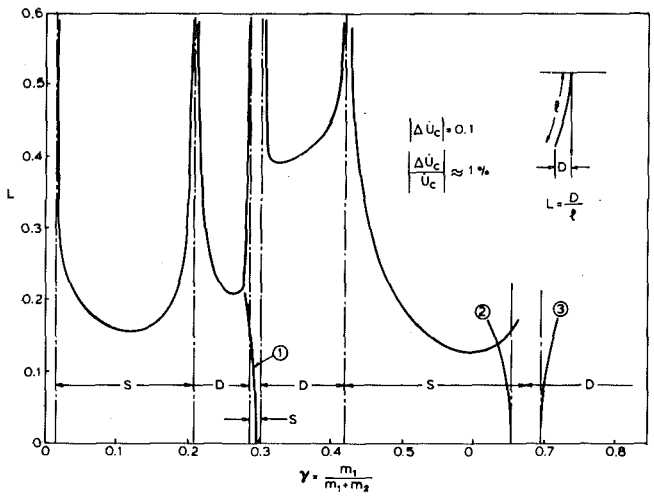


Fig. 3 Limit cycle amplitude versus γ

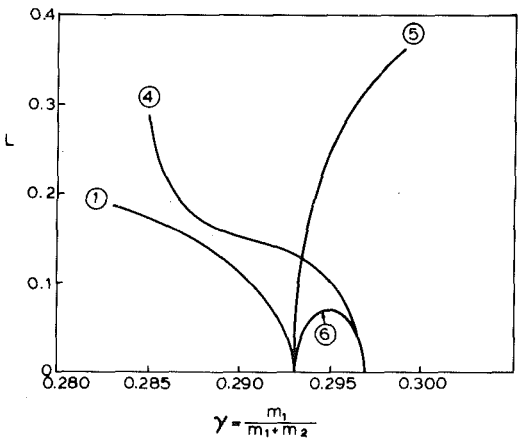


Fig. 4 Limit cycle amplitude versus γ for γ in the neighborhood of 0.295

The arguments of the integrals in the aforementioned two equations are completely known and the integrations can be performed on the computer.

The behavior of the system depends on the values of $\dot{L}_{av}$ and $\dot{\phi}_{av}$. When $\dot{L}_{av}$ is zero, it indicates that for the given amplitude the linear terms are fully opposed by the nonlinear terms. In such a case the amplitude of motion is constant and we have what is known as a limit cycle. For a smaller amplitude, the linear terms dominate and for a larger amplitude the nonlinear terms dominate. The size of the disturbance to which the system is subjected therefore becomes important because it can destabilize a system which is linearly stable (in the small) if it brings the system outside of a limit cycle (provided the nonlinearities are destabilizing). A plot of the amplitude of the limit cycles as a function of the system's mass ratio is presented in (Fig. 3). Also indicated on this plot, by the letters D and S, are the regions where the nonlinearities destabilize and stabilize the system.

Discussion of Results

We observe in Fig. 3 that the amplitude of the limit cycle is above 0.15 for most values of γ which is an indication that the nonlinearities have a weak effect, thus requiring large amplitudes of motion to compensate for a small amount of linear damping or excitation. In that plot, $|\Delta \dot{U}_C| = 0.1$ represents a change of about 1 percent from the critical flow velocity but branches 1, 2, and 3 are plotted for values of $|\Delta \dot{U}_C|$ of about 1. which represents approximately a change of 10 percent. Therefore, in spite of the general weakness of nonlinearities, they can have a very strong effect for values of γ in the neighborhood of 0.3 and 0.68. A blowup of the region around $\gamma = 0.295$ is presented in Fig. 4. The cause of the complexity in that region lies in the multiple crossings of the imiginary axis of the root locus as shown in Fig. 5.

We can recognize that, for $\gamma = 0.293$, the curve in Fig. 5 may come extremely close to the imaginary axis. Under such conditions the smallest amount of stabilizing nonlinearity is sufficient to stabilize the system. This case gives rise to branch No. 1. Curves 4, 5, 6, between 0.293 and 0.297 are related to the three crossing points in Fig. 5. The region close to $\gamma = 0.67$ reflects exactly the same type of behavior of the root locus except that Fig. 3 shows the existence of an additonal branch to the right of that region, branch 3. This branch exists because the nonlinearities are destabilizing for γ close to 0.7.

The plot of Fig. 3 does not extend past $\gamma = 0.7$ because for values of greater than 0.7 the thickness of the pipe is so small that an analysis using shell theory is required. Finally, we note in Fig. 3 that the amplitude of the limit cycles becomes infinite for certain values of γ which indicates the total disappearance of nonlinear contributions for the corresponding mode shape.

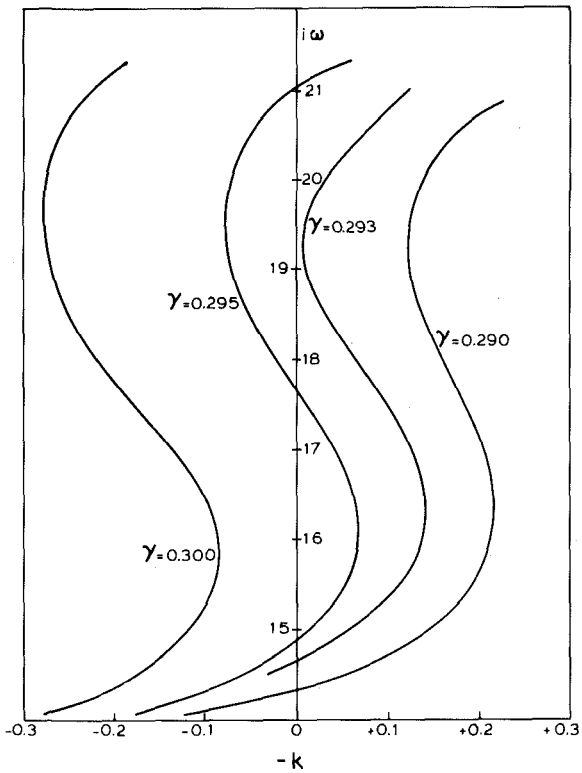


Fig. 5 Root locus as it crosses the imaginary axis

Conclusion

Because of the large amplitudes required to cause a small change (stability in the large) in the critical velocity for most mass ratios of the system, we conclude that, in general, we can rely in the linear predictions (stability in the small) as far as stability is concerned. However, in the neighborhood of $\gamma = 0.3$ and 0.68, the critical velocity can be changed by more than 10 percent due to the nonlinearities. This last fact results principally from the capricious behavior of the linear solution which permits the loss of stability for two different flow velocities. In this case, the small nonlinearities act only as trigger mechanisms. Finally, if very large amplitudes of motion are considered, a nonlinear analysis is unavoidable but the nonlinear terms which have been discarded in the present analysis should be investigated further to determine their importance.

Downloaded 01 May 2010 to 171.66.16.249. Redistribution subject to ASME license or copyright; see http://www.asme.org/terms/Terms_Use.cfm

References

1 Bourrières, F.-J., "Sur un phénomène d'oscillation auto-entretenue en mécaniqué de fluides reéls," *Publications Scientifiques et Techniques du Ministère de L'Air*, No. 147, 1939.

2 Paidoussis, M. P., and Issid, N. T., "Dynamic Stability of Pipes Conveying Fluid," *Journal of Sound and Vibration*, Vol. 33, No. 6, 1974, pp. 267–294.

3 Long, R. H., Jr., "Experimental and Theoretical Study of Transverse Vibration of a Tube Containing Flowing Fluids," ASME JOURNAL OF APPLIED MECHANICS, Vol. 22, 1955, pp. 55–68.

4 Benjamin, B. T., "Dynamics of a System of Articulated Pipes Conveying Fluid—I. Theory," *Proceedings of the Royal Society*, London, Vol. 261, 1961, pp. 457–486.

5 Benjamin, B. T., "Dynamics of a System of Articulated Pipes Conveying Fluid—II. Experiments," *Proceedings of the Royal Society*, London, Vol. 261, 1961, pp. 487–499.

6 Gregory, R. W., and Paidoussis, M. P., "Unstable Oscillation of Tubular Cantilevers Conveying Fluid—I. Theory, II. Experiments," *Proceedings of the Royal Society*, London, Vol. 293, 1966, pp. 512–542.

7 Rousselet, J., "Dynamic Behavior of Pipes Conveying Fluid Near Critical Velocities," PhD Dissertation, Stanford University, 1975.

8 Minorsky, N., *Nonlinear Oscillations*, Van Nostrand Co., 1962.

Downloaded 01 May 2010 to 171.66.16.249. Redistribution subject to ASME license or copyright; see http://www.asme.org/terms/Terms_Use.cfm

A. Unger
School of Engineering,
Tel Aviv University,
Tel Aviv, Israel

M. A. Brull[2]
Professor of Mechanics,
Tel Aviv University,
Tel Aviv, Israel

Parametric Instability of a Rotating Shaft Due to Pulsating Torque[1]

The torque transmitted by a shaft is usually a pulsating one. This torque may under certain conditions cause transverse parametric oscillations of the shaft leading to its failure. In this paper, an analytical numerical investigation is presented to determine the stability regions of the shaft due to a pulsating torque applied at its ends. The present work deals with three types of parametric instabilities. Unstable regions bounded by oscillatory motions characterized by period T and by period 2T and combination resonance. The results indicate that the most common and dangerous parametric instabilities arise as a result of combination resonance.

1 Introduction

The parametric instability of structures is an area of considerable current interest in mechanics. All of the latest works deal with the parametric instability of shafts due pulsating axial forces.

McLaclan [1] was the first to establish and summarize the mathematical knowledge on Mathieu equations, which are the basis for an understanding of the parametric instability phenomenon.

Later in 1964, Bolotin's extensive English translation appeared [2]. This book presents the most complete summary of the phenomena known up to 15 years ago. Bolotin investigates in his book the parametric instability regions which were defined 75 years ago by the French mathematician Floquet [3]. According to Floquet, a differential equation of the second-order, with time-varying coefficients has two sets of harmonic solutions, which form the limit between stable and unstable solutions. One set of solutions has a basic period equal to the natural period of the system without the pulsating component (Period T), and the second set are the solutions having a basic double period (Period $2T$).

Hsu [4] completed the basic knowledge to date on the parametric instability of a system having multiple degrees of freedom. He found that in a coupled system of Mathieu equations, there can exist, in addition to the known unstable regions (Periods T and $2T$) a new set of unstable regions called "combination resonance." Hsu also determined the conditions under which those new unstable regions can exist.

The phenomenon of combination resonance, was also investigated at the same time in the USSR. Valleev [5] published in 1963 a paper on the danger of the combination resonance phenomena.

Many works were published in the past 15 years in the field of parametric instability. But as far as is known to the authors, no theoretical work has been done on the specific subject, parametric excitation by a pulsating torque, on the bending stability of a continuous shaft. Eshleman [6] introduced the subject and developed the equation of motion and the corresponding boundary conditions, but he did not succeed in solving them. Eshleman went on to an experimental work on this subject. Without having a theoretical basis, Eshleman succeeded in proving the existence of transverse parametric instability regions of a rotating shaft, due to a pulsating torque. He did show experimentally on a shaft-disk system, that the T-type coupling exists between pulsating torque and lateral vibrations. In the present work, the existence of additional unstable regions are investigated.

The importance of these parametric phenomena is in the field of machinery shafting and especially in helicopter shafts, where the long shafts connecting the tail rotor to the power plant often operate at hypercritical angular velocities.

2 Equations of Motion

The equations of motion (see Fig. 1) of a circular cross-section shaft are well known (7), (8), and are given in an absolute coordinate system by

$$EI\frac{\partial^4 v}{\partial x^4} - T\frac{\partial^3 w}{\partial x^3} + m\frac{\partial^2 v}{\partial t^2} = 0$$
$$EI\frac{\partial^4 w}{\partial x^4} + T\frac{\partial^3 v}{\partial x^3} + m\frac{\partial^2 w}{\partial t^2} = 0 \qquad (1)$$

In writing these two coupled equations, the following assumptions were adopted:

1 The shaft is uniform and is suitably represented by classical (Euler-Bernoulli) beam theory.

2 The shaft rotates at a constant angular velocity Ω.

3 There is no dynamic coupling between the torsional and the transverse bending degrees of freedom.

---

[1] The results presented in this paper formed a part of a thesis submitted by the first author in partial fulfillment of the requirements for a PhD degree in the Department of Mechanics and Structures, School of Engineering, Tel Aviv University, Israel.

[2] In 1980–1982, Visiting Professor of Bioengineering, University of Pennsylvania, Philadelphia, Pa. 19104.

Contributed by the Applied Mechanics Division for publication in the JOURNAL OF APPLIED MECHANICS.

Discussion on this paper should be addressed to the Editorial Department, ASME, United Engineering Center, 345 East 47th Street, New York, N. Y. 10017, and will be accepted until two months after final publication of the paper itself in the JOURNAL OF APPLIED MECHANICS. Manuscript received by ASME Applied Mechanics Division, October, 1980; final revision, April, 1981.

Copyright © 1981 by ASME

Downloaded 01 May 2010 to 171.66.16.249. Redistribution subject to ASME license or copyright; see http://www.asme.org/terms/Terms_Use.cfm

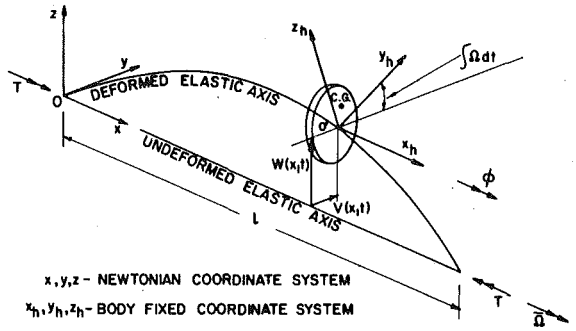


Fig. 1 General view of a continuous shaft system

Making use of the complex deflection $Z = v + iw$, equations (1) can be written in the form

$$EI\frac{\partial^4 Z}{\partial x^4} + iT\frac{\partial^3 Z}{\partial x^3} + m\frac{\partial^2 Z}{\partial t^2} = 0 \tag{2}$$

We now introduce the following dimensionless variables:

$$f = z/l; \quad \tau = \Omega t; \quad \xi = x/l; \quad L = Tl/EI; \quad p^2 = \frac{m}{EI}l^4\Omega^2$$

The equation of motion thus becomes

$$\frac{\partial^4 f}{\partial \xi^4} + iL\frac{\partial^3 f}{\partial \xi^3} + p^2\frac{\partial^2 f}{\partial \tau^2} = 0 \tag{3}$$

where L is the applied torque. We now assume a harmonic applied torque of the form

$$L(\xi, t) = L_0 + L_1 \cos \eta\tau \tag{4}$$

and the equation of motion is then given by

$$\frac{\partial^4 f}{\partial \xi^4} + i(L_0 + L_1 \cos \eta\tau)\frac{\partial^3 f}{\partial \xi^3} + p^2\frac{\partial^2 f}{\partial \tau^2} = 0 \tag{5}$$

Boundary Conditions

(a) Shaft Mounted in Long Bearings. The boundary conditions for nonself-aligning long bearings are merely the conditions of a clamped beam.

$$\left.\begin{aligned} f &= 0 \\ \partial f/\partial \xi &= 0 \end{aligned}\right\} \text{at} \quad \xi = 0 \quad \text{and} \quad 1 \tag{6}$$

(b) Shaft Mounted in Short Bearing. A shaft mounted in short bearings is equivalent to mounting in self-aligning bearings. This corresponds to hinged ends in the equivalent vibrating beam.

$$\left.\begin{aligned} &f = 0 \\ &\frac{\partial^2 f}{\partial \xi^2} + i(L_0 + L_1 \cos \eta\tau)\frac{\partial f}{\partial \xi} = 0 \end{aligned}\right\} \quad \text{at } \xi = 0 \text{ and } 1 \tag{7}$$

These boundary conditions are torque-dependent, and therefore time-dependent.

3 Solution of the Equations of Motion

As seen in the foregoing, both the equations of motion and the boundary conditions have time-varying coefficients for short bearing.

The general solution to this complex problem will be based on eliminating the space-dependence and then finding the unstable regions of the time-dependent problem.

In the following, each of these shaft problems will be examined separately.

3.1. Elimination of the Space-Dependence. *3.1.1 Shaft Mounted in Wide Bearings.* The solution is based on the method of separation of variables. Let us assume the existence of the following solution:

$$f(\xi, t) = \sum_{n=1}^{\infty} X_n(\xi) g_n(\tau) \tag{8}$$

Where the space-dependent functions $X_n(\xi)$ are a complete orthogonal set of functions filling the B.C. (6), hence

$$\left.\begin{aligned} X_n(0) &= 0 \\ X_n{}^{\mathrm{I}}(0) &= 0 \end{aligned}\right\} \text{at} \quad \xi = 0 \quad \text{and} \quad 1 \tag{9}$$

Choosing as the complete set the normal mode shapes of a shaft on long bearings, *without* a torque, one can write

$$X_n{}^{\mathrm{IV}} - X_n = 0 \tag{10}$$

and the orthogonality condition may be written by

Nomenclature

EI = flexural stiffness
v, w = rotor deflections
T = (a) torque; (b) excitation period
m = mass per unit length
t = time
l = length of shaft
$Z = v + iw$ = complex displacement
$f = Z/l$ = complex dimensionless displacement
$\tau = \Omega t$ = dimensionless time
$\xi = x/l$ = dimensionless coordinate along the shaft
$p^2 = m/EI\, l^4\Omega^2$ = nondimensional rotational speed
$L = Tl/EI$ = dimensionless torque
L_0, L_1 = constant and harmonic components of the dimensionless torque
η = nondimensional frequency of the harmonic torque component
$X_n(\xi)$ = space-dependent functions filling the B.C.
$g_n(\tau)$ = the time variation function of the nth shape
$\gamma_n{}^2 = \dfrac{ml^4\omega_m{}^2}{EI}$ = nondimensional natural frequencies of a clamped beam
$p_n{}^*$ = the critical speed of a shaft with no external torque applied on the shaft
N = number of mode shapes used in the Galerkin's approximation
M = an even integer, greater than N
η = ratio between harmonic torque frequency and Ω
ω = frequency
ϵ = excitation parameter
Γ = any finite real number (see equation (35))
δ = characteristic exponent
κ = number of terms accounting in expanding $g(\tau)$
λ = eigenvalue

Matrix Notation

A = torque effect matrix
F = real diagonal matrix, whose elements are the squares of the natural frequencies
g = a vector composed of the functions $g_m(\tau)$
$\chi(\tau)$ = periodic vector containing N terms (see equation (41))
a_k = vector of complex constants
b_k = vector of complex constants
G, G_b = complex matrices; see definition in equation (43)
H = imaginary matrix; see definition in equation (48)
U = cannonic form for extracting eigenvalues

Downloaded 01 May 2010 to 171.66.16.249. Redistribution subject to ASME license or copyright; see http://www.asme.org/terms/Terms_Use.cfm

$$\int_0^1 X_n(\xi)X_m(\xi)d\xi = \delta_{mn} \tag{11}$$

These functions are the orthonormal mode shapes of a beam clamped at both ends. The γ_n are the nondimensional natural frequencies of a clamped-clamped beam, and can be expressed by the natural frequencies

$$\gamma_n{}^2 = \frac{ml^4\omega_{0n}{}^2}{EI} \tag{12}$$

The p_n* are the nondimensional critical speeds of the shaft when no external torque is applied.

$$p_n{}^* = \gamma_n \tag{13}$$

One can find the analytical expressions for $X_n(\xi)$ in many references, such as Bishop [9].

Substituting equation (8) into equation (5) yields

$$\sum_{n=1}^{\infty} [X_n{}^{\mathrm{IV}}(\xi)g_n(\tau) + i(L_0 + L_1\cos\eta\tau)\mathrm{X_n{}^{III}}(\xi)g_n(\tau) + p^2X_n(\xi)\ddot{g}_n(\tau)] = 0 \tag{14}$$

The last equation is solved by using Galerkin's method. Multiplying both sides of equation (14) by $X_n(\xi)d\xi$, integrating within the limits $0 \le \xi \le 1$, and using (10) and (11), we obtain

$$q_m{}^2g_m(\tau) + i(L_0 + iL_1\cos\eta\tau)\sum_{n=1}^{\infty} g_n(\tau) \times \int_0^1 X_n{}^{\mathrm{III}}(\xi)X_m(\xi)d\xi + p^2\ddot{g}_n(\tau) = 0 \tag{15}$$

where $m = 1, 2, 3 \ldots \infty$.

Defining the integral

$$\int_0^1 X_m(\xi)X_n{}^{\mathrm{III}}(\xi)d\xi = 2a_{mn} \tag{16}$$

Choosing a truncated solution with N-terms

$$f(\xi, t) = \sum_{n=1}^{N} X_n(\xi)g_n(\tau) \tag{17}$$

the following set of equations is obtained:

$$\gamma_m{}^2g_m(\tau) + 2i(L_0 + L_1\cos\eta\tau)\sum_{n=1}^{N} a_{mn}g_n(\tau) + p^2\ddot{g}_n(\tau) = 0 \tag{18}$$

where $m = 1, 2 \ldots N$.

Equations (18) are coupled differential equations of the Mathieu type. They can be written in the following matrix form:

$$F \cdot g + 2i(L_0 + L_1\cos\eta\tau)Ag + p^2\ddot{g} = 0 \tag{19}$$

where F = real diagonal matrix ($N \times N$), containing along the diagonal the squared natural frequencies

$$F(i, i) = q_i{}^2 \tag{20}$$

g = an N-order vector containing the functions $g_m(\tau)$

$$g(i) = g_i(\tau) \tag{21}$$

A is defined as the torque effect matrix. It is a real matrix built from the a_{mn} terms. Numerical values for this matrix and the accuracy obtained by using it in calculating critical speeds are examined in the Appendix.

3.1.2 Shaft Mounted in Short Bearings. The boundary conditions of a shaft mounted in short bearings are homogeneous (7), but are time-dependent, which adds complexity to the problem. We will investigate the time-dependent behavior for the short bearings shaft, in a manner similar to the previous case, so that the remainder of the treatment can apply well to both cases.

Proceeding as before, and using the Galerkin method, we may write

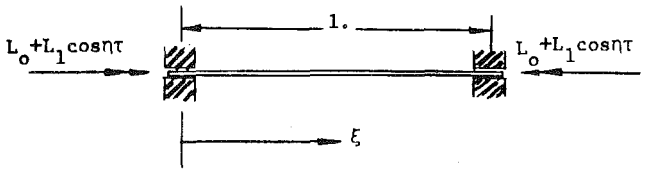


Fig. 2 Shaft mounted in long bearings

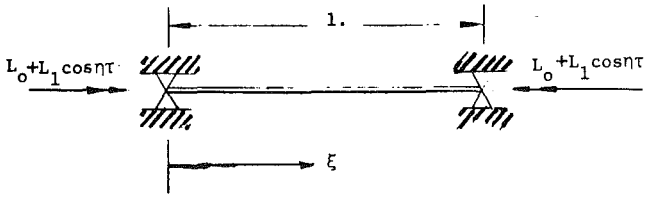


Fig. 3 Shaft mounted in short bearings

$$f(\xi, \tau) = \sum_{n=1}^{N} X_n(\xi)g_n(\tau) \tag{22}$$

where the function $f(\xi, \tau)$ has to satisfy the boundary conditions for all times. These boundary conditions lead to

$$\left.\begin{aligned} X_n &= 0 \\ X_n{}^{\mathrm{II}} &= 0 \\ X_n{}^{\mathrm{I}} &= 0 \end{aligned}\right\} \text{at} \quad \xi = 0 \quad \text{and} \quad 1 \tag{23}$$

Hence, the functions X_n have to satisfy six boundary conditions even though the differential equation (3) is the 4th order only. The $X_n(\xi)$ functions must satisfy two additional constraints, besides the four conditions necessary for a unique definition. These additional requirements are the main difficulty in selecting a suitable set of functions $X_n(\xi)$.

The complete set of functions satisfying the first two sets of boundary conditions in (23), can be written by

$$Z_n(\xi) = \sin n\pi\xi \tag{24}$$

We will now construct a new set of functions satisfying the two additional boundary conditions required in (23). This can be done by a combination with higher mode shapes such as

$$X_n(\xi) = \sin n\pi\xi - \frac{n}{M+n}\sin(M+n)\pi\xi \tag{25}$$

where M is an *even* integer greater than N.

The combined set of functions (25) is a complete set of orthogonal functions. Substituting (25) into (5) leads to the same expression as (14).

We can use these functions in connection with a modification of the Galerkin method, which is a special case of the method of weighted residuals.

Multiplying both sides of equation (14) by

$$Z_m(\xi) = \sin m\pi\xi \tag{26}$$

where $1 \le m \le N$, and integrating within $0 \le \xi \le 1$, yields the following form for the equation of motion:

$$m^4\pi^4g_m(\tau) + 2i(L_0 + L_1\cos\eta\tau)\sum_{n=1}^{N} a_{mn}g_n(\tau) + p^2\ddot{g}_n(\tau) = 0 \qquad 1 \le m \le N \tag{27}$$

where

Downloaded 01 May 2010 to 171.66.16.249. Redistribution subject to ASME license or copyright; see http://www.asme.org/terms/Terms_Use.cfm

$$a_{mn} = n\pi^3 \int_0^1 [-n^2 \cos n\pi\xi + (M+n)^2 \cos (M+m)\pi\xi] \sin m\pi\xi d\xi \quad (28)$$

We note that only the a_{mn} terms are somewhat dependent on the integer M, which corresponds to the higher mode shape entering into the solution (25). Evaluation of these terms (see the Appendix), clarifies the modified Galerkin method used, and its accuracy.

Equation (27) are similar to (18) and can be transformed into the matrix form (19). Thus we see that the conclusions resulting from a study of equation (19) can equally well be applied to both cases.

3.2 Stability Analysis. *3.2.1 Unstable Regions of Coupled Mathieu Equations.* The two basic problems in shafting have now been expressed by coupled sets of second-order differential equations of the Mathieu type (equation (19)).

Special attention has been paid in the literature [1–3] to the simplified Mathieu equation given by

$$\frac{d^2y}{dt^2} + \omega^2(1 - 2\mu \cos \theta t)y = 0 \quad (29)$$

One of the basic characteristics of this equation is that when ω and μ satisfy certain relations, a divergent solution is obtained.

We denote by $p_1 \ldots p_n$ the roots of the frequency equation without the pulsating torque

$$|(F + 2iL_0A) - p^2I| = 0 \quad (30)$$

so that these roots are the critical speeds of the shaft under constant torque.

It can be shown [4] that for small values of L_1, the following unstable regions can be obtained for a undimensional excitation frequency η_p, in the region of (*a*) p_i and the subharmonics resulting from it

$$\eta p \approx p_i/k; \quad i = 1, 2 \ldots N; \quad k = 1, 2 \ldots \infty \quad (31)$$

These unstable regions are characterized by harmonic solutions with period T bounding them, and therefore they would be called T-type unstable regions; (*b*) $2p_i$ and the subharmonics resulting from it

$$\eta p = \frac{2p_i}{2k-1}; \quad i = 1, 2 \ldots N; \quad k = 1, 2, \ldots \infty \quad (32)$$

These type of unstable regions are bounded by harmonic solutions having a fundamental period equal to twice that of the basic excitation. They are usually called the $2T$-type unstable regions. Those two aforementioned unstable regions were defined by the Floquet theory [3] and characterize uncoupled Mathieu equations; (c) $p_i \pm p_j$ and subharmonics obtained from this combination frequency

$$\left.\begin{aligned} \eta p &= \frac{p_i \pm p_j}{k}; \quad i \neq j; \quad i > j \\ i &= 1, 2 \ldots N; \quad j = 2, 3 \ldots N; \quad K = 1, 2 \ldots \infty \end{aligned}\right\} \quad (33)$$

In these combination regions, the system oscillates separately in the ith and jth mode shapes with corresponding nondimensional frequencies near to p_i and to p_j and with time increasing amplitudes. This character helps to identify experimentally the combination resonance phenomena.

3.2.2 Resonance Conditions According to Hsu. Hsu [4] defined conditions for obtaining unstable regions under small parametric excitation $\epsilon > 0$ for coupled Mathieu equations characterized by real matrices. In order to convert our system of equation (19) to the form defined by Hsu [4, equation (2)], substitute

$$\left.\begin{aligned} B^{(0)} &= \frac{1}{p^2}(F + 2iL_0A); \quad D = \frac{i}{p^2}A \\ \omega_j &= p_j/p; \quad \epsilon = 2L_1; \quad \theta = \eta \end{aligned}\right\} \quad (34)$$

where F and $B^{(0)}$ are real diagonal matrices. The rest of the matrices are real matrices too. The transformation (34) is applicable only for $L_0 = 0$. Following Hsu's developments we can find that his conclusions are quite applicable even if D is a pure imaginary matrix.

Note that our equation of motion can be transformed to the form used by Hsu, by describing the space-dependence by the complex shapes of the system under the constant torque term L_0. But, in such a case, the equivalent D matrix might be complex.

According to Hsu, the following conditions can lead to parametric instability for the particular case $L_0 = 0$:

(1) $\eta p = p_k + p_l + 2L_1\Gamma; \quad k \neq l$

Here Γ is a certain finite real number

$$(p_k + p_l) - L_1\left(-\frac{a_{kl}a_{lk}}{p_kp_l}\right)^{1/2} < \eta p < (p_k + p_l) + L_1\left(-\frac{a_{kl}a_{lk}}{p_kp_l}\right)^{1/2} \quad (35)$$

(2) $\eta p = p_l - p_k + 2L_1\Gamma; \quad l > k$

$$(p_l - p_k) - L_1\left(\frac{a_{kl}a_{lk}}{p_kp_l}\right)^{1/2} < \eta p < (p_l - p_k) + L_1\left(\frac{a_{kl}a_{lk}}{p_kp_l}\right)^{1/2} \quad (36)$$

(3) $\eta p = 2p_k + 2L_1\Gamma$

$$2p_k - L_1\frac{|a_{kk}|}{p_k} < \eta p < 2p_k + L_1\frac{|a_{kk}|}{p_k} \quad (37)$$

Conditions for the secondary regions were not given by Hsu. From the properties of torque effect matrix (see the Appendix) and Hsu's conditions for instability, we can derive the following conclusions:

(*a*) Since sign $(a_{kl}) = -$ sign (a_{lk}) (38)

only combination resonance of the sum type will occur.

(*b*) Since $a_{kl} = 0$ for $k + l$ even (39)

combination resonance of the sum type is based on frequencies whose order of summation is an odd integer

$$\left.\begin{aligned} (p_k + p_l) - L_1\left(-\frac{a_{kl}a_{lk}}{p_kp_l}\right)^{1/2} < \eta p < (p_k + p_l) + L_1\left(-\frac{a_{kl}a_{lk}}{p_kp_l}\right)^{1/2} \\ \text{where} \qquad k + l \quad \text{odd}; \quad k \neq l \end{aligned}\right\} \quad (40)$$

(*c*) The width of the main regions of the $2T$-type is equal to zero.

Note that these three conclusions are applicable for $L_0 = 0$ only. We may further find that some of these are applicable to the general case where $L_0 \neq 0$.

3.2.3 Estimation of Stability Boundaries. According to Floquet [3] the general solution for Mathieu equations is given by

$$g(\tau) = e^{\delta\eta\tau}\chi(\tau) \quad (41)$$

where $\chi(\tau)$ is a period vector of N terms. It's general periodicy is T. Bolotin [2] proved, that for a differential equation of the second-order (such as equation (19)), the second set of independent solutions has a period $2T$. $\delta\eta\tau$ is a characteristic exponent of the solution. Clearly, if δ has a positive real part for a given system at any particular forcing frequency ηp, an unstable solution results. The growth rate depends on the magnitude of the real part of δ.

Since our goal is to find the position and the nature of the instability zones, direct methods based on equation (41) can be used. Suitable quick methods, for this purpose are outlined below.

3.2 3.1 Direct Method Determining Stability Regions of T and 2T-Types. In lieu of equation (41) the unstable regions of the T and $2T$-type are bounded by harmonic solutions having periods T and $2T$. ($\delta = 0$). The stability boundaries can be determined by appropriate periodic substitutions.

(*a*) *Boundary of Unstable Regions of the T-Type.* The T-type unstable regions can be bounded by harmonic solutions having a basic period T.

Downloaded 01 May 2010 to 171.66.16.249. Redistribution subject to ASME license or copyright; see http://www.asme.org/terms/Terms_Use.cfm

$$g(\tau) = b_0 + \sum_{k=1}^{\infty} (a_k \sin k\eta\tau + b_k \cos k\eta\tau) \tag{42}$$

Substituting equation (47) into equation (20), the following linear homogeneous equation can be derived:

$$\left.\begin{aligned} (F - \eta^2 p^2 I + 2iL_0 A)a_1 + iL_1 A a_2 = 0 \\ (F - k^2\eta^2 p^2 I + 2iL_0 A)a_k + iL_1 A(a_{k-1} + a_{k+1}) = 0 \\ \text{for} \quad k = 2, 3, 4 \ldots \end{aligned}\right\} \tag{43}$$

$$\left.\begin{aligned} (F + 2iL_0 A)b_0 + iL_1 A b_1 = 0 \\ (F + 2iL_0 A - \eta^2 p^2 I)b_1 + 2iL_1 A b_0 + iL_1 A b_2 = 0 \\ (F - k^2\eta^2 p^2 I + 2iL_0 A)b_k + iL_1 A(b_{k-1} + b_{k+1}) = 0 \\ \text{for} \quad k = 2, 3, 4 \ldots \end{aligned}\right\} \tag{44}$$

Expressing b_0 by b_1 from the first equation of (44) the remaining two equations of (44) can be brought to a similar form as eqatuion (43)

$$\begin{aligned} \{F + 2iL_0 A - \eta^2 p^2 I + 2L_1{}^2(A - 2iL_0 A F^{-1} A) \\ \times (F + 4L_0{}^2 A F^{-1} A)^{-1} A\} b_1 + iL_1 A b_2 = 0 \end{aligned}$$

$$\begin{aligned} (F - k^2\eta^2 p^2 I + 2iL_0 A)b_k + iL_1 A(b_{k-1} + b_{k+1}) = 0 \\ \text{for} \quad k = 2, 3, 4 \ldots \end{aligned} \tag{45}$$

The two sets of equations (43) and (45) are infinite series of homogenous equations in a_k and $b_k (k = 1, 2, 4 \ldots \infty)$. These two sets are uncoupled, and as expected they reduce to an identical set in the case of $L_1 = 0$. Taking a finite number of terms $(k = 1, 2 \ldots K)$, the two sets (43) and (45) can be written in a common matrix form: (for example, for $K = 5$)

$$\begin{bmatrix} G \text{ or } G_b + \\ -\eta^2 p^2 I & H & & & \\ H & G + \\ & -2^2\eta^2 p^2 I & H & & \\ & H & G + \\ & & -3^2\eta^2 p^2 I & H & \\ & & H & G + \\ & & & -4^2\eta^2 p^2 I & H \\ & & & H & G + \\ & & & & -5^2\eta^2 p^2 I \end{bmatrix} \begin{Bmatrix} c_1 \\ c_2 \\ c_3 \\ c_4 \\ c_5 \end{Bmatrix} = 0 \tag{46}$$

Where the vector c_k is built from a_k or b_k, respectively,

$$c_k = a_k \text{ or } b_k \tag{47}$$

and

$$\left.\begin{aligned} G &= F + 2iL_0 A \\ G_b &= G + 2L_1{}^2(A - 2iL_0 A F^{-1} A(F + 4L_0{}^2 A F^{-1} A)^{-1} A \\ H &= iL_1 A \end{aligned}\right\} \tag{48}$$

The set of equations (46) has a nontrivial solution only if the determinant coefficients is equal to zero. This condition yields the critical excitation for which one might get an harmonic solution with a basic period T.

T-type unstable regions in the ηp versus L_1 plane for a given L_0, are given by the two sets of critical values of ηp obtained from equation (46). Practically, from the computational point of view, equation (46) can be transformed to the cannonical form eigenvalues

$$([U] - \lambda[I])\{c\} = 0 \tag{49}$$

$$[U] = \begin{bmatrix} G \text{ or } \\ G_b & H & & & \\ \left(\frac{1}{2}\right)^2 H & \left(\frac{1}{2}\right)^2 G & \left(\frac{1}{2}\right)^2 H & & \\ & \left(\frac{1}{3}\right)^2 H & \left(\frac{1}{3}\right)^2 G & \left(\frac{1}{3}\right)^2 H & \\ & & \left(\frac{1}{4}\right)^2 H & \left(\frac{1}{4}\right)^2 G & \left(\frac{1}{4}\right)^2 H \\ & & & \left(\frac{1}{5}\right)^2 H & \left(\frac{1}{5}\right)^2 G \end{bmatrix}; \quad \lambda = \eta^2 p^2 \tag{50}$$

(*b*) *Boundary Unstable Retions of the 2T-Type.* The development of the governing equations for defining the $2T$-type unstable regions, would be identical to what was done previously for the T-type. The harmonic solutions bounding the $2T$-type unstable regions are given by

$$g = \sum_{k=1,2}^{\infty} \left\{ a_k \sin\left(\frac{2k-1}{2}\right)\eta\tau + b_k \cos\left(\frac{2k-1}{2}\right)\eta\tau \right\} \tag{51}$$

Note that the a_k and b_k terms, appearing here are different from those of equation (42).

Substituting (51) into (19), performing trigonometric manipulators and equating common terms in τ, results the following sets of linear homogeneous equations:

$$\left.\begin{aligned} \left[F - \left(\frac{1}{2}\right)^2 \eta^2 p^2 I + i(2L_0 - L_1)A\right] a_1 + iL_1 A a_2 = 0 \\ \left[F - \left(\frac{2k-1}{2}\right)^2 \eta^2 p^2 I + 2iL_0 A\right] a_k + iL_1 A(a_{k-1} + a_{k+1}) = 0 \\ \text{for} \quad k = 2, 3 \ldots \infty \end{aligned}\right\} \tag{52}$$

$$\left.\begin{aligned} \left[[F - \left(\frac{1}{2}\right)^2 \eta^2 p^2 I + i(2L_0 + L_1)A\right] b_1 + iL_1 A b_2 = 0 \\ \left[F - \left(\frac{2k-1}{2}\right)^2 \eta^2 p^2 I + 2iL_0 A\right] b_k + iL_1 A(b_{k-1} + b_{k+1}) = 0 \\ \text{for} \quad k = 2.3 \ldots \infty \end{aligned}\right\} \tag{53}$$

The two foregoing homogeneous sets, can be brought to the cannonical form (49) in order to extract the eigenvalues. For the case of a finite set in (51) $k = 1, 2, \ldots 5$ $(K = 5)$, the matrix $[U]$ reduces to

Downloaded 01 May 2010 to 171.66.16.249. Redistribution subject to ASME license or copyright; see http://www.asme.org/terms/Terms_Use.cfm

$$[U] = \begin{bmatrix} \left(\frac{2}{1}\right)^2(G \pm H) & \left(\frac{2}{1}\right)^2 H & & & & \\ \left(\frac{2}{3}\right)^2 H & \left(\frac{2}{3}\right)^2 G & \left(\frac{2}{3}\right)^2 H & & & \\ & \left(\frac{2}{5}\right)^2 H & \left(\frac{2}{5}\right)^2 G & \left(\frac{2}{5}\right)^2 H & & \\ & & \left(\frac{2}{7}\right)^2 H & \left(\frac{2}{7}\right)^2 G & \left(\frac{2}{7}\right)^2 H & \\ & & & \left(\frac{2}{9}\right)^2 H & \left(\frac{2}{9}\right)^2 G \end{bmatrix}; \quad \lambda = \eta^2 p^2 \quad (54)$$

The $2T$-type unstable regions in the ηp versus L_1 plane, for a given L_0 are bounded by the two sets of critical values of ηp obtained from equation (49).

3.2.3.2 The Characteristic Exponent Method. This method consists of a numerical exploration in the ηp versus L_1 plane of the stability of equation (19) by using the general solution given in equation (41)

$$g(\tau) = e^{\delta \eta \tau} \chi(\tau) \quad (41)$$

The characteristic exponent $\delta\eta$ determines the stability of (41). Since the excitation parameters L_0, L_1, and ηp are given, the values of δ define whether the system is stable or not. The solutions (42) and (51) used to define the boundaries of the T and $2T$-type are particular cases of (41) where $\delta = 0$.

Since our goal is to develop a procedure for numerical search to determine whether a given point in the ηp versus L_1 plane (for a given L_0) is stable or not, we can express $\chi(\tau)$ by a basic periodic solution

$$\chi(\tau) = b_0 + a_1 \sin \eta\tau + b_1 \cos \eta\tau \quad (54)$$

By assuming the basic periodic solution (54) of period T in equation (41), we also include the solutions with the basic period $2T$, since those solutions are combined by the imaginary part of δ.

Substituting (54) into (19), and remembering the result must be valid for any time τ, the following homogeneous equations can be written in the matrix notation

$$\begin{bmatrix} F + 2iL_0A + \\ +\eta^2p^2\delta^2I & 0 & iL_1A \\ 0 & F + 2iL_0A + \\ & -\eta^2p^2I \\ & +\eta^2p^2\delta^2I & -2\eta^2p^2\delta^2I \\ 2iL_1A & 2\eta^2p^2I & F + 2iL_cA + \\ & & -\eta^2p^2I + \\ & & +\eta^2p^2\delta^2I \end{bmatrix} \begin{Bmatrix} b_0 \\ a_1\delta \\ b_1 \end{Bmatrix} = 0 \quad (55)$$

Equation (55) can be reduced by some matrix manipulation to the connical form (49) to extract the complex eigenvalues. The final expression for U is given by

$$U = \begin{bmatrix} -F - 2iL_0A & 0 & -iL_1A \\ & -F - 2iL_0A + & 2(-F - 2iL_0A + \\ -4iL_1A & & \\ & -3\eta^2p^2I & +\eta^2p^2I) \\ & & -F - 2iL_0A + \\ -2iL_1A & 2\eta^2p^2I & \\ & & +\eta^2p^2I \end{bmatrix}; \quad \lambda = \eta^2p^2\delta^2 \quad (56)$$

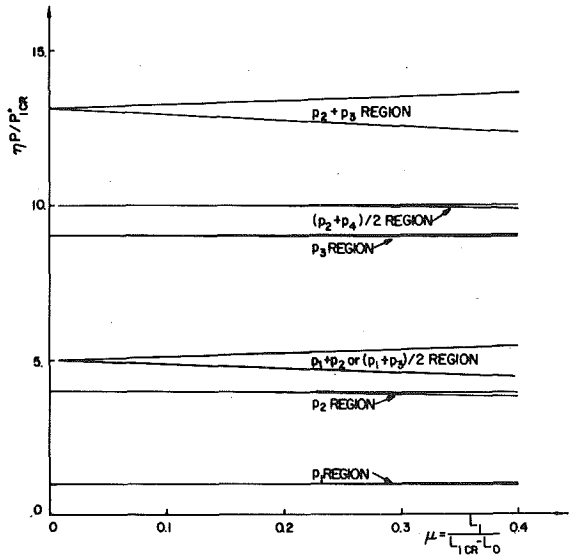


Fig. 4(*a*) Instability regions for a shaft supported by short bearings—$L_0 = 0$

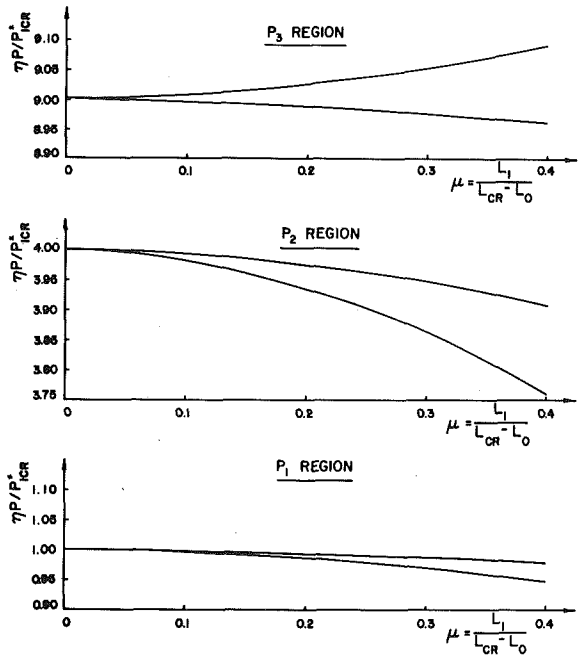


Fig. 4(*b*) Instability regions of period T for a shaft supported by short bearings—$L_0 = 0$

The stability of the system can be deduced directly from the value of the complex eigenvalue $\lambda = \lambda_R + i\lambda_I$.

Summarizing the Characteristic Exponent Method, we have to emphasize that, while it is of great generality in defining the three types of unstable regions, it is *very slow* and *time-consuming*. It requires meshing the plane ηp versus L_1 into a crowded net of points, and checking the stability of each one.

Computing time considerations lead us to use the direct method for defining the stability boundaries for the T and $2T$-type unstable regions, while using the generalized Characteristic Exponent Method for defining combination resonance regions.

4 Results

Instability regions of a rotating shaft due to parametric torque

Downloaded 01 May 2010 to 171.66.16.249. Redistribution subject to ASME license or copyright; see http://www.asme.org/terms/Terms_Use.cfm

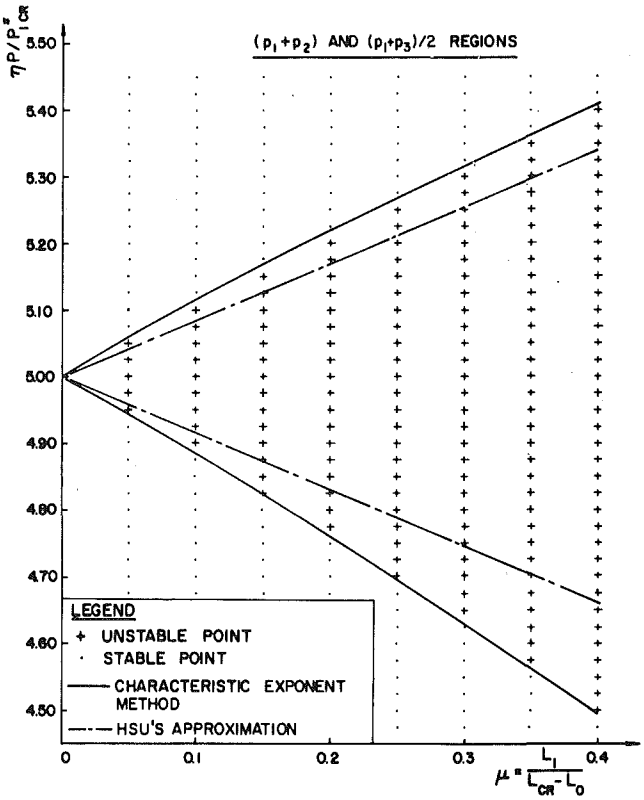


Fig. 4(*c*) Main regions of combination resonance for a shaft supported by short bearings—$L_0 = 0$

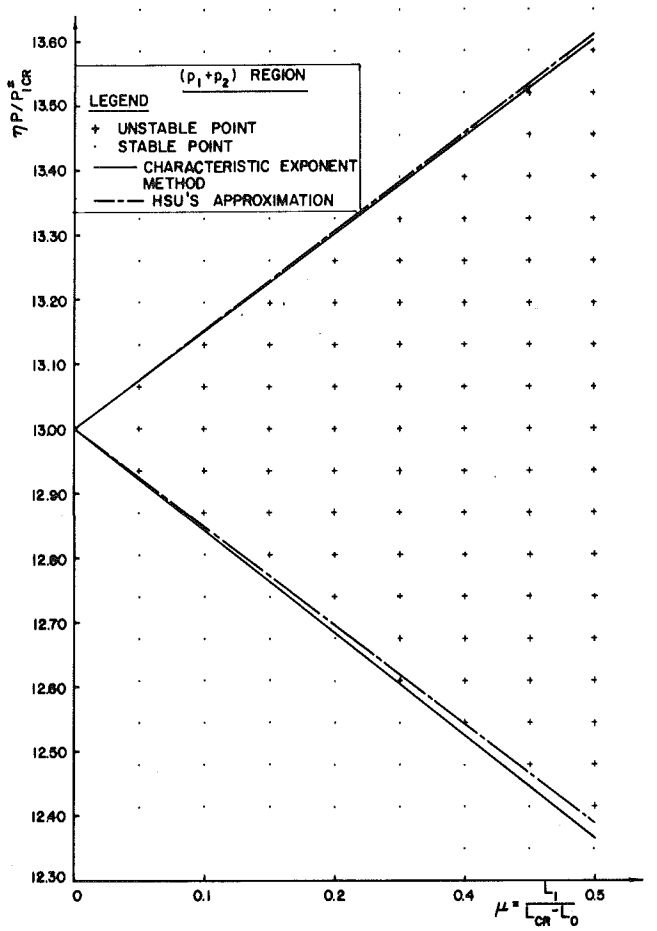


Fig. 4(*d*) Main regions of combination resonance for a shaft supported by short bearings—$L_0 = 0$

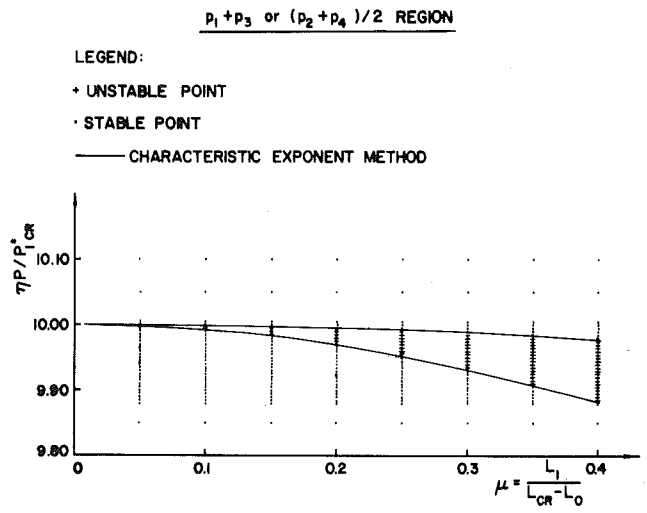


Fig. 4(*e*) Main regions of combination resonance for a shaft supported by short bearings—$L_0 = 0$

excitation, were calculated for shafts with wide and short bearings. The results are presented in Figs. 4–7.

Only the main and the first subharmonic instability regions obtained from the first three frequencies were presented. For convenience, some of the main unstable regions for the short bearing case were presented in a larger scale too. The basis for the calculations were the five first plane shapes ($N = 5$) in the space expansion, and $K = 5$ in the time domain expansion.

The instability regions were calculated for the following L_0 parameters:

$$L_0 = 0 \text{ and } 4.5 \text{ for the wide bearing case}$$

$$L_0 = 0 \text{ and } 3 \text{ for the short bearing case}$$

and were drawn in the $\eta p/p_{1\,cr}{}^*$ versus $\mu = L_1/L_{cr} - I_0$ plane. Where $p_{1\,cr}{}^*$ is the first nondimensional critical speed of the shaft with no torque applied ($L_0 = L_1 = 0$). This critical speed is equal to the natural frequency of the shaft in bending. L_{cr} is the dimensionless torque required to buckle the shaft in its first mode shape. The numerical values for $P_{1\,cr}{}^*$ and L_{cr} are tabulated in Table 1.

The abscissa μ in Figs. 4–7 was chosen as $\mu = L_1/L_{cr} - L_0$, since it is the ratio between the harmonic torque terms and the $L_{cr} - L_0$ term, which is a measure of the effective stiffness of the system under the constant torque L_0.

5 Discussion and Conclusions

Examination of the numerical results presented in Figs. 4–7 yields the following conclusions:

1 A shaft mounted in wide or short bearings has parametric instability regions of the T and $2T$ and combination resonance types. The combination resonance regions are based on sum of frequencies. The widest and the most dangerous instability regions are of the combination resonance type.

2 Compared to the principal unstable regions, the subharmonics are usually of narrow extent. It may, in fact, be very difficult to produce these subharmonic instabilities experimentally.

3 The basic unstable regions obtained numerically under a pure oscillating torque ($L_0 = 0$) are in an excellent engineering agreement with those derived by Hsu's [4] approximation.

(*a*) The width of the unstable region of the $2T$-type degenerate

Downloaded 01 May 2010 to 171.66.16.249. Redistribution subject to ASME license or copyright; see http://www.asme.org/terms/Terms_Use.cfm

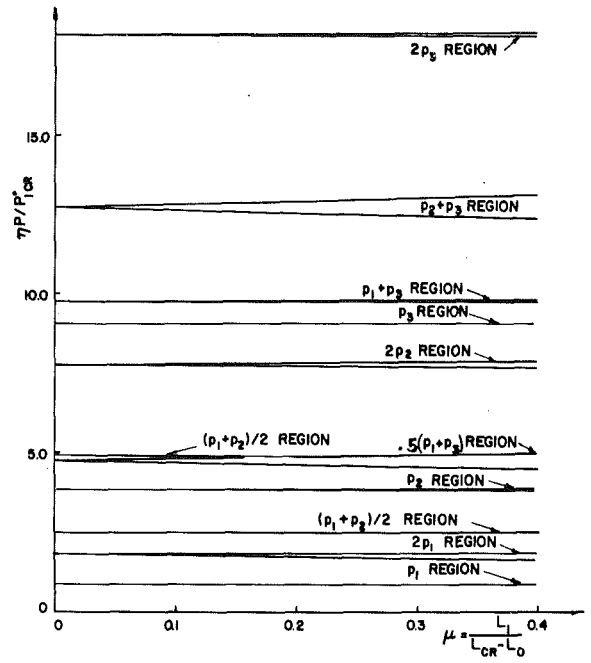


Fig. 5(*a*) Instability regions for a shaft supported by short bearings—$L_0 = 3$

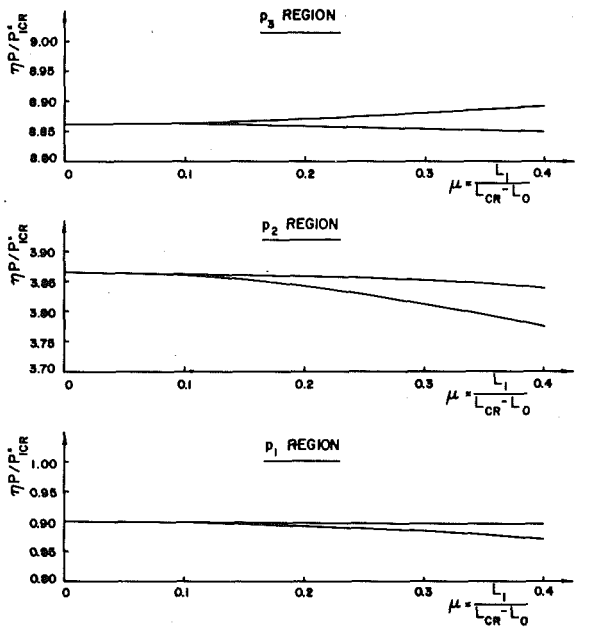


Fig. 5(*b*) Instability regions of period T for a shaft supported by short bearings—$L_0 = 3$

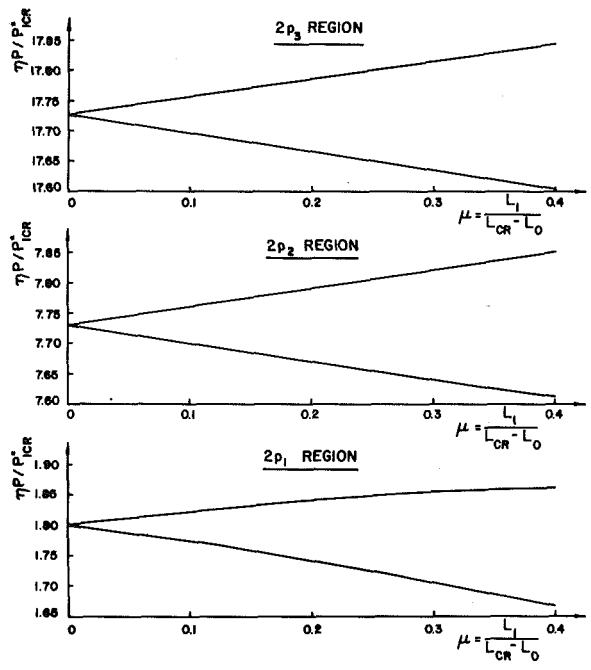


Fig. 5(*c*) Instability regions of period $2T$ for a shaft supported by short bearings—$L_0 = 3$

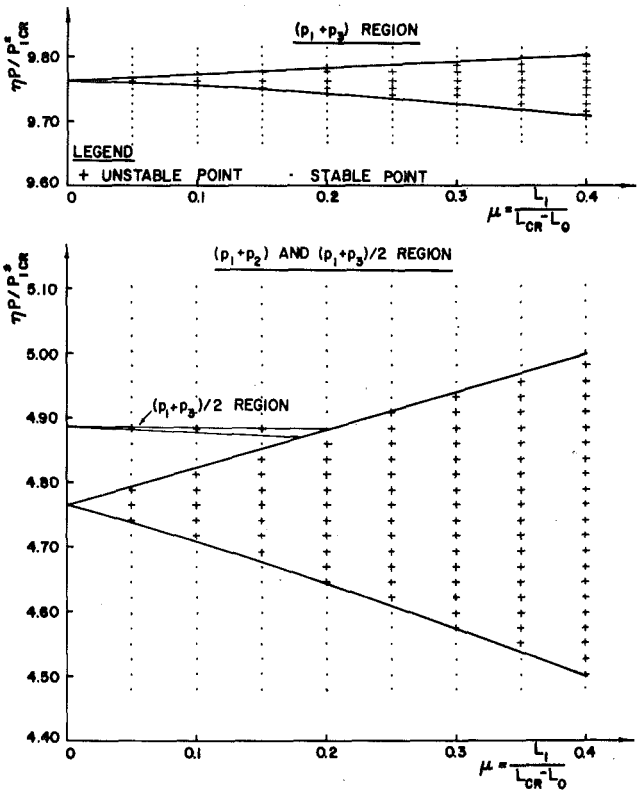


Fig. 5(*d*) Main regions of combination resonance for a shaft supported by short bearings—$L_0 = 3$

to a line. This characteristic is well known for physical systems where the $2T$-type instability dominates.

(*b*) Unstable combination resonance regions exist only for sums of frequencies. The possibility of existence of combination resonance regions based on difference of frequencies was checked numerically and no such instability was found.

(*c*) The main combination resonance regions are based on odd frequency sums. For example, no unstable region was obtained from the combination of $p_1 + p_3$. From the numerical results we can conclude that the first combination resonance subharmonic unstable regions are obtained for frequencies whose order summation is an odd

Table 1

	$p_{1\,\mathrm{cr}}{}^*$	L_{cr}
Shaft mounted in wide bearings	4.730041^2	8.9869
Shaft mounted in short bearings	π^2	2π

Downloaded 01 May 2010 to 171.66.16.249. Redistribution subject to ASME license or copyright; see http://www.asme.org/terms/Terms_Use.cfm

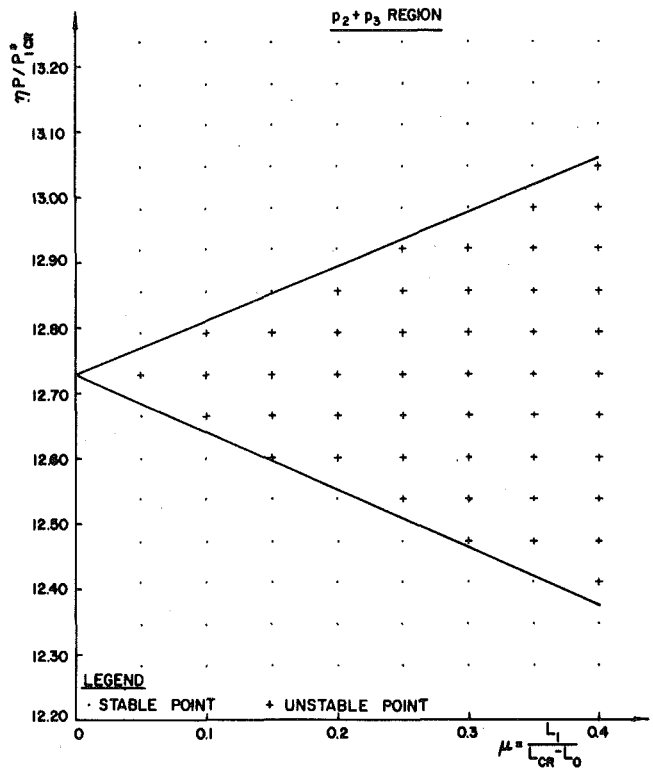


Fig. 5(*e*) Main regions of combination resonance for a shaft supported by short bearings—$L_0 = 3$

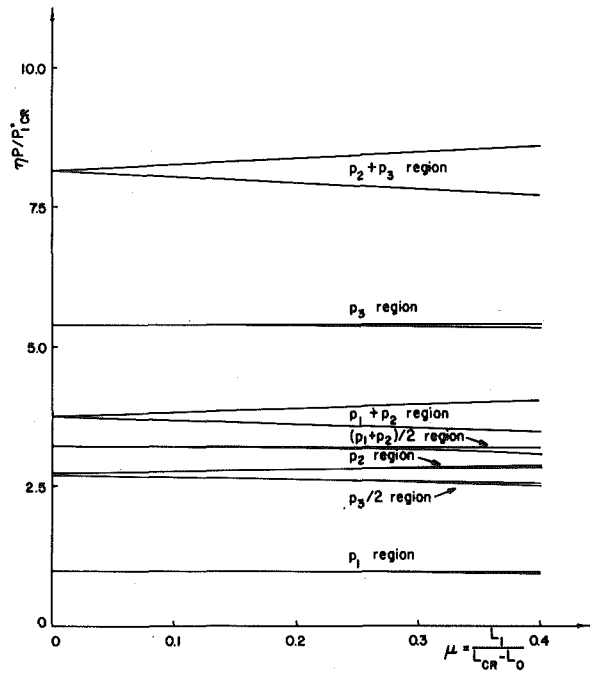


Fig. 6 Instability regions for a shaft supported by wide bearings—$L_0 = 0$

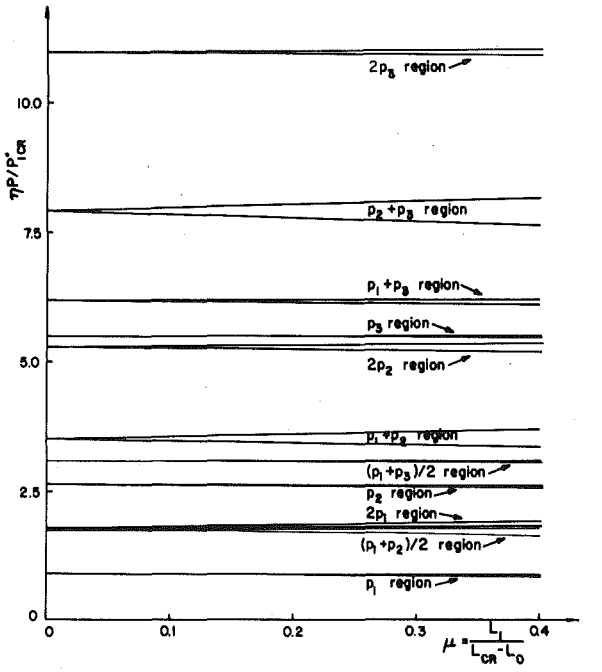


Fig. 7 Instability regions for a shaft supported by wide bearings—$L_0 = 4.5$

integer. Hence, narrow subharmonic regions of the $(p_i + p_j)/2$ type were obtained only when $i + j$ is odd.

4 For the cases where $L_0 \neq 0$:

(*a*) Unstable regions of the $2T$-type were obtained. In the cases checked, those regions were wider that the T-type regions, but substantially narrower than the combination resonance regions. The $2T$ subharmonic regions are very narrow compared to the main $2T$ region.

(*b*) In contrast to the results obtained for $L_0 = 0$, unstable regions of combination resonance were obtained from frequencies whose order summation is an even integer. The main regions based on $p_i + p_j$ where $i + j$ is even, are narrower than the regions based on frequencies whose order summation is odd, and their shape resembles that of subharmonics. (They *are not* bounded by two lines having opposite slopes.)

The restriction previously noted concerning the existence of combination resonance subharmonics in the case of $L_0 = 0$, does not apply for $L_0 \neq 0$.

References

1 McLaclan, N. W., *Theory and Application of Mathieu Functions*, Dover Publications, Inc., New York, 1964.

2 Bolotin, V. V., *The Dynamic Stability of Elastic Systems*, Holden-Day, Inc., 1964.

3 Floquet, G., "Sur les équations differentielles linéaires," *Ann. De L'école Normale Supèrieure*, Vol. 12, 1883, pp. 47–88.

4 Hsu, C. S., "On the Parametric Excitation of a Dynamic System Having Multiple Degrees of Freedom," ASME JOURNAL OF APPLIED MECHANICS, Vol. 30, 1963, pp. 367–372.

5 Valeev, K. G., "On the Danger of Combination Resonances," *Journal of Applied Mathematics and Mechanics* (translation of *Prikladnaia Matematika i Mekhanika*), Vol. 27, No. 6, 1963, pp. 1745–1759.

6 Eshleman, R. L., "On the Stability of Continuous Rotors," PhD Thesis, Illinois Institute of Technology, Jan. 1967.

7 Eshleman, R. L., and Eubanks, R. A., "On the Critical Speeds of a Continuous Rotor," ASME *Journal of Engineering for Industry*, Vol. 91, Nov. 1969, pp. 1180–1188.

8 Willems, N., and Holzer, S. M., "Critical Speeds of Rotating Shaft Subjected to Axial Loading and Tangential Torsion," ASME *Journal of Engineering for Industry*, Vol. 89, May 1967, pp. 259–264.

9 Bishop, R. E. D., and Johnson, D. C., *The Mechanics of Vibrations*, Cambridge, 1960.

Downloaded 01 May 2010 to 171.66.16.249. Redistribution subject to ASME license or copyright; see http://www.asme.org/terms/Terms_Use.cfm

Table 2 Variation of square root of the nondimensional critical speeds of a shaft in two wide bearing versus L_0. The calculation was made using the Galerkin method assuming five plane shapes ($N = 5$).

L_0	$\sqrt{p_1}$	$\sqrt{p_2}$	$\sqrt{p_3}$	$\sqrt{p_4}$	$\sqrt{p_5}$
0.	4.7300	7.8532	10.9956	14.1372	17.2788
2.	4.6854	7.8177	10.9695	14.1229	17.2975
3.5	4.5856	7.7423	10.9146	14.0949	17.3352
5.	4.4052	7.6198	10.8276	14.0557	17.3912
6.	4.2141	7.5075	10.7506	14.0252	17.4376
7.	3.9213	7.3660	10.6576	13.9930	17.4902
8.	3.4054	7.1897	10.5483	13.9604	17.5484

Table 3 Variation of the square root of the nondimensional critical speeds of a shaft in two wide bearings versus L_0. The results are obtained by the characteristic determinant method [6, 7].

L_0	$\sqrt{p_1}$	$\sqrt{p_2}$	$\sqrt{p_3}$	$\sqrt{p_4}$	$\sqrt{p_5}$
0.	4.7300	7.8532	10.9956	14.1372	17.2788
2.	4.6850	7.8170	10.9680	14.1140	17.2600
3.5	4.5850	7.7410	10.9090	14.0670	17.2200
5.	4.4043	7.6157	10.8154	13.9920	17.1572
6.	4.2124	7.5008	10.7323	13.9262	17.1026
7.	3.9175	7.3559	10.6308	13.8469	17.0373
8.	3.3951	7.1750	10.5090	13.7532	16.9607

Table 4 Variation of the square root of the nondimensional critical speeds of a shaft in short bearings versus L_0. The results were obtained by the modified Galerkin method using five plane shapes ($N = 5$), while $M = 6$.

L_0	$\sqrt{p_1}$	$\sqrt{p_2}$	$\sqrt{p_3}$	$\sqrt{p_4}$	$\sqrt{p_5}$
0.	3.1416	6.2832	9.4248	12.5664	15.7080
1.	3.1251	6.2712	9.4168	12.5603	15.7137
2.	3.0732	6.2348	9.3927	12.5426	15.7305
3.	2.9763	6.1724	9.3514	12.5141	15.7581
5.	2.5153	5.9564	9.2109	12.4311	15.8420
6.	1.7301	5.7905	9.1072	12.3809	15.8963

APPENDIX

Numerical Evaluation of the Torque Effect Matrix A and the Accuracy Obtained With It in Calculating Critical Speeds

(1) Shaft Mounted in Long Bearings. The analytical expressions for the $X_n(\xi)$ are given in (9).

The A matrix terms were calculated analytically according to their definition (16).

Using five modes, we can write the following numerical expression for the A matrix:

$$A = \begin{bmatrix} 0 & 61.032522 & 0 & 29.794096 & 0 \\ & 0 & 238.336920 & 0 & 107.583340 \\ & & 0 & 593.264200 & 0 \\ \text{Anti-} & & & 0 & 1091.087100 \\ \text{symmetric} & & & & 0 \end{bmatrix} \quad (57)$$

In order to check the accuracy of the Galerkin approximation made in the space-dependence, the critical speeds of a shaft under a constant torque L_0, were calculated according to equation (30), which is the cannonical form for extraction of eigenvalues.

Table 5 Variation of the square root of the nondimensional critical speeds of a shaft in short bearings versus L_0. The results were obtained by the modified Galerkin method using five plane shapes ($N = 5$) while $M \to \infty$.

L_0	$\sqrt{p_1}$	$\sqrt{p_2}$	$\sqrt{p_3}$	$\sqrt{p_4}$	$\sqrt{p_5}$
0.	3.1416	6.2832	9.4248	12.5664	15.7080
1.	3.1255	6.2716	9.4170	12.5605	15.7135
2.	3.0748	6.2364	9.3934	12.5432	15.7300
3.	2.9805	6.1759	9.3532	12.5153	15.7569
5.	2.5374	5.9666	9.2168	12.4340	15.8389
6.	1.8294	5.8058	9.1166	12.3845	15.8920

Table 6 Variation of the square root of the nondimensional critical speeds of a shaft in short bearings versus L_0. The results were obtained by the characteristic determinant method [6, 7].

L_0	$\sqrt{p_1}$	$\sqrt{p_2}$	$\sqrt{p_3}$	$\sqrt{p_4}$	$\sqrt{p_5}$
0.	3.1416	6.2832	9.4248	12.5664	15.7080
1.	3.1254	6.2714	9.4162	12.5590	15.7025
2.	3.0742	6.2354	9.3904	12.5400	15.6861
3.	2.9791	6.1734	9.3467	12.5059	15.6587
5.	2.5318	5.9566	9.2013	12.3953	15.5690
6.	1.8060	5.7885	9.0962	12.3169	15.5063

The results obtained by the Galerkin method were compared with results obtained by other well-known methods such as the characteristic determinant method described in [6, 7] which is assumed to be an exact numerical method (except for roundoff errors).

Comparing the results summarized in Tables 2 and 3, one can see that excellent accuracy is obtained by the present method. For example, an accuracy of 0.06 percent in $P_{1\,cr}$ and 0.04 percent in $P_{2\,cr}$ was obtained for $L_0 = 8$ by using only five plane shapes in the Galerkin approximation. The Galerkin method results are, as expected, substantially larger.

(2) Shaft Mounted in Short Bearings. The terms of the A matrix are defined by

$$2a_{mn} = \int_0^1 Z_m(\xi) X_n^{\mathrm{III}}(\xi) d\xi$$

$$= n\pi^3 \int_0^1 [-n^2 \cos n\pi\xi + (M+n)^2 \cos (M+n)\pi\xi] \sin m\pi\xi d\xi \quad (58)$$

yielding

$$a_{mn} = \begin{cases} 0 & \text{for } m+n \text{ even} \\ 2mn\pi^2 \left[\dfrac{(M+n)^2}{m^2-(M+n)^2} - \dfrac{n^2}{m^2-n^2}\right] & \text{for } m+n \text{ odd} \end{cases} \quad (59)$$

As just noted, the a_{mn} terms in equation (27) are the only terms in the equation depending on the integer M, which corresponds to the higher shapes combining the solution (25). Up to now, the only restrictions on M were

$$M - \text{is even} \quad M > N$$

It is natural to inquire about the behavior of the solution in the limit $M \to \infty$. For this limiting case, we obtain

$$\lim_{M\to\infty} a_{mn} = \begin{cases} 0 & \text{for } m+n \text{ even} \\ -\dfrac{2nm^3\pi^2}{m^2-n^2} & \text{for } m+n \text{ odd} \end{cases} \quad (60)$$

Downloaded 01 May 2010 to 171.66.16.249. Redistribution subject to ASME license or copyright; see http://www.asme.org/terms/Terms_Use.cfm

The physical meaning of $M \to \infty$ is that we assume in equation (25) the plane simply supported beam mode shapes

$$\lim_{M \to \infty} X_n(\xi) \to \sin n\pi\xi \tag{61}$$

with an infinitisimal correction accounting for clamping at both ends ($X_n^{\mathrm{I}}(\xi) = 0$ at $\xi = 0, 1$). According to (59) the limiting torque effect matrix A is given by (for $N = 5$)

$$A = \begin{bmatrix} 0 & 13.159473 & 0 & 5.263789 & 0 \\ -52.637890 & 0 & 94.748202 & 0 & 37.598493 \\ 0 & -213.183460 & 0 & 304.547790 & 0 \\ -84.220624 & 0 & -54.141830 & 0 & 701.838540 \\ 0 & -234.990580 & 0 & -1096.622700 & 0 \end{bmatrix} \tag{62}$$

In contrast to the wide bearing case, here the A is not an antisymmetric matrix. Its terms have only the sign changing property

$$\text{sign } (a_{mn}) = -\text{ sign } (a_{nm}) \tag{63}$$

Similarly to what was done for wide bearings, the critical speeds of a shaft under a constant torque $L_{\bar{0}}$ were calculated using the modified Galerkin method for M finite and infinite. The results were compared with those obtained by the characteristic deteminant method

As for wide bearings, one can see from Tables 4–6 that an excellent engineering accuracy is obtained by the modified Galerkin method. The accuracy decreases with increasing L_0. The limiting case $M \to \infty$ yields a better and more exact representation than that based on a finite value for M ($M = 6$). The critical speeds obtained with $M \to \infty$, are always higher than those obtained by the characteristic determinant method, while for the critical speeds obtained with a finite value for M, there is no consistency. Some of the critical speeds are higher, and some are lower than those obtained by the characteristic determinant method. The absolute error in the critical speeds obtained by the $M \to \infty$ representation are significantly lower than those obtained with a finite value of M.

Downloaded 01 May 2010 to 171.66.16.249. Redistribution subject to ASME license or copyright; see http://www.asme.org/terms/Terms_Use.cfm

S. L. Lau
Lecturer in Civil Engineering,
Hong Kong Baptist College,
224, Waterloo Road,
Kowloon, Hong Kong

Y. K. Cheung
Dean,
Faculty of Engineering
and Architecture,
University of Hong Kong,
Pokfulam Road,
Hong Kong

Amplitude Incremental Variational Principle for Nonlinear Vibration of Elastic Systems

The incremental method has been widely used in various types of nonlinear analysis, however, so far it has received little attention in the analysis of periodic nonlinear vibrations. In this paper, an amplitude incremental variational principle for nonlinear vibrations of elastic systems is derived. Based on this principle various approximate procedures can be adapted to the incremental formulation. The linear solution for the system is used as the starting point of the solution procedure and the amplitude is then increased incrementally. Within each incremental step, only a set of linear equations has to be solved to obtain the data for the next stage. To show the effectiveness of the present method, some typical examples of nonlinear free vibrations of plates and shallow shells are computed. Comparison with analytical results calculated by using elliptic integral confirms that excellent accuracy can be achieved. The technique is applicable to highly nonlinear problems as well as problems with only weak nonlinearity.

Introduction

Nonlinear effects have long been recognized to play an important role in the vibration analysis of many thin-walled structures. Usually, in nonlinear analysis, the elastic system is first reduced to a discrete system with one or more degrees of freedom by a suitable discretization procedure and a set of nonlinear ordinary differential equations in time is obtained. Such equations can be solved by one of the following methods:

1 **Harmonic Balance Method (Ritz and Galerkin Averaging Method) [1–5].** This approach involved making the average value of the virtual work per period vanish, and the resulting set of algebraic nonlinear equations is then solved numerically by iterative method or Newton-Raphson method.

2 **Perturbation Method [6–9].** The desired quantities are developed in powers of some small parameters, and the original nonlinear equation is then separated into a series of linear equations, which can be solved in a stepwise manner. Usually, this method can only be applied to a system with weak nonlinearity and the computation procedures become quite cumbersome if many terms in the perturbation series are required to achieve a desired degree of accuracy.

It is well known that incremental method has many advantages in static and dynamic response analysis of nonlinear systems, and yet, for one reason or other, it has received little attention in the analysis of nonlinear periodic vibrations and other related problems (dynamic instability, flutter, etc.). In many nonlinear problems, the responses are so complicated that many conventional numerical procedures fail to produce results which are convergent under all circumstances. However, with the incremental method convergence can always be guaranteed provided that a suitably small increment is chosen and a series of solutions can be obtained in a step-by-step manner starting from a known solution (usually the linear solution or simply the natural state at rest).

The purpose of this paper is to present the amplitude incremental variational principle for nonlinear vibrations of elastic systems. Based on this principle various approximate procedures such as the Rayleigh-Ritz method or the finite-element method can be used for formulating the incremental solution. To show the essence and the effectiveness of the present method, some typical examples of large-amplitude free vibrations of plates and shallow shells are presented herein. Comparison with other published results confirms that excellent accuracy can be achieved by the incremental method.

Amplitude Incremental Variational Principle

In formulating this variational principle, it is expedient to start from

Contributed by the Applied Mechanics Division and presented at the Winter Annual Meeting, Washington, D.C., November 15–20, 1981, of THE AMERICAN SOCIETY OF MECHANICAL ENGINEERS.

Discussion on this paper should be addressed to the Editorial Department, ASME, United Engineering Center, 345 East 47th Street, New York, N.Y. 10017, and will be accepted until March 1, 1982. Manuscript received by ASME Applied Mechanics Division, June, 1980; final revision, March, 1981. Paper No. 81-WA/APM-26.

Copyright © 1981 by ASME

Downloaded 01 May 2010 to 171.66.16.249. Redistribution subject to ASME license or copyright; see http://www.asme.org/terms/Terms_Use.cfm

the general theory of elasticity. The corresponding variational principle for the more common structures can always be derived from the general case by introducing appropriate assumptions.

In nonlinear theory of elasticity employing the Lagrangian approach, the strain components ϵ_{ij} are defined as

$$\epsilon_{ij} = \frac{1}{2}\left(\frac{\partial u_i}{\partial x_j} + \frac{\partial u_j}{\partial x_j} + \frac{\partial u_r}{\partial x_i}\frac{\partial u_r}{\partial x_j}\right) \quad (i, j, r = 1, 2, 3) \tag{1}$$

where $u_i (i = 1, 2, 3)$ denote the displacement components in a rectangular coordinate system and the corresponding stress components can be expressed as

$$\sigma_{ij} = \frac{\partial U}{\partial \epsilon_{ij}},$$

where U is the strain energy per unit volume. If Hookean solid is assumed, then

$$\sigma_{ij} = C_{ijkl}\epsilon_{kl}, \tag{2}$$

where the elasticity constants should satisfy the following symmetry conditions:

$$C_{ijkl} = C_{ijlk} = C_{jikl} = C_{klij}, \tag{2a}$$

The virtual work equation in terms of the initial geometry for a dynamic problem can be written as

$$\int\int\int_v \sigma_{ij}\delta\epsilon_{ij}dv - \int\int\int_v \overline{P}_i\delta u_i dv + \int\int\int_v \rho\left(\frac{\partial^2 u_i}{\partial t^2}\right)\delta u_i dv - \int\int_{s_\sigma} \overline{T}_i\delta u_i ds = 0, \tag{3}$$

where ρ denotes the density of the material, $\overline{P}_i$, $\overline{T}_i$ $(i = 1, 2, 3)$ denote the body force and surface force components, respectively, v denotes the volume of the body, and s_σ the surface on which traction $\overline{T}_i$ is prescribed.

Consider now only the periodic motion of the elastic system and introducing $\tau = \omega t$, where ω is the frequency of vibration, it is possible to integrate equation (3) with respect to time over one period to yield

$$\int_0^{2\pi}\left[\int\int\int_v \sigma_{ij}\delta\epsilon_{ij}dv - \int\int\int_v \overline{P}_i\delta u_i dv - \int\int_{s_\sigma}\overline{T}_i\delta u_i ds + \omega^2\int\int\int_v \rho\left(\frac{\partial^2 u_i}{\partial\tau^2}\right)\delta u_i dv\right]d\tau = 0$$

Integrating by parts and noting the periodic condition

$$u_i(\tau) = u_i(\tau + 2\pi), \quad (i = 1, 2, 3) \tag{4}$$

the foregoing equation can be rewritten as

$$\int_0^{2\pi}\left[\int\int\int_v \sigma_{ij}\delta\epsilon_{ij}dv - \int\int\int_v \overline{P}_i\delta u_i dv - \int\int_{s_\sigma}\overline{T}_i\delta u_i ds - \omega^2\int\int\int_v \rho\left(\frac{\partial u_i}{\partial\tau}\right)\delta\left(\frac{\partial u_i}{\partial\tau}\right)dv\right]d\tau = 0 \tag{5}$$

This variational equation is in fact a special form of Hamilton's principle for periodic motion.

Consider that the state of motion is subject to a small increment. The frequency of the vibrating system, which is amplitude-dependent, will be changed by a small increment $\Delta\omega$. In general, it can be stated that

$$u_i = u_i^{(0)} + \Delta u_i, \tag{6}$$

$$\overline{P}_i = \overline{P}_i^{(0)} + \Delta\overline{P}_i, \tag{7}$$

$$\overline{T}_i = \overline{T}_i^{(0)} + \Delta\overline{T}_i, \tag{8}$$

$$\omega = \omega_0 + \Delta\omega, \tag{9}$$

where $u_i^{(0)}, \overline{P}_i^{(0)}, \overline{T}_i^{(0)}$ denote the previous state of the periodic motion but with the frequency equal to $\omega_0 + \Delta\omega$ and ω_0 denote the previous frequency. Introducting equations (1) and (6) into the first integral of equation (5) and neglecting the small quantities of higher order, one can obtain

$$\int\int\int_v \sigma_{ij}\delta\epsilon_{ij}dv = \int\int\int_v \frac{1}{2}(\sigma_{ij}^{(0)} + \Delta\sigma_{ij})\times\left[\delta\frac{\partial\Delta u_i}{\partial x_j} + \delta\frac{\partial\Delta u_j}{\partial x_i} + \frac{\partial(u_r^{(0)} + \Delta u_r)}{\partial x_j}\delta\frac{\partial\Delta u_r}{\partial x_j} + \frac{\partial(u_r^{(0)} + \Delta u_r)}{\partial x_j}\delta\frac{\partial\Delta u_r}{\partial x_i}\right]dv \cong \int\int\int_v [\sigma_{ij}^{(0)}\delta\Delta\epsilon_{ij} + \Delta\sigma_{ij}\delta\Delta\epsilon_{ij} + \sigma_{ij}^{(0)}\cdot\frac{1}{2}\left(\frac{\partial\Delta u_r}{\partial x_i}\delta\frac{\partial\Delta u_r}{\partial x_j} + \frac{\partial\Delta u_r}{\partial x_j}\delta\frac{\partial\Delta u_r}{\partial x_i}\right)]dv, \tag{10}$$

where

$$\Delta\epsilon_{ij} = \frac{1}{2}\left(\frac{\partial\Delta u_i}{\partial x_j} + \frac{\partial\Delta u_j}{\partial x_i} + \frac{\partial u_i^{(0)}}{\partial x_i}\frac{\partial\Delta u_r}{\partial x_j} + \frac{\partial\Delta u_r}{\partial x_i}\frac{\partial u_r^{(0)}}{\partial x_j}\right) \tag{11}$$

and

$$\Delta\sigma_{ij} = C_{ijkl}\Delta\epsilon_{kl} \tag{12}$$

Similarly, by substituting equations (6) and (9) into the last term inside the bracket of equation (5) and neglecting the small quantities of higher order, it is possible to obtain

$$\omega^2\int\int\int_v \rho\left(\frac{\partial u_i}{\partial\tau}\right)\delta\left(\frac{\partial u_i}{\partial\tau}\right)dv = (\omega_0^2 + 2\omega_0\Delta\omega + \Delta\omega^2)\int\int\int_v \rho\frac{\partial(u_i^{(0)} + \Delta u)}{\partial\tau}\delta\frac{\partial\Delta u_i}{\partial\tau}dv \cong (\omega_0^2 + 2\omega_0\Delta\omega)\int\int\int_v \rho\frac{\partial u_i^{(0)}}{\partial\tau}\delta\frac{\partial\Delta u_i}{\partial\tau}dv + \omega_0^2\int\int\int_v \rho\frac{\partial\Delta u_i}{\partial\tau}\delta\frac{\partial\Delta u_i}{\partial\tau}dv. \tag{13}$$

With the relations given in equations (6)–(13), equation (5) is reduced to the form

$$\int_0^{2\pi}\left\{\int\int\int_v\left[\Delta\sigma_{ij}\delta\Delta\epsilon_{ij} + \sigma_{ij}^{(0)}\frac{1}{2}\delta\left(\frac{\partial\Delta u_r}{\partial x_i}\frac{\partial\Delta u_r}{\partial x_j}\right)\right]dv - \omega_0^2\int\int\int_v \rho\frac{\partial\Delta u_i}{\partial\tau}\delta\frac{\partial u_i}{\partial\tau}dv + \int\int\int_v \sigma_{ij}^{(0)}\delta\Delta\epsilon_{ij}dv - \int\int\int_v \overline{P}_i^{(0)}\delta\Delta u_i dv - \int\int_{s_\sigma}\overline{T}_i^{(0)}\delta\Delta u_i ds - \omega_0^2\int\int\int_v \rho\frac{\partial u_i^{(0)}}{\partial\tau}\delta\frac{\partial\Delta u_i}{\partial\tau}dv - \int\int\int_v \Delta\overline{P}_i\delta\Delta u_i dv - \int\int_{s_\sigma}\Delta\overline{T}_i\delta\Delta u_i ds - 2\omega_0\Delta\omega\int\int\int_v \rho\frac{\partial u_i^{(0)}}{\partial\tau}\delta\frac{\partial\Delta u_i}{\partial\tau}dv\right\}d\tau = 0 \tag{14}$$

It should be noted that all functions in this equation must be periodic and satisfy conditions similar to equation (4).

By using Gauss' theorem it can be established that

$$\int\int\int_v \sigma_{ij}^{(0)}\Delta\epsilon_{ij}dv = -\int\int\int_v \frac{\partial}{\partial x_j}\left[\sigma_{jk}^{(0)}\left(\delta_{ik} + \frac{\partial u_i^{(0)}}{\partial x_k}\right)\right]\times\Delta u_i dv + \int\int_s \sigma_{jk}^{(0)}\left(\delta_{ik} + \frac{\partial u_i^{(0)}}{\partial x_k}\right)n_j\Delta u_i ds,$$

where δ_{ik} is the Kronecker's notation, and n_j is the direction cosine of the normal to the surface.

Finally, assuming that the external forces are independent of deformation, equation (14) can be rewritten as the form

$$\delta\left\{\int_0^{2\pi}\left[\int\int\int_v\left(\frac{1}{2}C_{ijkl}\Delta\epsilon_{ij}\Delta\epsilon_{kl} + \frac{1}{2}\sigma_{ij}^{(0)}\frac{\partial\Delta u_r}{\partial x_i}\frac{\partial\Delta u_r}{\partial x_j}\right)dv \right. \tag{14a}$$

Downloaded 01 May 2010 to 171.66.16.249. Redistribution subject to ASME license or copyright; see http://www.asme.org/terms/Terms_Use.cfm

$$-\frac{\omega_0^2}{2}\int\int\int_v \rho\frac{\partial\Delta u_i}{\partial\tau}\frac{\partial\Delta u_i}{\partial\tau}dv\Big]d\tau$$
$$-\int_0^{2\pi}\Big[\int\int\int_v(\Delta\overline{P}_i+P_i^{(r)})\Delta u_i dv$$
$$+\int\int_{s_\sigma}(\Delta\overline{T}_i+T_i^{(r)})\Delta u_i ds$$
$$+2\omega_0\Delta\omega\int\int\int_v\rho\frac{\partial u_i^{(0)}}{\partial\tau}\frac{\partial\Delta u_i}{\partial\tau}dv\Big]d\tau\Big\}=0, \quad (14a)$$
(*Cont.*)

where

$$P_i^{(r)}=\frac{\partial}{\partial x_j}\left[\sigma_{jk}^{(0)}\left(\delta_{ik}+\frac{\partial u_i^{(0)}}{\partial x_k}\right)\right]-\rho\omega_0^2\frac{\partial^2 u_i^{(0)}}{\partial\tau^2}+\overline{P}_i^{(0)}, \quad (15)$$

$$T_i^{(r)}=\overline{T}_i^{(0)}-\sigma_{jk}^{(0)}\left(\delta_{ik}+\frac{\partial u_i^{(0)}}{\partial x_k}\right)n_j. \quad (16)$$

The quantities $P_i^{(r)}$, $T_i^{(r)}$, which will be called the residual load corrections, are obtained by evaluating the terms at the state before the current increment and will vanish when the previous state is an exact solution. Such corrections are extremely important as they prevent an approximate solution based on this incremental formulation from drifting away from the exact solution. Such techniques have already been widely used in nonlinear static analysis [10].

The last integral in equation (14*a*) represents the unbalanced kinetic energy of the previous state of motion due to the frequency shift $\Delta\omega$.

It is worthy of special mention that equation (14) is more general than equation (14*a*), because the former holds irrespective of the stress-strain relation and is applicable to nonconservative problems.

Plates and Shallow Shells

If von Karman's large deflection theory is adopted and the effects of rotary and in-plane inertia are neglected, the governing equations for plates can be formulated in terms of two functions, i.e., the deflection w and the Airy stress function ϕ as follows:

$$D\nabla^2\nabla^2 w=\frac{\partial^2 w}{\partial x^2}\frac{\partial^2\phi}{\partial y^2}+\frac{\partial^2 w}{\partial y^2}\frac{\partial^2\phi}{\partial x^2}-2\frac{\partial^2 w}{\partial x\partial y}\frac{\partial^2\phi}{\partial x\partial y}-\rho h\frac{\partial^2 w}{\partial t^2}+q, \quad (17)$$

$$\frac{1}{Eh}\nabla^2\nabla^2\phi=\left(\frac{\partial^2 w}{\partial x\partial y}\right)^2-\frac{\partial^2 w}{\partial x^2}\frac{\partial^2 w}{\partial y^2}, \quad (18)$$

This formulation retains the essential nonlinear features of the problem and is widely used in the literature.

A corresponding generalized variational principle which is equivalent to the aforementioned equations together with the boundary conditions was presented in [11], and the simplified form for periodic vibration problems can be written as

$$\delta\int_0^{2\pi}\Big[\int\int_A\Big(\frac{1}{2}\{\chi\}^T[D_b]\{\chi\}-\frac{1}{2}\{\Phi\}^T[D_m]\{\Phi\}$$
$$+\frac{1}{2}\{\theta\}^T[A]^T\{\Phi\}\Big)dxdy-\omega^2\int\int_A\frac{\rho h}{2}\left(\frac{\partial w}{\partial\tau}\right)^2 dxdy$$
$$-\int\int_A qw dxdy-\int_{C_R}\overline{R}_n w ds+\int C_M\overline{M}_n\frac{\partial w}{\partial n}ds\Big]d\tau=0, \quad (19)$$

where

$$[D_b]=\frac{Eh^3}{12(1-\nu^2)}\begin{bmatrix}1&\nu&0\\ \nu&1&0\\ 0&0&\frac{1-\nu}{2}\end{bmatrix},\quad [D_m]=\frac{1}{Eh}\begin{bmatrix}1&-\nu&0\\ -\nu&1&0\\ 0&0&2(1+\nu)\end{bmatrix},$$

$$\{\chi\}=\begin{Bmatrix}-\frac{\partial^2 w}{\partial x^2}\\ -\frac{\partial^2 w}{\partial y^2}\\ -2\frac{\partial^2 w}{\partial x\partial y}\end{Bmatrix},\quad \{\Phi\}=\begin{Bmatrix}\frac{\partial^2\phi}{\partial y^2}\\ \frac{\partial^2\phi}{\partial x^2}\\ -\frac{\partial^2\phi}{\partial x\partial y}\end{Bmatrix},$$

$$\{\theta\}=\begin{Bmatrix}\frac{\partial w}{\partial x}\\ \frac{\partial w}{\partial y}\end{Bmatrix},\quad [A]=\begin{bmatrix}\frac{\partial w}{\partial x}&0\\ 0&\frac{\partial w}{\partial y}\\ \frac{\partial w}{\partial y}&\frac{\partial w}{\partial x}\end{bmatrix},$$

E = Young's modulus,
ν = Poisson's ratio,
h = the thickness of the plate,
$\overline{M}_n$ = the bending moment prescribed along the boundary C_M,
$\overline{R}_n$ = the transverse shear force prescribed along the boundary C_R,
n = normal axis to the boundary of the plate in the middle surface,
A = the area of the middle surface.

and the subsidiary conditions are as follows:

(*i*) The deflection function w satisfies the prescribed geometrical boundary conditions

(*ii*) The Airy stress function ϕ satisfies all the boundary conditions (geometrical and mechanical).

The general formulation of the in-plane geometrical boundary conditions in terms of ϕ is in general very cumbersome (see [11]). Fortunately, in a number of simple cases commonly encountered in practice, it can be worked out without undue difficulty.

Using the procedure presented in the previous section, an amplitude incremental variational principle can be formulated as

$$\delta\int_0^{2\pi}\Big[\int\int_A\Big(\frac{1}{2}\{\Delta\chi\}^T[D_b]\{\Delta\chi\}-\frac{1}{2}\{\Delta\Phi\}^T[D_m]\{\Delta\Phi\}\Big)dxdy$$
$$+\int\int_A\Big(\frac{1}{2}\{\Delta\theta\}^T[\Delta A]^T\{\Phi^{(0)}\}+\{\Delta\theta\}^T[A^{(0)}]^T\{\Delta\Phi\}\Big)dxdy$$
$$-\omega_0^2\int\int_A\frac{\rho h}{2}\left(\frac{\partial\Delta w}{\partial\tau}\right)^2 dxdy$$
$$+\int\int_A(\{\Delta\chi\}^T[D_b]\{\chi^{(0)}\}-\{\Delta\Phi\}^T[D_m]\{\Phi^{(0)}\})\,dxdy$$
$$+\int\int_A\Big(\{\Delta\theta\}^T[A^{(0)}]^T\{\Phi^{(0)}\}+\frac{1}{2}\{\Delta\Phi\}^T[A^{(0)}]\{\theta^{(0)}\}\Big)dxdy$$
$$-(\omega_0^2+2\omega_0\Delta\omega)\int\int_A\rho h\left(\frac{\partial\Delta w}{\partial\tau}\right)\left(\frac{\partial w^{(0)}}{\partial\tau}\right)dxdy$$
$$-\int\int_A(q+\Delta q)\Delta w\,dxdy-\int_{C_R}(\overline{R}_n^{(0)}+\Delta\overline{R}_n)\Delta w ds$$
$$+\int_{C_M}(\overline{M}_n^{(0)}+\Delta\overline{M}_n)\frac{\partial\Delta w}{\partial n}ds\Big]d\tau=0. \quad (20)$$

If the deflection function also satisfies the mechanical boundary conditions on C_R and C_M, an alternative incremental Galerkin formulation can easily be derived from equation (20) by using Green's formula.

$$\int_0^{2\pi}\Big[\int\int_A(D\nabla^2\nabla^2(\Delta w)+\{\Delta\chi\}^T\{\Phi^{(0)}\}+\{\chi^{(0)}\}^T\{\Delta\Phi\})\delta\Delta w\,dxdy \quad (20a)$$

Downloaded 01 May 2010 to 171.66.16.249. Redistribution subject to ASME license or copyright; see http://www.asme.org/terms/Terms_Use.cfm

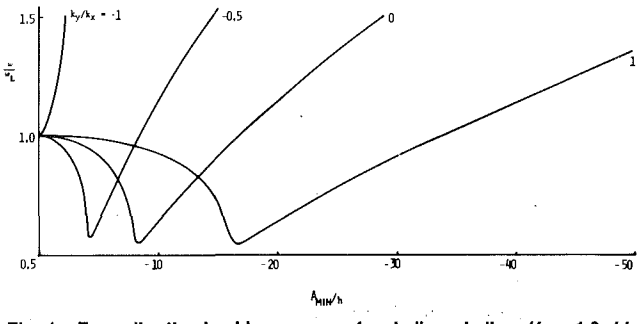


Fig. 1 Free-vibration backbone curves for shallow shells; $a/b = 1.0$, $hk_x = 0.001$, $ak_x = 0.4$, $\nu = 0.3$; number of terms $m = 4$, A_{min} = the minimum value of $A(t)$ (upward)

$$+ \int\int_A \rho h\omega_0{}^2 \frac{\partial^2 \Delta w}{\partial \tau^2}\delta\Delta w\, dxdy - \int\int_A \left(\frac{1}{Eh}\nabla^2\nabla^2(\Delta\phi) - \{\Delta\chi\}^T\{\overline{\chi}^{(0)}\}\right)\delta\Delta\phi\, dxdy + \int\int_A \left(D\nabla^2\nabla^2 w^{(0)} + \{\chi^{(0)}\}^T\{\Phi^{(0)}\} - q^{(0)} + \omega_0{}^2\rho h\frac{\partial^2 w^{(0)}}{\partial\tau^2}\right)\delta\Delta w\, dxdy - \int\int_A \left(\frac{1}{Eh}\nabla^2\nabla^2\phi^{(0)} - \frac{1}{2}\{\chi^{(0)}\}^T\{\overline{\chi}^{(0)}\}\right)\delta\Delta\phi\, dxdy - \int\int_A \Delta q\,\delta\Delta w\, dxdy + 2\omega_0\Delta\omega\int\int_A \rho h\frac{\partial^2 w^{(0)}}{\partial\tau^2} \times \delta\Delta w\, dxdy\Big]d\tau = 0, \quad (20a)$$

(Cont.)

where

$$\{\overline{\chi}^{(0)}\} = \left[\frac{\partial^2 w^{(0)}}{\partial y^2}, \quad \frac{\partial^2 w^{(0)}}{\partial x^2}, \quad -\frac{\partial^2 w^{(0)}}{\partial x\,\partial y}\right]^T.$$

This formulation may be convenient for some cases.

For the problem of nonlinear vibration of shallow shells, the foregoing variational principle can easily be generalized by adding into the square bracket of equation (20) the following terms:

$$-\int\int_A [\{k\}^T\{\Delta\Phi\}(w^{(0)} + \Delta w) + \{k\}^T\{\Phi^{(0)}\}\Delta w]\, dxdy \quad (20b)$$

where

$$\{k\} = [k_x, k_y, 2k_{xy}]^T$$

and k_x, k_y, and k_{xy} denote the curvature and twist of the middle surface of the shallow shell.

Numerical Examples

1 As the first example of application of the incremental variational principle, consider the free vibration of a simply supported rectangular plate (see Fig. 1).

For the fundamental frequency, the mode shape is assumed to be

$$w = A(t)\sin\frac{\pi x}{a}\sin\frac{\pi y}{b}, \quad (21)$$

where

$$A(t) = A_1\cos\omega t + A_3\cos 3\omega t \quad (22)$$

The corresponding stress function ϕ can be solved from equation (18) and is taken to be

$$\phi = Eh\frac{A^2(t)}{32}\left[\left(\frac{a}{b}\right)^2\cos\frac{2\pi x}{a} + \left(\frac{b}{a}\right)^2\cos\frac{2\pi y}{b}\right] + \frac{\overline{N}_x y^2}{2} + \frac{\overline{N}_y x^2}{2} \quad (23)$$

where $A(t)$ is expressed in terms of A_1 and A_3 by equation (22) and $\overline{N}_x$, $\overline{N}_y$ are the average external in-plane stress resultants acting at the edges.

If the edges are movable, then

$$\overline{N}_x = \overline{N}_y = 0 \quad (24)$$

However, if the edges are immovable, $\overline{N}_x$, $\overline{N}_y$ can then be determined by the conditions

$$\int_0^a \frac{\partial u}{\partial x}dx = 0, \quad \int_0^b \frac{\partial v}{\partial y}dy = 0,$$

which will in turn yield

$$\left.\begin{aligned}\overline{N}_x &= \frac{\pi^2}{8}\frac{b^2 + \nu a^2}{1-\nu^2}\frac{Eh}{a^2b^2}A^2(t),\\ \overline{N}_y &= \frac{\pi^2}{8}\frac{a^2 + \nu b^2}{1-\nu^2}\frac{Eh}{a^2b^2}A^2(t).\end{aligned}\right\} \quad (25)$$

Substituting equations (21)–(23) into variational equation (20a) and noting that the third and the fifth integrals vanish automatically due to the satisfaction of equation (18), the following incremental matrix equation is obtained:

$$([K_{ST}] - \omega_0{}^2[M_S])\begin{Bmatrix}\Delta A_1\\ \Delta A_3\end{Bmatrix} = \{R\} + 2\omega_0\Delta\omega\,[M_S]\begin{Bmatrix}A_1{}^{(0)}\\ A_3{}^{(0)}\end{Bmatrix} \quad (26)$$

where

$A_1{}^{(0)}$, $A_3{}^{(0)}$ = values of the coefficients A_1, A_3 at the previous state

ΔA_1, ΔA_3 = increments of A_1, A_3

$\{R\}$ = correction vector calculated from the fourth integral in equation (20a)

$[K_{ST}]$ = tangential stiffness matrix corresponding to vector $[\Delta A_1, \Delta A_3]^T$ calculated from the first integral in equation (20a)

$[M_S]$ = mass matrix corresponding to vector $[\Delta A_1, \Delta A_3]^T$ or $[A_1{}^{(0)}, A_3{}^{(0)}]^T$ calculated from the second or the last integral in equation (20a).

This set of equations is solved by the incremental method with one-step Newton-Raphson correction, using a TI-59 calculator. The corresponding linear solution with $A_1{}^{(0)}/h$ = an arbitrary small value, $A_3{}^{(0)}/h = 0$, and $\omega_0/\omega_L = 1$, where ω_L is the linear frequency

$$\omega_L{}^2 = \frac{\pi^4 Eh^2}{12a^4b^4(1-\nu^2)\rho}(a^2 + b^2)^2,$$

is taken as the starting point of solution. The algorithm used can be summarized as follows:

1 Two vectors $[\Delta A_1', \Delta A_3']^T$ and $[\Delta A_1'', \Delta A_3'']^T$ are solved separately with the first one corresponding to the right-hand side vectors $\{R\}$ and the second one to $2\omega_0[M_s][A_1{}^{(0)}, A_3{}^{(0)}]^T$ ($\Delta\omega$ assumed to be unity), respectively.

2 $\Delta\omega$ is now calculated from the prescribed increment ΔA_1:

$$\Delta\omega = (\Delta A_1 - \Delta A_1')/\Delta A_1''.$$

3 ΔA_3 is then computed from

$$\Delta A_3 = \Delta A_3' + \Delta\omega\Delta A_3''.$$

4 The new values of $A_1{}^{(0)}$, $A_3{}^{(0)}$, and ω_0 are updated by adding together the original values and the corresponding incremental values.

A series of frequency ratios for different amplitude ratios calculated with increment $\Delta A_1 = 0.1h$ are listed in Tables 1 and 2 for a square plate case and for a rectangular plate case, respectively.

In order to demonstrate the convergence and the accuracy of the present method, the fundamental frequency of a simply supported rectangular plate ($a/b = 2$) with immovable edges is calculated using different increments. The frequency ratios obtained are compared with the analytical results calculated from the elliptic integral [12] using the same mode assumption (see Table 3). The comparison shows that good accuracy can be achieved even with rather large increments and the errors decrease rapidly with the decrease of the increment.

Downloaded 01 May 2010 to 171.66.16.249. Redistribution subject to ASME license or copyright; see http://www.asme.org/terms/Terms_Use.cfm

Table 1 Frequency ratio ω/ω_L for a simply supported rectangular plate ($a/b = 1$)

The 1st Harmonic Amplitude A_1/h	Movable Edges ω/ω_L	Immovable Edges ω/ω_L
0.2	1.00512	1.01975
0.4	1.01950	1.07389
0.6	1.04425	1.16321
0.8	1.07833	1.27961
1.0	1.12085	1.41631
1.5	1.25858	1.81559
2.0	1.43095	2.26109
3.0	1.83984	3.21162
4.0	2.29522	4.19565
5.0	2.77385	5.19395

Table 2 Frequency ratio ω/ω_L for a simply supported rectangular plate ($a/b = 2$)

The 1st Harmonic Amplitude A_1/h	Movable Edges ω/ω_L	Immovable Edges ω/ω_L
0.2	1.00696	1.02443
0.4	1.02646	1.09090
0.6	1.05983	1.19919
0.8	1.10540	1.33832
1.0	1.16173	1.49951
1.5	1.34073	1.96171
2.0	1.55918	2.46927
3.0	2.06290	3.54038
4.0	2.61157	4.64234
5.0	3.18158	5.75729

Since only two harmonic terms have been used in the computations it is obvious that the present solution will not yield the exact solution by further and further reducing the increment.

It should be noted that the last row in Table 3 is the solution obtained by KBM method or the perturbation method [13] with the third-order approximation:

$$\omega/\omega_L = (1 + 3A_T{}^2\epsilon/8h^2 - 15A_T{}^4\epsilon^2/256h^4),$$

where A_T = the total amplitude and $\epsilon = 1.6281$ for the present case. Good results are obtained for small amplitudes using the perturbation method but the errors become larger as the vibration ceases to be a weak nonlinear phenomenon due to the increased amplitude.

Comparisons with other previously published results are given in Table 4, and the agreement is once again good for all cases.

2 As a second example, consider the interesting problem of the free vibration of simply supported rectangular shallow shells which was discussed by Leissa and Kadi [14].

For a simplified approach, it is reasonable to assume that the mode shape of vibration for the fundamental frequency take the form

$$w(x, y, t) = A(t) \cos\frac{\pi x}{a} \cos\frac{\pi y}{b}, \tag{27}$$

where a, b are the dimensions along the x and y-axes, respectively.

To satisfy the compatibility equation, the stress function is taken to be

$$\phi(x, y, t) = \frac{Eh\,A(t)a^2b^2}{\pi^2(a^2+b^2)^2}(b^2k_y + a^2k_x)\cos\frac{\pi x}{a}\cos\frac{\pi y}{b} - \frac{Eh\,A^2(t)}{32}\left[\left(\frac{a}{b}\right)^2\cos\frac{2\pi x}{a} + \left(\frac{b}{a}\right)^2\cos\frac{2\pi y}{b}\right]. \tag{28}$$

The deflection $A(t)$ has to be assumed as

$$A(t) = \sum_{n=0}^{m-1} A_n \cos n\omega t. \tag{29}$$

Table 3 Frequency ratio ω/ω_L for a simply supported rectangular plate ($a/b = 2$) with immovable edges

The 1st Harmonic Amplitude A_1/h		0.2	0.4	0.6	0.8	1.0
The 3rd Harmonic Amplitude A_3/h (calculated with $\Delta A_1/h=0.02$)		0.0004	0.0028	0.0081	0.0159	0.0254
Present Method $\Delta A_1/h$	0.4	1.0000	-	1.1713	-	1.4785
	0.2	1.0000	1.0979	1.1819	1.3363	1.4931
	0.1	1.0244	1.0909	1.1992	1.3383	1.4995
	0.05	1.0232	1.0929	1.2015	1.3402	1.5009
	0.025	1.0239	1.0937	1.2022	1.3407	1.5013
	0.02	1.0240	1.0938	1.2022	1.3407	1.5013
Analytical [12]		1.0242	1.0940	1.2023	1.3407	1.5011
Perturbation Method [13]		1.0242	1.0937	1.1997	1.3271	1.4552

Table 4 Frequency ratio ω/ω_L for rectangular plates with immovable edges

	ω/ω_L at A_T/h # 0.2	0.4	0.6	0.8	1.0
	Simply Supported, a/b = 1				
Present Method ($\Delta A_1/h$ =0.1)	1.0197	1.0732	1.1600	1.2713	1.4008
Chu-Herrman [6]	1.0195	1.0757	1.1625	1.2734	1.4024
* Rao et al [3] F.E.M.(4x4)	1.0185	1.0717	1.1534	1.2565	1.3753
	Simply Supported, a/b = 2				
Present Method ($\Delta A_1/h$=0.1)	1.0244	1.0876	1.1945	1.3270	1.4792
Chu-Herrman [6]	1.0241	1.0927	1.1975	1.3293	1.4808
* Rao et al [3] F.E.M (4x4)	1.0239	1.0918	1.1957	1.3264	1.4758

A_T = The total amplitude

* A special assumption is used in the formulation and the in-plane displacements are regarded as to be zero over the whole middle plane of the plate.

Owing to the satisfaction of the compatibility equation, equation (20a) with the additional terms (20b) is simplified to

$$\int_0^{2\pi}\left[\int\int_A\left(D\nabla^2\nabla^2(\Delta w) + \{\Delta\chi\}^T\{\Phi^{(0)}\} + \{\chi^{(0)}\}^T\{\Delta\Phi\} - \{k\}^T\{\Delta\Phi\} + \rho h\,\omega_0{}^2\frac{\partial^2\Delta w}{\partial\tau^2}\right)\delta\Delta w\,dxdy + \int\int_A\left(D\nabla^2\nabla^2 w^{(0)} + \{\chi^{(0)}\}^T\{\Phi^{(0)}\} - \{k\}^T\{\Phi^{(0)}\} + \rho h\omega_0{}^2\frac{\partial^2 w^{(0)}}{\partial\tau^2}\right)\delta w\,dxdy + 2\omega_0\Delta\omega\int\int_A\rho h\frac{\partial^2 w^{(0)}}{\partial\tau^2}\delta\Delta w\,dxdy\right]d\tau = 0. \tag{30}$$

Substituting equations (27)–(29) into the variational equation (30) and performing the integration, one can easily obtain a set of m linear equations (similar to equation (26)) governing the amplitude increments $\Delta A_n (n = 0, 1, 2, \ldots, m-1)$ and the frequency increment $\Delta\omega$.

An amplitude incrementation procedure, similar to [15], is used to solve the equations and the numerical results are depicted in Figs. 1 and 2. The computed frequency ratio ω/ω_L versus the dimensionless minimum deflection A_{min}/h relations are coincident with those of [14]. The backbone curves (see Fig. 1), except for the case of $k_y/k_x = -1$, demonstrate "soft" spring behavior for moderate large amplitudes and "hard" spring behavior for larger amplitudes. The physical explanation is clearly shown in Fig. 2 in which time histories of the de-

Downloaded 01 May 2010 to 171.66.16.249. Redistribution subject to ASME license or copyright; see http://www.asme.org/terms/Terms_Use.cfm

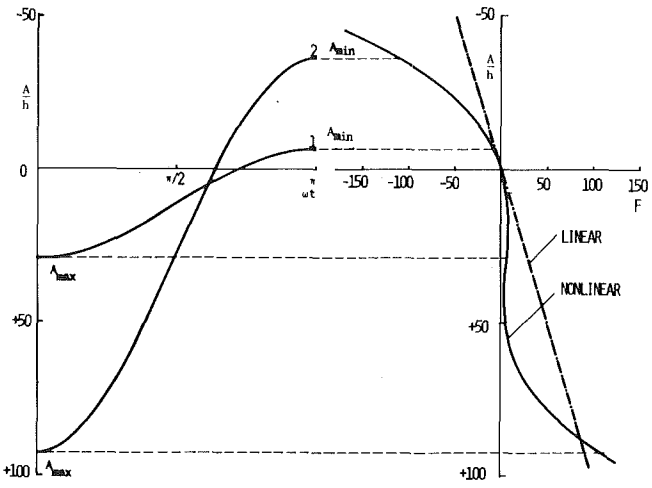


Fig. 2 Time history curves of deflection $A(\dot{t})$ and the equivalent elastic restoring force F versus deflection A for a spherical shallow shell; $k_x = k_y$, $a/b = 1.0$, $hk_x = 0.001$, $ak_x = 0.4$, $\nu = 0.3$; number of terms $m = 4$

flections $A(t)$ of two typical cases (softening and hardening types, respectively) of a spherical shallow shell are plotted. It can be seen that the nonsymmetry of the history curves are due to the nonsymmetrical nature of the dimensionless equivalent restoring force F which is plotted towards the right side in Fig. 2. For the particular example considered, the force F is given by (see [14])

$$F \cong \frac{A}{h} - 0.0416\left(\frac{A}{h}\right)^2 + 0.000475\left(\frac{A}{h}\right)^3, \tag{28}$$

For the smaller amplitude vibration (curve 1 in Fig. 2), the restoring force F remains almost always smaller than the corresponding linear one (shown by dash-dotted line) and the vibration is therefore of the softening type. At the same time, it is also clear from Fig. 2 that the vibration of the shell will become the hardening type at larger amplitudes (see curve 2), due to the fact that the elastic restoring force will be significantly bigger than the linear one for large deflections.

Concluding Remarks

1 An amplitude incremental variational principle for nonlinear periodic vibration problem is presented.

2 Based on this principle, the Rayleigh-Ritz method, especially the finite-element method can be adopted. In such procedures, only linearized equations have to be formulated and solved in each incremental step. This approach is essentially an incremental harmonic balance method, which would be quite useful for nonlinear structural vibration analysis, especially for problems with high nonlinearity.

3 Satisfactory numerical results can be obtained by the incremental harmonic balance method.

4 The tangential matrix ($[K_{ST}] - \omega_0^2[M_S]$) in equation (26) is symmetrical but, in general, indefinite.

References

1 Tseng, W. Y., and Dugundji, J., "Nonlinear Vibration of a Beam Under Harmonic Excitation," ASME JOURNAL OF APPLIED MECHANICS, Vol. 37, June 1970, pp. 292–297.

2 Evenson, D. A., "Nonlinear Flexural Vibration of Thin-Walled Circular Cylinder," NACA TN D-4090, Aug. 1967.

3 Rao, G. V., Raju, K. K., and Raju, I. S., "A Finite-Element Formulation for Large Amplitude Flexural Vibrations of Thin Rectangular Plates," *Computers and Structures*, Vol. 6, 1976, pp. 163–167.

4 Varadan, T. K., and Pandalai, K. A. V., "Nonlinear Flexural Oscillations of Orthotropic Shallow Spherical Shells," *Computers and Structures*, Vol. 9, 1978, pp. 417–425.

5 Ueda, T., "Nonlinear Free Vibrations of Conical Shells," *Journal of Sound and Vibration*, Vol. 64, No. 1, 1979, pp. 85–95.

6 Chu, H. N., and Herrmann, G., "Influence of Large Amplitudes on Free Flexural Vibrations of Rectangular Elastic Plates," ASME JOURNAL OF APPLIED MECHANICS, Vol. 23, 1956, pp. 532–540.

7 Atluri, S., "Nonlinear Vibrations of a Hinged Beam Including Nonlinear Inertia Effects," ASME JOURNAL OF APPLIED MECHANICS, Vol. 40, Mar. 1973, pp. 121–126.

8 Nayfeh, A. H., Mook, D. T., and Lobitz, D. W., "Numerical-Perturbation Method for the Nonlinear Analysis of Structural Vibration," *AIAA Journal*, Vol. 12, 1974, pp. 1222–1228.

9 Chen, J. C., and Babcock, C. D., "Nonlinear Vibration of Cylindrical Shells," *AIAA Journal*, Vol. 13, 7, 1975, pp. 868–876.

10 Stricklin, J. A., Haisler, W. E., and Von Riesemann, W. A., "Geometrically Nonlinear Structural Analysis by Direct Stiffness Method," *Journal of the Structural Division*, ASCE, Vol. 97, No. ST9, Sept. 1971, pp. 2299–2314.

11 Liu, S. N., (S. L. Lau in Cantonese), "On a Generalized Variational Principle and Some of Its Applications in the Theory of Elastic Shallow Shell," *Scientia Sinica*, Vol. 12, No. 10, 1963, pp. 1489–1506.

12 Timoshenko, S. P., Young, D. H., and Weaver, W., Jr., *Vibration Problems in Engineering*, 4th ed., Wiley, 1974.

13 Meirovitch, L., *Methods of Analytical Dynamics*, McGraw-Hill, New York, 1970.

14 Leissa, A. W., and Kadi, A. S., "Curvature Effects on Shallow Shell Vibrations," *Journal of Sound and Vibration*, Vol. 16, No. 2, 1971, pp. 173–187.

15 Haisler, W. E., Stricklin, J. A., and Key, J. E., "Displacement Incrementation in Nonlinear Structure Analysis by the Self-Correcting Method," *International Journal Num. Meth. Engng.*, Vol. 11, 1977, pp. 3–10.

Downloaded 01 May 2010 to 171.66.16.249. Redistribution subject to ASME license or copyright; see http://www.asme.org/terms/Terms_Use.cfm

Journal of Applied Mechanics

Brief Notes

A Brief Note is a short paper which presents a specific solution of technical interest in mechanics but which does not necessarily contain new general methods or results. A Brief Note should not exceed 1500 words *or equivalent* (a typical one-column figure or table is equivalent to 250 words; a one line equation to 30 words). Brief Notes will be subject to the usual review procedures prior to publication. After approval such Notes will be published as soon as possible. The Notes should be submitted to the Technical Editor of the JOURNAL OF APPLIED MECHANICS. Discussions on the Brief Notes should be addressed to the Editorial Department, ASME, United Engineering Center, 345 East 47th Street, New York, N. Y. 10017, or to the Technical Editor of the JOURNAL OF APPLIED MECHANICS. Discussions on Brief Notes appearing in this issue will be accepted until two months after publication. Readers who need more time to prepare a Discussion should request an extension of the deadline from the Editorial Department.

Aluminum Matrix Composite Elasticity Measured Ultrasonically

G. V. Blessing[1] and W. L. Elban[2]

Introduction

Many studies [1–3] have been made in the past decade to ultrasonically evaluate the elastic moduli of fiber-reinforced composites, in particular the organic matrix systems. The recent emergence of aluminum matrix composites, with greater specific strength and stiffness over a wider temperature range, has also led to ultrasonic evaluations [4–5] of their properties. We report here ultrasonic results obtained on two such composites with unidirectional fiber reinforcement: Graphite/Al (G/Al) and SiC/Al. Comparisons with theory and available mechanical property data are also made.

Experimental

Samples. Both composite systems possessed a nominal 30 volume percent unidirectional fiber-reinforcement in an aluminum matrix. The G/Al was continuous-fiber-reinforced plate 2.6mm thick, with a density of 2.44 gm/cm^3 for a 30 volume percent fiber content. The plate was fabricated [6] by diffusion bonding 1.2 mm dia precursor composite wires, previously formed by liquid metal (201 Al) infiltration of highly anisotropic Thornel 50 fiber tows.

The SiC/Al samples were taken from discontinuous-fiber-reinforced extruded rod (2024 Al matrix) 10 mm dia [7], with a density of 2.90 gm/cm^3 for a 32 volume percent fiber content. The SiC fibers were principally particulate of micrometer dimensions, with a small percentage of whiskers having an aspect ratio on the order of 30. The extrusion direction was taken to be the axis of symmetry for transverse isotropy.

Ultrasonic Technique. Ultrasonic velocity measurements of both longitudinal and shear waves were made in three principal directions in the composite samples: parallel, perpendicular, and 45° to the fiber direction. Two techniques for ultrasonic velocity measurements were used: pulse echo with a transducer—delay rod—sample arrangement, and through transmission with a second transducer attached to the previous arrangement. The through transmission technique was used on a second G/Al sample set to corroborate the pulse echo results for which a second echo was sometimes difficult to observe. The pulse echo technique utilized a sharp spike voltage excitation of the transducer to produce broadband ultrasonic pulses of about 0.5 microsec duration and a nominal center frequency of 5 MHz. Time-of-flight velocity measurements were made by pulse-echo-overlap with an oscilloscope internal time delay and digital readout. The through transmission technique utilized a tone burst excitation to produce a relatively narrowband signal at 5 MHz. With this technique, the time-of-flight measurements were made by noting the shift in time of the received signal upon sample removal. The estimated precision of the pulse echo and through transmission velocities were 1 and 1.5 percent, respectively.

By means of the stress-strain constitutive relationships for orthotropic media with transverse isotropy, the elastic coefficients C_{ij} were calculated from the material density and wave velocities [8]. The elastic engineering parameters: Young's and shear moduli, and Poisson's ratio, were in turn calculated from the C_{ij} [5].

Table 1 Ultrasonic wave speeds (in mm/μs) for Graphite/Al and SiC/Al

Wave Mode	G/Al[a]	G/Al[b]	SiC/Al[a]
Longitudinal: $\mathbf{k} \parallel 3$	8.64	8.33	7.67
Longitudinal: $\mathbf{k} \perp 3$	4.04	3.89	7.37
Shear: $\mathbf{k} \parallel 3, \epsilon \perp 3$	2.78	2.84	3.92
Shear: $\mathbf{k} \perp 3, \epsilon \parallel 3$	2.78	3.01	3.96
Shear: $\mathbf{k} \perp 3, \epsilon \perp 3$	2.07	2.09	3.85
Quasi-long: $\sphericalangle(\mathbf{k}, 3) = 45°$	6.17	6.27	7.46
Quasi-shear: $\sphericalangle(\mathbf{k}, 3) = 45°$ ϵ in plane $(\mathbf{k}, 3)$	3.07	2.78	4.10
Shear: $\sphericalangle(\mathbf{k}, 3) = 45°$ $\epsilon \perp$ plane $(\mathbf{k}, 3)$	2.45	2.30	3.92

[a] Pulse echo.
[b] Through transmission.

Results and Analysis

Table 1 lists velocities obtained on the three sets of composite samples for wave modes of propagation direction $\mathbf{k}$ and polarization ϵ. Table 2 compares the elastic moduli calculated from these velocities with their respective model predictions and available mechanical property data [9]. Tensile specimens of SiC/Al yielded values of 100

[1] Research and Technology Department, Naval Surface Weapons Center, Silver Spring, Maryland 20910; Present address: National Bureau of Standards, Ultrasonic Standards Group, Washington, D. C. 20234
[2] Research and Technology Department, Naval Surface Weapons Center, Silver Spring, Md. 20910.
Manuscript received by ASME Applied Mechanics Division, June, 1980; final revision, April, 1981.

Copyright © 1981 by ASME
Downloaded 01 May 2010 to 171.66.16.249. Redistribution subject to ASME license or copyright; see http://www.asme.org/terms/Terms_Use.cfm

Table 2 A comparison of composite moduli (in GPa) obtained ultrasonically with mechanical measurements and model predictions

	Graphite/Al				SiC/Al	
Modulus	Ultrasonic[a]	Ultrasonic[b]	Model	Mechanical	Ultrasonic[a]	Model
E_{33}	160.	161.	166.	135–165	131.	124.
E_{11}	29.8	29.9	31.7	32	116.	117.
G_{13}	18.9	19.7	18.5	17	45.1	45.5
G_{12}	10.5	10.6	10.6	—	42.9	40.7
ν_{13}	0.44	0.28	0.34	—	0.29	0.30

[a] Pulse echo.
[b] Through transmission.

to 130 GPa for E_{33} [10]. The second subscript is the stress direction, making E_{33} and G_{13} the axial or longitudinal moduli, and E_{11} and G_{12} the transverse moduli. A judicious choice of velocities based on sample path length, waveform clarity, and a minimization of error propagation in the C_{ij} derivation allowed for the calculation of the respective sets of G/Al moduli.

Two distinct mathematical models were used to predict the moduli based on material constituent properties. The composite cylinder assemblage model by Hashin [11] was applied to G/Al for its particular relevance to that composite's peculiar transverse properties: a matrix stiffer than the fiber in the transverse direction. An interpolated self-consistent model for short-fiber composites by Halpin and Tsai [12] was applied to SiC/Al.

Discussion

A comparison of the velocities in Table 1 for the two G/Al sample sets shows agreement for a majority of the data. The larger differences could be attributed to sample differences and the effect of geometric dispersion between the two ultrasonic techniques. The ultrasonic moduli calculated from these velocities are in good agreement with both theory and mechanical property data. The agreement between experiment and theory is especially significant for its corroboration of the composite cylinder assemblage model recently elaborated on for the special case of G/Al [11]. However, Poisson's ratio, which is highly dependent on the measurement sensitive C_{13} coefficient, could not be reliably evaluated by the ultrasonic method.

Good agreement is also observed between the ultrasonic results and the semiempirical model [12] applied to SiC/Al. While full alignment of the whiskers in the extrusion direction was assumed in the model calculations, the material's high degree of elastic isotropy confirms the SiC reinforcement to be largely particulate as noted earlier.

Conclusions

The ultrasonically measured elastic moduli of continuous-fiber G/Al and discontinuous-fiber SiC/Al composites are in good agreement with mechanical property data and selected theoretical models. In particular, the data for G/Al corroborates the composite cylinder assemblage model effective for the unusual transverse boundary condition between the aluminum matrix and graphite fibers.

Acknowledgments

The authors wish to thank A. L. Bertram for his computer analyses, to J. V. Foltz for many helpful discussions, and to Z. Hashin for an evaluation of his model's applicability to G/Al. This work was sponsored by the Naval Sea Systems Command Metal Matrix Block Program, and by the Naval Surface Weapons Center Independent Research Fund.

References

1 Dean, G. D., and Turner, P., "The Elastic Properties of Carbon Fibers and Their Composites," *Composites*, Vol. 4, 1973, pp. 174–180.

2 Smith, R. E., "Ultrasonic Elastic Constants of Carbon Fibers and Their Composites," *Journal of Applied Physics*, Vol. 43, No. 6, 1972, pp. 2555–2561.

3 Kriz, R. D., and Stinchcomb, N. W., "Elastic Moduli of Transversely Isotropic Graphite Fibers and Their Composites," *Experimental Mechanics*, Vol. 19, No. 2, 1979, pp. 41–49.

4 Read, D. T., and Ledbetter, H. H., "Elastic Properties of a Boron-Aluminum Composite at Low Temperatures," *Journal of Applied Physics*, Vol. 48, No. 7, 1977, pp. 2827–2831.

5 Blessing, V. G., Elban, W. L., and Foltz, J. V., "Ultrasonic Characterization of Aluminum Matrix Composites For Their Moduli," NBS Special Publication 596, Nov. 1980, pp. 137–146.

6 Plate fabricated by DWA Composite Specialties, Inc., Chatsworth, Calif. 91311.

7 Samples provided by A. P. Divecha, Naval Surface Weapons Center, Silver Spring, Md. 20910.

8 See, e.g., Mason, W. P., *Physical Acoustics and the Properties of Solids*, D. Van Nostrand Co. 1958, pp. 368–373.

9 Mechanical property data provided by NETCO, Long Beach, Calif. 90806.

10 Tensile data provided by C. R. Crowe, Naval Surface Weapons Center, Silver Spring, Md. 20910.

11 Hashin, Z., "Analysis of Properties of Fiber Composites With Anisotropic Constituents," ASME JOURNAL OF APPLIED MECHANICS, Vol. 46, 1979, pp. 543–550.

12 Ashton, J. E., Halpin, J. C., and Petit, P. H., *Primer on Composite Materials: Analysis*, Technomic Publishing Co., Westport, Conn., 1969, pp. 72–84.

Acoustoelastic Effect of Thickness Oscillations

M. Hirao,[1] Y. Miura,[2] and H. Fukuoka[1]

Application of stress to the solid material causes a slight change in the propagation velocities of elastic waves, which has been called acoustoelastic effect in general. Acoustoelasticity has been hoped to provide a new tool for the nondestructive stress measurement. For the thickness oscillations in plate, it was theoretically revealed [1] that the effect appears as (*i*) slight change in the resonance frequency and (*ii*) slow amplitude modulation of transverse (thickness-shear) mode unless polarized in the principal directions of stress. This Note offers some experimental results about the first result. Comparison with the sing-around method by the ultrasonic bulk waves will be presented about the third-order elastic constants obtained experimentally. Although the second result seems to be worth studying from the practical viewpoint, the corresponding experiment has not been available so far.

Change in Resonance Frequency

The acoustoelastic measurement of the thickness oscillations can be made by using oscillator with continuously variable frequency, frequency counter, oscilloscope, and testing machine as shown in Fig. 1. Monochromatic steady oscillation was sent out from the oscillator. One of the two PZT plates attached face to face on the specimen sides converted it into the thickness oscillation in plate. The other PZT plate transformed thus generated oscillation back into the electronic oscillation which was monitored by the oscilloscope. The pair of the PZT plates were of the same center frequency. It was nominally 10 MHz for longitudinal (L) mode and 5 MHz for transverse (T) mode.

When the frequency was scanned by the oscillator tuner, the amplitude of the thickness oscillation showed a series of distinct peaks with almost regular intervals. The frequency difference of two successive peaks equals the resonance frequency of the fundamental mode. With this value, the order of the overtones was experimentally determined.

Data were taken about the change in the resonance frequency as

[1] Department of Mechanical Engineering, Faculty of Engineering Science, Osaka University, Toyonaka, Osaka 560, Japan.
[2] Sakai Works, Nippon Steel Corporation, Sakai, Osaka 590, Japan.

Manuscript received by ASME Applied Mechanics Division, May, 1980; final revision, May, 1981.

Downloaded 01 May 2010 to 171.66.16.249. Redistribution subject to ASME license or copyright; see http://www.asme.org/terms/Terms_Use.cfm

Table 2 A comparison of composite moduli (in GPa) obtained ultrasonically with mechanical measurements and model predictions

	Graphite/Al				SiC/Al	
Modulus	Ultrasonic[a]	Ultrasonic[b]	Model	Mechanical	Ultrasonic[a]	Model
E_{33}	160.	161.	166.	135–165	131.	124.
E_{11}	29.8	29.9	31.7	32	116.	117.
G_{13}	18.9	19.7	18.5	17	45.1	45.5
G_{12}	10.5	10.6	10.6	—	42.9	40.7
ν_{13}	0.44	0.28	0.34	—	0.29	0.30

[a] Pulse echo.
[b] Through transmission.

to 130 GPa for E_{33} [10]. The second subscript is the stress direction, making E_{33} and G_{13} the axial or longitudinal moduli, and E_{11} and G_{12} the transverse moduli. A judicious choice of velocities based on sample path length, waveform clarity, and a minimization of error propagation in the C_{ij} derivation allowed for the calculation of the respective sets of G/Al moduli.

Two distinct mathematical models were used to predict the moduli based on material constituent properties. The composite cylinder assemblage model by Hashin [11] was applied to G/Al for its particular relevance to that composite's peculiar transverse properties: a matrix stiffer than the fiber in the transverse direction. An interpolated self-consistent model for short-fiber composites by Halpin and Tsai [12] was applied to SiC/Al.

Discussion

A comparison of the velocities in Table 1 for the two G/Al sample sets shows agreement for a majority of the data. The larger differences could be attributed to sample differences and the effect of geometric dispersion between the two ultrasonic techniques. The ultrasonic moduli calculated from these velocities are in good agreement with both theory and mechanical property data. The agreement between experiment and theory is especially significant for its corroboration of the composite cylinder assemblage model recently elaborated on for the special case of G/Al [11]. However, Poisson's ratio, which is highly dependent on the measurement sensitive C_{13} coefficient, could not be reliably evaluated by the ultrasonic method.

Good agreement is also observed between the ultrasonic results and the semiempirical model [12] applied to SiC/Al. While full alignment of the whiskers in the extrusion direction was assumed in the model calculations, the material's high degree of elastic isotropy confirms the SiC reinforcement to be largely particulate as noted earlier.

Conclusions

The ultrasonically measured elastic moduli of continuous-fiber G/Al and discontinuous-fiber SiC/Al composites are in good agreement with mechanical property data and selected theoretical models. In particular, the data for G/Al corroborates the composite cylinder assemblage model effective for the unusual transverse boundary condition between the aluminum matrix and graphite fibers.

Acknowledgments

The authors wish to thank A. L. Bertram for his computer analyses, to J. V. Foltz for many helpful discussions, and to Z. Hashin for an evaluation of his model's applicability to G/Al. This work was sponsored by the Naval Sea Systems Command Metal Matrix Block Program, and by the Naval Surface Weapons Center Independent Research Fund.

References

1 Dean, G. D., and Turner, P., "The Elastic Properties of Carbon Fibers and Their Composites," *Composites*, Vol. 4, 1973, pp. 174–180.

2 Smith, R. E., "Ultrasonic Elastic Constants of Carbon Fibers and Their Composites," *Journal of Applied Physics*, Vol. 43, No. 6, 1972, pp. 2555–2561.

3 Kriz, R. D., and Stinchcomb, N. W., "Elastic Moduli of Transversely Isotropic Graphite Fibers and Their Composites," *Experimental Mechanics*, Vol. 19, No. 2, 1979, pp. 41–49.

4 Read, D. T., and Ledbetter, H. H., "Elastic Properties of a Boron-Aluminum Composite at Low Temperatures," *Journal of Applied Physics*, Vol. 48, No. 7, 1977, pp. 2827–2831.

5 Blessing, V. G., Elban, W. L., and Foltz, J. V., "Ultrasonic Characterization of Aluminum Matrix Composites For Their Moduli," NBS Special Publication 596, Nov. 1980, pp. 137–146.

6 Plate fabricated by DWA Composite Specialties, Inc., Chatsworth, Calif. 91311.

7 Samples provided by A. P. Divecha, Naval Surface Weapons Center, Silver Spring, Md. 20910.

8 See, e.g., Mason, W. P., *Physical Acoustics and the Properties of Solids*, D. Van Nostrand Co. 1958, pp. 368–373.

9 Mechanical property data provided by NETCO, Long Beach, Calif. 90806.

10 Tensile data provided by C. R. Crowe, Naval Surface Weapons Center, Silver Spring, Md. 20910.

11 Hashin, Z., "Analysis of Properties of Fiber Composites With Anisotropic Constituents," ASME JOURNAL OF APPLIED MECHANICS, Vol. 46, 1979, pp. 543–550.

12 Ashton, J. E., Halpin, J. C., and Petit, P. H., *Primer on Composite Materials: Analysis*, Technomic Publishing Co., Westport, Conn., 1969, pp. 72–84.

Acoustoelastic Effect of Thickness Oscillations

M. Hirao,[1] Y. Miura,[2] and H. Fukuoka[1]

Application of stress to the solid material causes a slight change in the propagation velocities of elastic waves, which has been called acoustoelastic effect in general. Acoustoelasticity has been hoped to provide a new tool for the nondestructive stress measurement. For the thickness oscillations in plate, it was theoretically revealed [1] that the effect appears as (*i*) slight change in the resonance frequency and (*ii*) slow amplitude modulation of transverse (thickness-shear) mode unless polarized in the principal directions of stress. This Note offers some experimental results about the first result. Comparison with the sing-around method by the ultrasonic bulk waves will be presented about the third-order elastic constants obtained experimentally. Although the second result seems to be worth studying from the practical viewpoint, the corresponding experiment has not been available so far.

Change in Resonance Frequency

The acoustoelastic measurement of the thickness oscillations can be made by using oscillator with continuously variable frequency, frequency counter, oscilloscope, and testing machine as shown in Fig. 1. Monochromatic steady oscillation was sent out from the oscillator. One of the two PZT plates attached face to face on the specimen sides converted it into the thickness oscillation in plate. The other PZT plate transformed thus generated oscillation back into the electronic oscillation which was monitored by the oscilloscope. The pair of the PZT plates were of the same center frequency. It was nominally 10 MHz for longitudinal (L) mode and 5 MHz for transverse (T) mode.

When the frequency was scanned by the oscillator tuner, the amplitude of the thickness oscillation showed a series of distinct peaks with almost regular intervals. The frequency difference of two successive peaks equals the resonance frequency of the fundamental mode. With this value, the order of the overtones was experimentally determined.

Data were taken about the change in the resonance frequency as

[1] Department of Mechanical Engineering, Faculty of Engineering Science, Osaka University, Toyonaka, Osaka 560, Japan.
[2] Sakai Works, Nippon Steel Corporation, Sakai, Osaka 590, Japan.

Manuscript received by ASME Applied Mechanics Division, May, 1980; final revision, May, 1981.

Copyright © 1981 by ASME
Downloaded 01 May 2010 to 171.66.16.249. Redistribution subject to ASME license or copyright; see http://www.asme.org/terms/Terms_Use.cfm

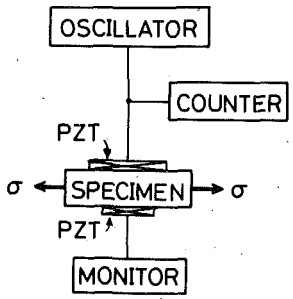


Fig. 1 Schematic diagram of resonance method

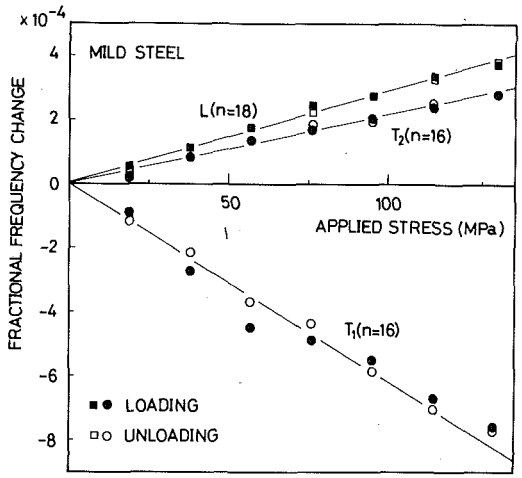


Fig. 2 Fractional change in resonance frequency versus tensile stress

a function of external stress. The resonance frequency under the given stress was determined from the frequency counter by tuning the oscillator so as to reach the maximum amplitude on the oscilloscope display. Typical result for the mild-steel plate of 5.15 mm thickness is presented in Fig. 2, where the load was uniaxial tension. The subscripts 1 and 2 of T-modes indicate, respectively, the parallel and normal polarizations with respect to the stress direction. The integer n denotes the mode order and the straight lines were drawn by processing the data with the method of least mean squares.

The resonance frequencies appear to vary linearly with the applied stress, which gives the experimental check to the theoretical result based on the second-order elasticity. The data scattering might be mainly due to the tuning error in obtaining the resonance maximum, because the so-called Q-value was not sufficiently large. For example, $Q = 20.2$ in the case of the 17th L-mode resonance. However, the careful manipulation of the tuner enabled the measurement of the change of resonance frequencies in units of kHz or less, as the stress is changed. Therefore, the accuracy in the order of 10^{-4} resulted for the fractional frequency change. If the resonance of the higher overtone is measured, the accuracy will be accordingly improved.

Third-Order Elastic Constants

The basic parameters which characterize the acoustoelastic effect of material are the third-order elastic constants. They correspond to the coefficients of the cubic-strain terms in the elastic energy and are indispensable in describing the nonlinear behavior of the material. The most remarkable advantage of the present resonance method is the ability to determine the third-order elastic constants in a rather simpler manner than have been reported [2–4]. For the isotropic case, three constants are independent with each other, so that the acoustoelastic data on the L and T-modes with the parallel and normal polarizations to the stress direction are required for the compatible determination.

Denoting by F the fractional change in the resonsnce frequency $(f - f_0)/f_0$ per unit uniaxial stress, f_0 being the value at stress-free condition, the third-order elastic constants ν_i $(i = 1, 2, 3)$ can be successively given by

$$\nu_3/\mu = 2\mu(F_{T1} - F_{T2}) - 1, \tag{1}$$

$$\nu_2/\mu = (3\lambda + 2\mu)(F_{T1} + F_{T2}) + (\lambda/2\mu - 1)\nu_3/\mu - \lambda/2\mu - 1, \tag{2}$$

$$\nu_1/\mu = 2(3\lambda + 2\mu)(\lambda + 2\mu)F_L/\mu + (\lambda/\mu)[(\lambda + 2\mu)/\mu + 2(\nu_2 + 2\nu_3)/\mu] - 2\nu_2/\mu, \tag{3}$$

where λ and μ are the Lamé (second-order) constants and equation (29) of [1] corrected for the thickness variation has been used. The third-order elastic constants deduced from the data of Fig. 2 are shown in Table 1. For comparison, those determined by the sing-around method [4] for the same material, but 20 mm thickness specimen, are presented. The correspondence between the both methods is fairly good. Therefore it can be concluded that the resonance method by thickness oscillations is a desirable technique to determine the third-order elastic constants of isotropic materials.

Table 1 Third-order elastic constants of mild steel ($\lambda = 10.49 \times 10^4$ MPa, $\mu = 8.28 \times 10^4$ MPa)

	ν_1	ν_2	ν_3
Resonance method	−0.33	−2.3	−2.0
Sing-around method	−0.27	−2.0	−2.0

(in unit of 10^5 MPa)

The theoretical analysis [1] also showed that the antisymmetric deformation with respect to the median plane of plate causes no frequency change of the thickness oscillations. This result was experimentally verified by purely bending the plate.

In [5], the dependence of the resonance frequency on the cut and azimuth angles, as well as on the applied stress, is discussed for the anisotropic material. There an agreement between the theory and the experiment in the case of quartz was found.

Acknowledgment

Discussions with Professor H. Toda are greatly appreciated.

References

1 Hirao, M., and Fukuoka, H., "Thickness Oscillations in Deformed Elastic Plate," ASME JOURNAL OF APPLIED MECHANICS, Vol. 46, 1979, pp. 663–666.

2 Hughes, D. S., and Kelly, J. L., "Second-Order Elastic Deformation of Solids," *Physical Reviews*, Vol. 92, 1953, pp. 1145–1149.

3 Smith, R. T., Stern, R., and Stephens, R. W. B., "Third-Order Elastic Moduli of Polycrystalline Metals From Ultrasonic Velocity Measurements," *Journal of the Acoustical Society of America*, Vol. 40, 1966, pp. 1002–1008.

4 Fukuoka, H., and Toda, H., "Preliminary Experiment on Acoustoelasticity for Stress Analysis," *Archives of Mechanics*, Vol. 29, 1977, pp. 673–686.

5 Lee, P. C. Y., Wang, Y. S., and Markenscoff, X., "High-Frequency Vibrations of Crystal Plates Under Initial Stresses," *Journal of the Acoustical Society of America*, Vol. 57, 1975, pp. 95–105.

Harmonic Waves in Fiber-Reinforced Orthotropic Elastic Composites

S. Nemat-Nasser[1] and M. Yamada[2]

The dispersive property of fiber-reinforced elastic composites con-

[1] Professor of Civil Engineering and Applied Mathematics, Northwestern University, Evanston, Ill. 60201. Mem. ASME.

[2] Visiting Scholar, Northwestern University, Evanston, Ill. 60201; on leave from Denkitsushin University, Chofu, Tokyo, Japan.

Manuscript received by ASME Applied Mechanics Division, January, 1981; final revision, April, 1981.

Downloaded 01 May 2010 to 171.66.16.249. Redistribution subject to ASME license or copyright; see http://www.asme.org/terms/Terms_Use.cfm

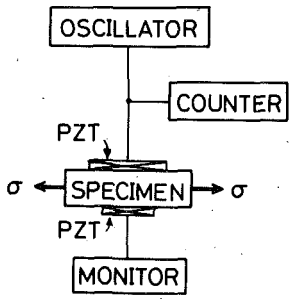


Fig. 1 Schematic diagram of resonance method

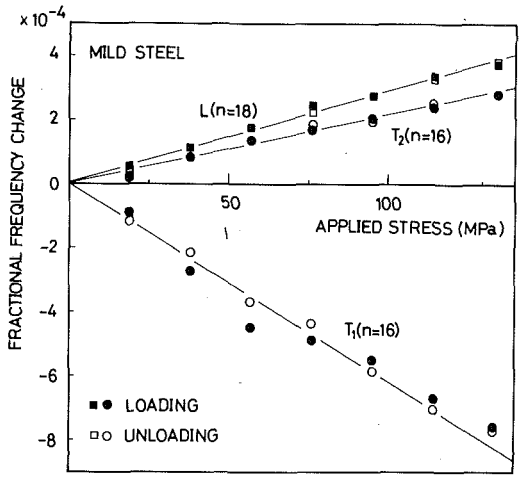


Fig. 2 Fractional change in resonance frequency versus tensile stress

a function of external stress. The resonance frequency under the given stress was determined from the frequency counter by tuning the oscillator so as to reach the maximum amplitude on the oscilloscope display. Typical result for the mild-steel plate of 5.15 mm thickness is presented in Fig. 2, where the load was uniaxial tension. The subscripts 1 and 2 of T-modes indicate, respectively, the parallel and normal polarizations with respect to the stress direction. The integer n denotes the mode order and the straight lines were drawn by processing the data with the method of least mean squares.

The resonance frequencies appear to vary linearly with the applied stress, which gives the experimental check to the theoretical result based on the second-order elasticity. The data scattering might be mainly due to the tuning error in obtaining the resonance maximum, because the so-called Q-value was not sufficiently large. For example, $Q = 20.2$ in the case of the 17th L-mode resonance. However, the careful manipulation of the tuner enabled the measurement of the change of resonance frequencies in units of kHz or less, as the stress is changed. Therefore, the accuracy in the order of 10^{-4} resulted for the fractional frequency change. If the resonance of the higher overtone is measured, the accuracy will be accordingly improved.

Third-Order Elastic Constants

The basic parameters which characterize the acoustoelastic effect of material are the third-order elastic constants. They correspond to the coefficients of the cubic-strain terms in the elastic energy and are indispensable in describing the nonlinear behavior of the material. The most remarkable advantage of the present resonance method is the ability to determine the third-order elastic constants in a rather simpler manner than have been reported [2–4]. For the isotropic case, three constants are independent with each other, so that the acoustoelastic data on the L and T-modes with the parallel and normal polarizations to the stress direction are required for the compatible determination.

Denoting by F the fractional change in the resonsnce frequency $(f - f_0)/f_0$ per unit uniaxial stress, f_0 being the value at stress-free condition, the third-order elastic constants ν_i $(i = 1, 2, 3)$ can be successively given by

$$\nu_3/\mu = 2\mu(F_{T1} - F_{T2}) - 1, \tag{1}$$

$$\nu_2/\mu = (3\lambda + 2\mu)(F_{T1} + F_{T2}) + (\lambda/2\mu - 1)\nu_3/\mu - \lambda/2\mu - 1, \tag{2}$$

$$\nu_1/\mu = 2(3\lambda + 2\mu)(\lambda + 2\mu)F_L/\mu + (\lambda/\mu)[(\lambda + 2\mu)/\mu + 2(\nu_2 + 2\nu_3)/\mu] - 2\nu_2/\mu, \tag{3}$$

where λ and μ are the Lamé (second-order) constants and equation (29) of [1] corrected for the thickness variation has been used. The third-order elastic constants deduced from the data of Fig. 2 are shown in Table 1. For comparison, those determined by the sing-around method [4] for the same material, but 20 mm thickness specimen, are presented. The correspondence between the both methods is fairly good. Therefore it can be concluded that the resonance method by thickness oscillations is a desirable technique to determine the third-order elastic constants of isotropic materials.

Table 1 Third-order elastic constants of mild steel ($\lambda = 10.49 \times 10^4$ MPa, $\mu = 8.28 \times 10^4$ MPa)

	ν_1	ν_2	ν_3
Resonance method	−0.33	−2.3	−2.0
Sing-around method	−0.27	−2.0	−2.0

(in unit of 10^5 MPa)

The theoretical analysis [1] also showed that the antisymmetric deformation with respect to the median plane of plate causes no frequency change of the thickness oscillations. This result was experimentally verified by purely bending the plate.

In [5], the dependence of the resonance frequency on the cut and azimuth angles, as well as on the applied stress, is discussed for the anisotropic material. There an agreement between the theory and the experiment in the case of quartz was found.

Acknowledgment

Discussions with Professor H. Toda are greatly appreciated.

References

1 Hirao, M., and Fukuoka, H., "Thickness Oscillations in Deformed Elastic Plate," ASME JOURNAL OF APPLIED MECHANICS, Vol. 46, 1979, pp. 663–666.

2 Hughes, D. S., and Kelly, J. L., "Second-Order Elastic Deformation of Solids," *Physical Reviews*, Vol. 92, 1953, pp. 1145–1149.

3 Smith, R. T., Stern, R., and Stephens, R. W. B., "Third-Order Elastic Moduli of Polycrystalline Metals From Ultrasonic Velocity Measurements," *Journal of the Acoustical Society of America*, Vol. 40, 1966, pp. 1002–1008.

4 Fukuoka, H., and Toda, H., "Preliminary Experiment on Acoustoelasticity for Stress Analysis," *Archives of Mechanics*, Vol. 29, 1977, pp. 673–686.

5 Lee, P. C. Y., Wang, Y. S., and Markenscoff, X., "High-Frequency Vibrations of Crystal Plates Under Initial Stresses," *Journal of the Acoustical Society of America*, Vol. 57, 1975, pp. 95–105.

Harmonic Waves in Fiber-Reinforced Orthotropic Elastic Composites

S. Nemat-Nasser[1] and M. Yamada[2]

The dispersive property of fiber-reinforced elastic composites con-

[1] Professor of Civil Engineering and Applied Mathematics, Northwestern University, Evanston, Ill. 60201. Mem. ASME.

[2] Visiting Scholar, Northwestern University, Evanston, Ill. 60201; on leave from Denkitsushin University, Chofu, Tokyo, Japan.

Manuscript received by ASME Applied Mechanics Division, January, 1981; final revision, April, 1981.

Copyright © 1981 by ASME
Downloaded 01 May 2010 to 171.66.16.249. Redistribution subject to ASME license or copyright; see http://www.asme.org/terms/Terms_Use.cfm

sisting of orthotropic materials is studied. Based on a new quotient recently proposed by one of the authors, approximate dispersion curves are obtained, and the influence of anisotropy is illustrated.

Introduction

While most composites consist of anisotropic constituents, isotropic fibers and matrix are assumed in most estimates, as otherwise laborious and complicated calculations are required. To illustrate the effect of anisotropy on the dynamic behavior of fiber-reinforced composites, their dispersive characteristics are studied in the present work using the new quotient method which has been developed by Nemat-Nasser [1], and further illustrated in [2, 3]. Harmonic waves in composites have been examined by a number of authors, e.g., Achenbach and Herrmann [4], Wheeler and Mura [5], Nelson and Navi [6], and others, but for isotropic fibers and matrix. In this work it is shown for various wave propagation directions that the effect of anisotropy can be significant.

It is noted that the method of the new quotient provides a rather powerful means for estimating the eigenvalues of elastic composites, in which large variations in material properties occur. This fact has been extensively documented in [1–3], where comparison with other methods is made, bounds on eigenvalues are presented, and the rate of convergence is numerically tested. In particular, it is shown that, for waves propagating normal to layers in a composite consisting of two alternating layers with mass density ratio of 3 and elastic modulus ratio of 100, negligibly small errors for the first eigenvalue at all wave numbers result from a three-term exponential approximation by the new quotient, while the corresponding Rayleigh quotient yields more than 100 percent error; for the new quotient, even the third eigenvalue is estimated in this case by a less than 20 percent error; see also [7]. In a recent work Babuška and Osborn [8] have proved that the method of the new quotient has a convergence rate which is one order better than that of the Rayleigh quotient for one-dimensional composites. Although a similar proof does not exist for the two-dimensional composites considered in the present Note, bounds given in [2] and other related facts seem to suggest that the method should remain effective beyond the one-dimensional layered composites.

Statement of Problem

Consider harmonic waves in a fiber-reinforced composite which consists of orthotropic infinitely extended cylindrical fibers with rectangular or elliptical cross sections, and an orthotropic matrix, Fig. 1. The eigenfrequencies are defined by the following eigenvalue problem:

$$\sigma_{jk,k} + \lambda\rho u_j = 0, \quad \sigma_{jk} = C_{jkmn}u_{m,n}, \tag{1}$$

$$u_j(\mathbf{x} + \mathbf{l}^\beta) = u_j(\mathbf{x})e^{i\mathbf{q}\cdot\mathbf{l}^\beta}, \quad \sigma_{ji}(\mathbf{x} + \mathbf{l}^\beta) = \sigma_{ji}(\mathbf{x})e^{i\mathbf{q}\cdot\mathbf{l}^\beta}, \quad j, k, m, n, \beta = 1, 2, \tag{2}$$

where the elasticity tensor $C_{jkmn}(\mathbf{x})$ and the mass-density $\rho(\mathbf{x})$ are continuous and continuously differentiable functions in both the matrix and the reinforcing subregions; $\lambda = \omega^2$, $\sigma_{jk}e^{\pm i\omega t}$, and $u_j e^{\pm i\omega t}$ are the stress and displacement fields, $\mathbf{q}$ is the wave vector, $\mathbf{l}$ is the periodicity vector, and comma followed by an index denotes partial differentiation with respect to the corresponding coordinate.

Equations (1) and (2) are the Euler-Lagrange equations of the quotient

$$\lambda_N = \frac{\langle \sigma_{jk}, u_{j,k}\rangle + \langle u_{j,k}, \sigma_{jk}\rangle - \langle D_{jkmn}\sigma_{jk}, \sigma_{mn}\rangle}{\langle \rho u_j, u_j\rangle}, \tag{3}$$

where

$$\langle gu_i, v_j\rangle = \int_V gu_i v_j^* dV, \tag{4}$$

and where g is a real-valued weighting function, * denotes the complex conjugate, the integration is carried out over the cross section of a typical unit cell, Fig. 1, and D_{jkmn} is the elastic compliance tensor; λ_N is called the new quotient.

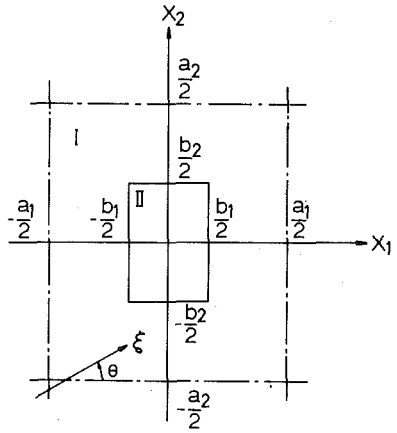


Fig. 1(a) A typical unit cell for a composite with rectangular fibers

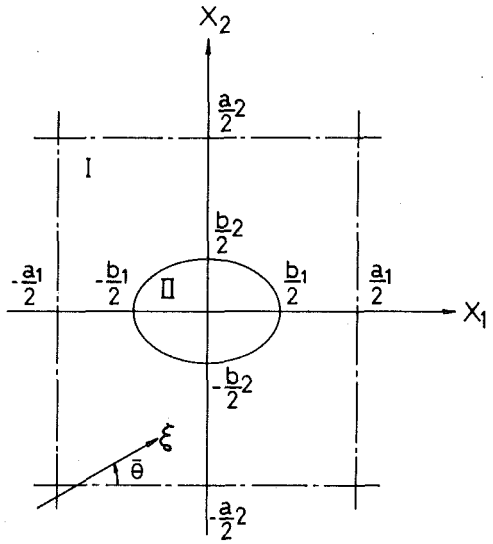


Fig. 1(b) A typical unit cell for a composite with elliptical fibers

For an approximate solution, set

$$u_j = \sum_{\alpha,\beta=0}^{M'} U_j^{\alpha\beta} f^{\alpha\beta}, \quad \sigma_{jk} = \sum_{\alpha,\beta=0}^{M'} S_{jk}^{\alpha\beta} f^{\alpha\beta},$$

$$f^{\alpha\beta} = \exp\,[i\{(q_1 + 2\pi\alpha)x_1 + (q_2 + 2\pi\beta)x_2\}], \tag{5}$$

where q_1 and q_2 are the components of the wave vector. Substitute (3) into (5) and upon rendering λ_N stationary, obtain

$$[\Omega - \mathbf{H}\Phi^{-1}\mathbf{H}^*]\mathbf{U} = \mathbf{0}. \tag{6}$$

The matrix Ω is defined as follows:

(*a*) Composites With Rectangular Fibers (Fig. 1(*a*)):

$$\Omega(I_1, J_1) = \frac{\bar{\omega}^2}{d}\begin{cases} \dfrac{(\theta-1)}{(\bar{n}_1 + \bar{n}_2\theta)}A_{\delta\beta}A_{\gamma\alpha}, & \alpha \neq \gamma, \beta \neq \delta, \\ \dfrac{(\theta-1)n_2}{(\bar{n}_1 + \bar{n}_2\theta)}A_{\delta\beta}, & \alpha = \gamma, \beta \neq \delta, \\ \dfrac{(\theta-1)m_2}{(\bar{n}_1 + \bar{n}_2\theta)}A_{\gamma\alpha}, & \alpha \neq \gamma, \beta = \delta, \\ 1, & \alpha = \gamma, \beta = \delta, \end{cases} \tag{7}$$

$$\Omega(I_2, J_2) = \Omega(I_1, J_1) \text{ and } \Omega(I_2, J_1) = \Omega(I_1, J_2) = 0; \tag{8}$$

(*b*) Composites With Elliptical Fibers (Fig. 1(*b*)):

Downloaded 01 May 2010 to 171.66.16.249. Redistribution subject to ASME license or copyright; see http://www.asme.org/terms/Terms_Use.cfm

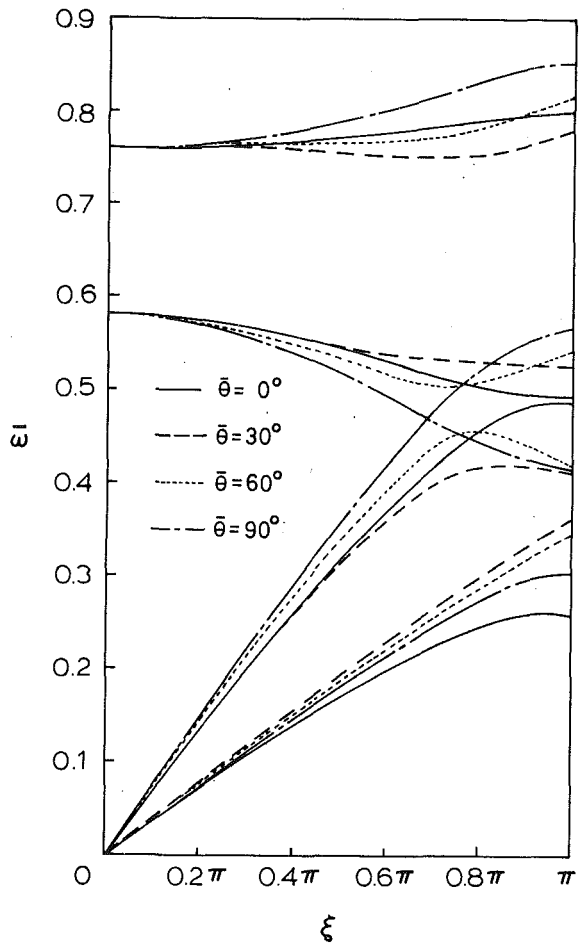


Fig. 2(a) Frequency $\bar{\omega} = \omega a_1(\bar{\rho}/\bar{C}_{1111})^{1/2}$ versus wave number $\xi = a_1(q_1^2 + q_2^2)^{1/2}$ for the indicated propagation angle $\bar{\theta}$ in isotropic composites with rectangular fibers; $\gamma = 100$, $\theta = 3$, $m_2 = 0.75$, $n_2 = 0.5$, $\bar{n}_2 = 0.38$, $\nu^{(1)} = \nu^{(2)} = 0.3$

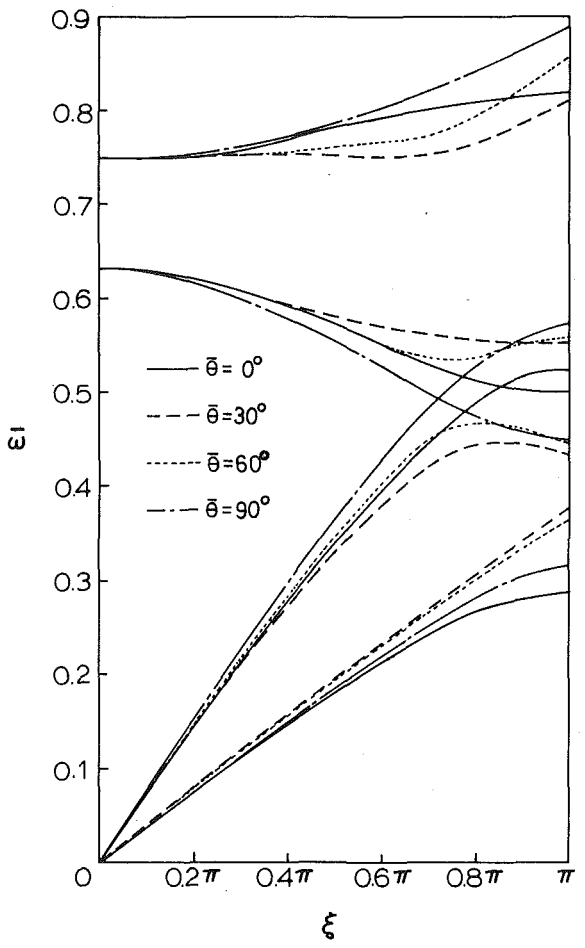


Fig. 2(b) Frequency $\bar{\omega} = \omega a_1(\bar{\rho}/\bar{C}_{1111})^{1/2}$ versus wave number $\xi = a_1(q_1^2 + q_2^2)^{1/2}$ for the indicated propagation angle $\bar{\theta}$ in isotropic composites with elliptical fibers; $\gamma = 100$, $\theta = 3$, $m_2 = 0.75$, $n_2 = 0.5$, $\bar{n}_2 = 0.29$, $\nu^{(1)} = \nu^{(2)} = 0.3$

$$\Omega(I_1, J_1) = \frac{\bar{\omega}^2}{d} \begin{cases} \dfrac{(\theta - 1)}{(\bar{n}_1 + \bar{n}_2\theta)} & \dfrac{m_2 n_2 J_1(R)}{2\{n_2^2(\alpha - \gamma)^2 + m_2^2(\beta - \delta)^2\}^{1/2}} \\ & \text{if } \alpha \neq \gamma, \text{ and/or } \beta \neq \delta, \\ 1 & \text{if } \alpha = \gamma, \beta = \delta, \end{cases} \tag{9}$$

where $J_1(R)$ is the Bessel function of the first kind and first order with argument

$$R = \pi\{n_2^2(\alpha - \gamma)^2 + m_2^2(\beta - \delta)^2\}^{1/2}. \tag{10}$$

The matrix Φ is defined as follows:

$$\Phi(I_1, J_1) = \begin{cases} \dfrac{(\gamma_{1111} - 1)}{(\bar{n}_1 + \bar{n}_2\gamma_{1111})} A_{\delta\beta}A_{\gamma\alpha}, & \alpha \neq \gamma, \beta \neq \delta, \\ \dfrac{(\gamma_{1111} - 1)n_2}{(\bar{n}_1 + \bar{n}_2\gamma_{1111})} A_{\delta\beta}, & \alpha = \gamma, \beta \neq \delta, \\ \dfrac{(\gamma_{1111} - 1)m_2}{(\bar{n}_1 + \bar{n}_2\gamma_{,1111})} A_{\gamma\alpha}, & \alpha \neq \gamma, \beta = \delta, \\ 1, & \alpha = \gamma, \beta = \delta, \end{cases} \tag{11}$$

$$\Phi(I_2, J_2) = \frac{4R_{1212}}{(\bar{n}_1 + \bar{n}_2\gamma_{1212})} \begin{cases} (\gamma_{1212} - 1)A_{\delta\beta}A_{\gamma\alpha}, & \alpha \neq \gamma, \beta \neq \delta, \\ (\gamma_{1212} - 1)n_2 A_{\delta\beta}, & \alpha = \gamma, \beta \neq \delta, \\ (\gamma_{1212} - 1)m_2 A_{\gamma\alpha}, & \alpha \neq \gamma, \beta = \delta, \\ (\bar{n}_1 + \bar{n}_2\gamma_{1212}), & \alpha = \gamma, \beta = \delta, \end{cases} \tag{12}$$

$$\Phi(I_3, J_3) = \begin{cases} \dfrac{(\gamma_{2222} - 1)R_{2222}}{(\bar{n}_1 + \bar{n}_2\gamma_{1111})} A_{\delta\beta}A_{\gamma\alpha}, & \alpha \neq \gamma, \quad \beta \neq \delta, \\ \dfrac{(\gamma_{2222} - 1)R_{2222}}{(\bar{n}_1 + \bar{n}_2\gamma_{1111})} n_2 A_{\delta\beta}, & \alpha = \gamma, \beta = \delta, \\ \dfrac{(\gamma_{2222} - 1)R_{2222}}{(\bar{n}_1 + \bar{n}_2\gamma_{1111})} m_2 A_{\gamma\alpha}, & \alpha \neq \gamma, \beta = \delta, \\ 1, & \alpha = \gamma, \beta = \delta, \end{cases} \tag{13}$$

$$\Phi(I_1, J_3) = \frac{R_{1122}}{(\bar{n}_1 + \bar{n}_2\gamma_{1111})} \begin{cases} (\gamma_{1122} - 1)A_{\delta\beta}A_{\gamma\alpha}, & \alpha \neq \gamma, \beta \neq \delta, \\ (\gamma_{1122} - 1)n_2 A_{\delta\beta}, & \alpha = \gamma, \beta \neq \delta, \\ (\gamma_{1122} - 1)m_2 A_{\gamma\alpha}, & \alpha \neq \gamma, \beta = \delta \\ (\bar{n}_1 + \bar{n}_2\gamma_{1122}), & \alpha = \gamma, \beta = \delta, \end{cases} \tag{14}$$

$$\Phi(I_3, J_1) = \Phi(I_1, J_3), \tag{15}$$

$$\Phi(I_1, J_2) = \Phi(I_2, J_1) = \Phi(I_2, J_3) = \Phi(I_3, J_2) = 0.$$

The matrix $\bar{H}$ is defined as follows:

Downloaded 01 May 2010 to 171.66.16.249. Redistribution subject to ASME license or copyright; see http://www.asme.org/terms/Terms_Use.cfm

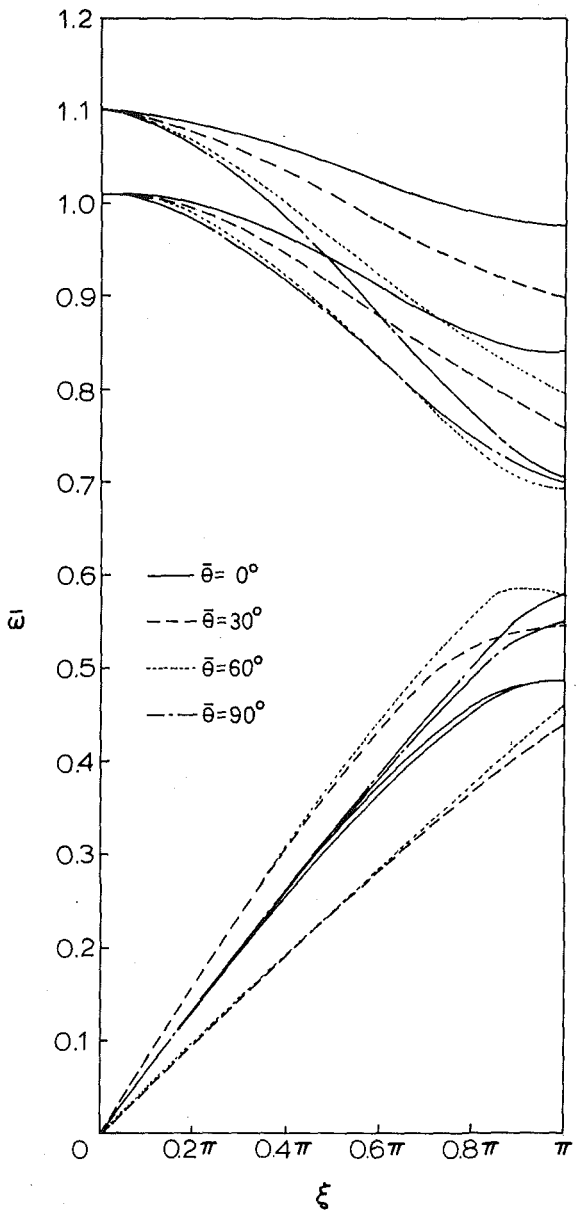


Fig. 3(*a*) Frequency $\bar{\omega} = \omega a_1(\bar{\rho}/\bar{C}_{1111})^{1/2}$ versus wave number $\xi = a_1(q_1^2 + q_2^2)^{1/2}$ for the indicated propagation angle $\bar{\theta}$ in orthotropic composites with rectangular fibers; $\gamma = 100$, $\theta = 3$, $m_2 = 0.75$, $n_2 = 0.5$, $\bar{n}_2 = 0.38$, $\nu^{(2)} = 0.3$, $\bar{c}_{22}^{(1)} = 4.0$, $\bar{c}_{12}^{(1)} = 0.25$, $\bar{c}_{66}^{(1)} = 1.0$

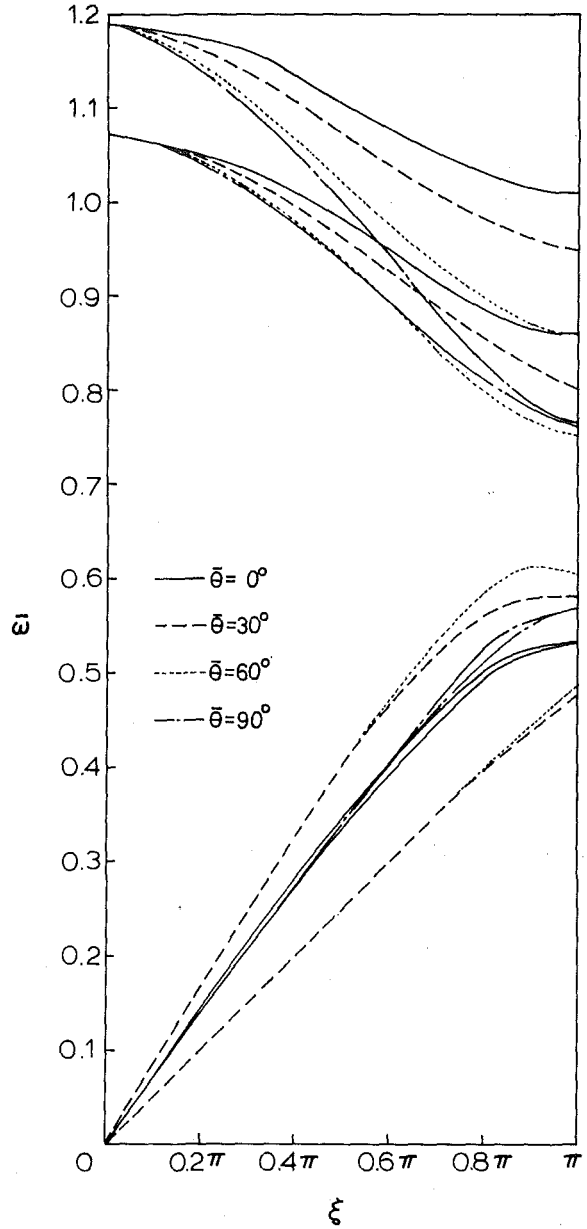


Fig. 3(*b*) Frequency $\bar{\omega} = \omega a_1(\bar{\rho}/\bar{C}_{1111})^{1/2}$ versus wave number $\xi = a_1(q_1^2 + q_2^2)^{1/2}$ for the indicated propagation angle $\bar{\theta}$ in orthotropic composites with elliptical fibers; $\gamma = 100$, $\theta = 3$, $m_2 = 0.75$, $n_2 = 0.5$, $\bar{n}_2 = 0.29$, $\nu^{(2)} = 0.3$, $\bar{c}_{22}^{(1)} = 4.0$, $\bar{c}_{12}^{(1)} = 0.25$, $\bar{c}_{66}^{(1)} = 1.0$

$$\bar{H}(I_1, J_1) = -i\begin{cases} q_1 + 2\pi\gamma & \text{if } \alpha = \gamma \quad \text{and} \quad \beta = \delta, \\ 0 & \text{if } \alpha \neq \gamma \quad \text{or} \quad \beta \neq \delta, \end{cases} \tag{16}$$

$$\bar{H}(I_2, J_1) = -i\begin{cases} (q_2 + 2\pi\delta)n_0 & \text{if} \quad \alpha = \gamma \quad \text{and} \quad \beta = \delta, \\ 0 & \text{if} \quad \alpha \neq \gamma \quad \text{or} \quad \beta \neq \delta, \end{cases} \tag{17}$$

$$\bar{H}(I_2, J_2) = \bar{H}(I_1, J_1), \quad \bar{H}(I_3, J_2) = \bar{H}(I_2, J_1), \quad \bar{H}(I_1, J_2) = \bar{H}(I_3, J_1) = 0, \tag{18}$$

where

$$I_1 = (\alpha + 1 + M') + (\beta + M')(2M' + 1),$$
$$J_1 = (\gamma + 1 + M') + (\delta + M')(2M' + 1),$$
$$\alpha, \beta, \gamma, \delta = 0, \pm 1, \ldots, \pm M'$$
$$I_2 = I_1 + (2M' + 1)^2, \quad J_2 = J_1 + (2M' + 1)^2,$$
$$I_3 = I_2 + (2M' + 1)^2, \quad J_3 = J_2 + (2M' + 1)^2, \tag{19}$$

and

$$\bar{\omega}^2 = \omega^2 a_1{}^2\bar{\rho}/\bar{C}_{1111}, \quad \bar{\rho} = \rho^{(1)}\bar{n}_1 + \rho^{(2)}\bar{n}_2,$$
$$\bar{C}_{1111} = c_{11}{}^{(1)}\bar{n}_1 + c_{11}{}^{(2)}\bar{n}_2,$$
$$\bar{n}_1 = 1 - \bar{n}_2, \quad \bar{n}_2 = \frac{b_1 b_2}{a_1 a_2}, \quad n_0 = \frac{a_1}{a_2}, \tag{20}$$

$$\theta = \frac{\rho^{(2)}}{\rho^{(1)}}, \quad n_2 = \frac{b_1}{b_2}, \quad m_2 = \frac{b_2}{a_2},$$
$$d = 1/(\bar{C}_{1111}\bar{D}_{1111}), \quad \bar{D}_{1111} = D_{1111}{}^{(1)}\bar{n}_1 + D_{1111}{}^{(2)}\bar{n}_2,$$
$$A_{\delta\beta} = \frac{\sin\pi(\delta - \beta)m_2}{\pi(\delta - \beta)}, \quad A_{\gamma\alpha} = \frac{\sin\pi(\gamma - \alpha)n_2}{\pi(\gamma - \alpha)},$$
$$D_{1111}{}^{(i)} = \frac{c_{22}{}^{(i)}}{A^{(i)}}, \quad D_{1122}{}^{(i)} = -\frac{c_{12}{}^{(i)}}{A^{(i)}},$$
$$D_{2222}{}^{(i)} = \frac{1}{A^{(i)}}, \quad D_{1212}{}^{(i)} = \frac{1}{4c_{66}{}^{(i)}},$$
$$A^{(i)} = c_{11}{}^{(i)}c_{22}{}^{(i)} - \{c_{12}{}^{(i)}\}^2, \quad i = 1, 2; \tag{20}$$

(Cont.)

the subscript (i) refers to the materials I and II for $i = 1$ and $i = 2$, respectively.

Numerical Results

Figs. 2 and 3 give the dispersion curves which relate the dimensionless frequency $\bar{\omega} = \omega a_1(\bar{\rho}/\bar{C}_{1111})^{1/2}$ to the dimensionless wave

Downloaded 01 May 2010 to 171.66.16.249. Redistribution subject to ASME license or copyright; see http://www.asme.org/terms/Terms_Use.cfm

number $\xi = a_1(q_1^2 + q_2^2)^{1/2}$. The following values for the parameters are used: $\gamma = 100$, $\theta = 3$, $m_2 = 0.75$, and $n_2 = 0.5$. Fiber is assumed to be isotropic. Note that in these figures the lowest set of curves is for the shear waves, the second set is for the longitudinal waves, and the other curves are the optical branches.

In Fig. 2, the matrix is also assumed to be isotropic. The effect of the propagation direction $\bar{\theta}$ is shown in Figs. 2(a) and 2(b).

In Figs. 3(a) and 3(b), the matrix is isotropic, but the fibers are not. The prominent effect of the parameters $\bar{c}_{22}$, $\bar{c}_{12}$, and $\bar{c}_{66}$ is shown.

Acknowledgment

This work has been supported by the U. S. Army Research Office under Grant DAAG29-79-C-0168 to Northwestern University.

References

1 Nemat-Nasser, S., "General Variational Methods for Elastic Waves in Composites," *Journal of Elasticity*, Vol. 2, 1972, pp. 73–90.

2 Nemat-Nasser, S., Fu, F. C. L., and Minagawa, S., "Harmonic Waves in One, Two, and Three-Dimensional Composites: Bounds for Eigenfrequencies," *International Journal of Solids and Structures*, Vol. 11, 1975, pp. 617–642

3 Minagawa, S., and Nemat-Nasser, S., "On Harmonic Waves in Layered Composites," ASME JOURNAL OF APPLIED MECHANICS, Vol. 44, 1977, pp. 689–695.

4 Achenbach, J. D., and Hermann, G., "Dispersion of Free Harmonic Waves in Fiber-Reinforced Composites," *AIAA Journal*, Vol. 6, 1968, pp. 1832–1836.

5 Wheeler, P., and Mura, T., "Dynamic Equivalence of Composite Material and Eigenstrain Problems," ASME JOURNAL OF APPLIED MECHANICS, Vol. 40, 1973, pp. 498–502.

6 Nelson, R., and Navi, P., "Harmonic Wave Propagation in Composite Materials," *Journal of the Acoustical Society of America*, Vol. 57, 1975, pp. 773–781.

7 Nemat-Nasser, S., and Minagawa, S., "Harmonic Waves in Layered Composites: Comparison Among Several Schemes," ASME JOURNAL OF APPLIED MECHANICS, Vol. 42, 1975, pp. 699–704.

8 Babuška, I., and Osborn, J. E., "Numerical Treatment of Eigenvalue Problems for Differential Equations With Discontinuous Coefficients," *Mathematics of Computation*, Vol. 32, 1978, pp. 991–1023.

Closed-Form Approximations for Forces on Conical Penetrators Into Dry Porous Rock[1]

D. B. Longcope,[2] and M. J. Forrestal[2]

In a recent paper [1], a model to predict forces on conical-nosed penetrators into dry rock targets is developed. The governing equations are written in Lagrangian coordinates and reduced, via a similarity transformation, to nonlinear ordinary differential equations which are solved numerically. In the present Note, the governing equations for the model of [1] are written in Eulerian coordinates, linearized, and closed-form solutions are obtained with an iterative technique. This solution is compared with the exact results from [1] and excellent agreement is shown for a wide range of practical parameters.

Formulation of the Problem

As shown in Fig. 1, a conical-nosed rigid projectile penetrates a uniform target at normal incidence. The analysis is simplified to one-dimensional wave propagation in the radial coordinate by applying the cylindrical cavity expansion approximation which considers the target as thin independent layers normal to the penetration direction. For dry porous rock, the target can be described by the linear hydrostat and linear shear failure-pressure relations

$$p = K(1 - \rho_0/\rho) \tag{1a}$$

$$\tau = \sigma_r - \sigma_\theta = \mu p \tag{1b}$$

where ρ_0, ρ are density in the undeformed and deformed configurations, p is pressure, and σ_r, σ_θ are the radial and circumferential stress components measured positive in compression. The equations of mass and momentum conservation in cylindrical Eulerian coordinates [2], the material description given by equations (1), and the assumption that $\sigma_z = \sigma_\theta$, where σ_z is the axial stress, are the field equations for the problem.

As the penetrator passes through a given target layer the radial particle velocity at the cavity wall is $v = V \tan \phi$, where V is the penetrator velocity and ϕ is half the cone angle. It is shown in [1] that particle velocity and radial stress are zero at the wave front. These are the boundary conditions for the problem.

The governing equations are reduced to ordinary differential equations via a similiarity transformation. Following the procedure outlined in [3], the dimensionless variables S, U, and ξ are introduced.

$$S = \sigma_r/\overline{K}, \quad U = v/c, \quad \xi = r/ct, \quad c^2 = \overline{K}/\rho_0 \tag{2a}$$

$$\bar{\mu} = 3\mu/(3 + 2\mu), \quad \overline{K} = (3 + 2\mu)K/3 \tag{2b}$$

where c is the wave front velocity obtained in [1]. The transformed equations of conservation of mass and radial momentum are, respectively,

$$\frac{dU}{d\xi} + \frac{U}{\xi} = \frac{1}{1 - S} \times (\xi - U)\frac{dS}{d\xi} \tag{3a}$$

$$\frac{dS}{d\xi} + \frac{\bar{\mu}}{\xi} S = \frac{1}{1 - S} \times (\xi - U)\frac{dU}{d\xi} \tag{3b}$$

and the boundary conditions are

$$U(\xi = \epsilon) = \epsilon, \quad \epsilon = V \tan \phi/c \tag{3c}$$

$$S(\xi = 1) = 0 \tag{3d}$$

Solution

Equations (3a, b) are linearized and reduce to

$$\frac{dU}{d\xi} + \frac{U}{\xi} = \xi \frac{dS}{d\xi} \tag{4a}$$

$$\frac{dS}{d\xi} + \frac{\bar{\mu}}{\xi} S = \xi \frac{dU}{d\xi} \tag{4b}$$

These equations are solved by an iterative procedure which starts by setting the right side of equation (4a) to zero. Thus

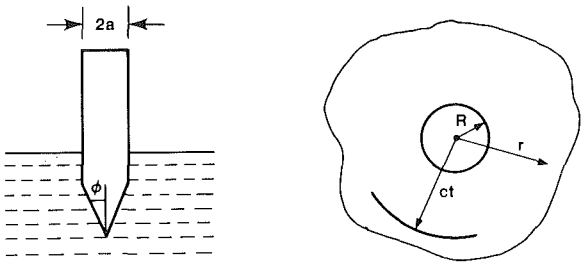


Fig. 1 Geometry of the problem

[1] This work was supported by the U. S. Department of Energy and the U. S. Army, Pershing II Project Manager's Office.

[2] Sandia National Laboratories, Albuquerque, New Mex. 87185. Mems. ASME.

Manuscript received by ASME Applied Mechanics Division, March, 1981; final revision, May, 1981.

Downloaded 01 May 2010 to 171.66.16.249. Redistribution subject to ASME license or copyright; see http://www.asme.org/terms/Terms_Use.cfm

number $\xi = a_1(q_1^2 + q_2^2)^{1/2}$. The following values for the parameters are used: $\gamma = 100$, $\theta = 3$, $m_2 = 0.75$, and $n_2 = 0.5$. Fiber is assumed to be isotropic. Note that in these figures the lowest set of curves is for the shear waves, the second set is for the longitudinal waves, and the other curves are the optical branches.

In Fig. 2, the matrix is also assumed to be isotropic. The effect of the propagation direction $\bar{\theta}$ is shown in Figs. 2(*a*) and 2(*b*).

In Figs. 3(*a*) and 3(*b*), the matrix is isotropic, but the fibers are not. The prominent effect of the parameters $\bar{c}_{22}$, $\bar{c}_{12}$, and $\bar{c}_{66}$ is shown.

Acknowledgment

This work has been supported by the U. S. Army Research Office under Grant DAAG29-79-C-0168 to Northwestern University.

References

1 Nemat-Nasser, S., "General Variational Methods for Elastic Waves in Composites," *Journal of Elasticity*, Vol. 2, 1972, pp. 73–90.

2 Nemat-Nasser, S., Fu, F. C. L., and Minagawa, S., "Harmonic Waves in One, Two, and Three-Dimensional Composites: Bounds for Eigenfrequencies," *International Journal of Solids and Structures*, Vol. 11, 1975, pp. 617–642

3 Minagawa, S., and Nemat-Nasser, S., "On Harmonic Waves in Layered Composites," ASME JOURNAL OF APPLIED MECHANICS, Vol. 44, 1977, pp. 689–695.

4 Achenbach, J. D., and Hermann, G., "Dispersion of Free Harmonic Waves in Fiber-Reinforced Composites," *AIAA Journal*, Vol. 6, 1968, pp. 1832–1836.

5 Wheeler, P., and Mura, T., "Dynamic Equivalence of Composite Material and Eigenstrain Problems," ASME JOURNAL OF APPLIED MECHANICS, Vol. 40, 1973, pp. 498–502.

6 Nelson, R., and Navi, P., "Harmonic Wave Propagation in Composite Materials," *Journal of the Acoustical Society of America*, Vol. 57, 1975, pp. 773–781.

7 Nemat-Nasser, S., and Minagawa, S., "Harmonic Waves in Layered Composites: Comparison Among Several Schemes," ASME JOURNAL OF APPLIED MECHANICS, Vol. 42, 1975, pp. 699–704.

8 Babuška, I., and Osborn, J. E., "Numerical Treatment of Eigenvalue Problems for Differential Equations With Discontinuous Coefficients," *Mathematics of Computation*, Vol. 32, 1978, pp. 991–1023.

Closed-Form Approximations for Forces on Conical Penetrators Into Dry Porous Rock[1]

D. B. Longcope,[2] and M. J. Forrestal[2]

In a recent paper [1], a model to predict forces on conical-nosed penetrators into dry rock targets is developed. The governing equations are written in Lagrangian coordinates and reduced, via a similarity transformation, to nonlinear ordinary differential equations which are solved numerically. In the present Note, the governing equations for the model of [1] are written in Eulerian coordinates, linearized, and closed-form solutions are obtained with an iterative technique. This solution is compared with the exact results from [1] and excellent agreement is shown for a wide range of practical parameters.

Formulation of the Problem

As shown in Fig. 1, a conical-nosed rigid projectile penetrates a uniform target at normal incidence. The analysis is simplified to one-dimensional wave propagation in the radial coordinate by applying the cylindrical cavity expansion approximation which considers the target as thin independent layers normal to the penetration direction. For dry porous rock, the target can be described by the linear hydrostat and linear shear failure-pressure relations

$$p = K(1 - \rho_0/\rho) \tag{1a}$$

$$\tau = \sigma_r - \sigma_\theta = \mu p \tag{1b}$$

where ρ_0, ρ are density in the undeformed and deformed configurations, p is pressure, and σ_r, σ_θ are the radial and circumferential stress components measured positive in compression. The equations of mass and momentum conservation in cylindrical Eulerian coordinates [2], the material description given by equations (1), and the assumption that $\sigma_z = \sigma_\theta$, where σ_z is the axial stress, are the field equations for the problem.

As the penetrator passes through a given target layer the radial particle velocity at the cavity wall is $v = V \tan \phi$, where V is the penetrator velocity and ϕ is half the cone angle. It is shown in [1] that particle velocity and radial stress are zero at the wave front. These are the boundary conditions for the problem.

The governing equations are reduced to ordinary differential equations via a similiarity transformation. Following the procedure outlined in [3], the dimensionless variables S, U, and ξ are introduced.

$$S = \sigma_r/\overline{K}, \quad U = v/c, \quad \xi = r/ct, \quad c^2 = \overline{K}/\rho_0 \tag{2a}$$

$$\bar{\mu} = 3\mu/(3 + 2\mu), \quad \overline{K} = (3 + 2\mu)K/3 \tag{2b}$$

where c is the wave front velocity obtained in [1]. The transformed equations of conservation of mass and radial momentum are, respectively,

$$\frac{dU}{d\xi} + \frac{U}{\xi} = \frac{1}{1-S} \times (\xi - U)\frac{dS}{d\xi} \tag{3a}$$

$$\frac{dS}{d\xi} + \frac{\bar{\mu}}{\xi} S = \frac{1}{1-S} \times (\xi - U)\frac{dU}{d\xi} \tag{3b}$$

and the boundary conditions are

$$U(\xi = \epsilon) = \epsilon, \quad \epsilon = V \tan \phi/c \tag{3c}$$

$$S(\xi = 1) = 0 \tag{3d}$$

Solution

Equations (3*a*, *b*) are linearized and reduce to

$$\frac{dU}{d\xi} + \frac{U}{\xi} = \xi \frac{dS}{d\xi} \tag{4a}$$

$$\frac{dS}{d\xi} + \frac{\bar{\mu}}{\xi} S = \xi \frac{dU}{d\xi} \tag{4b}$$

These equations are solved by an iterative procedure which starts by setting the right side of equation (4*a*) to zero. Thus

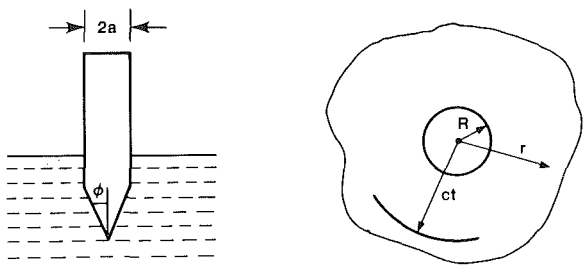


Fig. 1 Geometry of the problem

[1] This work was supported by the U. S. Department of Energy and the U. S. Army, Pershing II Project Manager's Office.

[2] Sandia National Laboratories, Albuquerque, New Mex. 87185. Mems. ASME.

Manuscript received by ASME Applied Mechanics Division, March, 1981; final revision, May, 1981.

Copyright © 1981 by ASME
Downloaded 01 May 2010 to 171.66.16.249. Redistribution subject to ASME license or copyright; see http://www.asme.org/terms/Terms_Use.cfm

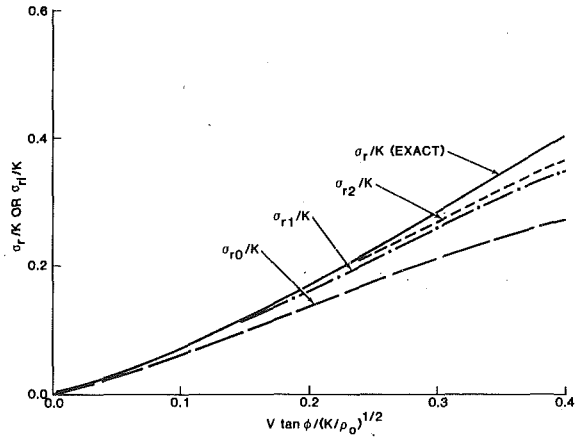


Fig. 2 Radial stress on the penetrator nose for $\mu = 1.0$

$$\frac{dU_0}{d\xi} + \frac{U_0}{\xi} = 0 \tag{5a}$$

which has solution

$$U_0 = \epsilon^2 \xi^{-1} \tag{5b}$$

with application of the boundary condition (3c). This solution is substituted into equation (4b) to give

$$\frac{dS_0}{d\xi} + \frac{\bar{\mu}}{\xi} S_0 = -\epsilon^2 \xi^{-1} \tag{5c}$$

which has solution

$$S_0 = \frac{\epsilon^2}{\bar{\mu}} \xi^{-\bar{\mu}} - \frac{\epsilon^2}{\bar{\mu}} \tag{5d}$$

with the application of the boundary condition (3d). As justification for starting the iteration procedure by neglecting the right side of equation (4a), the approximations (5b, d) may be substituted back into equations (4a, b). When scaled so that the left sides are of order unity, $O(1)$, the right sides of equations (4a, b) are $O(\epsilon^{2-\bar{\mu}})$ and $O(\epsilon^{\bar{\mu}})$, when ξ is $O(\epsilon)$. Typically, $\bar{\mu} = 0.6$ ($\mu = 1$) and the right side of equation (4a) is of higher order than the right side of equation (4b).

The procedure leading to equations (5b, d) is repeated two more times and formulas for the radial stress are given by

$$S_1 = \frac{-1}{\bar{\mu}} \left[\epsilon^2 + \frac{\epsilon^{4-\bar{\mu}}}{2-\bar{\mu}}\right] - \frac{(1-\bar{\mu})}{2(2-\bar{\mu})} \epsilon^2 \xi^{2-\bar{\mu}} + \left[\frac{1}{\bar{\mu}} + \frac{(1-\bar{\mu})}{2(2-\bar{\mu})}\right] \epsilon^2 \xi^{-\bar{\mu}} + \frac{\epsilon^{4-\bar{\mu}} \xi^{-\bar{\mu}}}{\bar{\mu}(2-\bar{\mu})} \tag{6}$$

$$S_2 = C_1(\xi^{-\bar{\mu}} - 1) + (C_2 + C_3)\xi^{-\bar{\mu}} - C_2 \xi^{2-\bar{\mu}} - C_3 \xi^{4-\bar{\mu}} \tag{7a}$$

in which

$$C_1 = \frac{\epsilon^2}{\bar{\mu}} + \left[\frac{1}{\bar{\mu}(2-\bar{\mu})} + \frac{(1-\bar{\mu})}{2(2-\bar{\mu})^2}\right] \epsilon^{4-\bar{\mu}} + \frac{\epsilon^{6-\bar{\mu}}}{\bar{\mu}(2-\bar{\mu})^2} + \frac{(1-\bar{\mu})}{2\bar{\mu}(4-\bar{\mu})} \epsilon^{6-\bar{\mu}} \tag{7b}$$

$$C_2 = \left[\frac{(1-\bar{\mu})}{2(2-\bar{\mu})} + \frac{\bar{\mu}(1-\bar{\mu})^2}{4(2-\bar{\mu})^2}\right] \epsilon^2 + \frac{(1-\bar{\mu})}{2(2-\bar{\mu})^2} \epsilon^{4-\bar{\mu}} \tag{7c}$$

$$C_3 = \frac{(1-\bar{\mu})(3-\bar{\mu})}{8(4-\bar{\mu})} \tag{7d}$$

As discussed in [1], the radial stress component on the surface of the conical nose is spatially uniform for a given penetrator velocity V and the resultant axial force on the penetrator nose is given by

$$F = \pi a^2 \sigma_r(\xi = \epsilon) \tag{8}$$

where a is the radius of the penetrator afterbody.

Numerical Results and Discussion

Comparisons of radial stresses at the cavity wall from the iterative solutions $\sigma_{ri} = \overline{K} S_i(\xi = \epsilon)$ and the exact solution $\sigma_r(\xi = \epsilon)$ given in [1] are shown in Fig. 2 for $\mu = 1$. For $[V \tan \phi/(K/\rho_0)^{1/2}] \leq 0.4$, which covers a wide range of practical parameters for penetration into dry porous rock targets, the closed-form expression for σ_{r2} is within 10 percent of the exact solution. For other values of μ, $0 < \mu < 1.5$, the accuracy of σ_{r2} is equivalent to that for $\mu = 1$.

It is interesting to point out that several empirical relations [4] used to estimate depth of penetration have represented the resisting force as an integer power series in the penetrator velocity. For the present target model the approximate solution has noninteger powers in the penetrator velocity which are a function of the shear strength parameter μ. Also, a recent solution for a locked hydrostat and a linear shear failure-pressure relation [5] predicts forces proportional to the square of the penetration velocity.

Acknowledgment

The authors would like to acknowledge initial discussion with T. G. Priddy regarding cavity expansion models of target response and their approximate solution.

References

1 Forrestal, M. J., Longcope, D. B., and Norwood, F. R., "A Model to Estimate Forces on Conical Penetrators Into Dry Porous Rock," ASME JOURNAL OF APPLIED MECHANICS, Vol. 48, Mar. 1981, pp. 25–29.

2 Malvern, L. E., *Introduction to the Mechanics of a Continuous Medium*, Prentice-Hall, Inc. 1969, pg. 668.

3 Zel'dovich, Y. B., and Raizer, Y. P., *Physics of Shock Waves and High-Temperature Hydrodynamic Phenomena*, Vol. II, Chapter XII, Academic Press, 1967.

4 Backman, M. E., and Goldsmith, W., "The Mechanics of Penetration of Projectiles Into Targets," *International Journal of Engineering Science*, Vol. 16, 1978, pp. 38–40.

5 Forrestal, M. J., Norwood, F. R., and Longcope, D. B., "Penetration Into Targets Described by Locked Hydrostats and Shear Strength," *International Journal of Solids and Structures*, Vol. 17, 1981, pp. 915–924.

An Improvement of the Stress Calculations in Plane Elasticity by Use of Spline Functions

J. C. Boyer[1] and P. Trompette[2]

In finite-element models based on simple displacement approximations, i.e., linear, the stress calculations are often lacking in accuracy especially for the highly stressed parts of the structure. For this reason it can be necessary to perform supplementary calculations, usually either refining the finite-element mesh or using higher-order approximation functions. These imply changes in the input data and consequently require more time to prepare and compute.

Several authors have previously attempted to improve the finite-element stress results without modifying the initial mesh or the type of the finite element:

Turner, Martins, and Weikel [1], discuss an averaging technique based on equivalence of nodal forces and element stresses; Oden and Brauchli [2], and Oden and Reddy [3], use the concept of conjugate approximations; Loubignac, Cantin, and Touzot [4], calculate the equilibrium of the finite element by an iterative method.

[1] Assistant, Laboratoire de Mécanique des Solides, I.N.S.A.—Lyon, 20, avenue Albert Einstein, 69621 Villeurbanne Cédex—France.

[2] Professor, Laboratoire de Mécanique des Structures—ERA 911, I.N.S.A.—Lyon, 20, avenue Albert Einstein, 69621, Villeurbanne, Cedex—France. Mem. ASME.

Manuscript received by ASME Applied Mechanics Division, January, 1981.

Downloaded 01 May 2010 to 171.66.16.249. Redistribution subject to ASME license or copyright; see http://www.asme.org/terms/Terms_Use.cfm

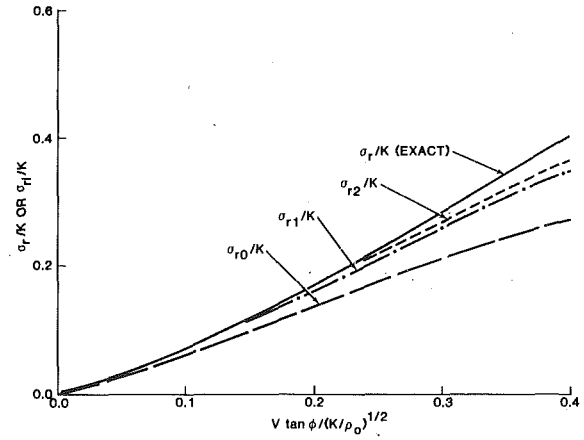


Fig. 2 Radial stress on the penetrator nose for $\mu = 1.0$

$$\frac{dU_0}{d\xi} + \frac{U_0}{\xi} = 0 \tag{5a}$$

which has solution

$$U_0 = \epsilon^2 \xi^{-1} \tag{5b}$$

with application of the boundary condition (3c). This solution is substituted into equation (4b) to give

$$\frac{dS_0}{d\xi} + \frac{\bar{\mu}}{\xi} S_0 = -\epsilon^2 \xi^{-1} \tag{5c}$$

which has solution

$$S_0 = \frac{\epsilon^2}{\bar{\mu}} \xi^{-\bar{\mu}} - \frac{\epsilon^2}{\bar{\mu}} \tag{5d}$$

with the application of the boundary condition (3d). As justification for starting the iteration procedure by neglecting the right side of equation (4a), the approximations (5b, d) may be substituted back into equations (4a, b). When scaled so that the left sides are of order unity, $O(1)$, the right sides of equations (4a, b) are $O(\epsilon^{2-\bar{\mu}})$ and $O(\epsilon^{\bar{\mu}})$, when ξ is $O(\epsilon)$. Typically, $\bar{\mu} = 0.6$ ($\mu = 1$) and the right side of equation (4a) is of higher order than the right side of equation (4b).

The procedure leading to equations (5b, d) is repeated two more times and formulas for the radial stress are given by

$$S_1 = \frac{-1}{\bar{\mu}} \left[\epsilon^2 + \frac{\epsilon^{4-\bar{\mu}}}{2-\bar{\mu}}\right] - \frac{(1-\bar{\mu})}{2(2-\bar{\mu})} \epsilon^2 \xi^{2-\bar{\mu}} + \left[\frac{1}{\bar{\mu}} + \frac{(1-\bar{\mu})}{2(2-\bar{\mu})}\right] \epsilon^2 \xi^{-\bar{\mu}} + \frac{\epsilon^{4-\bar{\mu}} \xi^{-\bar{\mu}}}{\bar{\mu}(2-\bar{\mu})} \tag{6}$$

$$S_2 = C_1(\xi^{-\bar{\mu}} - 1) + (C_2 + C_3)\xi^{-\bar{\mu}} - C_2 \xi^{2-\bar{\mu}} - C_3 \xi^{4-\bar{\mu}} \tag{7a}$$

in which

$$C_1 = \frac{\epsilon^2}{\bar{\mu}} + \left[\frac{1}{\bar{\mu}(2-\bar{\mu})} + \frac{(1-\bar{\mu})}{2(2-\bar{\mu})^2}\right] \epsilon^{4-\bar{\mu}} + \frac{\epsilon^{6-\bar{\mu}}}{\bar{\mu}(2-\bar{\mu})^2} + \frac{(1-\bar{\mu})}{2\bar{\mu}(4-\bar{\mu})} \epsilon^{6-\bar{\mu}} \tag{7b}$$

$$C_2 = \left[\frac{(1-\bar{\mu})}{2(2-\bar{\mu})} + \frac{\bar{\mu}(1-\bar{\mu})^2}{4(2-\bar{\mu})^2}\right] \epsilon^2 + \frac{(1-\bar{\mu})}{2(2-\bar{\mu})^2} \epsilon^{4-\bar{\mu}} \tag{7c}$$

$$C_3 = \frac{(1-\bar{\mu})(3-\bar{\mu})}{8(4-\bar{\mu})} \tag{7d}$$

As discussed in [1], the radial stress component on the surface of the conical nose is spatially uniform for a given penetrator velocity V and the resultant axial force on the penetrator nose is given by

$$F = \pi a^2 \sigma_r(\xi = \epsilon) \tag{8}$$

where a is the radius of the penetrator afterbody.

Numerical Results and Discussion

Comparisons of radial stresses at the cavity wall from the iterative solutions $\sigma_{ri} = \overline{K} S_i(\xi = \epsilon)$ and the exact solution $\sigma_r(\xi = \epsilon)$ given in [1] are shown in Fig. 2 for $\mu = 1$. For $[V \tan \phi/(K/\rho_0)^{1/2}] \leq 0.4$, which covers a wide range of practical parameters for penetration into dry porous rock targets, the closed-form expression for σ_{r2} is within 10 percent of the exact solution. For other values of μ, $0 < \mu < 1.5$, the accuracy of σ_{r2} is equivalent to that for $\mu = 1$.

It is interesting to point out that several empirical relations [4] used to estimate depth of penetration have represented the resisting force as an integer power series in the penetrator velocity. For the present target model the approximate solution has noninteger powers in the penetrator velocity which are a function of the shear strength parameter μ. Also, a recent solution for a locked hydrostat and a linear shear failure-pressure relation [5] predicts forces proportional to the square of the penetration velocity.

Acknowledgment

The authors would like to acknowledge initial discussion with T. G. Priddy regarding cavity expansion models of target response and their approximate solution.

References

1 Forrestal, M. J., Longcope, D. B., and Norwood, F. R., "A Model to Estimate Forces on Conical Penetrators Into Dry Porous Rock," ASME JOURNAL OF APPLIED MECHANICS, Vol. 48, Mar. 1981, pp. 25–29.

2 Malvern, L. E., *Introduction to the Mechanics of a Continuous Medium*, Prentice-Hall, Inc. 1969, pg. 668.

3 Zel'dovich, Y. B., and Raizer, Y. P., *Physics of Shock Waves and High-Temperature Hydrodynamic Phenomena*, Vol. II, Chapter XII, Academic Press, 1967.

4 Backman, M. E., and Goldsmith, W., "The Mechanics of Penetration of Projectiles Into Targets," *International Journal of Engineering Science*, Vol. 16, 1978, pp. 38–40.

5 Forrestal, M. J., Norwood, F. R., and Longcope, D. B., "Penetration Into Targets Described by Locked Hydrostats and Shear Strength," *International Journal of Solids and Structures*, Vol. 17, 1981, pp. 915–924.

An Improvement of the Stress Calculations in Plane Elasticity by Use of Spline Functions

J. C. Boyer[1] and P. Trompette[2]

In finite-element models based on simple displacement approximations, i.e., linear, the stress calculations are often lacking in accuracy especially for the highly stressed parts of the structure. For this reason it can be necessary to perform supplementary calculations, usually either refining the finite-element mesh or using higher-order approximation functions. These imply changes in the input data and consequently require more time to prepare and compute.

Several authors have previously attempted to improve the finite-element stress results without modifying the initial mesh or the type of the finite element:

Turner, Martins, and Weikel [1], discuss an averaging technique based on equivalence of nodal forces and element stresses; Oden and Brauchli [2], and Oden and Reddy [3], use the concept of conjugate approximations; Loubignac, Cantin, and Touzot [4], calculate the equilibrium of the finite element by an iterative method.

[1] Assistant, Laboratoire de Mécanique des Solides, I.N.S.A.—Lyon, 20, avenue Albert Einstein, 69621 Villeurbanne Cédex—France.

[2] Professor, Laboratoire de Mécanique des Structures—ERA 911, I.N.S.A.—Lyon, 20, avenue Albert Einstein, 69621, Villeurbanne, Cedex—France. Mem. ASME.

Manuscript received by ASME Applied Mechanics Division, January, 1981.

Copyright © 1981 by ASME
Downloaded 01 May 2010 to 171.66.16.249. Redistribution subject to ASME license or copyright; see http://www.asme.org/terms/Terms_Use.cfm

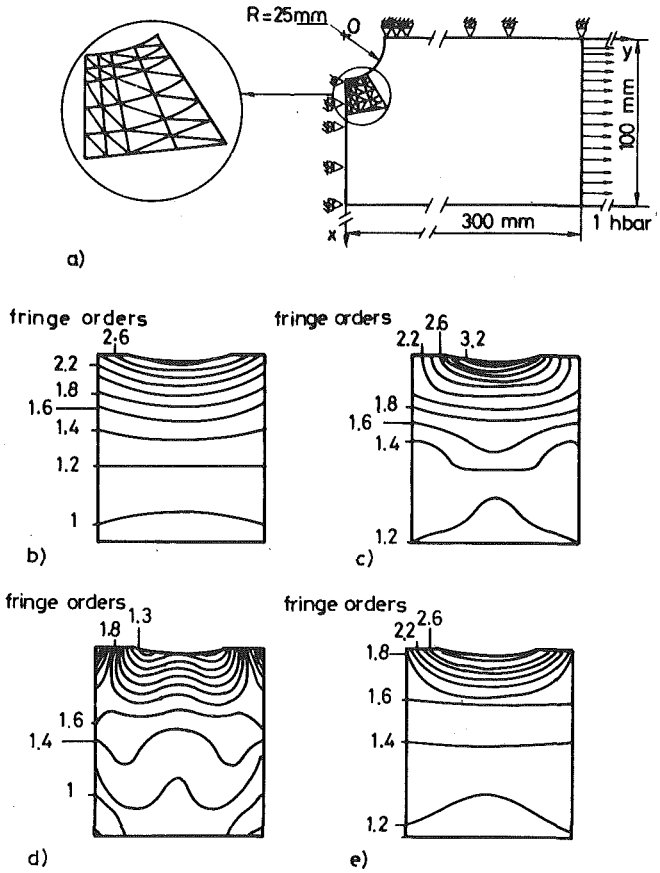


Fig. 1 Plate with circular hole; (*a*) finite-element mesh in the studied area; (*b*)–(*e*) isochromatic patterns; (*b*) theory [8]; (*c*) constant stress triangle; (*d*) consistent stress [2]; (*e*) spline interpolation

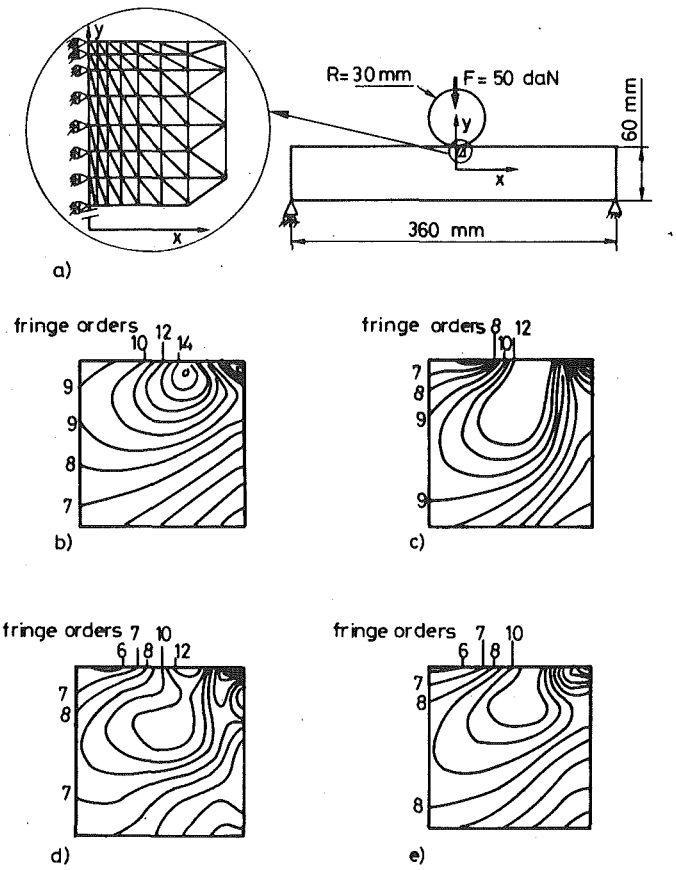


Fig. 2 Beam under Hertzian load; (*a*) finite-element mesh in the studied area; (*b*)–(*e*) isochromatic patterns; (*b*) experiment [9]; (*c*) constant stress triangle; (*d*) consistent stress [2]; (*e*) spline interpolation

There a completely different approach is described which is summarized as follows:

1 It is supposed that the displacement field deduced from the initial mesh is precise enough to be the basis of the following calculations.

2 From the preceding discrete data, the interopolation spline functions are generated and provide a continuous displacement field, for a part or the totality of the structure.

3 The derivatives of these spline functions give the strains and finally the stresses.

The basic idea of this process is to take into account information additional to that given by one finite element. It is hoped and verified on several stress-concentration problems in two-dimensional elasticity that this "wider starting point" is also a "better starting point." Only two examples are presented here.

On the other hand, the continuity of the displacements and strain fields allow more accurate stress calculations over any part of the studied area, as it also simplifies the computer graphic plottings.

It is pointed out that this approach must not be confused with those using spline functions as shape functions of a finite element.

Displacement Interpolation by Spline Functions

The procedure previously described needs the use of bivariate splines, deduced from any type of finite-element mesh which means any bidimensional point set data. The bivariate spline functions developed here require the combination of two univariate splines. The followed procedure has been first developed by Gordon [5], who demonstrates how the values of a function at the nodes of any rectangular mesh and the values of the derivatives at the boundary can be used to determine the bivariate spline functions. Nevertheless the work of Gordon is insufficient in finite-element analysis for which the meshes are not necessarily rectangular. This is the reason why it has been extended by [7] as it can be demonstrated that the top values of the rectangular mesh may be replaced by those of neighboring points in the B splines determination. Conversely the FE mesh no longer needs to be rectangular. The different steps are given in [7], in accordance with the general spline theory described by Greville [6].

Applications

Before presenting the different results obtained by this method, the choice of some parameters must be discussed.

Degree of the Splines. It has been shown in [7] that the accuracy increases with the spline degree but the improvement in accuracy is rapidly limited in percentage values, so it is suggested that quintic splines be selected. They are a satisfactory compromise between the computer time and the accuracy.

Interpolation Point Number. This parameter has a small effect on the stress accuracy. It may be sufficient to retain the points necessary to determine the spline functions which are $(h + 1)^2$ for B splines of degree h.

Interpolation Domain. It has been shown in [7] that the results are rather unsatisfactory at the corner nodes of the interpolation domain. This is why it is recommended that the interpolation be carried out over a domain larger than the studied area. In the following examples four supplementary points have been taken in one direction.

Example 1

This is a rectangular plate with a circular hole under uniform tension; see Fig. 1(*a*). Due to symmetry only a quarter of the plate is divided in 130 elements (132 nodes). The four Figs. 1(*b*)–1(*e*) represent the isochromatic patterns, respectively, obtained with the theory [8],

Downloaded 01 May 2010 to 171.66.16.249. Redistribution subject to ASME license or copyright; see http://www.asme.org/terms/Terms_Use.cfm

the constant stress triangle element (CST), Oden's method of consistent stress, and the spline functions. In the studied area, the improvements are easily established both for the shape and the levels of the fringes.

Example 2

This second example is related to the Hertz contact problem and concerned a rectangular simply supported beam loaded in its center by means of an elastic disk. For this example the reference results are experimental and have been obtained with the aid of photoelastic models [9]. The dimensions and the load values are shown in the figure. In this example, it is found that the improvements with regard to the direct method are significant. It seems that the Oden's method is more sensitive to the conditions of symmetry than the spline functions (see the shapes of the isochromatics in Fig. 4(*d*).

Conclusions

It has been shown that the use of spline functions to interpolate the discrete finite-element displacement field is an effective means of improving the final stress field.

On the other hand, the continuity of all the functions obtained is of considerable value either for the computer graphics or the determination of the stress values on boundaries.

It must be pointed out that extra computing effort required to implement this method is not significant. The input data of the finite-element method can be used again and the coefficients of the splines are obtained in solving only one band linear system.

This method, of course, is still limited to the two-dimensional space as the three-dimensional interpolation problem is not yet satisfactorily resolved.

References

1 Turner, M. J., Martin, H. C., and Weikel, B. C., "Further Developments and Applications of the Stiffness Method," *Matrix Methods of Structural Analysis*, 1st ed., Vol. 1, Macmillan, New York, 194, pp. 203–266.

2 Oden, J. T., and Brauchli, H. J., "On the Calculation of Consistent Stress Distributions in Finite-Element Approximations," *International Journal for Numerical Methods in Engineering*, Vol. 3, n° 3, 1971, pp. 317–325.

3 Oden, J. T., and Reddy, J. N., "Note on an Approximate Method for Computing Consistent Conjugate Stresses in Elastic Finite Elements," *International Journal for Numerical Methods in Engineering*, Vol. 6, n° 1, 1973, pp. 55–61.

4 Loubignac, G., Cantin, G., and Touzot, G., "Continuous Stress Fields in Finite-Element Analysis," *AIAA Journal*, Vol. 15, n° 11, 1977, pp. 1645–1647.

5 Gordon, W. J., "Spline-Blended Surface Interpolation Through Curve Networks," *Journal of Mathematics and Mechanics*, Vol. 18, n° 10, 1969, pp. 931–951.

Greville, T. N. E., "Introduction to Spline Functions," *Theory and Applications of Spline Functions*, Academic Press, New York, 1969, pp. 1–35.

7 Boyer, J. C., "Utilisation des fonctions splines pour la détermination des contraintes. Cas des structures planes," Thesis, University of Lyon, 1979.

8 Howland, R. C. J., "On the Stresses in the Neighbourhood of a Circular Hole in a Strip Under Tension," *Philosophical Transactions of the Royal Society*, Series A, Vol. 229, n° 671, janu. 1930, pp. 49–87.

9 Berveiler, M., "Détermination des contraintes de contact dans une poutre soumise à la flexion par une charge hertzienne," Thesis, University of Metz, 1971.

Boundary Condition Independence in Coupled Thermoelasticity

E. V. Wilms[1] and H. Cohen[2]

We investigate the temperature and strain in a thermoelastically coupled half space. Two sets of boundary conditions are considered:

Conditions *A*:

$$\sigma(0, t) = \mathrm{H}(t), \tag{1a}$$

$$T(0, t) = 0. \tag{1b}$$

Conditions *B*:

$$\sigma(0, t) = \mathrm{H}(t), \tag{2a}$$

$$T_x(0, t) = 0. \tag{2b}$$

Here σ is the dimensionless stress, T is the temperature, and H is the Heaviside function. It is shown that for certain ranges of the space and time variables x and t, the strain and temperature are the same for the isothermal boundary condition (1*b*) as for the insulated boundary condition (2*b*).

The governing equations are

$$u_{xx} - \frac{1}{v^2} u_{tt} - \frac{\beta}{\rho v^2} T_x = 0, \tag{3a}$$

$$T_{xx} - \frac{c}{v^2} T_t - \frac{\rho c \epsilon}{\beta} u_{xt} = 0. \tag{3b}$$

Here u is the displacement in the direction of the space variable x, which is positive to the right. $v = [(\lambda + 2\mu)/\rho]^{1/2}$ is the dilatational wave speed, where λ and μ are the elastic constants and ρ is the mass density. $c = v^2/k$ is the characteristic thermoelastic frequency [1], where k is the thermal diffusivity. $\epsilon = \beta^2 T_0/c_v(\lambda + 2\mu)$ is the thermoelastic coupling constant, where $\beta = \alpha(3\lambda + 2\mu)$, α is the linear coefficient of expansion, T_0 is the absolute reference temperature, and c_v is the specific heat. The dimensionless stress is

$$\sigma = u_x - \frac{\beta}{\rho v^2} T.$$

Equations (3) have been extensively investigated, see, for example, [2, 3]. Boundary conditions *A* were used in [4, 5], where identical results, which were valid for long time and distance, were obtained.

In the present Note, we apply boundary conditions *B* and obtain results identical to those obtained in [4, 5] for conditions *A*. The method of solution is an iterative procedure which was used in [5, 6]. We take the initial displacement and temperature identically zero and take the Laplace transformation of equations (3) with respect to time. Here we employ the notation $\tilde{f}(s) = \mathcal{L}\{f(t)\}$. We also employ the conditions that $u_x \to 0$ and $T \to 0$ as $x \to \infty$. The first step in the iteration procedure is as follows. Set $T_x = 0$ in (3*a*) and solve for u_x subject to condition (2*a*) and $T(0, t) = 0$. Substitute the resulting expression for u_x into (3*b*) and solve for T subject to condition (2*b*). The resulting expression for T is substituted into (3*a*) and u_x is solved subject to (2*a*). This procedure is repeated for a total of three iterations. The first-order terms in ϵ corresponding to the first iteration yield

$$\frac{\tilde{T}(x, s)}{\rho v^2/\beta} = \epsilon \left[\left(\frac{1}{(s - c)} - \frac{1}{s} \right) e^{-sx/v} - \frac{c^{1/2}}{s^{1/2}(s - c)} e^{-(s/k)^{1/2}x} \right], \tag{4a}$$

$$\tilde{u}_x(x, s) = \left[\frac{1}{s} + \epsilon \left\{ \frac{1}{(s - c)} - \frac{1}{s} - \frac{c^{3/2}}{s^{1/2}(s - c)^2} - \frac{c^{1/2}}{s^{1/2}(s - c)} - \frac{cx}{2v(s - c)} \right\} \right] e^{-sx/v} + \epsilon \frac{c^{3/2}}{s^{1/2}(s - c)^2} e^{-(s/k)^{1/2}x}. \tag{4b}$$

To carry out the inversion of equations (4) back to the time domain, tables of inverse Laplace transforms must be used, e.g., [7, 8]. For example, we have the following inversions:

[1]Associate Professor, Department of Civil Engineering, University of Manitoba, Winnipeg, Canada, R3T 2N2.

[2]Professor, Department of Civil Engineering, University of Manitoba, Winnipeg, Canada, R3T 2N2.

Manuscript received by ASME Applied Mechanics Division, April, 1981.

Downloaded 01 May 2010 to 171.66.16.249. Redistribution subject to ASME license or copyright; see http://www.asme.org/terms/Terms_Use.cfm

the constant stress triangle element (CST), Oden's method of consistent stress, and the spline functions. In the studied area, the improvements are easily established both for the shape and the levels of the fringes.

Example 2

This second example is related to the Hertz contact problem and concerned a rectangular simply supported beam loaded in its center by means of an elastic disk. For this example the reference results are experimental and have been obtained with the aid of photoelastic models [9]. The dimensions and the load values are shown in the figure. In this example, it is found that the improvements with regard to the direct method are significant. It seems that the Oden's method is more sensitive to the conditions of symmetry than the spline functions (see the shapes of the isochromatics in Fig. 4(*d*).

Conclusions

It has been shown that the use of spline functions to interpolate the discrete finite-element displacement field is an effective means of improving the final stress field.

On the other hand, the continuity of all the functions obtained is of considerable value either for the computer graphics or the determination of the stress values on boundaries.

It must be pointed out that extra computing effort required to implement this method is not significant. The input data of the finite-element method can be used again and the coefficients of the splines are obtained in solving only one band linear system.

This method, of course, is still limited to the two-dimensional space as the three-dimensional interpolation problem is not yet satisfactorily resolved.

References

1 Turner, M. J., Martin, H. C., and Weikel, B. C., "Further Developments and Applications of the Stiffness Method," *Matrix Methods of Structural Analysis*, 1st ed., Vol. 1, Macmillan, New York, 194, pp. 203–266.

2 Oden, J. T., and Brauchli, H. J., "On the Calculation of Consistent Stress Distributions in Finite-Element Approximations," *International Journal for Numerical Methods in Engineering*, Vol. 3, n° 3, 1971, pp. 317–325.

3 Oden, J. T., and Reddy, J. N., "Note on an Approximate Method for Computing Consistent Conjugate Stresses in Elastic Finite Elements," *International Journal for Numerical Methods in Engineering*, Vol. 6, n° 1, 1973, pp. 55–61.

4 Loubignac, G., Cantin, G., and Touzot, G., "Continuous Stress Fields in Finite-Element Analysis," *AIAA Journal*, Vol. 15, n° 11, 1977, pp. 1645–1647.

5 Gordon, W. J., "Spline-Blended Surface Interpolation Through Curve Networks," *Journal of Mathematics and Mechanics*, Vol. 18, n° 10, 1969, pp. 931–951.

Greville, T. N. E., "Introduction to Spline Functions," *Theory and Applications of Spline Functions*, Academic Press, New York, 1969, pp. 1–35.

7 Boyer, J. C., "Utilisation des fonctions splines pour la détermination des contraintes. Cas des structures planes," Thesis, University of Lyon, 1979.

8 Howland, R. C. J., "On the Stresses in the Neighbourhood of a Circular Hole in a Strip Under Tension," *Philosophical Transactions of the Royal Society*, Series A, Vol. 229, n° 671, janu. 1930, pp. 49–87.

9 Berveiler, M., "Détermination des contraintes de contact dans une poutre soumise à la flexion par une charge hertzienne," Thesis, University of Metz, 1971.

Boundary Condition Independence in Coupled Thermoelasticity

E. V. Wilms[1] and H. Cohen[2]

We investigate the temperature and strain in a thermoelastically coupled half space. Two sets of boundary conditions are considered:

Conditions *A*:

$$\sigma(0, t) = \mathrm{H}(t), \tag{1a}$$

$$T(0, t) = 0. \tag{1b}$$

Conditions *B*:

$$\sigma(0, t) = \mathrm{H}(t), \tag{2a}$$

$$T_x(0, t) = 0. \tag{2b}$$

Here σ is the dimensionless stress, T is the temperature, and H is the Heaviside function. It is shown that for certain ranges of the space and time variables x and t, the strain and temperature are the same for the isothermal boundary condition (1*b*) as for the insulated boundary condition (2*b*).

The governing equations are

$$u_{xx} - \frac{1}{v^2} u_{tt} - \frac{\beta}{\rho v^2} T_x = 0, \tag{3a}$$

$$T_{xx} - \frac{c}{v^2} T_t - \frac{\rho c \epsilon}{\beta} u_{xt} = 0. \tag{3b}$$

Here u is the displacement in the direction of the space variable x, which is positive to the right. $v = [(\lambda + 2\mu)/\rho]^{1/2}$ is the dilatational wave speed, where λ and μ are the elastic constants and ρ is the mass density. $c = v^2/k$ is the characteristic thermoelastic frequency [1], where k is the thermal diffusivity. $\epsilon = \beta^2 T_0/c_v(\lambda + 2\mu)$ is the thermoelastic coupling constant, where $\beta = \alpha(3\lambda + 2\mu)$, α is the linear coefficient of expansion, T_0 is the absolute reference temperature, and c_v is the specific heat. The dimensionless stress is

$$\sigma = u_x - \frac{\beta}{\rho v^2} T.$$

Equations (3) have been extensively investigated, see, for example, [2, 3]. Boundary conditions *A* were used in [4, 5], where identical results, which were valid for long time and distance, were obtained.

In the present Note, we apply boundary conditions *B* and obtain results identical to those obtained in [4, 5] for conditions *A*. The method of solution is an iterative procedure which was used in [5, 6]. We take the initial displacement and temperature identically zero and take the Laplace transformation of equations (3) with respect to time. Here we employ the notation $\tilde{f}(s) = \mathcal{L}\{f(t)\}$. We also employ the conditions that $u_x \to 0$ and $T \to 0$ as $x \to \infty$. The first step in the iteration procedure is as follows. Set $T_x = 0$ in (3*a*) and solve for u_x subject to condition (2*a*) and $T(0, t) = 0$. Substitute the resulting expression for u_x into (3*b*) and solve for T subject to condition (2*b*). The resulting expression for T is substituted into (3*a*) and u_x is solved subject to (2*a*). This procedure is repeated for a total of three iterations. The first-order terms in ϵ corresponding to the first iteration yield

$$\frac{\tilde{T}(x, s)}{\rho v^2/\beta} = \epsilon \left[\left(\frac{1}{(s - c)} - \frac{1}{s} \right) e^{-sx/v} - \frac{c^{1/2}}{s^{1/2}(s - c)} e^{-(s/k)^{1/2}x} \right], \tag{4a}$$

$$\tilde{u}_x(x, s) = \left[\frac{1}{s} + \epsilon \left\{ \frac{1}{(s - c)} - \frac{1}{s} - \frac{c^{3/2}}{s^{1/2}(s - c)^2} - \frac{c^{1/2}}{s^{1/2}(s - c)} - \frac{cx}{2v(s - c)} \right\} \right] e^{-sx/v} + \epsilon \frac{c^{3/2}}{s^{1/2}(s - c)^2} e^{-(s/k)^{1/2}x}. \tag{4b}$$

To carry out the inversion of equations (4) back to the time domain, tables of inverse Laplace transforms must be used, e.g., [7, 8]. For example, we have the following inversions:

[1]Associate Professor, Department of Civil Engineering, University of Manitoba, Winnipeg, Canada, R3T 2N2.

[2]Professor, Department of Civil Engineering, University of Manitoba, Winnipeg, Canada, R3T 2N2.

Manuscript received by ASME Applied Mechanics Division, April, 1981.

Copyright © 1981 by ASME

Downloaded 01 May 2010 to 171.66.16.249. Redistribution subject to ASME license or copyright; see http://www.asme.org/terms/Terms_Use.cfm

$$\mathcal{L}^{-1}\left\{\frac{e^{-sx/v}}{s}\right\} = \mathrm{H}\left(t - \frac{x}{v}\right), \tag{5a}$$

$$\mathcal{L}^{-1}\left\{\frac{e^{-sx/v}}{(s-c)}\right\} = \mathrm{H}\left(t - \frac{x}{v}\right) e^{c(t-x/v)},$$

or

$$= \mathrm{H}(\tau(1-n))e^{\tau(1-n)}, \tag{5b}$$

$$\mathcal{L}^{-1}\left\{\frac{e^{-sx/v}}{s^{1/2}(s-c)}\right\} = H\left(t - \frac{x}{v}\right) c^{-1/2} e^{c(t-x/v)} \operatorname{erf}\left(c\left(t - \frac{x}{v}\right)\right)^{1/2},$$

or

$$= H(\tau(1-n))c^{-1/2}e^{\tau(1-n)} \operatorname{erf}(\tau(1-n))^{1/2}, \tag{5c}$$

$$\mathcal{L}^{-1}\left\{\frac{e^{-(s/k)^{1/2}}}{s^{1/2}(s-c)}\right\} = \frac{1}{2} c^{-1/2} e^{ct}\left\{e^{-(c/k)^{1/2}x} \operatorname{erfc}\left(\frac{x}{2(kt)^{1/2}} - (ct)^{1/2}\right)\right.$$
$$\left. - e^{(c/k)^{1/2}x} \operatorname{erfc}\left(\frac{x}{2(kt)^{1/2}} + (ct)^{1/2}\right)\right\},$$

or

$$= \frac{1}{2} c^{-1/2} e^{\tau}\left\{e^{-n\tau} \operatorname{erfc}\left(\tau^{1/2}\left(\frac{n}{2} - 1\right)\right)\right.$$
$$\left. - e^{n\tau} \operatorname{erfc}\left(\tau^{1/2}\left(\frac{n}{2} + 1\right)\right)\right\}. \tag{5d}$$

Here $\tau = ct$ and $n = x/vt$. Hence $n = 1$ corresponds to the wavefront defined by

$$\mathrm{H}\left(t - \frac{x}{v}\right)$$

The remaining two transformed expressions in (4) may be inverted using the relation: If

$$\mathcal{L}^{-1}\left\{\frac{\bar{f}(s)}{(s-c)^n}\right\} = F(t, c),$$

then

$$\mathcal{L}^{-1}\left\{\frac{\bar{f}(s)}{(s-c)^{n+1}}\right\} = \frac{1}{n}\frac{\partial}{\partial c} F(t, c).$$

Consider the identity $\operatorname{erfc}(-x) = 2 - \operatorname{erfc}(x)$. The function $\operatorname{erfc}(x)$ is negligibly small for all positive arguments $x \geq 3$. Also $\operatorname{erf} x \cong 1$ for large x. Since c is very large (1.73×10^{11} sec^{-1} for copper), τ is very large and $\operatorname{erfc}(\tau)^{1/2}((n/2) - 1) \cong 2$ for $n < 1$. Also $\operatorname{erf}(\tau(1-n))^{1/2} \cong 1$ for $n < 1$. Further $e^{\tau(1+n)} \operatorname{erfc}(\tau)^{1/2}((n/2) + 1) \cong 0$ for all n. Using these values inversions (5c) and (5d) become

$$\mathcal{L}^{-1}\left\{\frac{e^{-sx/v}}{s^{1/2}(s-c)}\right\} = \mathrm{H}(\tau(1-n))c^{-1/2}e^{\tau(1-n)}, \tag{5c}'$$

$$\mathcal{L}^{-1}\left\{\frac{e^{-(s/k)^{1/2}x}}{s^{1/2}(s-c)}\right\} = c^{-1/2}e^{\tau(1-n)}. \tag{5d}'$$

Further, we also have for large time

$$\mathcal{L}^{-1}\left\{\frac{e^{-sx/v}}{s^{1/2}(s-c)^2}\right\} = \mathrm{H}(\tau(1-n))c^{-3/2}\left(-\frac{1}{2} + \tau(1-n)\right)e^{\tau(1-n)}, \tag{5e}$$

$$\mathcal{L}^{-1}\left\{\frac{e^{-(s/k)^{1/2}x}}{s^{1/2}(s-c)^2}\right\} = c^{-3/2}\left(-\frac{1}{2} + \tau\left(1 - \frac{n}{2}\right)\right)e^{\tau(1-n)}. \tag{5f}$$

Then using the foregoing relations, the inversions of equations (4) are, for $n < 1$, namely, to the left of the wavefront defined by $\mathrm{H}(t - (x/v))$:

$$\frac{T(x, t)}{\rho v^2/\beta} = -\epsilon, \tag{6a}$$

$$u_x(x, t) = 1 - \epsilon. \tag{6b}$$

If the iterative procedure is continued for three iterations we obtain

$$\frac{T(x, t)}{\rho v^2/\beta} = -\epsilon + \epsilon^2 - \epsilon^3, \tag{7a}$$

$$u_x(x, t) = 1 - \epsilon + \epsilon^2 - \epsilon^3, \tag{7b}$$

or approximately

$$\frac{T(x, t)}{\rho v^2/\beta} = -\frac{\epsilon}{1+\epsilon}, \tag{7a}'$$

$$u_x(x, t) = \frac{1}{1+\epsilon}. \tag{7b}'$$

Equations (7)′ are identical to the results obtained in [4, 5] for conditions A, to the left of the wavefront defined by $\mathrm{H}(t - (x/v))$ and a very short distance away from the boundary $x = 0$. Hence there is a certain degree of boundary condition independence for wave propagation in a thermoelastically coupled half space.

References

1 Chadwick, P., "Thermoelasticity, the Dynamical Theory," eds., Sneddon, I. N., and Hill, R., *Progress in Solid Mechanics*, Vol. 1, North-Holland Publishing Company, Amsterdam, Holland, 1960, Chapter 6.

2 Nowacki, W., *Dynamic Problems of Thermoelasticity*, eds., Francis, P. H., and Hetnarski, R. B., Noordhoff International Publishing, Leyden, The Netherlands, 1975.

3 Boley, B. A., and Tolins, I. S., "Transient Thermoelastic Boundary-Value Problems in the Half Space," ASME JOURNAL OF APPLIED MECHANICS, Vol. 29, 1962, pp. 637–642.

4 Daimaruya, M., and Ishikawa, H., "On the Propagation of Thermoelastic Waves According to the Coupled Thermoelastic Theory," *Bulletin of the Japan Society of Mechanical Engineers*, Vol. 17, 1974, pp. 991–999.

5 Wilms, E. V., "On Coupling Effects in Transient Thermoelastic Problems," ASME JOURNAL OF APPLIED MECHANICS, Vol. 31, 1964, pp. 719–722.

6 Soler, A. I., and Brull, M. A., "On the Solution to Transient Coupled Thermoelastic Problems by Perturbation Techniques," ASME JOURNAL OF APPLIED MECHANICS, Vol. 32, 1965, pp. 389–399.

7 Erdelyi, A., Editor, *Tables of Integral Transforms*, Vol. 1, *Bateman Manuscript Project*, McGraw-Hill, New York, 1954.

8 Carslaw, H. S., and Jaeger, J. C., *Conduction of Heat in Solids*, 2nd ed., Oxford at the Clarendon Press, 1959.

The Annular Membrane Under Axial Load

D. J. Allman[1] and E. H. Mansfield[2]

An exact solution is given of the nonlinear differential equations for the large deflection behavior of an initially unstressed annular membrane under axial load for the case of Poisson's ratio equal to one third.

Analysis

The membrane equations derived by Föppl [1, 2] can be written in the form

$$\left.\begin{aligned} q + \diamond^4(\Phi, w) = 0, \\ \nabla^4\Phi + \tfrac{1}{2}Et \diamond^4(w, w) = 0, \end{aligned}\right\} \tag{1}$$

[1] Principal Scientific Officer, Royal Aircraft Establishment, Farnsborough, England

[2] Chief Scientific Officer, Royal Aircraft Establishment, Farnsborough, England.

Manuscript received by ASME Applied Mechanics Division, February, 1981; final revision, May, 1981.

Downloaded 01 May 2010 to 171.66.16.249. Redistribution subject to ASME license or copyright; see http://www.asme.org/terms/Terms_Use.cfm

$$\mathcal{L}^{-1}\left\{\frac{e^{-sx/v}}{s}\right\} = \mathrm{H}\left(t - \frac{x}{v}\right), \tag{5a}$$

$$\mathcal{L}^{-1}\left\{\frac{e^{-sx/v}}{(s-c)}\right\} = \mathrm{H}\left(t - \frac{x}{v}\right) e^{c(t-x/v)},$$

or

$$= \mathrm{H}(\tau(1-n))e^{\tau(1-n)}, \tag{5b}$$

$$\mathcal{L}^{-1}\left\{\frac{e^{-sx/v}}{s^{1/2}(s-c)}\right\} = H\left(t - \frac{x}{v}\right) c^{-1/2} e^{c(t-x/v)} \operatorname{erf}\left(c\left(t - \frac{x}{v}\right)\right)^{1/2},$$

or

$$= H(\tau(1-n))c^{-1/2}e^{\tau(1-n)} \operatorname{erf}(\tau(1-n))^{1/2}, \tag{5c}$$

$$\mathcal{L}^{-1}\left\{\frac{e^{-(s/k)^{1/2}}}{s^{1/2}(s-c)}\right\} = \frac{1}{2} c^{-1/2} e^{ct}\left\{e^{-(c/k)^{1/2}x} \operatorname{erfc}\left(\frac{x}{2(kt)^{1/2}} - (ct)^{1/2}\right)\right.$$
$$\left. - e^{(c/k)^{1/2}x} \operatorname{erfc}\left(\frac{x}{2(kt)^{1/2}} + (ct)^{1/2}\right)\right\},$$

or

$$= \frac{1}{2} c^{-1/2} e^{\tau}\left\{e^{-n\tau} \operatorname{erfc}\left(\tau^{1/2}\left(\frac{n}{2} - 1\right)\right)\right.$$
$$\left. - e^{n\tau} \operatorname{erfc}\left(\tau^{1/2}\left(\frac{n}{2} + 1\right)\right)\right\}. \tag{5d}$$

Here $\tau = ct$ and $n = x/vt$. Hence $n = 1$ corresponds to the wavefront defined by

$$\mathrm{H}\left(t - \frac{x}{v}\right)$$

The remaining two transformed expressions in (4) may be inverted using the relation: If

$$\mathcal{L}^{-1}\left\{\frac{\bar{f}(s)}{(s-c)^n}\right\} = F(t, c),$$

then

$$\mathcal{L}^{-1}\left\{\frac{\bar{f}(s)}{(s-c)^{n+1}}\right\} = \frac{1}{n}\frac{\partial}{\partial c} F(t, c).$$

Consider the identity $\operatorname{erfc}(-x) = 2 - \operatorname{erfc}(x)$. The function $\operatorname{erfc}(x)$ is negligibly small for all positive arguments $x \geq 3$. Also $\operatorname{erf} x \cong 1$ for large x. Since c is very large (1.73×10^{11} sec^{-1} for copper), τ is very large and $\operatorname{erfc}(\tau)^{1/2}((n/2) - 1) \cong 2$ for $n < 1$. Also $\operatorname{erf}(\tau(1-n))^{1/2} \cong 1$ for $n < 1$. Further $e^{\tau(1+n)} \operatorname{erfc}(\tau)^{1/2}((n/2) + 1) \cong 0$ for all n. Using these values inversions (5c) and (5d) become

$$\mathcal{L}^{-1}\left\{\frac{e^{-sx/v}}{s^{1/2}(s-c)}\right\} = \mathrm{H}(\tau(1-n))c^{-1/2}e^{\tau(1-n)}, \tag{5c}'$$

$$\mathcal{L}^{-1}\left\{\frac{e^{-(s/k)^{1/2}x}}{s^{1/2}(s-c)}\right\} = c^{-1/2}e^{\tau(1-n)}. \tag{5d}'$$

Further, we also have for large time

$$\mathcal{L}^{-1}\left\{\frac{e^{-sx/v}}{s^{1/2}(s-c)^2}\right\} = \mathrm{H}(\tau(1-n))c^{-3/2}\left(-\frac{1}{2} + \tau(1-n)\right)e^{\tau(1-n)}, \tag{5e}$$

$$\mathcal{L}^{-1}\left\{\frac{e^{-(s/k)^{1/2}x}}{s^{1/2}(s-c)^2}\right\} = c^{-3/2}\left(-\frac{1}{2} + \tau\left(1 - \frac{n}{2}\right)\right)e^{\tau(1-n)}. \tag{5f}$$

Then using the foregoing relations, the inversions of equations (4) are, for $n < 1$, namely, to the left of the wavefront defined by $\mathrm{H}(t - (x/v))$:

$$\frac{T(x, t)}{\rho v^2/\beta} = -\epsilon, \tag{6a}$$

$$u_x(x, t) = 1 - \epsilon. \tag{6b}$$

If the iterative procedure is continued for three iterations we obtain

$$\frac{T(x, t)}{\rho v^2/\beta} = -\epsilon + \epsilon^2 - \epsilon^3, \tag{7a}$$

$$u_x(x, t) = 1 - \epsilon + \epsilon^2 - \epsilon^3, \tag{7b}$$

or approximately

$$\frac{T(x, t)}{\rho v^2/\beta} = -\frac{\epsilon}{1+\epsilon}, \tag{7a}'$$

$$u_x(x, t) = \frac{1}{1+\epsilon}. \tag{7b}'$$

Equations (7)′ are identical to the results obtained in [4, 5] for conditions A, to the left of the wavefront defined by $\mathrm{H}(t - (x/v))$ and a very short distance away from the boundary $x = 0$. Hence there is a certain degree of boundary condition independence for wave propagation in a thermoelastically coupled half space.

References

1 Chadwick, P., "Thermoelasticity, the Dynamical Theory," eds., Sneddon, I. N., and Hill, R., *Progress in Solid Mechanics*, Vol. 1, North-Holland Publishing Company, Amsterdam, Holland, 1960, Chapter 6.

2 Nowacki, W., *Dynamic Problems of Thermoelasticity*, eds., Francis, P. H., and Hetnarski, R. B., Noordhoff International Publishing, Leyden, The Netherlands, 1975.

3 Boley, B. A., and Tolins, I. S., "Transient Thermoelastic Boundary-Value Problems in the Half Space," ASME JOURNAL OF APPLIED MECHANICS, Vol. 29, 1962, pp. 637–642.

4 Daimaruya, M., and Ishikawa, H., "On the Propagation of Thermoelastic Waves According to the Coupled Thermoelastic Theory," *Bulletin of the Japan Society of Mechanical Engineers*, Vol. 17, 1974, pp. 991–999.

5 Wilms, E. V., "On Coupling Effects in Transient Thermoelastic Problems," ASME JOURNAL OF APPLIED MECHANICS, Vol. 31, 1964, pp. 719–722.

6 Soler, A. I., and Brull, M. A., "On the Solution to Transient Coupled Thermoelastic Problems by Perturbation Techniques," ASME JOURNAL OF APPLIED MECHANICS, Vol. 32, 1965, pp. 389–399.

7 Erdelyi, A., Editor, *Tables of Integral Transforms*, Vol. 1, *Bateman Manuscript Project*, McGraw-Hill, New York, 1954.

8 Carslaw, H. S., and Jaeger, J. C., *Conduction of Heat in Solids*, 2nd ed., Oxford at the Clarendon Press, 1959.

The Annular Membrane Under Axial Load

D. J. Allman[1] and E. H. Mansfield[2]

An exact solution is given of the nonlinear differential equations for the large deflection behavior of an initially unstressed annular membrane under axial load for the case of Poisson's ratio equal to one third.

Analysis

The membrane equations derived by Föppl [1, 2] can be written in the form

$$\left.\begin{aligned} q + \diamond^4(\Phi, w) = 0, \\ \nabla^4\Phi + \tfrac{1}{2}Et \diamond^4(w, w) = 0, \end{aligned}\right\} \tag{1}$$

[1] Principal Scientific Officer, Royal Aircraft Establishment, Farnsborough, England

[2] Chief Scientific Officer, Royal Aircraft Establishment, Farnsborough, England.

Manuscript received by ASME Applied Mechanics Division, February, 1981; final revision, May, 1981.

Copyright © 1981 by ASME

Downloaded 01 May 2010 to 171.66.16.249. Redistribution subject to ASME license or copyright; see http://www.asme.org/terms/Terms_Use.cfm

where t is the thickness, Φ is the middle-surface force function, E is Young's modulus, q is the normal pressure, w is the deflection, and the operator $\Diamond^4$ is defined in polar coordinates by

$$\Diamond^4(\Phi, w) = \frac{\partial^2\Phi}{\partial r^2}\left(\frac{1}{r}\frac{\partial w}{\partial r} + \frac{1}{r^2}\frac{\partial^2 w}{\partial\theta^2}\right) - 2\frac{\partial}{\partial r}\left(\frac{1}{r}\frac{\partial\Phi}{\partial\theta}\right)\frac{\partial}{\partial r}\left(\frac{1}{r}\frac{\partial w}{\partial\theta}\right) + \frac{\partial^2 w}{\partial r^2}\left(\frac{1}{r}\frac{\partial\Phi}{\partial r} + \frac{1}{r^2}\frac{\partial^2\Phi}{\partial\theta^2}\right).$$

Consider now an initially unstressed annular membrane whose outer boundary at r_2 is fixed and whose inner boundary at r_1 is attached to a floating rigid boss to which an axial load P is applied. The deflection of the membrane is accordingly independent of θ and equations (1) may be written as

$$\frac{d}{dr}\left(\frac{d\Phi}{dr}\frac{dw}{dr}\right) = 0,$$
$$\frac{d}{dr}\left[r\frac{d}{dr}\left\{\frac{1}{r}\frac{d}{dr}\left(r\frac{d\Phi}{dr}\right)\right\} + \tfrac{1}{2}ET\left(\frac{dw}{dr}\right)^2\right] = 0. \tag{2}$$

We search for a solution in the form

$$w(r) = k(r_2^\alpha - r^\alpha), \tag{3}$$

which satisfies the condition that $w(r_2) = 0$, and

$$\Phi(r) = cr^\beta, \tag{4}$$

where k, c, α, β are constants.

Substitution into equations (2) yields

$$\alpha\beta ckr^{\alpha+\beta-2} = \text{constant}, \tag{5}$$

and

$$c\beta^2(\beta-2)r^{\beta-2} + \tfrac{1}{2}Etk^2\alpha^2 r^{2\alpha-2} = \text{constant} \tag{6}$$

It follows from a consideration of the indices in equations (5) and (6) that

$$\alpha = 2/3, \quad \beta = 4/3. \tag{7}$$

These values of α, β mean that equation (5) is automatically satisfied while equation (6) also requires that

$$c = \frac{3}{16}Etk^2. \tag{8}$$

Now, the stress resultants in the radial and circumferential directions are

$$N_r = \frac{1}{r}\frac{d\Phi}{dr}, \quad N_\theta = \frac{d^2\Phi}{dr^2}, \tag{9}$$

and hence equilibrium of the load P yields

$$P = -2\pi r N_r\frac{dw}{dr} = \frac{16\pi}{9}ck, \tag{10}$$

in virtue of equations (3), (4), and (7).

It follows from equations (8) and (10) that

$$\left.\begin{aligned} k &= \left(\frac{3P}{\pi Et}\right)^{1/3}, \\ c &= \frac{3}{16}\left(\frac{9EtP^2}{\pi^2}\right)^{1/3}. \end{aligned}\right\} \tag{11}$$

It is also necessary to consider the radial displacements u at the inner and outer boundaries. In this connection we note that

$$u = r\epsilon_\theta, \tag{12}$$

and the circumferential strain is given by

$$\epsilon_\theta = \frac{1}{Et}(N_\theta - \nu N_r), \tag{13}$$

where ν is Poisson's ratio.

It follows from equations (4), (9), (12), and (13) that

$$u = \frac{4cr^{1/3}}{3Et}(\tfrac{1}{3} - \nu), \tag{14}$$

and the vanishing of u at the boundaries is seen to be fortuitously satisfied if $\nu = 1/3$, which is typical of many elastic materials.

References

1 A. Föppl, *Vorlesungen über Technische Mechanik*, Vol. 5, 1907, p. 132.

2 Stoker, J. J., *Nonlinear Elasticity*, Nelson, 1968, Chapter 3.

On Plastic Strain in Porous Materials

M. M. Carroll,[1] J. F. Schatz,[2] and S. E. Yamada[2]

The formulation of continuum theories for inelastic response usually involves the definition of plastic strains or plastic strain increments. For solid materials, these are usually defined in terms of the residual deformation resulting from a loading-unloading stress cycle. For porous materials, the residual deformation may involve both irreversible and reversible deformation mechanisms in the solid matrix. We treat the special case of hydrostatic response of dry or fluid-saturated isotropic porous materials and we show that a particular definition of the plastic volume strain increment isolates the irreversible deformation mechanism, thereby making it perhaps the most useful definition for theoretical purposes.

Introduction

In recent years there has been much interest in the development and application of continuum theories to describe the mechanical response of materials in which porosity plays a significant role. Such materials include soils and rocks, metals, polymers, biological tissue, and ceramics. The geotechnical applications in which soils and rocks are important (mining, oil, and gas recovery, geothermal and geopressured systems, earthquake prediction, nuclear waste isolation, military site design) have added a considerable impetus to current research. In many cases, these applications require detailed modeling of the material behavior, including inelastic response, fracturing, thermal and chemical effects, and fluid-solid interactions.

Most of the theories which have been developed to describe the mechanical response of porous materials beyond the elastic range bear some similarity to the classical elastic-plastic theories for nonporous materials. While the notions of normality and associative flow rules are not always adopted, the kinematical description usually involves a resolution of the strain, strain rate or strain increment into elastic and plastic components. The definition of the plastic strain for nonporous materials is usually associated with the identification of residual strains resulting from a loading–unloading stress cycle.

In the present Note we address the question of defining the plastic strain increment for a dry or fluid-saturated porous material as the residual strain resulting from a loading–unloading stress cycle. We

[1] Professor, Department of Mechanical Engineering, University of California, Berkeley, Calif. 94720. Mem. ASME.

[2] Terra Tek, Inc., Salt Lake City, Utah 84108.

Manuscript received by ASME Applied Mechanics Division, July 1980.

Downloaded 01 May 2010 to 171.66.16.249. Redistribution subject to ASME license or copyright; see http://www.asme.org/terms/Terms_Use.cfm

where t is the thickness, Φ is the middle-surface force function, E is Young's modulus, q is the normal pressure, w is the deflection, and the operator $\Diamond^4$ is defined in polar coordinates by

$$\Diamond^4(\Phi, w) = \frac{\partial^2\Phi}{\partial r^2}\left(\frac{1}{r}\frac{\partial w}{\partial r} + \frac{1}{r^2}\frac{\partial^2 w}{\partial\theta^2}\right) - 2\frac{\partial}{\partial r}\left(\frac{1}{r}\frac{\partial\Phi}{\partial\theta}\right)\frac{\partial}{\partial r}\left(\frac{1}{r}\frac{\partial w}{\partial\theta}\right) + \frac{\partial^2 w}{\partial r^2}\left(\frac{1}{r}\frac{\partial\Phi}{\partial r} + \frac{1}{r^2}\frac{\partial^2\Phi}{\partial\theta^2}\right).$$

Consider now an initially unstressed annular membrane whose outer boundary at r_2 is fixed and whose inner boundary at r_1 is attached to a floating rigid boss to which an axial load P is applied. The deflection of the membrane is accordingly independent of θ and equations (1) may be written as

$$\frac{d}{dr}\left(\frac{d\Phi}{dr}\frac{dw}{dr}\right) = 0,$$
$$\frac{d}{dr}\left[r\frac{d}{dr}\left\{\frac{1}{r}\frac{d}{dr}\left(r\frac{d\Phi}{dr}\right)\right\} + \tfrac{1}{2}ET\left(\frac{dw}{dr}\right)^2\right] = 0. \tag{2}$$

We search for a solution in the form

$$w(r) = k(r_2^\alpha - r^\alpha), \tag{3}$$

which satisfies the condition that $w(r_2) = 0$, and

$$\Phi(r) = cr^\beta, \tag{4}$$

where k, c, α, β are constants.

Substitution into equations (2) yields

$$\alpha\beta ckr^{\alpha+\beta-2} = \text{constant}, \tag{5}$$

and

$$c\beta^2(\beta-2)r^{\beta-2} + \tfrac{1}{2}Etk^2\alpha^2 r^{2\alpha-2} = \text{constant} \tag{6}$$

It follows from a consideration of the indices in equations (5) and (6) that

$$\alpha = 2/3, \quad \beta = 4/3. \tag{7}$$

These values of α, β mean that equation (5) is automatically satisfied while equation (6) also requires that

$$c = \frac{3}{16}Etk^2. \tag{8}$$

Now, the stress resultants in the radial and circumferential directions are

$$N_r = \frac{1}{r}\frac{d\Phi}{dr}, \quad N_\theta = \frac{d^2\Phi}{dr^2}, \tag{9}$$

and hence equilibrium of the load P yields

$$P = -2\pi r N_r\frac{dw}{dr} = \frac{16\pi}{9}ck, \tag{10}$$

in virtue of equations (3), (4), and (7).

It follows from equations (8) and (10) that

$$\left.\begin{aligned} k &= \left(\frac{3P}{\pi Et}\right)^{1/3}, \\ c &= \frac{3}{16}\left(\frac{9EtP^2}{\pi^2}\right)^{1/3}. \end{aligned}\right\} \tag{11}$$

It is also necessary to consider the radial displacements u at the inner and outer boundaries. In this connection we note that

$$u = r\epsilon_\theta, \tag{12}$$

and the circumferential strain is given by

$$\epsilon_\theta = \frac{1}{Et}(N_\theta - \nu N_r), \tag{13}$$

where ν is Poisson's ratio.

It follows from equations (4), (9), (12), and (13) that

$$u = \frac{4cr^{1/3}}{3Et}(\tfrac{1}{3} - \nu), \tag{14}$$

and the vanishing of u at the boundaries is seen to be fortuitously satisfied if $\nu = 1/3$, which is typical of many elastic materials.

References

1 A. Föppl, *Vorlesungen über Technische Mechanik*, Vol. 5, 1907, p. 132.

2 Stoker, J. J., *Nonlinear Elasticity*, Nelson, 1968, Chapter 3.

On Plastic Strain in Porous Materials

M. M. Carroll,[1] J. F. Schatz,[2] and S. E. Yamada[2]

The formulation of continuum theories for inelastic response usually involves the definition of plastic strains or plastic strain increments. For solid materials, these are usually defined in terms of the residual deformation resulting from a loading-unloading stress cycle. For porous materials, the residual deformation may involve both irreversible and reversible deformation mechanisms in the solid matrix. We treat the special case of hydrostatic response of dry or fluid-saturated isotropic porous materials and we show that a particular definition of the plastic volume strain increment isolates the irreversible deformation mechanism, thereby making it perhaps the most useful definition for theoretical purposes.

Introduction

In recent years there has been much interest in the development and application of continuum theories to describe the mechanical response of materials in which porosity plays a significant role. Such materials include soils and rocks, metals, polymers, biological tissue, and ceramics. The geotechnical applications in which soils and rocks are important (mining, oil, and gas recovery, geothermal and geopressured systems, earthquake prediction, nuclear waste isolation, military site design) have added a considerable impetus to current research. In many cases, these applications require detailed modeling of the material behavior, including inelastic response, fracturing, thermal and chemical effects, and fluid-solid interactions.

Most of the theories which have been developed to describe the mechanical response of porous materials beyond the elastic range bear some similarity to the classical elastic-plastic theories for nonporous materials. While the notions of normality and associative flow rules are not always adopted, the kinematical description usually involves a resolution of the strain, strain rate or strain increment into elastic and plastic components. The definition of the plastic strain for nonporous materials is usually associated with the identification of residual strains resulting from a loading–unloading stress cycle.

In the present Note we address the question of defining the plastic strain increment for a dry or fluid-saturated porous material as the residual strain resulting from a loading–unloading stress cycle. We

[1] Professor, Department of Mechanical Engineering, University of California, Berkeley, Calif. 94720. Mem. ASME.

[2] Terra Tek, Inc., Salt Lake City, Utah 84108.

Manuscript received by ASME Applied Mechanics Division, July 1980.

Copyright © 1981 by ASME

Downloaded 01 May 2010 to 171.66.16.249. Redistribution subject to ASME license or copyright; see http://www.asme.org/terms/Terms_Use.cfm

simplify the analysis by treating the special case of hydrostatic loading and, because of the importance of fluid-solid interactions in geotechnical applications, we include both a confining pressure and a pore pressure.

The total volume strain of the porous material has a component due to compaction of the solid matrix and a component due to pore collapse. Solid compaction is usually an elastic (reversible) deformation governed by the solid pressure and pore collapse is usually an inelastic (irreversible) deformation governed by the effective pressure. (The solid pressure and the effective pressure are defined in equation (4)). Because the solid pressure depends on the porosity, the addition and removal of increments of confining pressure and pore pressure gives rise to a residual solid pressure and hence to a residual solid volume strain. Thus cycling the confining pressure and the pore pressure gives rise to a residual total strain which involves the reversible solid compaction as well as the irreversible pore collapse. It is desirable, both in developing theoretical models and in interpreting experimental data, to separate the irreversible and reversible deformation mechanisms. We show there is a particular definition of the plastic volume strain which effects this separation.

Hydrostatic Response of Porous Materials

Consider a representative sample of porous material under confining pressure P and pore pressure P_p, i.e., it is subjected to uniform normal traction P on its outer boundary B and uniform normal traction P_p on the pore boundaries B_p;

$$t_i = -Pn_i \quad \text{on} \quad B, \quad t_i = -P_p n_i \quad \text{on} \quad B_p. \tag{1}$$

We assume that the overall response of the porous material and the local response of the solid matrix are isotropic.

The volumetric state of the sample may be described by specifying any two of the kinematic variables V, V_s, V_p, and ϕ which represent, respectively, the total volume, the solid volume, the pore volume, and the porosity and are related through

$$V = V_s + V_p, \quad \phi = V_p/V. \tag{2}$$

Equations (2) imply that

$$V = V_s/(1-\phi), \; dV/V = dV_s/V_s + d\phi/(1-\phi) \tag{3}$$

and the second of these equations resolves the total volume strain dV/V into a component due to solid compaction and one due to pore collapse. An important aspect of this resolution is that solid compaction is usually an elastic (reversible) process while pore collapse may be a plastic (irreversible) process.

The forces which govern the processes of solid compaction and pore collapse are, respectively, the "solid pressure" P_s and the "effective pressure" $\hat{P}$, defined by

$$P_s = \frac{P - \phi P_p}{1-\phi}, \quad \hat{P} = P - P_p. \tag{4}$$

This is exactly so in the linear theory and is a very plausible assumption in the nonlinear theory (Carroll [1, 2]). The loading described by equation (1), with $P \neq P_p$, gives rise to a nonuniform, nonhydrostatic stress state in the solid matrix. However, the average stress theorem implies the average stress in the solid matrix is a hydrostatic pressure P_s given by the first equation (4). In the linear theory, the induced (zero-average) shear stresses do not cause any solid compaction, and equal confining pressure and pore pressure (which give rise to a uniform pressure in the solid matrix) do not change the porosity. Thus the solid volume strain is proportional to the solid pressure and the change in porosity is proportional to the effective pressure. In the nonlinear theory, it is plausible to assume the zero-average stresses again does not cause solid volume compaction and equal increments of confining pressure and pore pressure leave the porosity unchanged. This implies response laws of the form

$$P_s = F(V_s/V_{s0}), \quad \hat{P} = \mathcal{F}(\phi, \phi_0) \tag{5}$$

for solid compaction and pore collapse.

The first of equations (5) is generally path-independent, with F being the volumetric response function of the solid material in the absence of pores. The pore collapse relation, however, is usually rather complex, with $\mathcal{F}$ being a path-dependent functional determined by the response of the solid material and by the pore geometry. The path-dependence is a consequence of the fact that pore collapse is due primarily to induced shearing—in fact it is due solely to induced shearing for an incompressible matrix material with arbitrary pore geometry and also for any matrix material with spherical pores [1].

Plastic Strain Increment

We now turn to the question of defining the plastic volume strain increment by finding the residual volume strain $\Delta V/V$ resulting from an incremental loading–unloading cycle. It seems natural to assume a cycle of both the confining pressure P and the pore pressure P_p, since they are, at least in principle, measurable and controllable. Thus we consider the effect of adding and removing incremental pressures δP and δP_p.

It is clear, from the second equation (4), that this involves adding and removing an effective pressure increment $\delta\hat{P}$. Beyond the elastic range, this will give rise to a residual porosity change $\Delta\phi$, of the form

$$\Delta\phi = \mathcal{G}(\hat{P})\, \delta\hat{P}, \tag{6}$$

where $\mathcal{G}$ is a path-dependent functional which is determined by the pore collapse response functional $\mathcal{F}$. Because of this residual porosity change, it is evident from the first equation (4) that adding and removing confining pressure and pore pressure increments gives rise to a residual change ΔP_s in the solid pressure. It is easily seen that this residual change is given by

$$\Delta P_s = \hat{P}\Delta\phi/(1-\phi)^2. \tag{7}$$

This change in the solid pressure in turn gives rise to a residual change ΔV_s in the solid volume, which is found from the first equation (5) in the form

$$\Delta V_s/V_s = -\Delta P_s/K_s, \tag{8}$$

where K_s is the tangent bulk modulus of the solid material. Equations (7) and (8), with the second equation (3), give the residual volume strain as

$$\Delta V/V = [1 - \hat{P}/(1-\phi)K_s]\, \Delta\phi/(1-\phi), \tag{9}$$

with $\Delta\phi$ given by equation (6).

It is evident from equation (9) that addition and removal of both confining pressure and pore pressure increments gives rise to a residual volume strain which involves both irreversible pore collapse and reversible solid compaction. Knowledge of $\hat{P}$, ϕ, K_s, thus allows $\Delta\phi$ to be determined directly from equation (9).

Suppose, instead, one were to add and remove solid pressure and effective pressure increments δP_s and $\delta\hat{P}$. Then the residual volume strain

$$\Delta V/V = \Delta\phi/(1-\phi), \tag{10}$$

with $\Delta\phi$ again given by equation (6), should be due solely to pore collapse. From a theoretical point of view, it is attractive to adopt the pairs $(P_s, \hat{P})$ and (V_s, ϕ) as pressure and kinematic variables, since this leads to a clear separation of the two volume compaction processes. In particular, it affords a convenient definition of the plastic volume strain increment as the residual volume strain in equation (10), which involves only the irreversible pore collapse. This may be the best approach in developing a constitutive theory. Unfortunately, from the experimental point of view, the solid pressure P_s is not a convenient pressure because it is not directly measurable or controllable but must be calculated from the first equation (4). Drained tests on fully saturated materials are most useful in this regard, since

Downloaded 01 May 2010 to 171.66.16.249. Redistribution subject to ASME license or copyright; see http://www.asme.org/terms/Terms_Use.cfm

measurement of extruded fluid volume gives the change in pore volume.

In many applications, the difference between equations (9) and (10) will be insignificant. The significance of the correction term increases with the effective pressure $\hat{P}$ and depends on the porosity and on the tangent bulk modulus K_s.

It is important to point out that the problem in defining the plastic strain increment is not due solely to cycling the pore pressure. It persists for dry porous materials and for drained tests at constant pore pressure on saturated materials,[3] as is easily seen from equations (4). The problem is evern more complicated in the case of nonhydrostatic loading.

In conclusion, we point out that the definition of the plastic strain has some implications with regard to "effective stress laws" for failure and flow of saturated porous materials. It is usually assumed (Garg and Nur [3], Rice [4]) that yield surfaces and flow rules for saturated materials are obtained from the corresponding dry or undrained response by replacing the stress σ_{ij} by the effective stress

$$\hat{\sigma}_{ij} = \sigma_{ij} + P_p\, \delta_{ij}. \tag{11}$$

Rice [4] has obtained the theoretical result that the plastic strain is governed by the effective stress law (11). The result obtained here shows that this is the case for plastic volume strain defined in accordance with equation (10). The residual volume strain given by equation (9), however, is governed by the effective stress law (11) only if the matrix material has a constant tangent bulk modulus.

References

1 Carroll, M. M., "Compaction of Dry or Fluid-Filled Porous Materials," *Journal of the Engineering Mechanics Division, ASCE*, to appear.

2 Carroll, M. M., "Mechanical Response of Fluid-Saturated Porous Materials," *Proceedings of the 15th International Congress of Theoretical and Applied Mechanics*, to appear.

3 Garg, S. K., and Nur, A., "Effective Stress Laws for Fluid-Saturated Porous Rocks," *Journal of Geophysical Research*, Vol. 78, 1973, p. 5911.

4 Rice, J. R., "Pore Pressure Effects in Inelastic Constitutive Formulations for Fissured Rock Masses," in *Advances in Civil Engineering Through Engineering Mechanics*, Vol. 295, ASCE, New York, 1977.

[3] In some rocks and soils, chemomechanical effects may give rise to differences between dry and drained material response.

Critical Compressive Stress of a Beam-Column to a Second Order

D. Chattoraj[1] and S. K. Bose[2]

Buckling of a beam-column under axial loads at the ends is considered as a three-dimensional stability problem. Displacement and stress fields are written in terms of Neuber-Papkovich potentials. These are then approximated to forms containing one more higher-order term than those corresponding to the Euler-Bernoulli equations. These expressions yield a modified formula for the bending moment. The energy method applied to the equations yield a modified form of Euler critical load and Shanley tangent modulus formula. The effect of the second-order modification is to decrease the critical load. For mild steel this decrease exceeds 5 percent for the slenderness ratio less than 25.

Introduction

In the theory of elastic and inelastic buckling of a beam-column, the latter is usually regarded as a linear continuum without shear deformations (Timoshenko and Gere [1]). In this Note we shall consider a circular beam-column and treat it as a three-dimensional problem. The exact solution of the Lamé equations are used to obtain approximate form of the Euler-Bernoulli expression for the bending moment. The energy method (Timoshenko and Gere [1]) then yields the modified Euler critical load formula and the Shanley tangent modulus formula. The modifications are partly due to the contribution of shear deformations and partly due to the additional terms appearing in the normal stresses. The modifications have decreasing effect on the critical load in each case.

Displacement and Stress Field in the Buckled Beam

We consider a homogeneous and isotropic circular beam with simply supported ends and loaded symmetrically on both the ends, the resultant of the compressive load on each of the ends being P along the axial direction (Fig. 1). In addition to this load the beam-column is subjected to an infinitesimal lateral load Q at a distance c from one of the ends which contains the origin 0. Let the radius of cross section be a and length H, while we assume that the shear modulus and Poisson's ratio to be μ and ν, respectively. We employ cylindrical coordinates (r, θ, z) with the z-axis along the central axis of the undisturbed position of the beam-column. The plane of buckling is taken as the xz-plane.

In the interior of the cylinder $0 \le r \le a$, $0 \le z \le H$, the displacement field is given by (u_r, u_θ, u_z). In terms of Neuber-Papkovich potentials the displacement components can be written as

$$u_r = -\frac{1}{4(1-\nu)}\frac{\partial}{\partial r}(\delta + z\delta_1) - \frac{1}{4(1-\nu)}\left[(4\nu-1)\frac{\partial\delta_2}{\partial r} + r\frac{\partial^2\delta_2}{\partial r^2}\right] + \frac{1}{r}\frac{\partial\delta_3}{\partial\theta}$$

$$u_\theta = -\frac{1}{4(1-\nu)}\frac{\partial}{\partial\theta}\left[\frac{\delta}{r} + \frac{z}{r}\delta_1 + 2(2\nu-1)\frac{\delta_2}{r} + \frac{\partial\delta_2}{\partial r}\right] - \frac{\partial\delta_3}{\partial r}$$

$$u_z = \delta_1 - \frac{1}{4(1-\nu)}\frac{\partial}{\partial z}[\delta + z\delta_1] - \frac{1}{4(1-\nu)}\left[2\frac{\partial\delta_2}{\partial z} + r\frac{\partial^2\delta_2}{\partial r\partial z}\right] \tag{1}$$

where δ, δ_1, δ_2, and δ_3 are arbitrary harmonic functions.

A set of functions suitable for the buckling problem are

$$\delta_1 = 0$$

$$\delta = -4(1-\nu)\left[B_m^{(2)} + (4\nu-2)\frac{B_m^{(3)}}{k_m}\right]\frac{I_1(k_m r)}{k_m^2 I_1(k_m a)}\cos k_m z\cos\theta$$

$$\delta_2 = 4(1-\nu)\frac{B_m^{(3)}}{k_m}\frac{I_1(k_m r)}{k_m^2 I_1(k_m a)}\cos k_m z\cos\theta$$

$$\delta_3 = \left[B_m^{(1)} + \frac{B_m^{(3)}}{k_m}\right]\frac{I_1(k_m r)}{k_m^2 I_1(k_m a)}\cos k_m z\sin\theta \tag{2}$$

where $B_m^{(1)}$, $B_m^{(2)}$, $B_m^{(3)}$ are arbitrary constants and $k_m = m\pi/H$ ($m = 1, 2, 3, \ldots$). Using (2) in (1) the displacement components can be represented in series.

If we ignore the local effect of the infinitesimal lateral load Q, the

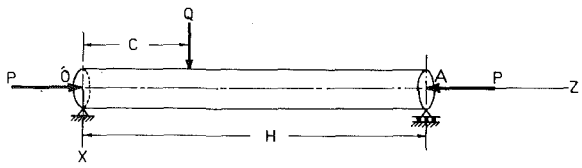


Fig. 1 The beam-column

[1] Assistant Professor, Department of Mathematics, Hooghly Mohasin College, Hooghly, India.

[2] Professor, Department of Mathematics, Regional Engineering College, Durgapur, India.

Manuscript received by ASME Applied Mechanics Division, October, 1980; final revision, February, 1981.

Downloaded 01 May 2010 to 171.66.16.249. Redistribution subject to ASME license or copyright; see http://www.asme.org/terms/Terms_Use.cfm

measurement of extruded fluid volume gives the change in pore volume.

In many applications, the difference between equations (9) and (10) will be insignificant. The significance of the correction term increases with the effective pressure $\hat{P}$ and depends on the porosity and on the tangent bulk modulus K_s.

It is important to point out that the problem in defining the plastic strain increment is not due solely to cycling the pore pressure. It persists for dry porous materials and for drained tests at constant pore pressure on saturated materials,[3] as is easily seen from equations (4). The problem is evern more complicated in the case of nonhydrostatic loading.

In conclusion, we point out that the definition of the plastic strain has some implications with regard to "effective stress laws" for failure and flow of saturated porous materials. It is usually assumed (Garg and Nur [3], Rice [4]) that yield surfaces and flow rules for saturated materials are obtained from the corresponding dry or undrained response by replacing the stress σ_{ij} by the effective stress

$$\hat{\sigma}_{ij} = \sigma_{ij} + P_p\, \delta_{ij}. \tag{11}$$

Rice [4] has obtained the theoretical result that the plastic strain is governed by the effective stress law (11). The result obtained here shows that this is the case for plastic volume strain defined in accordance with equation (10). The residual volume strain given by equation (9), however, is governed by the effective stress law (11) only if the matrix material has a constant tangent bulk modulus.

References

1 Carroll, M. M., "Compaction of Dry or Fluid-Filled Porous Materials," *Journal of the Engineering Mechanics Division, ASCE*, to appear.

2 Carroll, M. M., "Mechanical Response of Fluid-Saturated Porous Materials," *Proceedings of the 15th International Congress of Theoretical and Applied Mechanics*, to appear.

3 Garg, S. K., and Nur, A., "Effective Stress Laws for Fluid-Saturated Porous Rocks," *Journal of Geophysical Research*, Vol. 78, 1973, p. 5911.

4 Rice, J. R., "Pore Pressure Effects in Inelastic Constitutive Formulations for Fissured Rock Masses," in *Advances in Civil Engineering Through Engineering Mechanics*, Vol. 295, ASCE, New York, 1977.

[3] In some rocks and soils, chemomechanical effects may give rise to differences between dry and drained material response.

Critical Compressive Stress of a Beam-Column to a Second Order

D. Chattoraj[1] and S. K. Bose[2]

Buckling of a beam-column under axial loads at the ends is considered as a three-dimensional stability problem. Displacement and stress fields are written in terms of Neuber-Papkovich potentials. These are then approximated to forms containing one more higher-order term than those corresponding to the Euler-Bernoulli equations. These expressions yield a modified formula for the bending moment. The energy method applied to the equations yield a modified form of Euler critical load and Shanley tangent modulus formula. The effect of the second-order modification is to decrease the critical load. For mild steel this decrease exceeds 5 percent for the slenderness ratio less than 25.

Introduction

In the theory of elastic and inelastic buckling of a beam-column, the latter is usually regarded as a linear continuum without shear deformations (Timoshenko and Gere [1]). In this Note we shall consider a circular beam-column and treat it as a three-dimensional problem. The exact solution of the Lamé equations are used to obtain approximate form of the Euler-Bernoulli expression for the bending moment. The energy method (Timoshenko and Gere [1]) then yields the modified Euler critical load formula and the Shanley tangent modulus formula. The modifications are partly due to the contribution of shear deformations and partly due to the additional terms appearing in the normal stresses. The modifications have decreasing effect on the critical load in each case.

Displacement and Stress Field in the Buckled Beam

We consider a homogeneous and isotropic circular beam with simply supported ends and loaded symmetrically on both the ends, the resultant of the compressive load on each of the ends being P along the axial direction (Fig. 1). In addition to this load the beam-column is subjected to an infinitesimal lateral load Q at a distance c from one of the ends which contains the origin 0. Let the radius of cross section be a and length H, while we assume that the shear modulus and Poisson's ratio to be μ and ν, respectively. We employ cylindrical coordinates (r, θ, z) with the z-axis along the central axis of the undisturbed position of the beam-column. The plane of buckling is taken as the xz-plane.

In the interior of the cylinder $0 \le r \le a$, $0 \le z \le H$, the displacement field is given by (u_r, u_θ, u_z). In terms of Neuber-Papkovich potentials the displacement components can be written as

$$u_r = -\frac{1}{4(1-\nu)}\frac{\partial}{\partial r}(\delta + z\delta_1) - \frac{1}{4(1-\nu)}\left[(4\nu-1)\frac{\partial\delta_2}{\partial r} + r\frac{\partial^2\delta_2}{\partial r^2}\right] + \frac{1}{r}\frac{\partial\delta_3}{\partial\theta}$$

$$u_\theta = -\frac{1}{4(1-\nu)}\frac{\partial}{\partial\theta}\left[\frac{\delta}{r} + \frac{z}{r}\delta_1 + 2(2\nu-1)\frac{\delta_2}{r} + \frac{\partial\delta_2}{\partial r}\right] - \frac{\partial\delta_3}{\partial r}$$

$$u_z = \delta_1 - \frac{1}{4(1-\nu)}\frac{\partial}{\partial z}[\delta + z\delta_1] - \frac{1}{4(1-\nu)}\left[2\frac{\partial\delta_2}{\partial z} + r\frac{\partial^2\delta_2}{\partial r\partial z}\right] \tag{1}$$

where δ, δ_1, δ_2, and δ_3 are arbitrary harmonic functions.

A set of functions suitable for the buckling problem are

$$\delta_1 = 0$$

$$\delta = -4(1-\nu)\left[B_m^{(2)} + (4\nu-2)\frac{B_m^{(3)}}{k_m}\right]\frac{I_1(k_m r)}{k_m^2 I_1(k_m a)}\cos k_m z\cos\theta$$

$$\delta_2 = 4(1-\nu)\frac{B_m^{(3)}}{k_m}\frac{I_1(k_m r)}{k_m^2 I_1(k_m a)}\cos k_m z\cos\theta$$

$$\delta_3 = \left[B_m^{(1)} + \frac{B_m^{(3)}}{k_m}\right]\frac{I_1(k_m r)}{k_m^2 I_1(k_m a)}\cos k_m z\sin\theta \tag{2}$$

where $B_m^{(1)}$, $B_m^{(2)}$, $B_m^{(3)}$ are arbitrary constants and $k_m = m\pi/H$ ($m = 1, 2, 3, \ldots$). Using (2) in (1) the displacement components can be represented in series.

If we ignore the local effect of the infinitesimal lateral load Q, the

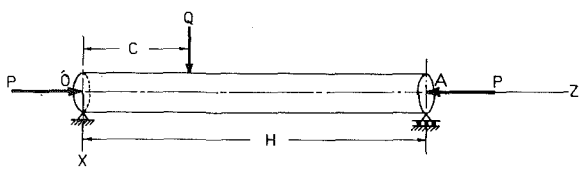


Fig. 1 The beam-column

[1] Assistant Professor, Department of Mathematics, Hooghly Mohasin College, Hooghly, India.

[2] Professor, Department of Mathematics, Regional Engineering College, Durgapur, India.

Manuscript received by ASME Applied Mechanics Division, October, 1980; final revision, February, 1981.

Copyright © 1981 by ASME

Downloaded 01 May 2010 to 171.66.16.249. Redistribution subject to ASME license or copyright; see http://www.asme.org/terms/Terms_Use.cfm

potential energy of deformation will substantially be the same, as in that of a buckled bar without a transverse load. We thus take

$$(\tau_{rr})_{r=a} = (\tau_{r\theta})_{r=a} = (\tau_{rz})_{r=a} = 0 \tag{3}$$

The stress components τ_{rr}, $\tau_{r\theta}$, τ_{rz} can then be computed from the generalized Hooke's law.

In our formulation, fifth and higher-order terms in a/H are neglected. This order of computation is sufficient for finding the first-order correction in the Euler critical load. Under this condition it can be shown that the three equations obtained from (3) are not independent. So, without loss of generality, we can take any two of them into consideration and get,

$$B_m{}^{(1)} = \left[\frac{1-4\nu}{4\nu-3} - \frac{3+2\nu}{(4\nu-3)^2}(k_m a)^2\right] B_m{}^{(2)}$$

$$B_m{}^{(2)} = \left[-(4\nu-3) + \frac{3+2\nu}{2}(k_m a)^2\right] \frac{B_m{}^{(3)}}{k_m} \tag{4}$$

Rejecting terms of the order of $(k_m r)^5$ the displacement components can then be written as

$$u_r = \left[u + \frac{\nu}{2} r^2 \frac{\partial^2 u}{\partial z^2} - \frac{8\nu+5}{192} r^4 \frac{\partial^4 u}{\partial z^4}\right] \cos\theta$$

$$u_\theta = \left[-u + \frac{\nu}{2} r^2 \frac{\partial^2 u}{\partial z^2} - \frac{8\nu-1}{192} r^4 \frac{\partial^4 u}{\partial z^4}\right] \sin\theta \tag{5}$$

$$u_z = \left[-r\frac{\partial u}{\partial z} - \frac{1}{4}\{(3+2\nu)a^2 - r^2\} r \frac{\partial^3 u}{\partial z^3}\right] \cos\theta$$

where u is the deflection of the central axis given by

$$u = \sum_{m=1}^{\infty} B_m{}^{(3)} \frac{\cos k_m z}{k_m{}^2 I_1(k_m a)} \tag{6}$$

If we drop the terms containing r^4 in (5), we get the expression given by Bose [2] for the Euler-Bernoulli buckling. Also, if M is the bending moment then we can show from (5) that

$$M = -\int_0^{2\pi}\int_0^a \tau_{zz} \cos\theta r^2 dr d\theta$$

$$= \frac{E\pi a^4}{4}\frac{\partial^2 u}{\partial z^2} - \frac{E\pi a^6(z-4\nu^2)}{48(1-2\nu)(1+\nu)}\frac{\partial^4 u}{\partial z^4} \tag{7}$$

The second term in the right-hand side represents a modification in the Euler-Bernoulli expression for the bending moment.

Using (4) and (6) in (5) we get,

$$u_r = \sum_{m=1}^{\infty} A_m \left[1 - \frac{\nu}{2}k_m{}^2 r^2 - \frac{8\nu+5}{192}k_m{}^4 r^4\right] \cos k_m z \cos\theta$$

$$u_\theta = \sum_{m=1}^{\infty} A_m \left[-1 - \frac{\nu}{2}k_m{}^2 r^2 - \frac{8\nu-1}{192}k_m{}^4 r^4\right] \cos k_m z \sin\theta \tag{8}$$

$$u_z = \sum_{m=1}^{\infty} A_m \left[k_m r - \frac{3+2\nu}{4}k_m{}^3 a^2 r + \frac{k_m{}^3 r^3}{4}\right] \sin k_m z \cos\theta$$

where $A_m = B_m{}^{(3)}/[k_m{}^2 I_1(k_m a)]$.

The Critical Load

We shall apply the energy method (Timoshenko and Gere [1] to calculate the critical load of deflection of the beam-column. In the equilibrium condition the displacement components are given by (8). The corresponding stress components are given by the generalized Hooke's law. The strain energy U of the buckled beam is thus

$$U = \frac{1}{2}\int_0^H \int_0^{2\pi}\int_0^a [\tau_{rr}e_{rr} + \tau_{\theta\theta}e_{\theta\theta} + \tau_{zz}e_{zz} + 2\tau_{r\theta}e_{r\theta}$$

$$+ 2\tau_{\theta z}e_{\theta z} + 2\tau_{zr}e_{zr}] r dr d\theta dz$$

$$= \frac{\mu}{2}\sum_{m=1}^{\infty} A_m{}^2 \pi H \left[(1+\nu)\frac{k_m{}^4 a^4}{4} - \frac{4\nu^2+14\nu+9}{48}k_m{}^6 a^6\right] \tag{9}$$

If a small displacement be imparted to the system leading to a change in U, then this change in U will be balanced by the work done by the external load during such a displacement. The equation obtained by equating the change in strain energy to the work done by the external load can be used to obtain the critical load of buckling. Let the small displacement be represented by a small variation dA_m in any constant A_m. So the small displacement of the central axis is $dA_m \cos k_m z$ and the change in U is given by

$$\Delta U = \frac{\partial U}{\partial A_m} dA_m = \mu\pi H \left[(1+\nu)\frac{k_m{}^4 a^4}{4}\right.$$

$$\left. - \frac{4\nu^2+14\nu+9}{48}k_m{}^6 a^6\right] A_m dA_m; \quad (m = 1, 2, 3, \ldots) \tag{10}$$

Again the displacement of the point of application of Q due to the change in A_m only, is $dA_m \sin k_m c$ and the work done by Q for the small variation imposed on A_m is $Q dA_m \sin k_m c$.

Due to the action of the load P the central axis of the column is deformed from its initial straight form to the buckled form in the equilibrium state. Denoting the displacement of the end A by λ we get as in [1],

$$\lambda = \frac{1}{2}\int_0^H \left(\frac{\partial U}{\partial z}\right)^2 dz = \frac{H}{4}\sum_{m=1}^{\infty} A_m{}^2 k_m{}^2$$

A small variation in the single coefficient A_m results in a change in λ. The change is

$$d\lambda = \tfrac{1}{2} k_m{}^2 H A_m dA_m$$

Therefore, the work done by P is $P k_m{}^2 H A_m dA_m/2$. Equating the change in strain energy to the total work done by external loads, we obtain

$$A_m = \frac{2Q}{k_m{}^2 H} \frac{\sin k_m c}{2\mu\pi\left[(1+\nu)\frac{k_m{}^2 d^4}{4} - \frac{4\nu^2+14\nu+9}{48}k_m{}^4 a^6\right] - P} \tag{11}$$

Therefore,

$$U = \frac{2Q}{H}$$

$$\times \sum_{m=1}^{\infty} \frac{\sin k_m c \cos k_m z}{2\mu\pi\left[(1+\nu)\frac{k_m{}^4 a^4}{4} - \frac{4\nu^2+14\nu+9}{48}k_m{}^6 a^6\right] - P k_m{}^2} \tag{12}$$

It follows from (12) that however small the lateral load Q may be, the deflection will increase considerably if the load P approaches its critical value P_{cr} given by

$$P_{cr} = \frac{E\pi k_m{}^2 a^4}{4} - \frac{E\pi(4\nu^2+14\nu+9)}{48(1+\nu)}k_m{}^4 a^6,$$

$$(m = 1, 2, 3, \ldots) \tag{13}$$

where E is the Young's modulus of the column.

The smallest value of P_{cr} is obtained from (13) by taking $m = 1$ and we get,

$$P_{cr} = \frac{E\pi^3 a^4}{4H^2} - \frac{E\pi^5(4\nu^2+14\nu+9)}{48(1+\nu)H^4}a^6 \tag{14}$$

The term $P_{Euler} = E\pi a^4/(4H^2)$ represents the well-known Euler load. It corresponds to an analysis in which the displacement components contain terms upto third-order in r. The next higher-order analysis shows that the critical load is less than the Euler load by

$$\frac{E\pi^5(4\nu^2+14\nu+9)}{48(1+\nu)H^4}a^6$$

The critical value of the compressive stress now becomes

$$\sigma_{cr} = \frac{P_{cr}}{\pi a^2} = \frac{E\pi^2}{(l/a)^2} - \frac{E\pi^4(4\nu^2+14\nu+9)}{3(1+\nu)(l/a)^4} \tag{15}$$

where l is the "effective length" $2H$ of the beam-column.

As an illustration we consider a beam-column of mild steel with $E = 2.069 \times 10^5$ MPa and $\nu = 0.29$. The Euler compressive stress $\sigma_{Euler} = E\pi^2/(l/a)^2$ and its modified form (15) for different values of l/a are tabulated in Table 1.

Downloaded 01 May 2010 to 171.66.16.249. Redistribution subject to ASME license or copyright; see http://www.asme.org/terms/Terms_Use.cfm

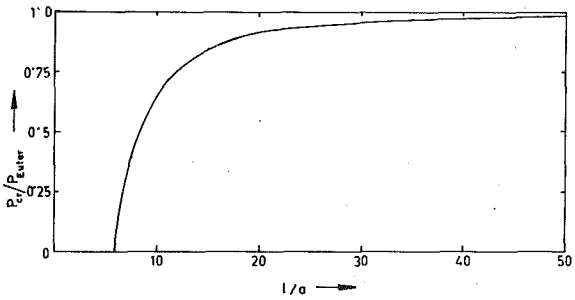


Fig. 2 Variation of P_{cr}/P_{Euler} with slenderness ratio l/a

In Fig. 2 we also give the plot of P_{cr}/P_{Euler} ($= \sigma_{cr}/\sigma_{Euler}$). Since its expression is negative for $l/a < 5.845$, this portion of the graph is not shown.

For higher modes of buckling $m > 1$, it is apparent from (13) that the percentage reduction is higher than that in the first mode.

Buckling of Inelastic Beam-Column

The buckling of inelastic beam-columns have been studied in the literature by taking the tangent modulus E_t for the Young's modulus E. Making this change in equation (15), the critical value of the compressive stress for buckling of an inelastic beam-column is

$$\sigma_{cr} = E_t \left[\frac{\pi^2}{(l/a)^2} - \frac{4\nu^2 + 14\nu + 9}{3(1+\nu)} \frac{\pi^4}{(l/a)^4}\right] \tag{16}$$

If we drop the second term in the right-hand side of (16), we obtain the well-known Shanley tangent modulus formula. In an earlier attempt to incorporate the additional effect of shear distortion in the formula, Hill and Sewell [3] gave a new formula, which to the order $(a/l)^4$ is

$$\sigma_{cr} = E_t \left[\frac{\pi^2}{(l/a)^2} - \frac{3 + 3\nu - 2\nu^2}{3(1+\nu)} \frac{\pi^4}{(l/a)^4}\right] \tag{17}$$

Equations (16) and (17) are of similar form. The larger coefficient of the second term in (16) shows that σ_{cr} given by this formula is lesser than that given by (17).

Table 1

l/a	Euler compressive stress σ_{Euler} in MPa	Modified compressive stress σ_{cr} in MPa equation (15)	Percentage reduction
15	9.076×10^3	7.697×10^3	15.2
20	5.105×10^3	4.669×10^3	8.5
25	3.267×10^3	3.088×10^3	5.5
30	2.269×10^3	2.183×10^3	3.8

Acknowledgment

The authors wish to thank a referee for suggesting the plot of the critical load and therby improving the presentation of the results.

References

1 Timoshenko, S. P., and Gere, J. M., *Theory of Elastic Stability*, McGraw-Hill, New York, 1961.

2 Bose, S. K., "On the Vibrations of a Circular Tower Due to Rayleigh Waves," *Bulletin of the Calcutta Mathematical Society*, Vol. 63, 1971, pp. 101–113.

3 Hill, R., and Sewell, M. J., "A General Theory of Inelastic Column Failure—I," *Journal of Mechanics and Physics of Solids*, Vol. 8, No. 2, 1960, pp. 105–111.

On a Bénard Convection in the Presence of Dielectrophoretic Forces

A. Georgescu[1] and O. Polotzka[2]

In this Note we shall study the influence of dielectrophoretic forces on some Bénard convection by means of a method which leads to shorter numerical calculations than the classical one.

Consider a viscous fluid layer between two flat electrods located at $x = \pm 0.5$ heated from below subjected to dielectrophoretic forces. Suppose that the perturbation of the layer's equilibrium have the form $f(x,y) = f(z)e^{-iky}$ (y-axis is perpendicular to the x-axis), the boundaries are kept at constant temperature, the velocity vanishes at the boundaries, and the charge on the electrods is kept constant. Then the problem governing the linear neutral stability (in the case when the principle of the exchange of stabilities holds) of the mentioned equilibrium against the foregoing perturbations consists of the following equations [1]:

$$(D^2 - k^2)\theta + v = 0, \tag{1}$$

$$(D^2 - k^2)v - k^2R(1 + El)\theta - k^2 REl \cdot D\varphi = 0, \quad x \in (-0.5; 0.5) \tag{2}$$

$$(D^2 - k^2)\varphi + D\theta = 0, \tag{3}$$

and the boundary conditions

$$v = Dv = \theta = D\varphi = 0 \quad \text{at} \quad x = \pm 0.5. \tag{4}$$

Here θ and φ are the temperature and the electric potential of the perturbation, respectively, v is the velocity component along the x-axis, k is the wave number in the y-direction, $D = d/dx$, R is the Rayleigh number, and El is a dimensionless number proportional to the square of the electric field. For El fixed, we shall deduce from the problem (1)–(4) the neutral curve $R = R(k)$ which separates the domain of stability from that of instability. In other words the values R on these curves are the ones at which the convection sets in from the rest. Since R is proportional to the difference between the temperatures of the electrode, it follows that from the knowledge of the neutral curve we can deduce the thermal gradient at which the convection sets in.

The eigenvalue problem (1)–(4) has R as eigenvalue and (θ, v, φ) as eigenfunction. The parameters El and k are fixed. The characteristic equation associated with the eigenvalue problem (1)–(4) will yield the neutral curve. More precisely $R(k)$ shall be the least solution the characteristic equation and, therefore, least eigenvalue of (1)–(4).

The classical (in hydrodynamic and hydromagnetic stability theory) Chandrasekhar's method of deriving the characteristic equation for problems similar to (1)–(4) consists of writing (1)–(4) as a variational problem and solving it by developing the unknowns in an orthonormal set of functions f_n dense in L^2 $(-0.5; 0.5)$ which satisfy all the boundary conditions. As a result the characteristic equation is $A = 0$ where A is an infinite determinant. In Budiansky and DiPrima's approach the initial problem is put, by appropriate splittings and introducing new unknowns into self-adjoint form. The expansion functions f_n may not satisfy all the boundary conditions. The remaining boundary conditions introduce some constraints, and finally the characteristic equation is $B = 0$ where B is an infinite series. To

[1] Institute of Mathematics, Str. Academiei 14, 780 15 Bucharest 1 Romania.

[2] Institute of Research and Development for Electronics Components, Baneasa, Romania.

Manuscript received by ASME Applied Mechanics Division, December, 1980; final revision, June, 1981.

Downloaded 01 May 2010 to 171.66.16.249. Redistribution subject to ASME license or copyright; see http://www.asme.org/terms/Terms_Use.cfm

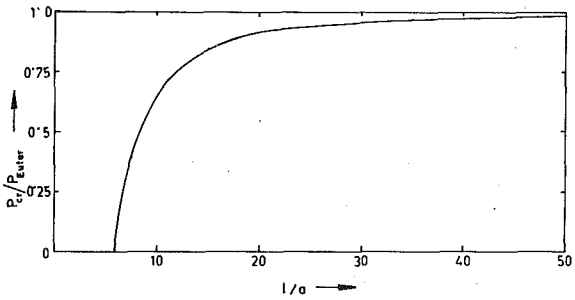


Fig. 2 Variation of P_{cr}/P_{Euler} with slenderness ratio l/a

In Fig. 2 we also give the plot of P_{cr}/P_{Euler} ($= \sigma_{cr}/\sigma_{Euler}$). Since its expression is negative for $l/a < 5.845$, this portion of the graph is not shown.

For higher modes of buckling $m > 1$, it is apparent from (13) that the percentage reduction is higher than that in the first mode.

Buckling of Inelastic Beam-Column

The buckling of inelastic beam-columns have been studied in the literature by taking the tangent modulus E_t for the Young's modulus E. Making this change in equation (15), the critical value of the compressive stress for buckling of an inelastic beam-column is

$$\sigma_{cr} = E_t \left[\frac{\pi^2}{(l/a)^2} - \frac{4\nu^2 + 14\nu + 9}{3(1+\nu)} \frac{\pi^4}{(l/a)^4}\right] \tag{16}$$

If we drop the second term in the right-hand side of (16), we obtain the well-known Shanley tangent modulus formula. In an earlier attempt to incorporate the additional effect of shear distortion in the formula, Hill and Sewell [3] gave a new formula, which to the order $(a/l)^4$ is

$$\sigma_{cr} = E_t \left[\frac{\pi^2}{(l/a)^2} - \frac{3 + 3\nu - 2\nu^2}{3(1+\nu)} \frac{\pi^4}{(l/a)^4}\right] \tag{17}$$

Equations (16) and (17) are of similar form. The larger coefficient of the second term in (16) shows that σ_{cr} given by this formula is lesser than that given by (17).

Table 1

l/a	Euler compressive stress σ_{Euler} in MPa	Modified compressive stress σ_{cr} in MPa equation (15)	Percentage reduction
15	9.076×10^3	7.697×10^3	15.2
20	5.105×10^3	4.669×10^3	8.5
25	3.267×10^3	3.088×10^3	5.5
30	2.269×10^3	2.183×10^3	3.8

Acknowledgment

The authors wish to thank a referee for suggesting the plot of the critical load and therby improving the presentation of the results.

References

1 Timoshenko, S. P., and Gere, J. M., *Theory of Elastic Stability*, McGraw-Hill, New York, 1961.

2 Bose, S. K., "On the Vibrations of a Circular Tower Due to Rayleigh Waves," *Bulletin of the Calcutta Mathematical Society*, Vol. 63, 1971, pp. 101–113.

3 Hill, R., and Sewell, M. J., "A General Theory of Inelastic Column Failure—I," *Journal of Mechanics and Physics of Solids*, Vol. 8, No. 2, 1960, pp. 105–111.

On a Bénard Convection in the Presence of Dielectrophoretic Forces

A. Georgescu[1] and O. Polotzka[2]

In this Note we shall study the influence of dielectrophoretic forces on some Bénard convection by means of a method which leads to shorter numerical calculations than the classical one.

Consider a viscous fluid layer between two flat electrods located at $x = \pm 0.5$ heated from below subjected to dielectrophoretic forces. Suppose that the perturbation of the layer's equilibrium have the form $f(x,y) = f(z)e^{-iky}$ (y-axis is perpendicular to the x-axis), the boundaries are kept at constant temperature, the velocity vanishes at the boundaries, and the charge on the electrods is kept constant. Then the problem governing the linear neutral stability (in the case when the principle of the exchange of stabilities holds) of the mentioned equilibrium against the foregoing perturbations consists of the following equations [1]:

$$\left.\begin{aligned} &(D^2 - k^2)\theta + v = 0, && (1)\\ &(D^2 - k^2)v - k^2R(1 + El)\theta - k^2 REl \cdot D\varphi = 0, && (2)\\ &(D^2 - k^2)\varphi + D\theta = 0, && (3)\end{aligned}\right\} x \in (-0.5; 0.5)$$

and the boundary conditions

$$v = Dv = \theta = D\varphi = 0 \quad \text{at} \quad x = \pm 0.5. \tag{4}$$

Here θ and φ are the temperature and the electric potential of the perturbation, respectively, v is the velocity component along the x-axis, k is the wave number in the y-direction, $D = d/dx$, R is the Rayleigh number, and El is a dimensionless number proportional to the square of the electric field. For El fixed, we shall deduce from the problem (1)–(4) the neutral curve $R = R(k)$ which separates the domain of stability from that of instability. In other words the values R on these curves are the ones at which the convection sets in from the rest. Since R is proportional to the difference between the temperatures of the electrode, it follows that from the knowledge of the neutral curve we can deduce the thermal gradient at which the convection sets in.

The eigenvalue problem (1)–(4) has R as eigenvalue and (θ, v, φ) as eigenfunction. The parameters El and k are fixed. The characteristic equation associated with the eigenvalue problem (1)–(4) will yield the neutral curve. More precisely $R(k)$ shall be the least solution the characteristic equation and, therefore, least eigenvalue of (1)–(4).

The classical (in hydrodynamic and hydromagnetic stability theory) Chandrasekhar's method of deriving the characteristic equation for problems similar to (1)–(4) consists of writing (1)–(4) as a variational problem and solving it by developing the unknowns in an orthonormal set of functions f_n dense in L^2 $(-0.5; 0.5)$ which satisfy all the boundary conditions. As a result the characteristic equation is $A = 0$ where A is an infinite determinant. In Budiansky and DiPrima's approach the initial problem is put, by appropriate splittings and introducing new unknowns into self-adjoint form. The expansion functions f_n may not satisfy all the boundary conditions. The remaining boundary conditions introduce some constraints, and finally the characteristic equation is $B = 0$ where B is an infinite series. To

[1] Institute of Mathematics, Str. Academiei 14, 780 15 Bucharest 1 Romania.

[2] Institute of Research and Development for Electronics Components, Baneasa, Romania.

Manuscript received by ASME Applied Mechanics Division, December, 1980; final revision, June, 1981.

Copyright © 1981 by ASME
Downloaded 01 May 2010 to 171.66.16.249. Redistribution subject to ASME license or copyright; see http://www.asme.org/terms/Terms_Use.cfm

Table 1 The values of $R(k)$ on the neutral curve

$El\backslash k$	1	1.5	2	2.5	3	3.5	4	4.5	5	5.5	6	6.5	7	7.5	8	8.5	9	9.5	10
0		3090	2175	1820	1710	1740	1875	2110	2435	2870	3415	4090	4915	5905	7080				
0.5	5595	2825	1900	1525	1380	1365	1435	1580	1795	2085	2455	2915	3475	4145	4945	5885	6980		
1	5360	2605	1690	1310	1155	1120	1160	1260	1420	1635	1915	2260	2685	3195	3800	4510	5340		
2	4945	2255	1380	1025	875	825	840	900	1000	1145	1330	1565	1845	2190	2595	3070	3630	4275	5015
5	4010	1600	890	620	505	460	260	305	530	600	695	810	955	1125	1330	1570	1850	2015	2550
10	3050	1080	560	370	295	265	260	270	295	335	300	365	525	620	730	865	1015	1110	1310

obtain a better approximation by the first method one has to consider a determinant corresponding to a $n+1$ by $n+1$ matrix, while by the second method only the $n+1$th term in the series has to be added. Thus it follows that there is considerable reduction of computations. On the other hand, since the variational formulation for self-adjoint operators requires half the functions than in the case of nonself-adjoint operators, it also shows another advantage of the second method. DiPrima [2] studied only systems containing $D^{2s}f$, s-integer number. The appearance in (1)–(4) of odd derivatives increases the difficulty of reducing (1)–(4) to a self-adjoint form. In [3] we indicated some means to get this form for problems which contain odd derivatives. In the sequel we shall apply this extended Budiansky-DiPrima method to the problem (1)–(4). We can write the problem (1)–(4) in a self-adjoint form. We introduce the new function $u = -k^2R(1+El)\theta - k^2REl\cdot D\varphi$ such that $u(\pm 0.5) = 0$. Then (1)–(4) reduces to

$$\left.\begin{aligned} &(D^2-k^2)\theta = -v, && (5)\\ &(D^2-k^2)v^2 = -u, && (6)\\ &(D^2-k^2)u + k^2R(D^2-k^2)\theta \\ &\qquad - k^4REl\theta = 0, && (7)\\ &u = v = Dv = \theta = 0 && (8) \end{aligned}\right\} x \in (-0.5; 0.5)$$

which may be written as $Lf = 0$ where the operator L is self-adjoint. We used the notations $f = (u, v, \theta)$, $\mathcal{D} = \{f \in [C^\infty(-0.5; 0.5)]^3; u, v, \theta$ satisfy (8)$\}$ and $L:\mathcal{D} \to [C^0(-0.5; 0.5]^3$. Define now the functional $J:\mathcal{D} \to R$ by $J(f) = (Lf, f)$, where $(.,.)$ is the usual scalar product in $L^2(-0.5; 0.5)$. We have

$$J(f) = \int_{-0.5}^{0.5} -2D\theta Du - 2k^2\theta u + 2uv + k^4v^2 + (D^2v)^2 + 2k^2(Dv)^2 - k^2R(D\theta)^2 - k^4R(1+El)\theta^2\}dx.$$

The following variational principle holds $Lf = 0$ if $\delta J(f) = 0$ where δ is the variation. Therefore to solve (1)–(4) is equivalent to solving the variational problem: find the stationary points of the functional J. To solve this last problem we expand u, v, θ in the Fourier series

$$u = \sum_{n=1}^{\infty} u_{2n-1}E_{2n-1}, \quad v = \sum_{n=1}^{\infty} v_{2n-1}E_{2n-1}, \quad \theta = \sum_{n=1}^{\infty} \theta_{2n-1}E_{2n-1},$$

where the set $\{E_m\}$ $m \in N$, $E_m = \sqrt{2}\cos m \times \pi$ is dense in $L^2(-0.5, 0.5)$. A backward integration technique yields:

$$Du = -\sum_{n=1}^{\infty} (2n-1)\pi u_{2n-1}F_{2n-1}, Dv = -\sum_{n=1}^{\infty} (2n-1)\pi v_{2n-1}F_{2n-1},$$

$$D\theta = -\sum_{n=1}^{\infty} (2n-1)\pi\theta_{2n-1}\cdot F_{2n-1},$$

$$D^2v = \sum_{n=1}^{\infty} (2n-1)^2\pi^2 v_{2n-1}E_{2n-1}$$

where $F_m = \sqrt{2}\sin m \times \pi$.

The functional J becomes

$$J(f) = \sum_{n=1}^{\infty} \{-2(2n-1)^2\pi^2\theta_{2n-1}u_{2n-1} - 2k^2\theta_{2n-1}u_{2n-1} + 2u_{2n-1}v_{2n-1} + k^4v^2_{2n-1} + 2k^2(2n-1)^2\pi^2v^2_{2n-1} + (2n-1)^4\pi^4v^2_{2n-1} - k^2R(2n-1)^2\pi^2\theta^2_{2n-1} - k^4R(1+El)\theta^2_{2n-1}\}.$$

On putting $A_n = (2n-1)^2\pi^2 + k^2$, J may be written in the form

$$J(f) = \sum_{n=1}^{\infty} \{-2A_n\theta_{2n-1}u_{2n-1} + 2u_{2n-1}v_{2n-1} + A_n{}^2v^2_{2n-1} - k^2R(A_n + k^2El)\theta_{2n-1}\}.$$

Note that the boundary condition $u = 0, v = 0, \theta = 0$ are automatically satisfied by the choice of expansion functions. The conditions $Dv = 0$ at $x = \pm 0.5$ introduce the constraint

$$\Gamma = \sum_{n=1}^{\infty} (2n-1)\pi v_{2n-1}(-1)^{n+1} = 0.$$

Our variational problem consists now in finding the coefficients u_{2n-1}, v_{2n-1}, and θ_{2n-1} satisfying the constraint $\Gamma = 0$ and for which the functional J (now depending on these coefficients) is stationary. Denoting by λ the Lagrange multiplier, the variational problem is reduced to the algebraic system

$$\frac{\partial(J-\lambda\Gamma)}{\partial\theta_{2n-1}} = \frac{\partial(J-\lambda\Gamma)}{\partial u_{2n-1}} = \frac{\partial(J-\lambda\Gamma)}{\partial v_{2n-1}} = 0, \quad \Gamma = 0.$$

This gives

$$A_nu_{2n-1} + k^2R(A_n + k^2El)\theta_{2n-1} = 0, \tag{9}$$

$$A_n\theta_{2n-1} - v_{2n-1} = 0, \tag{10}$$

$$2u_{2n-1} + 2A_n{}^2v_{2n-1} = \lambda(2n-1)\pi(-1)^{n+1}, \tag{11}$$

$$\sum_{n=1}^{\infty} (2n-1)\pi(-1)^{n+1}v_{2n+1} = 0. \tag{12}$$

Elimination of $u_{2n-1}, v_{2n-1}, \theta_{2n-1}$ between these equations leads to the characteristic equation

$$\sum_{n=1}^{\infty} \frac{A_n{}^2(A_n - k^2)}{A_n{}^4 - Rk^2(A_n + k^2El)} = 0. \tag{13}$$

Since

$$\sum_{n=1}^{\infty} \frac{1}{A_n - k^2} = \frac{1}{8}$$

the convergence of the forergoing series can be improved by adding this equality to (13) to obtain

$$\frac{1}{8} + \sum_{n=1}^{\infty} \frac{-2k^2A_n{}^3 + Rk^2(A_n + k^2El) + k^4A_n{}^2}{[A_n{}^4 - Rk^2(A_n + k^2El)](A_n - k^2)} = 0. \tag{14}$$

This characteristic equation may also be obtained by a direct Fourier series technique. The convergence of the series, the continuity of the functions, some other mathematical details have been proved in [3].

In solving equation (14) we used the chord method; 20 terms in the series of (14) have been taken. Our numerical results given in Table 1 agree perfectly with those of [1] obtained by means of Chandrasekhar's method. From Table 1 it can be seen that the dielectrophoretic forces favor an earlier appearance of the convective motion; that is, the equilibrium state is an increasing function of El.

References

1 Turnbull, J. R., "Effect of Dielectrophoretic Forces on the Bénard Instability," *The Physics of Fluids*, Vol. 12, 9, 1969, pp. 1809–1815.

2 DiPrima, R. C., "Some Variational Principles for Problems in Hydrodynamic and Hydromagnetic Stability," *Quarterly Journal of Applied Mathematics*, Vol. 18, 4, 1961, pp. 375–385.

3 Georgescu A., *Hydrodynamic Stability Theory*, to be published by Sijthoff & Noordhoff.

Downloaded 01 May 2010 to 171.66.16.249. Redistribution subject to ASME license or copyright; see http://www.asme.org/terms/Terms_Use.cfm

Journal of Applied Mechanics

Discussion

Reexamination of Unsteady Fluid Dynamic Forces on a Two-Dimensional Finite Plate at Small Mach Numbers[1]

C. H. Ellen.[2] Matsuzaki and Ueda[1] have presented a rederivation of expressions in a slightly more restricted form ($M = 0$) than those derived originally in [1]. In stating that the earlier derivation has obtained expressions for the generalized pressures at low frequencies they appear to ignore the fact that precisely the same limits have been applied to obtain their result which, apparently, has a typographical error in equation $(37d)$[3] and which does not give an explicit form for Q_{nn} [1]. They confirm that Weaver and Unny [2] have introduced a zero-order error by changing the lower limit of integration (otherwise the same result may be derived from their integrals), but do not appear to agree that a similar problem exists with Ishii's results [3]. The point is that Ishii states in his Appendix that $a^R{}_{mn}$ $(M, k = 0) = (1 - M^2)^{-1/2}\, a^R{}_{mn}$ $(M = 0, k = 0)$ (in his notation), a result which is incorrect and acknowledged to be incorrect in the discussion of Matsuzaki and Ueda (see also Table 2 of footnote one): this, together with the absence of any reference to singular terms in [3], is the basis of the comments made in [1].

However the purpose of this Discussion is not to go over what would appear to be old and well-known ground but to raise the question of the relevance and the use of this form of two-dimensional fluid dynamics in the study of the panel stability problem. As the frequency of oscillation becomes small the acoustic wavelength increases but must remain small compared with the panel width if the two-dimensional theory is to remain valid. This presents obvious difficulties to any analysis of the nature of panel motion in the neighborhood of a panel divergence condition or at low frequencies when the panel dimensions will violate this theoretical restriction. (In a wind tunnel experiment one might expect conditions to approach two-dimensionality if wall boundary-layer effects can be minimized.) The alternative approach is to examine stability when the acoustic wavelength is large compared with both panel dimensions: use of three-dimensional fluid dynamics generates the generalized pressures given in [1], again at "low frequency" only in the sense that the acoustic wavelengths are large compared with the panel dimensions. With these forms, the neighborhood of a divergence instability, which is, of course, identical for panels in two-dimensional flows and high aspect ratio panels in three-dimensional flows, may be examined with confidence. For a panel (or membrane) in an otherwise rigid surface it has been established generally that, as long as the frequency is not so large that the acoustic wavelengths are small compared with the panel dimensions, the only instability must be a divergence [4, 5]. Therefore the use of an approximate modal approach to examine theoretical oscillatory instabilities appears to serve no purpose unless some distinctly different feature is under examination. (The problem of instability prediction using a truncated convergent series is well known and graphically illustrated by the "supersonic membrane paradox" [6, 7].)

Recent work has identified the importance of the environment of the panel in controlling the type of instability which is likely to occur. When the trailing edge of a panel is free, oscillatory-type instabilities are present but these appear to be suppressed when the trailing edge is fixed [4, 5, 8]. While it has been shown that, when the rigid attachments (upstream and downstream) to the panel are sufficiently large, the divergence instability condition approaches that of a panel in an infinite baffle [5], the theory also suggests that small mass ratio flutter instabilities are possible when the rigid attachment lengths are small in relation to the panel length.

In conclusion, therefore, the scope of this paper by Matsuzaki and Ueda[1] appears limited, both in theory and application, and it would be useful if the proposed additional paper on the stability analysis using the generalized forces obtained in footnote one takes into account the points raised in this Discussion.

References

1 Ellen, C. H., "The Stability of Simply Supported Rectangular Surfaces in Uniform Subsonic Flow," ASME JOURNAL OF APPLIED MECHANICS, Vol. 40, 1973, pp. 68–72.

2 Weaver, D. S., and Unny, T. E., "The Hydroelastic Stability of a Flat Plate," ASME JOURNAL OF APPLIED MECHANICS, Vol. 37, 1970, pp. 823–827.

3 Ishii, T., "Aeroelastic Instabilities of Simply Supported Panels in Subsonic Flow," AIAA Paper No. 65-772, 1965.

4 Ellen, C. H., "The Stability of an Isolated Rectangular Surface Embedded in Uniform Subsonic Flow," ASME JOURNAL OF APPLIED MECHANICS, Vol. 44, 1977, pp. 201–206.

5 Shahrokh, K., and Ellen, C. H., "The Stability of Partially Rigid Two-Dimensional Surfaces in Uniform Incompressible Flow," *Journal of Sound and Vibration*, Vol. 65, No. 3, 1979, pp. 339–351.

6 Bolotin, V. V., *Nonconservative Problems in the Theory of Elastic Stability*, Macmillan, New York, 1963.

7 Ellen, C. H., "Approximate Solutions of the Membrane Flutter Problem," *AIAA Journal*, Vol. 3, No. 6, 1965, pp. 1186–1187.

8 Kornecki, A., Dowell, E. H., and O'Brien, J., "On the Aeroelastic Instability of Two-Dimensional Panels in Uniform Incompressible Flow," *Journal of Sound and Vibration*, Vol. 47, No. 2, 1976, pp. 163–178.

Authors' Closure

The authors would like to thank Dr. Ellen for his comments, especially on the similar applicability of our analysis to his corresponding one.

The main objective of the paper is to reexamine the previous aerodynamic analyses, that is, to clarify issues raised in several papers. Therefore, its scope is the same as those of the analyses reexamined. However, we show that there exists an essential difference between a compressible flow and an artificial incompressible model which is often adopted as a representative case. As a result, we indicated Ishii's error in the incompressible flow analysis which had been overlooked,

---

[1] By Y. Matsuzaki and T. Ueda, and published in the December, 1980, ASME JOURNAL OF APPLIED MECHANICS, Vol. 47, pp. 720–724.

[2] Associate Manager, Process Engineering, John Lysaght (Australia) Limited, Research & Technology Centre, P.O. Box 77, Port Kembla, 2505, N.S.W. Australia.

[3] A factor of $2/\pi$ appears to be missing from the "c" term.

Copyright © 1981 by ASME

Downloaded 01 May 2010 to 171.66.16.249. Redistribution subject to ASME license or copyright; see http://www.asme.org/terms/Terms_Use.cfm

and proposed a "zero-volume change" vibration mode for dynamic stability analysis.

The expression of equation (37*d*) contains an error as pointed out. However, all the numerical calculation was carried out by using the correctly expressed equation.

Next, let us reexamine Ishii's result for $M \neq 0$ in his Appendix. When $M \neq 0$ and $k = 0$, we obtain from equation (17) of our paper

$$\Phi^*(M \neq 0) = iU\xi/(\beta|\xi|)W^* \exp(-\zeta y)$$

because of $\zeta = \beta|\xi|$, while

$$\Phi^*(M = 0) = iU\xi/|\xi|W^* \exp(-\zeta y)$$

because of $\zeta = |\xi|$ for $M = k = 0$. Comparison between the equations yields $\Phi^*(M \neq 0) = (1 - M^2)^{-1/2}\Phi^*(M = 0)$. Therefore, it does not seem that Ishii's result is incorrect as far as the point just raised is concerned. However, we should repeat that his incompressible aeroforces are invalid for a symmetric natural mode when $k \neq 0$.

As for the proposed paper on the stability analysis, it has already been accepted for publication in this JOURNAL, and will soon be published [9]. In this area, several important problems remain to be resolved. It reexamines again an old and well-known problem, that is, the possibility of postdivergence flutter oscillation which is probably the most controversial point. Since a brief description of this topic is given in [9], we would refrain from repeating it here.

Finally, we'd like to indicate another typographical error: although the explanation in the text is correct, $k = 0$ should read $k = 1$ in the caption of Table 2 of our paper.

Reference

9 Matsuzaki, Y., "Reexamination of Stability of a Two-Dimensional Finite Panel Exposed to an Incompressible Flow," to be published in the ASME JOURNAL OF APPLIED MECHANICS.

A Correct Definition of Elastic and Plastic Deformation and Its Computational Significance[1]

J. Casey[2] and P. M. Naghdi.[3] Our purpose here is to discuss two points raised in a paper of Lubarda and Lee[1] and again in a more recent paper of Lee [1]. These points, which are both related to the use of full invariance requirements in plasticity, in the manner proposed by Green and Naghdi [2] are as follows:

(*a*) Whether it is necessary to demand independent invariance requirements for intermediate stress-free configurations associated with the decomposition of the deformation gradient in the form $\mathbf{F} = \mathbf{F}_e\mathbf{F}_p$; and

(*b*) whether it is possible to specify $\mathbf{F}_e$ to be a symmetric positive definite tensor in the construction of a general theory.[4]

With regard to (*a*), Lubarda and Lee[1] and again Lee [1] demand that only partial invariance requirements be satisfied. Similarly, with reference to (*b*), they assume that without loss in generality the elastic part $\mathbf{F}_e$ of the deformation gradient $\mathbf{F}$ can be chosen to be symmetric. We disagree with the contents of the authors' paper[1] and reference [1] insofar as (*a*) and (*b*) are concerned.

In our recent Brief Note [3], we emphasized the physical grounds for invoking full invariance requirements of the type proposed by Green and Naghdi [2], whenever use is made of intermediate stress-free configurations. Lubarda and Lee (footnote 1, p. 37 after equation (33)) appeal to only a restricted form of invariance requirements, and more recently Lee [1, p. 867] has objected to the use of full invariance requirements because they seem to him "to demand two objectivity checks for the single [current] configuration" and therefore to involve a redundancy. We discuss the two points (*a*) and (*b*) above using the notation of [3].

The invariance requirements in [2, 3] are based on the idea that all configurations, global or local, which differ from any physically possible configuration of a body by a rigid displacement are equivalent. All such configurations are physically indistinguishable and should therefore play an equal role in any theory of material behavior. The invariance requirements insure that these configurations enter the theory in a physically meaningful way. The intermediate stress-free configuration, if it exists, *is* a possible configuration of the body and can, in the words of Lee [1, p. 863], "be achieved physically by . . . *destressing.*" It was precisely because the intermediate stress-free configuration (whenever it exists) is physically realizable, that in [2, 3] it was assumed that this configuration is subject to *exactly the same* invariance requirements as any other possible configuration of the body. As a consequence, two different orthogonal tensors must appear in the transformation rules for certain fields. For example, when the present configuration and the intermediate stress-free configuration are subjected at time t to arbitrary independent rigid displacements, involving rotations $\mathbf{Q}(t)$ and $\bar{\mathbf{Q}}(t)$, respectively, the tensor $\mathbf{F}_e$ is transformed into

$$\mathbf{F}_e^+ = \mathbf{Q}(t)\mathbf{F}_e\bar{\mathbf{Q}}^T(t). \tag{1}$$

The reason for the appearance of two different rigid body rotation tensors in (1) is simple and may be explained even without appealing to either the stress-free nature of the intermediate configuration, or the elastic-plastic character of the body. To see this, consider any deformable body which is first deformed from a reference configuration κ_0 into a configuration κ_1, and then from κ_1 into the present configuration κ. The deformation gradient $\mathbf{F}$ in the configuration κ can then be expressed as[5]

$$\mathbf{F} = \mathbf{F}_2\mathbf{F}_1 \tag{2}$$

where $\mathbf{F}_1$ is the deformation gradient in the configuration κ_1 and $\mathbf{F}_2$ is the gradient in the configuration κ relative to the configuration κ_1. Since both κ_1 and κ are physically realizable configurations of the body, they are both subject to the usual invariance requirements. If κ_1 is replaced at time t_1 by a configuration κ_1^+ that differs from it by an arbitrary rigid displacement whose rotation tensor is $\mathbf{Q}_1(t_1)$, then $\mathbf{F}_1$ is transformed into

$$\mathbf{F}_1^+ = \mathbf{Q}_1(t_1)\mathbf{F}_1. \tag{3}$$

Similarly, if κ is replaced at the present time t by a configuration κ^+ that differs from κ by an arbitrary rigid displacement whose rotation tensor is $\mathbf{Q}(t)$, $\mathbf{F}$ is transformed into

$$\mathbf{F}^+ = \mathbf{Q}(t)\mathbf{F}. \tag{4}$$

The gradient in the configuration κ^+ relative to κ_1^+ is again given by the chain rule in the form

$$\mathbf{F}_2^+ = \mathbf{F}^+(\mathbf{F}_1^+)^{-1}. \tag{5}$$

From (2)–(5), it follows that

$$\mathbf{F}_2^+ = \mathbf{Q}(t)\mathbf{F}_2\mathbf{Q}_1^T(t_1). \tag{6}$$

Since the rigid displacements by which κ_1 is taken into κ_1^+ and κ is

---

[1] By V. A. Lubarda and E. H. Lee, and published in the March, 1981, issue of the ASME JOURNAL OF APPLIED MECHANICS, Vol. 48, pp. 35–40.

[2] Department of Mechanical Engineering, University of Houston, Houston, Texas 77004.

[3] Department of Mechanical Engineering, University of California, Berkeley, Calif. 94720.

[4] By a "general theory," we mean one that is at least broad enough to include anisotropic materials and to be valid for all possible motions of the elastic-plastic body.

[5] Since the two configurations κ_1 and κ are global, (2) is obtained by means of the chain rule. A similar form holds if κ_1 is only a local configuration.

Downloaded 01 May 2010 to 171.66.16.249. Redistribution subject to ASME license or copyright; see http://www.asme.org/terms/Terms_Use.cfm

and proposed a "zero-volume change" vibration mode for dynamic stability analysis.

The expression of equation (37*d*) contains an error as pointed out. However, all the numerical calculation was carried out by using the correctly expressed equation.

Next, let us reexamine Ishii's result for $M \neq 0$ in his Appendix. When $M \neq 0$ and $k = 0$, we obtain from equation (17) of our paper

$$\Phi^*(M \neq 0) = iU\xi/(\beta|\xi|)W^* \exp(-\zeta y)$$

because of $\zeta = \beta|\xi|$, while

$$\Phi^*(M = 0) = iU\xi/|\xi|W^* \exp(-\zeta y)$$

because of $\zeta = |\xi|$ for $M = k = 0$. Comparison between the equations yields $\Phi^*(M \neq 0) = (1 - M^2)^{-1/2}\Phi^*(M = 0)$. Therefore, it does not seem that Ishii's result is incorrect as far as the point just raised is concerned. However, we should repeat that his incompressible aeroforces are invalid for a symmetric natural mode when $k \neq 0$.

As for the proposed paper on the stability analysis, it has already been accepted for publication in this JOURNAL, and will soon be published [9]. In this area, several important problems remain to be resolved. It reexamines again an old and well-known problem, that is, the possibility of postdivergence flutter oscillation which is probably the most controversial point. Since a brief description of this topic is given in [9], we would refrain from repeating it here.

Finally, we'd like to indicate another typographical error: although the explanation in the text is correct, $k = 0$ should read $k = 1$ in the caption of Table 2 of our paper.

Reference

9 Matsuzaki, Y., "Reexamination of Stability of a Two-Dimensional Finite Panel Exposed to an Incompressible Flow," to be published in the ASME JOURNAL OF APPLIED MECHANICS.

A Correct Definition of Elastic and Plastic Deformation and Its Computational Significance[1]

J. Casey[2] and P. M. Naghdi.[3] Our purpose here is to discuss two points raised in a paper of Lubarda and Lee[1] and again in a more recent paper of Lee [1]. These points, which are both related to the use of full invariance requirements in plasticity, in the manner proposed by Green and Naghdi [2] are as follows:

(*a*) Whether it is necessary to demand independent invariance requirements for intermediate stress-free configurations associated with the decomposition of the deformation gradient in the form $\mathbf{F} = \mathbf{F}_e\mathbf{F}_p$; and

(*b*) whether it is possible to specify $\mathbf{F}_e$ to be a symmetric positive definite tensor in the construction of a general theory.[4]

With regard to (*a*), Lubarda and Lee[1] and again Lee [1] demand that only partial invariance requirements be satisfied. Similarly, with reference to (*b*), they assume that without loss in generality the elastic part $\mathbf{F}_e$ of the deformation gradient $\mathbf{F}$ can be chosen to be symmetric. We disagree with the contents of the authors' paper[1] and reference [1] insofar as (*a*) and (*b*) are concerned.

In our recent Brief Note [3], we emphasized the physical grounds for invoking full invariance requirements of the type proposed by Green and Naghdi [2], whenever use is made of intermediate stress-free configurations. Lubarda and Lee (footnote 1, p. 37 after equation (33)) appeal to only a restricted form of invariance requirements, and more recently Lee [1, p. 867] has objected to the use of full invariance requirements because they seem to him "to demand two objectivity checks for the single [current] configuration" and therefore to involve a redundancy. We discuss the two points (*a*) and (*b*) above using the notation of [3].

The invariance requirements in [2, 3] are based on the idea that all configurations, global or local, which differ from any physically possible configuration of a body by a rigid displacement are equivalent. All such configurations are physically indistinguishable and should therefore play an equal role in any theory of material behavior. The invariance requirements insure that these configurations enter the theory in a physically meaningful way. The intermediate stress-free configuration, if it exists, *is* a possible configuration of the body and can, in the words of Lee [1, p. 863], "be achieved physically by . . . *destressing.*" It was precisely because the intermediate stress-free configuration (whenever it exists) is physically realizable, that in [2, 3] it was assumed that this configuration is subject to *exactly the same* invariance requirements as any other possible configuration of the body. As a consequence, two different orthogonal tensors must appear in the transformation rules for certain fields. For example, when the present configuration and the intermediate stress-free configuration are subjected at time t to arbitrary independent rigid displacements, involving rotations $\mathbf{Q}(t)$ and $\bar{\mathbf{Q}}(t)$, respectively, the tensor $\mathbf{F}_e$ is transformed into

$$\mathbf{F}_e^+ = \mathbf{Q}(t)\mathbf{F}_e\bar{\mathbf{Q}}^T(t). \tag{1}$$

The reason for the appearance of two different rigid body rotation tensors in (1) is simple and may be explained even without appealing to either the stress-free nature of the intermediate configuration, or the elastic-plastic character of the body. To see this, consider any deformable body which is first deformed from a reference configuration κ_0 into a configuration κ_1, and then from κ_1 into the present configuration κ. The deformation gradient $\mathbf{F}$ in the configuration κ can then be expressed as[5]

$$\mathbf{F} = \mathbf{F}_2\mathbf{F}_1 \tag{2}$$

where $\mathbf{F}_1$ is the deformation gradient in the configuration κ_1 and $\mathbf{F}_2$ is the gradient in the configuration κ relative to the configuration κ_1. Since both κ_1 and κ are physically realizable configurations of the body, they are both subject to the usual invariance requirements. If κ_1 is replaced at time t_1 by a configuration κ_1^+ that differs from it by an arbitrary rigid displacement whose rotation tensor is $\mathbf{Q}_1(t_1)$, then $\mathbf{F}_1$ is transformed into

$$\mathbf{F}_1^+ = \mathbf{Q}_1(t_1)\mathbf{F}_1. \tag{3}$$

Similarly, if κ is replaced at the present time t by a configuration κ^+ that differs from κ by an arbitrary rigid displacement whose rotation tensor is $\mathbf{Q}(t)$, $\mathbf{F}$ is transformed into

$$\mathbf{F}^+ = \mathbf{Q}(t)\mathbf{F}. \tag{4}$$

The gradient in the configuration κ^+ relative to κ_1^+ is again given by the chain rule in the form

$$\mathbf{F}_2^+ = \mathbf{F}^+(\mathbf{F}_1^+)^{-1}. \tag{5}$$

From (2)–(5), it follows that

$$\mathbf{F}_2^+ = \mathbf{Q}(t)\mathbf{F}_2\mathbf{Q}_1^T(t_1). \tag{6}$$

Since the rigid displacements by which κ_1 is taken into κ_1^+ and κ is

---

[1] By V. A. Lubarda and E. H. Lee, and published in the March, 1981, issue of the ASME JOURNAL OF APPLIED MECHANICS, Vol. 48, pp. 35–40.

[2] Department of Mechanical Engineering, University of Houston, Houston, Texas 77004.

[3] Department of Mechanical Engineering, University of California, Berkeley, Calif. 94720.

[4] By a "general theory," we mean one that is at least broad enough to include anisotropic materials and to be valid for all possible motions of the elastic-plastic body.

[5] Since the two configurations κ_1 and κ are global, (2) is obtained by means of the chain rule. A similar form holds if κ_1 is only a local configuration.

Copyright © 1981 by ASME
Downloaded 01 May 2010 to 171.66.16.249. Redistribution subject to ASME license or copyright; see http://www.asme.org/terms/Terms_Use.cfm

taken into κ^+ are arbitrary, $\mathbf{Q}(t)$ will not equal $\mathbf{Q}_1(t_1)$ in general. Thus, even though only the usual invariance requirements have been invoked, we still must include two unequal orthogonal tensors in the transformation rule (6) for $\mathbf{F}_2$.

In plasticity, the intermediate configuration κ_1 is a local stress-free configuration, but since it is physically realizable whenever it exists, it is subject to the transformation rule (3). Consequently, in plasticity the tensor $\mathbf{F}_e$ (being the analogue of $\mathbf{F}_2$ above) satisfies the transformation rule (1), which has the same form as (6) with $\mathbf{Q}_1(t_1) = \bar{\mathbf{Q}}(t)$ and with t_1 differing from t by a constant.[6] Rather than involving a redundancy, the invariance requirements of [2, 3] treat all configurations of the body in the same manner. Lubarda and Lee[1] and Lee [1] are not consistent in their treatment of the intermediate stress-free configuration and the present configuration, since they assume that the intermediate stress-free configurations can be subjected only to *special* superposed rigid displacements, whereas the present configuration may be subjected to *arbitrary* rigid displacements. Indeed, in the invariance requirements used in Lubarda and Lee[1] and Lee [1], $\bar{\mathbf{Q}}(t)$ in (1) is taken equal to $\mathbf{Q}(t)$. This obviously involves a loss of generality and is in fact basically no different than what other authors (see [3] for references) have done in choosing $\bar{\mathbf{Q}}(t) = \mathbf{I}$, $\mathbf{I}$ being the identity tensor. As will be seen at the end of our discussion of the second point (b), the restriction $\mathbf{Q}(t) = \bar{\mathbf{Q}}(t)$ which Lubarda and Lee[1] place on their invariance requirements is closely related to their assumption that $\mathbf{F}_e$ be chosen symmetric.

It is appropriate to remark here on a further puzzling aspect of Lee's discussion of invariance requirements in [1]. While Lee admits that the intermediate stress-free configuration is a possible configuration,[7] he later regards it [1, p. 867] as involving only a "thought experiment" and claims [1, p. 866]: "The unstressed state . . . was envisaged and analyzed in order to select convenient variables with which to express the theory, but was not actually achieved during the stressing so that it is not necessary to impose a test of objectivity on that configuration."

Is Lee's distinction in regard to invariance requirements, between those assumed for the actual configurations and for possible configurations, valid? To examine this question, let us consider again the configurations κ and κ_1 that were introduced above in connection with the motion of a general deformable body. Thus, in another motion, let the body once more occupy the configuration κ but suppose that in this motion it did not pass through the configuration κ_1. (This thought experiment is a perfectly valid one.) For whatever purposes desired, one may still use the configuration κ_1 to express the deformation gradient $\mathbf{F}$ as a product in the form (2). Should we now alter the transformation rule (3)? Certainly not, since the configuration κ_1 is still a possible configuration, and must therefore enter the theory in a physically meaningful way. What matters is not whether a configuration is actually occupied in a given motion, but only that it can possibly be occupied in some motion. The transformation rule (6), and its analogue (1) for an elastic-plastic body, should therefore be retained.

Turning now to the second point (b), we recall that a polar decomposition of $\mathbf{F}_e$ yields

$$\mathbf{F}_e = \mathbf{R}_e \mathbf{M}_e, \tag{7}$$

where the tensors $\mathbf{R}_e$ and $\mathbf{M}_e$ are proper orthogonal and symmetric positive definite, respectively. Lubarda and Lee[1] (page 36) state: "For analytical convenience, and with no basic loss of generality, we take the elastic deformation gradient $\mathbf{F}_e$, associated with destressing, to be rotation free and hence given by $\mathbf{M}_e$, a symmetric matrix." Similar statements are repeated by Lubarda and Lee (see footnote 1, p. 36, before equations (14)) and reference [1, p. 864]. Corresponding to their assumption, Lubarda and Lee[1] and Lee [1] choose $\mathbf{R}_e = \mathbf{I}$, a choice which violates the invariance requirements of [2, 3]. Actually, this issue was discussed briefly in [3, p. 674]. To elaborate, even if for a particular choice of intermediate stress-free configuration $\mathbf{F}_e$ is symmetric, then by the transformation rule (1), it is not true that $\mathbf{F}_e$ will be symmetric in all intermediate stress-free configurations that can be obtained from the first by arbitrary rigid displacements; an inspection of (1) shows that even if $\mathbf{F}_e$ is symmetric, $\mathbf{F}_e^+$ will not be symmetric, since in general $\mathbf{Q}(t)$ will not be equal to $\bar{\mathbf{Q}}(t)$. In this connection, it should be noted that the statements "choose $\mathbf{F}_e$ symmetric positive definite" and "choose $\mathbf{F}_p$ symmetric positive definite" are not physically meaningful in that they do not contain invariant ideas. As regards point (b), we conclude that the invariance requirements in [2, 3] imply that $\mathbf{F}_e$ cannot be chosen symmetric in the context of a general theory of plasticity.

Lubarda and Lee[1] justify the restriction $\mathbf{Q}(t) = \bar{\mathbf{Q}}(t)$ on their invariance requirements on the grounds of the admissibility of the choice $\mathbf{F}_e = \mathbf{M}_e$, stating (footnote 1, p. 37): "Since elastic destressing is considered to occur without rotation, each element of the unstressed configuration must be subjected to the same rotation, $\mathbf{Q}(t)$, as the current configuration and this constraint must be introduced into the objectivity requirements." Lubarda and Lee[1] recognize the interconnection between points (a) and (b) and their special assumption that $\mathbf{F}_e$ can be chosen symmetric compels them to adopt restricted invariance requirements. In order to satisfy full invariance requirements their choice $\mathbf{F}_e = \mathbf{M}_e$ must be abandoned.

References

1 Lee, E. H., "Some Comments on Elastic-Plastic Analysis," *International Journal of Solids and Structures*, Vol. 17, 1981, pp. 859–872.

2. Green, A. E. and Naghdi, P. M., "Some Remarks on Elastic-Plastic Deformation at Finite Strain," *International Journal of Engineering Sciences*, Vol. 9, 1971, pp. 1219–1229.

3 Casey, J., and Naghdi, P. M., "A Remark on the Use of the Decomposition $\mathbf{F} = \mathbf{F}_e\mathbf{F}_p$ in Plasticity," ASME JOURNAL OF APPLIED MECHANICS, Vol. 47, 1980, pp. 672–675.

Authors' Closure

We thank Professors Casey and Naghdi for providing an opportunity to discuss our differences in approach to this question. We agree with the discussers that, in considering a constitutive relation, objectivity or invariance requirements must apply to all physically achievable states falling within its purview. In the paper under discussion we attained this objective by establishing objectivity of an arbitrarily deformed state. This avoids becoming involved in the unnecessarily elaborate mathematical structure used by the discussers in establishing objectivity simultaneously for many states, i.e., the state associated with general deformation and those associated states obtained from it by destressing. Objectivity of the latter states falls within the scope of the proof covering general deformation and there is thus no need to consider it separately.

We should perhaps clarify our use of the concept "physically achievable" for an elastic-plastic state. Since, apart from homogeneous deformation, virtually all elastic-plastic loading of a body will leave it in a state of residual stress when the loads are removed, the corresponding unstressed state can only be achieved by considering the body to be divided into infinitesimal elements. This corresponds to the standard method of measuring residual stresses by machining away parts of the body and measuring the consequent strain change in the remainder. In practice the elements cannot be reconstructed to reform the body because of the material lost in the form of machining chips, but in principle this could be done and is a useful concept in constructing a constitutive relation. Complete investigation of the constitutive relation can be obtained by considering only homogeneous deformation states and then the residual aspect and the appearance of nondifferentiable maps does not arise.

In the subject paper the condition at an arbitrary point on a general elastic-plastic deformation path, for a material element of the body, is analyzed in order to determine the constitutive relation connecting

[6] The invariance requirements always permit a translation in the time variable.

[7] See the quoted phrase in the fourth paragraph of this Discussion.

Downloaded 01 May 2010 to 171.66.16.249. Redistribution subject to ASME license or copyright; see http://www.asme.org/terms/Terms_Use.cfm

the stress and deformation histories to which the element has been subjected. Because of the incremental or flow-type nature of the plasticity law, strain *rate* appears in the constitutive relation. For application in stress and deformation analysis, total strain rate, and stress and stress rate are needed in the relation. Such a constitutive law is deduced from the kinematic relation expressing the total strain rate in terms of the elastic and plastic components, by substituting from the plasticity law and the time derivative of the usual elasticity law for the plastic and elastic strain rates, respectively. This yields a constitutive relation for the total strain rate in terms of the stress, stress rate, and variables expressing the history of deformation.

For the case when purely elastic deformation could occur in destressing to zero stress, the choice of destressing by pure deformation without rotation, expressed by the symmetric deformation gradient matrix $\mathbf{V}^e$, constitutes a correct definition of elastic deformation, although not the most general one since arbitrary rigid-body rotation of the unstressed state provides an alernative unstressed state. However, utilizing this particular choice of elastic deformation does permit convenient elimination of the elastic strain-rate term in the kinematic relation for total strain. Any rotation which might have been included in the elastic deformation is automatically embodied in the associated plastic deformation and is determined by the solution process to provide whatever compatability is needed in the configuration of the body on the general deformation path. Thus a correct, but not the most general, definition of elastic and plastic deformation is achieved.

In order to investigate objectivity of the resulting constitutive equation (to be used in stress and deformation analysis) which contains stress-rate and total strain-rate variables, we need only consider superposed arbitrary rigid rotation on the current state of the body on the general deformation path. This is done in the paper under discussion and the constitutive relation is found to be objective.

Since this applies for any general deformation history, we can choose the deformation path to follow pure elastic destressing with or without rotation from the considered state on the general deformation path, and this establishes objectivity of the unstressed state for rotations independent of that utilized in the objectivity check carried for the body on the general deformation path prior to destressing. Thus we established the full invariance requirement stressed by the discussers on the basis of a simpler analytical development. We thus assert that the statement that we "demand that only partial invariance requirements be satisfied" is incorrect. The fact that it is necessary to employ the constitutive relation containing only the current rate of total strain to substitute into the usual variational principle for determination of the velocity field eliminates the need to simultaneously include the plastic deformation gradient in establishing objectivity for any state. Although the subject paper considers only isotropic elastic and plastic laws, the approach explained in this Closure can be utilized for anisotropic laws by taking into account rotation of the anisotropic characteristics with the deformation of the unstressed state.

Professors Casey and Naghdi maintain that even when the intermediate (unstressed) configuration is not occupied in a given motion, the transformation law involving simultaneous independent rotations of the intermediate and final states must be included in the analysis. In this connection it is interesting to consider the analogous problem of the evaluation of thermal stresses. The theory can be formulated by considering an intermediate state in which the temperature variation occurs, and hence thermal expansion, but the condition of zero stress is maintained. This configuration would comprise an incompatible state of strain and hence a discontinuous map. Superimposing the thermal stresses then produces a compatible final configuration which can be expressed by a differentiable mapping from the initial undisturbed state at uniform temperature. The geometrical characteristics of the intermediate state have much in common with those of the unstressed state in elastic-plastic theory, yet to our knowledge the alleged difficulties often ascribed to the intermediate unstressed state in elastic-plastic theory have never been mentioned in the thermal stress case. Nor have we heard of prescribing an involved objectivity principle including independent rotations of the thermally expanded configuration and the final thermally stressed configuration. We are not surprised by this omission since it seems natural to us that since the purely thermally expanded configuration does not appear in the final thermoelastic constitutive relation, no advantage would accrue to offset the additional mathematical complexity of including independent rotation of the thermally expanded intermediate state.

We take this opportunity to mention that typographical errors appeared in equations (22), (40), and (61) of the subject paper and they have been corrected in an Erratum which appeared in the September, 1981, issue of the ASME JOURNAL OF APPLIED MECHANICS.

Basic Transport Equations in Ascending Equiangular Spiral Polar Coordinates[1]

C.-Y. Wang.[2] In this paper,[1] Dr. Ali stated that the torous seems to be the only curved tube which has been analyzed. This is not true. Sinusoidal, once-curved and twice-curved planar tubes (center line lies in a plane) have been studied by Murata, Miyake, and Inaba [1]. Helical tubes were recently investigated by Wang [2].

As soon as the Christoffel symbols for a curvilinear system are obtained, it is fairly easy to produce the field equations through tensors. Murata, et al. [1], developed the coordinate system for the general planar curved tube which would include Ali's work as a special case. The planar coordinates are always orthogonal. Wang [3] developed the coordinate system for the general nonplanar curved tube (arbitrary spatial curvature of the center line) which includes both the helical coordinates and Murata's coordinates as special cases.

It is uncertain that the ascending equiangular spiral polar coordinates are suitable for analytical and numerical work as claimed. This kind of geometry does not lead to an asymptotic state and conditions at both ends highly affect the field properties. Both analytical or numerical attempts would be very difficult.

References

1 Murata, S., Miyake, Y., and Inaba, T., "Laminar Flow in a Curved Pipe With Varying Curvature," *Journal of Fluid Mechanics*, Vol. 73, 1976, pp. 735–752.

2 Wang, C.-Y., "The Helical Coordinate System and the Temperature Distribution Inside a Helical Coil," ASME JOURNAL OF APPLIED MECHANICS, Vol. 47, 1980, pp. 951–953.

3 Wang, C.-Y., "On the Low Reynolds Number Flow in a Helical Pipe," *Journal of Fluid Mechanics*, Vol. 108, 1981, pp. 185–194.

[1] By S. Ali, and published in the March, 1981, issue of the ASME JOURNAL OF APPLIED MECHANICS, Vol. 48, pp. 190–192.

[2] Professor, Department of Mathematics, Michigan State University, East Lansing, Mich. 48824.

On the Uniqueness and Stability of Endochronic Theory[1]

I. S. Sandler.[2] In the paper,[1] the author presents several conclusions with respect to the uniqueness and stability properties of endochronic theories based on considerations first presented in [1]. Some of the conclusions of the author's paper,[1] however, are incorrect and

[1] By B. J. Hsieh, and published in the December, 1980, issue of the ASME JOURNAL OF APPLIED MECHANICS, Vol. 47, pp. 748–754.

[2] Weidlinger Associates, Consulting Engineers, 110 East 59 St., New York, N. Y. 10022.

Downloaded 01 May 2010 to 171.66.16.249. Redistribution subject to ASME license or copyright; see http://www.asme.org/terms/Terms_Use.cfm

the stress and deformation histories to which the element has been subjected. Because of the incremental or flow-type nature of the plasticity law, strain *rate* appears in the constitutive relation. For application in stress and deformation analysis, total strain rate, and stress and stress rate are needed in the relation. Such a constitutive law is deduced from the kinematic relation expressing the total strain rate in terms of the elastic and plastic components, by substituting from the plasticity law and the time derivative of the usual elasticity law for the plastic and elastic strain rates, respectively. This yields a constitutive relation for the total strain rate in terms of the stress, stress rate, and variables expressing the history of deformation.

For the case when purely elastic deformation could occur in destressing to zero stress, the choice of destressing by pure deformation without rotation, expressed by the symmetric deformation gradient matrix $\mathbf{V}^e$, constitutes a correct definition of elastic deformation, although not the most general one since arbitrary rigid-body rotation of the unstressed state provides an alernative unstressed state. However, utilizing this particular choice of elastic deformation does permit convenient elimination of the elastic strain-rate term in the kinematic relation for total strain. Any rotation which might have been included in the elastic deformation is automatically embodied in the associated plastic deformation and is determined by the solution process to provide whatever compatability is needed in the configuration of the body on the general deformation path. Thus a correct, but not the most general, definition of elastic and plastic deformation is achieved.

In order to investigate objectivity of the resulting constitutive equation (to be used in stress and deformation analysis) which contains stress-rate and total strain-rate variables, we need only consider superposed arbitrary rigid rotation on the current state of the body on the general deformation path. This is done in the paper under discussion and the constitutive relation is found to be objective.

Since this applies for any general deformation history, we can choose the deformation path to follow pure elastic destressing with or without rotation from the considered state on the general deformation path, and this establishes objectivity of the unstressed state for rotations independent of that utilized in the objectivity check carried for the body on the general deformation path prior to destressing. Thus we established the full invariance requirement stressed by the discussers on the basis of a simpler analytical development. We thus assert that the statement that we "demand that only partial invariance requirements be satisfied" is incorrect. The fact that it is necessary to employ the constitutive relation containing only the current rate of total strain to substitute into the usual variational principle for determination of the velocity field eliminates the need to simultaneously include the plastic deformation gradient in establishing objectivity for any state. Although the subject paper considers only isotropic elastic and plastic laws, the approach explained in this Closure can be utilized for anisotropic laws by taking into account rotation of the anisotropic characteristics with the deformation of the unstressed state.

Professors Casey and Naghdi maintain that even when the intermediate (unstressed) configuration is not occupied in a given motion, the transformation law involving simultaneous independent rotations of the intermediate and final states must be included in the analysis. In this connection it is interesting to consider the analogous problem of the evaluation of thermal stresses. The theory can be formulated by considering an intermediate state in which the temperature variation occurs, and hence thermal expansion, but the condition of zero stress is maintained. This configuration would comprise an incompatible state of strain and hence a discontinuous map. Superimposing the thermal stresses then produces a compatible final configuration which can be expressed by a differentiable mapping from the initial undisturbed state at uniform temperature. The geometrical characteristics of the intermediate state have much in common with those of the unstressed state in elastic-plastic theory, yet to our knowledge the alleged difficulties often ascribed to the intermediate unstressed state in elastic-plastic theory have never been mentioned in the thermal stress case. Nor have we heard of prescribing an involved objectivity principle including independent rotations of the thermally expanded configuration and the final thermally stressed configuration. We are not surprised by this omission since it seems natural to us that since the purely thermally expanded configuration does not appear in the final thermoelastic constitutive relation, no advantage would accrue to offset the additional mathematical complexity of including independent rotation of the thermally expanded intermediate state.

We take this opportunity to mention that typographical errors appeared in equations (22), (40), and (61) of the subject paper and they have been corrected in an Erratum which appeared in the September, 1981, issue of the ASME JOURNAL OF APPLIED MECHANICS.

Basic Transport Equations in Ascending Equiangular Spiral Polar Coordinates[1]

C.-Y. Wang.[2] In this paper,[1] Dr. Ali stated that the torous seems to be the only curved tube which has been analyzed. This is not true. Sinusoidal, once-curved and twice-curved planar tubes (center line lies in a plane) have been studied by Murata, Miyake, and Inaba [1]. Helical tubes were recently investigated by Wang [2].

As soon as the Christoffel symbols for a curvilinear system are obtained, it is fairly easy to produce the field equations through tensors. Murata, et al. [1], developed the coordinate system for the general planar curved tube which would include Ali's work as a special case. The planar coordinates are always orthogonal. Wang [3] developed the coordinate system for the general nonplanar curved tube (arbitrary spatial curvature of the center line) which includes both the helical coordinates and Murata's coordinates as special cases.

It is uncertain that the ascending equiangular spiral polar coordinates are suitable for analytical and numerical work as claimed. This kind of geometry does not lead to an asymptotic state and conditions at both ends highly affect the field properties. Both analytical or numerical attempts would be very difficult.

References

1 Murata, S., Miyake, Y., and Inaba, T., "Laminar Flow in a Curved Pipe With Varying Curvature," *Journal of Fluid Mechanics*, Vol. 73, 1976, pp. 735–752.

2 Wang, C.-Y., "The Helical Coordinate System and the Temperature Distribution Inside a Helical Coil," ASME JOURNAL OF APPLIED MECHANICS, Vol. 47, 1980, pp. 951–953.

3 Wang, C.-Y., "On the Low Reynolds Number Flow in a Helical Pipe," *Journal of Fluid Mechanics*, Vol. 108, 1981, pp. 185–194.

[1] By S. Ali, and published in the March, 1981, issue of the ASME JOURNAL OF APPLIED MECHANICS, Vol. 48, pp. 190–192.

[2] Professor, Department of Mathematics, Michigan State University, East Lansing, Mich. 48824.

On the Uniqueness and Stability of Endochronic Theory[1]

I. S. Sandler.[2] In the paper,[1] the author presents several conclusions with respect to the uniqueness and stability properties of endochronic theories based on considerations first presented in [1]. Some of the conclusions of the author's paper,[1] however, are incorrect and

[1] By B. J. Hsieh, and published in the December, 1980, issue of the ASME JOURNAL OF APPLIED MECHANICS, Vol. 47, pp. 748–754.

[2] Weidlinger Associates, Consulting Engineers, 110 East 59 St., New York, N. Y. 10022.

Copyright © 1981 by ASME
Downloaded 01 May 2010 to 171.66.16.249. Redistribution subject to ASME license or copyright; see http://www.asme.org/terms/Terms_Use.cfm

Journal of Applied Mechanics

Book Reviews

The Symmetric Eigenvalue Problem. By Beresford N. Partlett. Prentice-Hall, Englewood Cliffs, N.J. 07632. 1980. Pages xix–348. Price $25.

REVIEWED BY S. H. CRANDALL[1]

Eigenvalue problems are ubiquitous in engineering analysis. A generation ago the same engineer would formulate the physical problem, set up the associated eigenvalue problem, obtain a partial solution graphically or numerically, and interpret the result in terms of the physical system. Today thanks mostly to the great development of computers there is a considerable division of labor involved in accomplishing similar but more extensive goals. A numerical analyst designs an algorithm, a software specialist then creates a program which is eventually made accessible to the engineer with the eigenvalue problem. The present book is directed narrowly toward the numerical analysis underlying algorithms for the symmetric matrix eigenvalue problem. Only passing allusions are made to the physical problems from which eigenvalue problems arise or to the software developments which are required to implement the algorithms. The main feature of the book is the lucid description of the developments in numerical analysis of eigenvalue problems which have occurred during the past thirty years. These topics include triangular factorization, reduction to tridiagonal form, Jacobi rotations, QL and QR algorithms, Lanczos algorithms, Rayleigh quotient iteration, and subspace iteration. Matrices are called small if they can be stored and worked on entirely in the high-speed memory. It is claimed that the understanding of the methods for small matrices is now essentially complete. The problem for tomorrow is to reach a similar plateau for cost-effective methods applicable to very large matrices. Each chapter contains exercises for the reader. Material in the first nine chapters has been used in a senior level course in numerical analysis while later material has been used in a graduate seminar. The first 14 chapters deal with the problem $Ax = \lambda x$ for a single real symmetric matrix A while the final chapter extends most of the results to the generalized problem $Ax = \lambda Mx$ for two symmetric matrices A and M. Within the limits imposed the author has produced a carefully crafted exposition of the present state of understanding of algorithms for eigenvalue problems.

Nonlinear Oscillations. By Peter Hagedorn. Translated and edited from German to English by Wolfram Stadler. Oxford University Press, New York. 1981. Pages x–289. Price $85.

REVIEWED BY C. S. HSU[2]

It is a pleasure to call the reader's attention to the appearance of an English version of Professor Hagedorn's book on nonlinear oscillations. While there are several outstanding introductory mathematical books on nonlinear ordinary differential equations available, there is a dearth of modern textbooks which introduce the theory of nonlinear oscillations from the point of view of mechanics. In this respect this book fulfills a need and is a most welcome addition to the literature. The adoption of the book for classroom use may, however, be hindered by the cost factor.

For a review of the technical contents of the book the reader is referred to a review prepared by Professor Rosenberg and published in the March, 1979, issue of this JOURNAL, Vol. 46, p. 238.

Turbulence in the Free Atmosphere. By N. K. Vinnichenko, N. Z. Pinus, S. M. Shmeter, and G. N. Shur, (F. L. Sinclair, Trans.) Second Edition. Plenum Publishing Corp., New York. Pages xiii–310. Price $49.50.

REVIEWED BY J. L. LUMLEY[3]

This book, like the first edition published in 1968 in the USSR and in 1973 in the USA, is devoted mainly to the results of experimental, rather than theoretical, investigations of atmospheric turbulence affecting the flight of aircraft. The book does not deal with the microscale turbulence that affects the propagation of radio waves, light and sound in the atmosphere. The authors constitute the staff responsible for work of this nature at the Central Aerological Observatory at Dolgoprudnyi, the leading such group in the USSR.

The revised and enlarged second edition greatly expands on the original coverage of methods and apparatus for measurements of fluctuations of velocity and temperature, and has been updated to include the results of new experimental investigations of turbulence in clouds and in the tropopause. In particular, the section devoted to radar and laser methods has been enlarged, and an aircraft instrument for measurement of temperature fluctuations is described. Chapters 6–8 dealing with atmospheric convection, thermal turbulence, turbulence in clouds, and wave/turbulence interaction, have been radically revised and enlarged, bringing in much new experimental data, and reflecting the increase in understanding of the mechanisms responsible that has taken place in the time since publication of the first edition.

Injection and Mixing in Turbulent Flow. By J. A. Schetz. M. Summerfield, editor. Progress in Astronautics and Aeronautics, AIAA. New York. Vol. 68. Pages xvii–200. Price $17; Member, $27 List.

REVIEWED BY J. L. LUMLEY[3]

This useful book collects in one place a great deal of data on jets with/without coflowing streams, axial pressure gradients, net mo-

---

[1] Ford Professor of Engineering, Massachusetts Institute of Technology, Cambridge, Mass. 02139.

[2] Professor of Applied Mechanics, Department of Mechanical Engineering, University of California, Berkeley, Calif. 49720.

[3] Willis H. Carrier Professor of Engineering, Sibley School of Mechanical and Aerospace Engineering, Cornell University, Ithaca, New York 14853.

 Copyright © 1981 by ASME

Downloaded 01 May 2010 to 171.66.16.249. Redistribution subject to ASME license or copyright; see http://www.asme.org/terms/Terms_Use.cfm